

# Flexible formwork for concrete structures

John Joseph Orr

A thesis submitted for the Degree of Doctor of Philosophy

University of Bath

Department of Architecture and Civil Engineering

October 2012

## **COPYRIGHT**

Attention is drawn to the fact that copyright of this thesis rests with the author. A copy of this thesis has been supplied on condition that anyone who consults it is understood to recognise that its copyright rests with the author and that they must not copy it or use material from it except as permitted by law or with the consent of the author.

## **RESTRICTIONS ON USE**

This thesis may be made available for consultation within the University Library and may be photocopied or lent to other libraries for the purposes of consultation.





Every day you may make progress. Every step may be fruitful. Yet there will stretch out before you an ever-lengthening, ever-ascending, ever-improving path. You know you will never get to the end of the journey. But this, so far from discouraging, only adds to the joy and glory of the climb.

*Sir Winston Churchill*



# Abstract

Concrete, our most widely used construction material, is a fluid that offers the opportunity to economically create structures of almost any geometry. Yet this unique fluidity is seldom capitalised on, with concrete instead being cast into rigid prismatic moulds to create high material use structures with large carbon footprints. Our rate of concrete consumption means that cement manufacture alone is estimated to account for some 5% of global Carbon Dioxide emissions.

This dissertation shows that by replacing conventional orthogonal moulds with a flexible system comprised primarily of high strength, low cost fabric sheets, the fluidity of concrete can be utilised to create structurally optimised concrete structures. Flexible formwork therefore has the potential to facilitate the change in design and construction philosophy that will be required for a move towards a less material intensive, more sustainable, construction industry.

Optimisation and design processes developed in this thesis show that material savings of up to 40% are possible in flexibly formed concrete beams. Full scale structural testing of these processes is undertaken to verify the flexural and shear behaviours of non-prismatic elements. This is supported by further experimental and theoretical investigations into the durability of concrete cast in a permeable, flexible mould. Detailed analysis is provided alongside practical guidance for designers. Coupled with innovation in design and analysis techniques, flexible formwork is shown to provide a globally accessible method for the construction of low carbon, materially efficient and architecturally interesting concrete structures.

Recognising the impact construction has on the environment, design philosophies centred around the need to put material where it is required are becoming increasingly desirable. This can now be achieved by replacing rigid formworks with systems comprised of flexible sheets of fabric. This is a step change in the way we think about our new concrete structures.

# Declaration

The author wishes to declare that, except for commonly understood and accepted ideas, or where specific reference is made to the works of others, the content of this dissertation is his own work. This dissertation has not been submitted previously to any University or institution for any degree, diploma, or other qualification. The full length of this dissertation is 544 pages.

## Image credits

The images and figures in this thesis are the property of the author. Any images and figures in this thesis that have been used with permission are noted and the appropriate credit is given in the text or figure caption. In addition, the following images are used with permission:

Page xxxvi	'STS-135 Launch Countdown'. Bill Ingalls/NASA (2011). Available from <a href="http://tinyurl.com/c67htat">http://tinyurl.com/c67htat</a>
Page 464	'A New View of the Tarantula Nebula, PIA14415' X-ray: NASA/CXC/PSU/L.Townsley <i>et al.</i> ; Optical: NASA/STScI; Infrared: NASA/JPL/PSU/L.Townsley <i>et al.</i> Available from <a href="http://tinyurl.com/bqn39h8">http://tinyurl.com/bqn39h8</a>
Page 478	'The Water Planet'. NASA/Robert Simmon and Marit Jentoft-Nilsen (2010). Available from <a href="http://tinyurl.com/cajxyzz">http://tinyurl.com/cajxyzz</a>

# Acknowledgements

Thanks are due to Dr Antony Darby, Professor Tim Ibell and Dr Mark Evernden for their supervision and support of this thesis, to Dr Chris Williams and Dr Michael Patterson for their help with all things computational, and to Professor Mark West and Mr Ronnie Araya for providing me with the initial inspiration that led to the completion of this work.

Grateful thanks are extended to all at Atkins and the Engineering and Physical Sciences Research Council (EPSRC) for their generous sponsorship of this research as part of an Industrial Collaborative Award in Science and Engineering (CASE).

I am indebted to Professor Mike Otlet and Mr Dominic Pask for the invaluable advice and guidance they have given me throughout this research. Additional thanks are due to the entire team at Atkins, Oxford, for allowing me to participate in so many exciting projects.

The experimental work described in this thesis would not have been possible without the support, guidance and practical assistance provided by Brian Purnell, Will Bazeley, Sophie Hayward, Neil Price and Graham Mott in the Department of Architecture and Civil Engineering and Ursula Potter and John Mitchels in the Microscopy and Analysis Suite.

And finally, to Graham, Alison, Trevor, Rachel and Sarah - for supporting me throughout this journey, thank you.



# Table of contents

<b>Abstract</b>	<b>i</b>
<b>Declaration</b>	<b>ii</b>
<b>Acknowledgements</b>	<b>iii</b>
<b>List of figures</b>	<b>xi</b>
<b>List of tables</b>	<b>xxxi</b>
<b>Chapter 1    Introduction</b>	<b>1</b>
1.1. Introduction . . . . .	1
1.2. Fabric formwork . . . . .	3
1.3. Problem . . . . .	5
1.4. Aims . . . . .	5
1.5. Objectives . . . . .	7
1.6. Approach . . . . .	7
1.7. Funding and supervisory board . . . . .	7
1.8. Principal publications . . . . .	8
<b>Chapter 2    Fabric formwork</b>	<b>11</b>
<i>Literature review</i>	
2.1. Introduction . . . . .	11
2.2. Fabric formwork . . . . .	11
2.3. Construction methods . . . . .	17
2.4. Design . . . . .	22
2.5. Structural testing . . . . .	27
2.6. Permeable formwork . . . . .	35
2.7. Impacts . . . . .	41
2.8. Summary . . . . .	45
2.9. Goals . . . . .	46

<b>Chapter 3</b>	<b>Material behaviour</b>	<b>49</b>
	<i>Literature review</i>	
3.1. Introduction . . . . .		49
3.2. Concrete . . . . .		49
3.3. Fabric . . . . .		60
3.4. Reinforcement . . . . .		68
3.5. Conclusions. . . . .		80
<b>Chapter 4</b>	<b>Concrete behaviour</b>	<b>83</b>
	<i>Literature review</i>	
4.1. Introduction . . . . .		83
4.2. Prismatic beams . . . . .		83
4.3. Non-prismatic reinforced concrete beams. . . . .		95
4.4. Summary . . . . .		112
<b>Chapter 5</b>	<b>Design (1)</b>	<b>115</b>
	<i>Flexural behaviour</i>	
5.1. Introduction . . . . .		115
5.2. Approach . . . . .		115
5.3. Initial designs . . . . .		120
5.4. Testing matrix . . . . .		122
5.5. Detailed Design 1 - T-Beams. . . . .		124
5.6. Detailed Design 2 - Double T-Beam . . . . .		136
5.7. Detailed design 3 - Ultra-high Performance Fibre Reinforced Concrete . . . . .		145
5.8. Construction methods . . . . .		153
5.9. Conclusions. . . . .		154
<b>Chapter 6</b>	<b>Development (1)</b>	<b>157</b>
	<i>Flexural behaviour</i>	
6.1. Introduction . . . . .		157
6.2. Pull out tests . . . . .		159
6.3. Splayed bar beam tests . . . . .		172
6.4. Centre for Architectural Structures and Technology, Canada . . . . .		177
6.5. T Beams. . . . .		182
6.6. Double T Beams . . . . .		195
6.7. Ultra high performance fibre reinforced concrete fabric formed beams . . . . .		206
6.8. Material use . . . . .		215
6.9. Conclusions. . . . .		215



<b>Chapter 7</b>	<b>Design (2)</b>	<b>217</b>
	<i>Shear behaviour</i>	
7.1.	Introduction . . . . .	.217
7.2.	Detailed Design 4 - Variable section members in shear . . . . .	.218
7.3.	Conclusions. . . . .	.242
<b>Chapter 8</b>	<b>Development (2)</b>	<b>245</b>
	<i>Shear behaviour</i>	
8.1.	Introduction . . . . .	.245
8.2.	Three-metre span beams. . . . .	.246
8.3.	Tapered beams in shear . . . . .	.260
8.4.	Strut and tie model . . . . .	.284
8.5.	Analysis . . . . .	.301
8.6.	Flexible shear reinforcement . . . . .	.330
8.7.	Conclusions. . . . .	.340
<b>Chapter 9</b>	<b>Development (3)</b>	<b>343</b>
	<i>Durability enhancement</i>	
9.1.	Introduction . . . . .	.343
9.2.	Test Group 1 - Carbonation . . . . .	.344
9.3.	Test Group 2 - Chloride ingress . . . . .	.350
9.4.	Test Group 3 - Sorptivity . . . . .	.364
9.5.	Test Group 4 - Microscopy . . . . .	.373
9.6.	Test Group 5 - Surface hardness . . . . .	.390
9.7.	Discussion . . . . .	.399
9.8.	Conclusions. . . . .	.405
<b>Chapter 10</b>	<b>Analysis</b>	<b>409</b>
	<i>Fabric formed beams</i>	
10.1.	Introduction . . . . .	.409
10.2.	Load deflection predictions. . . . .	.409
10.3.	Deflection limits . . . . .	.421
10.4.	Modelling techniques . . . . .	.424
10.5.	Parametric studies . . . . .	.427
10.6.	Material use . . . . .	.433
10.7.	Conclusions . . . . .	.441

<b>Chapter 11</b>	<b>Design guide</b>	<b>443</b>
	<i>Steel reinforced fabric formed beams</i>	
11.1.	Introduction . . . . .	.443
11.2.	Symbols . . . . .	.443
11.3.	Process flow chart . . . . .	.445
11.4.	Sample beam design . . . . .	.447
11.5.	Profile Predictions . . . . .	.456
11.6.	Load Deflection Predictions. . . . .	.456
11.7.	Construction . . . . .	.457
11.8.	Detailing considerations. . . . .	.460
11.9.	Conclusions . . . . .	.463
<b>Chapter 12</b>	<b>Future work</b>	<b>465</b>
	<i>Proposals</i>	
12.1.	Introduction . . . . .	.465
12.2.	Optimised construction . . . . .	.465
12.3.	Construction processes. . . . .	.473
12.4.	Computational methods. . . . .	.474
12.5.	Shear behaviour . . . . .	.475
12.6.	Durability investigations . . . . .	.475
12.7.	Fire . . . . .	.476
12.8.	Conclusions . . . . .	.477
<b>Chapter 13</b>	<b>Conclusions</b>	<b>479</b>
	<i>Flexibly formed concrete structures</i>	
13.1.	Introduction . . . . .	.479
13.2.	Structural behaviour . . . . .	.480
13.3.	Durability . . . . .	.482
13.4.	Analysis . . . . .	.483
13.5.	Conclusion. . . . .	.484
<b>References</b>		<b>487</b>

[blank page]

[blank page]

# List of figures

<b>Chapter 1</b>	<b>Introduction</b>	<b>1</b>
Figure 1.1:	Left: World material expenditure in 2008 (material and price data after USGS (2011) and intended as an illustration only. Global GDP estimate courtesy the World Bank (2011). Right: Embodied energy of building materials (after Hammond and Jones, 2008)..	2
Figure 1.2:	Historical UK emissions to 2009 and reduction targets for the period to 2050 (DECC, 2011).	2
Figure 1.3:	The influence of the built environment on carbon emissions in 2008 (after BIS, 2010).	2
Figure 1.4:	Changes in energy use (estimated values, after Cole and Kernan (1996); Sturgis and Roberts (2010) and Lane (2007).	2
Figure 1.5:	Material savings achieved using fabric formwork..	4
Figure 1.6:	Casting concrete in fabric (left); Conventional and fabric cast surface finishes (centre); architectural uses (images courtesy Anne-Mette Manelius) (right).	4
Figure 1.7:	Process map.	6
Figure 1.8:	Road map.	6
<b>Chapter 2</b>	<b>Fabric formwork</b>	<b>11</b>
	<i>Literature review</i>	
Figure 2.1:	Lilienthal floor slab (Lilienthal, 1899).	12
Figure 2.2:	Patents by Waller (1934).	12
Figure 2.3:	Ctesiphon construction and example (images Courtesy of the Irish Architectural Archive (93/67 Waller Album) and Conlon (2011)).	12
Figure 2.4:	The work of Miguel Fisac: top, left to right: IBM offices Madrid, (image courtesy flickr: Una Ballena de seis ojos [cinemascope]), House in Almagro, Santa Ana Fisac - covered porch (images used under creative commons license). Bottom, l-r: MUPAG, and Editorial DÓLAR (both Madrid) (images courtesy Miguel Fisac Foundation, provided by <a href="http://tinyurl.com/yhabbyt">http://tinyurl.com/yhabbyt</a> ).	13
Figure 2.5:	'P-Wall' cast using fabric formwork (image courtesy P_Wall(2009) by Matsys / Andrew Kudless).	13
Figure 2.6:	Kenzo Unno.(l-r): Filter point walling, architectural use and frame restraint system (images courtesy Kenzo Unno and Mark West).	14
Figure 2.7:	Zero waste formwork (l); Fab-form products (r).	14
Figure 2.8:	Columns made at CAST (images courtesy CAST).	15
Figure 2.9:	Precast panels (images courtesy CAST).	15
Figure 2.10:	Beams (CAST, l and c) and Garbett (2008) (r).	15
Figure 2.11:	Trusses (images courtesy CAST).	15
Figure 2.12:	Shells (images courtesy CAST).	15

Figure 2.13: Apprentice sewing one half of an underwater bag (l); Indicative folded and expanded dimensions (r). . . . .	16
Figure 2.14: Spline mould construction method. . . . .	18
Figure 2.15: Keel mould construction method. . . . .	18
Figure 2.16: Pinch mould method. . . . .	18
Figure 2.17: Forming tables (after Bailiss, 2006 and Garbett, 2008). . . . .	19
Figure 2.18: Variable section beam formwork (after Garbett, 2008).. . . . .	19
Figure 2.19: Wall panels. Steel frame (l) and vertical sheets (r) (West, 2007). . . . .	20
Figure 2.20: The construction of 'Y' shaped columns.. . . .	20
Figure 2.21: Achieving a variable column geometry - examples courtesy CAST. . . . .	20
Figure 2.22: Fabric formwork groupings (after West et al., 2007). . . . .	21
Figure 2.23: Sectional analysis for a frame. . . . .	23
Figure 2.24: Jourawski's method for shear stress. . . . .	24
Figure 2.25: Shear distribution in a simple cracked section. . . . .	24
Figure 2.26: Sectional analysis technique for fabric formed elements (after Garbett, 2008). . . . .	25
Figure 2.27: BS8110 analysis, required depth based on equations for moment and shear capacity. . . . .	25
Figure 2.28: Summary of elements tested and material savings.. . . .	26
Figure 2.29: Prismatic (l) and Curved (r) beams (Hashemian, 2012). . . . .	28
Figure 2.30: Construction method (l); End plate detail (r). (Hashemian, 2012). . . . .	28
Figure 2.31: Failure, orthogonal beams with linear reinforcement (B1). (Hashemian, 2012). . . . .	28
Figure 2.32: Failure, orthogonal beams with curved reinforcement (B2). (Hashemian, 2012). . . . .	28
Figure 2.33: Failure, variable section beams (B3). (Hashemian, 2012).. . . . .	28
Figure 2.34: Load deflection response for a selection of beams tested (courtesy Hashemian, F). . . . .	29
Figure 2.35: End beam tests summary (after Hashemian, 2012). . . . .	29
Figure 2.36: Curved Cambered Beam tests - summary (after Hashemian, 2012). . . . .	30
Figure 2.37: Type A (l); Type B (r) (after Lee, 2010).. . . . .	31
Figure 2.38: Anchorage method (l); Maximum capacity results of tests undertaken (r) (Lee, pers. comm., 9th April 2010). . . . .	31
Figure 2.39: Beam profiles. Top (l-r) Bailiss (2006): Beams 1 & 2; 3; 4. Bottom (l-r) Garbett (2008): Beam 1; 2. . . . .	33
Figure 2.40: Test photographs (Garbett, 2008). Beam 1 (l) and Beam 2 (r). . . . .	33
Figure 2.41: Conventional (l) and permeable-mould cast concrete (r). . . . .	35
Figure 2.42: Essential components of a CPF system. . . . .	35
Figure 2.43: Variation in w/c ratio when concrete is cast in permeable moulds (after Price, 2000). . . . .	36
Figure 2.44: Durability of concrete structures - environmental penetration (after Price, 2000). . . . .	38
Figure 2.45: Test results. Left - right: Ghaib (2001); Abdelgadar (2009); small samples tested by Delijani (2010). . . . .	40
Figure 2.46: Embodied carbon reductions, and the role of fabric formwork. . . . .	42
Figure 2.47: Historical variations in construction industry wages and labour and material costs (data after LABORSTA, 2010; USGS, 2008). Values adjusted to 1998. . . . .	43

**Chapter 3 Material behaviour****49***Literature review*

Figure 3.1: Stress strain for uniaxial compression (l); Typical model for codified design (r) (after BS EN 1992-1-1 (2004)). . . . .	50
Figure 3.2: Uniaxial test data showing actual post peak behaviour (Kotsovos, 2007). . . . .	51
Figure 3.3: Triaxial stress strain plot (Kotsovos and Pavlovic, 1999). . . . .	51
Figure 3.4: General behaviour of fibre reinforced concrete (after Zia et al., 1994). . . . .	53
Figure 3.5: Compression tests at different time intervals for steam treated and untreated Ductal® samples (Graybeal, 2006a). . . . .	55
Figure 3.6: Short and long term shrinkage (l); Creep (r); both after Graybeal (2006a). . . . .	56
Figure 3.7: Flexural test. (l-r) Midspan deflection, Failure, Fibre detail (Graybeal, 2006b). . . . .	57
Figure 3.8: Shear failure in prestressed Ductal® cast I-beam. . . . .	57
Figure 3.9: Uni-axial stress strain model for Ductal® (after Graybeal, 2006b). . . . .	58
Figure 3.10: Fourth order bezier curve (l); Modelling the keel mould (r) (After Veenendaal, 2008). . . . .	62
Figure 3.11: Calculating concrete loads in a fabric formed structure (illustration after Veenendaal, 2008). . . . .	63
Figure 3.12: Hanging mould (l); Buckled column (c); Coordinates system for fabric curvature (r). . . . .	64
Figure 3.13: Hydrostatic shape plots during filling (l); Plot of T-Beam bulb shape (r). . . . .	65
Figure 3.14: Equilibrium considerations (l); and cross section predictions (r) (after Iosilevski, 2010). . . . .	65
Figure 3.15: Empirical method (after Bailiss, 2006). . . . .	66
Figure 3.16: Anchorage comparison in non-orthogonal structures(l); Standard bar bend shapes (r). . . . .	69
Figure 3.17: Reinforcing fabric formed concrete beams. . . . .	69
Figure 3.18: Anchorage methods in steel reinforced fabric formed beams (after Garbett, 2008). . . . .	69
Figure 3.19: Stress strain behaviour of steel bars (BS EN 1992-1-1 (2004) model) and FRP bars. . . . .	71
Figure 3.20: BPE model – Steel (l); FRP (r) (after Cosenza et al., 1997). . . . .	74
Figure 3.21: Pull out test (l); Modified pull out test (r) (after Chung, 2000). . . . .	76
Figure 3.22: Beam test for pull out strength (after Makitani et al, 1993) (l); Refined testing procedure (after Perera et al., 2009) (r). . . . .	76
Figure 3.23: Splayed bars (l), Experimental set up for pull out tests (r). . . . .	77
Figure 3.24: Non helically reinforced (l) and helically reinforced around splayed bar (r). . . . .	77
Figure 3.25: Cube test results for different splay lengths - without helix (Darby et al., 2007). . . . .	78
Figure 3.26: Cube test results for different splay lengths - with helix (Darby et al., 2007). . . . .	78
Figure 3.27: Participating fabric formwork - possible arrangements. . . . .	80

**Chapter 4 Concrete behaviour****83***Literature review*

Figure 4.1: Typical concrete stress-strain models (l) and sectional design method (r) (after BS EN 1992-1-1 (2004)). . . . .	84
Figure 4.2: Triaxial model for the compressive stress block (l); Radial stresses (r) (after Kotsovos and Pavlovic, 1999). . . . .	85
Figure 4.3: Six contributing factors for shear resistance (after Orr, 2009). . . . .	85

Figure 4.4: Biaxial tests on concrete. Strength plot (l); tension zone (r) (After Kupfer et al., 1969).	86
Figure 4.5: Dowel action. Beam behaviour with and without shear links (l); Longitudinal reinforcement slippage (r).	87
Figure 4.6: Size effects (l); Shear valley (r).	88
Figure 4.7: The truss analogy (l) and components of shear resistance (r) (after Orr, 2009).	88
Figure 4.8: Compressive force path (l); Detail at supports (c); Stresses on each concrete tooth (r) (after Kotsovos, 1988).	89
Figure 4.9: Load transfer at the supports.	90
Figure 4.10: Development of tensile forces in the compression path (after Kotsovos and Pavlovic (1999)).	90
Figure 4.11: Types of beam behaviour (after Kotsovos and Pavlovic (1999)).	90
Figure 4.12: Mohr's circle of strain (l) and Stress (r) for compression field theory (after Collins et al., 2008).	93
Figure 4.13: Haunched reinforced concrete sections (l-r: image credits 'ldawriter' at <a href="http://tinyurl.com/c3oqyzq">http://tinyurl.com/c3oqyzq</a> ; 'Tim k13' at Wikimedia Commons; 'seier+seier' at <a href="http://tinyurl.com/d577v4b">http://tinyurl.com/d577v4b</a> ).	95
Figure 4.14: Contributing factors to shear resistance in tapered and prismatic sections.	96
Figure 4.15: General behaviour of tapered beams with contribution from chords (after BS EN 1992-1-1 (2004)).	96
Figure 4.16: Additional tension force in the truss model (after Orr et al, 2011).	97
Figure 4.17: Typical simply supported haunched beams of increasing depth (l) and decreasing depth (r)	98
Figure 4.18: Tapered segments of continuous beams.	98
Figure 4.19: Vertical cut method (l) and Circular arc method for constant thickness wedge (r) (after Davies et al., 1973).	98
Figure 4.20: Simplified method for stress corrections (after Guyon, 1953)..	100
Figure 4.21: Specimen test variables (after Debaiky and El-Niema, 1982)..	102
Figure 4.22: Test results for negative and positive haunch beams (Debaiky and El-Niema, 1982)..	102
Figure 4.23: Equilibrium of haunched sections (after Debaiky and El-Niema, 1982).	103
Figure 4.24: T-Beam specimen test variables (El-Niema, 1988).	104
Figure 4.25: Results of 'T' beam tests by El-Niema (1988).	104
Figure 4.26: Comparison of Eq. 4.26 with test data.	104
Figure 4.27: Test summary (l); Critical section definition (r) (after MacLeod and Houmsi, 1994).	105
Figure 4.28: Load-displacement for haunched beams (l) and compression paths in prismatic and haunched sections (after MacLeod and Houmsi, 1994).	106
Figure 4.29: Test layouts by Rombach and Nghiep (2011).	107
Figure 4.30: Test data for elements showing shear failures and their crack patterns (Rombach and Nghiep, 2011).	108
Figure 4.31: Test data for haunched elements (after Rombach and Nghiep, 2011).	108
Figure 4.32: Variation of factors of safety against shear capacity with haunch angle to different design codes (after Rombach and Nghiep, 2011).	109
Figure 4.33: Behaviour of long and short tapered beams.	110

## Chapter 5    **Design (1)** *Flexural behaviour*

**115**

Figure 5.1: Augustine House (render by the author from the available drawings)..	116
--	-----



Figure 5.2: Carnival HQ (render by the author from the available drawings).	.117
Figure 5.3: Bending Moment Beam Design.	.120
Figure 5.4: Extended bending moment beam design.	.121
Figure 5.5: Portal frames using fabric formwork.	.121
Figure 5.6: T-Beam Design.	.121
Figure 5.7: 'T' beam element, and potential application to reinforced concrete frame construction.	.124
Figure 5.8: Use of precast beam elements.	.124
Figure 5.9: General arrangement for beam tests.	.124
Figure 5.10: Scaling test loads.	.126
Figure 5.11: Load cases for design (summary).	.126
Figure 5.12: T-Beam loading moment envelope.	.126
Figure 5.13: Four beams for testing.	.127
Figure 5.14: Flexural capacity at mid-span in as-built section, Load Case 2.	.128
Figure 5.15: Distribution of test loads (l); Vertical force and moment diagram comparison (r).	.128
Figure 5.16: Shear link design. Paperclip (l); Rectangle (r).	.129
Figure 5.17: Shear between web and flange (l); Shear between concrete casts (r) (after BS EN 1992-1-1 (2004)).	.129
Figure 5.18: Transverse reinforcement. Load case 1 (l) and Load case 2 (r).	.129
Figure 5.19: Recommended link spacing according to BS EN 1992-1-1 (2004).	.130
Figure 5.20: Design compromise for double cantilever fabric formed beams.	.132
Figure 5.21: Discrepancy in bar position, Load Case 1 and Load Case 2.	.132
Figure 5.22: The compression and tension force paths in a variable section fabric formed beam (illustrative).	.133
Figure 5.23: Tension path in the composite 'T' section (illustration).	.133
Figure 5.24: Forming a flat support.	.133
Figure 5.25: Section detail of support (l); Solution for multistorey construction (r).	.134
Figure 5.26: 'Pinch' in the T-beam designs.	.134
Figure 5.27: 'Pinch' beam design visualisation.	.135
Figure 5.28: Fabric formed double 'T' beam design.	.136
Figure 5.29: Loading envelope for 2m span double tee.	.137
Figure 5.30: Test arrangement.	.137
Figure 5.31: Reinforcement layout.	.137
Figure 5.32: The Double Keel Mould.	.137
Figure 5.33: Support detail.	.138
Figure 5.34: 4m span double T beams general arrangement.	.138
Figure 5.35: Moment and vertical force envelopes.	.139
Figure 5.36: Flexural design and beam profile.	.139
Figure 5.37: Double T Design, method 1.	.140
Figure 5.38: Moment-Shear interaction diagram as used in design method 1.	.140
Figure 5.39: Shear reduction due to the inclined bar.	.141
Figure 5.40: Double T Beam (6_4_1).	.141

Figure 5.41: Double T Beam (6_4_2).	.142
Figure 5.42: Prismatic section for material use comparison.	.142
Figure 5.43: Reinforcement summary, Beams 6_4_1 and 6_4_2.	.143
Figure 5.44: Beam dimensions in elevation.	.143
Figure 5.45: Construction details.	.144
Figure 5.46: Flexural design Model 1 for UHPFRC Beams 7_1, 7_2 and 7_3.	.145
Figure 5.47: Flexural design model 2 for UHPFRC beams.	.146
Figure 5.48: Sample cross section (l); Moment-Curvature analysis (r).	.146
Figure 5.49: Sectional diagrams at salient points shown in Figure 5.48.	.146
Figure 5.50: Load cases for design (summary).	.147
Figure 5.51: Scaling loads - Load case 1	.148
Figure 5.52: Scaling loads - Load case 2.	.148
Figure 5.53: T-Beam loading moment envelope.	.148
Figure 5.54: Test set up and test loads.	.149
Figure 5.55: UHPC Beam elevation and dimensions.	.149
Figure 5.56: Proposed design rendering, Beam 7_1, 7_2 and 7_3.	.150
Figure 5.57: Beam sections showing rib and double keel construction.	.150
Figure 5.58: Load envelope, Beams 7_4 and 7_5.	.151
Figure 5.59: Test loads, Beams 7_4 and 7_5.	.151
Figure 5.60: Beam 7_4 elevation, determined for flexure.	.151
Figure 5.61: Shear capacity of UHPFRC beam.	.152
Figure 5.62: Double T table formwork.	.152
Figure 5.63: Keel mould construction and prototype elements.	.153
Figure 5.64: Double bending moment shaped beam.	.153
Figure 5.65: Double keel method	.154
Figure 5.66: Double keel 'T Beam'.	.154

## Chapter 6 Development (1)

157

### *Flexural behaviour*

Figure 6.1: Summary of all structural testing undertaken and published results.	.158
Figure 6.2: Helix construction (l); Examples of helix construction (r).	.160
Figure 6.3: Test set up and variables.	.161
Figure 6.4: Test rig design (after Perera, 2009).	.162
Figure 6.5: Specimen construction process.	.162
Figure 6.6: Demoulded sections.	.162
Figure 6.7: Typical specimen failure mode (l) and crack pattern (r).	.164
Figure 6.8: Construction photos.	.164
Figure 6.9: Test details overview: Rectangular section (l); Tapered section (r).	.165
Figure 6.10: Strain gauge locations in Series 2 tests.	.165
Figure 6.11: Load-displacement plots for tests 2_1_0_0:0 to 2_6_2_90:30.	.166
Figure 6.12: Strain distribution for increasing load (Test 2_5_2_0:0).	.167

Figure 6.13: Strain gauges (Test 2_5_2_0:0).	.167
Figure 6.14: Splayed bar behaviour in Specimen 2_2_2_0:0.	.168
Figure 6.15: Closure of splay during pull out (l); Shape recovery of bar when removed from section (r).	.168
Figure 6.16: Idealised splayed bar behaviour during pull out.	.168
Figure 6.17: Fin-splay design details.	.169
Figure 6.18: Fin splay photographs.	.169
Figure 6.19: Catastrophic rupture of the CFRP bar (l-r).	.170
Figure 6.20: Test results (2A_1_2_90:30). Load-displacement (l); Bar strains (r).	.170
Figure 6.21: Loading envelope (l) and Splay dimensions (r).	.172
Figure 6.22: Beam 3_2 (l); Beam 3_3 (r).	.173
Figure 6.23: Construction method.	.173
Figure 6.24: Test photographs. Beam 3_2 (l); Beam 3_3 (r).	.174
Figure 6.25: CFRP Bar Rupture.	.174
Figure 6.26: Load-displacement response for Beam 3_2 and Beam 3_3.	.174
Figure 6.27: Beam 1. Construction method (top) and resulting beam.	.177
Figure 6.28: Double keel construction.	.178
Figure 6.29: Beam 2.	.178
Figure 6.30: Beam 3.	.178
Figure 6.31: Beam 4. Design (l); Construction failure (r).	.179
Figure 6.32: Beam 5. Formwork (l); Beam (r).	.179
Figure 6.33: Beam 6. Fabric stapled to mould (l); Beam cast (r).	.179
Figure 6.34: Beam 6.	.179
Figure 6.35: Beam 7.	.180
Figure 6.36: Beam 8 - design (l) and broken beam (r).	.180
Figure 6.37: Fabric formed beams and shell elements as a floor system.	.181
Figure 6.38: Keel dimensions.	.183
Figure 6.39: Beam 1 (all beams have the same top slab dimensions).	.183
Figure 6.40: Beam 2.	.184
Figure 6.41: Beam 3.	.184
Figure 6.42: Beam 4.	.184
Figure 6.43: Keel construction photos.	.184
Figure 6.44: Photo of the T Beam.	.184
Figure 6.45: Casting and demoulding 4m span T-beam.	.185
Figure 6.46: Test set up.	.186
Figure 6.47: Load-deflection plot for Load Case 2a.	.187
Figure 6.48: Load-deflection plot for Load Case 2b.	.187
Figure 6.49: Element 5_1_H_C before testing.	.188
Figure 6.50: Test photographs - 5_1_H_C.	.188
Figure 6.51: Strain gauge results, Beam 5_1_H_C.	.189
Figure 6.52: Beam 5_2_H_C crack distribution at failure.	.189

Figure 6.53: Strain gauge results, Beam 5_2_H_C. . . . .	.190
Figure 6.54: Beam 5_3_H_F test photographs and crack distribution at failure. . . . .	.191
Figure 6.55: Strain gauge results, Beam 5_3_H_F. . . . .	.191
Figure 6.56: Beam 5_4_H_F test photographs and crack patterns. . . . .	.192
Figure 6.57: Strain gauge results, Beam 5_4_H_F. . . . .	.192
Figure 6.58: Load capacity comparisons, load case 2. . . . .	.193
Figure 6.59: Construction photos, Beam 6_2_1. . . . .	.196
Figure 6.60: Testing arrangement, Beam 6_2_1. . . . .	.196
Figure 6.61: Load-deflection, Beam 6_2_1. . . . .	.196
Figure 6.62: Final failure mode, Beam 6_2_1. . . . .	.197
Figure 6.63: Cross section at 100mm from the supports (l); Predicted failure load using MCFT (r). . . . .	.197
Figure 6.64: Crack locations and reinforcement. . . . .	.197
Figure 6.65: Construction of Beam 6_4_1. . . . .	.198
Figure 6.66: Construction details - typical cross section through double T formwork. . . . .	.198
Figure 6.67: Casting and demoulding of Beam 6_4_1. . . . .	.199
Figure 6.68: Beam 6_4_1. . . . .	.199
Figure 6.69: Beam 6_4_1. . . . .	.199
Figure 6.70: Beam 6_4_2. . . . .	.199
Figure 6.71: Testing arrangement, for 6_4_1 and 6_4_2(i). . . . .	.200
Figure 6.72: Photos of seven point loading arrangement for 6_4_1 and 6_4_2(ii). . . . .	.201
Figure 6.73: Testing arrangement for Beam 6_4_2(ii). . . . .	.201
Figure 6.74: Cracking and failure mode for Beam 6_4_1. . . . .	.202
Figure 6.75: Load displacement - Beam 6_4_1 and 6_4_2(ii). . . . .	.202
Figure 6.76: Final failure mode for Beam 6_4_1. . . . .	.203
Figure 6.77: Cracking in Beam 6_4_2 at 60% of its design load. . . . .	.203
Figure 6.78: Beam 6_4_2(i) and 6_4_2(ii) test results comparison. . . . .	.204
Figure 6.79: Beam 6_4_2(ii) crack locations and failure mode. . . . .	.204
Figure 6.80: Final failure mode for Beam 6_4_2(ii). . . . .	.204
Figure 6.81: Formwork for UHPFRC beams 7_1 and 7_2. . . . .	.207
Figure 6.82: Pouring UHPFRC beam 7_1. . . . .	.207
Figure 6.83: Demoulded beam 7_1. . . . .	.207
Figure 6.84: Test set up, UHPFRC Beam 7_1. . . . .	.208
Figure 6.85: Crack distribution, Beam 7_1. . . . .	.208
Figure 6.86: Load - displacement response, UHPFRC Beam 7_1. . . . .	.209
Figure 6.87: Beam 7_3 construction (l) and test setup (r) photos for Beam 7_3. . . . .	.209
Figure 6.88: Test set up, Beam 7_3. . . . .	.210
Figure 6.89: Load-deflection, Beam 7_3. . . . .	.210
Figure 6.90: Failure mode and photographs - Beam 7_3. . . . .	.210
Figure 6.91: Construction sequence, Beam 7_4. . . . .	.211
Figure 6.92: Double T Beam cast using Ductal®. . . . .	.211

Figure 6.93: Testing arrangement, Beams 7_4 and 7_5. . . . .	.212
Figure 6.94: Test photographs, Beams 7_4 and 7_5. . . . .	.212
Figure 6.95: Load-midspan deflection, Beams 7_4 and 7_5.. . . .	.213
Figure 6.96: Cracking comparison. . . . .	.213
Figure 6.97: Failure location (l) and steel properties (r) in Beam 7_5 tested on coupon extracted from the failed beam at the quarter span. . . . .	.214
<b>Chapter 7      Design (2)</b>	<b>217</b>
<i>Shear behaviour</i>	
Figure 7.1: Summary of variable section members tested to assess shear capacity.. . . .	.218
Figure 7.2: Moment-shear interaction diagram. . . . .	.219
Figure 7.3: Failure modes in non-prismatic beams designed to the compressive force path method. . .	.221
Figure 7.4: The effect of adding vertical capacity. . . . .	.221
Figure 7.5: Design of variable section elements using the CFP method. . . . .	.222
Figure 7.6: Loading and moment envelope for Beam tests. . . . .	.223
Figure 7.7: Longitudinal steel profile, Beam 8_1. . . . .	.223
Figure 7.8: Moment shear interaction diagram, Beam 8_1. . . . .	.223
Figure 7.9: Moment shear interaction diagram, Beam 8_2. . . . .	.224
Figure 7.10: Beam 8_2 elevation and transverse steel requirements. . . . .	.224
Figure 7.11: Design basis, Beam 8_3i. . . . .	.225
Figure 7.12: Beam 8_3i. . . . .	.225
Figure 7.13: Beam 8_3ii. . . . .	.225
Figure 7.14: Test procedure and loading arrangement. . . . .	.228
Figure 7.15: Shear force diagrams and design point loads for each test. . . . .	.228
Figure 7.16: Reinforcement method showing anchorage and lap lengths.. . . .	.229
Figure 7.17: Design, Beam 9_1_CFP_V . . . . .	.230
Figure 7.18: Capacity envelope for Beam 9_1_CFP_V. . . . .	.230
Figure 7.19: Options for the reinforcement of Beam 9_1_CFP. . . . .	.230
Figure 7.20: Design method for BS EN 1992-1-1 (2004).. . . .	.231
Figure 7.21: Beam 9_1_EC2_V design. . . . .	.231
Figure 7.22: Test 9_2_CFP_V and 9_2_CFP_M. . . . .	.232
Figure 7.23: Beam 9_2_EC2_V and 9_2_EC2_M. . . . .	.233
Figure 7.24: Beam 9_3_CFP_V and 9_3_CFP_M. . . . .	.233
Figure 7.25: Beam 9_3_EC2_V and 9_3_EC2_M. . . . .	.233
Figure 7.26: Test 9_4_CFP_V and 9_4_CFP_M. . . . .	.234
Figure 7.27: Beam 9_4_EC2_V and 9_4_EC2_M. . . . .	.234
Figure 7.28: Comparison, Beams 9_1 to 9_4. . . . .	.235
Figure 7.29: Equivalent strut and tie model assumed for Eurocode 2 tapered model (l); potential for moment generation at the supports (r). . . . .	.236
Figure 7.30: Generic strut and tie model for a tapered section. . . . .	.236
Figure 7.31: Loading layout for Beam 9_2_STM. . . . .	.237

Figure 7.32: Strut definition (BS EN 1992-1-1 (2004), §6.5).	.238
Figure 7.33: Design model for Beam 9_2_STM.	.239
Figure 7.34: Force diagram for Beam 9_2_STM.	.240
Figure 7.35: Beam 9_2_STM.	.241
Figure 7.36: Support detail provided at one end of each STM beam.	.241
<b>Chapter 8      Development (2)</b>	<b>245</b>
<i>Shear behaviour</i>	
Figure 8.1: Beams 8_1 - 8_3 as tested.	.247
Figure 8.2: 3m span beam construction.	.248
Figure 8.3: Test set up.	.248
Figure 8.4: Load-midspan deflection summary.	.249
Figure 8.5: Crack propagation, Beam 8_1a.	.250
Figure 8.6: Transducer results for longitudinal steel in Beam 8_1a.	.250
Figure 8.7: Crack propagation, Beam 8_1b.	.250
Figure 8.8: Beam 8_1a (transducers placed at both ends of the Beam).	.251
Figure 8.9: Beam 8_1b failure, in sequence from (a) to (f) covering approximately 0.5 seconds. Explosive failure recorded at the pinned support, with considerable vertical displacement seen.	.251
Figure 8.10: Crack propagation, Beam 8_2a.	.252
Figure 8.11: Bar slip transducer results for Beam 8_2a.	.252
Figure 8.12: Crack propagation, Beam 8_2b.	.252
Figure 8.13: Beams 8_2a and 8_2b.	.252
Figure 8.14: Strain recorded in Beam 8_1b and Beam 8_2b.	.253
Figure 8.15: Crack propagation, Beam 8_3i.	.254
Figure 8.16: Crack propagation, Beam 8_3ii.	.254
Figure 8.17: Beam 8_3i (l) and 8_3ii (r) failure comparison.	.255
Figure 8.18: Beam 8_1b and 8_3(i) failure comparison.	.255
Figure 8.19: Tension forces in the end zone of Beam 8_3i.	.256
Figure 8.20: Proposed reinforcement layout for Beam 8_3i.	.256
Figure 8.21: Shear crack angles in 8_1b and 8_2a at 25kN load and Beam 8_3i at 21.5kN.	.257
Figure 8.22: Failure progression in Beam 8_3i showing development of flexure-shear failure cracks.	.257
Figure 8.23: Beams 9_1 to 9_4.	.261
Figure 8.24: Typical construction process.	.262
Figure 8.25: Typical test set up.	.262
Figure 8.26: Data collection for tapered beam tests.	.263
Figure 8.27: Crack patterns at failure for all EC2 and CFP beams tested.	.264
Figure 8.28: Load versus midspan deflection for Beams 9_1_EC2_V and 9_1_CFP.	.264
Figure 8.29: Beam 9_1_EC2_V Progression of cracking.	.265
Figure 8.30: Beam 9_1_EC2_V Failure.	.265
Figure 8.31: Beam 9_1_EC2_V strain gauge locations and readings.	.265
Figure 8.32: Cracking in Beam 9_1_CFP_V.	.266

Figure 8.33: Major cracking (l) and failure (r) of Beam 9_1_CFP_V. . . . .	.266
Figure 8.34: Beam 9_1_CFP_V strain gauge locations and readings. . . . .	.267
Figure 8.35: Bar arrangement and failure geometry. . . . .	.267
Figure 8.36: Load deflection plot for Beams 9_2_EC2(i) and 9_2_CFP(i). . . . .	.268
Figure 8.37: Crack progression and failure, Beam 9_2_EC2_M. . . . .	.268
Figure 8.38: Crack progression and failure, Beam 9_2_EC2_V(i). . . . .	.269
Figure 8.39: Bond failure in Beam 9_2_CFP (l) and crack pattern prior to failure (r). . . . .	.269
Figure 8.40: New test set up for Beam 9_2_CFP_M(i). . . . .	.269
Figure 8.41: Progression of cracking in Beam 9_2_CFP_M(i) and failure photographs. . . . .	.270
Figure 8.42: Setup and Progression of cracking in Beam 9_2_CFP_V(i). . . . .	.270
Figure 8.43: Beam 9_2_CFP_V(i) strain gauge locations and results. . . . .	.270
Figure 8.44: Reinforcement layouts and failure modes for Beams 9_2_CFP_V and 9_2_CFP_M. . . . .	.271
Figure 8.45: Load deflection plot - Beam 9_2_EC2(ii) and Beam 9_2_CFP(ii). . . . .	.271
Figure 8.46: Progression of cracking in Beam 9_2_EC2_V(ii). . . . .	.272
Figure 8.47: Cracking and failure in Beam 9_2_EC2_V(ii). . . . .	.272
Figure 8.48: Recorded strain variations, Beam 9_2_EC2_V(ii). . . . .	.272
Figure 8.49: Progression of cracking in Beam 9_2_EC2_M(ii). . . . .	.273
Figure 8.50: Cracking and failure in Beam 9_2_EC2_M(ii). . . . .	.273
Figure 8.51: Cracking and failure in Beam 9_2_CFP_M(ii). . . . .	.274
Figure 8.52: Photographs of displacement and failure mode in Beam 9_2_CFP_M(ii) (§8.3.7.3 on page 273). . . . .	.274
Figure 8.53: Cracking and failure in Beam 9_2_CFP_V(ii). . . . .	.275
Figure 8.54: Displacement photographs and failure in Beam 9_2_CFP_V(ii). . . . .	.275
Figure 8.55: Strain gauge location and results, Beam 9_2_CFP_V(ii). . . . .	.275
Figure 8.56: Load deflection plot for Beams 9_3. . . . .	.276
Figure 8.57: Crack location and progression in Beam 9_3_EC2_M. . . . .	.276
Figure 8.58: Cracking locations and failure mode (shown from two angles) for Beam 9_3_EC2_M. . . . .	.276
Figure 8.59: Crack locations and progression for Beam 9_3_EC2_V. . . . .	.277
Figure 8.60: Strain gauge locations and results, Beam 9_3_EC2_V. . . . .	.277
Figure 8.61: Crack distribution in Beam 9_3_CFP_M. . . . .	.278
Figure 8.62: Crack distribution and failure mode in Beam 9_3_CFP_V. . . . .	.278
Figure 8.63: Beam 9_3_CFP_V failure mode. . . . .	.278
Figure 8.64: Strain gauge locations and results, Beam 9_3_CFP_V. . . . .	.279
Figure 8.65: Load deflection plot for Beam 9_4_EC2 and Beam 9_4_CFP. . . . .	.279
Figure 8.66: Initial cracking (l) and failure mode (r) in Beam 9_4_EC2_M. . . . .	.279
Figure 8.67: Crack distribution in Beam 9_4_EC2_V. . . . .	.280
Figure 8.68: Failure at support location in beam 9_4_EC2_V. . . . .	.280
Figure 8.69: Horizontal displacement after failure of Beam 9_4_EC2_V. . . . .	.280
Figure 8.70: Strain gauge locations and results, Beam 9_4_EC2_V. . . . .	.281
Figure 8.71: Crack distribution, Beam 9_4_CFP_M. . . . .	.281



Figure 8.72: Crack propagation in Beam 9_4_CFP_V. . . . .	.282
Figure 8.73: Crack distribution and failure mode, Beam 9_4_CFP_V. . . . .	.282
Figure 8.74: Lateral motion of Beam 9_4_CFP_V at failure. . . . .	.282
Figure 8.75: Beam 9_2_STM layout. . . . .	.284
Figure 8.76: Construction of Beam 9_2_STM. . . . .	.285
Figure 8.77: Typical test set up, Beams 9_2_STM(i) and 9_2_STM(ii). . . . .	.285
Figure 8.78: Load versus deflection results for Beam 9_2_STM(i). . . . .	.286
Figure 8.79: Crack propagation in Beam 9_2_STM_1(i). . . . .	.286
Figure 8.80: Crushing in the top flange of Beam 9_2_STM_1(i). . . . .	.286
Figure 8.81: Bar strain, Beam 9_2_STM_1(i). . . . .	.287
Figure 8.82: Force comparison at the design load for Beam 9_2_STM_1(i). . . . .	.287
Figure 8.83: Behaviour analysis. . . . .	.287
Figure 8.84: Strut and tie model compared to recorded steel strains at peak load. . . . .	.288
Figure 8.85: Cracking in Beam 9_2_STM_2(i). . . . .	.288
Figure 8.86: Deformation and spalling in Beam 9_2_STM_2(i) beyond peak load. . . . .	.289
Figure 8.87: Force comparison at the design load for Beam 9_2_STM_2(i). . . . .	.290
Figure 8.88: Strut and tie model compared to recorded steel strains at peak load for Beam 9_2_STM_2(i). . . . .	.290
Figure 8.89: Strain gauge results for Beam 9_2_STM_2(i). . . . .	.290
Figure 8.90: Load versus deflection for Beam 9_2_STM_1(ii) and 9_2_STM_2(ii). . . . .	.291
Figure 8.91: Comparison between 9_2_STM_1(ii) and 9_2_STM_2(ii) . . . . .	.291
Figure 8.92: Cracking in Beam 9_2_STM_1(ii). . . . .	.291
Figure 8.93: Final failure in Beam 9_2_STM_1(ii). . . . .	.292
Figure 8.94: Recorded bar strains, Beam 9_2_STM_1(ii). . . . .	.292
Figure 8.95: Force comparison at the design load. . . . .	.293
Figure 8.96: Force comparison at the peak load. . . . .	.293
Figure 8.97: Cracking in Beam 9_2_STM_2(ii). . . . .	.293
Figure 8.98: Bar strains, Beam 9_2_STM_2(ii). . . . .	.294
Figure 8.99: Strut and tie model compared to recorded steel strains at the design load, Beam 9_2_STM_2 (ii). . . . .	.294
Figure 8.100: Test setup for Beam 9_2_STM(iii). . . . .	.295
Figure 8.101: Load versus deflection for Beam 9_2_STM(iii). . . . .	.295
Figure 8.102: Load versus deflection for Beam 9_2_STM_2(i) and 9_2_STM_2(iii). . . . .	.296
Figure 8.103: Cracking in Beam 9_2_STM_1(iii). . . . .	.296
Figure 8.104: Bar Strains - Beam 9_2_STM_ (iii). . . . .	.296
Figure 8.105: Strain gauge result comparison, Beam 9_2_STM_1(i) and (iii). . . . .	.297
Figure 8.106: Cracking in Beam 9_2_STM_2(iii). . . . .	.297
Figure 8.107: Failure of Beam 9_2_STM_2(iii). . . . .	.298
Figure 8.108: Bar strains - Beam 9_2_STM_2(iii). . . . .	.298
Figure 8.109: Bar forces comparison at the design load of 36kN, Beam 9_2_STM(iii). . . . .	.298
Figure 8.110: Summary of all beam tests in 9_2_STM series. . . . .	.299



Figure 8.111: Summary of all 9_2 Series Tests. . . . .	.300
Figure 8.112: Summary of all tests undertaken in §8.3 and §8.4. . . . .	.300
Figure 8.113: Method of analysis using DIC and GeoPIV. . . . .	.301
Figure 8.114: Displacement comparison - measured and interpolated results. . . . .	.302
Figure 8.115: Changes in principal strain $\epsilon_1$ for Beam 9_2_CFP_M(ii) over the loading cycle. . . . .	.302
Figure 8.116: Scale bar for all DIC results. . . . .	.303
Figure 8.117: Beam 9_2_EC2_V(i) at its peak load (§8.3.6.2). . . . .	.304
Figure 8.118: Beam 9_2_EC2_M(i) at it peak load (§8.3.6.1). . . . .	.304
Figure 8.119: Beam 9_2_EC2_V(ii) at its peak load (§8.3.7.1). . . . .	.305
Figure 8.120: Beam 9_2_EC2_M(ii) at its peak load (§8.3.7.2). . . . .	.305
Figure 8.121: Beam 9_3_EC2_M at its peak load (§8.3.8.1). . . . .	.306
Figure 8.122: Beam 9_3_EC2_M just beyond peak load (18kN, but showing shear failure mode). . . . .	.306
Figure 8.123: Beam 9_2_CFP_V(ii) at the design load (§8.3.7.4). . . . .	.307
Figure 8.124: Beam 9_2_CFP_V(ii), at failure (§8.3.7.4). . . . .	.307
Figure 8.125: Beam 9_2_CFP_M(ii) at the design load (§8.3.7.3). . . . .	.308
Figure 8.126: Beam 9_2_CFP_M(ii), at failure (§8.3.7.3). . . . .	.308
Figure 8.127: Beam 9_3_CFP_V at the design load (32kN) (§8.3.8.4). . . . .	.309
Figure 8.128: Beam 9_3_CFP_V, at its failure load (44kN) (§8.3.8.4). . . . .	.309
Figure 8.129: Beam 9_3_CFP_M at its design load (32kN) (§8.3.8.3). . . . .	.310
Figure 8.130: Beam 9_4_CFP_V at its design load (29kN) (§8.3.9.3). . . . .	.310
Figure 8.131: Beam 9_4_CFP_V at its peak load (80kN) (§8.3.9.3). . . . .	.311
Figure 8.132: Beam 9_4_CFP_M at its design load (29kN) (§8.3.9.4). . . . .	.311
Figure 8.133: Beam 9_2_CFP_M(ii) major strain direction over loading cycle. Principal strain $\epsilon_1$ in background. . . . .	.312
Figure 8.134: Beam 9_2_CFP_M(ii) minor strain direction over loading cycle. Principal strain $\epsilon_1$ in background. . . . .	.312
Figure 8.135: Change in strain direction, detail for Beam 9_2_CFP_M(ii). . . . .	.312
Figure 8.136: Beam 9_2_EC2_M(ii) major strain direction over loading cycle. Principal strain $\epsilon_1$ in background. . . . .	.313
Figure 8.137: Beam 9_2_EC2_M(ii) minor strain direction over loading cycle. Principal strain $\epsilon_1$ in background. . . . .	.313
Figure 8.138: Change in strain direction, detail for Beam 9_2_EC2_M(ii). . . . .	.313
Figure 8.139: Beam 9_2_STM_1(i), Design Load 36kN (§8.4.5.1). . . . .	.314
Figure 8.140: Beam 9_2_STM_1(ii), Design Load 36kN (§8.4.6.1). . . . .	.314
Figure 8.141: Beam 9_2_STM_1(ii), Peak Load (39kN) (§8.4.6.1). . . . .	.315
Figure 8.142: Beam 9_2_STM_1(iii), Design Load 36kN (§8.4.7.1). . . . .	.315
Figure 8.143: Beam 9_2_STM_2(i), Design Load 36kN (§8.4.5.2). . . . .	.316
Figure 8.144: Beam 9_2_STM_2(i), Peak Load 41.5kN (§8.4.5.2). . . . .	.316
Figure 8.145: Beam 9_2_STM_2(ii), Design Load 36kN (§8.4.6.2). . . . .	.317
Figure 8.146: Beam 9_2_STM_2(iii), Design Load 36kN (§8.4.7.2). . . . .	.317
Figure 8.147: Beam 9_2_STM_2(iii), Failure Load 40.6kN (§8.4.7.2). . . . .	.318

Figure 8.148: Beam 9_2_STM_2(i) major direction over loading cycle. Principal strain $\epsilon_1$ in background.	.318
Figure 8.149: Beam 9_2_STM_2(i) minor direction over loading cycle. Principal strain $\epsilon_1$ in background.	.319
Figure 8.150: Change in strain direction, detail for Beam 9_2_EC2_M(ii).	.319
Figure 8.151: Comparison between Beam 9_2_EC2_M(ii) and Beam 9_2_CFP_M(ii) at their respective peak loads for principal strain $\epsilon_2$ (top) and showing crack distributions overlain on $\epsilon_1$ strain plot (bottom).	.320
Figure 8.152: Failure modes for Beam 9_2_EC2_M(ii) and Beam 9_2_CFP_M(ii).	.321
Figure 8.153: Comparison of principal strains in Beams 9_3_EC2_M and 9_3_CFP_M at their respective failure loads.	.322
Figure 8.154: Comparison between Beam 9_2_EC2_M(ii) and Beam 9_2_STM_2(i) at their respective peak loads (top). Crack distributions at the peak load overlain on $\epsilon_1$ strain plot (bottom).	.323
Figure 8.155: Comparison of $\epsilon_{yy}$ strains in Beam 9_2_CFP_2(i) and the design model forces.	.324
Figure 8.156: Comparison between Beam 9_2_CFP_M(ii) and Beam 9_2_STM_2(i) at their respective peak loads (top). Crack distributions at the peak load overlain on $\epsilon_1$ strain plot (bottom).	.324
Figure 8.157: Comparison of overall beam geometry, 9_2_CFP; 9_2_EC2 and 9_2_STM.	.325
Figure 8.158: Crack propagation comparisons for Beam 9_2.	.326
Figure 8.159: Summary of all 9_2 Series Tests.	.328
Figure 8.160: Fully coated CFRP Grid, feasibility study.	.331
Figure 8.161: Partially bonded grids.	.331
Figure 8.162: Force envelope.	.332
Figure 8.163: Beam layouts.	.333
Figure 8.164: CFRP grid fabrication for Beam 10_1 (left) and Beam 10_2 (right).	.333
Figure 8.165: Test set up.	.334
Figure 8.166: Crack progression in Beam 10_3.	.334
Figure 8.167: Crack progression in Beam 10_2.	.335
Figure 8.168: Significant cracking in Beam 10_2 after the peak load.	.335
Figure 8.169: Failure of the partially coated CFRP grids in Beam 10_2.	.336
Figure 8.170: Crack progression in Beam 10_1.	.336
Figure 8.171: Significant cracking and post-peak behaviour in Beam 10_1.	.336
Figure 8.172: Failure of the CFRP grids.	.337
Figure 8.173: Load-displacement results.	.338
Figure 8.174: Summary failure diagrams.	.338

## Chapter 9 Development (3)

**343**

### *Durability enhancement*

Figure 9.1: Modified cube mould	.344
Figure 9.2: Cubes splitting method (l); and carbonation depth measurements (r).	.345
Figure 9.3: Carbonation depth examples at each testing stage.	.345
Figure 9.4: Comparison between samples exposed for 180 days to a 4% CO <sub>2</sub> environment and samples exposed for 180 days to atmospheric CO <sub>2</sub> levels.	.346
Figure 9.5: Carbonation depth results summary.	.346
Figure 9.6: Carbonation depth results plotted against the square root of time.	.347

Figure 9.7: Cylinder mould for Chloride Ingress test. . . . .	.352
Figure 9.8: Heated water bath (l); Samples coated in paraffin wax (r). . . . .	.353
Figure 9.9: Concrete sampling process. (l-r) Cutting equipment; sample broken down by depth; grinding. . . . .	.354
Figure 9.10: Specimen after sampling (l); Ground samples ready for chloride analysis (r). . . . .	.354
Figure 9.11: Analysis process (l-r): Sample weighed; Hot acid extraction of sample; Filtering of extracted sample; Titration with ammonium thiocyanate. . . . .	.355
Figure 9.12: The convection zone ( $\Delta x$ ) in a typical chloride profile with depth from an in-situ concrete structure (after Schiessl and Lay, 2005 and DD CEN 12390-11 (2010)). . . . .	.358
Figure 9.13: Chloride content with depth, results for test 1-1 to B-1 drawn using Eq. 9.10 and Table 9.9. . . . .	.359
Figure 9.14: Comparison of average chloride ingress profiles. . . . .	.361
Figure 9.15: Comparison of average chloride ingress profiles. . . . .	.362
Figure 9.16: Cumulative capillary absorption (i) versus $t^{1/2}$ for a 1:2 Portland cement:sand mortar, reproduced from Taylor et al., 1999) (l); 'Initial' and 'Secondary' sorptivities as defined by the ASTM C1585 (2004) method for sorptivity measured using water, where 'I' the change in mass divided by the product of the cross sectional area of the specimen and the density of water (r). . . . .	.365
Figure 9.17: Fabric base for concrete cylinder samples (l); Sample locations for sorptivity testing (r). . . . .	.366
Figure 9.18: Test method and set up (diagram after ASTM C1585, 2004).. . . . .	.367
Figure 9.19: Surface area of the fabric cast sample . . . . .	.368
Figure 9.20: Samples S1-S3, initial and secondary absorption plots, showing values for $S_i$ and $S_s$ . . . . .	.369
Figure 9.21: Results of Table 9.17. . . . .	.370
Figure 9.22: Prisms cast for Series 2.. . . . .	.373
Figure 9.23: Location of test wafers from each concrete prism. . . . .	.375
Figure 9.24: Resin coated samples (l); Polished sample (r). . . . .	.375
Figure 9.25: Imaging locations for Sample S1-T3, S2-T1 and S3-T2 (l-r). . . . .	.375
Figure 9.26: SEM Imaging for Sample S1-T3 showing Site 1 on the Timber and Fabric Faces (magnification at 30x, 100x and 1000x as noted). . . . .	.376
Figure 9.27: Composition with depth measured for Sample S3-T2 on Fabric and Timber faces (imaged at 100x magnification). . . . .	.376
Figure 9.28: Fabric cast face in the surface zone for sample S3-T2 (27x magnification (l) and 400x magnification (r)). . . . .	.376
Figure 9.29: Analysis sites for particle size distribution. . . . .	.377
Figure 9.30: Watershed grain size analysis example from SEM image (250x (top) and 500x (bottom) magnification shown). . . . .	.378
Figure 9.31: Samples for topology imaging in SEM. . . . .	.379
Figure 9.32: Imaging for Timber face (S1-TA) at 18x, 500x, 1000x and 2500x magnification. . . . .	.380
Figure 9.33: Imaging for Fabric Surface (S1-FA) at 18x, 500x and 1000x magnification. . . . .	.380
Figure 9.34: Detailed imaging of the fabric cast face. . . . .	.381
Figure 9.35: Comparison between concrete topology on timber cast face (l) with that found in the weave intersections on the fabric cast face (r). . . . .	.381
Figure 9.36: Void zones in the fabric cast concrete face at increasing magnification (l-r: x37, x110, x1000). . . . .	.382
Figure 9.37: EDS locations for sample S1-TB (l) and sample S1-FB (r). . . . .	.382
Figure 9.38: EDS Results for Sample S1-TB, Site 1. . . . .	.383
Figure 9.39: EDS Results for Sample S1-TB, Site 2. . . . .	.383

Figure 9.40: EDS Results for Sample S1-FB, Site 1. . . . .	.383
Figure 9.41: Distribution of Calcium (Ca(K $\alpha$ )) and Sodium (Na(K $\alpha$ )) compared to SEM image (l). . . . .	.384
Figure 9.42: EDS Results for Sample S1-FB to compare ridge (top) and intersection zones (bottom). . . . .	.385
Figure 9.43: Histogram showing distribution of elements in each pixel of the SEM image by weight % for Sample S1-FB, Site 1. . . . .	.386
Figure 9.44: Histogram showing distribution of elements in each pixel of the SEM image by weight % for Sample S1-TB, Site 1. . . . .	.386
Figure 9.45: Histogram showing distribution of elements in each pixel of the SEM image by weight % for Sample S1-TB, Site 2. . . . .	.387
Figure 9.46: Surface hardness specimen preparation.. . . .	.390
Figure 9.47: Test specimen with grid marked on the surface and held securely against a strong floor. . . . .	.391
Figure 9.48: Results for specimens 1.1 and 1.2 after 28 days and 90 days (left) and 180 days (right). . . . .	.392
Figure 9.49: Results for specimens 1.3 and 1.4 after 35 days and 95 days. . . . .	.392
Figure 9.50: Improvements in surface hardness with depth for Specimen 1.3 at 95 days (l); Average percentage improvement seen in the fabric cast face at each test depth (Specimen 1.3) (r). . . . .	.393
Figure 9.51: Composite photo of appearance of the concrete surface between 0 and 9mm from the timber cast face. . . . .	.394
Figure 9.52: Prism moulds for Series 2 hardness tests. . . . .	.395
Figure 9.53: Three Series 2 moulds (l); Casting (c); Demoulded prisms (r).. . . . .	.396
Figure 9.54: Securing series 2 prisms for surface hardness testing (l); Test locations (r). . . . .	.396
Figure 9.55: Surface hardness with depth for Samples 2.1-2.3.. . . . .	.397
Figure 9.56: Percentage difference in surface hardness between fabric and timber faces in Samples 2.1-2.3. . . . .	.397
Figure 9.57: Fabric cast concrete surface (l); Timber cast concrete surface (r), both surface cast from the same concrete mix. . . . .	.402
Figure 9.58: Results of surface hardness tests on seven different fabrics presented by Lee (2012) showing optimum pore sizes for woven and non-woven fabric types. . . . .	.403
Figure 9.59: Behaviour and construction of woven and non-woven fabrics. . . . .	.404
Figure 9.60: A summary of the proposed effects of casting concrete into fabric formwork in the surface zone. . . . .	.406
Figure 9.61: Reductions in embodied energy (data after Craig et al., 2009). . . . .	.407

## Chapter 10 Analysis

409

### *Fabric formed beams*

Figure 10.1: Moment-curvature relationship at a particular section. . . . .	.411
Figure 10.2: Load-deflection calculation for entire beam. . . . .	.411
Figure 10.3: Uni-axial stress strain model for Ductal® (after Graybeal, 2006b). . . . .	.412
Figure 10.4: Material model for steel (after BS EN 1992-1-1 (2004)). . . . .	.412
Figure 10.5: Results for Ductal® cast double T beam. . . . .	.413
Figure 10.6: Flowchart showing deflection calculation process. . . . .	.415
Figure 10.7: Summary of beam dimensions. . . . .	.416
Figure 10.8: Beam 5_1 and 5_2 boundary conditions for integrations. . . . .	.417
Figure 10.9: Predicted response of Beam 5_1 and 5_2, comparison with test data.. . . .	.418

Figure 10.10: Predicted response of Beam 5_3 and 5_4, comparison with test data. . . . .	.419
Figure 10.11: Predicted response (mid-span deflection versus total load) of Beam 6_4_1, comparison with test data. . . . .	.420
Figure 10.12: Deflection profile prediction for Beam 6_4_1, comparison with test data.. . . .	.420
Figure 10.13: Predicted response (mid-span deflection versus total load) of Beams 8_3i and 8_3ii, compared to test data. . . . .	.421
Figure 10.14: Principle of moment-rotation approach for a singly reinforced section (figure after Haskett et al., 2008). . . . .	.422
Figure 10.15: Method for cross sectional modelling. . . . .	.425
Figure 10.16: Generating three-dimensional images for beam design. . . . .	.425
Figure 10.17: Comparison between plaster model and computer approach (model images courtesy Professor Mark West, University of Manitoba). . . . .	.426
Figure 10.18: Three-dimensional images generated from the cross sectional modelling approach (clockwise from top left: Double T Beams; Double cantilever beam; Ribbed slab on fabric cast beams; Continuous beam).. . . . .	.426
Figure 10.19: Beam layout for sensitivity analysis. . . . .	.427
Figure 10.20: Sensitivity analysis results. . . . .	.428
Figure 10.21: Bar position for different values of $\alpha$ . . . . .	.428
Figure 10.22: The variable angle truss model for a tapered beam with an inclined tension chord.. . . .	.429
Figure 10.23: Reduction in shear carried by the web in beams with inclined tension chords. . . . .	.431
Figure 10.24: The variable angle truss model for a tapered beam with an inclined compression chord. . . . .	.431
Figure 10.25: Change in shear carried by the web in beams with an inclined compression chord. . . . .	.432
Figure 10.26: Materials used in the construction of Beam 5_1 and an equivalent strength prismatic section (denoted Beam 5_1_P).. . . . .	.433
Figure 10.27: Materials used in the construction of Beam 6_4_1 and an equivalent strength prismatic section (denoted Beam 6_4_1_P). . . . .	.435
Figure 10.28: Layout of prototype building showing geometry and overall forms. . . . .	.438
Figure 10.29: Typical sections through the fabric formed and conventionally cast structure. . . . .	.439
Figure 10.30: Future use of fabric cast shells as permanent formwork for in situ concrete construction.. . . .	.440

## Chapter 11 Design guide

**443**

### *Steel reinforced fabric formed beams*

Figure 11.1: Design process flow chart summary. . . . .	.445
Figure 11.2: Beam layout and load envelope (l), with indicative bending and shear envelopes shown (r). . . . .	.447
Figure 11.3: Stress strain profile for flexural capacity (note vertical component of bar is not included in shear force calculation for the BS EN 1992-1-1 method as per the recommendations found in Chapter 8 and the test results of this thesis). . . . .	.449
Figure 11.4: Anchorage and development lengths for flexural and transverse reinforcement. . . . .	.449
Figure 11.5: Construction joints, end zone detailing and other considerations. . . . .	.450
Figure 11.6: Cover requirements for longitudinal flexural reinforcement. . . . .	.450
Figure 11.7: Cross section and reinforcement layouts assumed in design process. . . . .	.451
Figure 11.8: Progression of beam section design. . . . .	.451
Figure 11.9: Indicative progression of beam section design for a continuous beam.. . . .	.452

Figure 11.10: Example continuous beam design to BS EN 1992-1-1 (2004) including transverse reinforcement. . . . .	.452
Figure 11.11: Beam designed according to the compressive force path method as described in this thesis. . . . .	.454
Figure 11.12: Comparison of BS EN 1992-1-1 (2004) and CFP method designs. . . . .	.455
Figure 11.13: Example beam profile render in 3D. . . . .	.456
Figure 11.14: Example formwork system, shown for a continuous beam. . . . .	.457
Figure 11.15: Construction process. . . . .	.458
Figure 11.16: Continuous beam design and options for cross section variations. . . . .	.459
Figure 11.17: End zone of a tapered beam (l); Anchorage using a looped bar (c); Using an 'L' bar (r). . . . .	.460
Figure 11.18: Splayed bar anchorage method for fabric formed beams. . . . .	.461
Figure 11.19: Detailing of simple supports. Column (l); Corbel (r). . . . .	.461
Figure 11.20: Detailing of fixed supports over a column (l); and at a corbel end (r). . . . .	.462
Figure 11.21: Theoretical profile of the beam (l); Additional depth at supports (c); Improved layout (r). . . . .	.462
<b>Chapter 12 Future work</b>	<b>465</b>
<i>Proposals</i>	
Figure 12.1: Design options for UHPFRC actively reinforced beams. . . . .	.466
Figure 12.2: Computational optimisation of a flat slab (Bak, 2011). . . . .	.467
Figure 12.3: Shell formwork floor system. . . . .	.468
Figure 12.4: Shell formwork construction. . . . .	.468
Figure 12.5: Form finding the shell using dynamic relaxation.. . . .	.468
Figure 12.6: The fabric formed flat slab. . . . .	.469
Figure 12.7: Support detail.. . . .	.469
Figure 12.8: Shell structures. CAST models (l) and 'Al-Akaria' shell design, courtesy Atkins UK (r). . . . .	.470
Figure 12.9: Fabric scale model for the 'Akaria' shell. . . . .	.470
Figure 12.10: Framing systems using fabric formwork. . . . .	.471
Figure 12.11: Drop in central span. . . . .	.471
Figure 12.12: Application of double cantilevered beam to building frame. . . . .	.471
Figure 12.13: Cantilever Beam Designs. . . . .	.472
Figure 12.14: Prefabricated framing system. . . . .	.472
Figure 12.15: Fabric sock design principles.. . . .	.473
Figure 12.16: Pre-sewn fabric 'sock'.. . . .	.473
Figure 12.17: Modelling concrete using random fibres (increasing load left-right, blue showing tension, red compression) (after Williams, 2012). . . . .	.474
Figure 12.18: Left: Spalling after the Channel Tunnel Fire, 1996 (Smith and Atkinson, 2010); Right: Fire damage during construction (Ingham, 2009). . . . .	.476
Figure 12.19: Protecting concrete from explosive spalling using polypropylene microfibres (Shuttleworth, 2001, cited by Smith and Atkinson, 2010). . . . .	.476

[blank page]

[blank page]



# List of tables

<b>Chapter 1</b>	<b>Introduction</b>	<b>1</b>
<b>Chapter 2</b>	<b>Fabric formwork</b>	<b>11</b>
	<i>Literature review</i>	
	Table 2.1: Material savings using fabric formwork. . . . .	26
	Table 2.2: Available structural test data for fabric formed concrete beams. . . . .	27
	Table 2.3: Test summary. . . . .	33
	Table 2.4: The benefits of a permeable formwork system (after Price, 2000 and DuPont, 2007). . . . .	38
	Table 2.5: Goals and proposed resolutions. . . . .	46
<b>Chapter 3</b>	<b>Material behaviour</b>	<b>49</b>
	<i>Literature review</i>	
	Table 3.1: Ultra high performance fibre reinforced concrete (FRC) (after Li, 2002). . . . .	54
	Table 3.2: Material properties of Ductal® (after Graybeal, 2006a). . . . .	54
	Table 3.3: Material characteristics (after Graybeal, 2006a). . . . .	55
	Table 3.4: Creep testing results (after Graybeal, 2006a). . . . .	56
	Table 3.5: Textile vocabulary (after ASTM, 1994). . . . .	60
	Table 3.6: Fabric properties. . . . .	61
	Table 3.7: Basic material properties of FRP bars. . . . .	71
	Table 3.8: 75mm Splayed bar, pull-out load improvement (Tallis, 2005). . . . .	77
<b>Chapter 4</b>	<b>Concrete behaviour</b>	<b>83</b>
	<i>Literature review</i>	
	Table 4.1: Summary of tests and analysis of results presented by MacLeod and Houmsi (1994). . . . .	106
	Table 4.2: Test results and failure load predictions to DIN 1045-1 (cited by Rombach and Nghiep (2011). . . . .	108
	Table 4.3: Design shear capacities to different design codes (Rombach and Nghiep, 2011). . . . .	109
<b>Chapter 5</b>	<b>Design (1)</b>	<b>115</b>
	<i>Flexural behaviour</i>	
	Table 5.1: Concrete frame analysis details (courtesy Atkins Ltd). . . . .	116
	Table 5.2: Augustine House, material use analysis. . . . .	116
	Table 5.3: Carnival HQ, material use analysis. . . . .	117
	Table 5.4: Construction methods. . . . .	122

Table 5.5: Reinforcement and concrete matrix. . . . .	.122
Table 5.6: Tests undertaken. . . . .	.123
Table 5.7: Material Properties. . . . .	.127
Table 5.8: Test load summary (see also Chapter 6). . . . .	.128
Table 5.9: Material use comparison. . . . .	.135
Table 5.10: Shear design for Method 2. . . . .	.141
Table 5.11: Material use saving summary for the Double T Beams 6_4_1 and 6_4_2 (with slab (l); without slab (r)). . . . .	.143
Table 5.12: Ductal® material properties. . . . .	.146
Table 5.13: Test load summary (see also Chapter 6). . . . .	.148
Table 5.14: Material Properties. . . . .	.149

## **Chapter 6      Development (1)      157**

*Flexural behaviour*

Table 6.1: Preliminary work.. . . .	.157
Table 6.2: Testing series outline. . . . .	.157
Table 6.3: Concrete mix properties. . . . .	.160
Table 6.4: Recorded concrete strength and standard deviation. . . . .	.160
Table 6.5: Recorded concrete flexural tensile strength. . . . .	.160
Table 6.6: FRP Material Properties. . . . .	.160
Table 6.7: Test details. . . . .	.161
Table 6.8: Monitoring details. . . . .	.162
Table 6.10: Test results. . . . .	.163
Table 6.11: Test details. . . . .	.164
Table 6.12: Failure load summary. . . . .	.165
Table 6.13: Test details. . . . .	.169
Table 6.14: Member details. . . . .	.173
Table 6.15: Beam summary. . . . .	.182
Table 6.16: Concrete mix ratios. . . . .	.182
Table 6.17: Concrete mix properties. . . . .	.183
Table 6.18: Test failure modes and ultimate capacity. . . . .	.186
Table 6.19: Concrete mix design per m <sup>3</sup> , Beam 6_2_1. . . . .	.195
Table 6.20: Concrete mix design, Beam 6_4_1 and 6_4_2. . . . .	.195
Table 6.21: Concrete mix properties. . . . .	.195
Table 6.22: Test Results, Beams 6_4_1 and 6_4_2. . . . .	.200
Table 6.23: Ductal® mix proportions (prescribed by Lafarge, July 2010). . . . .	.206
Table 6.24: Cube strength test results. . . . .	.206
Table 6.25: Material savings demonstrated in Chapter 6. . . . .	.215

<b>Chapter 7</b>	<b>Design (2)</b>	<b>217</b>
	<i>Shear behaviour</i>	
Table 7.1:	Summary of tapered beam tests.	.228
<b>Chapter 8</b>	<b>Development (2)</b>	<b>245</b>
	<i>Shear behaviour</i>	
Table 8.1:	Concrete mix design per m <sup>3</sup> .	.246
Table 8.2:	Concrete properties in compression.	.246
Table 8.3:	Concrete properties in tension.	.247
Table 8.4:	Test failure modes and ultimate capacity.	.249
Table 8.5:	Capacity prediction comparisons, Beams 8_1 - 8_2.	.258
Table 8.6:	Capacity prediction comparisons, Beams 8_3(i) and 8_3(ii).	.259
Table 8.7:	Concrete mix design per m <sup>3</sup> .	.260
Table 8.8:	Concrete properties - compression.	.260
Table 8.9:	Test failure modes and ultimate capacity.	.263
Table 8.10:	Concrete mix design per m <sup>3</sup> .	.284
Table 8.11:	Concrete properties - compression.	.284
Table 8.12:	Test failure modes and ultimate capacity for STM series tests.	.285
Table 8.13:	DIC data summary.	.303
Table 8.14:	CFRP Grid by Fortress Stabilisation, Material Properties.	.331
Table 8.15:	Epoxy resin as used in all tests.	.331
Table 8.16:	Concrete strengths as measured at testing.	.334
<b>Chapter 9</b>	<b>Development (3)</b>	<b>343</b>
	<i>Durability enhancement</i>	
Table 9.1:	Summary of tests in Chapter 9.	.343
Table 9.2:	Concrete mix per m <sup>3</sup> , durability tests.	.343
Table 9.3:	Fabric properties.	.343
Table 9.4:	Summary of carbonation depths.	.346
Table 9.5:	Calculated values of the coefficient of carbonation.	.347
Table 9.6:	Chloride ingress test date summary.	.352
Table 9.7:	Correlating compressive strength results.	.355
Table 9.8:	Chloride content results by sample.	.356
Table 9.9:	Variable values for each test series.	.360
Table 9.10:	Reduction in $D_{nss}$ when using fabric cast concrete.	.360
Table 9.11:	Reduction in $K_{Cr}$ when using fabric cast concrete.	.360
Table 9.12:	Reduction in $D_{nss}$ when using fabric cast concrete.	.362
Table 9.13:	Reduction in $K_{Cr}$ when using fabric cast concrete.	.362
Table 9.14:	Specimens for sorptivity testing.	.366
Table 9.15:	Sample weights, to 7 days.	.367
Table 9.16:	Summary of measured absorption rates.	.369

Table 9.17: Samples 1-6, comparison of I at different time steps. . . . .	.370
Table 9.18: Initial surface absorption of samples 1-3. . . . .	.371
Table 9.19: Summary of test prisms for Series 2 and Series 3 tests. . . . .	.374
Table 9.20: Concrete compressive strength summary.. . . .	.374
Table 9.21: Summary of grain size results. . . . .	.378
Table 9.22: Median value in weight % for each element. . . . .	.387
Table 9.23: Average value for each element by weight %. . . . .	.388
Table 9.24: Surface hardness test details. . . . .	.390
Table 9.25: Recorded cube strengths for surface hardness tests. . . . .	.391
Table 9.26: Summary of surface hardness results for Specimens 1.1, 1.2, 1.3 and 1.4. . . . .	.391
Table 9.27: Fabric types used in Series 2 surface tests. . . . .	.395
Table 9.28: Test specimens. . . . .	.395
Table 9.29: Summary of surface hardness results for Specimens 2.1-2.3.. . . .	.396
Table 9.30: Summary of test results. . . . .	.400
Table 9.31: Summary of concrete mix used for durability tests. . . . .	.400
<b>Chapter 10 Analysis</b>	<b>409</b>
<i>Fabric formed beams</i>	
Table 10.1: Beams subject to the analysis method. . . . .	.416
Table 10.2: Equations for beam properties. . . . .	.416
Table 10.3: Embodied energy of Beam 5_1 (all values taken as 'Cradle to Gate' values where possible from Hammond and Jones, 2011). . . . .	.434
Table 10.4: Embodied energy of equivalent strength Beam 5_1_P (all values taken as 'Cradle to Gate' values where possible from Hammond and Jones, 2011. . . . .	.434
Table 10.5: Savings in embodied energy for Beam 5_1 when compared to Beam 5_1_P. . . . .	.434
Table 10.6: Embodied energy of Beam 6_4_1 (all values taken as 'Cradle to Gate' values where possible from Hammond and Jones, 2011). . . . .	.436
Table 10.7: Embodied energy of equivalent strength Beam 6_4_1_P (all values taken as 'Cradle to Gate' values where possible from Hammond and Jones, 2011. . . . .	.436
Table 10.8: Savings in embodied energy for Beam 6_4_1 when compared to Beam 6_4_1_P. . . . .	.436
Table 10.9: Material use comparison for Beams 5_1 and 6_4_1 considering concrete and steel only. . . . .	.437
Table 10.10: Material use summary for the example fabric formed building shown in Figure 10.28 and Figure 10.29. . . . .	.439
Table 10.11: Material use summary for the example prismatic building shown in Figure 10.28 and Figure 10.29. . . . .	.439
Table 10.12: Changes in material use, arranged by structural element (excluding core walls). . . . .	.439
<b>Chapter 11 Design guide</b>	<b>443</b>
<i>Steel reinforced fabric formed beams</i>	
Table 11.1: Partial factors applied to loads (BS EN 1990 (2002)). . . . .	.447
Table 11.2: Material Savings achieved in example beam design. . . . .	.455
Table 11.3: Summary of anchorage methods for fabric formed beam. . . . .	.461

[blank page]



# Chapter 1 Introduction

## 1.1. Introduction

The language and technology of concrete construction has changed dramatically over the past two thousand years - from dome of the Pantheon, through its renaissance in the 1800s, and up to the work of Nervi and other modern masters of this fluid material. Throughout this, concrete has been cast almost exclusively into wooden or steel moulds to create prismatic elements. Nervi himself noted that:

*'although reinforced concrete has been used for over a hundred years and with increasing interest during the last few decades few of its properties and potentialities have been fully exploited so far...the main cause of this is a trivial technicality: the need to prepare wooden forms' (Nervi, 1956)*

This triviality pervades the minds of Engineers even today, with increased cost being associated with concrete structures that deviate from the use of flat panels of timber or steel as formwork. Despite this, concrete remains one of the most widely used man made materials in the world, with global production of cement approaching  $2.8 \times 10^9$  t in 2008 (USGS, 2008). Cement accounts for a large proportion of the world's raw material expenditure, reaching nearly 33% of the total in 2008 (Figure 1.1(left)). Although concrete has a relatively low embodied energy (Figure 1.1(right)), its rate of consumption means that cement manufacture alone is estimated to account for between 3% and 5% of global carbon dioxide emissions (WRI, 2005).

Against a backdrop of carbon dioxide emissions reduction targets (Figure 1.2), a recognition of the impact construction has on the environment (Figure 1.3) and an increasing client focus on sustainability, design philosophies centred around the need to put material where it is required are becoming increasingly desirable. It is noted that:

*'shape is cheaper than material' (Beukers and van Hinte, 2005).*

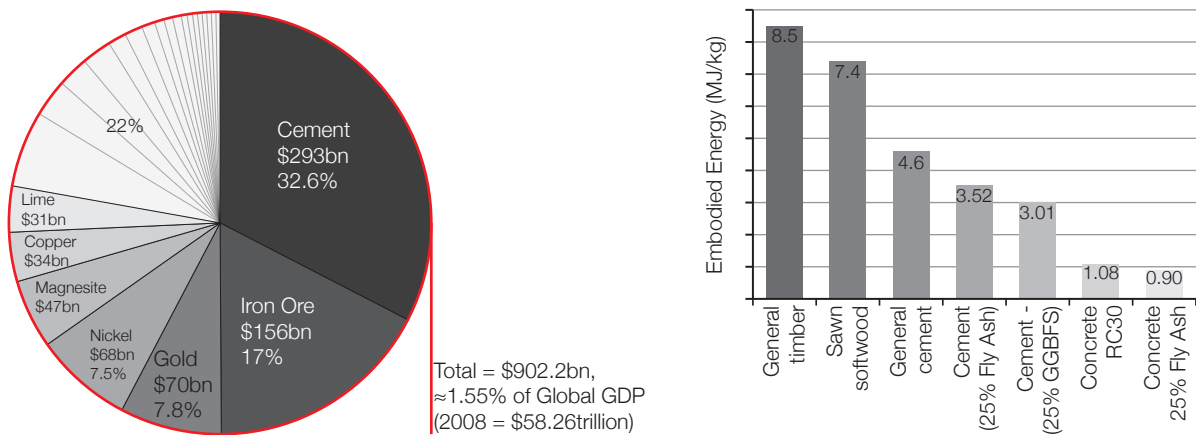


Figure 1.1: Left: World material expenditure in 2008 (material and price data after USGS (2011) and intended as an illustration only. Global GDP estimate courtesy the World Bank (2011). Right: Embodied energy of building materials (after Hammond and Jones, 2008).

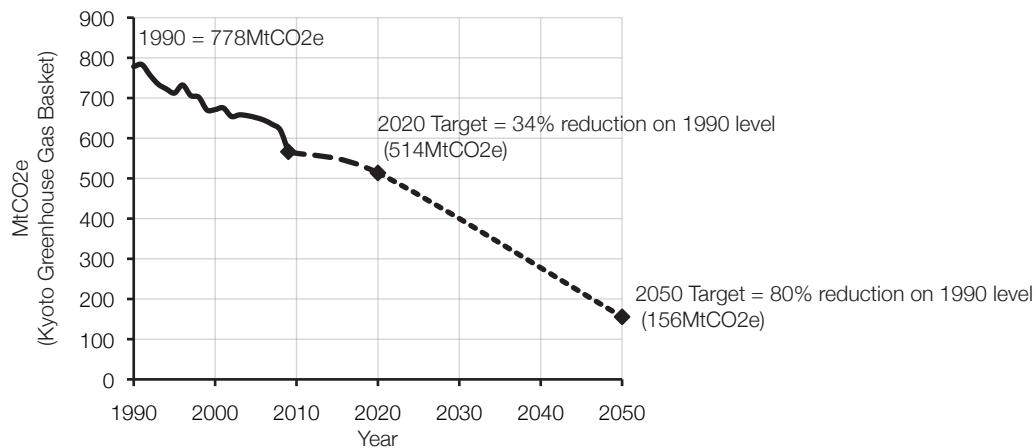


Figure 1.2: Historical UK emissions to 2009 and reduction targets for the period to 2050 (DECC, 2011).

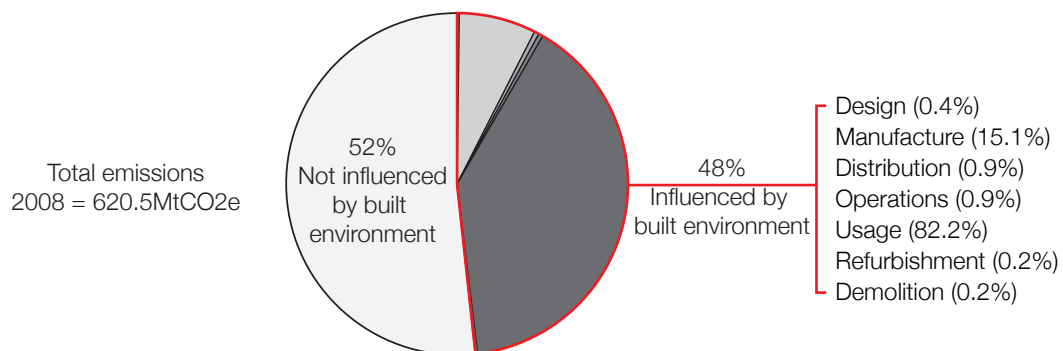


Figure 1.3: The influence of the built environment on carbon emissions in 2008 (after BIS, 2010).

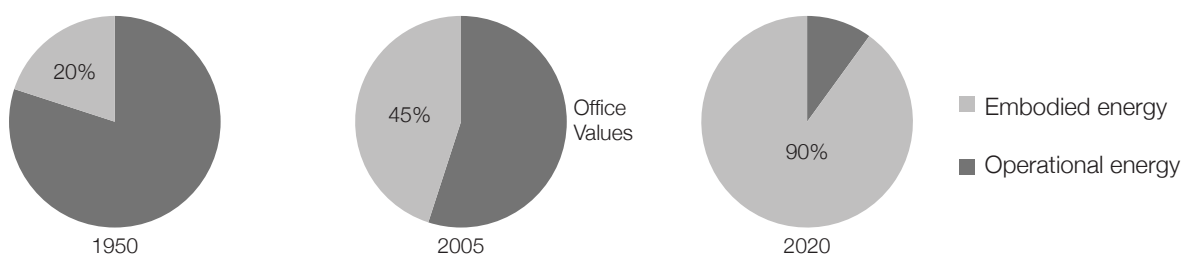


Figure 1.4: Changes in energy use (estimated values, after Cole and Kernan (1996); Sturgis and Roberts (2010) and Lane (2007).



Furthermore, the relative importance of embodied energy (the available energy that was used in the processes of making a product) over operational energy is changing, as is illustrated for office buildings in Figure 1.4. With increased energy efficiency, a structure built in 2050 may have a lower operational energy requirement than one built in 2005, thus making its embodied energy a more significant factor. This is further described by Thormark (2001), who studied low energy housing in Sweden as part of the CEPHUS project (see Schneiders, 2003) to find that embodied energy accounted for 40% of the total energy use in a 50 year life cycle.

The implication of this is that both construction and in-service energy use must be carefully considered to ensure that energy savings made during the life of the building are not offset by high initial energy requirements during construction. This thesis aims to address the requirement for low material use concrete structures through a step change in the way concrete is formed. Replacing flat sheets of timber and steel with a flexible mould, this system aims to capitalise on the fluidity of concrete by marrying it with the flexibility and strength of modern fabrics.

## **1.2. Fabric formwork**

Human bone is perhaps the ultimate material, having the optimum strength to resist the loads applied by our bodies, the optimum weight to prevent fatigue and the optimum connection detailing that allows us to move. Strong, cortical bone provides basic strength to the skeleton while lighter weight honeycombed bone provides support to both the cortical bone and the internal bone marrow (Standring, 2008).

The distribution of these two basic bone types varies both across the skeleton and over time, responding to the functional role of each member through the continual processes of bone matrix removal and replacement known as bone remodelling (Hamil and Knutzen, 2009). In long bones, the main shaft (or diaphysis) is usually a thick cylinder of compact bone enclosing the central marrow cavity (Standring, 2008) while flat, slender bones such as the ribs tend to have a uniformly cancellous internal structure enclosed by a layer of compact bone (Standring, 2008). By changing the load distribution on a mature skeleton, overall bone mass can be increased (Hamil and Knutzen, 2009) - as demonstrated by considering that the cortical bone in the dominant arm of a professional tennis player can be 35% thicker than in the contralateral arm (Komi, 1986).

The analogy of bone growth to sustainable structural design is thus apparent. Material, chosen from the palette available to the designer (including concrete to carry compression and reinforcement to carry tension), should be arranged in the manner which provides the most efficient response to the condition that the element is subjected to. This condition is not limited to just the structural loads on the element, but also to the consequences of failure, the role of the element in delivering the architectural intent, its construction cost and design feasibility. The changing loads on a structure over time may be met through the addition of prestress, strengthening or remedial works.

By applying simple optimisation methods in the design of reinforced concrete, elements whose form reflects this philosophy can quite readily be created. However, when using conventional formwork the trivial technicality

emphasised on Page 1 by Nervi (1956) immediately becomes a stumbling block. This thesis proposes that by replacing conventional formwork systems with flexible moulds made of fabric, reinforced concrete structures of almost any geometry can be created.

By removing concrete that serves little structural function, fabric formwork facilitates the construction of architecturally interesting, optimised structures. Analyses of existing buildings has shown that for a typical four-storey concrete structure only about 40% of the concrete is actually working to resist the applied loads (Wise, 2010) demonstrating that significant reductions in material use are indeed achievable.

This is illustrated by the three beams designed to carry a uniformly distributed load that are shown in Figure 1.5. The inefficiency of the prismatic element is immediately apparent, while the elements shaped in response to the loads applied to them provide a theoretical material savings of up to 46%. The construction of such non-prismatic elements is readily achieved using flat sheets of fabric, as will be shown in this thesis.

The advantages of fabric formwork are not simply limited to reductions in material use. By casting concrete into fabric excess water is allowed to bleed from the mould, resulting in an architecturally interesting, high quality surface finish (Figure 1.6). Exposing these surfaces internally not only avoids extraneous false ceilings and coverings, but also provides the potential for passive heating and cooling through the exposed thermal mass, adding further environmental and building physics design opportunities.

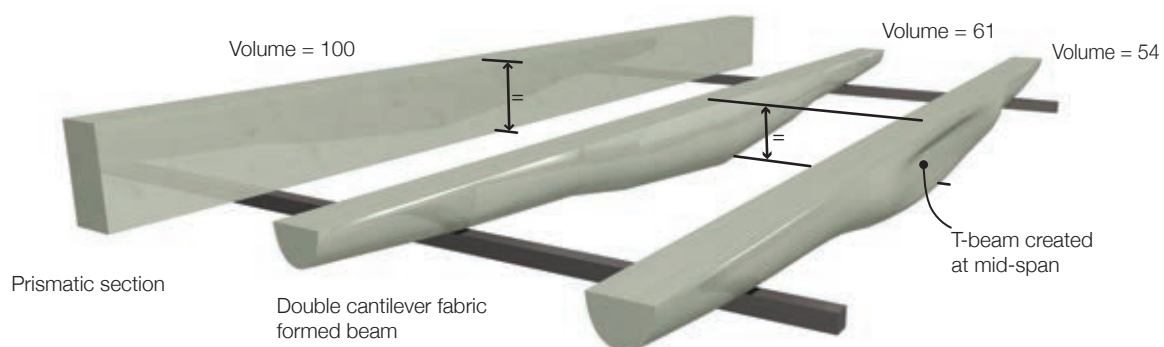


Figure 1.5: Material savings achieved using fabric formwork.

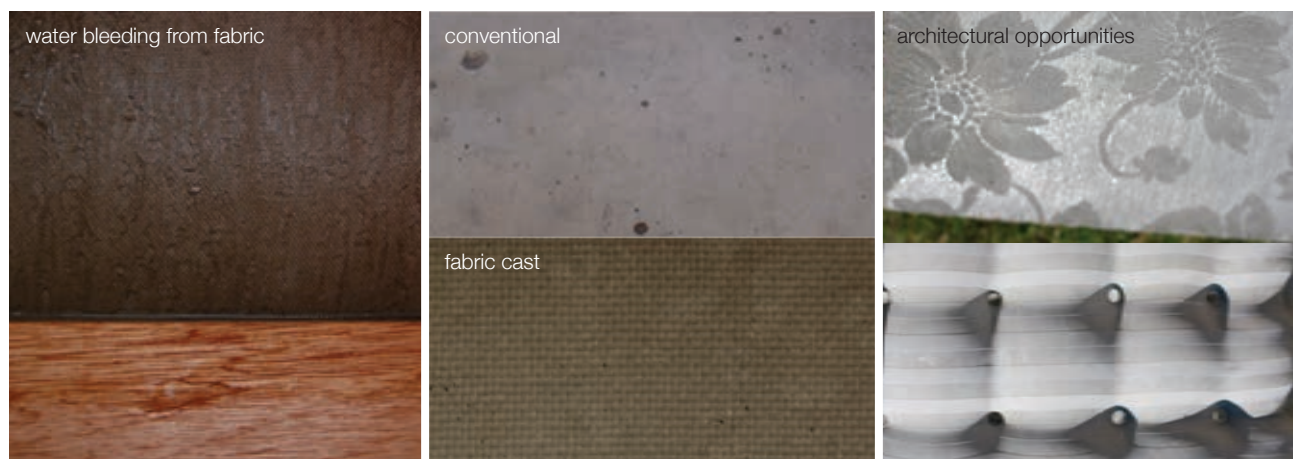


Figure 1.6: Casting concrete in fabric (left); Conventional and fabric cast surface finishes (centre); architectural uses (images courtesy Anne-Mette Manelius) (right).

### 1.3. Problem

The idea of casting variable section members is by no means a new one - the work of Pier Luigi Nervi and his contemporaries provide modern engineers and architects with ample precedent, yet in conventional construction such structures are comparatively rare. In discussing the work of Australian architect and engineer Harry Seidler, Abel (2004) echoes the words of Nervi to neatly illustrate the problem:

*"...if the natural forces of shear, tension and compression in a beam or support were clearly expressed, and any excess material was omitted, then what would be produced would be not only structurally efficient and economical to build, but also aesthetically pleasing. The only technical limitation was making the formwork to mould the resulting complex shapes."*

Innovation using fabric formwork has come from those designers who are not just trying to be free of straight lines, but who, like Nervi and Seidler, recognise the potential for inherent structural efficiency when concrete is cast in non-prismatic moulds. The research undertaken in the development of this thesis aims to address the concerns of optimisation, efficiency and construction from a structural engineering perspective, providing the technical guidance required to complement growing architectural interest in fabric formed concrete structures.

Yet obstacles stand in the way of fabric formwork as a mainstream construction method. Optimisation of concrete structures is complex and often time consuming and the structural behaviour of the resulting forms is not well understood at the ultimate limit state. When forms are generated, ensuring constructability and predicting the behaviour of its flexible mould during casting are further challenges. Finally, changes in the surface zone concrete of fabric cast elements are not well understood.

### 1.4. Aims

This dissertation brings together the three areas of focus identified in §1.3 to answer the question '*How can fabric formwork facilitate a sustainable future in concrete construction?*', with the following aims:

1. To demonstrate and understand the behaviour in shear and flexure at the ultimate limit state of optimised fabric cast beam elements;
2. To determine suitable construction processes, accurate methods for load-deflection prediction, and detailing considerations (including reinforcement anchorage) for fabric cast concrete structures;
3. To quantify and understand the changes in surface properties that occur when concrete is cast into a permeable mould.

The process undertaken in meeting these aims is illustrated in Figure 1.7 on page 6, and each has been achieved in this dissertation through a combination of experimental, theoretical and analytical work, much of which has been published. The full test matrix for shear, flexural and durability testing undertaken in this dissertation is provided in Table 5.6 on page 123.

The challenges, development and results of this dissertation are presented in thirteen chapters that are linked as shown by the road map in Figure 1.8, which is provided to guide the reader through the argument that fabric formwork can be used as a feasible alternative to conventional construction methods to provide durable, optimised, low carbon concrete structures.

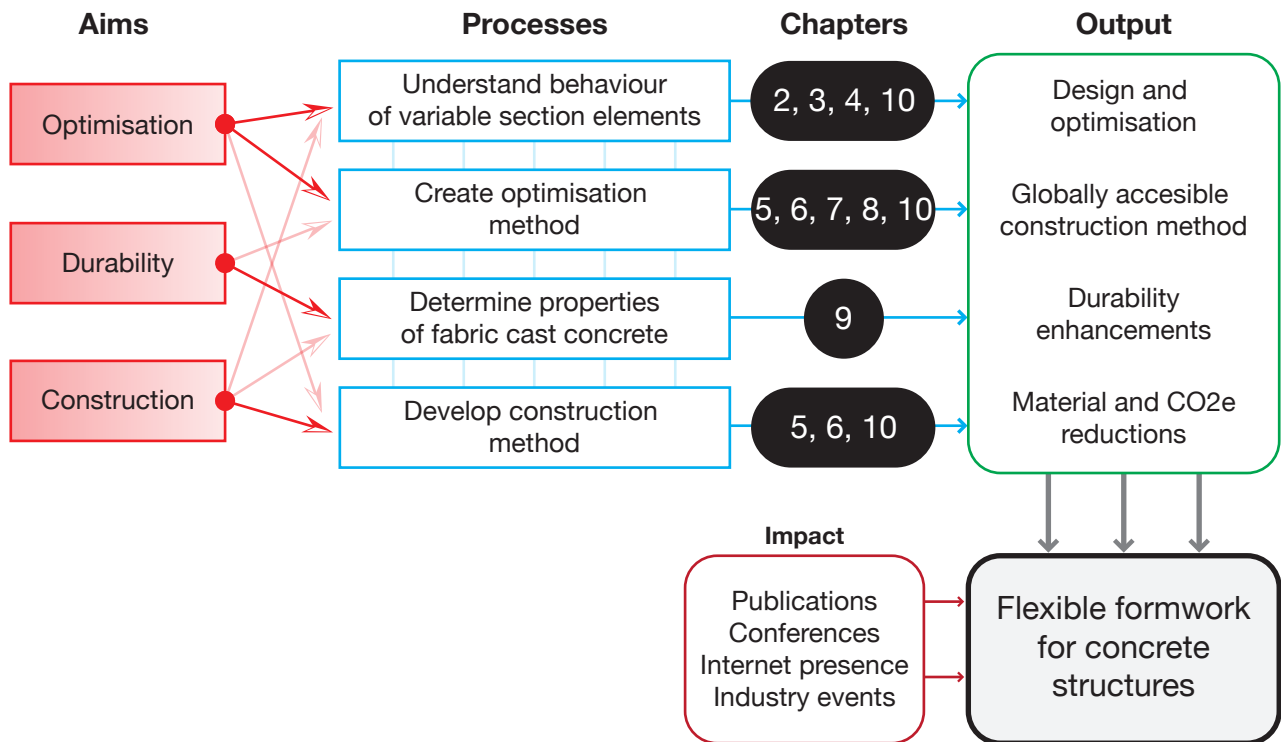


Figure 1.7: Process map.

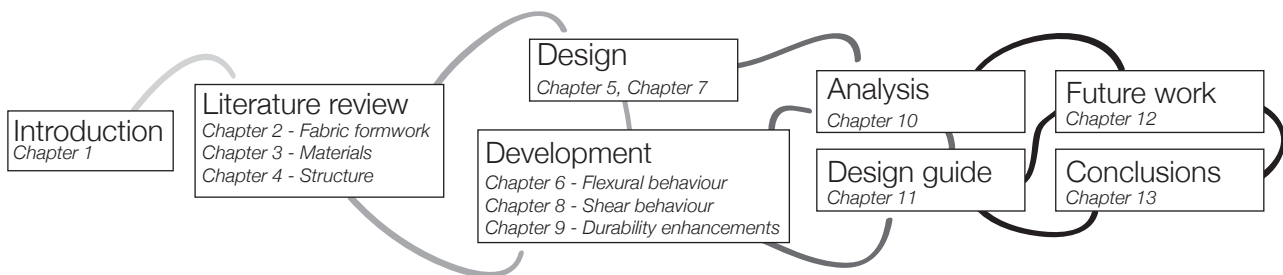


Figure 1.8: Road map.

## **1.5. Objectives**

From a series of initial design options shown in Chapter 5, a matrix of testing was determined. The tests undertaken, which are summarised on page 123, were chosen to address the following objectives:

1. Construction methods for fabric formed concrete beams;
2. The design, analysis and testing of fabric formed beams as elements in concrete framed structures;
3. The use of ultra-high performance concrete in fabric formed beams;
4. The anchorage behaviour of reinforcing bars with shallow end zones;
5. The shear behaviour of variable section concrete beams;
6. The changes in concrete surface properties arising from the use of fabric formwork.

## **1.6. Approach**

In Chapter 1 the central question that this thesis will address has been presented in brief. A historical background to fabric formwork, presented in Chapter 2, is followed by an analysis of the design and construction of fabric formed structures and available structural test data is presented before the advantages of fabric formwork are discussed. Chapter 3 details the three components of a fabric formed structure before the design challenges of both prismatic and non-prismatic of concrete are considered in Chapter 4. Following the aim of providing a sustainable future for concrete construction stated in the introduction, Chapter 5 and Chapter 7 present design work undertaken as part of this thesis.

Experimental work undertaken by the author is presented in Chapter 6, Chapter 8 and Chapter 9. Analysis of each section of work, focusing on flexural behaviour, shear behaviour and durability enhancements are presented within these Chapters, before more general analysis and parametric studies are provided in Chapter 10. Design guidance based on the work presented in this thesis is given in Chapter 11 before opportunities for future work are summarised in Chapter 12. Finally, conclusions encompassing the whole thesis are given in Chapter 13.

## **1.7. Funding and supervisory board**

This research has been funded as part of an Engineering and Physical Sciences Research Council Cooperative Award in Science and Engineering (EPSRC CASE), with Atkins as industrial sponsor and Professor Mike Otlet as industrial supervisor. Dr Antony Darby is the lead academic supervisor, supported by Professor Tim Ibell and Dr Mark Evernden.

## 1.8. Principal publications

### 1.8.1. Journal papers

1. Orr, J.J., Darby, A.P., Ibell, T.J., Denton, S.R., Shave, J.D., 2010. 'Shear design of circular concrete sections using the Eurocode 2 truss model'. *The Structural Engineer*, 88 (23/24), p26-33.

Paper (1) was awarded a Diploma of the Institution of Structural Engineers' Henry Adams Award, given for the best research paper published in 2010 in the Journal '*The Structural Engineer*'.

2. Orr, J.J., Darby, A.P., Ibell, T. J., Evernden, M.C., Otlet, M., 2011. 'Concrete structures using fabric formwork'. *The Structural Engineer*, 89 (8), p.20-26.

Paper (2) was awarded a Diploma of the Institution of Structural Engineers' Henry Adams Award, given for the best research paper published in 2011 in the Journal '*The Structural Engineer*'.

### 1.8.2. Conference Proceedings

1. Orr, J.J., Evernden, M.C., Ibell, T.J., Darby, A.P., 2012 [Editors]. *Proceedings of the Second International Conference on Flexible Formwork*. University of Bath, Bath, 27th - 29th June 2012.

### 1.8.3. Conference Papers

1. Orr, J.J., Ibell, T. J., Darby, A.P., 2010. Innovative concrete structures using fabric formwork. In: *Proceedings of the fourth international conference on Structural Engineering, Mechanics and Computation (SEMC 2010)*, 4th - 8th September 2010, Cape Town, University of Cape Town.
2. Ibell, T., Darby, A., Orr, J. and Evernden, M., 2010. The role of structural fabrics in a sustainable concrete infrastructure. In: *International Conference on Sustainable Built Environment (ICSBE 2010)*, 12th - 14th December 2010, Kandy, Sri Lanka.
3. Orr, J.J., Ibell, T. J., Darby, A.P., Evernden, M.C., 2011. Innovative reinforcement for fabric formed concrete structures. In: *10th International Symposium on Fiber Reinforced Polymer Reinforcement for Concrete Structures (FRPRCS-10)*, 2-4 April 2011, Tampa, Florida.
4. Orr, J.J., Darby, A.P., Ibell, T. J., Evernden, M.C., 2011. Fibre reinforced polymer grids as shear reinforcement in fabric formed concrete beams. In *Advanced Composites in Construction 2011 (ACIC 2011)*, 6-8 September, University of Warwick, UK.
5. Orr, J.J., Darby, A.P., Ibell, T. J., and Evernden, M.C., 2012. Fabric formwork for ultra high performance fibre reinforced concrete structures. In *federation internationale du beton (fib) Symposium: Concrete Structures for Sustainable Community*, 11-14 June, Royal Institute of Technology, Stockholm, Sweden.
6. Orr, J.J., Darby, A.P., Ibell, T. J., Evernden, M., 2012. Durability enhancements using fabric formwork. In *federation internationale du beton (fib) Symposium: Concrete Structures for Sustainable Community*, Stockholm, 11-14 June, Royal Institute of Technology, Stockholm, Sweden.

7. Orr, J., Darby, A., Ibell, T. and Evernden, M., 2012. Optimisation and durability in fabric cast 'Double T' beams. In: *Second International Conference on Flexible Formwork (icff2012)*, 27-29 June 2012, University of Bath.
8. Orr, J. J., Darby, A., Ibell, T., Evernden, M. and Otlet, M., 2012. Design of innovative fabric formed beams in shear. In: *18th IABSE Congress "Innovative Infrastructures - Towards Human Urbanism"*. Seoul, South Korea, 19-21 September 2012.
9. Orr, J., Darby, A., Ibell, T., Evernden, M., Lava, P. and Debruyne, D., 2013. The shear behaviour of non-prismatic reinforced concrete beams determined using digital image correlation. In: *5th International Conference on Optical Measurement Techniques for Systems & Structures, (OPTIMESS 2012)*, 4-5 April 2012, Universiteit Antwerpen, Belgium.

#### 1.8.4. Articles

1. Orr, J.J., Ibell, T. J., Darby, A.P., Evernden, M.C., 2010. Fibre reinforced polymer reinforcement for fabric formed concrete structures. *International Institute for FRP in Construction (IIFC) Newsletter, July 2010*
2. Paine, K. A., Darby, A. P., Ibell, T. J., Evernden, M., Ioannou, S., Orr, J. J., 2010. *Concrete materials and structures research at the University of Bath*. Concrete, 44 (6), pp. 55-57.
3. Orr, J.J., Darby, A.P., Ibell, T.J., Evernden, M., 2012. *Flexible formwork for visual concrete*. Concrete, 46 (5) pp. 14-16.

#### 1.8.5. Other

1. Chair of the organising committee and Editor of the Conference Proceedings for the Second International Conference on Flexible Formwork, held at the University of Bath, UK, from 27-29th June 2012.
2. Speaker at the BRE Trust Conference, The British Museum, London, 15th May 2012.
3. Invited speaker at the two day conference 'Surface Design Show', held at The Business Design Centre, London, 7th-9th February 2012.
4. Invited speaker at the one day conference 'Visual Concrete', held at the Building Centre, London, 19th October 2011.
5. Speaker at the Institution of Structural Engineers' Young Researchers' Conference 2011 (17/03/11): 'Flexibly formed concrete structures'.
6. Speaker at the Western Counties Branch of the Institution of Structural Engineers, joint presentation to an evening meeting (07/02/11): 'Low carbon structural engineering research'. Orr, J., Bawcombe, J., Gates, P., Ioannou, S., Grist, E., Gross, C., and Isaac, P., 2011.
7. Speaker in the Buro Happold 'SHARE' presentation series, 16th March 2011. 'Fabric formed concrete'. Orr, J., and Garbett, J., 2011.







# Chapter 2      Fabric formwork

## Literature review

### 2.1. Introduction

Chapter 2 provides a review of the literature relevant to the development of fabric formwork. The history, development, current use and technology behind fabric formwork is introduced and analysed before the three main components of a fabric formed structure are discussed in Chapter 3.

### 2.2. Fabric formwork

#### 2.2.1. History

Using sheets of fabric or paper draped between timber floorboards as formwork for a reinforced concrete floor slab, Gustav Lilienthal effectively initiated the use of fabric formwork in concrete construction. His idea, shown in Figure 2.1 and used in a number of housing projects in Germany, was patented in 1899 (Lilienthal, 1899). Following closely from the work of Lilienthal, but having the distinction of being rather more prolific, James Waller used hessian fabrics in a patented method for the construction of structural elements that he named the ‘*Nofrango*’ system (Figure 2.2). Similar patents used fabric as formwork in hydraulic structures including canals (Waller, 1934) and he later used sheets of hessian draped between temporary arched formwork to create thin, efficient corrugated shells in a construction system later named ‘*Ctesiphon*’ after the Taq-i Kisra arch in the ancient Mesopotamian city of the same name.

The Ctesiphon system was used in a number of building projects across Europe (some of which are detailed by Conlon (2011)), but along with the construction of concrete shells in general the method later fell out of favour due to its labour intensive construction method, poor thermal performance and serviceability issues. The work of Waller did, however, go on to influence some of the great shell builders including Felix Candela, who used the ‘Ctesiphon’ method in one of his first shell projects (Sutherland *et al.*, 2001).

Further influence on the development of fabric formwork can be found in the fields of offshore and geotechnical engineering. As early as 1922 it was proposed by Johann Störe to use concrete filled fabric bags in the construction of underwater concrete structures (Lamberton, 1989) and remains a successful implementation of the technology.

A patent application (Hillen, 1969) describes a method for the production of what are now referred to as concrete ‘mattresses’, formed using layers of material joined at regular intervals and pumped full of concrete. Hillen’s method was successful in both the Netherlands and the United States and was quickly refined into what is now known as ‘filter point’ mattresses (Lamberton, 1989). Later innovations included systems for pile jacketing (Bindhoff and King, 1982) and vertical formwork. Filter point linings are widely used today in lieu of stone rip-rap in offshore construction, primarily because they avoid uplift issues by allowing water pressures to dissipate through the filter points.

Early adopters of fabric formwork as a construction technology were quick to notice its unique advantage in acting as a drainage layer for freshly cast concrete and an innovative method to capitalise on this was later patented by Bilner (1936). The advantage of permeable formwork in providing improvements in concrete durability is described in more detail in §2.6 on page 35.

It was, however, the introduction in the late 1960s of low cost, high strength, durable synthetic fabrics that precipitated the first revolution in fabric formwork, allowing complex shapes to be successfully formed (Lamberton, 1989).

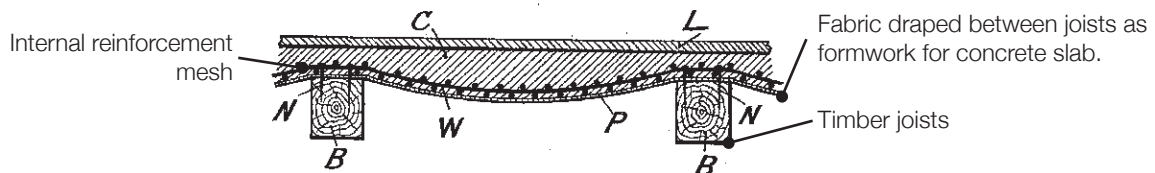


Figure 2.1: Lilienthal floor slab (Lilienthal, 1899).

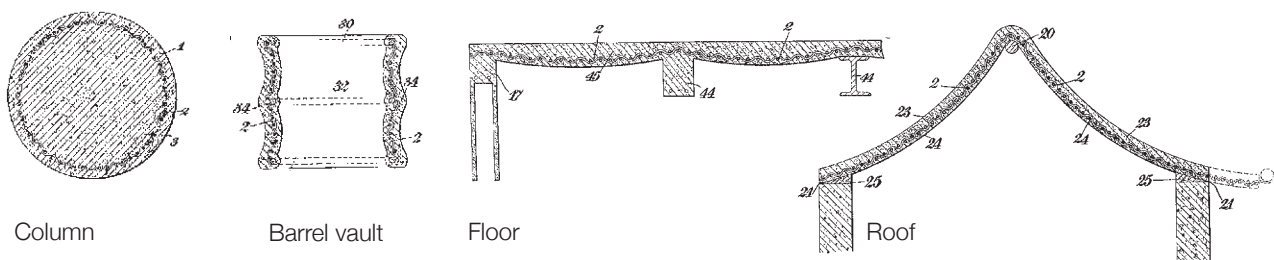


Figure 2.2: Patents by Waller (1934).



Figure 2.3: Ctesiphon construction and example (images Courtesy of the Irish Architectural Archive (93/67 Waller Album) and Conlon (2011)).

Initial interest in the use of fabric formwork as a construction method arose from its potential to reduce construction costs. Whilst the forms derived from the endeavours of Waller and Lilienthal may be described as architecturally significant, this was not necessarily the intention of those who designed them. The first true interest in the architectural possibilities of fabric formwork can perhaps be attributed to the Spanish architect Miguel Fisac (b.1913, d.2006), who in 1969 completed the 'MUPAG' centre in Madrid (Figure 2.4) where he developed and patented a method for the construction of prefabricated fabric formed wall panels. The influence of these architectural panels is seen in more recent work, such as '*P-Wall*' (Figure 2.5), exhibited at the Museum of Modern Art, New York in 2009.



Figure 2.4: The work of Miguel Fisac: top, left to right: IBM offices Madrid, (image courtesy flickr: Una Ballena de seis ojos [cinemascope]), House in Almagro, Santa Ana Fisac - covered porch (images used under creative commons license). Bottom, l-r: MUPAG, and Editorial DÓLAR (both Madrid) (images courtesy Miguel Fisac Foundation, provided by <http://tinyurl.com/yhabbyt>).



Figure 2.5: '*P-Wall*' cast using fabric formwork (image courtesy *P-Wall*(2009) by Matsys / Andrew Kudless).



Significant developments since the work of Miguel Fisac occurred simultaneously yet independently of each other. The Japanese architect Kenzo Unno developed a system for the in-situ casting of ‘zero waste formwork’ fabric formed concrete walls, as illustrated in Figure 2.6 and Figure 2.7(l), while commercial systems for the construction of simple fabric formed structures (Figure 2.7(r)) became available in the USA. Marketed under the ‘Fab-Form’ product name, their genesis can clearly be seen in the earlier work of Waller (Figure 2.2). Chandler and Pedreschi (2007) describe many further applications of fabric formwork that truly demonstrate its potential to realise complex architectural and geometric requirements.



Figure 2.6: Kenzo Unno. (l-r): Filter point walling, architectural use and frame restraint system (images courtesy Kenzo Unno and Mark West).

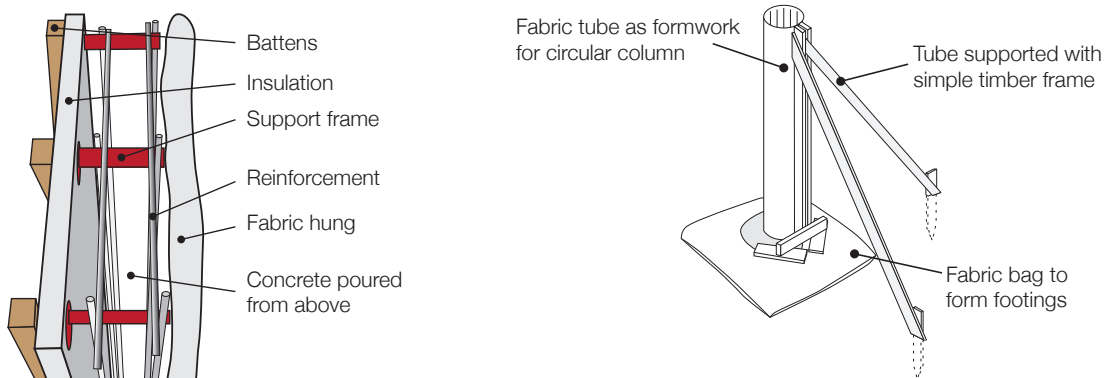


Figure 2.7: Zero waste formwork (l); Fab-form products (r).

### 2.2.2. Centre for Architectural Structures and Technology, University of Manitoba (CAST).

Perhaps the most influential area of research in recent years has been the work of Professor West at the University of Manitoba's Centre for Architectural Structures and Technology (CAST) - the world's first research centre dedicated to the development and promulgation of fabric formwork for concrete structures. The early work of Unno (Figure 2.6) has been developed at CAST to include precast panels which can be cast both horizontally and vertically. In general, these panels have been non-structural, but their funicular forms in fact make them well suited to load carrying. The method involves stretching fabric over a steel frame and pouring concrete to provide a lightweight panel whose support conditions can be altered as required to make multiple unique forms from a single mould. Vertically cast panels can be sprayed with shotcrete to produce interesting and beautiful forms, Figure 2.9.



Figure 2.8: Columns made at CAST (images courtesy CAST).



Figure 2.9: Precast panels (images courtesy CAST).



Figure 2.10: Beams (CAST, l and c) and Garbett (2008) (r).

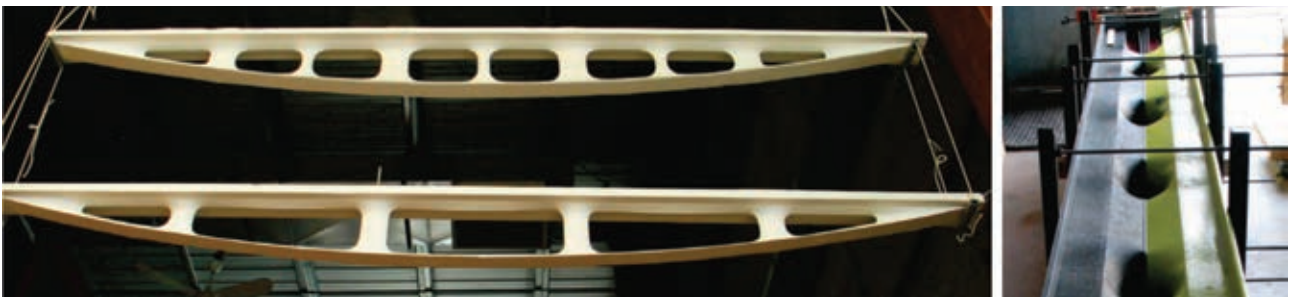


Figure 2.11: Trusses (images courtesy CAST).



Figure 2.12: Shells (images courtesy CAST).

The construction of beams and trusses has been investigated both at CAST and the University of Bath. Work at CAST has produced beams of up to 12m in span, as shown in Figure 2.10. At the University of Bath, Balliss (2006) and Garbett (2008) have both produced small span optimised beams of similar profiles, although problems have been encountered during testing (as discussed in §2.5 on page 27). Trusses, although more complex to form, can also be cast using fabric, as illustrated in Figure 2.11. As a truss works primarily with discrete tension and compression members, casting a concrete truss at first appears nonsensical. However, the bottom chord here is in fact a prestressed steel cable surrounded by concrete, thus creating an efficient and interesting structure.

Vaults and shells have long relied on fabric for form finding, with the process of hanging fabric between supports to determine a form being used extensively by both Isler and Gaudí (Chilton, 2000). Hanging models are in pure tension and by inverting the structure a pure compression form is found in a process that today may equally be carried out computationally using processes such as dynamic relaxation. Work at CAST has also investigated the use of fabric to form small span shells (Figure 2.12). Formed from a single sheet of fabric held on a timber frame these elements are cast by hand before being turned upside down for use in construction.

### 2.2.3. Offshore structures

Whilst the popularity of fabric as a construction method for shells, floors and panels has varied over the past one hundred years, construction using fabric formwork in offshore environments has remained successful and in the UK is estimated to be the predominant use for fabric formwork. The high cost, technical demands and potentially extreme environmental loading encountered when casting concrete underwater means that timber shuttering is often not a viable option. In addition, forms cast underwater tend to be mattresses, pillows or pile caps, which are both geometrically simple and have no real aesthetic requirements. Therefore, a fabric bag, with pre-sewn zips, folds and seams offers many advantages.

The current methods used in this field are exemplified by fabric pillows installed in Venice as part of a new flood defence system (M Hawkswood, *pers. comm.*, 21<sup>st</sup> October 2009). Each prefabricated fabric pillow (Figure 2.13) is lowered into position before a diver attaches a concrete hose onto a pre-sewn joint. The concrete is then pumped under pressure to inflate the entire structure underwater, with 'break-tags' used to ensure correct deployment of the fabric pillow. The construction of more conventional structures is described in §2.3.

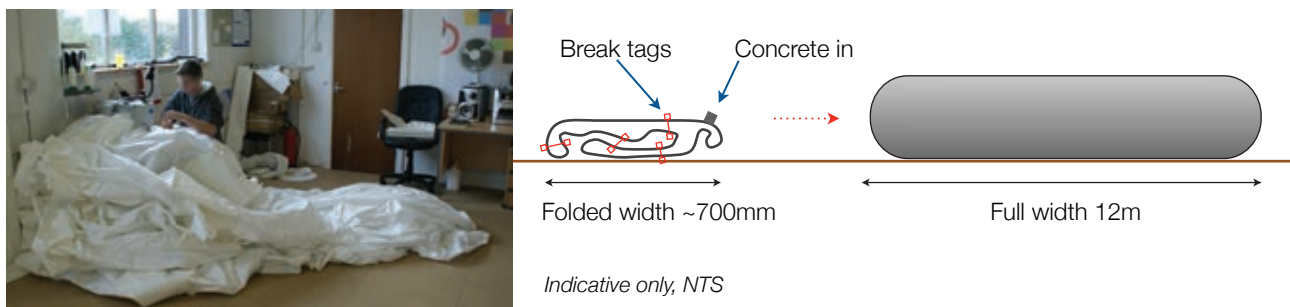


Figure 2.13: Apprentice sewing one half of an underwater bag (l); Indicative folded and expanded dimensions (r).



## 2.3. Construction methods

Construction of concrete structures using fabric formwork is at present limited to a small group of research centres and specialist companies. Some of the available techniques are presented in the following section, with the aim of informing the central argument that fabric formwork can provide a globally accessible method for the construction of low carbon, optimised concrete structures.

Eighty-four percent of the world's population lives in developing countries, defined by the World Bank (2009) as all countries with a gross national income (GNI) per capita of less than US\$11,906. Whilst a discussion of construction practices, techniques and quality across the globe is outside the scope of this thesis, it is apparent that in many parts of the developing world high quality concrete construction is not widely available. One aim of this thesis is therefore that construction using fabric formwork should be both cost effective and easily achieved.

Construction using fabric formwork may thus range from simple sheets of fabric secured on timber battens, reinforced with bent steel bars right through to three dimensionally woven fabric formed bags using advanced composites that may become a feasible alternative to the CNC machining of complex formwork shapes. Current methods used in fabric formed construction are presented below, where beams, columns, shells and wall panels are considered.

### 2.3.1. Beams

The construction of concrete beams using fabric formwork requires that the fabric be supported prior to casting in such a manner that it takes up the desired final geometry during the concreting process and retains it as the concrete hardens. In addition, provision must be made to support any internal reinforcement. These challenges have been addressed in a number of ways, the most relevant of which are described below.

#### 2.3.1.1. Flat sheet and spline mould

The flat sheet and spline mould method uses a metal bar to vertically pretension a single rectangular sheet of fabric held on a timber forming table, Figure 2.14. By pre-tensioning the fabric, the volume of concrete in the tension zone is reduced, optimising the beam section. A spline with sufficient elastic capacity must be used to pretension the fabric as any plastic deformation during or prior to pouring will change the shape of the beam.

#### 2.3.1.2. Keel mould

The keel mould (Figure 2.15) uses two sheets of fabric, held vertically and secured between sheets of plywood cut to the desired profile (the keel). The fabric is pretensioned from above to both form the desired shape and to prevent the fabric from wrinkling during casting.

### 2.3.1.3. Pinch mould

The pinch mould method has been used to create trusses. Two sheets of fabric, sandwiched between rigid panels, are 'pinched' together at predefined locations by protruding elements that control the cross section thickness. When set to meet in the centre, these pinches can be used to create truss elements, such as those shown in Figure 2.16. Whilst the method is relatively simple, more formwork is required and each timber pinch mould can only be used for a specific geometry.

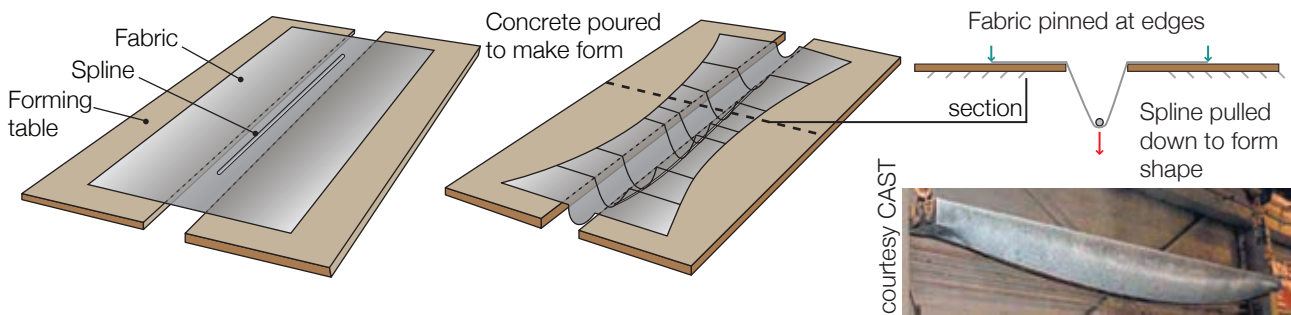


Figure 2.14: Spline mould construction method.

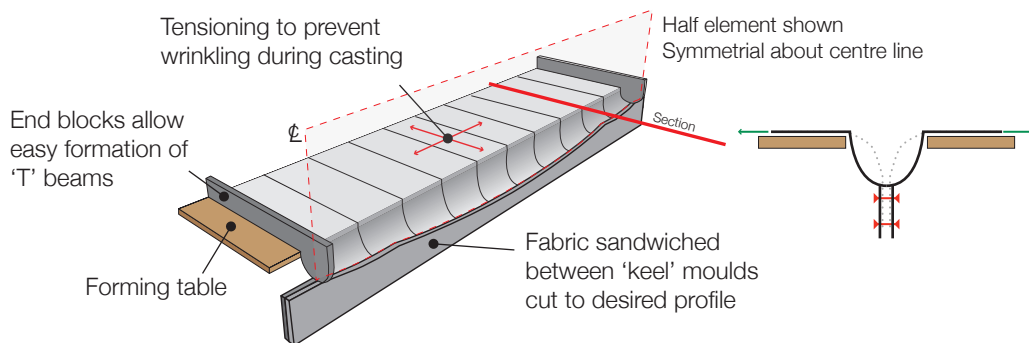


Figure 2.15: Keel mould construction method.

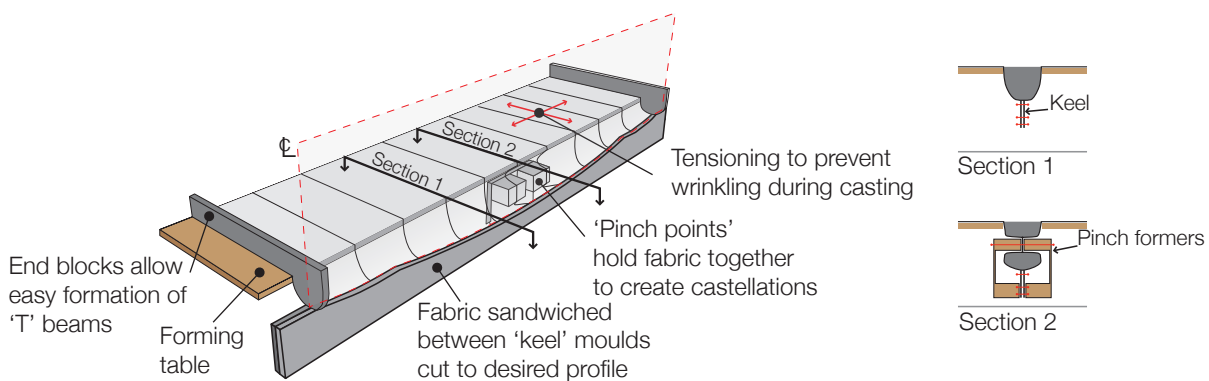


Figure 2.16: Pinch mould method.

### 2.3.1.4. Alternative methods

Following from the methods developed at CAST, Bailiss (2006) and Garbett (2008) used a 'U' shaped table to form optimised beams, Figure 2.17. The fabric is simply hung from a slot cut in the table top and concrete is poured into the mould to make the form. Wrinkling of the fabric is avoided by proper arrangement of fastenings and by pretensioning along the fabric edge. Work undertaken at the University of Edinburgh in the development of fabric formed T-beams (§2.5.2) has followed a broadly similar technique and was equally successful.



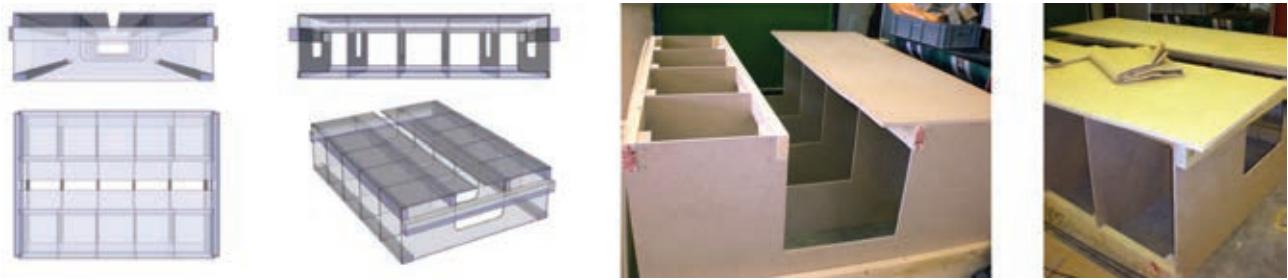


Figure 2.17: Forming tables (after Bailiss, 2006 and Garbett, 2008).

To achieve greater optimisation of the beam section, Garbett (2008) used external timber formers, clamped to the beam in the midspan to create a 'key' shaped profile, as shown in Figure 2.18. This construction method was shown to be less than ideal, as the timber was difficult to fix in position during casting and the resulting beam did not conform to the designed dimensions.



Figure 2.18: Variable section beam formwork (after Garbett, 2008).

### 2.3.2. Shells

The construction of shell structures has been carried out at CAST. The first shell was constructed in 2004, using a simple hanging sheet of geotextile fabric coated in Glass Fibre Reinforced Concrete (GFRC). More recently, rigid timber frames have had fabric hung between them, Figure 2.12. Some shells have been reinforced with Carbon Fibre grids and sections as thin as 30mm have been cast. The actual contribution of the carbon grids to the reinforcement of the shell was not determined at the time: this is an area that requires further investigation.

### 2.3.3. Wall panels

The construction of wall panels has been carried out at both CAST and the University of Edinburgh. The simplest method involves stretching a sheet of fabric over a steel frame, with supports underneath to produce patterns, corrugations and details as desired. Concrete is then sprayed or poured over the fabric to produce a lightweight funicular structure, Figure 2.19(l). Additional research at CAST has investigated methods to create thin shell panels by spraying a layer of shotcrete onto a suspended sheet, as shown in Figure 2.19(r).

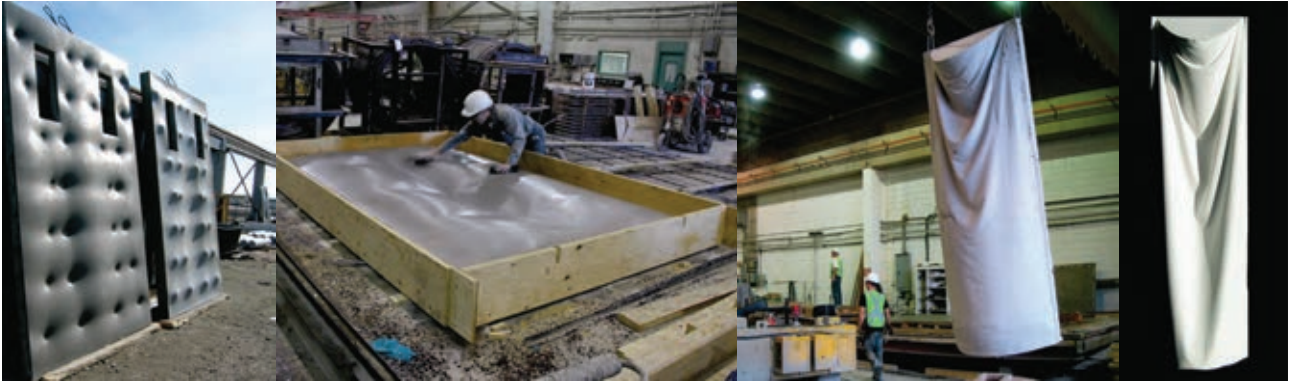


Figure 2.19: Wall panels. Steel frame (l) and vertical sheets (r) (West, 2007).

### 2.3.4. Columns

Circular column sections are easily created using single rectangular sheets of fabric, as shown in Figure 2.7 on page 14, and demonstrated in the commercially successful work of Fab-Form Industries. Researchers at CAST have also developed a method for the construction of columns with complex geometry using just two sheets of fabric and a plywood support system, as illustrated in Figure 2.20. Based on a comparison with work undertaken by Lafarge on the construction of similar 'Y' shaped columns, the steel moulds for which cost tens of thousands of Euros to manufacture (D Corvez, *pers. comm.*, June 28th 2010), the materials used could potentially cost just 1/1000<sup>th</sup> of their steel equivalent while also allowing each column to be different and providing a far more organic, tactile, architecturally interesting surface finish. Coupled with a simple construction method, these advantages are simply too great to be ignored.

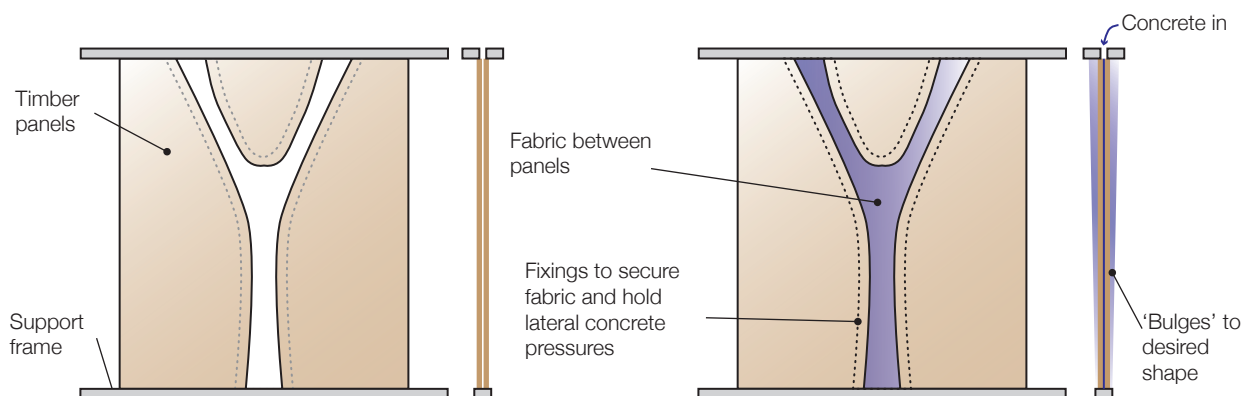


Figure 2.20: The construction of 'Y' shaped columns.



Figure 2.21: Achieving a variable column geometry - examples courtesy CAST.

### 2.3.5. Material consumption

The costs of conventional reinforced concrete construction generally associated with timber formwork (transport, storage and maintenance) may be reduced when fabric formwork is used, as evidenced by the projects presented above. Large volumes of timber may be required in conventional construction to resist the lateral loads generated by wet concrete during pouring and to provide a flat finished surface. In fabric formed structures, there is no desire for flat surfaces and hence this lateral force need not be resisted. Instead, the fluid pressures are used to create the desired shape. Pallet (1994) suggests that the use of fabric formwork may also achieve labour cost savings, as formwork stripping and work cycle times are improved when compared to timber formwork.

Furthermore, when used on ground bearing elements the fabric allows formwork for uneven or rocky ground to be produced quickly and efficiently. In addition to material savings in construction, the design of optimised concrete structures offers further and potentially more significant material use reductions, as described in this thesis.

### 2.3.6. Summary

Construction methods for fabric formed structures are unconventional and varied. The methods presented above are by no means exhaustive and it is likely that new construction techniques will be developed as applications require them. It is, however, clear that fabric formwork can provide a simple method by which low carbon, optimised concrete structures may be formed. From the work presented above, the use of fabric formwork can be divided into four main groups, as shown in Figure 2.22, that encompass the shells, beams, floor plates, columns and façade elements with which an entirely fabric formed structure could be constructed.

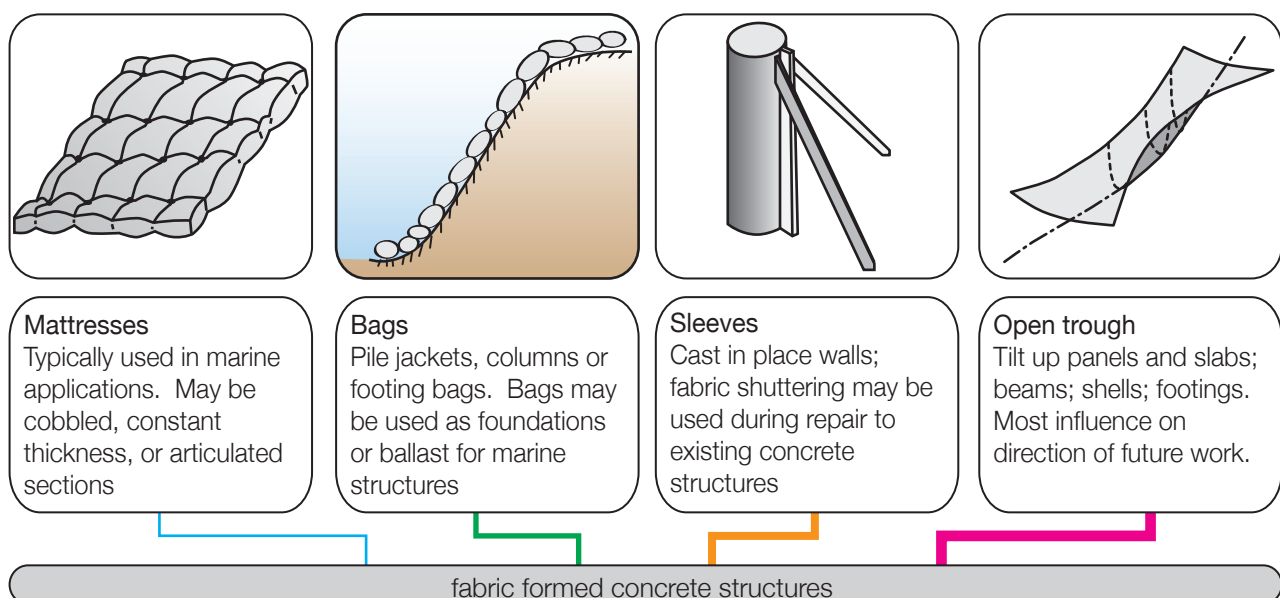


Figure 2.22: Fabric formwork groupings (after West et al., 2007).

§2.2 has provided a brief introduction to the history and construction of fabric formed concrete structures. Design techniques and structural test data are investigated in the following sections, before issues surrounding surface quality (§2.6) and material consumption (§2.7) are considered in greater detail.

## 2.4. Design

### 2.4.1. Introduction

The design and optimisation of reinforced concrete structures encompasses a broad spectrum of techniques that vary greatly in complexity, accuracy and popularity. Those that are, or have previously been, pertinent to the design of fabric formed structures are considered briefly in the following section. Greater detail for some of the methods later used in this thesis is provided in Chapter 3.

### 2.4.2. Graphic statics

Graphic statics, which describes a hand drawn method to investigate static forces, has been used since the 16<sup>th</sup> Century when the Dutch mathematician Simon Stevin first represented force as a vector (Allen *et al.*, 2010). Engineers including Varignon (1654-1722), Poleni (1683-1761), Maxwell (1831-1879) and Cremona (1830-1903) have all published work investigating the resolution of static forces, yet Karl Culmann (1821-1881) is widely considered as the founding father of graphic statics after his comprehensive thesis on graphical techniques (Culmann, 1865).

Simple examples of graphic statics (Allen *et al.*, 2010) may easily be extended to produce form-finding methods for funicular structures, cantilevers and arches, as well as constant force trusses. Graphic statics is particularly efficient for the design of trusses and this has been used by researchers at CAST (*pers comm.*, M West, 2010). An efficient truss may be designed to have a constant force in either top or bottom chord - in such a situation, the constant force members use material very efficiently, while in the other chord the force doesn't vary very much and diagonal members can often be eliminated (Allen *et al.*, 2010).

The constant force truss thus has a direct corollary with the design of fabric formed beams, where a constant force in the 'tension chord' of the reinforced concrete beam is assumed at the ultimate limit state (§2.4.3.2 and Chapter 5). In addition, by designing the fabric formed beam to follow the bending moment diagram (as is the case for a constant force truss) the vertical component of force in the longitudinal steel theoretically balances the applied vertical force for equilibrium and thus such beams may be termed 'zero resultant shear' elements. The practical difficulties of achieving such a design are addressed and explained in Chapter 8 on page 245.

### 2.4.3. Sectional analysis methods

Sectional analysis methods are deeply embedded in codes of practice for concrete structures and deal with combinations of axial load, moments and shear forces to assess the load resistance of structural elements. Such approaches often require that certain assumptions be made (such as plane sections remaining plane) but they are nevertheless powerful design tools. Using sectional analysis techniques requires the design process to be split into distinct tasks. In the frame subjected to the loads shown in Figure 2.23(l), the member forces are first determined by elastic analysis. With these values, the concrete section is analysed by considering the response of the cracked section at each point, as illustrated in Figure 2.23(r).

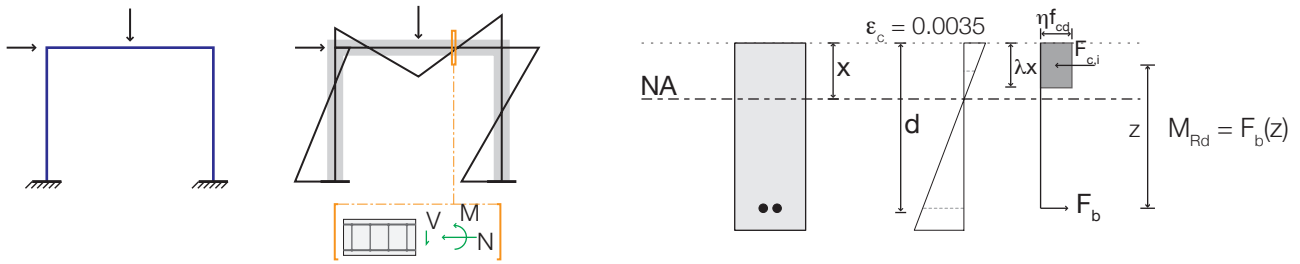


Figure 2.23: Sectional analysis for a frame.

#### 2.4.3.1. Shear stresses

Most designers are comfortable with the analysis of concrete sections in flexure, and this is reflected in design codes of practice (although fundamental assumptions such as the biaxial behaviour of concrete in compression have been challenged, as discussed in §3.2.1 on page 49). In contrast, the analysis of concrete sections in combinations of shear and bending is less well understood, but recent advances are beginning to redress this. In particular, the use of modified compression field theory for sectional analysis (described in §4.2.5.3 on page 92 and utilised in Chapter 5 and Chapter 6) has been successful (Bentz, 2000b).

Traditionally, shear stress calculations are undertaken using Jourawski's method, which assumes that plane sections remain plane and that the section behaves as a linear elastic material. Consider the beam shown in Figure 2.24, where a free body diagram is drawn for the shaded element between cut planes 'A' and 'B'. By drawing the stress profile at both faces, the difference in moment between the two sides is demonstrated by the change in gradient of the stress profiles. The change in moment requires a horizontal force 'H' to be applied to satisfy equilibrium and the vertical shear stress on the cut face (1) is then found to be equal to 'H' by summing moments about a suitable point. This derivation is used to determine the familiar Eq. 2.1. Hence, the shaded region defines the shear stress profile of the section (Bentz, 2000b), and the shaded area at any depth is proportional to the derivative of the shear stress with respect to beam depth.

In a section with a linear variation in stress between points this relationship yields the familiar parabolic variation in stress. For non-linear materials, it may be sensible to assume that plane section remain plane, but the variation in stress over the depth of the element should be determined based on the change in longitudinal stiffness of the element over its depth. Such a procedure was undertaken by Bentz (2000b) by dividing the element into multiple horizontal layers. The shear stress distribution in a cracked concrete section is illustrated in Figure 2.25.

Bentz (2000b) provides a full description of a 'longitudinal stiffness method' that follows this procedure, and by dividing the element into sections of approaching zero width, more accurate calculations of vertical shear stress distribution in any cross sectional shape can be determined. However, such an approach is computationally intense and not well suited to design codes of practice for complex shapes. Most concrete design codes instead continue to rely on empirical equations for shear capacity, a topic covered in much greater detail in §3.5.



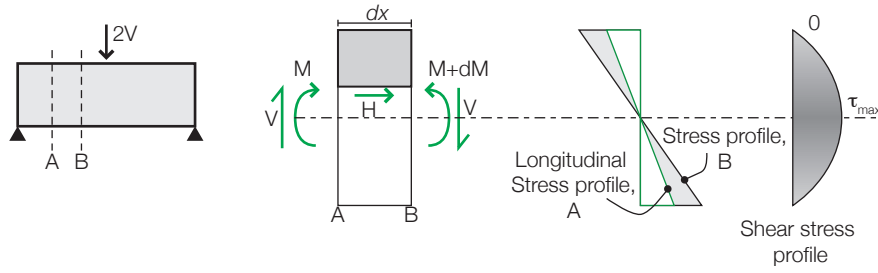


Figure 2.24: Jourawski's method for shear stress.

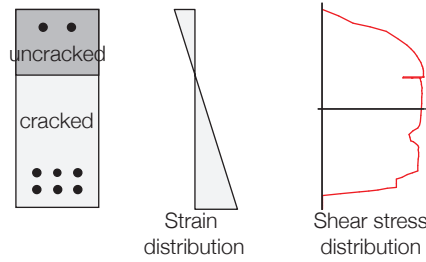


Figure 2.25: Shear distribution in a simple cracked section.

$$v = \frac{VQ}{Ib} \quad \text{Eq. 2.1}$$

Where  $V$  = total shear force;  $Q$  = first moment of area;  $I$  = Second moment of area;  $b$  = width of section

#### 2.4.3.2. Codified design

The codified design of fabric formed concrete members has been undertaken at the University of Bath, where a method for the flexural design of bending moment shaped fabric formed beams to BS8110-1 (1997) was developed by Bailiss (2006) and later used by Garbett (2008). Flexural strength is determined by using the plane sections hypothesis, which is widely accepted as an accurate and reliable design method that itself forms the basis of many concrete design codes, including BS EN 1992-1-1 (2004) and ACI 318 (2005). For steel reinforced structures, requiring the steel to yield defines the lever arm required to resist the applied moment, which in turn defines the section depth, as given by Eq. 2.2 and summarised in Figure 2.26. Empirical equations were used by both Bailiss and Garbett to predict the hydrostatic shape of the beams, test details of which are provided in §2.5 on page 27.

$$d = \left( \frac{0.45F_c}{0.67f_{cu}(0.9b)} \right) + \left( \frac{M}{F_s} \right) + \left( \frac{\phi}{2} \right) + c \quad \text{Eq. 2.2}$$

Where  $F_c$  is the force in the concrete compression block;  $f_{cu}$  = concrete compression strength,  $b$  = breadth,  $M$  = moment,  $F_s$  is the force in steel;  $\phi$  is bar diameter, and  $c$  is the concrete cover

For a beam without transverse reinforcement, the section depth,  $d$ , required to carry shear forces is determined by equating the shear stress on the section under consideration (Eq. 2.3) to the concrete shear capacity ( $v_c$ ) as determined in BS8110-1 (1997) (Eq. 2.4), resulting in Eq. 2.5.

$$v = \frac{V}{bd} \quad \text{Eq. 2.3}$$

$$v_c = 0.79 \left( \frac{100A_s}{bd} \right)^{1/3} \left( \frac{400}{d} \right)^{0.25} \left( \frac{f_{cu}}{25} \right)^{1/3} \left( \frac{2d}{a_v} \right) \quad \text{Eq. 2.4}$$

$$d_1 = \left( V / 0.79b \left( \frac{100A_s}{b} \right)^{1/3} 400^{0.25} \left( \frac{f_{cu}}{25} \right)^{1/3} \right)^{12/5} \quad \text{Eq. 2.5}$$

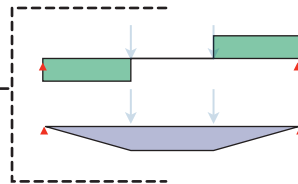
1. Define span, area of longitudinal steel and concrete strength.



2. Define loads



3. Divide into sections



2a. ULS shear and moment envelopes

3a. Analyse each section

Calculate beam effective depth separately for flexure and shear

Take maximum value for  $d$

Iterate for 'n' sections

4. Plot optimised shape

Figure 2.26: Sectional analysis technique for fabric formed elements (after Garbett, 2008).

By comparing the section depth required for moment and shear at each section along the length of the beam, the optimised beam elevation is plotted, as illustrated in Figure 2.27. However, design to BS8110-1 (1997) allows sections to have no shear reinforcement only when  $v < 0.5v_c$ , and it is therefore likely that previous method do not in fact satisfy BS8110-1 (1997). Instead, if  $v = 0.5v_c$  is used to determine an equation for  $d$ , then Eq. 2.6 is obtained, which results in a five-fold increase in the required effective depth of a section, Eq. 2.7. This is something of a concern, and suggests that the BS8110-1 (1997) empirical equations for  $v_c$  are unsuited to the analysis of fabric formed beams that are not transversely reinforced.

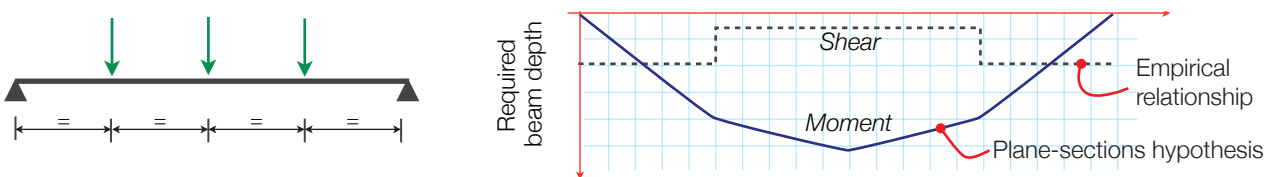


Figure 2.27: BS8110 analysis, required depth based on equations for moment and shear capacity.

$$d_2 = \left( V / 0.395b \left( \frac{100A_s}{b} \right)^{1/3} 400^{0.25} \left( \frac{f_{cu}}{25} \right)^{1/3} \right)^{12/5} \quad \text{Eq. 2.6}$$

$$\frac{d_2}{d_1} = 2^{12/5} = 5.28 \quad \text{Eq. 2.7}$$

#### 2.4.4. Material consumption

Fundamental to the design processes utilised in previous research has been the understanding that the resulting optimised element will consume less material than one designed as a prismatic member. Such savings in material use are taken in addition to those that arise by virtue of the simplified construction process (§2.3.5 on page 21). Previous research in which fabric cast elements have been designed and structurally tested (as is described in greater detail in §2.5) has allowed comparisons between the material use of the optimised element and that of a prismatic structure with the same ultimate load capacity to be made.

Analysis of the available data is presented in Table 2.1, where it can be seen that material savings of up to 50% are regularly achieved in fabric cast concrete beams, clearly demonstrating the potential for fabric formwork to provide a sustainable option for the construction industry. Further assessment of the results and structural tests undertaken in achieving these results is presented in §2.5 on page 27.

Table 2.1: Material savings using fabric formwork.

Centre	Researcher	Date	Material savings (% , as compared to an 'equivalent strength' prismatic section)
CAST, University of Manitoba	Hashemian, F., and West, M ( <i>pers comm.</i> , 29/04/10)	2010	30%
University of Edinburgh	Lee, D	2010	Up to 40%
University of Bath	Bailliss, J	2006	30-50%
University of Bath	Garbett, J	2008	30-50%

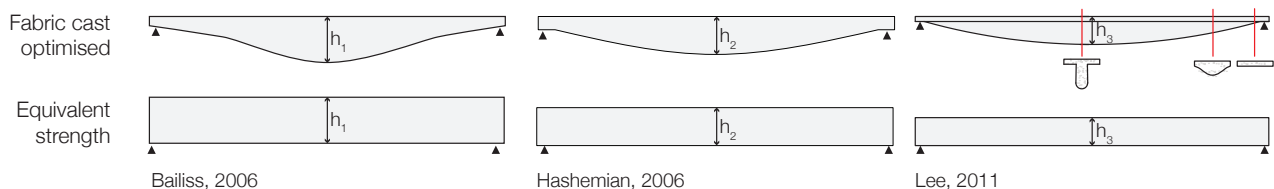


Figure 2.28: Summary of elements tested and material savings.

#### 2.4.5. Summary

Whilst the flexural analysis of fabric formed beams has previously been considered by applying a plane sections based approach, the empirical basis of most codified approaches to shear design is hard to verify for use in fabric formed members and approaches that combine shear and bending moments should instead be used. Such methods are developed and discussed in more detail in subsequent chapters before being applied to the design and analysis of fabric formed beams. This thesis concentrates primarily on the use of sectional analysis methods as they are well understood by practicing engineers, and can show significant accuracy when appropriate methods are used. Alternative methods are, however, discussed in §4.3 on page 95 and developed further in Chapter 10.



## 2.5. Structural testing

With the design and construction techniques for fabric formed structures explained in detail in the preceding sections, the current body of destructive testing data that exists for fabric formed beams is now considered, as summarised in Table 2.2.

*Table 2.2: Available structural test data for fabric formed concrete beams.*

Centre	Researcher	Date	Test Outline
CAST, University of Manitoba	Hashemian, F	2012	3 bending moment shaped, 4 orthogonal beams, 2 cambered bending moment shaped beams and a number of 'beam end' tests.
University of Edinburgh	Lee, D	2010	Bending moment shaped T-beams.
University of Bath	Bailliss, J	2006	Four tests on bending moment shaped beams, designed to BS8110
University of Bath	Garbett, J	2008	Two tests on bending moment shaped beams. Optimisation using external formers undertaken.

### 2.5.1. University of Manitoba

Hashemian (2012) considers the structural behaviour of bending moment-shaped reinforced concrete beams through a series of tests on prismatic and non-prismatic sections. Working from the hypothesis that by providing inclined compression or tension forces, diagonal tension at the support zones can be eliminated, the work considers elements without transverse reinforcement. In doing so, it is proposed that the material use requirements in terms of steel and concrete will be reduced.

Three series of tests were undertaken in this work. In the first, a comparison was made between the behaviour of bending moment shaped and prismatic sections, as detailed in Figure 2.29. Design of the steel position was undertaken using a sectional approach, satisfying the resisting moment along the length of the beam according to the provisions of CSA A23.3 (2004). The beams were cast in a timber mould rather than in fabric, (Figure 2.30(l)), a method that was undertaken to ensure complete repeatability of the tests.

All beams were tested in six point bending, with two 25mm diameter deformed steel bars as longitudinal reinforcement. No transverse reinforcement was used and anchorage of the longitudinal bars was provided by means of a structural weld to an end plate, Figure 2.30(r). Load-deflection predictions based on a finite element model were made for each test, and good agreement was found in the elastic range.

All beams were then tested to destruction. The prismatic beams with linear longitudinal steel (B1) all failed catastrophically in diagonal tension at the supports, Figure 2.31. This was the expected failure mode, as no transverse steel was present in any of the tests. The orthogonal beams with curved longitudinal reinforcement (B2) also failed close to the support zone in a more complex combination of failures, all of which propagated from the position of the tensile reinforcing steel, Figure 2.32. The variable section beams (B3) failed in a similar manner, Figure 2.33, suggesting a limited the influence of the inclined steel. Such results are in agreement with later work undertaken at the University of Bath (§2.5.3) and are discussed further in §8.2.5 on page 256.

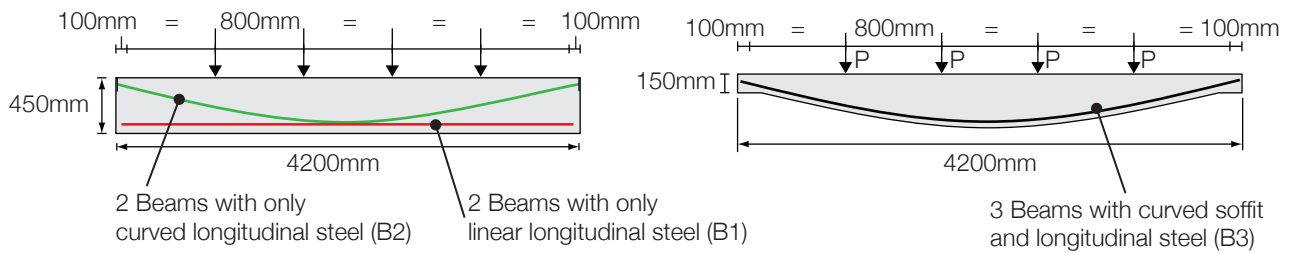


Figure 2.29: Prismatic (l) and Curved (r) beams (Hashemian, 2012).

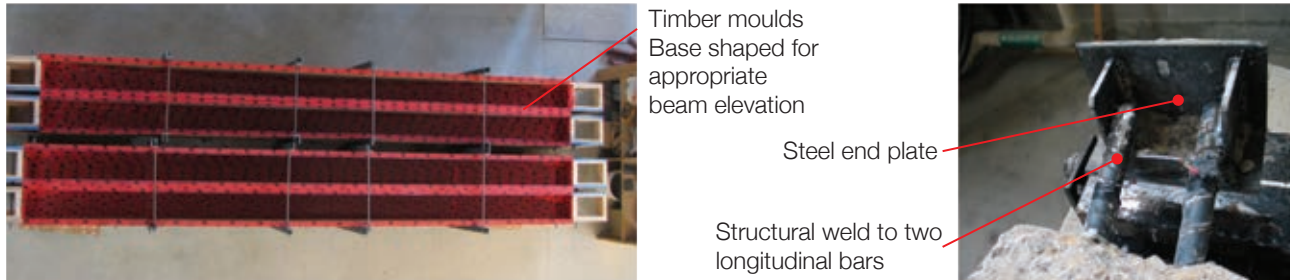


Figure 2.30: Construction method (l); End plate detail (r) (Hashemian, 2012).



Figure 2.31: Failure, orthogonal beams with linear reinforcement (B1) (Hashemian, 2012).

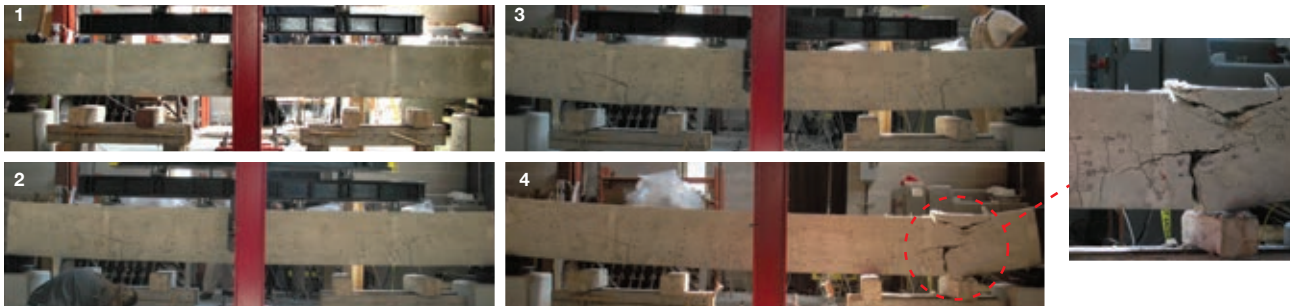


Figure 2.32: Failure, orthogonal beams with curved reinforcement (B2) (Hashemian, 2012).



Figure 2.33: Failure, variable section beams (B3) (Hashemian, 2012).

Load deflection results for all three sections are shown in Figure 2.34. Specimen B2 had the greatest capacity (200kN total), illustrating the beneficial effect of inclined reinforcement in providing shear capacity at the supports. B1 failed at 182kN, but exhibited a much stiffer response. B3 failed at 160kN, but interestingly appears to have precisely the same stiffness as the orthogonal beam with inclined steel.

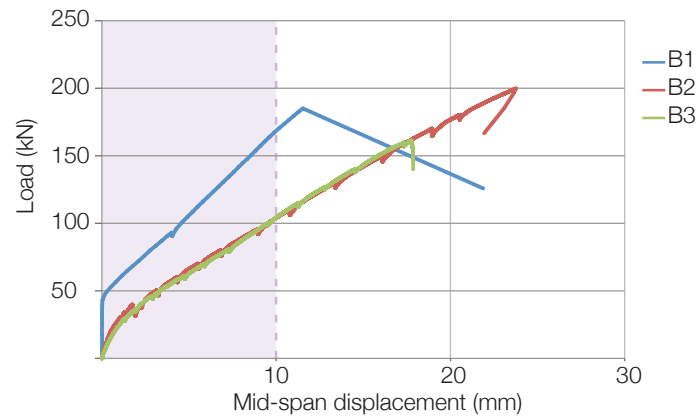


Figure 2.34: Load deflection response for a selection of beams tested (courtesy Hashemian, F).

It is notable that in all the curved beams (3 tests) failure occurred in a brittle manner at the end support. In the rectangular beams with inclined shear reinforcement an interesting failure mode (Figure 2.32) is recorded that bears resemblance to similar tests undertaken in §8.2.5. A control beam, designed to CSA A23.3 (with transverse reinforcement) had a ductile failure mode. This is considered further in this thesis, where the reasons for brittle failure modes in sections with inclined steel are explored in detail in Chapter 8, where design methods and an understanding of why such failures occur is presented.

Hashemian (2012) also made interesting comparisons between the beam tests at the serviceability limit state. If a new approach can be achieved in which diagonal tensile failure at the support is avoided, the performance of the variable section beam should equal that of the orthogonal beam with curved bars. Taking a 10mm deflection limit as the serviceability criteria for the beams, it is seen that those sections with curved bars carry 60% of the load of Beam 1. To achieve the full benefit of variable section beams the requirements for both serviceability and ultimate limit states must be carefully considered.

#### 2.5.1.1. End section tests

After carrying out the tests described above, Hashemian (2012) then considered the behaviour in shear of the tapered end zone in more detail through a series of eight 'end beam' tests. Some issues with the test method are identified by Hashemian (2012) and as such the result of these beam tests (summarised in Figure 2.35) were used primarily to verify and refine the Finite Element model developed later in the work. Similarly to the beam tests described above, all of the end beam test failed in a brittle manner at the support zone.

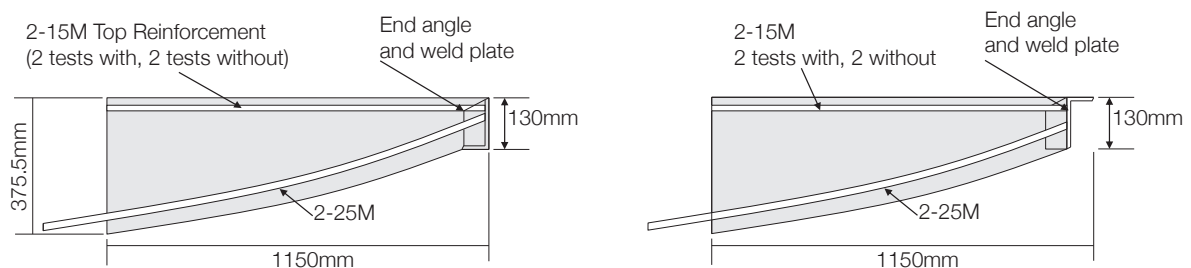


Figure 2.35: End beam tests summary (after Hashemian, 2012)

### 2.5.1.2. Cambered beam tests

Following from the results of beam and end-beam tests, Hashemian (2012) then considered the addition of a top camber to control the compression path towards the supports. This approach has interesting corollaries with the work undertaken in this thesis in both Chapter 6 and Chapter 8.

A summary of the cambered beams is provided in Figure 2.36. Although the addition of a camber does increase the concrete volume by 5%, it was shown by Hashemian (2012) that such an approach could provide additional strength to the beam section, although both beams tested did fail in a brittle manner (as shown in Figure 2.36).

It was also shown that in the cambered beam a greater proportion of the steel had yielded along the beam when compared to the rectangular beam (but crucially, the whole length of the bar had not yielded). The effect of assumptions relating to steel yielding and anchorage of the bars are explored in more detail in Chapter 7 and Chapter 8.

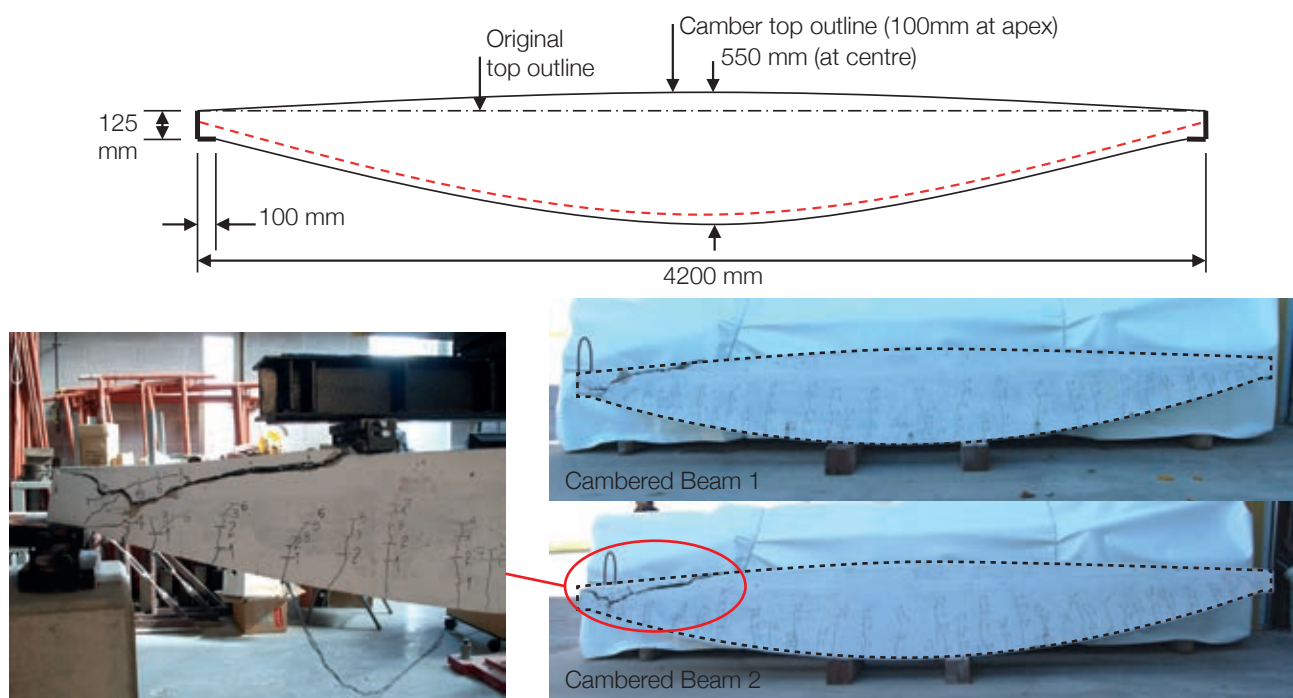


Figure 2.36: Curved Cambered Beam tests - summary (after Hashemian, 2012).

Hashemian (2012) set out to demonstrate that by providing inclined longitudinal steel, transverse reinforcement could be omitted in curved beams. Although the tests provided encouraging results, the presence of brittle failures in all the non-prismatic beams tested suggests the end zone behaviour should be considered in more detail. Approaches for the design of tapered end zones are considered in greater detail in Chapter 7.



### 2.5.2. University of Edinburgh

Work undertaken by Lee (2010) at the University of Edinburgh has focused on the design of T-Beam sections for use as precast floor elements, and again considered how elements could be designed without transverse reinforcement. Through a process of iteration the variables of flange thicknesses, web geometry, the percentage of steel reinforcement, the type of anchorage and the compression steel (Lee, 2010) were all studied.

Two beam designs and two longitudinal reinforcement layouts (Figure 2.37) were tested in twelve separate tests. Anchorage of the longitudinal bars was not possible by conventional means (such as hooks) due to the limited end zone space in the beam and was provided instead by a single or double orthogonal welded 'T' bar, as shown in Figure 2.38.

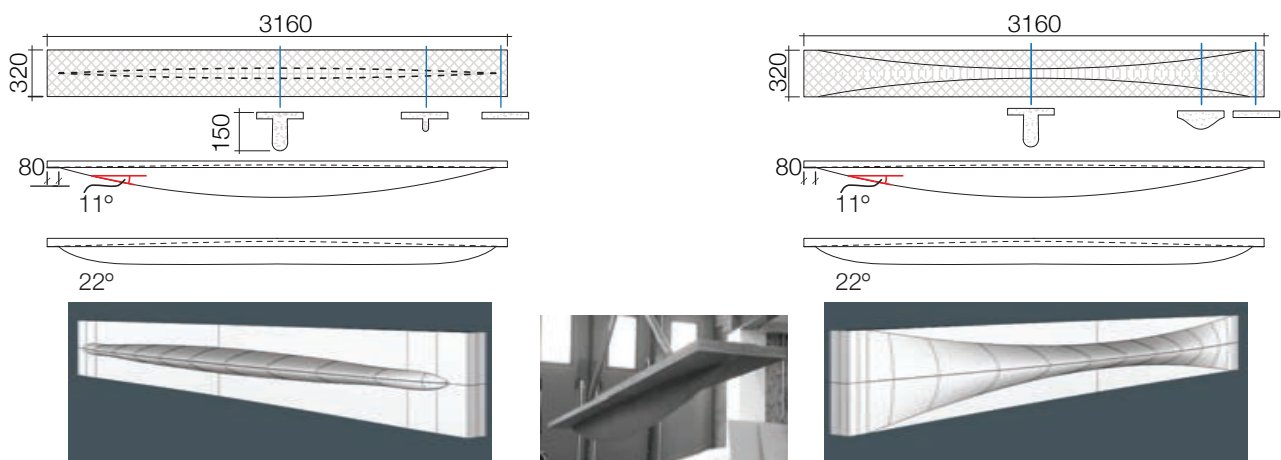


Figure 2.37: Type A (l); Type B (r) (after Lee, 2010).

Longitudinal reinforcement was designed initially to follow a catenary curve, with an  $11^\circ$  inclination required at the supports. Such a flat angle ensured that a significant horizontal component of force was created in the end zone of the beam, and it is suggested that this caused a 'pull out' type behaviour in which the concrete around the anchorage zone split in tension. By doubling the inclination of the bar to  $22^\circ$ , the horizontal component of force was reduced. The steeper bar, combined with a wider end zone (Type B, Figure 2.37(r)) was found to give the optimum beam behaviour, with only one test failing in shear at the supports.

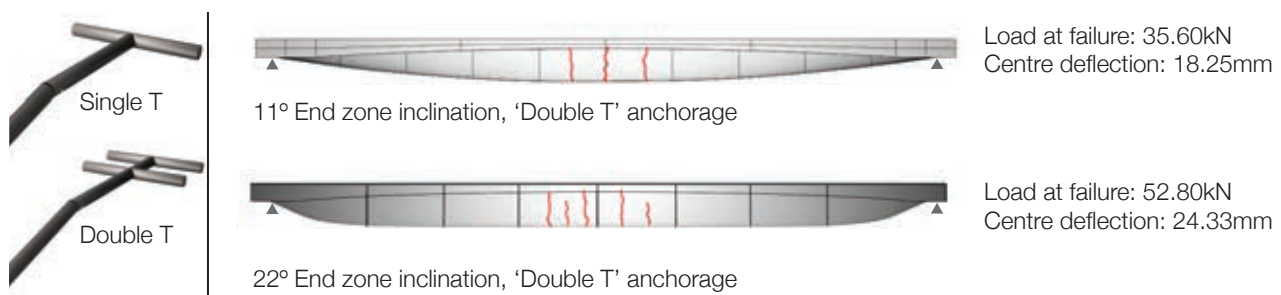


Figure 2.38: Anchorage method (l); Maximum capacity results of tests undertaken (r) (after Lee, 2010).

From the testing undertaken, Lee (2010) suggests that by increasing the end zone inclination, and using a wider web at the end zone, the beam behaviour can be optimised. The steeper angle reduces the horizontal component

of force in the bar, whilst the wider web zone provides a larger area to carry shear. The addition of a mesh of compression zone steel was also found to increase the section shear capacity. Lee (2010) further suggests that to encourage tension cracking in the midspan, a reduced web width is ideal (providing a reduced second moment of area once the section cracks).

The beams tested by Lee (2010) use plain reinforcing bar throughout, with a characteristic yield stress quoted as 355N/mm<sup>2</sup>. This makes comparisons with the behaviour of the anchorage zones in the beams tested in this dissertation difficult. There are, however, interesting comparisons to be made between the Single T and Double T anchorages proposed by Lee (2010) and the splayed bar anchorage that is used with success in both pull out and beam tests in §6.2 on page 159.

To demonstrate the material efficiencies that can be achieved with fabric formwork, the beams were compared to prismatic rectangular sections designed to BS8110-1 (1997) and material savings of up to 40% were recorded (Lee, *pers. comm.*, 9<sup>th</sup> April 2010). This is in line with results from other work and provides further verification of the potential for fabric formwork to reduce material consumption in the construction industry.

An embodied energy analysis of the T Beams as tested is also presented, in which values from The Inventory of Carbon and Energy (Hammond and Jones, 2011) are used. The analysis suggests that the fabric cast T beams can provide embodied energy reduction of up to 27% (not including the formwork). When the formwork is included, the fabric cast beam designed by Lee (2010) was in fact 14% more energy intensive than an equivalent strength prismatic element. This is discussed further in Chapter 10 on page 409, where additional embodied energy analyses are undertaken on the T and Double T beams cast as part of this dissertation. It is recognised that the formwork for a fabric cast beam can be quite energy intensive, and alternative construction processes should be investigated to address this.

Through an iterative design process, it is shown by Lee (2010) that effective anchorage of the plain reinforcing bar and an avoidance of brittle end failures can be achieved in fabric cast beams without transverse reinforcement.

### 2.5.3. University of Bath

Work at the University of Bath has approached fabric formed beams from a different perspective, and the incorporation of a topping slab has not been considered to date. Bailiss (2006) tested four and Garbett (2008) tested two beams of 2m span in five point bending with a total load of 15kN applied. All beams were designed to BS8110-1 (1997) following the processes described in §2.4.3.2. Each test is summarised in Table 2.3. Beam elevations and dimensions are illustrated in Figure 2.39. The structural behaviour of the beams was generally to fail at or close to the supports. This is an undesirable mode of failure, although it was generally accompanied by a degree of flexural cracking and deformation to warn of impending collapse, as illustrated in Figure 2.40.

Table 2.3: Test summary.

#	Concrete strength	Reinforcement	Fabric used	Design load	Failure load	Failure/Design	Failure mode
Bailliss (2006)							
1	52MPa	1 No. 8mm steel bar, $f_y = 460\text{MPa}$	Autway 240	15kN	15kN	100%	Shear crack opening close to support
2			Lotrak 50R	15kN	9kN	60%	Shear - Reinforcement placed incorrectly, so capacity overestimated.
3			Hessian	15kN	15kN	100%	Cracking at support.
4			Hessian	15kN	15kN	100%	Shear-flexure failure at the support.
Garbett (2008)							
1	36.4MPa	1 No. 8mm bar, $f_y = 460\text{MPa}$	Hessian	15kN	12.5kN	83%	Shear
2	34.9MPa		Hessian	15kN	21kN	140%	Shear

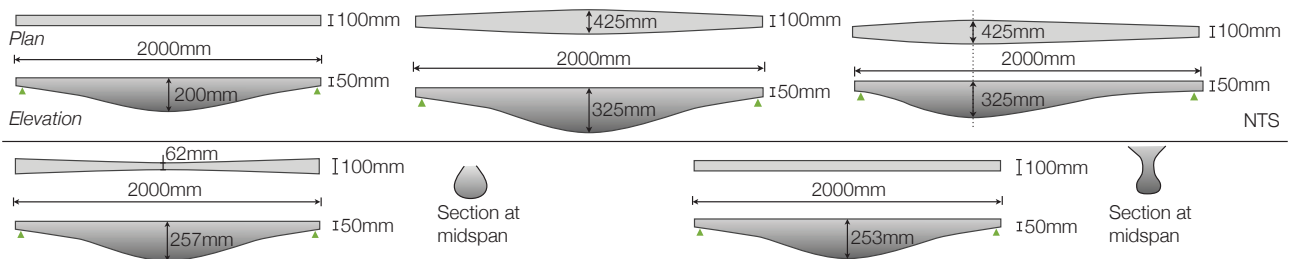


Figure 2.39: Beam profiles. Top (l-r) Baillis (2006): Beams 1 &amp; 2; 3 &amp; 4. Bottom (l-r) Garbett (2008): Beam 1; 2.



Figure 2.40: Test photographs (Garbett, 2008). Beam 1 (l) and Beam 2 (r).

#### 2.5.4. Summary

The available structural test data presented above, while limited in both size and scope, illustrates a number of potential issues for fabric formed concrete structures that are to be addressed in this thesis, including:

1. Premature shear failures;
2. Difficulties in construction;
3. Unconventional anchorage methods required.



Shear failures have been found to occur in many of the beams tested, suggesting either deficient design processes or a previously unknown behaviour of variable section concrete beams. The analysis and testing undertaken in subsequent chapters will therefore be key in determining feasible methods for the design of fabric formed beams.

Prior to this, the advantages and mechanisms of permeable formwork are described (§2.6) before the economics of construction using fabric formwork and issues surrounding material use and sustainability are discussed in §2.7, wherein further advantages of fabric formwork are highlighted.

## 2.6. Permeable formwork

In conventional reinforced concrete, orthogonal formwork moulds provide an impermeable seal between the wet concrete and the atmosphere. This ensures that the water content of the mixture does not change dramatically during the first hydration period (Ghaib and Gorski, 2001). When concrete is cast into permeable formwork the surface properties of the resulting concrete are changed as water is allowed to bleed from the mould.

Concrete cast into permeable moulds may be distinguished from concrete cast against impermeable moulds by 1) a darker surface finish; 2) a reduction in blow holes; and 3) a textured surface finish (Price, 2000) as illustrated in Figure 2.41.



Figure 2.41: The same concrete mix cast in conventional (l) and permeable moulds (r).

The advantages and behaviour of both fabric formwork and controlled permeability formwork systems are described in the following section. Work by the author to quantify the effects of using fabric cast concrete to provide durable concrete structures to achieve the aim of low carbon construction is described in full in Chapter 9

### 2.6.1. Controlled permeability formwork

Developed in Japan in the 1980s, controlled permeability formwork (CPF) describes a construction method in which water is allowed to drain from the surface of freshly cast concrete to provide a high quality, defect free finish (Price, 2000). Commercially available CPF systems broadly consist of three elements, as illustrated in Figure 2.42.

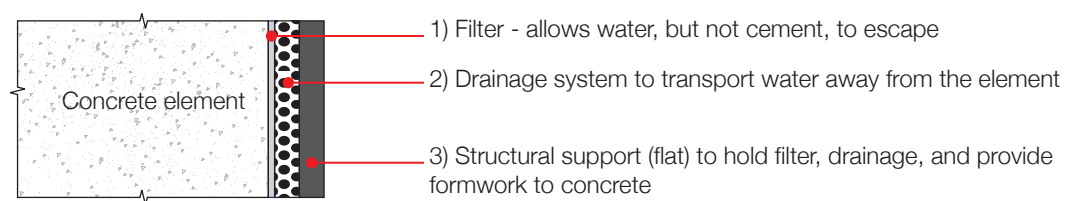


Figure 2.42: Essential components of a CPF system.

CPF systems can remove water from the concrete surface by 1) positive pressure under vibration, 2) hydrostatic pressure in the concrete mix, or 3) suction from an absorptive formwork system (Price, 2000). Absorption of water by the formwork system is unusual, with most systems instead relying on drainage as the means by which water is removed from the element.

During vibration, the concrete behaves similarly to a liquid and compression waves generated in the concrete compress the mix against the formwork (ACI 309, 1981). The resulting pore water pressure in the concrete then

pushes excess water through the filter and out of the concrete. This contrasts to impermeable formwork systems where air and water are trapped at the internal formwork surface.

### 2.6.1.1. Benefits

The amount of water drained from a concrete surface has a direct impact on its properties. Work by Kasai (1989) suggested that drainage rates of 1.5 litres/m<sup>2</sup> could be achieved from an initial water/cement ratio of 0.55, while a reduction in water/cement ratio to 0.45 provided a concomitant reduction in drainage rate to 1.1 litres/m<sup>2</sup>. These values were later verified by Shigekazu *et al* (1989), while DuPont (2007) suggest that their 'Zemdrain' product will drain up to 3 litres/m<sup>2</sup>. The obvious disadvantage of draining water from the concrete is that cement particles may also be removed and work by Rankilor (1994) suggests that fabric pore size should be no greater than 2.5 times the diameter of the cement grain (approximately 10-20µm) to prevent this.

The use of CPF is widely accepted to modify concrete properties close to the surface of the element. The most notable effect is a reduction in water/cement ratio, which contrasts to the increases in water/cement ratio seen at the surface of elements cast against impermeable formwork (Price, 2000), as illustrated in Figure 2.43. This effect was verified in experimental work by Price and Widdows (1991) in which electron microprobe analysis of a concrete panel was undertaken. It was found that the water/cement ratio of an element cast against CPF reduces towards the surface of the element, while in an element cast against impermeable formwork the water/cement ratio increases towards the surface. The same results have been found in work by Skjolsvold (1991, 1992, cited by Price, 2000) and Kasai *et al* (1988), where the cement content at the surface of CPF cast elements was found to rise by as much as 20kg/m<sup>3</sup> when compared to a conventionally cast element.

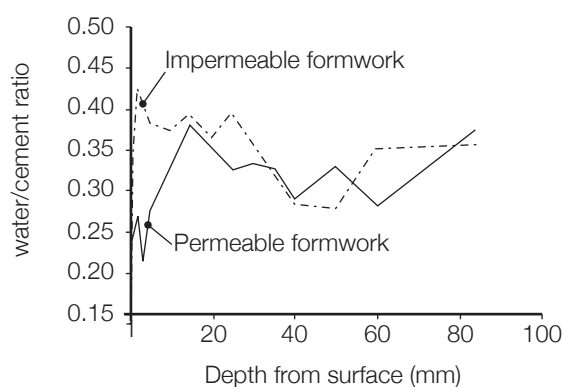


Figure 2.43: Variation in w/c ratio when concrete is cast in permeable moulds (after Price, 2000).

CPF has also been shown to reduce the porosity of concrete close to the cast face. Using mercury porosimetry Kasai *et al* (1988) investigated the distribution of pores in the surface 30mm of concrete panels. Over a range of pore sizes (1.5-2850nm), the CPF cast concrete was found to have up to 70% less pores (by volume) when compared to the same element cast against impermeable formwork. It was further found that whilst porosity increases towards the surface in conventionally cast elements, in elements cast against CPF porosity actually decreases towards the surface. Sha'a *et al* (1992, cited by Price, 2000) also showed that the size of capillary

pores in CPF cast concrete are reduced (from 1.5-3 $\mu$ m to 0.1-1 $\mu$ m), which, when combined with a reduction in water/cement ratio provide a dense, low porosity surface finish.

#### 2.6.1.1.1. Surface strength

Work by Price and Widdows (1991) and Serafini (1994) suggests that concrete cast into permeable moulds provides an increase in surface hardness (as measured using a Schmidt hammer) of approximately 20%, although work by Richardson (1994, cited by Price, 2000) suggests that this difference diminishes over time as the conventionally cast surface carbonates faster than that which was cast against a permeable mould.

Price (1991) also showed that permeable formwork can improve surface tensile strength, although the extent of this improvement is disputed. Price (2000) suggests that permeable moulds can provide a 250% increase in surface tensile strength, while DuPont (2007) suggest that a five-fold increase can be obtained.

#### 2.6.1.1.2. Durability

Deterioration of concrete structures takes place primarily because of environmental penetration into the concrete surface (Figure 2.44). Reductions in water/cement ratio in the surface zone are therefore expected to provide improvements in surface durability, potentially providing reductions in cover requirements for steel reinforced concrete structures. Available test data, some of which is summarised below, focuses mainly on CPF systems although similar results may be expected with fabric formwork.

The absorption of water by a concrete structure in service is a primary concern for durability, and can be assessed by both the sorptivity test and the initial surface absorption test (ISAT). Results from both types of test (as summarised by Price, 2000) suggest that permeable formwork systems provide concrete surfaces with a reduced ability to absorb water. The application of these results to fabric formwork construction will require additional testing.

Additional tests (DuPont, 2007) suggest that permeable formwork systems can also reduce the water permeability of concrete structures, although this is only of real concern in structures such as basements where water pressures may be high. The lower permeability of concrete cast in a permeable mould provides additional protection to the internal reinforcement by not only reducing carbonation rates, but also by slowing chloride and oxygen ingress into the concrete surface (Price, 2000).

Price and Widdows (1991) demonstrated that the depth of carbonation of concrete panels when cast against permeable moulds is reduced by approximately 20%, although the effect of using permeable formwork is greater at a higher concrete strength. Methods used to determine chloride ingress vary, but Price and Widdows (1991) showed that reductions of up to 40% may be achieved (using a diffusion cell). Skjolsvold (1991, cited by Price, 2000) found similar results using an electrically accelerated test. Tests to measure oxygen ingress are limited, but a study by Price and Widdows (1991) suggests oxygen diffusion may be reduced by 30% when cast against permeable formwork, a result later verified for a different CPF system by DuPont (2007).

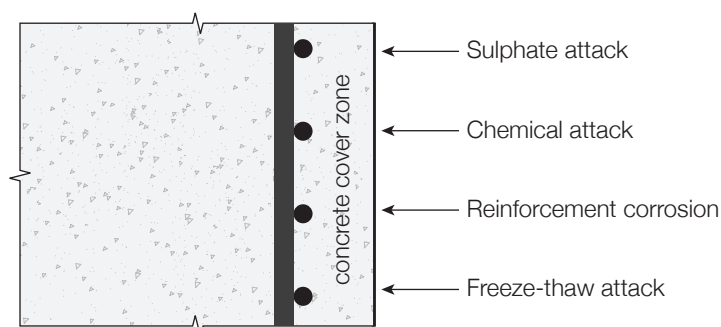


Figure 2.44: Durability of concrete structures - environmental penetration (after Price, 2000).

Whilst carbonation and chloride and oxygen ingress are essential ingredients for concrete deterioration, good design will ensure that concrete cast against impermeable moulds has an adequate design life. Using fabric formwork, the same durability may now be achieved with either reduced cover, or a reduced cement content.

The final effect to consider with regards to durability is the ability of algae and micro-organisms to grow on the concrete surface. The high pH of concrete after casting is degraded over time by carbonation, and eventually an environment attractive to organisms may develop. By slowing carbonation, permeable formwork systems also slow organic growth on the concrete surface through a reduction in porosity and water absorption. A summary of the benefits of a permeable formwork system are provided in Table 2.4, where a summary of data given by Price (2000) is provided alongside DuPont (2007) data for the Zemdrain system.

Table 2.4: The benefits of a permeable formwork system (after Price, 2000 and DuPont, 2007).

Property	Improvement with CPF (Price, 2000)		Improvement with Zemdrain (DuPont, 2007).
	Average	Range	
Surface hardness	+22%	+11 to +35%	+24%
Surface tensile strength	+94%	+6 to +260%	+70%
Abrasion depth	-76%	-95% to -51%	-50%
Sorptivity	-50%	-77% to -8%	-30%
10 minute ISAT*	-63%	-98% to -32%	-90%
Water permeability	-65%	-99% to -39%	-60%
Carbonation depth	-73%	-99% to -20%	-90%
Chloride diffusion	-55%	-84% to -25%	-70%
Oxygen diffusion	-25%		-25%
Air permeability	-76%	-96% to -28%	NA
Freeze-thaw damage	-67%	-99% to -7%	-95%
*Initial surface absorption test			

#### 2.6.1.2. Economics of permeable formwork

The economics of using controlled permeability formwork in construction are summarised by Price (2000) in terms of both costs (associated with additional construction time and materials) and benefits (long term durability improvements and additional service life). Based on real project data, the additional costs associated with CPF in construction ranged from £6 to £13 per m<sup>2</sup> of CPF surface. However, if the increased durability of concrete structures cast in CPF could allow designers to specify a lower strength concrete mix, potentially significant cost

savings may be achieved. Pallet (1994) provides data based on a hypothetical concrete building, in which an immediate saving of 3.9% over a conventionally cast structure was found through a reduction in required concrete strength, while long term savings of 7.4% were found through reduced maintenance requirements. The potential for such savings, combined with a reduction in material use provided by fabric formwork, form the beginnings of an economic argument for the use of fabric formwork.

### 2.6.2. Application to fabric formwork

The advantages of controlled permeability formwork, as described above, have to date not been considered in detail for fabric formed structures. Previous research has instead chosen to focus on determining the potential for strength improvements in fabric cast concrete.

Ghaib and Gorski (2001) carried out a comprehensive series of tests on fabric cast concrete and the results appeared to demonstrate significant improvements in compressive strength (Figure 2.45(l)). However, the work tested samples of different dimensions and omitted a number of important details, making the results hard to successfully interpret.

Abdelgader and El-Baden (2009) tested thirty-six cylindrical specimens using two different fabrics with water/cement ratios ranging from 0.5 to 0.75. The results showed there to be little improvement in the compressive strength of fabric cast concrete (Figure 2.45(centre)), although the comparison between 100mm diameter fabric cast samples and 150mm diameter steel cast samples again makes the results qualitative only.

Delijani (2010) carried out a more detailed study on both fabric cast cylinders ( $\varnothing 152\text{mm} \times 305\text{mm}$  tall) and short concrete columns ( $\varnothing 254\text{mm} \times 1500\text{mm}$ ). Whilst the compressive strength of the small cylinders was improved by approximately 19% when using fabric formwork (Figure 2.45(r)), improvements in strength were not replicated in the large columns. This demonstrates that permeable formwork can provide only a local improvement in concrete properties at the boundary between the element and the permeable formwork, but does not provide global increases in strength.

Far less research has considered durability effects in fabric cast concrete. West *et al* (2007) suggest that concrete cast into fabric exhibits an effect described as ‘case hardening’, in which a denser surface layer of concrete results in a more durable concrete structure with fewer surface voids. Whilst this statement is supported by work undertaken on controlled permeability formwork systems additional research is required to quantify the effect of casting concrete into fabric.

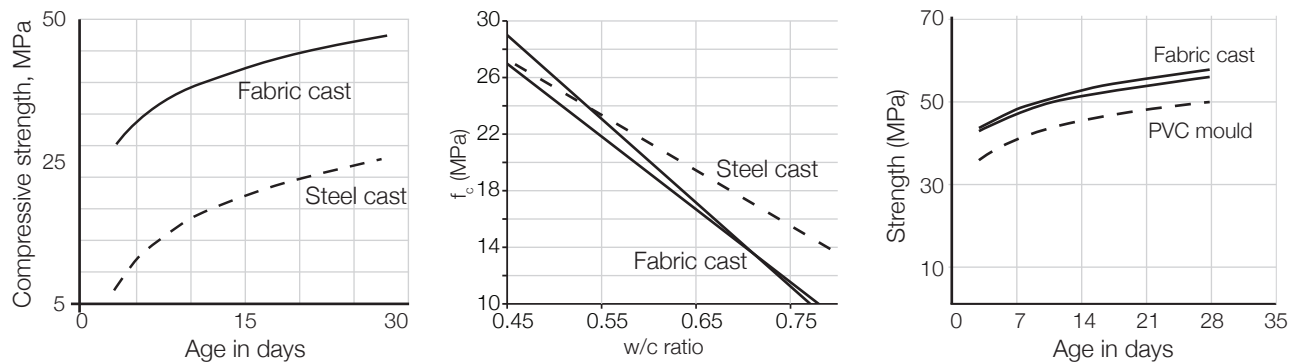


Figure 2.45: Test results. Left - right: Ghaib (2001); Abdelgadar (2009); small samples tested by Delijani (2010).

### 2.6.3. Conclusions

Controlled permeability formwork provides a suitable comparison technology to fabric formwork and the body of available test data suggests that casting concrete into permeable moulds provides a sensible method by which high quality concrete can be provided. However, the available systems can be expensive and time consuming to install, presenting an opportunity for fabric formwork to act as a sustainable alternative that does not require complex support systems, since the fabric acts as both filter and structural formwork.

The primary benefits of permeable formwork is therefore to provide improved durability and enhanced surface properties and this aspect of fabric formwork technology forms the focus of Chapter 9 (page 343).



## 2.7. Impacts

### 2.7.1. Introduction

The preceding sections have presented both architectural and structural applications for fabric formed concrete structures, emphasising the variety of potential approaches to the use of fabric formwork. On the one hand it may be viewed as a means to create the structurally and materially efficient shapes that would otherwise be expensive to form in conventional formwork; on the other it may be viewed as a means to create interesting, seductive and dynamic shapes that would be expensive (or impossible) to cast in conventional formwork. The two approaches need not be mutually exclusive.

The widespread use of fabric formwork may only be achieved if the economic and environmental advantage for its use can be comprehensively demonstrated alongside the provision of technical design and construction guidance. Considering the labour, material and environmental costs of construction, §2.7 sets out the arguments that underpin this thesis - that fabric formwork has the potential to facilitate a low carbon, sustainable concrete construction industry.

### 2.7.2. Material consumption

It has been shown above that fabric formwork offers the potential to reduce material consumption through both the design and construction processes (§2.3.5 and §2.4.4). The importance of this is demonstrated by considering a simple case study, presented by Thirion (2010), in which the utilisation (percentage of element capacity required to carry the design loads) of a low-rise London office structure was calculated. The analysis showed that embodied carbon savings of up to 60% could be achieved by following simple optimisation routines for the concrete frame and floor slab construction.

The importance of embodied carbon in the built environment is emphasised by our commitments to reduce carbon emissions, as introduced in §1.1 on page 1. These commitments may be realised through a reduction in the embodied energy associated with new concrete structures, which can be significantly influenced by fabric formwork. Shown in Figure 2.46 is one example of the role fabric formwork can play - where the design of a new structure is formed by a multi-disciplinary team who are able to develop an appropriate response to a particular local environment. From here, the efficiency of materials and their specification (putting material in the right place) is heavily influenced by fabric formwork. Appropriate choices, influenced by the life cycle requirements of the structure, may facilitate significant reductions in not only the embodied energy of the new structure but also in its operational energy, and subsequently in its end of life refurbishment, reuse or deconstruction.

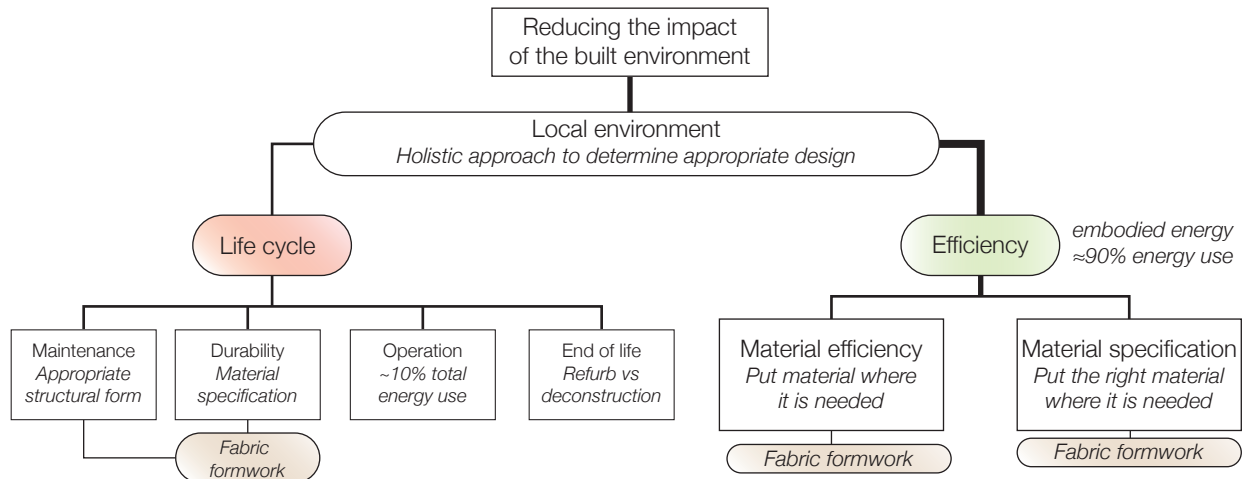


Figure 2.46: Embodied carbon reductions, and the role of fabric formwork.

### 2.7.2.1. Challenges

Elements produced using fabric formwork have the advantage that their shape can be optimised and material saved. However, this makes the section suitable for only one loading envelope, which must be carefully analysed. Under an extraordinary loading event, the optimised shape may become more susceptible to failure than a conventional prismatic member.

These concerns, whilst important, should not be viewed as detrimental to the success of fabric formwork and instead solutions should be found. A controlled collapse mechanism may be possible, and load redistribution to the surrounding structure is possible if connections are detailed correctly. Ibell *et al* (2007) argue that the advantages of fabric formwork, including material savings of up to 40%, improved durability, inexpensive formwork, and the ability to produce complex designs outweigh these concerns.

### 2.7.3. Labour and material costs

Construction costs, excluding operational costs, may be considered in terms of material and labour, with the relationship between the two having a historically strong influence on the prevalence of certain construction techniques (Meyer and Sheer, 2005). In the UK, high material costs and low labour costs in the 1950s and 1960s, in addition to social changes, helped to make material efficient but labour intensive shell structures popular with both architects and engineers.

Subsequently material costs have generally fallen and labour costs generally risen in the UK, making simple construction techniques that have minimal labour requirements more economically viable even though the resulting structures can consume more material. Coupled with the economic boom of the late 20th century, the way materials are used has changed dramatically. This relationship is illustrated for the thirty seven year period between 1970-2007 in Figure 2.47, where the historical price of cement and steel (all monetary values adjusted to 1998 levels) is plotted alongside available construction industry labour cost data.

In the period 1970-2010 a trend in increasing labour and falling material costs is apparent (although this does represent just one time period and historical steel price data was only available for the United States). There is insufficient available data to be able to plot the same graph over a longer time period, and the same data is not available for the majority of the globe.

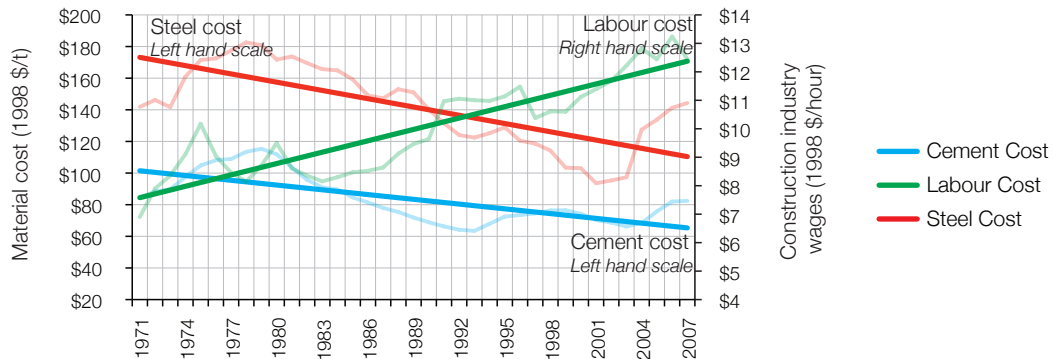


Figure 2.47: Historical variations in construction industry wages and labour and material costs (data after LABORSTA, 2010; USGS, 2008). Values adjusted to 1998.

The new emphasis on a low carbon economy may bring about a renaissance in the construction techniques that facilitate low material use structures, and fabric formwork has the potential to provide one way by which concrete elements of almost any geometry can be cast to provide a low impact construction industry.

#### 2.7.4. Environment

The vast quantities of cement manufactured each year result in significant greenhouse gas emissions (§1.1 on page 1). Whilst the raw materials used in concrete are unlikely to run out within the next 1,000 years (Craig *et al.*, 1996), the environmental impacts associated with wasteful consumption may be entirely avoidable if concrete is simply cast in optimised structures.

Cost savings found in optimised structures have the potential to bring short term economic benefits, while in the medium term it is only sensible to use materials in an efficient manner to minimise waste thus allowing fabric formwork to achieve a sustainable approach to construction and design. Although widely defined, sustainability in construction should embrace much more than simple reductions in material use, and for this reason fabric formed structural elements must be considered as part of an holistic approach to low impact construction in which sustainable objectives are embedded within the project specifications from the outset.

Therefore, meeting the needs of future generations does not mean present day development should cease; and the principles of sustainability should recognise that 'needs' are not the same for all people at all times. Prioritising and understanding the needs of the people affected by any development is a significant step towards achieving a sustainable design. Although sustainability is often correlated to reductions in material use, such comparisons are too simplistic - since to preserve a nonrenewable resource for every future generation would logically require all current consumption to cease entirely. Instead, for truly finite resources our best options are to 1) make them last longer, and 2) develop the new technologies that will release any dependence on the finite resource. Considerable

future work is envisaged in which the potential successors to our current construction materials and techniques are developed.

#### 2.7.4.1. Climate

The greenhouse gases that encircle the globe make the lower atmosphere warmer and the upper atmosphere cooler than they would be without them (the greenhouse effect) and theoretical surface temperatures of 60°C are prevented by the action of convection in the atmosphere (Spencer, 2008). Warm air rises from the surface, transporting heat to the upper atmosphere. Upon cooling this air then sinks, creating a system whose processes result in all global weather. The cooling effects of this system are quantitatively larger than the warming created by the greenhouse effect (Spencer, 2008).

Climate change, which describes variations in the mean surface temperature over time, has many influencing factors - one of which is the actions of humankind. Anthropogenic climate change is primarily concerned with increasing concentrations of certain gases within the atmosphere, the theoretical impact of which is to change the global climate response. The most widely reported data are emissions of carbon dioxide, the concentration of which has generally increased over the past fifty years, from 317ppm (1960) to 388ppm (2009) (Tans, 2010), representing an addition of one molecule of CO<sub>2</sub> to every 100,000 molecules of air every 7 years. Increases in global temperature, of approximately 0.2°C per decade since the 1980s (Hansen *et al*, 2006), are often cited as a consequence of changing gas concentrations in the atmosphere.

The theory of global warming, in which increasing greenhouse gas concentrations result in increased surface temperatures, more extreme weather and rising sea levels, is supported by sophisticated computer models (although such an approach can be difficult to verify as the interaction between water vapour, cloud cover and the oceans, which make up the essential building blocks of the global climatic system, is not entirely understood (Spencer, 2008)). Whilst there remains a large amount of work to be done in this field, it is apparent that the body of scientific evidence supports the notion that emissions of carbon dioxide (and the associated basket of Kyoto gases) should be reduced in the coming decades.

Pressure to act on greenhouse gas emissions has important economic implications. In a UK Government Commissioned Report, Stern (2007) argued that the cost of action far outweighed the costs of inaction, although the report has been criticised for both mishandling basic data (Carter *et al.*, 2006), and for its economic analyses (Byatt *et al.*, 2006; Nordhaus, 2007). A less dramatic approach is taken by Spencer (2008), who argues that proposals to tackle climate change should instead be met with two simple questions - 'How much will it cost?', and 'How much will it help?'.

The impact for the built environment in achieving the commitments made to reduce our carbon emissions (Figure 1.2) will be significant. The European Commission Roadmap to 2050 (EC, 2011) estimates that emissions reductions of 90% (greater than the average) are possible in the built environment, and this will occur in the

next 30-40 years. Indeed, requirements for all new buildings to be 'nearly zero energy' by 2020 already exist in European Union Directive 2010/31/EU (EC, 2010). Analysis by the European Commission further suggests that investment in upgrading work for existing infrastructure will require an extra €200bn in order to achieve the long term emissions reductions goals (EC, 2011).

Yet climate change is a problem of collective action in which the total benefit can only be gained if all emitting parties are willing to commit to and realise similar reductions in emissions. Fabric formwork may provide one means by which the impact of the built environment can be reduced. Helm and Hepburn (2011) and Aldy *et al* (2001) provide further discussion around this topic, which is deeply entwined with the future of the built environment.

## **2.8. Summary**

Chapter 2 has illustrated the history, design and construction methods used in fabric formed concrete structures, which have the following advantages:

1. Use less material - providing environmental and economic benefits to clients and designers;
2. Require a simple construction method that can easily be used to create unique shapes;
3. Allow scope for variable section elements that place material only where it is required.

Whilst dedicated research has been carried out in this field, a number of key issues that are to be addressed in this thesis have been raised, as summarised below:

1. Limited test data has highlighted an apparent propensity for variable section beams to fail in shear;
2. Permeable formwork systems can provide significant improvements in durability and surface behaviour, but little data is available for fabric formed structures;
3. Codified design methods and empirical equations for shear capacity are difficult to apply to fabric formed structures. Existing structural design codes need careful appraisal if they are to be applied to fabric formed structures;
4. Construction methods are widely applicable, but generally require refinement, full scale testing and verification;
5. Anchorage, shear, serviceability and secondary effects are potentially important for variable section members.

## 2.9. Goals

Chapter 2 has provided a brief introduction to the use, design and construction of fabric formed structures. Summarised below are the key goals for this work, including some thoughts on how they will be achieved. The over riding consideration is for the provision of efficient structures that both use less material and are architecturally interesting.

*Table 2.5: Goals and proposed resolutions.*

Goal	Resolution
Design	Build on existing precedent, including work at CAST. Codified approaches to be clarified, improved, or redeveloped. Design should consider both ultimate and serviceability limit states.
Optimisation routines	Key to ensuring a sensible design. Existing methods to be developed and improved.
Material use	Additionally consider the appropriate use of materials in fabric formed structures. This may include advanced composites, active reinforcement, or innovative concrete mixes.
Construction	Detailed methods for construction should be developed that are applicable across the world.
Test data	Destructive testing must be carried out to validate the above processes, and to provide a database for subsequent researchers.

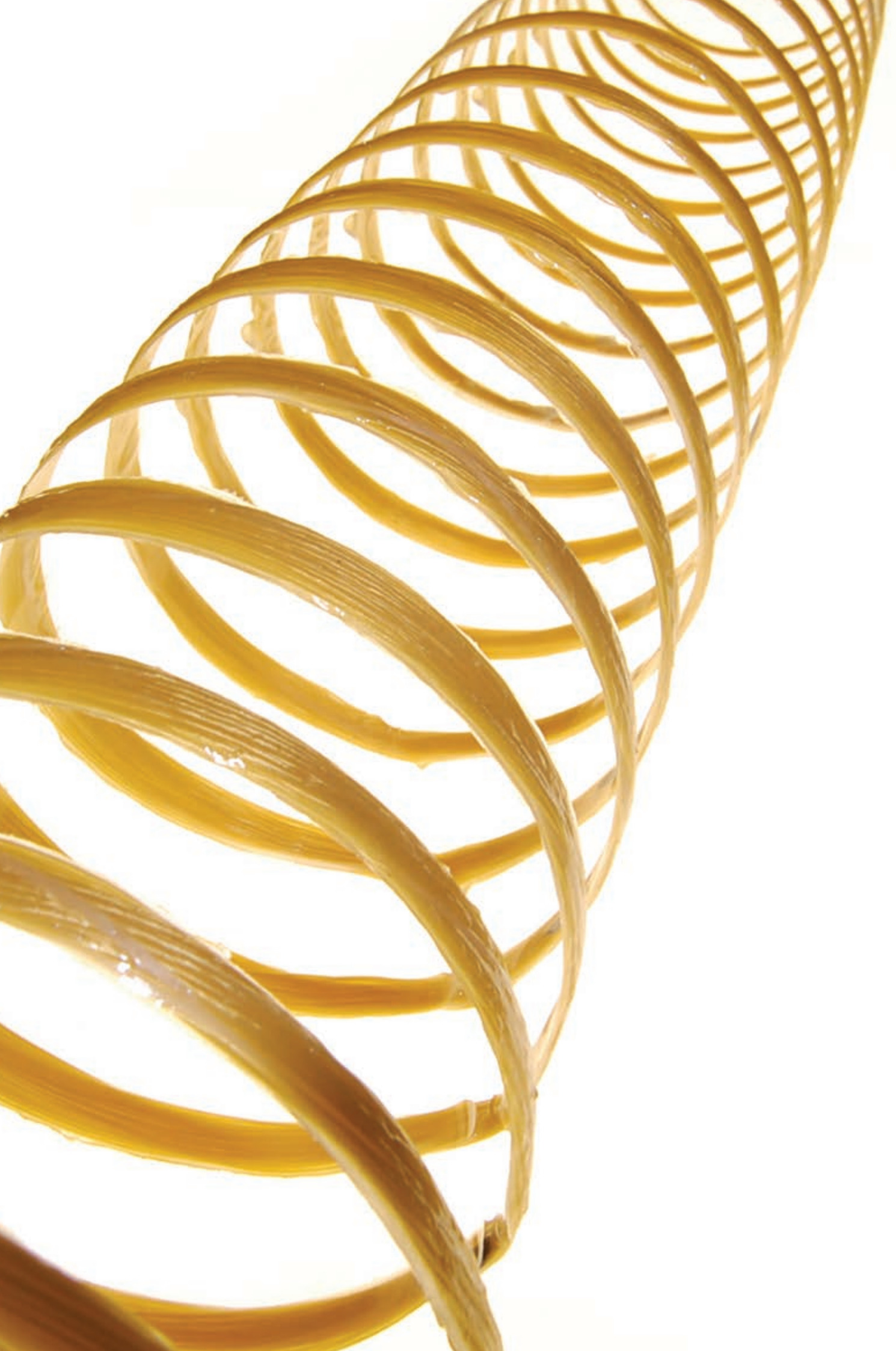
To begin to answer the questions posed in Chapter 1, a detailed analysis of the components of a fabric formed concrete structure is presented in Chapter 3. This analysis goes on to inform the development work required to both meet the stated goals and provide the evidence that underpins fabric formwork as a sustainable alternative to conventional construction methods.



---

[blank page]

---



# Chapter 3      Material behaviour

## Literature review

### **3.1. Introduction**

Chapter 3 provides a detailed investigation into the concrete, the fabric and the reinforcement that make up the principal components of a fabric formed concrete structure. In doing so this Chapter demonstrates some of the main challenges for the development of a sustainable construction industry using fabric formwork that are addressed in this thesis.

### **3.2. Concrete**

Concrete is the most widely used man-made material in the world, with consumption estimated at 1.5m<sup>3</sup> per person per year (USGS, 2008). Its basic components - cement, sand, aggregate, water and admixtures - form a unique, fluid material with a high compressive strength and low tensile strength. Architecturally, these properties give concrete great scope for innovation.

#### **3.2.1. Material behaviour**

The widespread use of concrete belies the difficulty with which constitutive material models for it are formed. Fundamentally, the compressive strength of a concrete structure is limited by the tensile strength of the material; indeed it is argued here that compression failures cannot occur in concrete, as coexisting tensile stresses will always cause the material to fail before a compression limit can be reached. The fundamental strength of concrete comes from the hardened cement paste that forms during hydration of the hydraulic cement, which is typically mixed with pulverised fuel ash (PFA) or ground granulated blast furnace slag (GGBS) to reduce its carbon content (although such mixtures do slow the rate of strength development).

The stress strain behaviour of concrete in uniaxial compression is illustrated in Figure 3.1(l). Concrete models for design most commonly assume the existence of some post-peak strength (Figure 3.1(r)), yet Kotosovos and Pavlovic (1999) suggest that this behaviour is solely a result of frictional resistance generated between steel loading platens and the concrete surface during uniaxial testing. By undertaking tests with progressively reduced friction coefficients, it was suggested that concrete in uniaxial compression has zero post peak strength, Figure 3.2. It is notable also that uniaxial testing results in peak concrete strengths at axial strains of approximately 0.002, significantly less than the 0.0035 level that is allowed in most design codes.

The behaviour of concrete is most commonly considered in terms of axial strain, yet its transverse behaviour is perhaps more important. Transverse strains in concrete increase rapidly at close to the peak compressive stress and this is accompanied by considerable volume dilation of the material (Kotsovos, 2007). By testing cylinders under triaxial conditions, it has been shown (Kotsovos and Pavlovic, 1999) that confining stresses of around 10% of the uniaxial cylinder compressive strength can give compressive strength increases of more than 50%, with this level of confinement having further been shown to exist in flexural members (Kotsovos, 1982).

Therefore the assumption of a uniaxial stress strain behaviour may not represent the actual behaviour of a concrete element. Kotsovos and Pavlovic (1999) argue that in ignoring the effect of transverse strains, most concrete material models must rely on the existence of post-peak softening behaviour as predicted by uniaxial testing in order to correctly predict the compressive behaviour of flexural concrete members. Ergo, the triaxial stress state of concrete in flexural compression zones is not ignored; rather it is incorrectly attributed to other effects, including post peak softening, aggregate interlock, and dowel action. This is discussed in greater depth in §4.2.1.

Concrete under triaxial stress has far greater strain capacity for the same peak stress than is found under uniaxial compression and this strain capacity is further improved by the application of a uniform confining pressure, as illustrated in Figure 3.3, a behaviour that is potentially important for sections with confined concrete in the compression zone. The same effect was also demonstrated by Park and Paulay (1975).

The tensile capacity of concrete is usually ignored for design purposes, but may be estimated at less than 20% of the uniaxial compressive strength (Park and Paulay, 1975). Kupfer *et al* (1969) concluded that whilst the biaxial strength of concrete may be up to 27% higher than the uniaxial strength, tensile strength remains approximately equal in both cases.

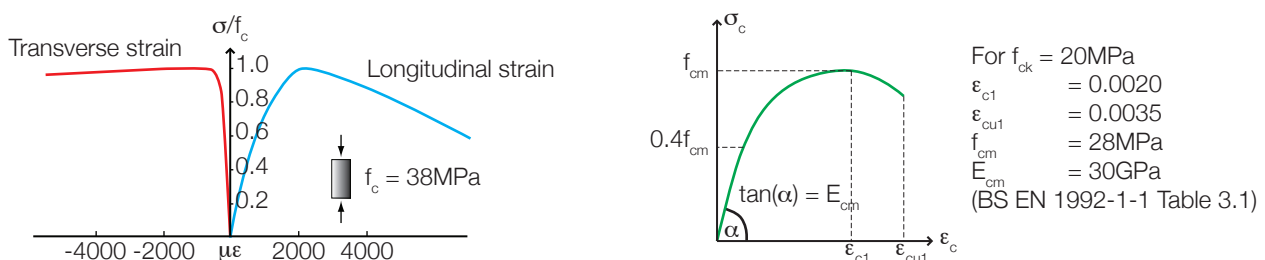


Figure 3.1: Stress strain for uniaxial compression (l); Typical model for codified design (r) (after BS EN 1992-1-1 (2004)).

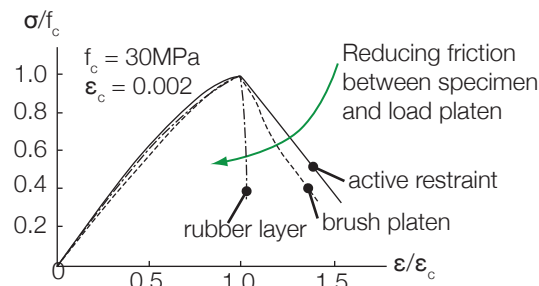


Figure 3.2: Uniaxial test data showing actual post peak behaviour (Kotsovos, 2007).

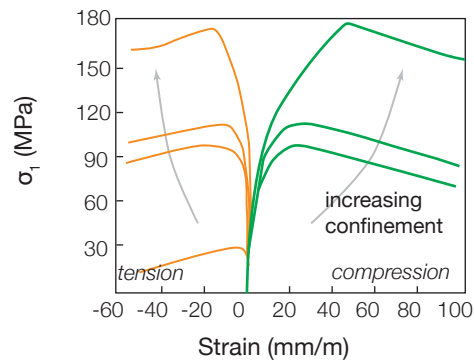


Figure 3.3: Triaxial stress strain plot (Kotsovos and Pavlovic, 1999).

The interfacial zone (between aggregate and cement paste) of the concrete is its strength limiting phase, and ensures that concrete fails at less than the strength of either of its main components and behaves inelastically in compression (even though both cement and aggregate in isolation present an elastic behaviour). The interfacial zone in young concrete has larger and more frequent voids in addition to considerable microcracking (Mehta *et al*, 2006) and it is this interfacial zone that ensures concrete is both weak in tension and has higher permeability than is found in a corresponding cement paste.

Aggregates are used to add dimensional stability, bulk, and are predominantly responsible for the elastic modulus of concrete. Aggregate strength is largely immaterial, but shape is an important factor (Kwan and Mora, 2001). The presence of voids, retained water and air as well as the cement, aggregate and admixtures used all influence the final concrete behaviour and strength.

#### 3.2.1.1. Influence of water

Abrams (1918) first determined empirical relationships between the water/cement ratio and concrete strength, Eq. 3.1, which have subsequently been refined (Teychenné *et al*, 1997). The relationship showed that an increase in the water/cement ratio provides a proportional increase in porosity, thereby reducing compressive strength. This direct relationship holds true in normal and low strength concrete. In high strength concrete, small changes in water/cement ratio can result in large increases in compressive strength, since the reduction occurs almost entirely at the interfacial zone (Mehta *et al*, 2006).

$$f_c = \frac{k_1}{k_2^{w/c}} \quad \text{Eq. 3.1}$$

Where  $f_c$  = compressive strength;  $w/c$  = water cement ratio;  $k_1$  and  $k_2$  are empirical constants.

A water/cement ratio of 0.28 is typically required to ensure hydration of all the cement in a typical concrete mix; yet typical water/cement ratios can be as high as 0.4-0.6, in part to provide workability. Water particles that collect next to timber formwork create 'bubbles' in the concrete, which results in a reduction in both durability and aesthetic quality.

Water content must be controlled if a high quality concrete is to be achieved. Water is necessary in the early stages after pouring for cement hydration, yet large amounts of retained water will evaporate after curing, leaving a network of open pores that result in poor durability. The potential for subsequent resaturation of these pores is dependent on the hydraulic conductivity of the surface,  $K$ , which may be determined in a basic form using Darcy's equation, Eq. 3.2. Permeability of the surface is critical as water is involved in nearly every deterioration process (Mehta *et al*, 2006) and so the rate of penetration will typically determine the rate of structural deterioration.

$$\frac{dq}{dt} = K \frac{\Delta H A}{L \mu} \quad \text{Eq. 3.2}$$

Where  $dq/dt$  = rate of fluid flow;  $\mu$  = viscosity of the fluid;  $\Delta H$  = hydraulic gradient;  $A$  = surface area;  $L$  = thickness of the solid.

Garboczi (1990) presents an extensive review of permeability in concrete structures, which concluded that further experimental validation was required to prove the usefulness of predictions for diffusivity in concrete elements when using simple models. Subsequent work by Mehta *et al* (2006) compared two sets of permeability data to show again the importance of the interfacial zone in determining concrete properties. Microcracking, which develops from the interfacial zone, provides a uniquely permeable route through the concrete, ensuring that the impermeable characteristics of cement paste are not replicated in the concrete structure. Water is therefore both crucial to the curing process and potentially detrimental to the long-term behaviour of the concrete structure.



### 3.2.2. High performance concrete (HPC)

Ordinary Portland cement based concrete suffers from a number of deficiencies, namely a low strength to weight ratio, poor impact resistance and a relatively high surface permeability. High performance concrete has been developed to overcome these issues. Lightweight aggregates improve strength to weight ratios, superplasticising admixtures reduce water/cement ratios to give both increased strength and reduced surface permeability, and fibre-reinforced concrete mixes are used where impact resistance is critical. However, reinforced concrete members that make use of high strength concrete then require additional tensile steel and hence compaction can become critical. High performance concrete may be specified with a slump of 250mm without overly high w/c ratios, although bleeding and segregation often occur during construction if vibrators are overused (Mehta *et al.*, 2006). Self consolidating (or rheoplastic) concrete was developed in the 1980s to prevent this.

Reinforcing plain concrete with steel or synthetic fibres helps the material to overcome the rapid propagation of microcracks under applied loading that are responsible for its low tensile strength. The types of fibres and volume fraction used are key to the success of such fibre reinforced concrete (FRC). Whilst plain concrete displays very little ductility, Figure 3.3, fibre reinforced concrete improves the resistance of a section to crack opening and propagation (Zia *et al.*, 1994). Figure 3.4 highlights the differences between plain and fibre reinforced concrete, and fibres have been found to be more effective in high strength concrete ( $>60\text{MPa}$ ) with increases in both ultimate capacity and ductility recorded (Zia *et al.*, 1994). SIFCON (Slurry infiltrated concrete) uses fibre volumes of  $>12\%$  to provide excellent ductility (see Fritz *et al.*, 1992) and SIMCON (Slurry infiltrated mat concrete) uses a mat of high aspect ratio fibres (ratios up to 500) to provide similar properties but using a fibre volume half that of SIFCON (Zia *et al.*, 1994).

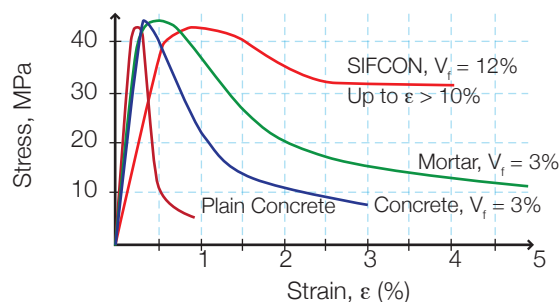


Figure 3.4: General behaviour of fibre reinforced concrete (after Zia *et al.*, 1994).

Three notable approaches to the use of ultra-high performance concrete are described in the following. Engineered cementitious composites (ECC) are highly ductile cement-synthetic fibre composites with tensile strain capacities of up to 7% (Li, 1998). Multiscale fibre reinforced concrete (MSFRC) was developed in France (Rossi, 2001) and fibre volume fractions of up to 7% can be used with both straight and hooked bars. Also in France, reactive powder concrete (RPC) was developed through an extensive optimisation process (Richard and Cheyrezy, 1995). RPC is a steel or organic fibre reinforced concrete that has no coarse aggregate and therefore shows much improved packing. Heat and pressure is often applied to RPC sections during curing and compressive strengths of up to 200MPa can be achieved after 3 days when cured at 90°C. Compressive strengths of up to 800MPa

have been achieved, but this requires curing at very high temperatures (400°C). The mechanical properties of some ultra-high performance fibre reinforced concrete mixes are compared to the properties of normal concrete in Table 3.1.

Table 3.1: Ultra high performance fibre reinforced concrete (FRC) (after Li, 2002).

	$\sigma_0^{(4)}$ (MPa)	$\sigma_t$ (MPa)	$\varepsilon_t$ (%)	E (GPa)	$G_c$ (kJ/m <sup>2</sup> ) <sup>(5)</sup>	$l_{ch}$ (m) <sup>(5)</sup>
Normal strength concrete	-	2-5	0.01	15-30	0.1-0.2	0.25-0.4
Steel FRC ( $V_f$ = 1% hooked end)	4 <sup>(5)</sup>	4.5	0.05-0.5	32.5	5	8
Carbon FRC ( $V_f$ = 2%)	5.5	5	0.1-0.2	5.6	1-3	0.2-0.7
Polymer FRC ( $V_f$ = 1% olefin)	0.75-1.5 <sup>(5)</sup>	4.5 <sup>(5)</sup>	0.1	30	1-4 <sup>(5)</sup>	1.5-6
SIFCON ( $V_f$ = 4-20% steel)	20-35	6-32 <sup>(5)</sup>	0.5	30-70	20-30 <sup>(5)</sup>	2-17
CRC <sup>(1)</sup> ( $V_f$ = 6% steel, with steel bars)	40	120	1-2	100	1200	8.3
RPC <sup>(2)</sup> 200 ( $V_f$ = 2.4% steel)	9.6	10-24 <sup>(5)</sup>	0.5-0.7	54-60	15-40 <sup>(5)</sup>	4.2-8.1
ECC <sup>(3)</sup> ( $V_f$ = 2% PE)	4.5-8 <sup>(5)</sup>	2.5	3-6	22-35	27	95-150
$\sigma_t$ = tensile strength; $\varepsilon_t$ = tensile strain; E = Young's Modulus; $G_c$ = Fracture Energy; $l_{ch}$ = characteristic length; $V_f$ fibre volume fraction						
Notes to Table 3.1: 1. Compact Reinforced Concrete; 2. Reactive Powder Concrete; 3. Engineered cementitious composite; 4. Peak value of an $\sigma$ - $\delta$ plot; 5. See also further notes in Li, 2002.						

Lafarge Cements have developed one such ultra-high strength concrete, marketed under the *Ductal*® brand name, the material properties of which are summarised in Table 3.2. The proprietary RPC mix, which uses either high carbon metallic fibres or a poly-vinyl alcohol (PVA) fibre, is altered for each specific application to ensure optimum performance (Lafarge, 2009). Available technical literature suggests that this material is ideally used in prestressed or post tensioned structures, where its high compressive strength is a great advantage. In addition, a relatively high tensile strength gives the material inherent shear capacity, a great advantage for fabric formed members where placement of shear reinforcement can be difficult. The material properties and use of Ductal® is discussed in greater detail below.

### 3.2.2.1. Ductal®

Ductal® is one of the only ultra-high performance (>150MPa compressive strength) concretes available in either the USA or Britain. The constituent parts of this granular mixture are described in Table 3.2, where fine sand (150-600µm in diameter) is the largest granular component and the smallest component, silica fume, is small enough to fill the interstitial voids between the cement and quartz. The reinforcing fibres are rather larger, at 0.2mm x 12.7mm, and are specified with very high tensile strengths ( $\geq 2,600$ MPa), that require careful quality control monitoring (Graybeal, 2006a).

Table 3.2: Material properties of Ductal® (after Graybeal, 2006a).

Material	Amount (kg/m <sup>3</sup> )	Percent by weight	Average size
Portland Cement	712	28.5	15µm
Fine Sand	1020	40.8	150-600µm
Silica Fume	231	9.3	<10µm
Ground Quartz	211	8.4	10µm
Superplasticiser	30.7	1.2	-
Accelerator	30.0	1.2	-
Steel Fibres	156	6.2	0.2 x 12.7mm

Material	Amount (kg/m <sup>3</sup> )	Percent by weight	Average size
Water	109	4.4	-

Table 3.3: Material characteristics (after Graybeal, 2006a).

Characteristic	Range	Characteristic	Range
Compressive strength (MPa)	180-225	Modulus of Elasticity (GPa)	55-58.5
Flexural Strength (MPa)	40-50	Chloride ion diffusion (m <sup>2</sup> /s)	$1.9 \times 10^{-14}$
Carbonation penetration depth (mm)	<0.5	Freeze-thaw resistance (RDM)	100%
Salt-scaling resistance (kg/m <sup>2</sup> )	<0.012	Entrapped air content	2-4%
Post-cure shrinkage (microstrain)	0	Creep coefficient	0.2-0.5

The remarkable properties of Ductal® are particularly evident when corrosion and chloride permeability are considered, with the mix being far more durable than most standard concrete mixes. The greatest compressive strengths are obtained by heat treatment of the concrete after pouring, with a standard procedure of steaming the UHPC at 90°C (95% RH) for 48 hours. The additional cost of such treatments, coupled with the difficulty of steam treating larger elements, may limit such processes to research applications. Under normal curing conditions, compressive strengths can be reduced by up to 60% (from 200MPa to 120MPa, for example, as shown by Graybeal (2006a)), a significant change. Steam treated mixes gain their strength very rapidly (within 3 days), with a slower progression found in untreated mixes, while it has also been shown that the application of steam treatment at some time after casting (up to 16 weeks) results in compressive strength increases of up to 30% (Graybeal, 2006a).

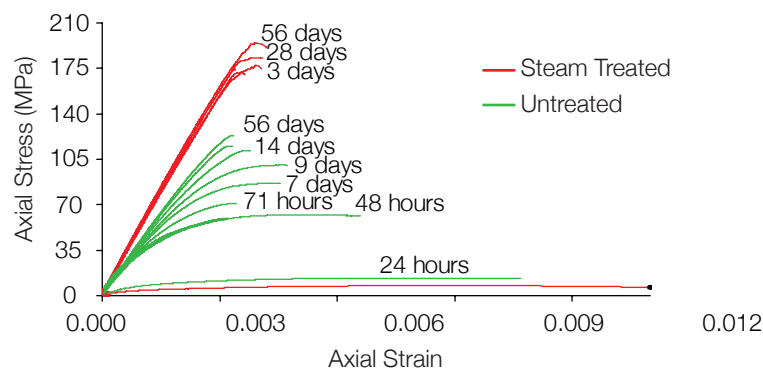


Figure 3.5: Compression tests at different time intervals for steam treated and untreated Ductal® samples (Graybeal, 2006a).

The tensile behaviour of Ductal® is also improved by steam treatment, although tensile strengths are now heavily influenced by the presence of steel fibres. Taking modified results of flexural strength tests, Graybeal (2006a) showed the tensile strength to be between 5 and 7% of compression strength (with slightly higher values recorded from split cylinder tests), and an equation for the tensile strength of Ductal® is given in Eq. 3.3.

The Young's modulus of concrete is often related to its compressive strength, and most concrete design codes have different formulae for determining such values. The extensive testing undertaken by Graybeal (2006a) allowed a linear regression analysis to be undertaken, with the resulting values for Young's Modulus predicted (for concrete strengths up to 131MPa) by Eq. 3.4.

$$f_{ct} = x\sqrt{f_c} \quad \text{Eq. 3.3}$$

When values are measured in psi;  $x = 7.8$  (steam treatment);  $x = 6.7$  (untreated);  $x = 8.3$  (delayed steam treatment)

$$E = 7.1 \times 10^6 e^{\left[ -\frac{1}{2} \left( \frac{\ln\left(\frac{f'_c}{44000}\right)}{1.7} \right)^2 \right]} \quad \text{Eq. 3.4}$$

Where both  $f'_c$  (the compressive strength at a particular age) and  $E$  are given in psi. Values in  $\text{kN/mm}^2$  are obtained by multiplying  $E$  by  $6.895 \times 10^{-6}$ .

The greater strength of steam treated members is offset by slightly higher ultimate shrinkage values (Graybeal, 2006a), although shrinkage in steam treated members occurs more rapidly (Figure 3.6(l)). The creep behaviour of Ductal® is also highly dependent on curing conditions, as shown in Figure 3.6(r), where the results of cylinders loaded to 40% of their anticipated ultimate compressive strength is shown. Creep coefficients<sup>1</sup> and specific creep<sup>2</sup> values for various curing conditions are shown in Table 3.4, with these values comparing favourably to ordinary Portland cement concrete.

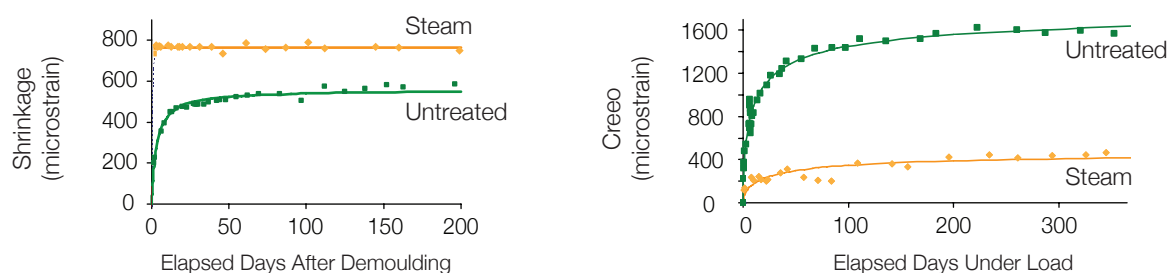


Figure 3.6: Short and long term shrinkage (l); Creep (r); both after Graybeal (2006a).

Table 3.4: Creep testing results (after Graybeal, 2006a).

Curing regime	Control strength (MPa)	Creep coefficient	Specific creep ( $\mu\epsilon/\text{MPa}$ )
Steam	188	0.29	5.7
Untreated	114	0.78	21.2

Steam treated Ductal® has been shown to have far greater abrasion resistance than the same untreated material, with an order of magnitude increase in material lost during various abrasion techniques reported by Graybeal (2006a). This characteristic is perhaps not directly relevant for fabric formed structures, but illustrates the potential for highly durable structures. One of the few full scale reported tests using this material is detailed below, with additional information and discussion provided by Graybeal (2006a, 2006b). The use and design of Ductal® cast fabric formed beam elements is provided in Chapter 5.

<sup>1</sup> Defined (Graybeal, 2006) as 'the final asymptotic amount of additional creep strain that occurs over time divided by the initial elastic strain that occurs when load is first applied'

<sup>2</sup> Specific creep is the creep coefficient divided by the elastic modulus of concrete

### 3.2.2.1.1. Full scale tests

Graybeal (2006b) undertook a series of tests on prestressed Ductal® cast concrete I-beams as part of a FHWA research assessment program into the material that resulted in an analytical uniaxial stress-strain model of Ductal® that may be useful in future design and analysis. AASHTO Type II cross section beams were tested in both flexure and shear, with the single flexural test (23.9m span, 910mm deep section) reaching a peak load and deflection of 790kN and 470mm respectively. Failure occurred at one central crack, which split the section into two pieces, Figure 3.7. Photographs of the failure surface highlight the fibre orientation within the section.



Figure 3.7: Flexural test. (l-r) Midspan deflection, Failure, Fibre detail (Graybeal, 2006b).

Three beam elements were then tested in shear and, having no shear links, relied solely on the tensile capacity of the concrete to resist shear failure. Failure in all cases was catastrophic, with highly linear cracks forming due to the lack of shear reinforcement and sizeable aggregate in the concrete matrix. Final failure occurs once the reinforcing fibres either debond and pull out or yield and fail along the crack. Once pull out occurs, failure propagates rapidly since the concrete itself has little tensile strength, suggesting that the inclusion of steel links could provide further ductility in shear failures. An empirical method to determine the shear capacity of such girders is proposed by Graybeal (2006b), but is not reproduced here.

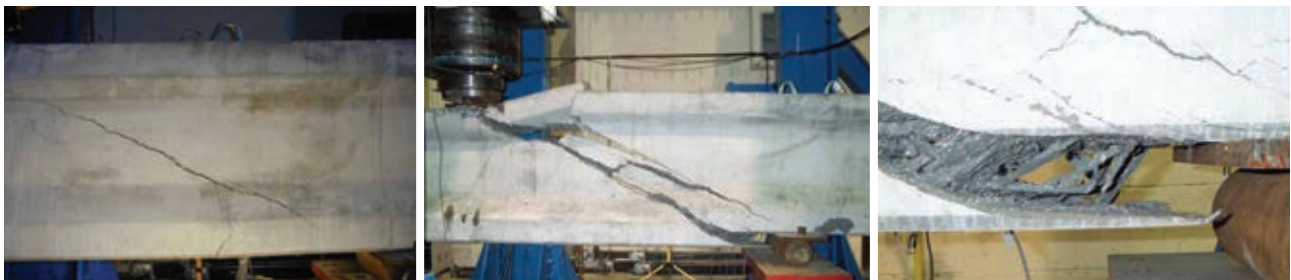


Figure 3.8: Shear failure in prestressed Ductal® cast I-beam.

### 3.2.2.1.2. Uniaxial stress-strain model for flexure

A uniaxial stress strain model of Ductal® was developed by Graybeal (2006b) from the flexural tests as described above and is presented in Figure 3.9 in both detailed and simplified forms. The model was developed by calculating strains at the midspan on vertical slices of the I-beam, from which stresses were calculated. By iteration, equilibrium of the concrete and prestressing strands was achieved at every load step, with the assumed uniaxial UHPC response repeatedly modified. The final curve is then formed of four parts. In compression, behaviour is defined by the Young's Modulus of the mix used (Graybeal, 2006b). Initially linear elastic tensile

behaviour gives way to a transition zone, during which cracking occurs, and after which the post-cracking curve is drawn.

Graybeal (2006b) provides a simplified uni-axial stress strain model that is determined by three conditions. First, the UHPC is assumed to be linear elastic up to 85% of its compressive strength. In tension, the material is assumed rigid plastic, with a conservative percentage of the post-cracking tensile capacity used as a maximum strength. Finally, an ultimate tensile strain of 0.007 is determined. This model has been used in analysing beam tests undertaken by the author, as described in §10.2.3 on page 412.

However, the presence of steel fibres is considered by the author likely to increase the confinement of the concrete compression zone, thereby ensuring a multiaxial rather than uni-axial stress state. The effect of this was not discussed in the above model.

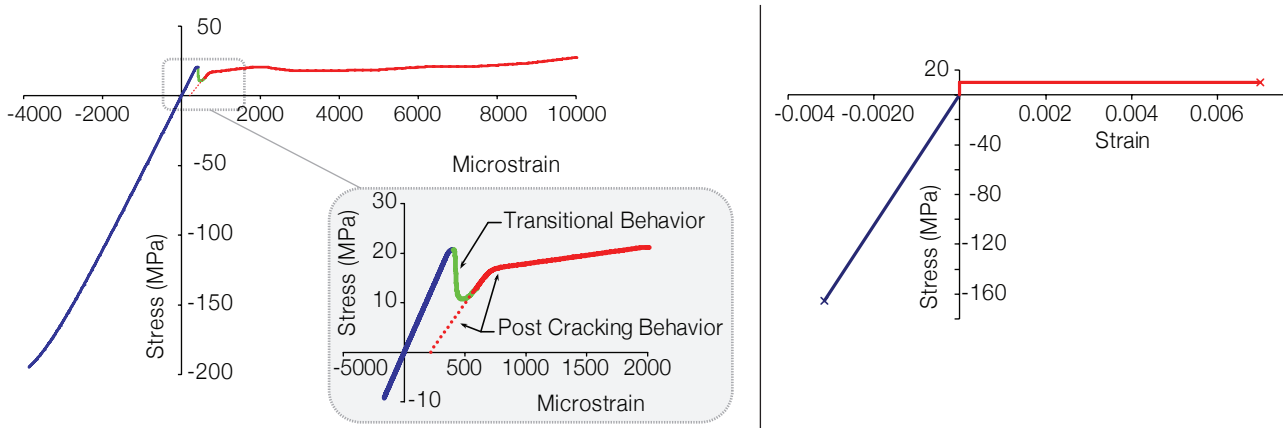


Figure 3.9: Uni-axial stress strain model for Ductal® (after Graybeal, 2006b).

### 3.2.2.1.3. Shear design model

The design of UHPFRC sections in shear has been the subject of numerous studies. Work by Graybeal (2006) suggests that the model proposed by the Association Française de Génie Civil (AFGC, 2002) may be used with success. The model allows the shear capacity of a UHPFRC element to be determined by Eq. 3.5, with the components of this given by Eq. 3.6 to Eq. 3.7. This model has been used in design and testing work undertaken by the author (as described in §5.7 on page 145 and §6.7 on page 206).

$$V_u = V_{Rb} + V_a + V_f \quad \text{Eq. 3.5}$$

Where  $V_{Rb}$  is the concrete contribution;  $V_a$  is the contribution of the reinforcement and  $V_f$  is the contribution of the fibres and:

$$V_{Rb} = \frac{0.21}{\gamma_E \gamma_b} k \sqrt{f_{cj}} b_0 d \quad \text{Eq. 3.6}$$

And for sections in compression,  $k = 1 + \frac{3(\sigma_{cm})}{f_{ij}}$ ; for sections in tension  $k = 1 - \frac{0.7\sigma_{tm}}{f_{ij}}$ ;  $\sigma_m$  = mean stress in the section of concrete under normal force;  $f_{cj}$  = compressive strength of the UHPFRC,  $b_0$  = web width;  $d$  = effective depth.



$$V_a = 0.9d \frac{A_t}{s_t} \frac{f_e}{\gamma_s} (\sin \alpha + \cos \alpha) \quad \text{Eq. 3.7}$$

Where  $d$  = effective depth;  $A_t$  = reinforcement area;  $s_t$  = spacing;  $f_e$  = yield strength;  $\gamma_s$  = partial safety factor;  $\alpha$  = angle of shear reinforcement

$$V_f = \frac{S \sigma_p}{\tan \beta_u} \quad \text{Eq. 3.8}$$

Where  $S = b_0 z$ ;  $b_0$  = web width;  $z$  = lever arm between compression and tension;  $\sigma_p$  = residual tensile strength of the fibres

### 3.2.3. Summary

The behaviour and material properties of concrete have been fully assessed and its use in fabric formed concrete structures discussed. Information pertinent to the design of fabric formed beams has been presented, and will be used in later analysis and design work. The following section discusses the behaviour, modelling and material properties of fabric for use in fabric formed structures.

### 3.3. Fabric

The critical aspect of fabric formwork for determining shape, workability and aesthetic is the fabric itself. Structural properties for commonly used materials are presented, before methods for modelling their behaviour when used as formwork are investigated. The American Society for Testing and Materials publication D123 (ASTM, 1994) provides an extensive forty-seven page reference guide to fabric terminology, a small sample of which is presented in Table 3.5 to aid the following discussion.

Table 3.5: Textile vocabulary (after ASTM, 1994).

Term	Definition	Term	Definition
Bursting Strength	The force or pressure required to rupture a textile by distending it with a force applied normal to the fabric surface	Mesh	The number of warp yarns or ends per linear inch followed by the number of filling yarns or picks per linear inch.
Cover	(in yarns) The outside layer of fibres that form the surface of a yarn.	Polyolefin	Any long chain synthetic polymer composed of at least 85% (by weight) of ethylene, propylene, or other olefin units (monomers).
Count	The number of ends (individual warp yarns) and picks (individual weft yarns) per inch.	Selvage	The woven edge portions of fabric parallel to the warp.
Denier	A direct numbering system for expressing linear density, equal to mass in grams per 9km of yarn, filament, fibre or strand.	Tenacity	The tensile stress of a material based on the linear density of the unstrained material.
Warp	Yarn arranged lengthways on a loom and crossed by the weft.	Weft	Also Fill. Short yarns running crossways on the loom.

Various fabrics have been used for the construction of fabric formed structures, including Hessian (Garbett, 2008; Bailiss, 2006) and some polyolefins (West, 2007), but relatively few tests have been undertaken to quantify the requirements for fabric formed structures. Bailiss (2006) tested a number of fabrics and determined that furniture grade hessian was the most workable material, preventing wrinkling of the fabric during casting. West (2007) has suggested that the woven polyolefin fabrics provide the best compromise between strength, workability and flexibility, and this advice was verified later by Delijani (2010). The properties and behaviour of some of these materials are presented below, with this data informing design and construction work presented later.

#### 3.3.1. Structural properties

Fabrics are anisotropic and tend to exhibit highly non-linear behaviour under loading. The different moduli of Elasticity in the warp and weft directions should be calculated by standard testing methods or be taken from manufacturer's data. Fabrics can suffer from relaxation and creep when loaded, and these effects are therefore important when fabric is used as formwork. Short term behaviour (during concrete curing) is critical and fabrics that display high degrees of relaxation or creep during this time should not be used. In the design of fabric structures (tension membranes for example), these non-linear characteristics are usually disregarded in favour of a conservative linear approximation of the fabrics' mechanical properties (Veenendaal, 2008) but it is possible to use non-linear computational models to more accurately predict the behaviour of the fabric.

The structural properties of some common fabrics used as fabric formwork as presented in Table 3.6, with all available data provided by the relevant manufacturer. Lotrak 300GT, Propex 2006 and Nova Shield have been

used at the University of Manitoba and the University of Edinburgh in previous beam tests (Veenendaal, 2008). Proserve Ltd supplies constant thickness and marine geotextiles for underwater construction, and these fabrics will be used in all subsequent testing in this thesis. However, almost any fabric can be used and future work should be aimed at quantifying the properties of multiple fabrics according to the relevant European ISO (or American ASTM) standard to aid designers.

Table 3.6: Fabric properties.

Name	Material		Tensile Strength		Elongation		Pore Size	Unit Weight	Tie Strength
	Warp	Weft	Warp	Weft	Warp	Weft			
Constant thickness mattress (Proserve Ltd)	Polypropylene	Polyester	45kN/m	25kN/m	20%	20%	330µm	0.41kg/m²	0.4kN
Marine Geotextile (Proserve Ltd)	Polyester (1100 dtex)		54kN/m		25%		423µm	0.23kg/m²	NA
Hessian	Requires testing								
Lotrak 300GT (Don&Low Ltd)	Polypropylene		30.7	30.7	15%	8%	425µm	-	NA
Propex 2006 (Propex Systems)	Polypropylene		40	40	-	-	297µm	-	NA
Nova Shield (ECP Ltd)	High density polyethylene		45.6	42.08	-	-	-	0.224kg/m²	NA

### 3.3.1.1. Creep and relaxation

Creep describes the extension with time of a material under constant stress. For fabrics, creep behaviour is important during fabrication (Cui and Wang, 1999) and some theoretical models exist to describe the creep behaviour of textiles. When used as formwork, fabric will creep under the weight of the concrete and the short term creep behaviour of all fabrics used should be determined prior to construction. Creep behaviour is important for approximately 24 hours after pouring, during which time the concrete mix may be sufficiently plastic to also deform during creep of the fabric.

### 3.3.2. Modelling

Modelling the hydrostatic shape of a fluid filled fabric envelope can be achieved in a number of ways. Schmitz (2006) used an iterative computational procedure to determine the shape of fluid filled wall panels, while Veenendaal (2008) implemented dynamic relaxation to predict the final shape of fabric formed beams. Bailiss (2006) developed empirical relationships that were later used by Garbett (2008), while Iosilevskii (2010) determined a complete mathematical solution to the problem.

#### 3.3.2.1. Dynamic relaxation

Veenendaal (2008) used Dynamic Relaxation to determine the behaviour of fabric filled with wet concrete. Dynamic Relaxation (see Barnes, 1998) is a method to solve static problems using a pseudo-dynamic approach in which Newton's second law is applied with a fictitious mass value that is calculated to ensure convergence. Models for both keel mould and pinch mould construction methods (§2.3 on page 17) were successfully developed in this way.

A keel mould (§2.3.1.2 on page 17) was modelled using a five point (fourth order) bezier curve, which can be described mathematically. The five point curve is also symmetrical about the midspan of the beam, thereby reducing the number of coordinate variables by a factor of four. The top flange geometry was also defined by bezier curves, allowing multiple beam geometries to be generated from a total of twelve variables.

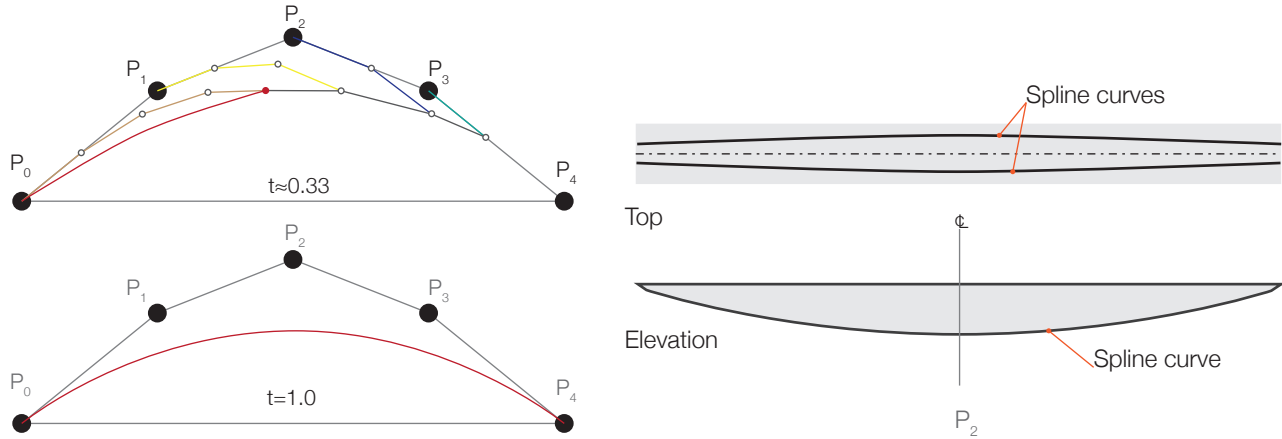


Figure 3.10: Fourth order bezier curve (l); Modelling the keel mould (r) (After Veenendaal, 2008).

The pinch mould was modelled based on an assumption of five pinch points along the length of the beam. Each 'pinch point' was modelled as a quadrilateral, giving nine variables for each pinch (four corners and a depth). A bottom 'spacer' was also added, allowing the bottom chord of the beam to be fixed in width. This gives a total of 36 variables (assuming a symmetrical beam), rather more than the twelve required to define the keel mould beam, but is still manageable from a computational perspective.

Veenendaal (2008) highlighted two important issues that arise when dynamic relaxation is applied to fabric formwork, namely that fluid pressure during casting are atypical loads for membrane structures, and that contact between the formwork and the fabric results in sharp corners that are generally not found in fabric tension structures. Methods to deal with these two phenomena are considered below.

#### 3.3.2.1.1. Fluid pressures

Calculating the fluid pressures in a fabric formed structure is key to determining its deformed shape. The concrete fluid pressure acts normal to the fabric surface and thus changes direction around the fabric element. Veenendaal (2008) provides a method for calculating the pressures at any point on a surface by dividing the fabric into triangles. The normal vector to each triangle is found using the cross product, Eq. 3.9, and the area and perimeter of each triangle is found using Heron's formula, Eq. 3.10. The normal vector for each node is then calculated as the weighted sum of the surrounding triangle normals, Eq. 3.12, before the unit vector is calculated, Eq. 3.13, and finally the concrete load on each node is determined, Eq. 3.14. The process is summarised in Figure 3.11.

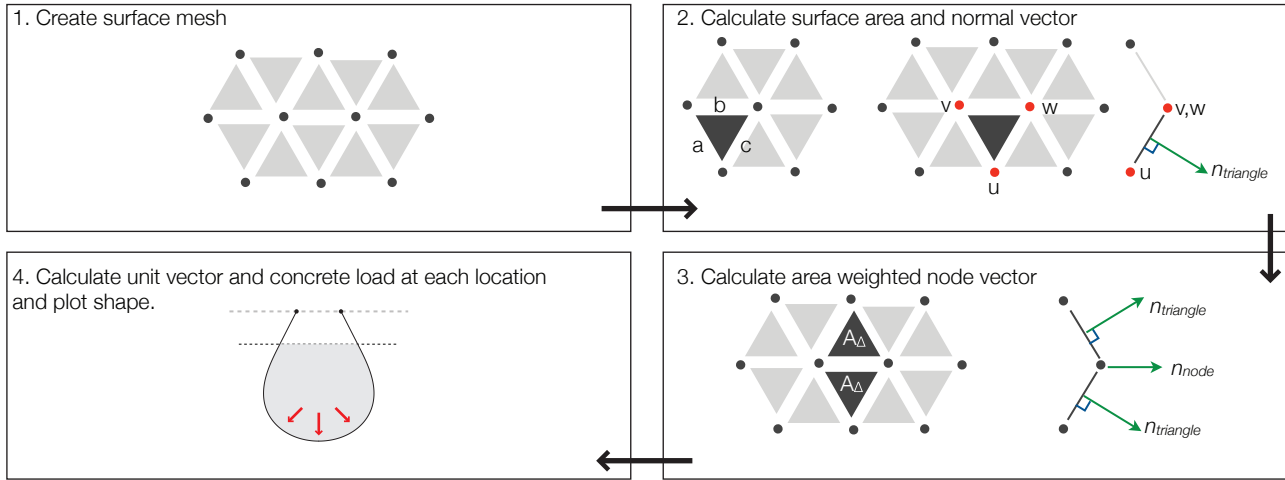


Figure 3.11: Calculating concrete loads in a fabric formed structure (illustration after Veenendaal, 2008).

$$\mathbf{n}_{triangle} = \mathbf{u} \times \mathbf{v} \quad \text{Eq. 3.9}$$

Where  $\mathbf{u}$  and  $\mathbf{v}$  are vectors describing a triangle of side length  $a, b, c$ .

$$Area = \sqrt{s(s-a)(s-b)(s-c)} \quad \text{Eq. 3.10}$$

$$\text{Where } s = \frac{a+b+c}{2} \quad \text{Eq. 3.11}$$

$$\mathbf{n}_{node} = \sum \frac{\mathbf{n}_{triangle}}{A_{triangle}} \quad \text{Eq. 3.12}$$

$$\hat{\mathbf{n}}_{node} = \frac{\mathbf{n}_{node}}{\|\mathbf{n}_{node}\|} \quad \text{Eq. 3.13}$$

$$q_c = \rho g h \cdot \hat{\mathbf{n}}_{node} \quad \text{Eq. 3.14}$$

### 3.3.2.1.2. Edge conditions

The second issue to consider when dynamic relaxation is applied to fabric formed structures are the edge conditions where the fabric and formwork meet. Typically, plywood sheets or steel tubes are used as edge members in forming tables and thus the computer analysis must ensure that the fabric can change direction around these fixed edges. Veenendaal (2008) identifies two conditions for the successful modelling of the edge condition when dynamic relaxation is used:

1. Elements on the edge must retain their correct length;
2. Nodes that pass over the edge must stay within the plane of the (now folded) fabric and the force and velocity vectors of the node should change accordingly.

### 3.3.2.2. Static approach

An alternative method for determining the hydrostatic shape is to consider a hanging mould that has been filled with fluid, Figure 3.12(l). The pressure in the fluid is given by Eq. 3.15, the tension,  $T$ , per unit width of fabric is constant, and the curvature of the fabric is given by Eq. 3.16. To determine the relationship between fluid volume

and external shape, the similar condition of a buckled column is then considered (Figure 3.12(c)). The curvature of the column is given by Eq. 3.17, and its internal moment is given by Eq. 3.18.

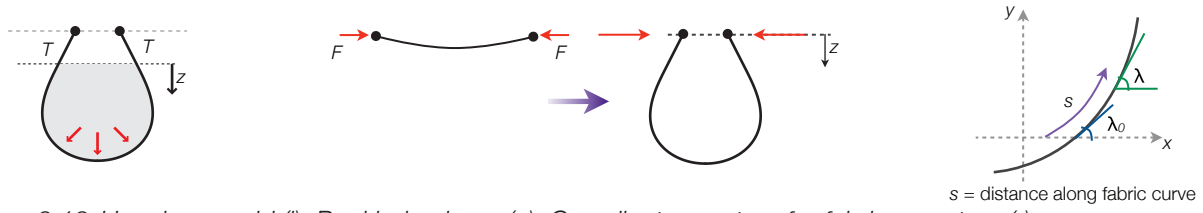


Figure 3.12: Hanging mould (l); Buckled column (c); Coordinates system for fabric curvature (r).

$$p = \rho g z \quad \text{Eq. 3.15}$$

$$\kappa = \frac{\rho g z}{T} \quad \text{Eq. 3.16}$$

$$\kappa = \frac{F}{EI} z \quad \text{Eq. 3.17}$$

$$M = EI\kappa = Fz \quad \text{Eq. 3.18}$$

Therefore, in the  $x$ - $y$  coordinates shown in Figure 3.12(r), the solution for  $s$  is determined as presented below. The resulting integral for  $s$  (Eq. 3.25) is solvable by numerical integration.

$$\kappa = \frac{d\lambda}{ds} = \frac{-y}{a^2} \quad \text{Eq. 3.19}$$

$$y = \int \sin \lambda \, ds \quad \text{Eq. 3.20}$$

Double integration of this gives:

$$\frac{d^2 y}{ds^2} = -\frac{\sin \lambda}{a^2} \quad \text{Eq. 3.21}$$

Which is then multiplied by:

$$\frac{d\lambda}{ds} \quad \text{Eq. 3.22}$$

To obtain:

$$\frac{d\lambda}{ds} \frac{d^2 \lambda}{ds^2} = \frac{d\lambda}{ds} \frac{-\sin \lambda}{a^2} \quad \text{Eq. 3.23}$$

$$\frac{1}{2} \left( \frac{d\lambda}{ds} \right)^2 = \frac{\cos \lambda - \cos \lambda_0}{a^2}$$

Thus:

$$\frac{d\lambda}{ds} = \frac{\sqrt{2(\cos \lambda - \cos \lambda_0)}}{a} \quad \text{Eq. 3.24}$$

And so:

$$s = \frac{a}{\sqrt{2}} \int \frac{d\lambda}{\sqrt{\cos \lambda - \cos \lambda_0}} \quad \text{Eq. 3.25}$$



The integration method presented above has been demonstrated using Excel spreadsheets (Foster, 2010) with these provide a simple and reliable calculation method to determine the hydrostatic shape. In addition, the method is able to predict the shape of 'part full' fabric bag, as well as that of a 'T-Beam', as illustrated in Figure 3.13.

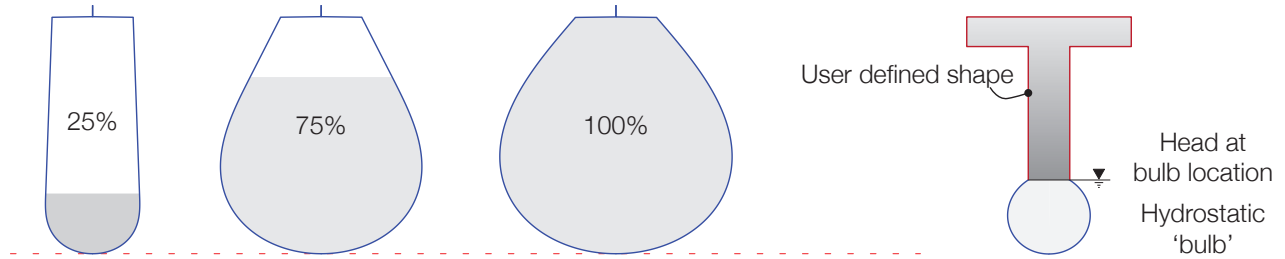


Figure 3.13: Hydrostatic shape plots during filling (l); Plot of T-Beam bulb shape (r).

Solutions for the exact hydrostatic shape of a fluid filled fabric bag are provided by losilevskii (2010), reproduced in Eq. 3.26 and Eq. 3.27. By considering equilibrium of a small element along the length of the perimeter (Figure 3.14(l)), integrals similar to those shown above are found, the solution to which requires the use of elliptic integrals. Elliptic integrals (see, for example, Abramowitz and Stegun, 2002) were first developed by Euler and Fagnolo to determine arc lengths around an ellipse, and although complex can be readily solved using Matlab if required. In addition to plotting the cross sectional shape, losilevskii (2010) shows that by knowledge of the edge tension in the fabric the area of the hanging shape can be calculated, Eq. 3.28.

$$\frac{x_s}{l} = \frac{E(\theta_s, k)}{K(k)} - \frac{1}{2} \frac{F(\theta_s, k)}{K(k)} \quad \text{Eq. 3.26}$$

$$\frac{y_s}{l} = \frac{k}{K(k)} \cos \theta_s \quad \text{Eq. 3.27}$$

$$A_c = l^2 \frac{k \sqrt{1 - k^2}}{K^2(k)} \quad \text{Eq. 3.28}$$

Where  $x_s, y_s$  are coordinates along the curve,  $l$  is the fabric perimeter length.  $F(\theta, k)$  is the incomplete elliptical of the first kind,  $K(k)$  is the corresponding complete elliptic integral of the first kind ( $k = F(\pi/2, k)$ ).  $E(\theta, k)$  is the incomplete elliptic integral of the second kind.

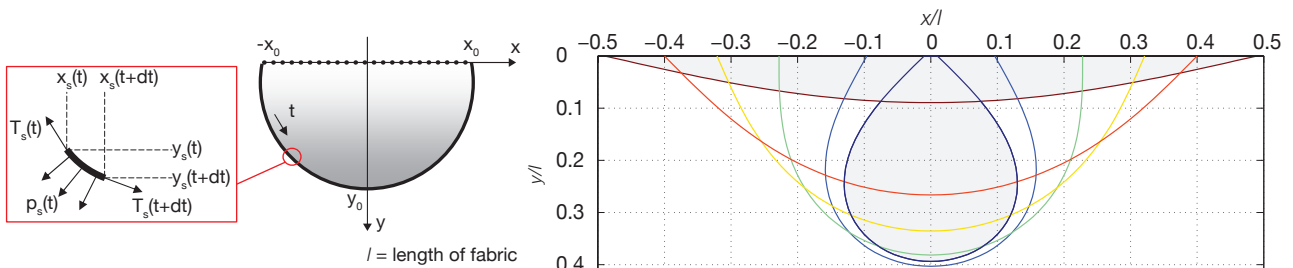


Figure 3.14: Equilibrium considerations (l); and cross section predictions (r) (after losilevski, 2010).

Using losilevskii's method, it is possible to plot a range of cross sectional shapes (Figure 3.14) based on the ratio of top width and draft to the fabric perimeter length. losilevskii (2010) further reveals a number of points that are pertinent to the design of fabric formed structures. First, the edges of the fabric are vertical when  $2x_d/l \approx 0.457$ .

Second, the maximum area of the section occurs when  $2x_g/l \approx 0.643$ , and third the maximum draft of the section occurs when  $2x_g/l \approx 0.195$ . These results come from numerical analysis of the relevant variables, and may be used to define design guidelines for fabric formed structures.

Iosilevskii's method provides 'exact' solutions to the shape of a fabric formed element. However, an empirical method first developed by Bailiss (2006) may also be used. Developed by photographing fluid filled fabric moulds, a relationship between top breadth, depth and cross sectional area was established, Eq. 3.29, Eq. 3.30 and Figure 3.15, that was subsequently used in work by both Garbett (2008) and Chawla (2010). Using the integration method outlined above, Foster (2010) showed that the empirical relationships provide a good estimation of the hydrostatic shape. The close agreement seen is pleasing, both in verifying the empirical approach and in providing evidence as to the accuracy of the integration method, which will be used in future work.

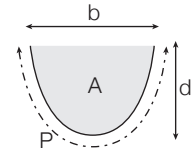
$$P = \frac{-(0.212b - d) \pm \sqrt{(0.212b - d)^2 - 4(0.396)(-0.49b^2)}}{2(0.396)} \quad \text{Eq. 3.29}$$

$$A = \left[ \left( \frac{\left( \frac{b}{P} \right) - 0.05}{0.65} \right) - 0.34 \right] (bd) \quad \text{Eq. 3.30}$$

Where  $b$  = top width;  $d$  = depth;  $P$  = cross section perimeter;  $A$  = cross sectional area.



Figure 3.15: Empirical method (after Bailiss, 2006).



### 3.3.3. Practical use

Most fabrics are untested for use in concrete construction and small panels should be tested prior to use. One of the great advantages of fabric formwork is that the fabric may be re-used for multiple elements, as shown in work that is currently underway in Chile to mass produce small, fabric formed, seating elements (*pers. comm.*, Prof. Mark West, May 2010). This work will be helpful in determining how many casts it is possible to produce from one sheet of fabric and the results are keenly anticipated. Past research at CAST has shown that a single sheet of fabric may be used 20 times before degradation occurs (*pers. comm.*, Prof. Mark West, May 2010).

### 3.3.4. Application

A method for solving the shape of the fluid filled fabric bag was adopted using an Excel based iterative routine based on the work of Foster (2010) throughout this thesis. Its use is highlighted in the following chapters, and a brief description of the process is provided in §10.4 on page 424.

### 3.3.5. Summary

The structural properties of fabric and methods to model its behaviour when filled with concrete have been presented, each of which has advantages and disadvantages. The dynamic relaxation and ANSYS routines developed by Veenendaal (2008) are accurate, reliable and adaptable, but the use of ANSYS is complex and requires significant computing power. Mathematical predictions of the hydrostatic shape are available, and can be solved using simple spreadsheets, making them attractive to designers. Relationships developed by Foster (2010) and Bailiss (2006) have been shown to be comparable to such mathematical approaches and have been adapted for use in this thesis.

### 3.4. Reinforcement

The reinforcement of orthogonally cast concrete structures has been the subject of considerable research over the past 100 years and codified design is predominantly based on the availability of deformed steel bars of various cross sections and longitudinal profiles. Variable section members, such as those formed using fabric, present significant challenges for conventional reinforcement design. This section assesses the problems and current design methods for the reinforcement of fabric formed concrete structures before alternative approaches, including the use of advanced polymers and prestressed reinforcement, are presented.

#### 3.4.1. Orthogonal structures

Reinforcement detailing in orthogonal structures is well covered in the technical literature. Of particular interest for comparison to fabric formed sections is the provision of anchorage to longitudinal bars, as variable section members often result in end zones with little space for standard detailing provisions, as shown in Figure 3.16. The design anchorage length for a steel bar to BS EN 1992-1-1 (2004) is given by Eq. 3.31, where coefficients are used to model 1) the effect of the shape of bars; 2) the effect of concrete cover; 3) the effect of confinement by transverse reinforcement; 4) the influence of welded transverse bars along the design anchorage length; and 5) for the effect of the pressure transverse to the plane of splitting along the design anchorage length (IStructE, 2006). The values of coefficients in Eq. 3.31 to Eq. 3.33 can be found in BS EN 1992-1-1 (2004) or the Standard Method of Detailing Concrete (IStructE, 2006).

$$l_{bd} = \alpha_1 \alpha_2 \alpha_3 \alpha_4 \alpha_5 l_{bd,rq} \geq l_{b,min} \quad \text{Eq. 3.31}$$

Where, for anchorages in tension:

$$l_{bd,rqd} = \frac{\sigma}{4} \left( \frac{\sigma_{sd}}{f_{bd}} \right); \quad \text{Eq. 3.32}$$

Where:

$\sigma_{sd}$  is the design stress of the bar at the position from where the anchorage is measured;

$$f_{bd} = 2.25 \eta_1 \eta_2 0.21 f_{ck}^{(2/3)}$$

$$l_{b,min} > \max \begin{cases} 0.3 l_{b,rqd}; \\ 10\emptyset; \\ 100mm; \end{cases} \quad \text{Eq. 3.33}$$

The application of these rules to variable section members is not addressed specifically, and therefore the provision of reinforcement anchorage in variable section members must be considered carefully in the design process.

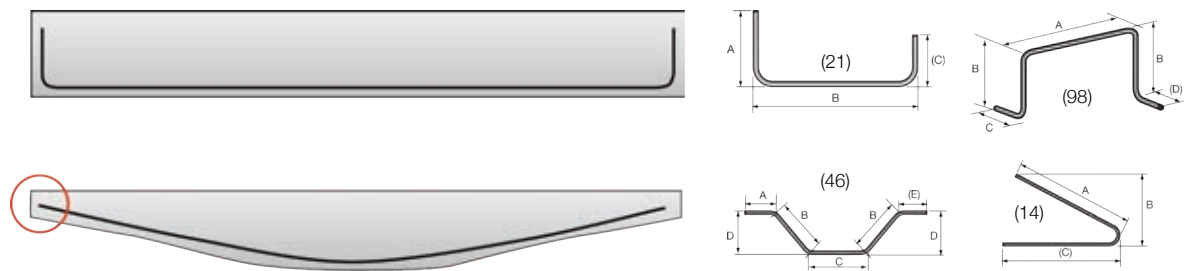


Figure 3.16: Anchorage comparison in non-orthogonal structures (l); Standard bar bend shapes (r).

### 3.4.2. Non-orthogonal structures

Work at the University of Bath has previously used deformed steel bars as reinforcement for flexibly formed concrete structures (Garbett, 2008). Current and proposed methods for the provision of longitudinal and transverse reinforcement in both passively and actively reinforced fabric formed structures are summarised in Figure 3.17. Each aspect is investigated separately in the following text.

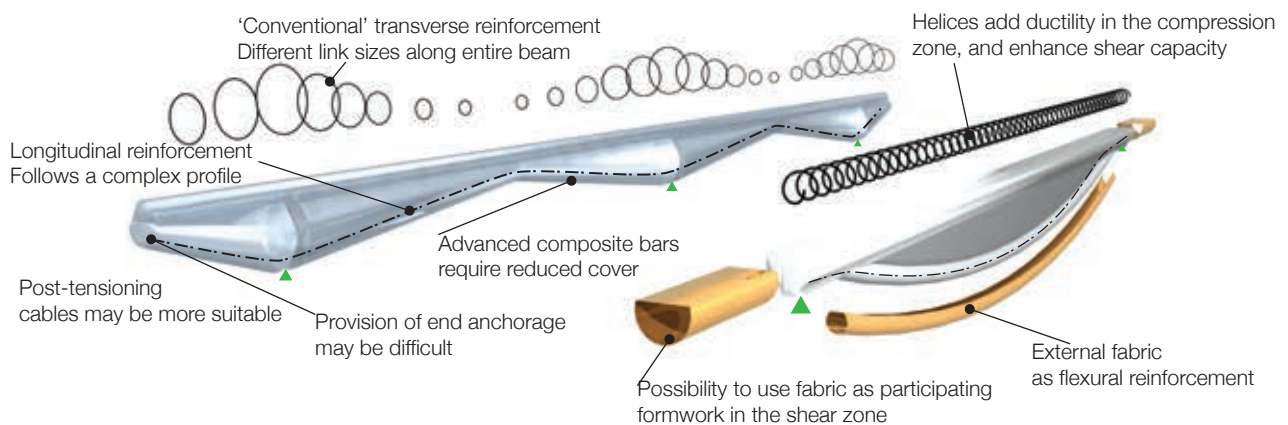


Figure 3.17: Reinforcing fabric formed concrete beams.

Providing sufficient anchorage to steel bars has previously been achieved using welded steel end plates, as illustrated in Figure 3.18. The longitudinal bar is firstly deformed into a predetermined shape, before being welded to angle brackets supported inside the fabric mould. The concrete is then poured over to obtain the reinforced beam.



Figure 3.18: Anchorage methods in steel reinforced fabric formed beams (after Garbett, 2008).

Whilst the welded plate has been found to provide sufficient anchorage, there are numerous problems that will limit its use on an industrial scale. Permanent deformation of the bar is required to ensure that it remains in the correct position during casting, a process that is time consuming and introduces the possibilities of construction errors (the effects of which are investigated in Chapter 10 on page 409). Once welded, cover to the steel at the end plate

is effectively zero, ensuring that such beams may not be suitable for use in exposed environments. In addition, all the beams tested to date (Figure 3.18) have been of small span (2m) with very low longitudinal reinforcement percentages (typical  $A_s = 113\text{mm}^2$ ). When multiple longitudinal bars are required, welding to a single end plate can become difficult.

The IStructE (2006) advise that welding be avoided wherever possible for reinforced concrete structures, as the combination of heat and rapid cooling can lead to brittle structures that are then susceptible to brittle fracture (CARES, 2004). Control of the welding process is essential to ensure that hydrogen is not absorbed during welding in the heat affected zone as this can additionally lead to brittle failure by hydrogen cracking in the steel (CARES, 2004). Poorly made welds potentially introduce defects into the steel, which then serve as stress raisers during loading and can lead to premature failures. Locational or structural welding must be carefully monitored during construction. The requirement for skilled workers coupled with the potential to introduce defects make welded joints an imperfect solution to the anchorage of longitudinal steel bars. It is therefore recommended that future steel reinforced fabric formed structures move away from welded end connections, and methods to do this are discussed in Chapter 6.

The flexible nature of fabric formwork for concrete beams makes the accurate positioning of longitudinal reinforcement difficult (Garbett, 2008). This is important for two reasons. First, the bending capacity of the section could potentially be compromised if the bars are too high and second, cover to the steel will be compromised if the bars are too low. Providing longitudinal reinforcement where very low cover can be specified is therefore an advantage for fabric formed sections, and this may be achieved through the use of advanced composite reinforcement.

### 3.4.3. Advanced composites

The use of fibre reinforced polymer (FRP) bars as reinforcement for concrete structures holds distinct advantages for designers, including high tensile strength and excellent durability, but their use in the construction industry has been limited. This section introduces the material and structural properties of FRP bars, and discusses how they can be used in fabric formed structures. Consideration is given to the bond between FRP and concrete in §3.4.3.4, before reinforced (§3.5) structures are discussed.

#### 3.4.3.1. Introduction

Fibre reinforced polymers (FRP) consist of fibres encased in a resin matrix. The resin matrix binds the fibres (which provide the strength of the composite), transferring loads between them whilst also providing protection. The most common fibres are glass, carbon, aramid and natural fibres such as hemp.

There are two major groups of resins: thermosets and thermoplastics. Thermoset resins are the most common, as they ensure rigidity of the FRP at high temperatures (Ibell and Darby, 2008). Thermoplastics are used where a remouldable shape is desired, but they have the distinct disadvantage of softening during fire. FRPs are strong in



the direction of the fibres, but exhibit linear elastic behaviour (Figure 3.19) and should therefore be considered as an entirely new material and not as a direct replacement for steel reinforcement in concrete structures.

Steel reinforced concrete structures obtain ductility during failure through yielding of the longitudinal steel. The brittle, linear elastic behaviour of FRP prohibits similar behaviour, and thus FRP reinforced concrete structures must be over reinforced to prevent catastrophic FRP failures. In turn, this means that ductility is obtained solely from the crushing behaviour of the concrete, which has been seen to be limited (§3.2). Helices in the compression zone have, however, been shown to improve ductility (Whitehead, 2002) and are used in subsequent testing programs (Chapter 5).

### 3.4.3.2. Properties

The properties of Carbon, Glass and Aramid fibre reinforced polymers are compared to steel in Figure 3.19, where the linear elastic tensile behaviour of FRP is evident. FRP bars also exhibit a size effect, with small diameter bars having higher tensile strengths than larger ones due to the effects of shear lag which develops between the fibres in larger diameter bars. The low stiffness of some FRP bars in compression means that they are not effective for use as compression reinforcement, since at the crushing strain of concrete very little stress would exist in the bars. FRP bars are also weak in shear, since transverse loading creates complementary longitudinal stresses in the bar, which in turn causes failure of the resin in uni-directional bars. The disadvantages of FRPs arise primarily from the use of epoxy resins. At around 85°C, epoxy resins lose their stiffness and thus the fibres are ineffective in carrying loads (Ibell, 2008). Epoxy resins are also highly flammable, and can emit toxic fumes to the surrounding area during fire. Fire resistant Phenolic resins are available, but have reduced aesthetic appeal.

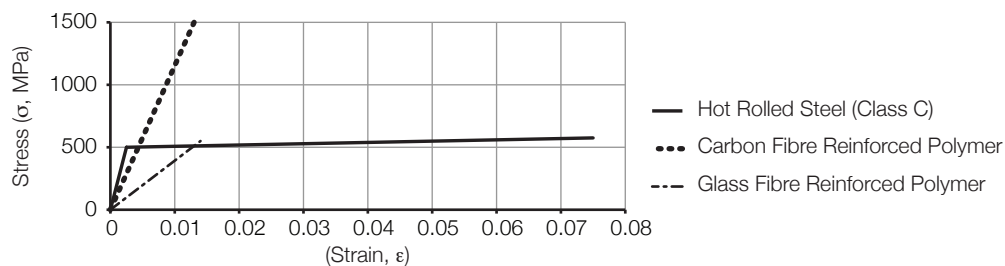


Figure 3.19: Stress strain behaviour of steel bars (BS EN 1992-1-1 (2004) model) and FRP bars.

Table 3.7: Basic material properties of FRP bars.

	Glass (GFRP)	Aramid (AFRP)	Carbon (CFRP)	Steel
Tensile strength (MPa)	550	1200	2000	500
Young's Modulus (GPa)	40	80	150	200
Rupture Strain (%)	1.4	1.5	1.3	10

### 3.4.3.3. Shaping

One of the main drawbacks of a fabric formed structure is the difficulty of installing passive longitudinal reinforcement that fits the desired beam profile. This section considers the development of curved and shaped FRP bars and how they might be used in fabric formed structures before the bond behaviour between FRP and concrete is considered.

Unlike steel, FRP bars cannot be bent on site and shaping must be done prior to the application of a thermoset matrix. Bent bars are therefore more expensive than straight bars. In addition, the bending process leads to stress concentrations resulting in large reductions in tensile strength. The corner bend radius has been found to be critical in determining the reduction in strength and available design guidance (TR55 (Loudon *et al.*, 2004), ACI440 (2006)) provides methods to calculate these strength reductions.

At present, the availability of shaped FRP bars is limited to glass and carbon fibre reinforced stirrups. The difficulty and expense of producing more complex shapes has prevented their use in fabric formed structures up to now. The following section considers how the creep and stress relaxation behaviour of FRP bars might be used to provide the required longitudinal reinforcement.

#### 3.4.3.4. Concrete bond behaviour

The bond between the reinforcement and concrete in reinforced and post tensioned concrete structures has been the subject of extensive research over the past century. The bond between polymeric reinforcement and concrete on the other hand, is less well documented and is often poorly considered in design codes. This section investigates the bond mechanisms that exist between concrete and fibre reinforced polymer bars used as passive reinforcement. Existing theoretical models are examined, and an innovative method to improve the pull out strength of FRP bars is assessed before conclusions are drawn.

#### 3.4.3.5. Introduction

The properties of deformed steel reinforcing bars are essentially the same the world over, a result of international standardisation of production techniques. FRP bars on the other hand suffer from far greater variation in properties, with each of the main manufacturers producing different products, making standardisation in the near future unlikely. This has hindered the development of design codes for FRP. The continuing development of FRP materials and manufacturing processes is a further difficulty for the analysis of bond behaviour, and older test results cannot necessarily be applied to improved FRP materials (Tepfers and De Lorenzis, 2003).

The anchorage behaviour of FRP bars is crucial to their success in fabric formed structures, which may have small end zones and short development lengths. FRP is often considered (and used) as a direct replacement for steel bars in passively reinforced concrete structures. The same bar dimensions, layouts and surface textures are produced, yet their behaviour is fundamentally different. The fact that steel is an elasto-plastic material is fundamental to this. A crack in the tension face of a bonded, steel reinforced concrete member causes the steel to strain and yield over the crack. This behaviour is the dominant response in the bar (Stratford and Burgoyne, 2003) and, coupled with the excellent bond between deformed steel bars and the surrounding concrete, ensures that bond strength between steel and concrete is often only critical in anchorage zones.

Figure 3.19 compares the idealised behaviour of FRP and steel bars. The linear elastic response seen in FRP bars means that any stress concentrations that develop over a crack can easily lead to brittle failure in the bar if slip is

prevented by good bond along its entire length. In a steel reinforced structure, local yielding of the steel over such cracks redistributes stresses and ensures that a ductile response is achieved. An overly strong bond between FRP and concrete is therefore detrimental to the behaviour of the structure and should be avoided. Equally, a completely unbonded bar would have very little anchorage and provides no real capacity to the section.

The middle ground, an intermittently bonded bar, is one that provides sufficient bond to develop stiffness but does not allow local failure of the FRP to occur (Lees and Burgoyne, 1999a). The behaviour of the FRP bar within the anchorage zone has been well documented (Lees and Burgoyne, 1999a,b) but only small amounts of work have focused on providing means to improve anchorage. Techniques used in steel structures (such as hooks) are not applicable to FRP reinforced construction, as bends introduced into a straight FRP bar can cause damage, leading to reductions in ultimate capacity. Preformed bends are both expensive and technically difficult and are therefore rarely used.

#### 3.4.3.6. Bond mechanisms

Bond stresses in reinforced concrete members arise from anchorage of the bars and from changes in bar force along the length of the member in regions of varying bending moment. The mechanisms of bond in steel reinforced sections are considered by Tepfers and De Lorenzis (2003) to be dependent on eight wide ranging parameters, including the geometry of the member, placement of the bar, cover depth, crack pattern and formation and confinement of the concrete by surrounding reinforcement.

In FRP reinforced sections, the number of variables is greater. The surface of FRP bars, whether they are coated or deformed, is generally weaker than steel and therefore the bars are unable to create stress concentrations in the concrete in the same manner as steel bars (Tepfers and De Lorenzis, 2003). This can delay the onset of cracking, which was also shown to be dependent on the surface finish of the FRP bar.

Understanding the bond between concrete and FRP is key to providing true composite action in an FRP reinforced section. The bond characteristic will be determined by the location and usage of the FRP. For example, pre-tensioned tendons must be adequately bonded to ensure prestressing forces are transferred (Lees and Burgoyne, 1999a) while transverse bars must be sufficiently partially bonded to ensure force transfer occurs without the possibility of local failure (Ibell and Burgoyne, 1999).

The load-slip relationship for FRP bars depends on the surface finish of the bar itself. The bond in plain bars is governed by shear, both between the concrete and the FRP and within the surface layers of the FRP itself by interlaminar shearing. The bond strength is thus normally very low (Darby *et al.*, 2007) and has large experimental variability. The behaviour of the FRP bar is thus considered to be governed by its shear and transverse properties, illustrating the importance of the resin matrix in providing bond strength.

For FRP bars with deformed surfaces, bond strength is influenced not only by the chemical adhesion of the bar and surrounding concrete, but also by friction and mechanical interlock in the system (Cosenza *et al.*, 1997).

Chemical adhesion develops at the bar-concrete interface and is the first mechanism to resist applied loads, but is relatively weak and fails after first slip of the reinforcement occurs. The weak adherence between epoxy resins used in FRP and concrete led to the development of sand coatings for FRP bars, allowing either mechanical interlock or frictional behaviour to provide bond strength post chemical adhesion failure.

### 3.4.3.7. Theoretical modelling of FRP bond behaviour

Theoretical modelling of FRP bond behaviour is an important step in developing accurate analysis techniques for FRP structures with active and passive reinforcement. Malvar (1994) provided the first empirically based model for determining the bond behaviour of FRP bars. However, its reliance on seven variables makes it slightly unwieldy, and only GFRP bars were considered.

Subsequent work has focussed mainly on the development of Eligehausen *et al.*'s (1983) model for steel reinforcement (the Bertero-Popov-Eligehausen model, BPE) as shown in Figure 3.20(l). When applied to steel reinforcement, this model includes an ascending branch, a plateau of constant bond stress and a descending branch, during which softening occurs (Choi, 2002). The model has been applied to FRP bars in numerous cases (for example Faoro, 1992; Alunno Rossetti *et al.*, 1995, cited by Choi, 2002). Cosenza *et al.* (1997) developed a modified BPE model, (Figure 3.20(r)) by considering that FRP bars cannot undergo a state of constant maximum bond stress. Therefore, the descending branch occurs immediately after maximum bond stress is achieved. The ascending branch relationship for both models is given by Eq. 3.34, while the descending slope for the modified model is given by Eq. 3.35. At large values of slip, it is also proposed that the bond stress remains constant at a value given by Eq. 3.36.

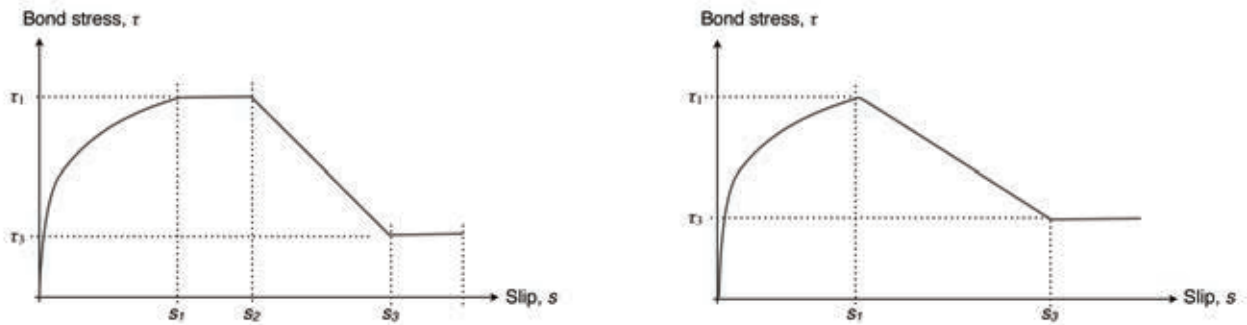


Figure 3.20: BPE model – Steel (l); FRP (r) (after Cosenza *et al.*, 1997).

$$\frac{\tau_R}{\tau_1} = \left( \frac{s}{s_1} \right)^\alpha \dots \text{for } (s < s_1) \quad \text{Eq. 3.34}$$

Where  $\tau_R$  is the bond stress;  $s$  is the bar slip;  $\alpha$  is a curve fitting parameter (empirically determined)

$$\frac{\tau_R}{\tau_1} = 1 - p \left( \frac{s}{s_1} - 1 \right) \dots \text{for } (s_1 \leq s \leq s_3) \quad \text{Eq. 3.35}$$

$$\tau_R = \tau_3 \dots \text{for } (s > s_3) \quad \text{Eq. 3.36}$$

Cosenza *et al* (1997) analysed the method against available test data and showed that good correlations can be achieved by correctly determining the curve fitting parameters,  $\alpha$  and  $\rho$ . However, this requires test data which can only be obtained by testing. The modified BPE model was rationalized (Cosenza *et al.*, 1997) by considering serviceability limits for an FRP reinforced concrete element. Cosenza *et al.* (1997) argue that only the ascending branch of the BPE model need be considered, thus ensuring that the bond stress remains below the maximum. A more refined model of the ascending branch is presented, Eq. 3.37, and subsequent analysis (Cosenza *et al.*, 1997) showed that this ascending branch model provides the best correlation with available test data.

$$\frac{\tau_R}{\tau_1} = \left(1 - e^{(-s/s_r)}\right)^\beta \quad \text{Eq. 3.37}$$

However, Choi and Ibell (2004), in considering primary anchorage zones in FRP prestressed structures, argue that bond behaviour at large values of slip may remain important since the reinforcement in such structures only becomes effective in the post-elastic stage. This means that values for  $s_3$  (Figure 3.20) and their corresponding bond strength are critical. In turn, this assertion means that the initial behaviour up to peak bond strength is less important, and a linear equation for the ascending branch may well be sufficient for design. This approach is also seen in work by Rostasy and Budelmann (1993), where a trilinear model was used to model pull out tests on GFRP bars.

#### 3.4.3.8. Experimental analysis

There have been numerous experimental studies into the bond of FRP bars embedded in concrete, with each leading to separate empirical formulae that may be applicable only to certain bar types or loading situations. There also exist a number of differences in behaviour between deformed steel and FRP bars. For steel reinforced structures, it is generally accepted that the bond strength is proportional to the square root of the concrete strength. For FRP reinforced structures, it has been found that the ultimate bond strength is independent of the concrete grade (Nanni *et al.*, 1995).

For steel reinforcement in the top of a concrete beam, it is generally assumed that compaction will be poor and so the bond strength is taken at around 70% of that used for bars in the tension zone, where good compaction can be assumed (Matthews *et al.*, 1999). However, tests on FRP reinforced structures with high degrees of confinement (Kanakubo *et al.*, 1993) showed little difference in the behaviour of top and bottom cast bars, suggesting again that anchorage failure in FRP bars takes place in the resin rather than in the concrete.

Two experimental techniques are used to determine the bond strength of reinforcing bars: pull out tests and beam tests. The pull out test, Figure 3.21(l), provides the simpler experimental technique and allows measurements of slip at both ends of the bar to be taken. However, pull out tests do not accurately model the behaviour of a tensile flexural reinforcing bar. During pull out, the concrete cubes are put into compression by the loading platens, which

effectively confine the concrete and reduce its propensity to suffer from tensile failure. This ensures that pull out testing provides an upper bound value to the bond-slip performance of FRP bars (Focacci *et al.*, 2000).

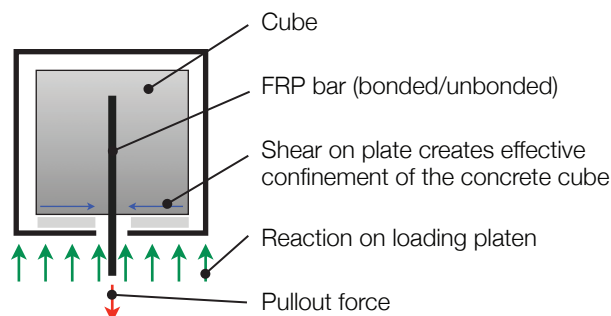


Figure 3.21: Pull out test (l); Modified pull out test (r) (after Chung, 2000).

The beam test (Figure 3.22) is considered to give more representative results, but is also time consuming to undertake. The method essentially requires a full model of the bar behaviour to be constructed, ensuring that the concrete around it remains in tension throughout the test. Most importantly, Benmokrane *et al.* (1996) showed that bond strengths determined by beam tests are lower than those from an equivalent pull out test, highlighting the need for caution when pull out tests are analysed

Early work by Makitani *et al* (1993) used the beam test to analyse the behaviour of aramid, carbon and glass bars. It was determined that the full tensile strength of the bar was achieved with a bond length of 40 times the bar diameter. Work at the University of Bath on the pull out strength of near surface mounted FRP reinforcement has refined the beam test arrangement to reduce experimental requirements, Figure 3.22(r), and this is used in subsequent work to determine the behaviour of an innovative anchorage method for FRP bars (Chapter 6 on page 157).

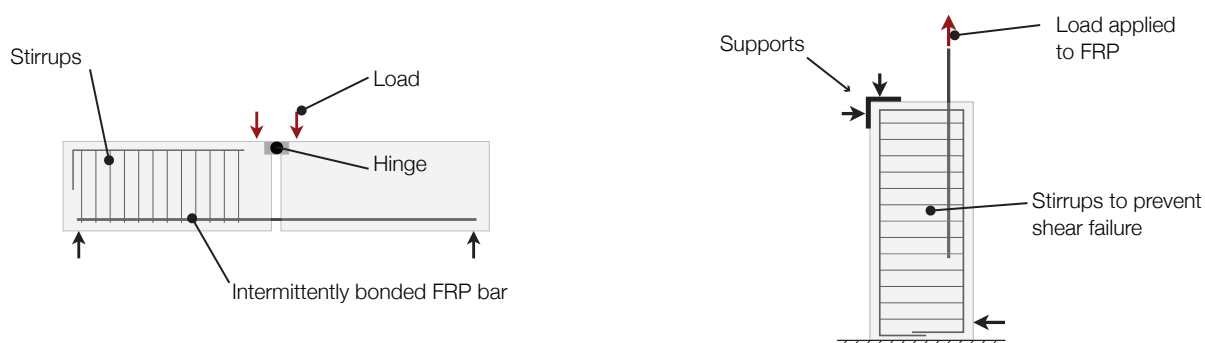


Figure 3.22: Beam test for pull out strength (after Makitani *et al.*, 1993) (l); Refined testing procedure (after Perera *et al.*, 2009) (r).

#### 3.4.3.8.1. Splayed bars

The experimental techniques presented thus far have considered bars with straight ends only. Darby *et al.* (2007) developed a splayed end arrangement for FRP bars that has been shown to give good improvements in bond strength, by using a wedge to resist large forces. Experimental testing has been undertaken using smooth



GFRP bars in pull out tests with a range of splay angles, both with and without confinement of the surrounding concrete, as shown in Figure 3.24.

It was found that even small splay angles can give an order of magnitude increase in bond when compared to a straight bar and that ductility can be improved through the addition of a confining helix, as illustrated in Figure 3.25 and Figure 3.26, where graphs are plotted for smooth GFRP bars with a  $3^\circ$  splay angle and leg lengths of 50-100mm (unsplayed smooth GFRP bars results are shown for comparison). A summary of the anchorage provided by  $3^\circ$  splayed bars is provided in Table 3.8.



Figure 3.23: Splayed bars (l), Experimental set up for pull out tests (r).

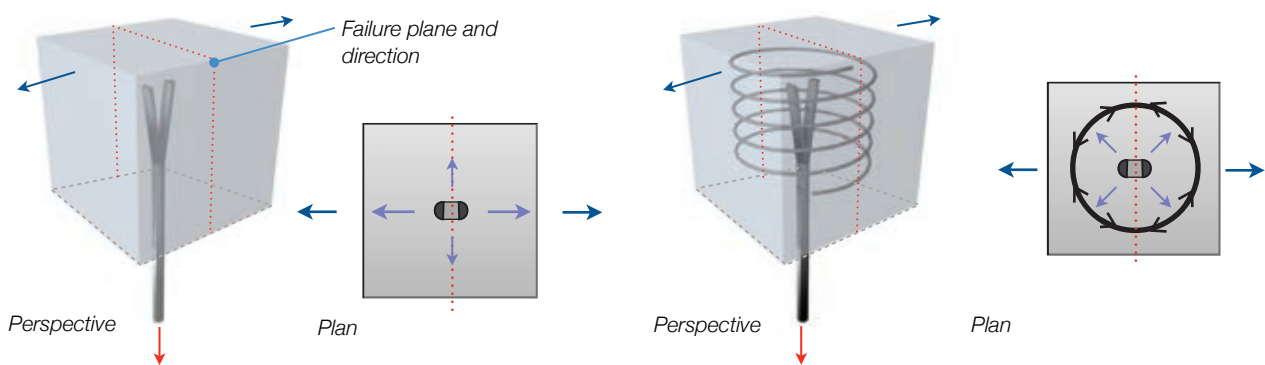


Figure 3.24: Non helically reinforced (l) and helically reinforced around splayed bar (r).

Table 3.8: 75mm Splayed bar, pull-out load improvement (Tallis, 2005).

Test	Maximum pull out load (kN)	Final displacement (mm)
Plain GFRP bar, $3^\circ$ splay	2.82	7.55
GFRP bar, $3^\circ$ splay, without concrete helix	21.89	26.59
GFRP bar, $3^\circ$ splay, with concrete helix	26.22	137.92

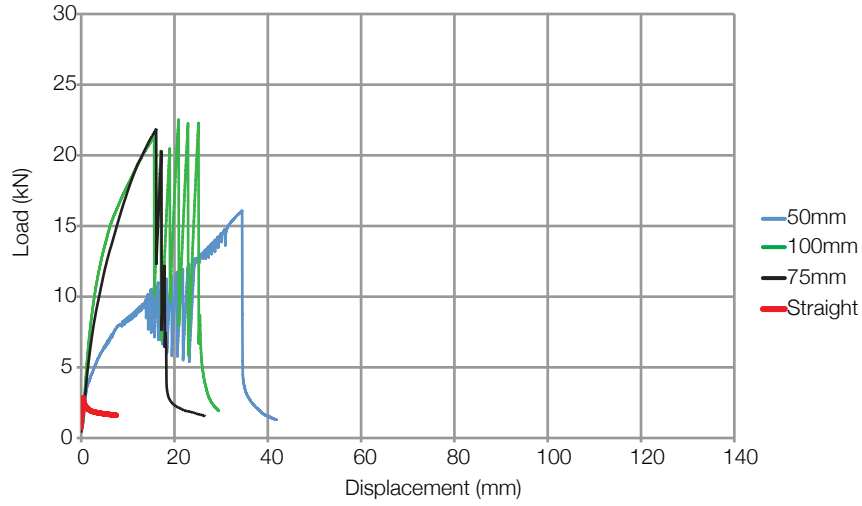


Figure 3.25: Cube test results for different splay lengths - without helix (Darby et al., 2007).

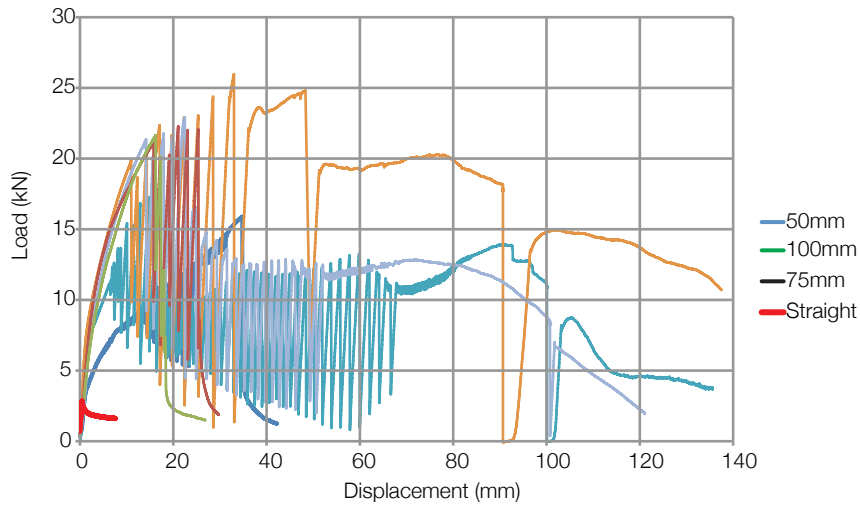


Figure 3.26: Cube test results for different splay lengths - with helix (Darby et al., 2007).

#### 3.4.3.9. Codified design

ACI 440 (2006) gives the development length of a straight bar by Eq. 3.38, rearranged in Eq. 3.39. FRP bars are assumed to fail by pull out where the concrete cover is greater than two times the bar diameter. Where it is less than this, splitting failure of the concrete is more likely to occur. Based on test data, the code recommends that a conservative estimate of the development length of an FRP bar controlled by pullout failure be given by Eq. 3.40.

$$l_{bf} \pi d \mu_f = A_{f,bar} f_{fu} \quad \text{Eq. 3.38}$$

$$l_{bf} = \frac{d_b f_{fu}}{4 \mu_f} \quad \text{Eq. 3.39}$$

Where:  $l_{bf}$  is the development length of the bar;  $d$  is the bar diameter;  $\mu_f$  is the average bond stress on the bar;  $A_{f,bar}$  is the area of one bar; and  $f_{fu}$  is the design tensile strength of the FRP bar.

$$l_{bf} = \frac{d_b f_{fu}}{18.5} \quad \text{Eq. 3.40}$$

$$l_{bf} = \frac{mm(Nmm^{-2})}{1} = Nmm^{-1} \quad \text{Eq. 3.41}$$

Eq. 3.40 provides a simple means to determine the development length of a straight bar, but fails a simple units test, Eq. 3.41. However, the equation may give reasonable results and should not be entirely disregarded during analysis. Until a theory exists that accounts for all the variables in bond behaviour, empirical relationships are the simplest way to determine anchorage length requirements for FRP structures.

#### 3.4.3.10. Conclusions

Quantifying the pull out resistance of FRP bars is essential for the development of usable design equations for fabric cast elements with non-metallic reinforcement. Simple pull out tests as described above can provide upper bound estimates of the pull out resistance of FRP bars, while beam tests yield lower capacities. Splayed bars have shown potential for considerable capacity improvements in pull out testing, but beams tests are now required to verify these results, and some steps towards this are made in Chapter 6. The following section considers a further innovation that may be possible for the reinforcement of fabric formed concrete structures, before methods for the design of reinforced and prestressed fabric formed concrete beams are assessed.

#### 3.4.4. Participating fabric formwork

One potential downside to the use of fabric formwork for concrete structures is that the fabric itself must be discarded after use. By using the fabric as participating, permanent formwork, this disadvantage could be eliminated. The use of woven advanced composite sheets is envisaged, as illustrated in Figure 3.27. However, participating formwork itself raises a number of new design issues that must be tackled before such a system can be used.

A participating fabric formwork system has the advantage that the formwork is not discarded after use. By providing a complete beam (with reinforcement) in one package, the construction process is greatly simplified and could feasibly be used anywhere in the world. However, a participating fabric system would require careful consideration of the bond between concrete and reinforcement, especially under cyclic loading which could result in delamination of the fabric. In addition, fire and vandalism to the principle reinforcement would be a critical concern.

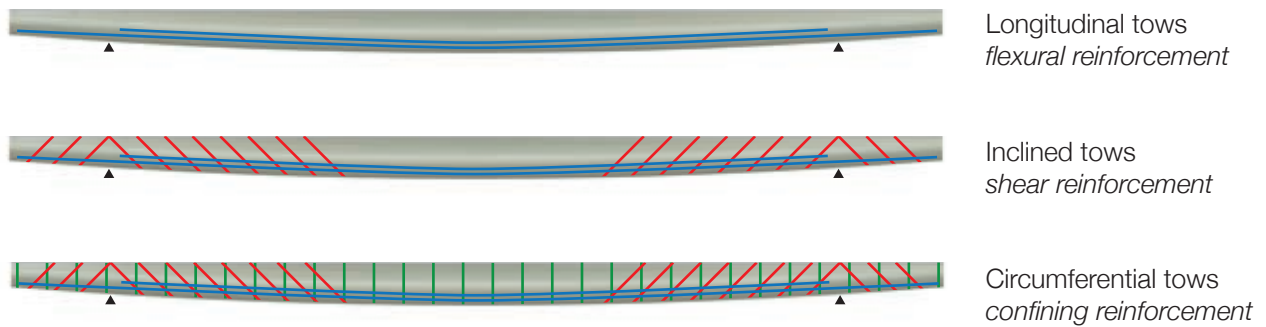


Figure 3.27: Participating fabric formwork - possible arrangements.

Investigations into the use of fibre reinforced polymers as shear reinforcement in flexibly formed concrete structures, described in Chapter 8, provide further introduction to the potential use of a participating fabric formwork construction system.

### 3.5. Conclusions

Chapter 3 has considered in detail the material behaviour of concrete, fabric and reinforcement systems. It has been seen that:

1. Ultra-high performance fibre reinforced concrete is an alternative to ordinary Portland cement concrete and can bring strength and construction advantages;
2. The behaviour of fabrics under hydrostatic and other loading can be modelled;
3. The reinforcement of fabric formed structures using either steel or advanced composite materials is a concern that may be met by innovative solutions such as the splayed bar.

These conclusions have informed the progress of Chapter 4, where a more detailed investigation into the behaviour of reinforced concrete members of prismatic and non-prismatic cross sections is presented.

[blank page]





# Chapter 4 Concrete behaviour

## Literature review

### 4.1. Introduction

The design of reinforced concrete structures is investigated with particular emphasis placed on the determination of shear capacity, an area of continued uncertainty for both prismatic and variable section elements. Methods for the assessment of prismatic steel reinforced concrete elements are presented before the effects of a variable section are considered. Such considerations will address how the design and analysis of optimised, non-prismatic concrete structures may be achieved to facilitate significant material use reductions and a sustainable future in concrete construction. Codified design methods (including BS EN 1992-1-1 (2004) and CSA A23.3 (2004)) are considered alongside other design approaches, including the compressive force path method.

### 4.2. Prismatic beams

#### 4.2.1. Flexural behaviour

The flexural strength of a reinforced concrete section can be predicted using the plane section hypothesis (plane sections remain plane, and strain levels in the reinforcing steel and concrete at an equal depth are the same, Figure 4.1), which forms the basis of most concrete design codes and has been verified through extensive testing, which for beams in flexure is both straightforward and provides generally unambiguous results (Bentz *et al.*, 2006).

Design to BS EN 1992-1-1 (2004) is defined based on strain levels in the section (Narayanan, 2002) and material stress strain models are provided for both steel and concrete. In contrast to the steel material model, the validity of the concrete model is open to criticism. In essence, the material model assumes that zero stress exists in the concrete below the neutral plane, with the compression zone stress being described by one of three models (Figure 4.1(l)).



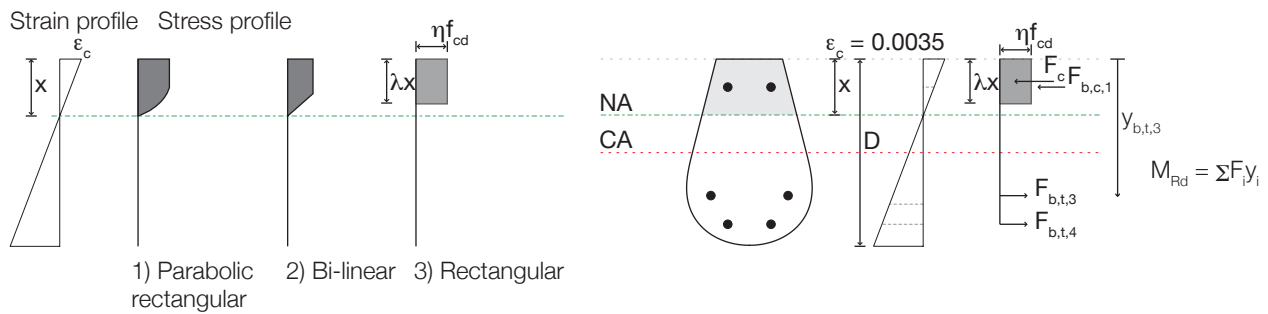


Figure 4.1: Typical concrete stress-strain models (l) and sectional design method (r) (after BS EN 1992-1-1 (2004)).

Kotsovos and Pavlovic (1999) considered the common assumption of uniaxial behaviour in the compression zone of flexural elements. From their work, described in §3.2.1 on page 49, it may be concluded that 'ductile' behaviour that has previously been attributed to strain-softening behaviour should more correctly be considered to arise from the complex triaxial state of stress that exists in the compression zone (Kotsovos and Pavlovic, 1999). A triaxial model, in which zero stress exists at the neutral axis, rising to a peak before decreasing at the extreme compression fibre was presented by Kotsovos and Pavlovic (1999) and is illustrated in Figure 4.2(l).

In addition to longitudinal stresses ( $\sigma_l$ ), secondary stresses exist within the concrete in both the transverse and radial directions ( $\sigma_t$  and  $\sigma_r$ ). Large transverse strains measured by Kotsovos and Pavlovic (1999) in tests on simply supported beams with two point loads, indicate the presence of a triaxial stress state in which the concrete in the central zone is restrained by the surrounding material. Tensile stresses in the adjacent material leads to a varying tension/compression state of stress, that ultimately reduces the beam's longitudinal strength and leads to collapse after horizontal splitting of the compression zone. Radial stresses occur along the length of the deformed beam, due to the inclination of the compression and tension forces in the longitudinal direction (Figure 4.2(r)). Such forces are only significant during plastic deformation, when large deflections cause corresponding increases in radial stresses that are estimated by Kotsovos and Pavlovic (1999) to be approximately equal to 10% of the concrete compressive strength.

The confinement provided by  $\sigma_t$  and  $\sigma_r$  is zero at the neutral axis, rising to a peak before reducing at the extreme compression fibre. The resulting stress distribution (Figure 4.2(l)) is comparable to that used in existing design codes, but this comparison should not necessarily be used as justification for the uniaxial concrete model, which, unlike the triaxial model, is unable to properly assess the failure behaviour of concrete in flexure-compression. However, the analysis put forwards by Kotsovos and Pavlovic (1999) shows that whilst the material models used by many concrete design codes are perhaps poorly constructed, they do provide an adequate representation of the behaviour of concrete.

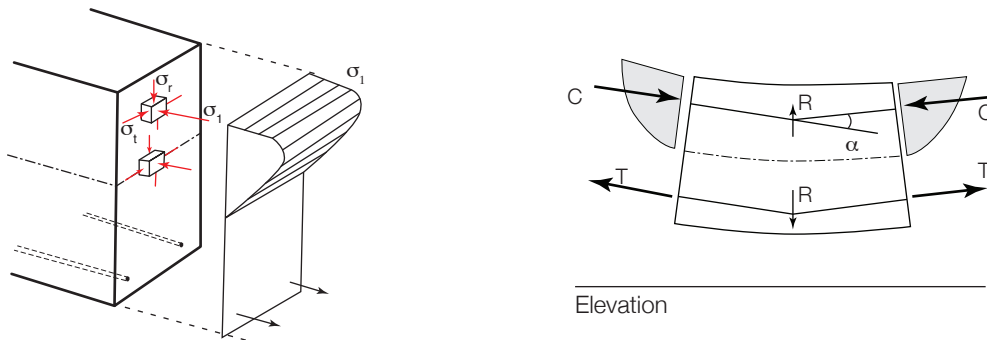


Figure 4.2: Triaxial model for the compressive stress block (l); Radial stresses (r) (after Kotsovos and Pavlovic, 1999).

#### 4.2.2. Shear behaviour

The shear behaviour of steel reinforced concrete is particularly important to understand where sections vary in depth. Fabric formed sections designed with adequate shear capacity according to BS8110-1 (1997) have been found in previous work to fail in this manner (Garbett, 2008); suggesting current codified methods are unable to account for the varying section shape found in fabric formed structures. This section introduces current approaches to shear design, and their application to fabric formed sections is assessed throughout.

There are often considered to be six contributing factors by which a reinforced concrete beam can carry shear, Figure 4.3. These mechanisms are investigated for steel reinforced structures in §4.2.3 below. The derivation of shear stresses through equilibrium considerations of a homogenous uncracked and isotropic beam is relatively straightforward, but the behaviour of the reinforced section is more complex. In a reinforced section, cracks will form when the principal tensile stress exceeds the tensile capacity of concrete (§4.2.3.2) and these diagonal cracks typically propagate from the tension face of the member towards the neutral axis. Initial cracking often occurs at  $45^\circ$  to the neutral axis, propagating as the applied loads are increased.

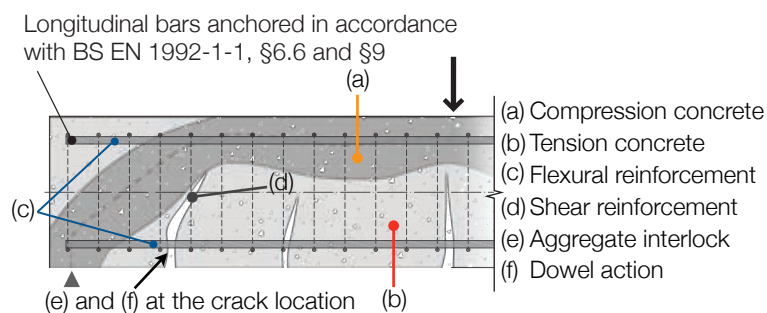


Figure 4.3: Six contributing factors for shear resistance (after Orr, 2009).

#### 4.2.3. Mechanisms to carry shear

##### 4.2.3.1. Concrete in compression

The uncracked compression zone is often considered to provide significant shear resistance in concrete sections (Park and Paulay, 1975), although the depth of this zone is highly dependent on the properties of the longitudinal steel. It is generally understood that the concrete section carries shear by a combination of the force

in the concrete and in the shear stirrups that confine it. Stratford (2008) argues that there are two mechanisms by which the compression concrete zone can carry shear, with these being a variation in axial force along the beam length and variation in the compressive force path depth.

#### 4.2.3.2. Concrete in tension

The tension zone contribution to shear strength is most commonly assumed to be zero in design. However, Figure 4.4 shows the results of extensive biaxial testing on plate sections, whereupon the small tensile capacity of concrete is evident. In codified design, it is only the Modified Compression Field Theory that fully considers concrete tensile strength (Orr, 2009). The tensile capacity of the concrete also influences the ability of a section to carry shear by aggregate interlock (§4.2.3.3).

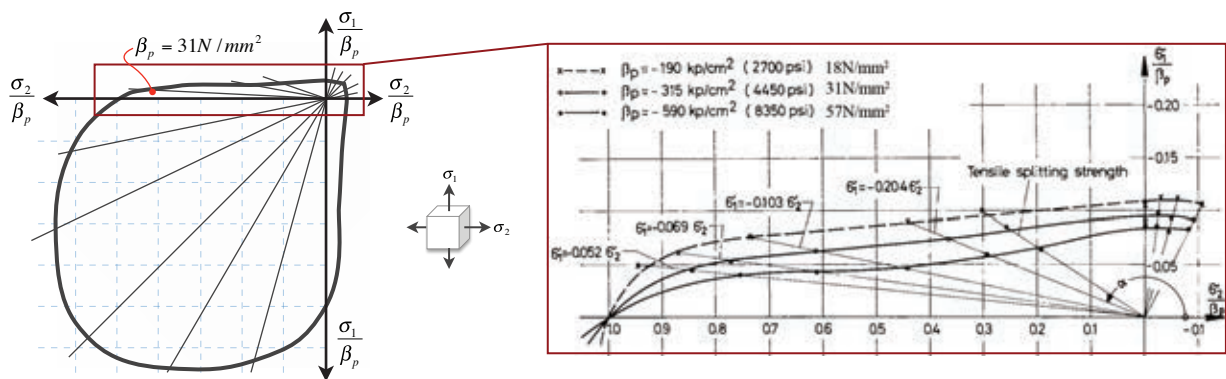


Figure 4.4: Biaxial tests on concrete. Strength plot (l); tension zone (r) (After Kupfer et al., 1969).

#### 4.2.3.3. Aggregate interlock

The interlock between aggregate particles (which account for typically 60-75% of the concrete volume) has been shown to carry significant shear force in comparison to the capacity of the uncracked concrete, with Taylor (1970) estimating it to be between 33 and 50% of the shear capacity of the uncracked section. In the more important cracked section, the degree to which shearing action occurs across the line of a crack is highly limited, and it has been shown (Walraven, 1981) that beyond a crack width of around 1mm, no aggregate interlock can occur. Kotsovos and Pavlovic (1999) provide additional experimental evidence to suggest that aggregate interlock has no role to play in the provision of shear resistance across inclined cracks.

This is explained by considering that at the tip of a crack, rotation will be the only relative movement between surfaces and thus there is no interlock to generate shear resistance. Under rotational displacement, there is no differential movement between internal faces of a crack, and hence the two surfaces cannot be considered to provide any shear resistance.

#### 4.2.3.4. Shear reinforcement and dowel action

Transverse reinforcement carries stress over cracks in the section as these cracks open under loading. It is important to define how many bars intersect such a crack to determine the resistance provided against shear. In addition to carrying shear, links both confine the concrete and may help to resist dowel failure in the longitudinal

steel. Confinement of the compression zone increases shear capacity by improving the rotation capacity of the section, and the links also prevent the section from splitting along the longitudinal reinforcement, Figure 4.5(l) (Stratford, 2008).

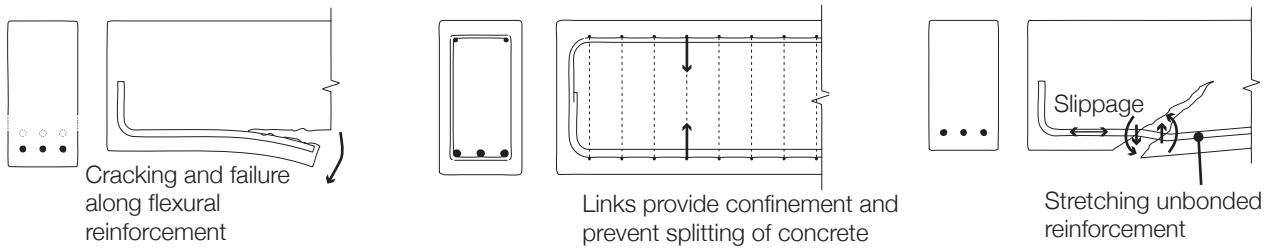


Figure 4.5: Dowel action. Beam behaviour with and without shear links (l); Longitudinal reinforcement slippage (r).

#### 4.2.3.5. Flexural reinforcement and dowel action

Longitudinal reinforcing bars provide shear resistance to the section through compatibility of the crack opening mechanism. This applies to deflections and rotations at the crack/bar interface, both parallel and perpendicular to the reinforcement (Stratford, 2008). In the axial direction, compatibility is ensured by the mechanisms illustrated in Figure 4.5(r). In design it may be assumed that the bars yield at ULS and hence extension of the deformed steel bar dominates the amount of slippage in the system. The component of force acting in shear in the flexural reinforcement is most commonly attributed to the effects of dowel action in the bar and the actual load carried in this mode has been shown to be small to the point of being negligible (Kotsovos and Pavlovic, 2006; Kotsovos and Pavlovic, 1999; Jelic, 2002).

#### 4.2.4. Size effect and failure modes

Size effects describe the reduction in strength of a concrete member as it increases in size. Work by Kani (1967) first discovered size effects in non-shear reinforced RC beams and a simple 'tooth' model for the concrete section was proposed wherein the cracked section is considered as a series of short cantilevering concrete teeth which resist applied loads from the flexural reinforcement. The size effect can also be considered in terms of the concrete crack width at failure, which is found to be a fairly constant 1mm irrespective of section size, implying that larger elements are more brittle. The graph illustrated in Figure 4.6(l) shows that failure loads decrease as 'size' (typically measured as member depth) increases. There are two zones of behaviour, with the initially flat line attributed to a linear relationship between nominal stress and section yield stress. Linear-elastic fracture mechanics is then used to consider the critical stress intensity factor ( $K_{IC}$ ) and analysis provides a 1:2 gradient relationship. The real section behaviour does not follow a perfectly plastic, brittle linear-elastic path; instead the quasi-brittle behaviour highlighted in Figure 4.6(l) is seen.

Shear failures are found to occur over a relatively small range of values of  $a/d$  (shear span/effective depth) as shown in Figure 4.6(r), with a critical load position at approximately  $2.5d$  (Kani, 1967). Deeper sections exhibit larger reductions in capacity. This 'Shear Valley' is obtained by dividing the ultimate failure moment by the calculated flexural moment to obtain what is termed the relative beam strength,  $r_v$ . Relative beam strength depends only on

the crack length and since crack lengths increase with beam depth, there is a reduction in strength as the section gets deeper. Figure 4.6(r) is an approximation of the shear valley, adapted from work by Bazant (1993) and Brown *et al* (2006), with a range of  $a/d$  from 1.0 to what is termed the transition point (the point at which full flexural failure is attained). Where  $a/d < 2.5$  there is an increase in capacity (shear enhancement) which must also be provided for in design.

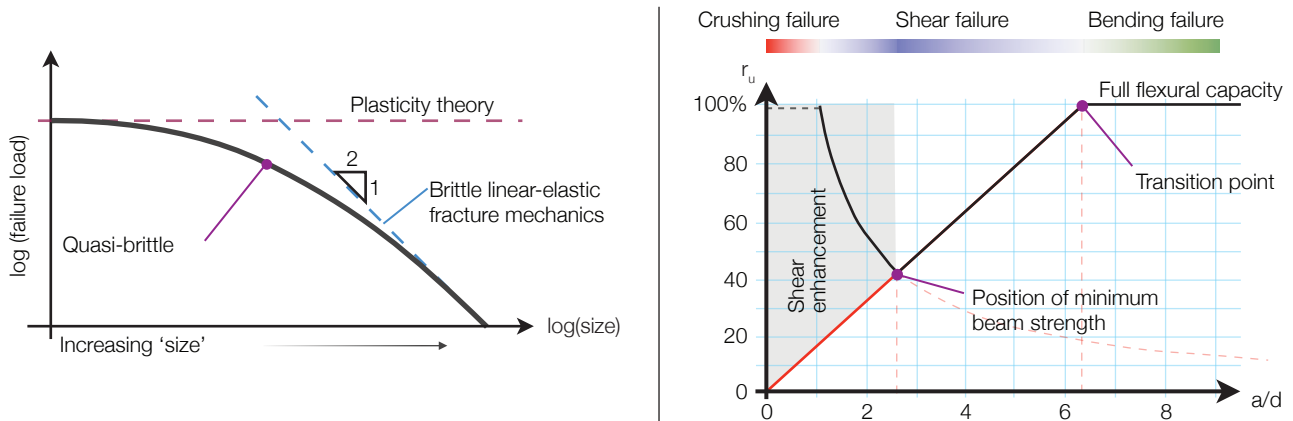


Figure 4.6: Size effects (l); Shear valley (r).

#### 4.2.5. Shear theories

There exist a number of methods for the design of steel reinforced concrete structures in shear, three of which are considered below for use in the design and testing work presented in later chapters.

##### 4.2.5.1. Truss analogy

The BS EN 1992-1-1 (2004) approach to shear design uses a variable angle truss model (Figure 4.6) that is based on methods previously used in BS 8110-1 (1997) that were first proposed by Ritter (1899) and Mörsh (1908) as a convenient design method for concrete structures. The basic premise of the model is that cracked concrete in the web of the section resists shear by a diagonal compressive stress in a concrete strut which pushes the flanges apart and causes tension in the stirrups which are then responsible for holding the section together. Mörsh's original model assumes that the angle from shear reinforcement to the beam axis ( $\alpha$ ) is  $90^\circ$  and the angle of the compression strut from the beam axis ( $\theta$ ) is  $45^\circ$ . The forces in the stirrups can then be determined from equilibrium considerations.

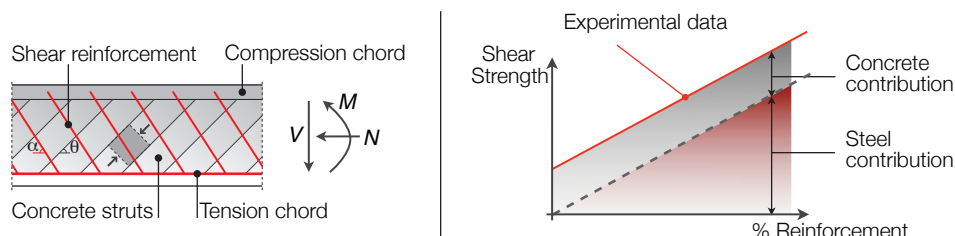


Figure 4.7: The truss analogy (l) and components of shear resistance (r) (after Orr, 2009).

Early researchers found that shear strength predictions according to the force in the stirrups underestimated the section shear strength by a fairly consistent value when using a  $45^\circ$  concrete strut model. To correct this, a 'concrete contribution' to shear resistance was added, as illustrated in Figure 4.6(r). This empirical factor was

used in BS 8110-1 (1997) and remains present in American design codes (ACI 318, 2005) but is not used in the Eurocode model.

Instead, it is assumed that once cracked, shear capacity comes solely from the links and the concrete is ineffective. However, the model allows the designer to choose the angle of the compression strut, with a flatter angle ensuring that more links are intersected, thus providing higher shear capacity. An additional tensile force, generated as a result of the compression strut inclination, is distributed between the tension and compression chords to satisfy equilibrium.

#### 4.2.5.2. Compressive force path method

The compressive force path method premises that the behaviour of a reinforced concrete beam can be simplified into three elements - a concrete frame, formed by drawing the path of the compressive stress resulting from applied loads, a steel tie of flexural reinforcement and a zone of concrete cantilevering teeth which form between successive cracks in the concrete section (Kotsovos and Pavlovic, 1999), as illustrated in Figure 4.8. Kotsovos and Pavlovic (1999) propose that the uncracked compression zone in a concrete beam sustains not only the compressive force that arises from bending loads, but also the entire shear force.

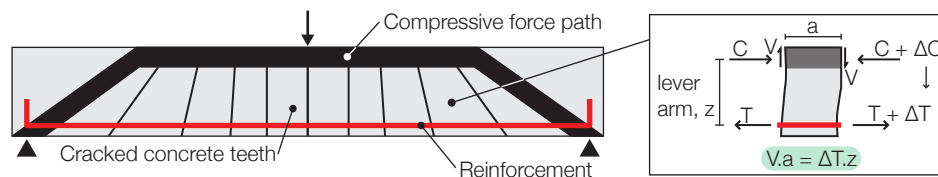


Figure 4.8: Compressive force path (l); Detail at supports (c); Stresses on each concrete tooth (r) (after Kotsovos, 1988).

Prior to flexural failure in a reinforced concrete beam, it can be seen that only a relatively small area of concrete remains uncracked - including a zone from the supports to the first inclined crack and the region along the top of the beam - yet the beam remains capable of transferring load to the supports. The concrete 'teeth' of the central zone effect this load transfer by moment equilibrium at each tooth, as shown in Figure 4.8(r). The shear forces on each end of a tooth are equilibrated by the force that develops due to a changing moment between the two sections, predominantly caused by a change in the internal compression (and equal tension) forces. The change ( $\Delta T$ ) in tensile force in the steel is thus the only force acting on the concrete tooth, which can be considered as a cantilever, fixed at its base to the compression zone. The bending that develops from the change in force in the longitudinal steel balances the moment across each tooth created by the shear forces acting in the compressive zone of the beam. Kotsovos and Pavlovic (1999) propose that this equilibrium condition describes the entire mechanism by which load (in the form of shear forces) is transferred through the beam.

Close to the supports, the typically larger inclined crack prevents this behaviour from continuing and load is now transferred as shown in Figure 4.9(l), with forces again being determined by equilibrium. The resultant compressive load ( $C'$ ) is angled through the section, indicating a change in direction of the compressive force path from horizontal at the mid span, to inclined close to the supports.

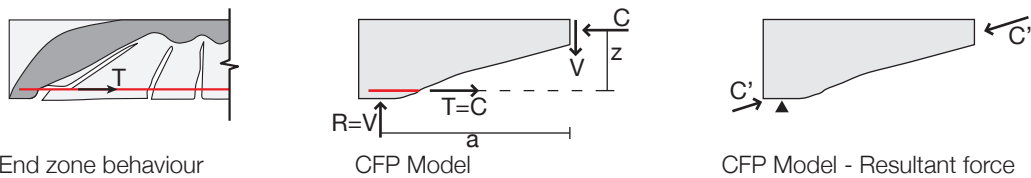


Figure 4.9: Load transfer at the supports.

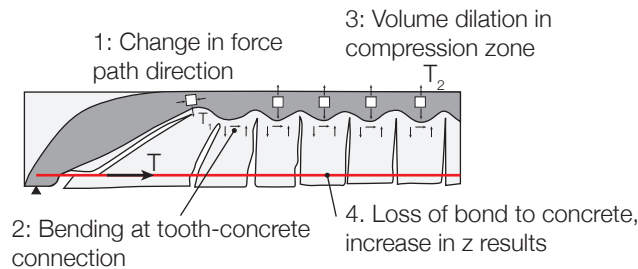


Figure 4.10: Development of tensile forces in the compression path (after Kotsovos and Pavlovic (1999)).

The compressive force path method proposes that ultimate failure must occur in the compressive path, since cracked concrete can be generally considered as concrete that has already failed and should therefore be ignored (Kotsovos and Pavlovic, 1999). Since concrete fails in tension, those regions of the path where tensile stresses may develop will be critical, and four such zones are discussed by Kotsovos and Pavlovic (1999) and illustrated in Figure 4.10.

At positions of change in force path direction, resultant tensile stresses are created. At the end zones, these tend to separate the upper (horizontal) compressive zone from the remainder of the beam through horizontal splitting of the section. At the 'cantilever' locations, tensile stresses are set up as the teeth bend, and in regions of deep flexural cracking volume dilation of the concrete in the compressive zone results in tensile stresses in the adjacent zones. Finally, failure can occur due to loss of the reinforcement bond that previously provided moment equilibrium with the applied shear forces. In this case, equilibrium is achieved by a change in lever arm, Figure 4.9(r), increasing compressive stresses in the concrete, again resulting in volume dilation of the compression concrete and tensile stresses in adjacent zones.

The compressive force path method differs from most codified approaches to shear design by positing that the total shear capacity is obtained solely from the uncracked compression concrete. Failure occurs due to tensile stresses in the section, which act transversely to the compressive stresses induced by the bending action of external loads. The force path method is further developed by considering four separate beam behaviours, as defined by their ratio of shear span to effective depth ( $a/d$ , Figure 4.6(r)), summarised in Figure 4.11.

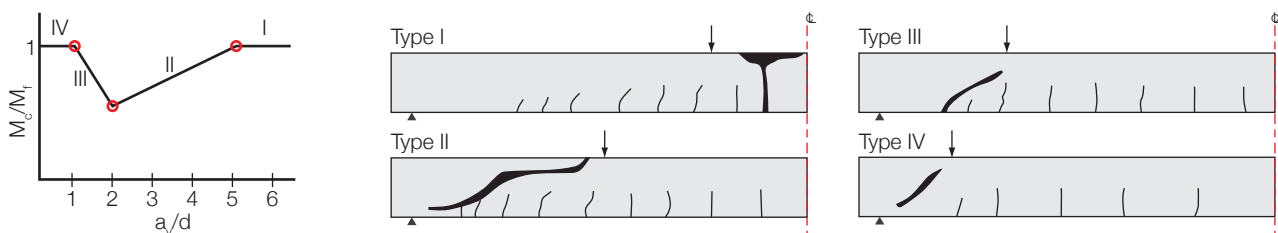


Figure 4.11: Types of beam behaviour (after Kotsovos and Pavlovic (1999)).



Ductile flexural behaviour is seen in Type 1 beams, while Type 2 and Type 3 beams exhibit brittle failure. Type 2 beams are generally seen to fail by extension of preexisting flexural cracks, while inclined cracking in the shear span of Type 3 beams occurs independently of any existing cracking. Type 4 behaviour can be either ductile or brittle, with brittle failure occurring in the uncracked end blocks close to the support, although both types have similar ultimate capacities (Kotsovos and Pavlovic, 1999).

Experimental results (Kotsovos, 1988) suggest that positioning shear stirrups in the centre span of a simply supported beam under two point loading can significantly increase capacity, even though the critical section approach would require shear links within the shear span. Similar tests on deeper beams revealed that shear stirrups do not have to be provided throughout the shear span in order to allow full flexural capacity to be reached. Beams tested with only partial shear reinforcement cannot conform to the truss analogy since there is no continuous vertical (or inclined) tension member but such sections are able to sustain higher load than that predicted by the truss analogy (Kotsovos, 1988). Therefore *'truss behaviour of a section is not a necessary condition for a beam to attain flexural capacity once shear capacity is exceeded'* (Kotsovos, 1988, p.74).

Tests undertaken by Salek *et al* (1995) compared the behaviour of indeterminate concrete frames designed to ACI 318 (1989) with identical frames designed using the compressive force path method. It was found that frames designed using the CFP method had much greater ductility than elements designed to ACI 318 (1989) simply through the correct positioning of transverse reinforcement to carry the tensile forces arising from changes in the direction of the compressive force path (Figure 4.10)

Jelic (2002) compared the behaviour of reinforced concrete beams designed using the compressive force path, BS EN 1992-1-1 (1991) and BS EN 1998-1 (1991) and the Greek Concrete Code (TCG, 1991). It was found that elements designed using the Eurocode methods tended to fail in diagonal tension below their design failure loads. More significantly, the elements designed in accordance with the Eurocode concept of 'critical regions' for ductility were found not to achieve the required levels of ductility. Elements designed using the CFP method often had less transverse reinforcement than required in an equivalent Eurocode design but displayed better ductility and load capacity through the correct positioning of this steel to prevent tension failures. Jelic (2002) suggests that the CFP method is superior to both Eurocode and Greek design models in terms of both ductility provision and ultimate limit state behaviour. There are corollaries between the results presented by Jelic (2002) and those found in this thesis for tapered beams, described in detail in Chapter 8 (page 245).

Whilst the literature suggests that the CFP method can indeed provide a more accurate representation of the behaviour of reinforced concrete beams than other design methods, the design method remains based on empirical equations originally derived by Whitney (1957), and subsequently modified by Bobrowski and Bardhan-Roy (1969) before their use in guidance on structural fire design (IStructE, 1975) and as such may be difficult to apply to general cases of concrete elements with any geometry.

The compressive force path method is described and used in §7.2.2 on page 219, but the empirical basis makes it potentially unattractive for use in fabric formed beam design where unconventional shapes are common. The provision of a design method that is applicable to any section geometry requires a sound theoretical basis that is verified by but not derived from available test data. One such approach, which has been developed in Canada over the past thirty years, is described below.

#### 4.2.5.3. Compression Field Theory

Compression field theory originates from work by Wagner (1929) on the post-buckling behaviour of metal beams with very thin webs. It was determined that post-buckling, the web of the beam no longer carries compression but instead resists shear by a field of diagonal tension. In concrete, the behaviour is reversed such that post-cracking the section no longer carries tension, instead resisting shear by a field of diagonal compression (Collins, 1978). In the development of the truss model, Mörsch was unable to calculate the angle of the compression field since there are four unknowns and three equations (Hawkins *et al.*, 2005). This problem is overcome in compression field theory by assuming that the principal compressive stress and principal compressive strain directions are coincident (Hawkins *et al.*, 2005).

Compression field theory in concrete was first developed for members in pure torsion (Mitchell and Collins, 1974) and then later for members in pure shear (Collins, 1978). For both problems the cracked sections have their own stress-strain relationships, distinct from those for the uncracked section, allowing equations for equilibrium and compatibility to be formulated. Equilibrium equations are found for the concrete, stirrups and longitudinal steel in a section by considering a location where the bending moment is zero. A Mohr's circle for strain is then considered to assess strain compatibility of the section, Figure 4.12(r). A fuller explanation of compression field theory can be found in Vecchio and Collins (1986) or Collins *et al* (2008).

The modified approach (MCFT) simplifies the concrete-steel boundary condition by allowing no slip to occur between the two materials and thus by compatibility any deformation (strain) in the steel is matched by equal strains in the concrete. Bentz *et al* (2006) determined relationships between the principal concrete stress and principal compressive and tensile strains to give simplified expressions (see Hoult *et al.*, 2008). The simplified MCFT approach was also developed to provide a set of equations for the American Association of State Highway and Transportation Officials Load and Resistance Factor Design Code (AASHTO LFRD), which had previously relied on a tabulated version of the MCFT equations. The simplifications, described in Mitchell and Collins (1974), are primarily based on strain limits in the steel and concrete.

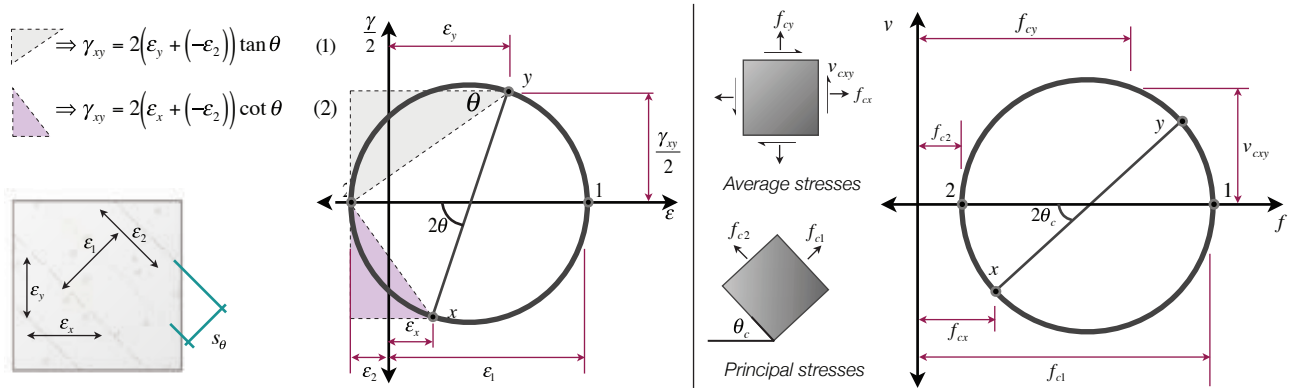


Figure 4.12: Mohr's circle of strain (l) and Stress (r) for compression field theory (after Collins et al., 2008).

$$f_{longitudinal} = E\varepsilon < f_y \quad \text{Eq. 4.1}$$

$$\tan \theta = \sqrt{\psi / 1 - \psi} \quad \text{Eq. 4.2}$$

$$f_v = f_y ; f_2 = f_c \quad \text{Eq. 4.3}$$

$$\text{Where } \psi = \frac{A_v f_y}{bs f_c} \quad \text{Eq. 4.4}$$

$$\varepsilon_y = \varepsilon_{yield} ; \varepsilon_2 = -\varepsilon_c$$

#### 4.2.6. Shear in sections reinforced with fibre reinforced polymer reinforcement.

Sections reinforced with advanced composites behave differently in shear to their steel reinforced counterparts. The use of lower bound plasticity design methods (such as the truss analogy) no longer apply to sections reinforced with linear elastic materials. In an FRP reinforced section, the concrete contribution to shear resistance is reduced as 1) FRP is less stiff than steel and so the compression zone is smaller, 2) dowel action in FRP bars is limited by longitudinal delamination in the resin, which occurs at far lower loads than in an equivalent steel bar and 3) the low stiffness of FRP ensures that cracks open more widely and so the influence of aggregate interlock is limited (Ibell and Darby, 2008). These effects ensure that the shear capacity of an FRP reinforced section is primarily dependent on the FRP.

FRP bars are difficult to manipulate and bend into a 'link' shape, suggesting that an alternative method for shear reinforcement is required. This is not widely recognised and FRP shear reinforcement is usually provided in shapes similar to their steel counterparts. In addition, the brittle nature of advanced composites suggests that existing techniques in American and European design codes for shear cannot be used, as they rely on the ductile behaviour of steel.

Early tests on beams with GFRP shear reinforcement (Nawy and Neuwerth, 1971; Nagaska *et al.*, 1993) were later considered by Clarke and Waldron (1996), and it was determined that a suitable factor of safety could be obtained by following a strain based approach. The strain approach assumes that shear failures occur when the longitudinal reinforcement strains reach 0.0025, equal to the yield strain of steel. The difference in Young's modulus, and hence stress, is accounted for by considering an effective area of longitudinal FRP reinforcement, which is dependent on the modular ratio between the FRP and steel, Eq. 4.5.

$$A_{eff} = A_s \frac{E_{FRP}}{E_{steel}} \quad \text{Eq. 4.5}$$

Where  $A_{eff}$  = Effective area of longitudinal reinforcement for determining shear strength;  $A_s$  = actual area of longitudinal reinforcement;  $E_{FRP}$  and  $E_{steel}$  = Young's moduli of FRP and steel respectively.

An alternative approach that is also based on the modification of existing formulae is the Sheffield modification, which considers that the strain at failure is typically higher than 0.0025 in FRP bars, and therefore allows a maximum strain of 0.0045 in the FRP. This in turn means that the effective area of FRP reinforcement (again based on the modular ratio) is 1.8 times that found when using the strain approach (Whitehead and Ibell, 2005).

Innovative methods for shear reinforcement were investigated by Ibell and Burgoyne (1999), who carried out a number of push off tests to determine the shear behaviour of concrete reinforced with GFRP stirrups and AFRP helices when compared to conventional steel stirrups. It was found that for sections reinforced with advanced composites, the shear strength of the section is determined by the link geometry and bond characteristics, not just the amount of reinforcement in the section.

Despite the complex nature of design using FRP shear reinforcement, the flexibility of carbon and aramid fibres prior to their coating in resin ensures that they can potentially be formed into reinforcement cages of almost any geometry. This aspect of FRP design is investigated in more detail in Chapter 6, where the behaviour of beams reinforced in shear with both resin-coated and uncoated carbon fibre reinforcement is considered and successfully tested experimentally.

### 4.3. Non-prismatic reinforced concrete beams

#### 4.3.1. Introduction

Conventionally cast non-prismatic concrete beams (Figure 4.13) can provide steel and concrete savings when compared to prismatic sections (Tena-Colunga *et al.*, 2008), in addition to being aesthetically pleasing. In the haunched section, it is often considered that a portion of what is normally termed the shear force may be carried by a suitably inclined top or bottom flange (which is normally arranged such that the inclination relieves some of the shear requirements of the section). However, research presented in the preceding Chapters suggests that the changes in the shear behaviour of haunched reinforced concrete sections are not yet fully understood, and that such approaches can lead to unconservative designs. This is an area of importance for optimised fabric formed beams, where variations in depth are commonplace.



Figure 4.13: Haunched reinforced concrete sections (l-r: image credits 'ldawriter' at <http://tinyurl.com/c3oqyzq>; 'Tim k13' at Wikimedia Commons; 'seier+seier' at <http://tinyurl.com/d577v4b>).

This section begins by defining the common types of passively steel reinforced concrete haunched sections before their structural behaviour is considered. Current codified design procedures are discussed and the available structural test data is analysed.

Following the analysis and assessment presented in this section, and to address the perceived gaps in knowledge of tapered reinforced concrete beams in shear, a series of structural tests were undertaken which are described in more detail in §7.2 on page 218 and analysed in §8.2 on page 246.

#### 4.3.2. Haunched concrete beams

##### 4.3.2.1. Flexural behaviour

The flexural design of concrete relies primarily on the assumption that plane sections before bending remain plane after bending. The applicability of this approach to tapered sections is, however, not immediately apparent, although work by Maki and Kuenzi (1965) and later by Davies *et al* (1973) suggests that for moderate tapers (a slope of less than 1:4, for example) such an approach does remain valid.

## 4.3.2.2. Shear behaviour

A comparison between the behaviour of prismatic and tapered concrete sections in shear is given in Figure 4.14. In sections that taper towards their supports, it is imaginable that the interaction of the diagonal cracks with the path of the compression force that reaches the supports is critical.

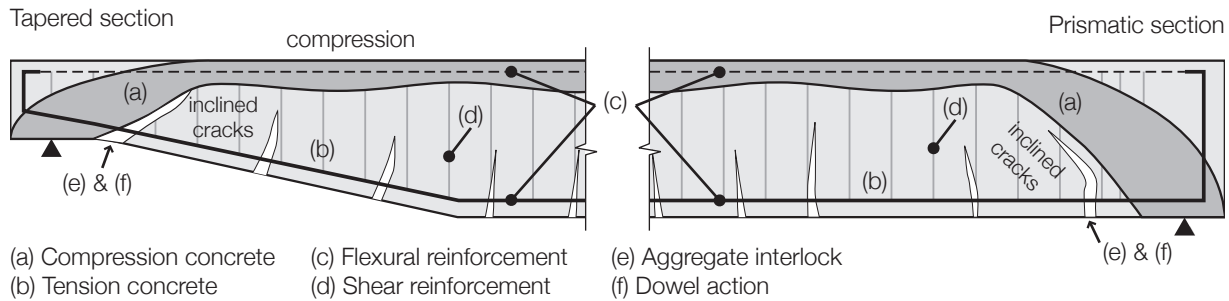


Figure 4.14: Contributing factors to shear resistance in tapered and prismatic sections.

The shear behaviour of steel reinforced concrete is thus particularly important to understand in members of variable depth. Previous work, in which optimised beams without shear reinforcement designed to BS 8110-1 (1997) were found to fail in shear (Garbett, 2008; Bailiss, 2006) suggests that codified methods are unable to fully account for the behaviour of the tapering beam sections that are often found in fabric formed structures.

In members of varying depth, the magnitude of the resultant shear force on a section may be affected by the presence of inclined forces in tension or compression, as illustrated for a section without transverse reinforcement in Figure 4.15. By taking a vertical cut on such a tapered beam, it is widely suggested that the resulting effective shear force for design should be given by Eq. 4.6 (see for example Paulay and Park, 1975; BS EN 1992-1-1, 2004).

$$V'_{Ed} = V_{Ed} - V_{ccd} - V_{td} \quad \text{Eq. 4.6}$$

Where  $V'_{Ed}$  is the design shear force;  $V_{Ed}$  is the shear force on the cross section;  $V_{ccd}$  is the vertical component of the inclined compression chord and  $V_{td}$  is the vertical component of the inclined tension chord (notation after BS EN 1992-1-1 (2004)).

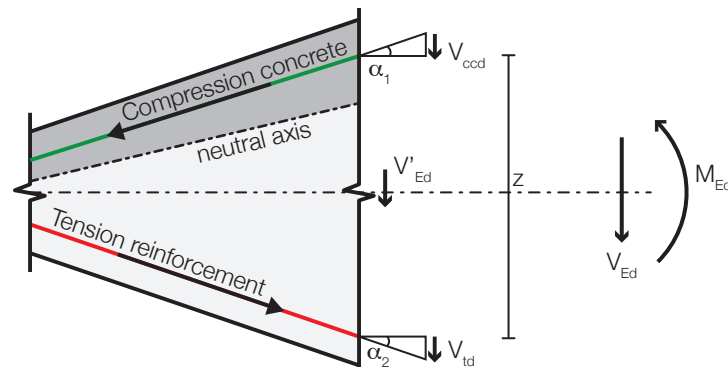


Figure 4.15: General behaviour of tapered beams with contribution from chords (after BS EN 1992-1-1 (2004)).

The values of force in the inclined chords may thus be given by Eq. 4.7, and this approach has been adopted in various guises in the literature (Paulay and Park, 1975; Debaiky and El-Neima, 1982; MacLeod and Houmsi, 1994; Rombach and Ngheip, 2011).

$$V'_{Ed} = V_{Ed} \pm \frac{M_{Ed}}{z} (\tan \alpha_1 + \tan \alpha_2) \quad \text{Eq. 4.7}$$

Where  $V'_{Ed}$  is the design shear force;  $V_{Ed}$  is the shear force on the cross section;  $M_{Ed}$  is the moment on the cross section; and  $\alpha_1$  and  $\alpha_2$  are the chord inclinations. The design shear force is reduced where the member depth increases in the direction of increasing moment.

However, in design using the truss model it is known that the inclined compression strut gives rise to an additional tension force. This force (given by the sum of normal stresses  $\sigma_x$  in Figure 4.16) provides an additional tension force (given for a member with vertical stirrups in Eq. 4.8) in both the compression and tension chords of the truss model. This simple consideration means that the force in the compression chord of the truss model is in fact reduced by the value of Eq. 4.8, and is thus smaller than the force given by Eq. 4.9 (the vertical component of which was used in Eq. 4.7 and has been recommended in the literature for use in the design of tapered sections in shear).

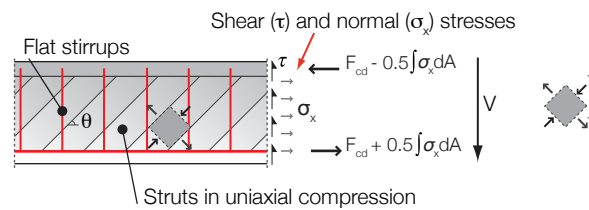


Figure 4.16: Additional tension force in the truss model (after Orr et al, 2011).

$$\Delta F = \frac{1}{2} \left( \frac{V}{\tan \theta} \right) \quad \text{Eq. 4.8}$$

Where  $\Delta F$  is the additional tension in both chords of the truss model;  $V$  is the applied shear and  $\theta$  is the angle of the compression struts.

$$F_c = \frac{M_{Ed}}{z} \quad \text{Eq. 4.9}$$

Where  $M_{Ed}$  is the design moment and  $z$  is the lever arm between chords.

Design using only Eq. 4.7 for structures with inclined compression chords can therefore give design values of the force in the web which are on the unsafe side. The formulation of complete forces for the variable angle truss model for variable depth elements is given in §10.5.3 on page 429. Rombach and Ngheip (2011), provide further data to support this analysis, as described in full in §4.3.6 on page 105.

#### 4.3.2.3. Beam types

Given the complexities of casting an element with two inclined chords, tests on tapered beams can generally be categorised into two main groups - 1) tests on simply supported beams, which may be either positively or negatively tapered (Figure 4.17), and 2) tests on the tapered support zones of continuous beams (Figure 4.18).

The compression paths illustrated in Figure 4.17 and Figure 4.18 show two distinct behaviours in non-prismatic beams: 1) elements with a strong compression arch (Figure 4.17(r) and Figure 4.18) and 2) elements with a flatter or weak compression arch (Figure 4.17(l)).



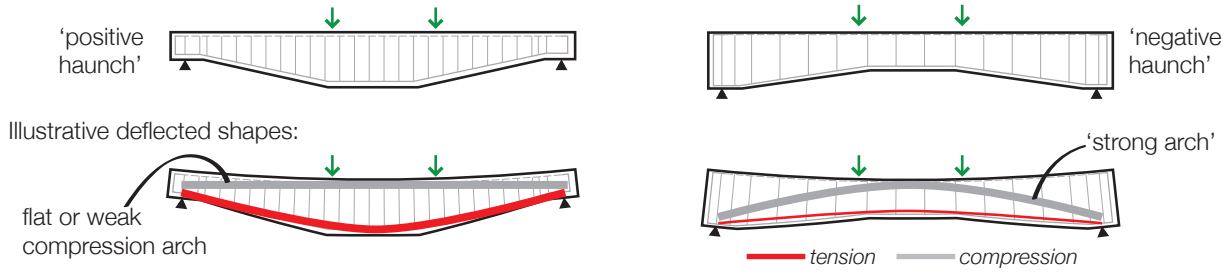


Figure 4.17: Typical simply supported haunched beams of increasing depth (l) and decreasing depth (r)

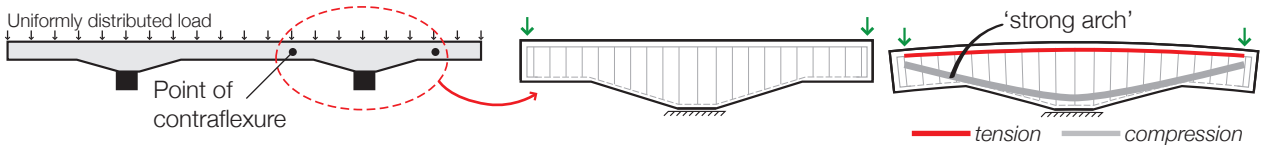


Figure 4.18: Tapered segments of continuous beams.

#### 4.3.3. Theoretical elastic stress distributions

In beams with changes in depth it is prescient to consider the stress state in the beam, and a number of theoretical methods have been developed to do this. Flexural design for concrete relies primarily on the assumption that plane sections remain plane, and early tests on tapered timber sections (Maki and Kuenzi, 1965) found that this assumption remains valid in tapered sections when the sloping face was inclined at a gradient of less than 1:4. The same result was reported for concrete sections by Davies *et al* (1973).

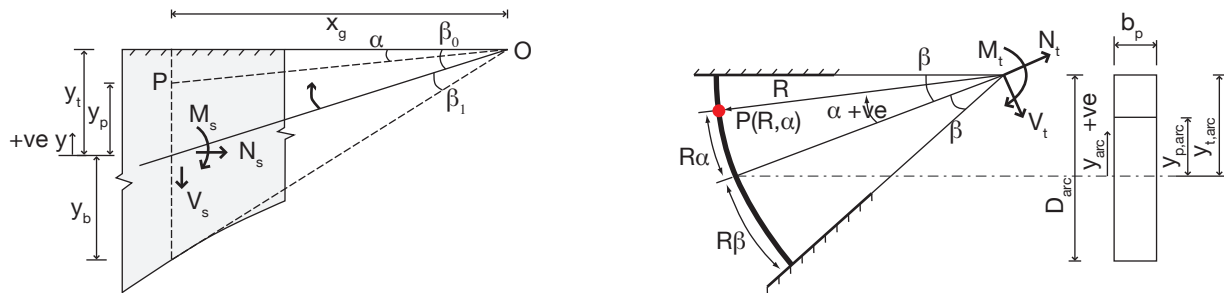


Figure 4.19: Vertical cut method (l) and Circular arc method for constant thickness wedge (r) (after Davies *et al.*, 1973).

The theoretical analysis of stress distribution in beams of varying depth was considered in detail by Davies *et al* (1973) who assessed two approaches to the problem. The vertical cut method (Figure 4.19(l)) simplifies the tapered section to a prismatic one, with stresses  $\sigma_x$  and  $\tau_{xy}$  being given by Eq. 4.10 and Eq. 4.11 respectively. Alternative approaches described by Davies *et al* (1973) include the circular arc method, which relates the radial and tangential stresses on an arc to forces applied at its tip.

$$\sigma_x = \frac{M_s y_p}{I_{xx}} + \frac{N_s}{A_p} \quad \text{Eq. 4.10}$$

$$\tau_{xy} = \frac{V_s \int y dA_x}{b_p I_{xx}} \quad \text{Eq. 4.11}$$

Where  $\sigma_x$  and  $\tau_{xy}$  are the normal and shear forces at a point on a vertical section due to stresses  $V_s$ ,  $M_s$ , and  $N_s$  as shown in Figure 4.19.

Guyon (1953), recognising that the stress equations for a prismatic member cannot be applied to a tapered one, provides an equation for modified external shear force that takes into account any inclination of the section, as given by Eq. 4.12. Principal stresses can then be evaluated using the resulting values of  $\sigma_x$  and  $\tau_{xy}$ . The reduction calculated by Eq. 4.13 is simply equal to that portion of the applied shear that is carried by the inclined flexural stresses (Davies *et al.*, 1973).

$$V_g = V_s - q \quad \text{Eq. 4.12}$$

$$q = \frac{M_s}{x_g} + N_s \beta_0 \quad \text{Eq. 4.13}$$

Where  $V_s$  = external shear force;  $V_g$  = modified shear force;  $q$  = upward force due to inclined flexural analysis (Guyon, 1953);  $M_s$  = moment acting at section;  $x_g$  = distance from wedge tip to section (Figure 4.19);  $N_s$  = normal force at section;  $\beta_0$  = angle of wedge (Figure 4.19(l)).

Circular arc theories, which were assessed in detail by Davies *et al* (1973), provide radial and tangential stresses as given by Eq. 4.14 - Eq. 4.16. For sections with large radii of curvature, where the angles  $\beta$  and  $\alpha$  are small (Figure 4.19) Davies *et al* (1973) suggest a simplified set of equations, derived by expanding the trigonometric relations and retaining only first order parts, as given in Eq. 4.17 and Eq. 4.18. A complete solution for sections with curved soffits is given by Wysiatycki (1957, cited by Davies *et al.*, 1973) that uses a complex variable to provide solutions for shear, moment and normal forces in the section. It is however, rather more difficult to apply and Davies *et al* (1973) concluded that any errors arising from use of Guyon's solution were small enough to be disregarded in most situations.

$$\sigma_a = 0 \quad \text{Eq. 4.14}$$

$$\sigma_r = \frac{N_t}{Rt} \frac{\cos \alpha}{\beta + \frac{1}{2} \sin 2\beta} + \frac{V_t}{Rt} \frac{\sin \alpha}{\beta - \frac{1}{2} \sin 2\beta} + \frac{2M_t}{R^2 t} \frac{2 \sin 2\alpha}{\sin 2\beta - 2\beta \cos 2\beta} \quad \text{Eq. 4.15}$$

$$\tau_{ra} = \frac{M_t}{R^2 t} \frac{\cos 2\alpha - \cos 2\beta}{\sin 2\beta - 2\beta \cos 2\beta} \quad \text{Eq. 4.16}$$

Where  $N_t$ ;  $V_t$ ;  $M_t$  = normal, shear and moment at wedge tip;  $\alpha$  = angular polar coordinate with origin at tip,  $\beta$  = angle defining extent of wedge;  $R$  = radius of curvature;  $t$  = wedge thickness (constant)

$$\sigma_r = \frac{N_t}{A_{arc}} + \frac{(V_t R + M_t) y_{arc}}{I_{arc}} \quad \text{Eq. 4.17}$$

$$\tau_{ra} = \frac{M_t}{R b_p I_{arc}} \int y_{arc} dArc \quad \text{Eq. 4.18}$$

Where 'arc' refers to the properties measured around the arc, and the integral is taken above the point under consideration (Davies *et al.*, 1973).

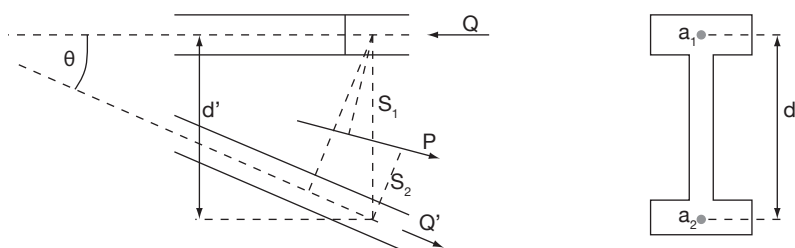


Figure 4.20: Simplified method for stress corrections (after Guyon, 1953).

The methods presented above can, however, further be approximated for general purposes. Consider a section with one horizontal and one inclined surface, Figure 4.20. In this I-section, the web may be disregarded and the forces on the section are reduced to  $Q$  and  $Q'$ , which themselves are related by Eq. 4.19. Then, the nominal stresses in each flange for this vertical section can be found, and are given by Eq. 4.20. The actual area on the section is then used to correct these stress values; in the horizontal flange the correction is zero, while the inclined bottom flange has a true stress as given by Eq. 4.21, which is related to the nominal stress on the vertical section by Eq. 4.22.

$$Q = Q' \cos \theta \quad \text{Eq. 4.19}$$

$$f_N = \frac{M}{d'a_1} \quad f'_N = \frac{M}{d'a'_2} \quad \text{Eq. 4.20}$$

$$f' = \frac{Q'}{a, \cos \theta} = \frac{Q}{a, \cos^2 \theta} = \frac{M}{d' a, \cos^2 \theta} \frac{1}{\cos^2 \theta} \quad \text{Eq. 4.21}$$

$$f' = f'_N \frac{1}{\cos^2 \theta} \quad \text{Eq. 4.22}$$

Where  $Q$ ,  $Q'$ ,  $d$ ,  $a_p$ ,  $a_2$  and  $\theta$  are given in Figure 4.20;  $f_N$  and  $f'_N$  are the nominal fibre stresses on the vertical section,  $f$  and  $f'$  are the actual fibre stresses ( $f = 0$ , in the horizontal top flange).

#### 4.3.4. Codified approaches

Whilst tapered sections are quite widely used in practice, analysis and design methods are infrequently included in concrete design codes. ACI 318 (2005) has no specific guidance for the shear design of haunched concrete sections, while CSA A23-3 (2004) suggests simply that the components of tension and compression in the direction of a shear force should be considered in design if their effect is unfavourable (and may be included if it is favourable). Greater attention is paid to the provisions of BS EN 1992-1-1 (2004) in the following section, before the available structural test data for tapered beams tested in shear is presented in §4.3.5.

#### 4.3.4.1. BS EN 1992-1-1 (2004)

BS EN 1992-1-1 (2004) allows the shear capacity of a tapered section with transverse reinforcement to be determined by Eq. 4.23, by the addition of vertical components of force in both the compression concrete and tension steel at the support zone, as described by Figure 4.15.

$$V_{Rd} = V_{Rd,s} + V_{ccd} + V_{td} \quad \text{Eq. 4.23}$$

Where  $V_{Rd,s}$  is the design value of the shear force which can be sustained by the yielding shear reinforcement;  $V_{ccd}$  is the design value of the shear component of the force in the compression area, in the case of an inclined compression chord;  $V_{td}$  is the design value of the shear component of the force in the tensile reinforcement, in the case of an inclined tensile chord

$$V_{Ed} - V_{ccd} - V_{td} \not> V_{Rd,max} \quad \text{Eq. 4.24}$$

Where  $V_{Ed}$  is the design value of the applied shear force and

$$V_{Rd,max} = \frac{b_w z f_{cd}}{\cot \theta + \tan \theta} \quad \text{Eq. 4.25}$$

Where  $b_w$  is the web width,  $z$  the lever arm,  $f_{cd}$  = design concrete strength;  $\theta$  = angle of the compression strut.

As described in §4.3.2.2, the truss model gives an additional tension force to be resisted by both chords of the truss model (see cl.6.2.3(7), BS EN 1992-1-1 (2004)), which must be included in the determination of the compression and tension forces (and their resulting vertical components) to ensure that the value of Eq. 4.23 is correct.

Limits are placed on Eq. 4.23 as shown in Eq. 4.24, where  $V_{Rd,max}$  is defined in BS EN 1992-1-1 (2004) as the design value of the maximum shear force which can be sustained by the member, limited by crushing of the compression struts and is given by an empirical equation. Thus, provided this limit is not exceeded the sum of  $V_{ccd}$  and  $V_{td}$  could feasibly be made equal to the applied shear force, negating the requirement for transverse steel ( $V_{Rd,s}$ ).

This premise forms the basis of a program of structural testing undertaken on tapered beams in shear, designed to the provisions of BS EN 1992-1-1 (2004) that is described in detail in §7.2 on page 218, where comparisons are made between the Eurocode 2, Compressive Force Path method and a strut and tie model for tapered beams loaded in shear.

4.3.5. Structural test data for tapered steel reinforced concrete beams

To determine the extent to which the behaviour of tapered beams differs from their prismatic counterparts, data from sixty seven tests on tapered reinforced concrete beams were collected from four different experimental test series, with each series being described in the following text.

Debaiky and El-Niema (1982) tested a total of thirty-three haunched reinforced concrete beams in four point bending. The beams, which are summarised in Figure 4.21, varied linearly in depth across the shear span, before becoming prismatic in the constant moment zone. Longitudinal reinforcement followed the soffit profile in all but six beams (Type ‘E’), where horizontal bars were added.

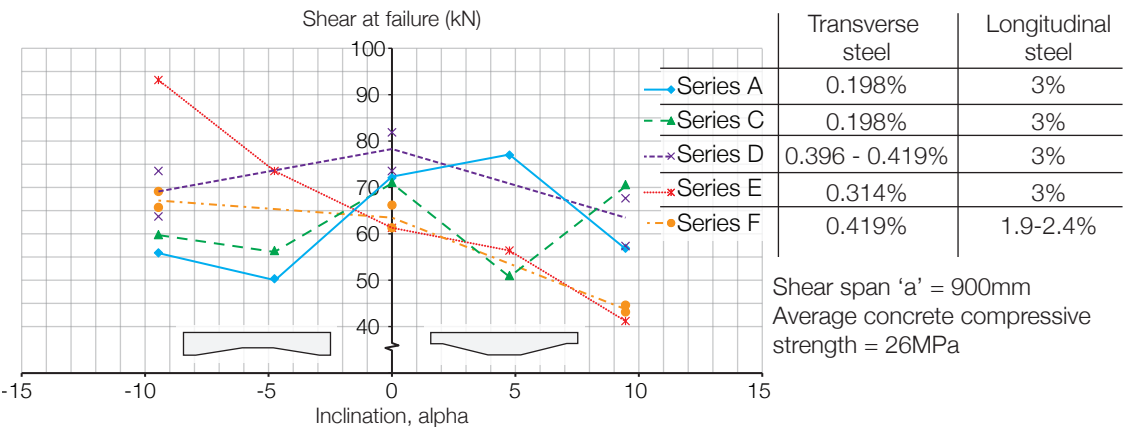
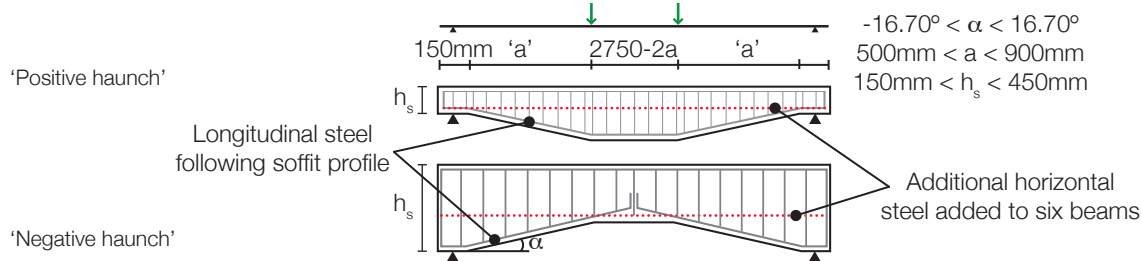


Figure 4.22: Test results for negative and positive haunch beams (Debaiky and El-Niema, 1982).

It was found that both crack number and location depended on the inclination of the haunch. Compared to a prismatic section, the total number of cracks was found to increase for beams with greater depth at the support and to decrease for sections that were shallower at the support. For sections shallower at the support, the position of the major shear crack moved closer to the support, as would be expected based on an assumption that cracking occurs at the weakest section.

Positively haunched beams were found to fail with diagonal shear cracks, while negatively haunched beams were found to be more likely to fail by concrete crushing at the supports. The test results (Figure 4.22) suggest that the shear capacity of both positively and negatively haunched beams is generally reduced when compared to a prismatic section.

Debaiky and El-Niema (1982) posit that the positively haunched section obtains shear capacity from its inclined longitudinal steel which offsets the weak arch that forms between the supports, while the negatively haunched section sees a negative contribution from the inclined longitudinal steel, thus reducing the beneficial effect of a deeper support section.

In tests of Series 'E' with additional horizontal steel, the ultimate shear capacity was seen to increase by up to 48% for negatively ( $\alpha = -9.46^\circ$ ) haunched beams, and decreased by up to 33% for positive haunch ( $\alpha = 9.46^\circ$ ) beams, when compared to the prismatic section ( $\alpha = 0^\circ$ ). These findings were further verified by later tests on haunched T-Beams (El-Niema, 1988), where the ultimate capacity of negatively haunched sections with horizontal reinforcement was found to be greater than that of positively haunched sections with inclined reinforcement.

In both experimental regimes, (El-Niema 1988; Debaiky and El-Niema, 1982) it was found that the negative haunch section was best reinforced with horizontal steel, and in this arrangement showed an increased ultimate shear capacity and improved deformation behaviour when compared to both prismatic and positively haunched sections. This suggests that for negatively haunched sections with reinforcement following the soffit, the tension tie is insufficient to hold the compression arch together, yet with the addition of horizontal bars this tying can be achieved.

#### 4.3.5.1. Analysis

Analysis of the haunched sections was undertaken by considering equilibrium of the end support, as illustrated in Figure 4.23, which was combined with the experimental results to determine an empirical equation for the shear capacity of haunched beams, as presented in Eq. 4.26. This equation is applied to the test data provided by Debaiky and El-Niema (1982) in Figure 4.26, where it is apparent that the method is broadly conservative.

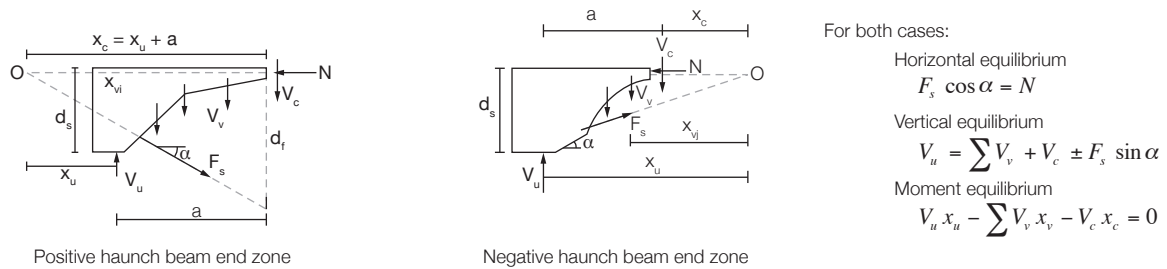


Figure 4.23: Equilibrium of haunched sections (after Debaiky and El-Niema, 1982).

$$\frac{V_u}{bd_s} = v_c (1 + 1.7 \tan \alpha) + \rho_v f_y + 0.25 \rho_w f_{yw} \sin \alpha \quad \text{Eq. 4.26}$$

Where:  $v_c$  = ACI 318 (1977) concrete shear strength (MPa);  $\rho_v f_y$  = longitudinal reinforcement percentage and yield stress;  $\rho_w f_{yw}$  = transverse reinforcement percentage and yield stress.

Eq. 4.26 was also used by El-Niema (1988) to predict the shear capacity of haunched 'T' beams. Ten beams were tested (summarised in Figure 4.24). The comparison of theoretical and experimental results is shown in Figure 4.25 and Figure 4.26, where it is apparent that the formula can estimate broad trends in the experimental data, but is generally unconservative.

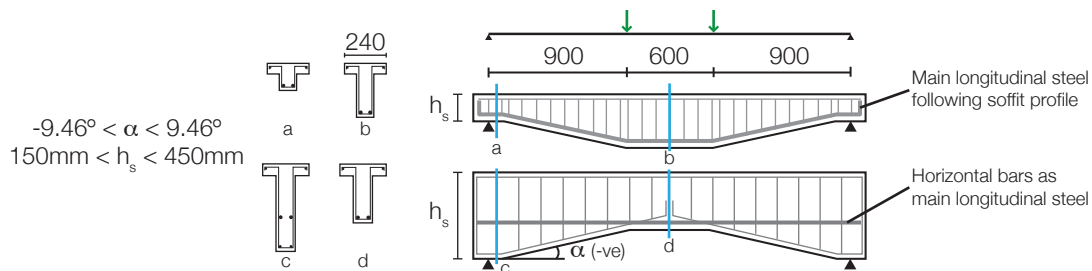


Figure 4.24: T-Beam specimen test variables (El-Niema, 1988).

The test results again show a decrease in predicted shear capacity for sections with positive haunches. Also shown in Figure 4.25 is the contribution to this shear capacity that arises from the transverse steel only according to Eq. 4.26.

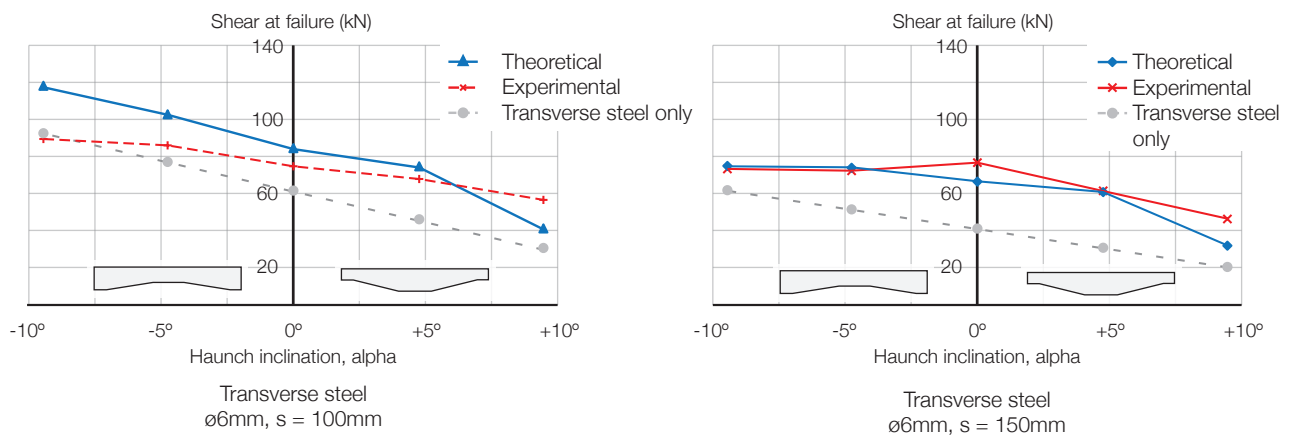


Figure 4.25: Results of 'T' beam tests by El-Niema (1988).

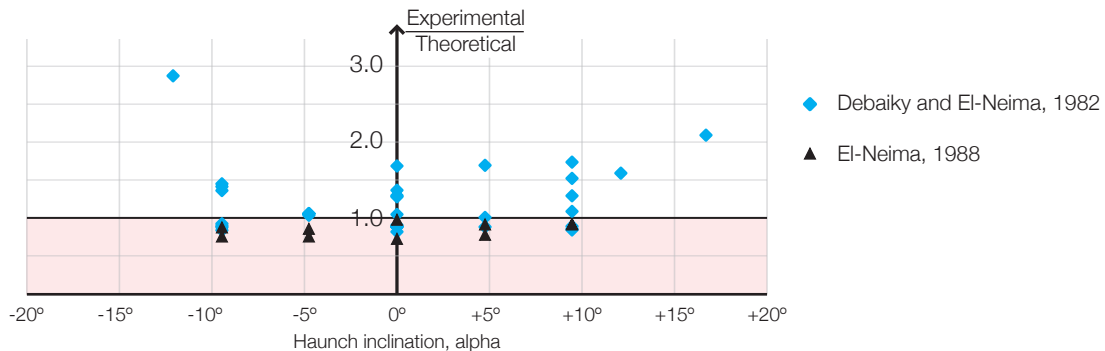


Figure 4.26: Comparison of Eq. 4.26 with test data.

It should be noted that whilst the above would appear to suggest that positively haunched sections are deficient in shear, many of the comparisons made are inherently unfair. None of the beams presented by Debaiky and El-Niema (1982) or Debaiky (1988) appear to have been designed to carry a specific load, and thus it is not surprising that there is a range of results. In particular, it is not surprising that the elements with the shallowest section at the support zone failed first.



#### 4.3.6. Continuous beams

Later work by MacLeod and Houmsi (1994) tested six cantilever haunch beams with a varying haunch angle (as summarised in Figure 4.27(l)). All of the beams were doubly reinforced with longitudinal bars extended beyond the supports and welded to steel plates to prevent anchorage failures, in a similar manner to that used in later fabric formed beams (§3.4).

Shear capacity predictions were again made based on Eq. 4.7, although the concept of a ‘critical section’ was introduced to determine minimum beam capacity. The critical section is found by considering the propagation of the inclined shear crack, and is based on the compressive force path concept (§4.2.5.2). MacLeod and Houmsi (1994) used experimentally determined crack inclinations from prototype beams to predict the critical section location and hence shear capacity. Clearly, such a method is not possible in all situations and a more robust method for assessing crack inclinations is required. However, their analysis revealed a general equation for  $C_h$  (Eq. 4.27), which correlates well with the presence of a ‘shear valley’ (Figure 4.6(r)) in which minimum beam strength occurs at approximately  $a_v = 2.5d$ . This formulation may be derived by considering the geometry of Figure 4.27.

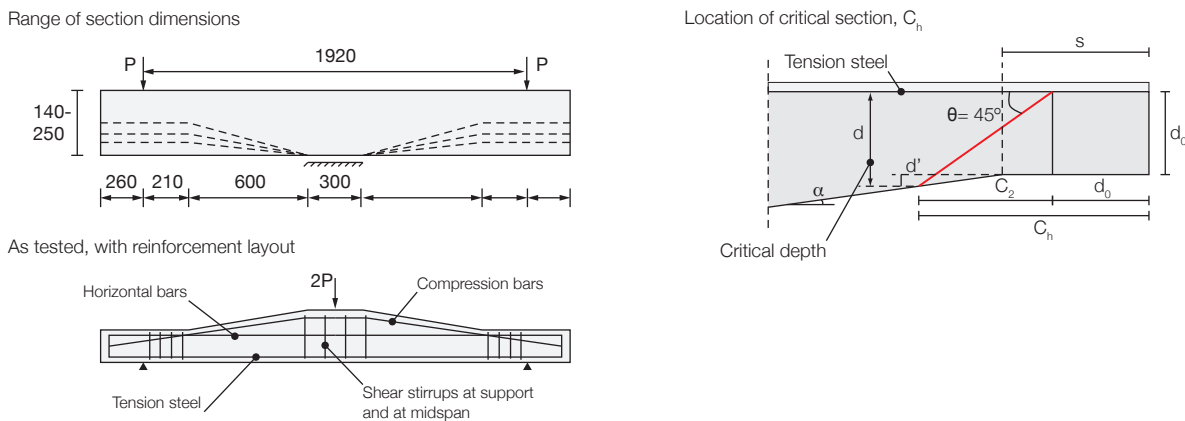


Figure 4.27: Test summary (l); Critical section definition (r) (after MacLeod and Houmsi, 1994).

$$C_h = d_0 + \frac{d_0 (1 + \tan \alpha) - S \tan \alpha}{\tan \theta - \tan \alpha} = 2.7 d_0 \quad \text{Eq. 4.27}$$

During testing it was found that the constant depth sections failed in a brittle manner, while the tapered sections displayed both greater deformation and load capacity at failure, as summarised in Figure 4.28(l). The tapered sections were found to have shear capacities up to 50% greater than the prismatic control specimen, a result that may be in part attributed to the inclination of the compression steel. More importantly, the compressive force path (Figure 4.28(r)) is straighter, and provides a vertical component of force that may resist applied shear. MacLeod and Houmsi (1994) suggest that the compressive path is narrower in the tapered section and hence must carry higher stresses than the prismatic section.

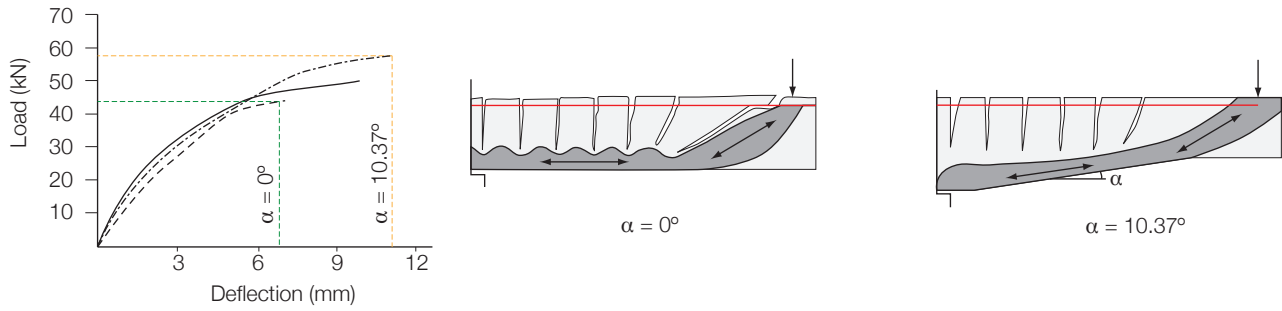


Figure 4.28: Load-displacement for haunched beams (l) and compression paths in prismatic and haunched sections (after MacLeod and Houmsi, 1994).

Analysis reveals that applying Eq. 4.7 at the critical section can give a good estimate of shear strength. However, the presence of some unconservative results led MacLeod and Houmsi (1994) to derive Eq. 4.28. The results of this equation are compared to the experimental data in Table 4.1. However, the empirical nature of Eq. 4.28 gives it limited applicability to the general shear design of tapered concrete beams.

Rombach and Nghiep (2011) suggest that the data provided by MacLeod and Houmsi (1994) does not provide any conclusive evidence for the behaviour of tapered beams, as evidenced by the fact that Beam 2 ( $\alpha = 4.7^\circ$ ) and Beam 3 (constant depth) were found to fail at almost identical loads. Furthermore Beam 5 and Beam 5R (identical layout with slightly different concrete measured strengths) were found to fail at quite different loads.

$$V_h = V_{pc} + \frac{M}{d_{cr}} F \tan \alpha \quad \text{Eq. 4.28}$$

$$F = 0.27(1 + \tan \alpha)^{10} \quad \text{Eq. 4.29}$$

Where  $V_{pc}$  = shear strength of constant depth beam with effective depth  $d_{cr}$ ;  $M$  = moment at critical section;  $d_{cr}$  = effective depth at critical section;  $F$  = Eq. 4.28, and  $\alpha$  = haunch slope.

Table 4.1: Summary of tests and analysis of results presented by MacLeod and Houmsi (1994).

	Depth (mm)			Haunch Length mm	Alpha Degrees	Cube strength MPa	Predicted failure (Eq. 4.82) kN	Measured failure kN	Measured/ Predicted
	Max	Min	Min/Max						
Beam 2	250	200	0.80	600	4.76	37.9	46.70	43.3	0.93
Beam 3	250	250	1.00	-	-	38	44.8	43.5	0.97
Beam 4	300	200	0.67	900	6.34	33.5	51.90	50.6	0.97
Beam 5	250	170	0.68	600	7.59	34.5	47.00	47.4	1.01
Beam 5R	250	170	0.68	600	7.59	33	46.30	50.2	1.08
Beam 6	250	140	0.56	600	10.39	33.2	46.60	57.2	1.23
Average								1.03	
Standard deviation								0.11	

Rombach and Nghiep (2011) presented a new set of test data based on the results of 18 further tests (summarised in Figure 4.29) that specifically addressed the issue of design to BS EN 1992-1-1 (2004). Adopting the design method described in §4.3.4 on page 100, Rombach and Nghiep (2011) provided capacity predictions for the tapered sections with and without the contribution of  $V_{ccd}$  (Figure 4.15 on page 96).

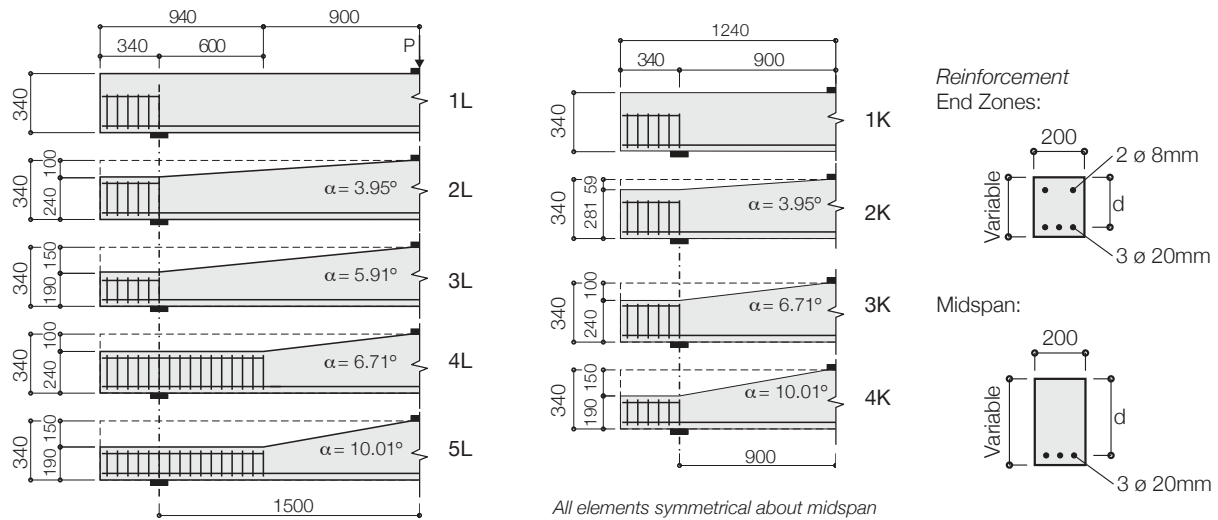


Figure 4.29: Test layouts by Rombach and Nghiep (2011).

The results are presented below in Table 4.2 and Figure 4.30 (note that specimens 4L and 5L failed in bending and are omitted from the results shown below) where it is apparent that simply applying an additional shear capacity provided by  $V_{ccd}$  does not accurately represent the behaviour of the tapered section. For the tapered sections, the average prediction using  $V_{ccd}$  was slightly unconservative and the prediction without  $V_{ccd}$  was slightly conservative (Table 4.2, note that no safety factors were included here).

This is highlighted in Figure 4.31, where the results for tapered beams that failed in shear only are presented. Plotted alongside this is a value for the capacity with just 50% of the value of  $V_{ccd}$  considered. This gives a slightly more consistent result, and appears to be predict the shear capacity rather well. However, the relative differences between the three data sets is quite small.

The limited data plotted in Figure 4.30 appear to suggest that in the beams with a span/depth ratio of 5 (Table 4.2), an increase in haunch inclination reduces the shear capacity of the section while in short beams ( $a/d = 3$ ) it increases the capacity of the section. It is considered here that the different ratios of span/depth simply provide the elements with different structural behaviour. Long elements ( $a/d = 5$ ) are flexural elements and thus a reducing depth at the support corresponds to a reduction in the shear capacity of the element. In short elements, the primary load carrying method is by arching and thus a steeper haunch provides a greater vertical component of force to resist shear. However, such statements require further verification, but taken with the test results presented above suggest that there is no great benefit to be found by including the inclination of the compression force in the design process.

It is interesting to note that the capacity predictions for prismatic sections (1L and 1K) were unconservative, with the short beam 1K being significantly unconservative, a potentially worrying result for the German Code that suggests the underlying behaviour of the section, irrespective of its haunch inclination, is not correctly understood at present.

Table 4.2: Test results and failure load predictions to DIN 1045-1 (cited by Rombach and Nghiep (2011)).

Beam	Alpha	a/d	$f_{ck}$ (MPa)	Test failure load (kN)	Predictions to DIN 1045-1			
					With $V_{ccd}$ (kN)	Actual/ Prediction	Without $V_{ccd}$ (kN)	Actual/ Prediction
1L-1	0	5	48.1	75.5	-	-	83	0.91
1L-2	0	5	49.2	79	-	-	83.5	0.95
2L-1	3.95	5	49.5	75	79	0.95	71.5	1.05
2L-2	3.95	5	50	74.5	79	0.94	71.5	1.04
3L-1	5.91	5	50.2	66.5	68.5	0.97	58.5	1.14
3L-2	5.91	5	51	69.5	69	1.01	58.5	1.19
1K-1	0	3	53.9	75.5	-	-	86.5	0.87
1K-2	0	3	54	69.5	-	-	86.5	0.80
2K-1	3.95	3	54.2	83.5	90	0.93	81.5	1.02
2K-2	3.95	3	54.2	85	90	0.94	81.5	1.04
3K-1	6.71	3	54.3	79.5	92	0.86	77.5	1.03
3K-2	6.71	3	54.3	80	92	0.87	77.5	1.03
4K-1	10.01	3	54.8	85	89	0.96	67	1.27
4K-2	10.01	3	54.8	84	89	0.94	67	1.25
Average					0.92		Average	1.04
Standard deviation (SD)					0.05		SD	0.14

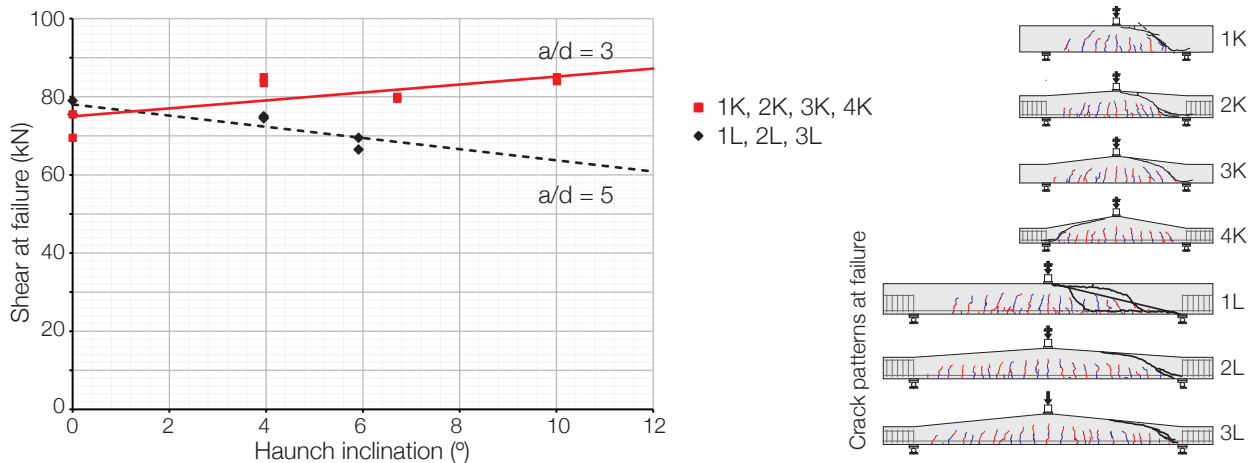


Figure 4.30: Test data for elements showing shear failures and their crack patterns (Rombach and Nghiep, 2011).

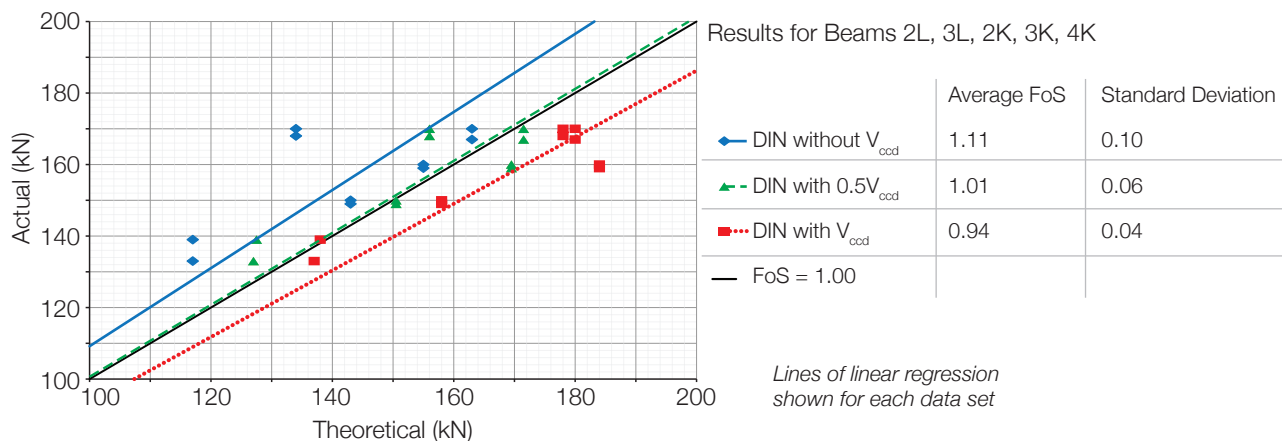


Figure 4.31: Test data for haunched elements (after Rombach and Nghiep, 2011).

The test results were then compared by Rombach and Nghiep (2011) with methods described in CSA A23.3 (2004), ACI 318 (2005), and the Swiss Concrete Design Code SIA 262 (2003, cited by Rombach and Nghiep, 2011). The exact methods used in implementing these codes were not described, but the results were presented and are compared in Table 4.3 and Figure 4.32, where the factor of safety for each design code and each beam layout is shown. Note that the values in Table 4.3 are design values and therefore include a factor of safety; predictions made in Table 4.2 do not include factors of safety (typically 1.80 for design to BS EN 1992-1-1 (2004)).

Table 4.3: Design shear capacities to different design codes (Rombach and Nghiep, 2011).

Beam	Alpha	a/d	Test results	Design shear capacity predictions					
			Failure load, $V_u$ (kN)	DIN (with $V_{cdd}$ )	DIN (without $V_{cdd}$ )	ACI (with $V_{cdd}$ )	ACI (without $V_{cdd}$ )	CSA	SIA
1L-1	0	5	75.5	44	44	51	51	65	52
1L-2	0	5	79	44	44	51	51	65	52
2L-1	3.95	5	75	38	42	38	42	62	51
2L-2	3.95	5	74.5	38	42	38	42	62	51
3L-1	5.91	5	66.5	31	36	30	35	61	51
3L-2	5.91	5	69.5	31	36	30	35	61	51
1K-1	0	3	75.5	47	47	55	55	81	64
1K-2	0	3	69.5	47	47	55	55	81	64
2K-1	3.95	3	83.5	44	49	48	53	77	62
2K-2	3.95	3	85	44	49	48	53	77	62
3K-1	6.71	3	79.5	42	50	43	51	75	61
3K-2	6.71	3	80	42	50	43	51	75	61
4K-1	10.01	3	85	35	48	36	49	72	60
4K-2	10.01	3	84	35	48	36	49	72	60

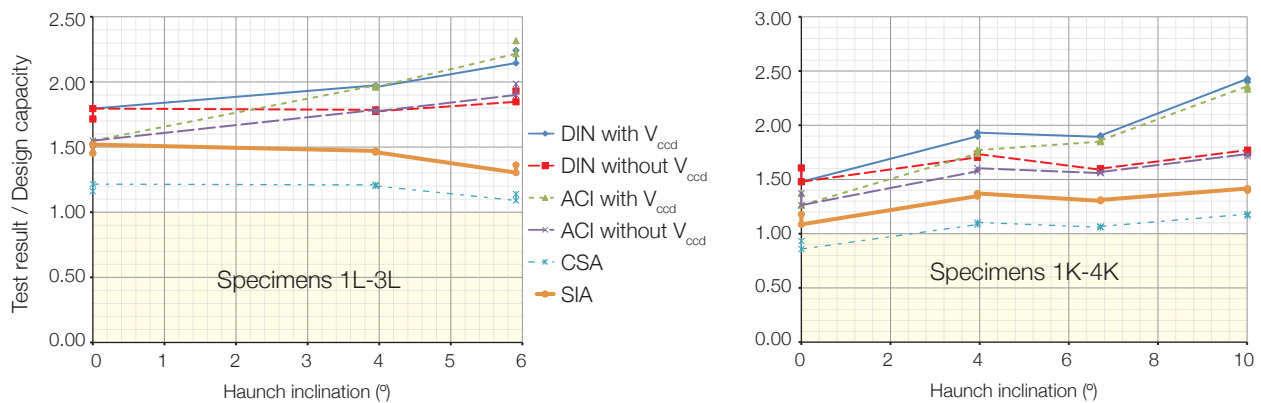


Figure 4.32: Variation of factors of safety against shear capacity with haunch angle to different design codes (after Rombach and Nghiep, 2011).

From Figure 4.32 it is clear that the effect of the haunch is not accurately considered in any of the methods analysed by Rombach and Nghiep (2011). Both CSA and SIA methods show little difference in capacity prediction between the haunched and prismatic sections (Table 4.3), while the DIN and ACI methods show increasing factors of safety with increasing haunch inclinations (up to 2.40 in Beam 4K).

In both CSA and SIA methods the shear capacity was calculated by Rombach and Nghiep (2011) in the area of maximum moment, which coincides with the area of maximum beam depth. The DIN and ACI methods on the other hand consider, more conventionally, the depth of the section at the supports as being critical, and it is this consideration that has led to higher factors of safety in the DIN and ACI approaches.

Rombach and Nghiep (2011) suggest that the DIN approach is the most reliable, yet this conclusion is not entirely borne out by the evidence presented. Comparisons between tests are difficult, since each has a different effective depth at the support, some of the tapers stop in mid-span, and only two values of  $a/d$  were considered.

In conclusion, Rombach and Nghiep (2011) accept that the use of an inclined compression chord to provide some shear capacity ( $V_{ccd}$ ) may not entirely represent the mechanical behaviour of the haunched beam, but that the effect of an inclined flange should not be ignored in design. It was recommended that only 50% of the value of  $V_{ccd}$  should be included (if it is a favourable effect) pending the results of further tests.

This rather unsatisfactory conclusion broadly represents all of the data presented for tapered beams in shear. There is yet to be a clear, satisfactory, widely applicable design method for such structures whose behaviour is borne out by the evidence of structural testing.

There also appears to be significant differences in the structural behaviour of short and long beams. Beam 4L and 5L were found by to fail in flexure, and have been omitted from the analysis above primarily because their structural layout is quite different to the remaining beam elements, as illustrated in Figure 4.33. In the short beams, the calculation of an equivalent to the shear valley (Figure 4.6 on page 88) seen in prismatic beams would be beneficial.

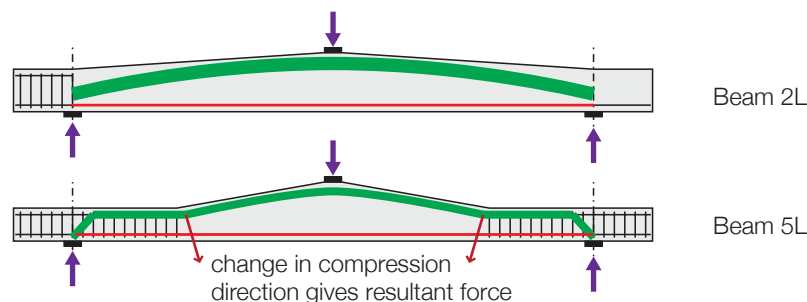


Figure 4.33: Behaviour of long and short tapered beams.

#### 4.3.7. Conclusions

The above has shown that various methods for determining the shear behaviour of tapered sections are available, but conclusive experimental data showing which method can provide accurate results is not available. There is considerable scatter in the available data, and some apparently contradictory results. The test data presents a confused picture, with some tapering elements appearing to show increases in capacity and other similar elements showing no improvement. This, coupled with the variations in design methods proposed, highlights the fact that the underlying behaviour is not yet fully understood.

For those sections with inclined tensile reinforcement (or a 'positive haunch'), shear capacity increases were found experimentally to be small or negative, while sections with horizontal tensile reinforcement and an inclined compression zone saw the potential for increases in capacity.

The final consideration for haunched concrete members is found by considering variations in the centroidal axis position, which are important for calculations of member stiffness (El-Mezaini *et al.*, 1991). A sloping centroidal axis causes a strong 'coupling' between bending, shear and axial forces in the variable section member, and should be considered carefully when hand calculations are undertaken for fixed end non-prismatic sections. The finite element modelling of such effects is considered in more detail by both Tena-Colunga (1996) and Balkaya (2001), who are in some disagreement as to the best method for such modelling. However, the poor quality of finite element modelling for cracked concrete precludes such arguments for ultimate limit state design.

The understanding of the behaviour of tapered sections in shear is fundamentally important to the future of fabric formed concrete structures, making the confusion presented in the tests shown above doubly important to unravel. This will be considered in a series of structural tests that are presented in §7.2 on page 218 and §8.2 on page 246.

The importance of a robust and easy to follow design method for tapered beams in shear is of critical importance to the effective use of fabric formed, non-prismatic, optimised concrete structures. Overly conservative approaches to shear design will dampen the potential material savings; while a failure to understand the structural behaviour could lead to equally catastrophic premature failures.

The potential advantages of a haunched section, including reduce material use, must thus be carefully considered against its potential pitfalls. In summary:

1. Haunched beams exhibit a different behaviour in shear to prismatic sections;
2. The categorisation of tapered beams according to the behaviour of their compression zone appears to be satisfactory (Figure 4.17);
3. Available test data suggests that simply supported beams with a positive haunch display a more brittle failure mode than beams with a negative haunch;
4. Available test data suggests that simply supported beams with a positive haunch have a reduced shear capacity than those with prismatic or negative haunch;
5. Continuous beam tests suggest that the BS EN 1992-1-1 (2004) design method is unable to account for the behaviour of the tapered section.

All of these concerns are considered in greater detail in the design and analysis of tapered reinforced concrete beams tested in shear that is presented in §7.2 on page 218 and §8.2 on page 246.



## **4.4. Summary**

Chapter 4 has provided a comprehensive assessment of the design of concrete structures, with particular attention given to the behaviour of non-prismatic structures. Combined with the assessment of the three components of a fabric formed structure presented in Chapter 3, a full understanding of the challenges facing the development of a sustainable construction industry is now apparent.

In Chapter 5 new work on the design of fabric formed structures is undertaken, before structural testing (Chapter 6) and analysis is undertaken with the aim of providing a stepping stone for the construction industry's use of fabric formwork for low carbon concrete design and construction.

[blank page]



# Chapter 5      Design (1)

## Flexural behaviour

### **5.1. Introduction**

The preceding Chapters provide information pertinent to the argument that fabric formwork can be used as a feasible method for the construction of low carbon concrete structures. A wide range of issues were considered that are now investigated in greater detail through a program of testing, analysis and development that is presented in the following Chapters. Chapter 5 sets out the philosophy of and reasoning behind a program of testing addressing flexural behaviour, the results of which are presented in Chapter 6. In Chapter 7 shear behaviour in non-prismatic beams is considered in detail, with the resulting structural testing and analysis being presented in Chapter 8.

Chapter 5 begins by again considering the feasibility of fabric formwork as an alternative to conventional construction methods. A new design methodology is presented, before a suitable range of structural tests are described. The development of construction methods is described alongside the structural test data in §5.8.

### **5.2. Approach**

The great advantage of fabric formwork is that it may be used in the construction of a very wide range of elements. This thesis will consider the use of fabric formwork as an alternative method for the construction of optimised beam elements with passive reinforcement only. Further work will be required to consider the use of actively reinforced fabric formed elements, in addition to shell structures, slabs, vaults and columns, as described in Chapter 12.

### 5.2.1. Benchmarking

Concrete framed buildings tend to make use of either in-situ reinforced concrete flat slabs or precast pre-tensioned elements. Post tensioned flat slabs offer material use advantages, but in practice are less common due to their increased design and construction requirements. A benchmark for material use in concrete framed structures is presented, with this analysis facilitating material use comparisons with the fabric formed elements presented in Chapter 10 (see §10.6.2 on page 438).

Two existing concrete framed structures were analysed, and whilst it is recognised that this sample does not necessarily provide a representation of all concrete construction in the United Kingdom, and to this end is rather limited, it does provide a starting point. The two structures to be analysed are described in Table 5.1. Concrete material volumes only are considered: steel usage, façade requirements, internal fittings and so forth are purposefully excluded.

Table 5.1: Concrete frame analysis details (courtesy Atkins Ltd).

	'Augustine House'	'Carnival Headquarters'
Location	Canterbury Christ Church University, CT1 2YA	West Quay Phase 3, Southampton.
Floor area	10,531m <sup>2</sup>	19,540m <sup>2</sup>
Purpose	Library and Student Services Centre	Headquarters for Carnival Shipping Lines
Completed	2009	2009
Structural layout	Braced RC Frame. RC Flat slab on a 7.2m x 9m grid (both structures have the same imposed loading).	Braced RC Frame. Post tensioned flat slab on a 7.5m x 9m grid

#### 5.2.1.1. Augustine House

Augustine House is a Library and Student Services centre for Canterbury Christ Church University, was designed by Architects Design Partnership and completed in 2009. The structure is divided into two four storey blocks that are connected by link bridges across a central atrium. Both blocks are braced RC frames, with 325mm flat slabs up to fourth floor and a 475mm roof slab. The building is illustrated in Figure 5.1, and the results of a material analysis are presented in Table 5.2.

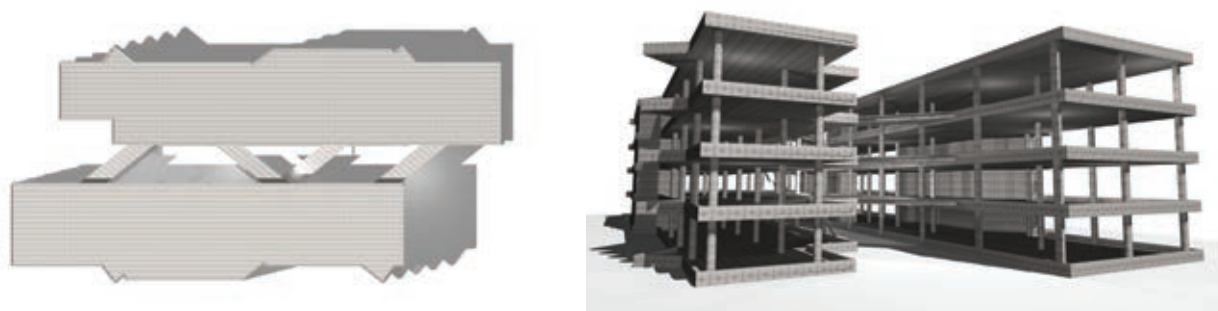


Figure 5.1: Augustine House (render by the author from the available drawings).

Table 5.2: Augustine House, material use analysis.

Item	Details	Concrete volume
RC Slab	10,531m <sup>2</sup>	4616m <sup>3</sup>
Upstands	385m, 0.6 x 0.25m	58m <sup>3</sup>
Columns	47 number, 600mm diameter	194m <sup>3</sup>

Item	Details	Concrete volume
Core walls	250mm thick, 178m total length	649m <sup>3</sup>
Total concrete volume (excluding foundations)		5517m <sup>3</sup>
m <sup>3</sup> concrete per m <sup>2</sup> floor area		0.52m <sup>3</sup> /m <sup>2</sup>

#### 5.2.1.2. Carnival HQ

Carnival HQ is located on a brownfield site previously used by Pirelli Cables. The building, which encloses a central atrium uses 300mm thick post-tensioned concrete slabs to maximise the space available for services and to minimise floor to floor heights. The project is illustrated in Figure 5.2 and the results of a material analysis are shown in Table 5.3.

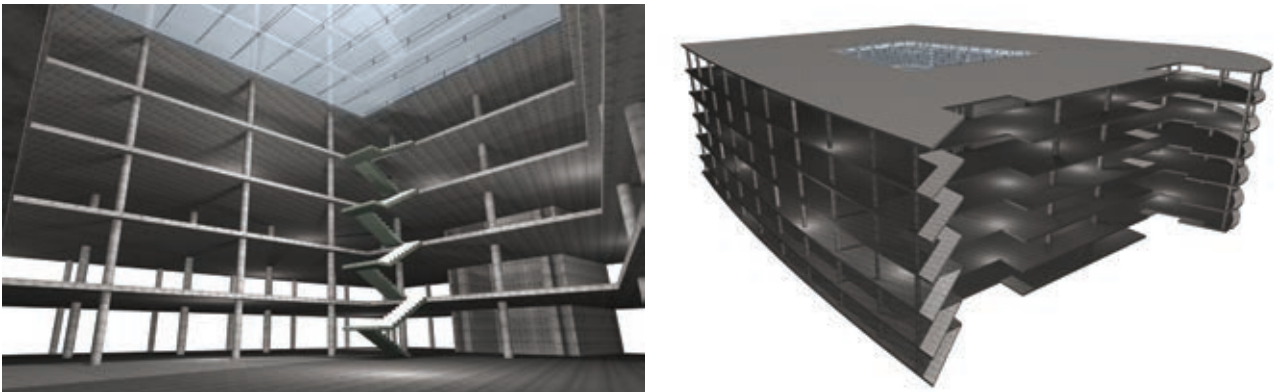


Figure 5.2: Carnival HQ (render by the author from the available drawings).

Table 5.3: Carnival HQ, material use analysis.

Item	Details	Concrete volume
PT Slab	19,540m <sup>2</sup>	6612m <sup>3</sup>
Columns	500mm - 750mm in diameter	297m <sup>3</sup>
Core walls	250mm thick, 147m total length	828m <sup>3</sup>
Total concrete volume (excluding foundations)		7737m <sup>3</sup>
m <sup>3</sup> concrete per m <sup>2</sup> floor area		0.40m <sup>3</sup> /m <sup>2</sup>

#### 5.2.1.3. Summary

The analysis undertaken above reveals that concrete volume savings are possible when post tensioned flat slabs are used (approximately 23% in this case). Fabric formed structures have already been seen (Chapter 2) to provide significant material savings, suggesting that there is scope in the construction industry to reduce material usage in both passively and actively reinforced concrete structures.

#### 5.2.2. Design influences

Presented on the following pages are a number of design influences for fabric formed construction that reflect the importance of not only structural efficiency but aesthetic appeal. These have been used to inform the development of this thesis. Following this, the work undertaken to achieve the goals set out in Table 2.5 on page 46 is described.

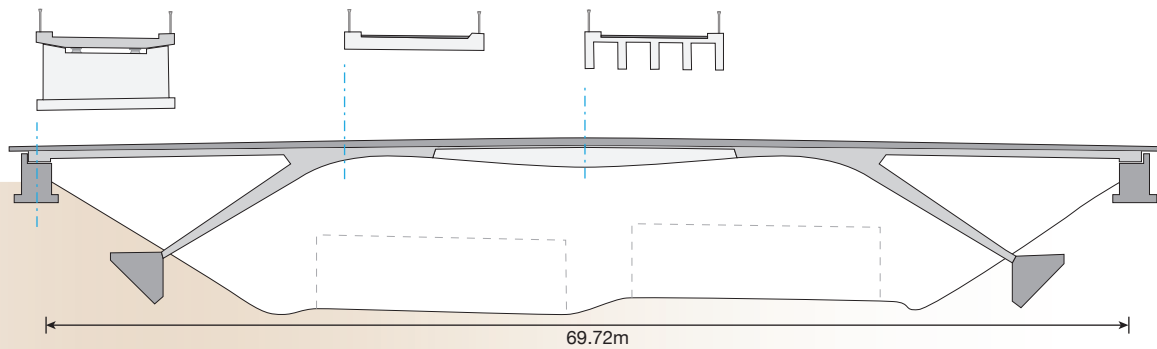


mark west

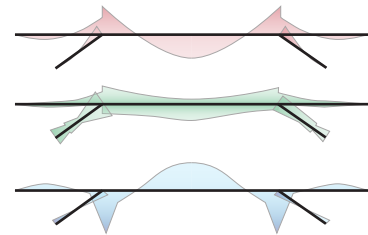
jorg schlaich



bridge over the A8 at kirchheim/teck (image: Schlaich and Schober, 1994)



bending moment diagrams



waclaw zalewski



'capital' precast system (images: Allen *et al.*, 2010)

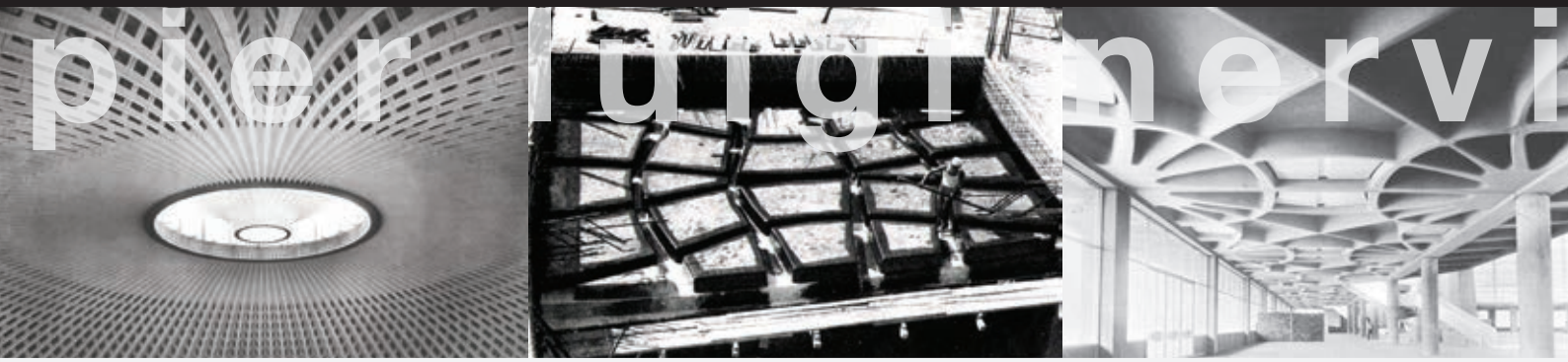
sumitomo construction company



shiosai bridge, japan

image courtesy 'Tawashi2006'





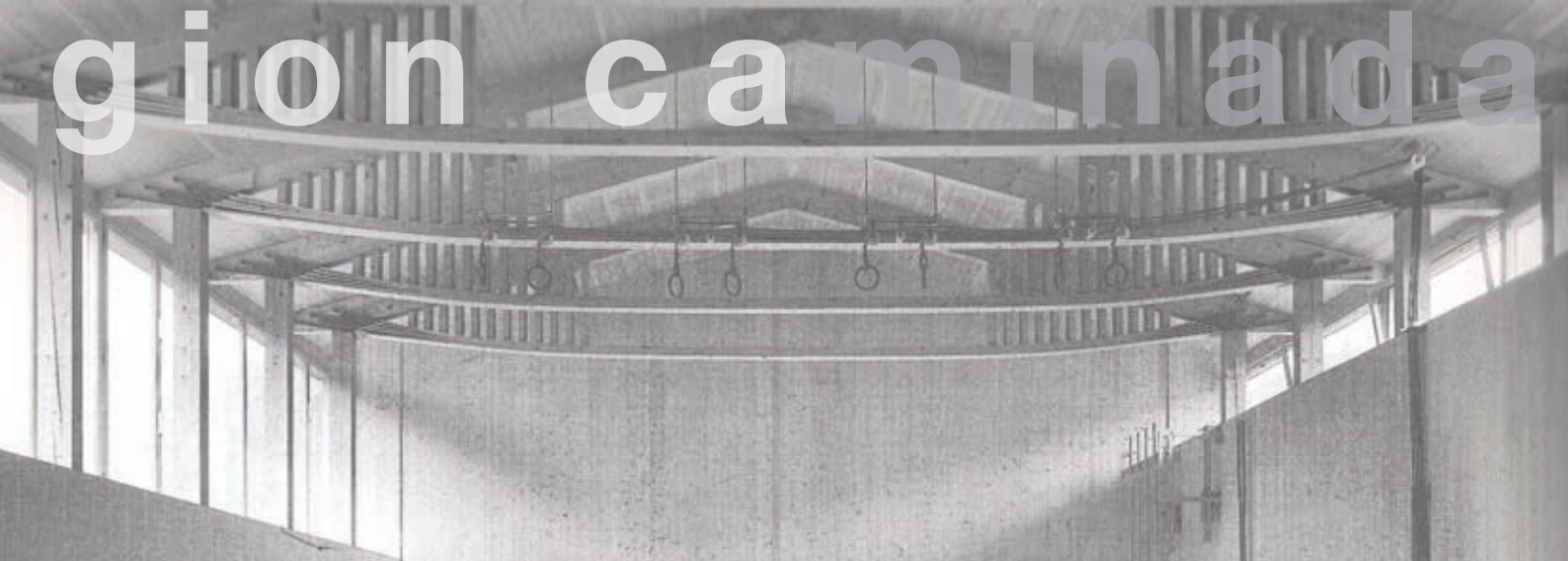
**Palazzo dello Sport, Rome and Palazzo del Lavoro** (images: Nervi, 1963)



**Exhibition Hall A, Turin; Palazetto dello Sport, Rome**



**Punt da Suransuns** (image credit: Chris Schroeer-Heiermann)



**Multipurpose Hall, Vrin** (image credit: Anna Lenz)

### 5.3. Initial designs

#### 5.3.1. Design options

Focusing on the use of fabric formwork to create optimised beams a number of design options were considered prior to structural design and testing of optimised fabric formed beams. Construction using bending moment shaped beams and precast fabric formed shell elements as permanent participating formwork for concrete slabs is illustrated in Figure 5.3 and Figure 5.4. The bending moment shaped beam presents some design issues such as shear behaviour and reinforcement anchorage in the support zone that are considered in subsequent Chapters.

By considering simply supported spans, the maximum shear and bending forces are located at different positions on the beam. To group the maximum shear and bending forces at the supports a cantilever frame construction method may alternatively be used, as shown in Figure 5.5. Here, precast variable section elements are tied together in-situ, with global stability provided by suitable core construction.

Whilst the use of 'beam' elements is advantageous for construction and transportation, they are invariably combined with an overtopping concrete floor slab. To address this, the following chapters have considered the design and construction of 'T' beams, as illustrated in Figure 5.6. Further development of this has led also to the design of 'double T' fabric formed beams, as described in §5.6 on page 136. Issues surrounding anchorage and shear remain prescient for such constructions and are addressed in §7.2 on page 218.

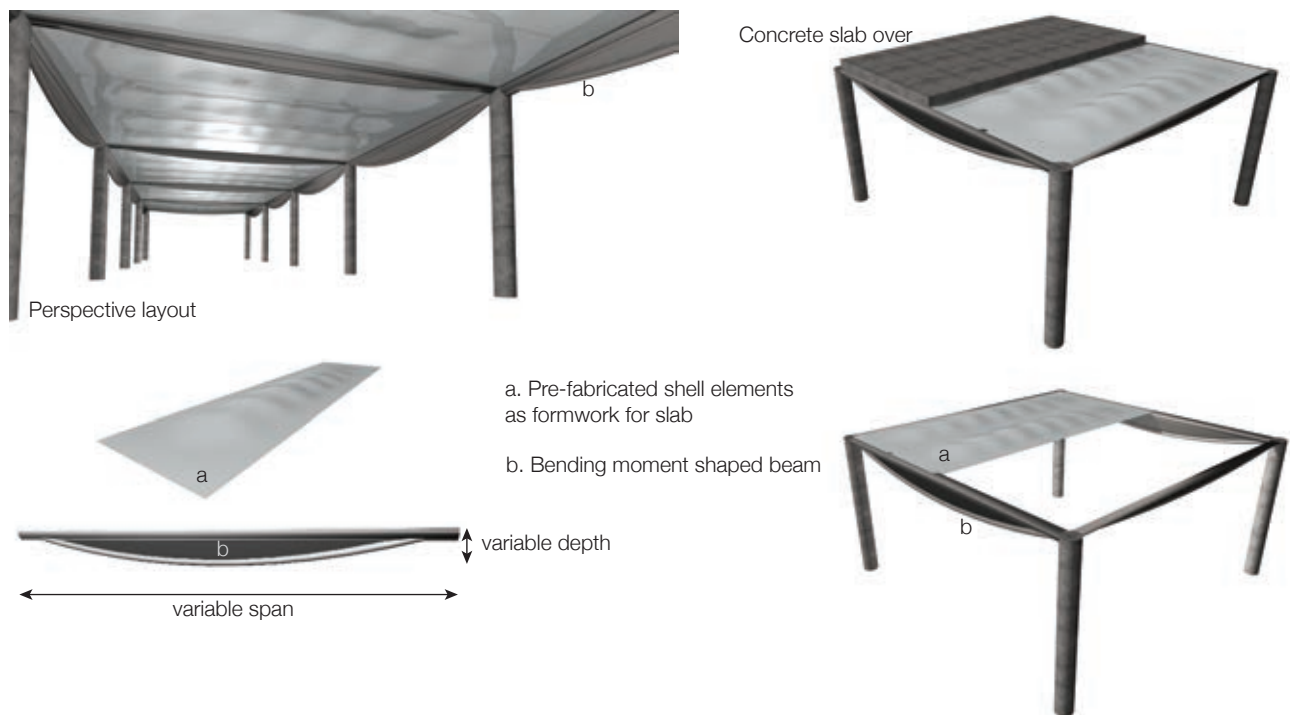


Figure 5.3: Bending Moment Beam Design.



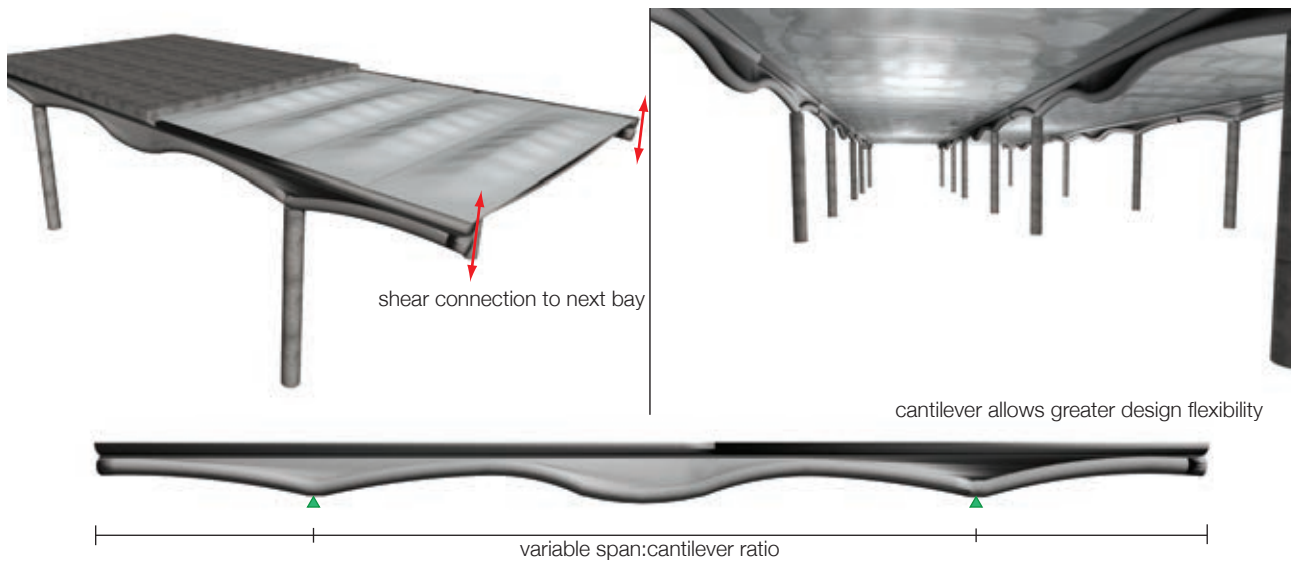


Figure 5.4: Extended bending moment beam design.

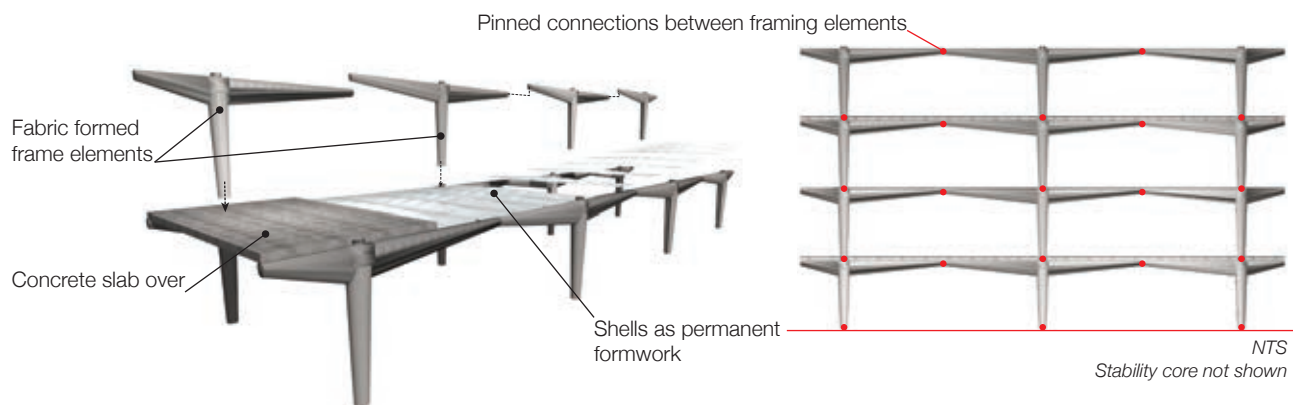


Figure 5.5: Portal frames using fabric formwork.

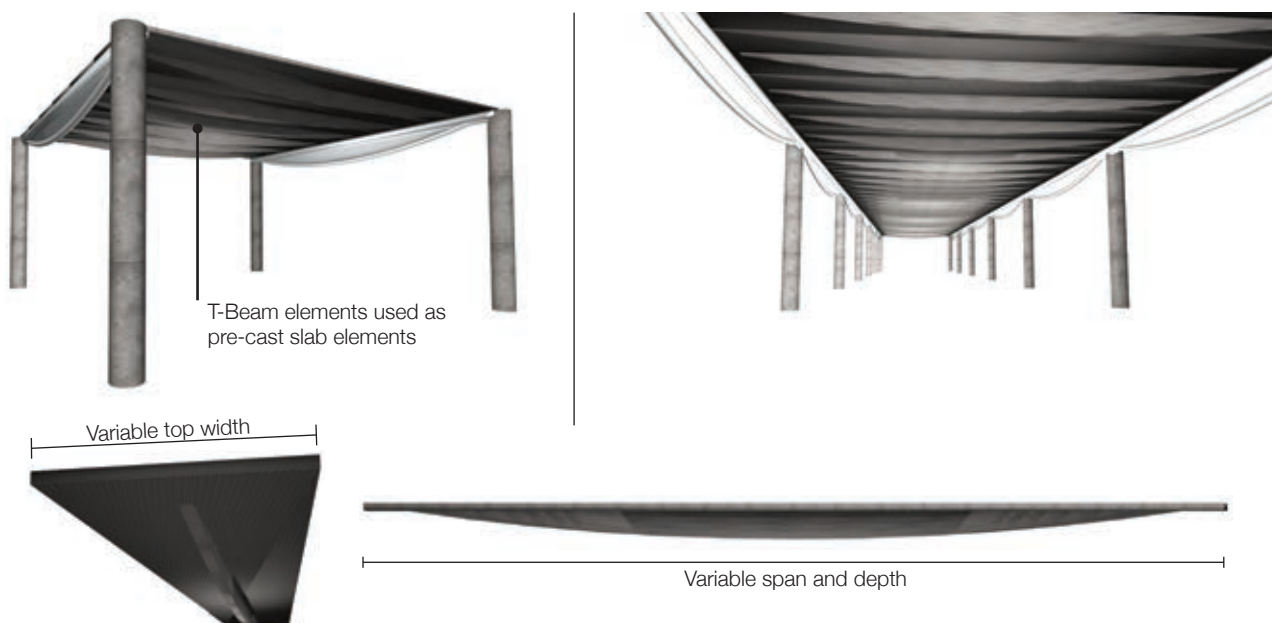


Figure 5.6: T-Beam Design.

## 5.4. Testing matrix

From the initial design options, a matrix of testing was determined based on combinations of construction and reinforcement methodologies for fabric formed beams (Table 5.4, Table 5.5). The tests undertaken, which are summarised in Table 5.6 and described in this thesis were chosen to address the following issues, as identified previously:

1. Construction methods for fabric formed concrete beams;
2. The design, analysis and testing of fabric formed beams as elements in concrete framed structures;
3. The use of ultra-high performance concrete in fabric formed beams;
4. The anchorage behaviour of reinforcing bars with shallow end zones;
5. The shear behaviour of variable section concrete beams;
6. The changes in concrete surface properties arising from the use of fabric formwork.

Each of these concerns deals directly with the main premise of this work, which is that fabric formwork can be used to facilitate a sustainable future for concrete construction. Each aspect is extensively investigated in this thesis, with the majority of the design work for subsequent structural testing being described in this Chapter.

Table 5.4: Construction methods.

	Bending moment shaped beams	Cantilever beams	T-Beams
Spline mould	(X)	(X)	(X)
Keel mould	X	X	X
Pinch mould	(X)	(X)	X

X = items tested in this thesis; (X) = alternative methods not used in this thesis.

Table 5.5: Reinforcement and concrete matrix.

		Longitudinal reinforcement	
		Steel	FRP
Shear reinforcement	FRP <sup>1</sup>	X	(X)
	Steel	X	(X)
	None	(X)	(X)
Concrete strength	Normal	X	X
	UHPFRC <sup>2</sup>	X <sup>3</sup>	(X)

X = items tested in this thesis; (X) = alternative methods not used in this thesis.

<sup>1</sup> FRP helices or draped stirrups for example as used by Whitehead, 2002; <sup>2</sup> Ultra high performance fibre reinforced concrete; <sup>3</sup> UHPFRC has higher tensile strength than normal strength concrete and is therefore also suitable for use in non-shear reinforced beams.

Table 5.6: Tests undertaken.

Issue	Description	Design details	Test details
Construction	Small span (1-2m) unreinforced beams constructed in fabric moulds to assess construction methods.	\$5.8 on page 153	
Anchorage	Thirteen tests undertaken to assess the use of splayed bars (§3.4.3.8.1) as anchorage for fabric formed beams. Complemented by later work undertaken at the University of Bath (see Kostova <i>et al</i> (2012)).	\$6.2 on page 159	
Reinforcement	Tests to determine the use of draped carbon fibre grids as shear reinforcement	\$8.6 on page 330	
T-Beam design and construction	4m span 'T' beam elements	\$5.5 on page 124	\$6.5 on page 182
	2m span 'double T' elements	\$5.6 on page 136	\$6.6 on page 195
	4m span 'double T' elements		
UHPFRC	2m span UHPFRC beam, single 'T' arrangement	\$5.7 on page 145	\$6.7 on page 206
	2m span UHPFRC beam, double 'T' arrangement		
Variable section beam tests	3m span beam with variable depth	\$7.2 on page 218	Chapter 8
	2m span beams with tapered ends		
Concrete properties	Chloride ingress tests	Chapter 9 on page 343	
	Carbonation		
	Schmidt hammer		
	Scanning electron microscopy		
	Sorptivity		

## 5.5. Detailed Design 1 - T-Beams

To address constructability concerns and the issue of premature shear failures seen in fabric formed structures (as described §2.5 on page 27) a series of 4m span beam tests was undertaken, chosen to model the behaviour of a beam and slab construction, as illustrated in Figure 5.7. Since the concrete slab now plays an important part in the behaviour of such an element, the system was designed as a 50% scale model of an 8m prototype concrete frame with 1m cantilevering sections beyond the column supports.

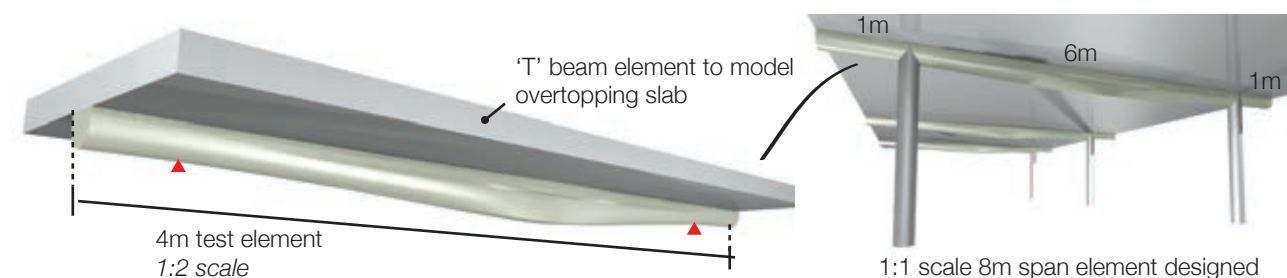


Figure 5.7: 'T' beam element, and potential application to reinforced concrete frame construction.

The elements are intended to model the use of a precast fabric formed beam, installed in a reinforced concrete frame and connected with an in-situ RC slab, as illustrated in Figure 5.8. In the experimental work described below, the 'beam' and 'slab' elements were cast together for ease of construction.

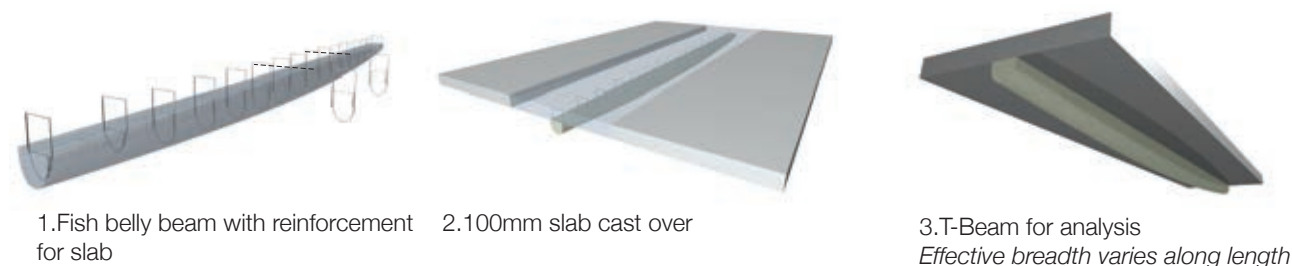


Figure 5.8: Use of precast beam elements.

Design will be undertaken assuming the beam element to be reinforced with four 10mm diameter bars, and two 12mm diameter bars, placed as illustrated in Figure 5.9 below. The 'T' beam top width was determined according to the provisions of BS EN 1992-1-1 (2004) as the maximum effective compression flange in such a construction typology.

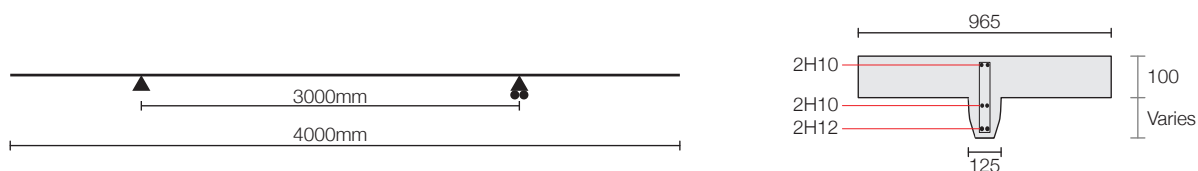


Figure 5.9: General arrangement for beam tests.

### 5.5.1. Methodology

Two design methods were used, contrasting previously used techniques with a new approach for the design of fabric formed beams. Design Method 1 replicates a technique found in previous work undertaken at the University of Bath where the beam is divided along its length into equally spaced sections, with each section then

designed to satisfy the moment applied to it according to the provisions of BS EN 1992-1-1 (2004). When steel bars are used as longitudinal reinforcement, they are first assumed to have yielded and thus provide a constant tension force along the length of the beam. This force is assumed to act horizontally, and thus the lever arm,  $z$ , can quickly be determined along the length of the beam to satisfy moment equilibrium, based on the applied loading envelope. This produces a steel profile whose depth is proportional to the bending moment on the section under consideration.

Design method 2 uses the vertical and horizontal components of the inclined bar force to satisfy the moment and shear force requirements of the beam. If the flexural reinforcement is placed at a depth proportional to the applied moment, then the vertical component of force in the bar is theoretically equal and opposite to the applied shear force everywhere along the element, as shown by Eq. 5.1.

$$\frac{dM}{dx} = V \quad \text{Eq. 5.1}$$

In Method 2, correct placement of the reinforcement is essential. The external dimensions of the beam may be altered for construction ease, but the internal reinforcement must follow the correct geometry to ensure the correct vertical component of force in the bar is present to resist the applied forces. Where this is not possible, vertical force capacity must be provided to the section and this is most easily achieved by the provision of transverse reinforcing steel.

The elements designed for testing according to Methods 1 and 2 use the same loading envelope, as summarised for the two load cases described below:

Load Case 1: Beam self weight plus a 200mm RC Flat Slab during construction;

Load Case 2: Full ultimate loading during which composite action with the topping slab is achieved.

Design loads are given in Figure 5.11 and the resulting bending moment diagram for design is given in Figure 5.12. The beams have been scaled by 50% to a 4m span test element, with an increase in dead load applied to account for the cubic loss in volume of the concrete element.



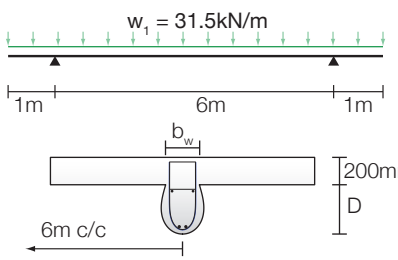
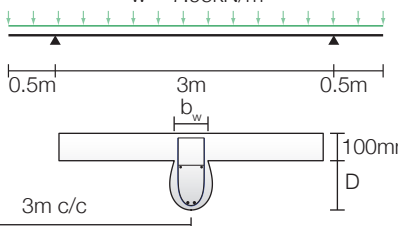
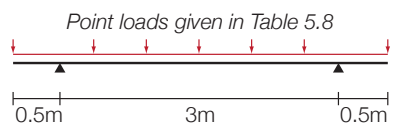
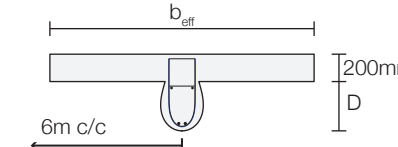
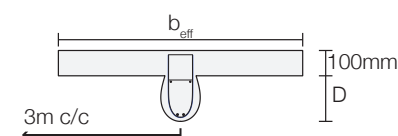
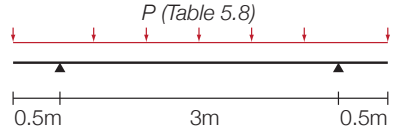
Load Case 1 : Beam Self Weight + Wet RC Slab		
<b>Prototype Loading</b> 200mm Slab, 6m Span = 28.8kN/m Beam Self Weight = 2.7kN/m (est.) $g_k$ = 31.5kN/m 	<b>50% Scale Dimensions for Testing</b> 100mm Slab, 3m Span = 7.2kN/m Beam Self Weight (est.) = 0.6kN/m Sum = 7.8kN/m Required Scale Load ( $0.5w_1$ ) = 15.75kN/m Additional load required = 7.95kN/m $w = 7.95\text{kN/m}$ 	<b>Applied loading for Testing</b> UDL = 7.8kN/m Additional UDL = 7.95kN/m All loads applied as point loads to give the same midspan bending moment. 
Load Case 2: Full dead and live load		
<b>Prototype Loading</b> 200mm Slab, 6m Span = 28.8kN/m Beam Self Weight = 2.7kN/m (est.) $g_k$ = 31.5kN/m $q_k$ (2.5kN/m <sup>2</sup> , 6m span) = 15kN/m $g_k + q_k$ = 46.5kN/m 	<b>50% Scale Dimensions</b> 100mm Slab, 3m Span = 7.2kN/m Beam Self Weight (est.) = 0.6kN/m $g_k$ = 7.8kN/m $g_{k, \text{additional}}$ = 7.95kN/m $g_{k, \text{total}}$ = 15.75kN/m $q_k$ (2.5kN/m <sup>2</sup> , 3m span) = 7.5kN/m $g_k + q_k$ = 23.25kN/m 	<b>Applied loading</b> Additional dead load and live load applied as point loads on the beam, as given below. The point loads are calculated to give the same bending moments as a UDL, but are easier to apply. 

Figure 5.10: Scaling test loads.

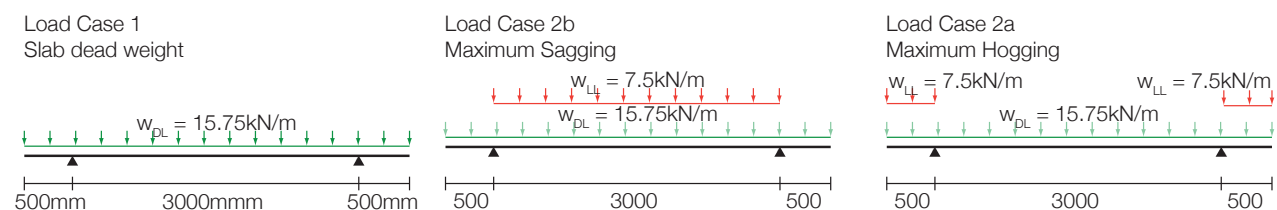


Figure 5.11: Load cases for design (summary).

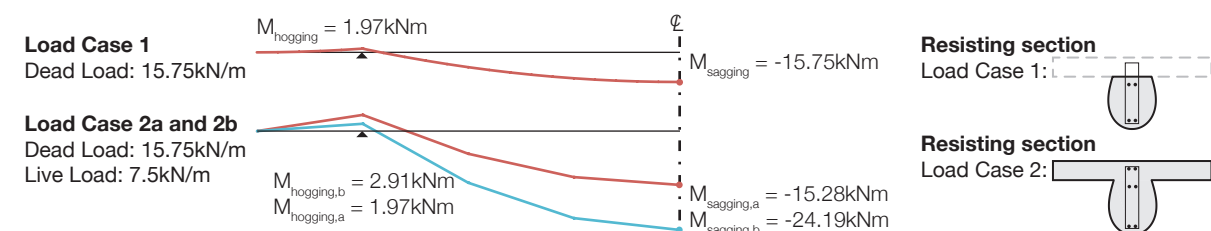


Figure 5.12: T-Beam loading moment envelope.

Four beams were thus designed, as described below and illustrated in Figure 5.13.

Beam 1, Method 1: Beam with designed links, and in areas where no links are required, minimum links to BS EN 1992-1-1 (2004). Curved longitudinal reinforcement placed at a constant cover from the beam soffit (This Beam is coded: 5\_1\_H\_C).

Beam 2, Method 1: Beam with designed links only, no links placed where not required according to MCFT.

Curved longitudinal reinforcement placed at a constant cover from the beam soffit (Code: 5\_2\_H\_C).

Beam 3, Method 2: Beam in which one set of longitudinal reinforcement follows the beam profile at a constant depth, while one curved bar is placed on the funicular line. Minimum links are provided along the beam length (Code: 5\_3\_H\_F).

Beam 4, Method 2: Beam with designed shear links at the support zone, in which the longitudinal reinforcement is placed on the funicular line only (Code 5\_4\_H\_F).

All beams were reinforced with two H12 bottom bars and four H10 top bars. Material properties are given in Table 5.7 and the overall section dimensions are provided in Figure 5.13.

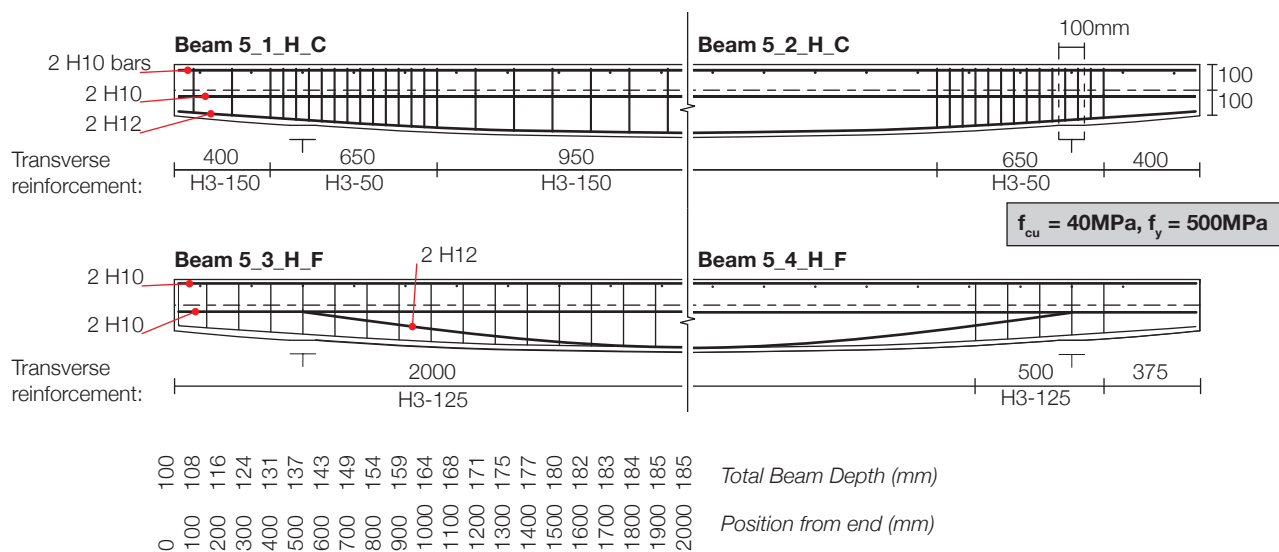


Figure 5.13: Four beams for testing.

Table 5.7: Material Properties.

Variable	Value	Variable	Value	Variable	Value	Variable	Value
Top steel	2H10	Link diameter	3mm	Concrete strength, $f_{cu}$	40N/mm <sup>2</sup>	Cover to steel	15mm
Bottom steel	2H12	Steel yield strength, $f_y$	500N/mm <sup>2</sup>	Top breadth	125mm		

### 5.5.2. Load capacity and response

By designing the beam to Load Case 1 and simply adding a 100mm top slab to the section, it was found that the as-built 'T' beam would have significantly more flexural and shear capacity than is required to carry the design loads. The flexural capacity of the section at mid span (Figure 5.14) is estimated by flexural analysis to be 40.5kNm, corresponding to a total applied load of 107kN (when applied in the ratio required for Load Case 2, and excluding self weight). This is significantly greater than the total design load of Load Case 2a (which is 65.2kN, as shown in Table 5.8), and it is therefore expected that the beam will exceed this requirement by some margin. These results are discussed further in Chapter 6.

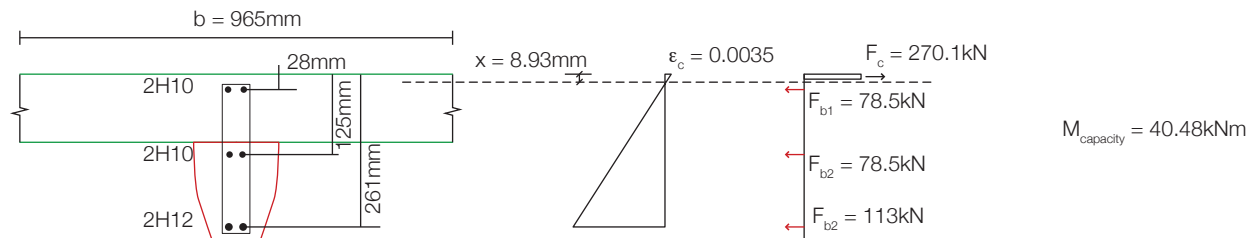


Figure 5.14: Flexural capacity at mid-span in as-built section, Load Case 2.

### 5.5.3. Test design loads

The moment envelope shown above will be approximated during testing using a nine point loading rig. By applying point loads, the distribution of vertical forces changes when compared to a uniformly distributed load and thus the beam must be designed for the test condition.

Since Load Case 1 is captured within the envelope of Load Cases 2a and 2b (as shown in Figure 5.12), only the Load Cases 2a and 2b will be applied in the testing process. Test loads are determined such that they give the same maximum and minimum moments as required in the loading envelope.

Vertical force and moment envelopes for the two conditions are compared in Figure 5.15(r) where it is apparent that the loading setup is well able to model a uniformly distributed load, although the shear forces can differ by up to 18% at the supports. The testing force envelopes shown below are then used in both Design Methods. During testing the dead load of the beam is subtracted from the values of P1 and P2.

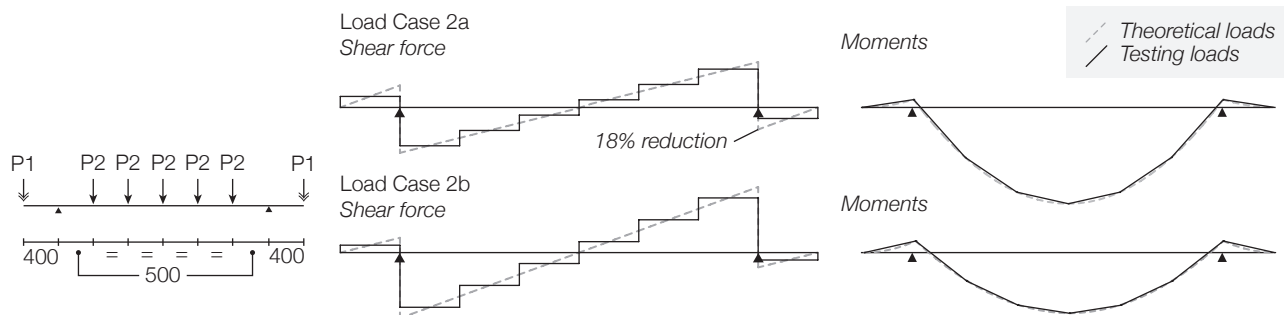


Figure 5.15: Distribution of test loads (l); Shear force and moment diagram comparison (r).

Table 5.8: Test load summary (see also Chapter 6).

Load Case	P1	P2	P1:P2	Total applied design load excluding selfweight
2a (maximum hogging)	5.87kN	6.69kN	1:1.14	45.18kN
2b (maximum sagging)	3.53kN	10.23kN	1:2.90	58.21kN

### 5.5.4. Transverse reinforcement design

Transverse reinforcement is designed to carry both transverse and longitudinal shear, as well as to confine the concrete section. To achieve this, 3mm diameter high yield steel 'paper clip' links have been designed, Figure 5.16(l), in order that a single bar can be bent to the correct shape. However, given the time required to produce complex links such as these, a simpler alternative design will be used in testing, Figure 5.16(r). Three design

conditions, transverse shear, shear between the web and flange and shear between concrete cast at different times (Figure 5.17) are to be satisfied by this transverse reinforcement.

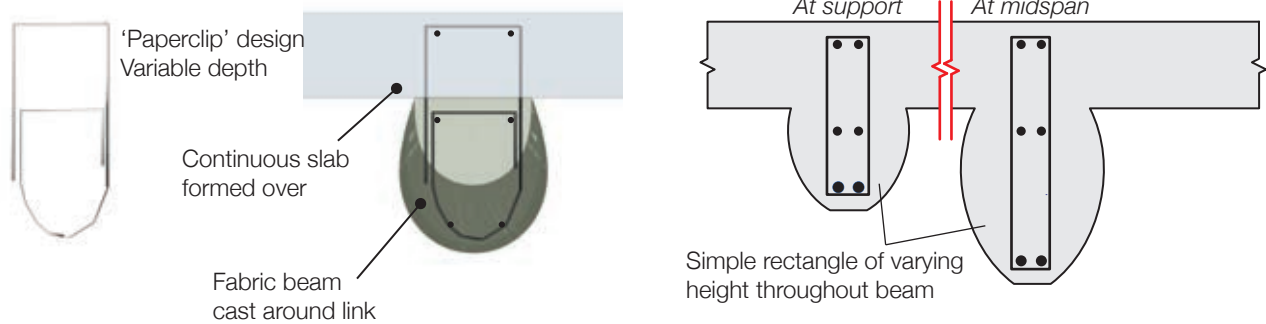


Figure 5.16: Shear link design. Paperclip (l); Rectangle (r).

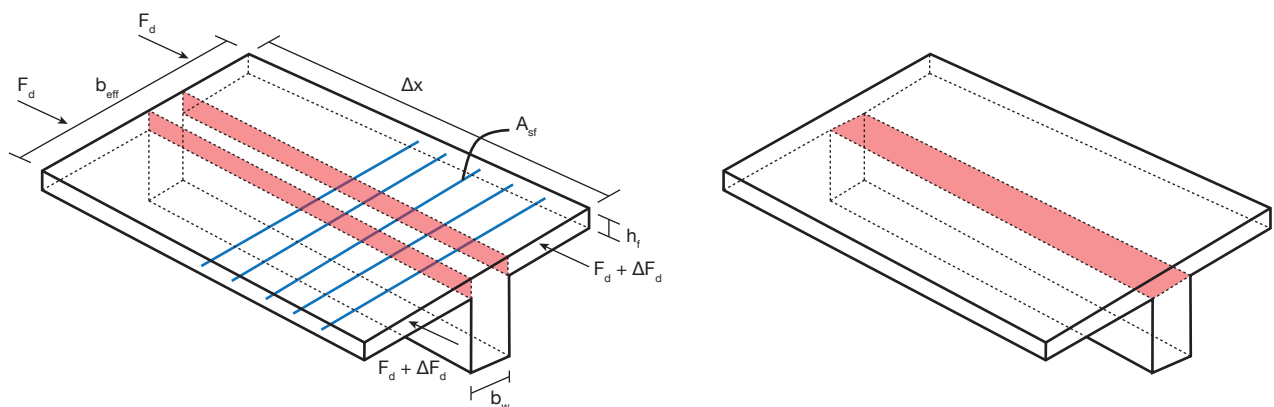


Figure 5.17: Shear between web and flange (l); Shear between concrete casts (r) (after BS EN 1992-1-1 (2004)).

#### 5.5.4.1. Transverse shear

The transverse shear capacity of the section must also be considered in both loading cases. In the service condition, the 'T' beam significantly adds to the shear capacity, as is shown below, where design is undertaken using the modified compression field theory and section capacities are calculated at critical sections, as shown in Figure 5.18. Shear critical zones are to be reinforced with 3mm diameter links at 50mm spacings, while reinforcement in the main span must also satisfy the requirements of §5.5.4.3.

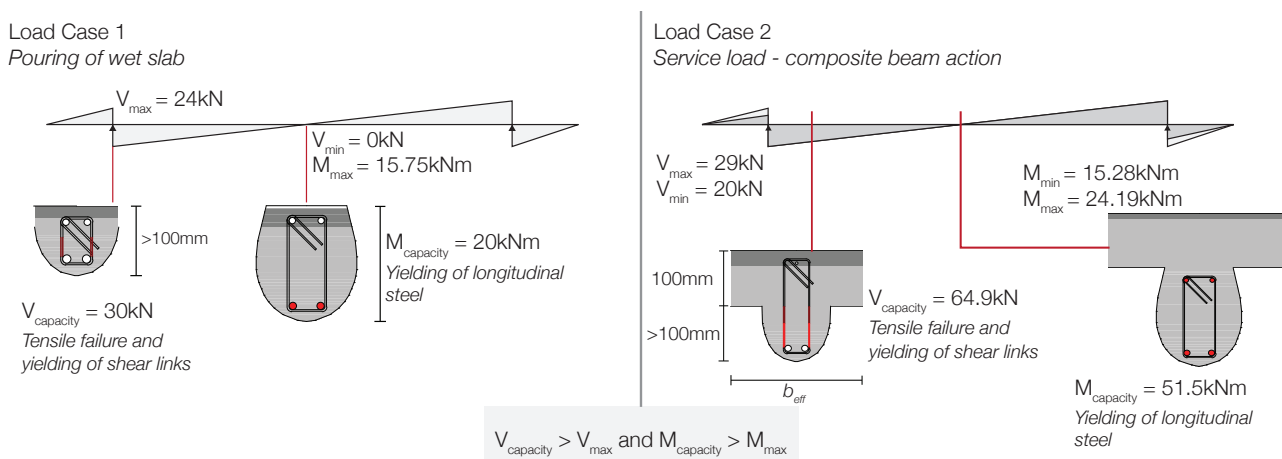


Figure 5.18: Transverse reinforcement. Load case 1 (l) and Load case 2 (r).

Undertaking detailed design to BS EN 1992-1-1 (2004) requires the maximum link spacing to be specified by Eq. 5.2, with resulting values along the length of the beam ranging from 75mm to 135mm, Eq. 5.3.

$$s_{l,max} = 0,75d(1 + \cot \alpha) \quad \text{Eq. 5.2}$$

$$s_{l,max} = 0,75(100) = 75\text{mm} \quad \& \quad s_{l,max} = 0,75(180) = 135\text{mm} \quad \text{Eq. 5.3}$$

In addition, BS EN 1992-1-1 (2004) cl.9.2.2(5) specifies a minimum ratio of transverse reinforcement, which is equated to the provided area of transverse reinforcement in Eq. 5.4. For a section with 3mm diameter links with a yield strength of 500MPa, a concrete strength of 40MPa and a beam breadth of 125mm, Eq. 5.4 is rearranged to show that a minimum spacing of 111mm is required, Eq. 5.5. The two requirements overlap, and result in a transverse reinforcement layout as show in Figure 5.19.

$$\left(0,08\sqrt{f_{ck}}\right)/f_{yk} = A_{sw}/sb_w \sin \alpha \quad \text{Eq. 5.4}$$

Where  $f_{ck}$  is the characteristic concrete strength,  $f_{yk}$  is the characteristic steel yield strength;  $A_{sw}$  is the area of transverse reinforcement;  $s$  is the spacing of transverse reinforcement along the beam axis;  $b_w$  is the beam web width;  $\alpha$  is the inclination of the reinforcement from the vertical.

$$s = \frac{A_{sw}f_{yk}}{b_w \sin \alpha \left(0,08\sqrt{f_{ck}}\right)} \quad \text{Eq. 5.5}$$

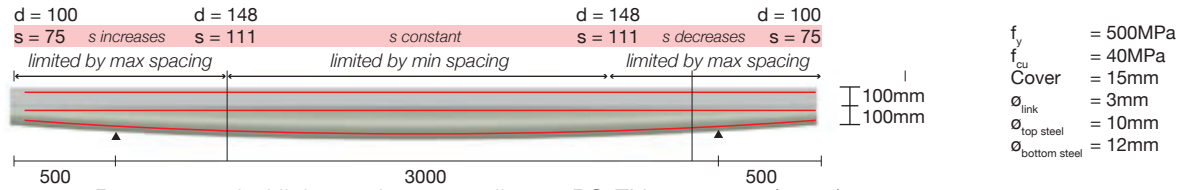


Figure 5.19: Recommended link spacing according to BS EN 1992-1-1 (2004).

#### 5.5.4.2. Shear between the web and the flange

The shear between web and flange is calculated as shown in Eq. 5.6, while the required area of reinforcement is given by Eq. 5.7. In this beam, the reinforcement is easily provided by 6mm diameter bars at 200mm spacing. Crushing of the web must also be checked, and is given by Eq. 5.8.

$$v_{Ed} = \frac{\Delta F_d}{h_f \Delta x} \quad \text{Eq. 5.6}$$

Where  $\Delta F_d$  is the change in normal force over a flange length  $\Delta x$ ; and  $h_f$  is the thickness of the flange in the section under consideration.

$$\frac{A_{sf}f_{yd}}{s_f} \geq v_{Ed} \frac{h_f}{\cot \theta_f} \quad \text{Eq. 5.7}$$

Where  $A_{sf}$  = area of transverse reinforcement at a spacing  $s_f$ ;  $\theta_f$  is the compression strut angle, which is given in the range  $1.0 \leq \cot \theta_f \leq 2.0$  (NA to BS EN 1992-1-1, Table NA.1, for compression flanges).

$$v_{Ed} \leq v_{fcd} \sin \theta_f \cos \theta_f \quad \text{Eq. 5.8}$$

### 5.5.4.3. Shear between concrete cast at different times

BS EN 1992-1-1 (2004) requires that the shear resistance between concrete cast at different times be greater than the design shear applied across the joint, Eq. 5.9. Maximum longitudinal shear occurs at the supports, where the minimum link spacing is determined by rearranging Eq. 5.11 to give Eq. 5.15. A minimum spacing of 154mm is thus satisfied along the beam by other transverse reinforcement considerations.

$$v_{Edi} \leq v_{Rdi} \quad \text{Eq. 5.9}$$

$$v_{Edi} = \frac{\beta V_{Ed}}{z b_i} \quad \text{Eq. 5.10}$$

$$v_{Rdi} = c f_{ctd} + \rho f_{yd} \quad \text{Eq. 5.11}$$

Where  $V_{Ed}$  is the transverse shear force;  $z$  is the lever arm of the composite section;  $b_i$  is the interface width;  $v_{Rdi}$  is the design shear resistance of the interface;  $c$  and  $\mu$  are factors that depend on the interface roughness and  $\rho$  is the reinforcement ratio.

$$\text{For load case 2: } v_{Edi} = \frac{29,000}{185(125)} = 1.25 \text{ Nmm}^{-2} \quad \text{Eq. 5.12}$$

Required reinforcement from Eq. 5.13:

$$\rho f_{yd} = v_{Rdi} - c f_{ctd} \quad \text{Eq. 5.13}$$

$$\rho = \frac{1.25 - 0.4(2.5)}{0.7(500)} = 0.073\% \quad \text{Eq. 5.14}$$

$$s = \frac{A_s}{b\rho} = \frac{2\pi(1.5^2)}{125(0.00073)} = 154 \text{ mm} \quad \text{Eq. 5.15}$$

Where  $f_{ctd} = 2.5 \text{ MPa}$  for  $f_c = 40 \text{ MPa}$  (BS EN 1992-1-1 3.1.6(2)P),  $c = 0.4$  and  $\mu = 0.7$

Values calculated at the support, where the lever arm is approximately 185mm and the section width 125mm. Factors for concrete roughness are taken from BS EN 1992-1-1 (2004).

### 5.5.5. Design compromise

Following the logic of the flexural design process, the shape of a uniformly loaded bending moment shaped, double cantilever beam is illustrated in Figure 5.20(top). Here, section depths at points of contraflexure are small and the beam elevation is considerably varied. However, this rather interesting shape is 'smoothed' by designing for an envelope of bending moments and shear forces. Most importantly, the presence of a construction constraint changes the overall beam geometry, such that a minimum depth for construction can be a guiding factor in design.

In the prototype 8m span beam, a top width of 250mm was chosen as a sensible value. At this width, a beam of less than 200mm in depth becomes difficult to construct, since the fabric will create a very shallow arc. This minimum depth of 200mm was therefore applied to the beam designs presented in this section. In the model as detailed in the above, these constraints are scaled down such that a minimum depth of 100mm is chosen. To avoid sharp changes in beam curvature, it is also proposed that a compromise be drawn between the absolute minimum depth of the beam and a desire for a more interesting shape, as shown in Figure 5.20(bottom).

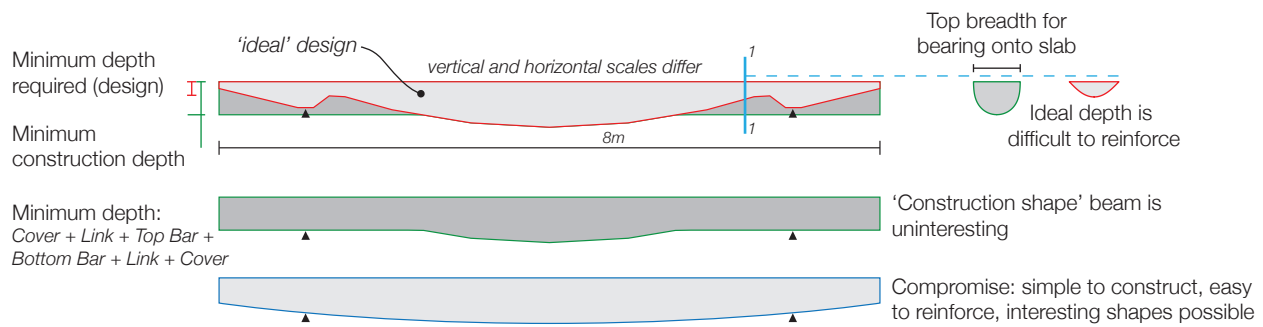


Figure 5.20: Design compromise for double cantilever fabric formed beams.

In addition, when a beam is designed to more than one load case, the ideal reinforcement position will vary between load cases. In this situation, a compromise must be sought in which the balance between constructability and efficiency is struck. This is illustrated in Figure 5.21, where the optimum bar positions for the two load cases described in Figure 5.12 are plotted.

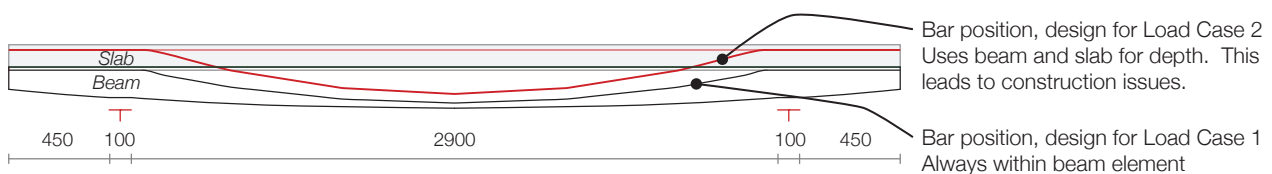


Figure 5.21: Discrepancy in bar position, Load Case 1 and Load Case 2.

It is thus not possible to provide passive reinforcement that can wholly satisfy the requirements of the beam (prior to casting the topping slab) and T-Beam (post casting of the topping slab). In addition, if the beam is indeed to be cast separately to the slab, connection must be made between the concrete cast at different times. Some form of transverse reinforcement is therefore required to carry the additional vertical force that arises because the bar is not inclined correctly for all load cases.

By positioning the flexural reinforcement at a depth proportional to the bending moment diagram, it is important to correctly assess behaviour at the supports. In the above design example, the sagging moment on the beam does not 'begin' until approximately 100mm inside either support (moving towards the centre of the beam). In this zone, the curved bar does not provide design resistance, instead the horizontal top bar is used to carry the hogging moments over the support.

In addition, the estimation of the actual location of the compression path is problematic. This is illustrated in Figure 5.23, where the change in direction of the compression force path coincides with the position of zero moment and crosses the tension steel. From there, the effective lever arm to the tension steel is determined as normal. It is considered that by 'draping' the flexural reinforcement, it is possible to guide the compression path into a desired location, so long as this remains within the confines of the physical section. Where the path changes direction, tensile forces result, as described by the compression force path method (§4.2.5 on page 88).



After casting the topping slab, transverse reinforcement is required to connect the tensile force paths from the two layers of horizontal reinforcement to the sagging reinforcement, as illustrated in Figure 5.24. The change from tension on the top face to tension on the bottom face is one that is not widely recognised in conventional concrete design, yet is of paramount importance here to prevent premature tensile failures in the section. The results of the testing regime will be fundamental in demonstrating that this has been achieved. It is also evident from Figure 5.23 that points of contraflexure are difficult to reinforce, and lead to a wide range of potential issues for construction and behaviour during loading.

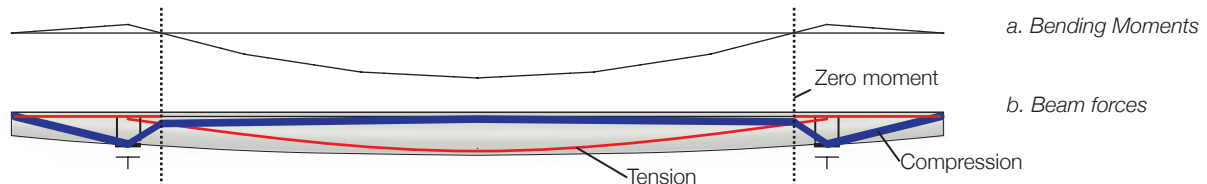


Figure 5.22: The compression and tension force paths in a variable section fabric formed beam (illustrative).

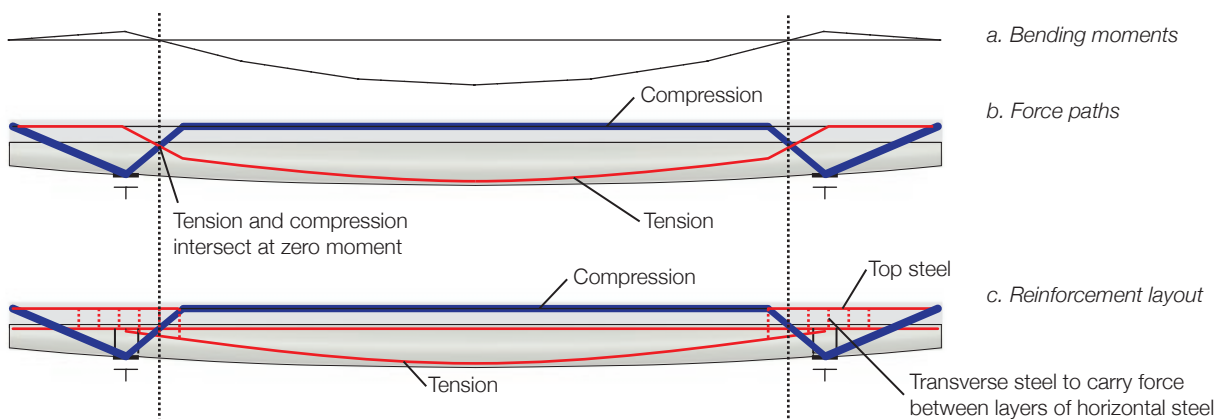


Figure 5.23: Tension path in the composite 'T' section (illustration).

#### 5.5.5.1. Support detail

Achieving a suitable beam-column connection is one aspect of fabric formwork that has not been fully addressed to date. It is now proposed to use a simple flat plate cast into the bottom of the beam, which has the simple effect of 'flattening' a continuous beam profile, Figure 5.24. The plate must be held securely in a level position during casting.

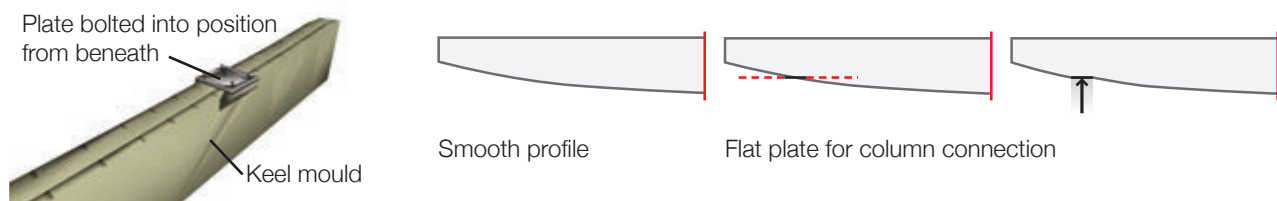


Figure 5.24: Forming a flat support.

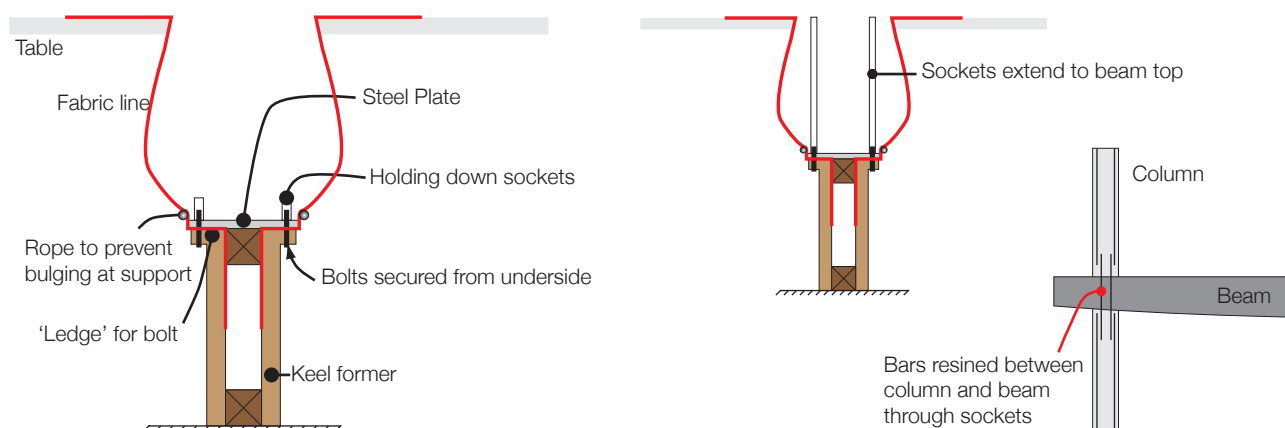


Figure 5.25: Section detail of support (l); Solution for multistorey construction (r).

Although the holding down bolts shown in Figure 5.25(l) are suitable for single level construction, in a multiple storey building continuity between levels may be achieved by casting full height sockets (or tubes) into the beam, Figure 5.25(r). The beam may then be placed over starter bars and grouted into position with ease, as is currently standard practice in precast concrete frame construction in the UK.

### 5.5.6. Material use

The above has provided a beam design that is both simple to construct and uses material efficiently. There are, however, further savings to be made by the introduction of a 'pinch' into the centre of the beam span, as shown in Figure 5.26. This would be achieved using the double keel mould (described in §6.4 on page 177), which provides additional material savings.

Concrete use is compared for the two fabric formed beam designs with an equivalent, 125mm x 250mm prismatic concrete section in Table 5.9, with concrete volumes in the fabric formed beam calculated from 3D Rhino models of the Beam elements. The reductions in material use are broadly in line with previous analysis and are therefore acceptable (note that the topping slab is constant in both fabric formed and prismatic beams and is therefore not included in the initial material use analysis. If the topping slab is included in the analysis, the material use savings are 'dampened' considerably, as shown in Table 5.9).

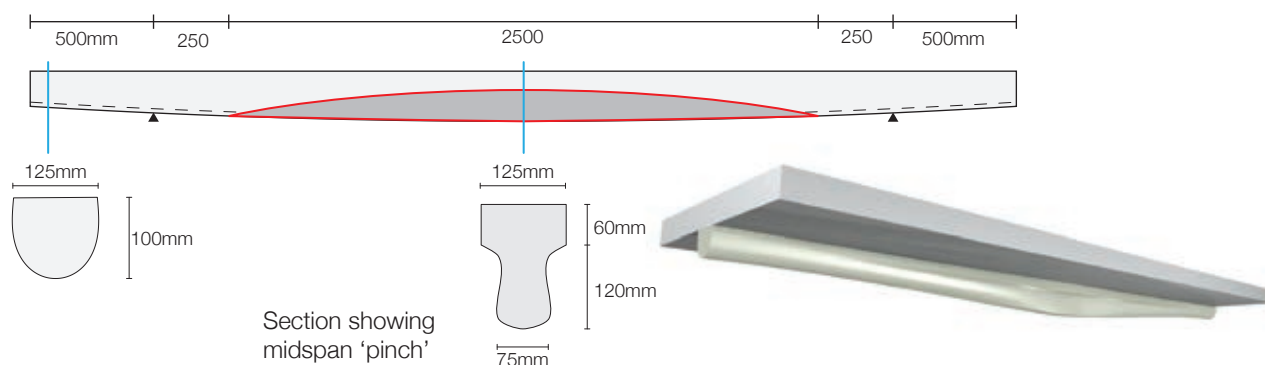


Figure 5.26: Pinch' in the T-beam designs.

Table 5.9: Material use comparison.

Beam	Volume excluding topping slab	Saving excluding topping slab	Volume including topping slab	Saving including topping slab
Prismatic	0.10m <sup>3</sup>	-	0.486m <sup>3</sup>	-
Fabric formed variable section beam	0.065m <sup>3</sup>	35%	0.451m <sup>3</sup>	7.2%
Fabric formed variable section beam with 'pinch mould'.	0.060m <sup>3</sup>	40%	0.446m <sup>3</sup>	8.2%



Figure 5.27: 'Pinch' beam design visualisation.

#### 5.5.7. Summary

In the above, the feasibility of using fabric formed beams in conventional design has been fully considered. The resulting section is designed for a moment envelope, is easy to construct and reinforce and has considerable material savings over its equivalent rectangular section. However, it is increasingly apparent that the real advantage of fabric formwork might be used in prestressed sections, where the full compression capacity of the concrete can be utilised.

The processes described above can easily be applied to less conventional designs - indeed fabric formwork not only provides a method by which material can be saved and improvements in surface durability and quality can be achieved, but also allows architects and engineers to realise their more unusual designs. The construction and testing of these beams is described in detail in §6.5 on page 182, where a journal paper including the results of these tests is detailed.

## 5.6. Detailed Design 2 - Double T-Beam

### 5.6.1. Introduction

Testing of the 4m span single 'T' design (§5.6) is described in §6.5 on page 182. Deep flexural cracking recorded in these tests demonstrates that a much shallower compression block is required to reach the maximum beam capacity than was provided. The simple scaling of beam and slab elements is therefore not an appropriate approach to demonstrate the efficiency of the fabric cast 'T' section.

In the following, the use of fabric formwork to create variable section 'Double T' beams is assessed, where these elements would be used as precast planks to support a thin structural topping. This contrasts to the previous approach in which a substantial top slab of 200mm was modelled in the 'T' beam tests.

Initial work was undertaken to refine the construction method for the double 'T', which has not been attempted before. Design calculations for a 2m span element are presented below, with test results presented in §6.6.2 on page 195. The results of these small tests then informed the design of larger, 4m span, elements (§5.6.4) the test results of which are presented in §6.6.3 on page 198.

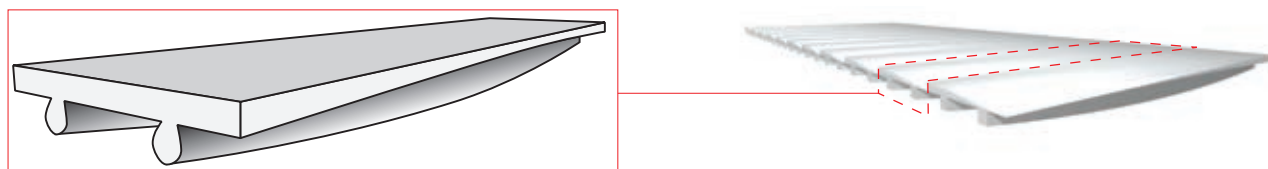


Figure 5.28: Fabric formed double 'T' beam design.

### 5.6.2. Design approach

To ensure that sufficient capacity is provided the beam is firstly design for flexure using the provisions of BS EN 1992-1-1 (2004), with the appropriate bar position for the loading envelope determined. Additional bars are added if required for construction purposes. The shear capacity of each section is then assessed using either the modified compression field theory or BS EN 1992-1-1 (2004) and the cross section may then be changed, or reinforcement added, if required.

### 5.6.3. Initial investigations

Initial work was undertaken to design and test a 2m span double 'T' element without transverse reinforcement. The loading envelope shown in Figure 5.29 was used to determine the test loads shown in Figure 5.30. The beam design (Figure 5.31) was determined in the same manner as described in §5.5.1 on page 124, where the flexural capacity of the element is matched to the requirements of the loading envelope and shear capacity is provided by the inclined longitudinal steel. Testing details for this beam are described in §6.6 on page 195, with these results going on to inform the design, construction and testing of 4m span prototype double tee beams as described in §5.6.4 on page 138.

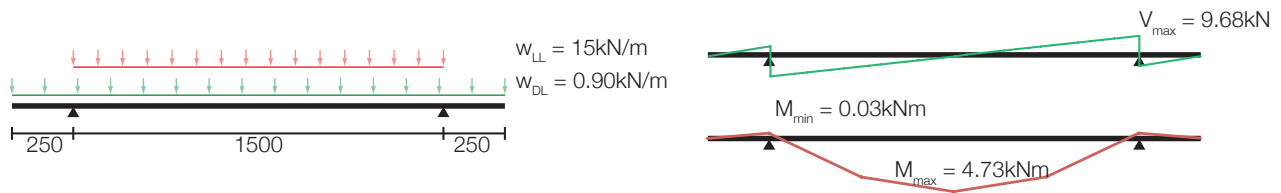


Figure 5.29: Loading envelope for 2m span double tee.

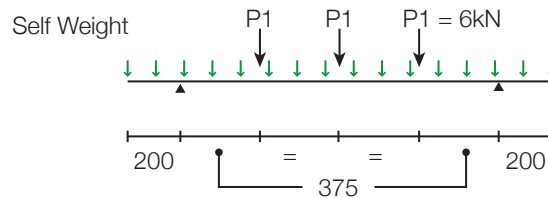


Figure 5.30: Test arrangement.

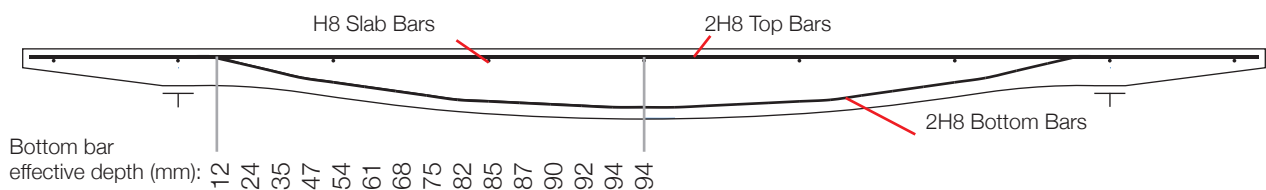


Figure 5.31: Reinforcement layout.

#### 5.6.3.1. Construction

Construction of the Double 'T' was undertaken in a new double keel mould, as illustrated in Figure 5.32. Here, three sheets of fabric are stretched between two keel moulds, and the requirements for accuracy in fitting the fabric are now greatly increased.

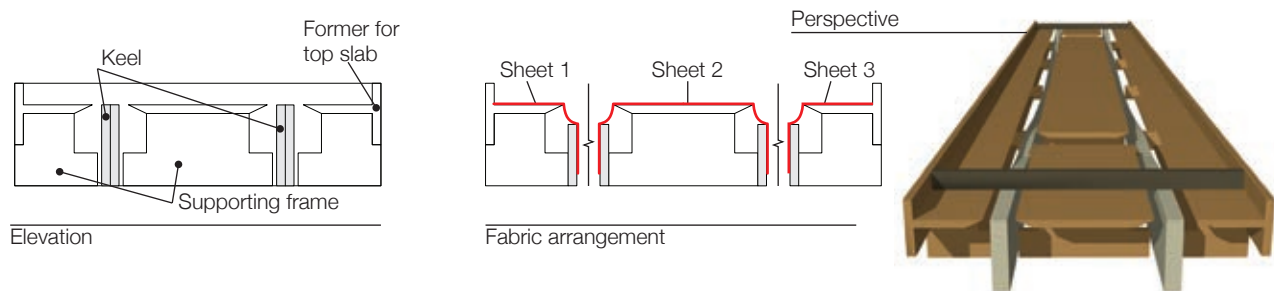


Figure 5.32: The Double Keel Mould.

At the supports, the previously described flat plate detail (Figure 5.25 on page 134) is replaced with a flat plate secured between the two keels to create a wide support zone, Figure 5.33. The detail is adaptable as desired to ensure that the fabric does not crease or wrinkle in the mould during casting.

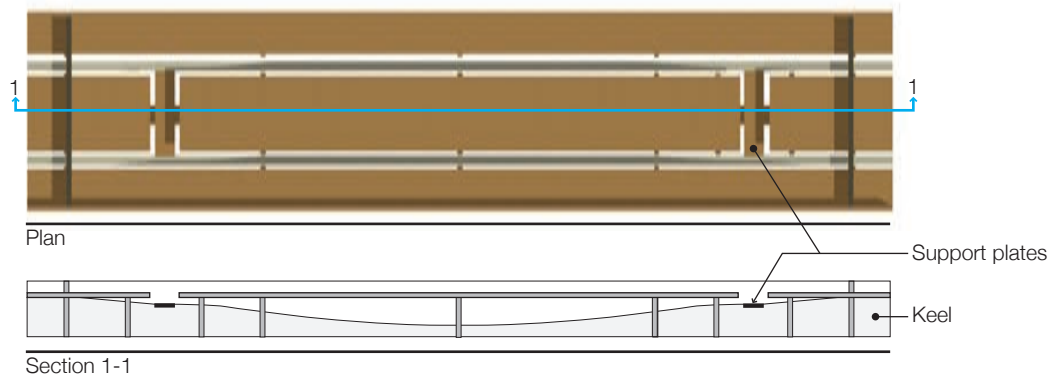


Figure 5.33: Support detail.

#### 5.6.4. Prototype Double T Beams

After completing the initial investigations described above, a series of four metre span double 'T' beams were designed. The general arrangement of these elements is shown in Figure 5.34, with the design loading envelope described in §5.6.4.1. The elements are intended to model the use of 8m span precast double T elements in a conventional concrete frame, which would be tied together with a structural topping.

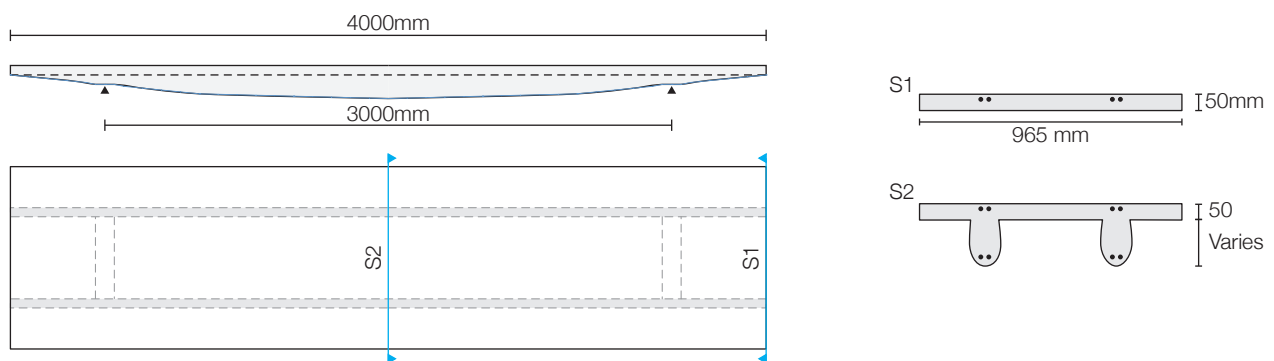


Figure 5.34: 4m span double T beams general arrangement.

##### 5.6.4.1. Load envelope

The beams were again designed for testing in nine point bending to the loading envelope shown in Figure 5.35. In contrast to those beams described in §5.5, the double T beams are to be tested in multiple load arrangements, with each specimen tested to destruction in a different way, as described fully in §6.6.3 on page 198. Two load cases are shown, representing maximum hogging and sagging moments in the element and include within them the construction load case.

It should be noted that the purpose of the loading envelope is to demonstrate a design method and to realise a specimen that can both be feasibly constructed and will provide useful test data and to this end the 50mm top flange of the model beam represents the top flange and structural topping of the 8m span prototype element.

Figure 5.35: Moment and shear force envelopes.

#### 5.6.4.2. Flexural design

All beams were reinforced with two number 8mm diameter high yield bars in the top and bottom of each flange. The section dimensions calculated required to satisfy the flexural requirements of the beam are shown in Figure 5.36.

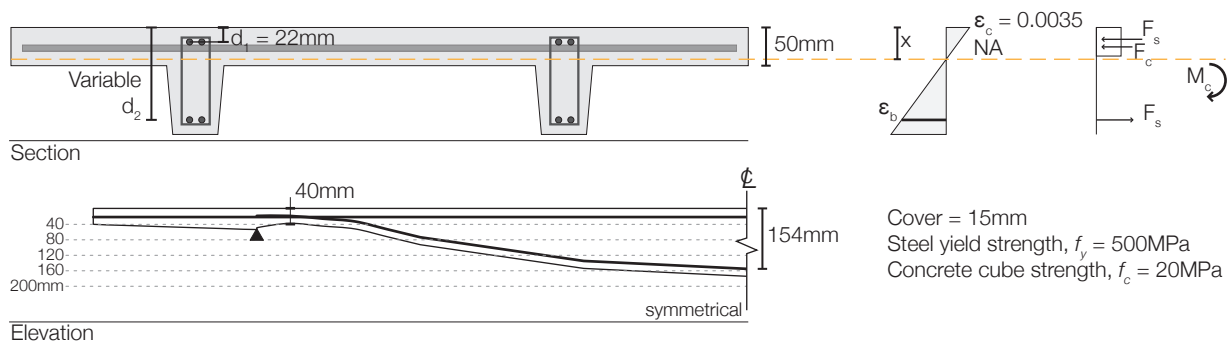


Figure 5.36: Flexural design and beam profile.

#### 5.6.4.3. Shear capacity

To assess the capacity of the section shown in Figure 5.36 to carry the design shear force two methods have been used. The first uses the Modified Compression Field Theory (described in §4.2.5.3 on page 92) to assess the capacity of the section, while the second uses a combination of the inclination of the longitudinal bar and conventional transverse reinforcement to provide shear capacity. In both cases, the combination forces of shear and moment have been carefully considered in the support zone, using both BS EN 1992-1-1 (2004) and MCFT approaches to check section capacities, to facilitate a ductile mid-span failure.

#### 5.6.4.3.1. Method 1

By designing the section using the MCFT, it is quickly apparent that a 40mm deep section at the support (Figure 5.36) is not able to carry the maximum design shear of over 20kN (Figure 5.35). The result of this analysis is a deeper and wider support zone, as shown in Figure 5.37, with closed links placed in both webs. The bar position determined in §5.6.4.2 solely for flexure is plotted on the section for comparison.



The loading condition on the beam results in zones of constant shear force with linearly variable moments. For a prismatic section, an increase in moment lowers the shear capacity of the section (as shown on the M-V diagram, Figure 5.38) and hence the beam increases in depth away from the supports (as the shear is constant but the moment increases). This beam design was not tested, as Method 2 (§5.6.4.3.2) was considered to provide a better design procedure.

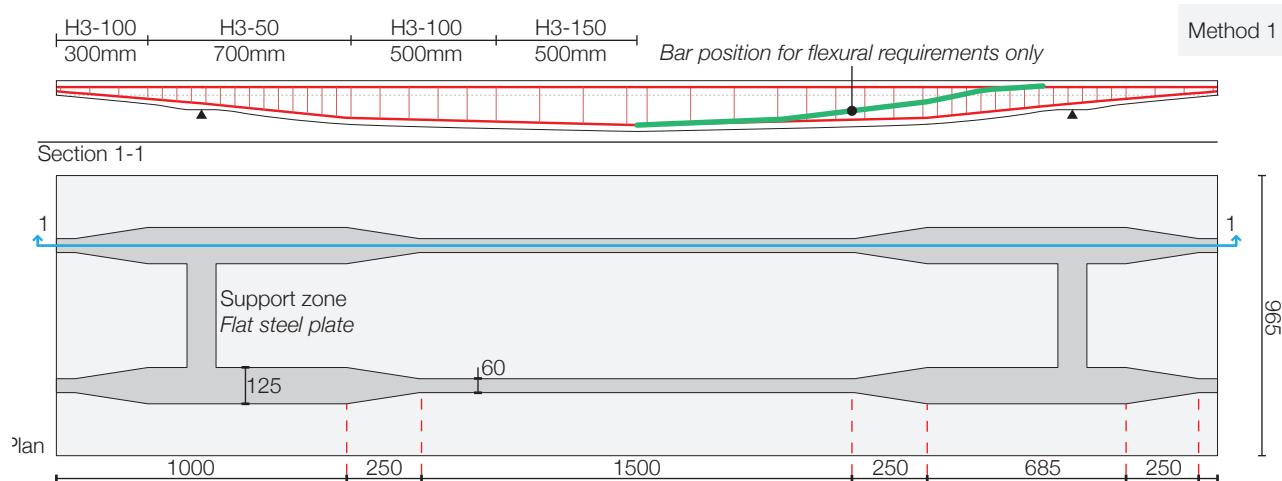


Figure 5.37: Double T Design, method 1.

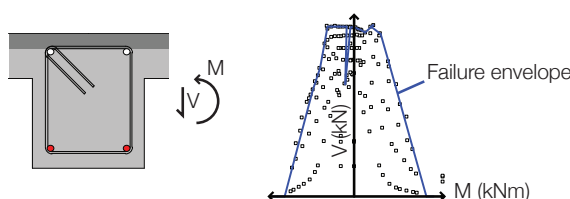


Figure 5.38: Moment-Shear interaction diagram as used in design method 1.

#### 5.6.4.3.2. Method 2

Method 2 considers separately the vertical and horizontal force components in the longitudinal reinforcement, allowing them to provide a reduction in shear at the supports, as illustrated in Figure 5.39. As a 40mm section depth at the support zone is not feasible for construction, the ideal case in which a 'zero shear' beam is produced will not be considered. Instead, a reduced shear force,  $V'$ , is calculated by Eq. 5.16. The results of this approach are summarised in Table 5.10 for the revised double T beam design. The resulting section has a constant web width of 60mm, providing significant reductions in material use over Design Method 1.

Two beams to this design are tested in Chapter 6 (Beam 6\_4\_1 and Beam 6\_4\_2). Transverse reinforcement in Beam 6\_4\_1 was calculated assuming a truss angle in the BS EN 1992-1-1 (2004) shear model of  $45^\circ$  and ensuring that the link spacing was never greater than the effective depth of the beam. The method was thus purposefully conservative at the support zone.

The exact transverse reinforcement required to carry the shear force was initially calculated for Beam 6\_4\_2, with these values then modified to facilitate easy construction and to ensure that the spacing of the links was not

greater than the effective depth of the beam. Beams 6\_4\_1 (Figure 5.40) and 6\_4\_2 (Figure 5.41) are therefore broadly similar in design approach.

$$V' = V - F_{s,v}$$

Eq. 5.16

Where  $V'$  is the reduced shear force,  $V$  is the design value of the shear force and  $F_{s,v}$  is the vertical component of force in the bar at the point under consideration

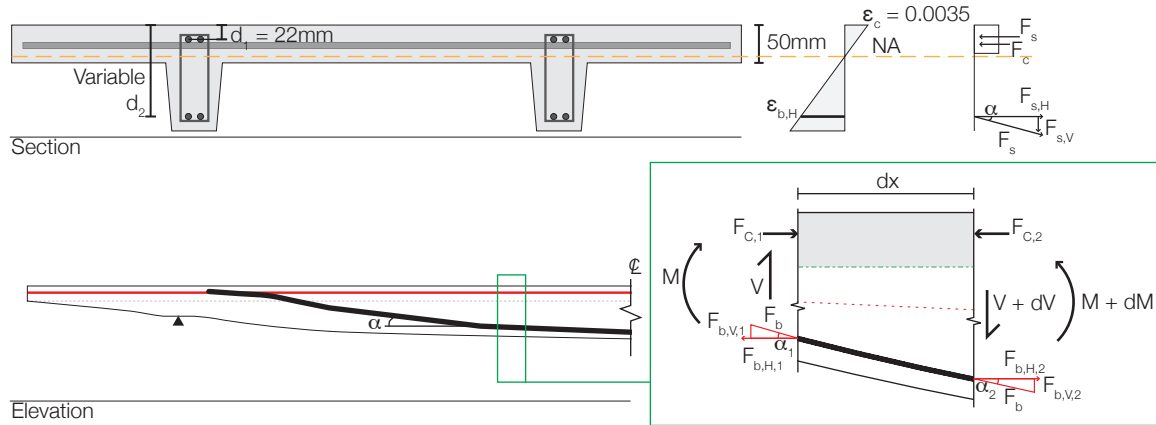


Figure 5.39: Shear reduction due to the inclined bar.

Table 5.10: Shear design for Method 2.

x (mm)	Design Envelope V, (kN)	Bar Depth	Gradient of Bar (rads)	Horizontal bar force $F_{s,2}$ (kN)	$F_{s,2,v}$ (kN)	V' (kN)	% Reduction
	(1)				(2)	(3) = (1) - (2)	= (3) / (1)
0.0	-4.0	36.3	0.083	-4.0	-0.3	-3.7	8%
500.0	-4.0	78.0	0.083	-4.9	-0.4	-3.6	10%
1000.0	20.2	128.0	0.100	100.5	10.0	10.2	49%
1500.0	12.1	140.5	0.025	100.5	2.5	9.6	21%
2000.0	4.0	153.0	0.025	100.5	2.5	1.5	62%

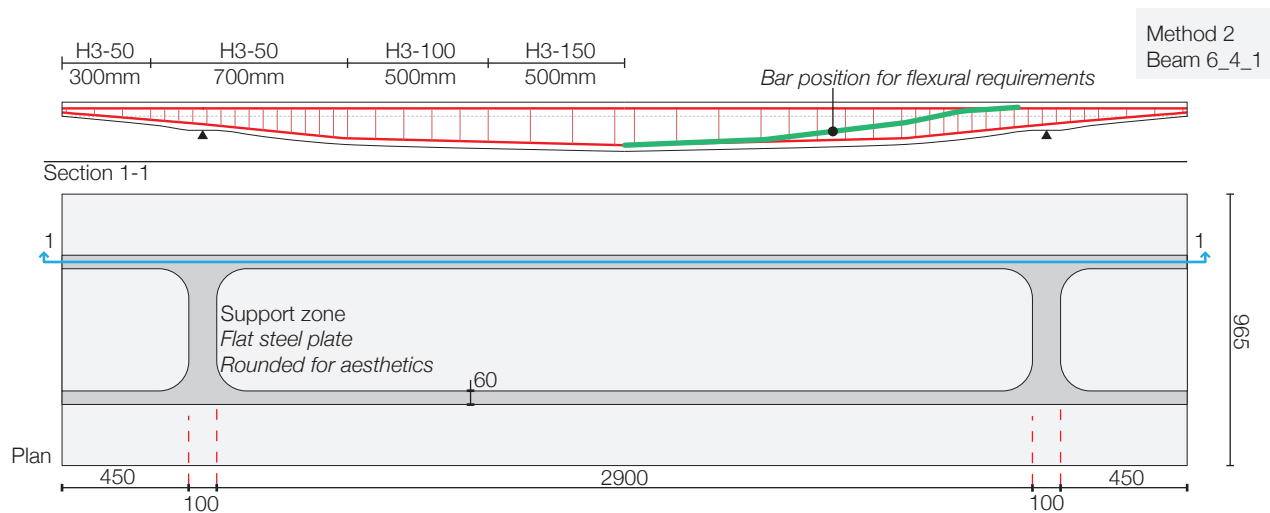


Figure 5.40: Double T Beam (6\_4\_1).

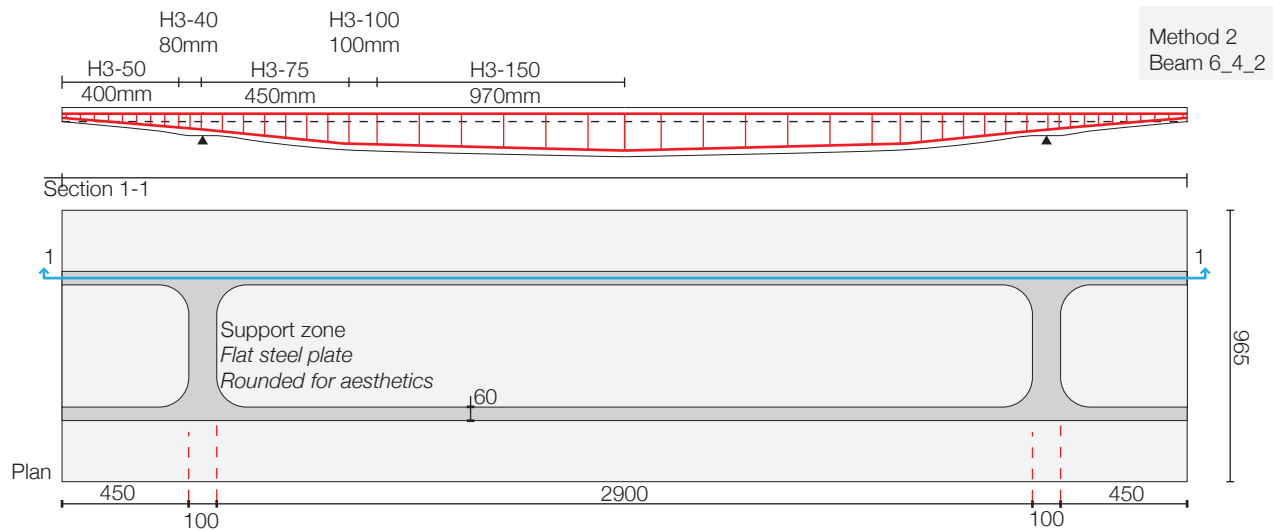


Figure 5.41: Double T Beam (6\_4\_2).

Whilst the Double T beam designed to Method 2 has a reduced web width at the support zone, there is considerable difficulty in providing transverse reinforcement to the beam as each link is replicated only four times. The use of flexible fibre reinforced polymers as reinforcement in such an element is considered in more detail in §8.6 on page 330, where it is shown that such an approach may also be used to provide transverse force capacity in variable section beams.

#### 5.6.4.4. Material savings

Material savings for construction methods 1 and 2 are predicted by comparing them to an equivalent strength prismatic section with the cross sectional dimensions shown in Figure 5.42 (denoted Beam 6\_C). The savings between these elements are summarised in Table 5.11. Note that the top slab ( $0.193\text{m}^3$ ) makes up a large percentage of the total concrete used, and thus the material comparisons are calculated both with and without the slab element. Without the slab, the considerable savings achieved in the optimised beams are apparent.

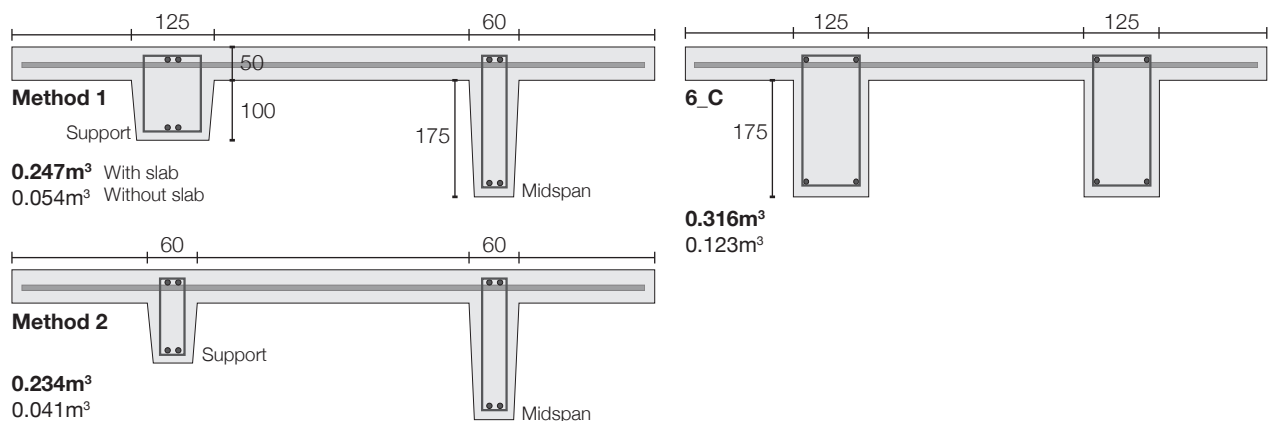


Figure 5.42: Prismatic section for material use comparison.

Table 5.11: Material use saving summary for the Double T Beams 6\_4\_1 and 6\_4\_2 (with slab (l); without slab (r)).

	6_C	Method 1	Method 2
6_C	-	22%	26%
Method 1	22%	-	5%
Method 2	26%	5%	-

	6_C	Method 1	Method 2
6_C	-	56%	67%
Method 1	56%	-	33%
Method 2	67%	25%	-

#### 5.6.4.5. Detailing

In addition to the steel designed above, transverse reinforcement is required in the top slab to carry load between the webs and to provide bending resistance. In both Beam 6\_4\_1 and Beam 6\_4\_2, this will be provided by 8mm diameter high yield bars at 200mm centres. The final reinforcement layout for the beams (excluding the transverse reinforcement) is summarised in Figure 5.43, and beam elevation dimensions are provided in Figure 5.44.

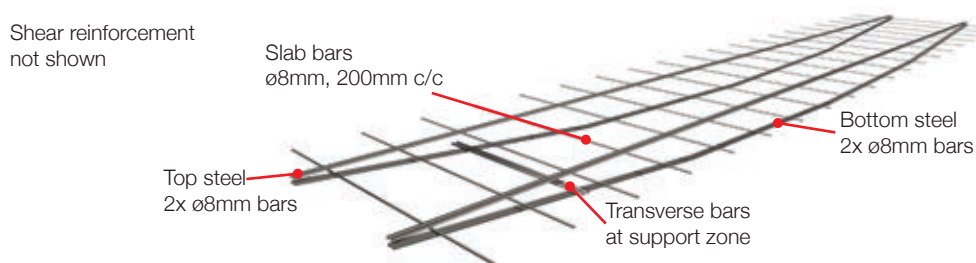


Figure 5.43: Reinforcement summary, Beams 6\_4\_1 and 6\_4\_2.

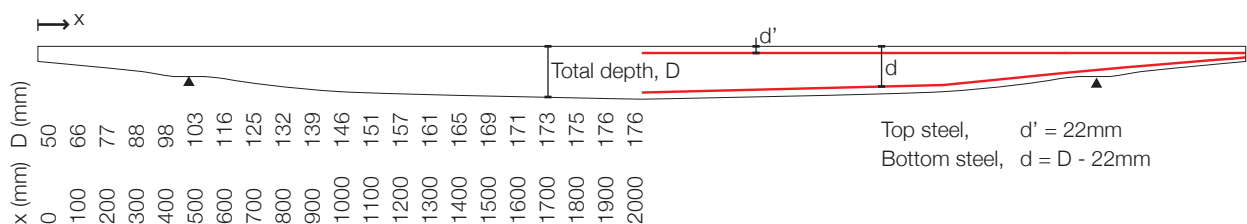


Figure 5.44: Beam dimensions in elevation.

#### 5.6.4.6. Construction method

The construction of Beam 6\_2\_1 was problematic (see §6.7.2 on page 207) and in the large scale tests an altered construction rig was produced, as illustrated in Figure 5.45. Here, the central 'table' is divided into two sections and may therefore move slightly during demoulding, preventing the formwork from becoming trapped in the fabric. Further construction information and photographs are provided in §6.6.3 on page 198.

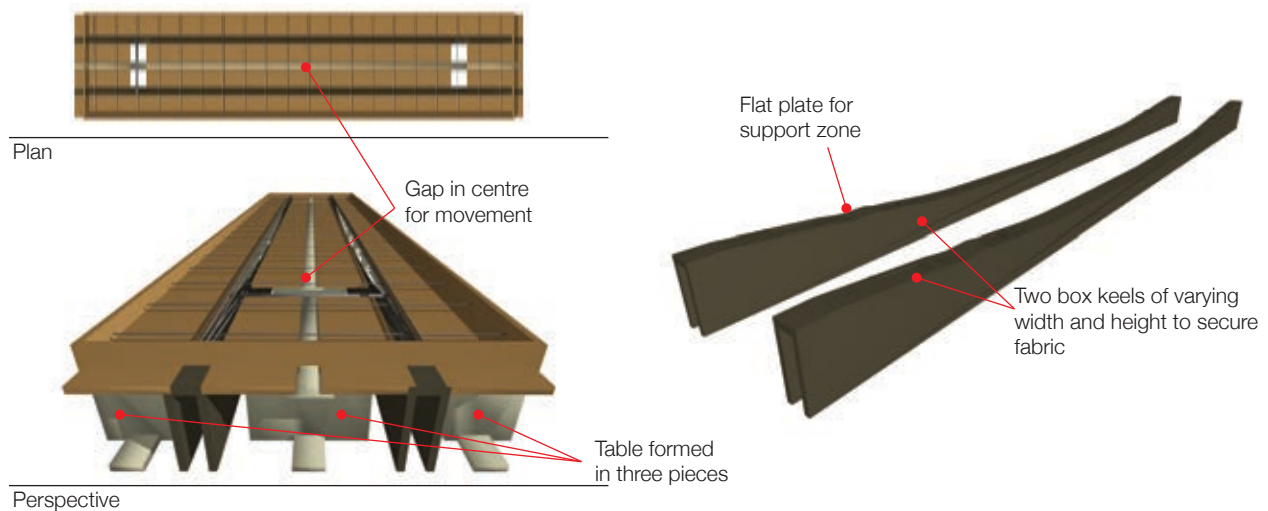


Figure 5.45: Construction details.

#### 5.6.5. Conclusion

Construction, testing and analysis of Beam 6\_2\_1, 6\_4\_1 and 6\_4\_2 are presented in Chapter 6 and Chapter 10. The design as described above provides significant material savings, a simple construction method and presents new opportunities for fabric formwork to facilitate a sustainable, low-carbon future in concrete construction.

In the following section, details of an alternative approach in terms of concrete technology and optimisation is described. The use of ultra-high performance concrete has been explored in this thesis because its requirement to be placed only where it is needed is well matched to the abilities and philosophy of flexible formwork systems.

## 5.7. Detailed design 3 - Ultra-high Performance Fibre Reinforced Concrete

### 5.7.1. Introduction

Ultra high performance fibre reinforced concrete (UHPFRC) offers two benefits for fabric formed construction. Its high strength should be utilised effectively, and fabric formwork allows the designer to put material only where it is needed. In addition, the presence of steel fibres is suggested to increase the shear capacity of the concrete section, which could allow the construction of variable section beams without complex and expensive steel shear reinforcement layouts.

These two issues are developed in this section through a collaboration with Lafarge. Instigated by the work undertaken in this dissertation, the University of Bath became the first centre in the UK to cast the UHPFRC produced by Lafarge known as Ductal® (as detailed in §3.2.2 on page 53). A sequence of work considering the structural behaviour and optimisation of UHPFRC Fabric Formed beams was developed in the following sequence:

1. Initial tests to determine behaviour of Ductal® cast in fabric formwork (§5.7.3), Beam 7\_1, 7\_2 and 7\_3;
2. 2m span 'Double T' beams cast with steel reinforcement (§5.7.4), Beam 7\_4 and 7\_5.

Following the successful casting and testing of these first fabric cast UHPFRC beams, the construction and testing of larger scale elements, undertaken in collaboration with Lafarge and the formwork manufacturer Cordek, is currently seeking funding.

### 5.7.2. Design models

#### 5.7.2.1. Flexural design

Two models for the flexural design of the initial UHPFRC beams described above were used. Model 1 does not consider the additional tensile strength of the concrete (Figure 5.46) and was used in the design of Beams 7\_1, 7\_2 and 7\_3. The second, more detailed model (Figure 5.47) was based on work proposed by Lafarge (§3.2.2.1 on page 54) and considers the full moment-curvature response of the fibre reinforced beam. This approach was used in the design of Beams 7\_4 and 7\_5.

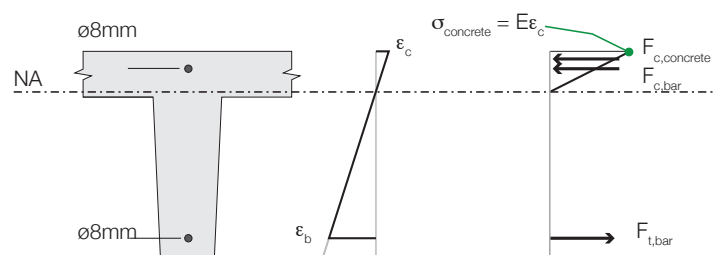


Figure 5.46: Flexural design Model 1 for UHPFRC Beams 7\_1, 7\_2 and 7\_3.

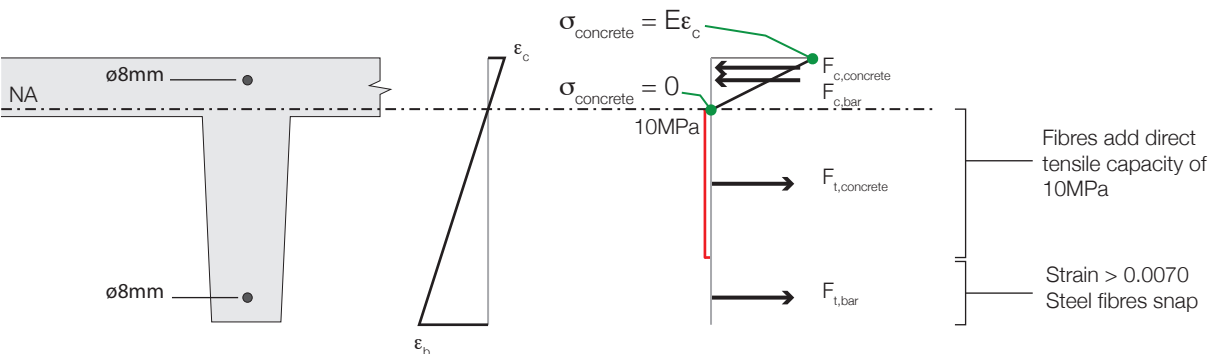


Figure 5.47: Flexural design model 2 for UHPFRC beams.

Flexural Design Model 2 allows the concrete to carry a direct tension of 10MPa up to a tensile strain of 0.0070 after which the steel fibres within the mix will fail in tension. By considering the moment curvature response of the Beam illustrated in Figure 5.48(l), it is clear that the maximum flexural capacity is obtained in this particular case when the tensile strain at the steel bar is just equal to 0.0070. This 'optimum position' may be found for any section geometry by moment-curvature analysis.

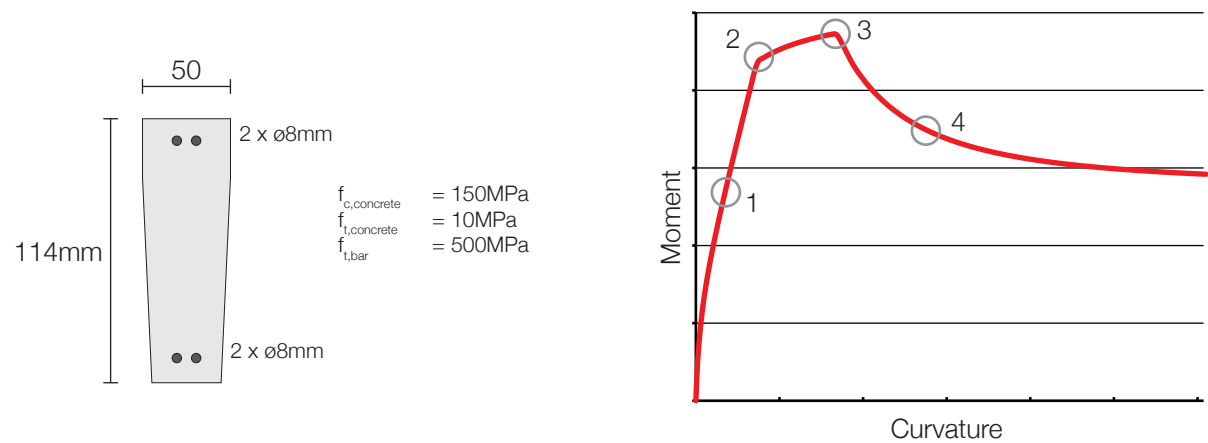


Figure 5.48: Sample cross section (l); Moment-Curvature analysis (r).

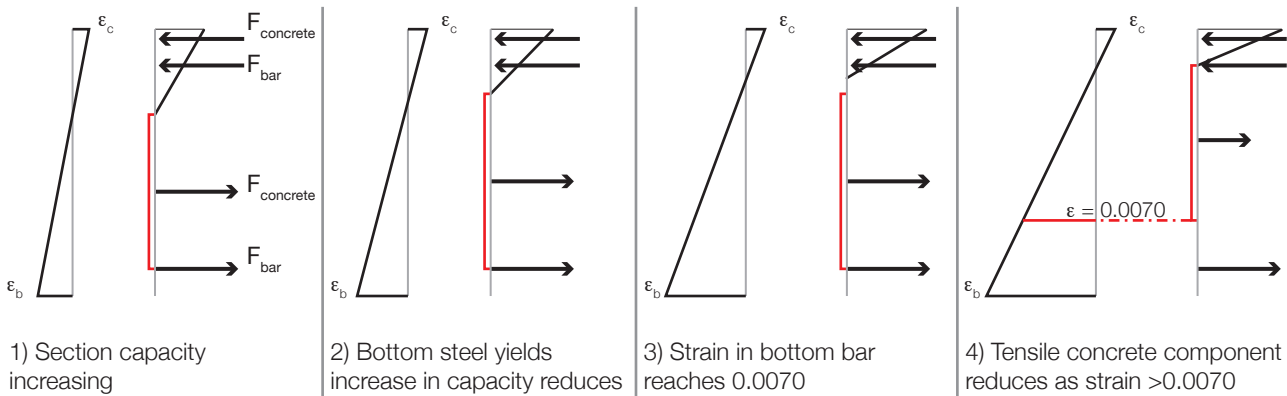


Figure 5.49: Sectional diagrams at salient points shown in Figure 5.48.

Table 5.12: Ductal® material properties.

Compressive strength (MPa)	Flexural strength (MPa)	Tensile strength (MPa)
120	40	10



### 5.7.2.2. Shear design

The additional concrete tensile capacity provided by using Ductal® has a relatively small impact on the section's flexural capacity, but is rather more important for shear design. The provision of transverse reinforcement to a continually varying depth beam is difficult and expensive, making it advantageous to provide all the tensile reinforcement through the concrete alone. The shear capacity of the beams described below has therefore been determined using the model proposed by the AFGC (2002) that is described in detail in §3.2.2.1.3 on page 58.

### 5.7.3. Initial designs - Beams 7\_1, 7\_2 and 7\_3

Recognising the potential economic benefits of casting complex shapes in fabric moulds, a series of tests were undertaken to determine the behaviour of fabric cast Ductal® T Beams. Modelling an 8m span element, 1/4 scale beams (2m span) were created in a fabric mould. Beams 7\_1 and 7\_2 were not reinforced with steel bars, but were cast to test the construction process. Beam 7\_3 was given designed steel reinforcement, as described below. All beams had the same external dimensions (taken from the design for Beam 7\_3).

With assistance from a Lafarge technical team, a special mix for this purpose was developed, the material properties of which are given in Table 5.12. The composition of the mix is detailed further in Table 6.23 on page 206.

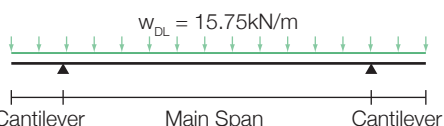
#### 5.7.3.1. Loading

The 'T' beam is envisaged to act as permanent formwork to an overtopping reinforced concrete flat slab, and its loading envelope is determined to reflect this. The loading envelope for the beam is defined in two cases, summarised below:

1. Beam self weight plus wet reinforced concrete flat slab during construction;
2. Full service loads, where composite action with topping slab is now achieved.

Prototype loads are scaled as shown in Figure 5.51, with load cases and a resulting bending moment envelope for design of the model element given in Figure 5.50 and Figure 5.53. The model is uniformly scaled and an increase in dead load is thus required to account for the cubic loss in volume of the concrete slab. This is calculated below as an equivalent line load.

Load Case 1  
Slab dead weight



Load Case 2  
Maximum Sagging

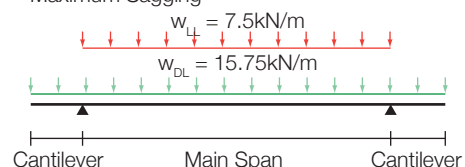
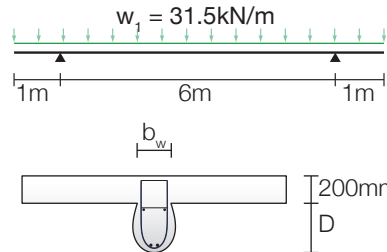


Figure 5.50: Load cases for design (summary).

**Load Case 1**  
**Beam self weight + wet reinforced concrete slab**

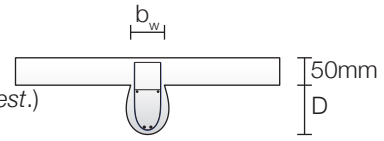
**Prototype Loading**

200mm RC Slab,  
6m Span = 28.8kN/m  
Beam Self Weight = 2.7kN/m (est.)  
 $g_k$  = 31.5kN/m



**25% Scale Dimensions**

50mm RC Slab,  
1.5m Span = 1.8kN/m  
Beam Self Weight = 0.2kN/m (est.)  
= 2.0kN/m



Required Scale Load =  $w_1 / 4 = 7.9\text{kN/m}$   
Additional load required = 5.9kN/m

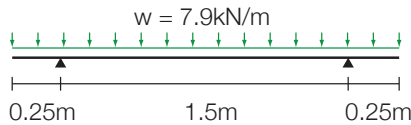


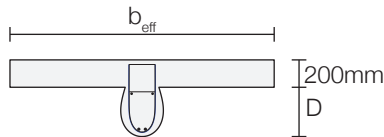
Figure 5.51: Scaling loads - Load case 1.

**Load Case 2**  
**Full dead and live load**

**Prototype Loading**

200mm RC Slab, 6m Span = 28.8kN/m  
Beam Self Weight = 2.7kN/m (est.)  
 $g_{k,1}$  = 31.5kN/m  
 $q_k$  (2.5kN/m<sup>2</sup>, 6m span) = 15kN/m

$g_k + q_k$  = 46.5kN/m



**25% Scale Dimensions**

50mm RC Slab, 1.5m Span = 1.8kN/m  
Beam Self Weight = 0.2kN/m  
 $g_{k,2}$  = 2.0kN/m  
 $g_{k,required}$  =  $g_{k,1} / 4 = 7.9\text{kN/m}$   
 $q_{k,2}$  (2.5kN/m<sup>2</sup>, 1.5m span) = 3.75kN/m

$g_{k,2} + q_{k,2}$  = 11.6kN/m  
=  $(g_{k,1} + q_{k,1})/4$

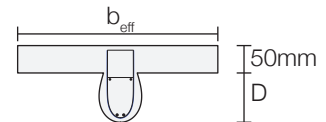
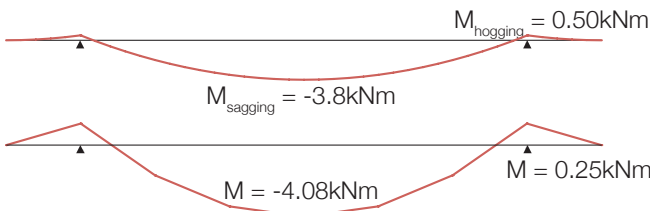


Figure 5.52: Scaling loads - Load case 2.



Load Case 1  
Self Weight + Slab

Resisting  
section



Load Case 2  
Full dead and live load

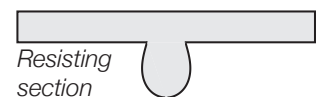


Figure 5.53: T-Beam loading moment envelope.

### 5.7.3.2. Test design loads

The moment envelope shown above will be approximated during testing using a seven point loading rig as shown in Figure 5.54 with loads applied as given in Table 5.13. Testing will be undertaken to Load Case 2 only, since this is the critical condition for the section that will be cast (top slab included).

Table 5.13: Test load summary (see also Chapter 6).

Load Case	$P1_{max}$	$P2_{max}$	P1:P2
2	0.98kN	5.77kN	1:5.88

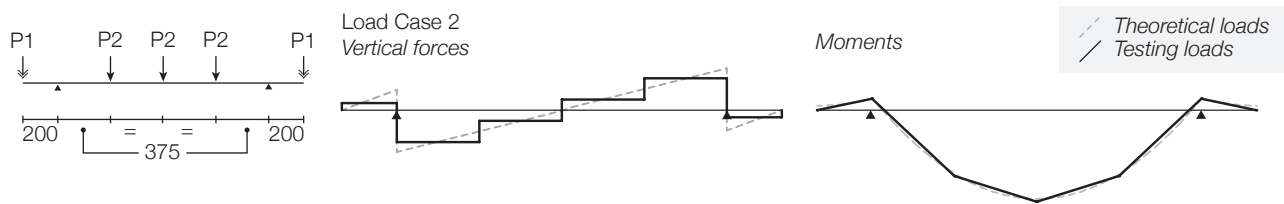


Figure 5.54: Test set up and test loads.

### 5.7.3.3. Flexural design

Beams 7\_1 and 7\_2 were constructed without internal steel reinforcement (§6.7.2 on page 207) but had the same external dimensions that were determined in the following for Beam 7\_3, which was designed using flexural design model 1 (Figure 5.46 on page 145). Beam 7\_3 was reinforced with two H8 bottom bars and one H8 top bar. Material properties are given in Table 5.14 and section depths at 100mm intervals along the beam are provided in Figure 5.55. A maximum section depth of just 101mm is required at the midspan, and 68mm at the supports (including the 50mm deep top slab).

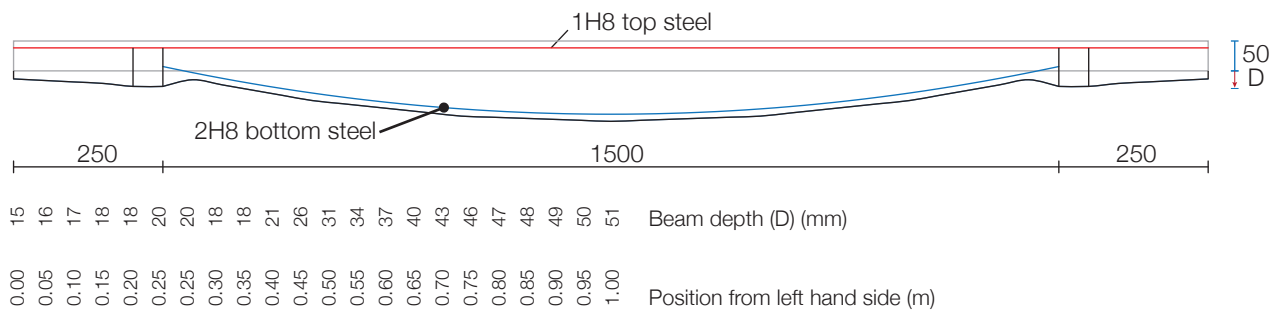


Figure 5.55: UHPC Beam elevation and dimensions.

Table 5.14: Material Properties.

Variable	Value	Variable	Value	Variable	Value
Top steel	2H8	Cover to steel	5mm	Concrete strength, $f_{cu}$	120N/mm <sup>2</sup>
Bottom steel	1H8	Steel yield strength, $f_y$	500N/mm <sup>2</sup>	Top breadth	62.5mm

### 5.7.3.4. Shear design

Shear forces in Beam 7\_3 are resisted by a combination of the inclined steel and the tensile strength of the fibre reinforced concrete. The calculations required to determine this capacity were undertaken as described for Beam 7\_4 in §5.7.4.3 on page 151. In this way, no transverse reinforcement was required along the length of the 'T' beams, considerably simplifying the construction process.

### 5.7.3.5. Beam layout and construction

The final UHPFRC model profile, as determined from the above calculations is given in Figure 5.55. The 'ribbed' slab construction method is illustrated in Figure 5.57, with cross sections shown at relevant positions. The beam design is similar to those shown in §5.5, yet is both shallower and has a less substantial slab system, allowing greater material savings to be achieved.

In the cantilever span, a minimum depth of 15mm was chosen at the end (8mm diameter reinforcement with 3.5mm cover) and this limit was extended along the beam, again illustrating the difficulty of modelling concrete structures. The support detail as shown in §5.5.5.1 on page 133 is also used in these beams.

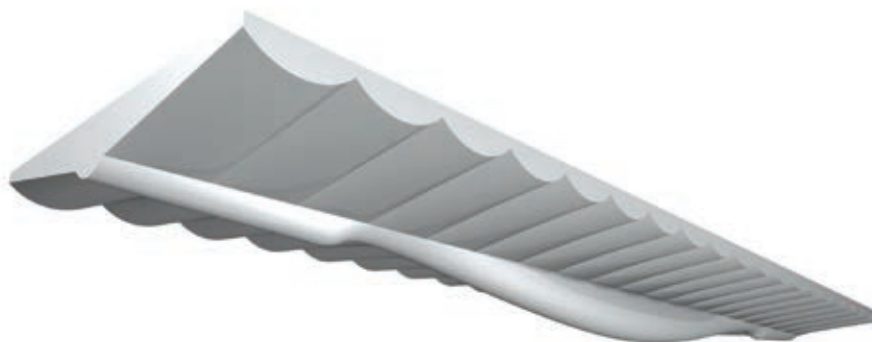


Figure 5.56: Proposed design rendering, Beam 7\_1, 7\_2 and 7\_3.

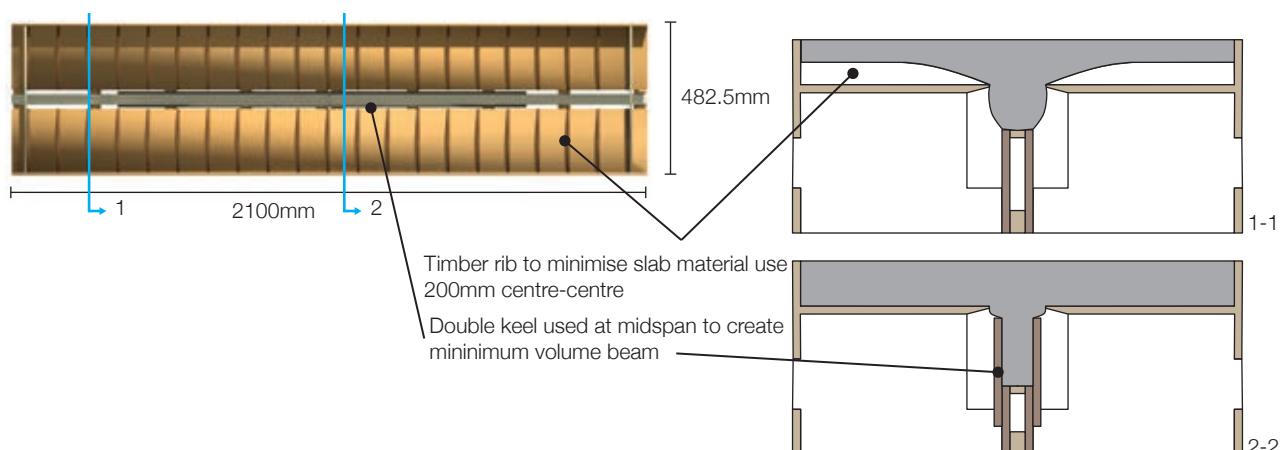


Figure 5.57: Beam sections showing rib and double keel construction.

#### 5.7.3.6. Summary

The construction and testing of the UHPFRC beams described above is provided in §6.7 on page 206. The successful outcome of these tests informed the development of the UHPFRC double T beams described in the following section.

#### 5.7.4. Double 'T' beam design, Beam 7\_4 and 7\_5

The first double 'T' beam cast in fabric formwork using Ordinary Portland Cement Concrete (§5.6 on page 136) failed in shear at the support zone (§6.6 on page 195). One solution to such a failure is to add sufficient tensile strength in the concrete such that it can carry the shear in the support zone without the need for transverse reinforcement, which in a constantly varying cross section can be costly to create.

Beam 7\_4 and Beam 7\_5 were therefore constructed to demonstrate the use of UHPFRC in variable section beams to allow the traditional transverse steel bars to be omitted from the design. The design of Beam 7\_4 is described below, with construction and testing details provided separately in Chapter 6 (Beam 7\_5 is identical).

### 5.7.4.1. Loads

The two metre span double tee beam was designed to the loads shown in Figure 5.58, where five point bending in the central span region was applied to model a uniformly distributed load.

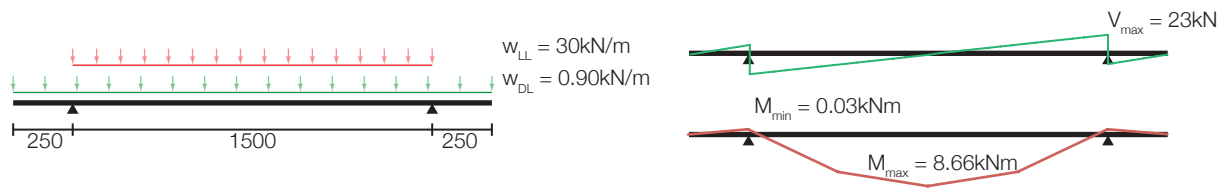


Figure 5.58: Load envelope, Beams 7\_4 and 7\_5.

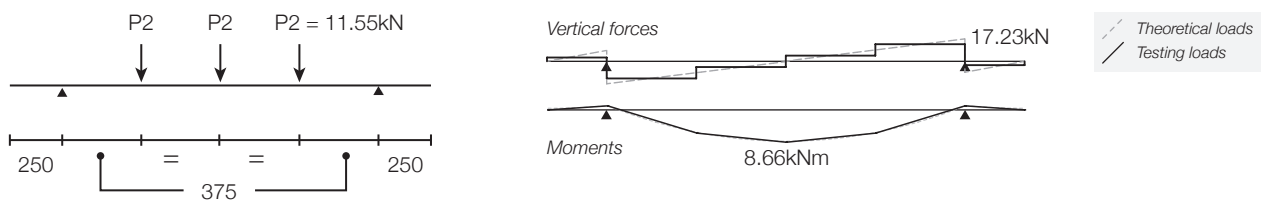


Figure 5.59: Test loads, Beams 7\_4 and 7\_5.

### 5.7.4.2. Flexural design

Beams 7\_4 and 7\_5 were designed using flexural design model 2 (Figure 5.47). A 'Double T' in cross section, two 8mm diameter bars were placed in each web to resist the design load envelope. The resulting design is provided in Figure 5.60, where salient dimensions are provided.

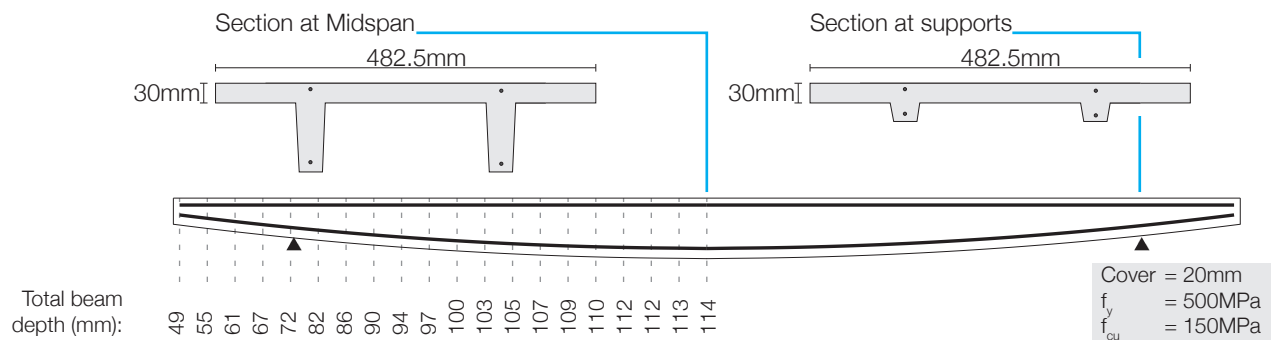


Figure 5.60: Beam 7\_4 elevation, determined for flexure.

In a similar manner to previous beams, the 'ideal' reinforcement profile has been smoothed for construction, to the continuous curve shown in Figure 5.60. The resulting steel profile is thus easier to construct and to install, and provides additional depth at the supports which, in structures using ordinary Portland cement concrete may be important and desirable for shear.

### 5.7.4.3. Shear design

The shear capacity of the 'Double T' beam was assessed using the AFGC (2002) design method described in §5.7.2.2 on page 147. The shear capacity of the section without transverse reinforcement is thus shown in Figure 5.61, where it is apparent that the dimensions required for flexural design are sufficient to provide the required shear capacity.

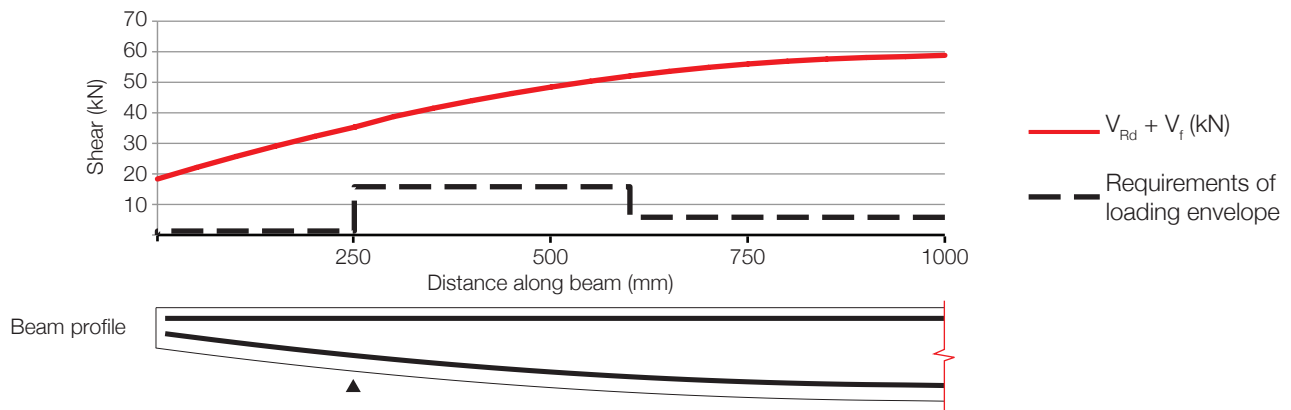


Figure 5.61: Shear capacity of UHPFRC beam.

#### 5.7.4.4. Construction

The formwork for Beam 7\_4 was modified from previous tests to allow re-use, as shown in Figure 5.62. The formwork follows all previous tests in using a simple 'keel' to provide a high construction tolerance with a simple construction process. Further construction and testing details are provided in §6.7.4 on page 211.

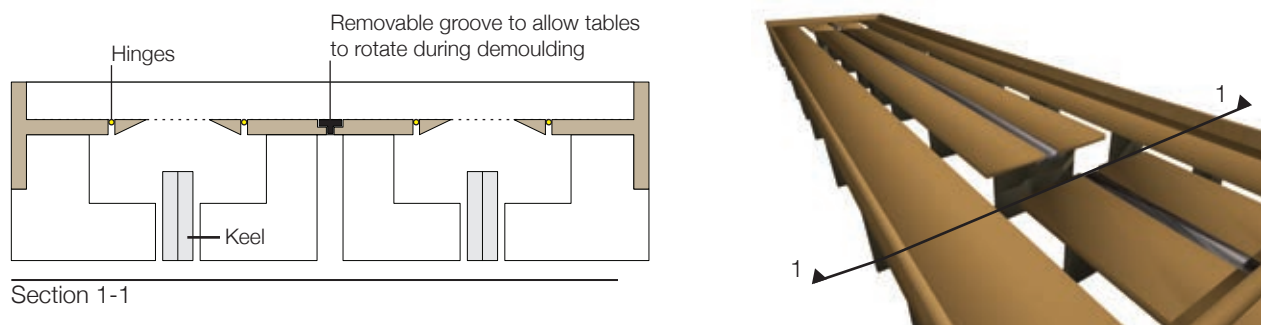


Figure 5.62: Double T table formwork.

#### 5.7.5. Conclusions

The use of ultra-high performance fibre reinforced concrete in conjunction with fabric formwork offers opportunities to create low material use, optimised structures. Test results, presented in Chapter 6, have verified the design methods used in this section although further work is required to properly assess the shear capacity of steel-fibre reinforced concrete structures. Following from the test data presented in Chapter 6, analysis of UHPFRC beams cast in fabric is presented separately in Chapter 10.

The preceding sections have concentrated on flexurally dominated elements, and test results presented in Chapter 6 have shown that the current design methods for such elements are satisfactory. In Chapter 7, the final aspect of the test matrix shown in §5.4 on page 122 is considered; namely the behaviour of tapered beams in shear critical loading.

## 5.8. Construction methods

Construction methods for the elements designed in this Chapter to be cast in fabric formwork were trialled in a series of small beam tests. These preliminary investigations, which considered both keel and double keel moulds, influenced the formwork designs for full scale elements, as described above and in Chapter 6.

### 5.8.1. Keel Mould

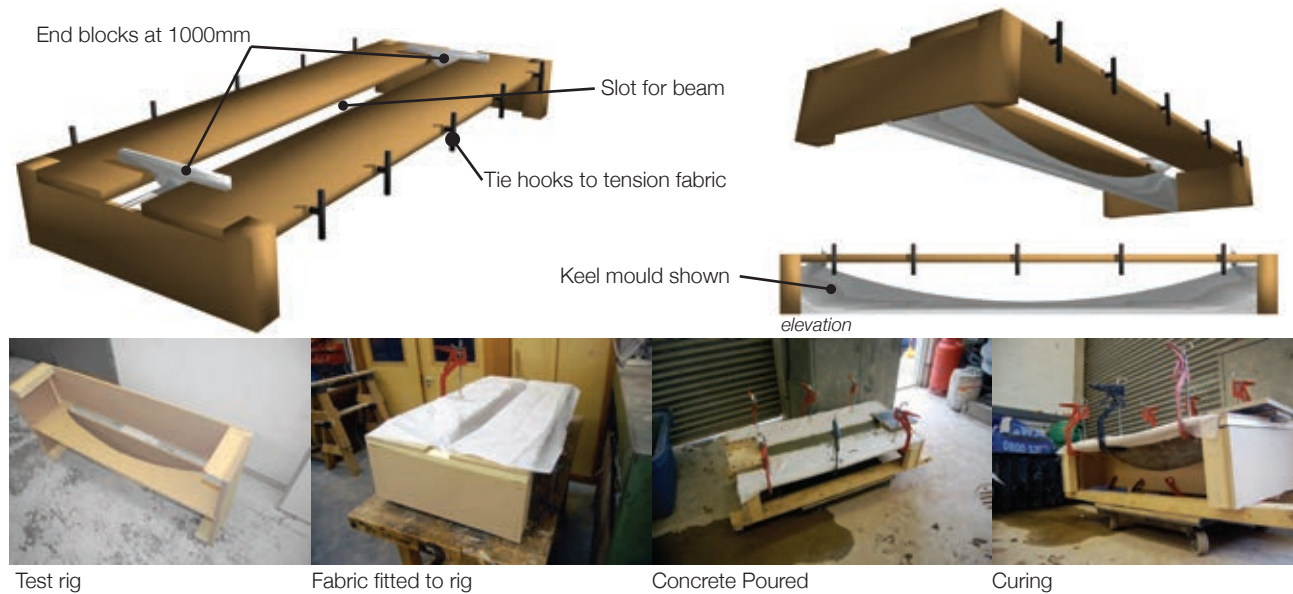


Figure 5.63: Keel mould construction and prototype elements.

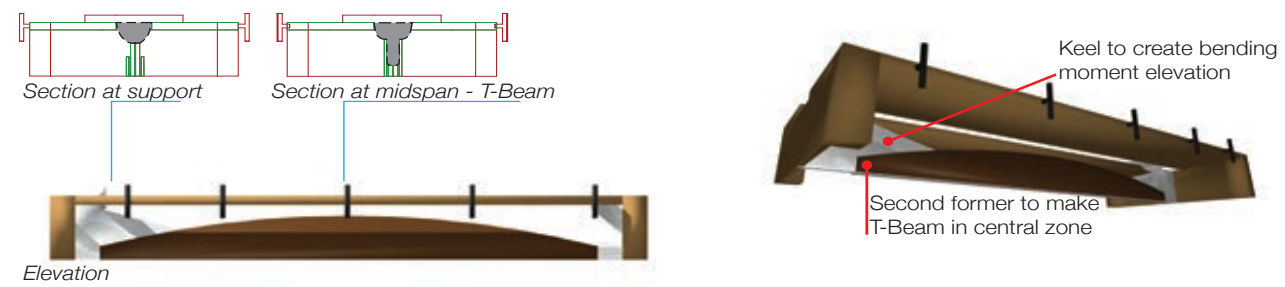


Figure 5.64: Double bending moment shaped beam.

The keel method provides the simplest construction method for fabric formed beams, and will be used in future work. The advantage of this method is that a range of keel designs can be produced, each optimised for a separate load envelope, allowing multiple beam designs to be made on the same forming table.

The double keel method was developed in February 2010 at the University of Bath in order to create bending moment shaped 'T-Beams'. Using the same 1m span as shown in the above, the double keel (as illustrated in Figure 5.65) allows T-Beams to be created with simple additions to the keel mould. The resulting beam, which is shown in Figure 5.66, provides excellent material savings, as the bending moment shape is further optimised by removing concrete in the tension zone. The double keel is essentially a variant of the 'pinch' method, described in Chapter 2.





Elevation  
Figure 5.65: Double keel method.



Figure 5.66: Double keel 'T Beam'.

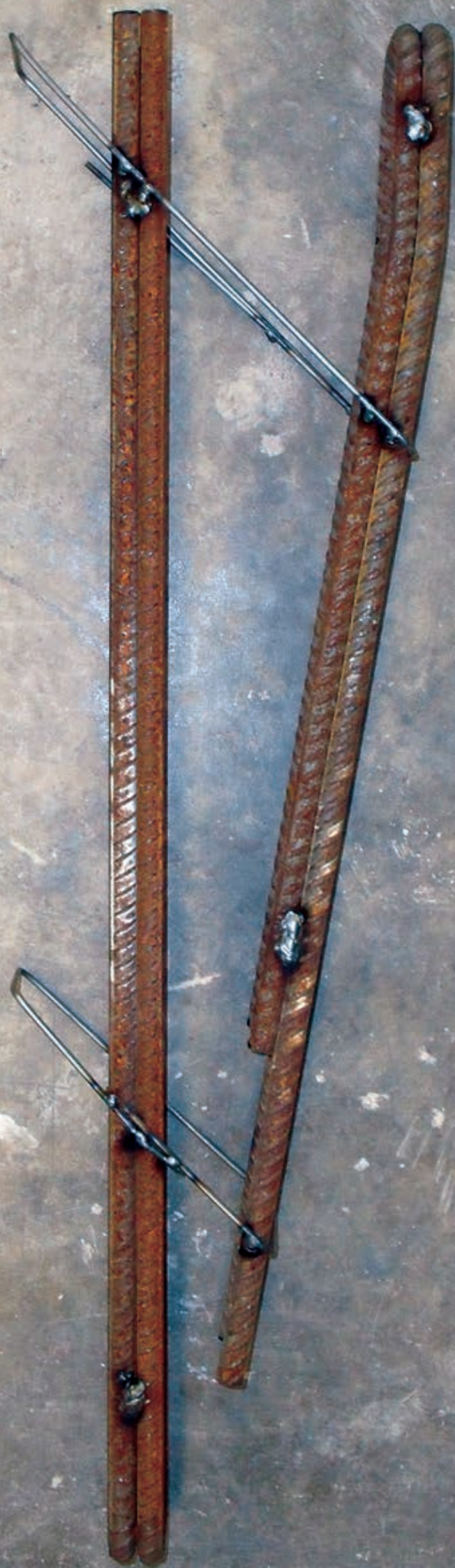
## 5.9. Conclusions

To answer the range of issues described in the goals set out in §5.4 on page 122 a comprehensive series of structural tests was required. The methodology and rationale behind those which address flexural behaviour has been presented in this Chapter. Each test area has built on one particular aspect of testing or new knowledge that became available during the testing program.

Test data, results and analysis for the beam designs presented in this Chapter are provided in full in Chapter 6. In Chapter 7 shear behaviour in non-prismatic beams is considered in detail, with the resulting structural testing and analysis being presented in Chapter 8.

[blank page]





# Chapter 6 Development (1)

## Flexural behaviour

### 6.1. Introduction

To develop the design and construction methods required to demonstrate fabric formed construction as a sustainable construction method, a series of experimental testing programmes have been identified in previous Chapters to meet the testing matrix described in §5.4 on page 122. An initial program of investigative work on construction methods was carried out before the ten periods of structural testing described in this Chapter were undertaken. The test series are presented in Chapter 6 and Chapter 8, as summarised in Table 6.2 and Figure 6.1.

Table 6.1: Preliminary work.

Series	Details	Number	Testing dates
A	Construction methods	Multiple	February 2010

Table 6.2: Testing series outline.

Series	Details	Number of tests	Reference
1	Pull out tests on tapered concrete section	4	§6.2
2	Pull out tests on rectangular and tapered concrete section	6	§6.3
3	Pull out test using redeveloped splayed bar design and 2m span beam tests	3	§6.3
4	Fabric beam tests at CAST	8	§6.4
5	4m span fabric formed T beams	4	§6.5
6	2m and 4m span double T beams	4	§6.6
7	2m span UHPFRC beams	5	§6.7
8	3m span variable section beams	6	§8.2 on page 246
9	2m span tapered beams in shear	21	§8.3 on page 260
10	3m span beams using CFRP shear reinforcement	3	§8.6 on page 330



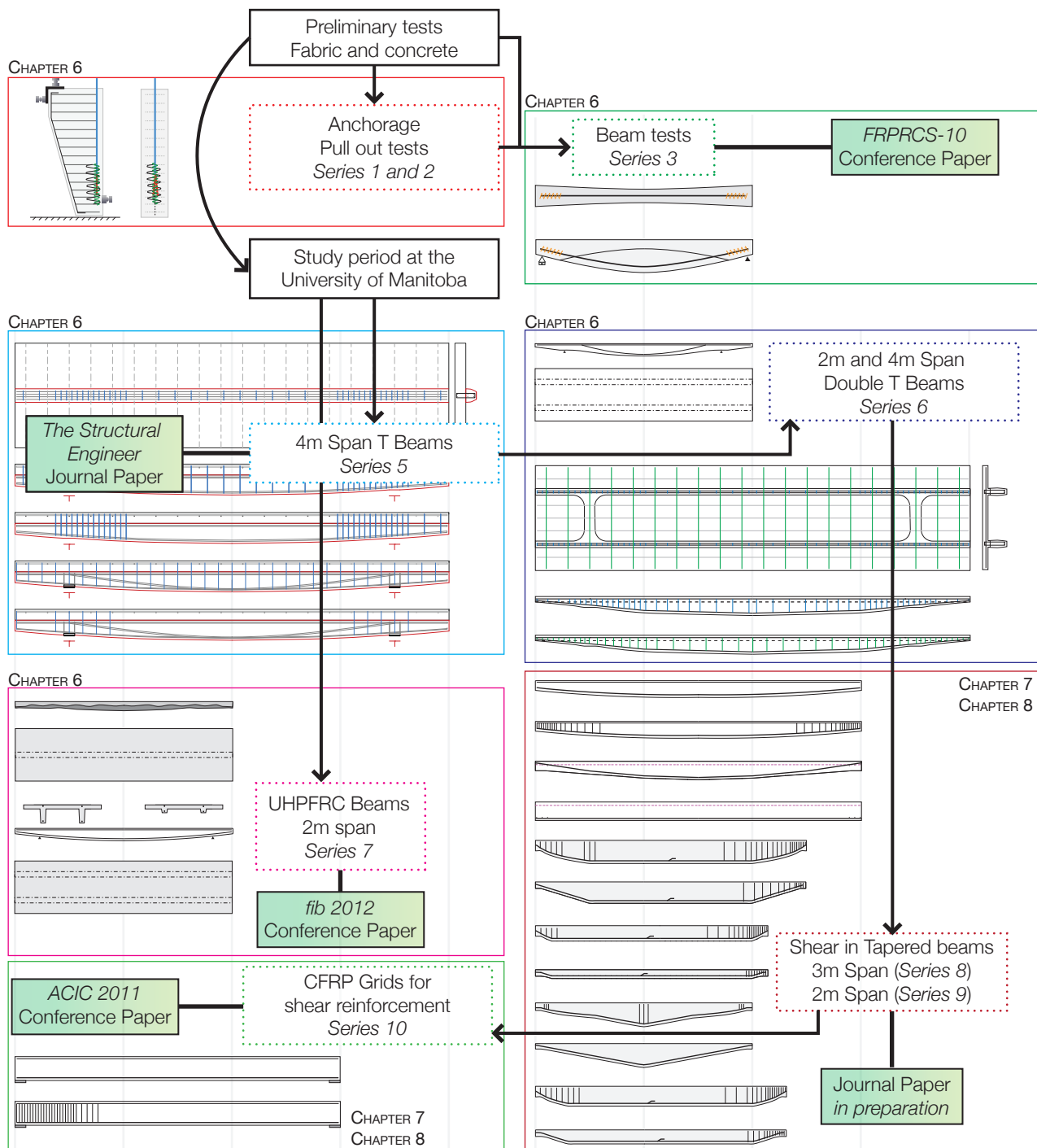


Figure 6.1: Summary of all structural testing undertaken and published results.

## 6.2. Pull out tests

Fibre reinforced polymer (FRP) reinforcement offers potential advantages for variable section fabric formed beams, as it is lightweight and can be shaped easily (see §8.6 on page 330). Where additional carbon reductions are sought through the use of low carbon cements (such as supersulfated cements), their increased susceptibility to carbonation requires protective measures to be taken for steel reinforcement - making FRP alternatives which are unaffected by changes in pH more desirable (Ioannou *et al.*, 2011).

In addition, it has been seen (Chapter 2) that the anchorage of reinforcing bars in simply supported beams with shallow end zones poses a significant challenge. Previous work (§2.5 on page 27) has considered the use of external welded plate connections (Hashemian, 2012) and orthogonal welded bars (Lee, 2010). In general, however, welding is best avoided in steel reinforcement (as discussed in §3.4.2 on page 69), and external plates can be undesirable from an aesthetic point of view.

In light of this, and to satisfy the testing matrix (§5.4 on page 122), a new method to provide anchorage for FRP bars has been developed using splayed bars (Darby *et al.*, 2007) as explained in §3.4.3.8.1 on page 76. Simple pull out tests have shown that the method is effective (Figure 3.26 on page 78) but it has not been analysed fully in beam tests. A program of tests using both varying and constant depth concrete sections was devised and run to investigate the behaviour of splayed FRP bars in beam sections and to ascertain any additional capacity gained by the addition of helical reinforcement. This section describes the program methodology and provides detailed experimental results which are analysed before conclusions are drawn.

### 6.2.1. Test series

Three experimental series were run and a total of eleven beam sections were tested. Series 1 investigated solely varying section depth members, and four tests were carried out. Series 2 investigated both constant depth and varying depth sections, and a total of six tests were undertaken. Series 3 used an improved splay design, and just one varying depth section was tested. Varying depth sections were used in an attempt to model the shape and behaviour of bending moment shaped beams, where shear issues have been seen to be important. All tests used the same concrete mix, FRP bars and helical reinforcement (when required), details of which are provided below.

#### 6.2.1.1. Construction details and material properties

The concrete mix used for all splayed bar pull out tests is detailed in Table 6.3. Average cube (100mm) compressive strengths for each test series are shown in Table 6.4. The flexural tensile strength of each mix was tested in three point bending in accordance with BS EN 12390-5 (2009) (using a 100x100x507mm prism), the results of which are shown in Table 6.5.

Table 6.3: Concrete mix properties.

Quantities	Cement (kg)	Water (kg)	Fine aggregate (0.5-5mm) (kg)	Soft sand	Coarse aggregate (10-12mm) (kg)
Per m <sup>3</sup>	450	190	633	72	1055

Table 6.4: Recorded concrete strength and standard deviation.

Series	7 Days (1 cube)		At testing (3 cubes)		14 Days (3 cubes)		28 Days (3 cubes)	
	f <sub>c</sub> (MPa)	SD	f <sub>c</sub> (MPa)	SD	f <sub>c</sub> (MPa)	SD	f <sub>c</sub> (MPa)	SD
1	40.6	-	41.6	1.2	46.0	2.00	49.2	2.50
2	43.9	-	47.1	2.54	50.6	3.24	54.7	2.42
3	46.4	-	48.9	0.52	52.2	3.18	55.9	2.31

Where f<sub>c</sub> = concrete compressive strength; SD = standard deviation on test results.

Table 6.5: Recorded concrete flexural tensile strength.

Series	Flexural Strength (MPa)	Series	Flexural Strength (MPa)	Series	Flexural Strength (MPa)
1	4.53	2	5.36	3	4.29

Table 6.6: FRP Material Properties.

Usage	Name	Tensile Strength (MPa)	Young's Modulus (GPa)
Helices	Kevlar 49 Parafil Rope	1926	126.5
Pull out bars	CARBOPREE 10mm	2300	130

Helices were used in a total of five tests and were constructed using Kevlar 49 Parafil rope (manufactured by Linear Composites Ltd). The rope was coated with 'Ciba 5052' epoxy resin before being wrapped around a polyethylene coated plastic tube as shown in Figure 6.2. The epoxy was mixed in a ratio ten parts araldite to four parts hardener. The CFRP bar upon which the pull-out tests were undertaken was a CARBOPREE bar with a nominal 10mm diameter. Manufacturer's data is provided in Table 6.6.

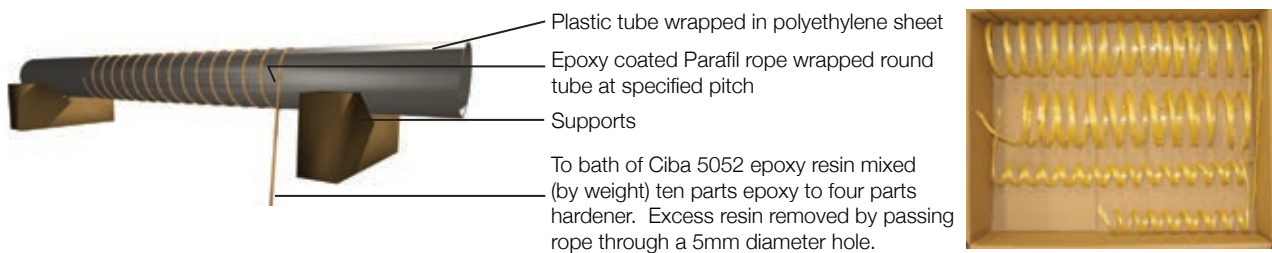


Figure 6.2: Helix construction (l); Examples of helix construction (r).



### 6.2.2. Series One

The experimental program for Series One consisted of four tests to investigate the effect of splay angle and helical confinement on the pull out resistance of  $\varnothing 10\text{mm}$  CARBOPREE Carbon FRP bars when cast in tapered concrete beams. The specimens were cast in standard  $110\text{mm} \times 220\text{mm}$  moulds, with blocking at one end to achieve the desired reduction in depth. Specimens were cast horizontally and tested vertically. The test layout is based on previous work at the University of Bath (Perera *et al.*, 2009) and is illustrated in Figure 6.3.

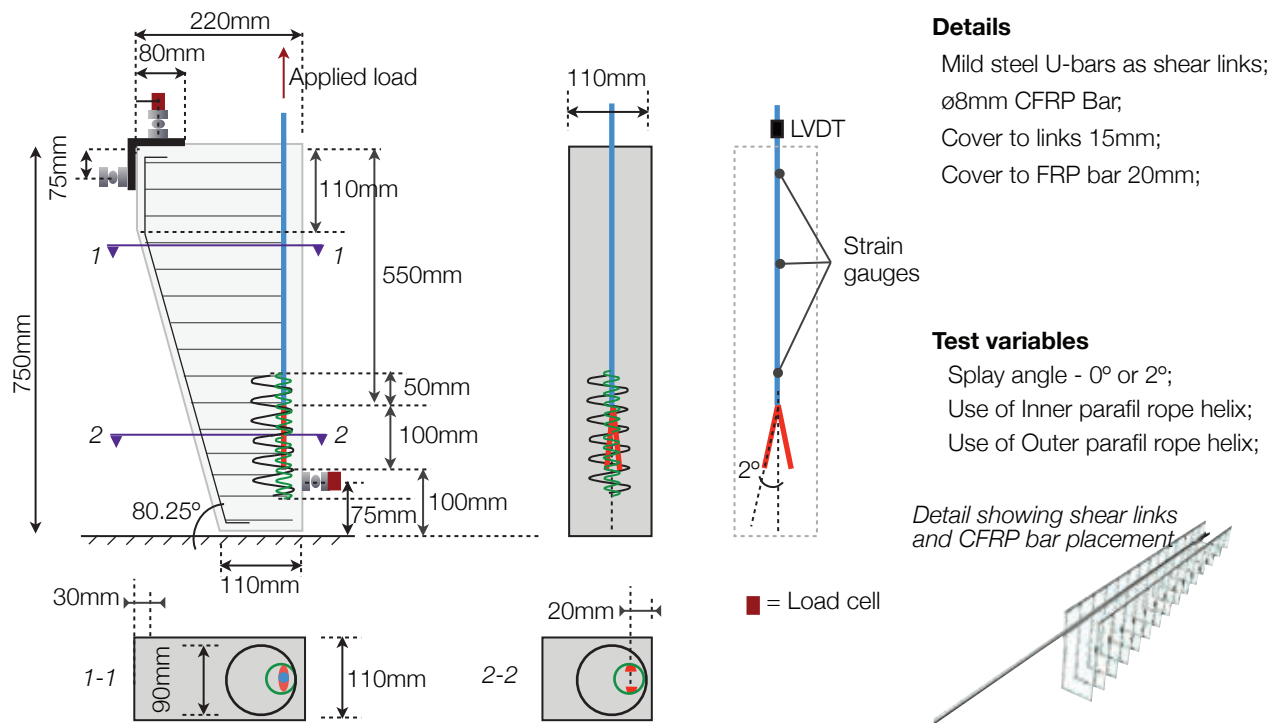


Figure 6.3: Test set up and variables.

#### 6.2.2.1. Test Details

Tests undertaken are detailed in Table 6.7 and are named according to the following convention:

*Program\_Test\_Splay Angle\_Outer helix diameter:Pitch\_Inner helix diameter:Pitch*

The specimens were held in a steel rig, shown in Figure 6.4, which provided three points of support to prevent the section from rotating. All specimens were tested using a 2MN capacity universal testing machine at a cross head displacement rate of  $0.5\text{mm/min}$ . The CFRP bars were gripped by placing two 2mm aluminium tabs between the bar and the machine jaw in an effort to prevent premature failure of the bar.

Table 6.7: Test details.

Test designation	Concrete Batch	CFRP Splay Angle	Outer Helix Diameter	Outer Helix Pitch	Inner Helix Diameter	Inner Helix Pitch
1_1_0_0:0_0:0	1	0	0	0	0	0
1_2_2_0:0_0:0	1	2	0	0	0	0
1_3_2_90:30_0:0	2	2	90	30	0	0
1_4_2_90:30_30:30	2	2	90	30	30	30

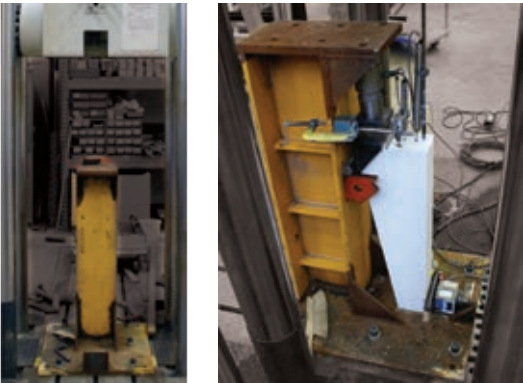
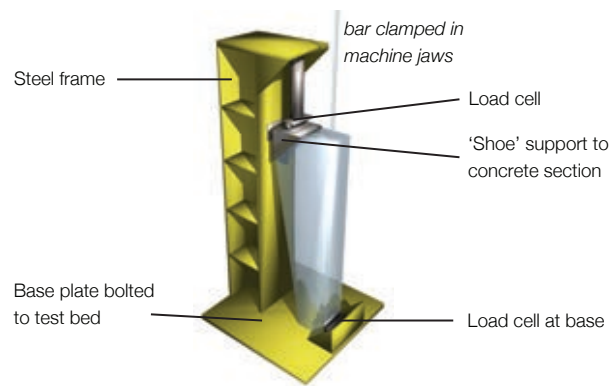


Figure 6.4: Test rig design (after Perera, 2009).

6.2.2.2. Construction

Construction of the test specimens is illustrated in Figure 6.5 for Test 1\_3\_2\_90:30\_0:0. The pitch and diameter of the single helix specimen (1\_3\_2\_90:30\_0:0) was large enough to allow for good concrete compaction, while the double helix specimen (1\_4\_2\_90:30\_30:30) was considerably more difficult and is not recommended for future tests.

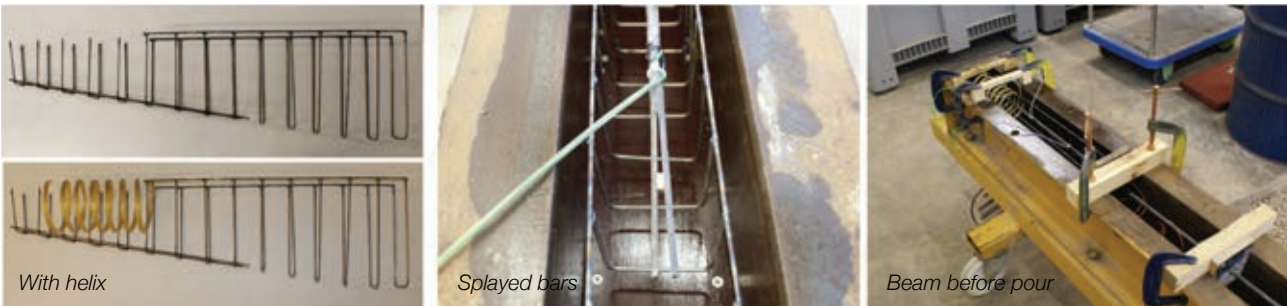


Figure 6.5: Specimen construction process.



Figure 6.6: Demoulded sections.

6.2.2.3. Monitoring

The monitoring arrangement for all Series 1 tests is illustrated in Figure 6.3. 500kN load cells were located at the supports to measure reactions and two linear variable displacement transducers were used to measure the bar slip. Strain gauge position information for each test is shown in Table 6.8.

Table 6.8: Monitoring details.

Test	Gauges	Location (measured from tip of splay)			
		1	2	3	4
1_1_0_0:0_0:0	2	151	704		

Test	Gauges	Location (measured from tip of splay)			
		1	2	3	4
1_2_2_0:0_0:0	2	153	702		
1_3_2_90:30_0:0	4	150	320	510	715
1_4_2_90:30_30:30	2	150	335		

Assuming a bar bond stress of 4MPa the theoretical force at which bar slip would occur for a straight bar is estimated in Eq. 6.1. The manufacturer was unable to provide an estimate of bond strength, and 4MPa was chosen as an initial estimate that sat within the bounds of results found by other researchers. For bars with a splayed end, an order of magnitude increase in capacity (as seen in previous tests, §3.4.3.8.1 on page 76 would result in a failure load equal to the breaking capacity of the bar, Eq. 6.3.

$$F_{ult} = 2\pi r l \tau \quad \text{Eq. 6.1}$$

$$F_{ult} = 2\pi(5)(650)(4) = 81.7kN \quad \text{Eq. 6.2}$$

$$F_{ult} = 4.5^2 \pi(2800) = 180kN \quad \text{Eq. 6.3}$$

#### 6.2.2.4. Test results

The tests were carried out with minimum longitudinal steel in an attempt to model the real behaviour of an FRP reinforced beam. However, each test failed in shear and thus the pull out strength of the bars was not determined. The test results are summarised in Table 6.10, and cracking patterns illustrating the shear failures are shown in Figure 6.7. The ultimate bar strength is calculated assuming a 10mm diameter, 2300MPa capacity CFRP bar (manufacturer's data), giving an ultimate breaking capacity of 180.6kN. The bond stress at failure is calculated using Eq. 6.4.

$$\tau = \frac{F_{ult}}{2\pi r l_b} \quad \text{Eq. 6.4}$$

Where  $F_{ult}$  is the ultimate load;  $r$  is the bar radius and  $l_b$  is the embedded length (650mm)

Table 6.10: Test results.

Specimen	Ultimate load (kN)	Ultimate load/Ultimate bar strength	Average bond stress at failure (MPa)	Failure Mode
1_1_0_0:0_0:0	71.05	39%	3.48	Concrete shear
1_2_2_0:0_0:0	74.47	41%	3.65	Concrete shear
1_3_2_90:30_0:0	53.11	29%	2.60	Concrete shear
1_4_2_90:30_30:30	74.14	41%	3.63	Concrete shear

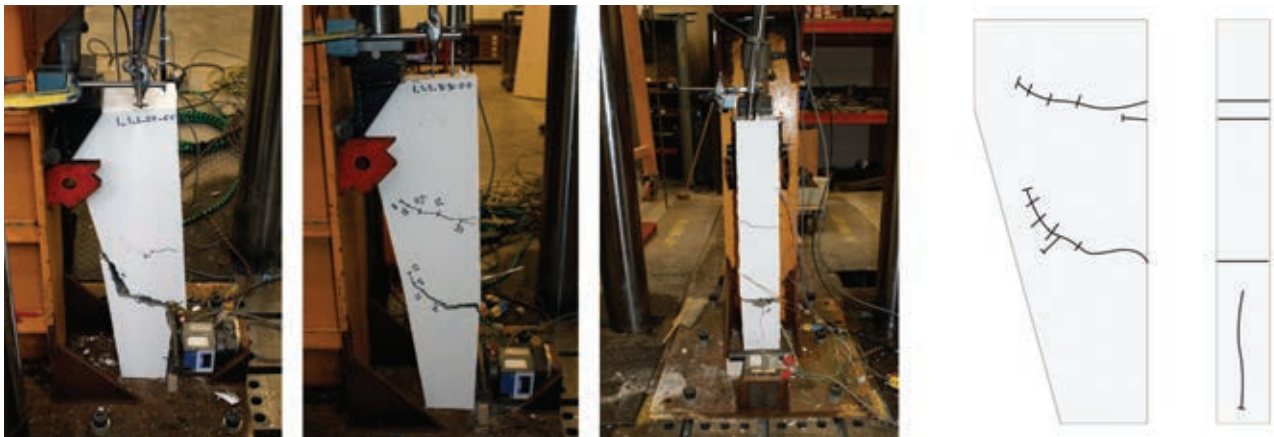


Figure 6.7: Typical specimen failure mode (l) and crack pattern (r).

6.2.3. Series Two

After Series 1 did not provide the required test information, Series Two followed a modified design. Longitudinal steel was added to the concrete section, the area of which was calculated to ensure it would not yield prior to failure of the CFRP Bar at 180kN total load. 12mm diameter deformed steel bars were used, and coupon tests revealed an average ultimate tensile strength of 654MPa.

In addition, Series 2 included a second section design (Figure 6.9) with a constant section. Helices were again used in the end zone, but the ‘double helix’ design of Test 1\_4\_2\_90:30\_30:30 was not replicated due to compaction difficulties experienced in Round 1. Construction of the elements is illustrated in Figure 6.8.



12mm bars spot welded for construction      Tapered section cage      Rectangular section cage, with helix

Figure 6.8: Construction photos.

Three tests were carried out with each design, as summarised in Table 6.11 and were named as follows:

*Program\_Test\_Splay Angle\_Outer helix diameter:Pitch*

Table 6.11: Test details.

Test designation	Section (Figure 6.9)	Concrete Batch	CFRP Splay angle	Outer helix diameter	Outer helix pitch
2_1_0_0:0	Rectangular	3	0	0	0
2_2_2_0:0	Rectangular	3	2	0	0
2_3_2_90:30	Rectangular	4	2	90	30
2_4_0_0:0	Tapered	3	0	0	0
2_5_2_0:0	Tapered	4	2	0	0
2_6_2_90:30	Tapered	4	2	90	30

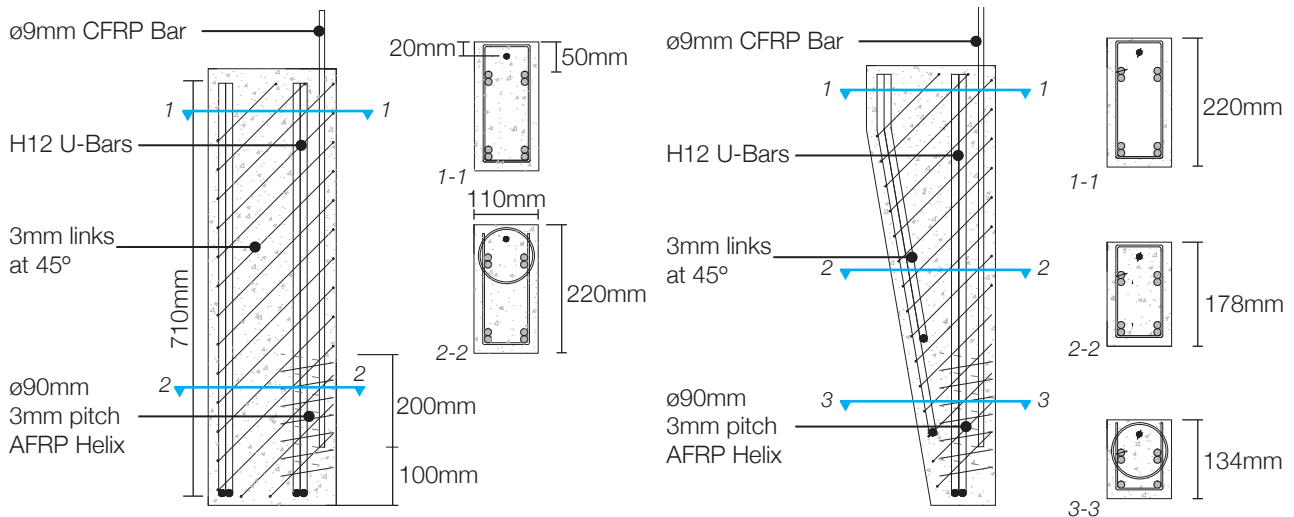


Figure 6.9: Test details overview: Rectangular section (l); Tapered section (r).

### 6.2.3.1. Monitoring

The monitoring arrangement for Series 2 is shown in Figure 6.5 and is similar to Series 1. Each section was monitored by two load cells and linear variable displacement transducers were used to measure bar slip.



Figure 6.10: Strain gauge locations in Series 2 tests.

### 6.2.3.2. Results

The peak and failure loads for each test are presented in Table 6.12 below, where it is clear that all six tests failed at approximately the same load. An equivalent bond stress is calculated for each test, based on a 9.3mm diameter straight bar (this being the average of the actual bars, as measured using a micrometer) with a bonded length of 650mm. Load displacement plots for all six tests are shown in Figure 6.11. Strain gauge readings for Test 2\_5\_2\_0:0 are plotted on a beam elevation at different values of applied load in Figure 6.12 to illustrate the development of strains in the FRP bar during loading. Complete strain gauge readings are plotted for test 2\_5\_2\_0:0 in Figure 6.13; the remaining five tests show essentially the same patterns and are therefore omitted.

Table 6.12: Failure load summary.

Test	Failure Mode	Ultimate Load Capacity (kN)	Equivalent bond stress (MPa)	Notes
2_1_0_0:0	Pull out	92.05	4.85	
2_2_2_0:0	Pull out	93.46	4.92	



Test	Failure Mode	Ultimate Load Capacity (kN)	Equivalent bond stress (MPa)	Notes
2_3_2_90:30	Pull out	98.16	5.17	
2_4_0_0:0	Pull out	96.63	5.09	
2_5_2_0:0	Bar failure	86.01	4.53	CFRP Bar ruptured.
2_6_2_90:30	Pull out	99.07	5.22	

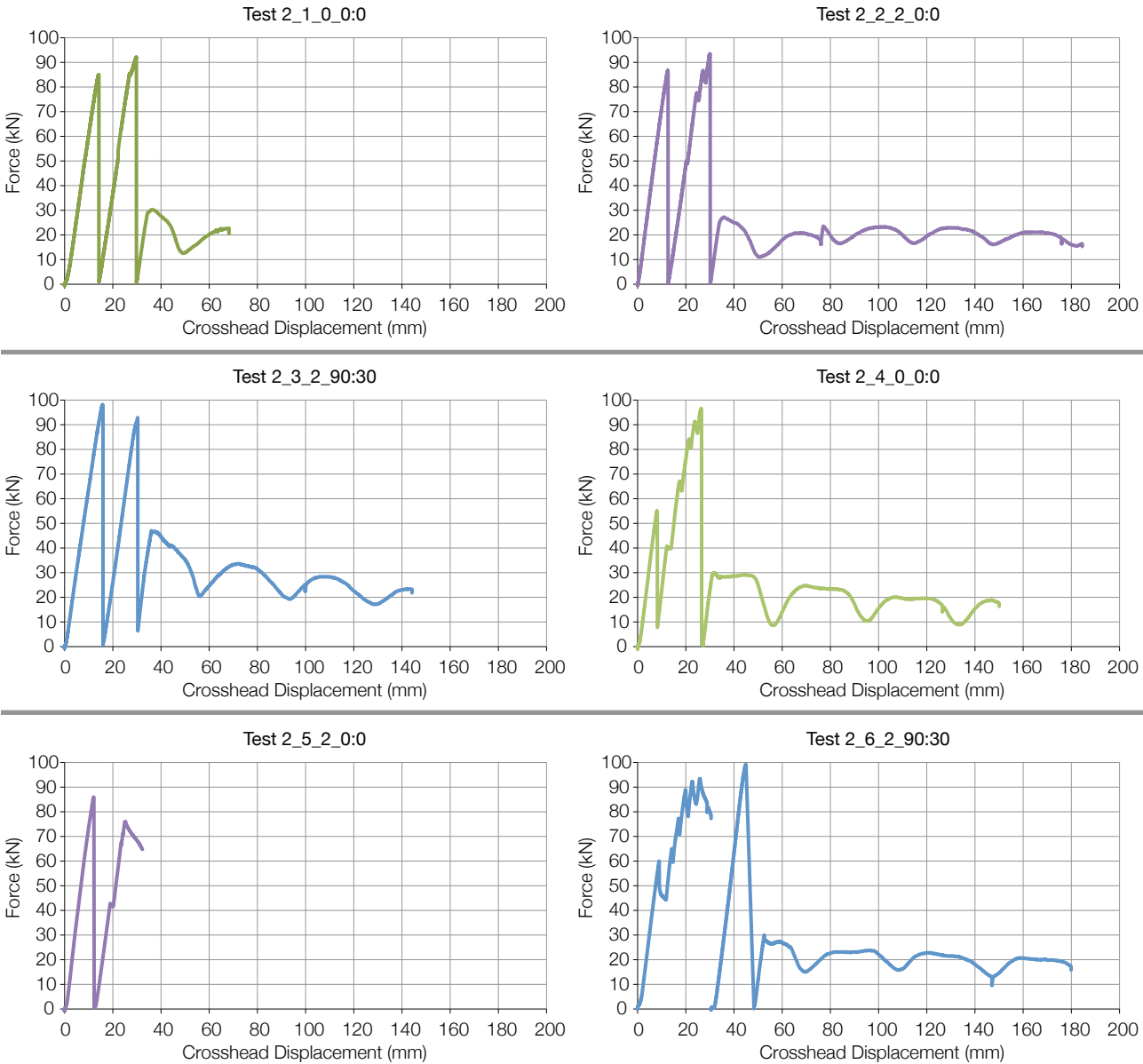


Figure 6.11: Load-displacement plots for tests 2\_1\_0\_0:0 to 2\_6\_2\_90:30.

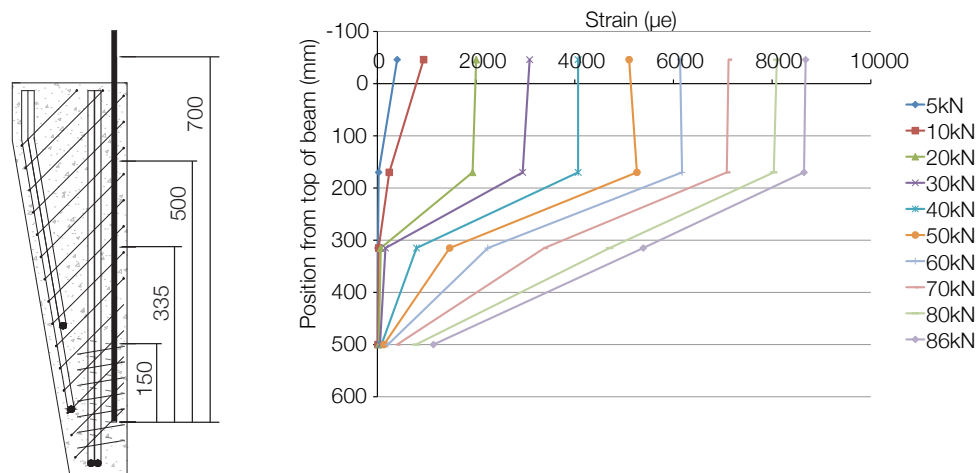


Figure 6.12: Strain distribution for increasing load (Test 2\_5\_2\_0:0).

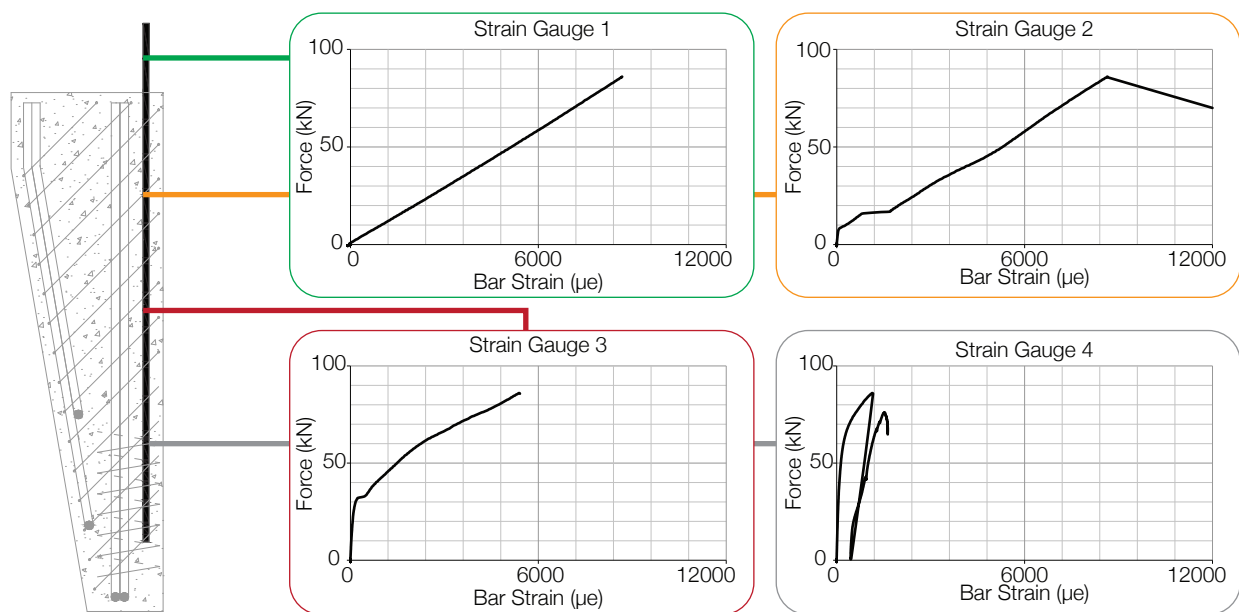


Figure 6.13: Strain gauges (Test 2\_5\_2\_0:0).

### 6.2.3.3. Analysis

It is evident from Figure 6.11 that the failure load and mode was similar for all six tests, and the initial stiffness illustrated by the load-displacement graphs are essentially identical. Two load peaks are seen in each test; the first represents the break down in chemical adhesion of the bar and the second is considered to represent mechanical friction (or tensile capacity of the concrete).

Subsequently, a wave like load-displacement is seen as the bar is pulled out of the concrete section. This line corresponds to the pitch of the helical surface deformations in the CFRP bars, as illustrated in Figure 6.15 and shows that a certain degree of load capacity is retained by mechanical interlock at very high displacements (typically the bars were pulled out by 150mm).

The addition of splayed bars and helices appears to have had no effect on either ultimate capacity or ductility during failure, contrary to previously obtained test results in cubes. During pull out, the behaviour of the splay



appears to be dependent on the stiffness of the concrete that surrounds it. If the concrete has greater stiffness than the splayed bars, then they will be forced closed by the action of pulling the bar out of the concrete and thus provide no wedging action in the section. In this situation, the addition of a helix will have little effect on the failure mode as no lateral forces are generated by the bar to be resisted by the helix.

To illustrate this behaviour, Test Specimen 2\_2\_2\_0:0 was cut into three pieces and the splayed bar was revealed, Figure 6.14. It is clear that whilst the wedge used to hold the splay open is intact, the ends of the splay have been closed by the surrounding concrete, Figure 6.15(l). Hence, during pullout the bar remains straight and the splay has no effect, although once removed from the section the bar regains its splayed shape, Figure 6.15(r). It is unclear why this effect was not influential in previously undertaken cube tests (Tallis, 2005), where excellent load capacity increases were seen using the same wedging design. The envisaged behaviour of the splay during pull out is illustrated in Figure 6.16.

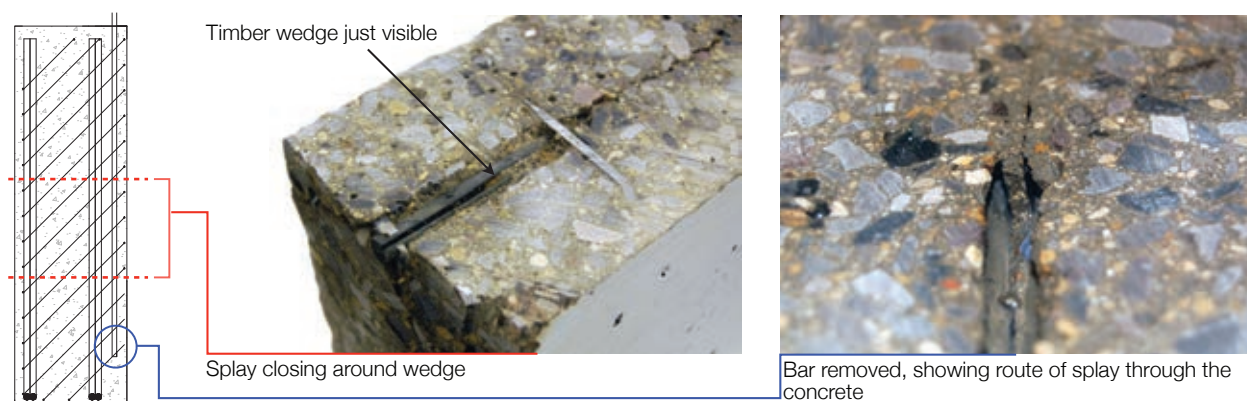


Figure 6.14: Splayed bar behaviour in Specimen 2\_2\_2\_0:0.

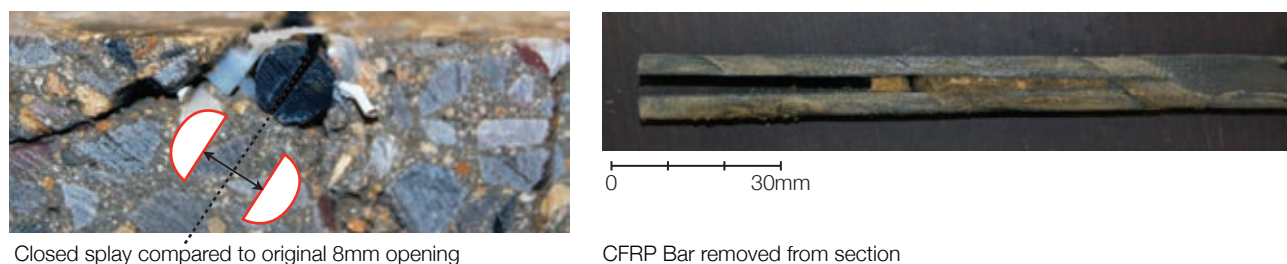


Figure 6.15: Closure of splay during pull out (l); Shape recovery of bar when removed from section (r).

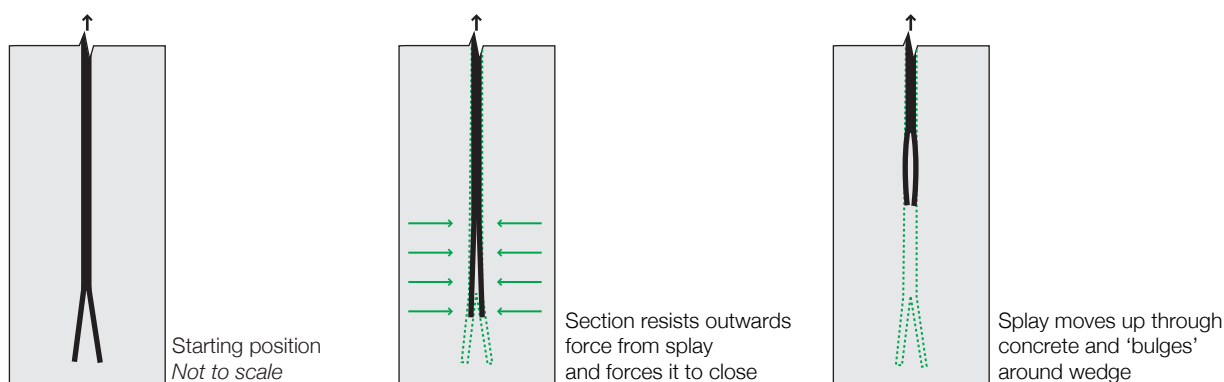


Figure 6.16: Idealised splayed bar behaviour during pull out.

The tests provide good data on the bond strength of the CFRP bar during pull out. As the section did not fail in shear, the bond stress along the length of the bar at ultimate load represents the maximum capacity of the bar. In §6.2.2 the equivalent bond stress at failure ranged from 2.60-3.65MPa (Table 6.10). In the second series of pull out tests, the bond stress ranges from 4.53-5.22MPa (Table 6.11) and this compares well with the previously assumed values of 4MPa.

Whilst the behaviour of the splayed bar has been unsatisfactory in Series 1 and 2, a simple solution to improve the behaviour of the splay has been developed and is investigated in Series 3, §6.2.4

#### 6.2.4. Series Two A

The final round of pull out testing investigates the effect of a ‘fin splay’ on the pull out resistance of a CFRP bar, as illustrated in Figure 6.17. One test was carried out on a tapered section of identical design, material properties and construction methods to Test 2\_6\_2\_90:30 (§6.2.3), as summarised in Table 6.13.

The revised splay design is achieved using a single piece of Perspex cut to the correct dimensions and bonded to the carbon bar using a two part araldite adhesive as shown in Figure 6.18. The fin is designed to ensure that the splay is maintained throughout the application of load, avoiding the problems seen in Series 1 and 2.

Table 6.13: Test details.

Test designation	Section (Figure 6.9)	Concrete Batch	CFRP Splay angle	Outer helix diameter	Outer helix pitch
2A_1_2_90:30	Tapered	5	2	90	30

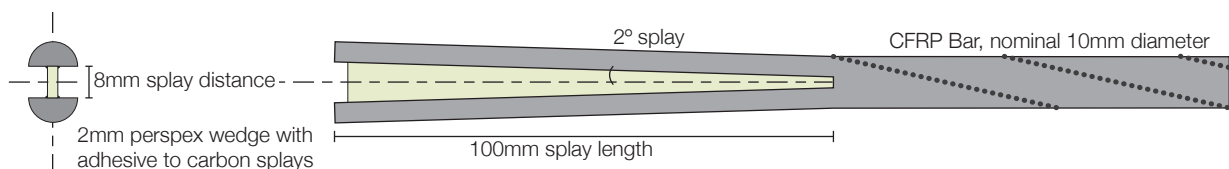


Figure 6.17: Fin-splay design details.



Figure 6.18: Fin splay photographs.

### 6.2.4.1. Results

The specimen was constructed and tested in the same manner as in Series 1 and 2 and loading was also applied using the same loading method. The specimen failed by rupture of the CFRP bar in the jaws of the testing machine (Figure 6.19) at a peak load of 89kN (Figure 6.20). Strain gauge results (recorded along the CFRP bar) are provided in Figure 6.20. Strain gauge 4 (located at the splay) failed prior to testing. Strain gauge 2 failed during loading, at 50kN.

The failure load of the bar is significantly below the ultimate capacity of the 10mm bar (180kN, Table 6.6), and suggests that the machine jaws induced strain concentrations in the bar during the test, or that the jaws were too tight, causing the failure. The results of this test are therefore inconclusive, since the bar did not fail in the splayed area.



Figure 6.19: Catastrophic rupture of the CFRP bar (l-r).

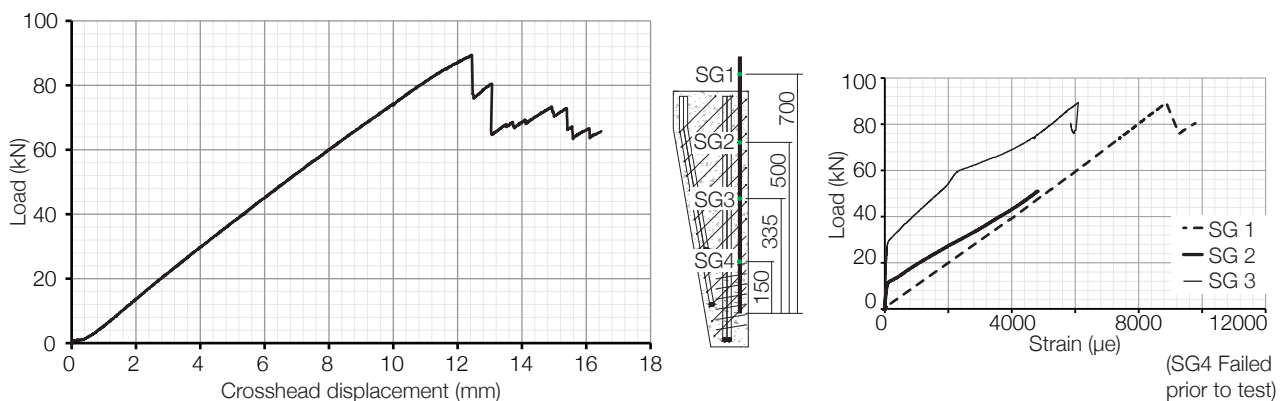


Figure 6.20: Test results (2A\_1\_2\_90:30). Load-displacement (l); Bar strains (r).

### 6.2.4.2. Summary

The test results of this Series were unable to conclusively demonstrate the efficacy of the anchorage method. The premature bar failure seen in Series 3 may have been caused by defects in the bar, but is more likely to have been exacerbated by the high gripping forces required at the cross head during loading.

To overcome this issue, the splayed bar method was used in a scale fabric formed beam test, which is described in 6.3 on page 172. This work demonstrated that it is possible to achieve full anchorage of both steel and FRP bars using the proposed method.

The work described in §6.2 provided some of the background studies for much more detailed work that is currently being undertaken at the University of Bath under a research grant funded by the Leverhulme Trust. For this reason further work on the splayed bar was not undertaken by the author beyond that which is presented in §6.3.

### 6.3. Splayed bar beam tests

#### 6.3.1. Introduction

Following the work presented in §6.2, two beam tests were undertaken to confirm the behaviour of the splayed bar anchorage system in 2m span fabric formed beams using both steel and advanced composite longitudinal reinforcement.

#### 6.3.2. Test details

Two beams were designed, one with steel reinforcement and the other with CFRP reinforcement. The layout of both was determined such that their capacities in flexure and shear were equal to the requirements of their loading envelope along the length of the beam. This was achieved using the provisions of BS EN 1992-1-1 (2004) for the steel reinforced section, and ACI 440 (2006) for the carbon fibre reinforced section, with the loading envelope shown in Figure 6.21(l) providing the capacity requirements.

The beams were designed with a 'T' section at their mid span, transitioning to a hydrostatic cross section 500mm from the supports. This ensured that a sufficient concrete area was provided in areas of high shear, while also minimising the beam's cross sectional area in those regions dominated by flexural capacity. Material properties of the concrete, steel and FRP reinforcement are provided in Table 6.14. The required beam dimensions were determined at 20 sections along the length of the beam.

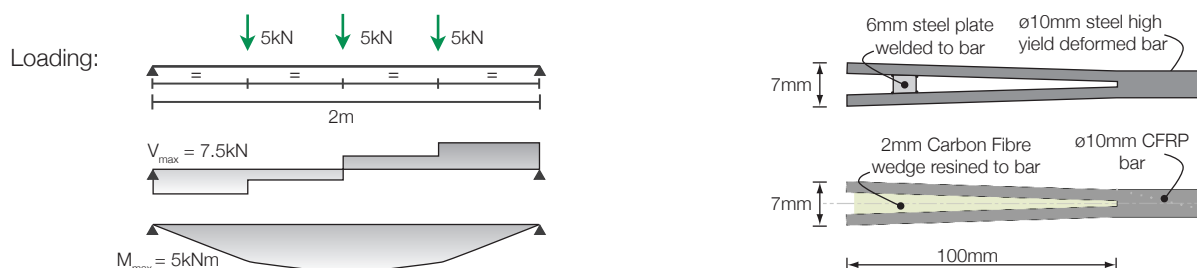


Figure 6.21: Loading envelope (l) and Splay dimensions (r).

Beam 3\_2 (Figure 6.22(l)) was longitudinally reinforced with a single 10mm diameter high yield steel bar, both ends of which were splayed as shown in Figure 6.21(r). The bar was confined in the end zone with a helix constructed of 3mm diameter high tensile steel wire (outer diameter 30mm, with a pitch of 40mm). Beam 3\_3 (Figure 6.22(r)) was longitudinally reinforced with a single 10mm diameter carbon fibre reinforced polymer (CFRP) bar, both ends of which were splayed as shown in Figure 6.21(r) that was confined in the end zone with a helix constructed using AFRP rope (Kevlar 49, as described in §6.2) impregnated with epoxy resin. Salient dimensions of the beams, which vary in both cross section and elevation, are provided in Figure 6.22.

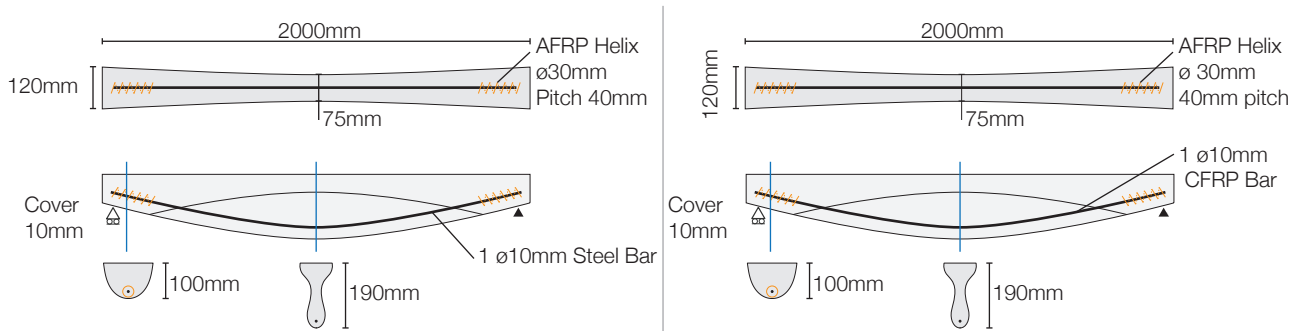


Figure 6.22: Beam 3\_2 (l); Beam 3\_3 (r).

Table 6.14: Member details.

#	Span	Top width	Section depth	Longitudinal reinforcement	Concrete cube strength (at testing)
3_2	2m	75-120mm	100-300mm	Ø10mm deformed steel, $f_y = 500\text{MPa}$	42MPa
3_3	2m	75-120mm	100-300mm	Ø10mm CFRP, $f_{tu} = 2300\text{GPa}$	41MPa

The beams were constructed in a hanging hessian fabric mould that was fixed in position along two line supports, with the 'T' section created using curved timber formers, as shown in Figure 6.23. Each beam was loaded through three jacks, positioned a quarter-span apart. A load cell and displacement transducer was connected to the bottom of each jack and strain gauges were placed at four points along the length of each reinforcing bar. A plug placed at each end of the reinforcement to facilitate the measurement of any bar slip during testing.

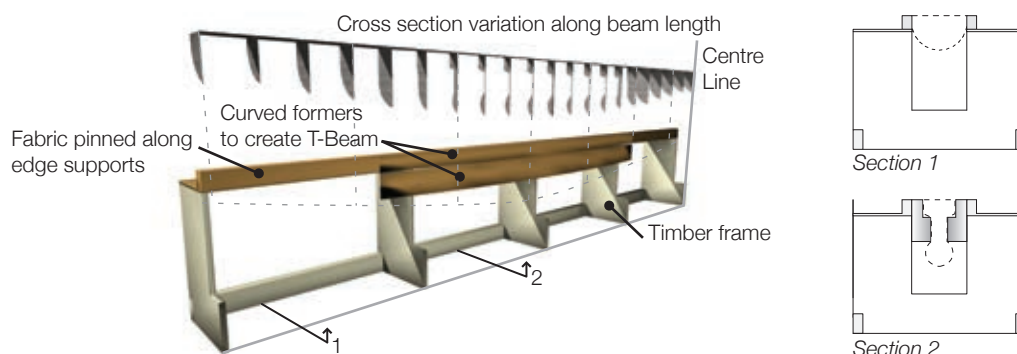


Figure 6.23: Construction method.

### 6.3.3. Results

Beam 3\_2 was tested first, with load applied in 2kN increments. After an approximately linear initial load-displacement response, Beam 3\_2 exhibited considerable ductility before failing at a total load of 26kN, considerably greater than the design load. Flexural cracking, as shown in Figure 6.24(l), was considerable, and failure occurred due to crushing of the compression zone after the longitudinal steel had yielded. Cracking was well distributed along the length of the beam, indicating a constant stress in the bar, as expected by merit of the design procedure used. Removal of the end plugs on the longitudinal bar after testing revealed that the splayed anchor in Beam 3\_2 had moved by less than 1mm when compared to its original position.



Beam 3\_3 (Figure 6.24(r)) displayed a similar response to Beam 3\_2 in the serviceability condition, yet failed in a more brittle diagonal tension mode close to the supports after displaying some flexural cracking in the main span. A wide inclined crack opened up close to the roller support at a total load of approximately 27kN (First Peak 1, Figure 6.24(r)). Load was then reapplied and the beam reached a second peak of 25kN before complete failure of the CFRP bar occurred. Analysis of the beam revealed that the splayed anchor had slipped by less than 1mm and that failure occurred after the CFRP bar ruptured at the position of the inclined crack, as shown by the photographs in Figure 6.25. The load displacement responses of both beam tests are shown in Figure 6.26, where a reduction in stiffness is seen in Beam 3\_3 under reloading.

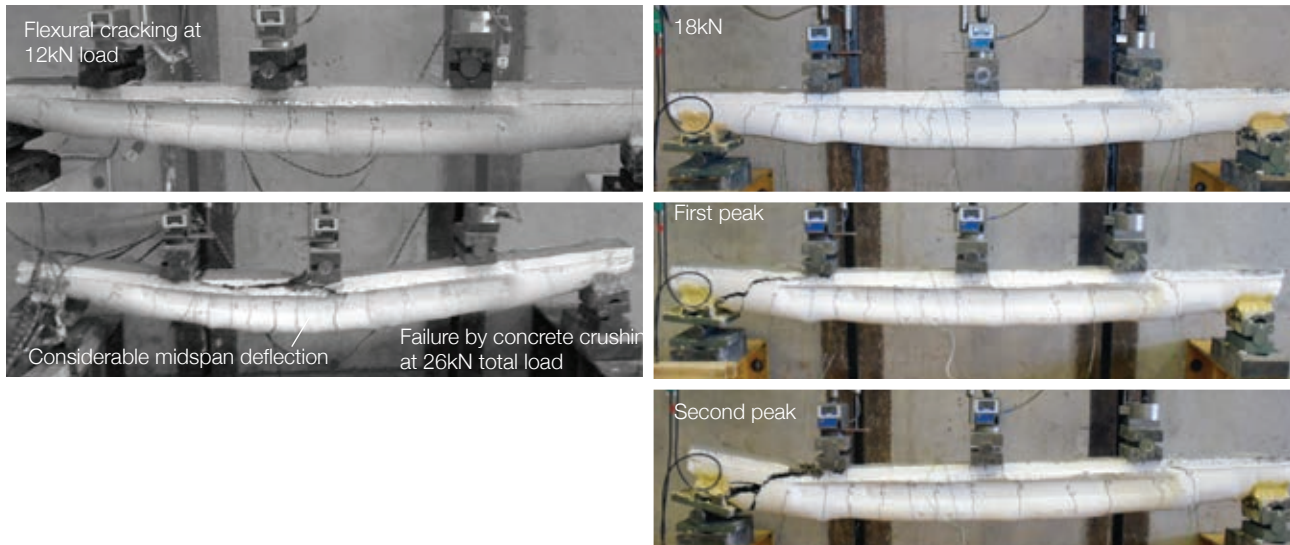


Figure 6.24: Test photographs. Beam 3\_2 (l); Beam 3\_3 (r).

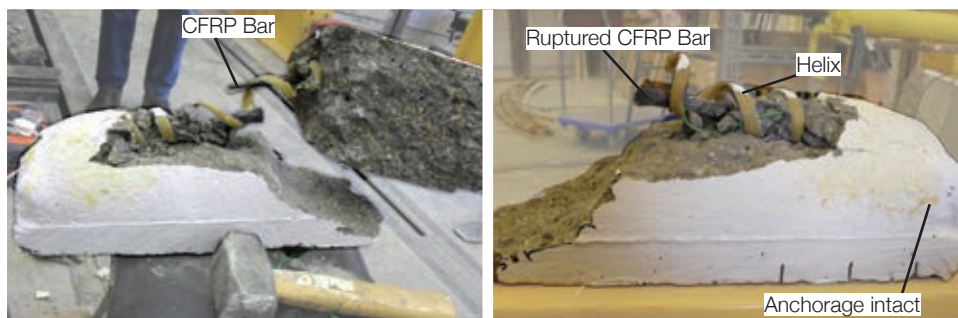


Figure 6.25: CFRP Bar Rupture.

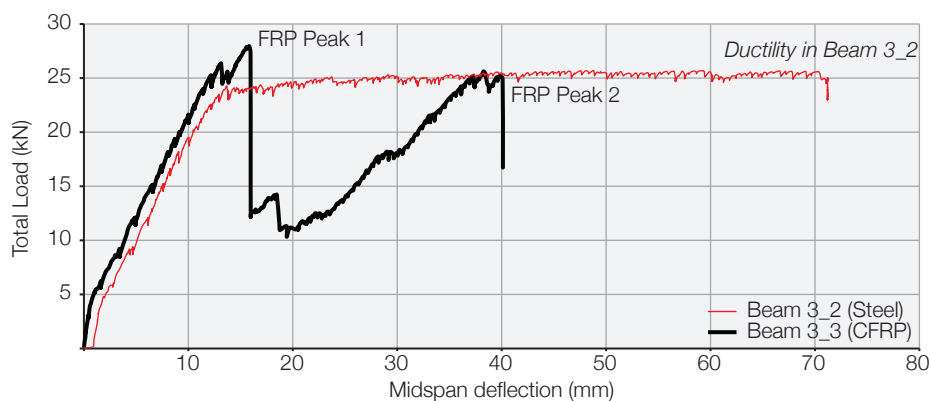


Figure 6.26: Load-displacement response for Beam 3\_2 and Beam 3\_3.



### 6.3.4. Analysis

Figure 6.26 illustrates that the serviceability behaviour of both beams was very similar, as was their peak load capacity. Beam 3\_2 displayed a more desirable failure mode, moving from linear elastic to plastic behaviour to show considerable ductility. Although the ultimate load (26kN) was higher than the design load (15kN), this can in part be attributed to an increased steel yield stress in the real section over that assumed for design, along with a slightly altered beam section in testing due to variability in construction. A total of 58mm deflection at a constant load of 23kN was recorded, and the splayed anchor was successfully used to provide anchorage to the steel bar.

The behaviour of Beam 3\_3 was less ideal, since the section was designed to fail by concrete crushing at the mid span before the CFRP bar was able to rupture. At the initial peak load the average bar stress at a position 500mm from the support was far less than the bar's ultimate tensile capacity, as shown in Eq. 6.5-Eq. 6.6. This suggests that failure of the CFRP occurred due to a high local strain across the crack, which in turn confirms that a proper assessment of the bond between the fibre reinforced polymer bar and its surrounding concrete is of great importance.

$$F_f = \frac{M}{z} = \frac{13,000 \times 500}{140} = 46.4 \text{ kN} \quad \text{Eq. 6.5}$$

$$\sigma_f = \frac{46429}{78} = 595 \text{ N / mm}^2 \quad \text{Eq. 6.6}$$

In a hypothetical, fully bonded section the strain in the longitudinal reinforcement and its surrounding concrete are the same. At the onset of cracking, local strains in the bar increase rapidly and since fibre reinforced polymer bars are unable to yield and maintain compatibility by stretching plastically, they will fail as soon as a limiting strain capacity is reached (Lees and Burgoyne, 1999). Conversely, in a section with zero bond between the bar and concrete, strains in the reinforcement are low since it is able to move relative to the concrete and whilst failure due to high local strains may now be prevented, lower strains in the reinforcement limit the moment capacity of the section. It is therefore important that some medium value of bond is achieved to obtain the best of both situations. In tests on prestressed aramid fibre reinforced beams, Lees and Burgoyne (1999) showed that such a partial bond was able to provide both high moment and high rotation capacity.

Although the failure mode of Beam 3\_3 was not ideal, the test showed that the helically confined splayed bar is an effective means by which full anchorage may be provided when advanced composite reinforcement is used, allowing the bar to develop its full strength without slipping at the end zones. The provision of helical confinement is considered to be important for both cases, potentially preventing premature tensile splitting of the end zone as the force on the splayed bar increases under loading, although this improvement has not been quantified. Whitehead and Ibell (2005) further showed that the provision of helical confinement increases the shear capacity of advanced composite reinforced beams, although this effect was not considered during the design process.

### 6.3.5. Conclusions

The testing described above has shown that the splayed bar may be used to provide anchorage in both steel and FRP reinforced fabric formed beams and that the use of a circular helix to confine the concrete is a logical method to prevent premature splitting failures when such an anchorage is used. When used with advanced composite bars, the splayed anchor may allow a greater proportion of the tensile capacity of the bar to be utilised. Additional testing using a modified pull-out method is currently underway to provide further verification of the results presented in this section.

A post-failure assessment of Beam 3\_3 showed that the section was in fact over designed for the chosen loading envelope, and would ideally have been slightly shallower. As tested, Beam 3\_3 was still an over reinforced section and thus the failure mode was unexpected. However, both tests were successful in demonstrating the efficacy of the splayed bar as an anchorage method.

In design, the provision of ductility is imperative. Where advanced composite reinforcement is used, the section must be over reinforced to facilitate a crushing failure and local overstrains must be avoided by proper assessment of the bond between concrete and FRP.

Compared to a 100x175mm prismatic beam, the fabric formed beams tested provided a 25% saving in total concrete volume ( $0.0261\text{m}^3$  compared to  $0.035\text{m}^3$ ). This is slightly less than has been achieved in previous work, although the beams were both over designed, failing at nearly twice their design load, suggesting that even greater material savings could have been achieved. Further testing is desirable and an improved section design method may lead to more efficient predictions of failure loads. The splayed bar, whilst not entirely verified in smaller scale beam-element tests presented in §6.2, can now be considered to provide sufficient anchorage when combined with helical confinement, and will be used in future beam tests.

The technical design considerations of §6.2 and §6.3 are contrasted in the following, where the details of a testing regime undertaken at the Centre for Architectural Structures and Technology (CAST), University of Manitoba, Winnipeg in May 2010 are given. With the expert guidance of Professor Mark West, construction methods, theory and design philosophies are presented that influenced later work undertaken at the University of Bath.

## 6.4. Centre for Architectural Structures and Technology, Canada

### 6.4.1. Introduction

The following section details work undertaken at the University of Manitoba's Centre for Architectural Structures and Technology during a two week study visit in April 2010. Part sponsored by a Royal Academy of Engineering Travel Grant, the work focused mainly on the construction and philosophical basis of fabric formwork, and the following has been partly taken from a report submitted to the Academy in May 2010. The beams described herein form Test Series 4.

During the initial period at CAST, three beams were constructed. The first (Figure 6.27), which was formed using a single rectangular sheet of fabric, was only moderately successful as the wrong sort of fabric was used in its construction (polyester, instead of nylon). There was considerable wrinkling along the top of the beam (Figure 6.27) and although this can make an interesting architectural feature, it was not desired here.



Figure 6.27: Beam 1. Construction method (top) and resulting beam.

Beam 1 has a hydrostatic cross section shape, and is thus fatter at the base than at the top. This shape is inefficient in a reinforced concrete beam, since below the neutral axis the concrete is in tension and thus adds no capacity to the section. To reduce the concrete volume in each the beam, the 'double keel' mould was utilised.

Construction using the double keel method is illustrated for Beams 2 and 3 in Figure 6.28, with the results shown in Figure 6.29 and Figure 6.30. Beam 3 was developed as a refinement of Beam 2, whereby the support location is accentuated and defined more clearly. The differences are mainly aesthetic, and do not add significantly to the construction complexity.

Following the work done on Beams 2 and 3, a fourth beam was cast to a slightly modified design (Figure 6.31). This beam was the first to suffer a failure during casting, where the formwork was badly detailed and the plaster

was able to escape from the bottom of the mould (Figure 6.31). This led to a redesign of the formwork, creating a better seal at the base of the formwork.

A fifth beam was then cast, making use of the new keel design. This aspect of the model production is unique, since a completely watertight mould is not required when concrete is used. However, the casting failure does highlight the need for a robust mould and forming method. This was achieved in the next iteration, as shown in Figure 6.32, where the double cantilever beam was formed using a single sheet of fabric.



Figure 6.28: Double keel construction.

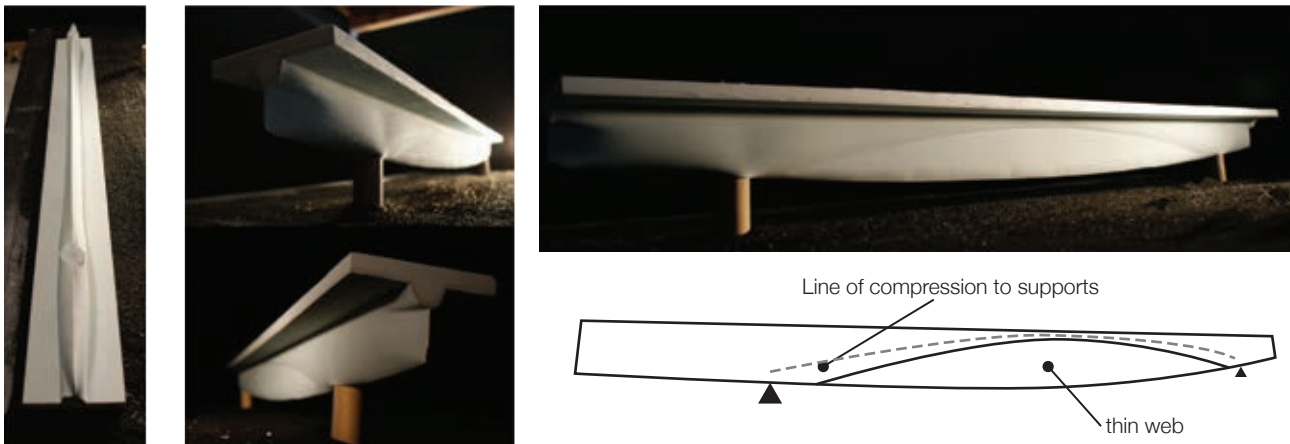


Figure 6.29: Beam 2.

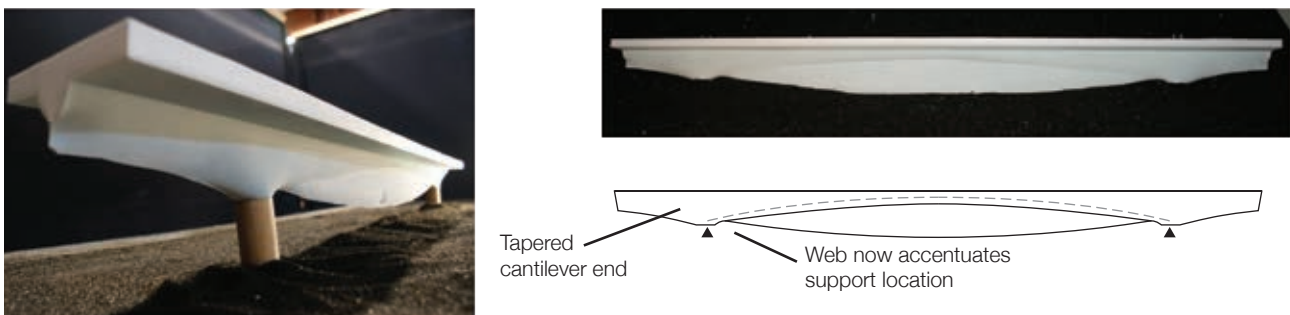


Figure 6.30: Beam 3.





Figure 6.31: Beam 4. Design (l); Construction failure (r).



Figure 6.32: Beam 5. Formwork (l); Beam (r).

#### 6.4.2. Design development

After the success of the double keel mould as a construction method, Professor West and the author worked on a simpler beam design that satisfies the same structural principles, but moves away from distinct cantilevered ends and is more streamlined in appearance. This design was chosen to speed up construction, allowing a single mould to be reused multiple times without having to re-set and attach the internal fabric. The principle of re-use was tested in the lab, and the beams thus made are shown in Figure 6.34.



Figure 6.33: Beam 6. Fabric stapled to mould (l); Beam cast (r).



Figure 6.34: Beam 6.

Following this, the double keel method was applied again, allowing Beam 7 to see even greater material savings over Beam 6. This design is to be used in structural tests of reinforced concrete beams (4m span) at the University of Bath in the Summer of 2010.



Figure 6.35: Beam 7.

In the final period spent at CAST, ideas for hollow beams and trusses were developed, including one with a 'compression arch' in the web zone, as shown in Figure 6.36. This type of beam, where the web material is removed, has implications both for architectural expression and practical design (allowing services to be threaded through the beam zone, for example). Unfortunately the plaster model broke in the centre span, illustrating the difficulty of accurate scaling in models, and the delicacy of plaster.

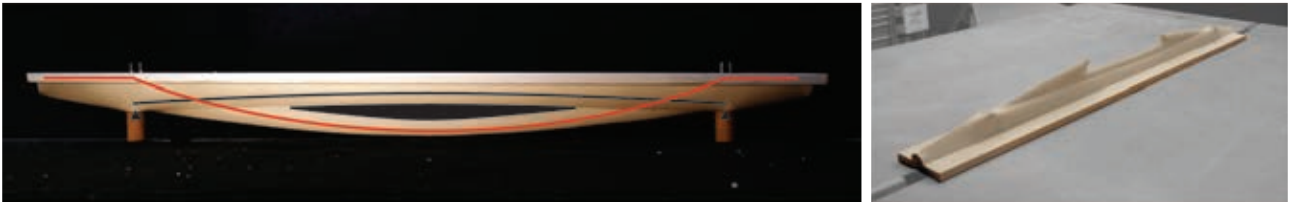


Figure 6.36: Beam 8 - design (l) and broken beam (r).

#### 6.4.3. Conclusions

The work undertaken with Professor West at CAST was instrumental in improving the understanding of fabric formwork technology and construction. Whilst some of the work has been shown in this report, much more was discussed informally with Professor West and his team and these ideas informed the development of this thesis. Two potential applications of the beams designed and built above are shown in Figure 6.37 on page 181, where a precast shell element was used to represent a potential floor construction method.

The design methods and construction techniques detailed above were utilised in subsequent structural testing of fabric cast beams, as is described in more detail in the following sections.



Figure 6.37: Fabric formed beams and shell elements as a floor system.



## 6.5. T Beams

### 6.5.1. Introduction

Building on the work presented above, and in the first significant step towards satisfying the aims of the testing matrix (§5.4 on page 122), four steel reinforced ‘T’ beams elements were tested to the designs presented in §5.5 on page 124. A summary of the beam layouts is provided in Table 6.15, where they are named according to the following convention (variables in square parentheses):

*Program [5] \_Test Number [1-4] \_Shape [Hydrostatic] \_Reinforcement {Constant Cover/Funicular}*

The testing of passively reinforced fabric formed beams is intended to satisfy the following criteria, for development into longer span beams in future work:

1. Prevention of shear failures;
2. Detailing at support connections;
3. Verification of serviceability behaviour.

Table 6.15: Beam summary.

Test	Span (m)	Section	Reinforcement	Code
1	4	Hydrostatic	Constant cover, minimum links along length	5_1_H_C
2	4	Hydrostatic	Constant cover, designed links only	5_2_H_C
3	4	Hydrostatic	Funicular, minimum links along length	5_3_H_F
4	4	Hydrostatic	Funicular, designed links	5_4_H_F

#### 6.5.1.1. Material properties

Concrete compressive strengths for each of the beams at testing is provided in Table 6.17. Beam 5\_1\_H\_C was cast using the mix described in Table 6.16, while the remaining beams were cast using a ready-mix supplier, greatly expediting the construction process. Some difficulties did occur and mixes for Beams 5\_2\_H\_C and 5\_4\_H\_F unfortunately had a slump of greater than 100mm. All longitudinal bars were of deformed steel with average tensile and yield strengths of 664MPa and 567MPa respectively. Shear links, when used, were constructed of 3mm high yield steel wire with an average ultimate strength of 782MPa. The beams were cast exclusively in Proserve Geotextile Fabric, as detailed in Table 3.6 on page 61.

Table 6.16: Concrete mix ratios.

Quantities	Cement (kg)	Water (kg)	Fine aggregate (0.5-5mm) (kg)	Soft sand	Coarse aggregate (10-12mm) (kg)
per 200kg	37.5	15.83	52.75	6	87.92
per m <sup>3</sup>	450	190	633	72	1055



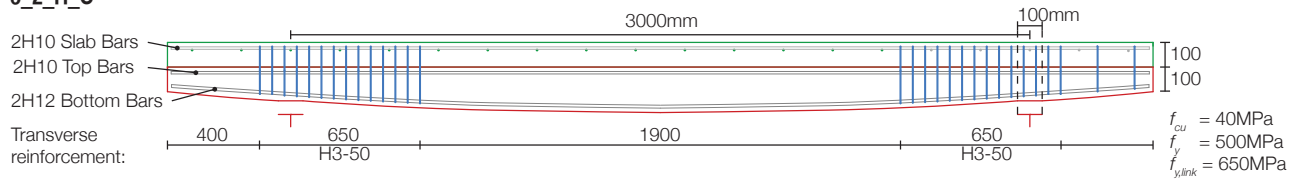
**5.2\_H\_C**

Figure 6.40: Beam 2.

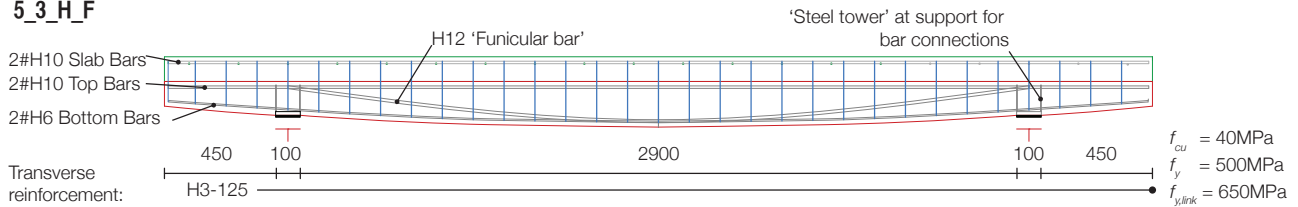
**5.3\_H\_F**

Figure 6.41: Beam 3.

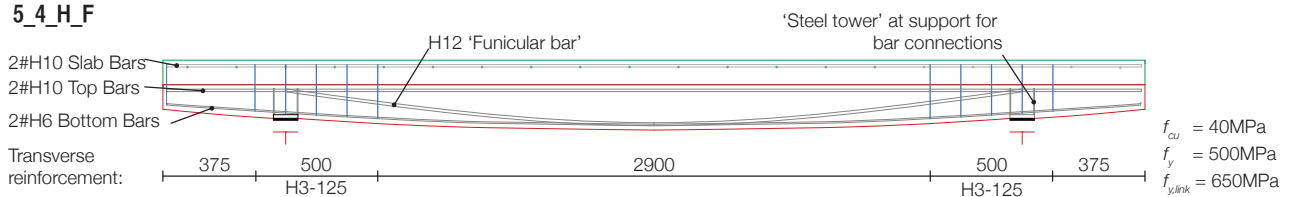
**5.4\_H\_F**

Figure 6.42: Beam 4.

**6.5.3. Construction**

Beam construction was undertaken using a 4m long forming table, as described previously. The table is able to accommodate a wide range of keel moulds and may be used in future tests. The four beams were all poured in the same mould, and thus a staggered construction program was required. The process of casting and demoulding is illustrated in Figure 6.45 below.



Figure 6.43: Keel construction photos.



Figure 6.44: Photo of the T Beam.

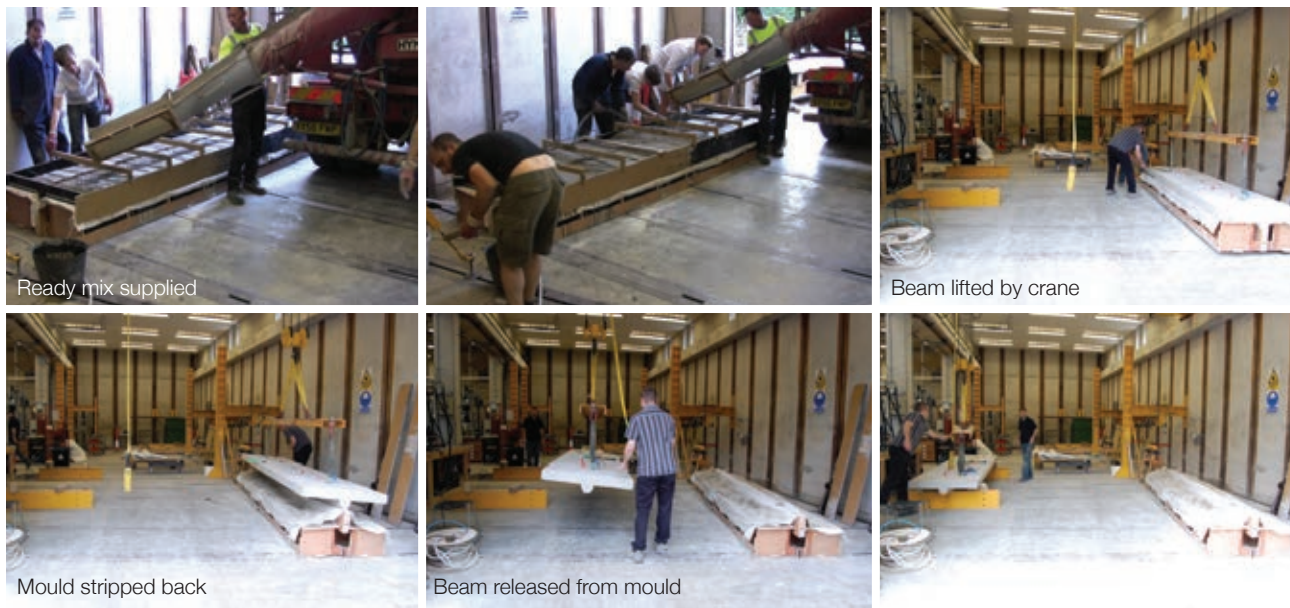


Figure 6.45: Casting and demoulding 4m span T-beam.

#### 6.5.4. Testing

##### 6.5.4.1. Arrangement

After curing for 14 days, the beams were tested in 9 point bending to model the presence of a uniformly distributed load on the beam, as shown in Figure 6.46. A test frame was specially constructed around each element. Load cells and displacement transducers were arranged as shown, while each member had between five and seven strain gauges positioned on its main longitudinal steel bars.

All beams were tested to the same load cases (2a and 2b) as described in §5.5 on page 124. Two values of load (P1 and P2, Figure 6.46) were applied through hydraulic jacks and continually monitored using the attached load cells. The beams were initially loaded to the design value of Load Case 2a (maximum hogging), before all loads were removed.

Load case 2b was then applied up to the design load (58kN total applied load). Cracking was monitored throughout. After the design loads had been achieved, the loads were increased in the ratio as determined by Load Case 2b up until the end jacks had exhausted their stroke. From this point, the beams were loaded to destruction. Beams 2, 3, and 4 were loaded only with the central point load, while Beam 1 was loaded with the central 5 loads to failure.

Displacements at Load Case 2a, Load Case 2b and the ultimate mid span deflection are summarised in Table 6.18 where the maximum load carried by the beam is also given. Further results are provided below.

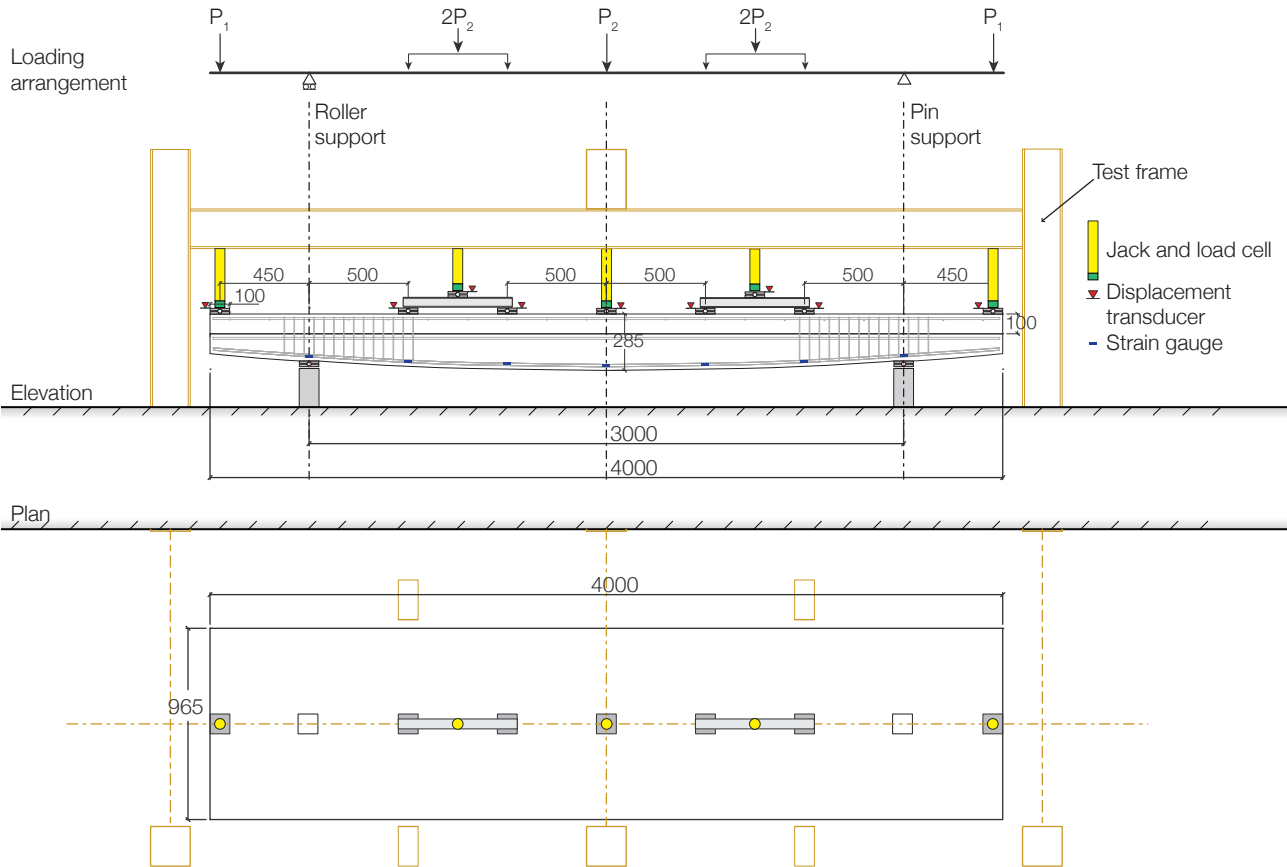


Figure 6.46: Test set up.

Table 6.18: Test failure modes and ultimate capacity.

Test	Load Case 2a		Load Case 2b		Failure		Failure mode
	Load ( $2P_1 + 5P_2$ ) (kN)	Mid span deflection (mm)	Load ( $2P_1 + 5P_2$ ) (kN)	Mid span deflection (mm)	Failure load (kN)	Mid span deflection (mm)	
5_1_H_C	44.9	3.11	58.4	7.41	113.8	89.3	Flexure
5_2_H_C	46.0	2.11	58.6	6.66	118.7	85.8	Flexure
5_3_H_F	47.0	2.68	58.6	7.13	114.9	89.1	Flexure
5_4_H_F	44.6	2.46	57.7	6.52	132.7	89.1	Flexure

### 6.5.5. Results

Load deflection plots for all four beams for Load Case 2a and Load Case 2b to failure are provided in Figure 6.47 and Figure 6.48 before more detailed analysis is undertaken for each beam test.

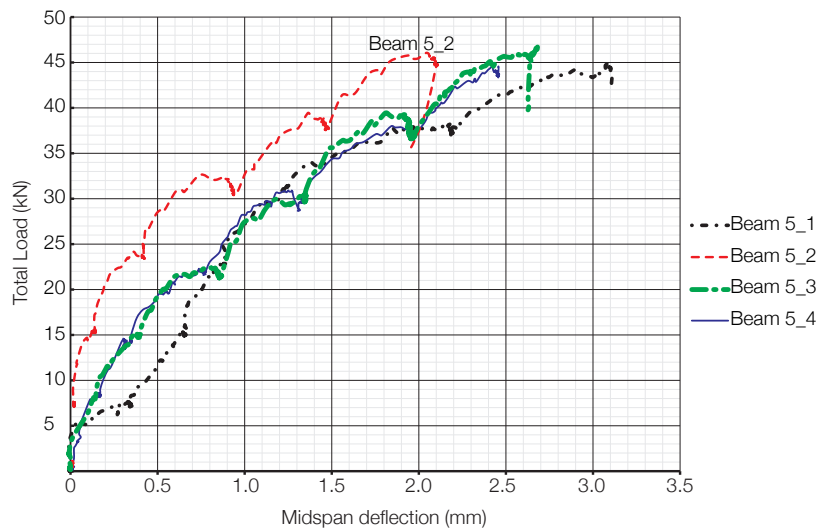


Figure 6.47: Load-deflection plot for Load Case 2a.

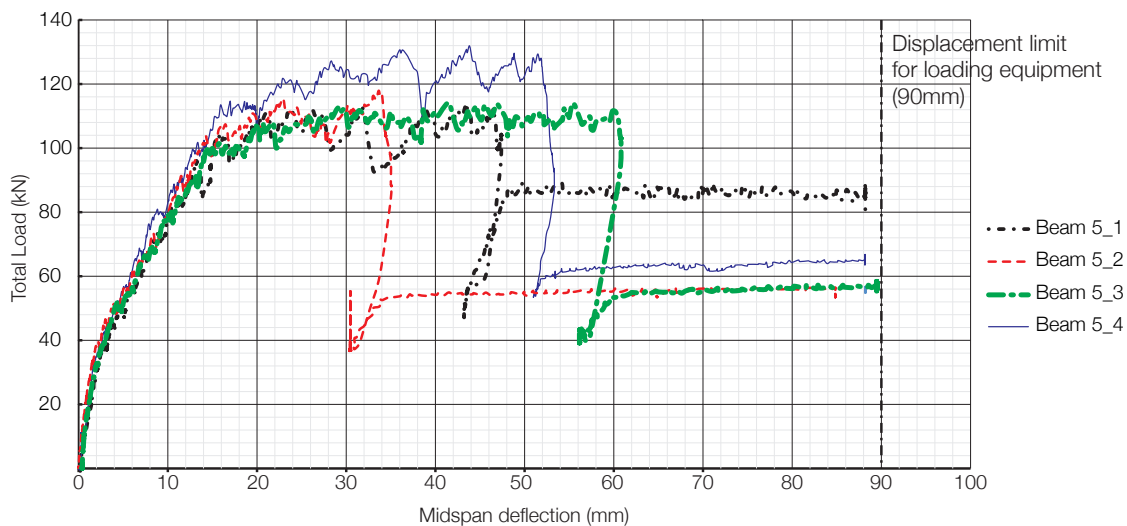


Figure 6.48: Load-deflection plot for Load Case 2b.

#### 6.5.5.1. Beam 5\_1\_H\_C

Beam 1 was loaded in 5kN increments until the design value of Load Case 2a had been reached. All load was then released. The beam was checked for cracking, before load was again applied in the manner required for Load Case 2b. Upon reaching the design load, the element was assessed for cracking before all loads were increased. A maximum load capacity of 113.8kN was recorded. At approximately 48mm central deflection the loads P1 were removed and the beam was taken to failure by crushing at the mid span by the application of the five point central loads (P2).

Photographs of the section under testing and at failure are provided in Figure 6.49 and Figure 6.50. Beam 5\_1\_H\_C was monitored throughout by seven strain gauges applied to the bottom tensile reinforcement (12mm bar), located as shown in Figure 6.51 where strain gauge readings for Load Case 2 until failure are provided.





Figure 6.49: Element 5\_1\_H\_C before testing.



Figure 6.50: Test photographs - 5\_1\_H\_C.

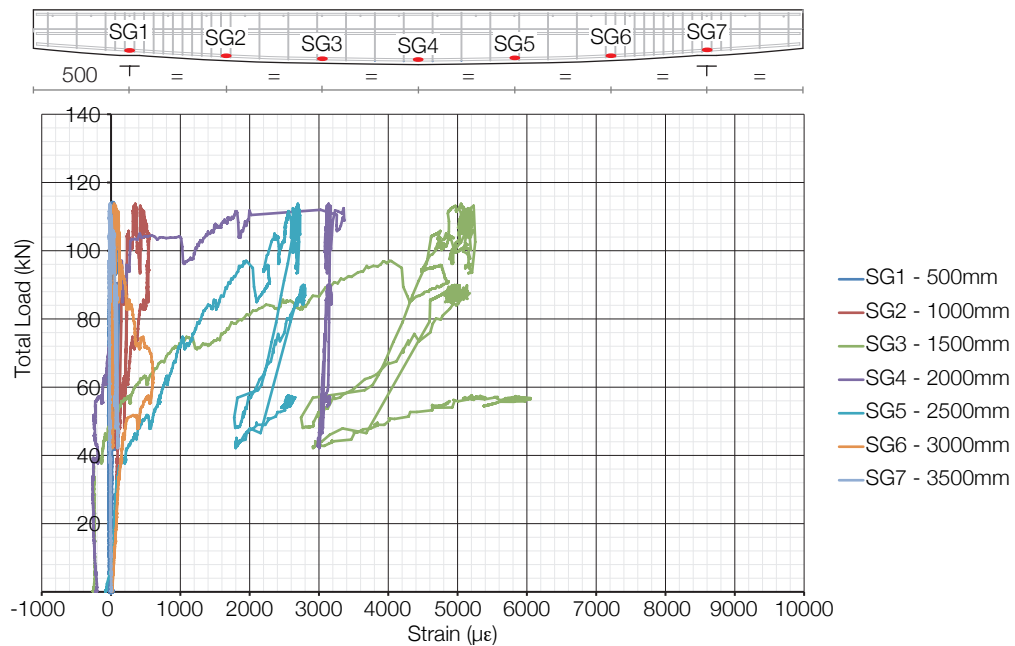


Figure 6.51: Strain gauge results, Beam 5\_1\_H\_C.

#### 6.5.5.2. Beam 5\_2\_H\_C

Beam 2 was loaded to the design value of Load Case 2a before all loads were released. The design value of Load Case 2b was then applied, before all loads were increased in the same ratio and the steel yielded. A maximum load capacity of 118.7kN was recorded. At approximately 35mm central deflection all loads, except for the central point load, were removed as two load cells were close to being pushed off their supports. Load was then applied through the central point (P2) only, until the section crushed at the mid span.

Photographs of the section under testing and at failure are provided in Figure 6.52

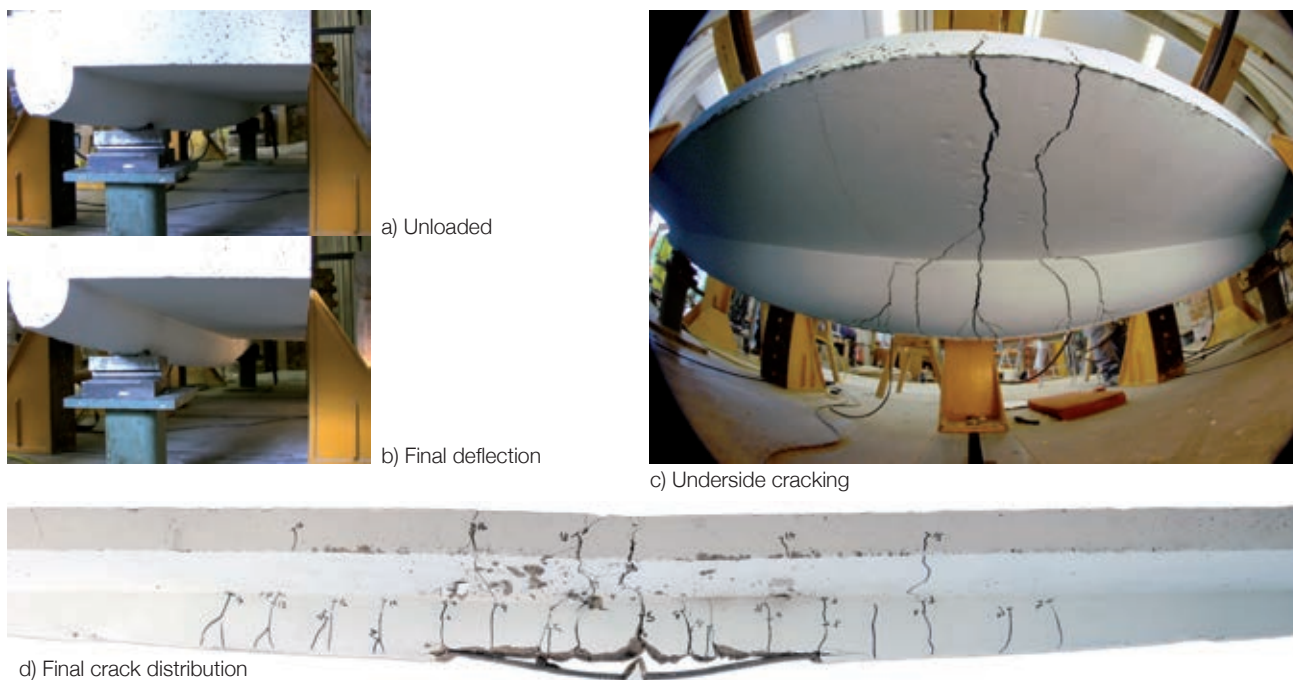


Figure 6.52: Beam 5\_2\_H\_C crack distribution at failure.

Beam 5\_2\_H\_C was monitored throughout by seven strain gauges applied to the bottom tensile reinforcement (12mm bar), located as shown in Figure 6.53 where strain gauge readings for Load Case 2b until failure are provided.

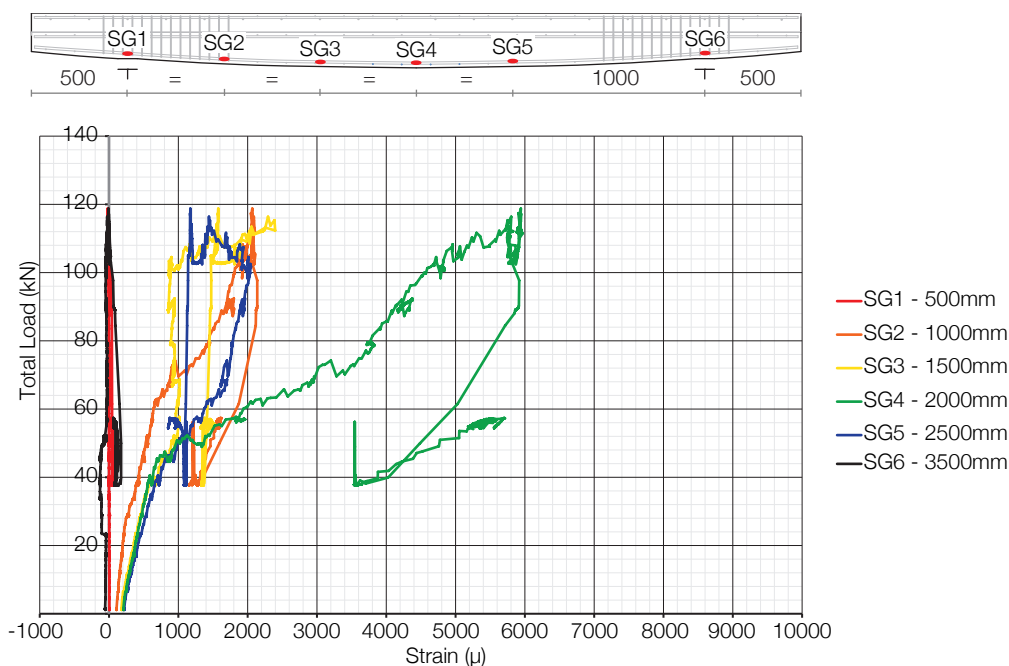
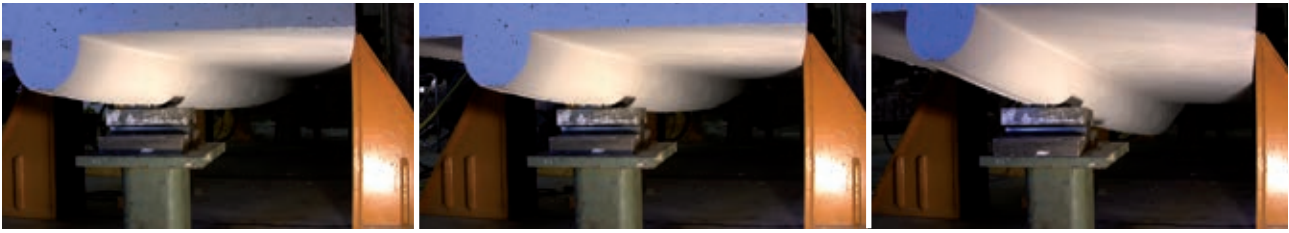


Figure 6.53: Strain gauge results, Beam 5\_2\_H\_C.

#### 6.5.5.3. Beam 5\_3\_H\_F

Beam 3 was loaded to the design value of Load Case 2a before all loads were released. The design value of Load Case 2b was then applied, before all loads were increased in the same ratio and the steel yielded. A maximum load capacity of 114.9kN was recorded. At approximately 62mm central deflection all loads, except for the central point load, were removed. Load was then applied through the central point (P2) only, until the section failed in a ductile manner.

Photographs of the section under testing and at failure are provided in Figure 6.54. Beam 5\_3\_H\_F was monitored throughout by seven strain gauges applied to the bottom tensile reinforcement (12mm bar), located as shown in Figure 6.55, where strain gauge readings for Load Case 2b until failure are provided.



Element Deflections over Load Case 2b

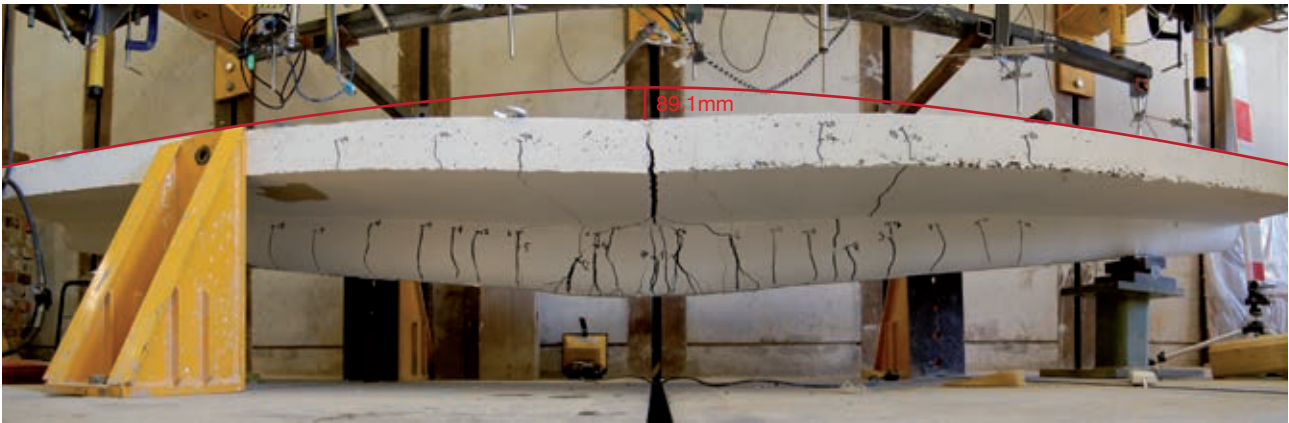


Figure 6.54: Beam 5\_3\_H\_F test photographs and crack distribution at failure.

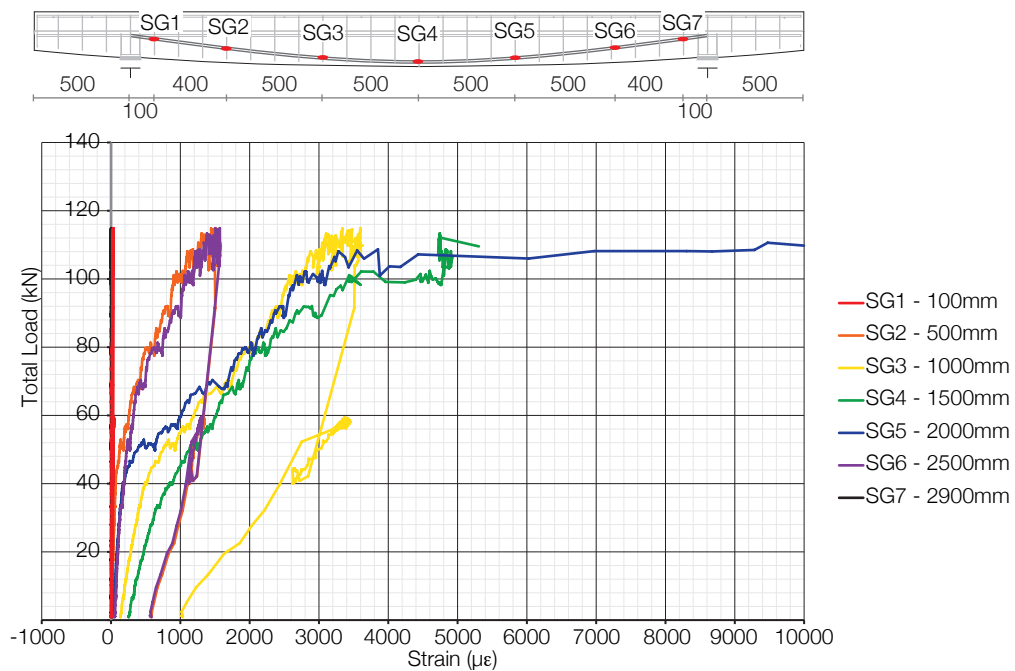


Figure 6.55: Strain gauge results, Beam 5\_3\_H\_F.

#### 6.5.5.4. Beam 5\_4\_H\_F

Beam 4 was loaded to the design value of Load Case 2a before all loads were released. The design value of Load Case 2b was then applied, before all loads were increased in the same ratio and the steel yielded. A maximum load capacity of 132.7kN was recorded. At approximately 53mm central deflection all loads, except for the central point load, were removed. Load was then applied through the central point (P2) only, until the section failed in a ductile manner.



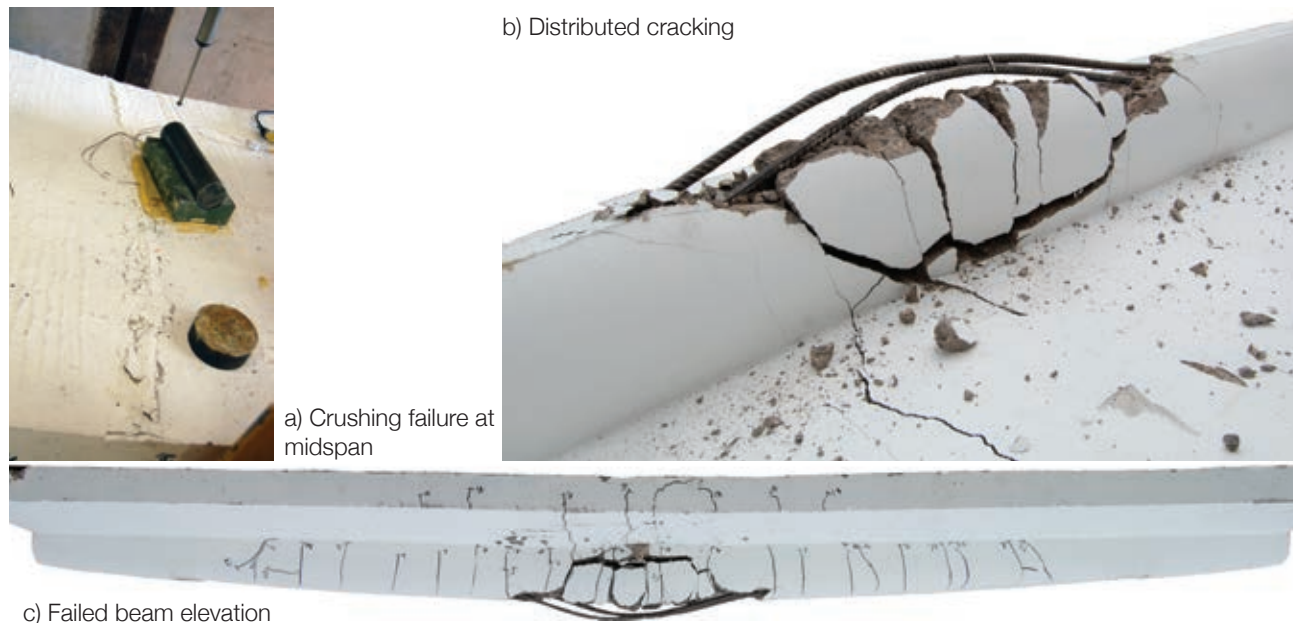


Figure 6.56: Beam 5\_4\_H\_F test photographs and crack patterns.

Photographs of the section under testing and at failure are provided in Figure 6.56. Beam 5\_4\_H\_F was monitored throughout by seven strain gauges applied to the bottom tensile reinforcement (12mm bar), located as shown in Figure 6.57, where strain gauge readings for Load Case 2b until failure are provided.

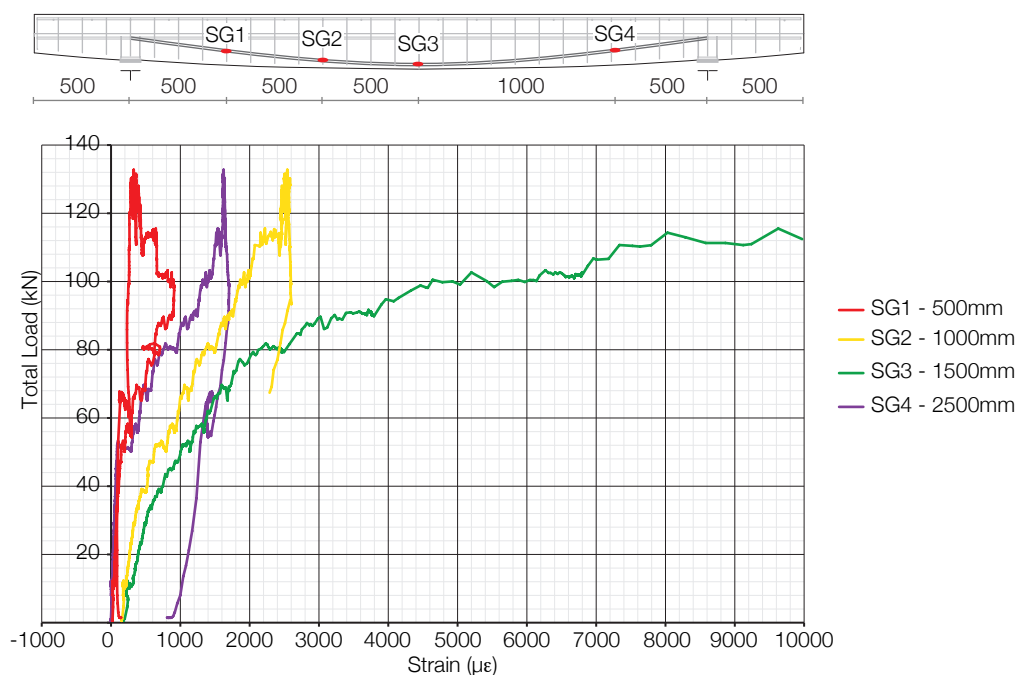


Figure 6.57: Strain gauge results, Beam 5\_4\_H\_F.

#### 6.5.6. Discussion

The test results presented above show that both design methods can be used to successfully avoid premature failures at the supports. In addition, the use of MCFT to assess shear capacity is seen to be successful. By assessing the ultimate moment capacity at the mid span of the beam, and ensuring that the support zone has

sufficient transverse capacity to allow this condition to be reached, the design of fabric formed elements can be achieved successfully.

As discussed in §4.5.7, by designing the beam first to Load Case 1 and then simply adding a 100mm deep slab adds significant capacity to the section that is not required to carry the loads of Load Case 2, as illustrated in Figure 5.14 on page 128. The predicted load capacity of the section at mid span of 107kN is significantly greater than the design load envelope, but corresponds well to the actual load capacity of the section, as is also shown in Figure 6.58.

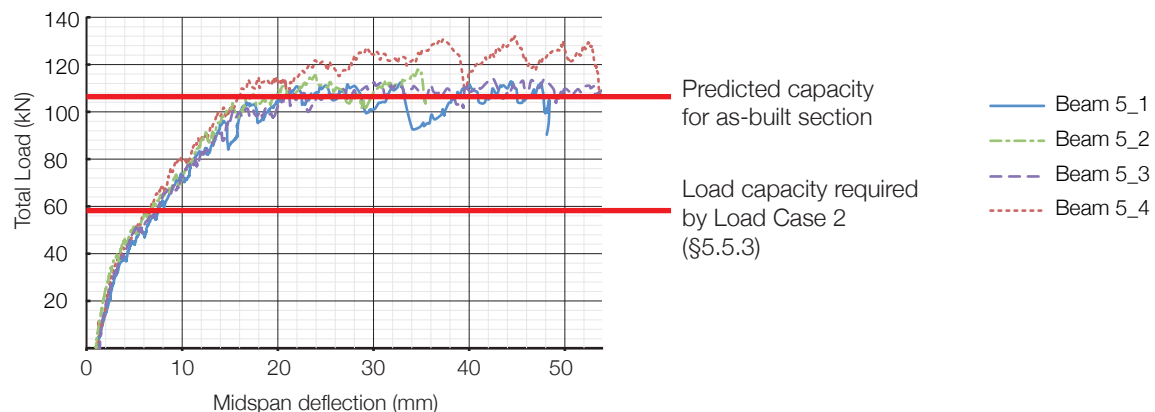


Figure 6.58: Load capacity comparisons, load case 2.

From the above it is now apparent that whilst the beam capacity can be predicted, it has far exceeded the ‘design’ loads required of it. This is quite simply a factor of the two load cases chosen - and by adding a 100mm flat slab to the precast beam (to model the insitu floor slab), significant capacity is gained. Therefore, future work will consider the construction of precast ‘T’ beam elements, in which the top slab may be much thinner, and simply provides the required design load capacity and reduces unnecessary material use.

The results have satisfied the primary aim of this round of testing - showing that ductility can be achieved, and providing new structural test data for fabric formed beam elements. The elements all reached their design loads, and the capacity requirements of §5.5 were met. However, flexural cracking at mid span in the top slab shows that much of the concrete in the slab was not utilised. A more sensible design, discussed below, would consider the use of a variable depth slab that ensures the compression zone is only in compression and flexural cracking is limited to the ‘beam’ element.

Whereas the tests described above model the use of a precast ‘beam’ element with an in-situ concrete slab, future work will instead consider the use of precast ‘T’ and ‘Double T’ beams. Such elements would be designed so as to minimise the presence of flexural cracking in the top slab, thus fully utilising the concrete compression zone. An over topping structural screed would then be used to tie the elements together, as is well understood in conventional precast construction.



Forming the Double 'T' using fabric will be the focus of initial investigations, with structural testing undertaken to ensure that the element utilises its full flexural capacity without failing in shear at the supports.

#### 6.5.7. Conclusion

The tests described above have successfully demonstrated the design and construction methods for fabric formed beams first presented in Chapter 5. The results demonstrate feasible design and construction methods for fabric cast beams whose primary failure mode is in flexure.

This section has demonstrated that fabric formwork can be used in the construction of structurally optimised, low material use, 'T' beam elements. The testing of these elements did, however, demonstrate further opportunities for material use reductions, which are explored in the construction and structural testing of 'Double T' beams, undertaken for the first time here, in the following section.

## 6.6. Double T Beams

### 6.6.1. Introduction

The design and construction of double T beams was undertaken to build on the work described in §6.5 and provide a greater level of optimisation in fabric cast construction. Described below are the results of the construction of one 2m span 'Double T' beam, and two 4m span 'Double T' beams. Further tests were undertaken on Double T beams cast using ultra-high performance fibre reinforced concrete, with this work described later in §6.7.

The beams described in this section are numbered to the following convention:

1. Beam 6\_2\_1: 2m span double T beam (§6.6.2);
2. Beam 6\_4\_1: 4m span double T beam (§6.6.3);
3. Beam 6\_4\_2: 4m span double T beam (§6.6.3).

Concrete compressive strengths for each of the beams at testing is provided in Table 6.21. Beam 6\_2\_1 was cast using the mix described in Table 6.19, which was prepared by the author. The remaining beams were cast using a ready-mix supplier (a C32/40 mix, described in Table 6.20), greatly expediting the construction process. All longitudinal bars were of high yield deformed steel with average ultimate and yield strengths of 664MPa and 567MPa respectively.

Table 6.19: Concrete mix design per m<sup>3</sup>, Beam 6\_2\_1.

Cement (CEM IIbv)	4-8mm aggregate	0-5mm aggregate	Water
304kg	1300kg	614kg	182kg

Table 6.20: Concrete mix design, Beam 6\_4\_1 and 6\_4\_2.

Designation	Aggregate size and type	Cement (BS EN 197-1 (2000))	Consistence	MCC
C32/40	10mm limestone	CIIIA+SR42.5L	70	370

Table 6.21: Concrete mix properties.

Batch	7 Days (1 cube)		14 Days (3 cubes)		28 Days (3 cubes)		At testing (3 cubes)		Testing date
	$f_c$ (MPa)	SD	$f_c$	SD	$f_c$	SD	$f_c$	SD	
1 (Beam 6_2_1)	-	-	-	-	-	-	26.5	1.22	29 days
2 (Beam 6_4_1)			19.1	0.38	22.7	3.35	23.7	1.66	30 days
3 (Beam 6_4_2)	21.4	1.73	-	-	33.8	2.47	31.8	2.64	27 days
Where $f_c$ = average concrete cube (100mm) compressive strength; SD = standard deviation on test results.									

### 6.6.2. Beam 6\_2\_1

Initial work was undertaken on a 2m span element to determine a suitable construction method for the following larger elements. The beam design and reinforcement details are provided in Chapter 5, with material properties for all beams as built given in §6.6.1.

Construction of Beam 6\_2\_1 was undertaken using the double keel mould described in §5.6.3 on page 136 and shown in Figure 6.59. Testing of the beam was undertaken in five point bending, Figure 6.60, to the loading envelope also described in §5.6. Construction of the beam was successful, but difficulties in demoulding of the element led to a change in formwork design for the larger beam elements described in §6.6.3.



Figure 6.59: Construction photos, Beam 6\_2\_1.

#### 6.6.2.1. Testing

Beam 6\_1\_2 was tested in five point bending, as shown in Figure 6.60. The final load versus mid span deflection plot for the beam is presented in Figure 6.61. Beam 6\_2\_1 failed in a brittle shear mode close to its supports at a total load of 11.51kN (at 4.9mm mid span deflection), as shown in Figure 6.62.

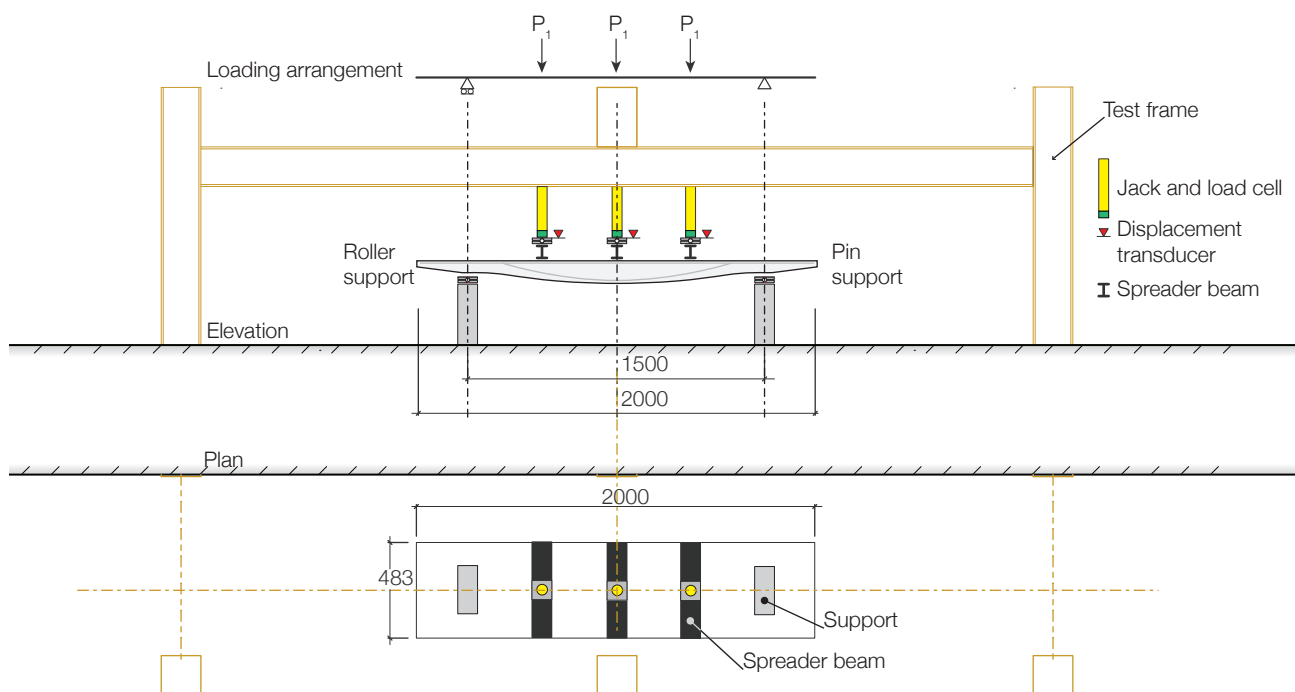


Figure 6.60: Testing arrangement, Beam 6\_2\_1.

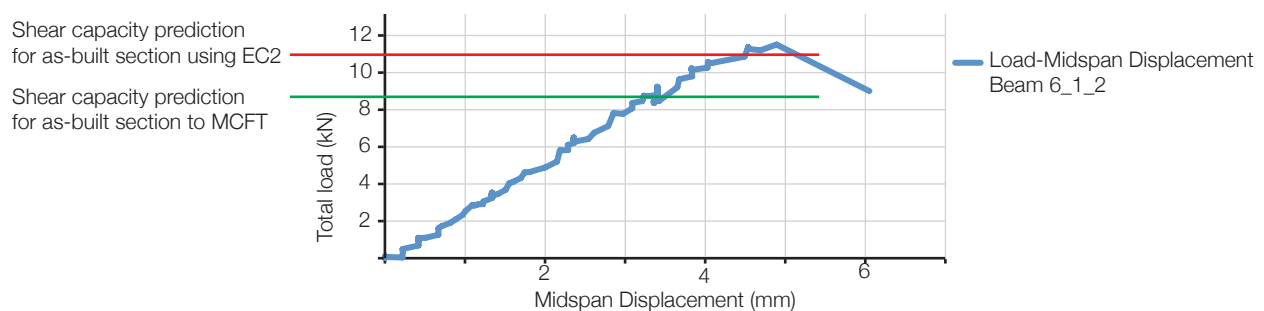


Figure 6.61: Load-deflection, Beam 6\_2\_1.



Figure 6.62: Final failure mode, Beam 6\_2\_1.

#### 6.6.2.1.1. Shear capacity assessment

Beam 6\_2\_1 was not provided with any transverse steel and was thus expected to fail in shear. Analysis of the as-built section using MCFT (carried out using Response-2000 detailed by Bentz, 2000) predicts a capacity for the beam of 8.6kN, as shown in Figure 6.63.

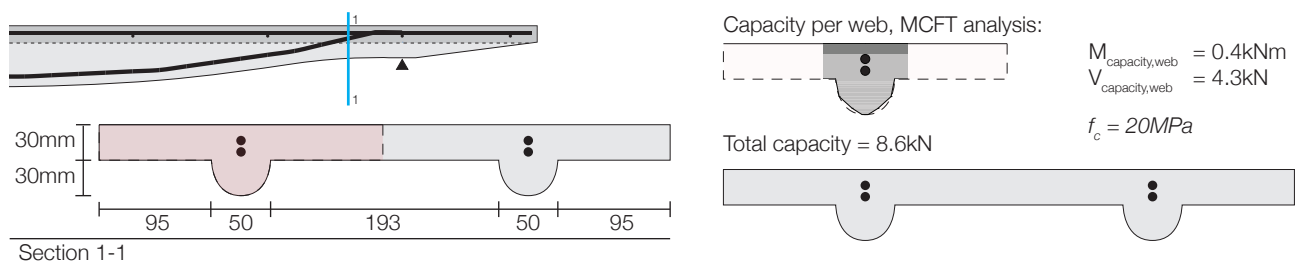


Figure 6.63: Cross section at 100mm from the supports (l); Predicted failure load using MCFT (r).

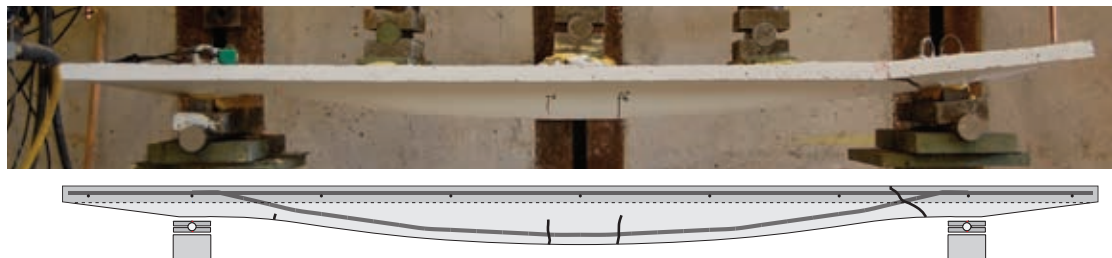


Figure 6.64: Crack locations and reinforcement.

Calculations undertaken using an approach based on BS EN 1992-1-1 (2004) predict a shear capacity for each web of 5.8kN, giving a total capacity for the beam of 11.6kN (as plotted on Figure 6.61). Thus the empirical basis of BS EN 1992-1-1 (2004) in this case provides a less conservative prediction than the MCFT approach.

BS EN 1992-1-1 (2004) §6.2.2:

$$V_{Rd,c} = C_{Rd,c} k (100 \rho_1 f_{ck})^{1/3} b_w d \quad \text{Eq. 6.7}$$

$$V_{Rd,c} = (0.18)(2.00)(100(0.02)(20))^{1/3} (100)(47) = 5.8 \text{ kN} \quad \text{Eq. 6.8}$$

Beam 6\_2\_1 demonstrated a feasible construction method for Double T beams formed in fabric. The test result illustrates the requirement for transverse reinforcement, although relatively accurate failure predictions were

achieved with both MCFT and BS EN 1992-1-1 (2004). In the following, prototype 4m span Double T beams are constructed and tested.

### 6.6.3. Prototype double 'T' beam tests

In light of the tests undertaken and shown above, a series of four metre span double T beams were constructed and tested. The design of these elements is described in §5.6.4 on page 138 with construction and test data presented below. Concrete material properties are recorded in Table 6.21.

#### 6.6.3.1. Construction

Two double T beams (numbered 6\_4\_1 and 6\_4\_2) were constructed in a special fabric mould that was based on work presented in §6.6.2 on page 195 and is shown below in Figure 6.65. Four flat sheets of fabric are firmly secured between two keels, with flat timber plates used to form the support points. Careful construction is required to ensure both beams are symmetrical and that the supports are level. The reinforcement cage is hung in the mould, ensuring that the reinforcement in the webs does not touch the fabric. This was achieved by placing the top slab steel on chairs and hanging the longitudinal reinforcement from it, as illustrated in Figure 6.67.

Lifting eyes were placed at the support points and the moulds were filled with concrete. After curing for at least a week to achieve the required strength to lift the beam, the formwork was stripped by hand. This was made easy by the fact that the keel moulds were not connected to the tables, but were just held in place by the weight of the concrete above. The full sequence of casting and demoulding is illustrated in Figure 6.67, and one of the resulting beams is shown in Figure 6.68. The beam reinforcement layouts are highlighted in Figure 6.69 and Figure 6.70.

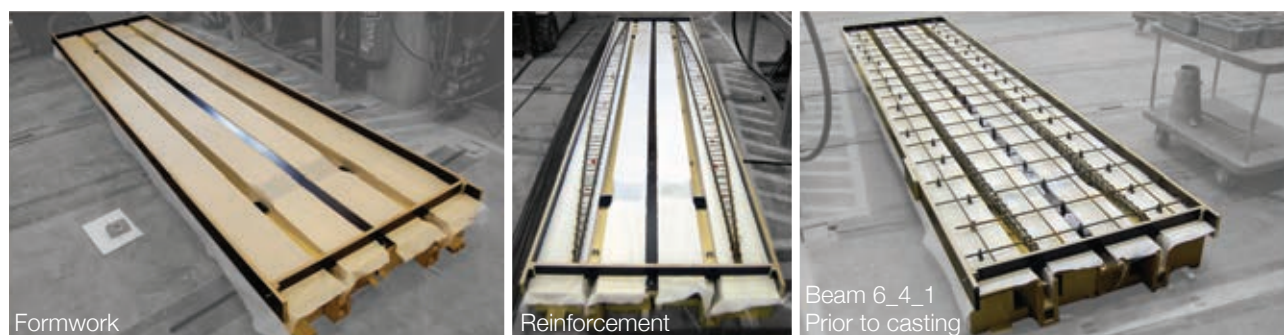


Figure 6.65: Construction of Beam 6\_4\_1.

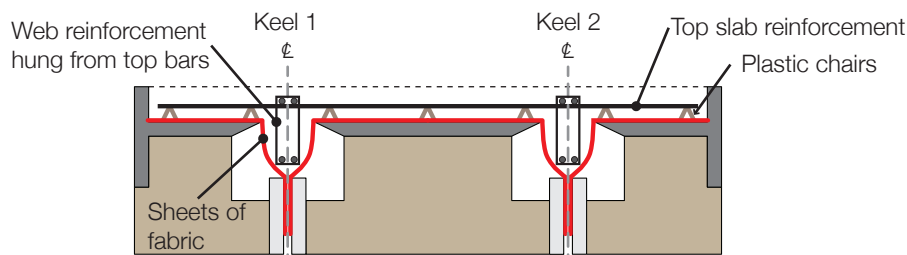


Figure 6.66: Construction details - typical cross section through double T formwork.



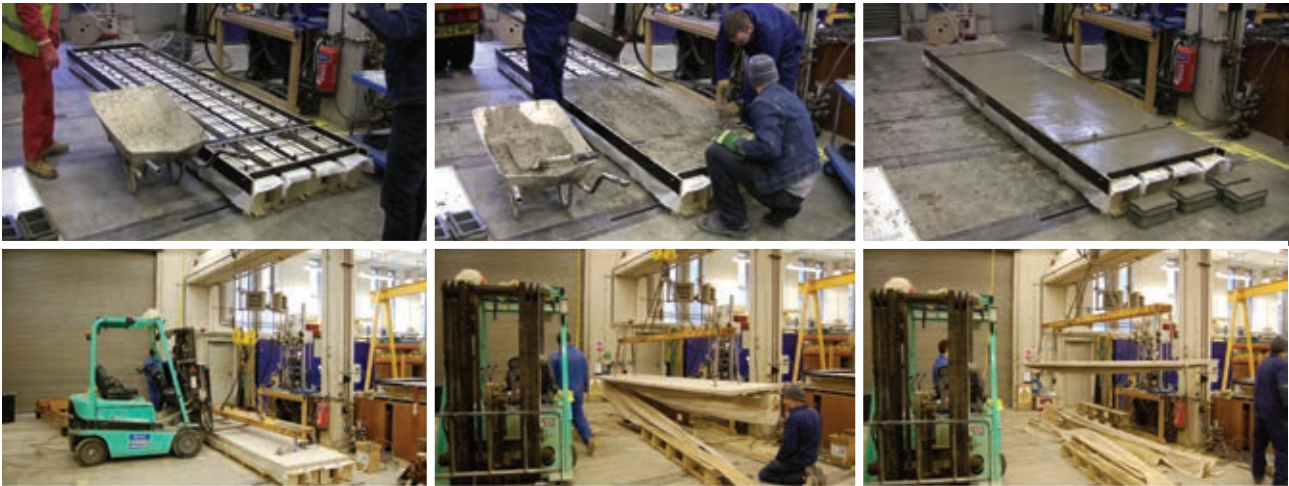


Figure 6.67: Casting and demoulding of Beam 6\_4\_1.



Figure 6.68: Beam 6\_4\_1.

### 6.6.3.2. Beam layouts

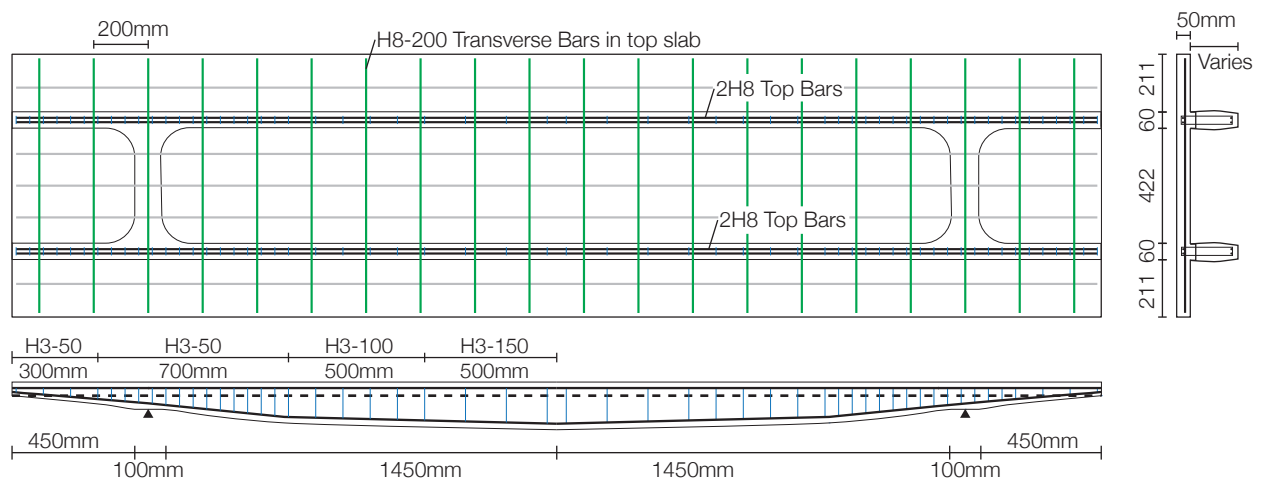


Figure 6.69: Beam 6\_4\_1.

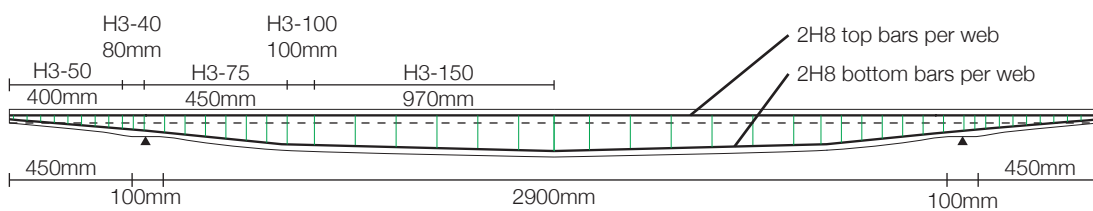


Figure 6.70: Beam 6\_4\_2.

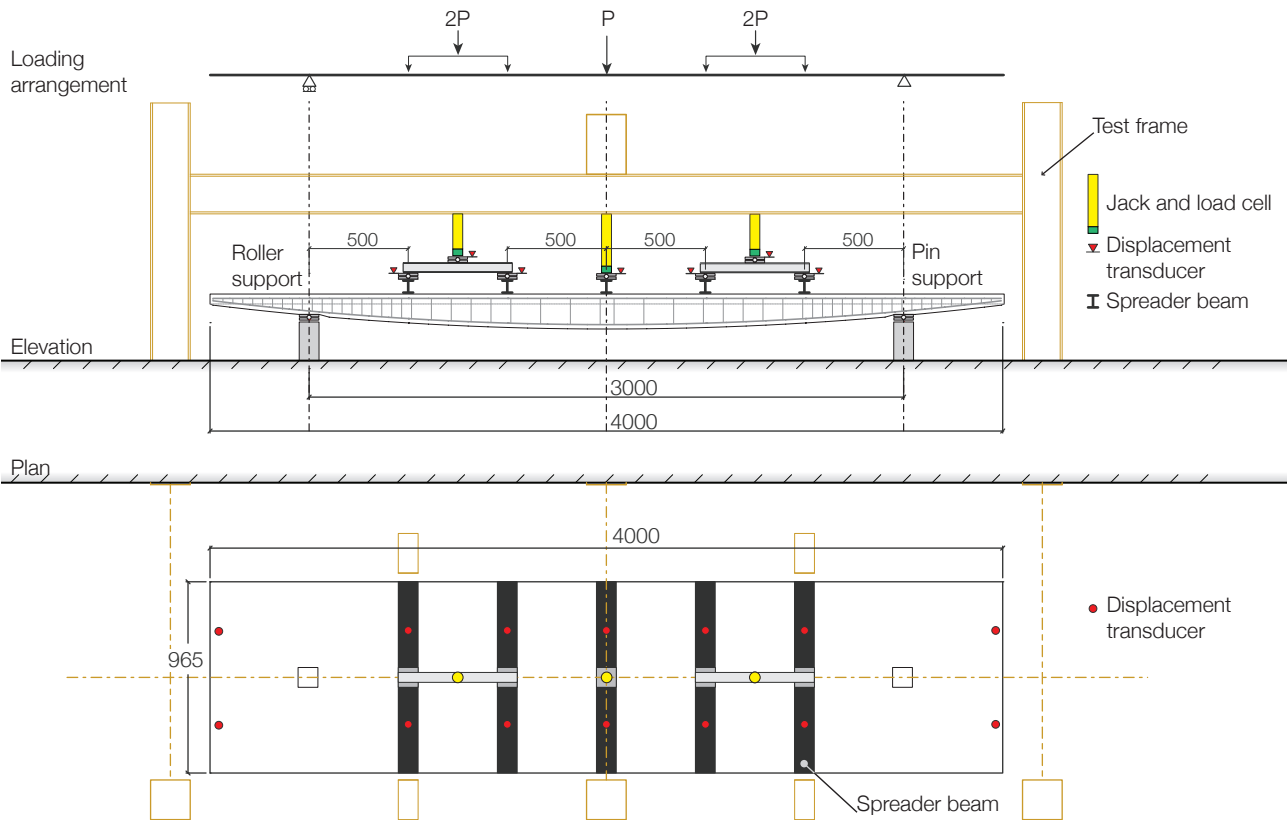


6.6.3.3. Testing

Beams 6\_4\_1 and 6\_4\_2 were tested in accordance with the design presented in §5.6.4 on page 138. Beam 6\_4\_1 was tested in seven point bending to failure (as shown in Figure 6.71 and Figure 6.72), while Beam 6\_4\_2 was tested in seven point bending to 60% of its design load (designated load case (i)) before being unloaded and then tested to failure by the application of two point loads (load case (ii)), as shown in Figure 6.73. Test results for both beams are summarised in Table 6.22.

Table 6.22: Test Results, Beams 6\_4\_1 and 6\_4\_2.

Test	Load Case 1		Failure		Failure mode
	Load (kN)	Mid span deflection (mm)	Failure load (kN)	Mid span deflection (mm)	
6_4_1	30.72kN	21.47mm	34.52kN	87.64mm (maximum)	Flexure
6_4_2(i)	18.43kN	12.87mm	-	-	-
6_4_2(ii)	-	-	34.51kN	84.41mm	Flexure



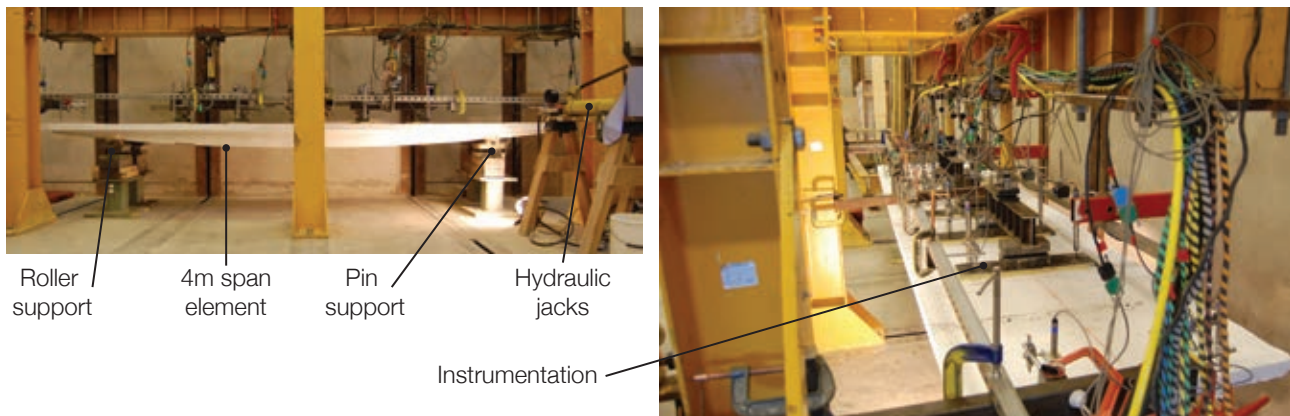


Figure 6.72: Photos of seven point loading arrangement for 6\_4\_1 and 6\_4\_2(i).

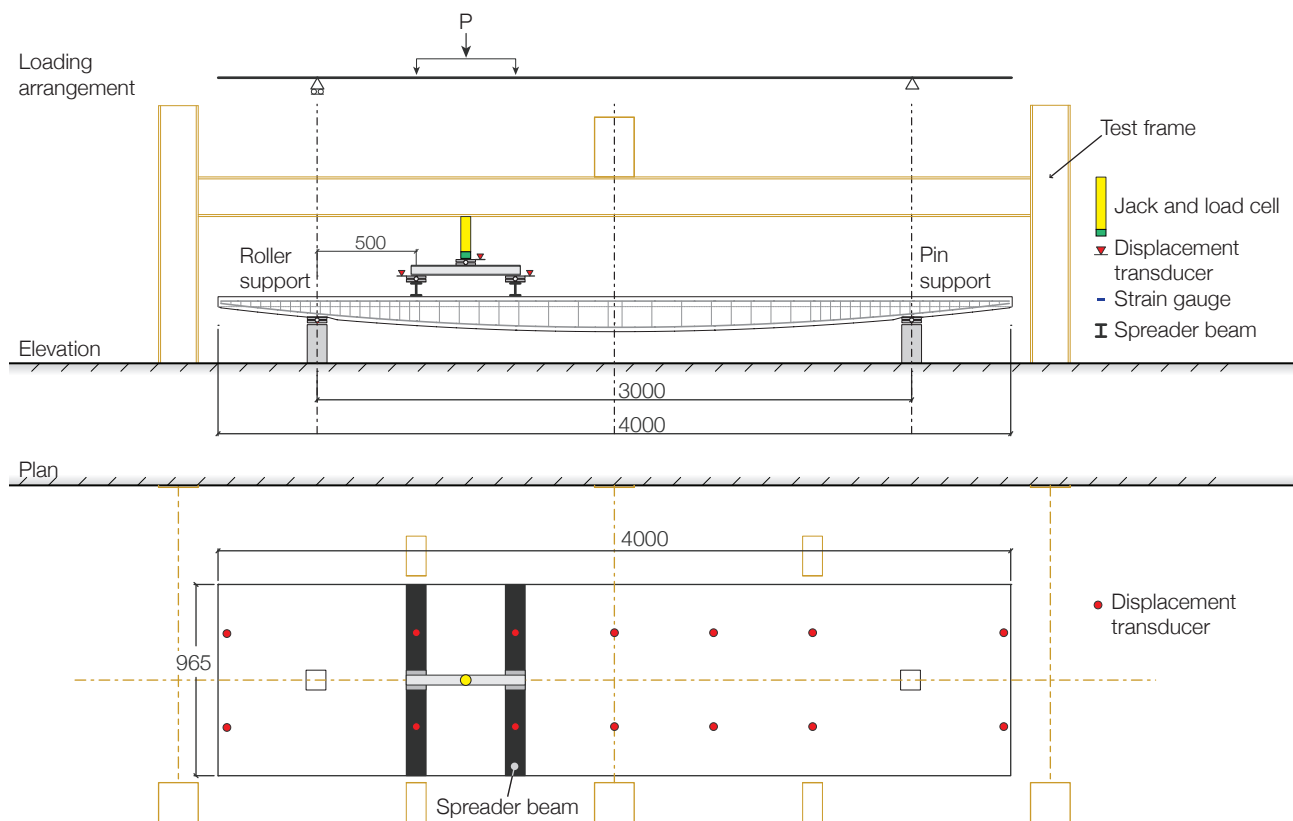


Figure 6.73: Testing arrangement for Beam 6\_4\_2(ii).

#### 6.6.3.4. Results

Beam 6\_4\_1 was tested first with all loads applied in 1kN increments. Upon loading, first cracking was noted at a total applied load of 5kN, after which the cracks propagated as shown in Figure 6.74. A peak load of approximately 33kN was reached at a mid span deflection of 23mm, after which considerable ductility in the beam was seen, with a maximum mid-span deflection of 87.6mm recorded at the end of the test.

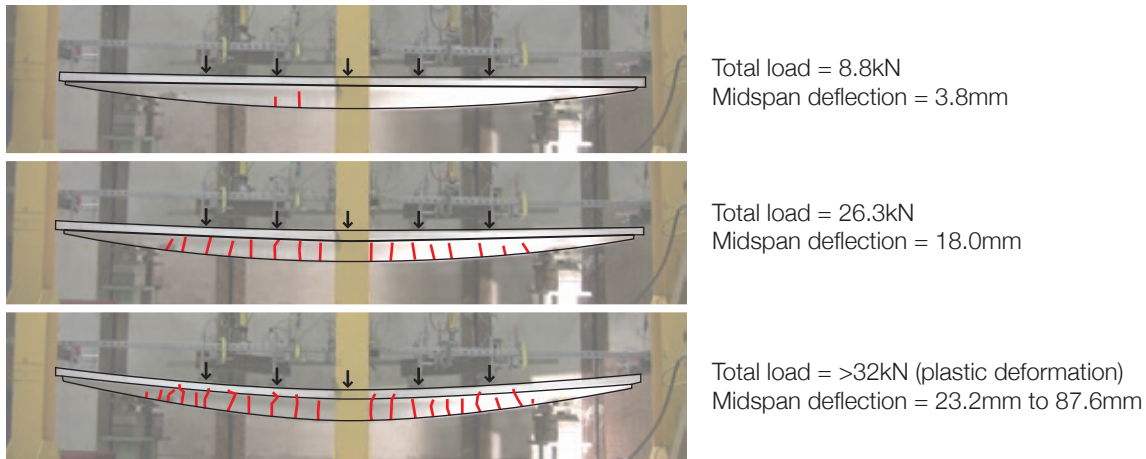


Figure 6.74: Cracking and failure mode for Beam 6\_4\_1.

A load-midspan displacement plot for Beam 6\_4\_1 to failure is presented in Figure 6.75. The beam exceeded the predicted design load by approximately 16% and this is explained by considering the design assumption of the steel yield strength ( $f_y = 500\text{MPa}$ ). Increasing this value of  $f_y$  to 550MPa, a reasonable increase based on steel bar tests, the flexural capacity of the Beam 6\_4\_1 increases to 18.54kNm (from 16.92kNm), which corresponds to an increase in load from 30.72kN to 34.32kN, close to the actual failure load. Photos from the testing and failure of Beam 6\_4\_1 are provided in Figure 6.76 where the considerable deformation can be seen (the maximum deflection was equivalent to around span/30 at the end of the test).

Also plotted on Figure 6.75 is a vertical line located at a common serviceability limit state requirement of span/250 (12mm), where it is apparent that this is achieved at 60% of the design load based on tests carried out on Beam 6\_4\_2.

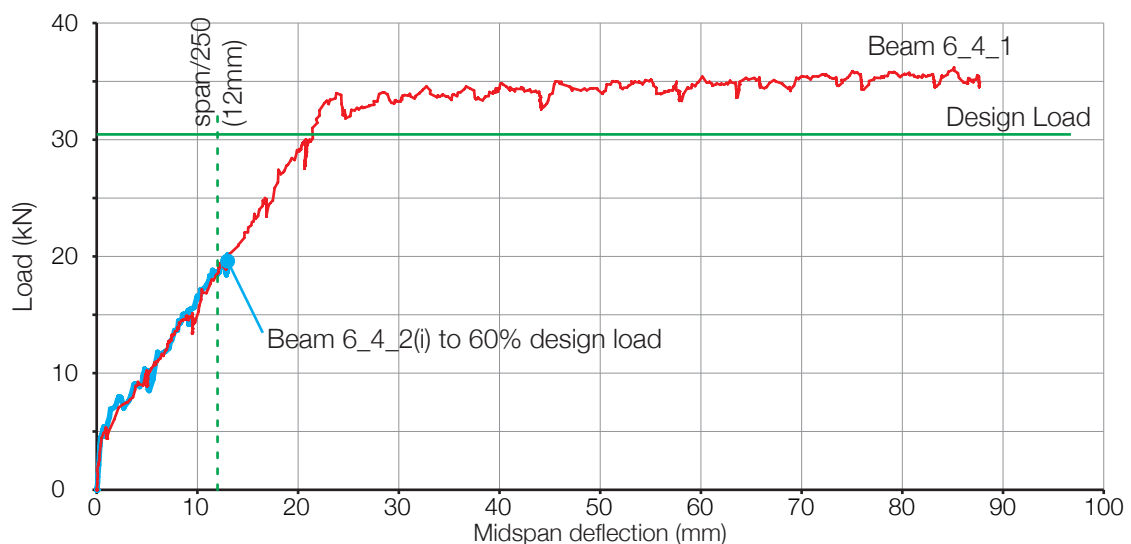


Figure 6.75: Load displacement - Beam 6\_4\_1 and 6\_4\_2(i).

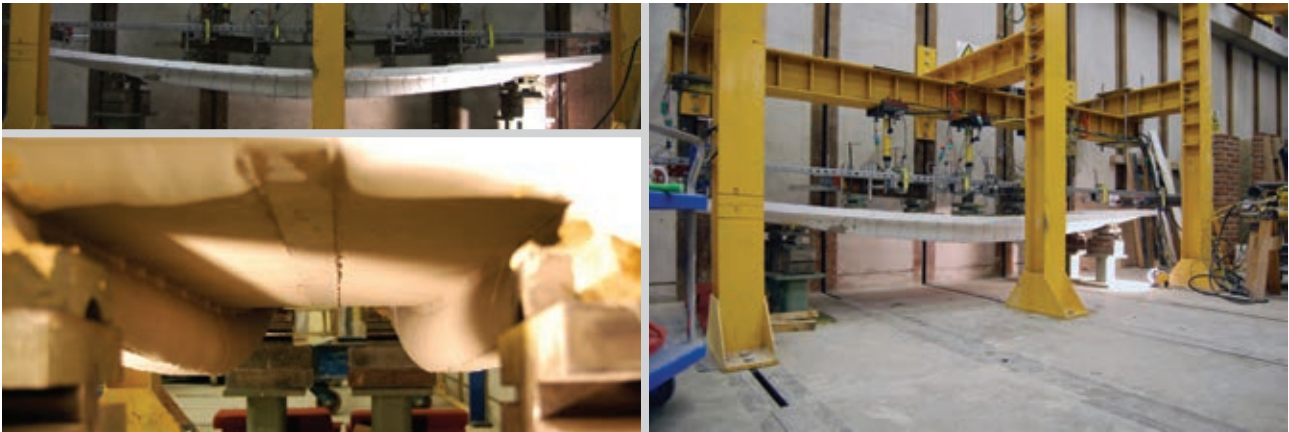


Figure 6.76: Final failure mode for Beam 6\_4\_1.

Beam 6\_4\_2 was then tested in the same loading condition as Beam 6\_4\_1. Its behaviour up to 60% of the design load exactly mirrored that of Beam 6\_4\_1, as shown in the load displacement plot (Beam 6\_4\_1(i) in Figure 6.75). The resulting crack pattern for Beam 6\_4\_2(i) is shown in Figure 6.77.

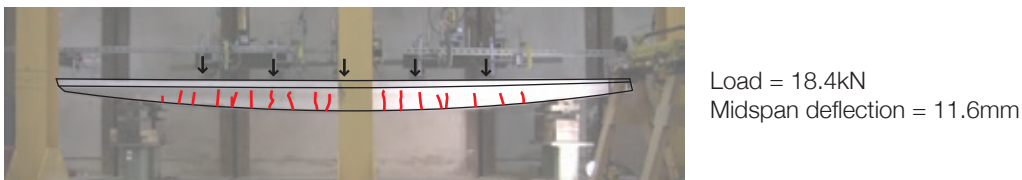


Figure 6.77: Cracking in Beam 6\_4\_2 at 60% of its design load.

Beam 6\_4\_2 was then tested in a second loading configuration (Figure 6.73), with the results of this shown in Figure 6.78, where the displacement at 1000mm from the left hand support is plotted against the total applied load. The results from Beam 6\_4\_2(i) (tested to 60% design load) are plotted as a comparison that shows the residual deformation in test 6\_4\_2(ii) from the previous test (6\_4\_2(i)).

Upon further loading, the Beam 6\_4\_2(ii) exhibited excellent ductility, and after reaching its maximum load of 30kN displayed a plateau of deflection up until approximately 107mm (Figure 6.78). Given the asymmetric loading, the beam deformation was correspondingly asymmetric, as shown in the failure photographs (Figure 6.80). The observed crack patterns for the beam are illustrated in Figure 6.79. Final failure for the beam was seen in crushing of the top concrete slab, as illustrated in Figure 6.80.

The beam design has thus been shown to perform well under the applied loading and has stayed within the failure envelope shown in Figure 5.35 on page 139. The load (Figure 6.73) required to create the design envelope moment in the beam was calculated at 30.2kN, and this was found to correlate well with the measured values presented in Figure 6.78.

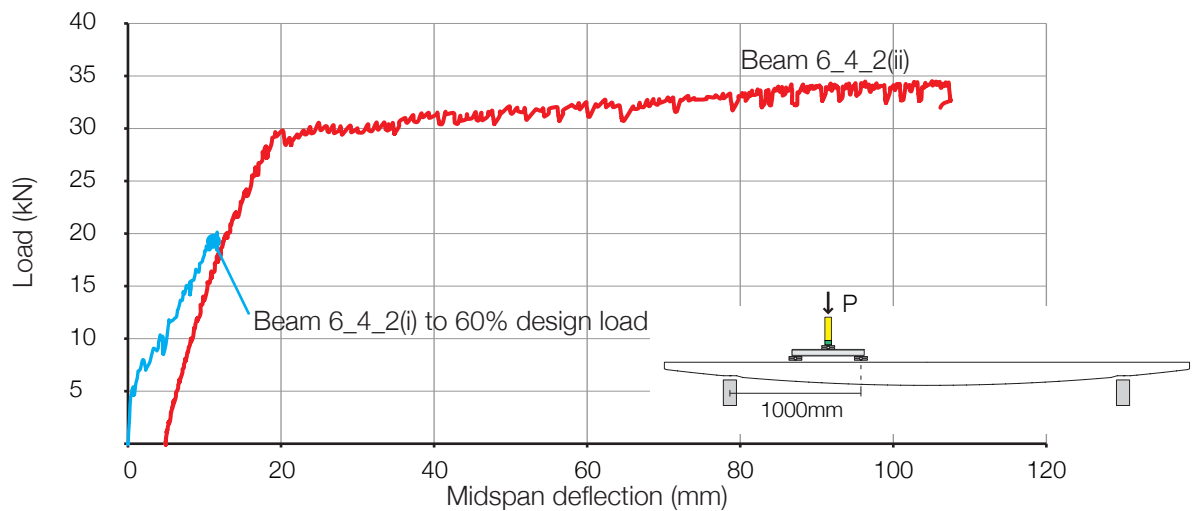


Figure 6.78: Beam 6\_4\_2(i) and 6\_4\_2(ii) test results comparison.

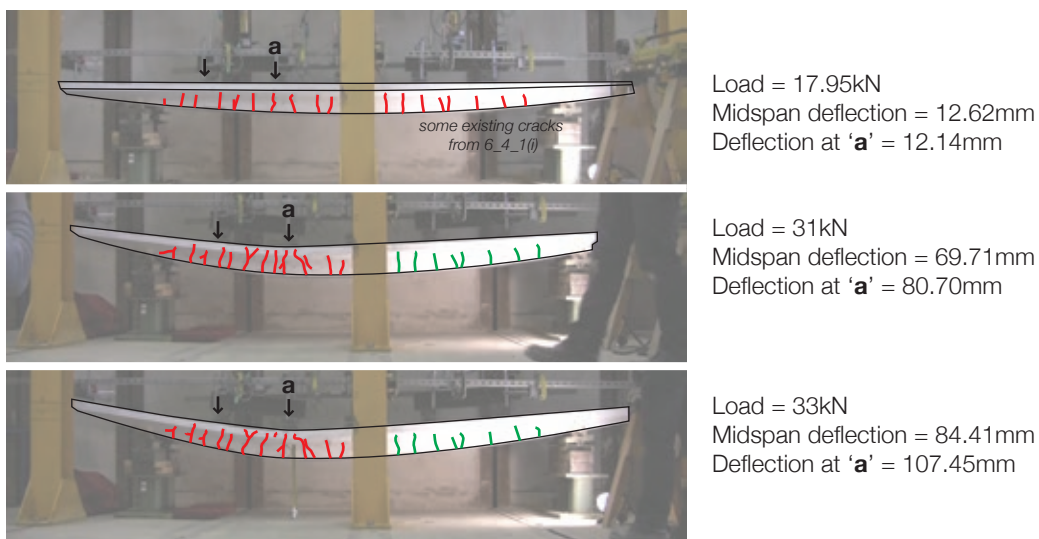


Figure 6.79: Beam 6\_4\_2(ii) crack locations and failure mode.



Figure 6.80: Final failure mode for Beam 6\_4\_2(ii).



#### 6.6.4. Conclusions

Following the publication of the structural tests presented in §6.5 on page 182, double T beams cast in fabric formwork have been designed, built and tested. These beams followed much the same principle as previous tests and showed that better design methods can achieve more efficient designs, as demonstrated by the material savings of up to 78% (Table 5.11 on page 143).

Such results suggest significant reductions in embodied energy are achievable when using fabric formwork, as has been demonstrated in work by Lee (2010) and is shown in Chapter 10. This further demonstrates the importance of fabric formwork in achieving a sustainable concrete construction industry.

The ductile load-deflection response seen in each of the Double T beam tests are desirable, and predictable. The success of the design method to create the beams is further enhanced by analysis in §10.2 on page 409 which shows how their load-deflection response may be predicted prior to testing.

The construction of the 4m span double tee beams was complicated slightly by the large number of links, each of which had different overall dimensions. Whilst this simply slowed down the construction of the prototype elements, such a slow construction process will add significant labour time and in turn, cost. The additional cost could potentially outweigh the economic advantage of the reductions in material use that have been achieved, hampering the implementation of fabric formwork in the cost conscious construction industry.

Whilst the tests were undoubtedly successful, the widespread use of fabric formwork will rely on its cost efficiency. Two further approaches were therefore taken to address this issue. The first approach was to use fibre reinforced polymer reinforcement as an alternative to steel bars. This was successfully achieved using Carbon Fibre grids as shear reinforcement in work that is presented in §8.6 on page 330. The second approach was to investigate the use of advanced concrete technology to facilitate the removal of all the internal transverse reinforcement. This was achieved using an ultra high performance fibre reinforced concrete supplied by Lafarge, design work for which is presented in §5.7 on page 145, with test data presented in the following section.



## 6.7. Ultra high performance fibre reinforced concrete fabric formed beams

### 6.7.1. Introduction

As described in §5.7 on page 145, a unique collaboration with Lafarge has been undertaken to utilise ultra-high performance fibre reinforced concrete (Ductal®) in fabric formed beam elements. Described below is the construction and testing of five beams cast using Ductal®, which are numbered as follows:

1. Preliminary tests on elements without steel reinforcement (Beams 7\_1 and 7\_2), §6.7.2;
2. Single 'T' beam with steel longitudinal reinforcement (Beam 7\_3), §6.7.3;
3. Double 'T' beam with steel longitudinal reinforcement (Beams 7\_4 and 7\_5), §6.7.4

Beams 7\_1 and 7\_2 were designed solely to demonstrate that Ductal® could be cast successfully into fabric, while Beam 7\_3 was reinforced with longitudinal steel bars to demonstrate the feasibility of the design method presented in §5.7 on page 145.

Two 2m span double 'T' beams were then cast to demonstrate the potential for using Ductal® to provide transverse force capacity in sections that are difficult to reinforce with conventional bars. The same Ductal® mix was used for all tests, as detailed in Table 6.23, with compressive test results for each of the beams described in the following sections provided in Table 6.24.

Table 6.23: Ductal® mix proportions (prescribed by Lafarge, July 2010).

Lafarge Mix: Grey Ductal® G2 with Ductal® F2 and metallic fibres			
	Accelerant, Ductal® A2		
	0%	1%	2%
Grey premix G2	25kg	25kg	25kg
Water	1558g	1494g	1429g
Superplasticiser Ductal® F2	342.5g (326ml)	342.5g (326ml)	342.5g (326ml)
Accelerant Ductal® A2	0	149.8g (103.3ml)	299.7g (206.7ml)
Metal fibres	1840g	1840g	1840g
Volume	11.47 litres	11.52 litres	11.56 litres

Table 6.24: Cube strength test results.

Batch	At testing			Testing age
	Number of cubes	$f_c$ (N/mm <sup>2</sup> )	SD	
Beam 7_3	3	166.2	5.16	21 Days
Beam 7_4	2	159.1	5.01	25 Days
Beam 7_5	1	99.7	-	7 days

Where  $f_c$  = average concrete cube (100mm) compressive strength; SD = standard deviation on test results.

### 6.7.2. Preliminary tests

To assess the feasibility of casting Ductal® into fabric, two beams were cast into a single 'T' mould (Figure 6.81 and Figure 6.82). The beams were demoulded after just 12 hours, Figure 6.83. Two beams were cast in this manner without additional steel reinforcement, and one of these was tested to destruction. A third beam was cast in the same mould and the resulting beam is shown Figure 6.87.

Construction of the beams was successful and thus the use of UHPFRC with fabric formwork was demonstrated for the first time.



Figure 6.81: Formwork for UHPFRC beams 7\_1 and 7\_2.



Figure 6.82: Pouring UHPFRC beam 7\_1.

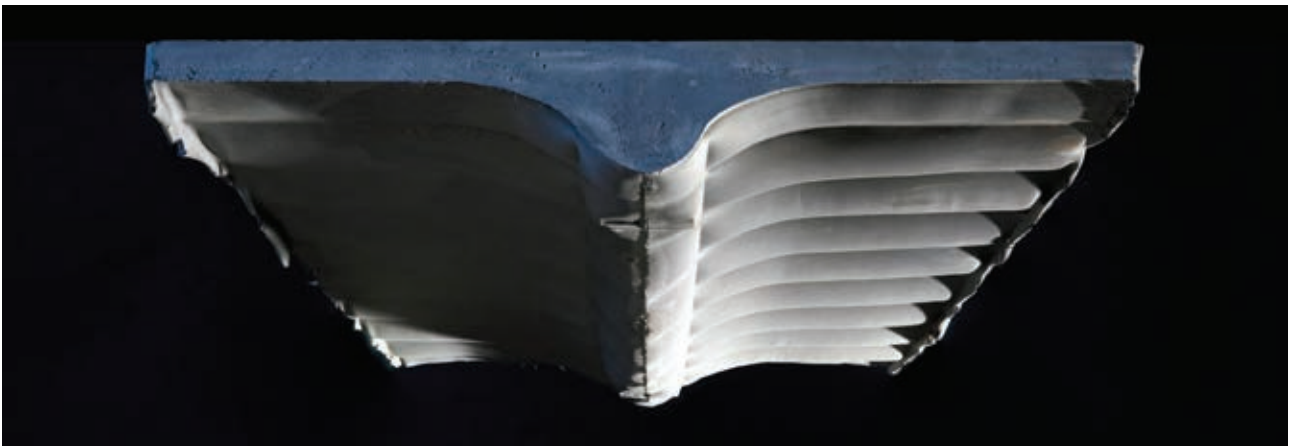


Figure 6.83: Demoulded beam 7\_1.

## 6.7.2.1. Testing

Beam 7\_1 was tested to destruction in three-point bending, as shown in Figure 6.84. Load was applied in 1kN increments and cracking began in the mid span at 9kN. This central crack grew under increasing load until a maximum load of 9.7kN was achieved. The beam suffered no further cracking along its span (Figure 6.85) but began to deflect considerably, as shown in the load deflection plot presented in Figure 6.86. After a mid span deflection of 91mm (span/16) the test was stopped.

Beam 7\_1 demonstrated the flexural strength provided by the steel fibres, and achieved a deformable failure even without internal steel reinforcement. This encouraging result informed the development and testing of the double T beams described in §6.7.4.

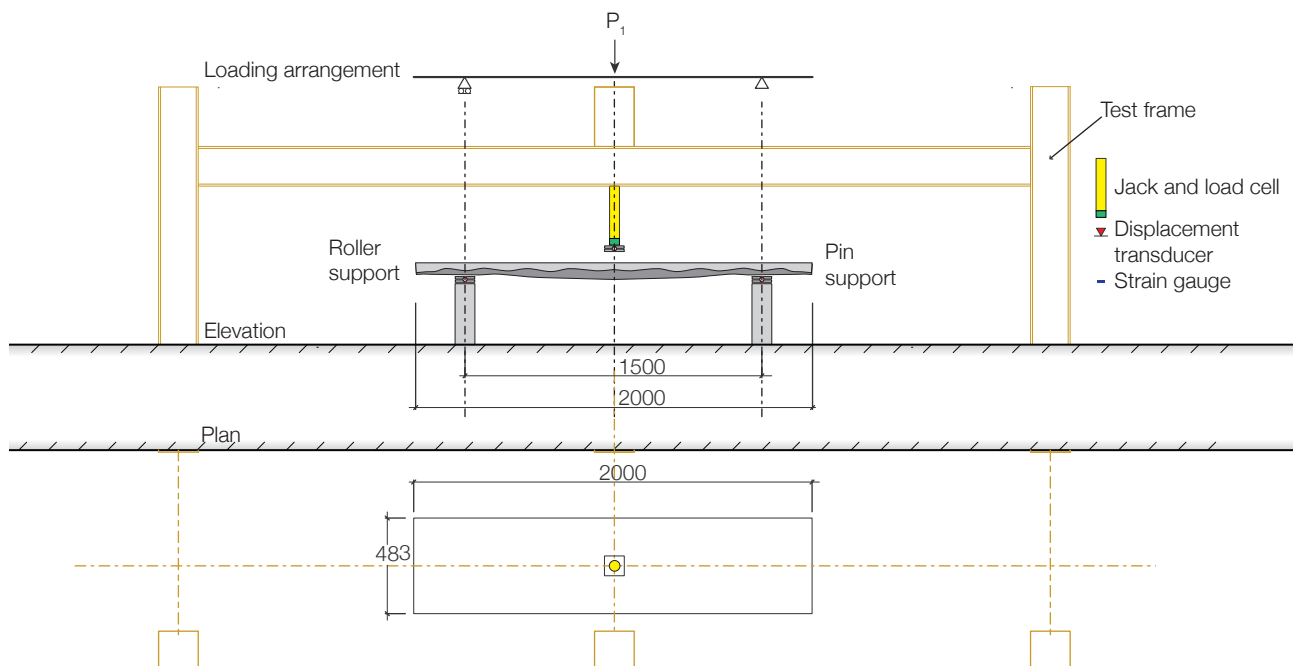


Figure 6.84: Test set up, UHPFRC Beam 7\_1.

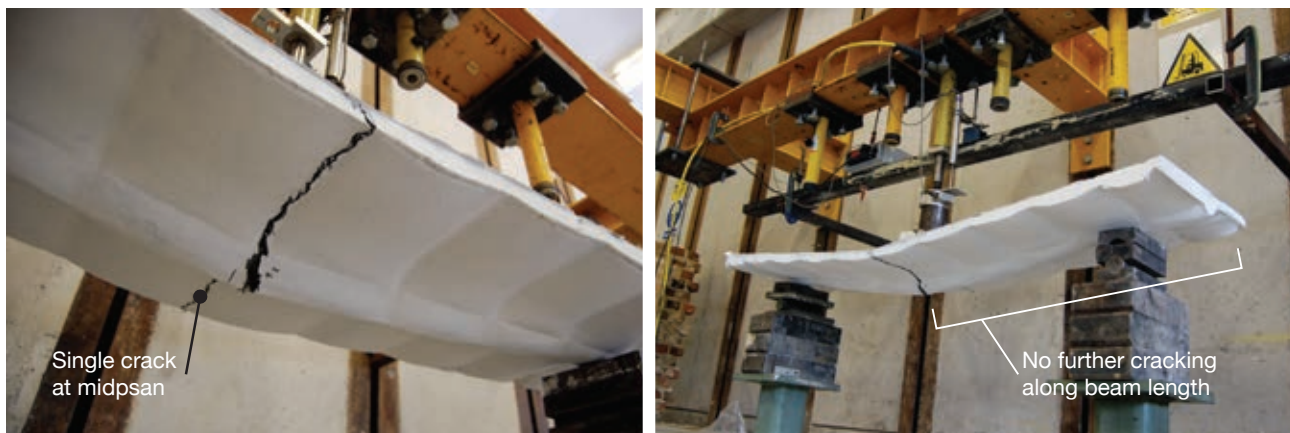


Figure 6.85: Crack distribution, Beam 7\_1.

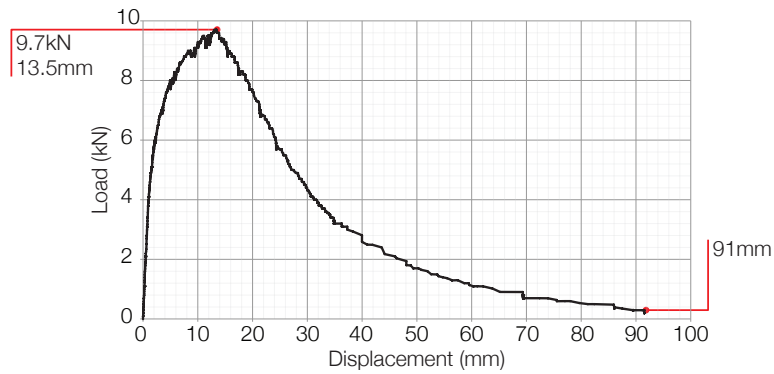


Figure 6.86: Load - displacement response, UHPFRC Beam 7\_1.

### 6.7.3. Development

Following the success of the unreinforced beam tests, Beam 7\_3 was designed and built with internal steel reinforcement, as described in §5.7.3 on page 147.

Beam 7\_3 was tested in seven point bending in the loading frame shown in Figure 6.88 (all monitoring equipment used is also shown). Load was applied incrementally according to the ratio defined in the beam design (see Table 5.13 on page 148). First cracking was recorded at a total applied load of 36.7kN, and cracking was distributed along the length of the beam, although larger cracks were seen at the end with a roller support.

By 53kN total load the cracks had reached and penetrated the top flange of the beam and failure was recorded at a final total applied load of 89.7kN. Failure was recorded in crushing of the compression zone of the beam, as shown in Figure 6.90. The final load-displacement plot is provided in Figure 6.89.

The beam considerably exceeded its design load level, although it should be recognised that this was calculated without considering the additional capacity provided to the section by the tensile strength of the concrete. The increase in load capacity suggests that the steel fibres must be included in the design and analysis of such beams as they provide a significant increase in strength.

Failure of Beam 7\_3 did not occur at the mid span and the beam formed a hinge at its third-span point, as can be seen in Figure 6.90. This suggests the section here was weaker under its ultimate loading envelope than that at the mid-span, although the presence of a roller support may also have influenced the test behaviour.



Figure 6.87: Beam 7\_3 construction (l) and test setup (r) photos for Beam 7\_3.



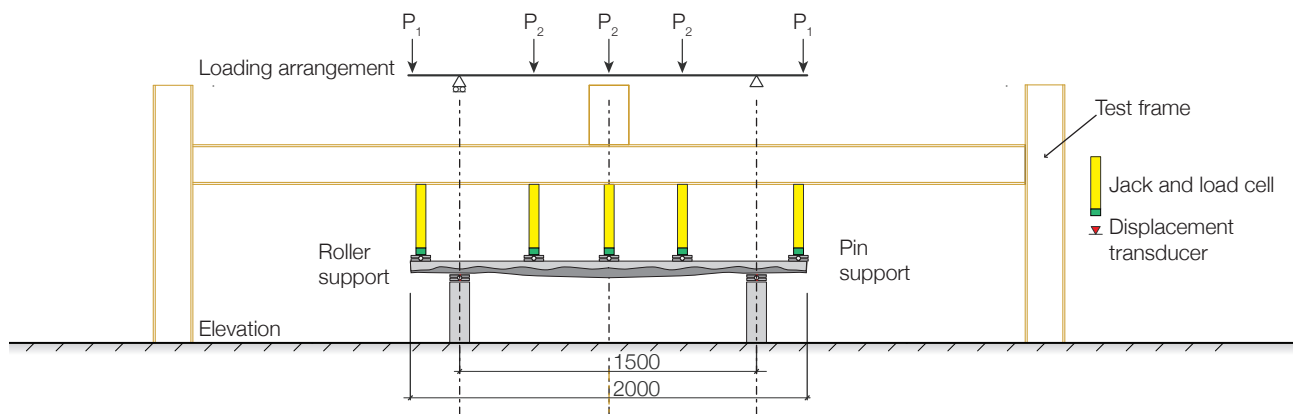


Figure 6.88: Test set up, Beam 7\_3.

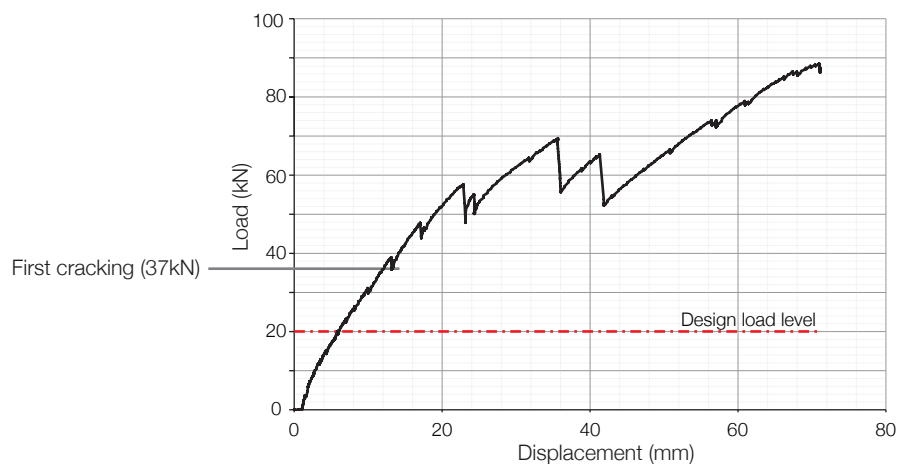


Figure 6.89: Load-deflection, Beam 7\_3.

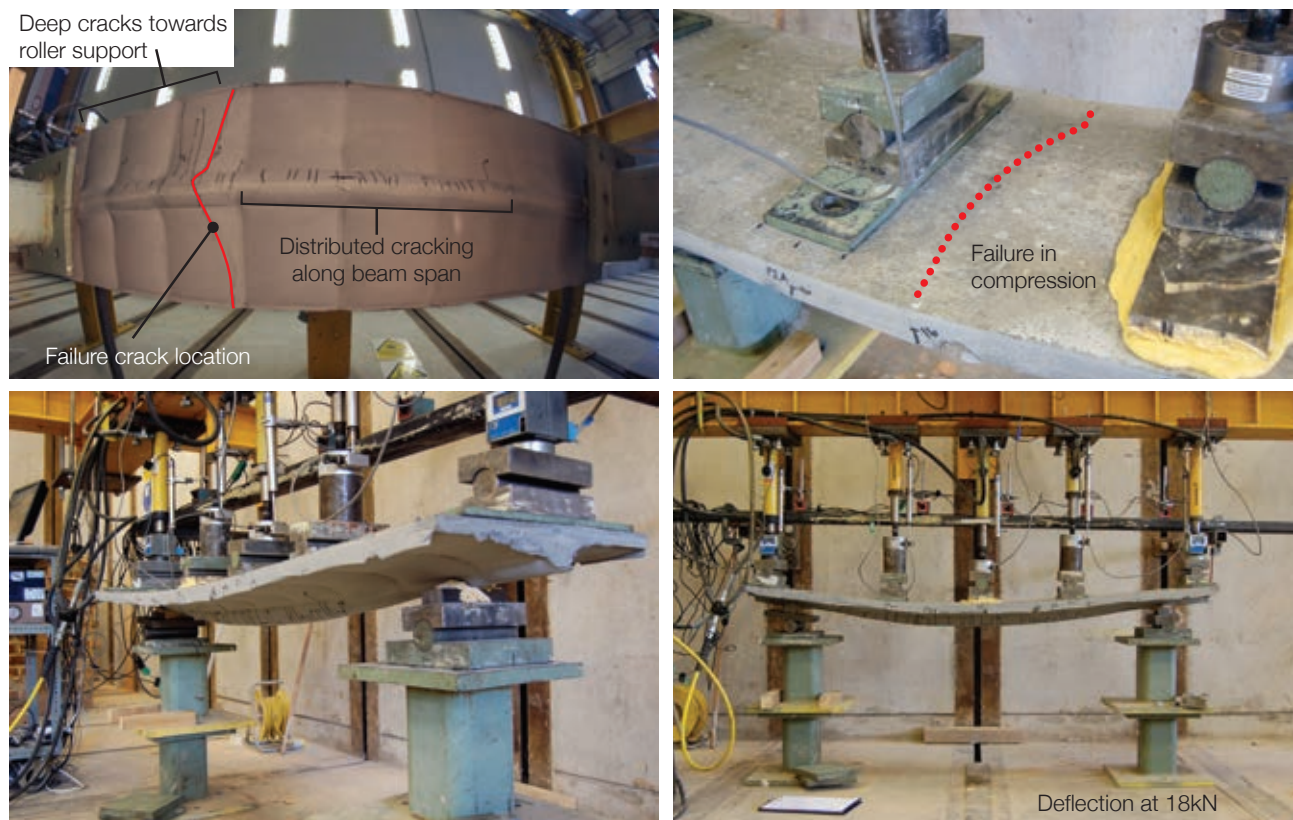


Figure 6.90: Failure mode and photographs - Beam 7\_3.

Following the single T beams described above, two further 'Double T' beams were designed and tested using UHPFRC. The various reasons why such elements are desirable was discussed in §6.6 on page 195. The results of the construction and testing of these beams is described below.

#### 6.7.4. Double T Beams using UHPFRC

The provision of adequate shear reinforcement in beams with constantly varying cross sections is difficult. One solution to this problem is to use UHPFRC to provide the tensile capacity required to carry the shear applied to the beam. This theory was tested by reconsidering Beam 6\_2\_1 (see §6.7.4 on page 211) which failed in shear, and casting the same design using Ductal®.

Structural design calculations are provided in §5.7.4.3 on page 151, where shear capacity is provided by the tensile strength of the concrete and the vertical component of force in the inclined longitudinal bar. The construction sequence is illustrated in Figure 6.91, with the resulting beam being shown in Figure 6.92. Two beams (7\_4 and 7\_5) were cast in the same mould.



Figure 6.91: Construction sequence, Beam 7\_4.

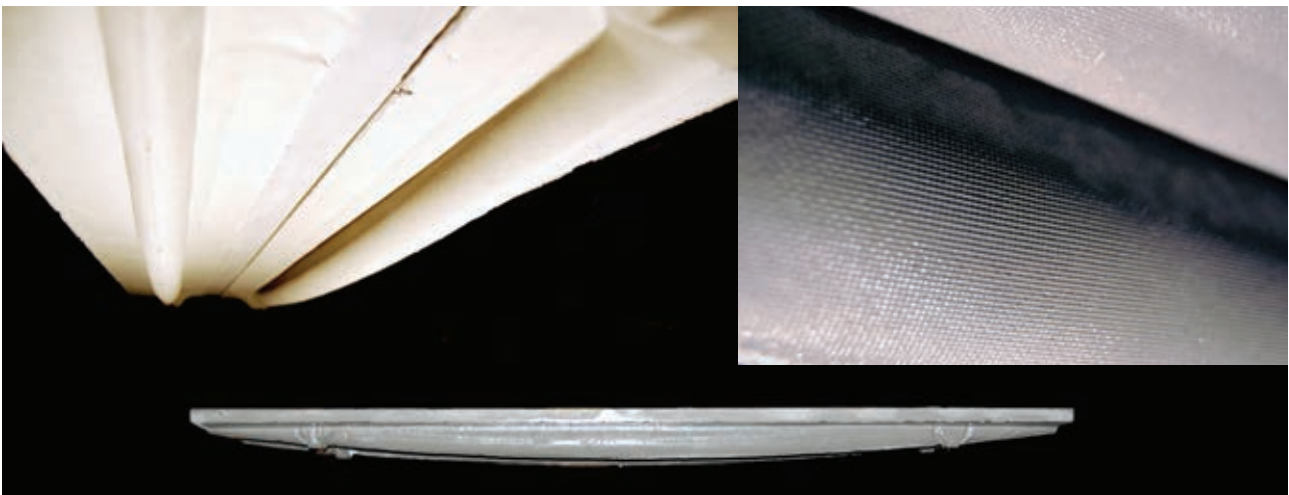


Figure 6.92: Double T Beam cast using Ductal®.

##### 6.7.4.1. Structural testing

Both beams were loaded in five point bending in 1kN increments (load  $P_1$ , applied through the test frame shown in Figure 6.93) and displacements were monitored at each load point. The beams were tested at different ages, and hence the concrete strength was quite different (Table 6.24 on page 206). However, the lower concrete



strength in Beam 7\_5 actually has relatively little influence on the theoretical beam capacity, which is limited to a greater degree by the capacity of the longitudinal reinforcing bar.

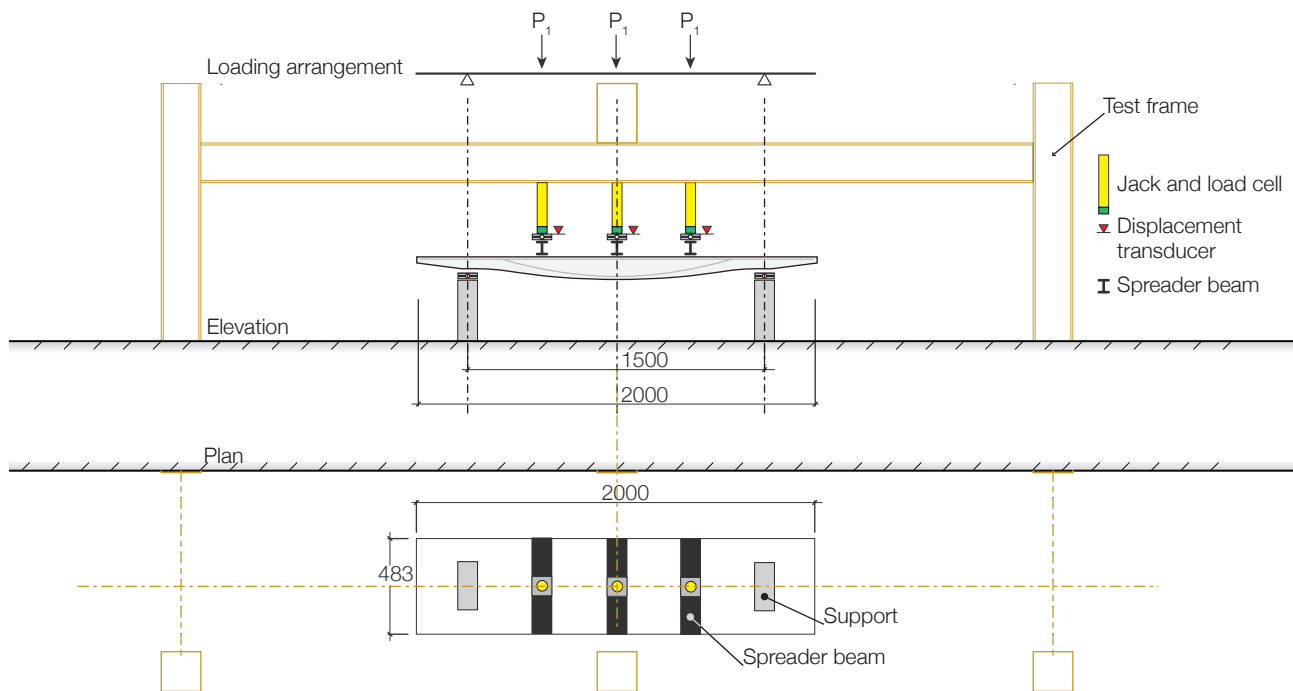


Figure 6.93: Testing arrangement, Beams 7\_4 and 7\_5.

Photographs of the beam through the loading stages and at failure are provided in Figure 6.94. A load-midspan deflection plot is provided for both beams in Figure 6.95, where it is apparent that the flexural load capacity predictions using a concrete tensile strength of 10MPa are quite accurate. Beam 7\_5 was slightly under capacity, and its internal steel reinforcing bar was found to snap at the point indicated in Figure 6.95.

Plotted alongside the test results for Beams 7\_4 and 7\_5 in Figure 6.95 is the results of Beam 6\_2\_1, which had the same external geometry and internal reinforcement, but was cast using an Ordinary Portland Cement Concrete. The difference in behaviour is stark, and demonstrates how UHPFRC can be used to guard against shear failures to facilitate increases in flexural capacity.

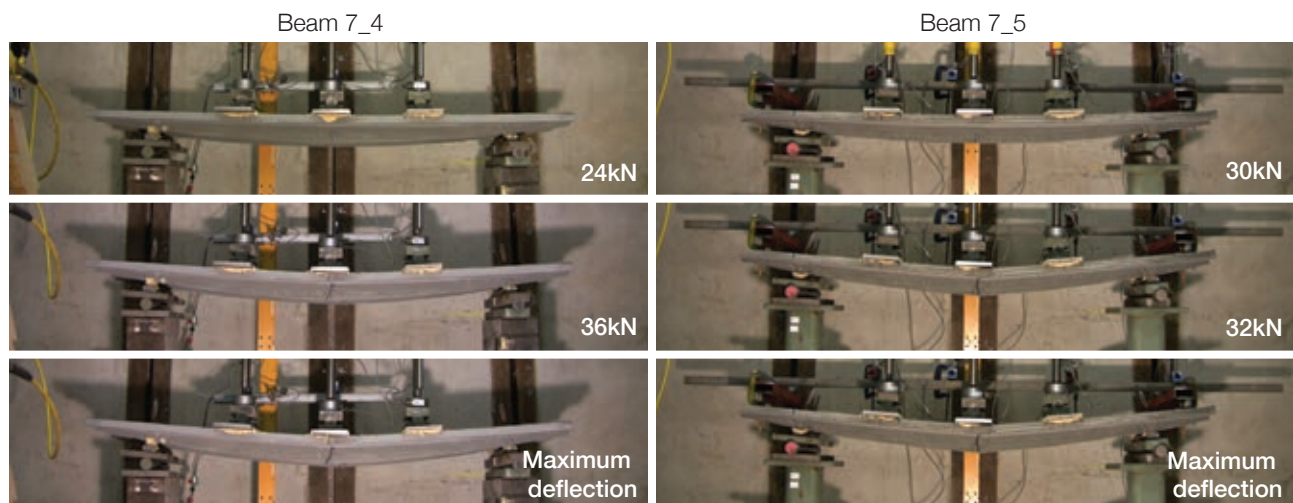


Figure 6.94: Test photographs, Beams 7\_4 and 7\_5.

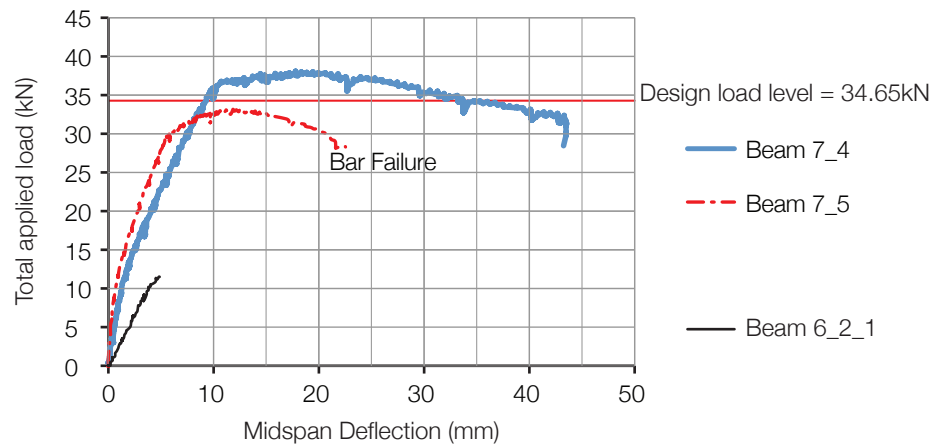


Figure 6.95: Load-midspan deflection, Beams 7\_4 and 7\_5.

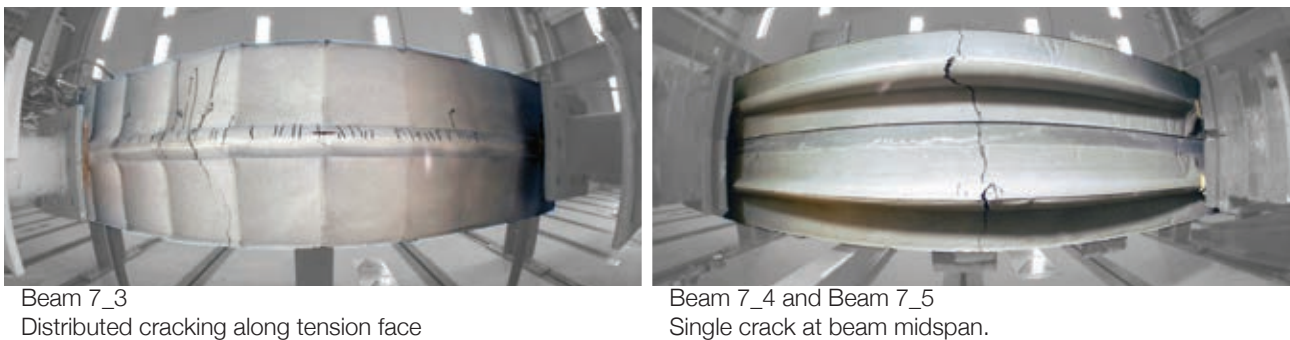


Figure 6.96: Cracking comparison.

Both Double-T beams failed in flexure, showing some ductility at their peak load. However, the failure mode and crack pattern in both beams was considerably different to that seen previously in Beam 7\_3. A comparison between the two sets of tests is shown in Figure 6.96.

The behaviour of Beam 7\_5 is not considered to be typical of Ductal® cast beams and is thought to have arisen because of a construction error. In general, bars inside fabric formed beams are not welded - in Beam 7\_5 a vertical spacer had been welded to the longitudinal steel at mid span. Post failure assessment (Figure 6.97) showed the location of this weld to correspond to the position of failure, suggesting excessive strain hardening had taken place prior to the application of load.

A sample of steel, taken from around the third-span position, was then tested in tension, where it was found to display considerable ductility (>10%), as shown in Figure 6.97. This result is in line with other tests undertaken on steel bars used in the preparation of all tests in this thesis, and corroborates that it was a localised failure as a result of a construction error.

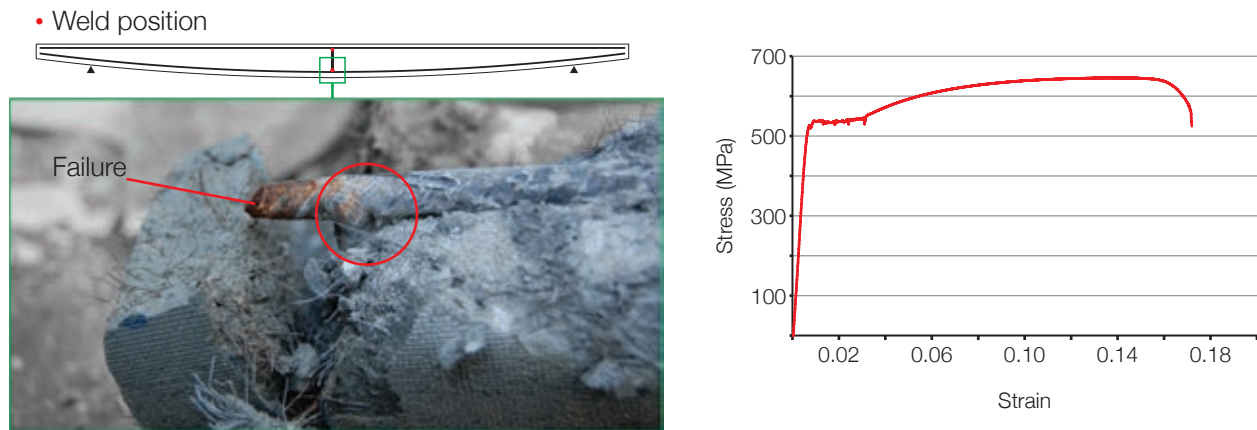


Figure 6.97: Failure location (l) and steel properties (r) in Beam 7\_5 tested on coupon extracted from the failed beam at the quarter span.

#### 6.7.5. Conclusions

The model UHPFRC beams demonstrated that fabric formwork may be used as an economic alternative to timber moulds for complex structures, allowing optimised shapes to be easily be cast. This work has demonstrated to the Lafarge technical team that fabric formwork may indeed be used with Ductal®, and a wide range of future work is planned (Chapter 12).

With the structural test data showing that reasonable capacity predictions and optimisation may be undertaken using the design models presented in Chapter 6, further analysis is give in Chapter 10 where the full load-deflection response of the UHPFRC Fabric Cast beams is predicted and verified against the test data.

The results of the small structural test may prove useful for later analysis and design techniques using Ductal®, although it is envisaged that such an element would include some active or passive reinforcement. This is an area of continuing development that is being partly assisted by the technical team of Lafarge, Paris.

## 6.8. Material use

A summary of the beam tests undertaken in Chapter 6 and their relative savings in material use is provided in Table 6.25. Alongside this information is a summary of further testing undertaken by others, whereupon the improvements in design method and construction can be seen. This material use data again demonstrates that fabric formwork may be used in conjunction with simple optimisation routines to create architecturally interesting, structurally optimised concrete structures.

Table 6.25: Material savings demonstrated in Chapter 6.

Beam description	Material saving when compared to equivalent strength prismatic element	Reference
4m span T Beam	35-40%	§5.5.6 on page 134
4m span double T Beam	26-78%	Table 5.11 on page 143
2m span UHPFRC beam	NA	
4.2m span bending moment shaped beams	30%	Hashemian, F., 2012
3.16m span T beams	40%	Lee, D., 2010
2m span bending moment shaped beams	30-50%	Bailiss, J., 2006
2m span bending moment shaped beams	40%	Garbett, J., 2008
<b>Average:</b>	<b>41%</b> (upper and lower average values 33.5% and 46.3%)	

## 6.9. Conclusions

Chapter 6 has demonstrated that the methods presented in Chapter 5 may be used to design and construct optimised, fabric cast concrete beams. The body of test data described above satisfies one of the aims presented in the testing matrix (§5.4 on page 122), addressing the flexural design and behaviour of variable section beams.

The research presented in this chapter, and supported by further analysis in Chapter 10, has demonstrated that:

1. Anchorage of steel and FRP bars may be achieved using the 'splayed bar' method;
2. A maximum material saving of 78% was achieved in a fabric cast beam failing in flexure, when compared to an equivalent strength prismatic beam;
3. Overall material savings of between 30% and 40% could readily be achieved in concrete construction by undertaken simple optimisation processes and using fabric formwork as the construction process;
4. Ultra-high performance fibre reinforced concrete can successfully be used in fabric formed elements, and its use should now be extended to panels, slabs and shells for full effect.

To facilitate the use of fabric formwork, a design method that accurately addresses the shear behaviour of non-prismatic concrete beams is required. This issue, which has previously been of concern, is addressed in the following chapter. Combined with the results presented here, a full design method is presented in Chapter 11.





# Chapter 7      Design (2)

## Shear behaviour

### 7.1. Introduction

In Chapter 5, Detailed Design Sections 1, 2, and 3 (§5.5, §5.6 and §5.7 respectively) led to a considerable program of structural testing and analysis that was presented in Chapter 6. In Chapter 7, Detailed Design Section 4 (§7.2 on page 218) considers the shear behaviour of tapered and non-prismatic concrete beams. Structural testing and results are then presented in Chapter 8.

The aims of this thesis, as described in the testing matrix (§5.4 on page 122), are addressed in Chapter 7 and Chapter 8 through the consideration of the shear behaviour of variable cross section concrete beams. Chapter 7 begins by considering the application of the compressive force path method to variable section beams, before comparisons are made to with BS EN 1992-1-1 (2004). A new strut and tie based approach is then presented. All structural test data and results are shown separately in Chapter 8.

Analysis of the tapered beam tests is also provided in Chapter 8, where the use of digital image correlation techniques is presented for the analysis of concrete structures that has provided new insights into the behaviour of tapered beams in shear.



## 7.2. Detailed Design 4 - Variable section members in shear

### 7.2.1. Introduction

The development of a comprehensive design model for fabric cast beams requires that both their flexural and shear behaviour is well understood. In this section, the shear behaviour of tapered reinforced concrete beams is assessed in detail with the view of providing such an approach. Test data and analysis of the designs presented below is given separately in Chapter 8 on page 245.

Four sets of test data are presented. Initial work considered how the Compressive Force Path method could be applied to tapered beams subject to uniform loading, with the aim of showing a transition point between flexural and shear failures. This is presented in §7.2.2.

Following from the result of this testing program, three further test programs on a total of 19 tapered reinforced concrete beams were undertaken. In these, non-prismatic elements subject to point loads applied at various shear spans were design according to BS EN 1992-1-1 (2004), the Compressive Force Path Method, as well as a new strut-and-tie based approach. The methodology behind these tests is described in §7.2.3 on page 227.

A distinct requirement for clear guidance on the behaviour of tapered beams in shear is apparent in previous work (§2.5 on page 27) and this section, along with the test data and analysis presented later, serves to begin to satisfy this requirement. As such, it builds on the successful testing of the flexurally dominated beams described in §5.5-§5.7 above to provide a complete method for the design of fabric formed elements such that the central thesis of this work can be satisfied to ensure that fabric formwork can facilitate a sustainable future in concrete construction. The relevant test information is provided in Chapter 8 and analysis of these results is summarised in Chapter 10.

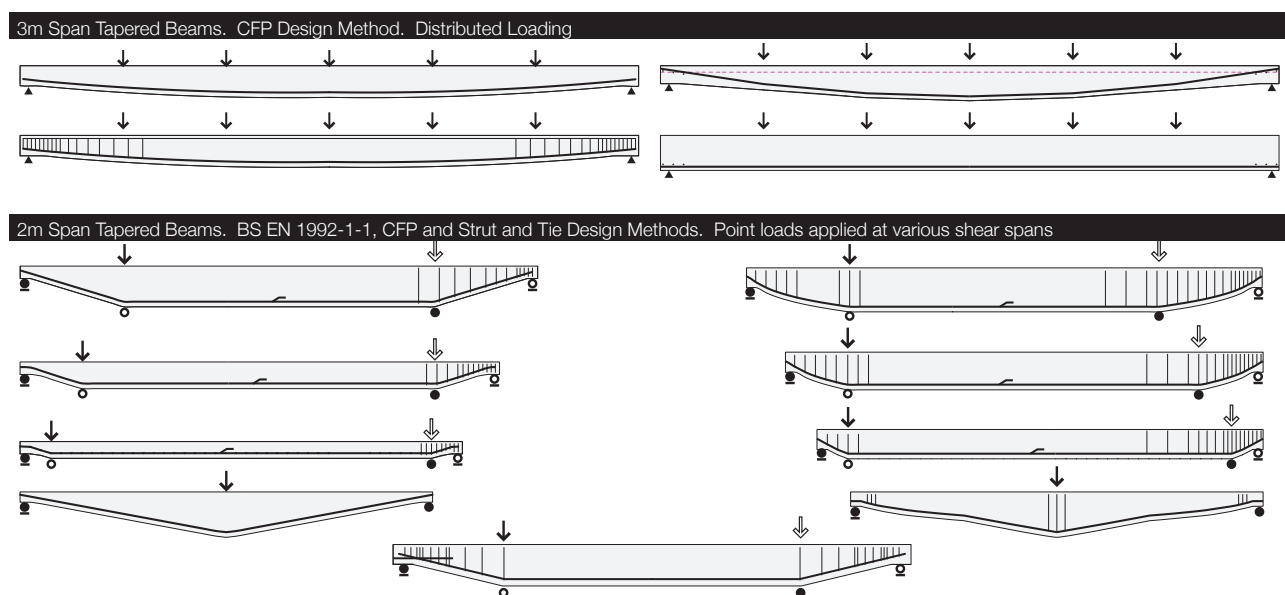


Figure 7.1: Summary of variable section members tested to assess shear capacity.

### 7.2.2. Variable section beams using the compressive force path method.

The compressive force path method was introduced in §4.2.5.2 on page 89, but to this point has not been used in the design of variable section beams.

The compressive force path method is applied to the design of reinforced concrete beams by considering the two potential failure modes for the section: ductile flexure or brittle flexure-shear. The flexural resistance of a section is determined by considering the theory of plane sections, while the combined flexure-shear resistance is determined by empirical equations based on original tests by Whitney (1957) that were later modified by Bobrowski and Bardhan-Roy (1969) and Kotsovos *et al* (1987).

The empirical equation for the moment on a section corresponding to shear failure ( $M_{cx}$ ) is given by Kotsovos *et al.* (1987) by Eq. 7.1. Thus, for a particular prismatic concrete element two lines can be drawn on a moment-shear interaction diagram. A horizontal line drawn at the flexural capacity of the section ( $M_f$ ) demarcates the maximum moment capacity of the section. The empirical equation for  $M_{cx}$  (Eq. 7.1) is then plotted on the same diagram by varying the shear span ( $a_{vx}$ ) to produce a hyperbolic curve. The resulting interaction diagram is illustrated in Figure 7.2.

$$M_{cx} = 0.875a_{vx}d \left( 0.342b_1 + 0.3 \frac{M_f}{d^2} \sqrt{\frac{z}{a_{vx}}} \right) \sqrt{\frac{16.66}{\rho_w f_y}} \quad \text{Eq. 7.1}$$

Where the subscript x denotes a given cross-section at a distance x mm from the support;  $M_{cx}$  is the moment corresponding to shear failure (Nmm);  $M_f$  is the flexural capacity (Nmm);  $a_{vx}$  is the ratio  $M_{ax} / V_{ax}$  (mm);  $M_{ax}$  and  $V_{ax}$  are the applied bending moment (Nmm) and shear force (N) on the section; z is the lever arm (mm); d is the effective depth (mm);  $\rho_w$  is the ratio of the area of tension steel to the web area of concrete to effective depth;  $f_y$  is the characteristic strength of the tension steel (N/mm<sup>2</sup>);  $b_1$  is the web width (mm).

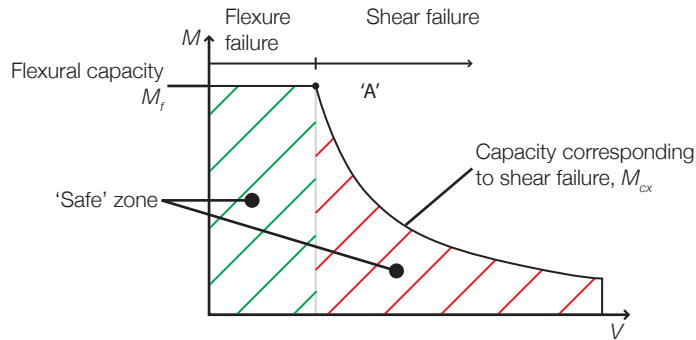


Figure 7.2: Moment-shear interaction diagram.

For the particular section under consideration, the values of coexisting moment and shear can then be plotted, and provided that they lie beneath the curve (within the hatched area shown on Figure 7.2), the compressive force path theory suggests that the section will be safe to carry the applied loads. The intersection of the two curves (marked by point 'A' in Figure 7.2) divides the failure mode of the section between a brittle flexure-shear and a ductile flexural failure.

### 7.2.2.1. Application to variable section beams

The design method described by Bobrowski and Bardhan-Roy (1969) and later by Kotsovos *et al* (1987) was applied to prismatic sections and thus only one design chart (Figure 7.2) was required to assess multiple points along the length of a beam. To apply the method to variable section members, a modified chart must be drawn, the proposed design procedure for which is outlined below and described in Figure 7.5 on page 222.

The beam is initially divided into sections, and at each section the required effective depth for flexural capacity according to the plane sections theory is determined. Each section is then assessed against Eq. 7.1 to determine a value of  $M_{cx}$  for the section. The corresponding shear capacity is then given by Eq. 7.2. The effective depth required for shear is then iterated until the value of  $V_{cx}$  on the section is equal to the shear force from the applied loads. The effective depth for design is then taken as the greater of the value determined for flexural requirements and the value determined for shear requirements.

$$V_{cx} = \frac{M_{cx}}{a_{vx}} \quad \text{Eq. 7.2}$$

Where  $V_{cx}$  is the shear force corresponding to shear failure (N);  $a_{vx}$  and  $M_{cx}$  are defined previously.

In those sections where the effective depth is determined by shear requirements, the moment capacity of the section will be equal to the moment causing shear failure (Eq. 7.1) and so whilst the theoretical capacity of the section will be sufficient to carry the loads, ultimate failure will be in a brittle shear mode. This condition is illustrated in Figure 7.3 with the line denoted '*Minimum Capacity Failure Envelope*'.

To guard against such shear failure, it is therefore proposed to increase the capacity of every section such that it remains in the flexural failure zone shown in Figure 7.2. If the shear capacity of a section that fails in a ductile manner is given by Eq. 7.3, and the shear capacity of a section failing in a brittle manner is given by Eq. 7.2, then for those sections where  $V_{cx} < V_f$ , additional vertical force capacity should be added such that  $V_{cx} > V_f$ , and this may be achieved by providing transverse steel reinforcement, the required area of which is given by Eq. 7.4. The addition of vertical force capacity to a section simply has the effect of ensuring ductile failure, as shown in Figure 7.4. This condition is illustrated in Figure 7.3 in the line denoted '*Capacity required for flexural failure*', where it is clear that to achieve flexural failure in the end zones considerable additional shear capacity is required.

$$V_f = \frac{M_f}{x} \quad \text{Eq. 7.3}$$

Where  $V_f$  is the shear force corresponding to flexural failure;  $x$  is the distance of the section from the support (mm) and  $M_f$  is defined previously.

$$A_{sv} = \frac{V_f - V_c}{f_{yv}} \quad \text{Eq. 7.4}$$

The design of variable section members with distributed loads using the compressive force path method is presented in §7.2.2.2 (test results presented in Chapter 8). The method is then extended to tapered beams with shear critical loading conditions in §7.2.3 on page 227).

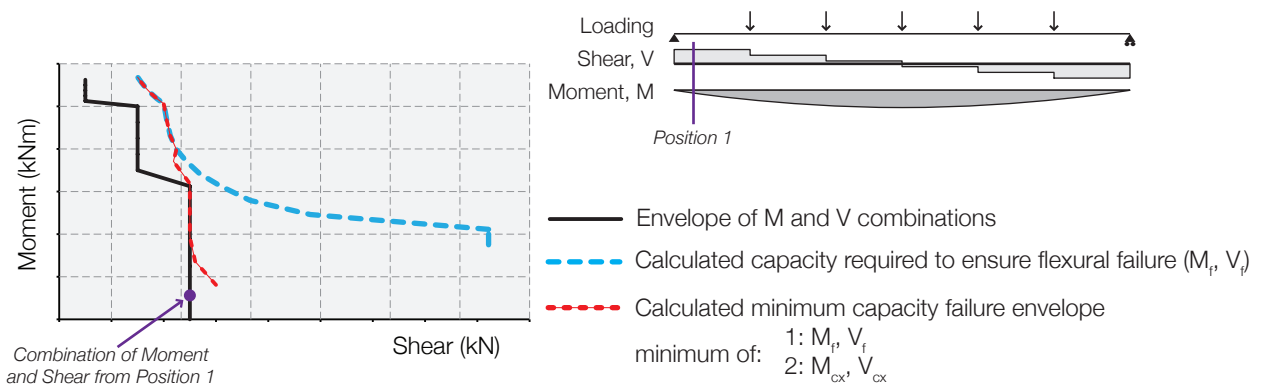


Figure 7.3: Failure modes in non-prismatic beams designed to the compressive force path method.

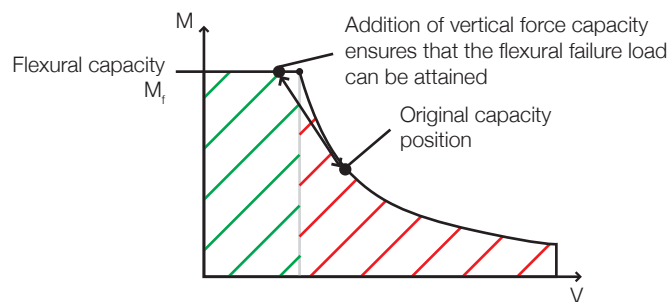


Figure 7.4: The effect of adding vertical capacity.

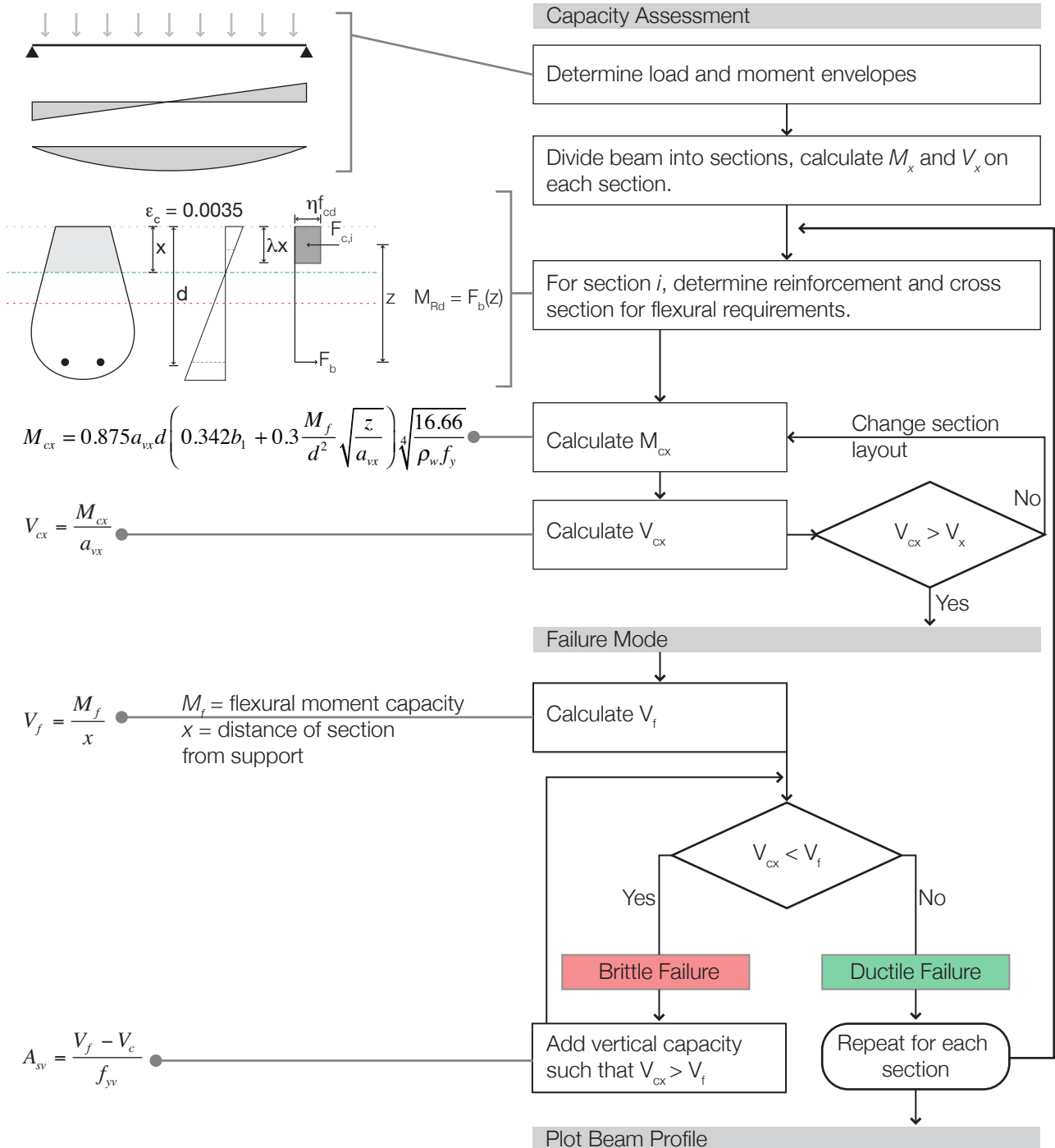


Figure 7.5: Design of variable section elements using the CFP method.

### 7.2.2.2. Beam design

To assess the use of the compressive force path method for design, tests were undertaken on three metre span beams to the loading envelope shown in Figure 7.6. The Beams are denoted 8\_1, 8\_2 and 8\_3.

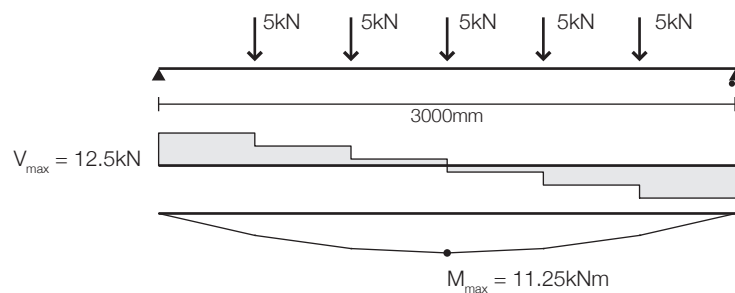


Figure 7.6: Loading and moment envelope for Beam tests.

#### 7.2.2.2.1. Beam 8\_1

Beam 8\_1 was designed in accordance with the method outlined above, but with an additional design step added to account for constructional issues with variable section beams. After assessing value for  $M_{cx}$  and  $M_f$  at each section and ensuring that the beam had sufficient capacity to carry the design loads, the reinforcement profile was simplified into one curve, Figure 7.7. From this curve, values for  $M_{cx}$  and  $M_f$  were re-calculated to ensure the beam capacity remained sufficient. The same profile was used in Beams 8\_2 and 8\_3i, the design of which described in §7.2.2.2.2 and §7.2.2.2.3.

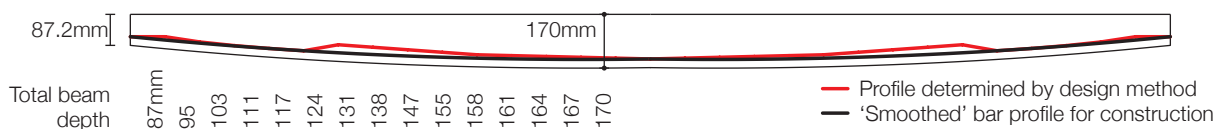


Figure 7.7: Longitudinal steel profile, Beam 8\_1.

The moment-shear interaction diagram for Beam 8\_1 is shown in Figure 7.7, where it is apparent that at high values of vertical force the section is predicted to fail in shear (although it is predicted to reach its design load).

The construction and testing of Beam 8\_1 is described in §8.2 on page 246.

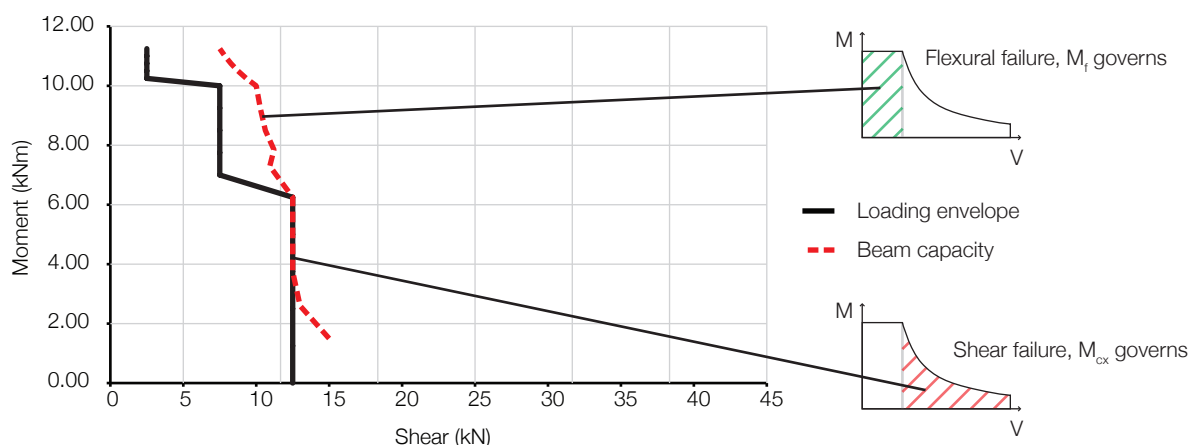


Figure 7.8: Moment shear interaction diagram, Beam 8\_1.



## 7.2.2.2.2. Beam 8\_2

Since it is preferable ensure that all beams fail in a ductile manner a further beam design was produced in which every section on the length of the beam was provided with sufficient shear capacity to achieve its flexural failure capacity ( $M_f$ ). This beam was denoted 8\_2 and the resulting interaction diagram is presented in Figure 7.9, where the increase in capacity requirements predicted to achieve ductile failure is shown. The required shear capacity is achieved using 3mm diameter links, as shown in Figure 7.10.

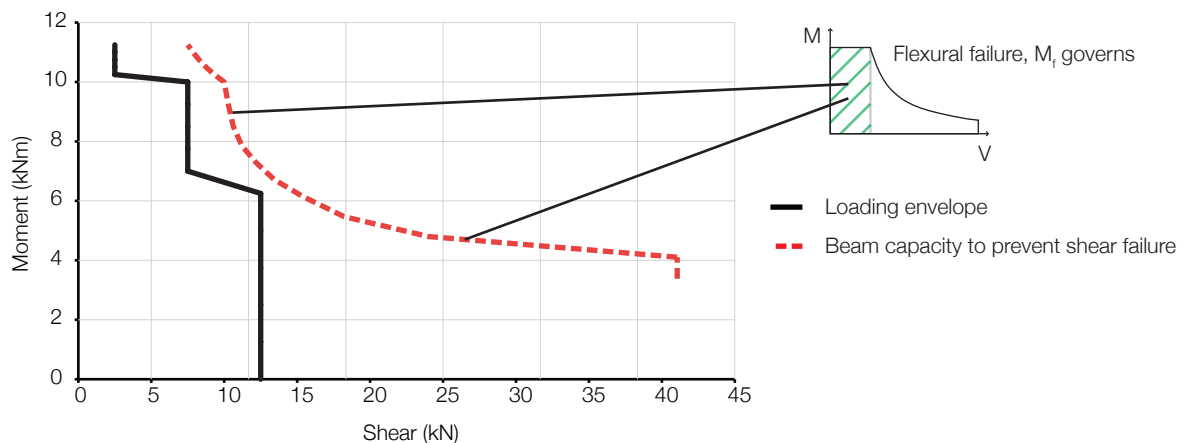


Figure 7.9: Moment shear interaction diagram, Beam 8\_2.

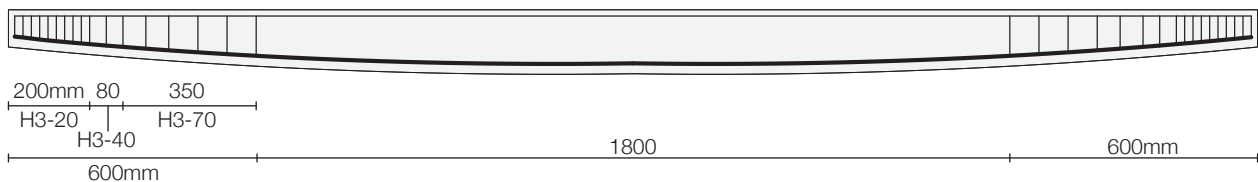


Figure 7.10: Beam 8\_2 elevation and transverse steel requirements.

By ensuring that every section remains within the 'ductile zone' (Figure 7.2) it is hoped that a satisfactory design method has been achieved. Transverse reinforcement is provided here through the use of conventional steel links, although it may also be possible to provide reinforcement through the use of used carbon fibre reinforced polymer (CFRP) grids (as described in §8.6 on page 330)

## 7.2.2.2.3. Beam 8\_3

The beams tested above have taken a shear theory derived for prismatic beams and applied it to elements with inclined reinforcement. To assess the difference between the two layouts, a final test was undertaken on one variable section beam (8\_3i) and one prismatic beam (8\_3ii).

Using the same load envelope as for Beams 8\_1 and 8\_2, the variable section beam (8\_3i) was designed by considering shear capacity in the section to come solely from the inclination of the reinforcing bar, as discussed previously and shown in Figure 7.11, where it was shown that by placing the bar at a depth proportional to the bending moment at each section the vertical component of force in the bar can be made equal to the applied shear force.

The design for Beam 8\_3i is thus shown in Figure 7.12. The beam was designed with two 10mm diameter H500C bars as flexural reinforcement, and anchorage at the end zone was provided by three bars welded orthogonally to the longitudinal steel. It should be noted that Beam 8\_3i differs from Beam 8\_1a primarily by the fact that the longitudinal bars extend to the top of the section at the support, where there is zero moment.

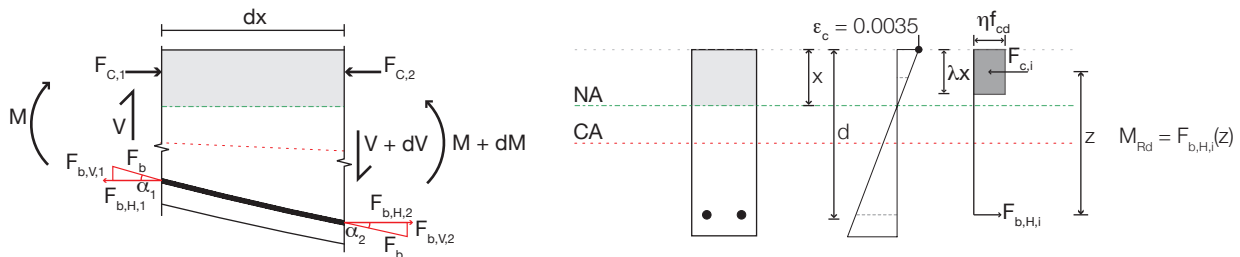


Figure 7.11: Design basis, Beam 8\_3i.

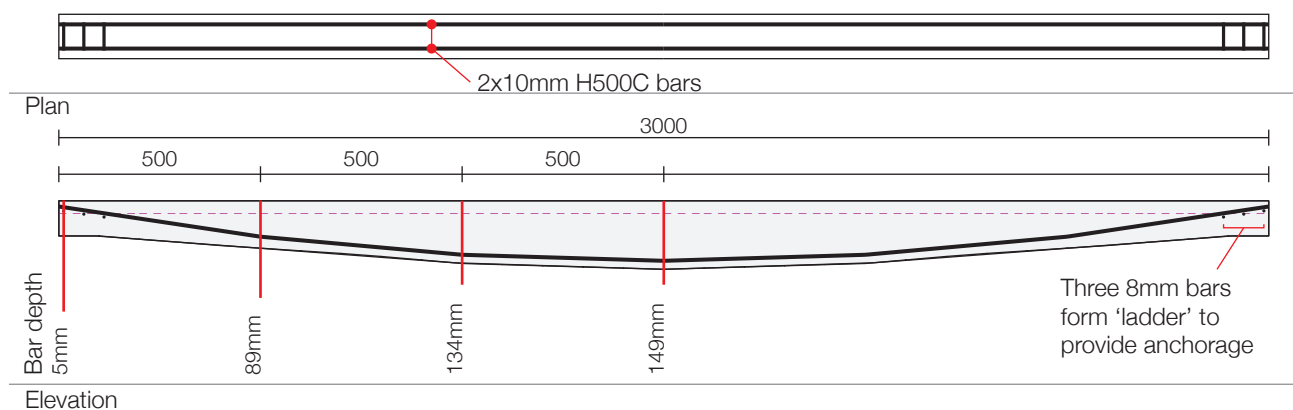


Figure 7.12: Beam 8\_3i.

To provide a meaningful assessment of the behaviour of Beam 8\_3i, a second Beam (8\_3ii) was cast with a prismatic cross section (Figure 7.13). The reinforcement has the same effective depth at mid span as found in Beam 8\_3i. Whilst it has sufficient flexural capacity along its length, it must resist shear from capacity of the concrete alone. Analysis of the beam using the empirical BS EN 1992-1-1 (2004) approach (Eq. 7.6) estimates a shear capacity for Beam 8\_3ii of 18kN at the supports, suggesting that the beam will fail in flexure (since the design support reaction is only 12.5kN, Figure 7.6).

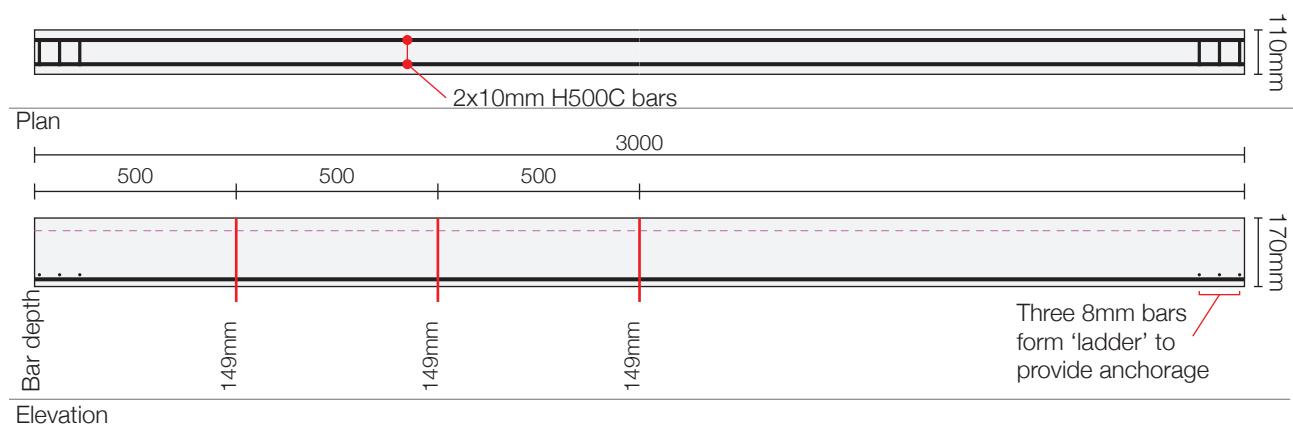


Figure 7.13: Beam 8\_3ii.

$$V_{Rd,c} = C_{Rd,c} k \left( 100 \rho_1 f_{ck} \right)^{1/3} + k_1 \sigma_{cp} b_w d \leq \left( v_{\min} + k_1 \sigma_{cp} \right) b_w d \quad \text{Eq. 7.5}$$

$$V_{Rd,c} = \left[ \frac{0.18}{1} (2) (100 (0.01) 30)^{1/3} + 0 \right] 110 (149) \leq (0.54 + 0) 110 (149) \quad \text{Eq. 7.6}$$

$$V_{Rd,c} = 18 \text{ kN} \quad \text{Eq. 7.7}$$

### 7.2.2.3. Discussion

Construction and testing details for Beams 8\_1, 8\_2 and 8\_3 are presented in §8.2 on page 246. The results demonstrate that the compressive force path method may be able to estimate the transition between flexure and shear failures quite well. It is also seen that the provision of inclined steel reinforcement in non-prismatic beams does not guard against shear failure, since the path of the compression force must still be controlled in the support zone. In addition, the results show that the empirical BS EN 1992-1-1 (2004) equation (Eq. 7.5) can provide conservative estimations of the shear strength of prismatic elements without transverse reinforcement.

In light of these tests and the analysis and discussion presented in Chapter 8, further work was undertaken to determine how the BS EN 1992-1-1 (2004) and compressive force path methods differ for elements with tapering sections loaded in shear, as presented in §7.2.3. A further comparison is provided using a strut and tie model, and the three approaches have yielded important conclusions for the shear design of non-prismatic elements, as described in Chapter 8 and Chapter 10.

### 7.2.3. Shear behaviour of tapered beams

Whilst the tests designed above and presented in §8.2 on page 246 have demonstrated that the proposed design method for variable section beams using the compressive force path method (Figure 7.5) can provide conservative results, it is applied only to beams with a uniformly distributed load and the method remains unadopted by code writers. In addition, the results of Beams 8\_3i and 8\_3ii demonstrate that the use of inclined bars can offer additional difficulties for designers.

The Eurocode BS EN 1992-1-1 (2004) allows additional shear capacity to be generated in sections with inclined compression and tension chords, as is described in §4.3.4 on page 100 and Figure 4.15 on page 96. The application of this design method is questioned by test data in the literature showing premature failures in beams with inclined reinforcement. This specific aspect of design to BS EN 1992-1-1 (2004), which is of crucial importance for non-prismatic beam behaviour is assessed in the designs presented in the following section.

To determine the most appropriate method for the design of tapered beams in shear a series of beam tests were undertaken to consider the differences between:

1. Design using BS EN 1992-1-1 (2004) (denoted 'EC2' beams);
2. Design using the compressive force path method (denoted 'CFP' beams); and
3. A strut and tie model of the tapered beam (denoted 'STM' beams, these are presented in §7.2.4).

A total of nine beam designs were created for this test series. This resulted in a total of twenty-four tests, as summarised in Table 7.1 and Chapter 8 on page 245. In the following sections, the design process and test methodology for each beam is presented.

#### 7.2.3.1. Test methodology

Tapered beams with shear spans of 150, 300, 500 and 1000mm were designed using the EC2 and CFP methods, while only a 500mm shear span was considered in the STM approach. All beams had a total span during testing of 2000mm. To facilitate the testing program, beams with shear spans of  $\leq 500$ mm were cast with two tapered ends and tested twice, as shown in Figure 7.14.

The beams were numbered according to their shear span and design methodology. For EC2 and CFP beams, their predicted failure mode is also denoted as shown below and summarised in Table 7.1, where *CFP* = compressive force path method, *EC2* = Eurocode method (BS EN 1992-1-1 (2004)); *STM* = Strut and Tie Model; *V* = predicted shear failure, *M* = predicted flexural failure.

*Beam Number\_Design Method\_Predicted Failure mode*  
*[9\_1, 9\_2, 9\_3, 9\_4]\_[CFP, EC2, STM]\_[V, M]*

Two elements of Beam 9\_2\_EC2 and 9\_2\_CFP were tested, and these are denoted (i) and (ii). Three elements of design Beam 9\_2\_STM were tested, denoted (i), (ii) and (iii), further details are provided in §7.2.4.

Table 7.1: Summary of tapered beam tests.

Beam Number	Design Method	Predicted failure mode	Beam Number	Design Method	Predicted failure mode
9_1	EC2	V	9_1	CFP	V
9_2(i)	EC2	V / M	9_2(i)	CFP	V / M
9_2(ii)	EC2	V / M	9_2(ii)	CFP	V / M
9_3	EC2	V / M	9_3	CFP	V / M
9_4	EC2	V / M	9_4	CFP	V / M
9_2(i), (ii) and (iii)	STM	See §7.2.4 on page 236			

All beams have a top breadth of 110mm and are reinforced on their tension face with two 10mm diameter high yield bars ( $f_y = 500\text{MPa}$ ). Where links are used, these are 3mm diameter plain bars with  $f_y \geq 500\text{MPa}$  unless noted otherwise. All links are supported using 3mm bars in the compression zone, the presence of which is ignored for design purposes as they have a negligible effect on flexural capacity. The design concrete strength is 40MPa throughout. To ensure that all beams except Beam 9\_1 had the same maximum support reaction, the design point load ( $P$ ) was varied between the tests. A summary of the design loads and resulting shear force diagrams for each beam is provided in Figure 7.15.

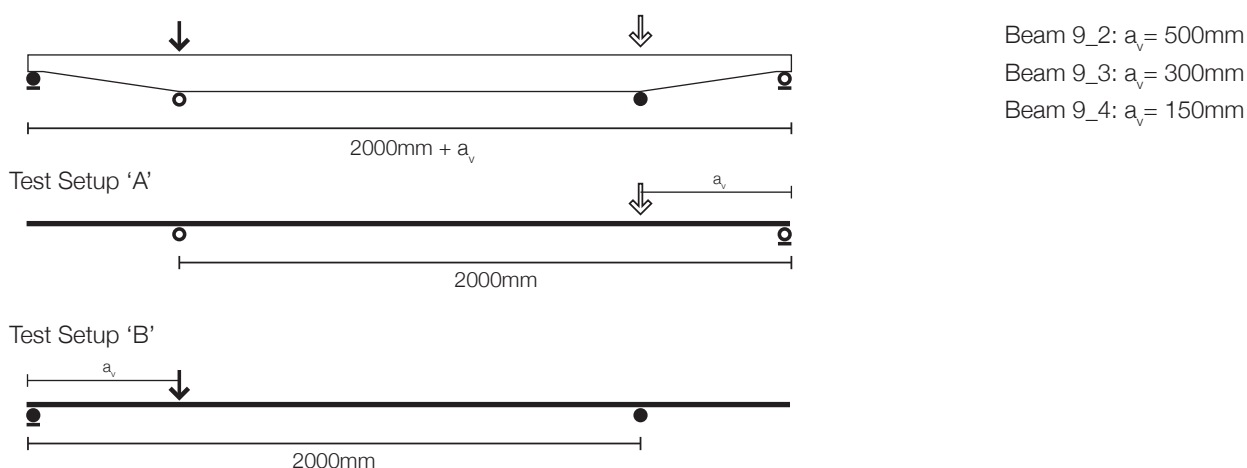


Figure 7.14: Test procedure and loading arrangement.

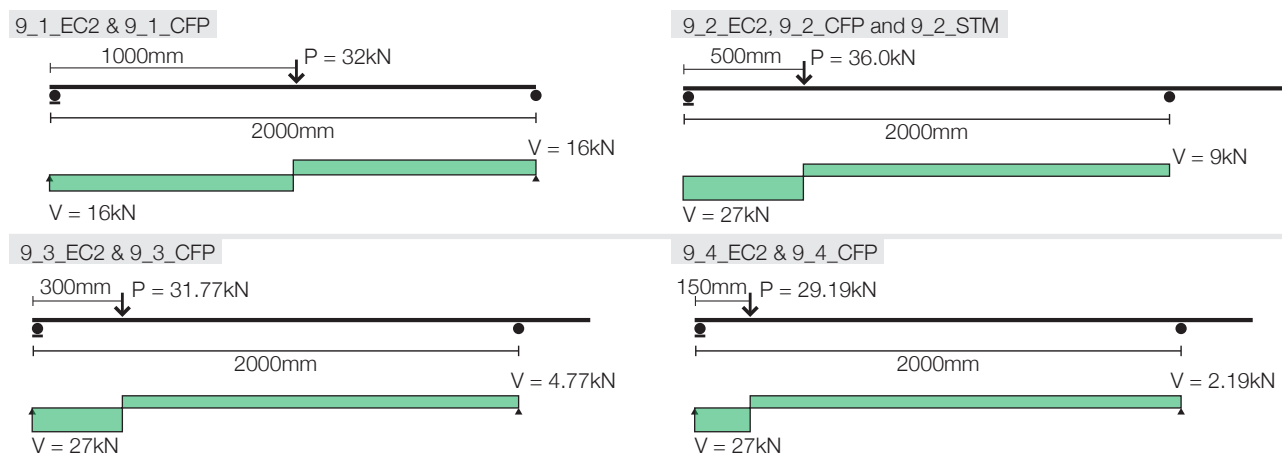


Figure 7.15: Shear force diagrams and design point loads for each test.

### 7.2.3.2. Anchorage

As has been discussed in the preceding sections, anchorage of the flexural reinforcement in elements with a near uniform stress in the flexural reinforcement (which occurs in optimised beams as a virtue of the design process) is critical. This is explored in the use of splayed bars in §3.4 on page 68 and §6.2 on page 159.

In the designs presented below two U-bars have been arranged to provide the required anchorage in the end zones of the beams. The bars are given sufficient lap length in the centre of the beam span (Figure 7.16) to ensure that force transfer can occur (no welding is used). This method, whilst not practical for every situation, was intended to remove the potential for anchorage failures of the longitudinal reinforcement prior to the determination of a flexural or shear type failure.

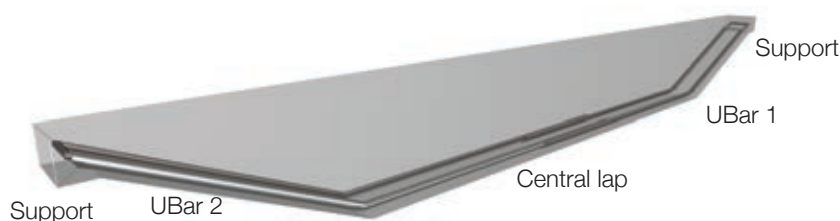


Figure 7.16: Reinforcement method showing anchorage and lap lengths.

### 7.2.3.3. Data collection and test monitoring

All of the tapered beam tests described in both §7.2.3 and §7.2.4 were monitored with a range of strain gauges and displacement transducers during testing (as detailed in Chapter 8). In addition to this, Digital Image Correlation (DIC) was used throughout the load cycle for all beams to determine strain distributions within the concrete section. The procedure, results and analysis for this are provided in §8.5 on page 301, where it is seen that this innovative analysis method can provide a unique insight into the behaviour of the EC2, CFP and STM beams. The results of the digital image correlation technique have provided an additional means by which the design models presented in this Chapter can be compared and their relative merits assessed.

### 7.2.3.4. Beam 9\_1

Beam 9\_1 is designed with an applied load of  $P = 32\text{kN}$  applied at a shear span of 1000mm. Two elements were designed and tested in this layout, using the CFP and EC2 approaches.

#### 7.2.3.4.1. Compressive force path method

It has already been seen (§7.2.2) that when using the compressive force path method transverse reinforcement may be added to variable section beams to prevent shear failures. Following the method presented in Figure 7.5, Beam 9\_1\_CFP\_V is shown in Figure 7.17. In this case shear failure is predicted to occur at the design maximum shear load of 16kN, as shown in Figure 7.18, where the values of  $V_a/V_{cx}$  along the beam are plotted (where  $V_a$  is the actual shear force and  $V_{cx}$  is the shear force corresponding to failure in shear). The external dimensions for Beam 9\_1\_CFP\_V are shown in Figure 7.17.



Transverse bars are provided at the position of the application of the load and at the theoretical change in compressive force path direction, as described by Kotsovos and Pavlovic (1999), which here is taken as a distance from the support of two times the effective depth of the beam at the support,  $d$ .

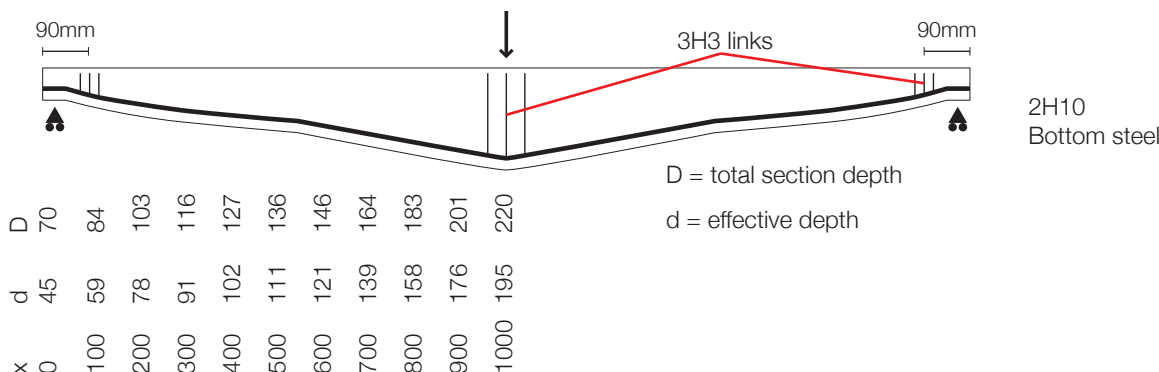


Figure 7.17: Design, Beam 9\_1\_CFP\_V.

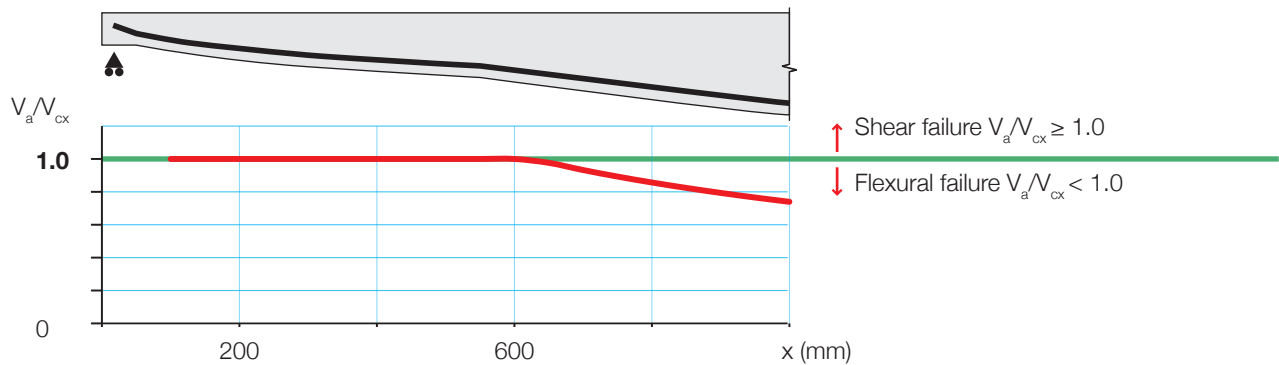


Figure 7.18: Capacity envelope for Beam 9\_1\_CFP\_V.

The designs presented for Beam 9\_1\_CFP could be improved upon in construction by using a layout of reinforcement such as that shown in Figure 7.19. Such an approach would necessitate an iterative design in which the general layout required was determined, and then a modified layout using multiple curved bars was reassessed and checked. This may be incorporated in future work.

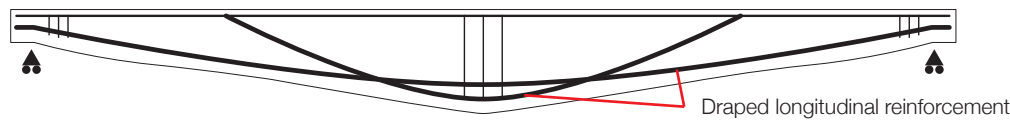


Figure 7.19: Options for the reinforcement of Beam 9\_1\_CFP.

#### 7.2.3.4.2. BS EN 1992-1-1 Method

Beam 9\_1\_EC2\_V was designed using the method set out in BS EN 1992-1-1 (2004), wherein the vertical component of force in the longitudinal bar can be used as an effective shear link, as described in §4.3.4 on page 100, by Figure 7.20 and Eq. 7.8-Eq. 7.13. By iterative design, equilibrium is satisfied to ensure the beam can provide both the flexural and shear requirements of the load envelope. This iterative process was undertaken along the length of the beam, with the resulting beam element shown in Figure 7.21. Although BS EN 1992-1-1 (2004)

does not set out methods for determining failure modes as described in §7.2.3.4.1 above, it may be reasonable to suggest that where full flexural and shear capacities are utilised, shear failure will occur first.

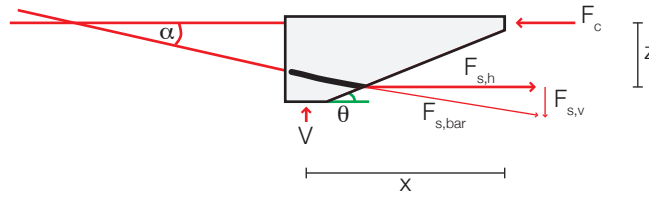


Figure 7.20: Design method for BS EN 1992-1-1 (2004).

Taking moments at C

$$F_{s,h}z + F_{s,v} \cot \theta = V_s x \quad \text{Eq. 7.8}$$

$$F_{s,h} = \frac{M}{z} + \frac{F_{s,v}}{2} \cot \theta \quad \text{Eq. 7.9}$$

Choosing the angle ' $\alpha$ ', and beginning with the assumption that  $F_{bar} = A_s f_y$

$$F_{s,h} = F_{bar} \cos \alpha \quad \text{Eq. 7.10}$$

$$F_{s,v} = F_{bar} \sin \alpha \quad \text{Eq. 7.11}$$

Iterate  $z$  and ' $\alpha$ ' such that  $F_{s,v} = V$  and  $F_{s,h}z = M$ .

At the supports, ensure maximum compression in inclined strut is less than allowable by Eq. 7.12, hence a minimum depth at the support is given by Eq. 7.13.

$$V_{Rd,max} = \frac{b_w z f_{cd}}{\cot \theta + \tan \theta} \quad \text{Eq. 7.12}$$

Where  $b_w$  is the web width,  $z$  the lever arm,  $f_{cd}$  = design concrete strength;  $\theta$  = angle of compression strut. Therefore, the minimum lever arm may be given by:

$$z_{min} = \frac{V (\cot \theta + \tan \theta)}{b_w f_{cd}} \quad \text{Eq. 7.13}$$

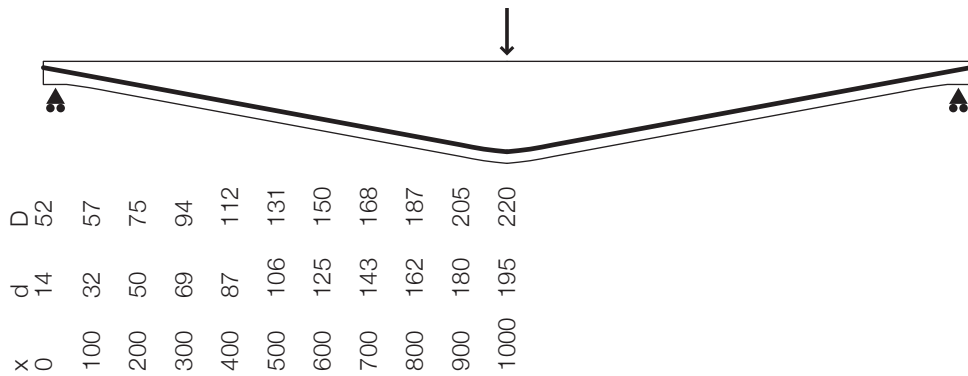


Figure 7.21: Beam 9\_1\_EC2\_V design.

### 7.2.3.5. Beams 9\_2

In contrast to Beam 9\_1, where the element was tested only once, Beam 9\_2 and subsequent elements were tested in two setups 'A' and 'B', providing two designs for each element, as described below. Beam 9\_2 was designed for a point load  $P = 36\text{kN}$  applied at  $a_v = 500\text{mm}$ . The layout of Beam 9\_2 was designed using all three methods - EC2, CFP and STM. The STM approach is described in further detail separately in §7.2.4.

7.2.3.5.1. CFP Method

Beam 9\_2 was the first beam designed to be tested twice and a detailed assessment was undertaken such that test Set Up 'A' would provide a flexural failure (all sections shear capacity  $> V_f$ ) and test Set Up 'B' a shear type failure (all sections shear capacity  $= V_{cx}$ ). The same process was undertaken for Beams 9\_3 and 9\_4.

Tensile steel is provided in Beam 9\_2\_CFP\_V such that the full load envelope can be achieved, but failure will be in shear. Beam 9\_2\_CFP\_M is designed to achieve its full flexural capacity. Note that the two tests 9\_2\_CFP\_V and 9\_2\_CFP\_M are carried out on the same beam specimen, as described in Figure 7.14.

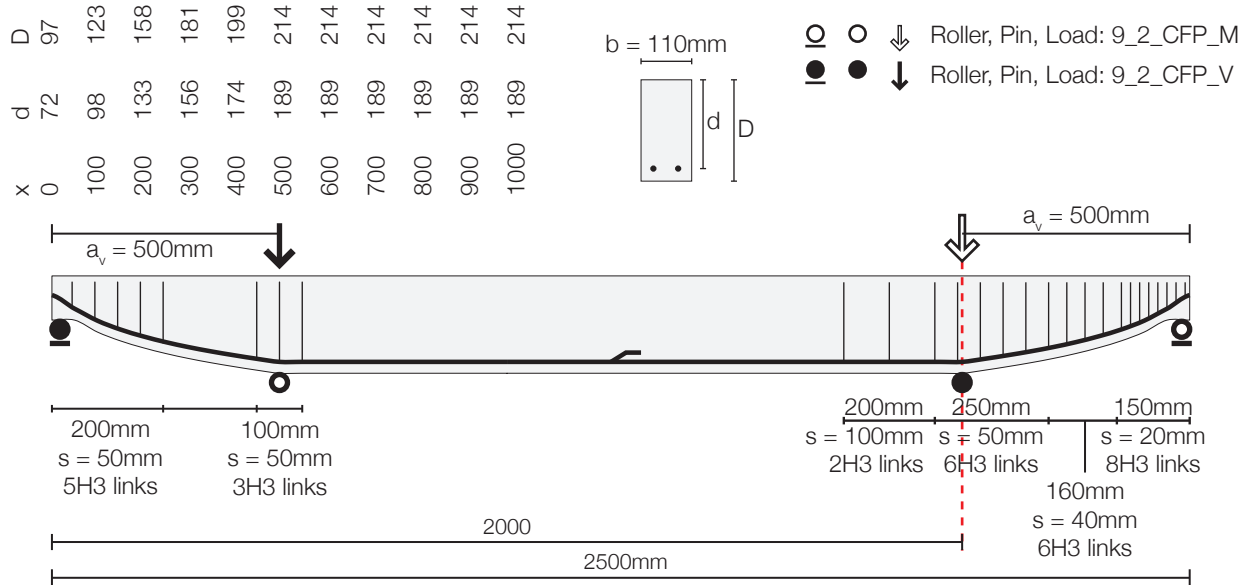


Figure 7.22: Test 9\_2\_CFP\_V and 9\_2\_CFP\_M.

7.2.3.5.2. EC2 Method

In Beam 9\_2\_EC2 element 'V' relies solely on the inclined bar for flexural and shear capacity, as described or Beam 9\_1\_EC2 above, while element 'M' is arranged such that the inclined flexural reinforcement is disregarded for shear design and the entire vertical force capacity is taken from the transverse steel reinforcement (as given by BS EN 1992-1-1 (2004)). Both 'V' and 'M' type beams have identical external geometries, which is determined in the design process by the requirements of layout 'V'. Both layouts are shown in Figure 7.23 for Beam 9\_2\_EC2, with the same design process being undertaken for Beams 9\_3\_EC2 and 9\_4\_EC2.

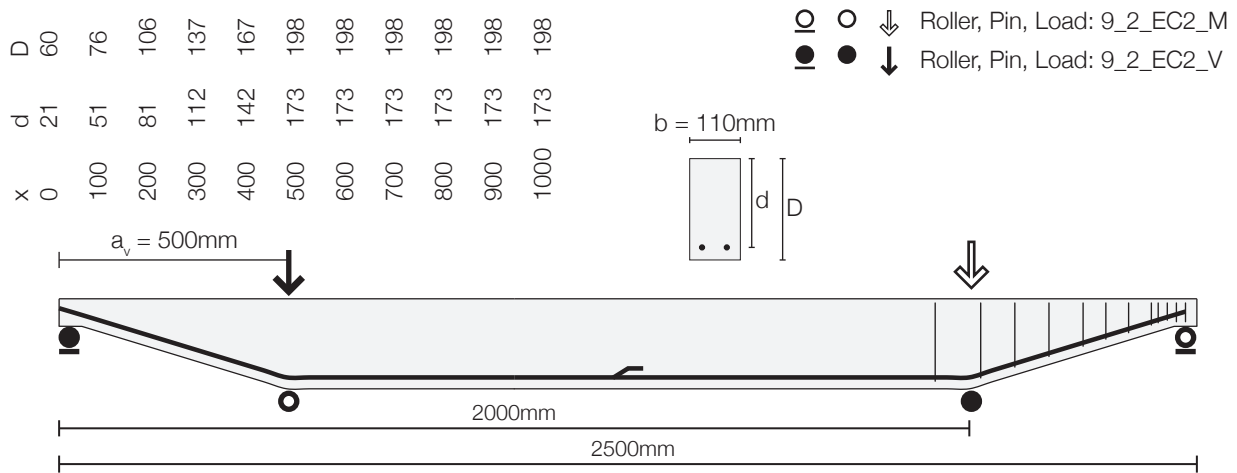


Figure 7.23: Beam 9\_2\_EC2\_V and 9\_2\_EC2\_M.

## 7.2.3.6. Beam 9\_3

Beam 9\_3 was designed for a point load of 31.76kN applied at a shear span of 300mm.

## 7.2.3.6.1. CFP Method

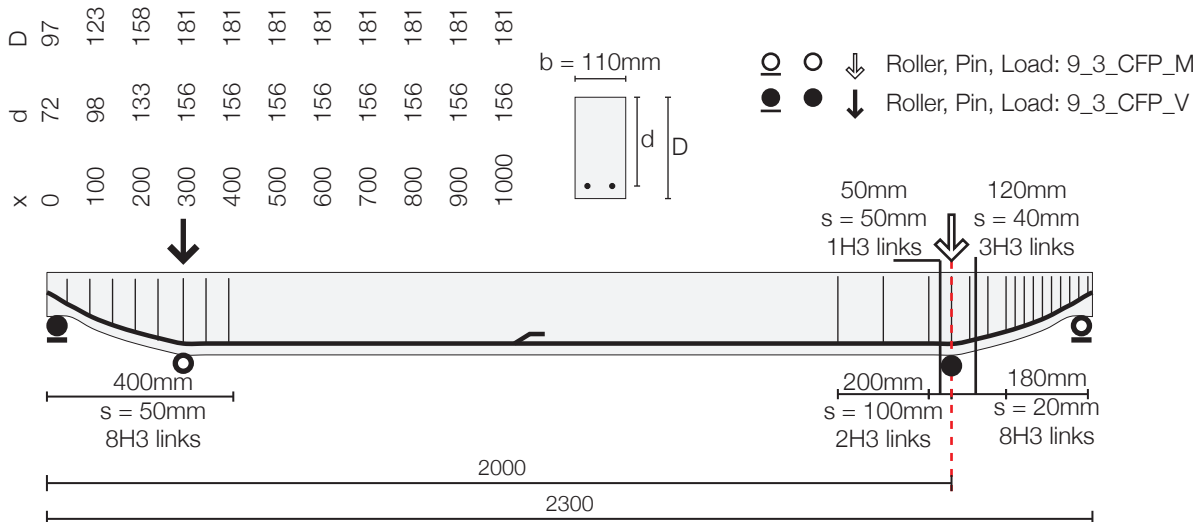


Figure 7.24: Beam 9\_3\_CFP\_V and 9\_3\_CFP\_M.

## 7.2.3.6.2. EC2 Method

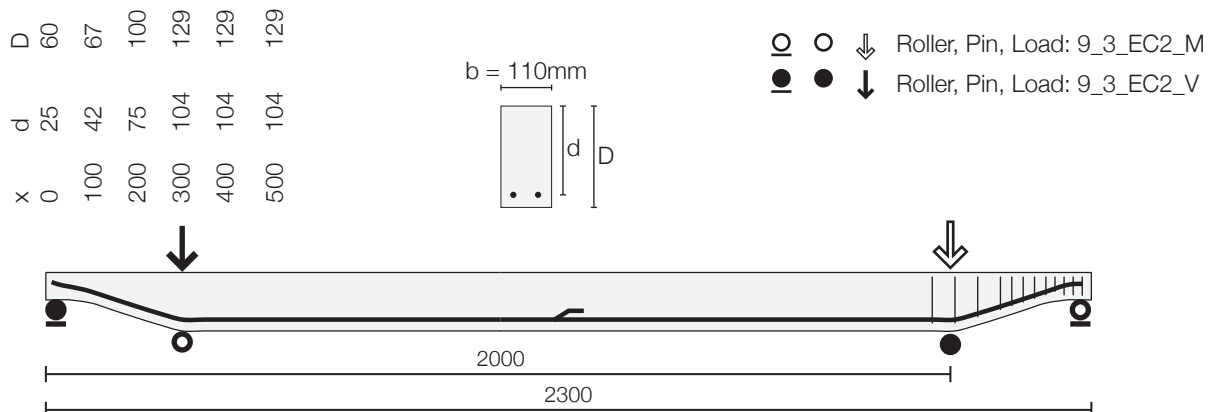


Figure 7.25: Beam 9\_3\_EC2\_V and 9\_3\_EC2\_M.

### 7.2.3.7. Beam 9\_4

Beam 9\_4 was designed for a point load of 29.19kN applied at a shear span of 150mm.

#### 7.2.3.7.1.CFP Method

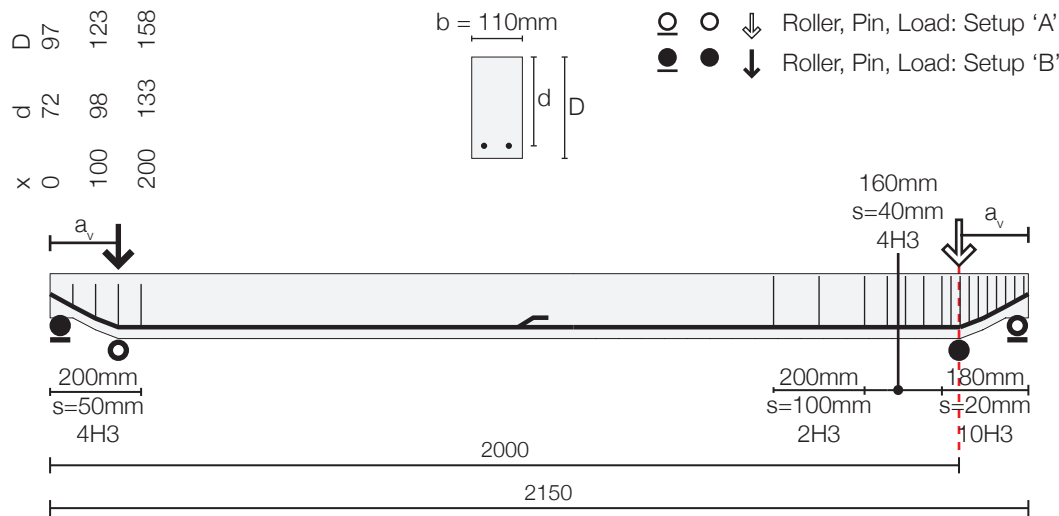


Figure 7.26: Test 9\_4\_CFP\_V and 9\_4\_CFP\_M.

#### 7.2.3.7.2.EC2 Method

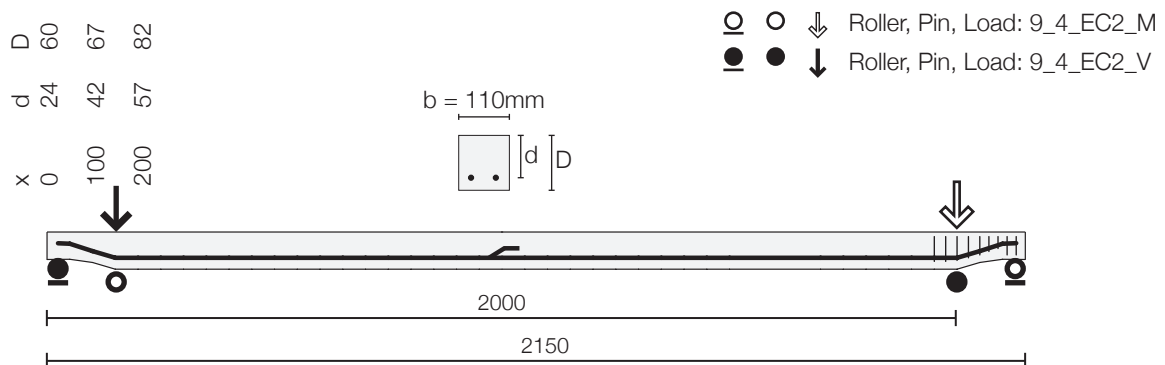


Figure 7.27: Beam 9\_4\_EC2\_V and 9\_4\_EC2\_M.

#### 7.2.3.8. All beams comparison

From the designs undertaken to BS EN 1992-1-1 and the CFP method, it is clear that at short shear spans, the BS EN 1992-1-1 (2004) design approach shown above results in shallower cross sections, as is illustrated for all beam sections in Figure 7.28.

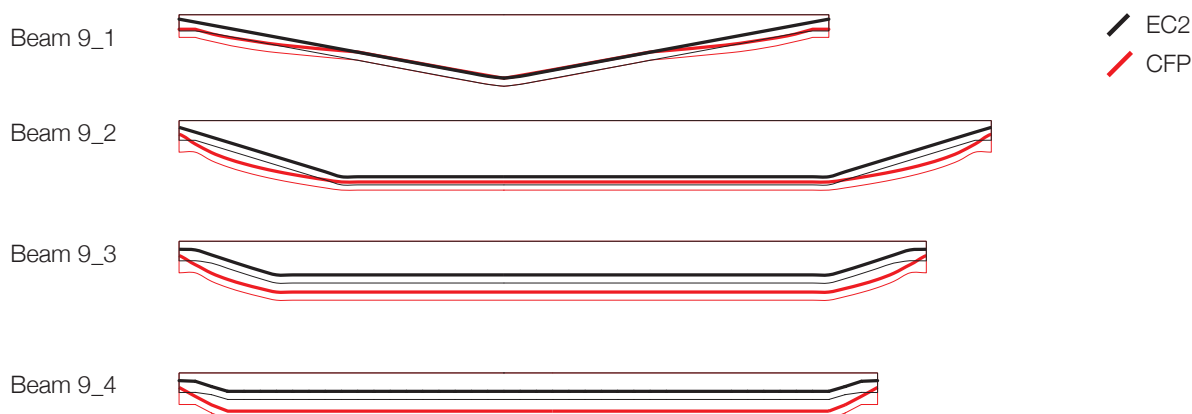


Figure 7.28: Comparison, Beams 9\_1 to 9\_4.

#### 7.2.3.9. Discussion

The logical extension of the BS EN 1992-1-1 (2004) design approach, which allows inclined tension and compression forces to contribute to the shear capacity of a tapered beam, has resulted in the range of beam geometries shown in the above section.

The testing, construction and analysis of the beams presented above is described in §8.3 on page 260. The results of these tests show that the BS EN 1992-1-1 (2004) method may not be applicable to tapered beams and that the current provisions could lead to unconservative designs. This testing program led to the development of a strut and tie based model for tapered beam sections, which is described in §7.2.4. The test designs described in both §7.2.4 and §7.2.3 form the basis of a conference paper described in Chapter 8.



### 7.2.4. Strut and Tie Modelling

Following the test results of the tapered beams designed using the EC2 and CFP approaches (described in §7.2.3 above), it was clear that an alternative approach was required to apply the provisions of BS EN 1992-1-1 (2004) to tapered beams. In this section a strut and tie based approach is presented, with test data and analysis provided in §8.4 on page 284.

#### 7.2.4.1. Model basis

The 'EC2', or BS EN 1992-1-1 (2004) based model used above has been arranged in some situations such that the inclined tension chord provides the entire vertical force capacity for the section. This requires the tapered beam to have a design model such as that shown in Figure 7.29(l) (note that the top chord is not horizontal in this figure), where the anchorage of the longitudinal steel is a crucial requirement to develop the required bar forces. It is clear that should the compression and tension forces not 'line up' precisely then the system will generate additional moments over the supports and no longer work as desired (Figure 7.29(r)).

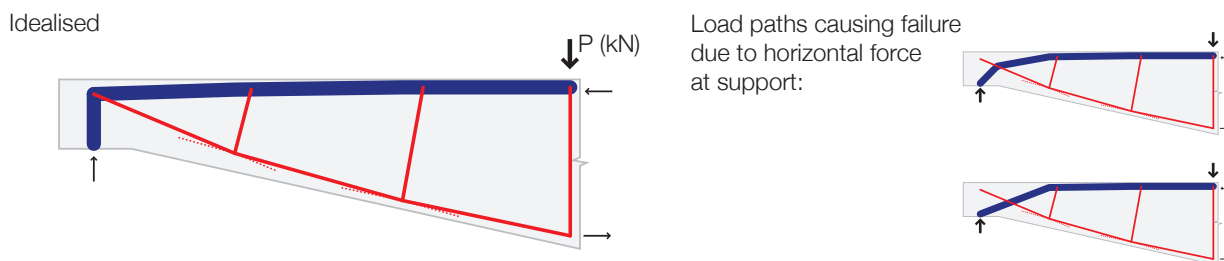


Figure 7.29: Equivalent strut and tie model assumed for Eurocode 2 tapered model (l); potential for moment generation at the supports (r).

The test results of Beams 9\_1\_EC2 to 9\_4\_EC2 demonstrate that this may not be possible to ensure with small section depths and narrow support zones, and the 'EC2' beam series consistently failed to reach its design load. In light of this, a modified strut and tie model is proposed which allows the concrete strut to be inclined at the support zone in what is a more conventional approach, summarised in Figure 7.30. Such an approach, however, requires that at the change in direction of the compression force, significant vertical forces are generated that must be resisted either by the concrete in tension or steel ties, as described below.

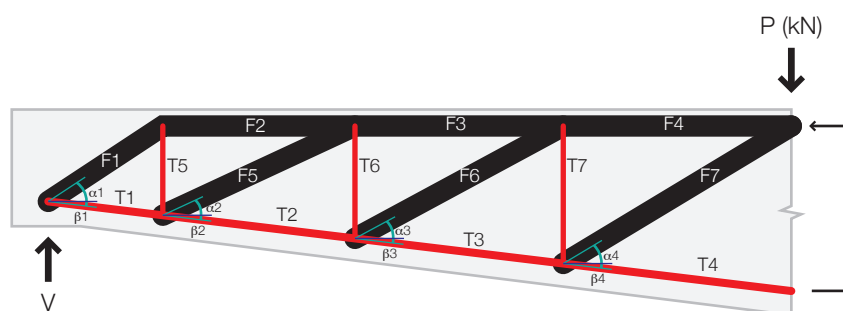


Figure 7.30: Generic strut and tie model for a tapered section.

From the model shown in Figure 7.30 it is apparent that the position of the bottom tension tie can not be in the ideal position for any load case (since it does not coincide with the top compression chord at the position of zero

moment) and hence the vertical force carried in the longitudinal steel will always be less than the applied shear force. This leads then to suggest that it is the capacity of the vertical steel ties which are critical in carrying the shear forces of such a design. In this model, the minimum section depth is defined by the minimum of:

1. Area required for anchorage of the longitudinal reinforcement, using the provisions of BS EN 1992-1-1 (2004);
2. Development length for the transverse reinforcement, such that it can be adequately anchored in the section to provide the required vertical capacity;
3. The capacity of the inclined concrete strut;
4. A minimum section depth to prevent splitting of the end anchorage zone.

From Figure 7.30 it is clear that the force in 'T5', the first vertical tie, is equal to the reaction minus any force carried in the inclined tension chord, 'T1'. This is a departure from the model shown in Figure 7.29 on page 236, where the inclined tension chord was proposed to carry the majority of the vertical force, and thus ensures that the tapered beam relies on transverse reinforcement and the concrete web in a much more significant way. In addition, the proposed model no longer requires the steel to yield and hence the force generated in 'T1' may in fact be relatively small, leaving the majority of the vertical force component to be carried in 'T5'.

By following the model shown above a series of equations can be formed for the force in each member of the strut and tie model which are dependent on the angles ' $\alpha$ ' and ' $\beta$ ', and the position of the change in direction of the concrete strut ( $F1-F2-F3-F4$ ). With these variables, parametric studies of a particular beam can be undertaken to determine feasible cases that provide the required beam capacity. This principle was applied to the design of one beam, described in §7.2.4.2. Three beams of the same design were tested, as described in §8.4 on page 284. The beam was further detailed by considering a minimum support width required in BS EN 1992-1-1 (2004) for beam elements, which resulted in a 100mm wide support plate.

#### 7.2.4.2. Beam layouts

The beam designed for this model was loaded and arranged in the same way as described for Beams 9\_2\_EC2 and 9\_2\_CFP described in §7.2.3 on page 227, and is designated 9\_2\_STM. The loading layout is shown in Figure 7.31.

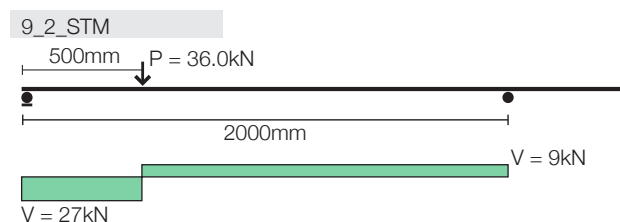


Figure 7.31: Loading layout for Beam 9\_2\_STM.

### 7.2.4.3. Beam design

Following the model above, the beam layout shown in Figure 7.35 was designed. The capacity of the concrete struts was limited by the provisions of BS EN 1992-1-1 (2004), which is summarised in Eq. 7.14, and the ties were limited by the capacity of the yielding steel provided at each position. In addition, a maximum link spacing of 75% of the effective depth was applied along the beam length, and the support zone was sized according to BS EN 1992-1-1 (2004), which resulted in a 100mm wide support. These constraints resulted in a deeper and wider support zone than has previously been calculated.

$$\sigma_{Rd,max} = f_{cd} \quad \text{Eq. 7.14}$$

Where  $\sigma_{Rd,max}$  is the compressive stress in a concrete strut (Figure 7.32) and  $f_{cd}$  is the design strength of the concrete ( $f_{cd} = \alpha_{cc} f_{ck} / \gamma_m$  where  $\alpha_{cc}$  is a coefficient for long term behaviour and  $\gamma_m$  is the partial safety factor for concrete, which is taken as 1.00 for these calculations).

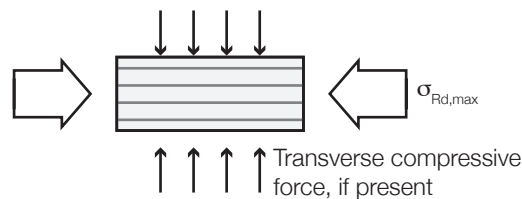


Figure 7.32: Strut definition (BS EN 1992-1-1 (2004), §6.5).

In contrast to the proposed BS EN 1992-1-1 (2004) method, the new strut and tie approach does not require that all the steel is yielding. Instead, it is proposed that plastic behaviour, which is desired for a ductile response, can be provided by ensuring that the steel yields in certain positions only. In the proposed methodology, this yielding is to occur beneath the point of load application (at the position of maximum moment and beam depth, and away from the support location). It is proposed that this mechanism will provide ductility to the beam response.

At the failure load, it is likely that the steel flexural and transverse reinforcement close to the support will still be in its elastic range (indeed this is predicted by the design model for Beam 9\_2\_STM, as described below), yet this is acceptable for this load case as the failure process is governed by the yielding of the steel at the deepest section.

To monitor the development of forces in the steel reinforcement, each STM model beam is monitored with strain gauges placed on the flexural reinforcement. In addition, digital image correlation is used to monitor the behaviour of the concrete section during the loading process. This innovative analysis technique allowed strains developing during the loading cycle to be determined. Test results, shown in 8.5 on page 301, demonstrate an excellent correlation between the forces predicted in the design model (shown in §7.2.4.4) and the actual forces recorded during testing.

This design process was undertaken using a simple spreadsheet method based on the solving of the required equations for equilibrium at each node, and these equations are presented in more detail in §7.2.4.4.

#### 7.2.4.4. Model equations

A strut and tie model for the Beam described above is provided based on the generic model shown in Figure 7.30. The layout has been simplified to include three truss 'bays'. The design is initiated by calculating the required depth at the position of maximum moment that will ensure the predefined area of internal flexural steel reinforcement steel has yielded in this location. This depth then provides the overall geometry of the model, defining the angles  $\alpha_1 - \alpha_6$ . The force in each section of the truss model is limited as described in §7.2.4.3 (concrete crushing and steel yielding), but each element is not required to be at its maximum capacity. It is required, however, that the tension path form a straight line between nodes.

With the forces in each tie thus determined, and equilibrium of the entire section checked, the provision of transverse reinforcement is calculated based on the discrete forces in the vertical truss elements, with additional bars provided between the 'ties' to guard against premature failure in a mass concrete section.

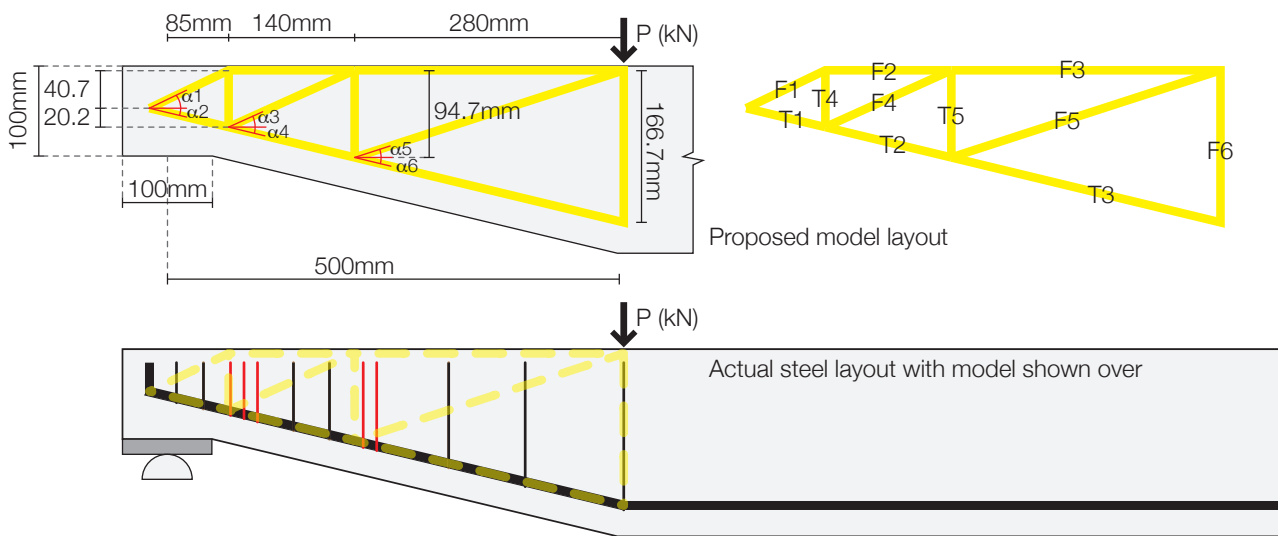


Figure 7.33: Design model for Beam 9\_2\_STM.

From these variables, equations for the force in each strut and tie are produced as shown in Eq. 7.15-Eq. 7.25. In the design process the model geometry is altered iteratively to provide a suitable layout of reinforcement that provide the required shear and flexural capacities along the length of the tapered beam. The variables chosen for Beam 9\_2\_STM are given in Figure 7.33, with the resulting forces in the STM model for this beam at its design load provided in Figure 7.34. All transverse reinforcement was provided by 3mm diameter plain bars.

$$F_{t1} = \frac{V \cos \alpha_1}{\cos(90 - \alpha_1 - \alpha_2)} \quad \text{Eq. 7.15}$$

$$F_{c1} = \frac{F_{t1} \cos \alpha_2}{\cos \alpha_1} \quad \text{Eq. 7.16}$$

$$F_{c2} = F_{c1} \cos \alpha_1 \quad \text{Eq. 7.17}$$

$$F_{t4} = F_{c1} \sin \alpha_1 \quad \text{Eq. 7.18}$$

$$F_{t2} = \frac{F_{t1} \sin(\alpha_2 + \alpha_3) + F_{t4} \sin(90 - \alpha_3)}{\sin(\alpha_3 + \alpha_4)} \quad \text{Eq. 7.19}$$

$$F_{c4} = \frac{F_{t4} + F_{t1} \sin \alpha_2 - F_{t2} \sin \alpha_4}{\sin \alpha_3} \quad \text{Eq. 7.20}$$

$$F_{c3} = F_{c2} + F_{c4} \cos \alpha_3 \quad \text{Eq. 7.21}$$

$$F_{t5} = F_{c4} \sin \alpha_3 \quad \text{Eq. 7.22}$$

$$F_{t3} = \frac{F_{t5} \sin(90 - \alpha_5) + F_{t2} \sin(\alpha_4 + \alpha_5)}{\sin(\alpha_5 + \alpha_6)} \quad \text{Eq. 7.23}$$

$$F_{c5} = \frac{F_{t3} \cos \alpha_6 - F_{t2} \cos \alpha_4}{\cos \alpha_5} \quad \text{Eq. 7.24}$$

$$F_{c6} = F_{t3} \sin \alpha_6 \quad \text{Eq. 7.25}$$

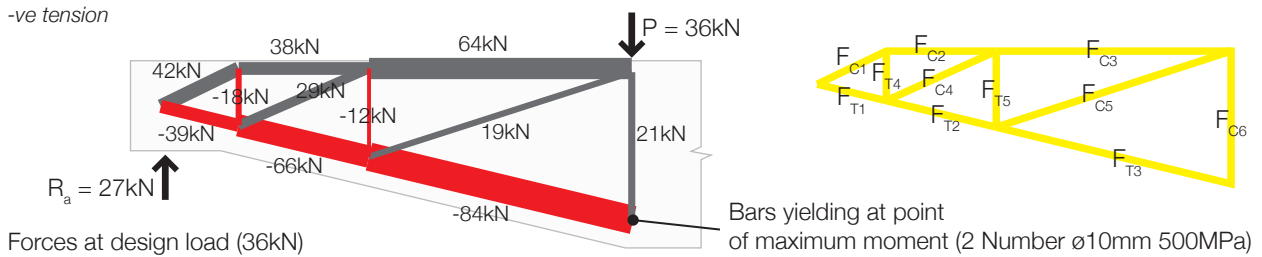


Figure 7.34: Force diagram for Beam 9\_2\_STM.

The maximum beam depth under the point load was defined by the moment capacity required at this position. Flexural tension reinforcement was then placed as a straight line between these two points, with the result that its inclination did not provide the full shear capacity to the section and that the ties therefore had to provide much of this capacity. This is thus likely to be a limitation on the minimum section depths that can be achieved in full size elements cast in fabric formwork, and as such may limit the ultimate material savings that are possible with this method.

At the support, the forces must still line up quite precisely, and thus it was decided that at one end the beam would be cast around a steel angle, anchored into the concrete by a 10mm reinforcing bar, as shown in Figure 7.36. This is the only difference between the two ends of the beam, which are to be tested in the same manner as described in §7.2.3.1 on page 227.

The final beam design is shown in Figure 7.35 and was constructed and tested as described in §8.4 on page 284. A comparison between the beam layout and the Strut and Tie model is given in Figure 7.34, where the magnitude of the forces in each element is described by the corresponding line thickness.

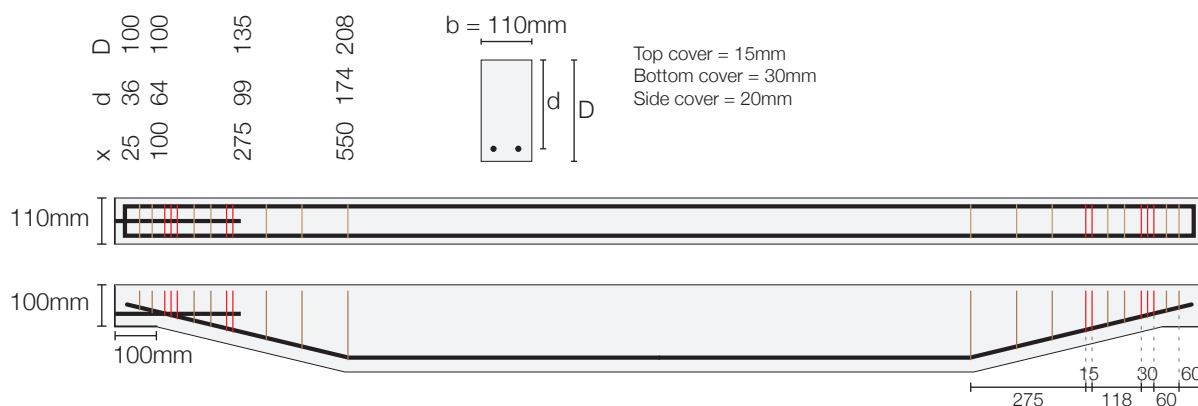


Figure 7.35: Beam 9\_2\_STM.

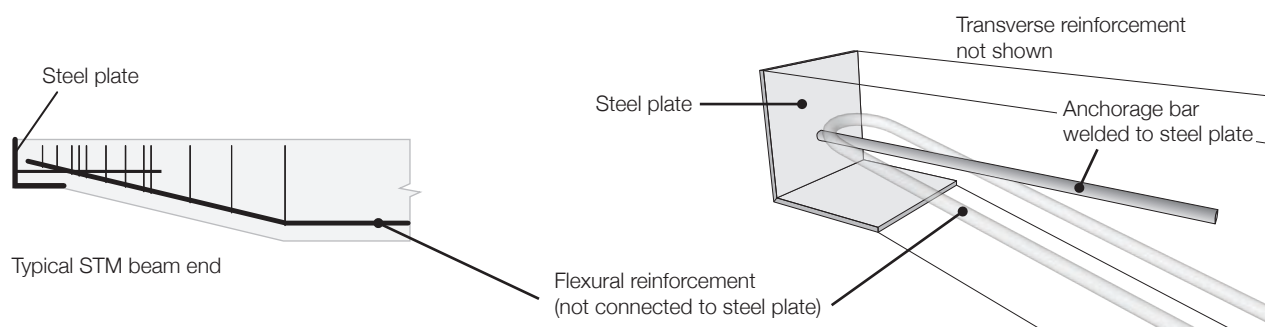


Figure 7.36: Support detail provided at one end of each STM beam.

#### 7.2.4.5. Discussion

The design model presented above has been applied to the testing of three identical tapered beams, numbered 9\_2\_STM(i), (ii) and (iii). These tests are presented in full in Chapter 8, where the use of digital image correlation techniques is again applied to analyse the distribution of forces within the element during loading.

The design methods presented above provide a range of alternative approaches for shear design, and the results presented in subsequent section demonstrate that it is possible to provide conservative designs for tapered beams in shear. It is seen, however, that the application of the 'EC2' model is less certain, with results providing cause for concern that add to those seen in previous tests data provided in the literature (Nghiep and Rombach, 2011, see also §4.3.6 on page 105).

Analysis of the test data presented in later chapters provides clear evidence of the differences between the design methods and has helped shape design guidance presented in Chapter 11.

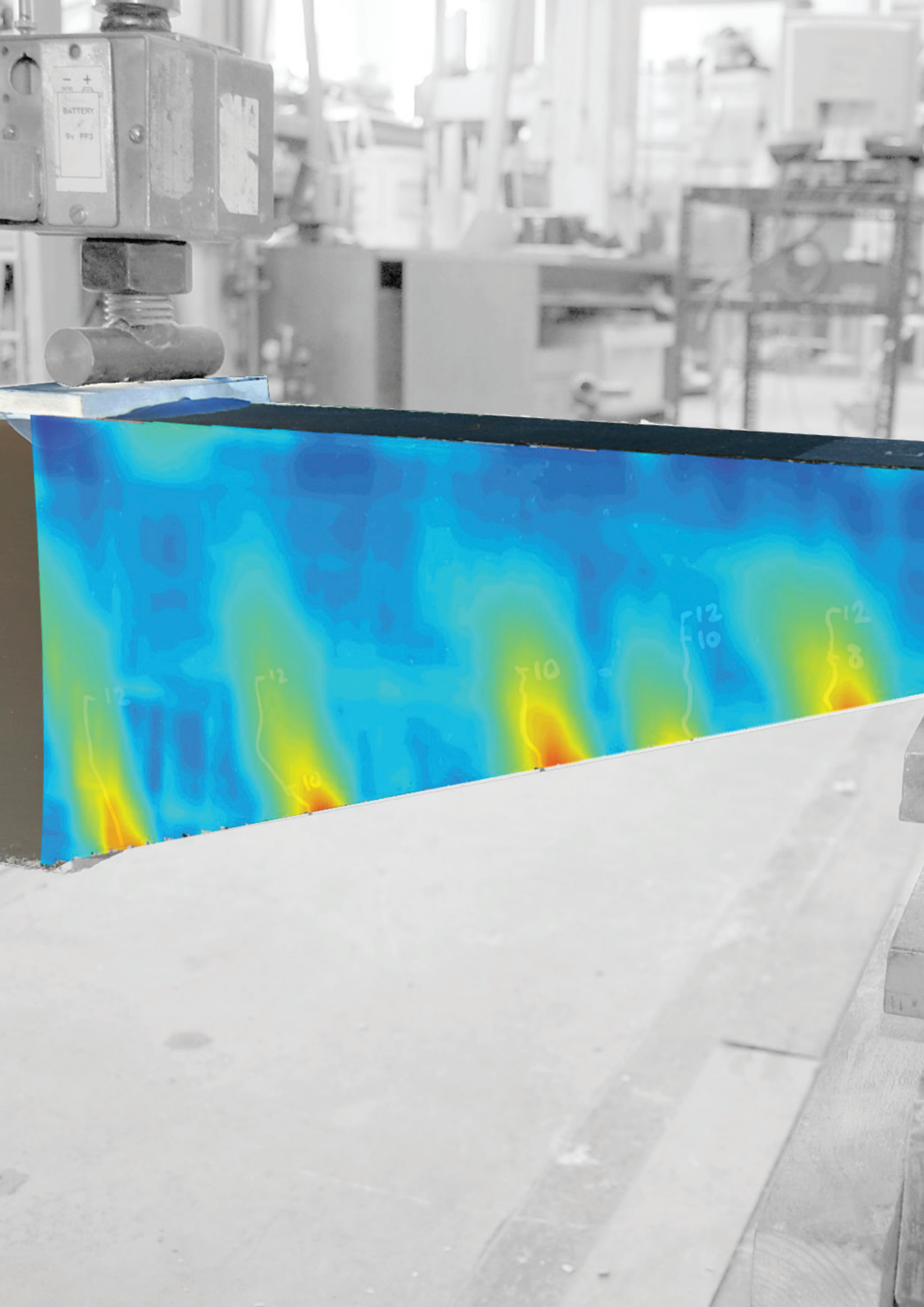


### **7.3. Conclusions**

The aims of the testing programme of this thesis (as set out in §5.4 on page 122) resulted in a comprehensive series of structural tests. Chapter 7 has presented the design of those tests relating to shear behaviour. Test data, results and analysis for the beam designs presented in this Chapter are provided in full in Chapter 8.

In addition to the structural testing, additional work undertaken to assess the durability benefits for concrete cast in fabric formwork are presented separately in Chapter 9. While each of these test series can be viewed alone, the results presented in Chapter 6, Chapter 8 and Chapter 9 are most advantageously considered together such that they support the thesis that fabric formwork can facilitate a sustainable future in concrete construction through its ability to harness a flexible mould to create optimised, durable, architecturally interesting concrete structures.

[blank page]



# Chapter 8 Development (2)

## Shear behaviour

### 8.1. Introduction

In Chapter 6 a body of test data and analysis was presented to demonstrate how fabric formwork can facilitate the construction of optimised beams subject to uniformly distributed loads that fail in flexure. Throughout this thesis it has been seen that experimentally verified, robust and simple to use design guidance for calculating the shear capacity of such elements is not readily available, and that load capacity predictions using existing methods can be unconservative.

To address this aspect of the test matrix described in §5.4 on page 122, the following chapter details further tests undertaken to establish the shear behaviour of tapered concrete sections. Three test series (Table 6.2 on page 157 and Figure 6.1 on page 158 ) are presented, with further analysis and development provided in Chapter 10. A total of nineteen beams with a variable cross section were tested with the following aims:

1. To determine a design method that can predict both flexural and shear type failures;
2. To demonstrate the provision of transverse reinforcement to move a section from a shear to a flexural failure mode;
3. To provide a simple method for the design of transverse reinforcement in variable section beams;
4. To provide a method for the provision of nonmetallic reinforcement in variable section fabric formed beams.

The first test series considered beams with a continuously varying cross section subject to distributed loads and is presented in §8.2. Results of this series are then extended and developed throughout the Chapter, including through the use of digital image correlation (§8.5) to analyse strain distributions during loading.

## 8.2. Three-metre span beams

### 8.2.1. Introduction

To address the aims presented above, an initial series of tests were undertaken on 3m span beams subjected to a uniformly distributed load and designed using the compressive force path (CFP) method described in §7.2 on page 218.

The beams described in this section are numbered to the convention described below. Two beams of type 8\_1 and 8\_2 were tested, and one each of Beam 8\_3i and 8\_3ii (a total of six specimens).

1. Beam 8\_1a and 8\_1b: 3m span bending moment shaped beam designed to the CFP method without transverse reinforcement;
2. Beam 8\_2a and 8\_2b: 3m span bending moment shaped beam designed to the CFP method with transverse reinforcement provided by 3mm diameter steel bars;
3. Beam 8\_3i: 3m span bending moment shaped beam with variable depth longitudinal steel, without transverse reinforcement;
4. Beam 8\_3ii: 3m span prismatic beam with constant depth longitudinal steel, without transverse reinforcement.

The longitudinal bars in beam 'a' of each test were extended beyond the mould to allow their displacement (bar slip) under loading to be monitored, while the bars of Beam 'b' of each test were kept within the section. Beam 8\_3 (denoted *i* and *ii*) was designed in a different manner, as shown in Figure 8.1. Concrete tensile and compressive strengths for each beam, taken from 100mm cubes, are provided in Table 8.2 and Table 8.3<sup>1</sup>.

Table 8.1: Concrete mix design per m<sup>3</sup>.

Cement (CEM IIbv)	4-8mm aggregate	0-5mm aggregate	Water
450kg	1055kg	705kg	190kg

Table 8.2: Concrete properties in compression.

Beam	7 Days (3 cubes)		14 Days (3 cubes)		28 Days (3 cubes)		Testing date
	$f_c$ (MPa)	SD	$f_c$	SD	$f_c$	SD	
8_1a	34.5	-(1)	39.7	0.50	-(2)	-	14 days
8_1b	29.6	-(1)	35.6	0.98	-(2)	-	14 days
8_2a	36.2	2.27	46.4	0.62	48.5	3.74	7 days
8_2b	38.5	1.16	48.3	0.21	53.3	0.28	7 days
8_3i	30.1	0.68	37.4	0.04	38.8	0.28	28 days
8_3ii	30.1	1.38	37.4	0.19	41.1	2.46	28 days

Where  $f_c$  = average concrete cube (100mm) compressive strength; SD = standard deviation on test results. (1): only one cube tested; (2) no cubes tested.

<sup>1</sup> Compressive strength determined in accordance with BS EN 12390-3:1990. Tensile splitting test carried out on 100mm cubes as discussed in BS EN 12390-6:1990, this method is generally considered to provide tensile strengths 10% greater than those of a 100mm diameter cylinder.

Table 8.3: Concrete properties in tension.

Beam	At testing (3 cubes)		Testing date
	$f_t$	SD	
8_1a	3.6	0.42	14 days
8_1b	3.7	0.28	14 days
8_2a	4.1	0.28	7 days
8_2b	3.6	0.54	7 days

Where  $f_t$  = average concrete cube (100mm) splitting tensile strength; SD = standard deviation on test results.

### 8.2.2. Beam layouts

Beams 8\_1 - 8\_3 are illustrated again in Figure 8.1, to the designs presented in §7.2 on page 218. Longitudinal reinforcement was kept constant throughout, although in Beam 8\_2 two additional three millimetre bars were placed in the top zone of the beam to support the transverse reinforcement. The additional compression capacity provided by these bars is negligible and was therefore ignored in the analysis.

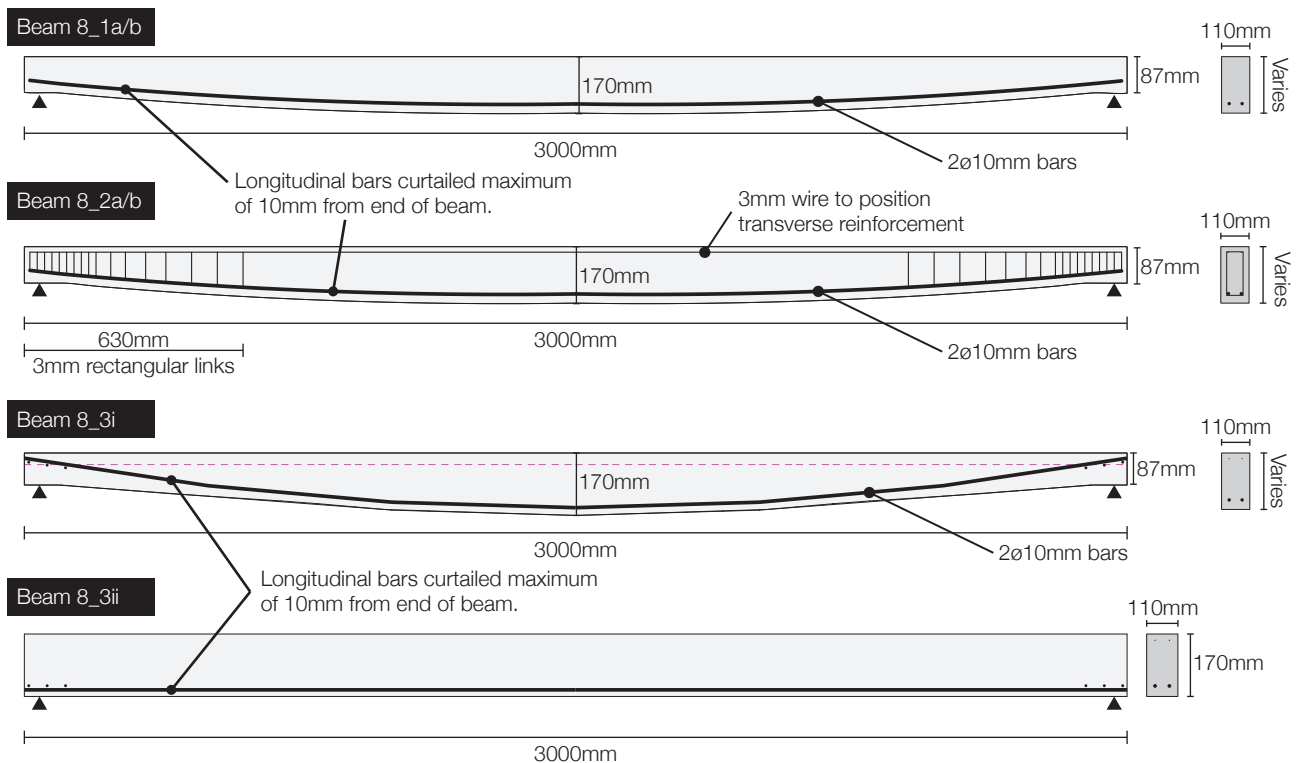


Figure 8.1: Beams 8\_1 - 8\_3 as tested.

### 8.2.3. Construction

In contrast to previous tests, the 3m span beams were constructed in conventional steel moulds, using timber formwork to create the desired beam profile. This allowed for quick construction of multiple identical elements, and is illustrated in Figure 8.2.



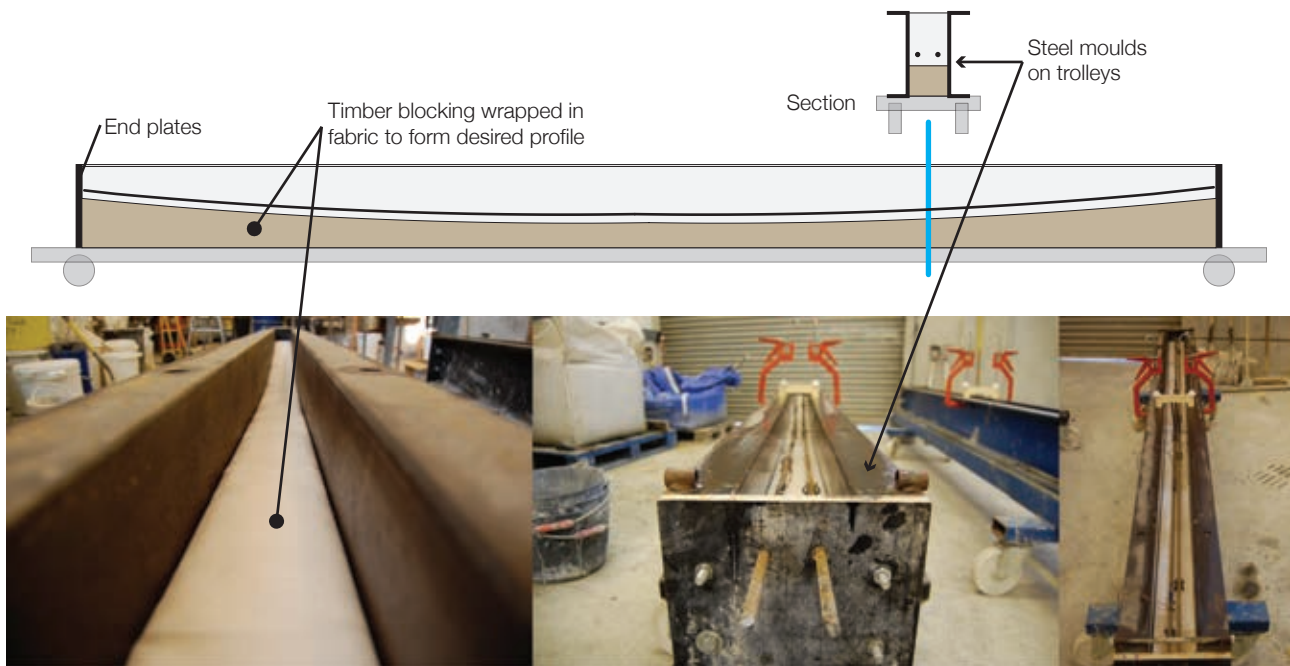


Figure 8.2: 3m span beam construction.

#### 8.2.4. Testing

After curing for a minimum of 7 days, the beams were tested in seven point bending, as shown in Figure 8.3. Load cells and displacement transducers were arranged as shown, while Beams 8\_1 and 8\_2 had five strain gauges positioned on one of their longitudinal steel reinforcing bars, with a further displacement transducer placed to monitor the protruding bar in one of each of the beam tests, as described previously.

All beams were tested to the same load cases, with load applied through hydraulic jacks and continually monitored using the attached load cells. After the design loads had been achieved, the loads were increased until the end jacks had exhausted their stroke or the beam had failed. Displacements and failure modes are summarised in Table 8.4, where the maximum load carried by each beam is also given. A summary of load versus midspan deflection for all beams is shown in Figure 8.3, with more detailed results provided in the following sections.

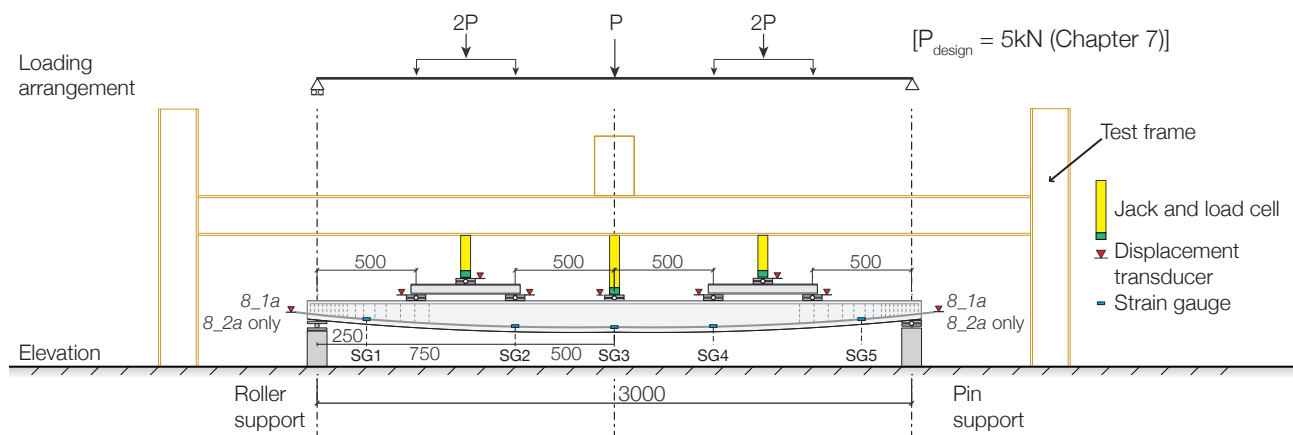


Figure 8.3: Test set up.

Table 8.4: Test failure modes and ultimate capacity.

Beam	Design load, 5P (Figure 8.3, kN)	Initial midspan deflection at design load (mm)	Maximum load (kN)	Failure load (kN)	Midspan deflection at failure (mm)	Failure Mode
8_1a	25	30.976	27.5	25.9	70.4	Flexure
8_1b	25	42.565	26.1	26.1	46.1	Shear
8_2a	25	38.293	26.9	24.7	89.8	Flexure
8_2b	25	41.290	26.8	21.1	121.0	Flexure
8_3i	25	-	19.9	19.9	37.25	Shear
8_3ii	25	26.39	27.8	23.8	48.3	Flexure

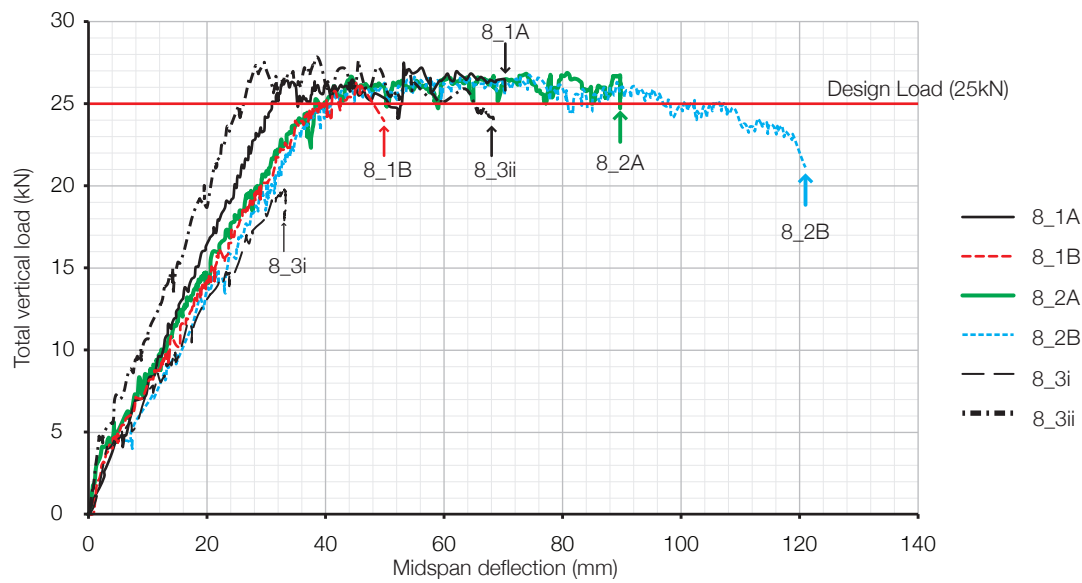


Figure 8.4: Load-midspan deflection summary.

#### 8.2.4.1. Beam 8\_1

Beam 8\_1 was designed to carry a total vertical load of 25kN, but was predicted by the design method to fail in shear at the support zone and did not have any transverse reinforcement. Beam 8\_1a was tested first with load applied in 1kN increments. Flexural cracking was first recorded at 5kN total load, and propagated as shown in Figure 8.5. Inclined cracking was not recorded in the end zone of the beam, which displayed considerable ductility upon reaching the design load of 25kN, and a maximum midspan displacement of 74.7mm was recorded ( $span/40$ ).

Beam 8\_1b was tested in the same manner, with first cracking again recorded at a total applied load of 5kN. The cracks propagated as shown in Figure 8.7, and began to incline in the support zone at the design load of 25kN. Failure followed, in an explosive shear mode, captured from the test video in Figure 8.9 on page 251.

Whilst both Beam 8\_1a and Beam 8\_1b reached the design load, only Beam 8\_1b was found to fail in a predominantly shear mode, with the resulting explosive failure provided a clear demonstration as to why such failures must be avoided. Beam 8\_1a showed a ductile flexural failure, reaching a significant midspan deflection before crushing of the compression zone was seen (Figure 8.8). The difference in failure mode illustrates that this beam is on the cusp of the design shear-flexure failure mode envelope that is described in §7.2 on page 218.

Whilst Beam 8\_1a had a slightly improved anchorage length due to the protruding longitudinal bars (Figure 8.8), data taken from displacement transducers that were placed to monitor the bars during testing showed that they did not move significantly during each test. This data is shown in Figure 8.6, where the differential slip results from both ends of one longitudinal bar are presented. The data appears to show that the bar monitored at the roller end showed a gradually increasing slip of up to 4mm at the maximum load - in contrast to the results at the pinned end where the slip reaches approximately 0.15mm at the same load point, before increasing rapidly.

Intrusive surveys of Beam 8\_1b, which failed in shear and had its longitudinal steel curtailed at the end of the beam (Figure 8.1), also showed that the steel bars did not slip significantly during testing, indicating that anchorage of the bars was sufficient and the difference in failure mode should therefore not be exclusively attributed to slip in the longitudinal reinforcing bars.

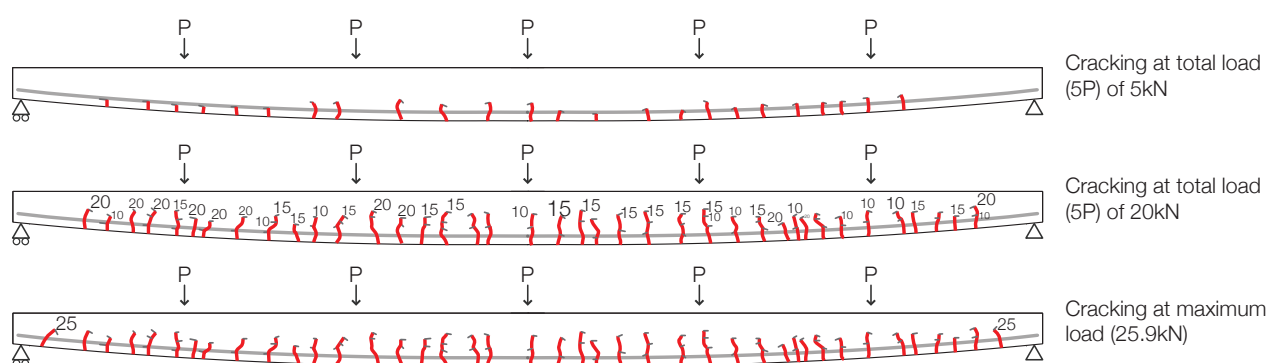


Figure 8.5: Crack propagation, Beam 8\_1a.

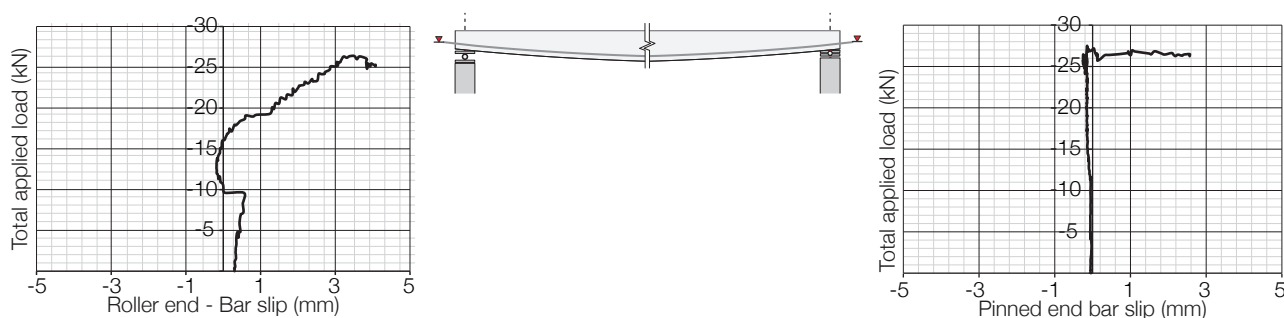


Figure 8.6: Transducer results for longitudinal steel in Beam 8\_1a.

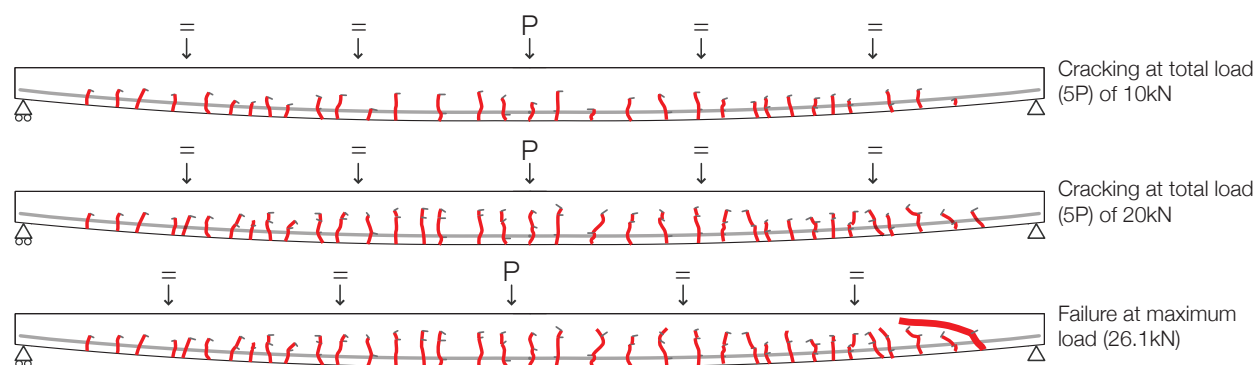


Figure 8.7: Crack propagation, Beam 8\_1b.

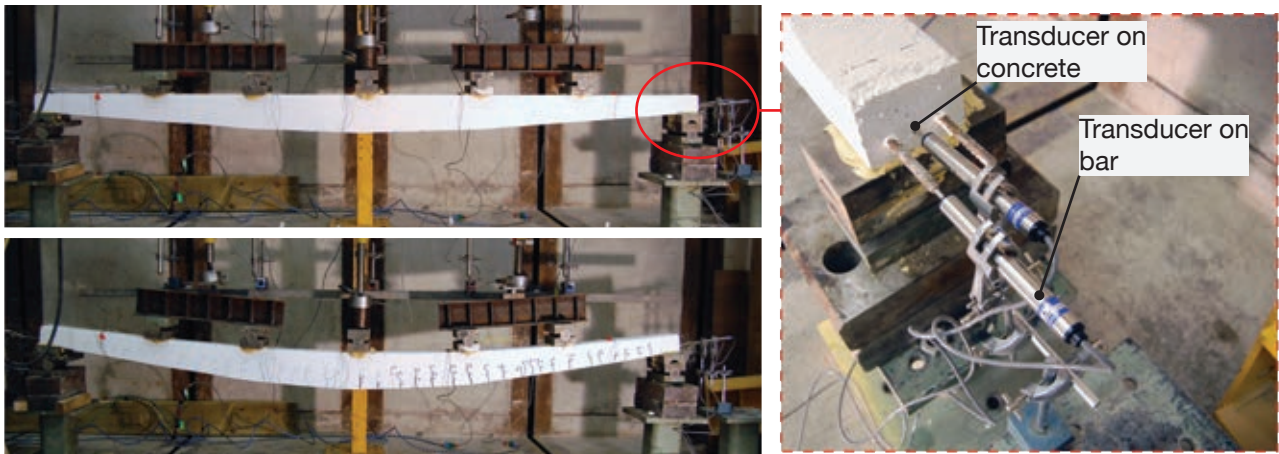


Figure 8.8: Beam 8\_1a (transducers placed at both ends of the Beam).

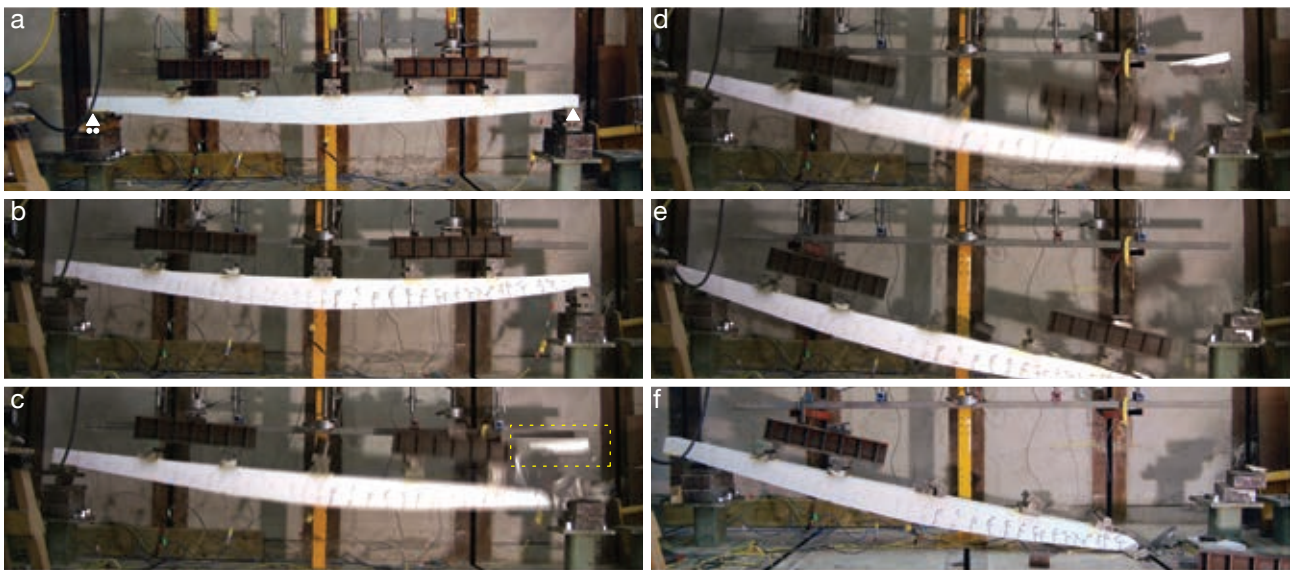


Figure 8.9: Beam 8\_1b failure, in sequence from (a) to (f) covering approximately 0.5 seconds. Explosive failure recorded at the pinned support, with considerable vertical displacement seen.

#### 8.2.4.2. Beam 8\_2

Beams 8\_2a and 8\_2b, which were provided with transverse reinforcement, were then tested under the same setup as used in Beam 8\_1. Upon loading of Beam 8\_2a, cracking was first recorded at 5kN total load and propagated as shown in Figure 8.10 before failure in flexure-compression. Significant ductility at the maximum load was recorded, with a midspan displacement of 89.7mm (span/33) recorded at failure. Displacement transducers placed on one longitudinal bar of Beam 8\_2a recorded small amounts of slip (maximum of 0.349mm) for the bar at the roller end of the beam, while at the pinned end a gradually increasing value of slip was recorded. During the recorded ductile behaviour, this reached a maximum of 2.56mm, as shown in Figure 8.11. These results are similar, but more pronounced, than those seen for Beam 8\_1a (Figure 8.6).

Beam 8\_2b was then loaded in the same manner and initial cracking was again recorded at 5kN. Distributed cracking in the beam span increased under loading, before the element failed in the same manner as Beam 8\_2a, as shown in Figure 8.12.



Both Beam 8\_2a and 8\_2b exhibited a flexural failure mode, thus providing the ductile response predicted by the design method as shown in Figure 8.13. These results have thus demonstrated that the CFP method may be used to successfully design shear reinforcement in variable section beams, and that it can also quite accurately predict the change in behaviour from flexural failures seen in Beam 8\_2 to the shear failure seen in Beam 8\_1b.

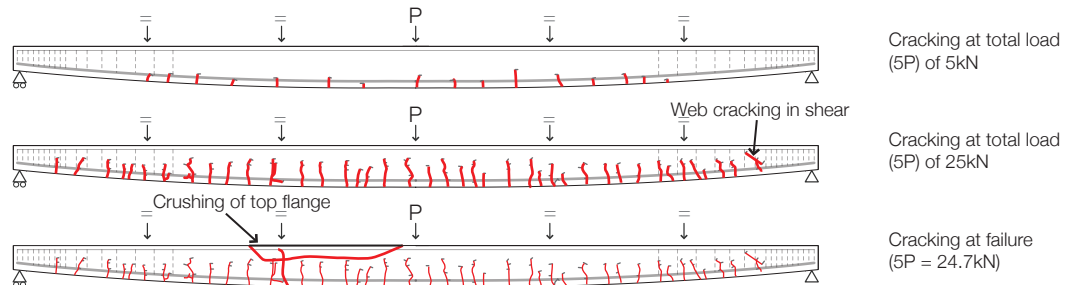


Figure 8.10: Crack propagation, Beam 8\_2a.

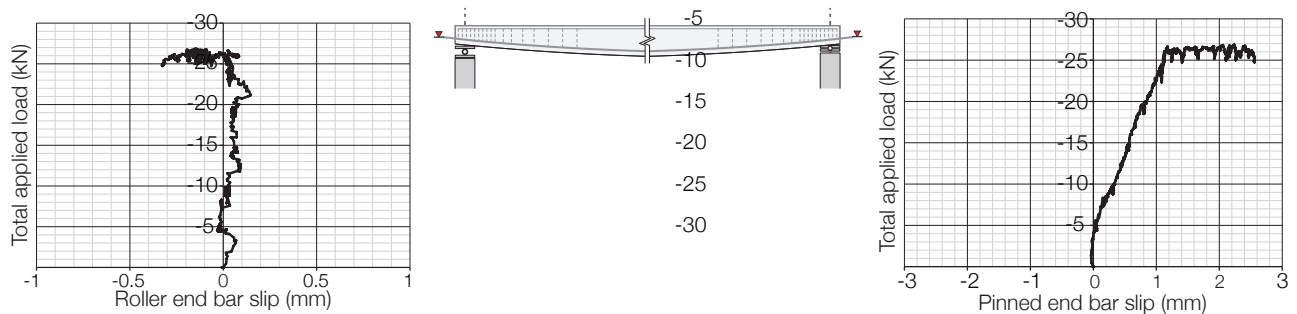


Figure 8.11: Bar slip transducer results for Beam 8\_2a.

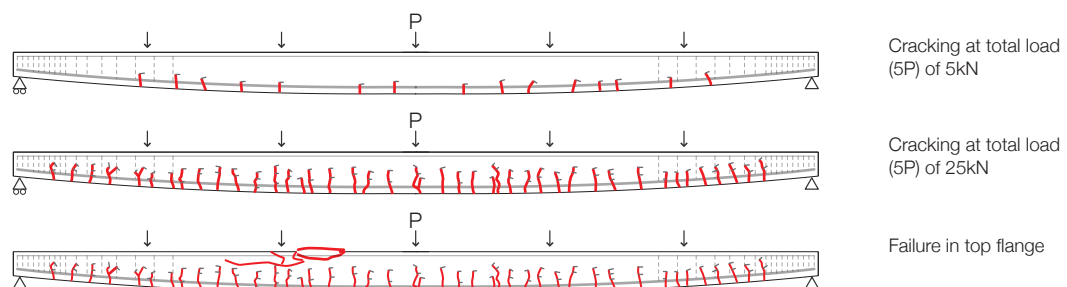


Figure 8.12: Crack propagation, Beam 8\_2b.

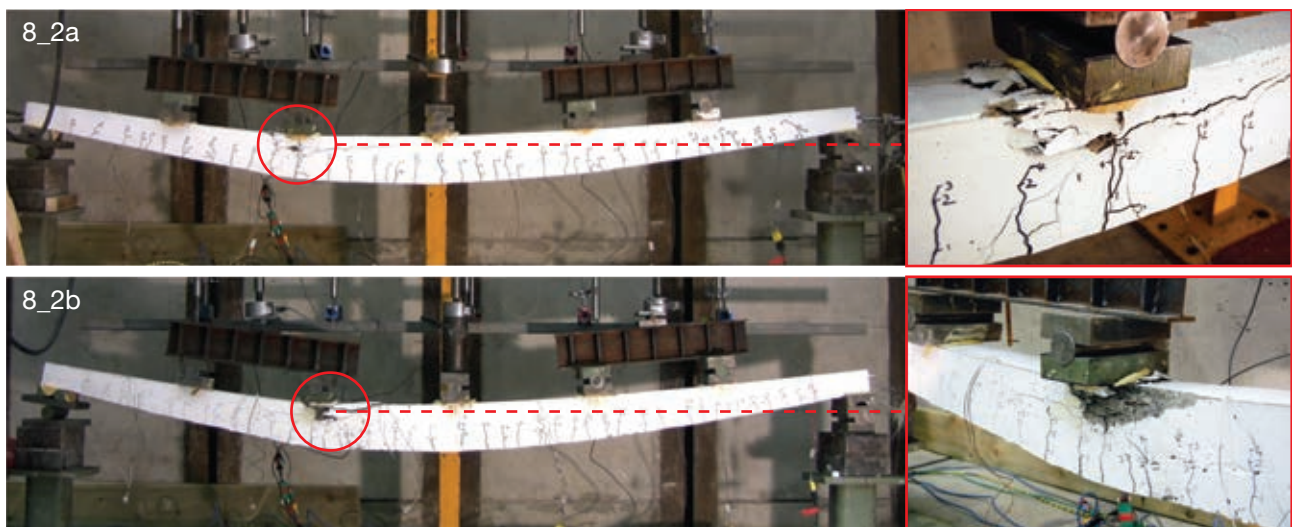


Figure 8.13: Beams 8\_2a and 8\_2b.

### 8.2.4.2.1. Bar strains

Five strain gauges were placed along one longitudinal reinforcing bar in each of the beam tests (as shown in Figure 8.3 on page 248). Two strain gauges in Beam 8\_2b failed during the construction process, but the remaining were functioning throughout the test. A comparison between the recorded bar strains in Beams 8\_1b and 8\_2b is provided in Figure 8.14 whereupon it is seen that the presence of the transverse reinforcement in Beam 8\_2b has not significantly altered the strain in the longitudinal reinforcement.

In Beam 8\_1a, none of the strain gauges recorded steel yielding, while in Beam 8\_1b only Strain Gauges 2 and 3 (Figure 8.3 on page 248) were yielding at failure. In Beam 8\_2a Strain Gauge 5 is seen to yield just prior to failure, and in Beam 8\_2b none of the gauges record a yielding of the steel. This contrasts to the Eurocode design approach, which assumes the full steel capacity may be utilised in its calculation of flexural and shear capacities.

The similarities in strain carried in the flexural reinforcement of beams with and without transverse reinforcement suggests that in a section without transverse reinforcement the ability of the section to carry shear appears to be significantly determined by the capacity of the web (either concrete alone or with transverse reinforcement). This may demonstrate how Beam 8\_1 was more susceptible to a brittle failure than Beam 8\_2. It should be further noted that the design method does not account for the inclination of the longitudinal steel reinforcement; this aspect is considered in greater detail in §8.3 on page 260.

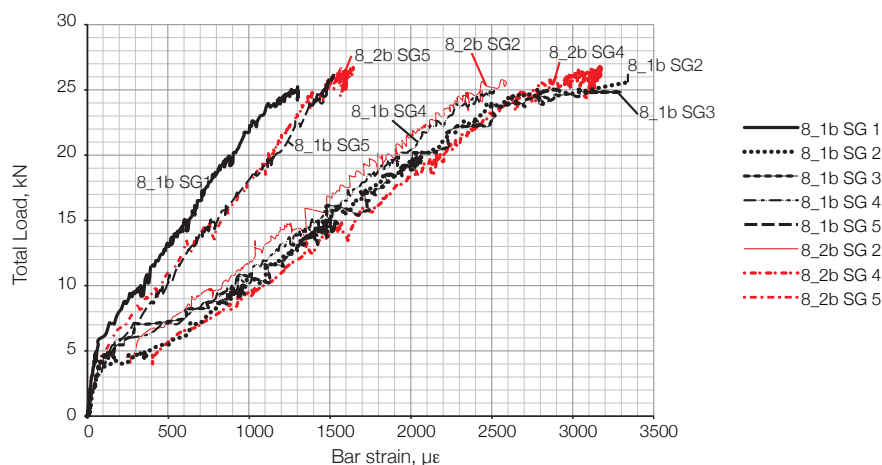


Figure 8.14: Strain recorded in Beam 8\_1b and Beam 8\_2b.

### 8.2.4.3. Beam 8\_3i and Beam 8\_3ii

Following the beams tested above and designed using the compressive force path model, two final tests were undertaken to determine the practical effect of a tapered versus prismatic beam when loaded in seven point bending. The designs for Beam 8\_3i and 8\_3ii are presented in §7.2 on page 218.

The variable depth Beam 8\_3i was tested first in an identical setup to that used for Beams 8\_1 and 8\_2. Cracking again commenced at a total applied load of 5kN, but in this case there were immediately deep cracks in the support zones, as shown in Figure 8.15. A large inclined crack formed at the pinned support at an applied load of 10kN, and grew horizontally (as shown in Figure 8.15) up to a total load of 20kN, whereupon failure was recorded



at an applied load of 21.5kN. The presence of such a horizontal crack was not seen in any other tests in this series. The failure mode was not as violent as seen in Beam 8\_1b, which also failed in shear (but reached its design load of 25kN), as illustrated in Figure 8.18. Strain gauges were not placed on the internal steel reinforcement in this test, and thus additional comparisons with Beams 8\_1 and 8\_2 are difficult to draw.

The prismatic Beam 8\_3ii was then tested in the same manner, and cracking again commenced at a total load of 5kN, before propagating as shown in Figure 8.16. Inclined flexural cracks began to form near the support zone at 20kN applied load, but failure was eventually found to occur in a flexural mode at the midspan at slightly above the design load of 25kN (Figure 8.17(r)). As strain gauges were not placed on the internal reinforcement in this test, it is not possible to determine the state of the steel bars at failure, although it can be assumed for Beam 8\_3ii that the bars will have yielded at the midspan.

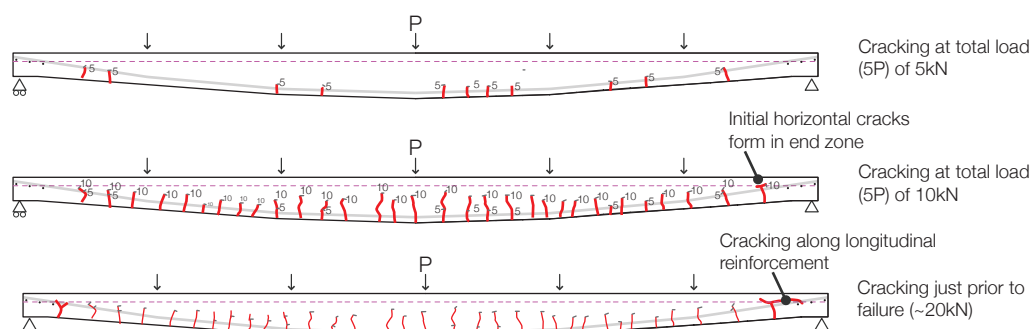


Figure 8.15: Crack propagation, Beam 8\_3i.

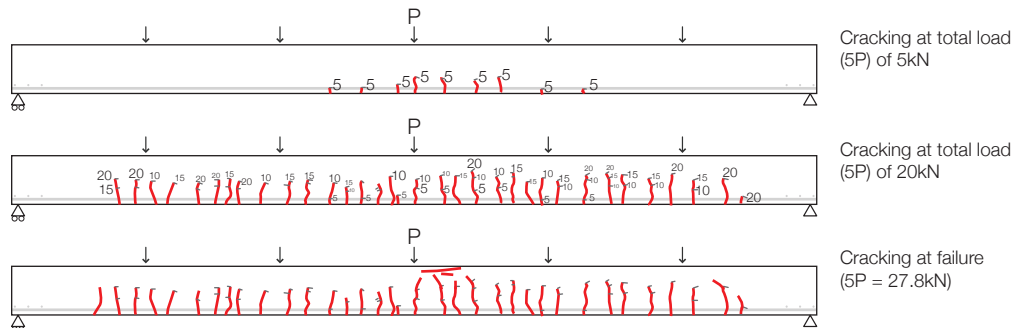


Figure 8.16: Crack propagation, Beam 8\_3ii.

These results are enlightening for a number reasons. First, the use of an inclined bar to provide full shear capacity to the section has not been successful. The results suggest that the assumption that the steel reinforcement yields are not necessarily valid. This conclusion is again explored in more detail in §8.3 on page 260. The results further suggest that tapered beams may always require some form of shear reinforcement to guard against brittle failures such as those seen in Beam 8\_3i.

Second, the comparison between Beam 8\_3i and Beam 8\_1b (Figure 8.18) demonstrates the difference in crack patterns at failure that result from moving the longitudinal reinforcement away from the bottom face of the beam. Beams 8\_1, 8\_2, and 8\_3i all share the same external geometry, and thus the differences between them (as shown in the load-deflection response, Figure 8.4 on page 249) arise from variations in internal steel layouts only.

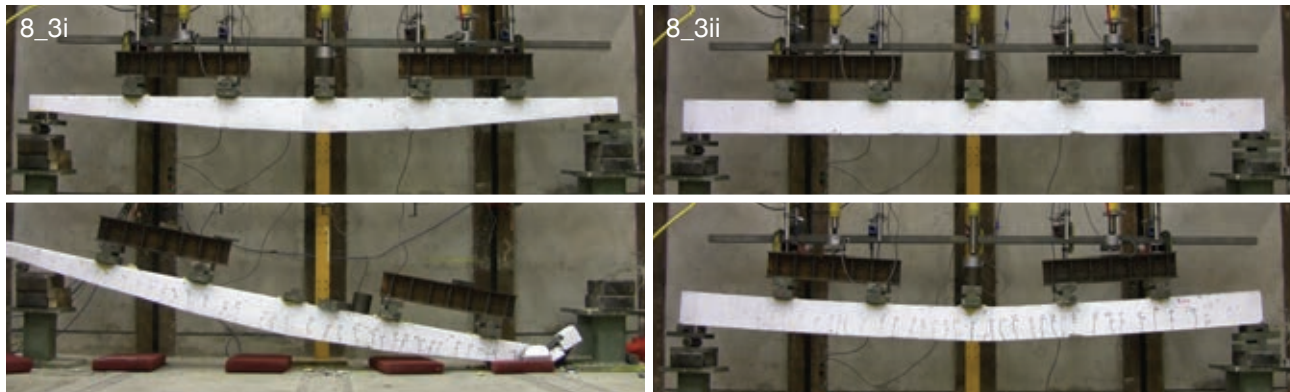


Figure 8.17: Beam 8\_3i (l) and 8\_3ii (r) failure comparison.

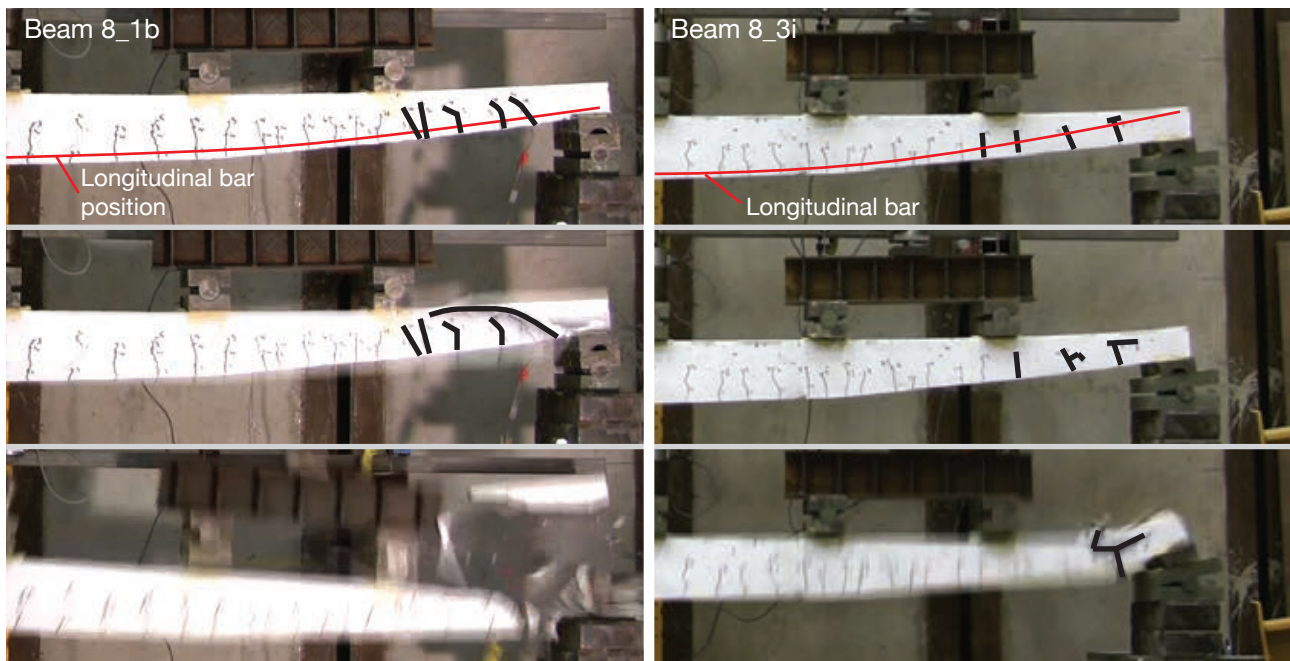


Figure 8.18: Beam 8\_1b and 8\_3(i) failure comparison.

The idealised behaviour of Beam 8\_3i that has been assumed through the design process is illustrated in Figure 8.19(a). Here, the compression force reaches the support without any inclination, and the effective depth of the tension steel increases in proportion to the moment requirement of the loading envelope. In this way, the moment capacity above the support is zero, and increases away from the it. There is no horizontal load on the support, and the system in equilibrium. It is clear, however, that this is not how beams behave in their end zones.

When the compression force meets the support at an inclined angle, there must be a resolution of this force, which in the case of Beam 8\_3i is not provided by the tension steel but by the tension capacity of the concrete. Hence, the crack pattern shown is a vertical crack through the concrete up to the tension bar followed by an inclined crack along the bottom of the steel (Figure 8.18(r)).

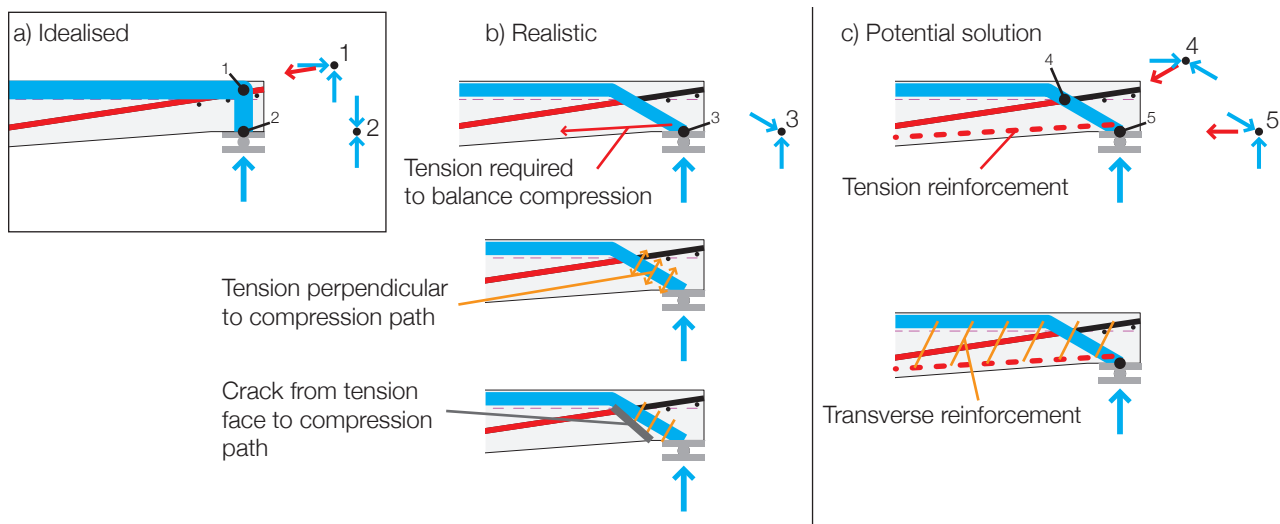


Figure 8.19: Tension forces in the end zone of Beam 8\_3i.

In addition, compression in the inclined strut has coexisting tension forces in the orthogonal direction (Figure 8.19(b)), which must be carried by either the concrete or transverse steel reinforcement. In Beam 8\_3i, the concrete must resist these tension forces. Without the provision of transverse reinforcement the behaviour of the beam at its supports is inadequate and hence failure occurs here.

Therefore, it is to be recommended for the design of a simply supported beam that:

1. Additional longitudinal reinforcement be placed along the bottom face of the beam to carry the tension force, with the resulting increase in moment capacity accounted for in the analysis (Figure 8.20); and/or
2. Transverse reinforcement be placed at the end zone to carry the tension forces Figure 8.19(c).

It should be noted that in reality the simply supported design condition (without any lateral constraints) does not usually exist and a degree of continuity between elements may perhaps facilitate the flow of forces described above. This is illustrated in tests on the tapered beams presented in §8.3.9.4 on page 281.

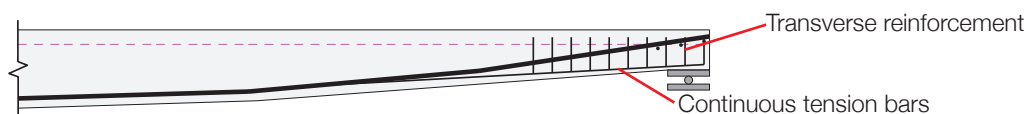


Figure 8.20: Proposed reinforcement layout for Beam 8\_3i.

### 8.2.5. Shear failures

In considering the potential for developing a variable angle truss model (§4.3 on page 95) for tapered beams, it is useful to compare cracking angles at failure in Beams 8\_1b, 8\_2a and 8\_3i, as shown in Figure 8.21.

By comparing Beams 8\_1b and 8\_2a, it is apparent that the addition of transverse reinforcement to the beam section (all have the same longitudinal steel layouts and external geometry) allows cracks to develop at a steeper angle close to the support zone. This is in contrast to the behaviour of Beam 8\_3i (discussed above) in which the crack first reaches the longitudinal steel in a vertical direction, before moving horizontally along the line of tension reinforcement, as shown in Figure 8.21.

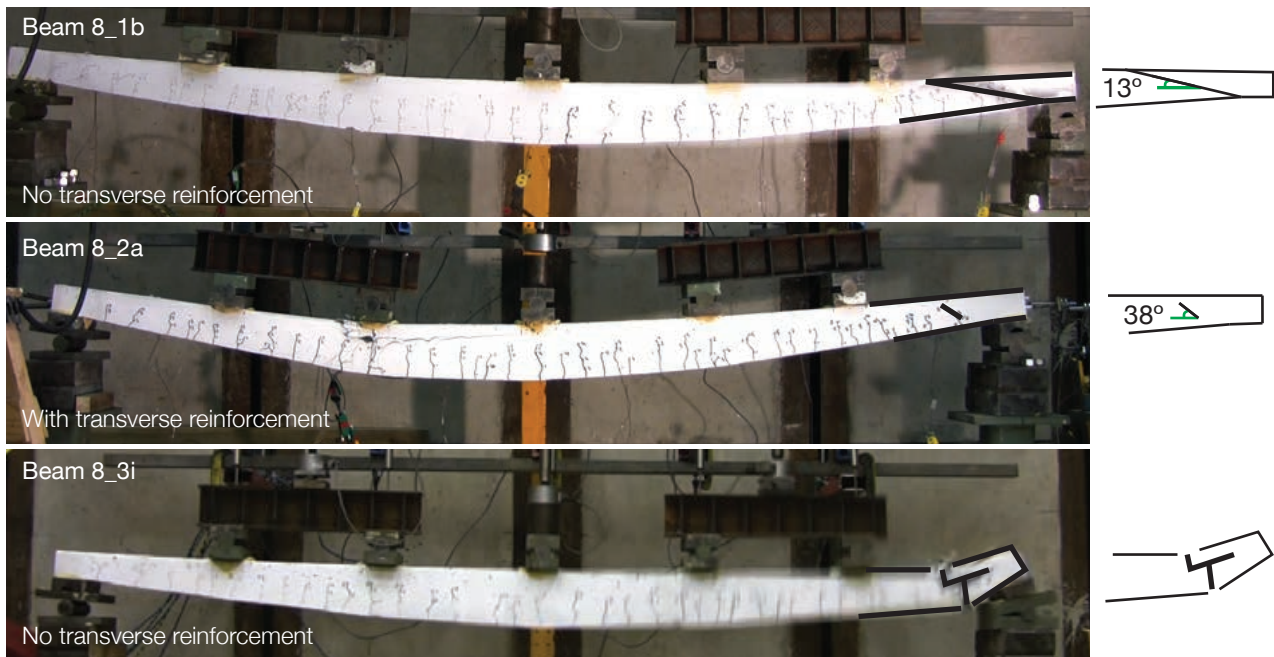


Figure 8.21: Shear crack angles in 8\_1b and 8\_2a at 25kN load and Beam 8\_3i at 21.5kN.

The crack pattern seen in Beam 8\_3i suggests an unconventional shear failure occurred in the beam due to the shallow effective depth of the longitudinal steel reinforcement. This is illustrated in Figure 8.22, where video stills show how the failure progressed from the horizontal cracking seen along the compression path to an abrupt failure of the compression path that relinquished the beam of its entire capacity as the compression block had no other place to move to. The resulting failure then bent the flexural reinforcement at the point of compression failure.



Figure 8.22: Failure progression in Beam 8\_3i showing development of flexure-shear failure cracks.

The failures recorded in Beam 8\_3i show similarities with failures seen in both prismatic and non-prismatic beam tests undertaken by Hashemian (2012), as described in §2.5.1 on page 27. It is thus apparent that both the longitudinal and transverse reinforcement positioning must be carefully designed to avoid such failures, as described later in §8.5 on page 301.

### 8.2.6. Capacity predictions

Capacity predictions for each of Beams 8\_1, 8\_2, and 8\_3 were undertaken using 1) the method proposed in BS EN 1992-1-1 (2004); 2) the compressive force path method and 3) the modified compression field theory. The results of this analysis are presented below to provide a further illumination into the behaviour of the elements.

For the Eurocode predictions, all sections along the length of the beam were assessed, and the position determining the overall strength of the element provided the maximum beam capacity. Assessment using the MCFT method was undertaken using the software 'Response-2000' (Bentz, 2000) with each section along the length of the



beam analysed to determine which was critical (the software at present does not include a method for analysing tapered beams, so this does not include the effects of inclined longitudinal reinforcement, which may have a contribution to make to the section's shear capacity as discussed later in this Chapter). The results for Beams 8\_1 and 8\_2 are provided in Table 8.5 and for Beams 8\_3 in Table 8.6. The results are not combined as the two sets of beams have quite different designs.

Table 8.5 shows that, as known from the design method, the CFP approach is consistently accurate for Beams 8\_1 and 8\_2. Design checks on the same beams using BS EN 1992-1-1 (2004) are generally more conservative, with a wider range of predicted capacities reflected in a higher standard deviation. The MCFT approach for the same beams is less conservative and more consistent than the Eurocode method, but is not as accurate as the CFP method.

For Beam 8\_3i (Table 8.6) predictions using the CFP method are very conservative, and this may reflect the empirical nature of the moment capacity equation (Eq. 7.1 on page 219), which may be unduly influenced by the very shallow support zone of this particular beam design. The low capacity prediction is contrasted with a more accurate prediction for Beam 8\_3ii using the same method. Analysis using BS EN 1992-1-1 (2004) is equally inconclusive, showing a better average capacity prediction, but overestimating the strength of Beam 8\_3i by 25%.

The MCFT method follows a similar pattern to the results of the CFP method - under predicting Beam 8\_3i and over predicting Beam 8\_3ii. This may again have been influenced by the very shallow effective depth in the support zone of Beam 8\_3i. In contrast, the Eurocode approach over predicted the capacity of Beam 8\_3i as it uses the inclined longitudinal bar as shear reinforcement, whilst this is not incorporated into the CFP design method and clearly did not have the desired effect on the failure load of the beams. This aspect and apparent failing of the design method using BS EN 1992-1-1 (2004) is investigated in much greater detail in §8.3 on page 260.

Table 8.5: Capacity prediction comparisons, Beams 8\_1 - 8\_2.

Beam	Maximum load (kN) [A]	CFP Capacity Prediction [B]	[A] / [B]	EC2 Capacity Prediction [C]	[A] / [C]	MCFT Capacity Prediction [D]	[A] / [D]
8_1a	27.50	25.00 (1)	1.10	17.00 (1)	1.62	20.40	1.35
8_1b	26.10	24.40 (1) (3)	1.04	16.39 (1)	1.59	19.40	1.35
8_2a	26.90	25.00 (2)	1.08	25.00 (2)	1.08	22.80	1.18
8_2b	26.80	25.00 (2)	1.07	25.00 (2)	1.07	22.80	1.18
		Average	<b>1.08</b>	Average	<b>1.34</b>	Average	<b>1.26</b>
		Standard deviation, $\sigma$	<b>0.01</b>	$\sigma$	<b>0.31</b>	$\sigma$	<b>0.10</b>
(1) Predicted shear failure; (2) Predicted flexural failure; (3) Lower value reflecting lower concrete strength in tested beam than assumed during design.							

Table 8.6: Capacity prediction comparisons, Beams 8\_3(i) and 8\_3(ii).

Beam	Maximum load (kN) [A]	CFP Capacity Prediction [B]	[A] / [B]	EC2 Prediction [C]	[A] / [C]	MCFT Capacity [D]	[A] / [D]
8_3i	19.90	12.85 (1)	1.55	25.00	0.80	13.00	1.53
8_3ii	27.80	29.00 (2)	0.96	25.00 (1)	1.11	34.00	0.82
		Average	<b>1.25</b>	Average	<b>0.95</b>	Average	<b>1.17</b>
		$\sigma$	<b>0.42</b>	$\sigma$	<b>0.22</b>	$\sigma$	<b>0.50</b>
(1) Predicted shear failure; (2) Predicted flexural failure							

### 8.2.7. Conclusions

The tests undertaken suggest that the compressive force path method may be successfully used for tapered sections carrying uniformly distributed loads with little modification. The test results presented in this Chapter raise interesting questions as to what shear failures actually represent - Beam 8\_3i failed catastrophically, but in a failure mode that is more akin to a flexural failure than most shear failures and reflects quite closely the chosen position of the longitudinal bar. This interesting detail provides us with new questions surrounding how combinations of moment and shear should be addressed in sections with very small effective depths.

Analysis using three different design methods has shown some significant differences between them, but has also shown that a safe design method for some tapered beams is available in the form of the compressive force path method or the modified compression field theory. The extension of the compressive force path method to include tapered beams in shear critical loading is discussed in greater detail in the following section. The results have further suggested that the BS EN 1992-1-1 (2004) allowance for inclined tension bars to provide shear resistance may be unconservative, and this is also analysed (and further confirmed) in §8.3.

The results of previous tests (as discussed in Chapter 2) which suggested that variable depth beams are more likely to fail in shear than in flexure when they are not transversely reinforced have been partially verified by the tests described in this section.

In the tests described above, relatively little instrumentation was used and this has made further analysis of the beam behaviour difficult, particularly where failures have occurred and originated in the concrete and not the steel. In an attempt to better monitor the behaviour of the concrete, digital image correlation (DIC) is used in the following section to monitor strain distributions within the concrete during loading. In this way, the behaviour of tapered beams loaded predominantly in shear is considered in more detail. Results of the DIC analysis are presented in §8.5 on page 301.



### 8.3. Tapered beams in shear

#### 8.3.1. Introduction

Following the tests presented in §8.2, a second series of more detailed tests was undertaken considering beams loaded predominantly in shear (point loads applied close to the support zone). This test series was focused on determining the detailed changes in behaviour that have been seen in previous tests between elements designed using the compressive force path and BS EN 1992-1-1 (2004) design methods. The design process undertaken for these elements is presented in §7.2 on page 218. Additional tests using a strut-and-tie model are presented separately in §8.4 on page 284, with all the test results then being analysed in §8.5 on page 301.

Each beam except Beam 9\_1 was tested twice, as described by Figure 7.14 on page 228 and a summary of the beam layouts is provided in §8.3.2. Two elements of Beam 9\_2\_EC2 and 9\_2\_CFP were constructed, and are therefore denoted (i) and (ii). A total of ten specimens were cast, resulting in a total of eighteen tests in §8.3.

The concrete mix design is given in Table 8.7 and the measured concrete strengths at testing are given in Table 8.8. The beams were tested at either 10 or 14 days.

Table 8.7: Concrete mix design per m<sup>3</sup>.

Cement (CEM IIbv)	4-8mm aggregate	0-5mm aggregate	Water
450kg	1055kg	705kg	190kg

Table 8.8: Concrete properties - compression.

Beam	10 Days (3 cubes)		14 Days (3 cubes)		28 Days (3 cubes)		Testing date
	$f_c$	SD	$f_c$	SD	$f_c$	SD	
9_1_EC2	-	-	38.6	2.35	43.6	1.18	14 days
9_2_EC2(i)	-	-	44.9	2.16	45.7	2.29	14 days
9_2_EC2(ii)	38.5	0.22	-	-	46.7	3.06	10 days
9_3_EC2	-	-	38.6	2.35	43.6	1.18	14 days
9_4_EC2	-	-	44.9	2.16	45.7	2.29	14 days
9_1_CFP	46.7	0.39	-	-	53.7	1.04	10 days
9_2_CFP(i)	35.2	1.81	-	-	44.8	1.06	10 days
9_2_CFP(ii)	39.5	1.02	-	-	52.6	0.29	10 days
9_3_CFP	45.2	0.06	-	-	48.4	2.17	10 days
9_4_CFP	45.2	0.06	-	-	48.4	2.17	10 days

Where  $f_c$  = average of three concrete cube (100mm) compressive strength tests; SD = standard deviation on test results.

#### 8.3.2. Beam layouts

Beams 9\_1 - 9\_4 are illustrated again in Figure 8.23. Longitudinal reinforcement was kept constant throughout, using two H10 U-bars arranged as shown in Figure 7.16 on page 229. Two three millimetre bars were placed in the top zone of the beam to support transverse reinforcement.

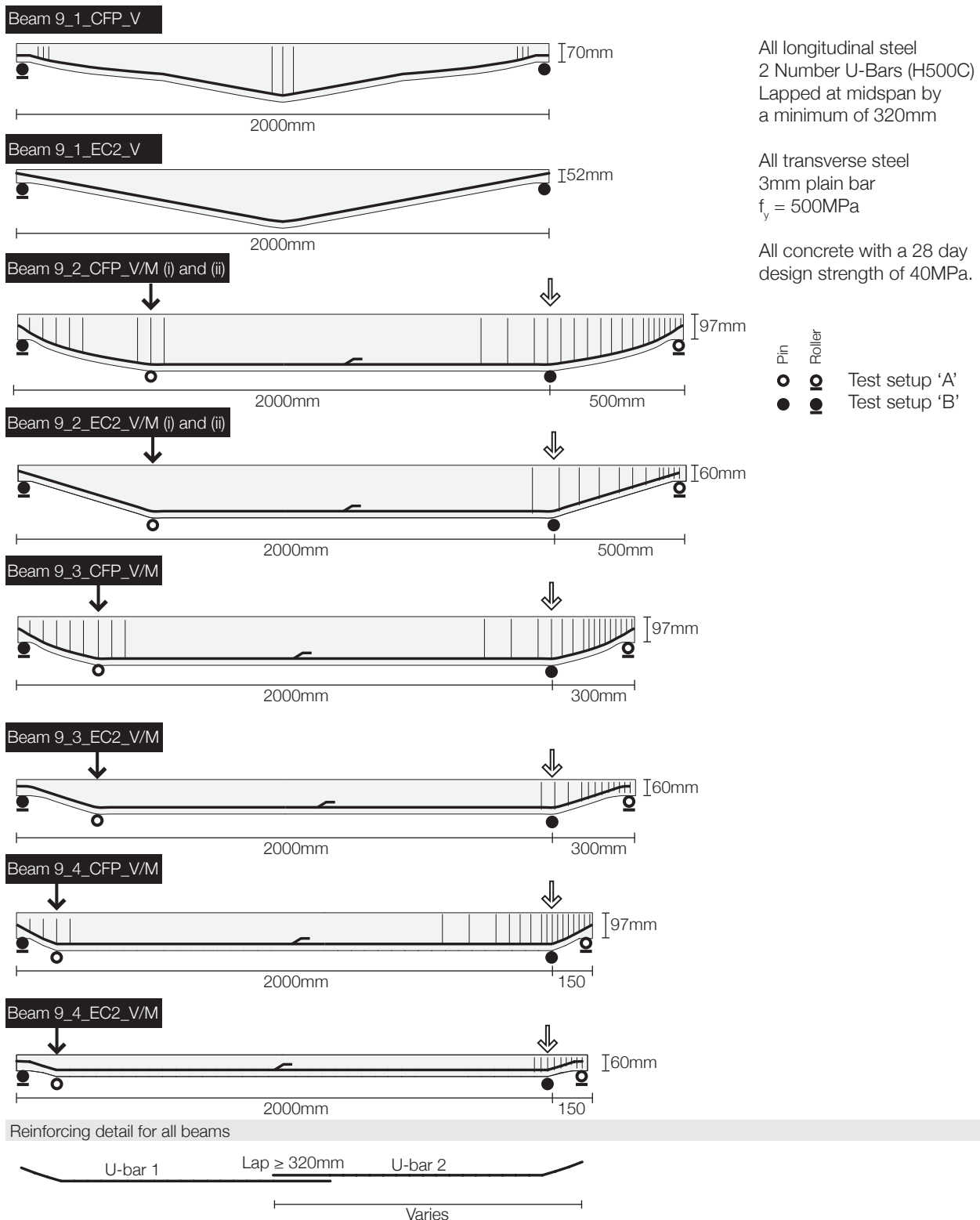


Figure 8.23: Beams 9\_1 to 9\_4.

### 8.3.3. Construction

Construction of all beams was undertaken in a steel mould shaped using timber blocks to create the required beam profile (Figure 8.24). The beams were cast in sets of four that were all demoulded 3 days after casting and cured in laboratory conditions prior to testing.

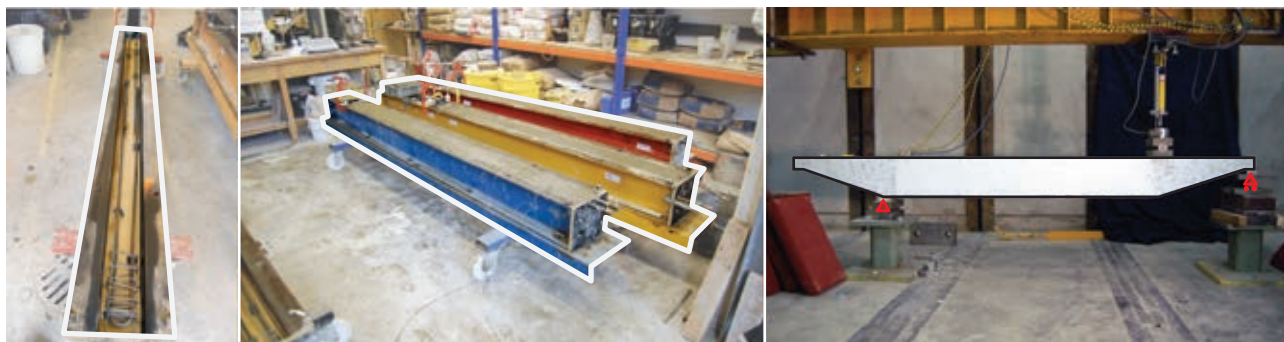


Figure 8.24: Typical construction process.

#### 8.3.4. Testing

Each beam was monitored using strain gauges on one of the longitudinal steel bars and a linear variable displacement transducer was placed at the point of load application, as shown in Figure 8.25. All tests were recorded using both a high definition video and a still digital camera to allow strain distributions in the concrete section to be determined using digital image correlation, as described in §8.3.4.1.

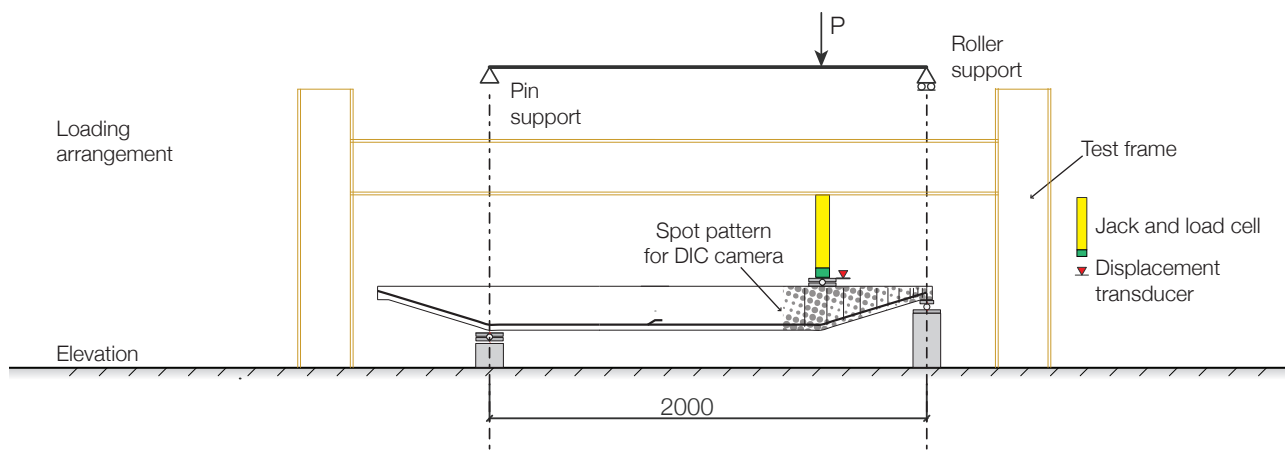


Figure 8.25: Typical test set up.

##### 8.3.4.1. Digital Image Correlation (DIC) strain monitoring

In order to determine the strains within the concrete section during testing, a DIC system was used for the majority of beam tests presented in this section. Digital Image Correlation is an optical method that compares a series of high resolution digital images to determine changes between them and can be used to measure displacements and strains (the most common implementation of DIC methods being found in optical computer mice). The equipment used to collect the required data is shown in Figure 8.26.

The beams were prepared by painting a random pattern of black dots onto the white painted concrete surface (Figure 8.113). During each of the tests (except Beam 9\_1) described in this chapter, images were collected at each loading increment for processing using the DIC equipment. All images and loading data were correlated to provide an accurate record of the loading cycle for each beam. A variety of software, some of which was developed by the author was then used to determine strains on the concrete section through the loading cycle, as described in §8.5 on page 301.

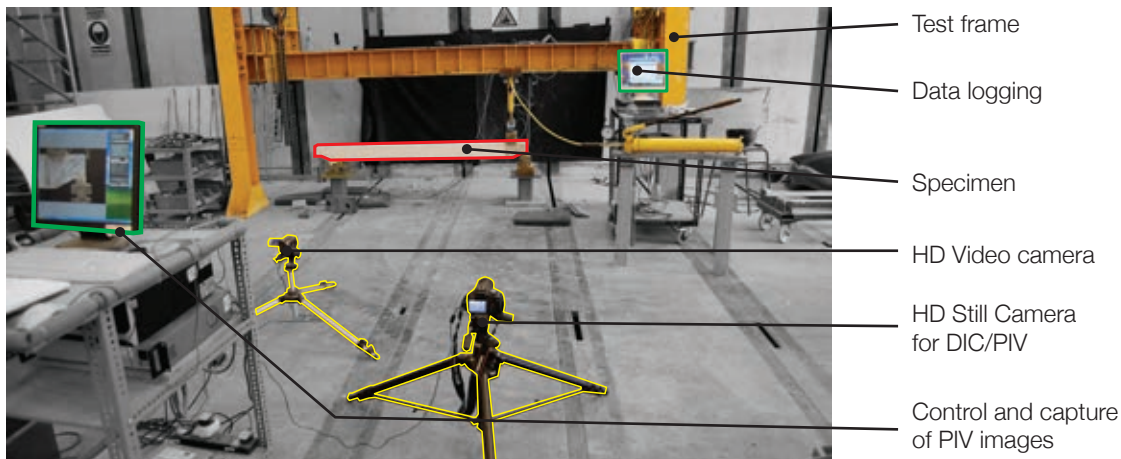


Figure 8.26: Data collection for tapered beam tests.

A summary of the test results is provided in Table 8.9, where the failure mode and ultimate load capacity has been recorded. The tests are described in the following sections according to the Beam Number (9\_1, 9\_2, 9\_3, 9\_4). A summary of the crack patterns at failure for all the beams tested is further provided in Figure 8.27 on page 264.

Table 8.9: Test failure modes and ultimate capacity.

	Design maximum load, P (kN) [A]	Maximum load achieved in test (kN) [B]	Failure mode	[B] / [A]
9_1_EC2_V	32.00	18.95	Shear	0.59
9_2_EC2_V(i)	36.00	7.75	Shear	0.22
9_2_EC2_M(i)	36.00	13.56	Shear	0.38
9_2_EC2_V(ii)	36.00	28.20	Shear	0.78
9_2_EC2_M(ii)	36.00	32.08	Shear	0.89
9_3_EC2_V	31.77	17.12	Shear	0.54
9_3_EC2_M	31.77	18.80	Shear	0.59
9_4_EC2_V	29.19	26.12	Shear	0.89
9_4_EC2_M	29.19	9.64	Anchorage	0.33
<b>Average [B] / [A]:</b>				<b>0.58</b>
9_1_CFP_V	32.00	29.6	Shear	0.93
9_2_CFP_V(i)	36.00 (See results)	41.6	-	1.16
9_2_CFP_M(i)	36.00 (See results)	51.5	-	1.43
9_2_CFP_V(ii)	36.00	46.9	Flexure	1.30
9_2_CFP_M(ii)	36.00	48.6	Flexure	1.35
9_3_CFP_V	31.77	43.8	Shear	1.38
9_3_CFP_M	31.77	31.5	-	0.99
9_4_CFP_V	29.19	84.5	Compression	(2.89)*
9_4_CFP_M	29.19	28.7	-	0.98
<b>Average [B] / [A]:</b>				<b>1.19</b>
* 9_4_CFP_V omitted from average result calculated due to test set up (see §8.3.9.3 on page 281).				

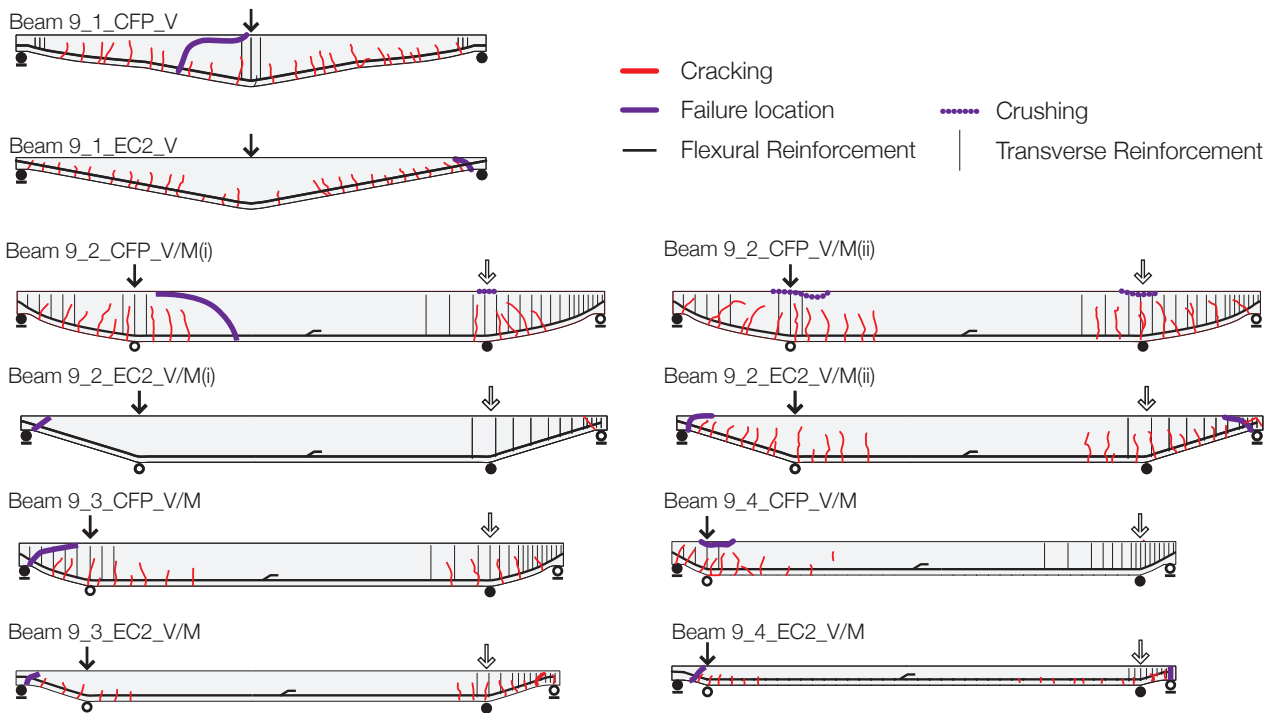


Figure 8.27: Crack patterns at failure for all EC2 and CFP beams tested.

### 8.3.5. Test results: Beam 9\_1

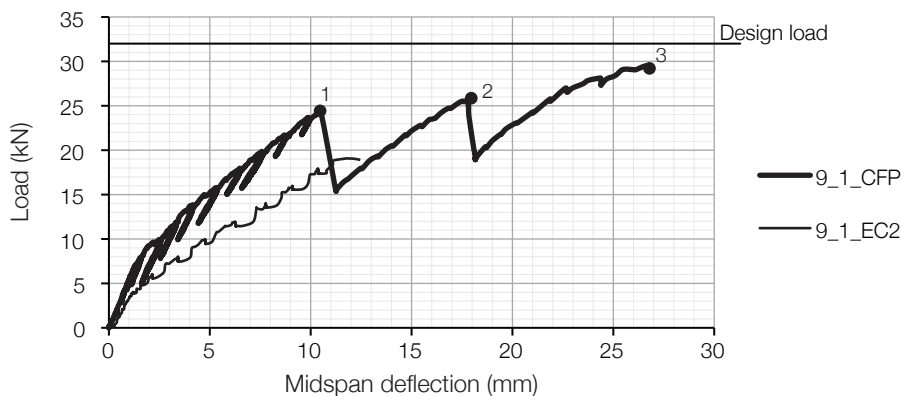


Figure 8.28: Load versus midspan deflection for Beams 9\_1\_EC2\_V and 9\_1\_CFP.

#### 8.3.5.1. Beam 9\_1\_EC2\_V

Beam 9\_1\_EC2\_V was the first element to be tested, and had a design load of 32kN. Load was applied in increments of 2kN. Cracking began at 6kN and propagated as shown in Figure 8.29 up to 12kN, when inclined cracks formed in the end zones of the beam. The formation of these cracks was quickly followed by catastrophic failure of the beam at just 60% of its design load (18.95kN), as seen in Figure 8.30. A load deflection plot for Beam 9\_1\_EC2 is given in Figure 8.28.

The results from strain gauges placed along the length of the beam are provided in Figure 8.31. Up to 4kN applied load, the gauges all provide identical readings. Beyond this initial load, the readings diverge significantly. Up to an applied load of 10kN, gauges 01 and 02 provided almost identical readings, while gauge 03 (located closer to the mid-span) showed a higher strain. After 10kN, the recorded strain in gauge 01 begins to reduce (the gauge is

located beyond the position of final failure). This behaviour is most likely attributable to a failure of the strain gauge, rather than an actual reduction in the strain in the steel bar.

A maximum strain of  $1400\mu\epsilon$ , recorded in gauge 02, indicates that none of the internal reinforcement was close to yield in this test ( $\sim 2750\mu\epsilon$ ), demonstrating that the design method presented in Chapter 5 is unable to account for the behaviour of the beam as tested since the method assumes the steel has indeed yielded along its length. DIC analysis was not undertaken for this beam.

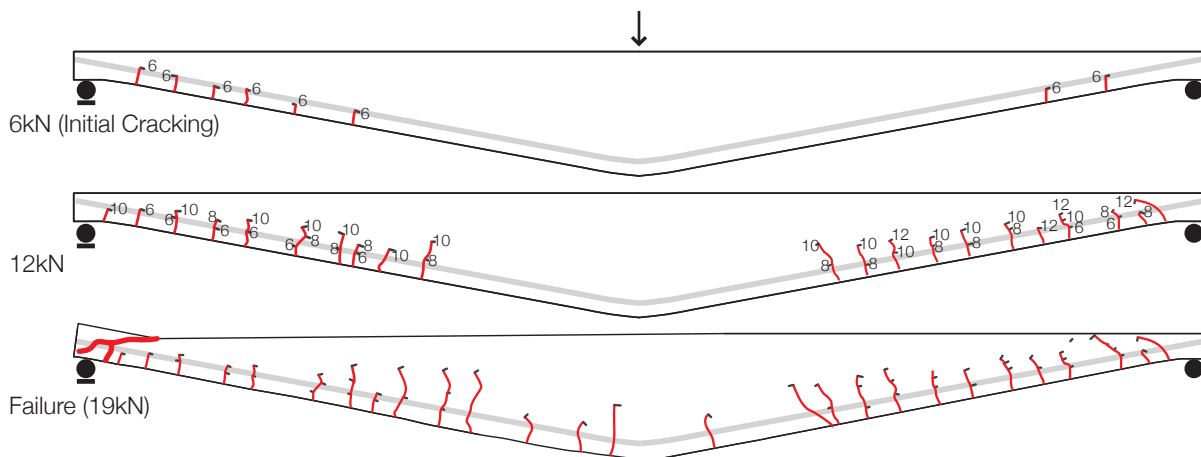


Figure 8.29: Beam 9\_1\_EC2\_V Progression of cracking.



Figure 8.30: Beam 9\_1\_EC2\_V Failure.

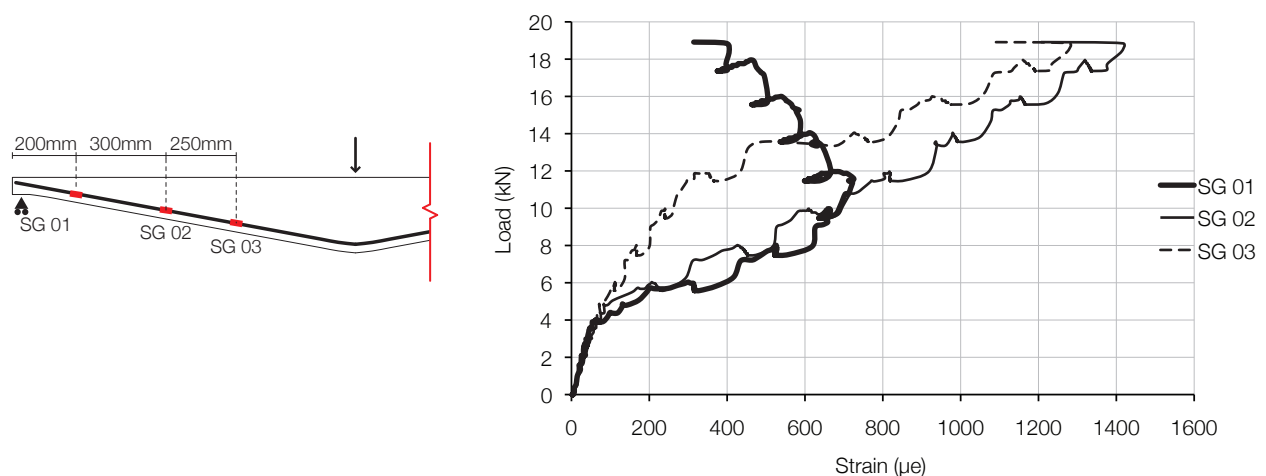


Figure 8.31: Beam 9\_1\_EC2\_V strain gauge locations and readings.

Beam 9\_1\_EC2\_V was examined after failure and it was found that the anchorage had pulled through the end zone of the beam, as shown in Figure 8.30. Given that the deep inclined cracks formed prior to failure, it is



suggested that the progression of these cracks under increasing load was the primary cause of failure, which in turn allowed the bar to be pull through the end block.

### 8.3.5.2. Beam 9\_1\_CFP\_V

Beam 9\_1\_CFP\_V also had a design load of 32kN. Load was applied in increments of 2kN and cracking began at 8kN. Distributed cracks then propagated along the beam up to around 24kN, as shown in Figure 8.31. Major cracking at around 24kN occurred along the line of the longitudinal reinforcement (Figure 8.33), in addition to vertical cracks in the centre of the beam span. The beam lost load on the formation of this crack pattern, which occurred first near to the pinned support. Upon reapplication of the load (see point '1' on the load deflection plot shown in Figure 8.28), the same crack pattern occurred on the roller side of the beam at approximately 25kN (Figure 8.33). Load was again lost (point '2' in Figure 8.28) and was again reapplied.

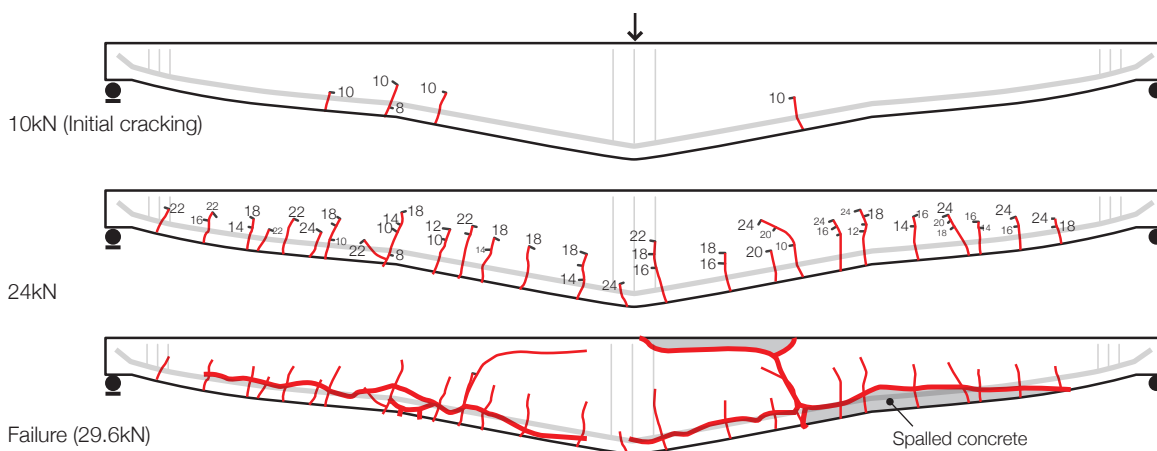


Figure 8.32: Cracking in Beam 9\_1\_CFP\_V.

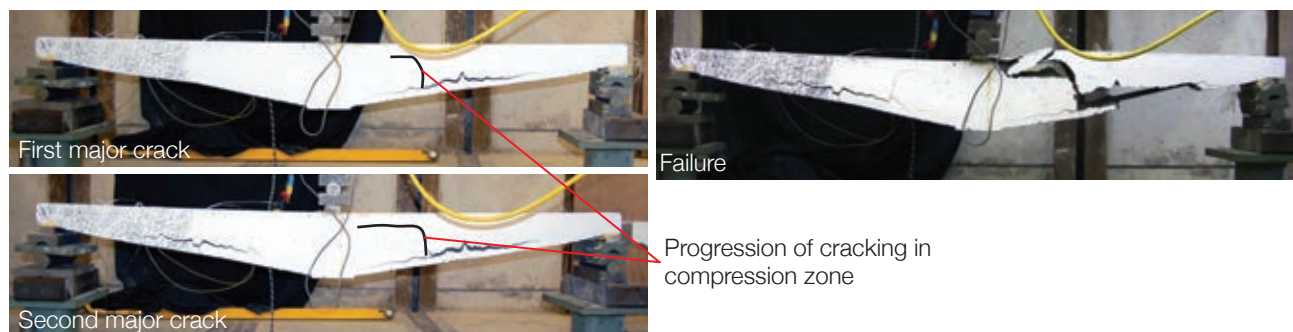


Figure 8.33: Major cracking (l) and failure (r) of Beam 9\_1\_CFP\_V.

Horizontal cracks beneath the compression zone of the beam at midspan then propagated towards the point load while the larger cracks around the longitudinal reinforcement began to open. A final shear failure occurred at 29.6kN, with the primary crack being located close to the point load, as shown in Figure 8.33. The support zones of the beam remained undamaged in comparison to Beam 9\_1\_EC2\_V and demonstrated that full anchorage of the longitudinal reinforcement could be achieved with sufficient end zone depth.

Thus, whilst the end zone of Beam 9\_1\_CFP was just 18mm (34%) deeper than Beam 9\_1\_EC2 (70mm versus 52mm), it appears that this difference, combined with the inclusion of a small amount of transverse reinforcement, was enough to allow the beam to reach its design load without failure occurring in the support zone.

Strain gauges placed along the flexural reinforcement show further changes in behaviour when compared to Beam 9\_1\_EC2. A maximum strain was recorded in Gauge 03, located towards the midspan. Gauge 01, which was located close to the support (Figure 8.34) showed the lowest bar strains, as would be expected.

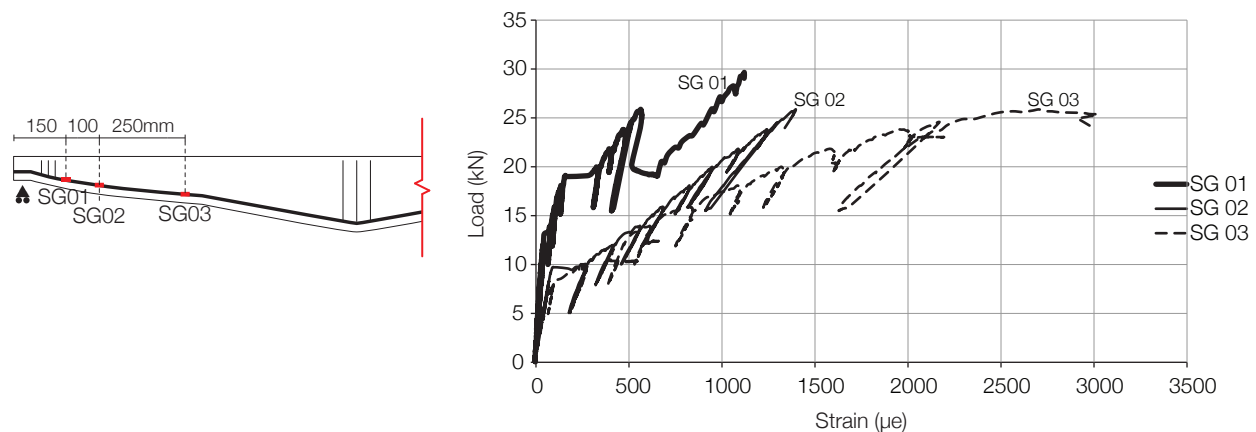


Figure 8.34: Beam 9\_1\_CFP\_V strain gauge locations and readings.

The design of Beam 9\_1\_CFP required that the longitudinal steel be bent into an unusual shape to achieve an increase in depth towards the support, as shown in Figure 8.35, and it is likely that this geometrical arrangement contributed to the unusual crack patterns seen. It is therefore to be recommended that where the tension bar changes direction unfavourably, transverse reinforcement should be provided to carry the resultant tensile force. One of the alternative reinforcement arrangements (Figure 7.19 on page 230) may therefore have been better suited to this particular beam, although it was chosen to follow only the design guidance to create the optimised section without further alterations.

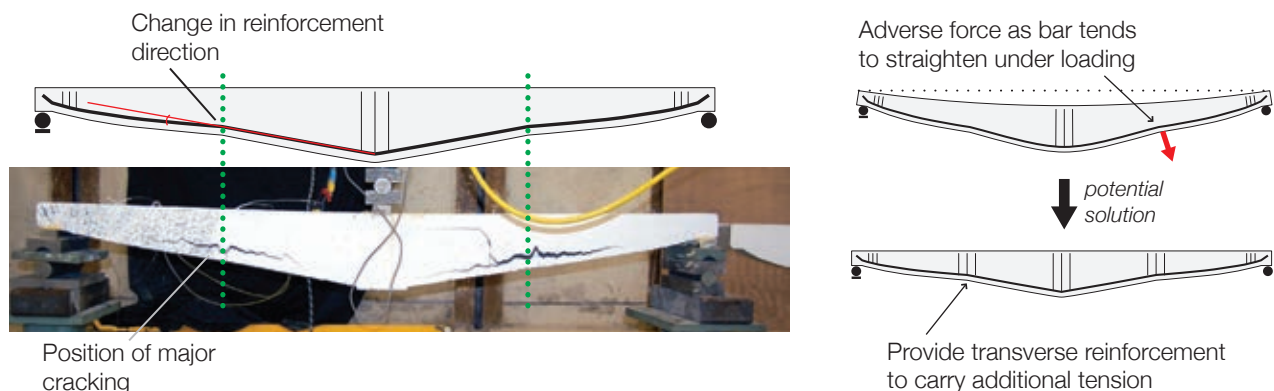


Figure 8.35: Bar arrangement and failure geometry.

### 8.3.6. Test results: Beam 9\_2(i)

Beam 9\_2 was the first element in this series to be tested in two loading arrangements, as described in Figure 7.14 on page 228. In addition to this, two sets of tests were undertaken (denoted (i) and (ii)), resulting in a total of four beams and eight tests.

A load deflection plot for beams 9\_2(i) only is provided in Figure 8.36 (note that deflection is measured at the point of load application in all tests, and the load values for Beam 9\_2\_CFP(i) have been modified as described in the text below to account for a change in their span). Results for Beam 9\_2(ii) are presented in §8.3.7 on page 271.

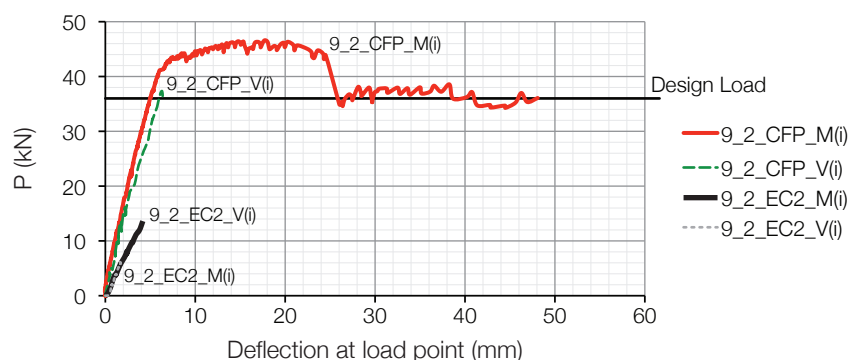


Figure 8.36: Load deflection plot for Beams 9\_2\_EC2(i) and 9\_2\_CFP(i).

#### 8.3.6.1. Beam 9\_2\_EC2\_M(i)

Beam 9\_2\_EC2\_M(i) was tested first. Load was applied in 2kN increments. At 8kN, cracking began at the support point and propagated a short distance into the tapered beam span, as shown in Figure 8.37. At 14kN, with little cracking found on the face and with very little warning, the beam failed with a single crack in the end zone. This represents failure at an applied load of just 38% of the design failure load. Strain gauges were not placed in this end of the beam.

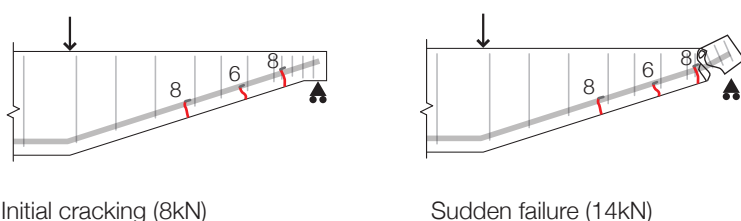


Figure 8.37: Crack progression and failure, Beam 9\_2\_EC2\_M.



#### 8.3.6.2. Beam 9\_2\_EC2\_V(i)

Beam 9\_2\_EC2\_V behaved in a similar manner to Beam 9\_2\_EC2\_M(i), but failed at the lower load of just 7kN, with a single inclined crack located at the support point. Very little deflection or cracking was recorded prior to this failure, which is illustrated in Figure 8.38. Strain gauges (placed at 100mm, 200mm and 500mm from the roller support in the tapered end) had a maximum reading of just 358 $\mu\epsilon$  at peak load. The poor behaviour suggests that anchorage of the longitudinal steel may not have been achieved and that the shear capacity of the

concrete was exceeded prior to the bar capacity being utilised to any significant amount. A second, identical, beam was tested to verify these results and showed slightly better behaviour, as described in §8.3.7 on page 271.

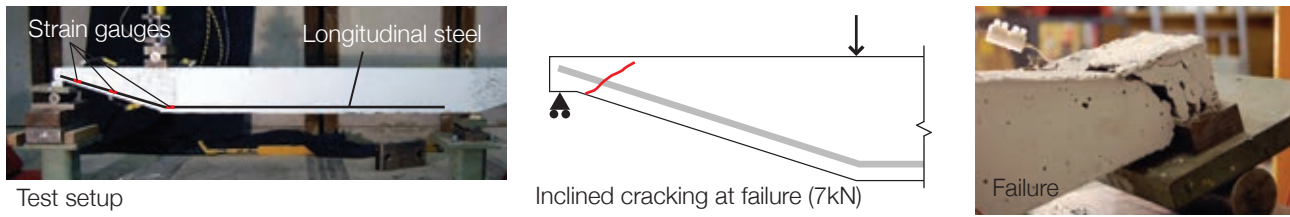


Figure 8.38: Crack progression and failure, Beam 9\_2\_EC2\_V(i).

### 8.3.6.3. Beam 9\_2\_CFP\_M(i)

Beam 9\_2\_CFP\_M was loaded in 2kN increments, in the same manner as described above. The beam suffered an unexpected bond failure in the midspan and broke in two at an applied load of 24.9kN, Figure 8.39(l). Some cracking in the tapered end had been recorded up to this point Figure 8.39(r), but it should be noted that the load was below the design failure load of 36kN.

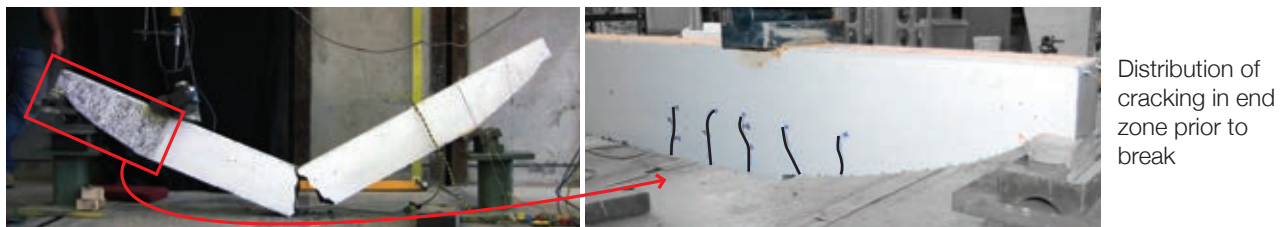


Figure 8.39: Bond failure in Beam 9\_2\_CFP (l) and crack pattern prior to failure (r).

Since the full capacity of the beam had not been reached, the two beam ends were tested with a reduced shear span of 1150mm, as shown in Figure 8.40. To enable comparisons between sets of results, the applied load was adjusted by a factor of 78/115 to ensure that the vertical load at the tapered end was the same as if it was a 3m span beam. The load-deflection plot in Figure 8.36 has been modified in this way to make it comparable to the other test data presented in this Chapter.

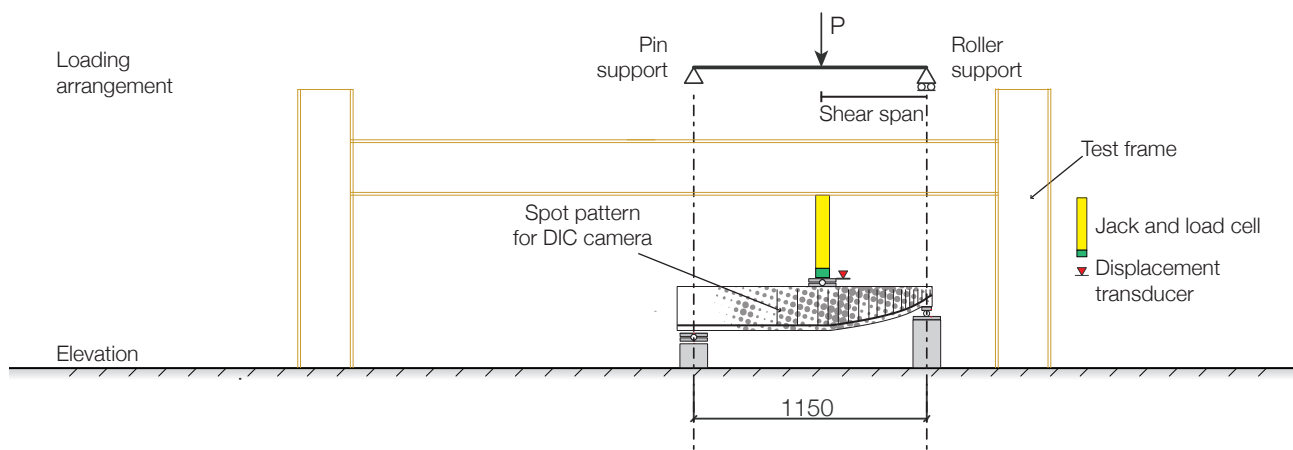


Figure 8.40: New test set up for Beam 9\_2\_CFP\_M(i).

Upon reloading of the shorter beam 9\_2\_CFP\_M, cracking was found to propagate towards the point load but there were few cracks closer to the support (Figure 8.41). The shear force at the tapered end of the beam

exceeded the design value of 27kN (Figure 7.14 on page 228), and a maximum applied load of 46.4kN was achieved in the test. During this time, the element demonstrated some ductility before final failure in a combination of shear and flexure, as illustrated in Figure 8.41 and Figure 8.36 on page 268.

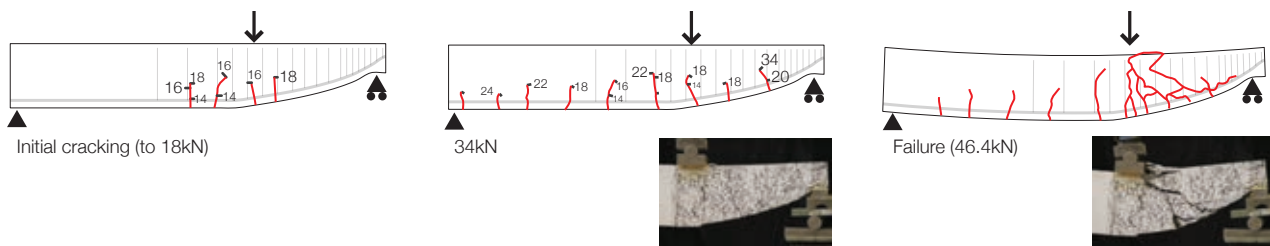


Figure 8.41: Progression of cracking in Beam 9\_2\_CFP\_M(i) and failure photographs.

#### 8.3.6.4. Beam 9\_2\_CFP\_V(i)

Beam 9\_2\_CFP\_V(i) was then tested, again with the shorter span of 1150mm. Load was applied in 2kN increments and cracking propagated initially in much the same way as Beam 9\_2\_CFP\_M(i) up to an applied load of 29.8kN, before the inclined cracks began to turn towards the point load at 36kN (Figure 8.42(l)). A continuation of the loading rate led to a sudden shear failure in the prismatic zone of the beam shortly after at 37.5kN, as shown in Figure 8.42(r).

Strain gauges (located as shown in Figure 8.42) gave a maximum reading of 1764 $\mu\epsilon$  in Strain Gauge 02 (Figure 8.43) prior to failure, again below the yield strain of the steel bar - suggesting that the full capacity of the steel was not used in the development of significant shear strength. This provides some support to the assertion that the compression force path provides the majority of the shear resistance of the tapered beam section.

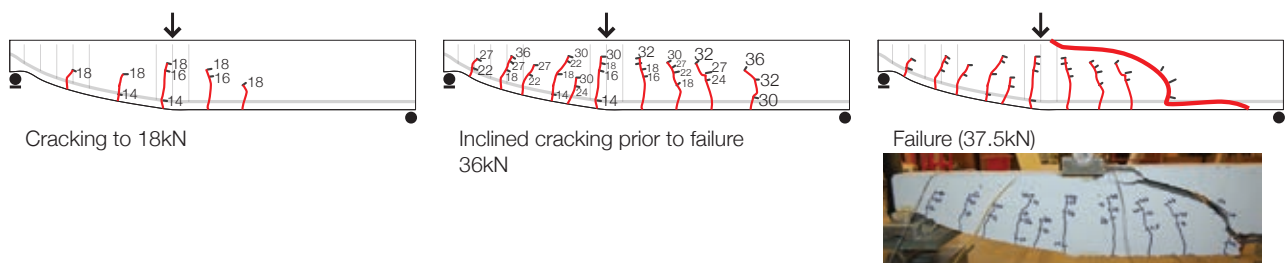


Figure 8.42: Setup and Progression of cracking in Beam 9\_2\_CFP\_V(i).

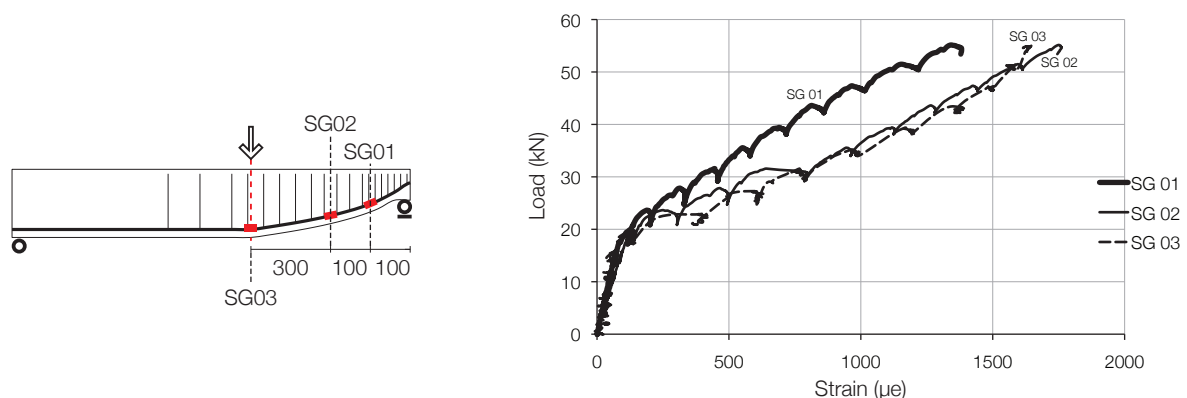


Figure 8.43: Beam 9\_2\_CFP\_V(i) strain gauge locations and results.

Figure 8.44 provides a comparison between the reinforcement layouts and failure modes for Beams 9\_2\_CFP\_M(i) and 9\_2\_CFP\_V(i). With the shorter span providing a higher reaction on the prismatic side than it was originally designed for, the failure seen in the modified beam test 9\_2\_CFP\_V(i) was not entirely unexpected.

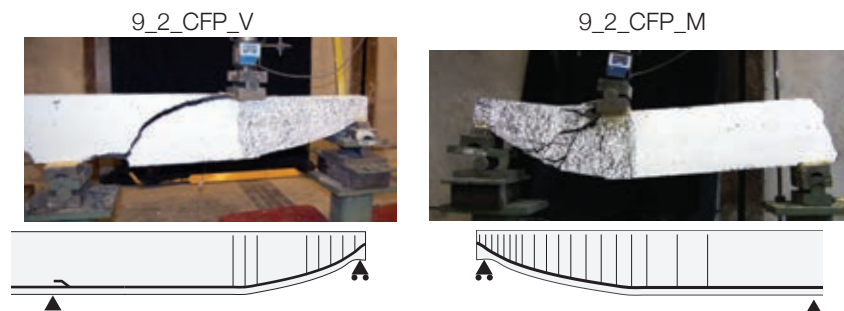


Figure 8.44: Reinforcement layouts and failure modes for Beams 9\_2\_CFP\_V and 9\_2\_CFP\_M.

### 8.3.7. Test Results - Beam 9\_2(ii)

The tests described in §8.3.6 on Beams 9\_2(i) were considered carefully before it was decided to test two further beams of the same designs, denoted Beam 9\_2(ii). Load versus deflection plots for these repeated tests are shown in Figure 8.45 (deflection again being measured at the position of load application).

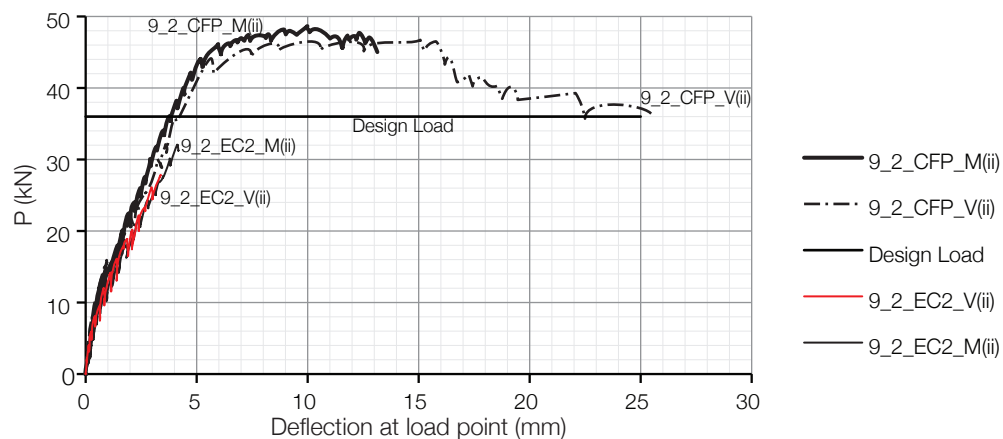


Figure 8.45: Load deflection plot - Beam 9\_2\_EC2(ii) and Beam 9\_2\_CFP(ii).

#### 8.3.7.1. Beam 9\_2\_EC2\_V(ii)

Beam 9\_2\_EC2(ii), which had a design load of 36kN, was tested in two loading arrangements ('V' and 'M') and Beam 9\_2\_EC2\_V was tested first. Load was applied in 2kN increments and cracking was first noted at 8kN (located next to the roller support). Cracking then progressed along the beam span, moving from the support towards the loading point as shown in Figure 8.46. The beam failed at an applied load of 28kN in the support zone (Figure 8.47). This failure load represents a considerable increase over Beam 9\_2\_EC2(i), with the most likely reason for this increase in capacity being a better bar anchorage in this beam test.

This potential explanation is explored further in Chapter 10 on page 409, where the influence of small construction errors leading to significant changes in structural behaviour are explored.



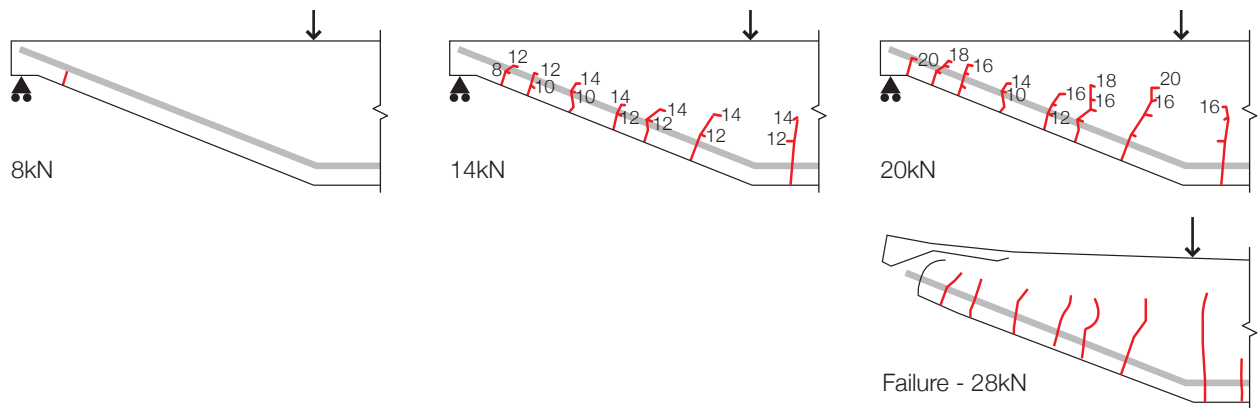


Figure 8.46: Progression of cracking in Beam 9\_2\_EC2\_V(ii).



Figure 8.47: Cracking and failure in Beam 9\_2\_EC2\_V(ii).

Strain gauges placed as shown in Figure 8.48 show that the strain in the longitudinal reinforcement increased linearly prior to cracking, after which strains generally increased more rapidly. It is interesting to note that strain Gauge 03, placed near to the support, initially follows the same pattern as Gauges 01 and 02, before a reduction in the rate of strain increase occurs, after which it stays approximately constant under an increasing load. The same effect was seen in Beam 9\_1\_EC2 (Figure 8.31 on page 265).

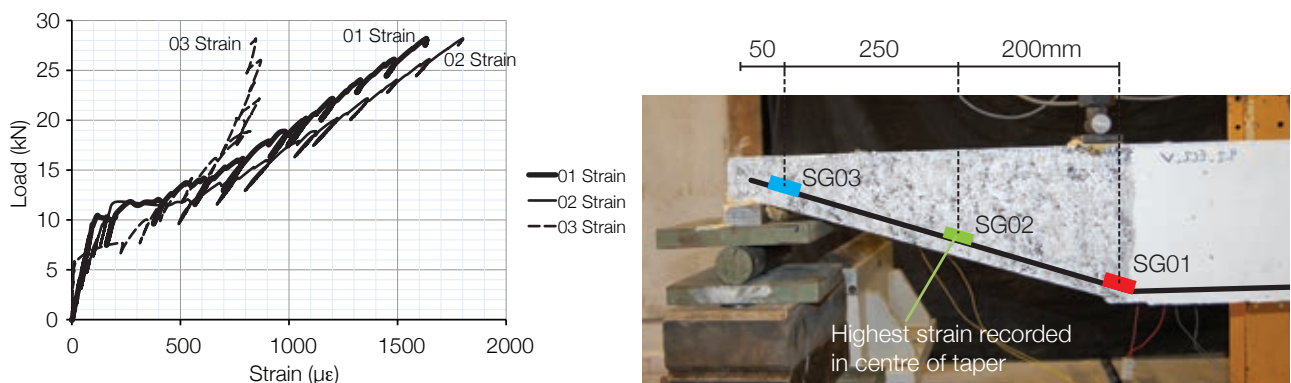


Figure 8.48: Recorded strain variations, Beam 9\_2\_EC2\_V(ii).

### 8.3.7.2. Beam 9\_2\_EC2\_M(ii)

Beam 9\_2\_EC2\_M was then tested and loaded in the same manner as Beam 9\_2\_EC2\_V(ii). The beam again cracked at around 8kN, with first cracks appearing next to the support point. These cracks then progressed along the length of the tapered section up to a maximum load of 32kN, Figure 8.49. Deeper and more numerous cracking occurred in the end zone, and failure was marked by the familiar end shape shown in Figure 8.50. Strain gauges were not placed in this end of the beam.

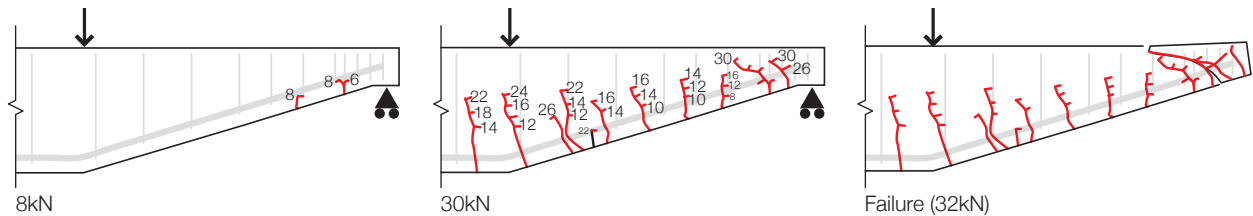


Figure 8.49: Progression of cracking in Beam 9\_2\_EC2\_M(ii).

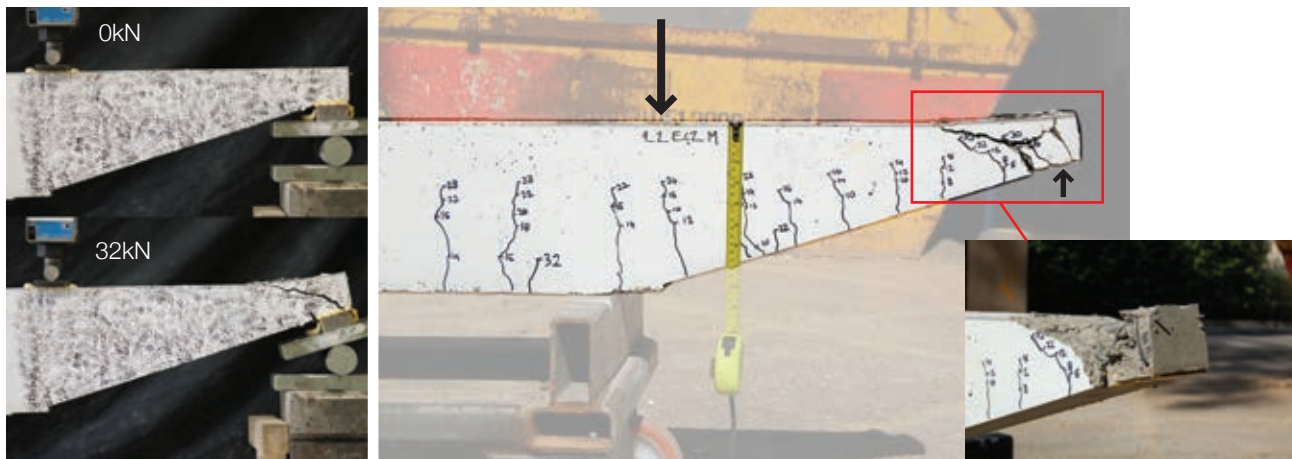


Figure 8.50: Cracking and failure in Beam 9\_2\_EC2\_M(ii).

### 8.3.7.3. Beam 9\_2\_CFP\_M(ii)

Beam 9\_2\_CFP\_M(ii) was tested first, with load again applied in 2kN increments. Similarly to Beam 9\_2\_CFP(i) cracking began directly beneath the support point at an applied load of 12kN (Figure 8.51). This contrasts to the behaviour of Beam 9\_2\_EC2(i) and (ii), where first cracking was seen at the end of the tapered section, close to the support. Cracking in Beam 9\_2\_CFP\_M(ii) progressed under increasing load into the tapered end and along the main span, with the first inclined crack appearing at the support point at 16kN. Under increasing applied load the cracks extended into the beam as shown in Figure 8.51.

The inclined crack at the support was measured up to 44kN applied load. Beyond this point the beam displayed considerable displacement during its ductile behaviour, before a combined crushing and shear failure occurred beneath the point of load application, Figure 8.52. The inclined cracks did not grow any further. A maximum load of 48.6kN was carried by the beam. There were no strain gauges placed in this end of the beam.

Loading was stopped after 13mm displacement at the load point (Figure 8.45 on page 271) to ensure the beam remained intact for the second test, described below.

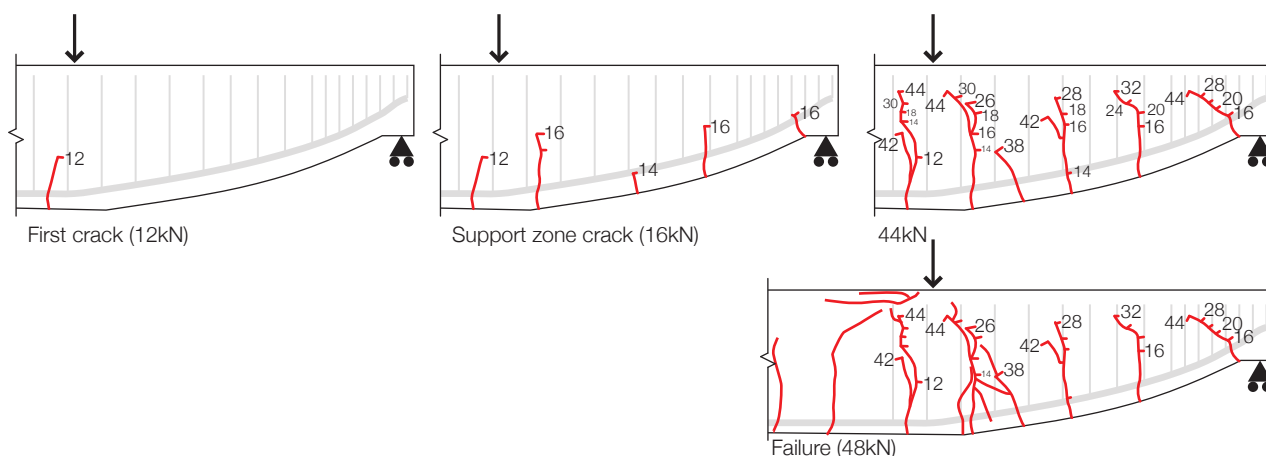


Figure 8.51: Cracking and failure in Beam 9\_2\_CFP\_M(ii).

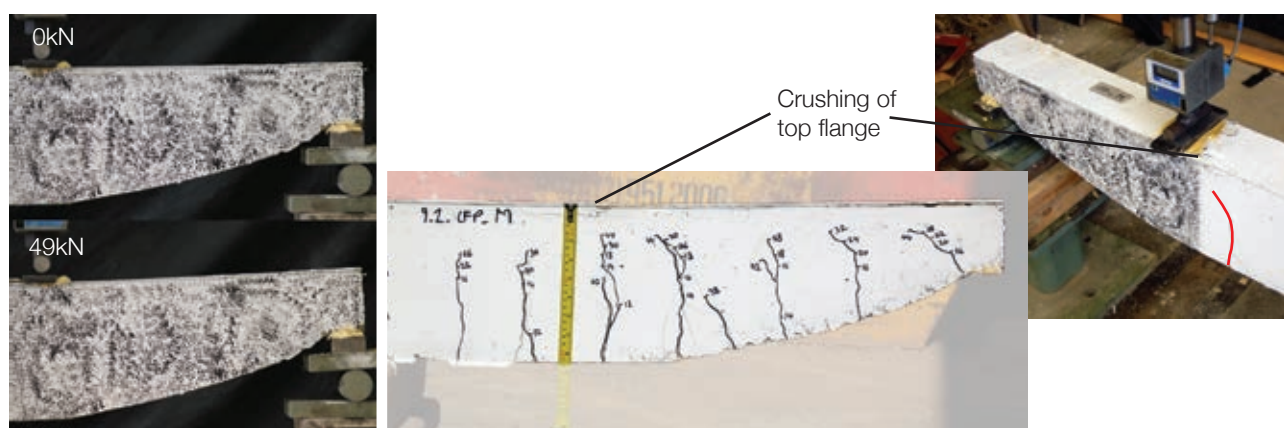


Figure 8.52: Photographs of displacement and failure mode in Beam 9\_2\_CFP\_M(ii) (§8.3.7.3 on page 273).

#### 8.3.7.4. Beam 9\_2\_CFP\_V(ii)

Beam 9\_2\_CFP\_V was then tested under the same loading regime. Initial cracks again formed beneath the load point at 12kN applied load, as shown in Figure 8.53. The crack distribution then spread along the beam, and cracks did not occur close to the support until an applied load of 26kN, after which they quickly grew and propagated in the direction of load application. The distribution of cracking is similar to that of Beam 9\_2\_CFP\_M(ii) but considerable difference in the angle of propagation of the cracks was seen, due primarily to Beam 9\_2\_CFP\_V(ii) having fewer transverse bars (see also Figure 8.23 on page 261).

The beam again showed considerable displacement in its response to increasing load. A maximum load of 46.9 kN was recorded. After displaying some plastic behaviour at the peak load, the capacity of the beam dropped (Figure 8.45 on page 271) as the beam redistributed stresses. The drop in capacity also coincided with large crushing in the compression zone, as shown in Figure 8.54.

Three strain gauges were placed on the longitudinal steel as shown in Figure 8.55. Strain gauge 02 stopped reading at an applied load of 28kN. Strain gauge 01 recorded that the bar yielded at an applied load of 38kN (close to the design load of 36kN, where the bar is assumed to have yielded), thus verifying the design used in the main span of the beam.

Strain gauge 03, placed in the support zone, recorded low strains (maximum of  $849\mu\epsilon$ ), again demonstrating the effect of the compressive force path on the behaviour of the longitudinal steel. Further analysis of the beam failure and behaviour is provided in §8.5 on page 301, where the digital image correlation data collected throughout the test is analysed.

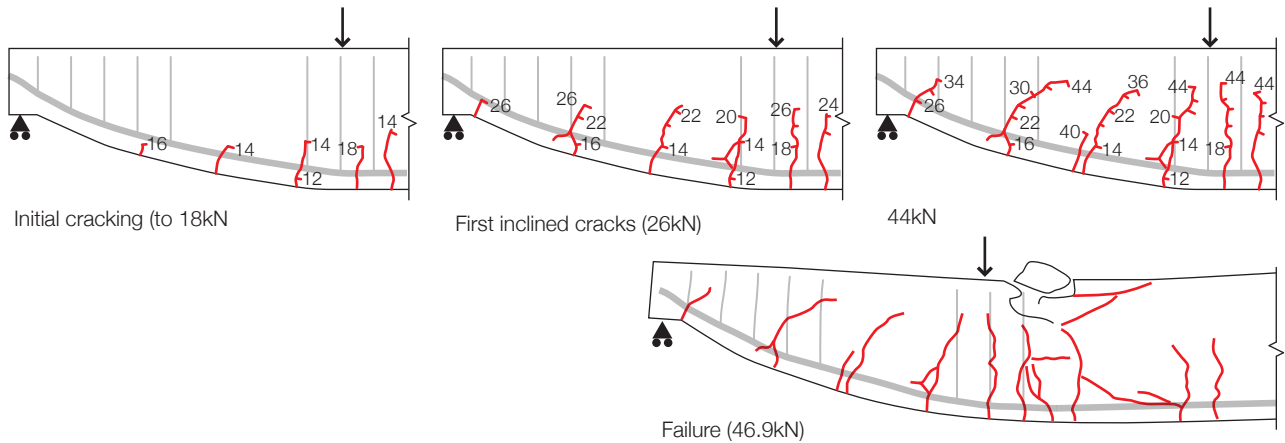


Figure 8.53: Cracking and failure in Beam 9\_2\_CFP\_V(ii).



Figure 8.54: Displacement photographs and failure in Beam 9\_2\_CFP\_V(ii).

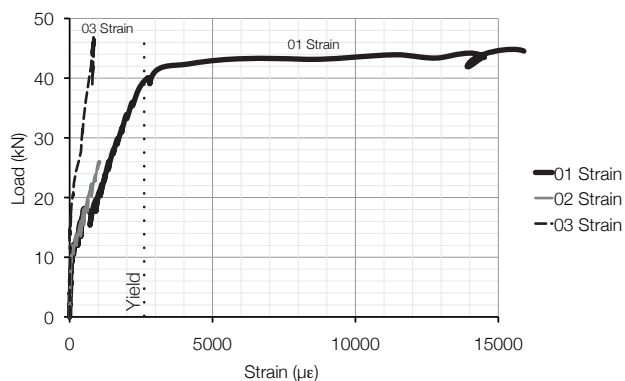


Figure 8.55: Strain gauge location and results, Beam 9\_2\_CFP\_V(ii).



## 8.3.8. Test Results: Beam 9\_3

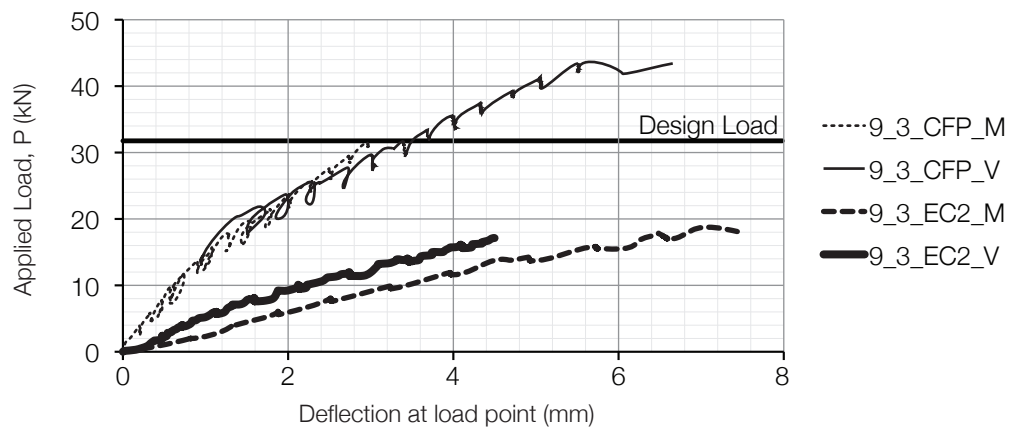


Figure 8.56: Load deflection plot for Beams 9\_3.

## 8.3.8.1. Beam 9\_3\_EC2\_M

Beam 9\_3 had a design load of 31.77 kN (Figure 7.15 on page 228). Beam 9\_3\_EC2\_M was tested first, with load applied in increments of 2 kN. Cracking was first recorded close to the support at an applied load of 6 kN, as shown in Figure 8.57. Cracking then propagated along the beam as shown in Figure 8.57, before failure occurred at 18.80 kN (59% of the design load). A load deflection plot for the beam is shown in Figure 8.56.

An unusual shear crack was formed in the tapered section, curving away from the applied load on one face, and towards it on the other (as shown in Figure 8.58). These cracks were accompanied by a local concrete failure in the top face of the beam.

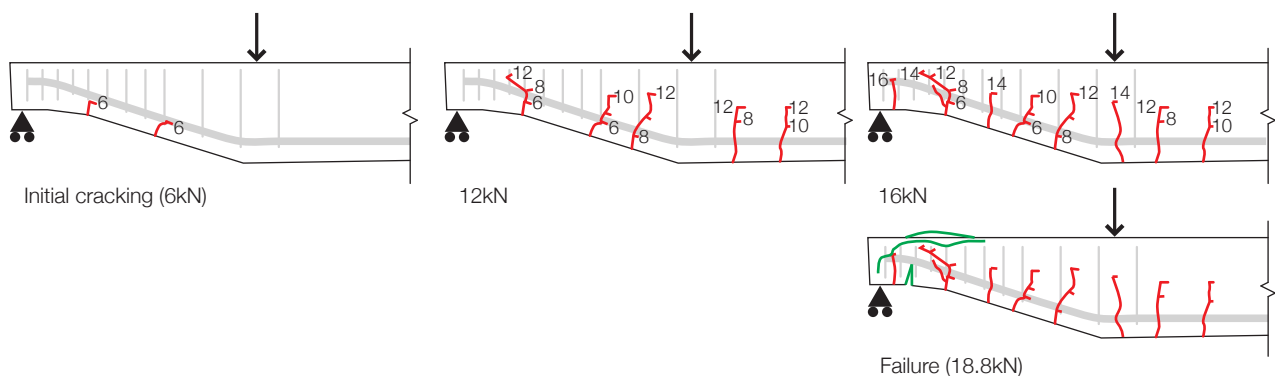


Figure 8.57: Crack location and progression in Beam 9\_3\_EC2\_M.



Figure 8.58: Cracking locations and failure mode (shown from two angles) for Beam 9\_3\_EC2\_M.

### 8.3.8.2. Beam 9\_3\_EC2\_V

Beam 9\_3\_EC2\_V displayed similar behaviour to Beam 9\_3\_EC2\_M. Initial cracks formed in the end zone at 6kN, before propagating as shown in Figure 8.59. An established pattern of crack formation is now seen, wherein the ‘EC2’ beams have cracking commencing at the support end of the beam, while ‘CFP’ beams have cracking commencing towards the loading point.

Under increasing load, Beam 9\_3\_EC2\_V failed at the support zone at an applied load of 17kN (53% of the design load), with a deep inclined crack forming rapidly in this position. A load deflection plot for the beam is shown in Figure 8.56.

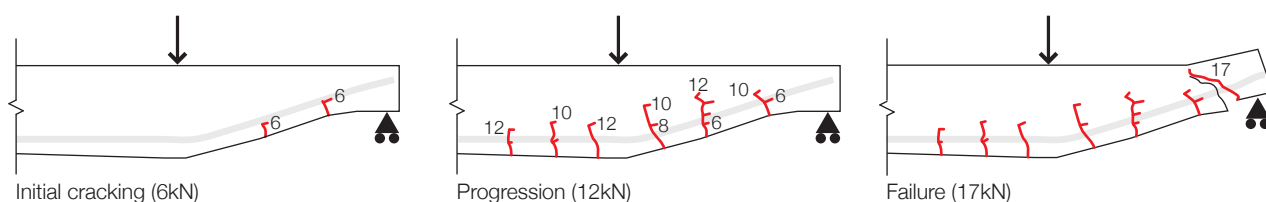


Figure 8.59: Crack locations and progression for Beam 9\_3\_EC2\_V.

Strain gauges, placed as shown in Figure 8.60, reveal that in Beam 9\_3\_EC2\_V the longitudinal reinforcement had begun to yield ( $\epsilon = 2950\mu\epsilon$ ) in the position beneath the loading point at an applied load of 17kN. At the same load, the remainder of the steel was seen not to have yielded.

This data, which is supported by previous ‘EC2’ series tests, demonstrates again that the assumption in the design model that the steel will yield everywhere is not borne out in the experimental data. The beam clearly failed to achieve the expected capacity and thus the results for Beam 9\_3\_EC2 again suggest that the design method to BS EN 1992-1-1 (2004) is unable to account for the behaviour of tapered beams in shear in some situations.

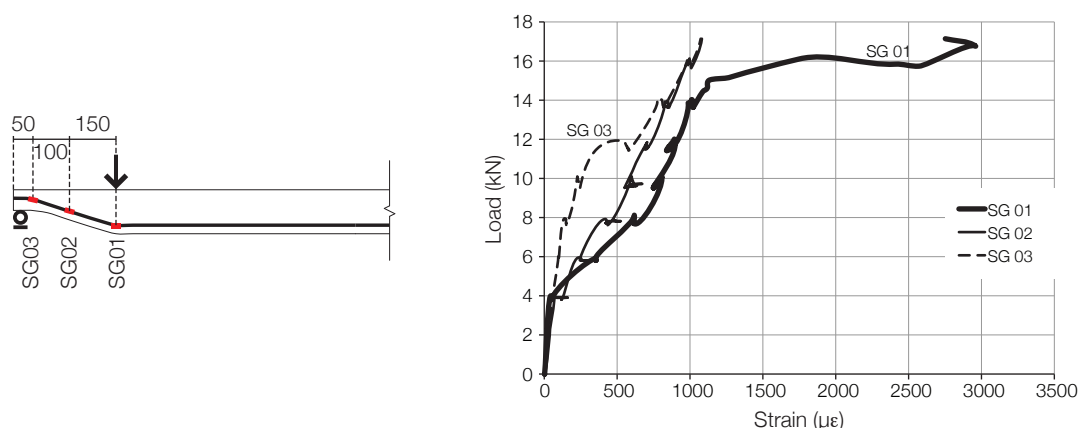


Figure 8.60: Strain gauge locations and results, Beam 9\_3\_EC2\_V.

### 8.3.8.3. Beam 9\_3\_CFP\_M

Beam 9\_3\_CFP was tested in the same manner as previous beams. Under the applied load, cracking was first noted at 16kN and was located beneath the point load, as shown in Figure 8.61. At 16kN a small inclined crack formed next to the point load, before cracking propagated towards the roller support as shown in Figure 8.61. This behaviour is common with all beams designed to the compressive force path method, but contrasts



to those designed using BS EN 1992-1-1 (2004), where cracking tends to propagate from the tip of the tapered section. The beam was taken to its design load of 32kN before the load was released. No strain gauges were placed in this end of the beam span.

Beam 9\_3\_CFP\_M was not tested beyond its design load of 32kN to ensure an intact specimen remained for the second test, Beam 9\_3\_CFP\_V. This experimental technique has, however, meant that the ultimate failure mode (flexure or shear) of this specimen is not known.

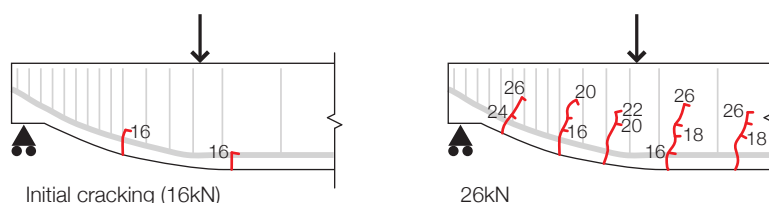


Figure 8.61: Crack distribution in Beam 9\_3\_CFP\_M.

#### 8.3.8.4. Beam 9\_3\_CFP\_V

Beam 9\_3\_CFP\_V was tested with load applied in 2kN increments. Cracks again formed directly under the point load at 14kN total load. Cracking through the section then progressed as shown in Figure 8.62. A steep inclined crack at the support location, which formed at 22kN, propagated diagonally through the section towards the point load. The beam went on to exceed its design load, failing at this diagonal crack location at 43.8kN applied load (Figure 8.62). Photographs of the failure location during the final stages of loading are provided in Figure 8.63.

The failure of Beam 9\_3\_CFP\_V is as predicted by the design method, which was arranged such that the beam would have sufficient transverse and flexural capacity to reach the design load (32kN) but that it would ultimately fail in shear.

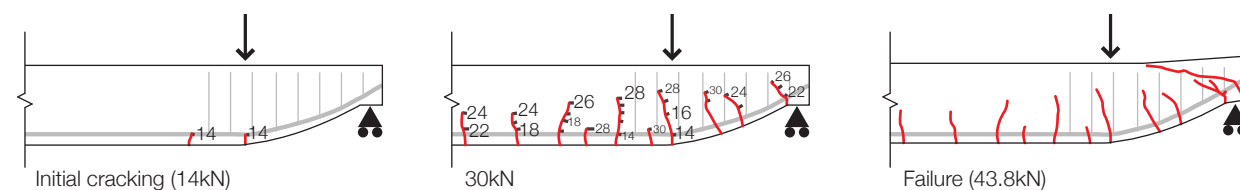


Figure 8.62: Crack distribution and failure mode in Beam 9\_3\_CFP\_V.

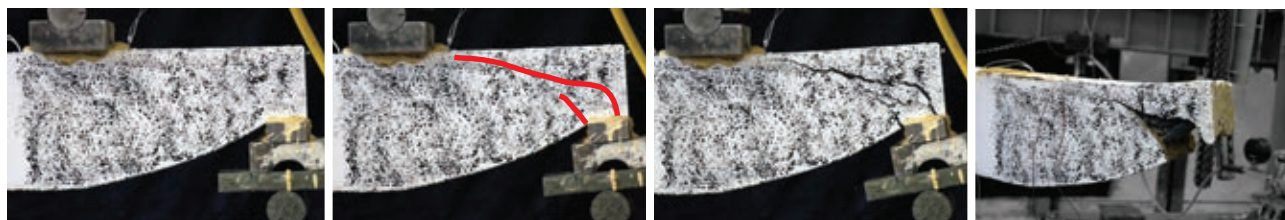


Figure 8.63: Beam 9\_3\_CFP\_V failure mode.

Three strain gauges were placed in the taper of Beam 9\_3\_CFP\_V. Whilst one gauge failed during construction, the results of the remaining gauges are provided in Figure 8.64. The results show that at the point of first cracking (14kN) the strain in the bar rapidly increases, as expected. Gauges 01 and 02 provide initially similar results,

before gauge 01 reduces slightly at higher loading. The beam therefore behaved in a similar manner to the other beams designed using the compressive force path method.

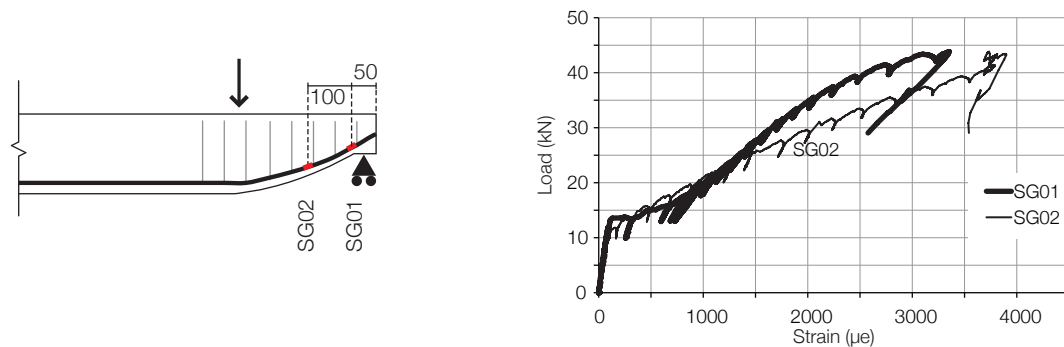


Figure 8.64: Strain gauge locations and results, Beam 9\_3\_CFP\_V.

### 8.3.9. Test Results - Beam 9\_4

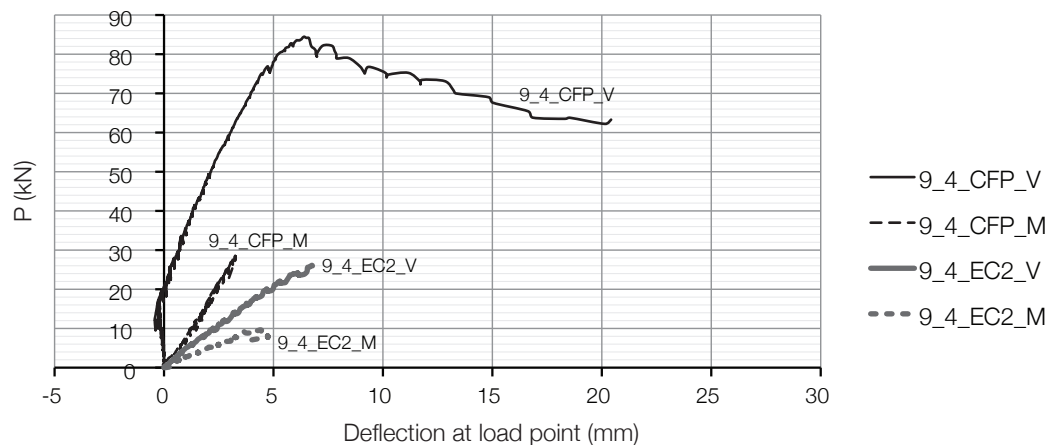


Figure 8.65: Load deflection plot for Beam 9\_4\_EC2 and Beam 9\_4\_CFP.

#### 8.3.9.1. Beam 9\_4\_EC2\_M

Beam 9\_4, with a design load of 29.2kN, was not monitored using the DIC system described in §8.3.4.1 on page 262. During testing load was applied in 2kN increments, with cracks forming initially at 4kN (Figure 8.66). At approximately 8kN, the beam failed with a single vertical crack forming over the support point as shown in Figure 8.66 (27% of the design load). A load deflection plot for the beam is provided in Figure 8.65. Given the nature of the failure, it is likely that the longitudinal reinforcement had moved away from its intended location during construction, leading to a premature failure at the support zone in the concrete section. A similar failure was also seen in Beam 9\_2\_EC2\_M(i).

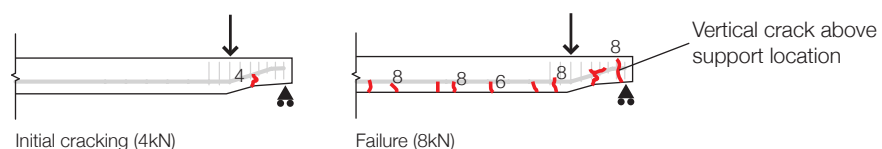


Figure 8.66: Initial cracking (l) and failure mode (r) in Beam 9\_4\_EC2\_M.

## 8.3.9.2. Beam 9\_4\_EC2\_V

Beam 9\_4\_EC2\_V was then tested under the same loading regime as Beam 9\_4\_EC2\_M. Cracking again began close to the support point at an applied load of 6kN. The element deflected very little, and cracks propagated along the length of the beam under increasing load. At an applied load of 22kN the first inclined cracks formed at the support and this was closely followed by total failure of the beam at 26kN (90% of the design load). The load deflection plot for the beam is shown in Figure 8.65.

The much higher capacity of Beam 9\_4\_EC2\_V when compared to Beam 9\_4\_EC2\_M suggests that the presence of transverse steel in Beam 9\_4\_EC2\_M has in fact been detrimental during the construction process, where the small section size and complex steel layout may have resulted in small errors that led to the premature failure.

Failure of Beam 9\_4\_EC2\_V is illustrated in Figure 8.67. After failure, the end zone was inspected, where it was seen that the anchorage zone had been split apart (Figure 8.68). At the failure load, the beam was seen to move considerably off of its supports, suggesting the presence of a horizontal reaction at the support, contrary to the assumptions of the design method. The extent of this displacement is shown in Figure 8.69.

Strain gauges located on the beam as shown in Figure 8.70(l) show that at failure the longitudinal reinforcement was close to yield in the end zone (Strain Gauge 1) and was approaching yield at Strain Gauge 2.

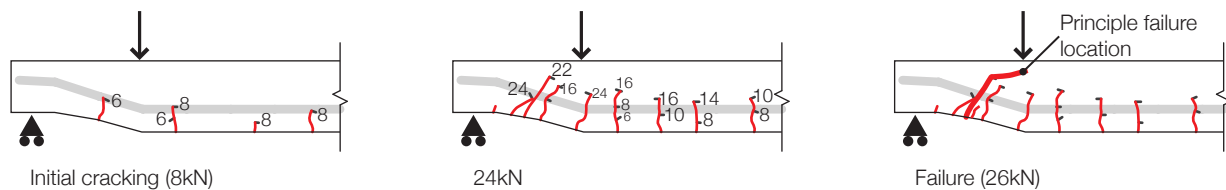


Figure 8.67: Crack distribution in Beam 9\_4\_EC2\_V.

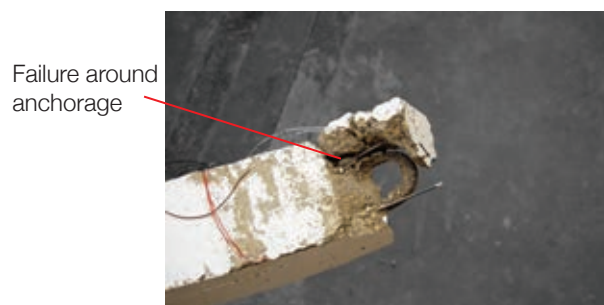


Figure 8.68: Failure at support location in beam 9\_4\_EC2\_V.



Figure 8.69: Horizontal displacement after failure of Beam 9\_4\_EC2\_V.

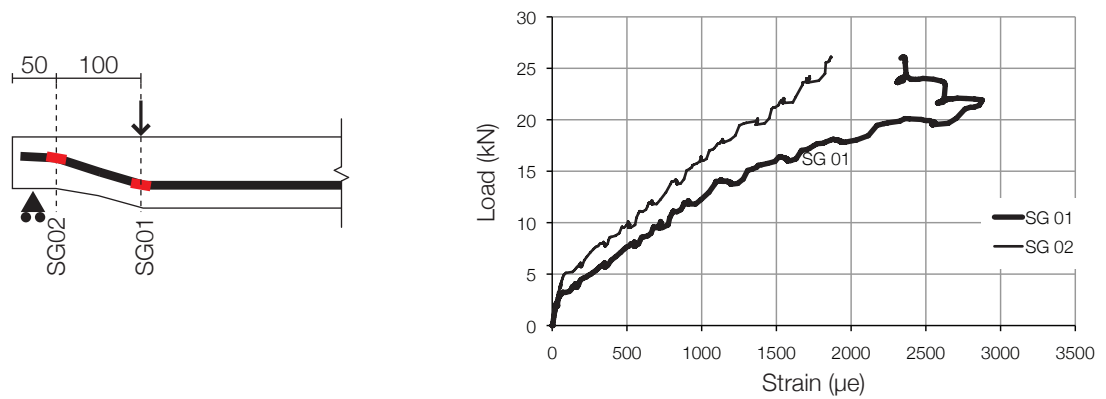


Figure 8.70: Strain gauge locations and results, Beam 9\_4\_EC2\_V.

### 8.3.9.3. Beam 9\_4\_CFP\_M

Beam 9\_4\_CFP\_M (Figure 8.71) was tested first, and was taken initially to its design load of 29.2kN. Load was applied in 2kN increments, and cracks were first noted at an applied load of 14kN. Upon increasing the load cracking was distributed along the face of the beam, as shown in Figure 8.71. The design load of 29.2kN was reached without failure and the load was then released to carry out the second test. Strain gauges were not present in this end of the beam. A load deflection plot for the beam is provided in Figure 8.65 on page 279

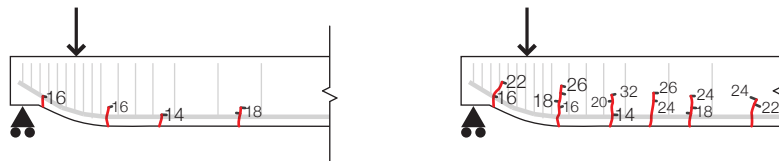


Figure 8.71: Crack distribution, Beam 9\_4\_CFP\_M.

### 8.3.9.4. Beam 9\_4\_CFP\_V

Beam 9\_4\_CFP\_V was then tested. In this test, a pinned support was placed at the end of the tapered beam section (Figure 8.72), which had a significant impact on the test results. Although this was not the intended test layout, the results did provide further interesting discussion surrounding the realistic modelling of concrete structures during experimental testing.

It can be seen in the results that a direct strut between the load and support was formed, providing the beam with significant capacity over any other test. Upon failure, the beam was seen to move laterally by a significant amount (Figure 8.74) as the support failed, showing the magnitude of the horizontal reaction generated by this strut at the support.

Load was applied in 2kN increments and first cracking was recorded at 14kN in a similar manner to Beam 9\_4\_CFP\_M. A similar distribution of crack formation was recorded in the initial loading phase, but the element went on to behave considerably differently to other tests, as illustrated in the load deflection plot in Figure 8.65 on page 279. The beam reached a maximum load of 84.5kN - significantly more than the design load of 29.2kN, and significantly more than predicted by any of the design methods.

Considerable deformability was seen in the test at peak loads, with deep inclined cracks forming in the end zone leading to crushing of the compression face. The final crack pattern in the tapered zone is shown in Figure 8.72 and Figure 8.73 (the beam set up is identical to 9\_4\_CFP\_M).

The use of a pin and roller for the tests carried out in this thesis was discussed in detail, and was chosen as a suitable representation of a simply supported beam. However, the position of the pin and roller in asymmetrically loaded tests does have a significant impact on their behaviour, and in particular for beams with short shear spans. This data is potentially important in reinforced concrete design, where rarely are elements truly simply supported, instead having a degree of connection provided to the surrounding vertical frame elements.

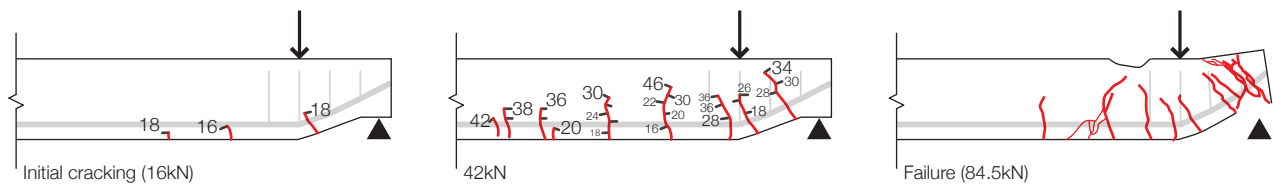


Figure 8.72: Crack propagation in Beam 9\_4\_CFP\_V.

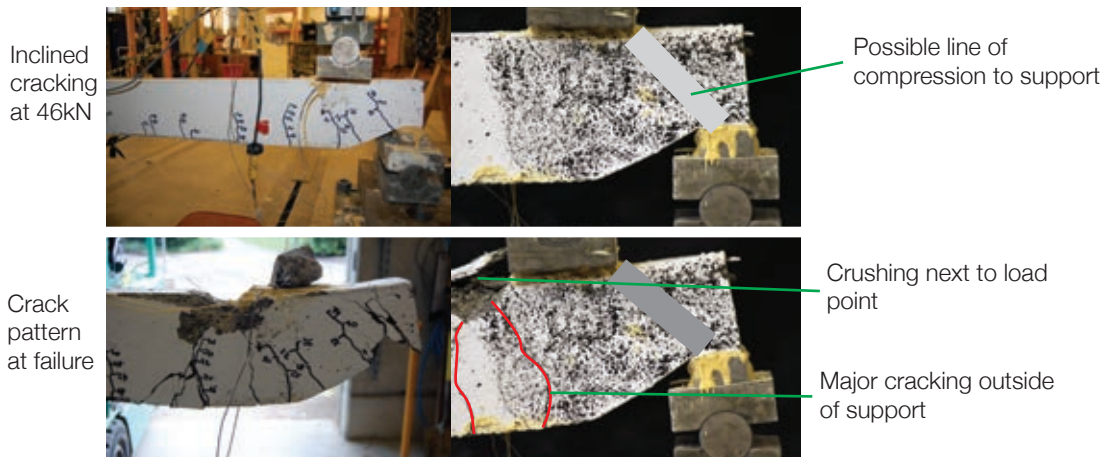


Figure 8.73: Crack distribution and failure mode, Beam 9\_4\_CFP\_V.

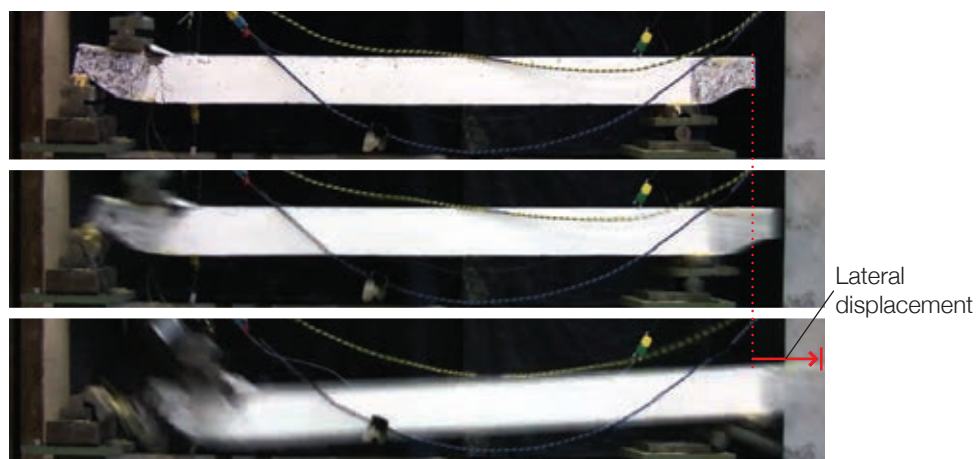


Figure 8.74: Lateral motion of Beam 9\_4\_CFP\_V at failure.

### 8.3.10. Discussion

The results of eighteen beam tests undertaken on ten specimens are presented and discussed in the preceding sections, through which comparisons have been made between the BS EN 1992-1-1 (2004) (EC2) and compressive force path (CFP) design methods. Beams designed using the 'CFP' method, on average, exceed their design load by 19% and displayed a ductile failure mode, while Beams designed using the 'EC2' method are found to be unconservative, reaching just 58% of their design load on average.

The data presented suggests that the EC2 design method can lead to unconservative designs for tapered beams in shear when the current provisions are applied. The results, which are summarised in Table 8.9 on page 263, show that the alternative compressive force path design method, which is equally simple to use, provides consistent results on the conservative side of failure.

All of the beams tested in this section were designed to have equal likelihood of shear and flexural failures, in contrast to previous work where deliberate 'over-designing' in shear has been undertaken in an attempt to prevent such failures. The results of these tests are thus far more informative, as they require full utilisation of the section's capacity and thus in turn require accurate predictions of what that capacity actually is.

The results suggest two things. First, that the combined actions of moment and shear must be considered in elements where both are critical. In conventional prismatic concrete beam design, it more common to have high utilisation of one action (for example, shear) with a low utilisation of another (for example, flexure). In the optimised beams cast using fabric formwork that are proposed in this thesis, high utilisation of both shear and flexure together is a requirement of the design process.

Secondly, the tests suggest that simplified optimisation methods may not necessarily be appropriate for elements of complex geometry. The behaviour of the beams tested has demonstrated that the method following guidance in BS EN 1992-1-1 (2004) may be inappropriate for tapered beams in shear critical loading. Much better behaviour, and closer correlation to the design predictions, is obtained through the use of the compression force path method.

Further analysis of the beam tests described above is undertaken using digital image correlation, as described in §8.5, where the differences in strain distributions created in the different models is seen. In addition, the results presented above are compared and analysed against the results presented in §8.4, where elements designed using a new strut and tie model are presented. A favourable and predictable behaviour is seen in elements with tapered ends using this approach.



## 8.4. Strut and tie model

### 8.4.1. Introduction

Following from the tests presented in §8.3 a series of tests were undertaken on three beam specimens designed according to the strut and tie model presented in §7.2.4 on page 236. The beams were tested in the same load condition as Beams 9\_2\_EC2 and 9\_2\_STM presented in §8.3 (shear span of 500mm), allowing comparisons to be made between the three design methodologies.

The beams were cast using the concrete mix shown in Table 8.10, with the resulting compressive strengths shown in Table 8.11. The average concrete compressive strength at testing was 35.9MPa. Test results are presented below, with discussion, analysis and comparisons to §8.3 provided in subsequent sections. All beams in this test series were monitored using digital image correlation, as described in §8.3.4.1 on page 262.

Table 8.10: Concrete mix design per  $m^3$ .

Cement (CEM IIbv)	4-8mm aggregate	0-5mm aggregate	Water
450kg	1055kg	705kg	190kg

Table 8.11: Concrete properties - compression.

Beam	7 Days (3 cubes)		10 Days (3 cubes)		14 Days (3 cubes)		28 Days (3 cubes)		Testing date
	$f_c$	SD	$f_c$	SD	$f_c$	SD	$f_c$	SD	
9_2_STM (i)	NA	-	38.2	1.05	45.0	2.98	45.5	1.75	10 days
9_2_STM (ii)	35.1	1.95	NA	-	46.1	1.80	51.3	0.78	7 days
9_2_STM (iii)	34.5	2.38	NA	-	NA	-	48.4	1.26	7 days

Where  $f_c$  = average of three concrete cube (100mm) compressive strength tests; SD = standard deviation on test results.

### 8.4.2. Beam Layouts

Beam 9\_2\_STM is illustrated in Figure 8.75, with the full design provided in §7.2.4 on page 236. Longitudinal reinforcement was kept constant throughout, using two H10 U-bars arranged as shown in Figure 7.16 on page 229. Two three millimetre bars were placed in the top zone of the beam to support transverse reinforcement. Two test set ups were used, with set up '2' having an additional steel plate in the end zone anchored with a 10mm diameter deformed steel bar. Three beams of this design were tested (denoted *i*, *ii* and *iii*), as described in the following sections.

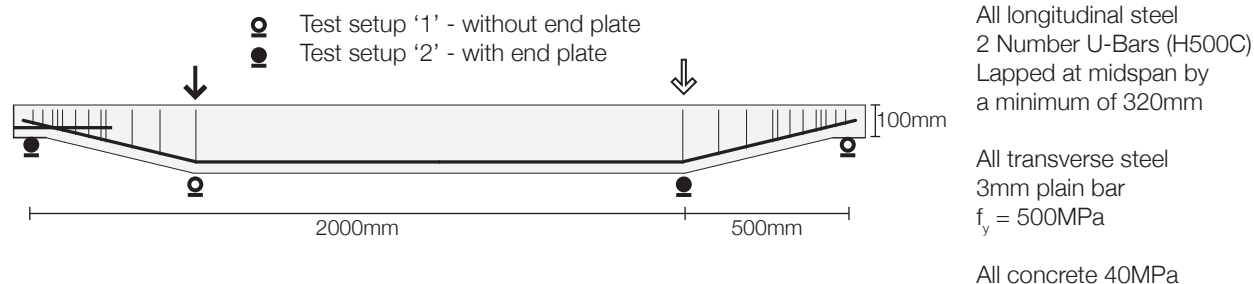


Figure 8.75: Beam 9\_2\_STM layout.

### 8.4.3. Construction

The construction of Beam 9\_2\_STM was made again in a steel mould, shaped internally using timber blocks (Figure 8.76). The beam was demoulded after 3 days and cured in laboratory conditions prior to testing.

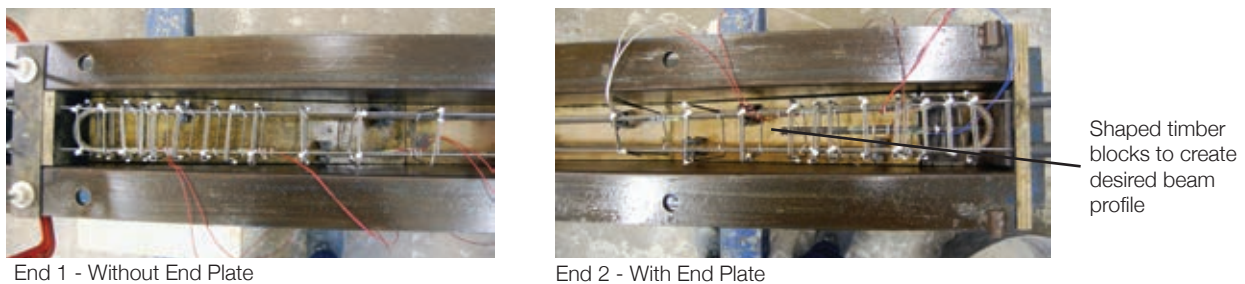


Figure 8.76: Construction of Beam 9\_2\_STM.

### 8.4.4. Testing

Testing was undertaken as described in §8.3.4 on page 262. Each beam was monitored with six strain gauges placed on the longitudinal reinforcement and a linear variable displacement transducer was placed at the point of load application and at the beam midspan, as shown in Figure 8.77. All tests were recorded using a video and a still camera to allow concrete strains to be determined using digital image correlation (§8.3.4.1 on page 262).

Beams (i) and (ii) were supported on two bridge bearings (as opposed the pin and roller set up used in Beam (iii)) to reflect the conditions of a simply supported beam in practice. A summary of the test results is provided in Table 8.12, and described below in §8.4.5 - §8.4.7.

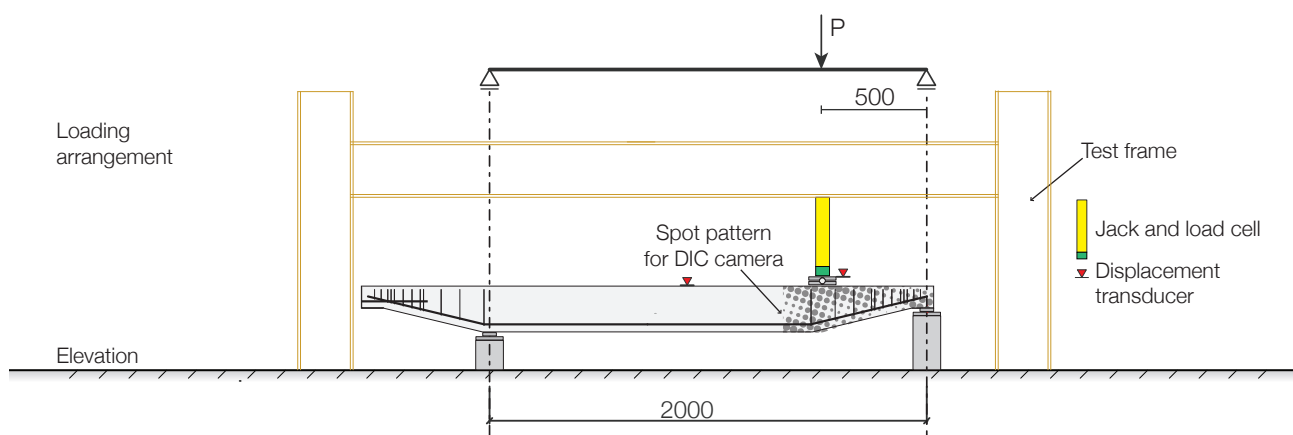


Figure 8.77: Typical test set up, Beams 9\_2\_STM(i) and 9\_2\_STM(ii).

Table 8.12: Test failure modes and ultimate capacity for STM series tests.

	Design maximum load, P (kN) [A]	Maximum load achieved in test (kN) [B]	Failure mode	[B] / [A]
9_2_STM_1 (i)	36.00	41.81	Shear/Flexure	1.16
9_2_STM_2 (i)	36.00	41.45	Shear/Flexure	1.15
9_2_STM_1 (ii)	36.00	38.73	Flexure	1.08
9_2_STM_2 (ii)	36.00	37.85	Flexure	1.05
9_2_STM_1 (iii)	36.00	37.42	Flexure	1.04
9_2_STM_2 (iii)	36.00	40.59	Flexure	1.13
Average [B] / [A]:				1.10

## 8.4.5. Test results: Beam 9\_2\_STM(i)

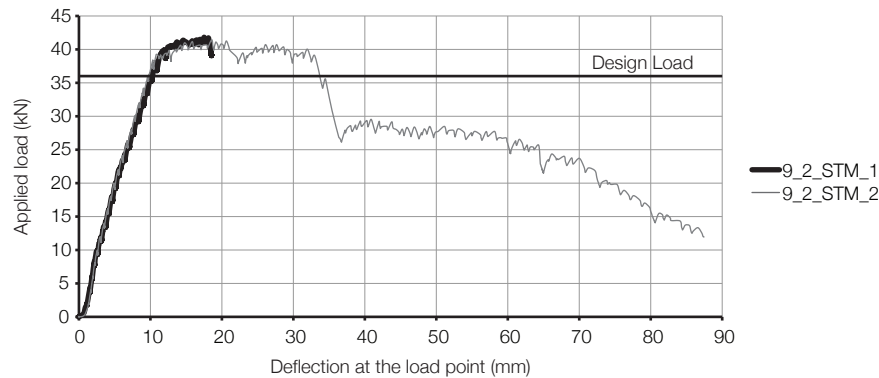


Figure 8.78: Load versus deflection results for Beam 9\_2\_STM(i).

## 8.4.5.1. Beam 9\_2\_STM\_1(i)

As noted in Figure 8.75, each symmetrical beam was tested twice (once for each tapered end, with the tests denoted '1' and '2' respectively). Beam 9\_2\_STM\_1(i) was tested first. Load was applied in 2kN increments, and cracking was first noted at 10kN, occurring directly beneath the load point. Cracking propagated along the tapered end of the beam as shown in Figure 8.79, before reaching a peak load of 41.81kN. A displacement at the point of load application of 17.5mm was recorded at this peak load (Figure 8.78).

Ductility at the peak load was recorded (Figure 8.78), before crushing began to occur on the top face of the beam as shown in Figure 8.79. To avoid significant damage to the beam that would prevent the testing of Beam 9\_2\_STM\_2(i), the test was stopped at a peak displacement of 18.5mm.

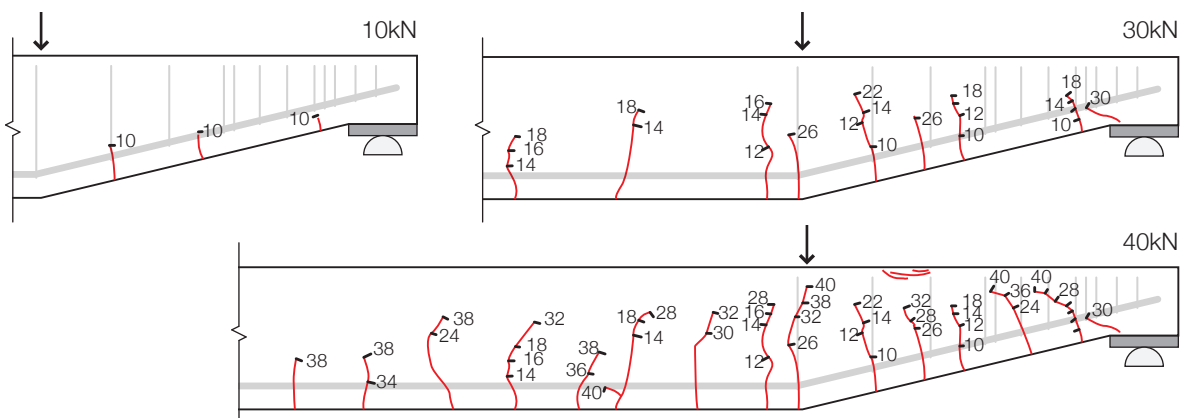


Figure 8.79: Crack propagation in Beam 9\_2\_STM\_1(i).

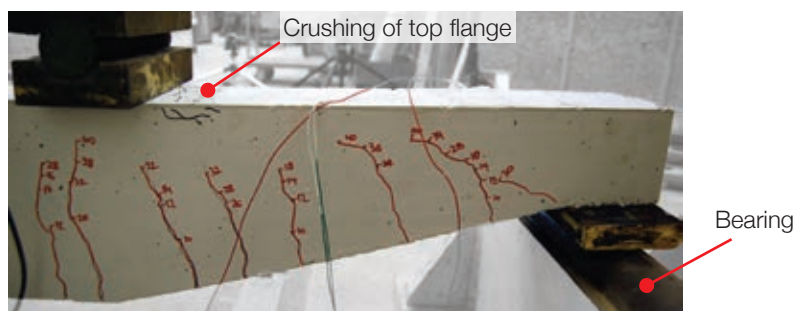


Figure 8.80: Crushing in the top flange of Beam 9\_2\_STM\_1(i).

Strain gauges, placed on the longitudinal reinforcement as shown in Figure 8.81, showed an linear increase in strain up to the cracking load. After this point, the strain in Gauge 3 increased rapidly up to yield, which occurred at the maximum load (corresponding to the flexural capacity of the beam). The strain recorded in Gauges 1 and 2 did not reach yield. After a sudden increase in strain at 23kN applied load, the recording on Gauge 2 was seen to reduce towards the maximum load.

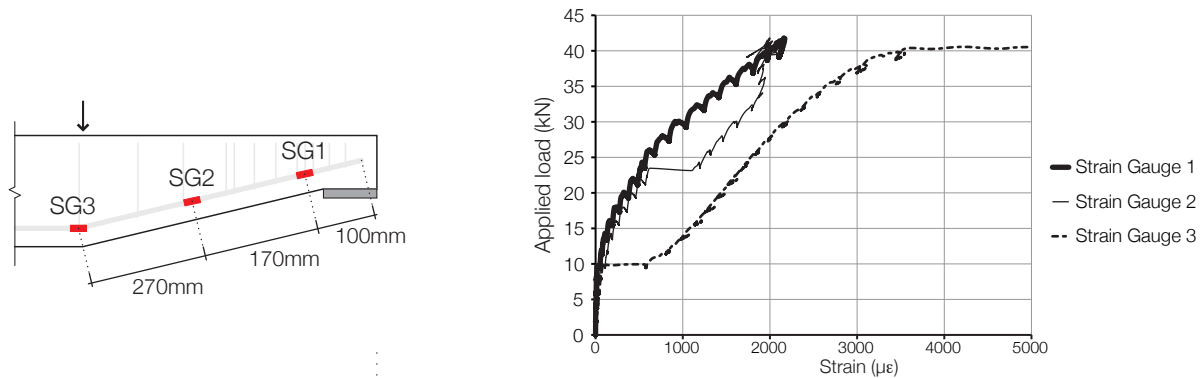


Figure 8.81: Bar strain, Beam 9\_2\_STM\_1(i).

At the design load of 36kN, strain gauge readings from the test data suggest that the force in the bar is distributed as shown in Figure 8.82. This is compared to the values assumed in the design using the strut and tie model in the same Figure, where good agreement is seen. Whilst the design model assumes a constant force in each tie, the reality of the test demonstrates that the force is more likely to vary along the length of the tie due to the presence of additional struts and vertical ties that transfer load.

This linear variation in strain in the steel may arise due to the increased number of vertical ties in the real beam, which act to increase the number of compression struts in the system. It is also recognised that the beam does not behave as a discrete strut and tie model, and is instead a distributed mesh of load paths that the strut and tie model is a simplification for, as illustrated in Figure 8.83.

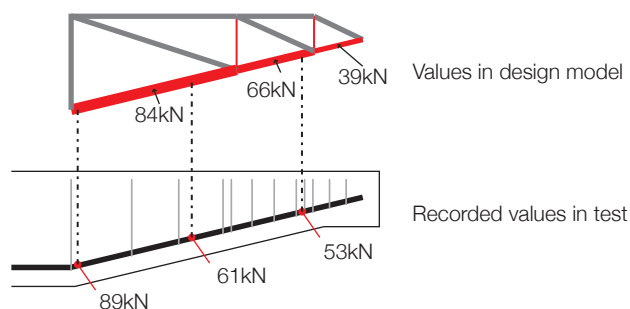


Figure 8.82: Force comparison at the design load for Beam 9\_2\_STM\_1(i).

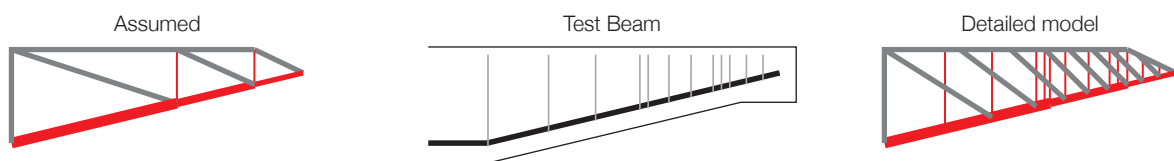


Figure 8.83: Behaviour analysis.

At the maximum load carried by Beam 9\_2\_STM\_1(i) of 40kN, strain gauge readings at positions 1 and 2 suggest the force in the bar at these locations was 66.8kN and 64.3kN respectively. This is again compared to the values estimated by the strut and tie model in Figure 8.84. The bar at Gauge 3 was seen to yield at a strain of  $3400\mu\epsilon$ , which provides a yield stress in the steel of 697MPa. This is considerably more than the 550MPa assumed during design, and thus accounts for the increased capacity of the beam beyond the 36kN design value.

It is seen in the results that the strain in the bar at Gauge 2 was slightly less than the strain in the bar at Gauge 1 at the peak load. This is not considered to be significant, and may have simply arisen due to a failure of the strain gauge at this location. The effect was not repeated in the remaining tests (Beams 9\_2\_STM\_1(ii) and (iii)).

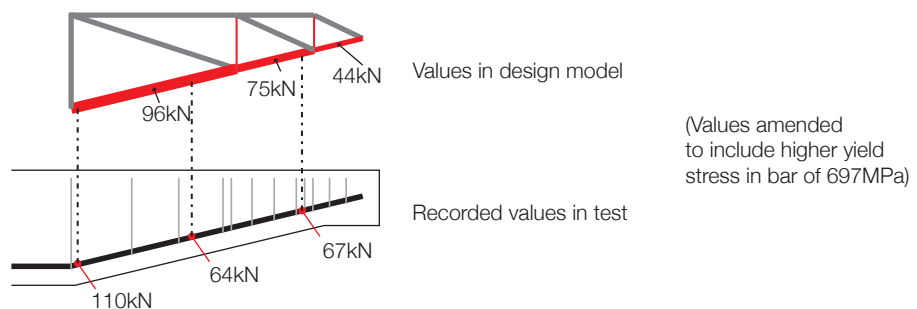


Figure 8.84: Strut and tie model compared to recorded steel strains at peak load.

#### 8.4.5.2. Beam 9\_2\_STM\_2(i)

Beam 9\_2\_STM\_2(i) was then tested in the same manner as Beam 9\_2\_STM\_1(i). Cracking was noted first at an applied load of 10kN and was located between the loading point and the support point. Cracking then propagated along the length of the beam as shown in Figure 8.79. A peak load of 41.45kN was achieved by the beam, reached initially at 10.8mm deflection at the load point.

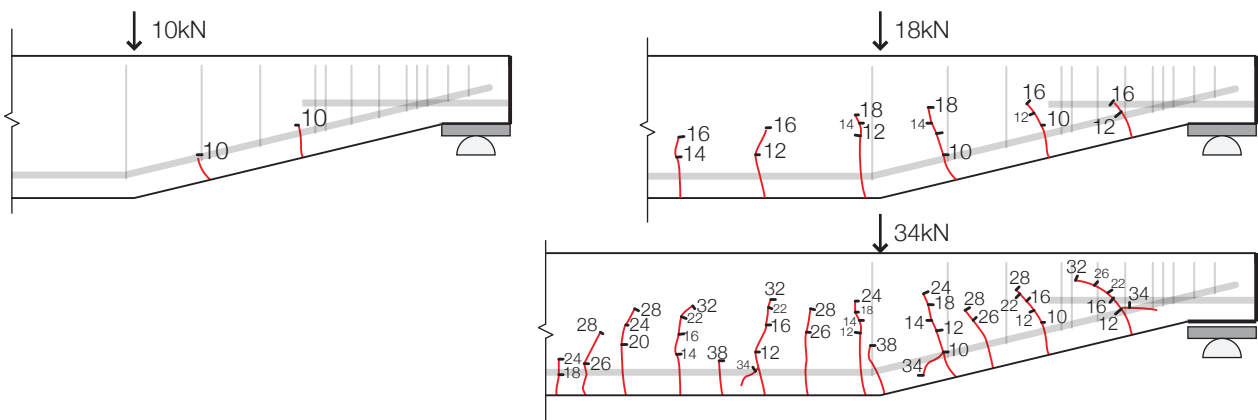


Figure 8.85: Cracking in Beam 9\_2\_STM\_2(i).

Ductility at this peak load was recorded, with the beam maintaining an applied load of approximately 40kN between 10.8mm and 32.5mm displacement (recorded beneath the load point), as shown in Figure 8.78. Crushing began in the same position as seen in Beam 9 2 STM 1(i), and in this test the beam was taken to destruction.

A wedge of concrete was initially pushed from the face of the beam, and the load dropped from its peak value to a second plateau at around 28kN (Figure 8.78) as the beam redistributed stresses. This load was maintained

through significant deformation (36.4mm to 58.4mm) during which time spalling of the concrete face occurred (Figure 8.86). Beyond this point the load capacity again fell, reaching 12kN at 88mm deflection at which point the test was stopped. The descending branch of this does not represent ductility in the beam, as the load capacity is not constant, but shows the extent to which deformation of the section can be accommodated.

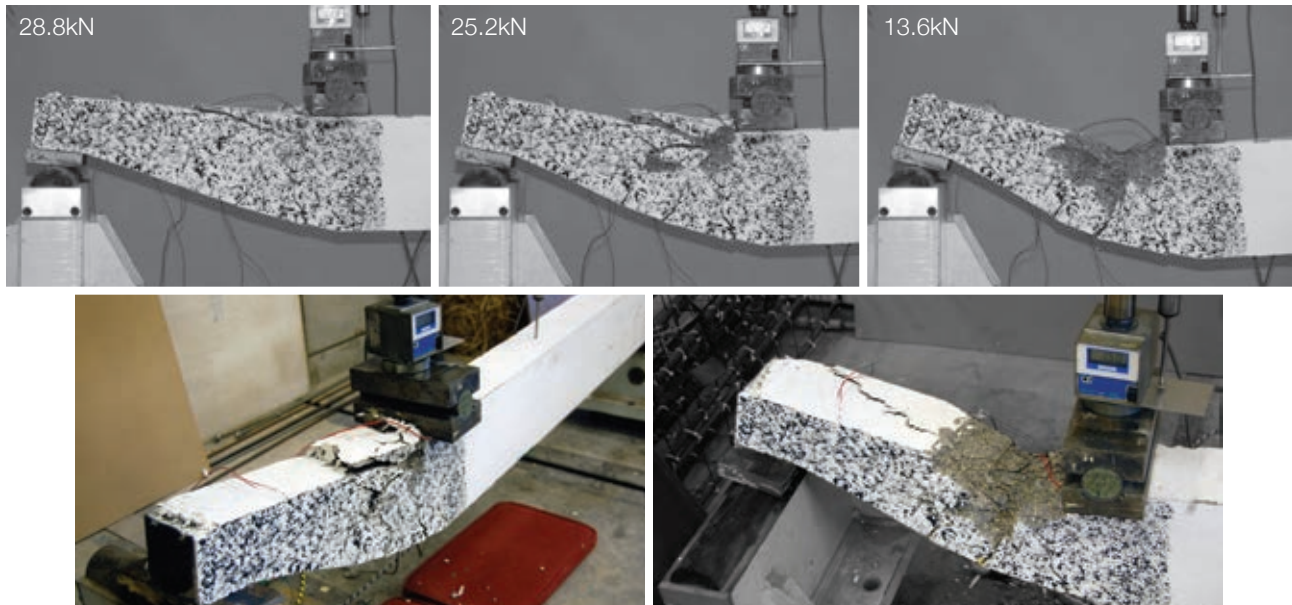


Figure 8.86: Deformation and spalling in Beam 9\_2\_STM\_2(i) beyond peak load.

Strain gauges were positioned on the main steel in the same manner as seen in Beam 9\_2\_STM\_1(i). The results, shown in Figure 8.89, illustrate a similar pattern with the bar at Gauge 3 yielding at the peak load of around 40kN. Gauge 2 showed a peculiar behaviour in which the strain dropped significantly and then decreased after an applied load of 30kN. Strain gauge 1 shows again that the strain in the bar at the end of the beam was quite low.

At the design load of 36kN, the forces in the bar are compared to the design model in Figure 8.89. The results show excellent correlation in the end zone and beneath the point load, but there is a significant drop in the middle of the tapered section due to the results of Strain Gauge 2. Whilst this may have suggested that the horizontal steel has taken up much of the load, the results of Beam 9\_2\_STM\_2(ii) (§8.4.6.1 on page 291) and the fact that the load will go to the stiffest (most highly stressed) point in the beam when it is behaving elastically and therefore should go to the flexural reinforcement, demonstrate that this is likely to be an anomaly. Although it is found in other tests that the force in the horizontal anchorage bar is not insignificant at peak loads (see §8.4.6.2 on page 293), it remains likely that cracking in the midspan has simply damaged Strain Gauge 2 in this test.

The same comparison is made at the peak load of Beam 9\_2\_STM\_2(i) in Figure 8.88. Here, the bar was seen to yield at around 2800 $\mu\epsilon$  (Figure 8.89), and this was included in the force calculation. The falling strain in the bar at Gauge 2 is again seen in Figure 8.89, where at the peak load it recorded an anomalous force of 11kN. However, good correlations are again seen in the remaining two strain gauge positions, and further comparisons between test data and the predictions of the design model for subsequent tests show that excellent correlations can be achieved between the design model and the test data.



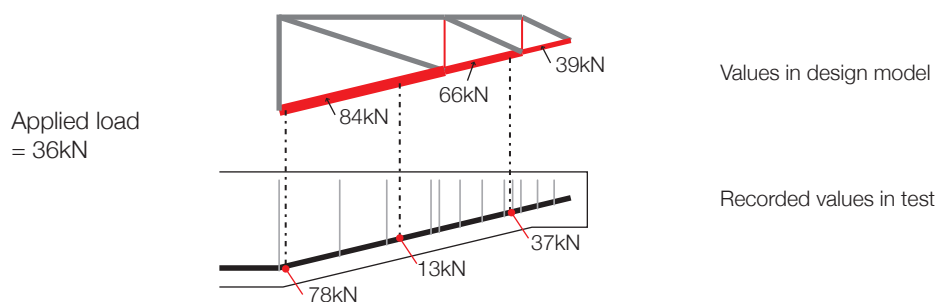


Figure 8.87: Force comparison at the design load for Beam 9\_2\_STM\_2(i).

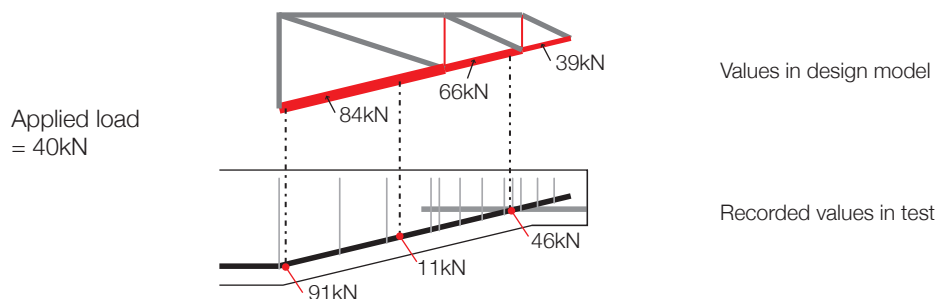


Figure 8.88: Strut and tie model compared to recorded steel strains at peak load for Beam 9\_2\_STM\_2(i).

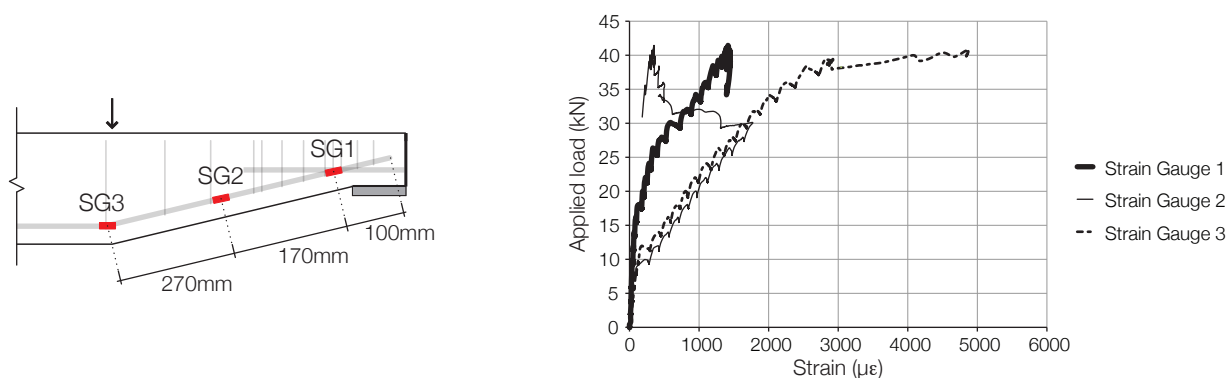


Figure 8.89: Strain gauge results for Beam 9\_2\_STM\_2(i).

#### 8.4.6. Test results - Beam 9\_2\_STM(ii)

The results of Beam 9\_2\_STM(i) suggest that the presence of an external plate with internal anchoring bar does not affect the load behaviour of the beam. Potentially erroneous strain gauge readings recorded in Beam 9\_2\_STM\_1(i) led to a second, identical beam being tested. In this test, the beam was tested in reverse order with Layout 1 being taken to its peak load and Layout 2 taken to destruction, thus allowing the assumption that the two layouts have the same overall behaviour to be verified. In addition, in Beam 9\_2\_STM\_1(ii) extra strain gauges were installed on the horizontal anchoring bar to determine its behaviour during the tests.

Load-deflection results for Beam 9\_2\_STM(ii) are shown in Figure 8.90. Shown in Figure 8.91 is a comparison between beam 9\_2\_STM\_2(i) and Beam 9\_2\_STM\_1(ii), both of which were tested to destruction. Beam 9\_2\_STM\_2(i) showed a higher peak load, which was maintained during a period of ductility at this load value before dropping off, while Beam 9\_2\_STM\_1(ii) the beam showed more gradual reduction in capacity from its peak. In summary, however, the two beams when tested to destruction show almost identical behaviour and hence the presence of the end plate and bar can be said to not adversely affect the behaviour of the section.

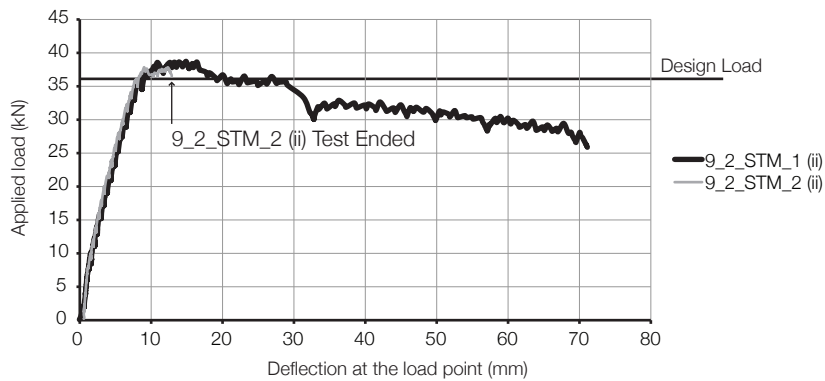


Figure 8.90: Load versus deflection for Beam 9\_2\_STM\_1(ii) and 9\_2\_STM\_2(ii).

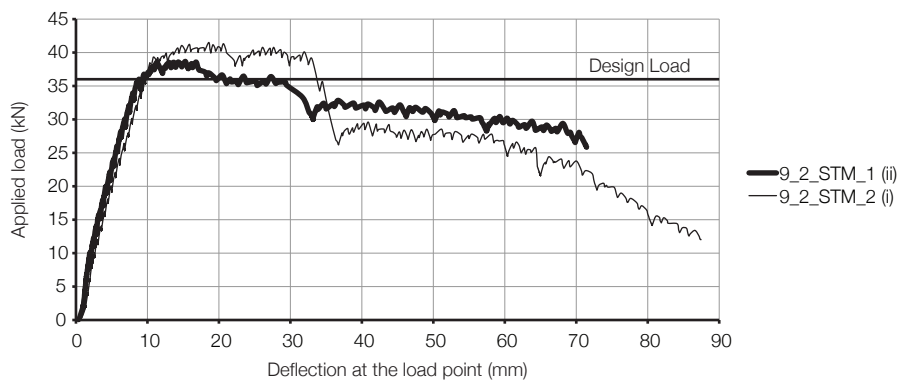


Figure 8.91: Comparison between 9\_2\_STM\_1(ii) and 9\_2\_STM\_2(i)

#### 8.4.6.1. Beam 9\_2\_STM\_1(ii)

Beam 9\_2\_STM\_1(ii) was tested after Beam 9\_2\_STM\_2(ii) (§8.4.6.2 on page 293). Load was applied to the beam in 2kN increments, and cracking was first noted at 8kN in the support zone, before further cracking beneath the load application point was recorded at 10kN. Cracking along the length of the tapered section then propagated as shown in Figure 8.92, before the section reached a peak applied load of 37.8kN. This value is slightly below that recorded in Beam 9\_2\_STM\_1(i), but is close to the design load of 36kN. The beam displayed some ductility prior to a slowly reducing load capacity as the beam crushed in the compression zone (Figure 8.90).

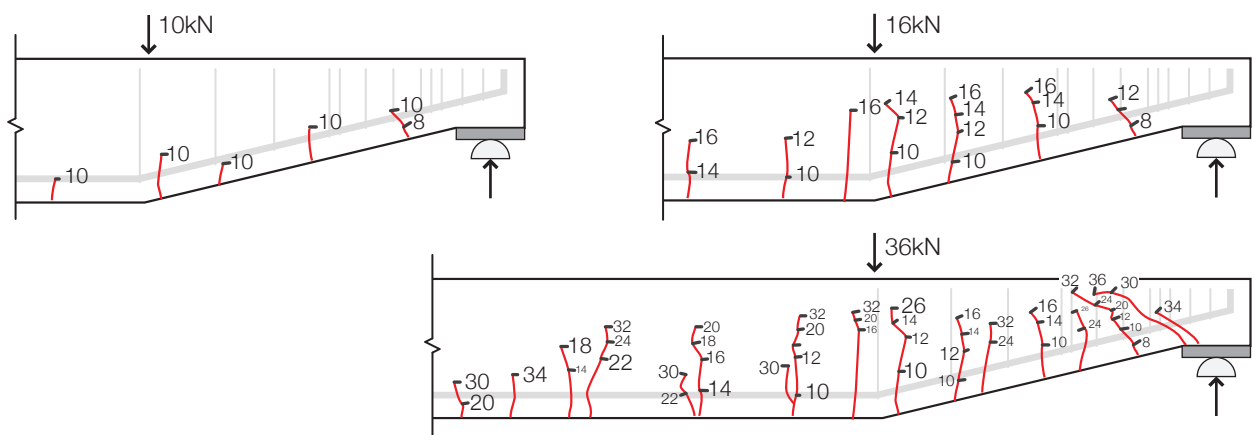


Figure 8.92: Cracking in Beam 9\_2\_STM\_1(ii).

Beam 9\_2\_STM\_1(ii) was tested to destruction in order to determine the full load deflection response of the section. The final failure mode is illustrated in Figure 8.93, where progressive images are shown for increasing

deflection at the load point. The failure is comparable to that recorded for Beam 9\_2\_STM\_2(i), which was also tested to destruction (Figure 8.86 on page 289).

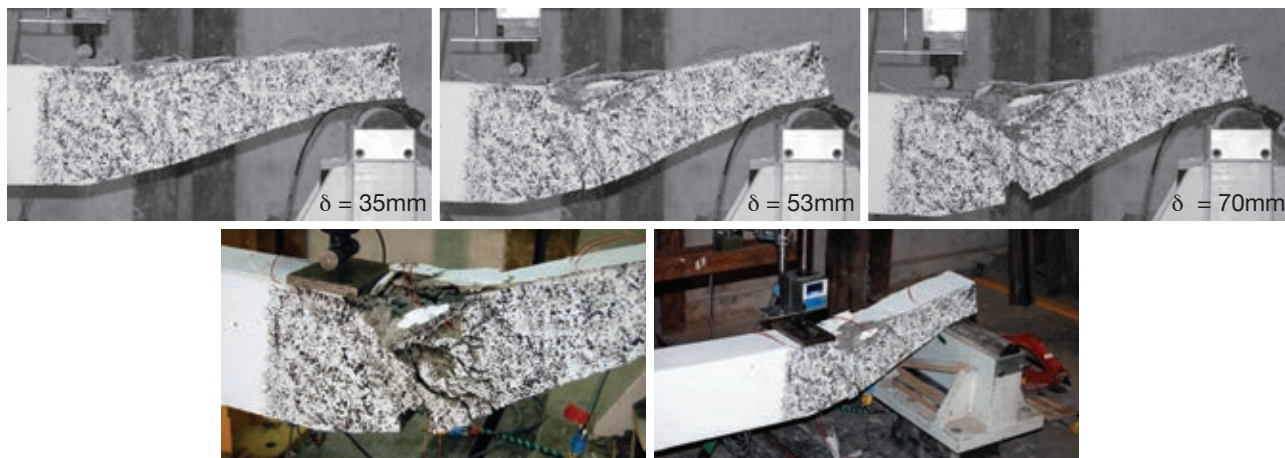


Figure 8.93: Final failure in Beam 9\_2\_STM\_1(ii).

Strain gauges were placed on the longitudinal steel as shown in Figure 8.94, with the results showing that Gauge 1 had yielded at the peak load (~36kN), while the other two gauges had not. The results from Gauges 1 and 2 are almost identical throughout the loading cycle, which is a different behaviour to that seen in Beam 9\_2\_STM\_1(i) (§8.4.5.1 on page 286), but this difference is not considered to be significant.

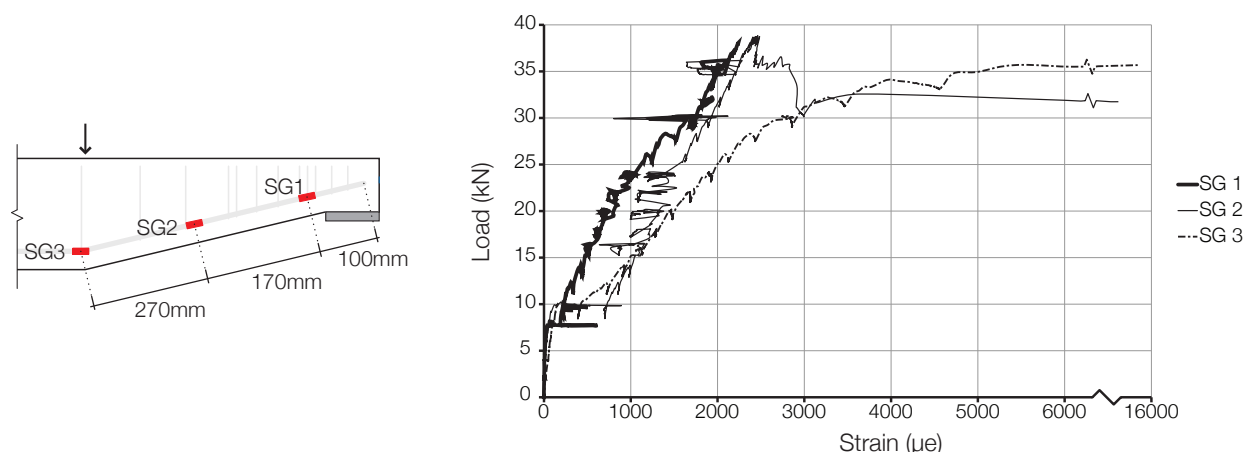


Figure 8.94: Recorded bar strains, Beam 9\_2\_STM\_1(ii).

A comparison between the recorded bar forces (calculated from strain gauge readings) and those predicted in the design model is made for Beam 9\_2\_STM\_1(ii) in Figure 8.95, where the bar yield stress is taken as 650MPa based on the strain gauge results collected during testing. At the design load of 36kN, it is seen that the model has mildly underestimated the forces in the steel, although the correlation remains acceptable and provides a good indication of the actual forces in the steel. A further comparison is made for the forces at peak load in Figure 8.96, where again it is seen that the model underestimates the steel forces.

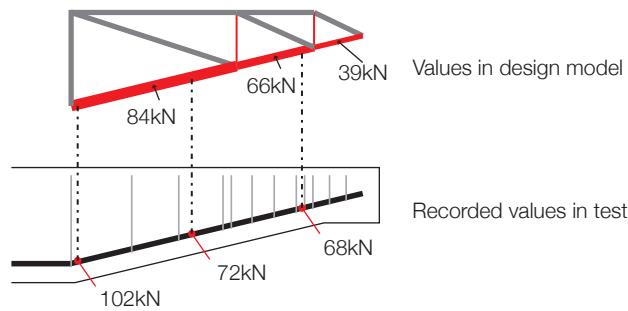


Figure 8.95: Force comparison at the design load.

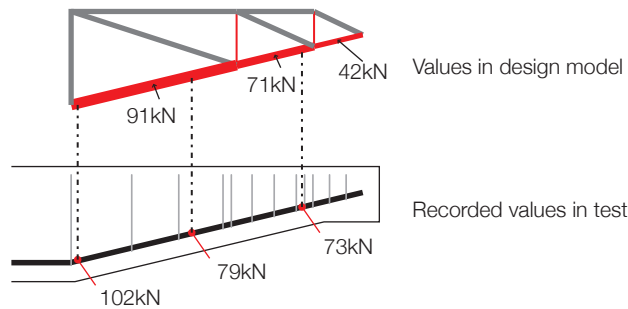


Figure 8.96: Force comparison at the peak load.

#### 8.4.6.2. Beam 9\_2\_STM\_2(ii)

Beam 9\_2\_STM\_2(ii) was tested with load applied in 2kN increments. Cracking was first noted at 10kN, both in the support zone and directly beneath the load point. Cracking propagated along the tapered end of the beam as shown in Figure 8.97, before reaching a peak load of 37.85kN (displacement at this load was recorded at 8.6mm). As shown in Figure 8.90, the beam showed almost identical behaviour to Beam 9\_2\_STM\_1(ii). At the peak load, a small degree of ductility, taking the beam to 12mm displacement, was recorded before the test was stopped to avoid damage to the beam that would have prevented the testing of Beam 9\_2\_STM\_1(ii).

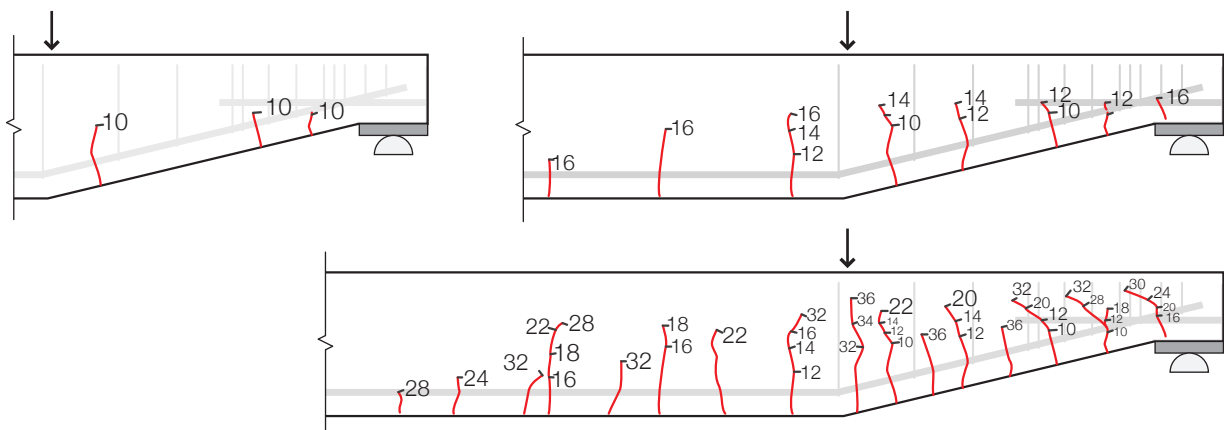


Figure 8.97: Cracking in Beam 9\_2\_STM\_2(ii).

Strain gauges were placed both on the flexural reinforcement (three gauges), and on the horizontal bar (two gauges) welded to the external plate, the results of which are shown in Figure 8.98. Of the three gauges on the flexural reinforcement, one failed during testing. The remaining two gauges show a linear increase in strain up to cracking, after which the strain in the bar increases rapidly. Neither gauge recorded a yielding of the steel, but it

is likely that the bar had yielded in the position of the failed gauge (based on the evidence of Beam 9\_2\_STM\_2(i), §8.4.5.2 on page 288).

The results of Gauge 2 do not show a reduction in strain at higher loads, as was seen in Beam 9\_2\_STM\_2(i), suggesting that result seen in Beam 9\_2\_STM\_2(i) was an anomaly and can be disregarded.

The gauges on the horizontal bar demonstrate that the bar does carry some load (up to a maximum of  $900\mu\epsilon$  (a stress of 180MPa). At an applied load of approximately 25kN (Figure 8.98), the strain in both gauges on the horizontal bar remained approximately constant, suggesting that at higher loads the stiffer flexural reinforcement was picking up the majority of the load in the beam.

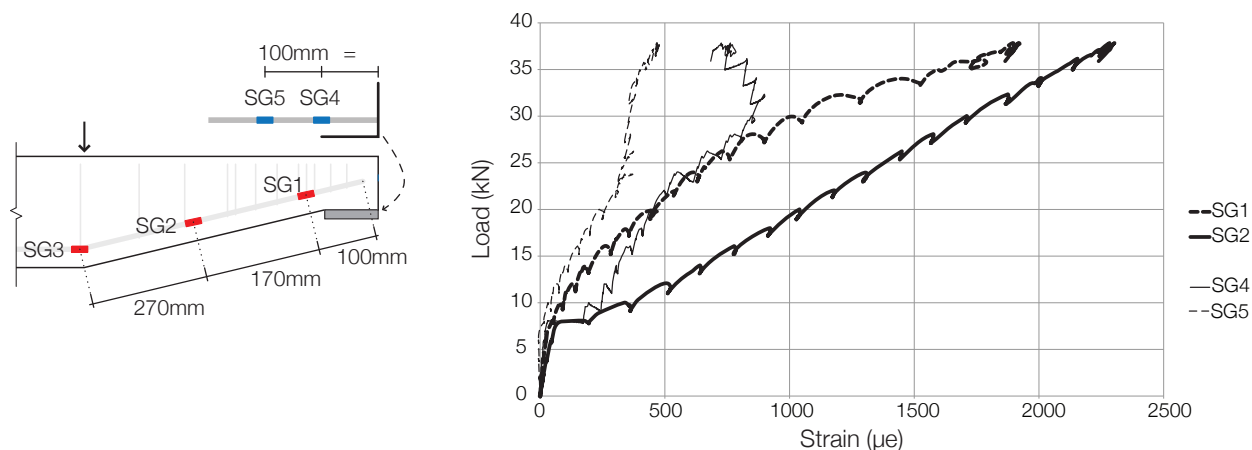


Figure 8.98: Bar strains, Beam 9\_2\_STM\_2(ii).

In the same way as presented for Beam 9\_2\_STM\_2(i), comparisons have been made between the model and experimental values for the forces in the flexural reinforcement. These comparisons are made for the design load (36kN) in Figure 8.99. A second comparison for the peak load (37.85kN) was not made as it is very similar to the design load. In addition to the forces in the flexural reinforcement, the experimentally recorded forces in the horizontal bar are also included in Figure 8.99.

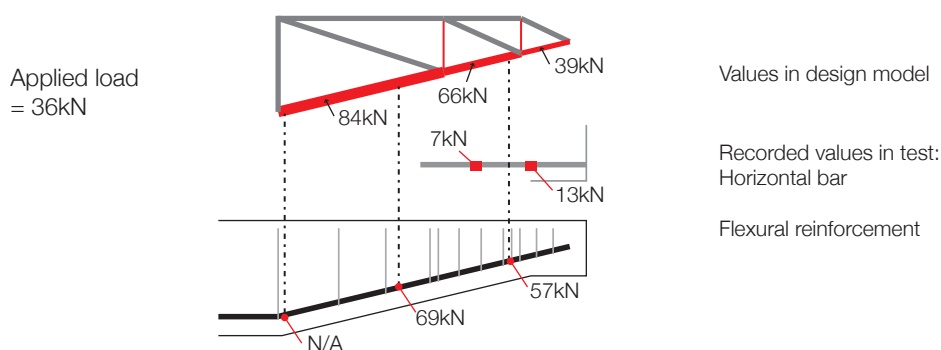


Figure 8.99: Strut and tie model compared to recorded steel strains at the design load, Beam 9\_2\_STM\_2 (ii).

It is apparent that the horizontal bar affects the internal distribution of stresses prior to peak load capacity. However, the global behaviour of the beam is not adversely affected and hence the option for an external plate anchored to an internal deformed bar remains feasible.

The critical element in the designed section is the first vertical tension tie, which, according to the design model, must carry almost the entire vertical force (§7.2.4 on page 236). The achievement of this load carrying method is demonstrated in the results, and is further assessed in the DIC results presented in §8.5, where the distribution of vertical strains at the support are seen clearly.

#### 8.4.7. Test results: Beam 9\_2\_STM(iii)

A final beam, of the same design as (i) and (ii) presented above, was tested to check the behaviour of the support conditions on the strut and tie model behaviour. In previous tests (§8.3 on page 260) a simple pin and roller arrangement has been used, while in the tests presented above (Beams 9\_2\_STM (i) and (ii)) a friction bearing support was used. After the results presented above, a final test was undertaken on a beam supported on the pin and roller arrangement shown in Figure 8.100, to match that used in the previous ‘EC2’ and ‘CFP’ series of tests.

The beam was tested in the same manner as Beam 9\_2\_STM(i). The full load deflection results are provided in Figure 8.101. A comparison between Beam 9\_2\_STM\_2(i) and 9\_2\_STM\_2(iii) is provided in Figure 8.102, where it is clear that the support conditions have made little difference to the overall behaviour of the beam, and hence justifies the choice of support for the previous two tests.

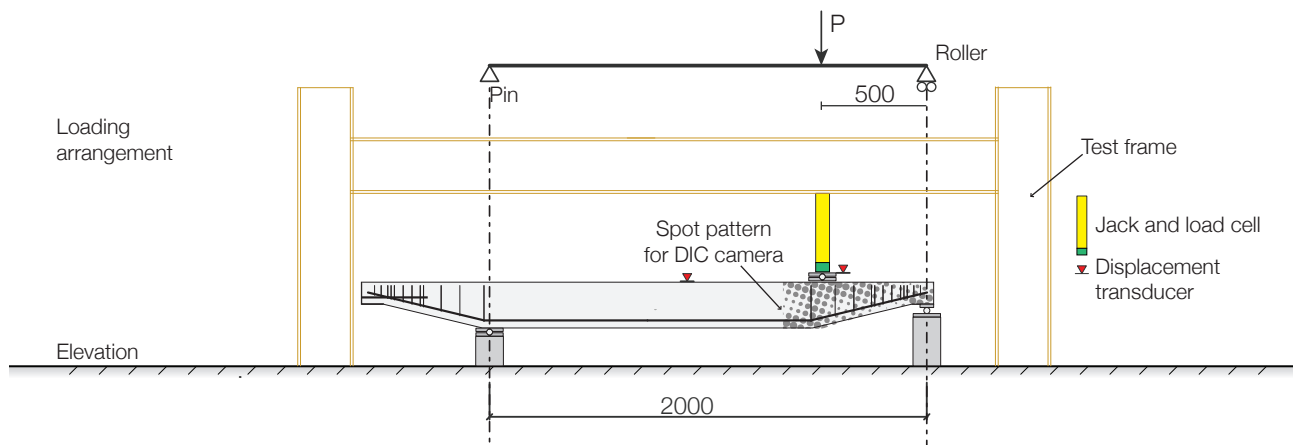


Figure 8.100: Test setup for Beam 9\_2\_STM(iii).

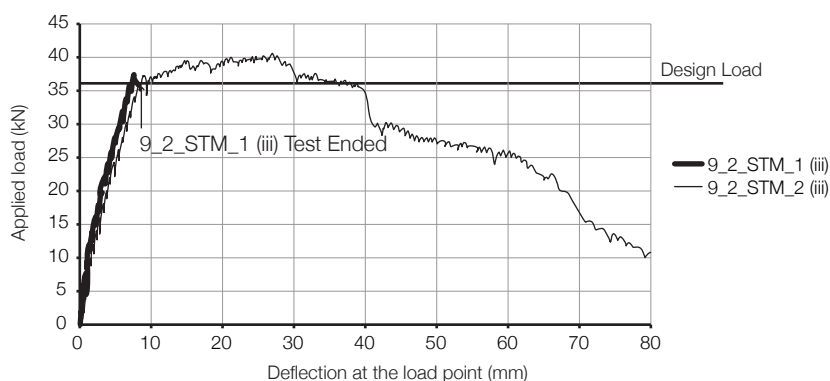


Figure 8.101: Load versus deflection for Beam 9\_2\_STM(iii).



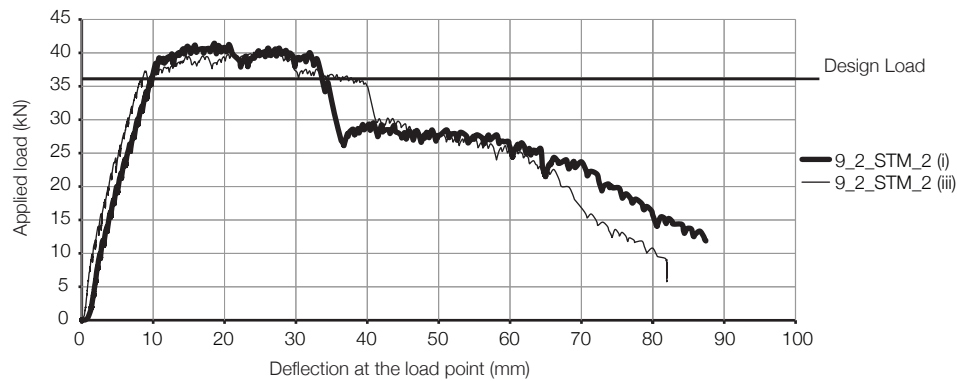


Figure 8.102: Load versus deflection for Beam 9\_2\_STM\_2(i) and 9\_2\_STM\_2(iii).

#### 8.4.7.1. Beam 9\_2\_STM\_1(iii)

Beam 9\_2\_STM\_1(iii) was tested first, in the manner shown in Figure 8.100. Load was applied in 2kN increments, and cracking was first noted at 8kN, close to the support zone as shown in Figure 8.103. Cracking propagated along the tapered end of the beam as shown in Figure 8.103, before reaching a peak load of 36kN, at which point the test was stopped to enable the second test to be undertaken. The beam was not taken past the design load in this test. Strain gauges, placed on the longitudinal reinforcement as shown in Figure 8.104, recorded a similar behaviour to that seen in previous tests, as shown in Figure 8.105, and the bar forces were again found to correlate to the design model (Figure 8.109 on page 298), as was also seen previously in §8.4.5 on page 286 and §8.4.6 on page 290.

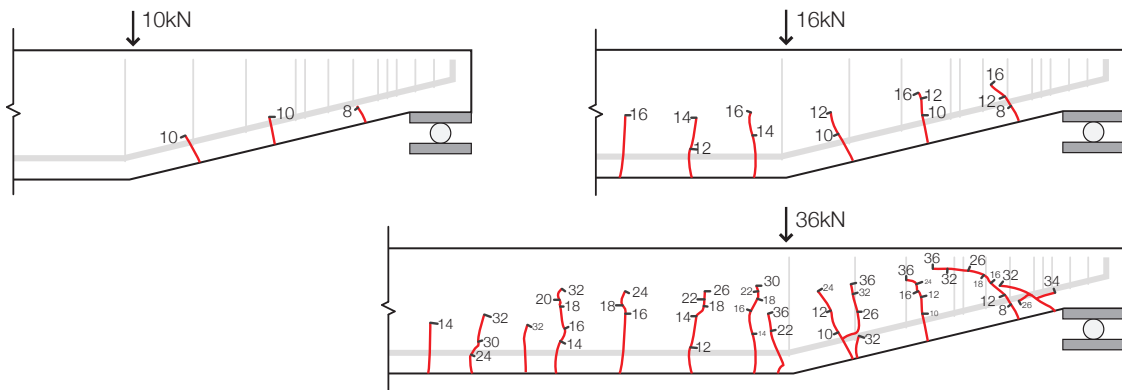


Figure 8.103: Cracking in Beam 9\_2\_STM\_1(iii).

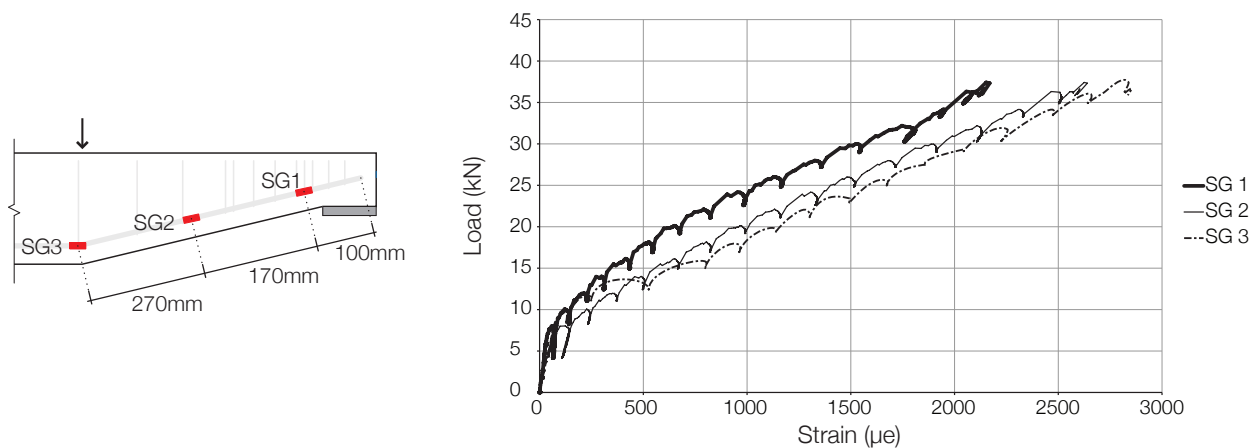


Figure 8.104: Bar Strains - Beam 9\_2\_STM\_1 (iii).

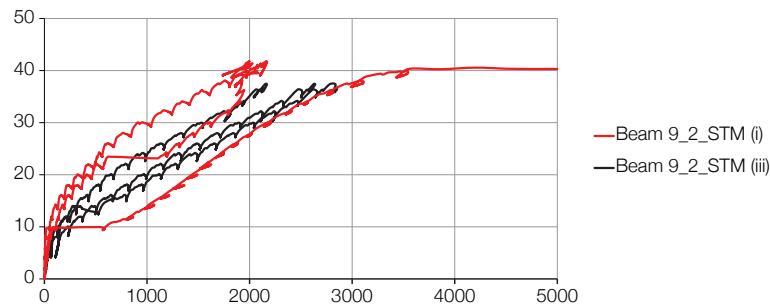


Figure 8.105: Strain gauge result comparison, Beam 9\_2\_STM\_1(i) and (iii).

#### 8.4.7.2. Beam 9\_2\_STM\_2(iii)

Beam 9\_2\_STM\_2(iii) was subsequently tested to destruction. Load was applied in 2kN increments, with first cracking appearing at 8kN in the midspan of the tapered section. Cracking then propagated as shown in Figure 8.106, with final failure of the beam occurring in the manner shown in Figure 8.107. A good correlation is seen between the results of this test and that of Beam 9\_2\_STM\_2(i) and (ii). The results of five strain gauges are provided in Figure 8.108 where again a good correlation in behaviour is seen between this and other beam tests. The roller support has had little influence on the global behaviour of the beam as tested.

The strain gauge results collected in both Beam 9\_2\_STM\_1(iii) and 9\_2\_STM\_2(iii) are again compared to the results of the design model in Figure 8.109 (at the design load of 36kN). The same correlation as seen previously is again shown, and Figure 8.109 also demonstrates how the presence of the end plate affects the distribution of forces within the beam.

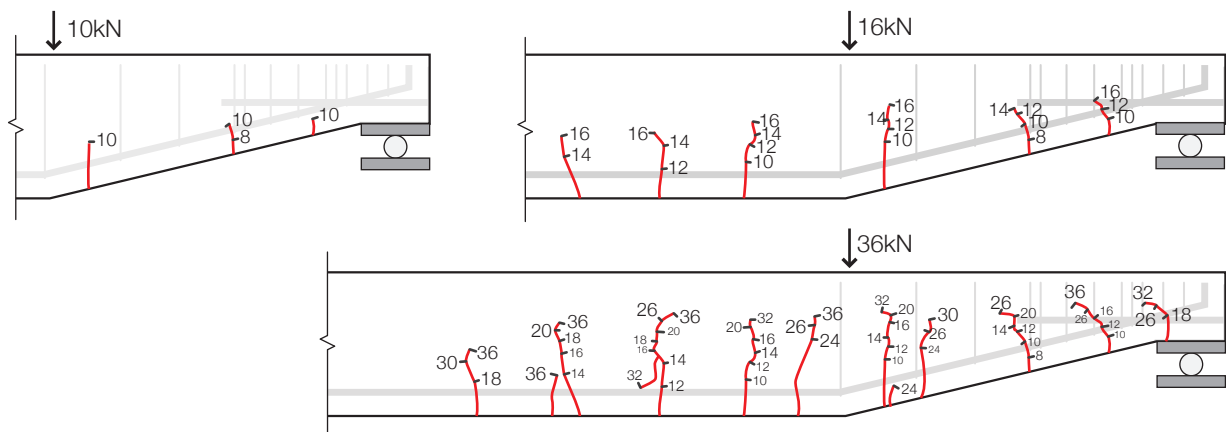


Figure 8.106: Cracking in Beam 9\_2\_STM\_2(iii).

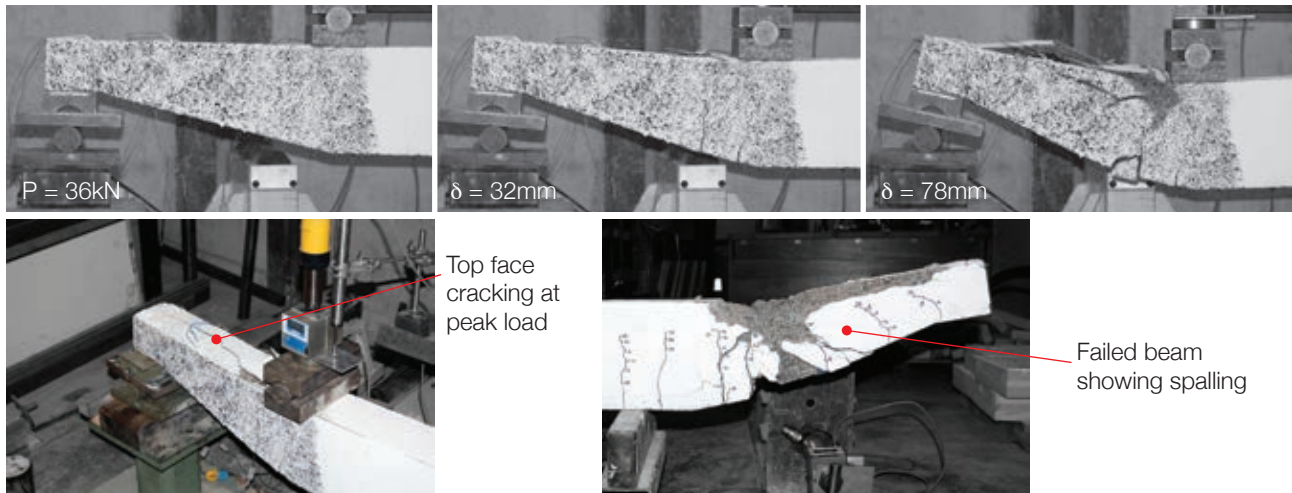


Figure 8.107: Failure of Beam 9\_2\_STM\_2(iii).

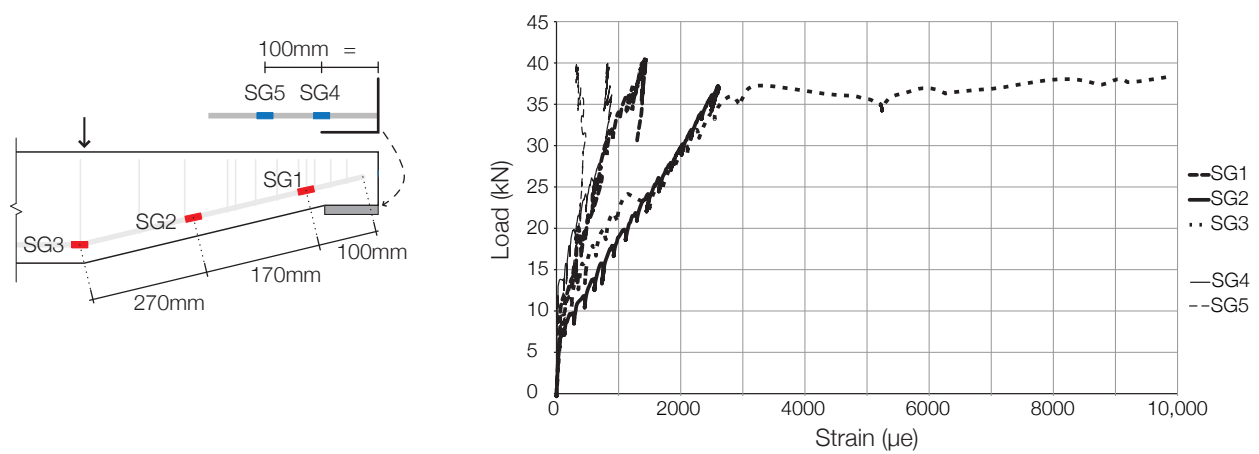


Figure 8.108: Bar strains - Beam 9\_2\_STM\_2(iii).

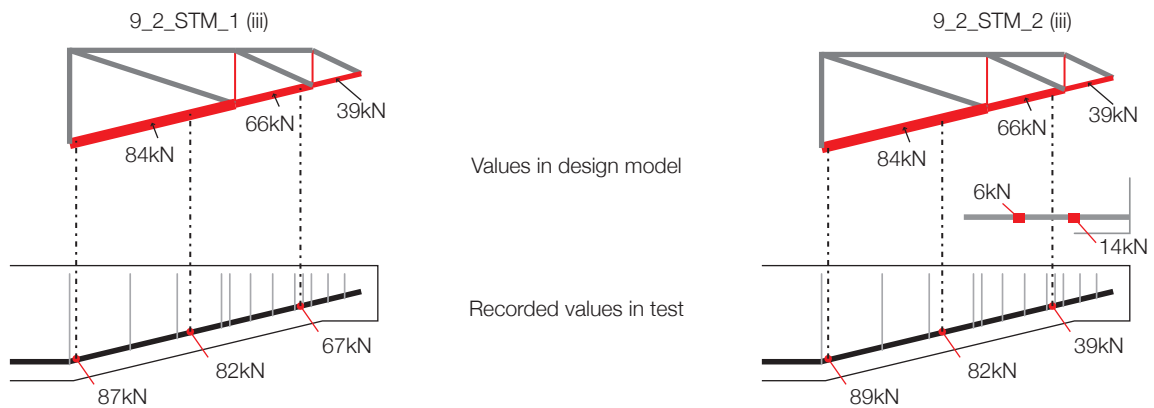


Figure 8.109: Bar forces comparison at the design load of 36kN, Beam 9\_2\_STM(iii).

### 8.4.8. Discussion

The beams tested in this section have shown that a simple design model using a modified strut and tie approach can provide accurate predictions of both the global failure load and internal forces in a tapered beam loaded in shear. Discussion of each test has been provided alongside the test data. The results show that designs using the proposed model exceed the design load by, on average, 10% (Table 8.12 on page 285). This contrasts favourably with much of the data presented in §8.3 on page 260, and suggests that the design model is well suited to tapered beams.

Within this test series two smaller studies have also been undertaken. The first to determine the effect of an end plate, and the second to consider the how the support conditions affect the tested elements.

The test results show that the presence of an external plate does not affect the global behaviour of the beam, but that the use of an internal bar to anchor the plate does attract load away from the flexural reinforcement. This is in itself not a negative aspect to the design, but should be incorporated into any future test methodologies.

The support conditions are modelled in the design as a pin and roller, as is conventional. In tests (i) and (ii), an alternative sliding bearing was used. To ensure that this did not provide any additional horizontal restraint (through friction) to the beam, test (iii) was undertaken with a conventional pin and roller. No difference was seen in the results and the original test method was accepted. This is shown in Figure 8.110, where a summary of all the tests undertaken in the ‘STM’ series is provided.

A final summary of the data collected on tapered beams in shear is provided in Figure 8.111 (where all the beams with a 500mm shear span are shown) and in Figure 8.112 (where all the beams tested are shown). The data suggests that there exist considerable differences between the design models used in this work. These differences are analysed in the following section with the aid of Digital Image Correlation undertaken on the high resolution images collected during the testing program. The data of §8.3 and §8.4 is presented and analysed, with the results facilitating good comparisons between the structural behaviour of the three models presented in this thesis.

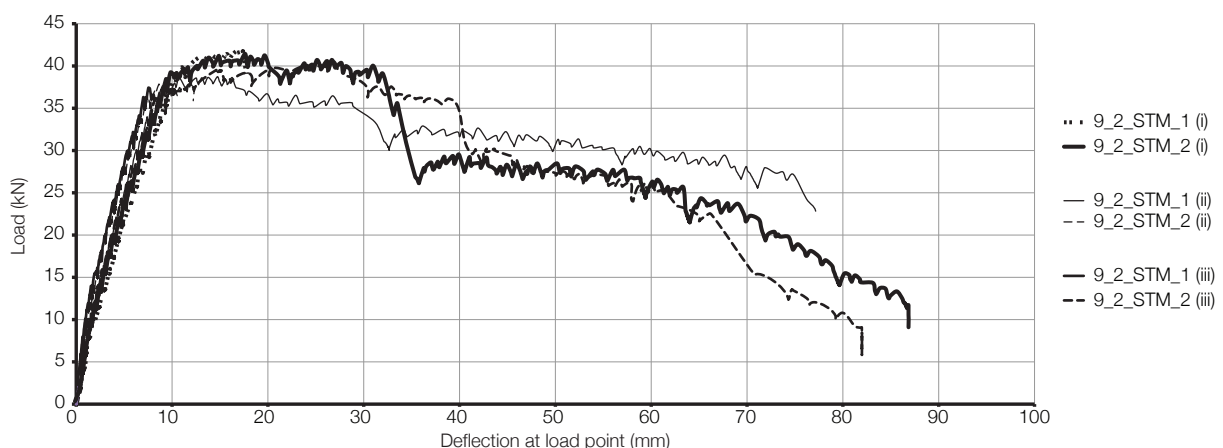


Figure 8.110: Summary of all beam tests in 9\_2\_STM series.

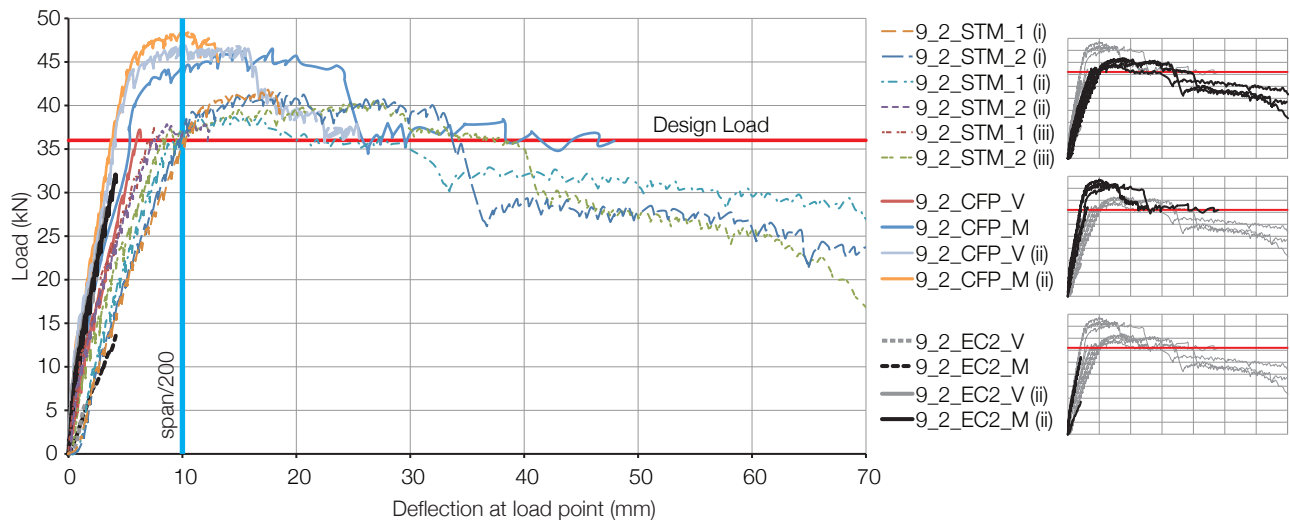


Figure 8.111: Summary of all 9\_2 Series Tests.

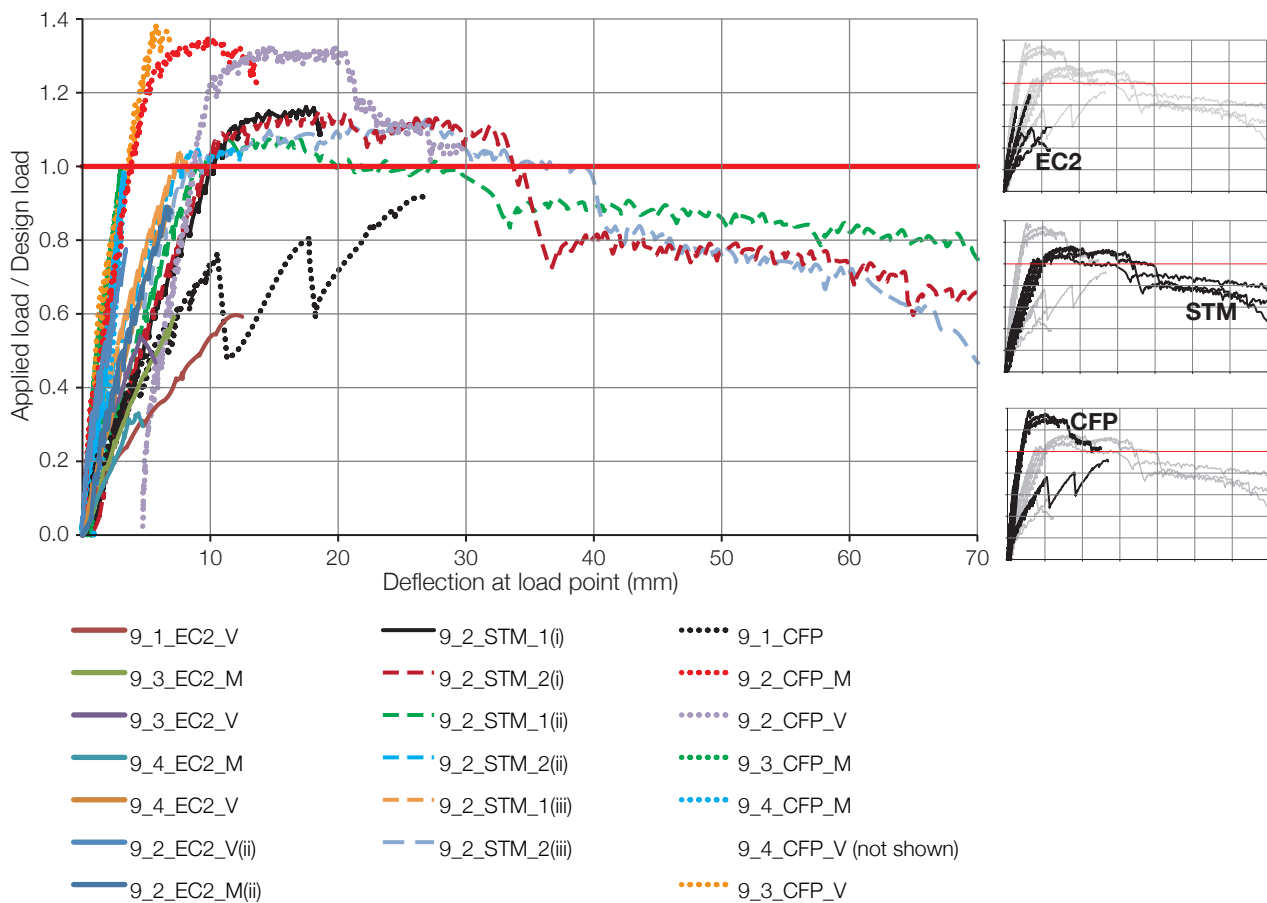


Figure 8.112: Summary of all tests undertaken in §8.3 and §8.4.

## 8.5. Analysis

### 8.5.1. Introduction

The primary method of analysis for each of the beams described in this Chapter will be through the use of digital image correlation. The results and analysis of test series CFP and EC2 (§8.3) are presented first, with STM (§8.4) tests described after. General conclusions pertaining to all of the tests are then made.

As described in §8.3.4.1 on page 262 digital image correlation was employed to monitor the strain distribution in each of the tests undertaken. DIC employs a static camera to take photos of a unique and random pattern, painted on the side of each beam, which is then processed to determine displacement and strain distributions, Figure 8.113.

Initial work was undertaken using ‘GeoPIV<sup>2</sup>’, which uses normalised cross-correlation to calculate changes in a sequence of images. Further details on the working of this programme can be found in Bisby *et al* (2007) and White *et al* (2001a and 2001b). Limitations found in the use of this software led to the programming of a new script for the commercial software ‘DigiFlow’ (Dalziel, 2011) which proved enormously useful for in initial programming work, but was eventually superseded by the use of freeware software ‘MatchID’ (Lava and Debruyne, 2010) supplied by the Catholic University College Ghent.

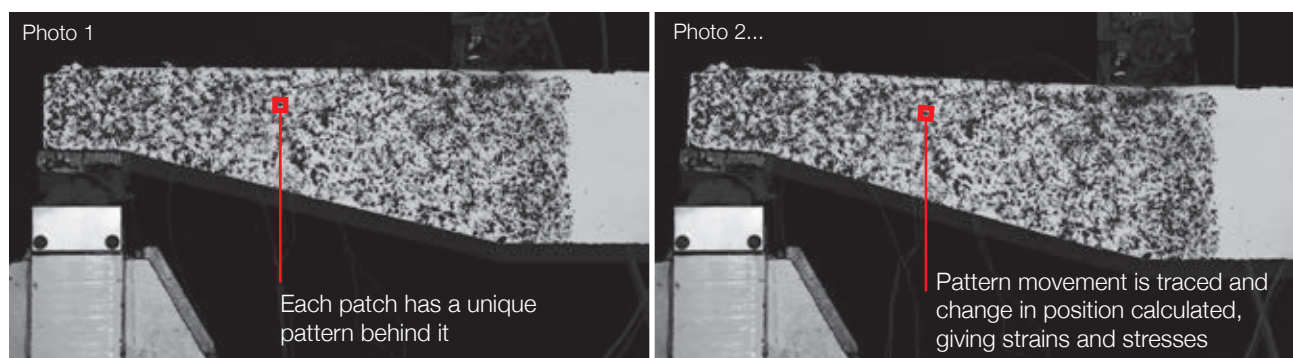


Figure 8.113: Method of analysis using DIC and GeoPIV.

### 8.5.2. Methodology

For each beam test described in §8.3, a series of fourteen-megapixel still images were taken of the tapered end of the beam under loading. The images are correlated to each incremental loading point, which was normally undertaken in 2kN intervals. The images were scaled, converted to black and white and processed as tagged image format files, which were then input to the workspace in MatchID.

For each beam, correlation was undertaken using the approximated normalized sum of squared differences (ASSD) technique. This method, which uses the correlation coefficient (Pan *et al.*, 2009) was chosen over other methods (such as gradient-based or cross correlation techniques) as it provides accurate results with good performance (Lava *et al.*, 2009). The method and derivation of the equations are described in more detail by Pan *et al* (2009) and Pan (2011). A sixteen pixel subset and eight pixel step size were used to provide a good level of accuracy with a reasonable processing time.

<sup>2</sup> Particle Image Velocimetry (PIV) was originally developed for fluids applications and its principles and use are reviewed by Adrian (1991).



Upon completion of the correlation, interpolation between calculated points was carried out using a bicubic interpolation (Debruyne and Lava, 2011). The initial calculations are carried out to determine the displacement field for the beam, from which strains are then calculated using the Levenberg-Marquardt routine (a general numerical solution for fitting a nonlinear function to parameters of the function, described by Debruyne and Lava, 2011). The strain tensor used for the calculations of  $\epsilon_{xx}$ ,  $\epsilon_{yy}$ ,  $\epsilon_{xy}$ ,  $\epsilon_1$  and  $\epsilon_2$  described in the following was a logarithmic Euler-Almansi strain tensor (a full description of this can be found in Hjelmstad, 2005). Interpolation was carried out using a bilinear quadrilateral method (Debruyne and Lava, 2011).

The calculated  $\epsilon_{xy}$  strains were not used in the following analysis as they add little to, and can confuse, the analysis of a concrete beam. The analysis of a typical beam described above was completed in under an hour, which compares favourably to the seven hours required using the scripts originally written for *DigiFlow*. To ensure that the results were correctly assessed, the displacements recorded during testing were compared to those interpolated from the DIC data. A comparison for two beams is shown in Figure 8.114.

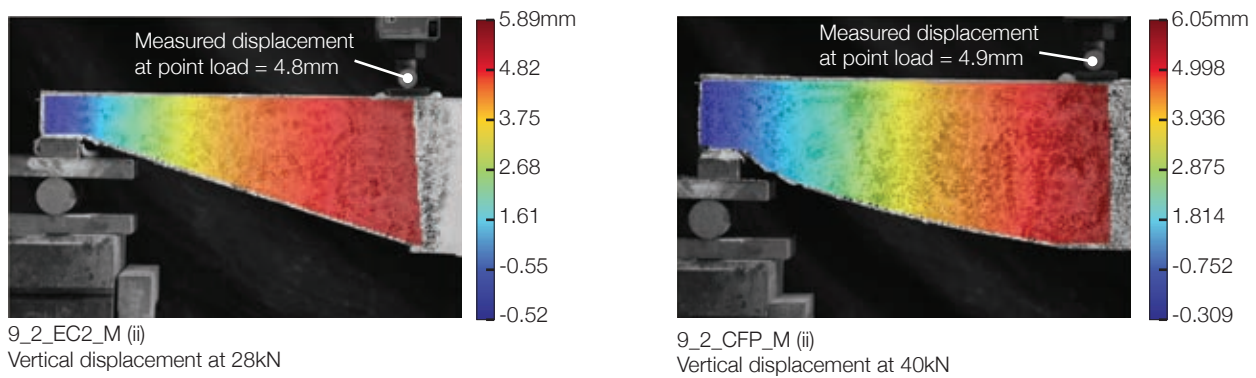


Figure 8.114: Displacement comparison - measured and interpolated results.

As data is collected throughout the loading cycle, plots of the full behaviour of each beam can be made (as shown in Figure 8.115 for strain  $\epsilon_1$  in Beam 9\_2\_CFP\_M(ii)). The results of the full strain analysis are presented in the following section, before a discussion of their pertinent results is given in §8.5.5 on page 319.

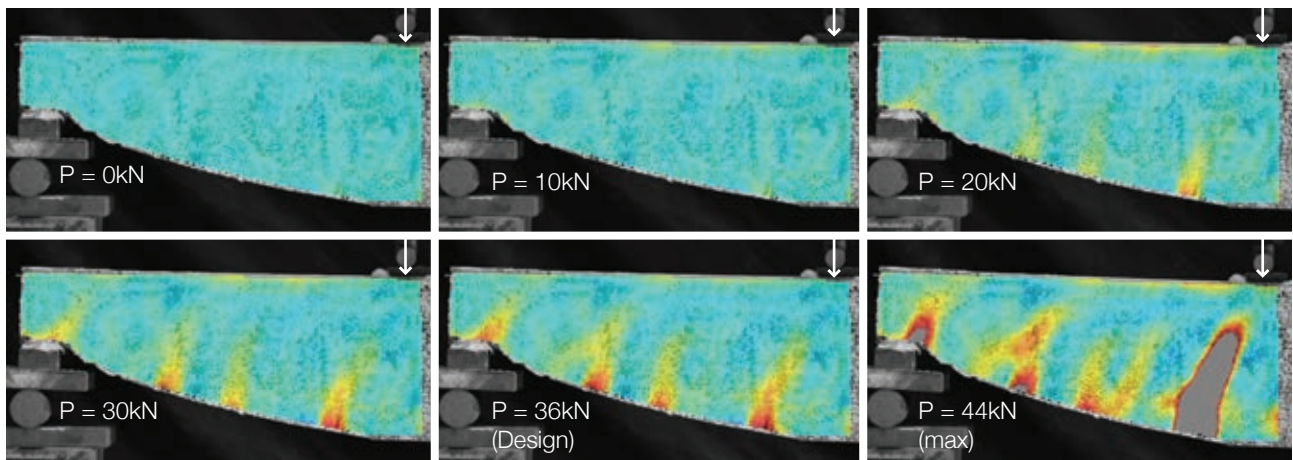


Figure 8.115: Changes in principal strain  $\epsilon_1$  for Beam 9\_2\_CFP\_M(ii) over the loading cycle.

### 8.5.3. EC2 and CFP Beam Results

In the following section results for the 'EC2' and 'CFP' beam test series are presented. For the beams listed in Table 8.13, the strains at the design load (where it was achieved) and at peak load are presented separately. The results are grouped according to the design method. The colour scale representing the strain value is kept constant throughout, as shown in Figure 8.116 (where the approximate cracking strain of concrete is highlighted as a reference point). Deflection plots, which were also calculated as part of the DIC analysis method are not shown as this data can be seen in the load-deflection graphs provided in previous sections.

Beam 9\_3\_EC2 was subject to DIC data collection, but an error in the camera set up rendered the images collected for Beam 9\_3\_EC2\_V impossible to analyse, and this was not realised until after the tests had been completed. In Beams 9\_4\_EC2, 9\_1\_EC2 and 9\_1\_CFP, DIC data was not collected.

Images for Beam 9\_2\_CFP\_V(ii) were found to be difficult to analyse, and hence there are some areas of missing data in these results that are particularly noticeable in the  $\epsilon_2$  results. In general, however, the patterns are in line with those seen for 9\_2\_CFP\_M(ii) and are hence included in Figure 8.123 and Figure 8.124.

Table 8.13: DIC data summary.

EC2 Test Series	DIC	CFP Test Series	DIC
9_1_EC2_V	No - data not collected	9_1_CFP	No - data not collected
9_2_EC2_V(i)	Yes (Peak Load)	9_2_CFP_V(i)	Yes, but results omitted in preference to (ii)
9_2_EC2_M(i)	Yes (Peak Load)	9_2_CFP_M(i)	Yes, but results omitted in preference to (ii)
9_2_EC2_V(ii)	Yes (Peak Load)	9_2_CFP_V(ii)	Yes (Design Load and Peak Load)
9_2_EC2_M(ii)	Yes (Peak Load)	9_2_CFP_M(ii)	Yes (Design Load and Peak Load)
9_3_EC2_V	No - flawed data collection	9_3_CFP_V	Yes (Design Load and Peak Load)
9_3_EC2_M	Yes (Peak Load)	9_3_CFP_M	Yes (Design Load and Peak Load)
9_4_EC2_V	No - data not collected	9_4_CFP_V	Yes (Design Load and Peak Load)
9_4_EC2_M	No - data not collected	9_4_CFP_M	Yes (Design Load and Peak Load)

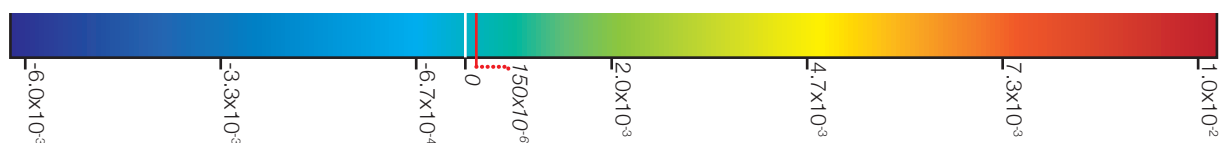


Figure 8.116: Scale bar for all DIC results.

Results are provided for  $\epsilon_{xx}$ ,  $\epsilon_{yy}$ ,  $\epsilon_1$ , and  $\epsilon_2$  for completeness. The differences (which can be inferred from the intensities of the colour plots) between the principal strains and the 'x' and 'y' strains helps to illustrate how the Mohr's circle is rotated. It is recognised that in the concrete section cracking will occur according to the largest tensile principal strain.

In addition to the presentation of strain plots, analysis was undertaken to provide strain direction information at the design and/or peak loads for each beam (as relevant), and this information is provided in §8.5.3.3 on page 312.

8.5.3.1. Beam Series ‘EC2’ results

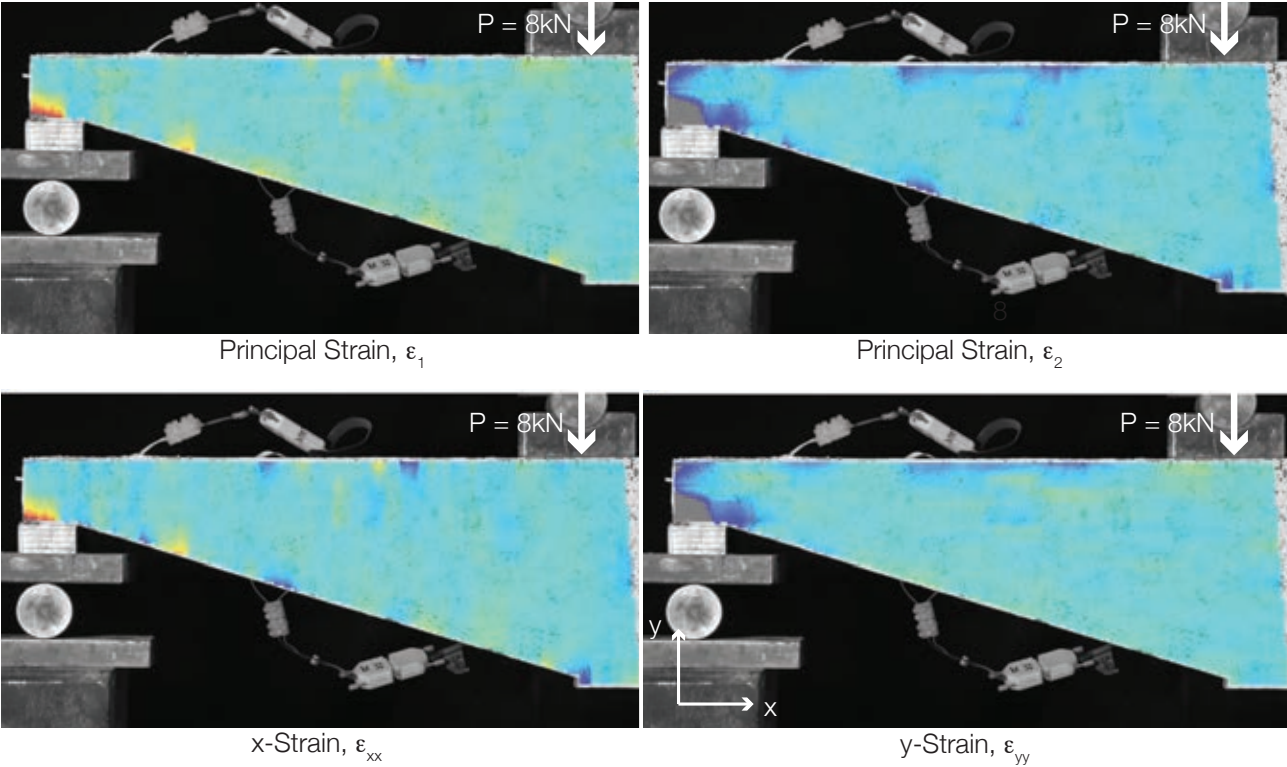


Figure 8.117: Beam 9\_2\_EC2\_V(i) at its peak load (§8.3.6.2).

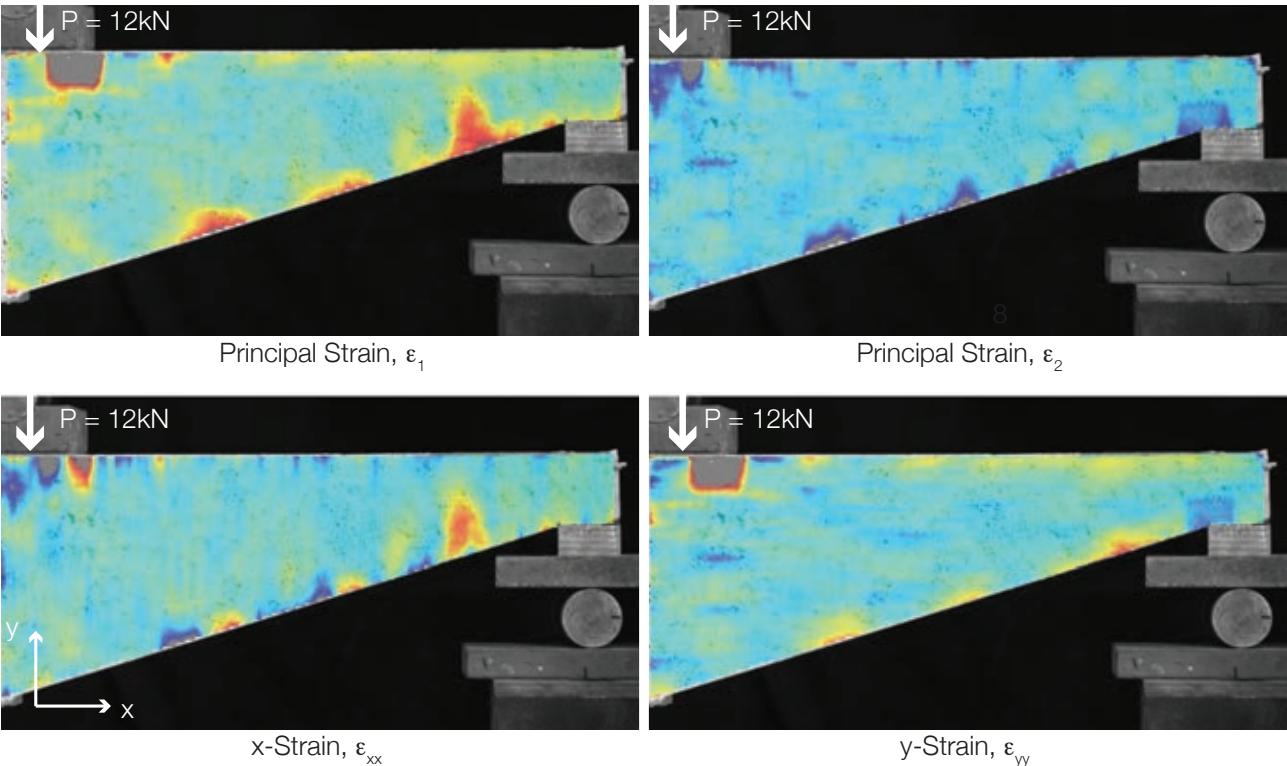
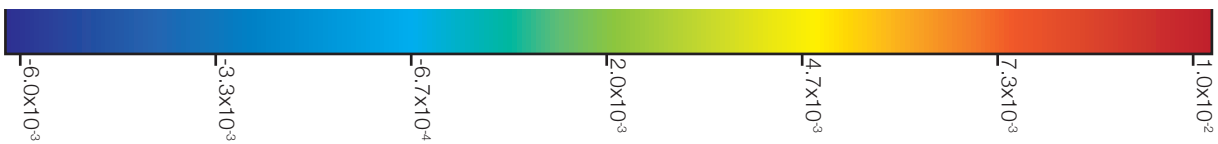


Figure 8.118: Beam 9\_2\_EC2\_M(i) at it peak load (§8.3.6.1).





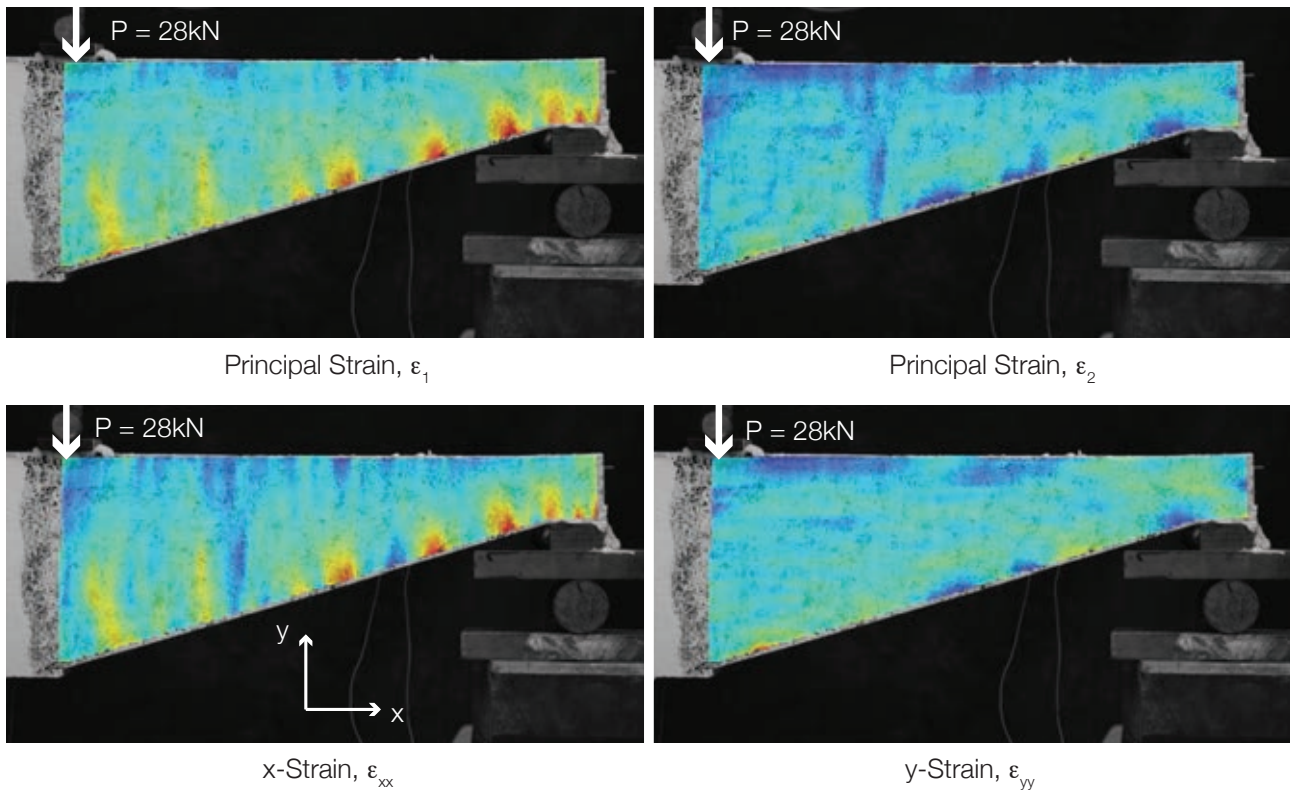


Figure 8.119: Beam 9\_2\_EC2\_V(ii) at its peak load (§8.3.7.1).

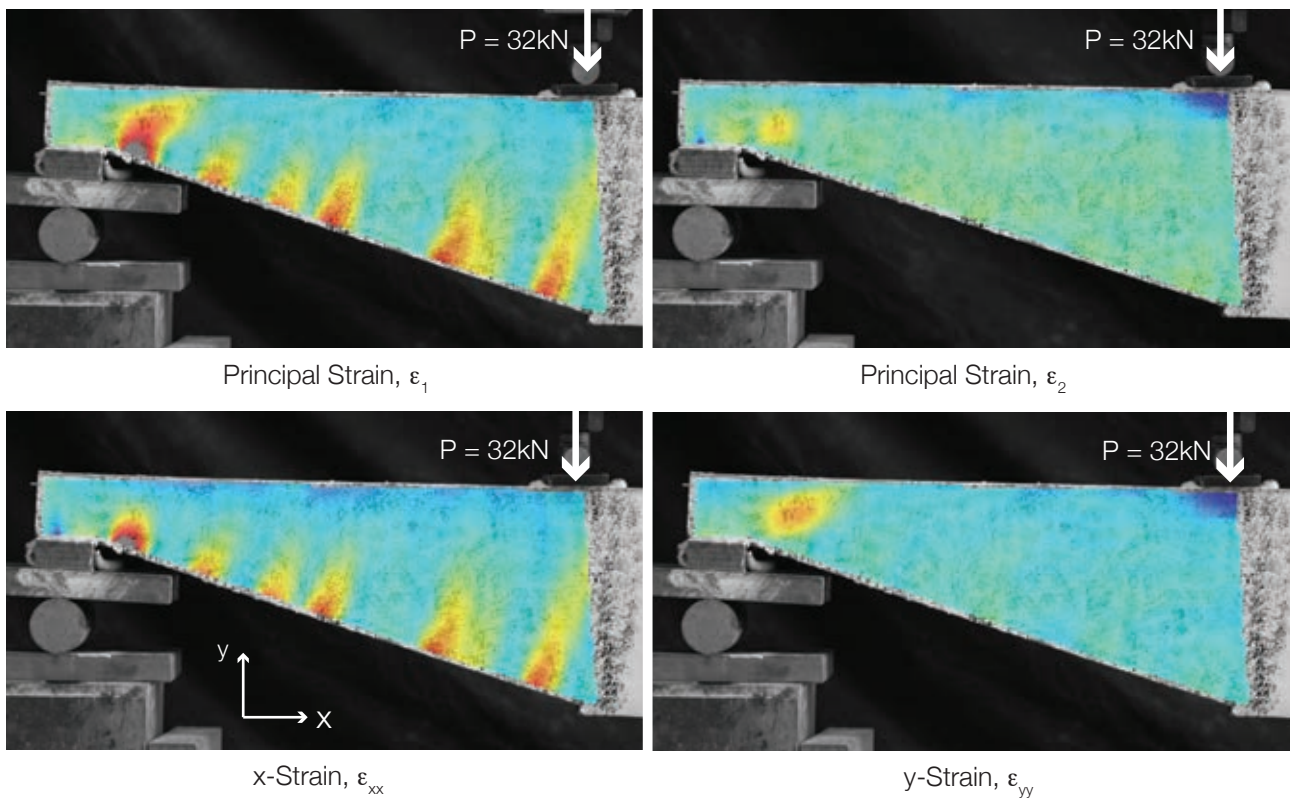
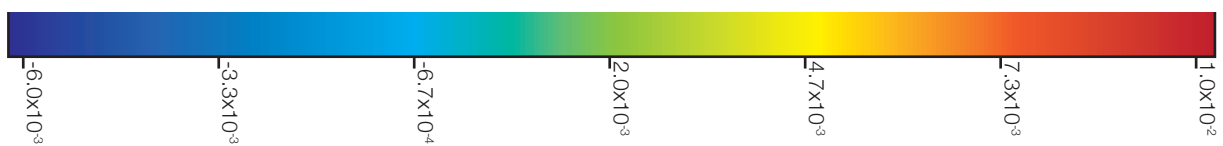


Figure 8.120: Beam 9\_2\_EC2\_M(ii) at its peak load (§8.3.7.2).



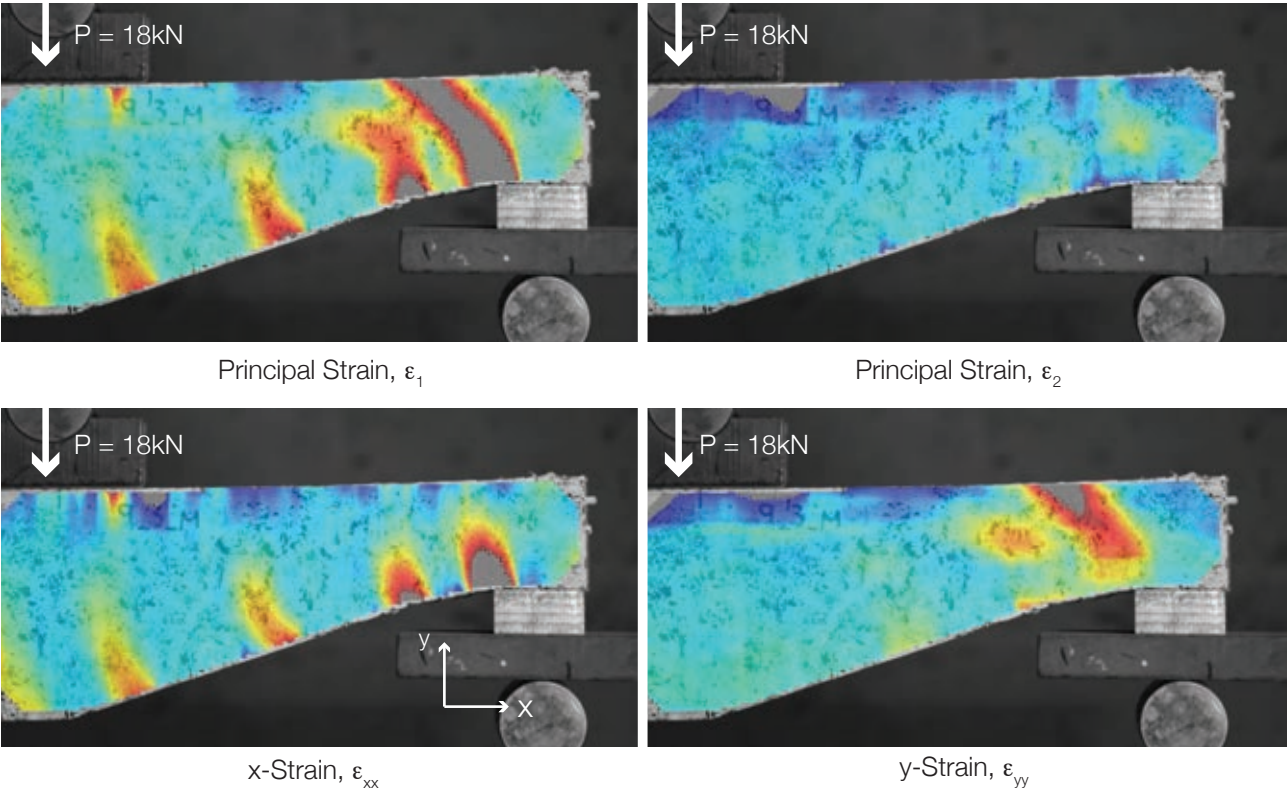


Figure 8.121: Beam 9\_3\_EC2\_M at its peak load (§8.3.8.1).

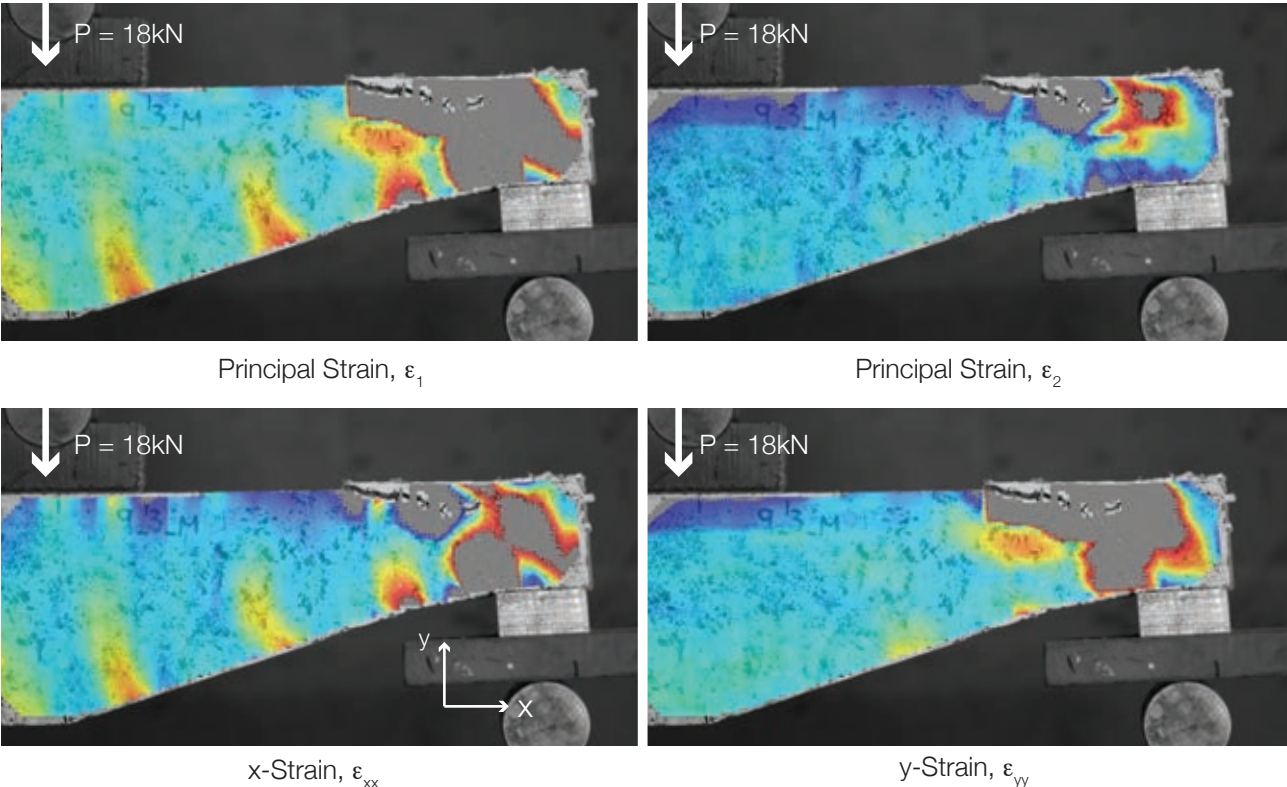
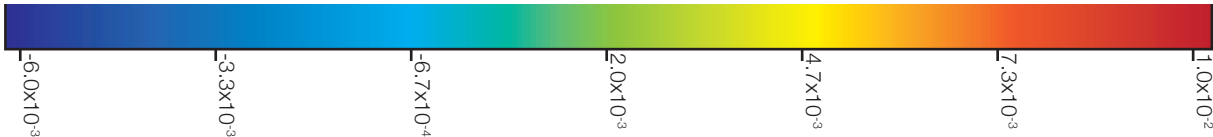


Figure 8.122: Beam 9\_3\_EC2\_M just beyond peak load (18kN, but showing shear failure mode).





## 8.5.3.2. Beam Series 'CFP' results

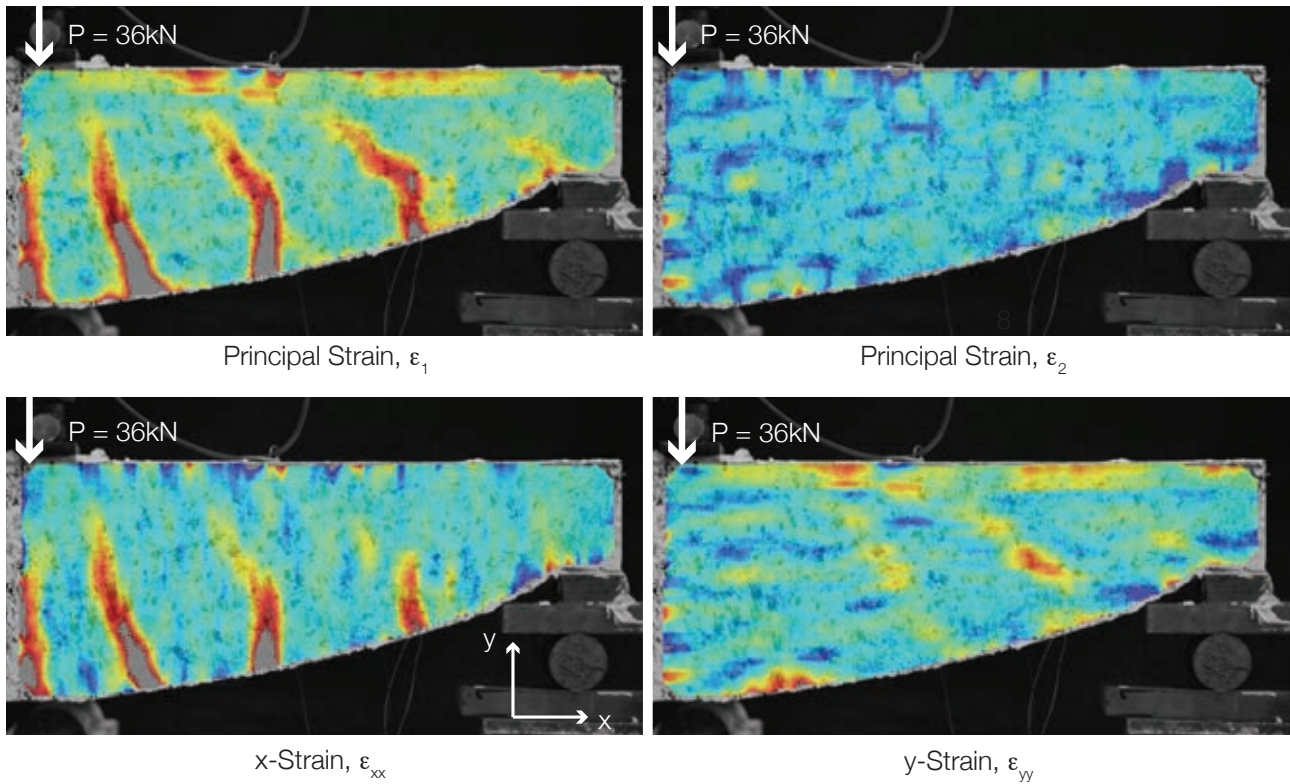


Figure 8.123: Beam 9\_2\_CFP\_V(ii) at the design load (§8.3.7.4).

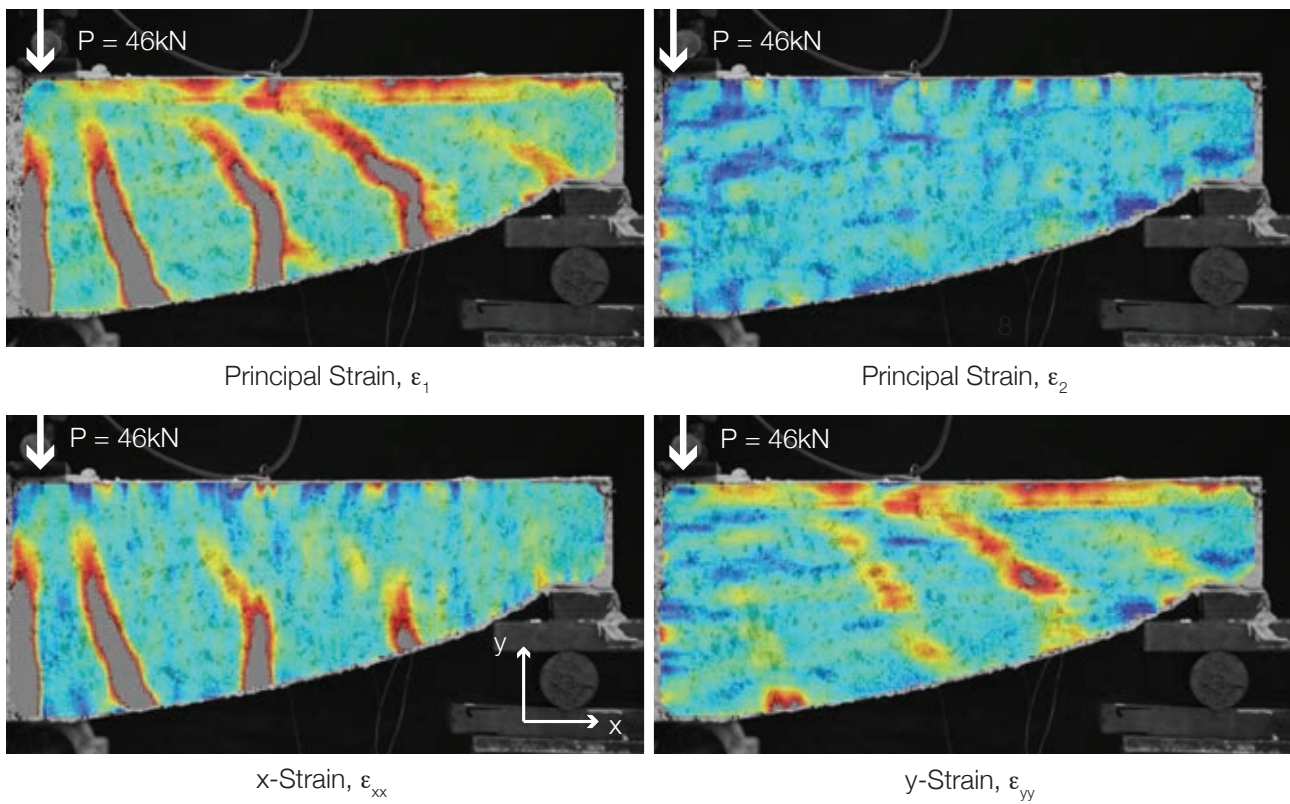
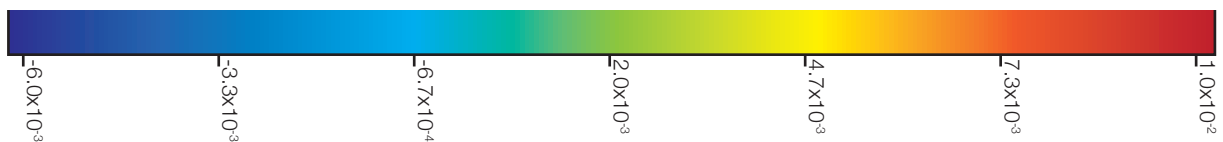


Figure 8.124: Beam 9\_2\_CFP\_V(ii), at failure (§8.3.7.4).





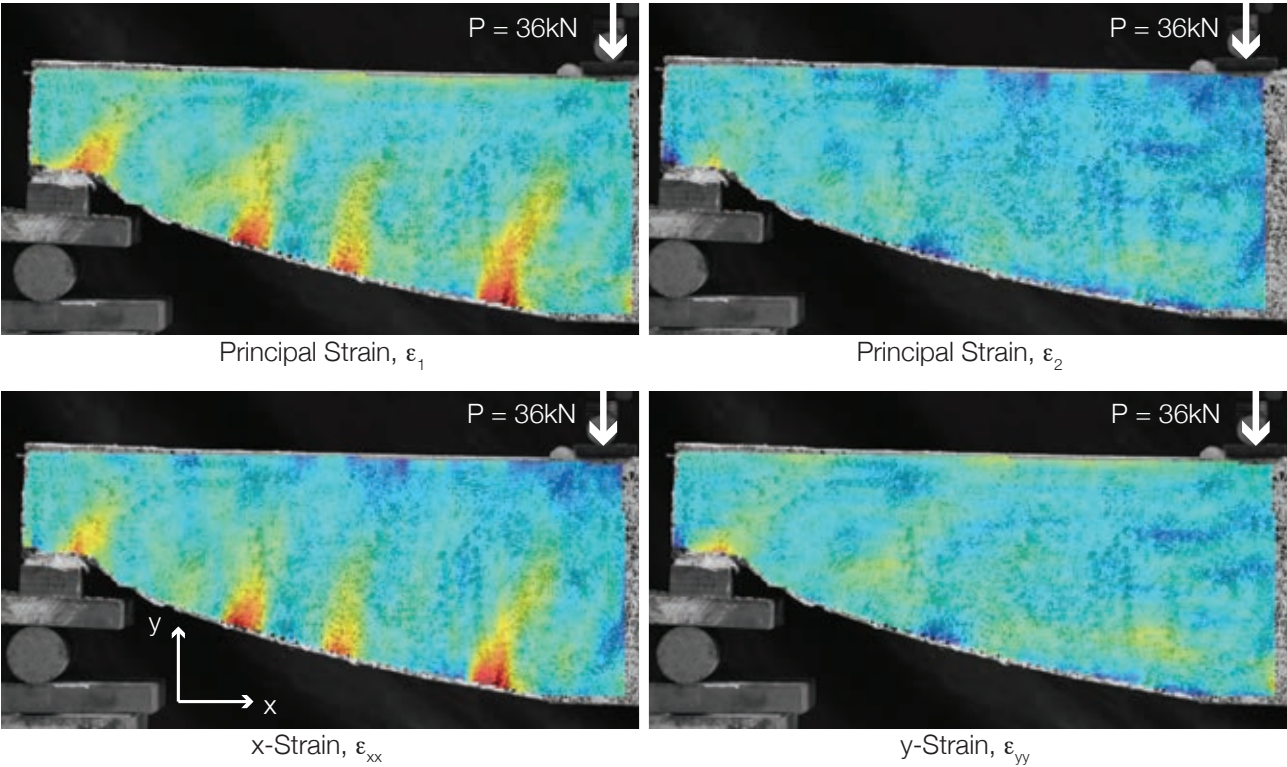


Figure 8.125: Beam 9\_2\_CFP\_M(ii) at the design load (§8.3.7.3).

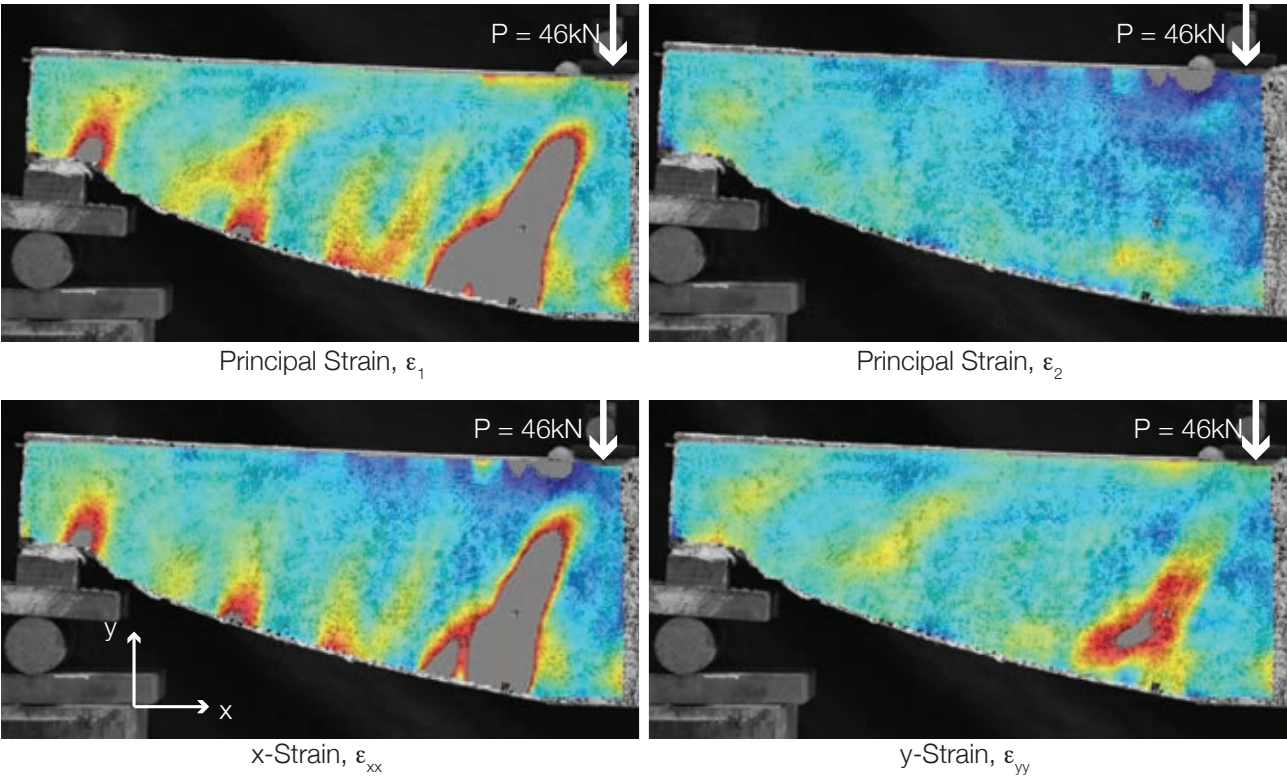
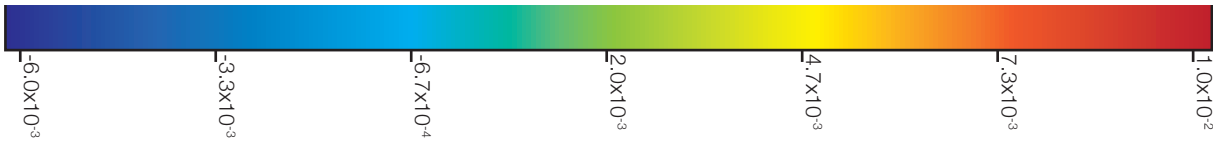


Figure 8.126: Beam 9\_2\_CFP\_M(ii), at failure (§8.3.7.3).





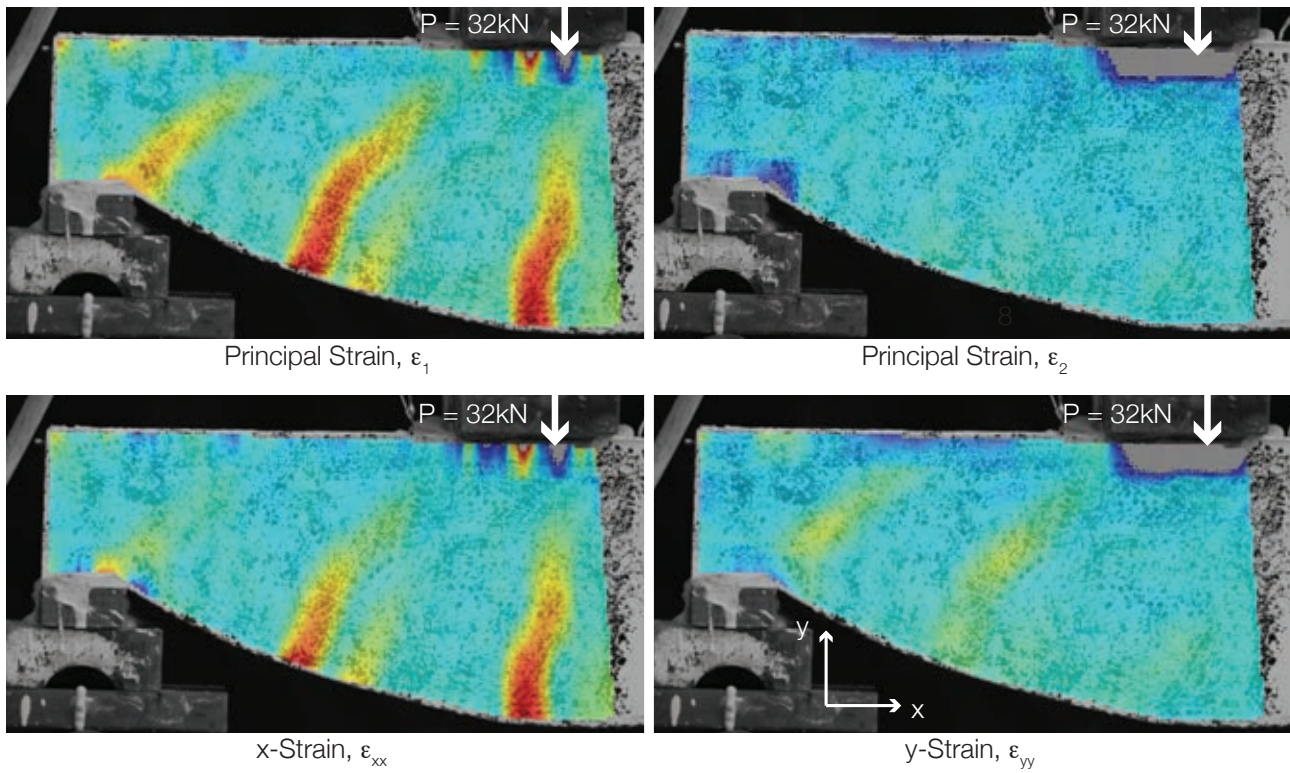


Figure 8.127: Beam 9\_3\_CFP\_V at the design load (32kN) (§8.3.8.4).

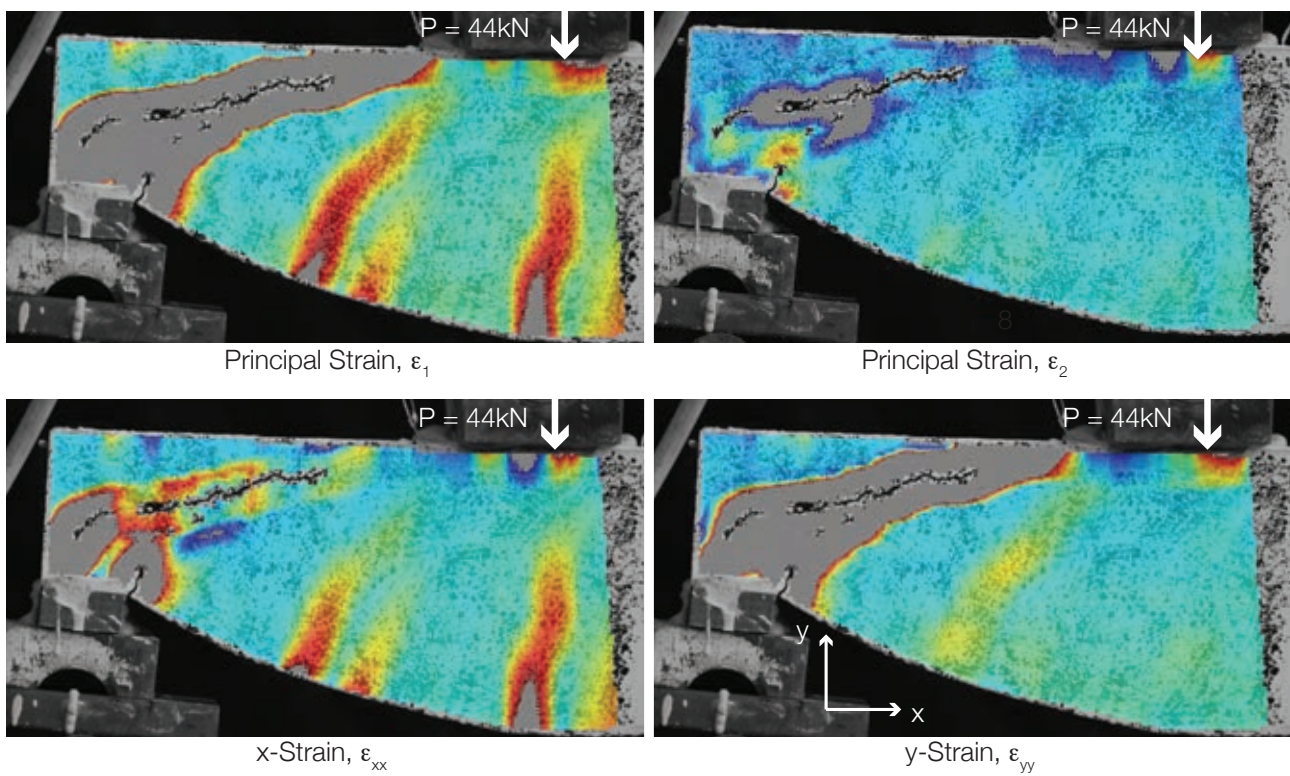
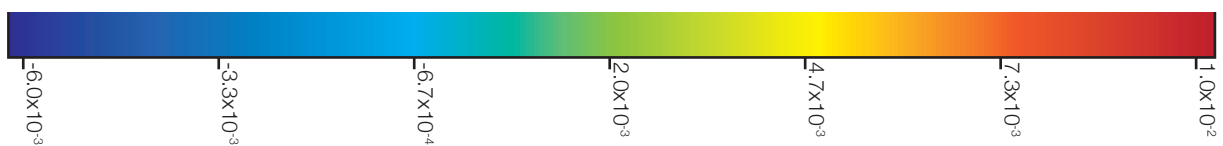


Figure 8.128: Beam 9\_3\_CFP\_V, at its failure load (44kN) (§8.3.8.4).





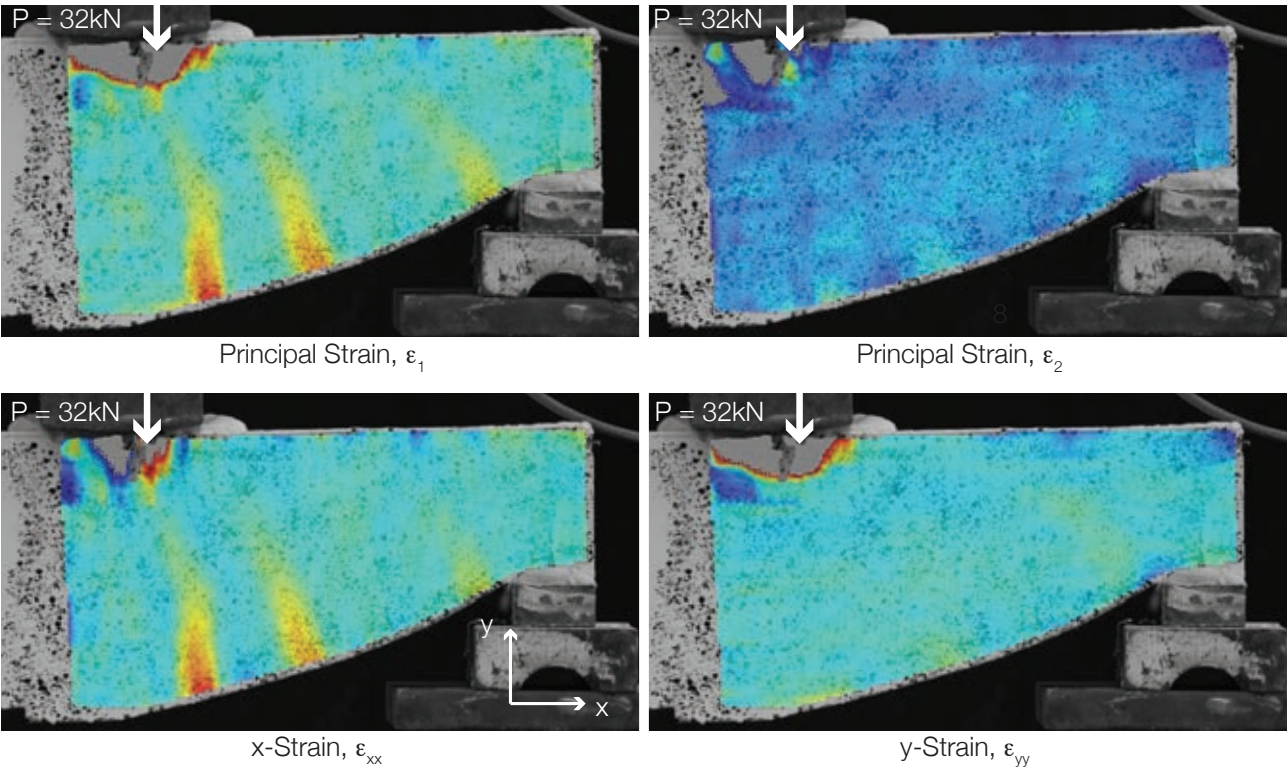


Figure 8.129: Beam 9\_3\_CFP\_M at its design load (32kN) (§8.3.8.3).

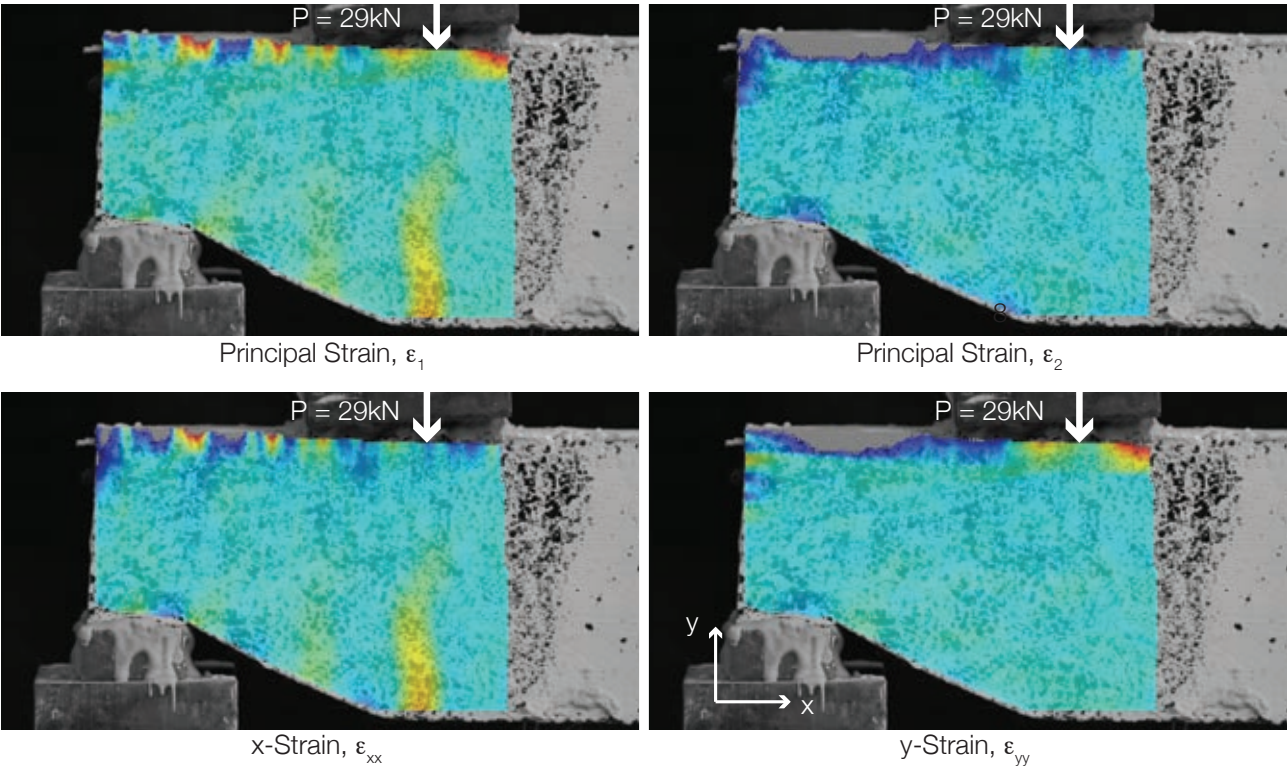
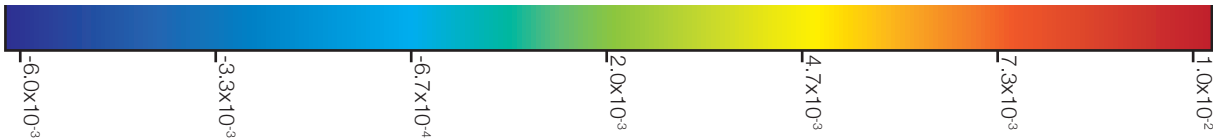


Figure 8.130: Beam 9\_4\_CFP\_V at its design load (29kN) (§8.3.9.3).



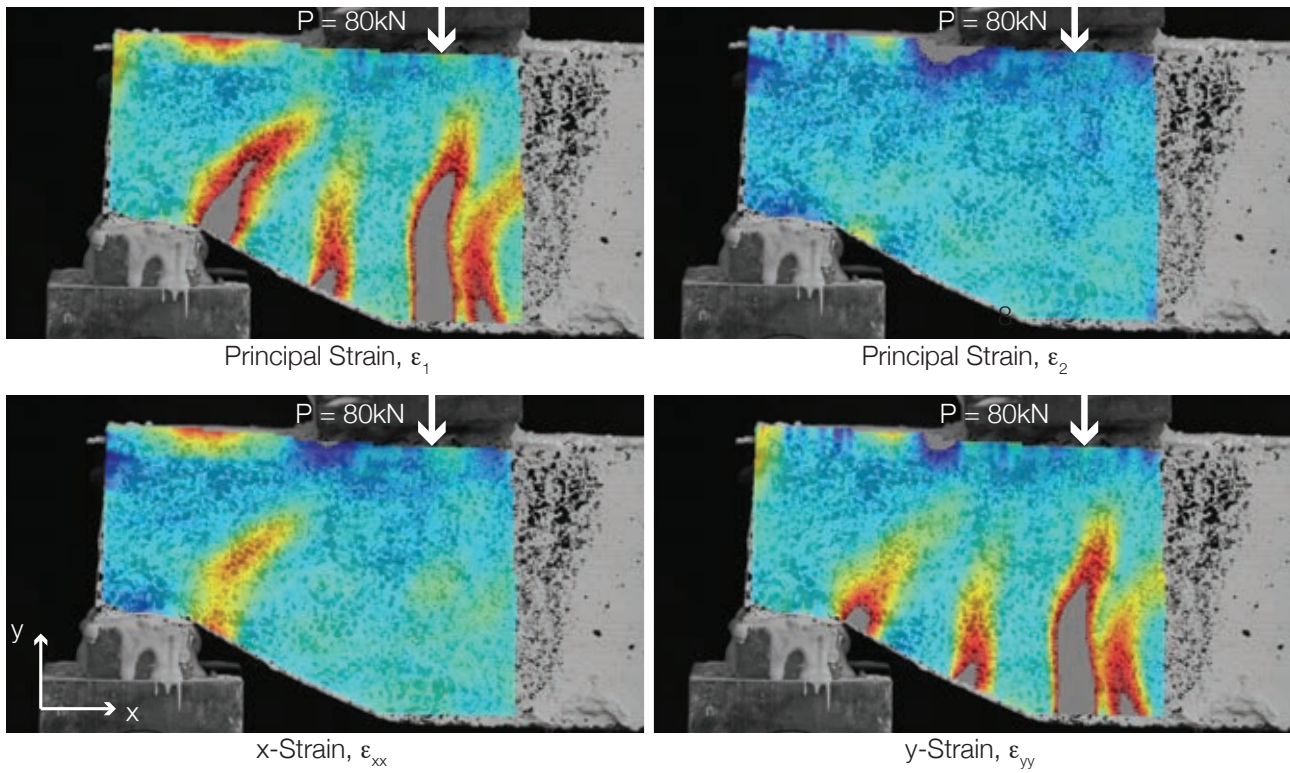


Figure 8.131: Beam 9\_4\_CFP\_V at its peak load (80kN) (§8.3.9.3).

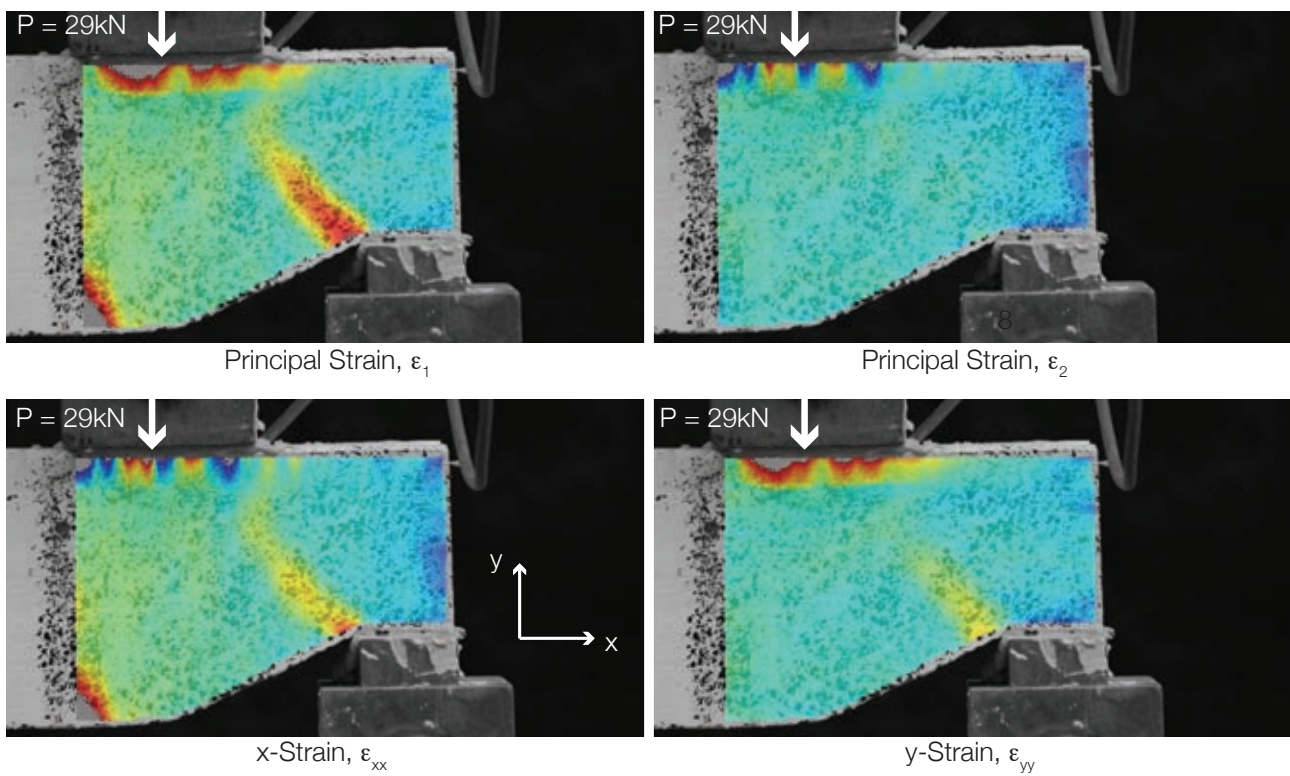
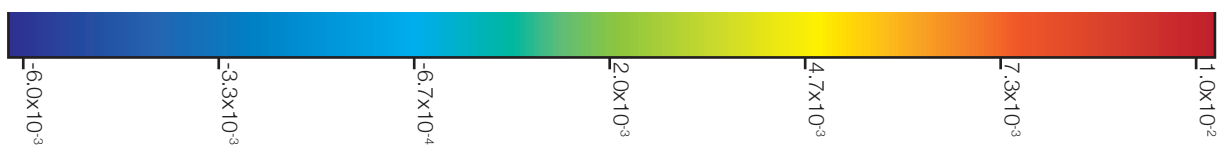


Figure 8.132: Beam 9\_4\_CFP\_M at its design load (29kN) (§8.3.9.4).





## 8.5.3.3. Strain direction plots for EC2 and CFP beams

The collected data and processing technique allowed the calculation of both major and minor strain directions. This is shown in Figure 8.133 and Figure 8.134 for Beam 9\_2\_CFP\_M(ii), and in Figure 8.136 and Figure 8.137 for Beam 9\_2\_EC2\_M(ii), before comparisons between the two are made. The analysis is shown across the loading cycle, where the rotation of the concrete strain direction at higher loads can be seen.

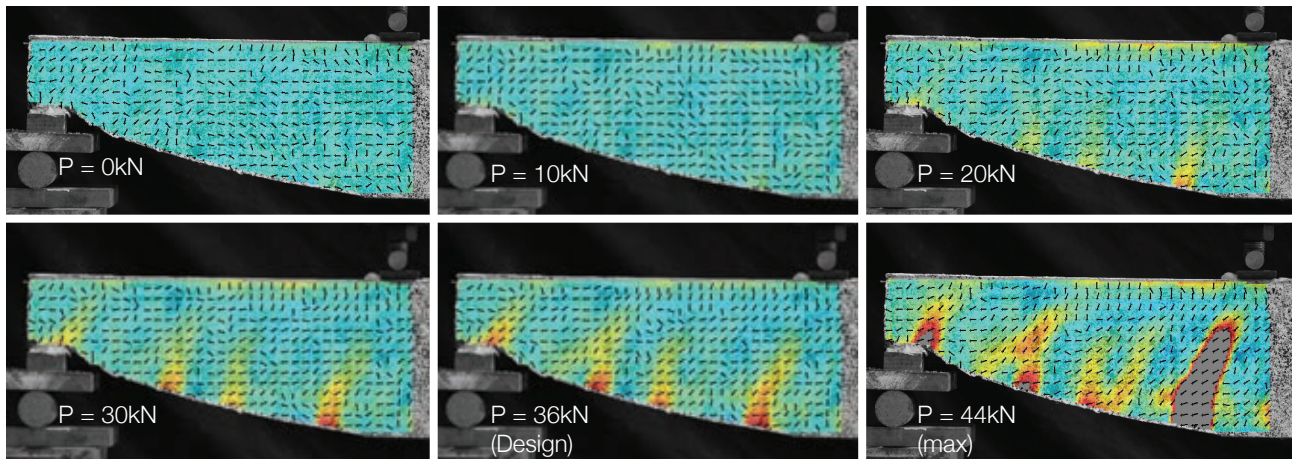


Figure 8.133: Beam 9\_2\_CFP\_M(ii) major strain direction over loading cycle. Principal strain  $\epsilon_1$  in background.

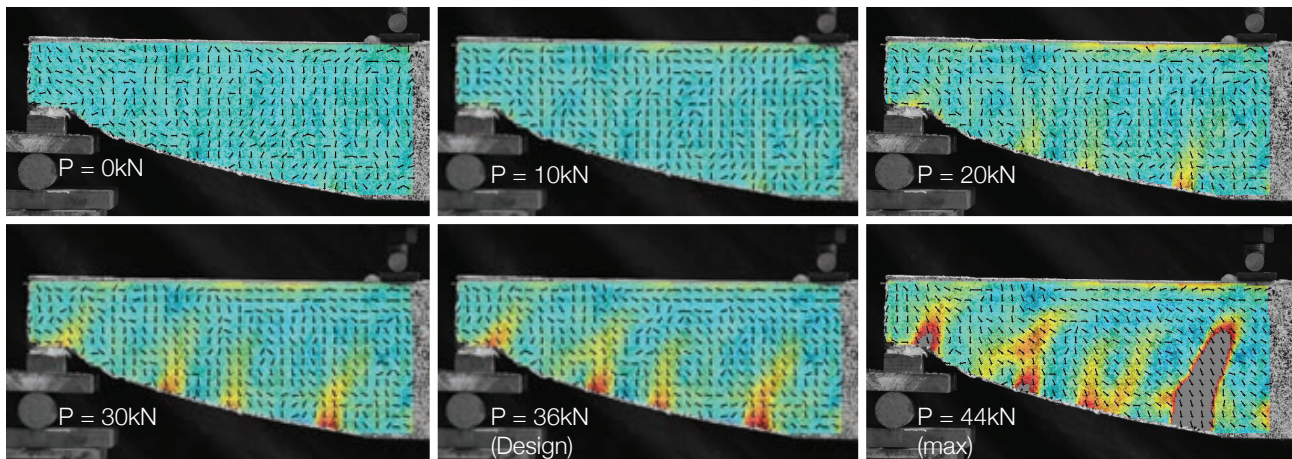


Figure 8.134: Beam 9\_2\_CFP\_M(ii) minor strain direction over loading cycle. Principal strain  $\epsilon_1$  in background.

To illustrate these changes, a close up of one area on Beam 9\_2\_CFP\_M(ii) is shown in Figure 8.135, where the change in both principal directions is shown. The ‘imaginary’ struts that are considered to form in concrete structures during loading can now be envisaged.

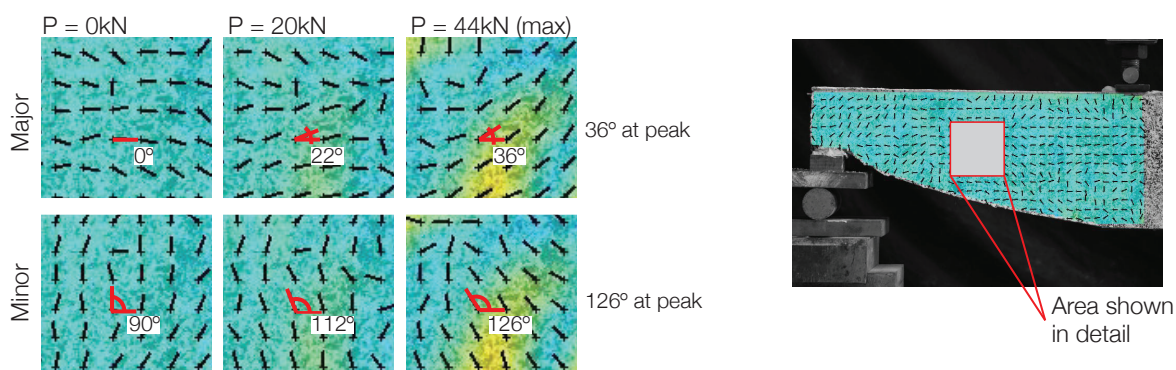


Figure 8.135: Change in strain direction, detail for Beam 9\_2\_CFP\_M(ii).



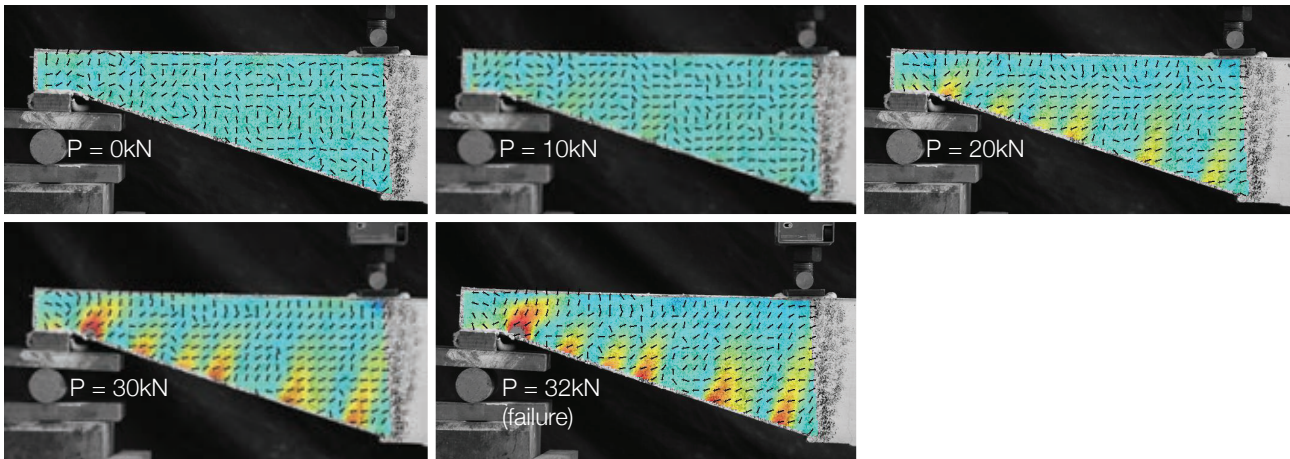


Figure 8.136: Beam 9\_2\_EC2\_M(ii) major strain direction over loading cycle. Principal strain  $\epsilon_1$  in background.

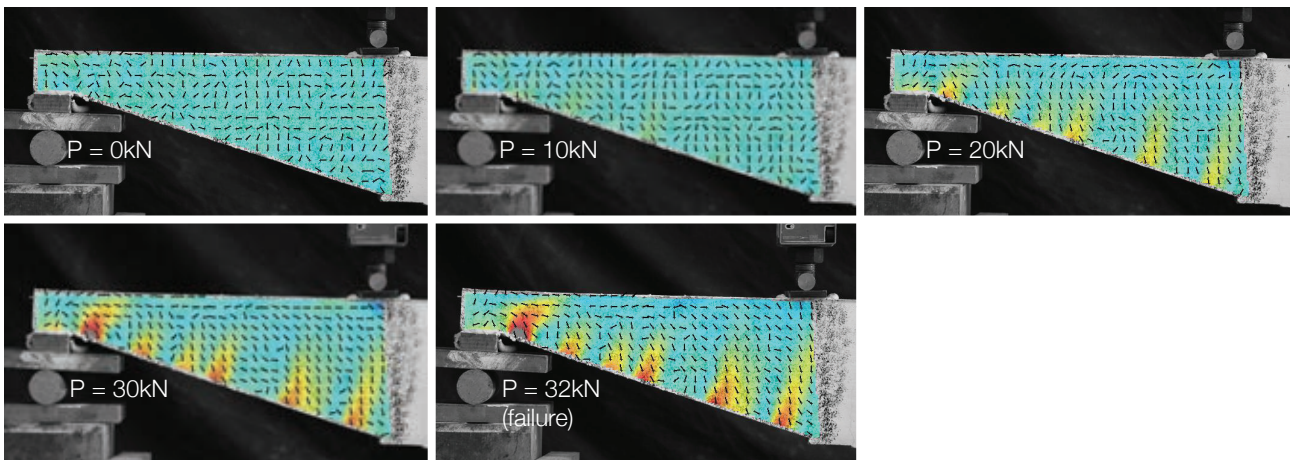


Figure 8.137: Beam 9\_2\_EC2\_M(ii) minor strain direction over loading cycle. Principal strain  $\epsilon_1$  in background.

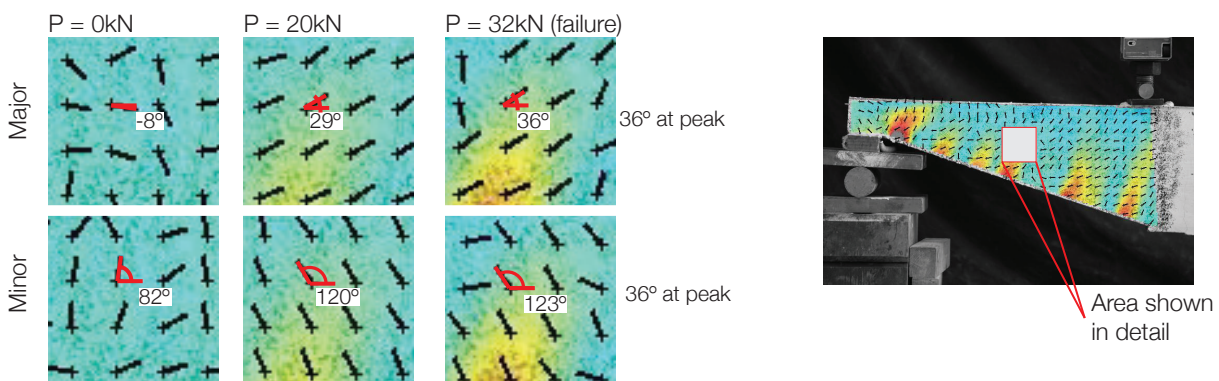


Figure 8.138: Change in strain direction, detail for Beam 9\_2\_EC2\_M(ii).

The strain direction plots provide a useful method to show how the element carries the load applied to it and how the direction of the imaginary struts rotates with increasing load, as shown in Figure 8.135 for Beam 9\_2\_CFP\_M(ii). A close up of the results for Beam 9\_2\_EC2\_M(ii) is given in Figure 8.138. The two beams show much the same behaviour in the locations chosen for analysis (web sections approximately half way along the shear span, in the location of an inclined concrete strut). This suggests that the behaviour of the concrete as a ‘truss’ may be taken as an accurate description of its behaviour at peak loads, where the inclined struts can be seen in both Figure 8.133 and Figure 8.136 (both showing the major strain direction over the loading cycle).



## 8.5.4. STM Model DIC Results

DIC data was also collected for the beams designed using the proposed strut and tie model (STM), described in §8.4, as outlined in §8.4.4. The results for each beam are presented at the design load (36kN), and if relevant at the failure load of the beam. The results have been scaled to match the results presented in §8.5.3 for ease of comparison.

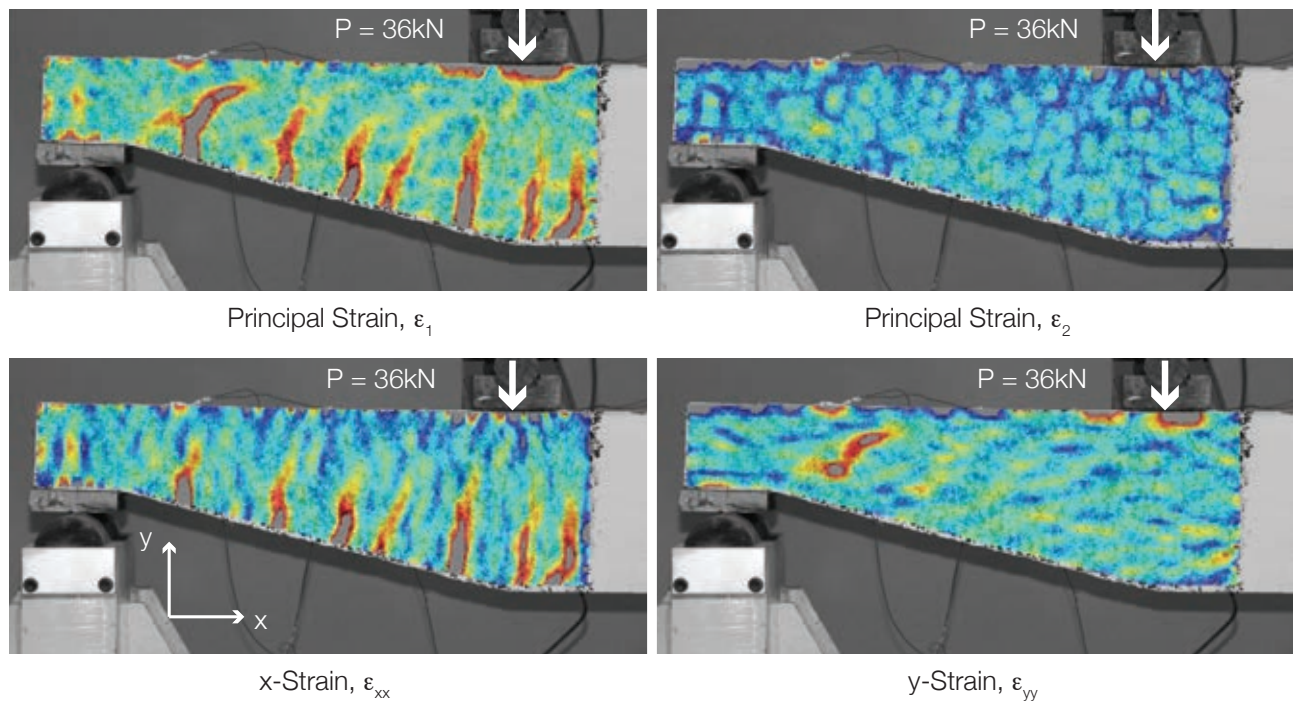


Figure 8.139: Beam 9\_2\_STM\_1(i), Design Load 36kN (§8.4.5.1).

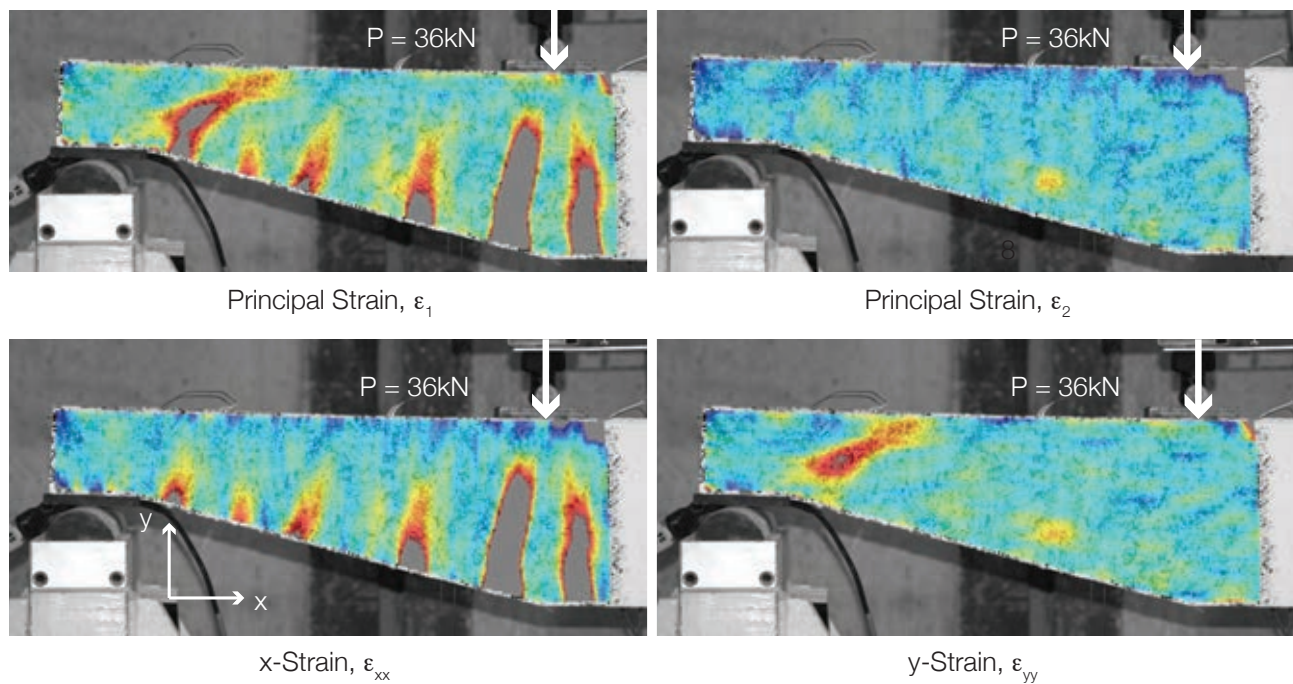
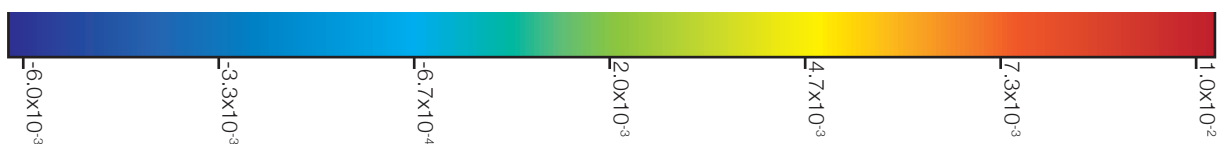


Figure 8.140: Beam 9\_2\_STM\_1(ii), Design Load 36kN (§8.4.6.1).



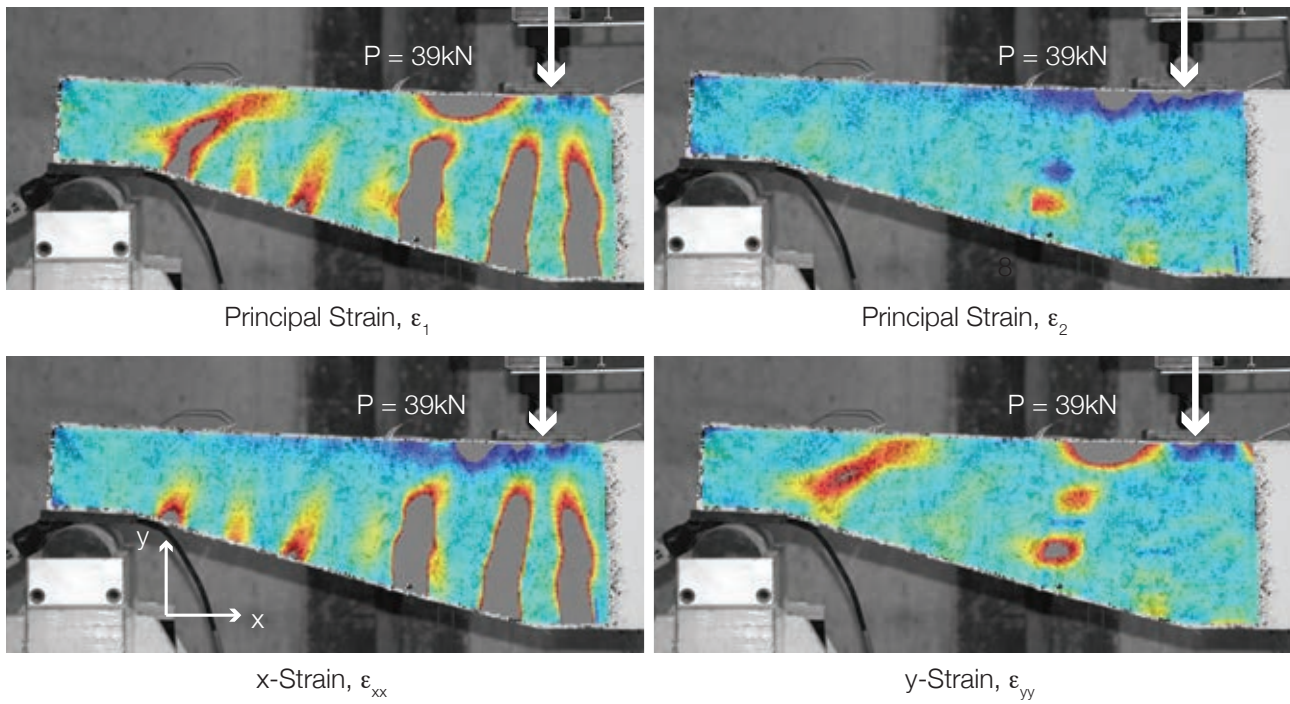


Figure 8.141: Beam 9\_2\_STM\_1(ii), Peak Load (39kN) (§8.4.6.1).

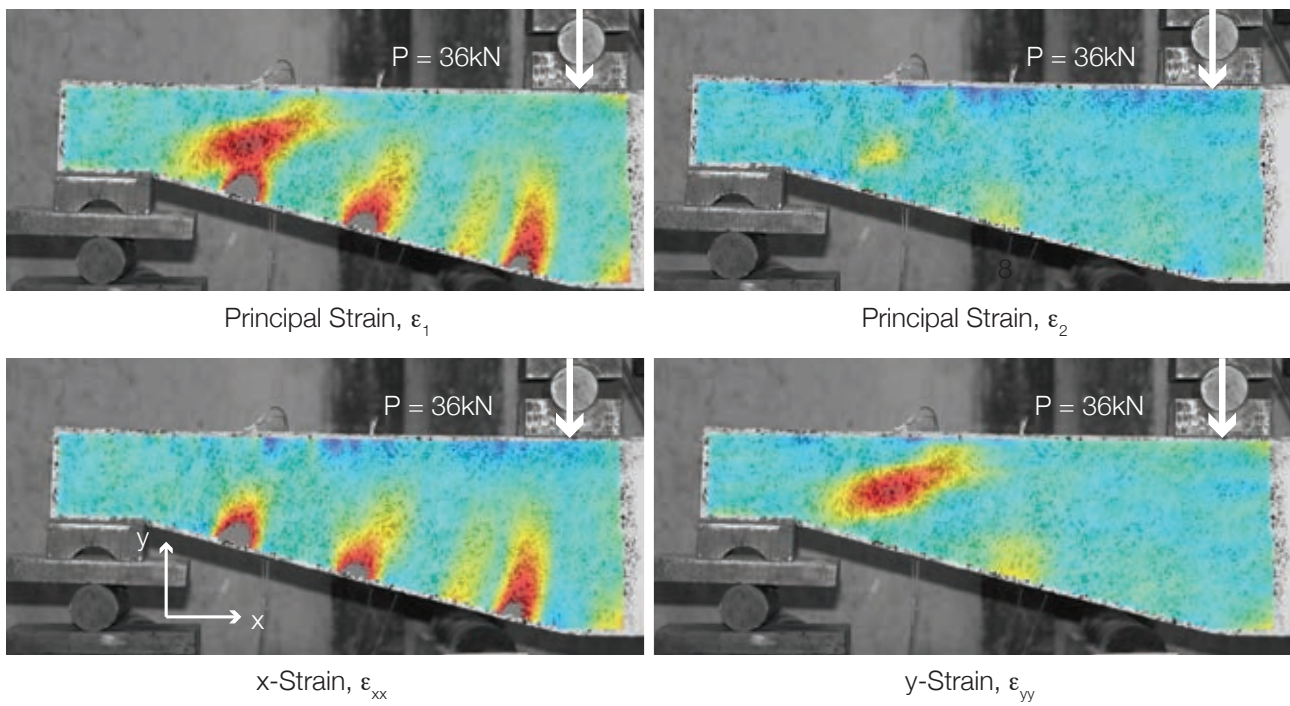
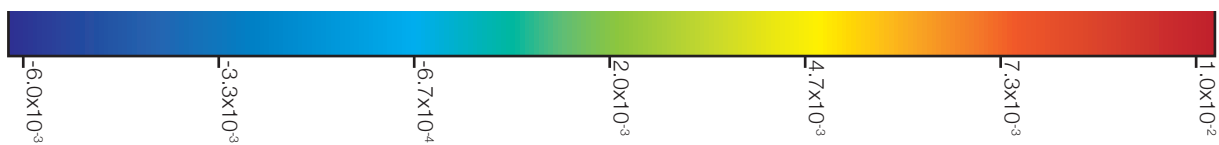


Figure 8.142: Beam 9\_2\_STM\_1(iii), Design Load 36kN (§8.4.7.1).





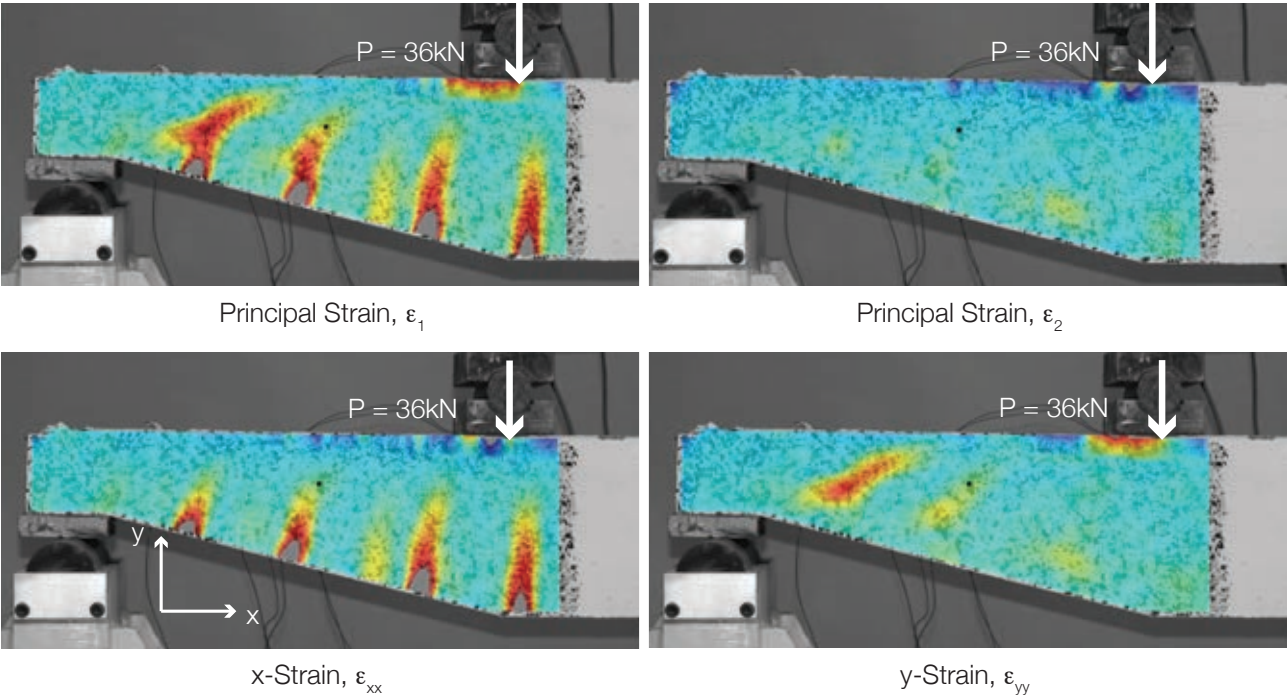


Figure 8.143: Beam 9\_2\_STM\_2(i), Design Load 36kN (§8.4.5.2).

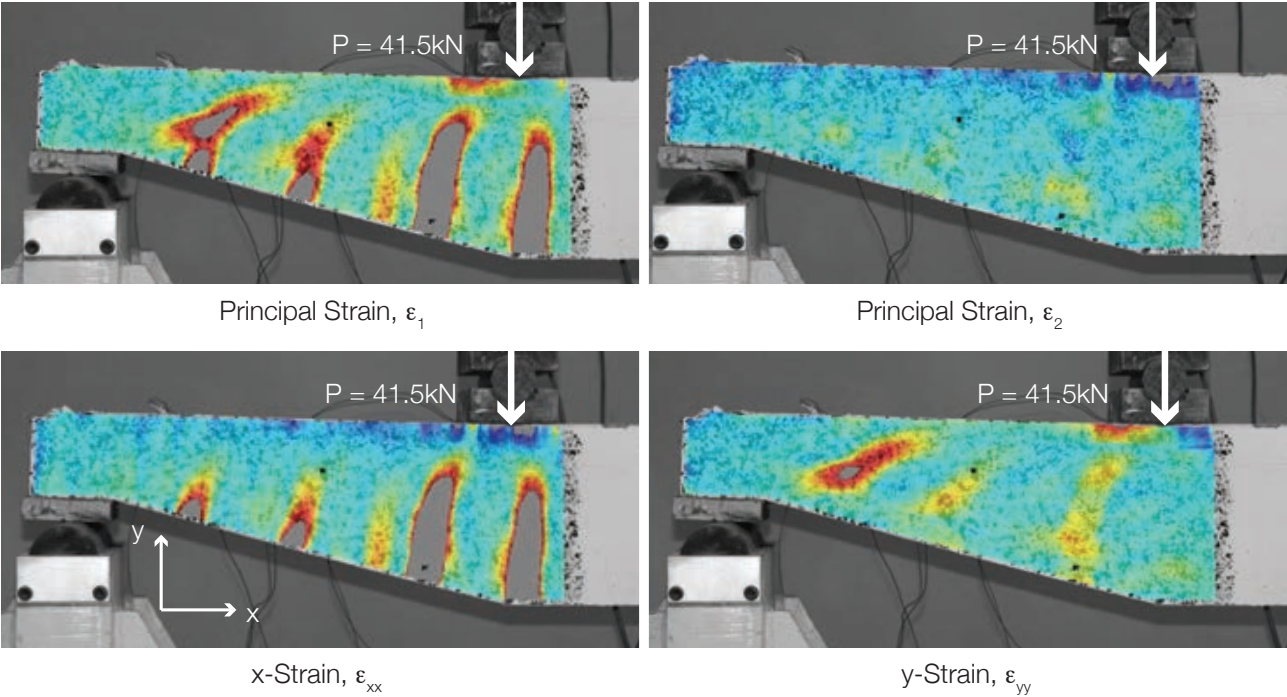
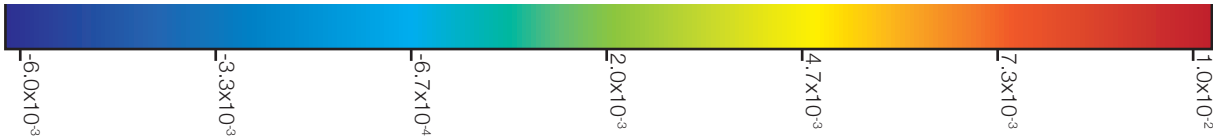


Figure 8.144: Beam 9\_2\_STM\_2(i), Peak Load 41.5kN (§8.4.5.2).



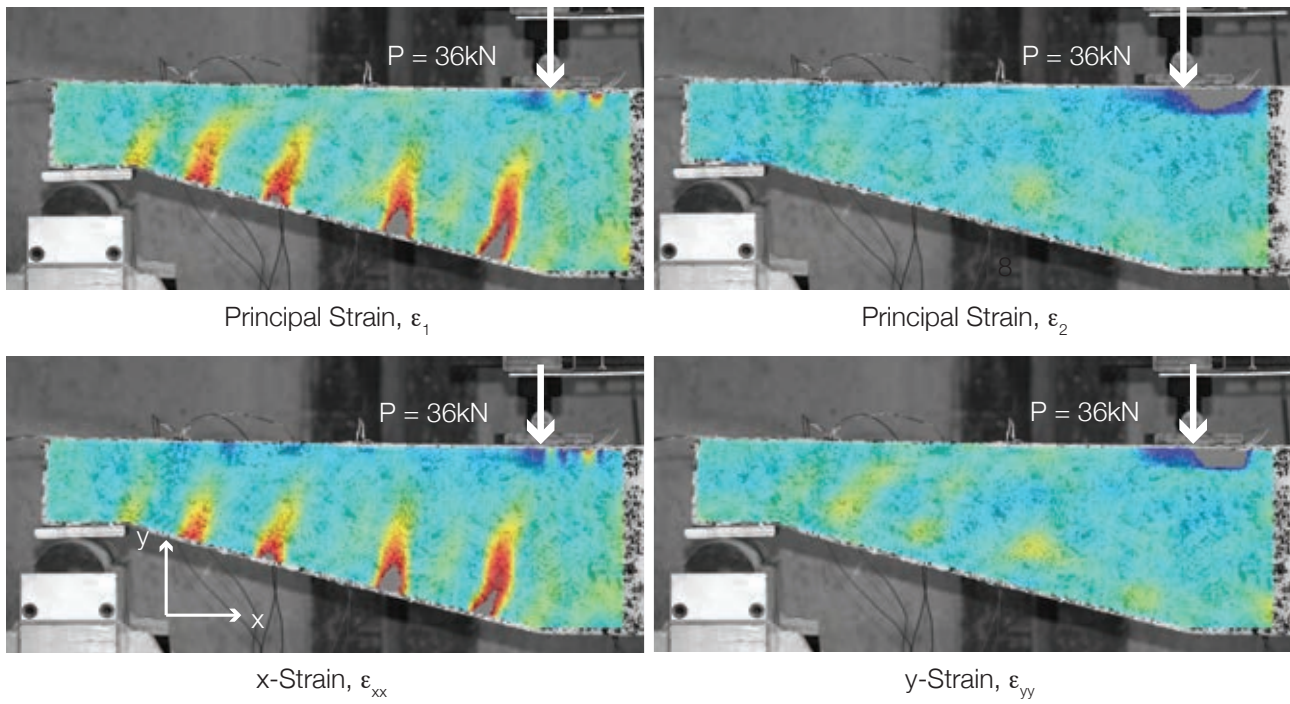


Figure 8.145: Beam 9\_2\_STM\_2(ii), Design Load 36kN (§8.4.6.2).

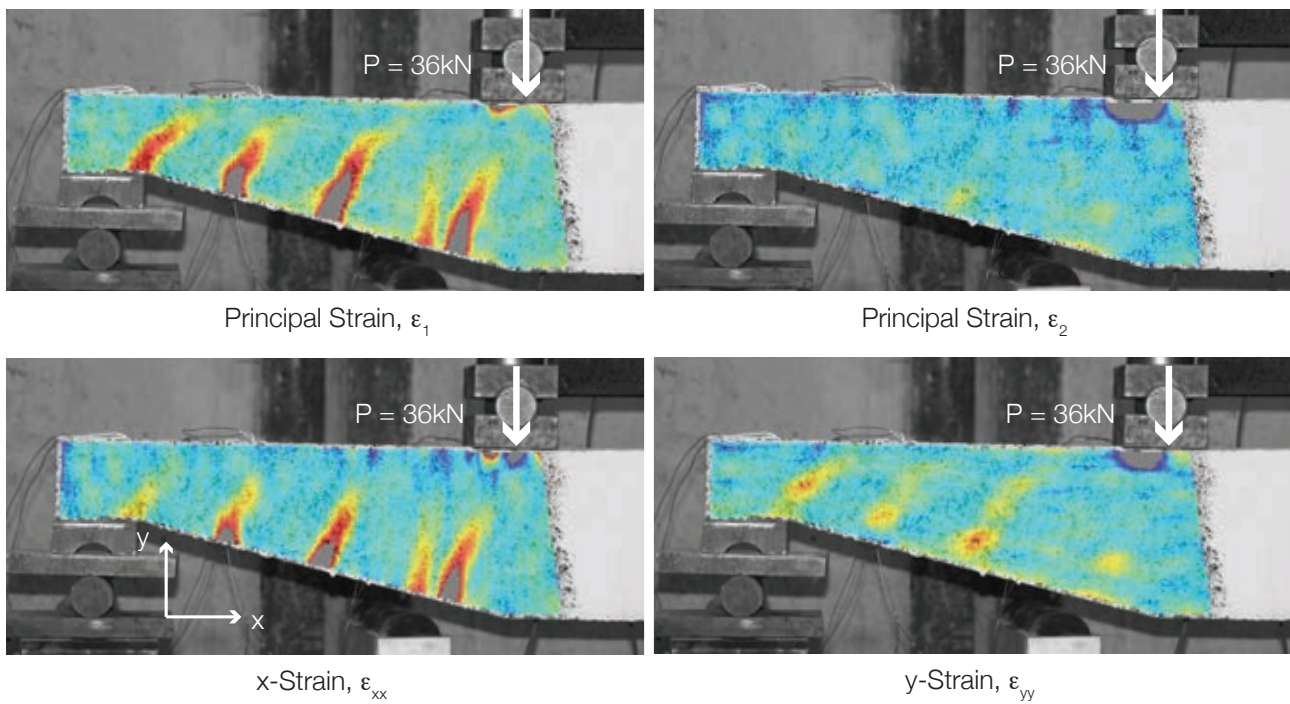
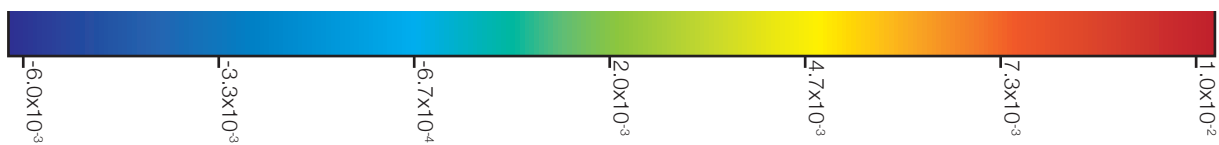


Figure 8.146: Beam 9\_2\_STM\_2(iii), Design Load 36kN (§8.4.7.2).





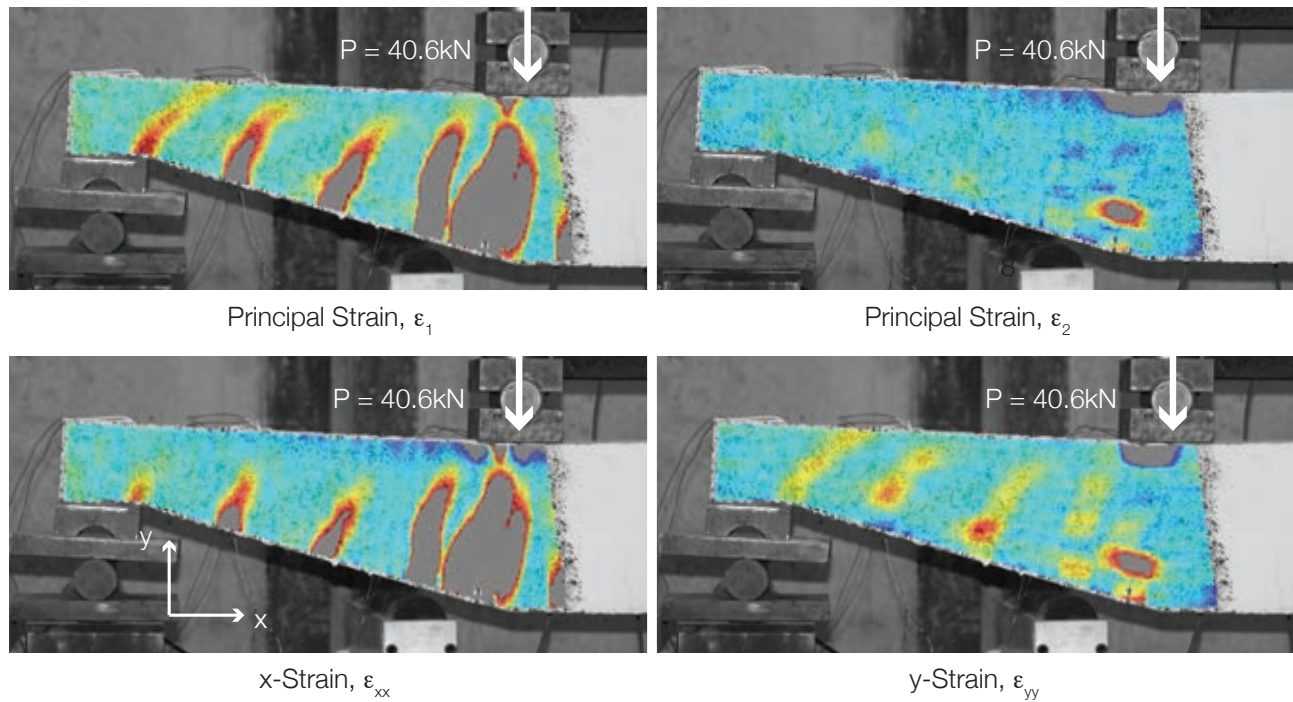
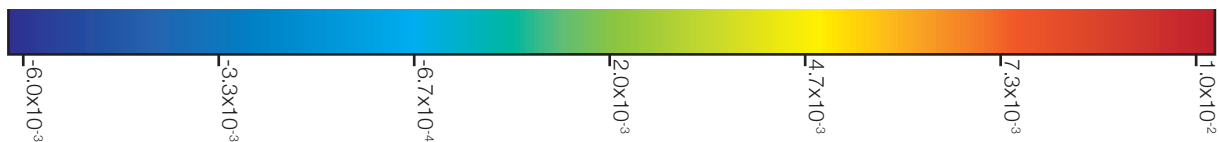


Figure 8.147: Beam 9\_2\_STM\_2(iii), Failure Load 40.6kN (§8.4.7.2).



#### 8.5.4.1. Strain direction plots

As is presented for Beam 9\_2\_EC2\_M(ii) and 9\_2\_CFP\_M(ii) in §8.5.3.3 on page 312, strain direction plots over the loading cycle were also collected for the 'STM' beam tests. One extract of this data is provided in Figure 8.148 and Figure 8.149 (below) for Beam 9\_2\_STM\_2(i).

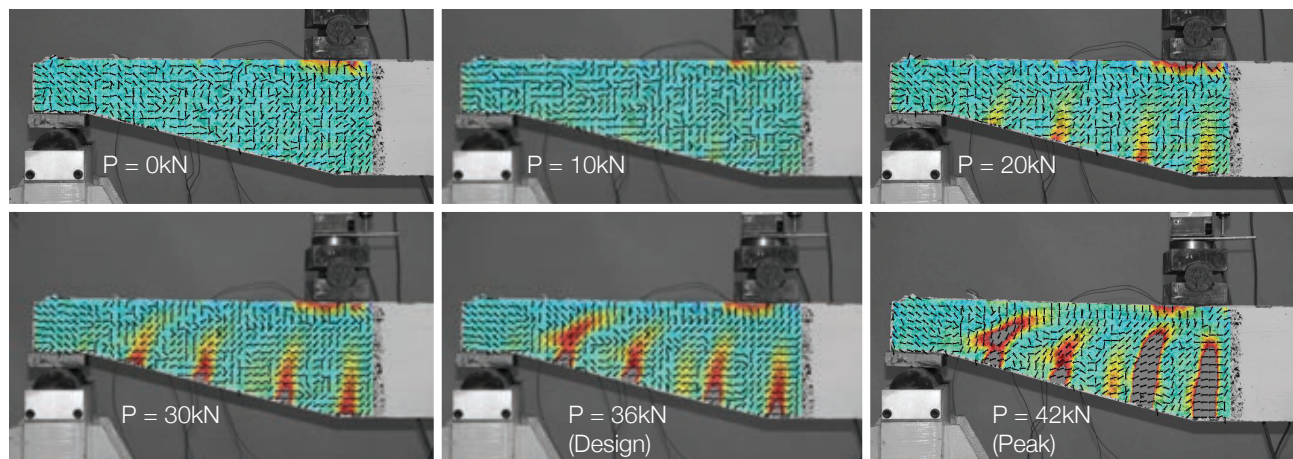


Figure 8.148: Beam 9\_2\_STM\_2(i) major direction over loading cycle. Principal strain  $\epsilon_1$  in background.

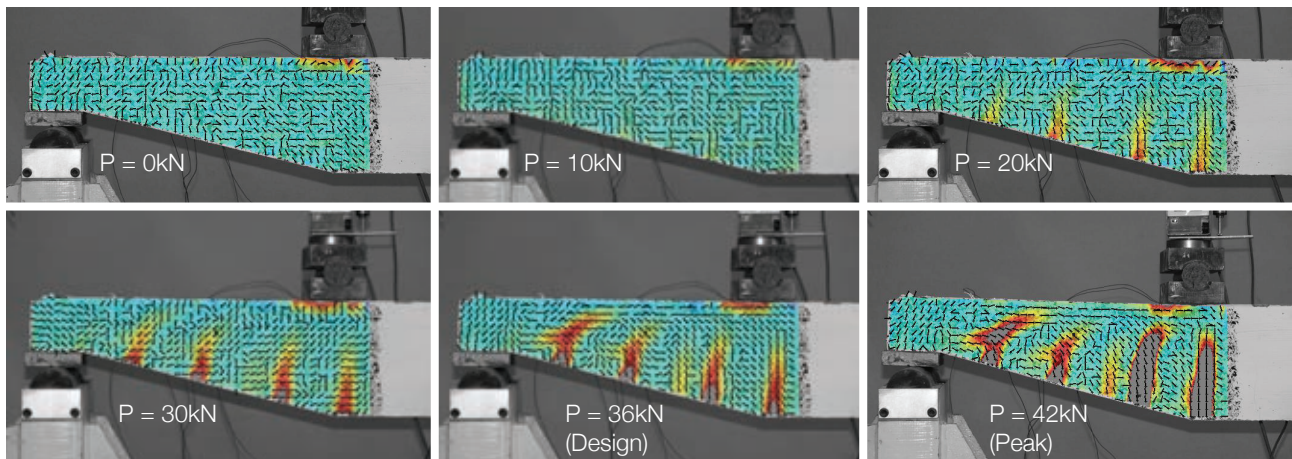


Figure 8.149: Beam 9\_2\_STM\_2(i) minor direction over loading cycle. Principal strain  $\epsilon_1$  in background.

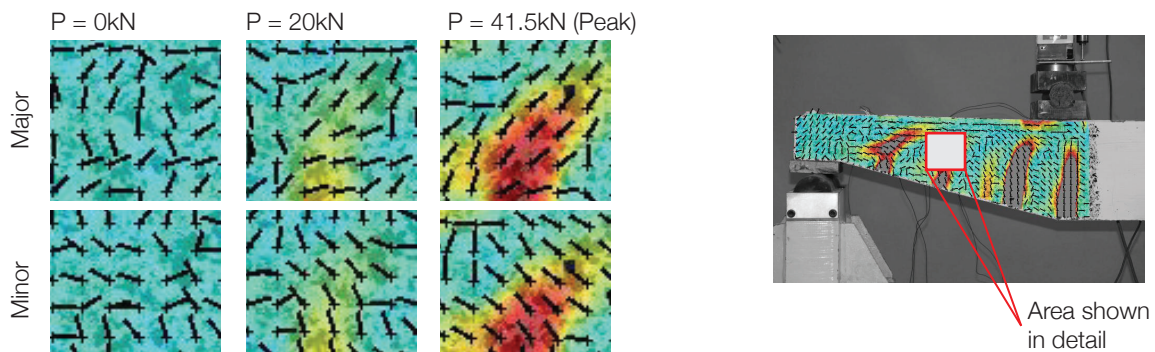


Figure 8.150: Change in strain direction, detail for Beam 9\_2\_EC2\_M(ii).

The strain direction plots again provide a useful method to show how the strain direction changes over the loading cycle. The two beams show much the same behaviour, with their concrete struts (chosen as the area shown in detail in the figures above) appearing to rotate as the load is increased, up to the position at which the maximum load capacity is reached. This again demonstrates how an ‘imaginary truss’ may be formed within the concrete section that evolves over time.

#### 8.5.5. Analysis

The digital image correlation technique has successfully been applied to the analysis of tapered beams loaded in shear. With data collected throughout the loading cycle, plots of the full behaviour of each beam can be made, as shown above. This provides a new dimension to the analysis to concrete beam behaviour, where steel strains and element displacements have previously been the most widely collected test data. In the following section, comparisons are made between the various design approaches, supported by the results of the DIC analysis. DIC results are presented at the same scale as the images given in the previous sections for ease of comparison.



### 8.5.5.1. CFP and EC2 Beams

The test results presented above show that the EC2 and CFP beams display contrasting behaviour under loading. The EC2 beams described above reached on average just 58% of their design load, while the CFP beams exceeded the design load by around 20% (Table 8.9 on page 263). In addition, the CFP beams displayed a more favourable failure mode, with ductility seen in the test results in combinations of flexure and flexure-shear. By contrast, all the EC2 beams failed in a less desirable brittle manner.

In the EC2 series, elements with transverse reinforcement (denoted 'M') were found to behave almost identically to those without transverse reinforcement ('V'). It was proposed in the design model for 'V' type beams that the inclined steel reinforcement would both carry the entire shear force and act as flexural reinforcement. This was not achieved, as the beams failed to reach their design loads, but more importantly there was no significant difference in failure load between the 'V' and 'M' type beams. This suggests that the transverse reinforcement, which is generally placed in concrete sections to increase their shear capacity, did not achieve this aim.

By contrast, the effective placement of transverse reinforcement forms a central design criterion for the compressive force path method (as described by Kotsovos and Pavlovic, 1999), with vertical steel provided only where it is needed in positions where tension forces are developed (as described in §4.2.5.2 on page 89). The difference between the two design methods is highlighted in Figure 8.151, where the  $\epsilon_1$  results for Beam 9\_2\_EC2(ii) and Beam 9\_2\_CFP\_M(ii) are presented at their respective peak loads. Also shown in Figure 8.151 is an overlay on the strain plot of the crack and reinforcement locations.

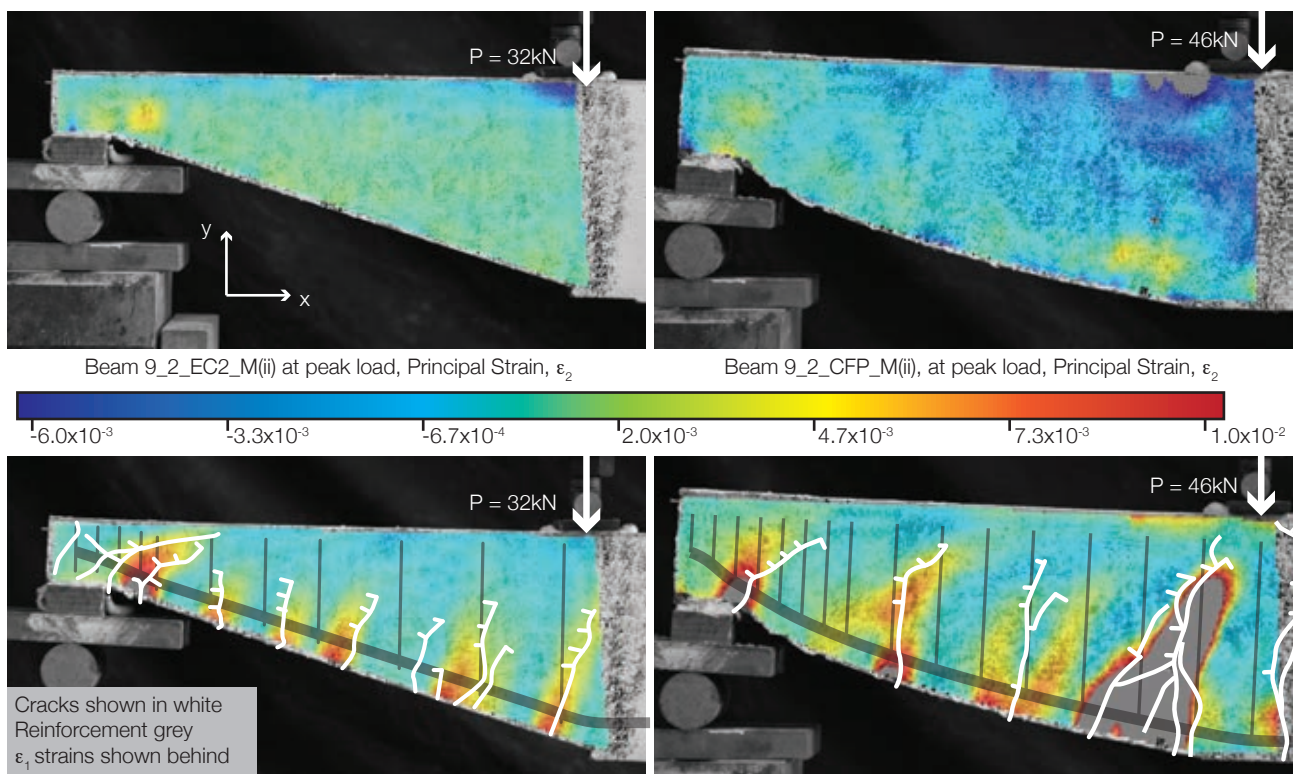


Figure 8.151: Comparison between Beam 9\_2\_EC2\_M(ii) and Beam 9\_2\_CFP\_M(ii) at their respective peak loads for principal strain  $\epsilon_2$  (top) and showing crack distributions overlain on  $\epsilon_1$  strain plot (bottom).

The plots illustrate how the distribution of vertical strains in the two beam designs differ. In the EC2 beam, which failed at an applied load 14kN less than that for the CFP beam, a concentration of vertical strain in the support zone can be seen, while much lower strains in the ‘body’ of the tapered beam are evident (full plots for  $\epsilon_{xx}$  and principal strains can be seen in Figure 8.120 on page 305).

By contrast, strains in the CFP beam are at their greatest concentration beneath the load point, at the position of maximum moment. Moving from this position to the support location, three bands of inclined zones of higher vertical strains can then be seen, with the magnitude of the maximum strain at the support being lower than that in the EC2 Beam. These zones can be imagined to demarcate the concrete ‘teeth’ described by the CFP model. This is further reflected by the much deeper cracking that was able to occur before failure in the CFP beam.

In the EC2 beam, cracks at the support dominate the failure mode. A line drawn over the top of the maximum crack depth for the 9\_2\_EC2\_M(ii) and 9\_2\_CFP\_M(ii) beams (Figure 8.152) shows how the effectiveness of the EC2 beam design is governed by the behaviour of its end zone, suggesting a shear critical design method. In the CFP designed beam, the neutral axis (denoted by the tip of the cracks) is consistent throughout the tapered section of the beam, suggesting a greater potential utilisation of the section at its peak load.

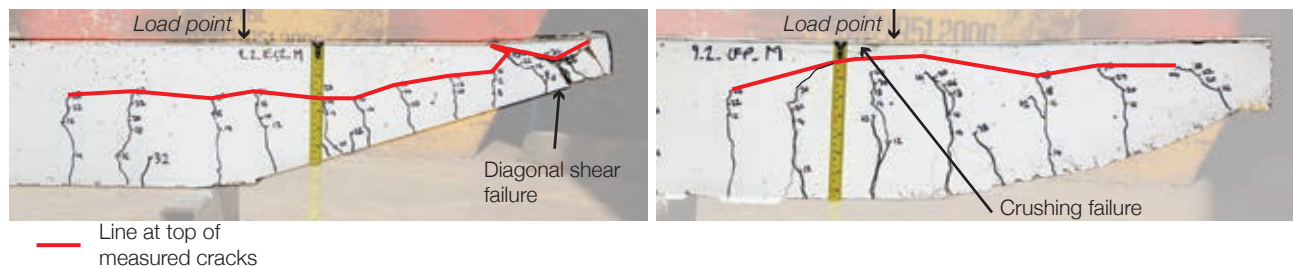


Figure 8.152: Failure modes for Beam 9\_2\_EC2\_M(ii) and Beam 9\_2\_CFP\_M(ii).

In the EC2 beam series, the 9\_2 test series provided the largest data set for analysis and thus has been the focus of this section. Data for Beam 9\_3\_EC2\_M was also collected, and can be compared to Beam 9\_3\_CFP\_M. In comparing the behaviours of Beams 9\_3\_EC2 (Figure 8.121 and Figure 8.122 on page 306) and 9\_3\_CFP (Figure 8.129 on page 310), it is clear that they display the same general behaviour as those of the 9\_2 test layout. For Beam 9\_3\_EC2\_M, Figure 8.122 is provided to display how the strain distribution changed just after formation of the first large shear crack that is recorded in Figure 8.121.

In Beam 9\_3\_EC2\_M, a peak of principal strain  $\epsilon_2$  is seen concentrated at the supports just prior to failure (which occurs at just over half of the design load). This contrasts to the behaviour of Beam 9\_3\_CFP, which achieved its design load of 32kN while also showing a more advantageous distribution of strain throughout the section. The principal strains for Beams 9\_3\_EC2\_M and 9\_3\_CFP\_M at their respective failure loads are compared in Figure 8.153 overleaf, where these differences are apparent. This provides additional weight to the analysis provided for tapered beams designed using the CFP and EC2 models described in the above sections.

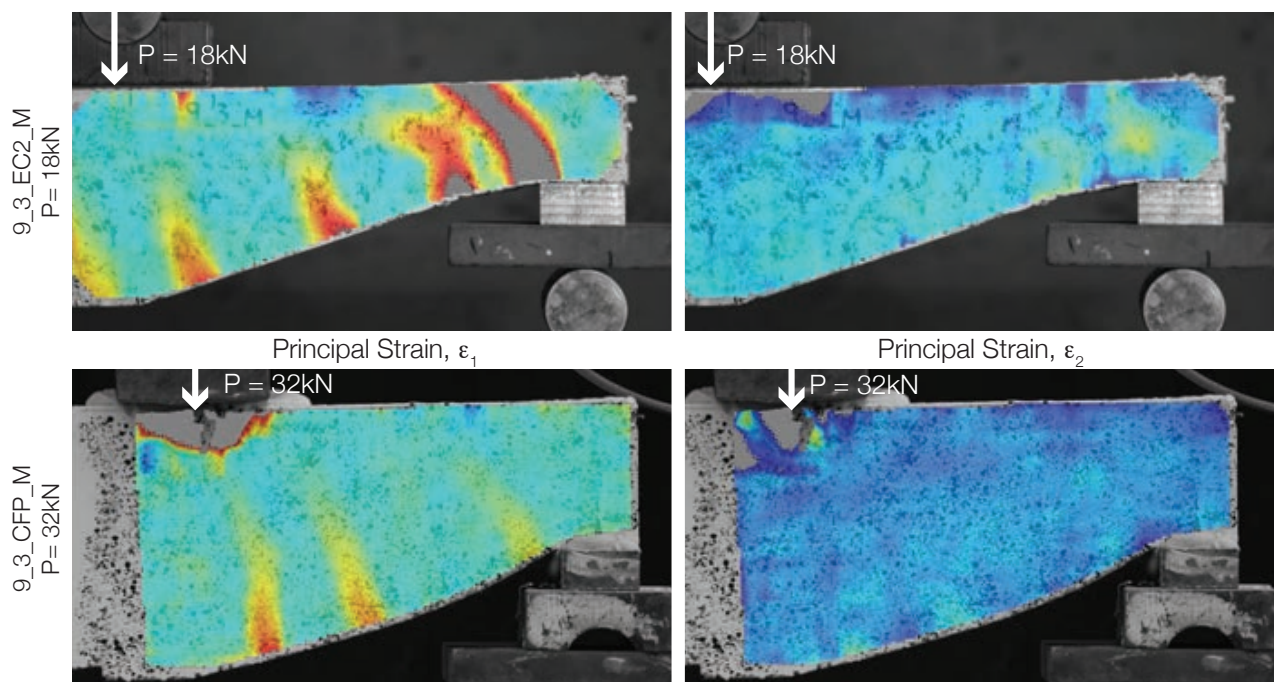


Figure 8.153: Comparison of principal strains in Beams 9\_3\_EC2\_M and 9\_3\_CFP\_M at their respective failure loads.

It is thus apparent that by controlling the compression path the CFP method is better able to facilitate a conservative design prediction whose failure mode may also be predicted. The DIC analysis presented in this section has shown how the behaviour of the EC2 and CFP beams differs, and whilst data was not collected for all the EC2 beams (much more was collected for the CFP beams) their failure modes recorded in the testing (§8.3) are all consistent with the behaviour seen in Beam 9\_2\_EC2(ii) and reproduced above.

#### 8.5.5.2. STM Beams

To address the need for a design method that does not rely on empirical formulae (as the CFP model does), the STM model was developed, as described in §7.2.4 on page 236. As noted in Table 8.12 on page 285, this design method resulted in elements that exceeded their design load by 10% on average during the testing program presented above. This is less conservative than was seen for the CFP method but remains an advantageous position, and compares well to the generally unconservative EC2 model described above.

The STM model may therefore provide a design method that gives a simple means by which the element capacity can be checked that does not rely on assumptions of steel yielding, as is done in the EC2 model. This aspect is discussed in greater detail below.

Strain plots for the STM beams show reduced concentrations of vertical strain at the supports and more widely spaced cracking along the beam when compared to the EC2 Model. These results are therefore similar in many respects to those seen for the CFP model. The differences are highlighted in Figure 8.154 where a comparison between the EC2 and STM results for vertical strains in Beam 9\_2 at their respective failure loads is presented.



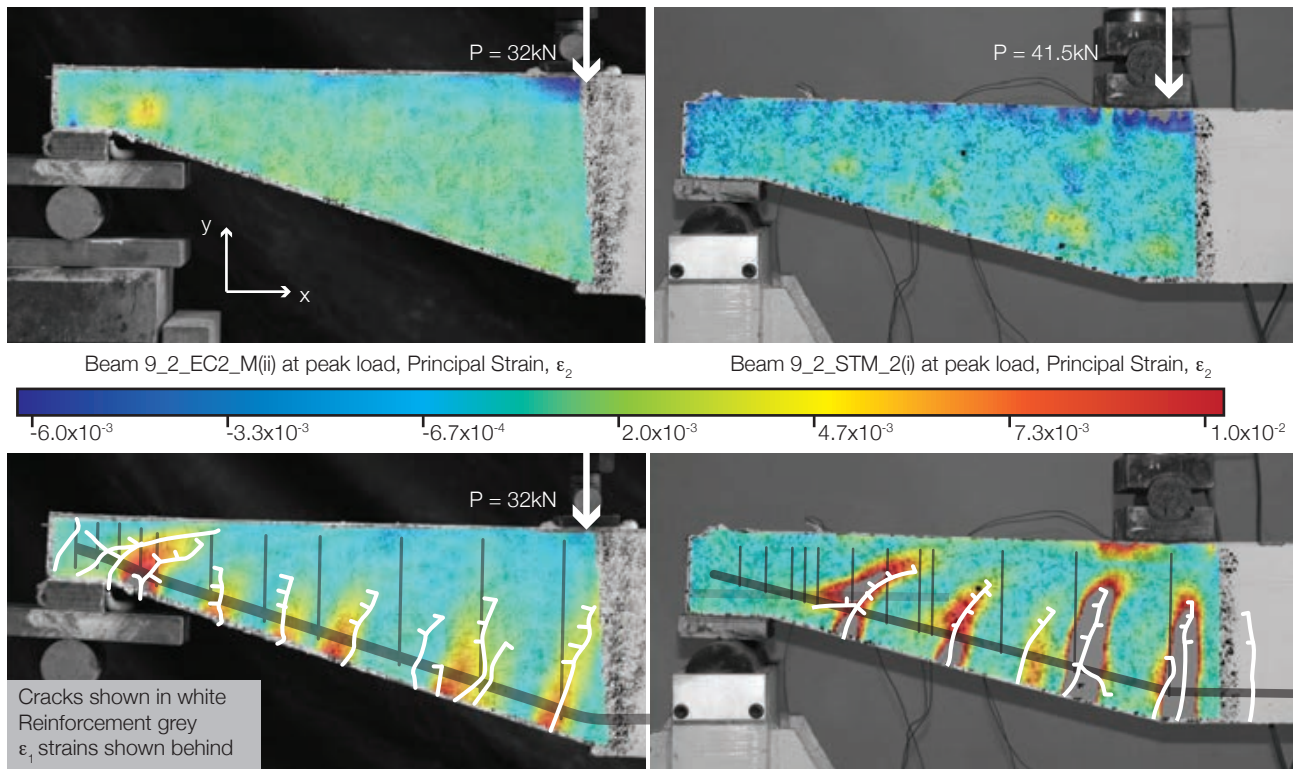


Figure 8.154: Comparison between Beam 9\_2\_EC2\_M(ii) and Beam 9\_2\_STM\_2(i) at their respective peak loads (top). Crack distributions at the peak load overlain on  $\epsilon_1$  strain plot (bottom).

The crack (and strain) distributions seen in the STM beam series demonstrate the advantages of the design method. By moving strain concentrations away from the support, where their influence in the EC2 beam has been seen to cause failures below the design load in shear the STM model beams are able to fail in a ductile manner (as shown in the test results presented in the preceding sections).

The STM beams have a deeper support section than those designed using the EC2 model. The reasons for this increase in depth, aside from the simple reality that the EC2 beam series was undertaken first and these were seen to be deficient in the support zone, are described by the design model. As is presented in §7.2.4 on page 236, anchorage of the transverse reinforcement and the provision of development lengths for the reinforcement, coupled with the provision of a straight force line between tension nodes for the reinforcement, necessarily leads to a requirement for a minimum beam depth. In the designs presented and tested in this thesis, this minimum depth was almost identical to that required in the CFP design, with the STM model requiring a 100mm end depth compared to 97mm for the CFP beam and 60mm for the EC2 beam.

The presence of a high vertical strain a small distance from the support in the STM beam is correlated to the design layout in Figure 8.155. In the design, the contribution of the first vertical link is critical, as the force in this link is approximately equal to the full reaction force (§7.2.4 on page 236). As has been shown in the above, the forces predicted in the model correlate well to the recorded steel strains (as recorded using strain gauges and shown in Figure 8.84 on page 288), and the results of Figure 8.155 demonstrate this close relationship further.

In addition to the comparison made between the STM and EC2 models in Figure 8.154, a further comparison is made between the STM and CFP results in Figure 8.156. Here, it is again apparent that the STM model provides advantages to the beam design by moving the areas of high tension away from the support zone. Whilst the STM and CFP beams both failed in a ductile manner, it may be surmised from these plots that the STM beam was closer to a brittle failure than the CFP beam. This may be reflected in the lower ultimate capacity of the STM beams (although both sets did reach their design load). In itself this is not a negative reaction to the STM design model, but does suggest that the manner in which the CFP beams were designed is well suited to a conservative design approach.

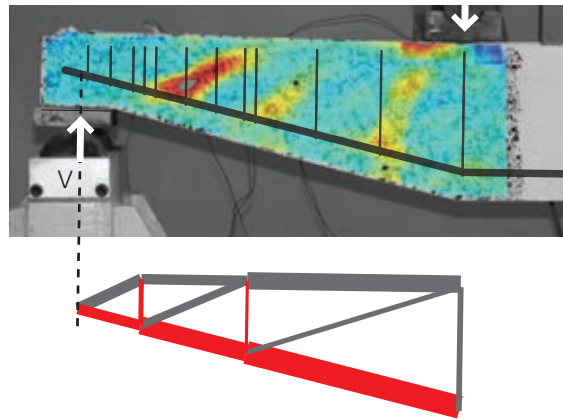


Figure 8.155: Comparison of  $\epsilon_{yy}$  strains in Beam 9\_2\_CFP\_2(i) and the design model forces.

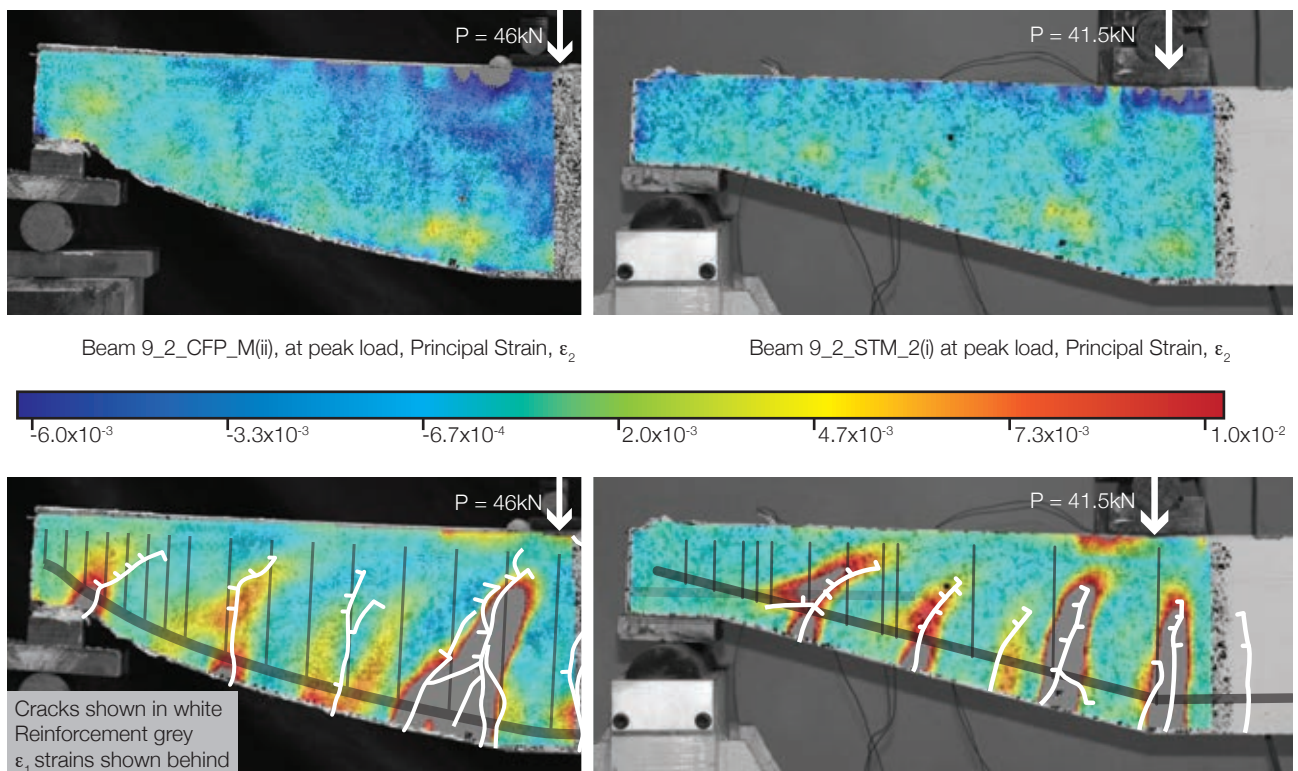


Figure 8.156: Comparison between Beam 9\_2\_CFP\_M(ii) and Beam 9\_2\_STM\_2(i) at their respective peak loads (top). Crack distributions at the peak load overlain on  $\epsilon_y$  strain plot (bottom).

### 8.5.5.3. Discussion

In the full test data presented in this Chapter, it was seen that there was no difference in overall behaviour for those STM beams with an external steel plate when compared to those without one. Although it might be expected that the internal anchorage bar for the external plate will help to reduce the degree of cracking in the end zone, this effect was not recorded in any detail in the tests. Although the horizontal anchoring bar does pick up some load, this was again not significant and has not unduly influenced the behaviour of the STM beam.

It may therefore be concluded that the external plate is neither required for, nor a hindrance to, the beam if it is used. For example in precast construction an external plate may become desirable for construction, mobility and installation reasons, but it would not be required purely for structural benefit.

A comparison between the overall profiles of the end zone of the three beam types is provided in Figure 8.157, where again the differences can be seen. Whilst from an objective standpoint the shallow support zone of the EC2 beam might be expected to yield the lowest capacities, it is the manner in which the STM and CFP models are able to adjust and control the behaviour of the beams that is most relevant about these results. In addition, it is only by pushing the EC2 model to its feasible limit that the deficiencies in such an approach have been revealed.

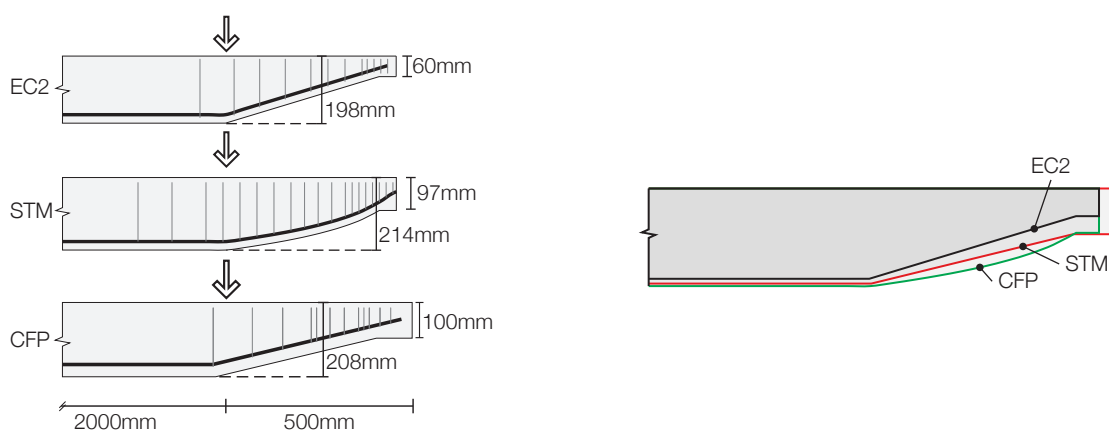


Figure 8.157: Comparison of overall beam geometry, 9\_2\_CFP; 9\_2\_EC2 and 9\_2\_STM.

#### 8.5.5.3.1. Crack progressions

The spread of the crack patterns in the CFP and STM beams (as is shown for all the beams in the results presented above) is summarised for all the Beam 9\_2 variants in Figure 8.158 on page 326. The advantage of the STM model over the EC2 approach is apparent from this Figure.

In the EC2 test results, the beams were found to crack initially at the end zone (where the regions of high strain are noted in the DIC results presented above), before limited crack progression towards the point of load application. In the STM model, cracking begins in the centre of the beam, before spreading both towards the support and towards the point of load application. In the CFP model, a much more advantageous distribution is seen, in which cracking begins beneath the load point, and spreads along the beam before failure.



This pattern of crack progression is seen in all the beams tested (see results presented above) and thus highlights the shear critical nature of the EC2 designs. By cracking in the end zone, it is clear that shear is the dominant condition at the ultimate load, and thus a brittle failure is created.

It is also important to note that in contrast to previous work in the testing of tapered, fabric formed beams (for example Garbett, 2008), where the shear loads were ‘over designed’ by 50% (while the flexural design was not altered), all of the beams tested in this thesis were assessed for the actual loads applied to the section, giving greater weight to the test results and analysis presented above.

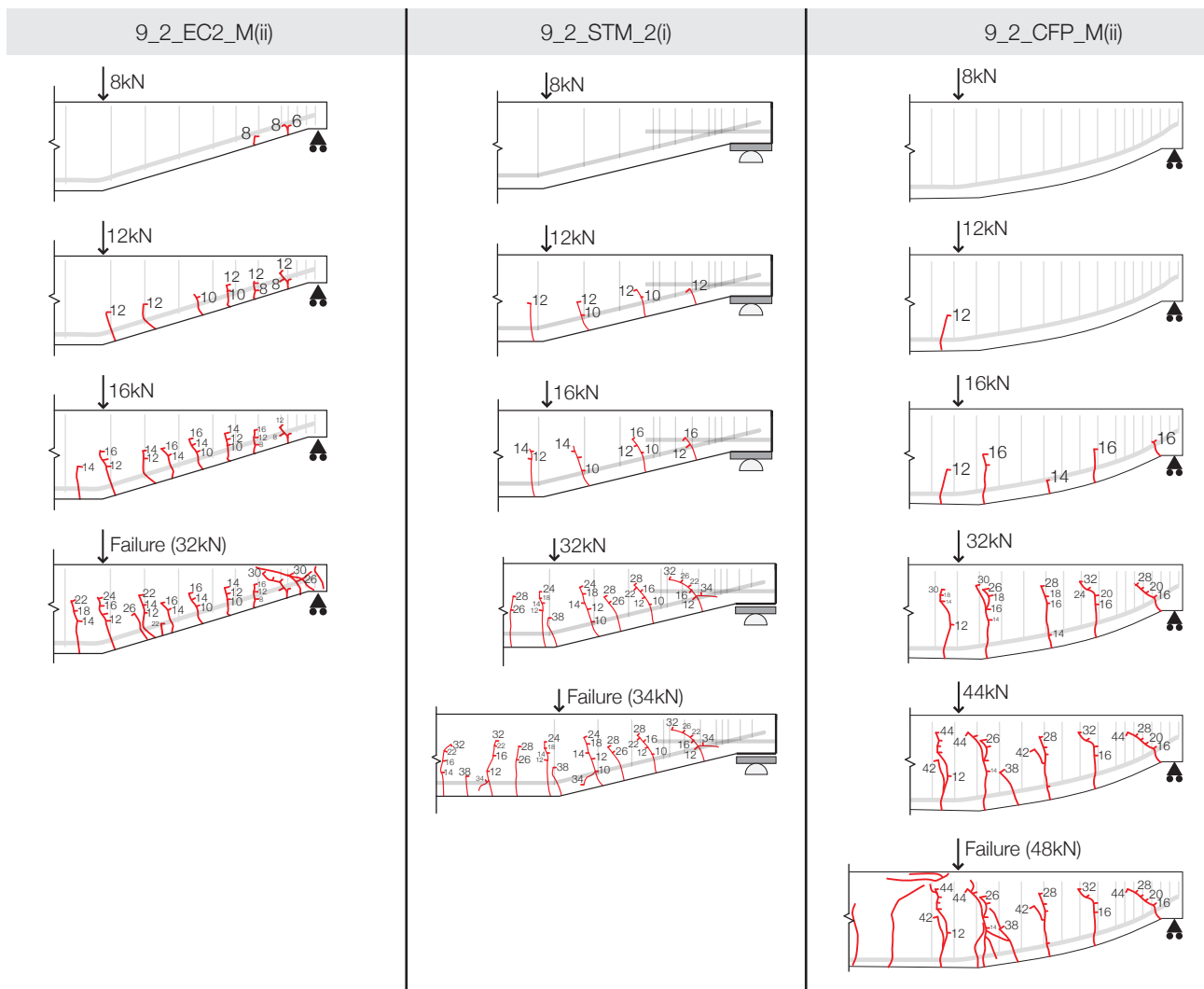


Figure 8.158: Crack propagation comparisons for Beam 9\_2.

The STM model appears to bring with it a new paradox for tapered beams. The EC2 model is, in itself, a strut and tie model that assumes the steel yields to get plastic behaviour and redistribute stresses. This approach forms the basis of the BS EN 1992-1-1 (2004).

The STM model, in which the steel is not assumed to be yielding in all positions, is therefore based on plastic theory but is applied to a situation where the behaviour is not plastic. The success of the STM model is found in providing a conservative design method for the tapered beams that works in reality because the element does not

fail in shear. By ensuring through the design method that the position at which the steel does yield is predicted and controlled, the element can be ensured to fail in a ductile manner. This ductile behaviour is ensured by controlling the yield position such that it occurs away from the support zone (and in the beams tested in this thesis occurs primarily beneath the loading point). This provides the element with the ductile behaviour that is desired in the design process, and that may not always be guaranteed in the EC2 method.

In this way, the STM and EC2 models are opposing in their fundamental approach. Whereas the STM model becomes a self-fulfilling prophecy in which the section is able to be designed to be ductile and so it is ductile, the EC2 model can become a vicious circle in which the ductile failure that is desired cannot be achieved because the steel is not able to yield prior to failure of the critical section. This fundamental result demonstrates the power of the STM method over the extension of the EC2 approach that has been used in this thesis.

### 8.5.6. Conclusions

The results presented in this section have shown that the STM and CFP methods provide a reliable design process that results in a more advantageous internal strain distribution. It is this distribution of strains that ensures a ductile response. The results show that the EC2 model presented in Chapter 5 is not able to model the behaviour of the tapered beam and whilst it is based on plastic theory, in which the steel is yielding to provide a strut and tie model, the actual behaviour of the beams in the end (disturbed) regions as recorded in the tests does not marry with the predictions of the design model.

This result should be compared to those of the STM model in which the forces predicted in the imaginary truss correlate well to those recorded using strain gauges during the tests. Additionally, the CFP method does not predict the force in the steel, but does allow the prediction of a flexural failure mode. Flexural, or flexure-shear failures were seen in all the CFP tests undertaken.

The importance of the compression path is demonstrated by both the CFP and STM design methods. In both, the change in direction of the compression path gives rise to the critical link position (close to the support which must carry almost the maximum shear force). The underlying approach of the two methods may therefore be considered to be quite similar.

The 9\_2 series of beam tests described and analysed in detail in this section has yielded the most informative results of all the tapered beams tested as part of this thesis. A reiteration of the differences in the design models, as reflected in the beams' load-deflection behaviour, is provided in Figure 8.159 on page 328, where the results of all 9\_2 series beam tests are presented. The advantages of the STM and CFP models, echoed in the strain profiles and discussion above, in providing a ductile, conservative load response, is seen.

For all tests, the shear force in the load envelope was the force used in the design, and there was no 'extra provision' of shear capacity to guard against shear failures (as seen in previous work). As such, the elements were theoretically able to fail in flexure or shear simultaneously. The nature of the results show that the EC2 model

is shear critical (and does not reach the predicted capacity, even in shear), while the STM is less shear dominant than the EC2 model, and the CFP model provides perhaps the ideal behaviour (limited cracking and lower strains in the end zone, leading to predictable and ductile failures).

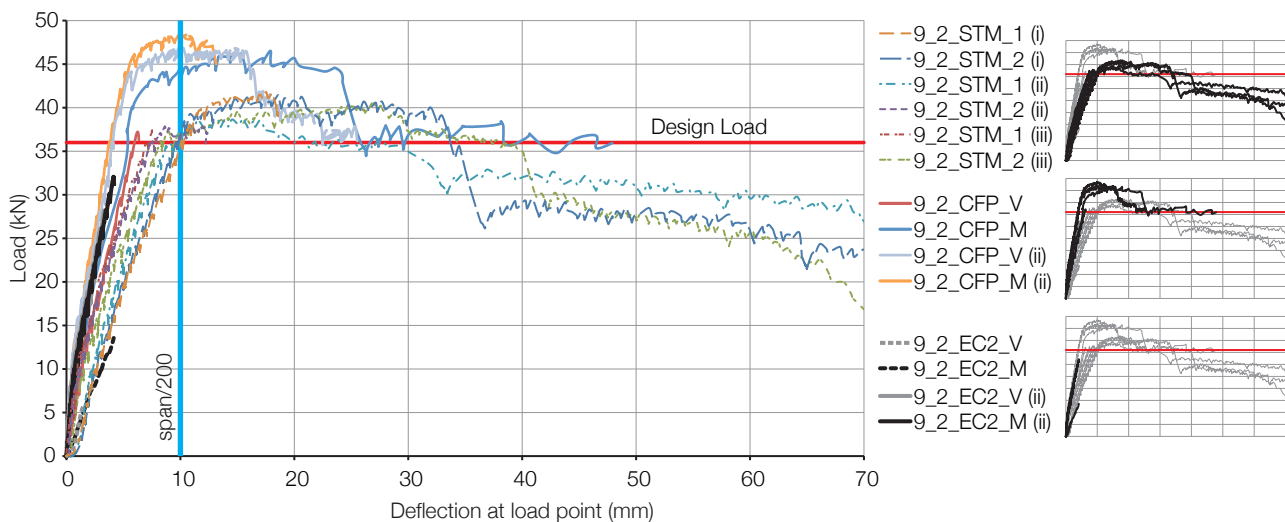


Figure 8.159: Summary of all 9\_2 Series Tests.

Conservative results from both the CFP and STM beam design methods, supported by DIC data showing how the internal strain distribution is altered in these design methods, suggests that they are better able to model the behaviour of tapered beams in shear. In light of the results presented for the EC2 beam series, it is recommended that tapered beams do not rely entirely on the contribution of their flexural steel to the shear capacity. This means that the value of the vertical component of the steel force ( $V_{td}$  in BS EN 1992-1-1 (2004), as shown in Figure 4.15 on page 96) should not comprise the full value of the shear resistance of the section until further guidance can be determined.

This conclusion is supported not only by the results of the tapered beams in Series 9, but also by the 3m-span beams subjected to uniformly distributed loads (§8.2 on page 246), where the contribution of the inclined steel was found to be negligible in some circumstances. In addition, the design and testing of Beams 8\_1 and 8\_2 has previously demonstrated the ability of the CFP method to predict the transition of a tapered concrete section between a brittle shear failure (without transverse reinforcement) and a ductile failure (with transverse reinforcement), in a manner that is not possible with other design procedures.

The DIC analysis undertaken in this section provides both a potential crack width measurement technique (by integration of the numerical output of the DIC results) and a means by which the cracked zones of each element can be monitored in detail over the loading cycle. The significant results of this analysis are that the tension zones seen in the EC2 beams at their supports are moved in both the STM and CFP beams to a distribution across the beam that satisfies the design model.

This Chapter has demonstrated that both the compressive force path (CFP) and strut-and-tie (STM) models provide an accessible method for the design of variable section beams. The provisions of BS EN 1992-1-1 (2004) appear to be unconservative in some situations. It is thus proposed that in the design of a fabric formed beam, the end zones (dominated by shear) should be analysed separately to those sections dominated by flexure. Such an approach is analogous to the 'Beam' and 'Disturbed' regions of the design models described originally by Schlaich *et al* (1987).

Whilst the proposed STM model has given good results, so too has the CFP method. To apply the CFP method with more confidence, further work is required to investigate in detail the genesis of the empirical equations provided by Kotsovos and Pavlovic (1999) and Bobrowski and Bardhan-Roy (1969). The quantity of test data collected for beams designed using the EC2 model was limited, and it is therefore recommended that additional work be undertaken to investigate the behaviour of a wider range of beam loading envelopes and shear spans. Such work should focus on realistic beam sizes, with conventional reinforcement layouts that could be rapidly adopted by industry.

This Chapter has shown that the proposed design method can lead to ductile, predictable responses in variable section beams. This result, which is expanded and confirmed in the design guidance provided in Chapter 11, is hugely important to the potential for fabric formwork to provide a means by which sustainable concrete design and construction can be achieved.

Throughout this thesis the use of simply-supported fabric formed beams has been considered (both in this Chapter and in Chapter 6). Many more challenges and opportunities will arise through the use of fabric formed, non-prismatic beams in frame elements, or in cast in-situ construction where the support conditions may allow moment to be carried. This provides additional optimisation challenges, since the position of an approximately zero moment will now be removed from the 'support' zone.

In light of the advancements made in this Chapter to provide a shear design method for non-prismatic reinforced concrete beams, a final objective to provide a practical means by which such structures can be reinforced, as identified in §5.4 on page 122, is addressed in the following section. The results demonstrate that advanced composite materials may provide a means by which economical reinforcement may be provided in the design of optimised, fabric formed concrete structures.

## 8.6. Flexible shear reinforcement

### 8.6.1. Introduction

The work presented above has demonstrated that variable section members are prone to shear failures if the moment-shear interaction is not correctly considered and that shear failures can be avoided through the use of an appropriate design method and steel bars as transverse reinforcement.

Whilst this has been successful, the construction of beams in which every link has different dimensions may be economically disadvantageous. It would therefore be advantageous to introduce a new process by which a variable depth reinforcement cage could quickly and easily be manufactured. One solution may be provided through the use of flexible carbon fibre grids, the first such use of which is described below.

### 8.6.2. Carbon fibre grids

Carbon fibre reinforced polymer grids are often used in place of welded wire steel mesh in architectural panels, prismatic beams (Chomarat, n.d.) and retrofit applications, where their high strength to weight ratio and stiffness are advantageous. However, they can be expensive and require specialist design knowledge to ensure failure modes remain safe.

When coated with resin, such grids are rigid and will readily snap if bent around too small a radius. This behaviour is ill suited to beams with a variable cross section, where complex curves may need to be accommodated if the grid is to be used as transverse reinforcement. It would therefore be advantageous to use an uncoated CFRP grid which could be simply draped into the desired profile before concrete is cast around it. Chung (1994) has shown that in contrast to both glass and aramid, carbon fibres have sufficient resistance to the alkaline environment within concrete to make such a solution feasible. However, the bond between concrete and CFRP when resin coated and when raw remains an issue of concern, since in both cases only the outermost fibres will be in contact with the concrete.

#### 8.6.2.1. Characterisation

A CFRP grid supplied by Fortress Stabilisation was used in the tests described in this paper. Material properties of the grid, which is supplied in 1.2m wide rolls with a 50mm mesh spacing, are given in Table 8.14. These properties were measured by tensile testing of individual tows (approximate external diameter 2.4mm). During manufacture the material is stitched into a grid and can easily be formed into any desired profile, as the tows are able to move over one another.

Initial work was undertaken to assess the feasibility of construction using the CFRP grid. A section of the CFRP grid was hung between timber supports to a predetermined profile before being coated with an araldite based epoxy resin (described in Table 8.15) and allowed to cure for 8 hours. The resulting element is shown in Figure 8.160.

Table 8.14: CFRP Grid by Fortress Stabilisation, Material Properties.

Property	Measured value	Property	Measured value	Property	Measured value
Ultimate tensile strength of a single CFRP tow	4226N	Strain in the tow at ultimate strength	0.013	Young's Modulus	74kN/mm <sup>2</sup>



a. Flexible grids



b. Coated in resin



c. Rigid mesh

Figure 8.160: Fully coated CFRP Grid, feasibility study.

Table 8.15: Epoxy resin as used in all tests.

	Component	Mixing – parts by weight	Pot life of mixed resin
Hardener	Aeropia Araldite HY5052	100	@18°C: 280 – 320 mins
Resin	Aeropia Aradur 5052	38	

The coating process is time consuming and difficult, making the use of the CFRP grid without a full resin coating a desirable alternative. However, such an approach could limit the effectiveness of the grid as very few of the individual carbon fibres within each tow would be bonded to the surrounding concrete. This may then allow the fibres to slip past one another, leading to a progressive failure of the tow.

A partially coated solution, as demonstrated elsewhere (Choi, 2002) and shown in Figure 8.161, may therefore be preferable. Coating the ends of each tow in resin prevents individual fibres from slipping past one another and, provided these ends remain anchored in the concrete, the tow may then be able to provide its full capacity. Such an approach would allow flexible grids to be used in conjunction with a flexible membrane in fabric formed concrete structures. To assess the use of both fully and partially coated grids, three 3m span concrete beams were tested.

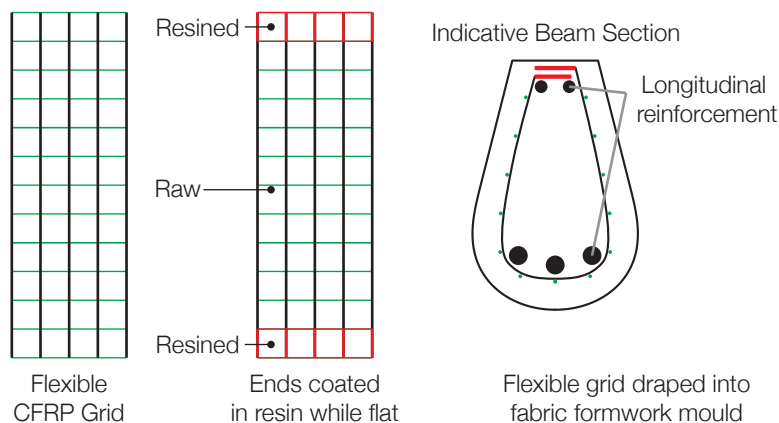


Figure 8.161: Partially bonded grids.



### 8.6.3. Structural testing

Three prismatic beams (110mm x 220mm x 3000mm) were tested. All beams were designed for three point loading, with the single point load located a distance of  $2.5d$  from the support, where  $d$  is the effective depth of the beam ( $d = 195\text{mm}$ ). All beams were longitudinally reinforced with two 10mm diameter high yield (assumed at  $550\text{N/mm}^2$  for design calculations) deformed steel bars with 20mm cover and had a design concrete cube strength of  $40\text{N/mm}^2$ . The resulting shear and bending moment diagrams are shown in Figure 8.162. Beams 10\_1 and 10\_2 were provided with transverse reinforcement in the form of a draped CFRP grid, the properties of which are described in the preceding section. A fully coated grid was used in Beam 10\_1, while in Beam 10\_2 a partially coated grid was used.

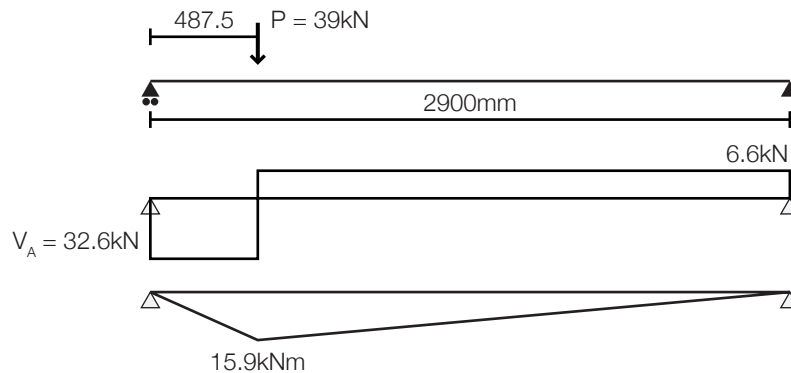


Figure 8.162: Force envelope.

The CFRP grid tow spacing required to resist the full shear force along the beam was determined using the variable angle truss approach for shear (Eq. 8.1), with the stress in the CFRP being initially given by the minimum of Eq. 8.2. This approach is taken from ACI440 (2006), where Eq. 8.2(a) is intended to prevent large shear crack widths and limits the strain in the FRP to 0.4% and Eq. 8.2(b) is intended to prevent the stirrup from snapping prematurely at the bend portions.

Taking this approach would thus limit the value of  $F_f$  to 1.341kN. However, given the limited test data used to determine  $E_f$  and that the manufacturer's available test data (Fortress Stabilisation, 2009) suggests a much higher value for  $E_f$  should be expected, it was decided for the purposes of this thesis to limit  $F_f$  to 1.902kN (representing a reduction of 55% on the ultimate tensile strength  $F_{fu}$ , Table 8.14) while also taking a truss angle of  $45^\circ$  in Eq. 8.1. Assuming plane sections remain plane, the neutral axis depth at the position of maximum moment (Figure 8.162) required to satisfy equilibrium was calculated as 27mm, giving a lever arm between the centres of tension and compression of 181mm. A CFRP grid spacing of 21mm is therefore required according to Eq. 8.3. Beam 10\_3 was not transversely reinforced, and using BS EN 1992-1-1 (2004) was predicted to fail in shear at  $P = 29\text{kN}$  ( $V_A = 24\text{kN}$ ). The resulting beam layouts are shown in Figure 8.163.

$$s = \frac{2F_f}{V}(z)(\cot \theta) \quad \text{Eq. 8.1}$$

Where  $s$  = spacing (mm);  $V$  = shear force (kN);  $F_f$  = tensile strength of each tow, as given by Eq. 8.2..

$$F_f = \min \begin{cases} a) 0.004 E_f A_f = 0.004 (74000) (4.53) = 1.341 kN \\ b) \left( 0.05 \frac{r_b}{d_b} + 0.3 \right) F_{fu} = (0.45) 4.226 = 1.902 kN \end{cases} \quad \text{Eq. 8.2}$$

Where  $s$  = spacing (mm);  $V$  = shear force (kN);  $F_f$  = tensile strength of each tow, as given by Eq. 8.2;  $A_f$  = area of tow;  $E_f$  = Young's Modulus;  $r_b$  is the bend radius,  $d_b$  is the bar diameter (the value  $r_b/d_b$  is taken as 3.0) and  $F_{fu}$  = ultimate tensile strength of each tow.

$$s = \frac{2(1.902)}{32.6} (181)(1) = 21 \text{ mm} \quad \text{Eq. 8.3}$$

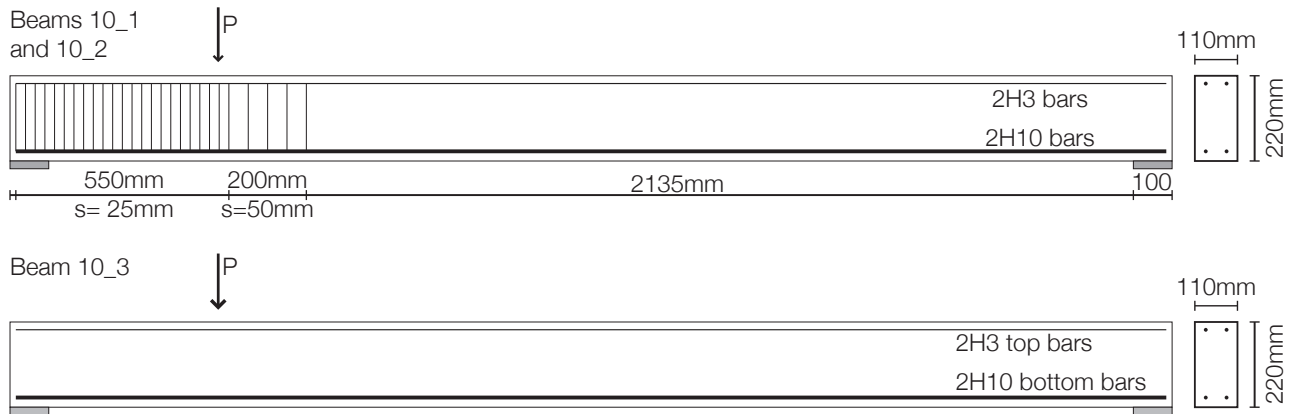


Figure 8.163: Beam layouts.

#### 8.6.4. Construction

The CFRP grids for Beams 10\_1 and 10\_2 were fabricated as described previously and shown in Figure 8.164. Three batches of the same concrete mix design were made, and the beams were cast in steel moulds of the required dimensions. A vibrating poker was used to achieve sufficient compaction of the mix. The beams were all demoulded after 72 hours. Six concrete cubes were cast for each beam, these were demoulded after 24 hours and dry stored at constant temperature and humidity until testing.

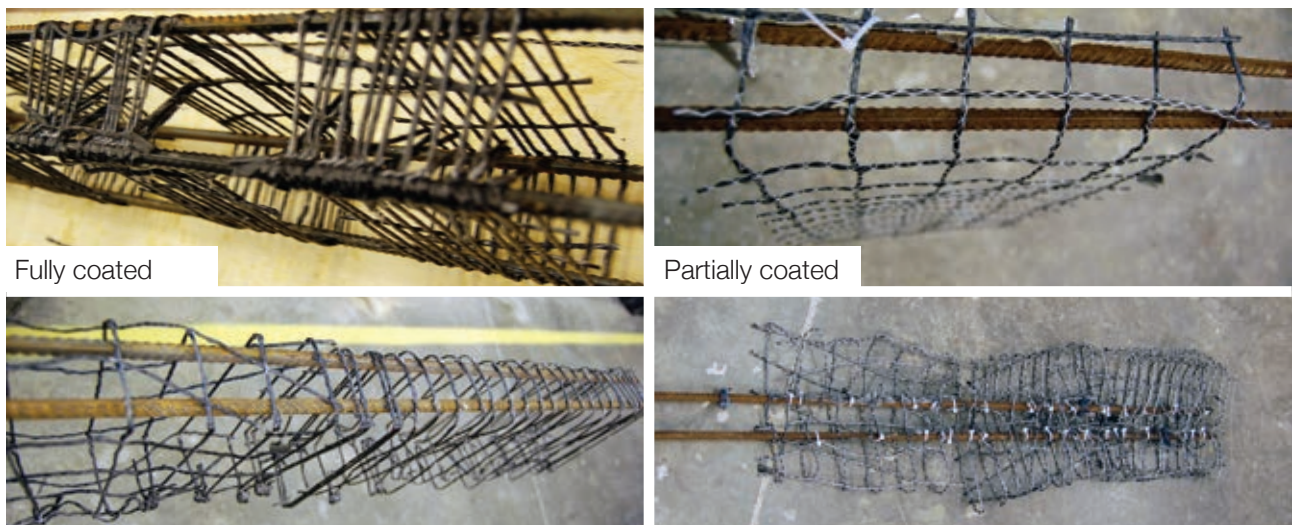


Figure 8.164: CFRP grid fabrication for Beam 10\_1 (left) and Beam 10\_2 (right).

### 8.6.5. Testing

All three beams were tested 7 days after casting. Concrete strengths were recorded prior to testing and are given in Table 8.16 (average compressive strength given by three 100mm cube tests). Load was applied to the beams by a hydraulic jack in 2kN increments, as measured by a load cell placed beneath the jack head. Displacements were measured below the load point and at the quarter points of each beam, as shown in Figure 8.165. The test results are summarised in Figure 8.173, with diagrams of each beam at failure provided in Figure 8.174.

Table 8.16: Concrete strengths as measured at testing.

Beam	Average compressive strength, $f_c$ (MPa)	Standard deviation on compressive strength, SD
9_1	38.2	0.89
9_2	38.2	1.09
9_3	38.7	0.64

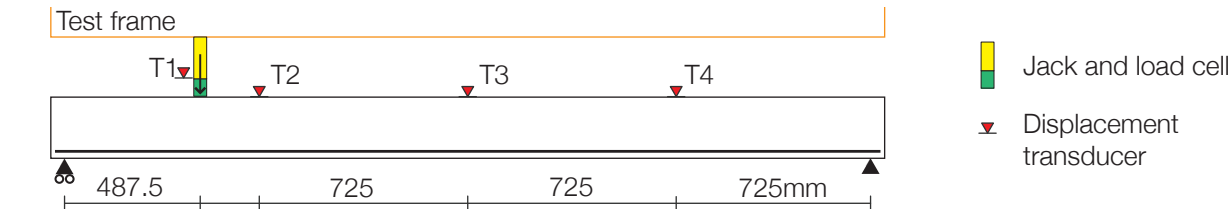


Figure 8.165: Test set up.

#### 8.6.5.1. Beam 10\_3

Beam 10\_3 (without transverse reinforcement) was tested as described above and first cracking was recorded at an applied load of 10kN. Further loading resulted in distributed cracking along the face of the beam, as shown in Figure 8.166. At an applied load of 18kN deep cracks to the left of the loading point began to curve towards the loading point. A maximum load of 35.8kN was sustained by the beam before failure occurred along a single inclined crack (highlighted in Figure 8.166) joining the support and point load in a shear failure.

The maximum load carried by the beam was slightly in excess of the predicted capacity of 29kN. A maximum displacement of 10.0mm was recorded at LVDT T1 (located under the point load) and 11.1mm at the midspan (T3, Figure 8.165). Beam 10\_3 provided an identical load-deflection behaviour to the initial stages of Beam 10\_1 and 10\_2, but did not achieve the same peak load and post-peak deformability, as shown in Figure 8.173 and discussed below.

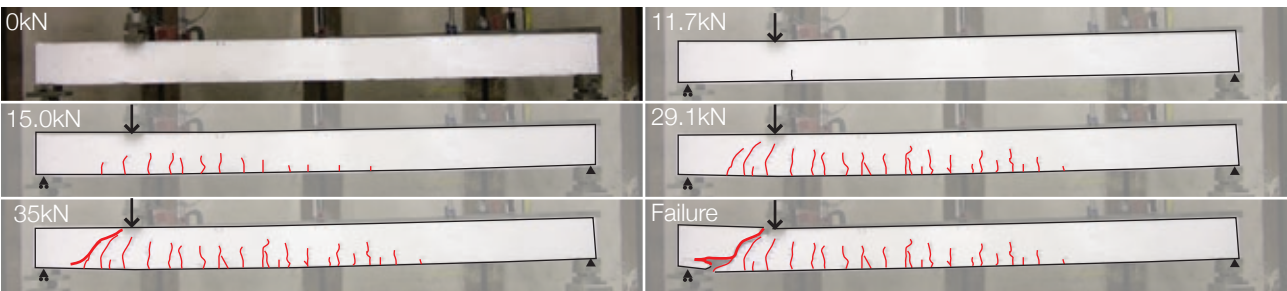


Figure 8.166: Crack progression in Beam 10\_3.

### 8.6.5.2. Beam 10\_2

Under the same experimental setup as Beam 10\_3, Beam 10\_2 (partially resin coated grids) was tested. Initial cracking beneath the point load was recorded at 12kN, after which cracking progressed along the beam as shown in Figure 8.167. Deep inclined cracking between the applied load and the roller support (left hand side in the photos) was recorded initially at 27kN, with this crack growing in size up to the maximum applied load of 49.5kN.

The beam held its maximum load of 49.5kN from a midspan displacement of 17mm up to 42mm (Figure 8.173), after which significant inclined cracking in the web (Figure 8.167(e)) was recorded and the load capacity dropped to 39kN (Figure 8.173). This load was held by the beam for a short time but under increasing displacement the inclined web cracks propagated and final failure was recorded as horizontal cracks formed in the top face of the beam (Figure 8.167(f)) and propagated through the compression zone. The beam displayed a maximum displacement of 93.3mm (LVDT T1, Figure 8.165) under the point load and 85.0mm at the midspan (LVDT T3).

After failure the beam was removed from its loading frame and the partially resin coated CFRP grids were inspected. The major failure was found to have occurred both within and outside the CFRP reinforced area (Figure 8.169(l)). Vertical CFRP tows were found to have snapped, with individual CFRP fibres now visible in areas without resin coating (Figure 8.169(r)).

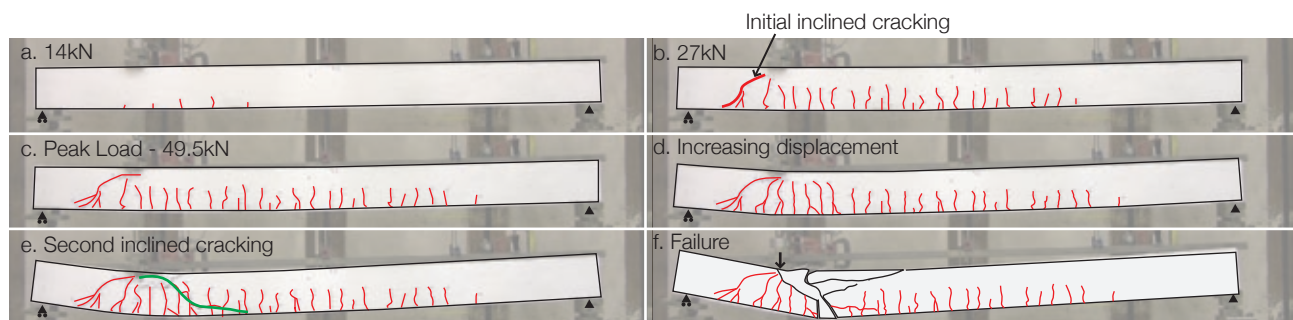


Figure 8.167: Crack progression in Beam 10\_2.

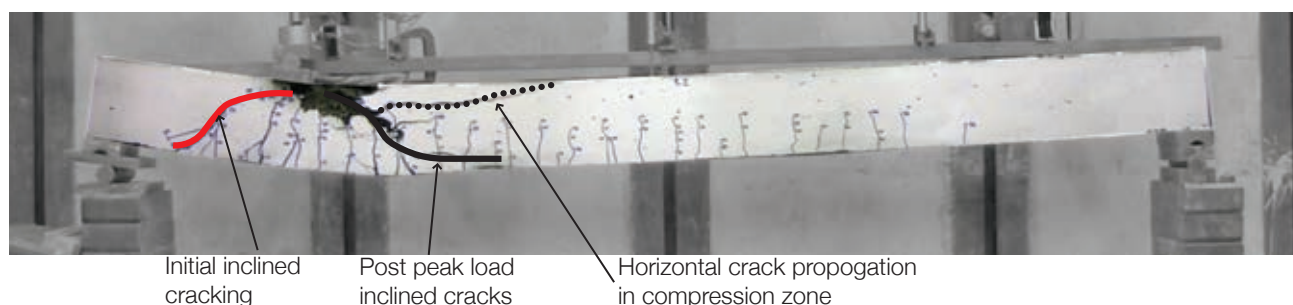


Figure 8.168: Significant cracking in Beam 10\_2 after the peak load.



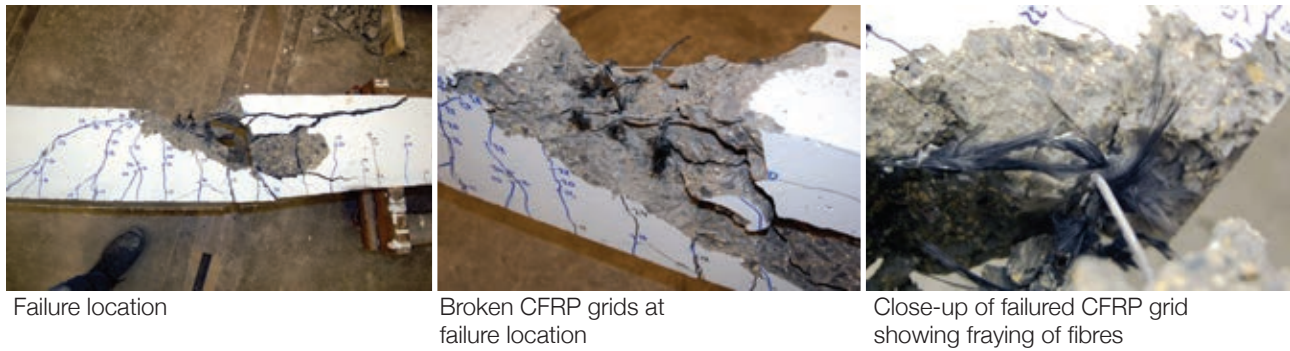


Figure 8.169: Failure of the partially coated CFRP grids in Beam 10\_2.

#### 8.6.5.3. Beam 10\_1

Beam 10\_1 (fully resin coated grids) was tested in the same manner as Beams 10\_2 and 10\_3. Initial cracking was recorded at 8kN, after which distributed cracking along the length of the beam with increasing load was recorded (Figure 8.170). The cracks propagated in a vertical direction until an applied load of 30kN was recorded, at which point those cracks between the point load and the roller support began to curve towards the point load (Figure 8.170(b)). A deep inclined crack formed at around 37kN, and propagated slightly up to the maximum applied load of 52.0kN (Figure 8.170(c)).

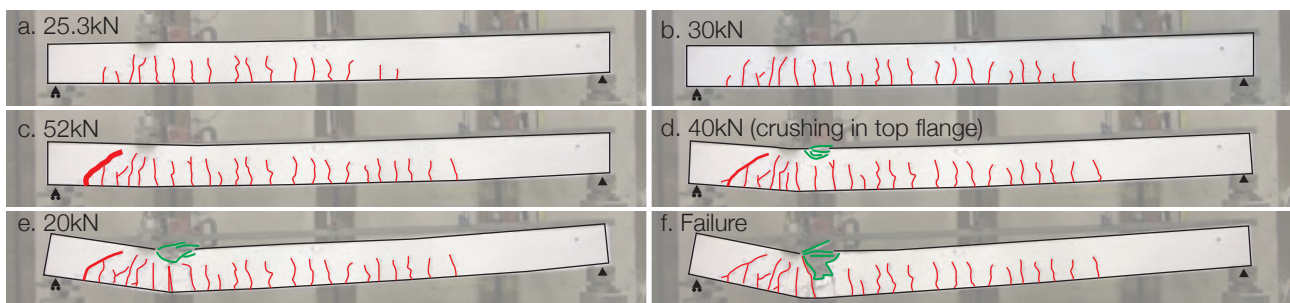


Figure 8.170: Crack progression in Beam 10\_1.

The beam displayed some deformability at this maximum load (Figure 8.170), reaching a midspan displacement of 29mm before losing some load. A second plateau at 39kN was then held by the beam and under increasing displacement inclined cracks formed in the web, existing cracks opened up and crushing of the top flange was observed (Figure 8.170(d)). The load was held up to a midspan displacement of 53mm, after which the capacity of the beam gradually dropped off and failure was recorded at a maximum midspan displacement of 71.1mm (Figure 8.170(f)).

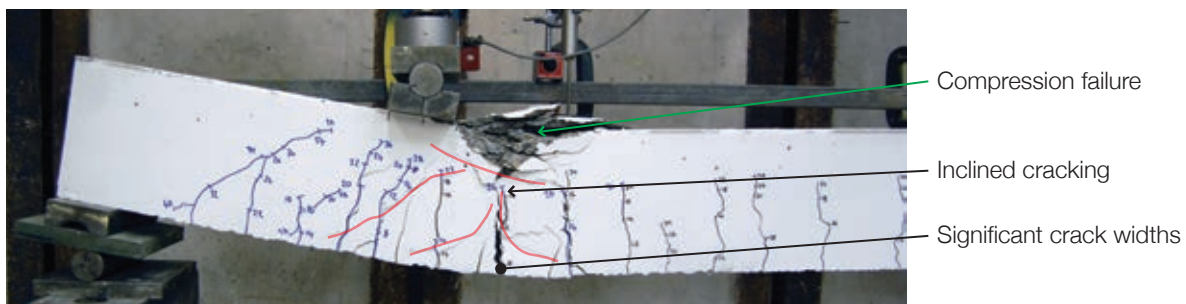


Figure 8.171: Significant cracking and post-peak behaviour in Beam 10\_1.

The beam was removed from its loading frame and resin coated CFRP grids were inspected. The grid was found to have failed in a number of vertical and horizontal tows, with the resin coated elements failing as shown in Figure 8.172. The fibres are not visible as they are entirely coated in resin. The CFRP grid was found to have effectively confined the internal concrete, that had then been crushed during loading, such that light tapping of the unloaded beam allowed a significant proportion of the internal concrete to fall through the CFRP grids (Figure 8.172(r)).

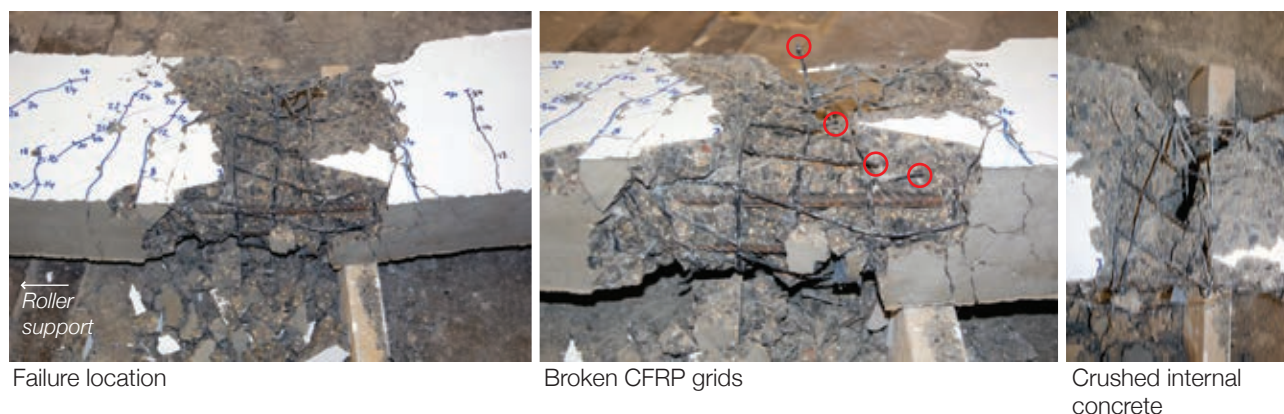


Figure 8.172: Failure of the CFRP grids.

#### 8.6.6. Discussion

Beam 10\_3 failed in shear at  $P = 35.8\text{kN}$ , an increase of 23% above the predicted failure load of  $29\text{kN}$ . Beam 10\_1 and Beam 10\_2 achieved higher peak loads of  $P = 49.5\text{kN}$  and  $P = 52.0\text{kN}$  respectively, with ultimate failure being a combination of shear-flexure. The ultimate capacity of both 10\_1 and 10\_2 was greater than the load corresponding to the flexural capacity of the steel reinforced section ( $P = 39\text{kN}$ ).

It is notable that both Beam 10\_1 and Beam 10\_2 exhibited deformability at their peak load - a peak displacement under the loading point of  $40\text{mm}$  for beam 10\_1 and  $33\text{mm}$  for Beam 10\_2 was recorded. Beyond this point the beams do not exhibit real deformability, as the tests were undertaken in displacement, rather than load, control. The full load-deflection plot for the test is, however, included in Figure 8.173 for completeness.

Beams 1 and 2 showed considerable inclined shear cracks prior to failure (Figure 8.174) but ultimately failed by crushing in the top face of the section. Failure of Beam 10\_1 was confined to a zone of approximately  $100\text{mm}$  in width while in Beam 10\_2 multiple large cracks formed to the right of the point of load application.

The apparent increase in load capacity over the theoretical predictions seen in Beams 10\_1 and 10\_2 may be partly attributed to the behaviour of the FRP-confined concrete (as discussed for steel reinforced sections in BS EN 1992-1-1 (2004)), and post-failure assessment of the sections revealed a considerable degree of crushing of the confined concrete which adds weight to this idea. Further capacity increases may also have arisen from the additional flexural capacity provided to the section by carbon fibre tows lying in the longitudinal direction of the beam. In addition the yield strength of the steel, assumed as  $550\text{N/mm}^2$  for design purposes, may have been exceeded in the test section.



In Beams 10\_1 and 10\_2 the increase in load capacity of the section was equivalent to a tensile force of 11kN applied at an effective depth equal to the steel reinforcement, and such a force may have been generated by just three of the CFRP tows in the longitudinal direction.

The subsequent drop in beam capacity from this peak value to the predicted flexural capacity of the section (as shown in Figure 8.173) represents the point at which the sections saw their second major cracking and the onset of crushing in the compression zone, which may have combined with strain failure (due to high displacements) of the CFRP grids at the same position, accompanied by stress redistribution in the concrete section. As the tests did not have strain gauges located on the CFRP grid it is difficult to more accurately determine the behaviour of the section, but these results do suggest that the CFRP grid may be used as both shear and flexural reinforcement in future tests.

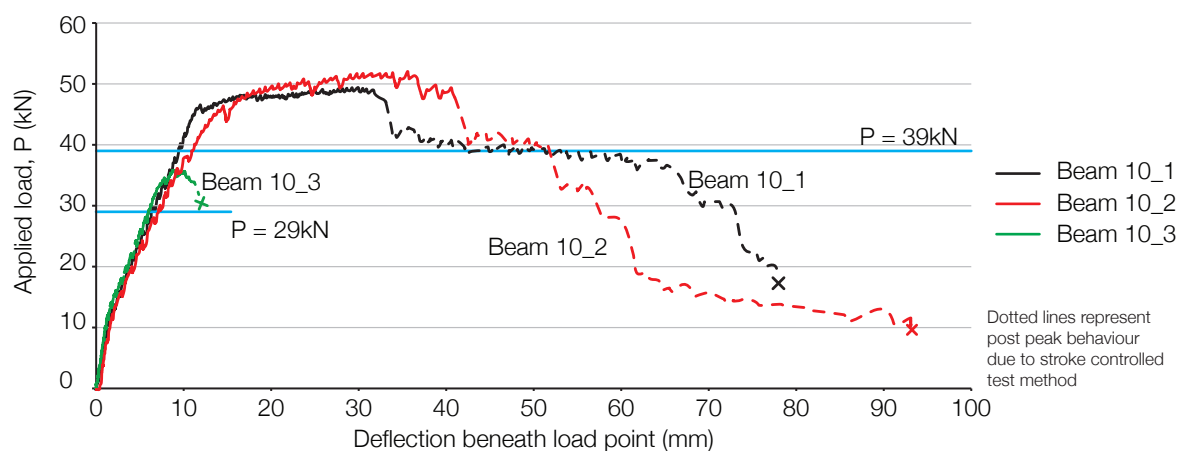


Figure 8.173: Load-displacement results.

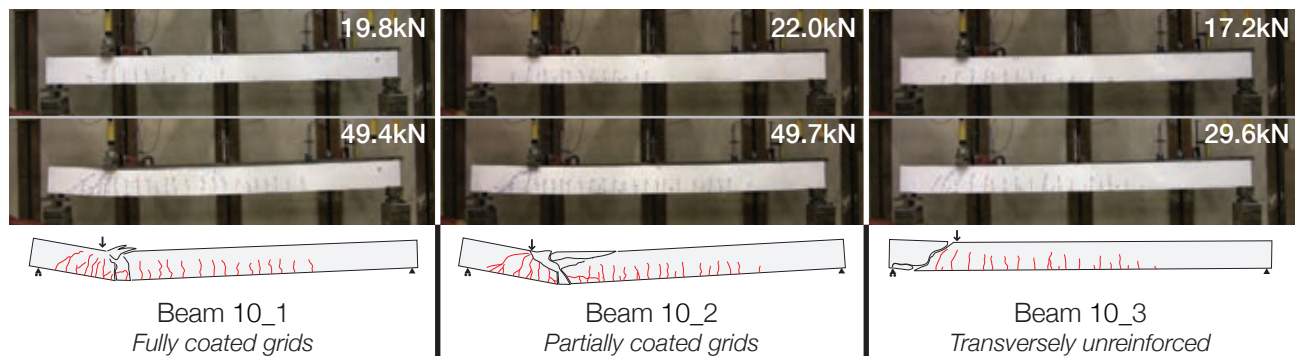


Figure 8.174: Summary failure diagrams.

### 8.6.7. Conclusions

In this section, advanced composites have been demonstrated for use as shear reinforcement in concrete beams reinforced in flexure using ductile deformed steel bars. Given that fibre reinforced polymer bars are relatively inefficient when used as passive flexural reinforcement due to their high strains (Burgoyne, 2001), such an approach is an attractive and logical proposition. Two methods for the fabrication of CFRP reinforcement have been demonstrated, wherein the use of partially bonded grids was seen to provide significant advantages in reducing construction time and complexity.

However, since Beam 10\_1 and Beam 10\_2 failed in a combination of flexure and shear further work is required to assess the full effect of the resin coating on the behaviour of the beams. Such tests would further help to verify the combined use of the ACI 440 (2006) and BS EN 1992-1-1 (2004) models for concrete structures reinforced in shear with fibre reinforced polymers.

The use of carbon fibre grids may now be considered in conjunction with fabric formwork. Here, partially bonded flexible grids hold significant advantages as they may simply be draped around the flexural reinforcement to take up the optimised shape of the surrounding fabric form. Such an approach would greatly simplify the transverse reinforcement of variable section members, making them more economical to construct.

In addition, it may be possible to utilise the longitudinal tows of the carbon fibre grid as flexural reinforcement in place of steel bars, thus facilitating the complete reinforcement of an optimised beam with one sheet of carbon fibre grid. Further work is required to demonstrate this concept.

Using fabric formwork to create an optimised external geometry in combination with steel flexural reinforcement and advanced composite grids as transverse reinforcement may facilitate the construction of materially efficient, low carbon concrete structures. Such an approach may help to precipitate the more widespread use of fabric formwork.

## 8.7. Conclusions

To support the argument that fabric formwork can be used to facilitate a sustainable future in concrete construction, two important steps have been made. In Chapter 6 it was demonstrated that fabric formwork may be used in the construction of optimised concrete structures whose dominant loading was in flexure. Addressing previous deficits in the knowledge and analysis of the shear behaviour of non-prismatic concrete structures, Chapter 8 has sought to demonstrate how their design in shear may be achieved.

The results of this Chapter have shown that control of the compression path as it moves through the optimised concrete beam is of primary importance. Using either a compressive force path or a new strut and tie model based approach, conservative designs have been achieved for structures loaded primarily in shear. The results of this test series have been supplemented and reinforced by innovative analysis of the tapered beam sections using digital image correlation.

Providing a suitable design method for optimised concrete structures requires that construction aspects have also been addressed. In light of this, initial steps towards the provision of advanced composite reinforcement in place of conventional steel reinforcement have been made. The additional design implications of such a move have been recognised, and it is likely that metallic reinforcement will remain the primary method of reinforcement in fabric formed concrete structures at the present time.

Advances in structural analysis and behaviour, revealed in both Chapter 8 and in Chapter 6, demonstrate the advantages of fabric formwork. In addition to the material use reduction benefits provided by fabric formwork, it is recognised that concrete cast in permeable moulds can provide significant concomitant benefits to the structure in terms of its whole life performance.

In light of the holistic approach to fabric formwork that has been taken throughout this thesis, and to demonstrate that sustainable design must consider not only reductions in material use at the point of design, but also the provision of durable concrete structures that will remain serviceable throughout their design life, the following Chapter presents the results of a program of accelerated durability testing. Chapter 9 will demonstrate that significant improvements in the life-cycle durability of fabric cast concrete can be achieved, adding additional weight to the central thesis that fabric formwork provides a method by which sustainable concrete construction can be achieved.

[blank page]





# Chapter 9 Development (3)

## Durability enhancement

### 9.1. Introduction

The advantages of a controlled permeability formwork system were initially introduced in §2.6 on page 35, where improvements in concrete properties and surface durability were described. This Chapter describes a series of tests undertaken to determine how the use of fabric formwork can provide a comparable outcome, as summarised in Table 9.1. The concrete mix described in Table 9.2 was used in all tests. A marine geotextile (Table 9.3) was used in the majority of the tests (and was also used in the beam tests described in Chapter 6). Two further fabrics described in Table 9.27 on page 395 were used as comparators to this fabric in Test Groups 3 and 4.

Table 9.1: Summary of tests in Chapter 9.

Test Group	Reference	Description
1	§9.2 on page 344	Rate of carbonation (comparing steel and fabric cast surfaces)
2	§9.3 on page 350	Resistance to chloride ingress (comparing steel and fabric cast surfaces)
3	§9.4 on page 364	Sorptivity testing (comparing steel and fabric cast surfaces)
4	§9.5 on page 373	Scanning electron microscopy imaging and elemental analysis
5	§9.6 on page 390	Surface hardness (comparing timber and fabric cast surfaces)

Table 9.2: Concrete mix per  $m^3$ , durability tests.

Cement (CEM IIbv)	Tap Water	Aggregate 0-5mm	Aggregate 5-10mm
450kg	180kg	531kg	1239kg

Table 9.3: Fabric properties.

Name	Material		Tensile Strength		Elongation		Pore Size
	Warp	Weft	Warp	Weft	Warp	Weft	
Marine Geotextile	Polyester (1100 dtex)		54kN/m		25%		423 $\mu$ m



## 9.2. Test Group 1 - Carbonation

Internal steel reinforcement in concrete structures is primarily protected from corrosion by the high alkalinity of concrete. Carbonation of the concrete mix, precipitated predominantly by the presence of carbon dioxide in the atmosphere, reduces the alkalinity of the concrete through the conversion of calcium hydroxide ( $\text{Ca}(\text{OH})_2$ ) in the cement paste to calcium carbonate ( $\text{CaCO}_3$ ) and water, as described in principle by Eq. 9.1. Carbonation occurs primarily by gaseous diffusion through air filled pores, and is often described using Fick's law (Steffens *et al.*, 2002, Papadakis *et al.*, 1991), as applied to the data collected in this thesis in §9.2.3 on page 346.



To determine the resistance of concrete to carbonation over its service life accelerated testing can be undertaken by exposing samples to an atmosphere of elevated carbon dioxide levels. Test methods vary from BS EN 13295 (2004) which recommends a 1%  $\text{CO}_2$  concentration, to a TFB<sup>1</sup> '*Bulletin du Ciment*' (1988, cited by Dunster, 2000) which uses a 100% carbon dioxide concentration. By comparison atmospheric carbon dioxide is currently estimated at 392 parts per million (Tans, 2010), or 0.039% of the atmosphere by volume, demonstrating the accelerated nature of such methods.

Previous work, outlined in Chapter 2, has suggested that carbonation depths can be reduced for concrete cast against permeable formwork. To determine and verify the extent to which this is true for fabric formwork a series of tests were carried on 100mm concrete cubes, using the accelerated test method described below.

### 9.2.1. Test method

The carbonation test undertaken is based on the NordTest NT BUILD 357 (1989) method. Cubes of 100mm side length were cast in the moulds shown in Figure 9.1(l), which allow the relative carbonation of fabric and steel cast concrete to be determined experimentally.

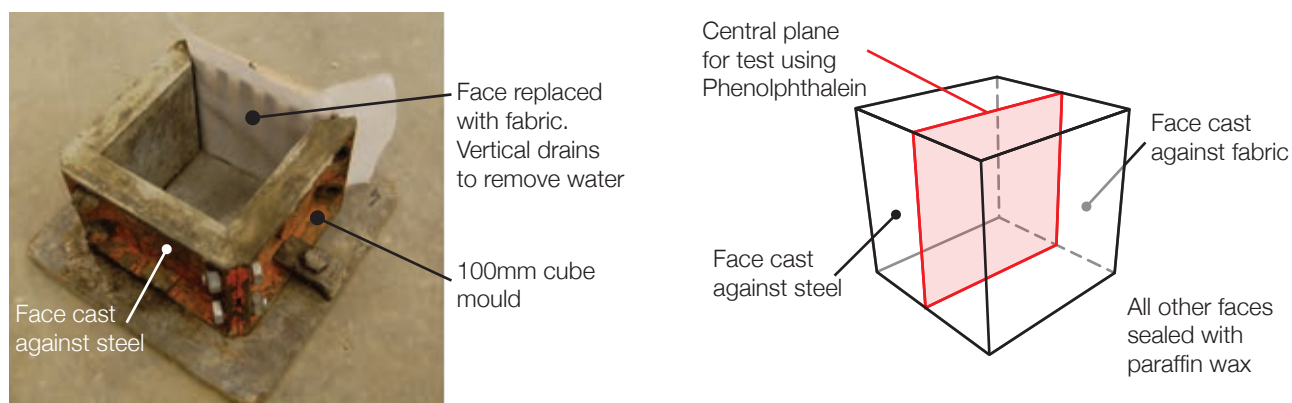


Figure 9.1: Modified cube mould.

The specimens were stripped 24 hours after casting, and cured in water ( $20^\circ\text{C} \pm 2^\circ\text{C}$ ) for 14 days, before being cured in air of  $50 \pm 5\%$  relative humidity,  $20^\circ\text{C} \pm 2^\circ\text{C}$  until 28 days, after which they were subjected to the carbonation test. Four sides of the cube (Figure 9.1(r)) were coated in paraffin wax, before the specimens were exposed to an

<sup>1</sup> Swiss '*Technische beratung für forschung und beton und zement*' (Technical Research and advice for cement and concrete), [www.tfb.ch](http://www.tfb.ch)

atmosphere containing 4% carbon dioxide with a relative humidity of between 55 and 65% by placing them in a carbonation chamber. The available literature (Jones *et al*, 1999 and Ho and Lewis, 1987, both cited by Dunster, 2000) suggests that under such a regime, one week in the carbonation chamber is equivalent to one year in natural indoor exposure conditions.

Carbonation depths were then recorded at 7, 14, 28, 90 and 180 days after placement in the carbonation chamber. Carbonation depths were recorded by first breaking the cube down its central plane by placing it in a compressive test machine between two metal bars (Figure 9.2(l)). The exposed surface of each cube half was then sprayed with a Phenolphthalein solution (1g Phenolphthalein in a solution of 500ml distilled water and 500ml ethanol) to reveal the extent of carbonation at each test stage. Carbonation depths on the face cast against fabric and the face cast against steel were recorded at four points along the exposed surface using callipers.

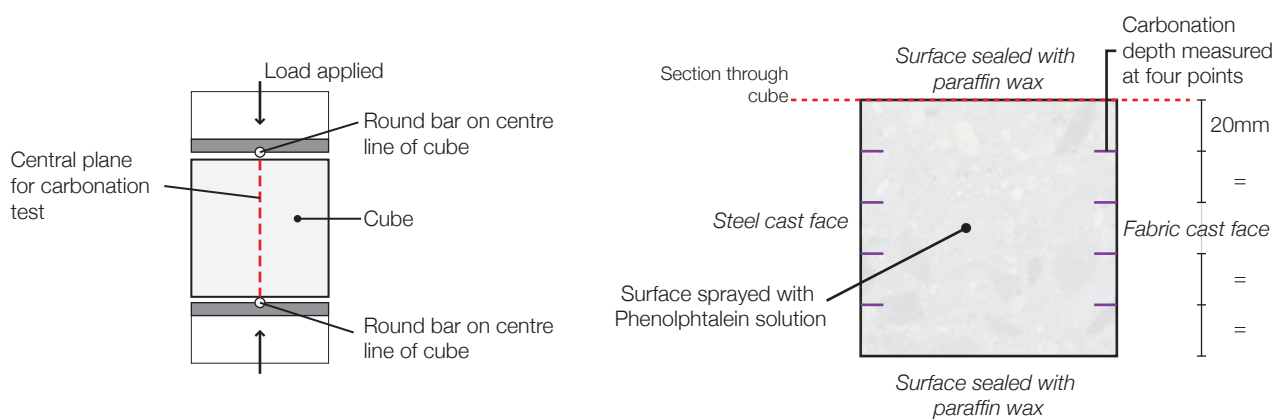


Figure 9.2: Cubes splitting method (l); and carbonation depth measurements (r).

A total of 15 cubes were tested and a further 6 cubes were cast and cured in the same manner to provide a reference 28 day compressive strength. The concrete mix used in all tests is described in Table 9.2.

### 9.2.2. Results

A summary of the carbonation depth measurements are provided in Table 9.4 on page 346. Photographs from each stage of testing are shown in Figure 9.3 and the results are presented graphically in Figure 9.5. The concrete mix used had an average compressive strength at 28 days of 45.3MPa. A further cube exposed to normal atmospheric carbon dioxide levels was further tested at 180 days, with the results of this being used to demonstrate the accelerated nature of this test series (Figure 9.4).

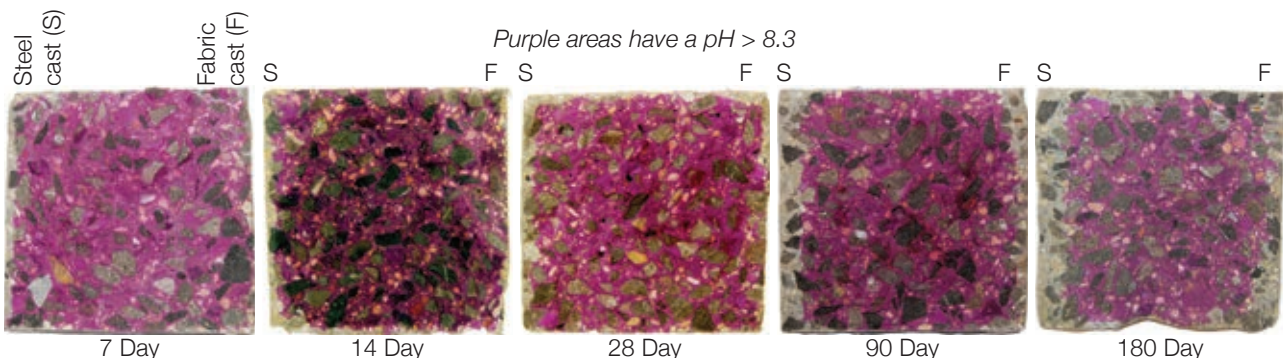


Figure 9.3: Carbonation depth examples at each testing stage.



Figure 9.4: Comparison between samples exposed for 180 days to a 4%  $\text{CO}_2$  environment and samples exposed for 180 days to atmospheric  $\text{CO}_2$  levels.

Table 9.4: Summary of carbonation depths.

Age	(1) Steel average carbonation depth (mm)	(2) Fabric average carbonation depth (mm)	Percentage change (1) to (2).
7 days	3.38	1.58	-53%
14 days	3.52	1.35	-62%
28 days	5.85	1.81	-69%
90 days	9.00	4.87	-46%
180 days	12.70	6.65	-48%

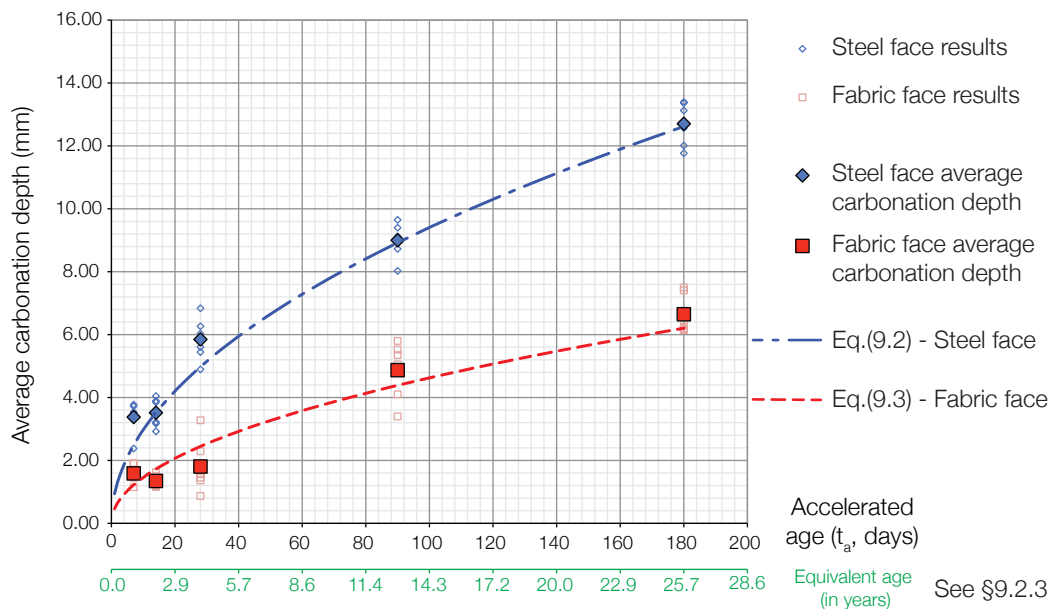


Figure 9.5: Carbonation depth results summary.

### 9.2.3. Analysis

The process of concrete carbonation is governed by the calcium hydroxide content of the concrete, in the manner described by Hunkeler (2005), since this predominantly defines the pH of the concrete. In turn, the pH is the primary factor in defining the potential for steel corrosion, since protection is only provided at pH values of greater than around 11 (Hunkeler, 2005). It is therefore critical from a durability perspective to be able to predict when this corrosion will begin.

Many of the available models for the prediction of concrete carbonation depth with age (Papadakis *et al.*, 1992; Liang *et al.*, 2002, Hunkeler, 2005) can be summarised by Eq. 9.2. The same form is taken in chloride ingress and sorptivity calculations, as presented in §9.3 on page 350 and §9.4 on page 364 respectively. The coefficient 'B' chosen in this analysis encompasses a range of variables and analytical methods that are beyond the scope

of this investigation. For example, Steffens *et al* (2002) and Saetta and Vitaliani (2004) present further models that incorporate the effects of heat, moisture and gas (primarily CO<sub>2</sub>) flows through concrete to provide a more detailed analytical model of the carbonation process and its prediction. To demonstrate the applicability of the  $t^{0.5}$  approach, the results presented in Figure 9.5 are redrawn in Figure 9.6 with a 'root time' x-axis, a common approach seen in the literature.

$$C_a = B\sqrt{t_a} \quad \text{Eq. 9.2}$$

Where  $C_a$  is the in situ depth of carbonation in mm;  $B$  is the coefficient of carbonation;  $t_a$  is the accelerated exposure time in days.

From the results presented in Table 9.4, two equations were determined to compare and predict the rate of carbonation in steel and fabric cast concrete members and are given by Eq. 9.3 and Eq. 9.4 respectively. Values for the coefficients of carbonation  $B_{\text{steel}}$  and  $B_{\text{fabric}}$  have been calculated by the linear relationships ascertained from Figure 9.6 and are given in Table 9.5 below, wherein a reduction in this coefficient of 50.1% is seen for concrete cast against fabric formwork.

$$C_{a,\text{steel}} = B_{\text{steel}}\sqrt{t_a} \quad \text{Eq. 9.3}$$

Where  $C_{a,\text{steel}}$  is the average accelerated carbonation depth in mm for concrete cast against a steel face at the accelerated age  $t_a$  days;  $B_{\text{steel}} = 0.968$

$$C_{a,\text{fabric}} = B_{\text{fabric}}\sqrt{t_a} \quad \text{Eq. 9.4}$$

Where  $C_{a,\text{fabric}}$  is the average accelerated carbonation depth in mm for concrete cast against a fabric face at the accelerated age  $t_a$  days;  $B_{\text{fabric}} = 0.483$

Table 9.5: Calculated values of the coefficient of carbonation.

Coefficient	Calculated value	
$B_{\text{steel}}$	0.968	
$B_{\text{fabric}}$	0.483	Saving 50.1% over $B_{\text{steel}}$

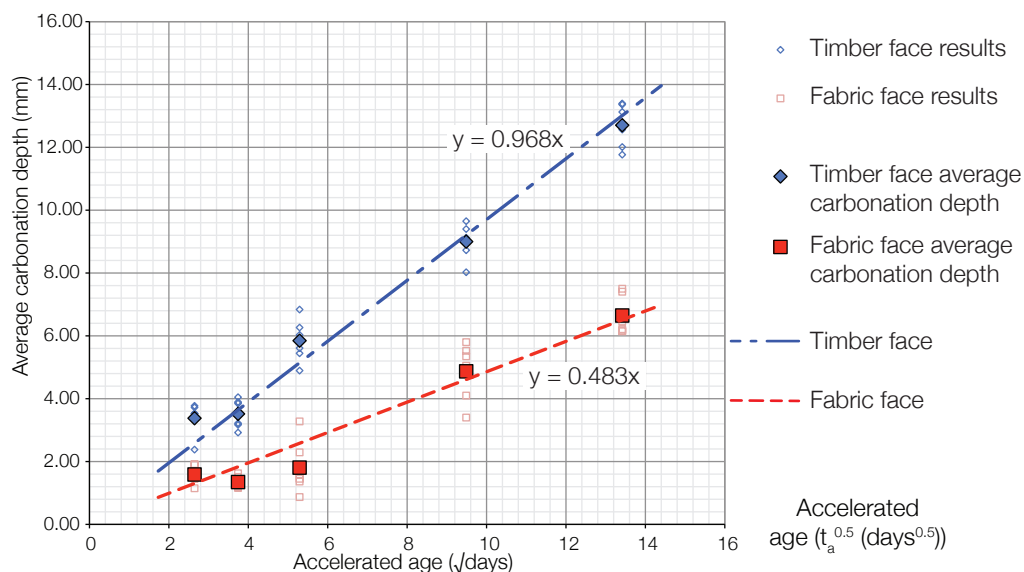


Figure 9.6: Carbonation depth results plotted against the square root of time.

Where estimated in-situ carbonation depths are required, Eq. 9.3 and Eq. 9.4 should be modified to account for the accelerated nature of the tests. The correlation between the test conditions and the in-situ behaviour of concrete has been described above and is incorporated in this analysis by the ratio  $\eta$ , described by Eq. 9.5, which estimates that one week in a 4% CO<sub>2</sub> environment is equivalent to one year under atmospheric conditions. The in-situ carbonation depths for steel and fabric faces are thus modified to give Eq. 9.6 and Eq. 9.7. This proposed correlation has been plotted beneath the results presented in Figure 9.5 on page 346.

$$\eta = \frac{\text{Accelerated days}}{\text{In-situ days}} = \frac{7}{365.25} \quad \text{Eq. 9.5}$$

$$C_{i, \text{steel}} = B_{\text{steel}} \sqrt{(\eta)t_i} \quad \text{Eq. 9.6}$$

Where  $C_{i, \text{steel}}$  is the average estimated in-situ carbonation depth in mm for concrete cast against a steel face at the age  $t_i$  days;  $B_{\text{steel}} = 0.968$

$$C_{i, \text{fabric}} = B_{\text{fabric}} \sqrt{(\eta)t_i} \quad \text{Eq. 9.7}$$

Where  $C_{i, \text{fabric}}$  is the estimated in-situ carbonation depth in mm for concrete cast against a fabric face at the age  $t_i$  days;  $B_{\text{fabric}} = 0.483$

From the analysis undertaken, a simple extrapolation of Eq. 9.5 and Eq. 9.6 may be undertaken for each concrete condition up to a service life of 80 years. Since the relationship of Eq. 9.2 is a linear one, the fabric cast face will continue to have an estimated carbonation depth 50% less than that found in the steel cast sample (calculated values of 22.9mm versus 11.4mm).

However, work by Martin *et al* (1975) and Kropp and Hilsdorf (1995) has suggested that the simple ' $\sqrt{t}$ ' law will over estimate the depth of carbonation over significant time periods as the rate of carbonation tends to slow over time. The exact influence of this process is not yet known in sufficient detail, but future publications may provide an alternative relationship to extrapolate the test data presented above beyond the available test dates.

#### 9.2.4. Conclusions

Accelerated carbonation testing was carried on specially prepared cubes with a maximum exposure time of 180 days, estimated to represent an in-situ structure after 25 years service life. The results presented above show considerable improvements in resistance to carbonation.

After 180 days, the fabric cast surface had a carbonation depth 48% less than its equivalent steel cast surface, and a coefficient of carbonation of 50% less than the steel cast surface. These results are quite remarkable and suggest that fabric cast concrete may have a durability against carbonation of almost double that of its conventionally cast counterpart. Alternatively, fabric cast concrete may be used to provide concrete structures with reduced cover distances that retain the same service life as one with a larger cover cast against an impermeable mould.

Whilst the coefficient of carbonation determined above is useful to provide comparisons between the two sets of data, further work is now required to determine how factors such as the water-cement ratio, aggregate-cement ratio, concentration of carbon dioxide, temperature and relative humidity during testing influence the value of this

coefficient. By testing a range of concrete strengths and fabric types, more complete guidance for designers may be developed.

The correlation between in-situ and accelerated test conditions is by no means certain, and the method used in the above analysis may be amended in light of new developments in any future publications. Carbonation tests on a 1960s reinforced concrete frame building with an average concrete compressive strength of 35MPa, obtained by the author as part of a separate study carried out for Atkins, found a maximum carbonation depth for internal structural elements of just 5mm. This would suggest that the correlation used above is conservative (assuming  $B_{steel}$  remains the same, the model given in Eq. 9.5 would suggest that the structure is only 4 years old).

It is not necessarily possible to extrapolate the results presented in this section for carbonation tests on small cubes to the behaviour in a large scale building structure, and this area will require further work before final conclusions can be drawn.

The data presented above suggests that even for a concrete cast against an impermeable mould the depth of carbonation after 80 years may be less than 25mm. Given that cover depths to reinforcing steel are usually in the order of 30-40mm, this would appear to suggest that there is little to be gained in the use of a permeable mould. However, the capacity of cement to bind chlorides (as described in §9.3) is also influenced by the degree of concrete carbonation. Carbonated cement pastes were found by Zibara (2001, cited by Yuan *et al.*, 2009) to have minimal binding capacity, resulting in more free chlorides whose primary impact is to initiate corrosion of internal reinforcement. Therefore, it is suggested that the protection afforded against carbonation by a permeable mould further helps to reduce the effects of chloride ingress on the concrete and its reinforcement. The effect of chloride ingress on fabric cast concrete is explored in more detail in the following section.



### 9.3. Test Group 2 - Chloride ingress

Similarly to carbonation, chloride ingress into concrete can have a significant impact on the durability of steel reinforced concrete structures as it increases the rate at which steel reinforcement corrodes by 1) destroying the passive layer of the reinforcement, 2) reducing the pore water pH, 3) increasing the internal moisture content through the hygroscopic nature of salts in concrete and 4) increasing the electrical conductivity of the mass concrete (Hunkeler, 2005).

Although Calcium Chloride ( $\text{CaCl}_2$ ) was used as an accelerating agent in the 1960s, increased steel corrosion led to a limit being placed on the anhydrous calcium chloride that could be present in concrete containing embedded steel, effectively banning the use of  $\text{CaCl}_2$  as an admixture in concrete. At present, BS EN 206-1 (2000) continues to recognise the importance of chloride content and specifies the allowable chloride contents in the concrete mix depending on a range of parameters. Thus, whilst there is no longer a significant risk of corrosion from chlorides within the concrete mix, environmental sources of chlorides, including de-icing salts and salt water, remain a threat.

The mechanisms of chloride ingress and its relationship with carbonation behaviour (as described in §9.2) is explored below. Following this the method and results of an accelerated testing regime are presented, in which the relative resistance of fabric and steel cast concrete to chloride ingress was investigated.

#### 9.3.1. Mechanisms

When unsaturated concrete is exposed to a chloride solution, it is absorbed into any unfilled spaces in the surface by capillary action (Bamforth and Price, 1997). Upon drying, water in the chloride solution evaporates, leaving the salts behind, which then build up over time until a stable surface level of chlorides is reached (Oshiro *et al.*, 1987, cited by Bamforth and Price, 1997). In addition to this surface build up, chloride ions migrate into the concrete through diffusion in the pore water.

The role of chlorides in concrete is complex, and not all chlorides are available to act as corrosion initiators (Glass and Buenfeld, 2000). Some chlorides present in a concrete mix are 'bound' to the cement matrix (particularly to the aluminates), while others are 'free' and are dissolved in the interconnected pores (Martin-Perez *et al.*, 2000). The 'binding capacity' of a particular concrete mix is dependent on its cement and mineral composition and a high binding capacity reduces both the rate of chloride ion transport through the concrete and the amount of free chlorides that then are able to initiate corrosion at the steel (Nilsson *et al.*, 1994). Cement binding also produces 'Friedel's Salt' (Yuan *et al.*, 2009), the structure of which retains chlorides, and the formation of which results in a less porous concrete structure - thus helping to further retard the transport of chlorides (Yuan *et al.*, 2009).

The amount of bound and free chlorides is not constant and can change over the life of a structure, and a significant source of such changes is carbonation. Reductions in concrete pH that arise from carbonation result both in the release of previously bound chlorides (by increasing the solubility of Friedel's Salt, which is then able

to release chlorides to act as corrosion initiators, as described by Suryavanshi and Narayan-Swamy (1996)) and the prevention of further chloride binding due to decomposition of the calcium silicate hydrate (CSH) resulting in there being fewer sites for binding to occur (Yuan *et al.*, 2009). Carbonation can therefore have a doubly negative impact on durability, and thus the importance of the results shown in §9.2 on page 344 is reiterated.

The mechanisms of transportation of chloride ions through the concrete section depend primarily on the exposure conditions, and there is usually more than one process involved. For sections that are entirely submerged (for example in-situ structures below low tide level, or in the accelerated tests described below), the primary chloride transport mechanism is by diffusion (CCAA, 2009). In such situations, Fick's second law of diffusion (Eq. 9.8) is generally used to describe the diffusion of the chloride ions, with an analytical solution to this equation being used in §9.3.4 (Eq. 9.10). This mechanism of chloride ingress is studied in the following sections, others (including capillary suction, absorption, adsorption, desorption and migration (as described by CCAA, 2009) are not studied here.

$$\frac{\partial C}{\partial t} = D \frac{\partial^2 C}{\partial x^2} \quad \text{Eq. 9.8}$$

Where  $C$  is the chloride concentration ( $\text{mol/m}^3$ ),  $t$  is time (secs),  $D$  is the diffusion coefficient ( $\text{m}^2/\text{s}$ ) and  $x$  is the position ( $\text{m}$ ).

Once chloride ions reach the steel layer, they begin to influence the formation of the passive oxide film that forms around steel reinforcement (Bamforth and Price, 1997). In chloride unaffected concrete, this oxide film is continually replenished by hydroxyl ions in the pore water. In the presence of even very low chloride ion concentrations, the rate of break down of the oxide film begins to increase up until a point at which the chloride ions reach a 'threshold layer' of concentration within the pore water and significant corrosion begins (Bamforth and Price, 1997). Beyond the threshold level, it has been seen that the rate of corrosion increases as the concentration of free chloride ions increases.

Although much work has been undertaken to assign a value to this critical chloride concentration threshold, its dependence on a wide range of variables (including cement type, water content and exposure conditions) has resulted in a significant spread of test data (Moreno *et al.*, 2004). In addition, the corrosion process is understood only through complex statistical approaches that depend on a random distribution of pores and particles in the concrete matrix and surface defects on the steel reinforcement (Breit, 1997, cited by Hunkeler, 2005).

Changes in the surface permeability of concrete cast in permeable moulds may be beneficial in increasing the chloride resistance of the surface zone and to assess the behaviour of fabric formed elements under chloride ingress a series of accelerated tests were carried, as described in §9.3.2.

### 9.3.2. Test method

To determine the relative resistance to chloride ingress of concrete cast against steel and against fabric, a series of accelerated tests were undertaken using the method described in NordTest 443 (1995) and the DD ENV 12390-11 (2010). The test results of three cylinders cast in conventional steel moulds, and four cylinders cast in fabric moulds were compared after exposure to Sodium Chloride (NaCl) for the durations described in Table 9.6. To achieve a fabric cast face, the bottom of a cylinder mould was replaced as shown in Figure 9.7.

Table 9.6: Chloride ingress test date summary.

Series	Mould Type	NaCl Exposure duration	Number of samples
A	Steel	53 days	2
B	Steel	90 days	1
1	Fabric	53 days	2
2	Fabric	90 days	2



Figure 9.7: Cylinder mould for Chloride Ingress test.

The chloride test is undertaken by exposing one plane of a concrete cylinder to a sodium chloride solution. After a specified period of time, layers of the concrete surface are removed and the chloride content ( $C_x$ ) of each layer measured. These results are compared to the initial chloride content of an unexposed sample of the same concrete ( $C_i$ ). The non-steady state chloride diffusion coefficient,  $D_{nss}$ , and the boundary condition of the chloride profile at the surface,  $C_s$ , are then calculated considering both the depth of the slice below the surface and the measured chloride content of that slice (DD CEN 12390-11, 2010). Analysis was undertaken using the process described in NT Build 443 (1995) to determine a value for a penetration parameter,  $K_{Cr}$ , which is used to compare sets of test results.

#### 9.3.2.1. Procedure

Seven concrete cylinders were cast using the mix shown in Table 9.2 on page 343. 100mm cubes were cast to provide a reference compressive strength of the concrete at each testing stage. The cylinders were demoulded after 24 hours and then air cured for 28 days before being cut in half along a plane perpendicular to the longitudinal axis of the cylinder. One half of the cylinder was used as the test specimen and the other half (named the reference half) was used to provide the reference chloride content,  $C_i$  (see §9.3.2.2).

After curing, the reference cylinder halves were stored in laboratory conditions. The test specimens were immersed in a Calcium Hydroxide ( $\text{Ca}(\text{OH})_2$ ) solution at  $23^\circ\text{C}$  for 24 hours before being weighed. Storage in the  $\text{Ca}(\text{OH})_2$  solution was continued until the change in mass of the cylinder over a period of 24 hours was less than 0.1%. This was typically found to occur within 3-4 days.

After achieving a constant mass, the test specimens were dried at room temperature and pressure, before all faces of the test specimen except that to be exposed to the Chloride Ingress test were coated in paraffin wax (Figure 9.8(r)). Once coated, the test specimen was again immersed in  $\text{Ca}(\text{OH})_2$  until a stable mass was achieved. Upon achieving a stable mass, the test specimen was placed in a solution of Sodium Chloride ( $165\text{g} \pm 1\text{g}$  NaCl per  $\text{dm}^3$  solution) in a temperature controlled bath held at  $23^\circ\text{C}$ , Figure 9.8(l). The storage vessel had a volume of  $0.002\text{m}^3$  and the solution temperature was measured and maintained continually by the storage vessel. Exposure to the NaCl solution lasted for either 53 or 90 days (Table 9.6).

The exposure concentration used was specified in NT Build 443 (1995) and is considerably greater than that recommended by DD CEN 12390-11 (2010), where a concentration of  $30\text{g}$  NaCl per  $0.97\text{dm}^3$  is specified (on the basis that this is approximately equal to the chloride concentration of Atlantic seawater). The NT Build 443 (1995) concentration is 5.34 times greater than this value, which demonstrates the accelerated nature of the test method. Comparisons between the results of these tests and other tests undertaken using DD CEN 12390-11 (2010) should, therefore, not be made.

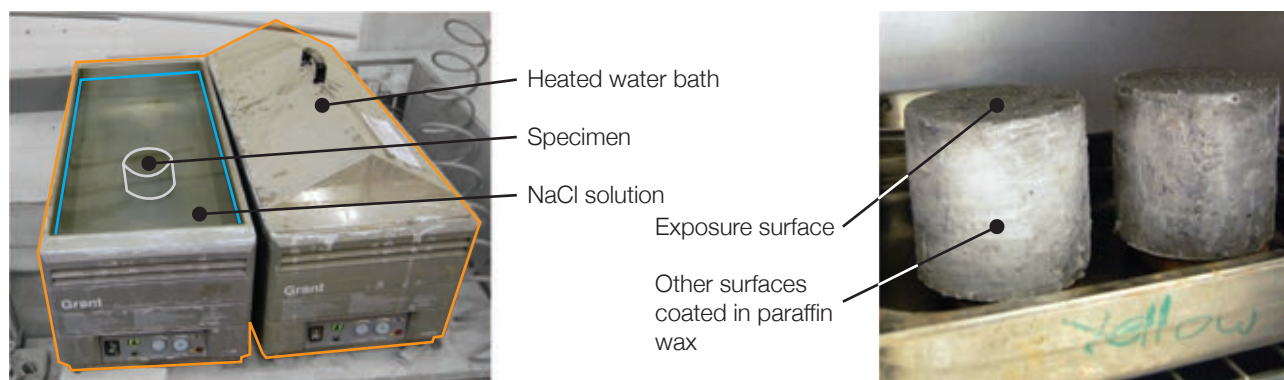


Figure 9.8: Heated water bath (l); Samples coated in paraffin wax (r).

#### 9.3.2.2. Chloride analysis

After the specified exposure time, the cylinders were removed from the NaCl bath and dried at  $105 \pm 5^\circ\text{C}$  for two hours before being placed in a desiccator for one hour to cool to room temperature. Samples were then taken from the concrete surface by dry grinding of the concrete face. Samples were prepared of between 1-5g in mass with a particle size of not greater than 1mm (achieved by sieving).

Samples were taken at 1, 3, 5, 7, 10, 13, 16 and 20mm from the surface to be tested in the exposed half of the cylinder. A separate sample was collected from the reference cylinder half to determine the initial chloride content  $C_i$ . All samples were collected by dry-cutting parallel grooves (at the correct depth) onto the concrete surface and using a hammer and chisel to remove the concrete to the chosen depth as shown in Figure 9.9. Each layer

sample was bagged separately and ground to pass a 1mm sieve, as described above and shown in Figure 9.10. The chloride content of each layer was then determined by Volhards Titration (see also NordTest 208 (1996) or BS EN 14629 (2007)).



Figure 9.9: Concrete sampling process. (l-r) Cutting equipment; sample broken down by depth; grinding.



Figure 9.10: Specimen after sampling (l); Ground samples ready for chloride analysis (r).

The theory of the test is that by adding silver nitrate to a solution with an excess of chloride ions, silver chloride precipitates. This excess of silver chloride is then titrated with a thiocyanate solution and the excess of thiocyanate ions is indicated by the formation of a red-iron(III) complex (giving the solution a weak red colour). The content of chlorides is then calculated as described below. Photographs from the titration process are shown in Figure 9.11.

The mass of all samples was first recorded in grams (to 0.001g) and placed in a 250ml beaker. After wetting with 50ml of water, 10ml of 5mol/l nitric acid and 50ml of hot water were added. The mixture was then heated and boiled for at least three minutes while stirring continuously. The mixture was immediately filtered through medium-textured paper (after which the beaker, stirrer and filter were washed to prevent cross contamination). Five millilitres of silver nitrate solution were added by pipette and the solution was stirred vigorously to precipitate the chlorides.

Five drops of ammonium ferric sulphate indicator solution (100ml of a cold saturate solution of  $\text{NH}_4\text{Fe}(\text{SO}_4)_2$  and 10ml diluted nitric acid) were added to the mixture, which was then titrated with an ammonium thiocyanate solution (0.1mol/l  $\text{NH}_4\text{SCN}$ ) one drop at a time. The volume of ammonium thiocyanate solution used was recorded and the chloride content as a percent of chloride ion by mass of the sample is then given by Eq. 9.9 (a second test on a blank reference sample was also undertaken). The results (§9.3.3) are analysed in accordance with the procedure set out in the draft ENV 12390-11 (2010) in 9.3.4



$$CC = 3.545f \left( \frac{V_2 - V_1}{m} \right) \quad \text{Eq. 9.9}$$

Where  $f$  is the molarity of the silver nitrate solution;  $V_1$  is the volume of ammonium thiocyanate solution used in the titration (ml);  $V_2$  is volume of the ammonium thiocyanate solution used in the blank titration (ml).



Figure 9.11: Analysis process (l-r): Sample weighed; Hot acid extraction of sample; Filtering of extracted sample; Titration with ammonium thiocyanate.

### 9.3.3. Results

The compressive strength results of cubes cast alongside the cylinders to be analysed are presented in Table 9.7. Chloride contents with depth for each test (determined using Eq. 9.9) are given in Table 9.8, with these results being analysed in §9.3.4 on page 357. Whilst there was a small difference in the 90 day compressive strength of the steel and fabric cast samples (~5MPa), it is not felt that this will unduly influence the results of the chloride testing.

However, following the work of Torrent and Jornet (1991), who demonstrated that the compressive strength and oxygen permeability of concrete can be related (with higher strength concrete having a generally lower surface permeability), it would be desirable to carry out further tests to verify these results.

Table 9.7: Correlating compressive strength results.

Series	Age at testing (days)	Cube strength (MPa)	Series	Age at testing (days)	Cube strength (MPa) <sup>1</sup>
A	53	-	1	53	54.0
B	90	46.7	2	90	53.0

Notes: <sup>1</sup> 100mm cube strength given as the average of a minimum of two cube tests undertaken in a universal testing machine.



Table 9.8: Chloride content results by sample.

Sample reference	Increment depth (mm)	Mass of sample	Chloride Cl- by % mass
Series 1, Sample 1 Fabric cast, 53 days	1	0.7	0.777
	3	3.4	0.463
	5	3.4	0.306
	7	2.8	0.200
	10	4.3	0.070
	13	4.3	0.041
	16	3.7	0.010
	20	5.1	0.004
	Initial	35	<0.004
Series 1, Sample 2 Fabric cast, 53 days	1	3.6	0.521
	3	2.5	0.340
	5	4.4	0.185
	7	4.4	0.104
	10	3.9	0.068
	13	2.7	0.026
	16	3.8	0.009
	20	5.6	0.003
	Initial	36.6	<0.003
Series 2, Sample 1 Fabric cast, 90 days	1	1.9	0.691
	3	2	0.405
	5	2.5	0.416
	7	5.6	0.174
	10	2.7	0.143
	13	3.8	0.093
	16	10.5	0.028
	20	9.6	0.007
	Initial	30.4	<0.004
Series 2, Sample 2 Fabric cast, 90 days	1	1.4	0.823
	3	2.9	0.366
	5	3.3	0.266
	7	2.7	0.147
	10	4.2	0.148
	13	4.8	0.099
	16	4.8	0.085
	20	4.6	0.019
	Initial	36	<0.003

Sample reference	Increment depth (mm)	Mass of sample	Chloride Cl <sup>-</sup> by % mass
Series A, Sample 1 Steel cast, 53 days	1	3.0	0.382
	3	2.0	0.361
	5	7.0	0.213
	7	3.0	0.308
	10	3.0	0.238
	13	4.0	0.192
	16	6.0	0.174
	20	6.0	0.064
	Initial	24.0	0.004
Series A, Sample 2 Steel cast, 53 days	1	4.0	0.466
	3	3.0	0.311
	5	4.0	0.230
	7	5.0	0.135
	10	5.0	0.149
	13	4.0	0.147
	16	5.0	0.028
	20	5.0	0.018
	Initial	19.0	0.004
Series B, Sample 1 Steel cast, 90 days	1	2.9	0.694
	3	3.2	0.550
	5	3.9	0.448
	7	3.6	0.411
	10	3.6	0.267
	13	5.1	0.188
	16	6.7	0.128
	20	6.9	0.067
	Initial	23.8	0.004

#### 9.3.4. Analysis

A regression analysis was undertaken to the procedure described in DD CEN 12390-11 (2010) to determine the chloride profile with depth for each concrete specimen. The second layer from the exposed surface (3mm depth) is the first point used in this analysis, avoiding the potential error associated with the convection zone that often arises at the surface. This zone, described by Schiessl and Lay (2005) and illustrated in Figure 9.12, occurs when a peak chloride concentration occurs away from the surface as chlorides are carried into the section in diffusion and removed from the immediate surface by water with a lower chloride concentration.

The final point used in the analysis is taken at the point where the chloride content reaches a value of between  $C_i$  and  $C_i + 0.015\%$  (where  $C_i$  is the initial chloride content measured from the reference cylinder half). Any layers deeper than this are not included in the regression analysis.

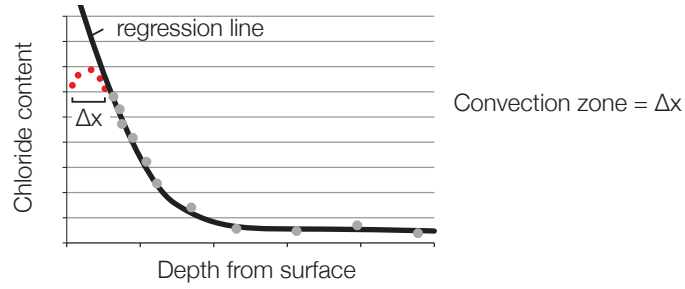


Figure 9.12: The convection zone ( $\Delta x$ ) in a typical chloride profile with depth from an in-situ concrete structure (after Schiessl and Lay, 2005 and DD CEN 12390-11 (2010)).

The calculated chloride content at the surface ( $C_s$ ) and the non-steady state chloride diffusion coefficient ( $D_{nss}$ ) are then determined by fitting Eq. 9.10 to the points determined during tested by means of a non-linear regression analysis using the method of least squares. Values thus determined for  $C_s$  and  $D_{nss}$  for each test are given in Table 9.9, with the corresponding graphs showing both the measured chloride contents and the results of the regression analysis (plotted against depth) shown in Figure 9.13 on page 359.

To facilitate further comparison of the data, NT Build 443 (1995) is used to calculate a chloride penetration parameter,  $K_{Cr}$ , Eq. 9.12. The parameter compares the chloride contents to a chosen reference chloride content, which is taken here as the recommended value of 0.05 mass % in NT Build 443 (1995). Results for the collected data are given in Table 9.9 on page 360, where  $K_{Cr}$  is reported in  $\text{mm/year}^{0.5}$ . Although this unit has little meaning, the parameter acts as a further useful comparator for the collected data. The values should only be used for comparing conditions similar to the tests, due to the high chloride concentration used.

$$C_x = C_i + (C_s - C_i) \left( 1 - \text{erf}_{(x)} \left[ \frac{x}{2\sqrt{D_{nss}t}} \right] \right) \quad \text{Eq. 9.10}$$

Where  $C_x$  is the chloride content measured at average depth  $x$  and exposure time  $t$ , % by mass of concrete;  $C_s$  is the calculated chloride content at the exposed surface, % by mass of concrete;  $C_i$  is the initial chloride content, % by mass of concrete;  $x$  is the depth below the exposed surface to the mid point of the ground layer, in metres (m);  $D_{nss}$  is the non-steady state chloride diffusion coefficient, in square metres per second ( $\text{m}^2\text{s}^{-1}$ );  $t$  is the exposure time, in seconds (s);  $\text{erf}(x)$  is the error function defined in Eq. 9.11:

$$\text{erf}_{(x)} z = \frac{2}{\sqrt{\pi}} \int_0^z \exp(-u^2) du \quad \text{Eq. 9.11}$$

$$K_{Cr} = 2\sqrt{D_{nss}} \text{erf}^{-1} \left( \frac{C_s - C_r}{C_s - C_i} \right) \quad \text{Eq. 9.12}$$

Where  $D_{nss}$  is the non-steady state chloride diffusion coefficient, in square metres per year ( $\text{m}^2\text{s}^{-1}$ )  $C_s$  and  $C_i$  are defined above;  $C_r$  is the selected reference chloride concentration (here taken as 0.05 mass%) and  $\text{erf}^{-1}$  is the inverse error function defined by Eq. 9.13. The results of  $K_{Cr}$  are reported in the text in units of  $\text{mm/year}^{0.5}$ .

$$\text{erf}^{-1}(z) = \frac{2}{\sqrt{\pi}} \int_0^z e^{t^2} dt \quad \text{Eq. 9.13}$$

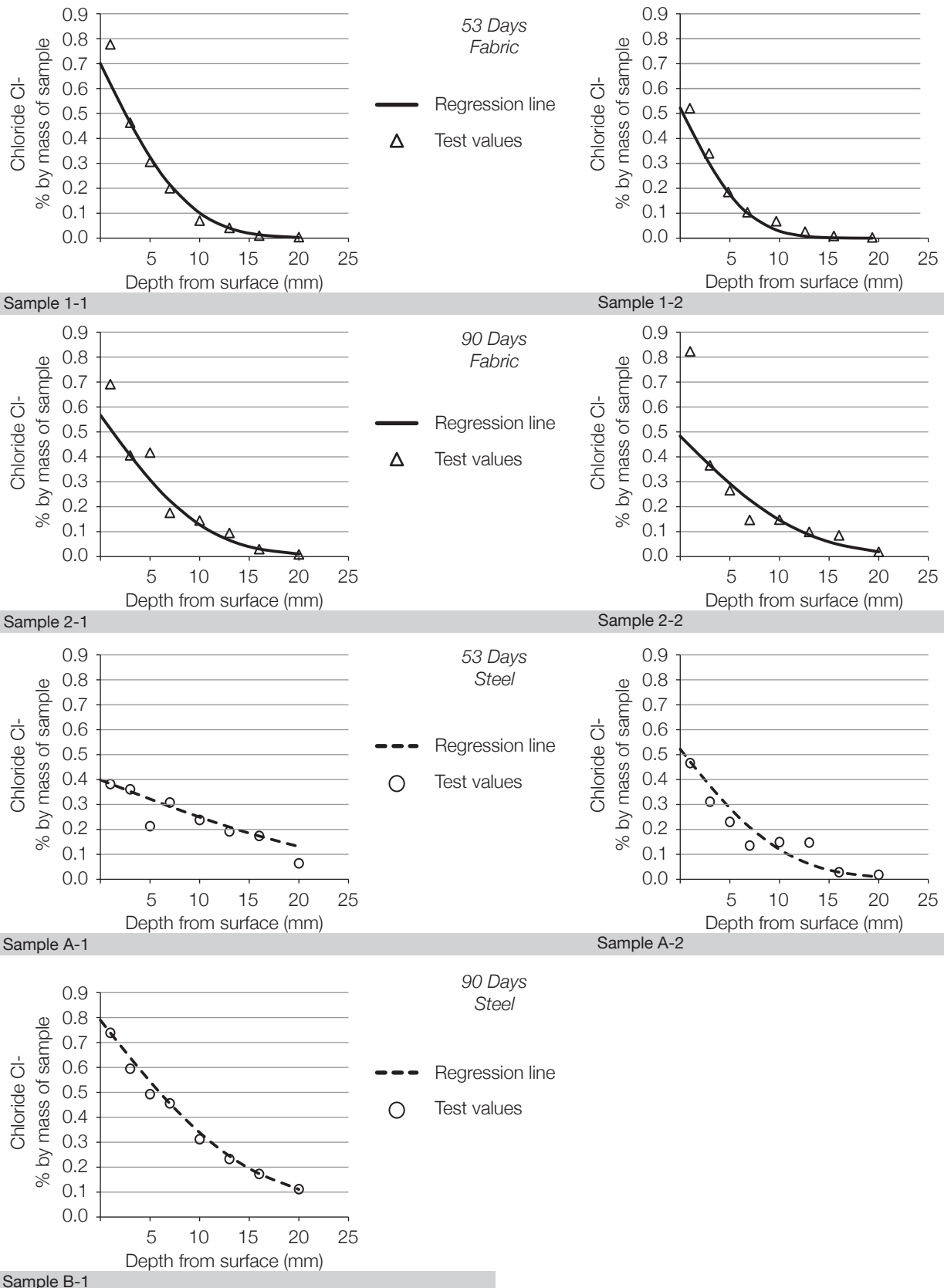


Figure 9.13: Chloride content with depth, results for test 1-1 to B-1 drawn using Eq. 9.10 and Table 9.9.

Table 9.9: Variable values for each test series.

Test	$D_{nss}$ ( $m^2s^{-1}$ )	$C_s$ (mass %)	$K_{Cr}$ (mm/year <sup>0.5</sup> )
1-1 Fabric cast, 53 days	$5.118 \times 10^{-12}$	0.700	32.40
1-2 Fabric cast, 53 days	$3.155 \times 10^{-12}$	0.522	23.51
2-1 Fabric cast, 90 days	$4.32 \times 10^{-12}$	0.567	28.17
2-2 Fabric cast, 90 days	$6.07 \times 10^{-12}$	0.483	31.86
A-1 Steel cast, 53 days	$45.8 \times 10^{-12}$	0.399	82.43
A-2 Steel cast, 53 days	$7.55 \times 10^{-12}$	0.521	36.36
B-1 Steel cast, 90 days	$8.88 \times 10^{-12}$	0.745	43.33

From the results presented above comparisons can be made between the chloride resistance of concrete cast in fabric compared to that cast in a steel mould by comparing the calculated values for the non-steady state chloride diffusion coefficient ( $D_{nss}$ ) and the penetration parameter ( $K_{Cr}$ ).

From the samples tested, it was found that  $D_{nss}$  reduces by 84.5% for fabric cast samples at 53 days and 41.5% for fabric cast samples at 90 days, as shown in Table 9.10, while  $K_{Cr}$  reduces by 53.9% at 53 days and 30.7% at 90 days.

It should be noted that Sample A-1 has a particularly flat chloride ingress profile when compared to Sample A-2 (Figure 9.13) and in the absence of further test data is to be considered as an outlier. If Sample A-1 is omitted from the analysis, it is found that after 53 days the fabric cast sample still shows a 45.2% reduction in its value of  $D_{nss}$  and a 23.1% reduction in  $K_{Cr}$ , which continues suggest that excellent resistance to chloride ingress is obtained when using fabric cast concrete. It is also possible that Sample A-1 was simply poorly made and thus may represent a real concrete structure in which some areas may have better compaction than others.

Table 9.10: Reduction in  $D_{nss}$  when using fabric cast concrete.

Age (days)	Fabric cast samples, Average value of $D_{nss}$ ( $m^2s^{-1}$ )	Steel cast samples, Average value of $D_{nss}$ ( $m^2s^{-1}$ )	% reduction when using fabric cast concrete
53	$4.14 \times 10^{-12}$	$26.7 \times 10^{-12}$	84.50
53 <sup>1</sup>	$4.14 \times 10^{-12}$	$7.55 \times 10^{-12}$	45.24
90	$5.20 \times 10^{-12}$	$8.88 \times 10^{-12}$	41.46
<sup>1</sup> Results at 53 days with potential outlier (Sample A-1) removed.			

Table 9.11: Reduction in  $K_{Cr}$  when using fabric cast concrete.

Age (days)	Fabric cast samples, Average value of $K_{Cr}$ (mm/year <sup>0.5</sup> )	Steel cast samples, Average value of $K_{Cr}$ (mm/year <sup>0.5</sup> )	% reduction when using fabric cast concrete
53	27.95	59.39	52.93
53 <sup>1</sup>	27.95	36.36	23.12
90	30.01	43.33	30.73
<sup>1</sup> Results at 53 days with potential outlier (Sample A-1) removed.			

A comparison between the average results of the steel and fabric cast samples is provided in Figure 9.14. It is clear that whilst the fabric cast samples had generally higher chloride concentrations in the surface zone (1-3mm depth), the lower diffusion coefficients found in these samples prevented the chlorides from penetrating deeper into the sample. This in turn suggests that the fabric cast concrete provides a higher level of chloride binding, preventing the chloride ions from navigating into the structure to cause corrosion of the internal steel.

Average results for samples tested at 53 days, as shown in Figure 9.14(l), show the two regression lines crossing over one another, with the concentration of chloride ions at the surface appearing to be greatest in the fabric cast sample. This result has arisen as Sample 1-1 (Figure 9.13) has a high chloride content at the surface when compared to all the other fabric cast samples (including those tested at 90 days). Given that the sampling method does not cover the entire cross section at each depth increment and that there may have been a concentration of sodium chloride at the location chosen for the sample that was not representative of the general sample, a second analysis was undertaken without this result.

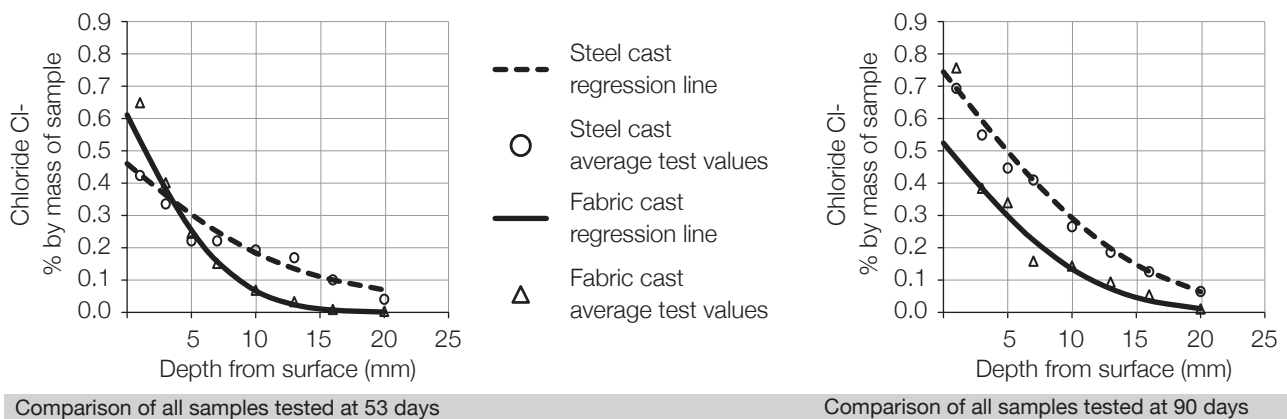


Figure 9.14: Comparison of average chloride ingress profiles.

The results at 53 and 90 days, excluding the results for Samples 1-1 and A-1, are again compared in Figure 9.15 (where the samples used in each comparison are noted beside the graphs). Percentage changes in the steady state diffusion coefficient between the two sets of samples are compared in Table 9.12, and for the penetration parameter in Table 9.13, where the significant advantage of fabric cast concrete is again apparent.

Both sets of results provide similar percentage values, and the results for  $K_{cr}$  may be used as comparators with future testing. It should be noted that whilst the comparison is now between two samples only, the results do not deviate from the general trends demonstrated above when all samples were included in the analysis.



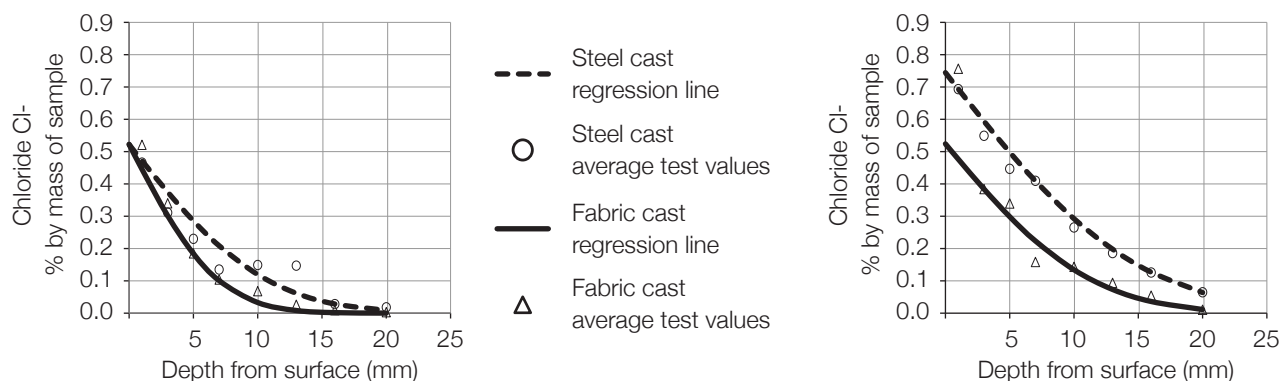


Figure 9.15: Comparison of average chloride ingress profiles.

Table 9.12: Reduction in  $D_{nss}$  when using fabric cast concrete.

Age (days)	Fabric cast samples, Average value of $D_{nss}$ ( $m^2s^{-1}$ )	Steel cast samples, Average value of $D_{nss}$ ( $m^2s^{-1}$ )	% reduction when using fabric cast concrete
53 <sup>1</sup>	$3.15 \times 10^{-12}$	$7.55 \times 10^{-12}$	58.24
90 <sup>2</sup>	$5.20 \times 10^{-12}$	$8.88 \times 10^{-12}$	41.46
<b>Average reduction</b>			<b>49.9%</b>

<sup>1</sup>Results at 53 days without Sample A-1 or Sample 1-1; <sup>2</sup>Results at 90 days unchanged.

Table 9.13: Reduction in  $K_{Cr}$  when using fabric cast concrete.

Age (days)	Fabric cast samples, Average value of $K_{Cr}$ (mm/year <sup>0.5</sup> )	Steel cast samples, Average value of $K_{Cr}$ (mm/year <sup>0.5</sup> )	% reduction when using fabric cast concrete
53 <sup>1</sup>	23.51	36.36	52.93
90 <sup>2</sup>	30.21	43.33	30.73
<b>Average reduction</b>			<b>41.8%</b>

<sup>1</sup>Results at 53 days without Sample A-1 or Sample 1-1; <sup>2</sup>Results at 90 days unchanged.

### 9.3.5. Conclusions

Concrete cylinders exposed to high concentrations of NaCl were used to determine the relative resistance to chloride ingress of fabric and steel cast concrete. Sixty three samples collected at incremental depths from the cast surface were analysed and the results show that significant improvements in chloride resistance can be obtained when using fabric cast concrete.

Average reductions in the non-steady state chloride diffusion coefficient of 49.9% and the chloride penetration parameter of 41.8% (Table 9.12 and Table 9.13) are in line with the results of tests reported by Price (2000), where 50% reductions in chloride diffusion were found when rigid, permeable formwork systems were used.

The reductions in chloride ingress seen in this test series could be attributed to a potential change in the binding capacity of the concrete through the formation of Friedel's salt (as described in §9.3.1 on page 350). Such a change would work to increase the binding capacity of the fabric cast concrete. However, given that this was not directly measured in this test series, it is not possible to make a firm conclusion at this point. An equally likely explanation may be found in physical changes in the structure of the concrete at the surface zone that occur through the use

of the permeable mould, and this aspect should be considered in future work. There therefore remains some ambiguity as to the exact mechanism by which improvements in chloride ingress in fabric cast concrete occur.

The test method used in this section intends to model predominantly the behaviour of chloride ion diffusion in the concrete, which is representative of the state of a submerged concrete structure (CCAA, 2009). Whilst such an approach allows the chloride permeability coefficient to be measured, and has become the standard test method for such situations, it does not consider other processes such as capillary suction, absorption, permeability, migration, adsorption and desorption that can occur in non-submerged concrete structures in service.

This is illustrated by Cady and Weyers (1983), who found that for structures subject to intermittent wetting and drying the maximum concentration of chloride ions can occur some distance from the cast concrete surface. Marchand and Samson (2009) provide some steps towards a model for chloride ingress which can account for such exposure conditions, but there is yet to be a codified test method for such conditions and hence the reliance on a chloride diffusion coefficient continues.

The sample size used in this section was relatively small, and only one fabric type and concrete mix was used. Concerns raised by Tang and Sorenson (2001) over the repeatability and errors associated with chloride penetration tests have not gone unnoticed, and in the analysis two data sets were cautiously omitted. To provide confidence in the results shown in this section, significant further work is required to generate a much larger data set. Further work is also required to classify the fabrics used for casting and, based on their pore size, provide a method by which the improvements in resistance to chloride ingress can be predicted. This may greatly assist designers of structures in areas of significant chloride exposure.

Changes in resistance to chloride ingress may also influence the carbonation properties of the concrete. It is known that carbonation can lead to the release of previously bound chlorides (§9.2.4 on page 348), but with an improved resistance to carbonation seen in fabric cast concrete (§9.2 on page 344) it is suggested that this impact may be offset. The combined testing of both carbonation and chloride ingress is therefore an additional topic for future work.

To determine further the pore structure changes that arise using fabric formwork, a series of tests to determine the sorptivity of such concretes were undertaken, presented in the following section. These tests are further supplemented by the use of both scanning electron microscopy and energy-dispersive X-ray spectroscopy to determine the chemical and structural composition of the surface zone of fabric cast concrete (§9.5 on page 373).

### 9.4. Test Group 3 - Sorptivity

In much of the available literature, the sorptivity (the rate of liquid absorption by capillary action) of a hydraulic cement concrete is related to its durability characteristics, as described by Hall (1989). In porous building materials, which often have bond (or Eötvös) numbers of less than 1.0 (Clift *et al.*, 1979), the force of gravity is not significant over time periods of several years (Lockington and Parlange, 2003) and the tests can be undertaken with vertical water ingress without concern as surface tension dominates.

In light of the advantageous tests presented in the §9.2-§9.3, Test Group 3 was undertaken to determine how the sorptivity behaviour of the concrete is affected by the use of a permeable mould. Presented below is an introduction to and discussion of sorptivity behaviour, before the chosen test method and its results are presented.

#### 9.4.1. Theoretical behaviour

Some of the first sorptivity profiles measured on porous materials in unidirectional tests showed a water absorption profile that advances with the square root of time (Gummerson *et al.*, 1979). The result is modelled in much of the literature by the non-linear diffusion equation given in Eq. 9.14 (Bazant and Najjar 1972, Hall and Yau 1987, Daian 1988, Hall 1989, Hall and Hoff 2002, Gummerson *et al.*, 1979, Carpenter *et al.*, 1993 and Pel 1995; all cited by Lockington and Parlange, 2003).

$$\frac{\partial \theta}{\partial t} = \frac{\partial}{\partial x} \left\{ D(\theta) \frac{\partial \theta}{\partial x} \right\} \quad \text{Eq. 9.14}$$

$\theta$  is the water content,  $D(\theta)$  is the hydraulic diffusivity ( $\text{mm}^2/\text{s}$ ),  $t$  the time (s) and  $x$  the spatial coordinate (mm)

Eq. 9.14 has the solution given by Eq. 9.15, provided there is a uniform initial water content and the specimen is placed in a reservoir (i.e. has a wet face) at the position  $x = 0$ .

$$x(\theta, t) = \phi(\theta) \sqrt{t} \quad \text{Eq. 9.15}$$

With the symbols as for Eq. 9.14

The sorptivity is thus often given simply as the volume of water absorbed by a specimen, Eq. 9.16 (Hall, 2007) and gives a linear increase with the square root of time. Results following this approach have been reported widely for masonry (Hall, 2007).

$$i = A + S\sqrt{t} \quad \text{Eq. 9.16}$$

Where  $i$  is the cumulative volume of absorbed liquid at time  $t$ ,  $S$  is the rate of absorption and  $A$  is a constant (Hall, 2007).

However, there is increasing work showing that in cementitious materials, the  $t^{0.5}$  relationship does not hold (Lockington and Parlange, 2003). There are many possible sources for such deviations from the expected  $t^{0.5}$  relationship according to Eq. 9.15, four of which are presented by Hall (2007). Strictly, the  $t^{0.5}$  relationship holds

only for one-dimensional absorption in an homogenous material, which for a cementitious material is required in both its structure and its initial moisture content - both of which may not be achieved. Aggressive drying to achieve a uniform moisture content can lead to damage of the cementitious specimen (in contrast to kiln fired brick, for example) and, more significantly, attaining experimental data of the actual moisture content in a concrete specimen is both difficult and rarely reported.

For cementitious materials, a potentially significant effect is the water-sensitivity of the material itself (Hall, 2007). Work by Taylor *et al.* (1999), in which the sorptivity of Portland cement mortars were measured using water and n-decane, show distinctly different behaviours (Figure 9.16(l)). Since the sorptivity behaviour measured using water falls below the n-decane line (which follows very well the expected 'root time' behaviour), can be described as 'subdiffusive'.

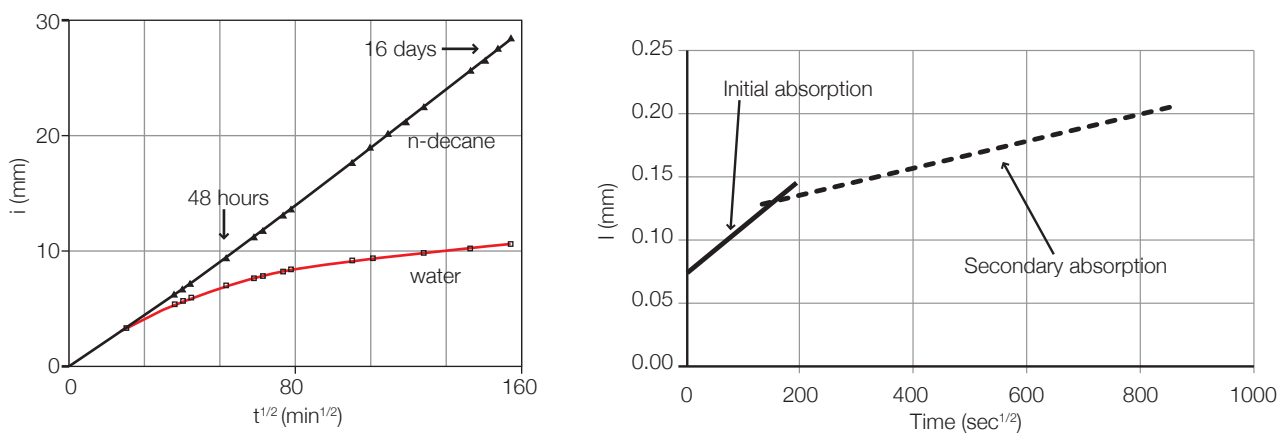


Figure 9.16: Cumulative capillary absorption ( $i$ ) versus  $t^{1/2}$  for a 1:2 Portland cement:sand mortar, reproduced from Taylor *et al.*, 1999) (l); 'Initial' and 'Secondary' sorptivities as defined by the ASTM C1585 (2004) method for sorptivity measured using water, where ' $i$ ' the change in mass divided by the product of the cross sectional area of the specimen and the density of water ( $r$ ).

With experimental data showing a clear difference between the sorptivities when using water and hydrocarbon liquids, it can be concluded that the effect arises due to chemical interaction between the water and the cementitious matrix (Hall, 2007). Attempts to model this behaviour include the work of Lockington and Parlange (2003), who approach the problem by allowing the diffusivity,  $D(\theta)$  (Eq. 9.14) to also vary with time, while Metzler and Klafter (2000) use a 'fractional diffusion' approach whose investigation is beyond the scope of this thesis.

One of the only published test procedures for sorptivity is the ASTM C1585 (2004), which recommends that tap water be used, but that two sorptivity values be calculated (Figure 9.16(r)). This approach was taken in preference to the use of n-decane, with the intention that more test data for comparison would be made available to follow the ASTM method than would use the experimental process of n-decane.

In this test series the sorptivity of concrete cast against steel and fabric was determined using the method set out in ASTM C1585 (2004), described below. The rate of water absorption is noted in the standard to depend on the concrete mix the presence of chemical admixtures, entrained air, cracks, formwork oils, the degree of hydration, chemical composition of the aggregates and cement, the curing duration, the moisture condition and the method

of placement (ASTM, 2004). Just one of these factors is to be considered in this test series - namely the curing condition at the face of the concrete.

#### 9.4.2. Test method

Twelve concrete cylinders ( $\phi 100 \times 200\text{mm}$ ) were used to determine the sorptivity characteristics of fabric and steel cast concrete, both at the cast face and at 25mm from the cast face, as described in Table 9.14. Samples 4-6 were included to provide an indication of the depth of any improvements in concrete properties beyond any found at the surface face. Six specimens with a fabric base (Figure 9.17(l)), and six with a steel base, were cast using the concrete mix described in Table 9.2 on page 343. Concrete strengths are also provided in Table 9.14.

Table 9.14: Specimens for sorptivity testing.

Sample	Face curing method	Test undertaken	Age at start of test	28 Day concrete strength
S1	Steel	Surface	28 days	38.1MPa
S2	Steel	Surface		
S3	Steel	Surface		
F1	Fabric	Surface		
F2	Fabric	Surface		
F3	Fabric	Surface		
S4	Steel	25mm from surface	28 days	35.2MPa
S5	Steel	25mm from surface		
S6	Steel	25mm from surface		
F4	Fabric	25mm from surface		
F5	Fabric	25mm from surface		
F6	Fabric	25mm from surface		

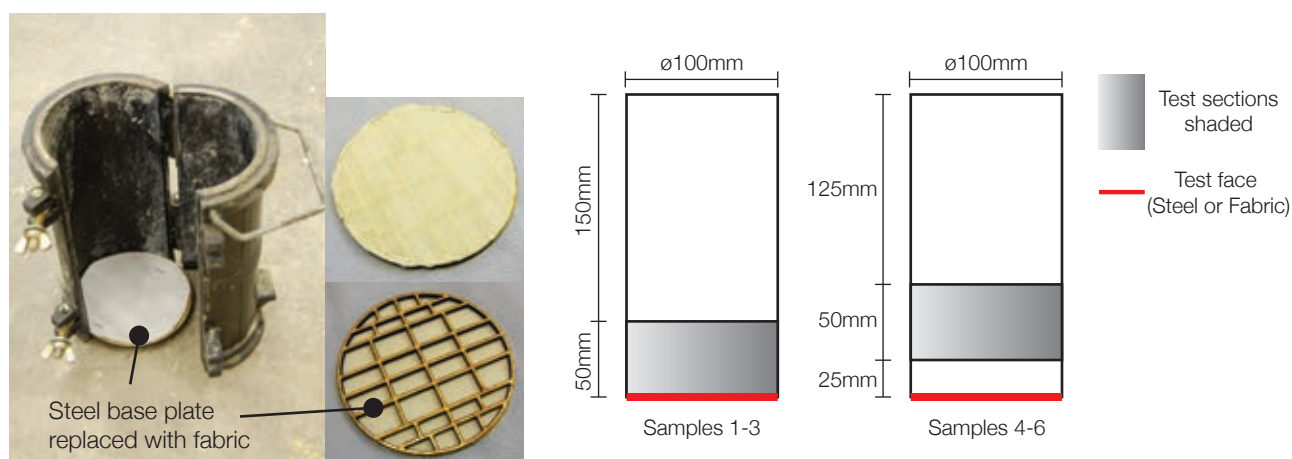


Figure 9.17: Fabric base for concrete cylinder samples (l); Sample locations for sorptivity testing (r).

The specimens were demoulded after 24 hours and a 50mm deep section was cut from six (three steel and three fabric cast) of the samples. The remainder had a 25mm section cut from the cast surface, with a 50mm deep section then cut from the remaining block (see Figure 9.17(r) for details). The discs were then marked and stored in an environmental chamber at  $50 \pm 2^\circ\text{C}$  and  $80 \pm 3\%$  relative humidity for 3 days. The specimens were then stored in a sealed container prior to testing.

After curing for 28 days as described above, each sample was removed from its container and its weight was recorded. The cylinder was then measured in four locations and the average diameter recorded (to 0.1mm). The cylinders sides were then sealed with paraffin wax and a plastic bag was secured over the unwaxed face opposite to the test face (Figure 9.18). The sample weight was again recorded as the initial mass for subsequent calculations.

Each specimen was then placed in a water bath, filled to the level shown in Figure 9.18 with water at  $23\pm2^{\circ}\text{C}$ , and supported off the base of the container. The mass of each specimen was then determined (by removing the sample from the water, blotting dry with a cloth, and weighing to 0.01g) at the following time intervals:  $60\pm2\text{s}$ ,  $5\text{min}\pm10\text{s}$ ,  $10\pm2\text{mins}$ ,  $20\pm2\text{mins}$ ,  $30\pm2\text{mins}$ ,  $60\pm2\text{mins}$ . After 1 hour, the measurements were taken at each hour up to 6 hours, then once a day until 7 days after the first test. With twelve cylinders, a total of 204 tests were undertaken. The results are presented in §9.4.3.

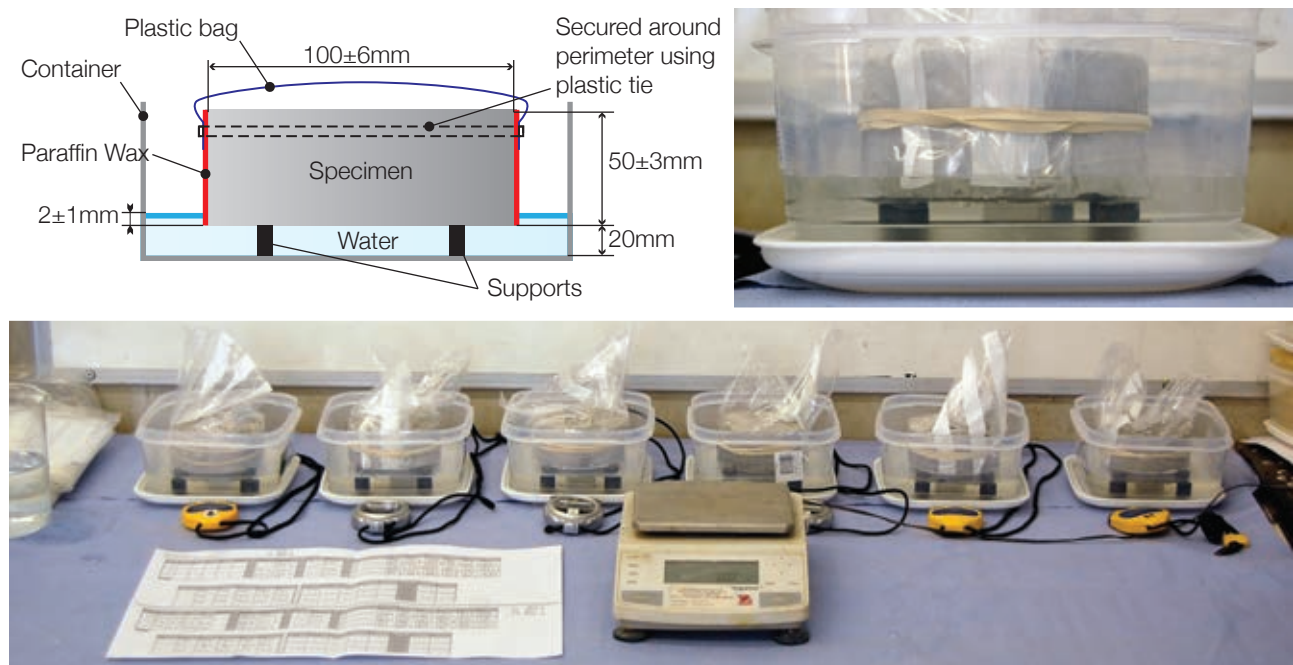


Figure 9.18: Test method and set up (diagram after ASTM C1585, 2004).

#### 9.4.3. Results

Mass results from 1 minute to 7 days for each sample are provided in full in Table 9.15.

Table 9.15: Sample weights, to 7 days.

Sample	Initial Weight	Average Diameter	+60s	+5mins	+10min	+20mins	+30mins	+60mins	+2hrs	+3hrs
S1	860.60	100mm	878.9	880.8	882.1	884	885.6	888.9	893.1	896.1
S2	868.70	100mm	885.9	888.1	889.6	891.8	893.3	896.5	900.5	903.5
S3	850.10	100mm	867.1	868.9	870.1	871.9	873.3	876.3	880.1	882.9
F1	852.10	100mm	853.8	855.8	857.3	859.2	860.7	864	868.6	871.8
F2	872.50	100mm	874.2	876.4	878.1	880.5	882.2	885.9	891.2	894.8
F3	895.50	100mm	896.8	898.4	899.6	901.3	902.6	905.6	909.9	913.2
S4	884.90	100mm	887.3	889.4	891.1	893.1	894.6	898.1	902.9	906.4



Sample	Initial Weight	Average Diameter	+60s	+5mins	+10min	+20mins	+30mins	+60mins	+2hrs	+3hrs
S5	922.20	100mm	924.2	926.2	927.6	929.4	930.8	933.8	938.1	941.3
S6	887.20	100mm	889.3	891.6	892.1	893.6	894.8	897.3	901	903.8
F4	869.10	100mm	871	873.2	874.7	876.7	878.3	881.3	885.7	888.8
F5	881.30	100mm	883.6	885.7	886.7	888.6	889.8	892.9	896.9	899.9
F6	873.70	100mm	875.9	878	879.3	881.4	882.6	885.9	890.5	893.8

Sample	+4hrs	+5hrs	+6hrs	+1 day	+2 days	+3 days	+4 days	+5 days	+6 days	+7 days
S1	874.3	876.1	877.6	880.8	881.1	881.6	881.7	881.8	882.0	882.1
S2	897.8	900	901.3	903.5	903.9	904.1	904.4	904.6	904.8	905
S3	916	918.4	920.3	926.2	926.6	927	927.1	927.3	927.4	927.6
F1	898.5	900.7	902.5	906.7	907.1	907.3	907.5	907.7	907.8	908
F2	905.8	907.7	909.3	912.9	913.3	913.6	913.7	913.9	914.0	914.2
F3	885	887	888.6	894.3	894.7	895	895.1	895.3	895.4	895.6
S4	891.1	892.5	893.5	895.8	896.2	896.4	896.6	896.8	897.0	897.0
S5	902.3	904.0	905.1	907.5	907.9	908.2	908.3	908.5	908.6	908.7
S6	896.5	898.5	899.9	902.8	903.3	903.5	903.7	903.9	904.1	904.2
F4	908.9	910.4	911.6	913.1	913.5	913.8	913.9	914.1	914.2	914.3
F5	943.9	945.5	946.8	950.1	950.5	950.7	950.9	951.0	951.2	951.3
F6	906.0	907.7	909.0	912.4	912.8	913.0	913.2	913.4	913.6	913.8

#### 9.4.4. Analysis

Following ASTM C1585 (2004), these results are analysed by considering a linear relationship between the values of  $time^{0.5}$  and the total change in mass of the specimen. The absorption,  $I$ , is given by Eq. 9.17. Two periods of water absorption are defined in the standard - an initial absorption up to 6 hours, followed by secondary absorption up until the end of the test. It should be noted that the area taken for each sample is the projected area of the cylinder, not the total surface area. This is important for the fabric cast specimen, where the cast face is not flat (Figure 9.19), but shows changes in elevation where the fabric has been able to bulge through the supporting frame.

$$I = \frac{m_t}{a/d} \quad \text{Eq. 9.17}$$

Where  $I$  is the absorption (in mm);  $m_t$  is the change in specimen mass in grams at the time  $t$ ;  $a$  is the exposed area of the specimen in  $mm^2$  and  $d$  is the density of water in  $g/mm^3$  (taken here as  $0.001g/mm^3$ ).

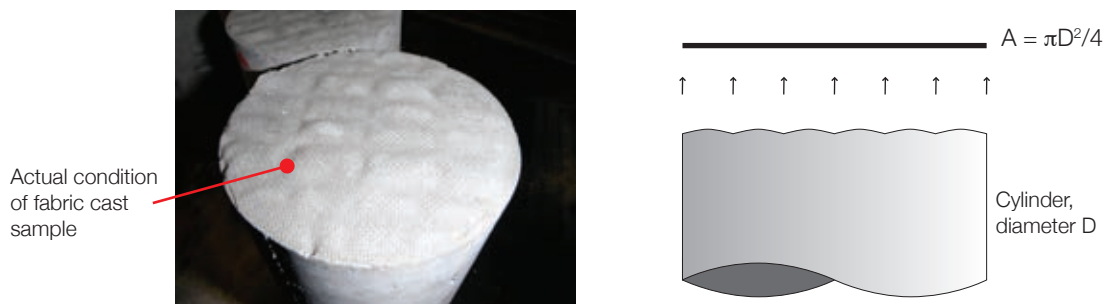


Figure 9.19: Surface area of the fabric cast sample.

The initial water absorption is calculated as the slope of a line of best fit plotted over the first six hours of data using a linear regression analysis, with all graphs plotted as  $mm$  versus  $time^{0.5}$ . A correlation coefficient of the linear regression of  $>0.98$  is expected, and the slope of the line is given by Eq. 9.18. The secondary rate of water absorption is taken as a linear relationship between the  $mm$  and  $time^{0.5}$  axes, and again a correlation coefficient of  $>0.98$  is expected for the results to be valid. The slope of the line is given by Eq. 9.19.

$$I = S_i \sqrt{t} + b \quad \text{Eq. 9.18}$$

Where  $S_i$  = the initial rate of absorption

$$I = S_s \sqrt{t} + b \quad \text{Eq. 9.19}$$

Where  $S_s$  = the secondary rate of absorption

Table 9.16: Summary of measured absorption rates.

Sample		S <sub>i</sub>	S <sub>s</sub>	Sample	S <sub>i</sub>	S <sub>s</sub>
S1	Shown in Figure 9.20.	0.0216	0.0003	S4	0.0228	0.0003
S2		0.0213	0.0003	S5	0.0210	0.0003
S3		0.0197	0.0003	S6	0.0180	0.0003
Average, S1-S3		0.021	0.0003	Average, S4-S6	0.0206	0.0003
F1		0.0221	0.0003	F4	0.0210	0.0003
F2		0.0254	0.0004	F5	0.0200	0.0003
F3		0.0217	0.0003	F6	0.0223	0.0003
Average, F1-F3		0.023	0.0003	Average, F4-F6	0.0211	0.0003

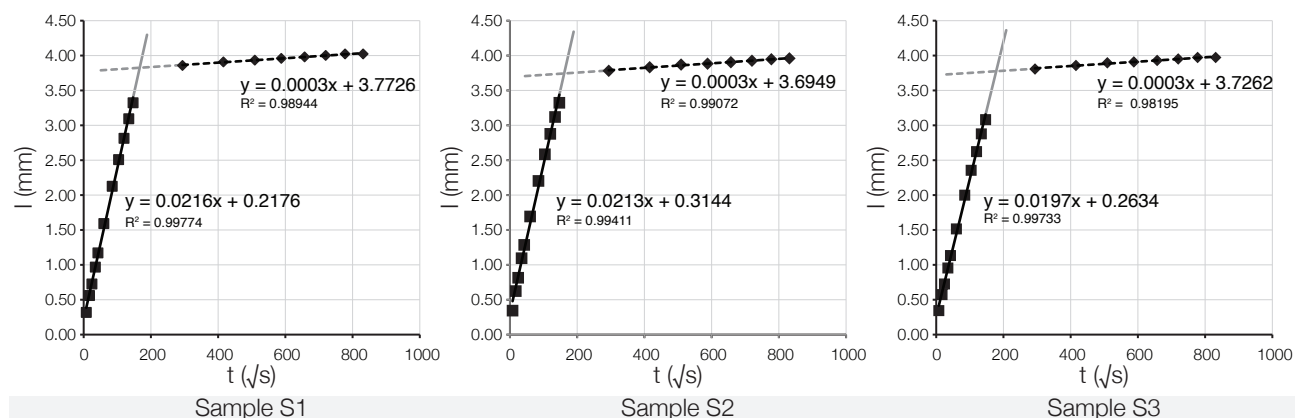


Figure 9.20: Samples S1-S3, initial and secondary absorption plots, showing values for  $S_i$  and  $S_s$ .

#### 9.4.4.1. Samples S1-S3 and F1-F3

The results appear to show little difference in the values of  $S_i$  and  $S_s$ , as measured according to ASTM C1585 (2004) for all samples. However, differences can be found by comparing the average values of  $I$  (Eq. 9.18) for Samples S1-S6 and F1-F6 over the first six hours of testing (the duration used for the calculation of  $S_i$ ). This data is provided in Table 9.17.

The process then highlights differences in the initial behaviour of the concrete that are masked by the calculation of  $S_i$  for the entire test duration (as shown previously in Table 9.16). The results are shown in Table 9.17, where the initial (<30 minutes) absorption of water by the fabric cast samples is up to 40% less than seen in the steel cast samples (Figure 9.21). This difference is then seen to drop off rapidly, such that the average absorption values over the next six hours ( $S_i$ ) are almost identical.

Table 9.17: Samples 1-6, comparison of  $I$  at different time steps.

Time (s)	Time ( $s^{0.5}$ )	Average value of $I$ (Eq. 9.17)						
		F1-F3 [A]	S1-S3 [B]	% Reduction, [B] to [A]		F4-F6 [C]	S4-S6 [D]	% Reduction, [D] to [C]
0	0	0.00	0.00	-		0.00	0.00	-
60	8	0.20	0.34	40.5		0.27	0.27	1.5
300	17	0.45	0.59	23.9		0.54	0.54	0.8
600	24	0.63	0.76	16.3		0.70	0.70	-0.6
1200	35	0.89	1.01	11.8		0.96	0.96	-3.7
1800	42	1.08	1.20	9.9		1.13	1.13	-2.7
3600	60	1.50	1.60	6.1		1.53	1.53	-3.2
7200	85	2.11	2.11	0.2		2.08	2.08	-2.7
10800	104	2.53	2.48	-2.1		2.48	2.48	-2.1
14400	120	2.89	2.77	-4.1		2.79	2.79	-2.0
18000	134	3.16	3.03	-4.2		3.01	3.01	-2.3
21600	147	3.36	3.24	-3.5		3.16	3.16	-1.8
86400	294	3.84	3.82	-0.6		3.48	3.48	-0.9
172800	416	3.88	3.87	-0.4		3.54	3.54	-1.0
259200	509	3.93	3.90	-0.8		3.57	3.57	-1.0
345600	588	3.95	3.92	-0.9		3.59	3.59	-1.0
432000	657	3.97	3.94	-0.9		3.61	3.61	-1.0
518400	720	3.99	3.96	-0.9		3.63	3.63	-1.1
604800	778	4.01	3.98	-0.9		3.64	3.64	-0.8
691200	831	4.02	3.99	-0.9		3.66	3.66	-1.1

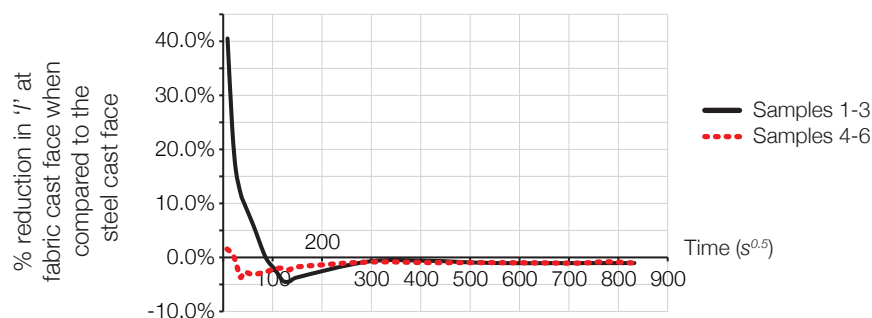


Figure 9.21: Results of Table 9.17.

Further details are revealed by considering the work of Buyle-Bodin and Hadjieva-Zaharieva (2002), who suggest the calculation of initial surface absorption ( $\text{kg/m}^2$ ) values for the first hour of a sorptivity test. This data is then distinguished from the sorptivity ( $\text{kg/m}^2\text{h}^{0.5}$ ) of the concrete collected over a longer time period. The importance of this difference in test length is highlighted by (Balayssac, 1992, cited by Buyle-Bodin and Hadjieva-Zaharieva,

2002) who showed that the initial water absorption is dependent primarily on larger pores (up to  $1.25\mu\text{m}$ ) while the longer term sorptivity is a measure of the presence of smaller pores (average size  $0.04\mu\text{m}$ ).

Analysis of the first hour of data for Samples S1-S3 and F1-F3 is presented in Table 9.18. The results show only a moderate reduction in the initial water absorption of the fabric cast concrete over the first hour of testing. This is good, if not entirely conclusive, evidence of a change in pore structure in the surface zone of fabric cast concrete. The subsequent similarities in sorptivity recorded over longer times (up to 6 hours) suggest that whilst there are less large pores in the fabric cast concrete, the number of the smallest pores is not reduced and hence over the longer time (where the smaller pores dominate the behaviour) the fabric and steel cast concretes have almost identical behaviours. This supports the results of previous work presented in §2.6.1.1 on page 36.

Table 9.18: Initial surface absorption of samples 1-3.

Sample	Mass change in first hour (g)	Surface area ( $\text{mm}^2$ )	Initial surface absorption ( $\text{kg}/\text{m}^2$ )
Average, F1 - F3	11.80	7854	1.50
Average, S1 - S3	12.57	7854	1.60
Reduction seen at the Fabric Face			6.25%

#### 9.4.4.2. Samples S4-S6 and F4-F6

Samples S4-S6 and F4-F6 were cut 25mm from the cast face of each sample, and show almost identical behaviours throughout the testing cycle. For completeness, comparisons between the values for  $I$  across the testing cycle are presented alongside those for Samples 1-3 in Table 9.17 and Figure 9.21.

The similarity of the results suggest that changes in the pore structure that occur in the surface zone are present within the initial 25mm of depth, and do not extend beyond this region. However, it is difficult to verify this assertion, since microcracking will be caused during the cutting of each of Samples S4-S6 and F4-F6, which will impact the surface behaviour of the specimen.

#### 9.4.5. Conclusions

The collected sorptivity test data has been used to determine both long term (up to 8 days), medium term (up to 6 hours) and short term (up to 1 hour) behaviour of the fabric cast concrete. In the short term, the data has been used to suggest that fabric cast concrete has fewer large pores and thus proportionally more smaller pores. Medium and long term data suggests little difference exists in the sorptivity behaviour of the fabric and steel cast specimens.

Whereas previous tests have shown clear advantages in the use of fabric formwork, they have also shown that these advantages are reduced over time (see Table 9.4 on page 346 for carbonation data and Table 9.13 on page 362 for chloride ingress data). Whilst both of tests still showed considerable advantages for the fabric cast concrete at the greater age, the reduction in improvement would suggest that over time the effect of the fabric cast face is less important to the internal condition.

Whilst the sorptivity data is presented to show potential changes in the pore structure of the concrete, it is also recognised that for chloride ingress mechanisms such as Friedel's salt formation have significant impacts on the durability behaviour. For carbonation, the size of the pore is important, but the effects of using water (additional hydration during absorption) may not be that useful in comparisons. Further work is therefore required to undertake sorptivity tests using n-decane, which has been shown to not interfere with the hydration properties of the cement.

It is premised that carbonation depths are reduced due to their being fewer large pores, which are formed due to an increased cement content at the surface zone. Cement is the smallest particle in the concrete mix and this, coupled with the removal of water from the surface, provides a denser surface structure. In addition, the presence of this cement encourages the formation of Friedel's salt, providing a much more difficult path for chloride ingress and thus providing the fabric cast concrete with a good resistance to both effects.

To provide further evidence for this summary, a fourth group of tests was undertaken using the scanning electron microscope and energy-dispersive X-ray spectroscopy, where images at high magnification and analysis of compounds present at the surface of both fabric and steel or timber cast concrete were collected. This test program is presented in the following section.

## 9.5. Test Group 4 - Microscopy

### 9.5.1. Introduction

The results presented in the preceding sections have demonstrated that significant improvements in the surface properties and durability of concrete cast using fabric formwork can be obtained. To determine in more detail the changes in structure and chemical composition that arise in the surface zone of fabric cast concrete, and to confirm changes in the pore structure and composition of the fabric cast concrete face, a further program of detailed tests was undertaken as part of Test Group 4, presented below as two test Series:

Series 1) Particle size measurements and imaging in cross section from the cast face;

Series 2) Scanning electron microscopy and X-Ray diffraction of the cast surfaces;

The tests of all series were undertaken with the help of the technicians at the University of Bath's Microscopy and Analysis Suite. The use of SEM to analyse concrete samples is a well established technique that can provide an insight into the processes at work within a specimen, and SEM (described in detail by Buschow *et al.*, 2001) allows information about surface topography and composition to be determined. The JEOL JSM6480LV SEM used in this thesis allows magnifications up to 300,000x and has a chamber for samples up to 200mm in width. An Oxford INCA X-ray analyser was also used for mapping and qualitative analysis of the samples.

### 9.5.2. Series 1

Series 1 of Test Group 4 was the first test series undertaken to determine what changes in the concrete composition and structure occur as a result of casting in fabric formwork. This work, which was undertaken to supplement the results presented for carbonation, chloride ingress, sorptivity and surface hardness testing, used cross sectional slices of concrete prisms to determine the changes in particle size and composition with depth from the cast surface (Figure 9.22). Three prisms were cast as part of this test series, and one of these was subsequently also used in Series 2 (§9.5.3 on page 379).

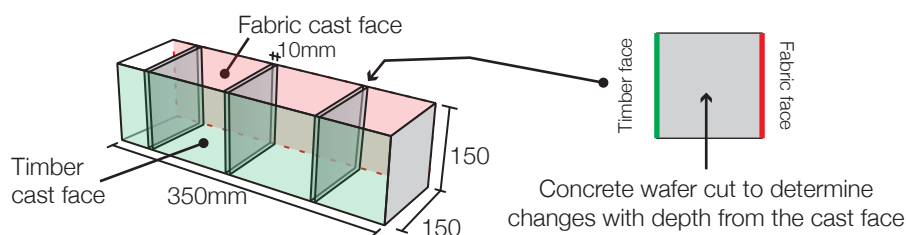


Figure 9.22: Prisms cast for Series 2.

#### 9.5.2.1. Test specimens

Three prisms (denoted S1, S2, and S3) were cast with the dimensions shown in Figure 9.22. The moulds were cleaned prior to casting and a new sheet of geotextile fabric (described in Table 9.3 on page 343) was placed in each mould. A summary of the prisms and the test undertaken on them is given in Table 9.19. Using the concrete



mix described in Table 9.2, concrete was placed in the moulds in five layers that were each compacted by hand. 100mm cubes cast alongside the specimens provide a reference 28 day concrete strength (Table 9.20).

Table 9.19: Summary of test prisms for Series 2 and Series 3 tests.

Prism	Cross section analysis (§9.5.2.2 and §9.5.2.3)			Surface topology analysis (§9.5.3)
	Slice	Sample identifier	Tested (Yes/No)	Sample details
S1	1	S1-T1	Y - Particle Size information	Samples S1-FA and S1-FB taken from fabric cast face; samples S1-TA and S1-TB taken from timber cast face.
S1	2	S1-T2	Y - Particle Size information	
S1	3	S1-T3	Y - Imaging with depth	
S2	1	S2-T1	Y - Imaging with depth	No sample taken.
S2	2	S2-T2	Y - Particle Size information	
S2	3	S2-T3	N	
S3	1	S3-T1	N	No samples taken.
S3	2	S3-T2	Y - Particle Size information and Imaging with depth	
S3	3	S3-T3	N	

Table 9.20: Concrete compressive strength summary.

Test series	Average cube strength after 28 days (MPa)*
Series 1	43.0
Series 2	43.0
*Average taken from three 100mm cube test.	

The specimens were demoulded 24 hours after casting before being cured at a constant temperature and humidity (21°C, 60% RH). After 21 days three 10mm thick wafers were cut from each prism, in the locations shown in Figure 9.23. These were then coated in clear optical resin (Araldite-DBF with Hardener HY 951 in a 10:1 ratio) and planed to a parallel finish (Figure 9.24(l)). Each wafer was then incrementally polished to a diamond grit size of 100x10<sup>-9</sup>m using a distilled water cooled polishing wheel (Figure 9.24(r)).

Of the nine wafers taken from the cast prisms, three were analysed for compositional data and three were analysed for particle size information (Table 9.19 on page 374). The remainder were not used due to time constraints. Each of the analysed samples was mounted on an aluminium platen before being vacuum coated with carbon (a layer of approximately 10x10<sup>-9</sup>m in thickness was applied to the surface) at a pressure of 1x10<sup>-5</sup> atmospheres to provide an electrically conductive layer for the imaging process. Degassing of the samples to the required vacuum level took approximately 48 hours, a reflection of their size and water and air content.

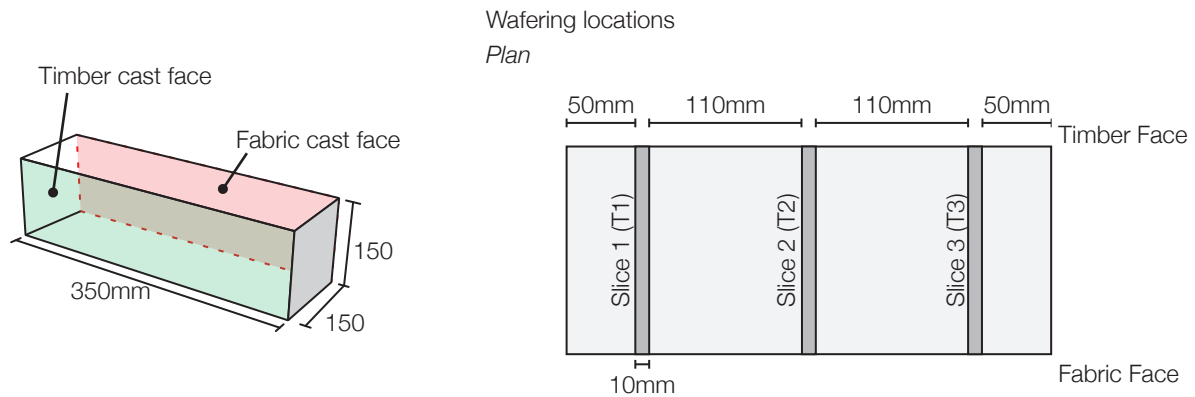


Figure 9.23: Location of test wafers from each concrete prism.

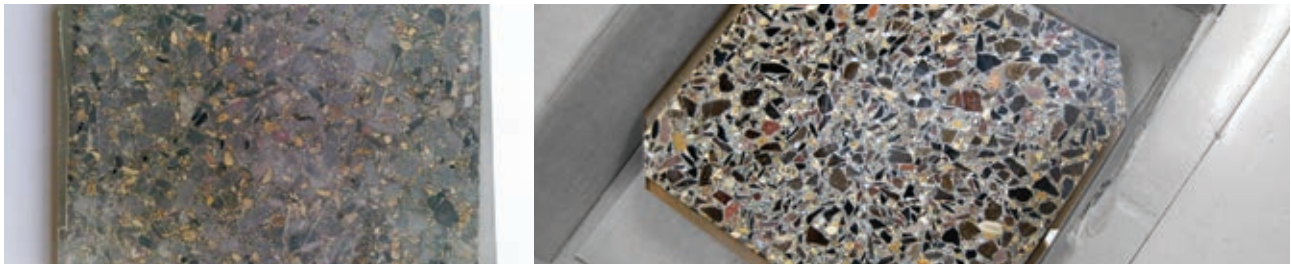


Figure 9.24: Resin coated samples (l); Polished sample (r).

#### 9.5.2.2. Analysis - Compositional data

Three wafers (S1-T3, S2-T1 and S3-T2) were analysed for particle size with depth from the cast face. Sites on each face of the wafers were chosen for imaging (located as shown in Figure 9.25) and images at increasing magnification were taken.

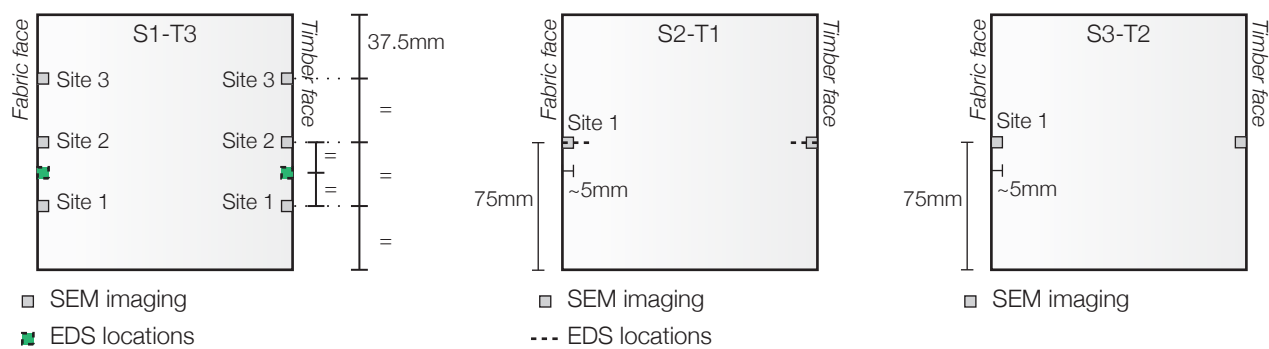


Figure 9.25: Imaging locations for Sample S1-T3, S2-T1 and S3-T2 (l-r).

Imaging results for Sample 1, Slice 3 (S1-T3) are shown in Figure 9.26, where the differences in surface morphology between the fabric and timber cast face can be seen (one site only is shown for comparison). Sample 3, Slice 2 (S3-T2) was then analysed by considering the changes in composition with depth between the fabric and timber samples. A composite image was generated at 100x magnification of the first 5mm of each sample, with the images being taken in the positions shown in Figure 9.25 and the resulting images shown in Figure 9.27. To illustrate more clearly the topology of the fabric cast face, images were taken in the surface zone of Sample S3-T2 at differing magnifications and are presented in Figure 9.28. The unique surface profile developed in the fabric cast face can be seen (compared to the flat surface of the timber cast face, Figure 9.26).

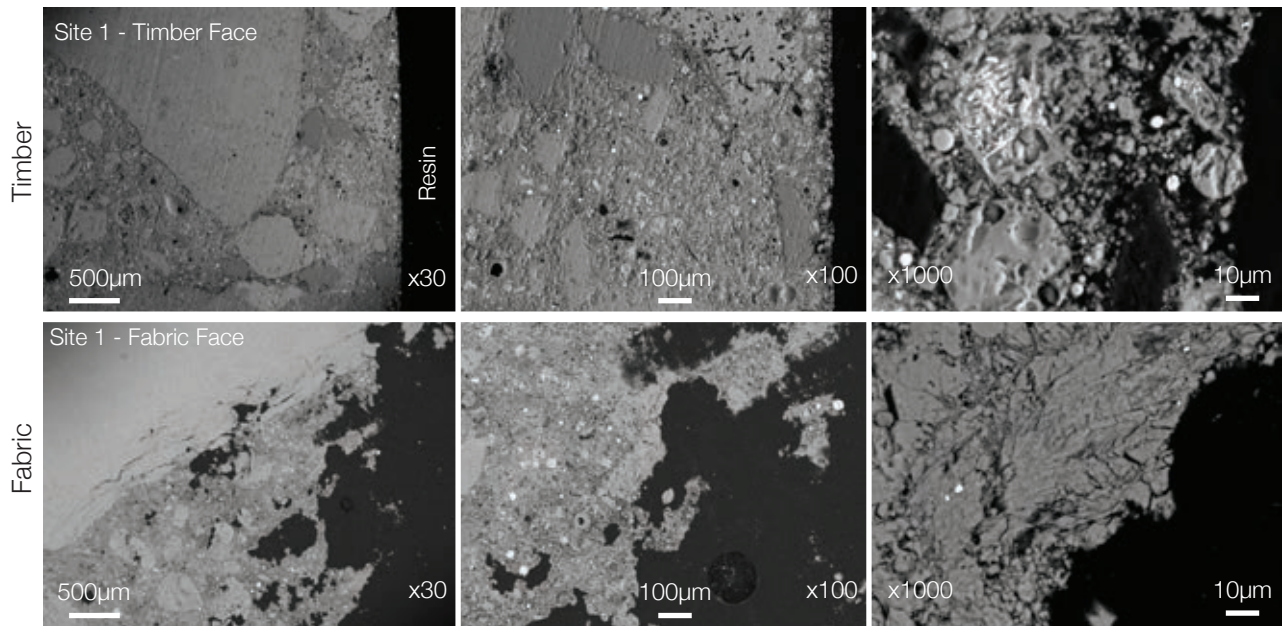


Figure 9.26: SEM Imaging for Sample S1-T3 showing Site 1 on the Timber and Fabric Faces (magnification at 30x, 100x and 1000x as noted).

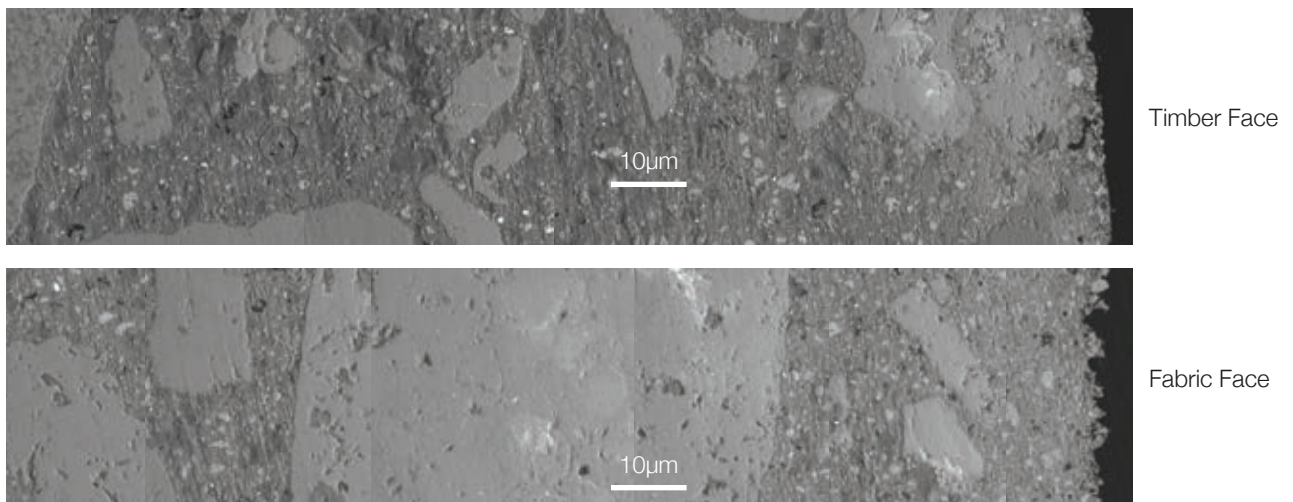


Figure 9.27: Composition with depth measured for Sample S3-T2 on Fabric and Timber faces (imaged at 100x magnification).

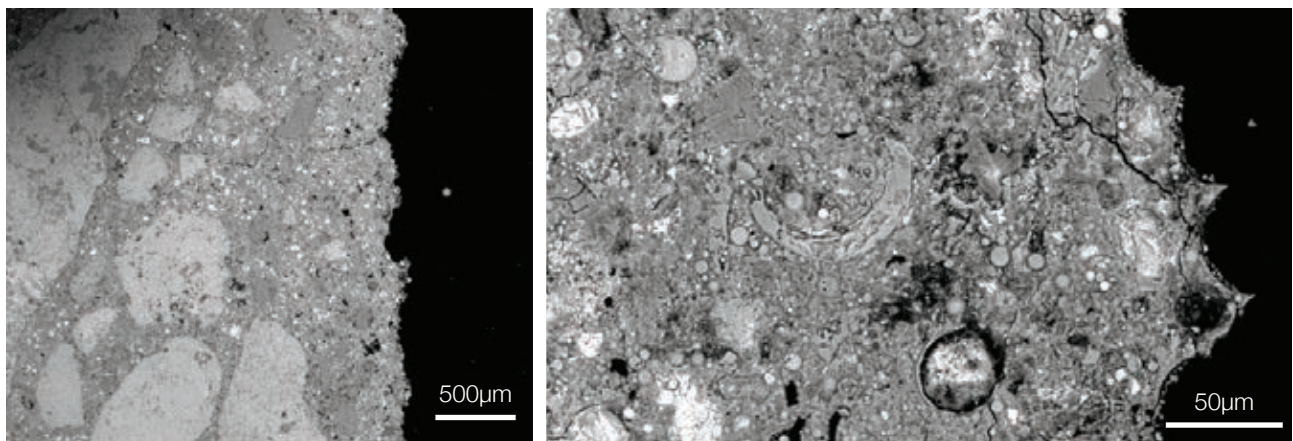


Figure 9.28: Fabric cast face in the surface zone for sample S3-T2 (27x magnification (l) and 400x magnification (r)).



### 9.5.2.3. Analysis - Particle size distribution

To determine how the particle size distribution varies between the fabric and timber cast faces a series of images were analysed using the open source analysis program 'ImageJ' (Ferreira and Rasband, 2011). Concrete slices S1-T2, S2-T2 and S3-T2 (see Table 9.19 on page 374) were coated in carbon before being imaged in a low-vacuum SEM mode to improve the contrast of the images at three sites on each face, as shown in Figure 9.29.

Images at 250x and 500x or 160x and 600x magnification were taken, with the 250x magnification image covering a distance of approximately 512µm, 500x magnification covering a distance of approximately 256µm, 160x magnification covering 1280µm, and the 600x magnification covering 213µm from the cast face. Each image was then processed by first converting it to a binary (black and white) image and marking grain sizes based on a watershed analysis, as described by Klapetek (2003) and illustrated in Figure 9.30. The results cover a maximum distance of 1.2mm from the cast surface, and whilst this is therefore a limited analysis, further time will be required to determine a fuller profile of the section from the surface into the cast concrete.

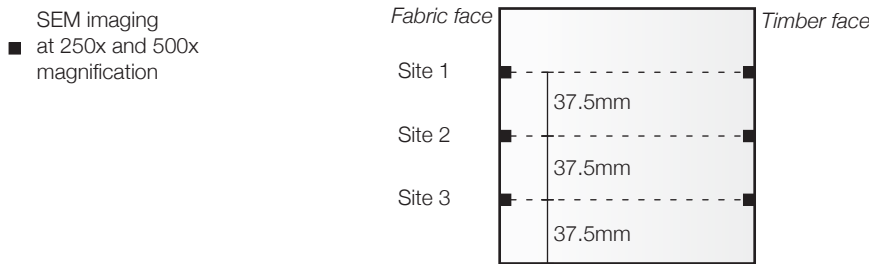


Figure 9.29: Analysis sites for particle size distribution.

ImageJ was used to determine the average particle size in each location and the results for all samples are provided in Table 9.21 on page 378. The results are arranged by image magnification, which is correlated to the distance from the cast surface that the image represents. The results are varied but on average show a significantly smaller particle size in the surface zone of the fabric cast member.

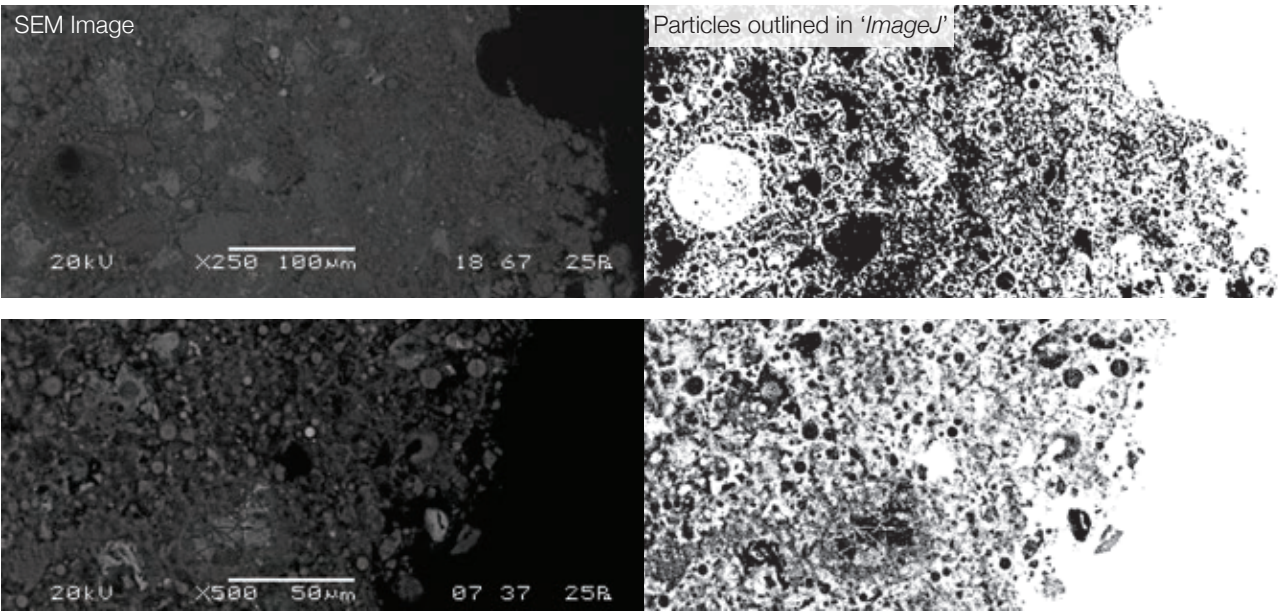


Figure 9.30: Watershed grain size analysis example from SEM image (250x (top) and 500x (bottom) magnification shown).

Table 9.21: Summary of grain size results.

Sample	Magnification	Average Particle Size		% reduction in fabric face
		Fabric face (μm)	Timber face (μm)	
1 (S1-T2)	500	0.714	3.772	81%
	250	2.025	7.247	72%
2 (S2-T2)	600	0.606	0.762	20%
	160	8.929	8.471	-5%
3 (S3-T2)	600	0.758	1.091	52%
	160	2.882	5.973	31%
4 (S1-T1)	600	0.536	0.369	-45%
	160	2.626	4.217	38%
Average				31%

9.5.2.4. Discussion - Series 1

The results of Series 1 have shown that topological differences between the fabric and timber cast faces can be seen and that the resulting composition in terms of particle size distribution may provide one reason by which the fabric cast face has shown significantly improved durability. Work is now required to build on these results to determine the porosity of the fabric and timber cast faces using the mercury intrusion porosimetry technique.

### 9.5.3. Series 2

The work presented in Series 1 above considered particle size differences between the fabric and timber cast concrete in cross section. To determine in more detail the changes in surface topology and properties, a further series of tests was undertaken on small prisms cut from the previously cast specimen S1 (Table 9.19 on page 374).

A 50x50x25mm prism was cut from both the fabric and timber cast faces and cut in half to provide a total of four samples from prism S1, as shown in Figure 9.31. The samples are identified as described in Table 9.19 on page 374.

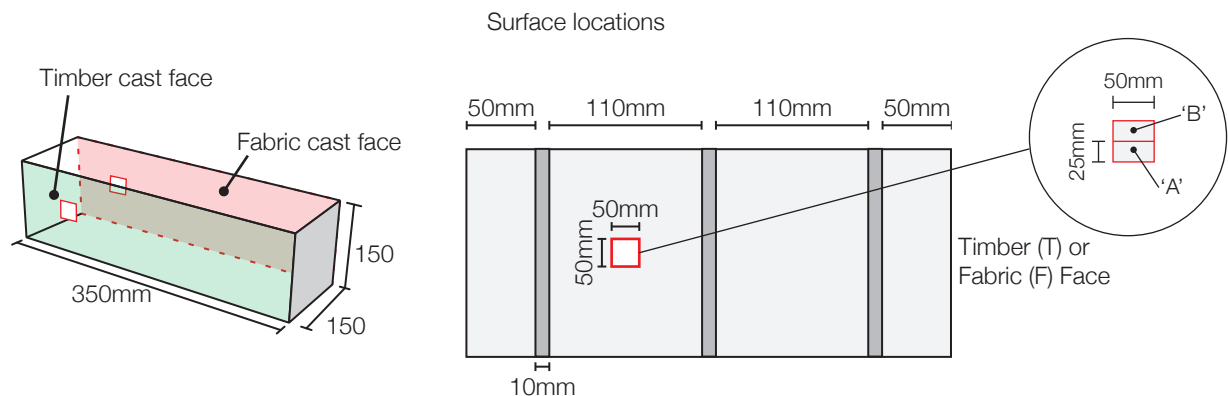


Figure 9.31: Samples for topology imaging in SEM.

All samples were tested 56 days after casting and had been stored in a constant temperature and humidity chamber (20°C, 60% RH) for this period. The samples were degassed for 96 hours to achieve the required vacuum level for SEM imaging, as described previously. Samples S1-FA and S1-TA were coated in conductive gold using a sputter coater and were imaged at progressively increasing magnifications. Samples S1-FB and S1-TB were coated in carbon and were then both imaged at increasing magnification and subjected to energy-dispersive X-ray spectroscopy to determine their chemical characteristics. The resulting images and EDS results are presented in the following sections.

#### 9.5.3.1. Results - SEM

Imaging of the timber cast surface of Sample S1-TA at increasing magnification is shown in Figure 9.32. At 18x magnification a large blow-hole is evident in the centre of the frame. At low magnifications the timber cast surface appears to be almost flat across the entire area. At increasing magnifications the distinctive structures of the surface concrete can be seen. These are subjected to EDS in §9.5.3.2.

Imaging of the fabric cast face of Sample S1-FA at increasing magnification is shown in Figure 9.33. At low magnifications the distinct changes in surface topography compared to the timber cast face are immediately evident, with deep furrows formed by the fabric fibres being visible at 18x magnification. An imprint of the fabric weave structure on the surface is clear, and the characteristic surface texture of the fabric cast concrete can be seen at all magnifications, creating weave areas and intersection areas between the individual fibre locations.



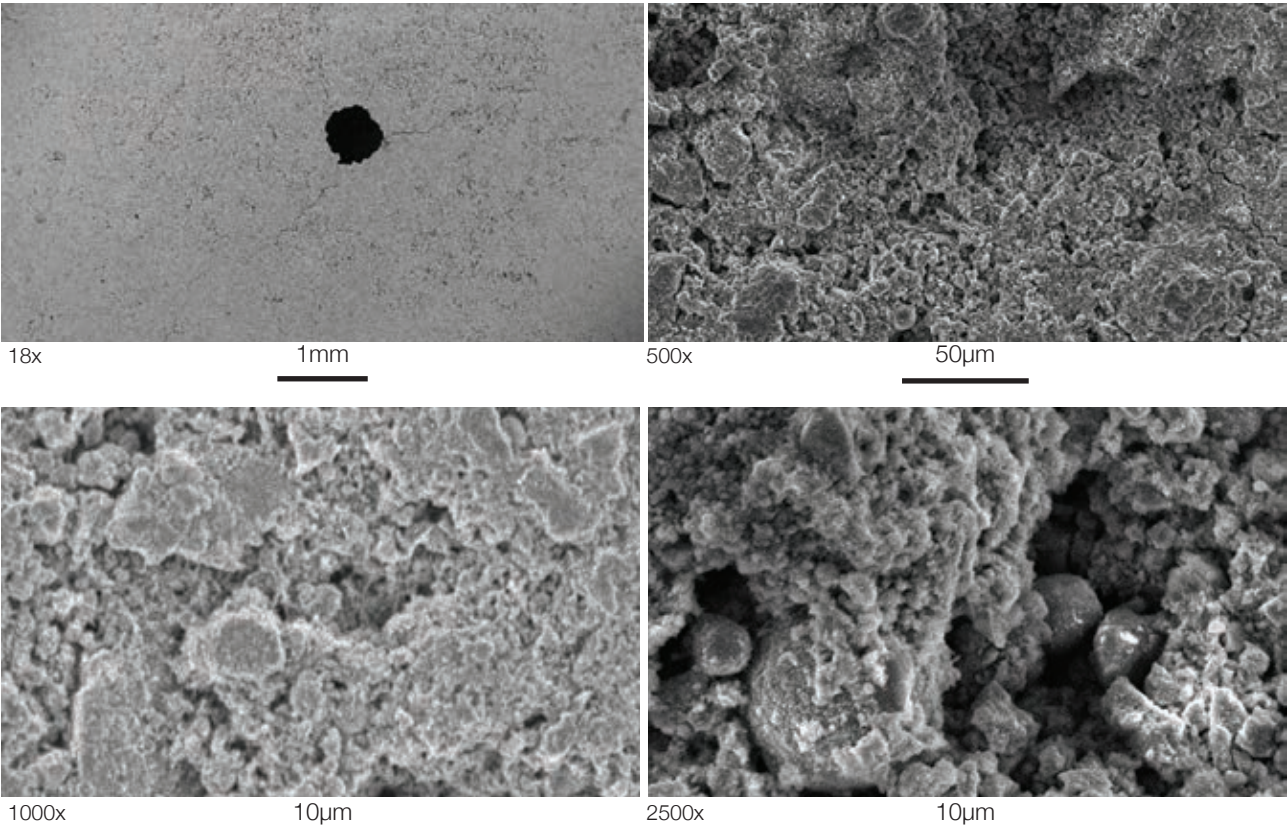


Figure 9.32: Imaging for Timber face (S1-TA) at 18x, 500x, 1000x and 2500x magnification.

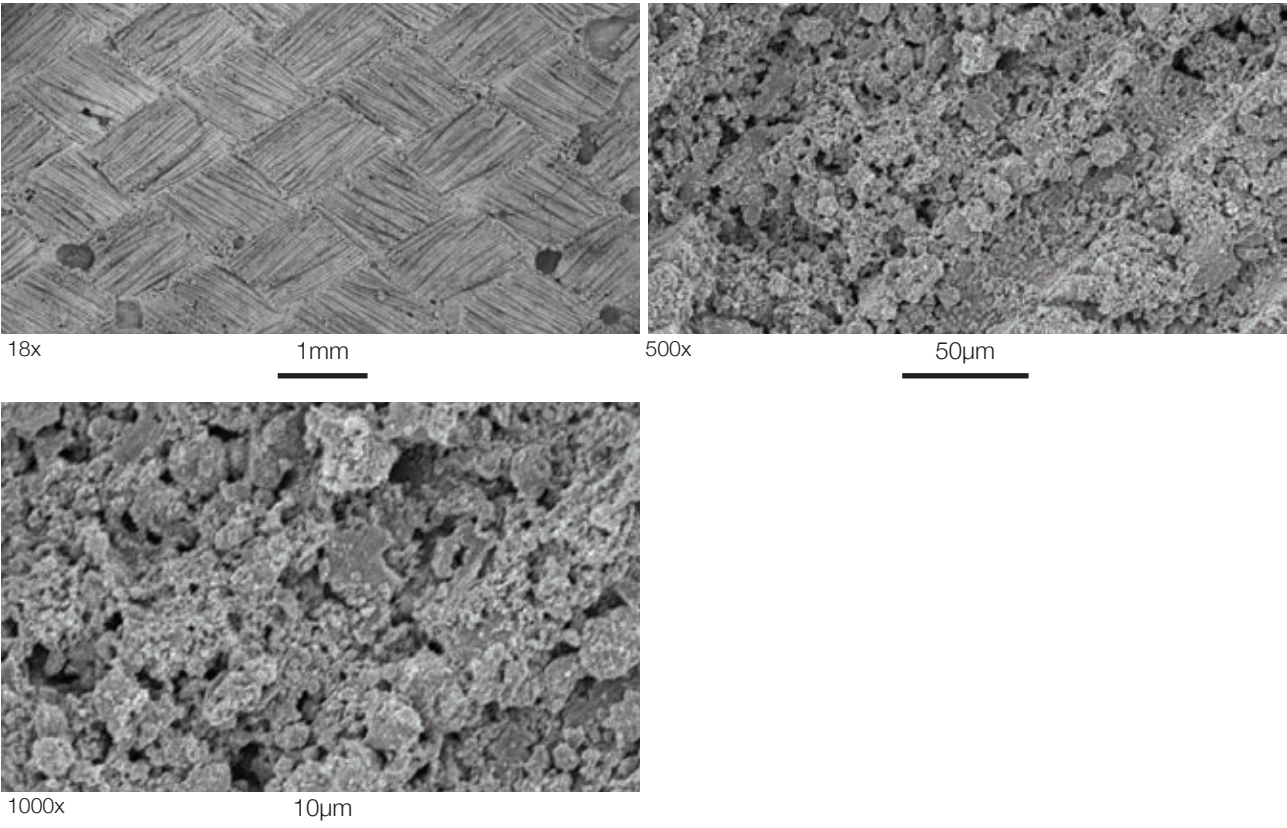


Figure 9.33: Imaging for Fabric Surface (S1-FA) at 18x, 500x and 1000x magnification.



Further investigation of the textured fabric cast surface was undertaken as shown in Figure 9.34. Imaging at higher magnification shows that furrowed areas of concrete form beneath the woven fabric fibres, and between the furrowed areas lie regions of material which have a similar appearance as those found in the timber cast as illustrated in Figure 9.35.

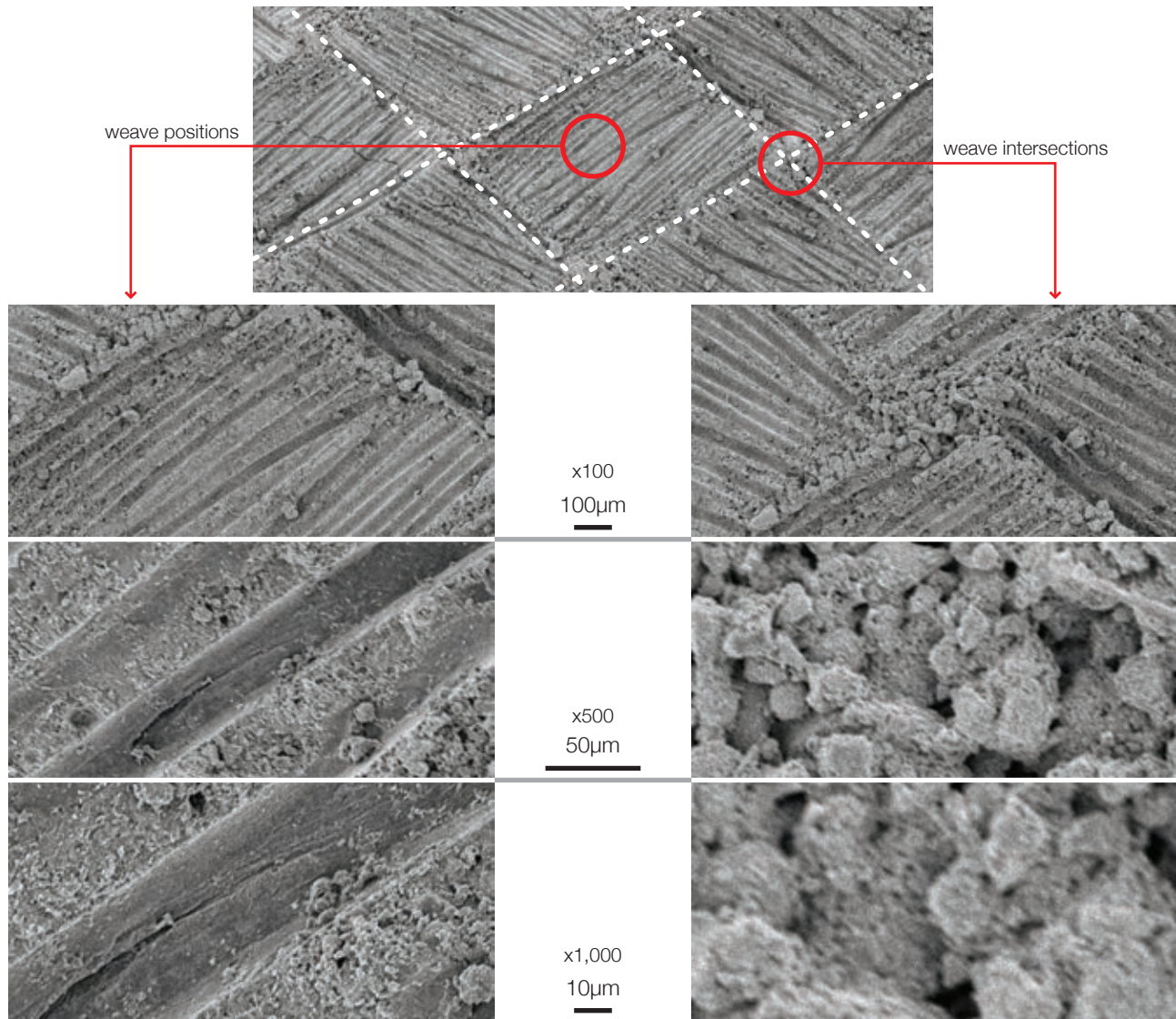


Figure 9.34: Detailed imaging of the fabric cast face.

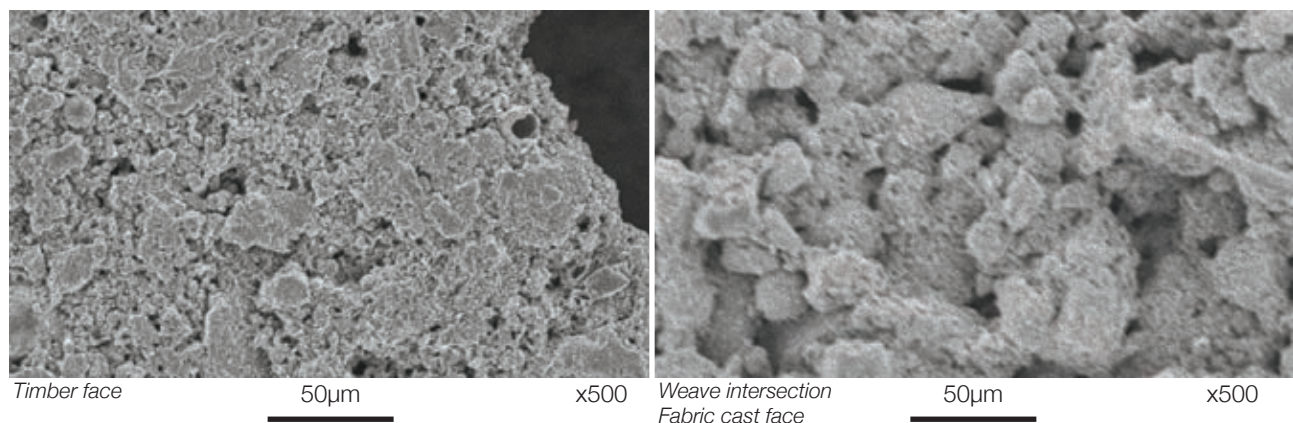


Figure 9.35: Comparison between concrete topology on timber cast face (l) with that found in the weave intersections on the fabric cast face (r).

Also evident on the fabric cast face are some areas without the characteristic surface texture of the majority of the surface, as shown in Figure 9.36(l). Further investigation of these areas shows their recessed topology to be similar to that found on the timber cast face. These voided areas were found predominantly in the intersection areas between fabric weaves, where the space between fabric fibres is the greatest, suggesting that it is from these areas that material is lost during the casting and curing process. It is therefore suggested by this that a reduction in the pore size of the woven fabric would ensure that material is not lost in these gaps, and a more uniform surface texture would result.

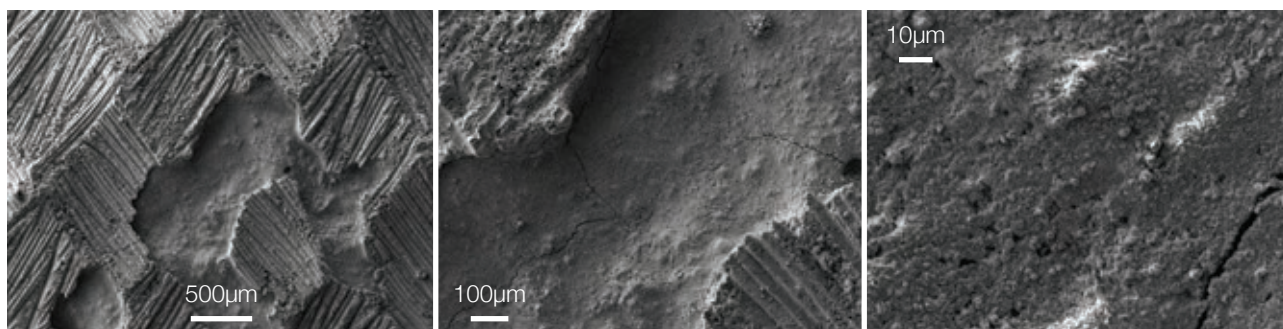


Figure 9.36: Void zones in the fabric cast concrete face at increasing magnification (l-r: x37, x110, x1000).

#### 9.5.3.2. Results - EDS

Samples S1-TB and S1-FB (Table 9.19) were subjected to EDS mapping in the locations shown in Figure 9.37. Mapping is undertaken by scanning the chosen surface area and taking a number of readings - in all of the following maps at least 1,000,000 readings were taken.



Figure 9.37: EDS locations for sample S1-TB (l) and sample S1-FB (r).

The resulting images and elemental maps are presented in Figure 9.38-Figure 9.40. Presented for each site are an SEM image of the site and a sum spectrum for the whole site, and intensity plots of Iron, Aluminium, Calcium and Silicon (shown as colour plots representing weight percentage for each element (i.e. varying between zero and 100%, shown as an intensity from black (0%) to red (100%)). Site 1 was imaged at 100x magnification, and Site 2 was imaged at 300x magnification. The resulting data was further analysed to provide the element maps described in §9.5.3.3 on page 385.

At each cast face there is a significant and almost uniform distribution of Calcium, which can be an indicator of the presence of Cement. Silicon is present across the surface, as are Aluminium, Potassium and Iron, with traces of the remaining elements visible. This pattern is replicated in both of the chosen test sites for Sample S1-TB.



Sample S1-FB was imaged at 30x magnification, and it is apparent from Figure 9.40 that the specimen has a lower intensity of Silicon on the surface, and a higher intensity of Calcium, when compared to Sample S1-TB, which suggests an increased presence of cement particles on the surface face.

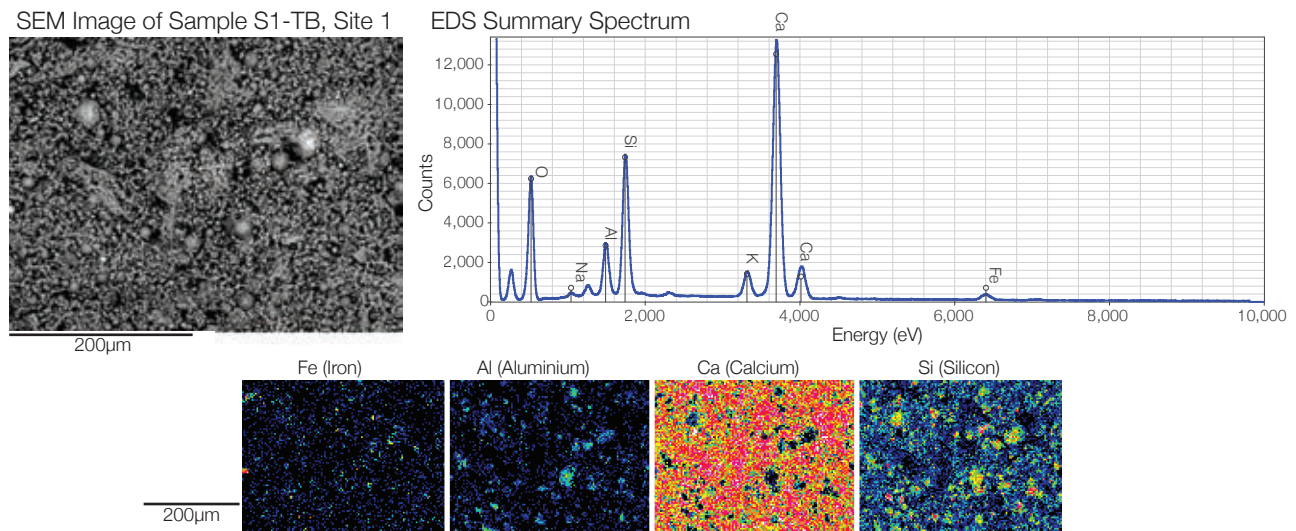


Figure 9.38: EDS Results for Sample S1-TB, Site 1.

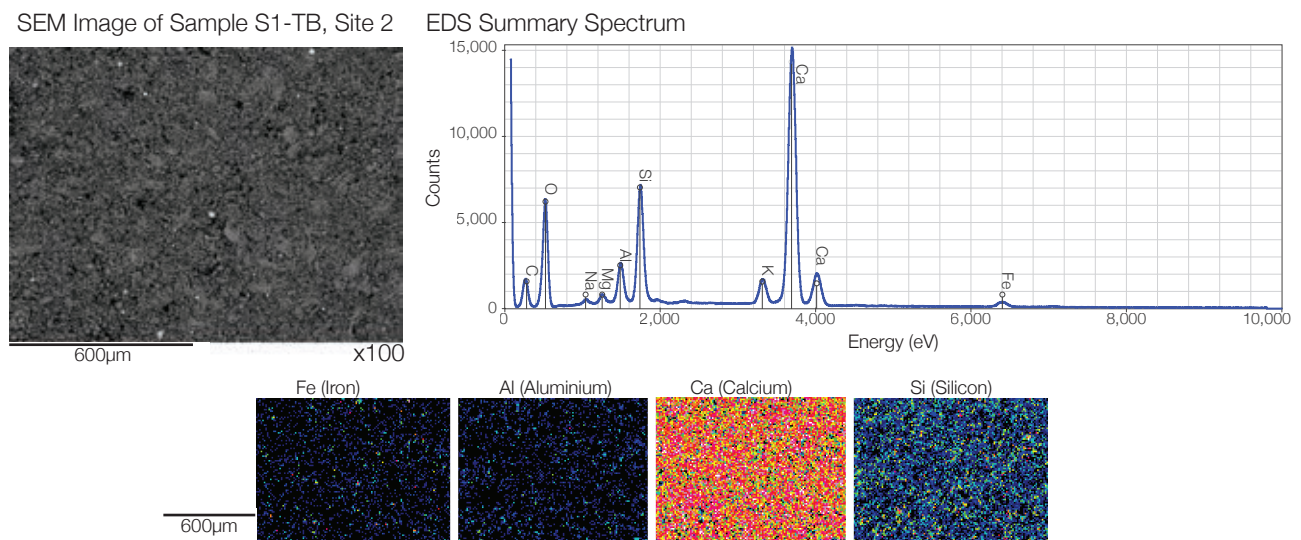


Figure 9.39: EDS Results for Sample S1-TB, Site 2.

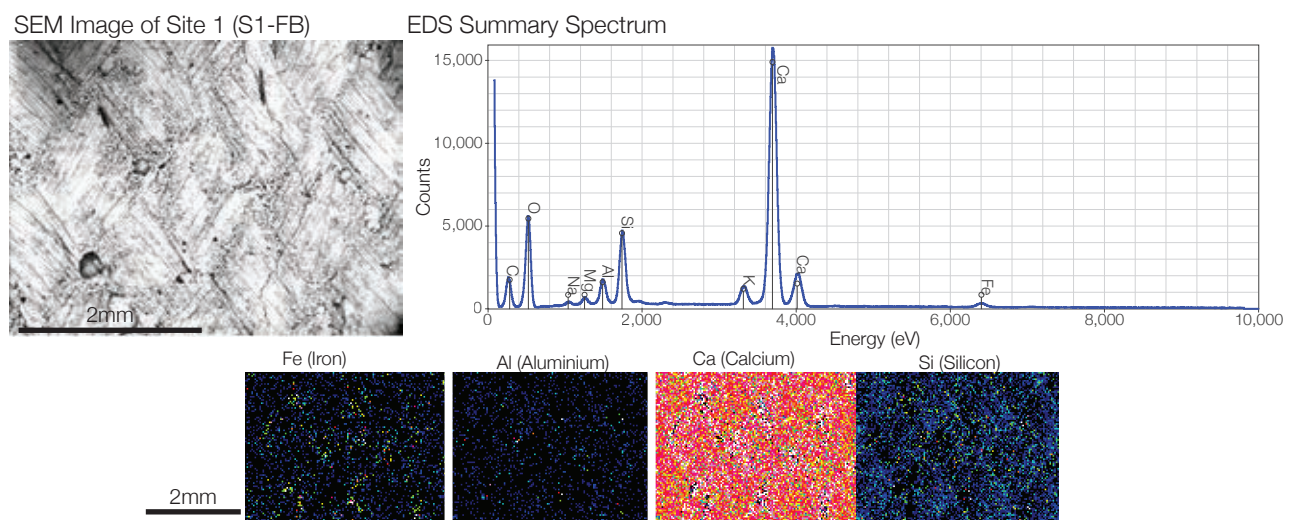


Figure 9.40: EDS Results for Sample S1-FB, Site 1.

Plots for the distribution of Calcium in Sample S1-FB are compared to the SEM imaging in Figure 9.41, where it is clear that compounds of Calcium form around the fabric fibres in greater concentrations than elsewhere. The familiar diagonal grid of fabric fibres can be seen in this distribution.

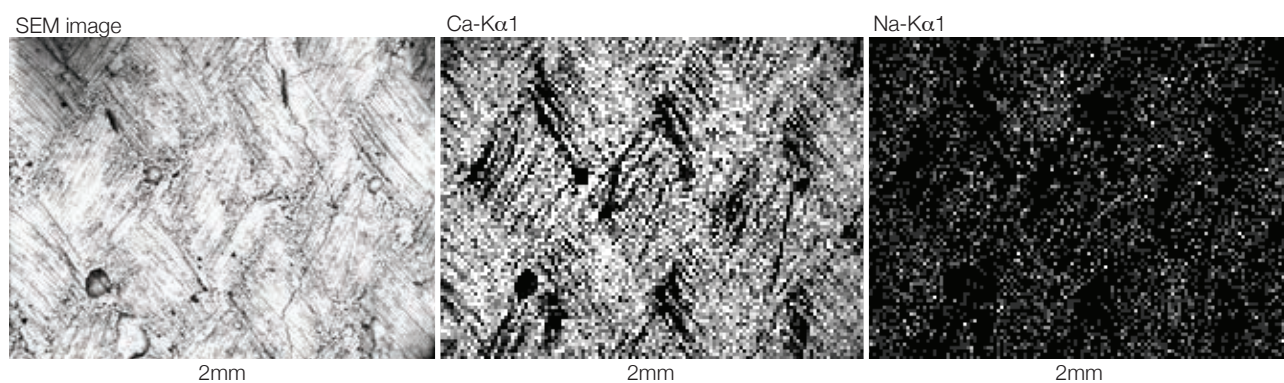


Figure 9.41: Distribution of Calcium ( $\text{Ca}(\text{K}\alpha)$ ) and Sodium ( $\text{Na}(\text{K}\alpha)$ ) compared to SEM image (I).

The compositional data presented shows that, for the sites analysed, the ‘fabric face’ tends to have less Silicon and marginally higher concentrations of Calcium. Given that Portland Cements are typically 60-65% calcium oxide ( $\text{CaO}$ ) then analysis for Calcium is suggested by Lamond (2006) as a good indicator of cement content on the surface, where the potential influence of non-siliceous aggregate is reduced.

It is also noted that Portland Cements do contain Silicon Dioxide (approximately 20% by weight, Lamond (2006)). Silicon counts are reduced significantly between the timber and fabric cast faces in samples S1-TB and S1-FB and this change is proposed to arise through a reduction in the presence of other, larger particles in the immediate surface zone of the fabric cast sample compared to the timber cast sample. These changes are thus postulated to demonstrate an increase in the relative concentration of cement particles at the surface zone, primarily demonstrated by an increase in Calcium ( $\text{CaO}$ ) recorded during the EDS testing. This higher concentration of smaller particles is in turn considered to be linked to the smaller pores recorded in the fabric cast concrete during sorptivity testing (§9.4 on page 364).

The fabric face of sample S1-FB was then subjected to EDS on the ridge structures that have been seen in all the preceding images, with the aim of determining the relative composition of the concrete surface at the weave and intersection positions. The results are shown in Figure 9.42, where it is apparent that in the weave positions the composition is predominantly of calcium compounds, while in the intersection areas silicon is present, indicating the larger sand particles tend to collect in these regions.

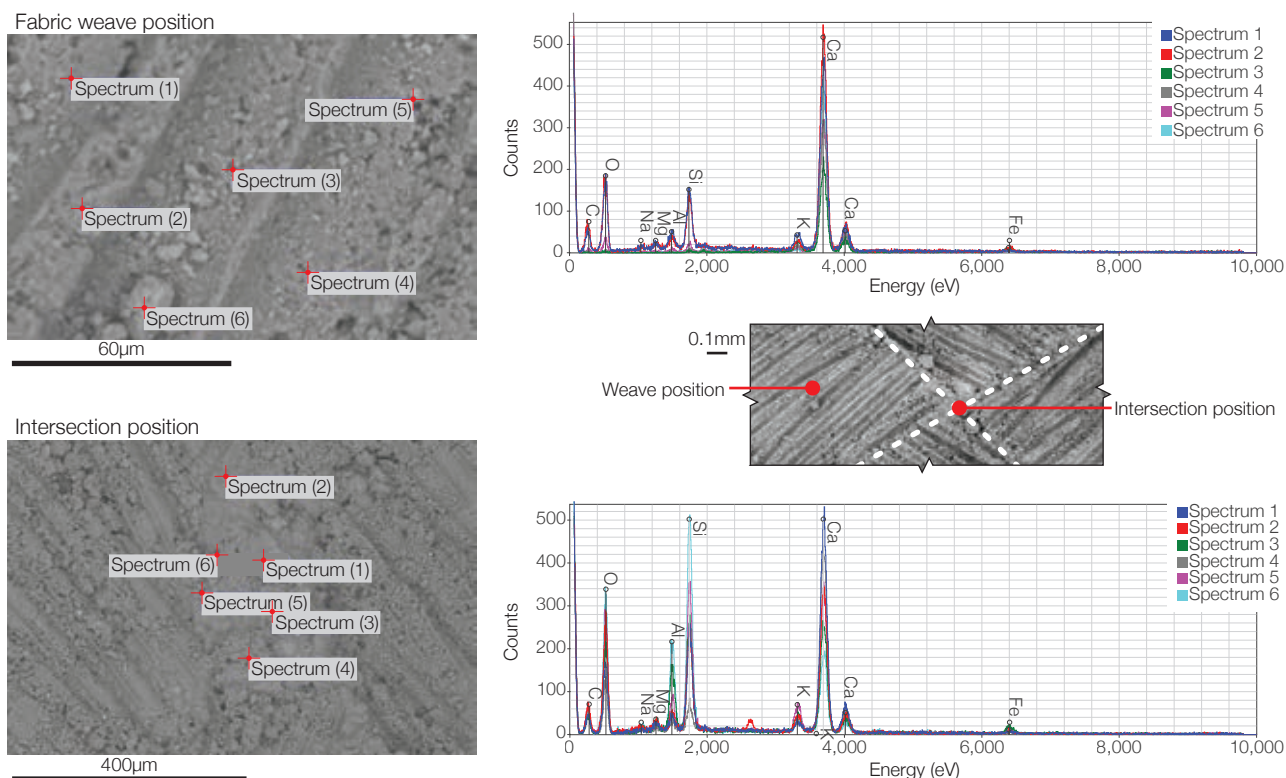


Figure 9.42: EDS Results for Sample S1-FB to compare ridge (top) and intersection zones (bottom).

#### 9.5.3.3. EDS Analysis

Each of the three element maps for the samples S1-TB (Site 1 and 2) and S1-FB (Site 1) was mapped using INCA software (provided by Oxford Instruments) to produce maps of the distribution of the eight elements identified in the sum spectra shown in Figure 9.38-Figure 9.40 on page 383 as being relevant to the analysis (these were Sodium, Magnesium, Aluminium, Silicon, Sulphur, Potassium, Calcium and Iron).

Each of the eight maps for each sample contains 12,288 pixels, with each given an intensity based on the percentage by weight of each element present. Three dimensional surface plots for each element at each of the three sample sites are shown to illustrate these results in Figure 9.43-Figure 9.45, where it can be seen that for some elements the majority of pixels have very low percentages by weight (the obvious exceptions to this being for Calcium and Silicon, which are presented in larger plots for clarity).



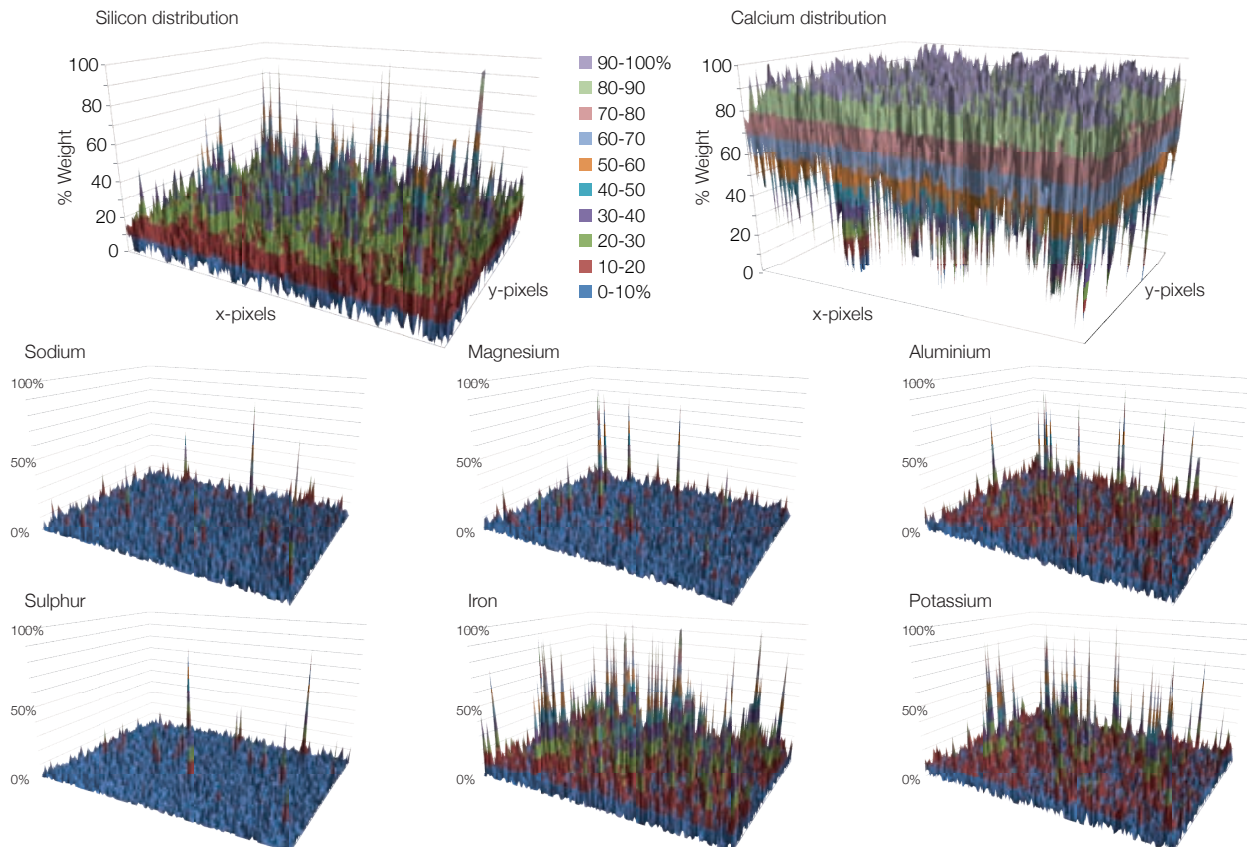


Figure 9.43: Histogram showing distribution of elements in each pixel of the SEM image by weight % for Sample S1-FB, Site 1.

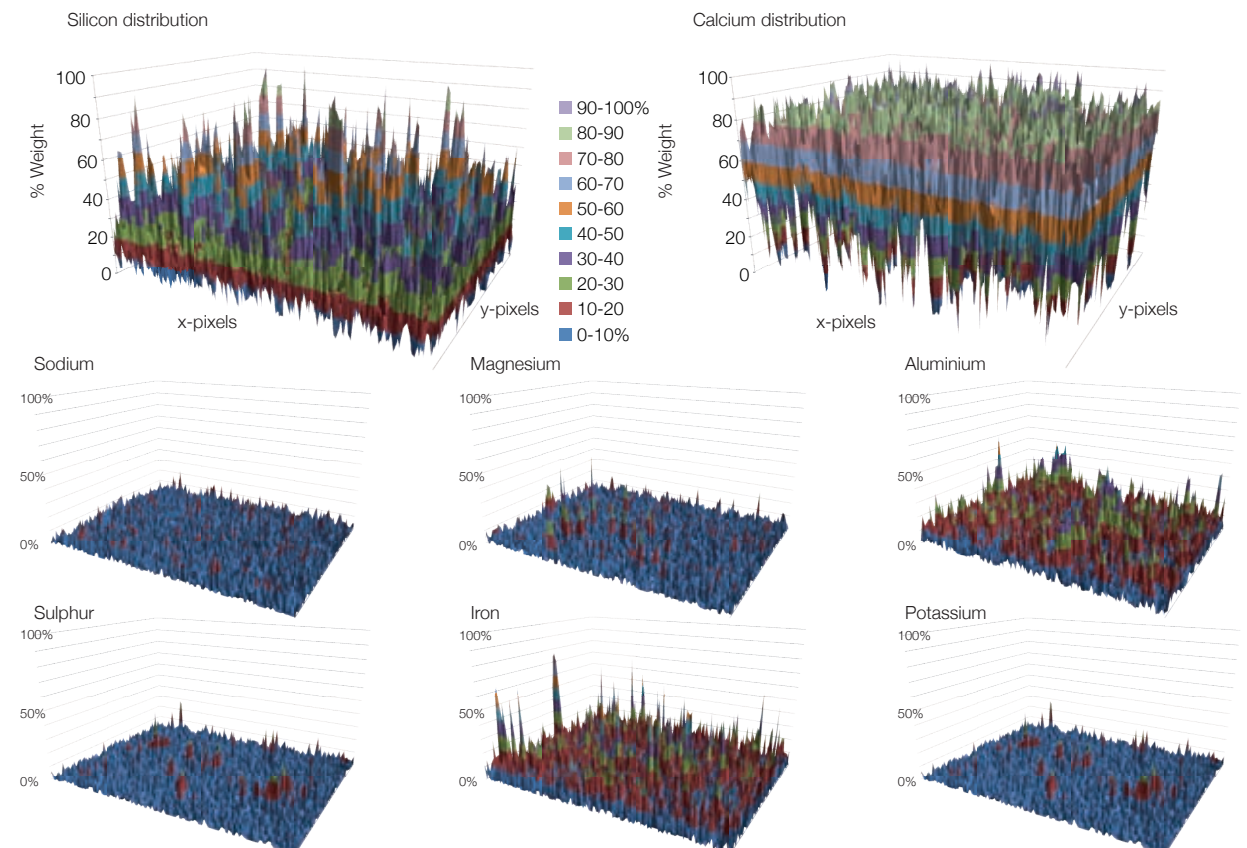


Figure 9.44: Histogram showing distribution of elements in each pixel of the SEM image by weight % for Sample S1-TB, Site 1.

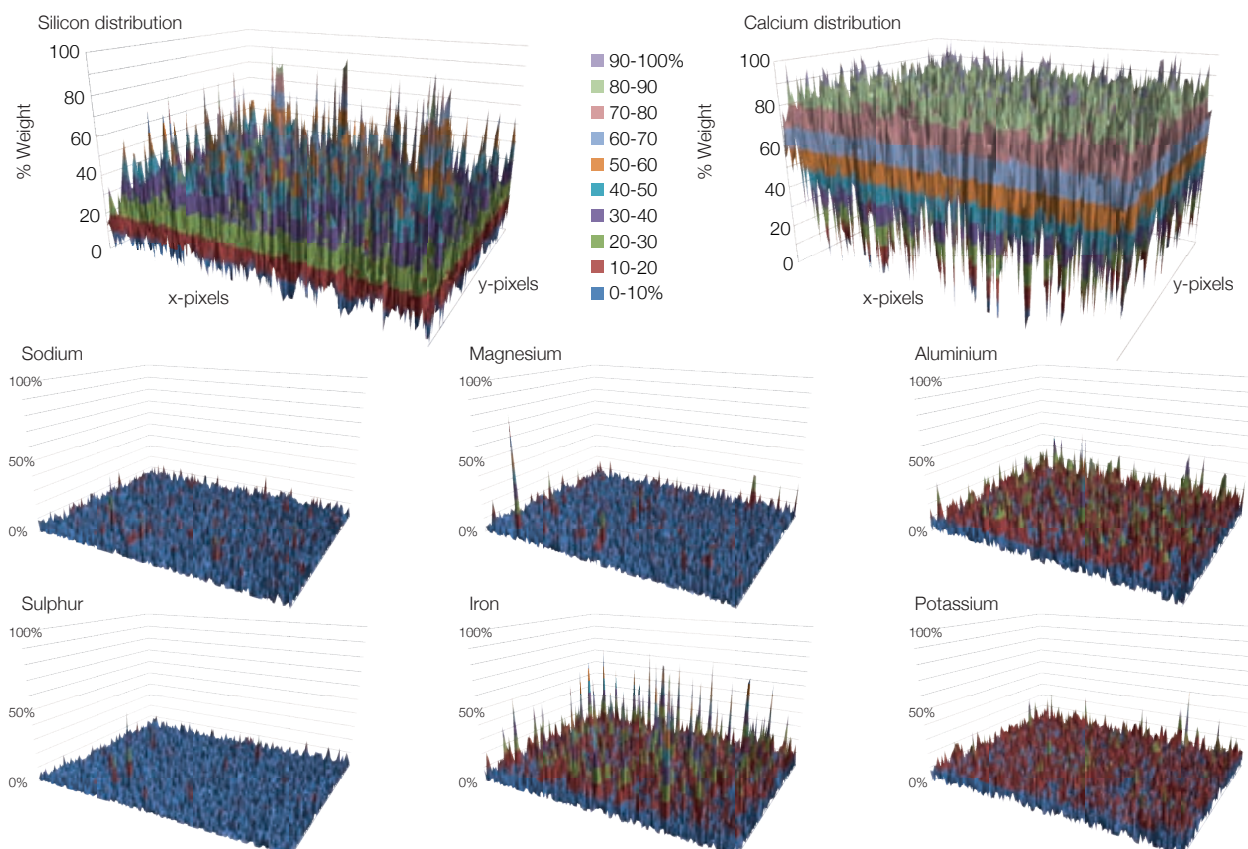


Figure 9.45: Histogram showing distribution of elements in each pixel of the SEM image by weight % for Sample S1-TB, Site 2.

The Spectra for sample S1-FB appear to demonstrate an increase in cement concentration at the fabric cast face when compared to the timber cast face, as a higher concentration of Calcium compounds were found in this area (Portland cements are typically 60% Calcium Oxide (Holland, 2005) and the typical constituents of a Portland cement include Tricalcium silicate ( $(\text{CaO})_3\text{SiO}_2$ ), Dicalcium silicate ( $(\text{CaO})_2\text{SiO}_2$ ), Tricalcium aluminate ( $(\text{CaO})_3\text{Al}_2\text{O}_3$ ), Tetracalcium aluminoferrite ( $(\text{CaO})_4\text{Al}_2\text{O}_3\text{Fe}_2\text{O}_3$ ) and Gypsum ( $\text{CaSO}_4\cdot 2\text{H}_2\text{O}$ )). It is, however, very difficult to draw firm conclusions from the EDS results as they represent just one small area of the sample.

In addition to the graphs for Sample S1-TB (Site 1 and Site 2) and Sample S1-FB (Site 1), the average and median values for each element by weight percentage were obtained from the matrix data, with this information presented in full in Table 9.22 and Table 9.23 on page 388. From these it can be seen that the mapped area of the fabric face had approximately 14% more Calcium, and 43% less Silicon, present at the surface, with the average values showing similar results (median values being preferred for comparison here as they reduce the influence of any outlying results).

Table 9.22: Median value in weight % for each element.

Sample	Na K	Mg K	Si K	Al K	S K	Fe K	Ca K	K K
Fabric	0.046	0.187	8.777	1.713	0.050	1.000	73.140	3.403
Timber SOI 1	0.098	0.626	16.351	4.326	0.109	1.126	62.373	4.249
Timber SOI 2	0.194	0.573	14.496	3.557	0.055	1.018	65.517	4.506
Average Timber	0.146	0.600	15.424	3.942	0.082	1.072	63.945	4.378
% Change at fabric face	-68%	-69%	-43%	-57%	-38%	-7%	14%	-22%

Table 9.23: Average value for each element by weight %.

Sample	Na K	Mg K	Si K	Al K	S K	Fe K	Ca K	K K
Fabric	1.772	1.929	10.777	3.806	1.224	5.097	70.387	5.008
Timber SOI 1	1.926	2.313	19.284	6.446	1.618	4.666	58.241	5.507
Timber SOI 2	2.036	2.210	16.940	5.377	1.384	4.388	62.095	5.570
Average Timber	1.981	2.262	18.112	5.911	1.501	4.527	60.168	5.538
% Change at fabric face	-11%	-15%	-40%	-36%	-18%	13%	17%	-10%

In mortar tests, El-Turki *et al* (2010) found that by dewatering (i.e. the removal of water from the cast face, in this case through the use of a porous brick substrate), a greater mortar strength was achieved. The increase in mortar strength recorded by El-Turki *et al* (2010) was found to arise through an initial reduction in the specimen's *water:cement* ratio as water was allowed to bleed from the surface. This process also resulted in a denser material structure. Once the dewatering process had reached equilibrium the remaining water, located close to the particles, then acted as sites for C-S-H (Calcium Silicate Hydrate) formation (which defines much of the strength of the mortar). This preferential formation of C-S-H is contrasted to the behaviour of a non-dewatered sample, where C-S-H can begin to form in any location with water present, resulting in lower mortar strengths. A similar effect may be happening in the fabric cast face.

However, since such an increase in C-S-H would also require that the recorded values for Silicon present on the surface should increase, the results presented in Table 9.22 and Table 9.23 may not support this hypothesis. Instead of an increase in cement content, a change in the presence of calcium hydroxide ( $\text{Ca}(\text{OH})_2$ ) at the surface of the fabric cast concrete face could be occurring. Such an effect would also help to explain the recorded reductions in silicon present at the surface. Further analysis on multiple samples is required to fully determine these changes in fabric cast concrete.

Further work is required to verify many of the results presented above. Opportunities and methods that could be used in such work are expanded and described by Stutzman (2000, 2004).

#### 9.5.3.4. Summary - Series 3

Series 3 of Test Group 4 has provided an indication of the changes in surface properties that arise in fabric cast concrete. The SEM imaging and EDS results show significant changes in the surface topology of fabric cast concrete, in addition to the distribution of elements at the surface zone. Higher concentrations of Calcium and reductions in Silica concentrations suggest smaller particles are collected at the surface zone, providing a dense region that provides the increased resistance to carbonation, chloride ingress and the improved surface hardness seen in durability tests.

Previous work (Price, 2000) shows a link between *water:cement* ratio and the improvements in surface properties found in permeable formwork. The challenge of measuring *water:cement* ratios in hardened concrete is, however, considerable. Much of the work undertaken to date uses optical techniques such as those described by Skjovsvoold (1991, cited by Price, 2000) and codified in NT Build 361 (1999). Using fluorescent dyes, a range of concretes with known *water:cement* ratios must be compared to the test specimen before its *water:cement* ratio can be estimated. Considerable preparation time is required, and the test accuracy is entirely dependent on the number of comparators that are cast. For this reason, this technique was not employed in these tests.

Additional future work should consider the design of a new fabric whose properties are optimised to modify the concrete surface to provide increases in durability whilst also retaining surface quality, shrinkage resistance and ease of construction.

Further discussion and analysis of the results of this and the preceding sections is presented in §9.7 on page 399. In the following, a final series of tests are undertaken to verify the increases in cement concentration seen at the surface of the fabric cast concrete. Since the relationship between concrete strength and cement content is well known, it is estimated that a reduced *water:cement* ratio will provide concrete with greater strength. A suitable means by which this can be determined is through the use of a surface hardness test, as is described in §9.6.

## 9.6. Test Group 5 - Surface hardness

In addition to improved resistance to carbonation and chloride ingress, as described in the preceding sections, reductions in the surface *water:cement* ratio may reasonably be expected to result in improvements in the surface strength of fabric cast concrete. This effect has been seen in the increased concentrations of cement in the fabric cast concrete, as revealed by EDS analysis in §9.5. To determine the magnitude of these changes, two series of tests were undertaken to compare the surface strength of timber and fabric cast concrete.

Series 1 considered the surface hardness of concrete prisms, while Series 2 was arranged to determine the depth to which any improvements in surface hardness extended beyond the cast face.

### 9.6.1. Series 1 - Prism testing

In Series 1 surface hardness tests were carried out using a Schmidt hammer on four prisms with dimensions 400x400x100mm. The test prisms were cast in special moulds (described in Table 9.24 and Figure 9.46) while conventional 100x100x100mm cubes were cast alongside to provide reference compressive strengths. The specimens were compacted in the moulds either by hand or using a vibrating poker. Specimens 1.1 and 1.2 were tested at 28 and 90 days, while Specimens 1.3 and 1.4 were tested at 35 and 95 days. Specimen 1.3 was then also tested at incremental depths from the surface, as described in §9.6.1.4 on page 393.

Table 9.24: Surface hardness test details.

Specimen	Test ages	Compaction	Number	Specimen	Test ages	Compaction	Number
1.1	28, 90 and 180 days	Vibrating poker	1	1.3	35 and 95 days	Hand	1
1.2	28, 90 and 180 days	Vibrating poker	1	1.4	35 and 95 days	Hand	1

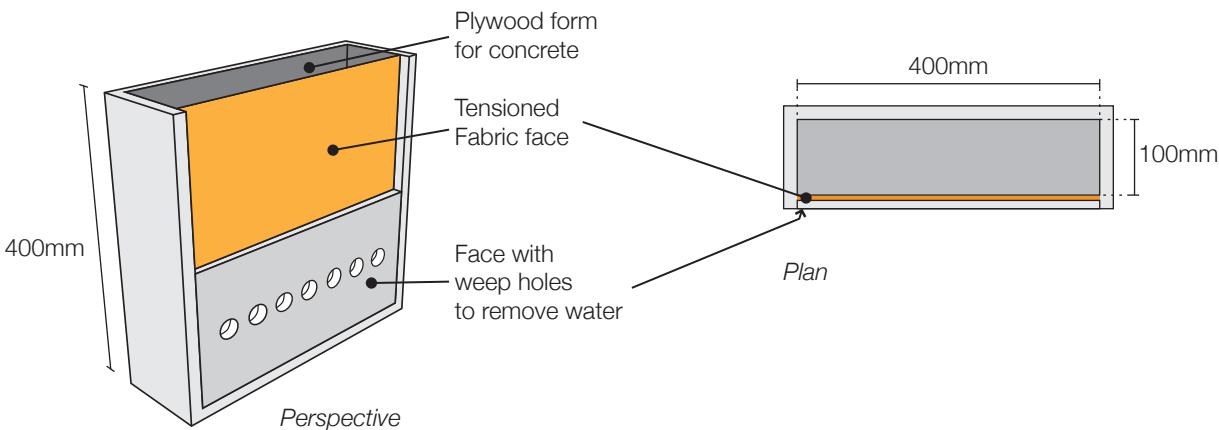


Figure 9.46: Surface hardness specimen preparation.

#### 9.6.1.1. Surface hardness test procedure

Surface hardness was measured using rebound hammer tests in accordance with BS EN 12504-2 (2001). Following mixing, concrete was placed in the moulds in four layers of equal depth and compacted. Specimens 1.1 and 1.2 were compacted using a vibrating poker, while Specimens 1.3 and 1.4 were compacted by hand



using a square compacting bar. All specimens were demoulded after 24 hours before being cured in a constant temperature and humidity chamber (21°C, 60% RH) prior to testing.

The test surfaces were first lightly ground to a smooth finish using an abrasive stone (to avoid the influence of surface texture on rebound results; as described by Cairns (1999)). A 50x50mm grid was marked onto the test faces, with the first test location being 50mm from a free edge, as illustrated in Figure 9.47. The specimen was then clamped to the floor and held in position using tensioned threaded rods, as illustrated in Figure 9.47. The specimen was orientated in the same direction as it was cast, and the same frame was used for all tests.

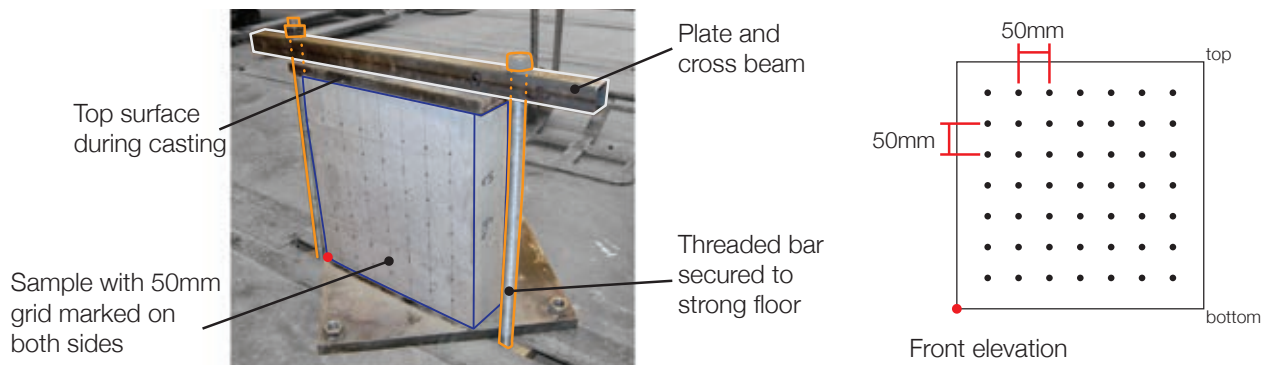


Figure 9.47: Test specimen with grid marked on the surface and held securely against a strong floor.

With the specimen secured, a Schmidt hammer with an impact energy of 2.207Nm was held perpendicularly to the concrete surface and released. The rebound number was recorded from the instrument and adjusted according to the manufacturers charts to provide an estimate of the in-situ concrete strength. The procedure was repeated at both test dates for each set of prisms.

#### 9.6.1.2. Surface hardness test results

All samples used the same mix design and cube strengths (average of three tests) for the specimens are presented in Table 9.25. Comparisons between the rebound number results as recorded by the Schmidt Hammer from both fabric and timber faces of each specimen are shown Figure 9.48-Figure 9.49 with percentage changes in surface hardness for each specimen summarised in Table 9.26. The distance from the top surface of the specimen is recorded and the seven tests are spaced 50mm apart across the face of the sample.

Table 9.25: Recorded cube strengths for surface hardness tests.

Specimen	Average cube strength after 28 days (MPa)	Average cube strength after 35 days (MPa)
1.1 and 1.2	42.2	-
1.3 and 1.4	44.6	51.9

Table 9.26: Summary of surface hardness results for Specimens 1.1, 1.2, 1.3 and 1.4.

Specimen	Test date (days after casting)	Average percentage improvement in surface hardness at the fabric face compared to the timber cast face
1.1 and 1.2	28	9%
1.1 and 1.2	90	5%



Specimen	Test date (days after casting)	Average percentage improvement in surface hardness at the fabric face compared to the timber cast face
1.1 and 1.2	180	3%
1.3 and 1.4	35	13%
1.3 and 1.4	95	7%

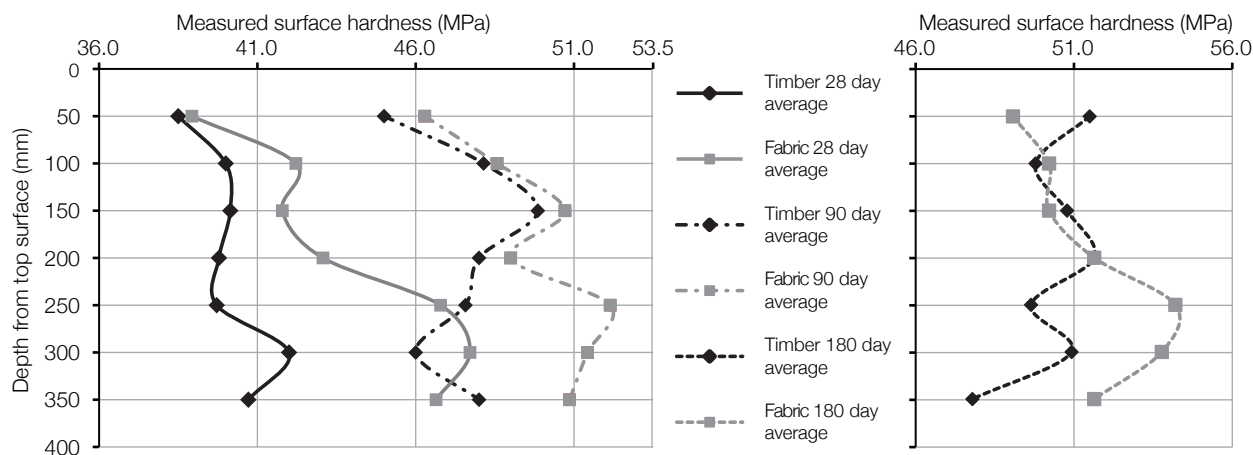


Figure 9.48: Results for specimens 1.1 and 1.2 after 28 days and 90 days (left) and 180 days (right).

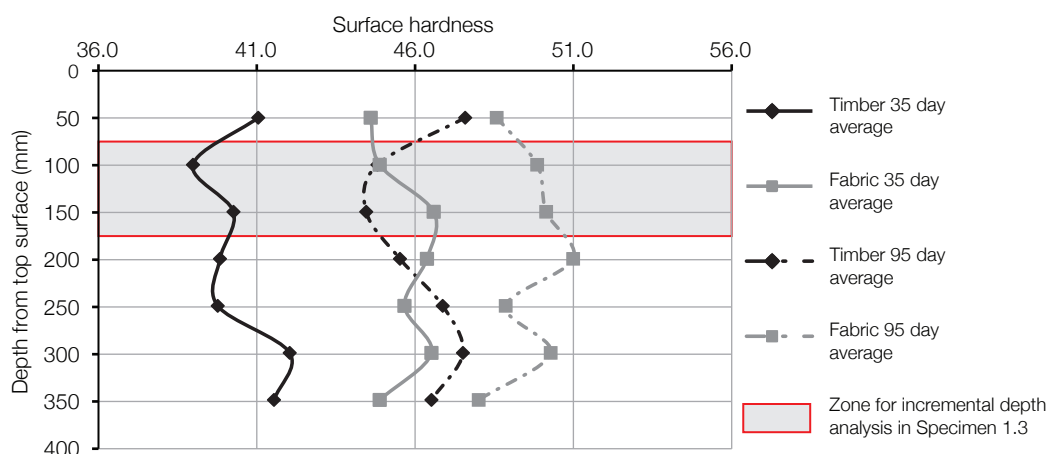


Figure 9.49: Results for specimens 1.3 and 1.4 after 35 days and 95 days.

### 9.6.1.3. Analysis

The test results for Series 1 show that fabric cast concrete can provide improvements in surface hardness of up to 18%, and these improvements can be attributed to the removal of excess pore water in the surface zone of the sample that results in a cement rich surface. Specimens 1.3 and 1.4, which were compacted by hand, show a consistent improvement in surface hardness with depth at both 35 and 90 days.

Specimens 1.1 and 1.2, which were compacted using a vibrating poker, show similar improvements beyond the mid-height of the sample, although this improvement appears to be more pronounced at the earlier test date. The lower surface hardness at the top of the sample suggests that the vibrating poker did not provide sufficient compaction to the top zone. In addition, the action of the vibrating poker encourages water to rise towards the top of the sample, where there is less hydrostatic pressure to drive it from the fabric surface. This effect may be partly responsible for the lower improvement in surface hardness seen in specimens 1.1 and 1.2.

The improvement in the surface hardness of the fabric cast concrete was found to reduce by up to 50% at the later test date. This suggests that the fabric cast surface achieves a higher surface hardness more quickly than the timber cast surface, with this difference changing over time. A series of tests over a much greater time period is required to verify these results and to supplement the limited data available in the literature.

Average improvements in surface hardness, given in Table 9.26 appear at first sight to be relatively small - between 5% and 13% - but it should be noted that tests at the top and bottom of all samples showed slightly lower surface hardness results than were seen around the mid-height. This suggests that both edge effects in the sample (particularly at the bottom) and hydrostatic pressure are important. Future work should consider carrying out tests on much larger wall panels to give more representative results over a greater surface area.

#### 9.6.1.4. Surface hardness at incremental depth

To determine how far into the sample the improvements in surface hardness penetrate Specimen 1.3 was analysed in greater detail, as described below. A prism with dimensions 150 x 400 x 100mm, was cut from Specimen 1.3 in the location shown in Figure 9.49 for further analysis. Using a water cooled diamond saw, a 3mm slice was cut from both the fabric and timber cast faces to expose the concrete beneath. The sample was then left to dry before being secured to the laboratory floor. Surface hardness readings were then taken in the same locations as carried out on the complete Specimen (as described above).

Two further cuts were then made and surface hardness readings at 3, 6 and 9mm from the cast face were collected. Greater depths were not tested as the sample had then begun to exhibit small cracks on the surface due to both the effect of the diamond saw and the impact hammer.

The results of these hardness tests with depth are summarised in Figure 9.50, where it is apparent that beyond approximately 9mm from the fabric cast face, there is only a small improvement in surface hardness. The graphs also illustrate that the improvement seen in the fabric cast face drops off very quickly, from almost 16% improvement at the surface (0mm) to just over 2% at 9mm from the surface. A photo at each depth increment reveals some of the changes taking place, as shown in Figure 9.51.

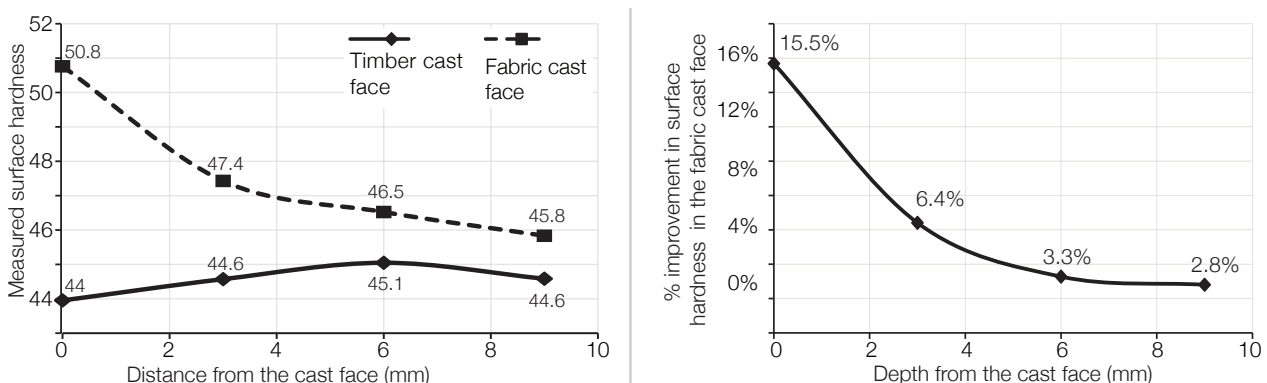


Figure 9.50: Improvements in surface hardness with depth for Specimen 1.3 at 95 days (l); Average percentage improvement seen in the fabric cast face at each test depth (Specimen 1.3) (r).

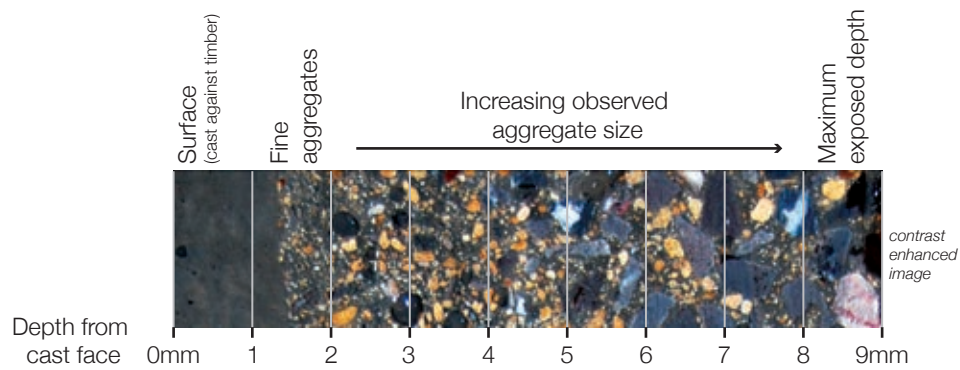


Figure 9.51: Composite photo of appearance of the concrete surface between 0 and 9mm from the timber cast face.

#### 9.6.1.5. Conclusions

Series 1 has shown that the expected increases in surface hardness due to reduced water:cement ratios at the surface of fabric cast concrete have been realised. The extent of these improvements has been determined for one fabric and concrete combination, and initial results suggest that such improvements extend to around 10mm depth from the cast face.

Further work is undertaken in §9.6.2 on page 395 to determine the depth to which the improvements seen above extend beneath the surface for a variety of fabric types.

### 9.6.2. Series 2 - Surface hardness with depth

Building on the work of Series 1, the aim of Series 2 was to determine the depth to which improvements in surface hardness were obtained in the fabric cast concrete and to compare the improvements between three fabric types. The fabric types chosen are detailed in Table 9.27, with Fabric 1 being used in all previous tests (previously described in Table 9.3 on page 343) and Fabrics 2 and 3 being provided by DuPont for the purpose of these tests.

Table 9.27: Fabric types used in Series 2 surface tests.

Designation	Name	Material		Tensile Strength		Elongation		Pore Size
		Warp	Weft	Warp	Weft	Warp	Weft	
Fabric 1	Marine Geotextile	Polyester (1100 dtex)		54kN/m		25%		423µm
Fabric 2	Zemdrain Classic	Polypropylene (black)		>18kN/m		NA		20µm
Fabric 3	Zemdrain MD	Polypropylene (white)		>19kN/m		NA		35µm

#### 9.6.2.1. Specimen details

Three specimens of dimensions 150 x 150 x 350mm were cast in special moulds (Figure 9.52) sized to pass through a diamond saw such that slices of concrete could be removed to allow the exposed concrete to be tested at increasing depths using a Schmidt hammer. The specimens are summarised in Table 9.28.

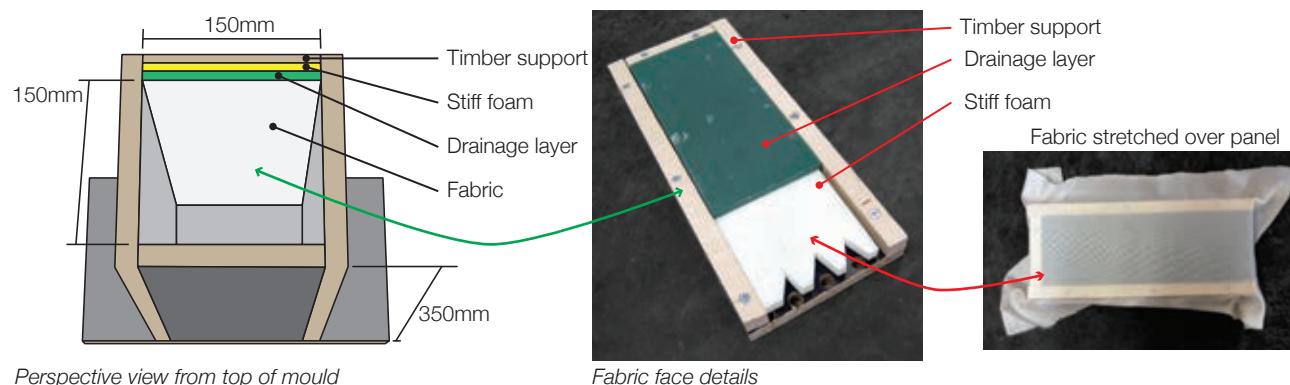


Figure 9.52: Prism moulds for Series 2 hardness tests.

Table 9.28: Test specimens.

Test specimen	Fabric type	Test age
2.1	1	28 days
2.2	2	28 days
2.3	3	28 days

#### 9.6.2.2. Test procedure

Following mixing to the mix design shown in Table 9.2 on page 343, concrete was placed in the moulds in five layers and compacted by hand (Figure 9.53(l)). The specimens were demoulded after 24 hours before being cured in a constant temperature and humidity room (21°C, 60% RH) for 28 days (Figure 9.53(r)).

After securing the specimens to the laboratory floor (Figure 9.54) the surface hardness of the cast face of each prism was tested as described in §9.6.1.1 on page 390. Upon completion of the first test, the specimen was removed from the test rig. The first 1mm of concrete was then removed from both fabric and timber cast faces using a diamond saw. After smoothing the cut surface with a grinding stone, the surface hardness was again measured using the Schmidt hammer and the results recorded.

The same procedure was then undertaken with further slices at 5mm and 10mm from the cast surface and all the results were collated. All hardness testing was undertaken on a dry surface.

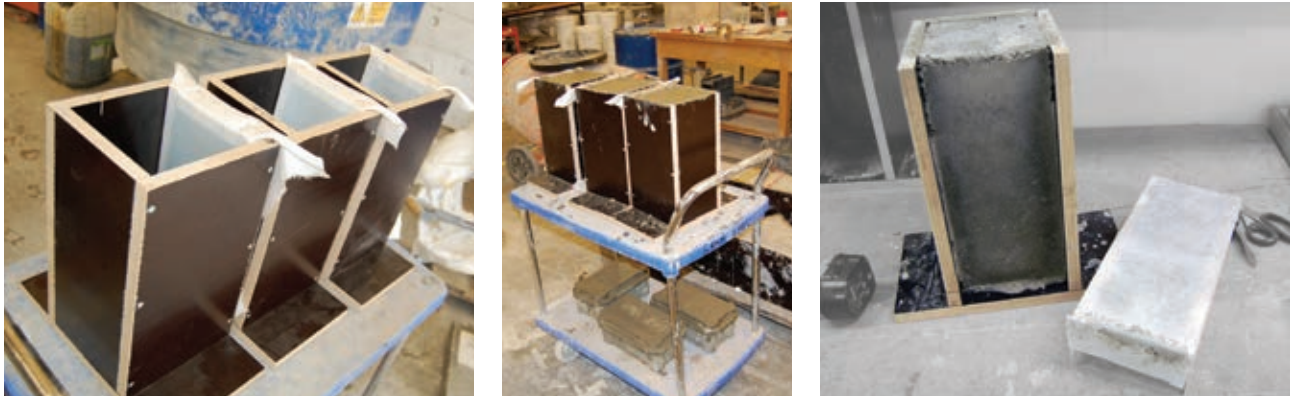


Figure 9.53: Three Series 2 moulds (l); Casting (c); Demoulded prisms (r).

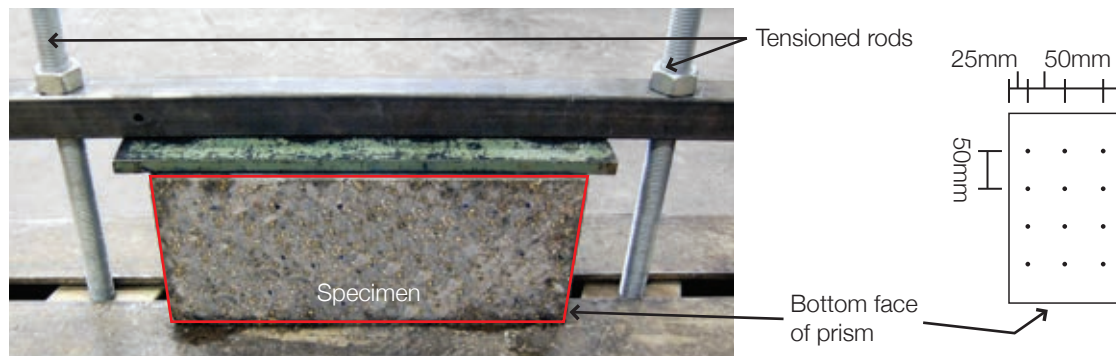


Figure 9.54: Securing series 2 prisms for surface hardness testing (l); Test locations (r).

### 9.6.2.3. Results

The results of Series 2 are presented in Table 9.29 below. A comparison between surface hardness in fabric and timber cast faces is provided in Figure 9.55, while the average percentage improvements for each fabric type are given in Figure 9.56 (error bars represent the manufacturer's prescribed range of potential error in readings taken on concrete surfaces).

Table 9.29: Summary of surface hardness results for Specimens 2.1-2.3.

	Specimen 2.1 (Fabric 1)			Specimen 2.2 (Fabric 2)			Specimen 2.3 (Fabric 3)		
	Timber Face	Fabric Face	%*	Timber Face	Fabric Face	%*	Timber Face	Fabric Face	%*
0mm	38	41	8.4%	37	40	9.5%	37	40	7.6%
5mm	41	45	11.1%	39	40	2.4%	37	40	7.1%
10mm	43	44	2.5%	40	40	-0.4%	39	38	-1.1%

\* Percentage improvement or reduction in surface hardness measured at the fabric cast face.

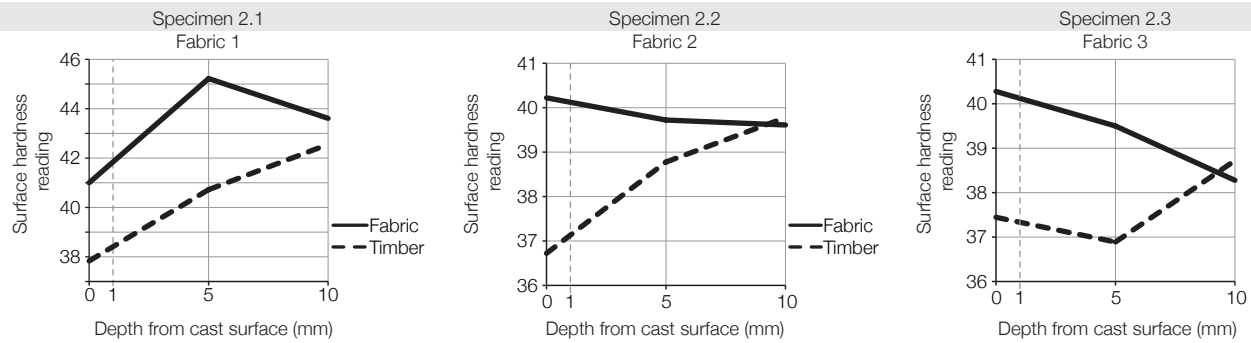


Figure 9.55: Surface hardness with depth for Samples 2.1-2.3.

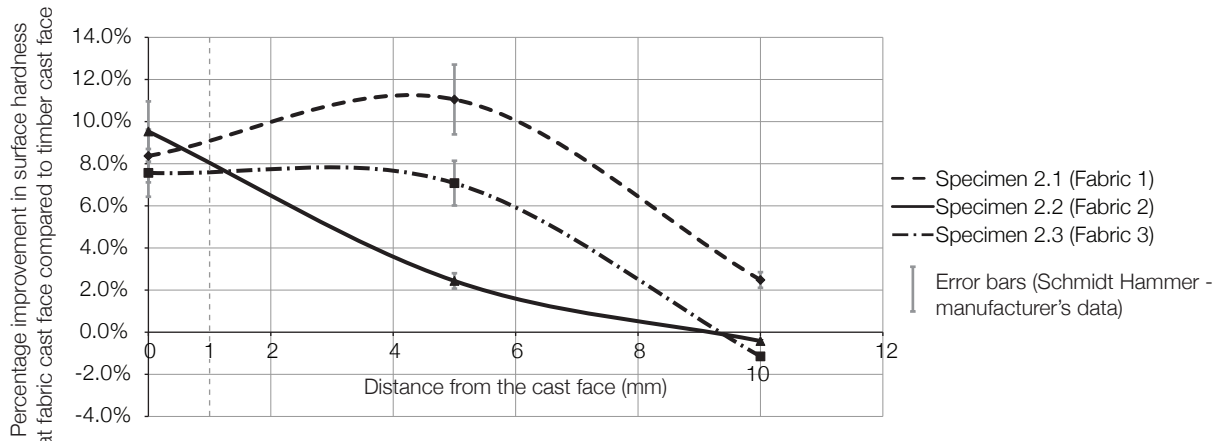


Figure 9.56: Percentage difference in surface hardness between fabric and timber faces in Samples 2.1-2.3.

#### 9.6.2.4. Analysis

The results presented show that the fabric cast face shows a small increase in surface hardness at the cast face (0mm) when compared to the timber cast concrete, of between 7.6% and 9.5% (Table 9.29). This increase is similar to that found in Series 1 (§9.6.1.2 on page 391) and suggests that the three fabrics create similar improvements at the surface zone.

Results with depth from the surface show the same general trend for all three fabrics, although Fabric 1 does show a small increase in surface hardness at 5mm depth from the surface. This result was not replicated in previous tests. The general trend is for the surface hardness of the fabric and timber faces to coincide at 10mm depth from the cast surface, suggesting that the property changes in the concrete due to the fabric occur in this relatively narrow zone.

#### 9.6.2.5. Conclusions

The results have shown that fabric cast concrete provides a small increase in surface hardness to accompany the other improvements shown in previous sections. The choice of fabric, and its pore size, appears to have only a small effect on the overall improvement in surface hardness. The range of results and limited test data require that further work be carried out to investigate this aspect of fabric cast concrete in further detail.



### 9.6.3. Conclusions -Test Group 5

Test Group 5 has shown that improvements in surface hardness can be attained using fabric cast concrete. These improvements are attributed to a reduction in the water:cement ratio at the surface zone of such concrete. This premise is supported by the work presented in Test Group 4 (§9.5 on page 373), where further samples were cast and their chemical composition determined using scanning electron microscopy and energy-dispersive X-ray spectroscopy.

From the initial series of tests on large concrete prisms, improvements in surface hardness of up to 13% were seen. It was proposed that compaction methods and depth of the concrete pour can influence these improvements. Work was then undertaken on a range of fabrics, with differing pore sizes, where it was found that similar improvements in surface hardness were found irrespective of the pore size (in the range 35-423µm).

Subsequently, smaller prisms were tested to determine the improvements in surface hardness with depth from the cast face. It was seen that the initial improvements in surface hardness seen at the cast fabric face are reduced with depth from this face, and appear to converge at approximately 10mm from the cast face.

Whilst the surface hardness method has given good results at the surface, the method of cutting slices from the samples to investigate differences in behaviour with depth was not ideal. Additional work, using more accurate cutting equipment, is now required to verify these results. It is also recognised that the effect of cutting the concrete will cause micro-cracking at the surface and this may further influence the results.

In addition, the combined effect of fabric pore size, compaction method, concrete strength and mix design must be investigated to fully understand their combined effects on the surface hardness results. Results from tests on seven fabric types and four concrete mixes are reported separately (Lee, 2012), and show that for surface hardness the optimum pore size is 100µm for non-woven fabrics and approximately 250µm for woven fabrics, as discussed in §9.7.3 on page 403.

## 9.7. Discussion

The tests in Chapter 9 provide a unique data set to demonstrate how fabric formed concrete can provide improvements in the long-term durability of concrete structures. Such advantages are in addition to those of material use reductions seen in previous Chapters.

It is thus proposed that by casting concrete into a permeable mould, excess pore water within the concrete is allowed to bleed from its surface. This has the following important effects:

1. There is a lower *water:cement* ratio at the surface zone;
2. There are fewer large pores at the surface;
3. There are more smaller (primarily cement) particles in the surface zone.

A reduction in the *water:cement* ratio ensures a greater concentration of cement particles and smaller pores (as shown by the initial surface absorption data presented in §9.4). This has the combined effect of constricting the flow of gases through the structure of the concrete (and hence providing the advantages for resistance to carbonation seen in §9.2), while the increased cement concentration provides ample sites for the formation of Friedel's salt, hampering the ingress of chlorides (as demonstrated in §9.3).

A summary of the test results presented in Chapter 9 is given in Table 9.30 below. Here, the significance of the effects and processes described and summarised above is apparent. The concrete and fabric properties used in the majority of the reported tests are reproduced in Table 9.31. Whilst this fabric choice has provided good durability benefits, the pore size of the fabric is sufficiently large to allow cement particles to leave the surface during the curing process. To ensure a fabric is used that allows only water to escape from the permeable mould, further work will be required to ensure not only that the pore size is correct but that the fabric provides the combinations of strength, stiffness and cost desired for fabric formed concrete structures.

Correlations between changes in durability with changes in the *water:cement* ratio of the constituent concrete are often made (c.f. Mehta and Monteiro, 2006). Such comparisons between durability and *water:cement* ratio reflect the fact that the chemical processes occurring in concrete during curing are still relatively unknown, and thus a broad comparison is often the best metric that can be reliably measured and compared.

Recognising this limitation the *water:cement* ratio of the fabric cast specimens was not investigated in detail, as its measurement with depth (such as was recorded by Price and Widdows (1991) and presented earlier (Figure 2.43 on page 36)) are determined either by laborious comparison with specimens of a known *water:cement* ratio (NT Build 361, 1999) using fluorescence microscopy (see Mayfield, 1990) or by the chemical analysis method given in BS 1881-124 (1988). Both methods require the laborious preparation of small samples and a skilled petrographer to properly interpret the results. The time and cost implications of such a test series excluded them from this thesis, but their incorporation in potential future work is discussed in Chapter 12.

Table 9.30: Summary of test results.

Test	Recorded improvement using fabric formwork
Carbonation - Coefficient of carbonation	50% (Table 9.5 on page 347)
Chloride ingress - Chloride Penetration parameter ( $K_{cr}$ )	42% (Table 9.13 on page 362)
Surface hardness	Up to 13% (Table 9.26 on page 391)

Table 9.31: Summary of concrete mix used for durability tests.

Strength at 28 days	Water/Cement ratio	Fabric pore size
40	0.40	400µm

### 9.7.1. Behaviour

The dominant process affecting the concrete in both the chloride ingress tests and carbonation tests described in Chapter 9 has been diffusion. To better understand this behaviour when related to fabric cast concrete, three factors of porosity, permeability and tortuosity are introduced below.

The porosity of a material may be defined as the ratio of void volume (pores) to the bulk volume, and is a static property of the material, Eq. 9.20 (after Lake, 1989). Permeability is defined in terms of fluid flow (Lake, 1989) and is most often given by Darcy's law (Eq. 9.21) (Martys *et al.*, 1994). Tortuosity, which describes how difficult it is to traverse between two points in comparison to the straight line distance between them, is dependent not on the size of pores in the sample but on the connectedness of the pores that allow diffusion to occur (Hall and Hoff, 2002).

$$\text{Porosity, } \phi = \frac{\text{interconnected pore volume}}{\text{bulk volume}} \quad \text{Eq. 9.20}$$

$$V = -\frac{k}{\eta} \frac{\Delta P}{L} \quad \text{Eq. 9.21}$$

Where  $V$  is the discharge;  $k$  is the permeability;  $\eta$  is the viscosity of the fluid;  $L$  is the length of the sample across which there is an applied pressure difference of  $\Delta P$ .

Predicting permeability based on the microstructure of a material has been widely studied (Martys *et al.*, 1994), and insights into the possible mechanisms by which fabric cast concrete achieves better resistance to chloride ingress and carbonation may be made by considering the semi-empirical, semi-theoretical Carman-Kozeny equation which introduces relationships between not only porosity and permeability but also the specific surface area and tortuosity of a sample. The equation, which is derived by combining the Hagen-Poiseuille equation (rearranged in Eq. 9.22 for average velocity in a laminar flow) with Darcy's law (Lake, 1989; Costa, 2006) is presented in many forms in the literature, one of which is shown in Eq. 9.23 (Scheidegger, 1974, cited by Martys *et al.*, 1994).

$$u_{z,avg} = \frac{D^2}{32\mu} \frac{\Delta P}{L} \quad \text{Eq. 9.22}$$

Where  $u_{z,avg}$  is the average velocity of the fluid;  $D$  is the pipe diameter;  $\mu$  is the dynamic viscosity of the fluid and  $\Delta P$  is the change in pressure over a length  $L$ .

$$k = \frac{\phi^3}{2s^2} \quad \text{Eq. 9.23}$$

Where  $k$  is the permeability;  $\phi$  is the porosity and  $s$  is the specific surface (total pore area/sample volume).

It can be seen that there exists a relationship between permeability, porosity and specific surface area that may be exploited by the use of fabric cast concrete. Developments by Lake (1989) determined the Carman-Kozeny equation in terms of specific surface area (Eq. 9.24), while Xi and Bazant (1999) later adapted it to provide a similar result, given in Eq. 9.25. Both approaches show the same relationship between porosity, tortuosity and specific surface area, wherein for a constant porosity an increase in the specific surface area provides a reduction in permeability for the material. However, adapting the Carman-Kozeny equation for cementitious materials has some limitations since not all of the porosity of the material is available to transport moisture, and the high specific surface area of cementitious materials can result in overestimates of the effect that they have on, for example, chloride diffusion, as discussed by Garboczi (1990).

$$k = \frac{\phi^3}{8\tau(1-\phi)^2 a_v^2} \quad \text{Eq. 9.24}$$

Where  $\phi$  = porosity (pore volume/bulk volume);  $\tau$  = tortuosity;  $a_v$  = specific surface area (area/unit mass)

$$D = \frac{V_p^3}{S^2 K_k} \quad \text{Eq. 9.25}$$

Where  $D$  is the diffusivity;  $V_p$  is the porosity;  $S$  is the specific surface area;  $K_k$  is the Kozeny constant ( $K_k = K_t \cdot K_s$ ),  $K_t$  = tortuosity and  $K_s$  = shape factor of the pores.

Chloride diffusion in concrete is considered in more detail by Xi and Bazant (1999), where the work of Christensen (1979) to describe Fick's Law (Eq. 9.8 on page 351) in terms of an effective diffusivity of the concrete based on the measurement of separate diffusivities for the cement paste and the aggregate inclusions is combined with temperature effects, chloride concentration dependence, and Eq. 9.25 to determine a general expression for chloride diffusivity. The equation was verified against available test data, but since the majority of the parameters required to implement this equation were not collected in the test data presented in this thesis it has not been possible to apply it to the fabric cast concrete tests.

Work described in §2.6.1.1 on page 36 has already shown that permeable formwork systems can provide significant reductions in surface porosity (as measured using mercury porosimetry). It has been shown for rock structures (Hall and Hoff, 2002) and for cementitious materials (Tumidajski *et al.*, 1996) that reductions in porosity can lead to increased tortuosity, suggesting that the reduced porosity of fabric cast concrete offers a more tortuous surface through which corrosion inducing substances (chloride ions or carbon dioxide) must diffuse.

From Eq. 9.24 and Eq. 9.25 it is apparent that changes in the porosity, specific surface area, and tortuosity of the sample subject to diffusion can combine to reduce the permeability of the concrete and to make the processes of both carbonation and chloride ingress more difficult. Increased tortuosity is premised to occur due to the mechanisms described above, but it is yet to be conclusively shown that fabric cast concrete has a greater specific surface area and reduced porosity when compared to concrete cast in an impermeable mould. Future work is required to address this knowledge deficit.

### 9.7.2. Visual concrete

The impetus behind the work presented in this Chapter has been to demonstrate that fabric cast concrete can be used to create durable structures, offering significant whole-life benefits for concrete construction. In addition, however, significant visual benefits are seen in the fabric cast surface texture, as discussed in Chapter 2 and seen in Figure 9.57.

A desire for architectural concrete finishes can often lead to cladding elements being fixed to primary structural elements, an approach that brings with it additional material and carbon costs. With fabric formwork, it may be possible to forego such additions by recognising that the primary structure will have significant visual impact.

Visual concrete finishes are most often achieved by specifying minimum cement contents to the concrete mix (Concrete Centre, 2012), with such mixes ensuring that sufficient fines reach the surface to avoid the pores and voids seen in some conventionally cast concrete surfaces. Such specifications are therefore based on visual, and not strength requirements.

When using fabric formwork, the surface of the finished element has an increased cement content (as seen in §9.5.3 on page 379) relative to the body concrete, providing the benefits without requiring a globally higher cement content. The concrete mix may then be designed for strength alone, avoiding unnecessary additions of cement that bring with them significant embodied carbon, whilst retaining the desired concrete finish.

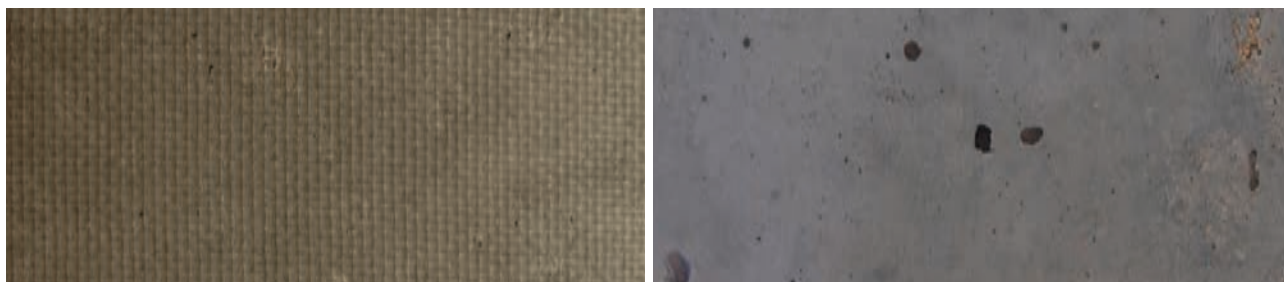


*Figure 9.57: Fabric cast concrete surface (l); Timber cast concrete surface (r), both surface cast from the same concrete mix.*

In this way, it may be possible to use fabric formwork in lieu of any increases in cement content to achieve the desired visual concrete surface. This effect is seen in Figure 9.57, where the same concrete mix (given in Table 9.2) is shown cast against a timber and a fabric surface. The fabric surface is often recognisable for its texture,

lack of blow holes, voids, and surface defects. In addition, the fabric surface shows a change in colour, which is a further result and illustration of the increased cement content at the surface of the fabric cast concrete.

### 9.7.3. Fabric properties

Throughout this thesis one fabric has been used for the casting of both full size structural elements and in the durability tests described in this Chapter. The properties of this woven fabric are given in Table 9.3 on page 343, where its pore size of 250 $\mu\text{m}$  is recorded. There is currently no known published guidance on suitable fabrics for use in flexible formwork construction, and this is considered in the following sections.

Fabrics are supplied either as woven or non-woven constructions, with the difference between them arising from the manufacturing process. Whereas woven fabrics are made up of yarns placed in the warp and weft directions, which may be arranged in any number of patterns depending on their intended use, non-woven fabrics are created by the thermal, mechanical or chemical bonding of fibres into flat sheets of fabric.

To create permeable, non-woven fabrics (typically using short polypropylene fibres heat bonded into sheets), the manufacturing process uses needling technology to accurately place the pores into the fabric, potentially allowing for greater control over the final pore size in the fabric.

Work by Lee (2012) was undertaken to determine the optimum pore size in both woven and non-woven fabrics for use as flexible formwork. A total of seven fabrics (three woven, four non-woven) were tested for carbonation resistance, surface hardness and pH with depth for each of three different concrete mixes. The results of this work suggest that the optimum pore size for woven and non-woven fabrics are not the same.

This is illustrated in Figure 9.58, where the percentage increase in surface hardness at the fabric cast face when compared to that at the timber cast face for a variety of fabric pore sizes is shown. From these results it could be argued that two peaks of improvements are seen, corresponding to different pore sizes for the woven and non-woven fabrics.

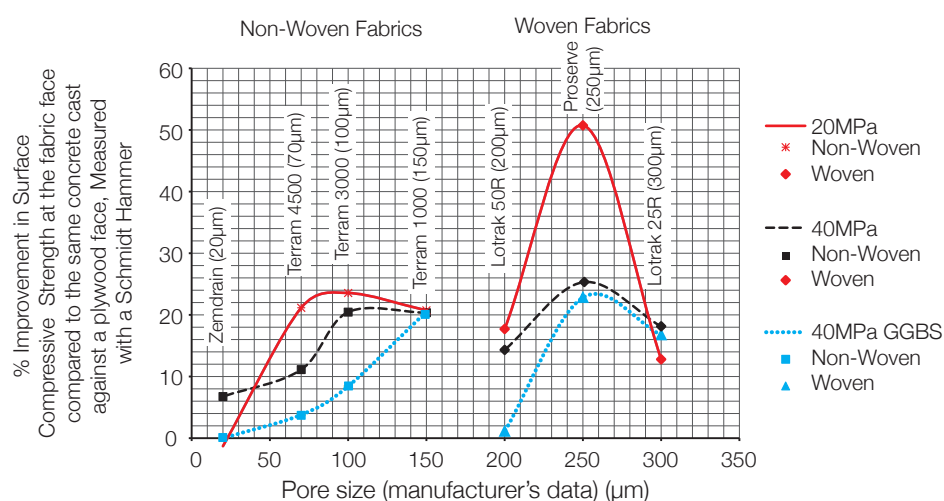


Figure 9.58: Results of surface hardness tests on seven different fabrics presented by Lee (2012) showing optimum pore sizes for woven and non-woven fabric types.



The work undertaken by Lee (2012) has shown that a greater understanding of the behaviour of the fabric formwork and its interaction with the surrounding concrete is required. Future work is required to determine how the correlations between pore size and improvements in durability properties arise, particularly when woven and non-woven fabrics are considered.

The two types of fabric have quite different fabrication methods, and the result of this may be to change the way in which water is able to flow and escape from the fabric surface. For example, the woven fabrics may offer a greater curved surface (on the individual yarns) along which water can travel, while in the non-woven fabric there exist only discrete holes created during the manufacturing process from which the water can escape (as illustrated in Figure 9.59). It is recommended that future work should focus on the correct modelling of fabric and its interaction with the surrounding concrete during and after casting, and this work could then consider how the various fabric typologies can positively influence concrete durability.

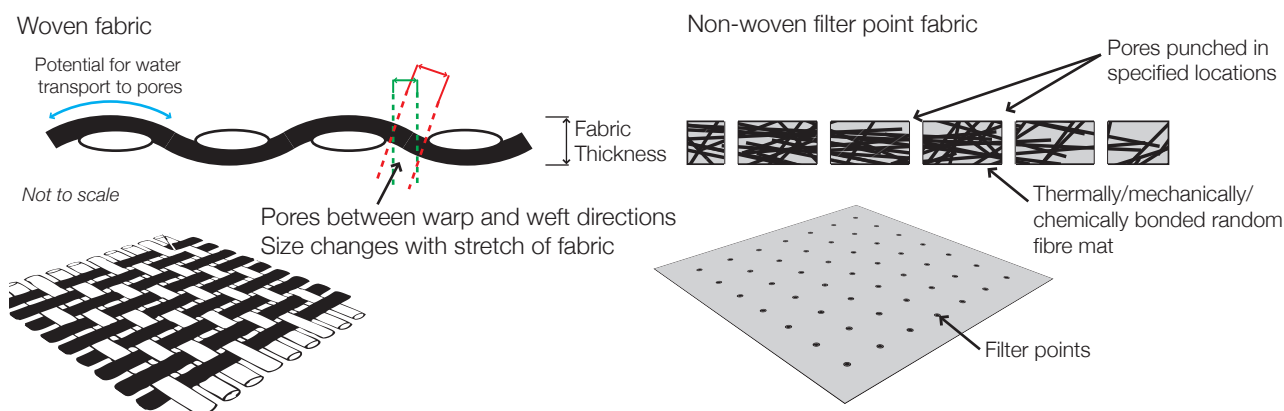


Figure 9.59: Behaviour and construction of woven and non-woven fabrics.

#### 9.7.4. Summary

Based on the experimental and analytical evidence presented it is premised that by casting concrete into a fabric mould three effects which serve to improve the durability of the fabric cast concrete surface occur:

1. Finer material collects in the surface zone as water is expelled from the cast surface, resulting in a more tortuous surface with fewer interconnected pores;
2. A greater concentration of cement particles (or a reduction in the *water:cement* ratio) at the surface may result in smaller pores to both constrict the flow of gases through the structure of the concrete and provide sites for the formation of Friedel's salt;
3. The macroscale surface texture provided to the concrete gives the fabric cast face a greater specific surface area when compared to the timber cast face, providing a larger area over which the contaminating material is spread.

From the combined results of Series 1, 2 and 3 it may be concluded that the action of casting concrete into fabric formwork changes the distribution and components of the concrete at the surface zone in such a way that a durable surface zone is formed.

Given that cement particle sizes are distributed between 5µm and 45µm, it may be sensible to require fabric cast concrete to use a fabric pore size of less than 45µm, wherein the amount of cement leaving the surface would be reduced.

The SEM and EDS work presented above has provided an insight into the processes behind this, but much greater work is required to fully map the behaviour of the fabric cast concrete. In particular, studies of the porosity (measured using mercury porosimetry) and specific surface area (inferred from gas diffusion tests) should be undertaken to develop a more sophisticated model for the fabric cast concrete. Additional work is required to verify the results of particle size analysis using SEM images. All of these aspects should be included in a period of future work, the aim of which would be to determine the ideal fabric for use as a durable formwork system and to fully quantify its benefits for designers.

Further work is also required to provide complete guidance for designers of visual concrete, such that the use of fabric formwork may be compared against existing metrics such as minimum cement and fines contents. By demonstrating an alternative to minimum cement content specifications, fabric formwork provides additional carbon savings to those achieved through the material use reductions seen in Chapter 5 and the whole life durability benefits demonstrated in this Chapter.

## 9.8. Conclusions

Within Chapter 9 five Groups of tests have been undertaken to determine how the presence of a permeable mould can affect the durability characteristics of concrete. The aim of these has been to determine further advantages of fabric formwork above those seen in Chapter 6, where significant reductions in material use have been recorded.

Initial accelerated tests on two of the most significant durability concerns, carbonation and chloride ingress, showed significant improvements in the fabric cast samples. Sorptivity data suggests that whilst fabric cast concrete has fewer large pores and thus a lower initial absorption rate than concrete cast against steel or timber, the presence of smaller pores on the surface ensure water uptake remains an important process. This then suggests that there are proportionally more small pores in the fabric cast concrete as a ratio of large to small pores, and hence the long term sorptivity values were found to be similar in both concrete finishes.

Faced with environmental effects, fabric cast concrete shows a number of advantages. Changes at the surface provide a harder finish, as measured using a rebound test (§9.6). Combined with a surface free from voids and blow holes, this provides the high quality visual finish that is described in much of the literature. A reduction in the volume of large pores at the surface, as suggested by sorptivity data (§9.4) provides a less permeable surface for carbonation and chloride ingress.

A potentially increased cement content at the surface would also encourage the formation of Friedel's Salt during chloride attack, further retarding the corrosion process, as discussed in §9.5.3.3 on page 385. Increased chloride binding by this higher cement content prevents depassivation of the steel, which is thus protected. In a similar way, the reduced pore area is considered to contribute to the concrete resistance to carbonation, which helps to prevent the reductions in concrete pH that can lead to corrosion. This web of advantages is illustrated in full in Figure 9.60

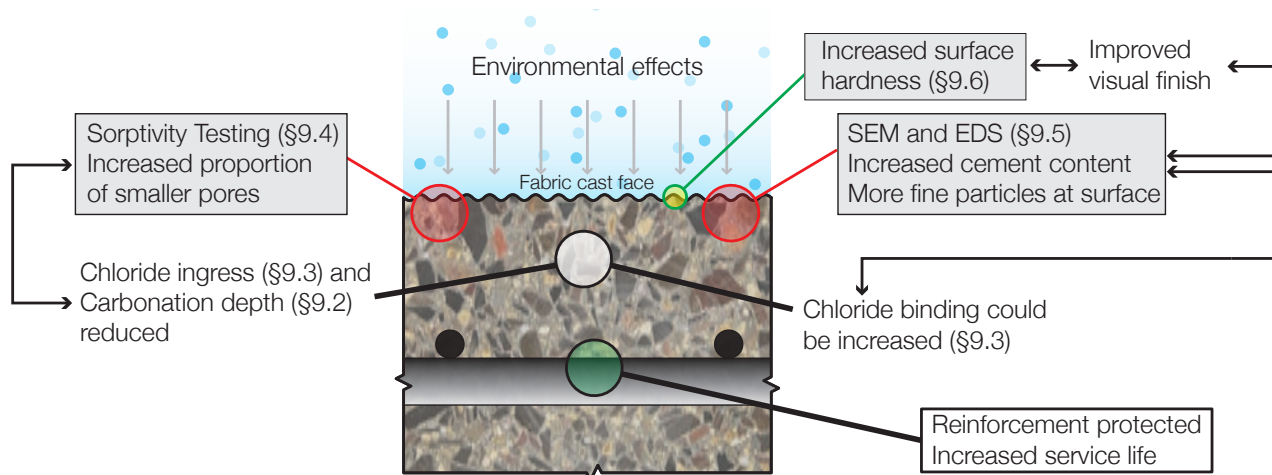


Figure 9.60: A summary of the proposed effects of casting concrete into fabric formwork in the surface zone.

From the tests undertaken in this thesis, it is clear that by casting concrete into a permeable mould significant durability benefits can be gained. This effect may allow designers to beneficially reduce their cover requirements, or, in designs governed by durability concerns, to reduce the specified concrete grade. Such reductions in concrete grade in turn facilitate further savings in embodied energy. For example, if a design required a C50 concrete solely to satisfy durability concerns, and if this could be replaced with a C20 concrete cast in fabric formwork, the resulting embodied energy savings would be approximately 38% (Figure 9.61). In conjunction with the material savings already achieved simply by casting optimised shapes and the potential additional carbon savings in using low-carbon cements, it is clear that fabric formwork offers an opportunity for significant embodied energy savings.

In addition, where the concrete surface is required to provide a visual grade finish, conventional approaches including increases in cement content, can be avoided through the use of fabric formwork. Such an approach further reinforces the specification of fabric cast concrete by its strength requirements only, utilising the construction method to provide the concomitant durability and visual benefits seen in this Chapter.

The majority of testing undertaken in this chapter has made use of a geotextile fabric (Fabric 1, described in Table 9.3 on page 343), and excellent results were obtained. Additional work, undertaken on two fabrics with smaller pore sizes provided by DuPont, showed improved surface properties when compared to Fabric 1. This suggests that the optimum fabric, combining flexibility, a low creep modulus, high strength and a small pore size, is yet to be

found for concrete structures cast using fabric formwork. There is plenty of scope to find such a material, and this should be considered as a separate research topic in the future.

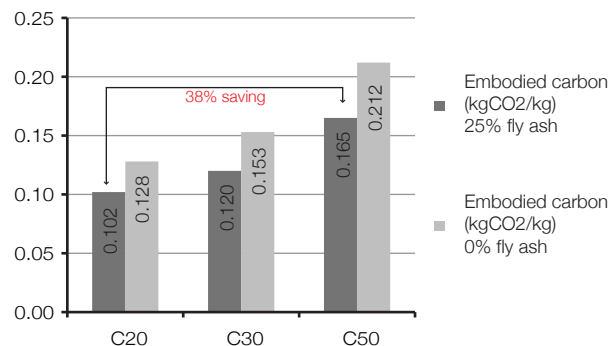
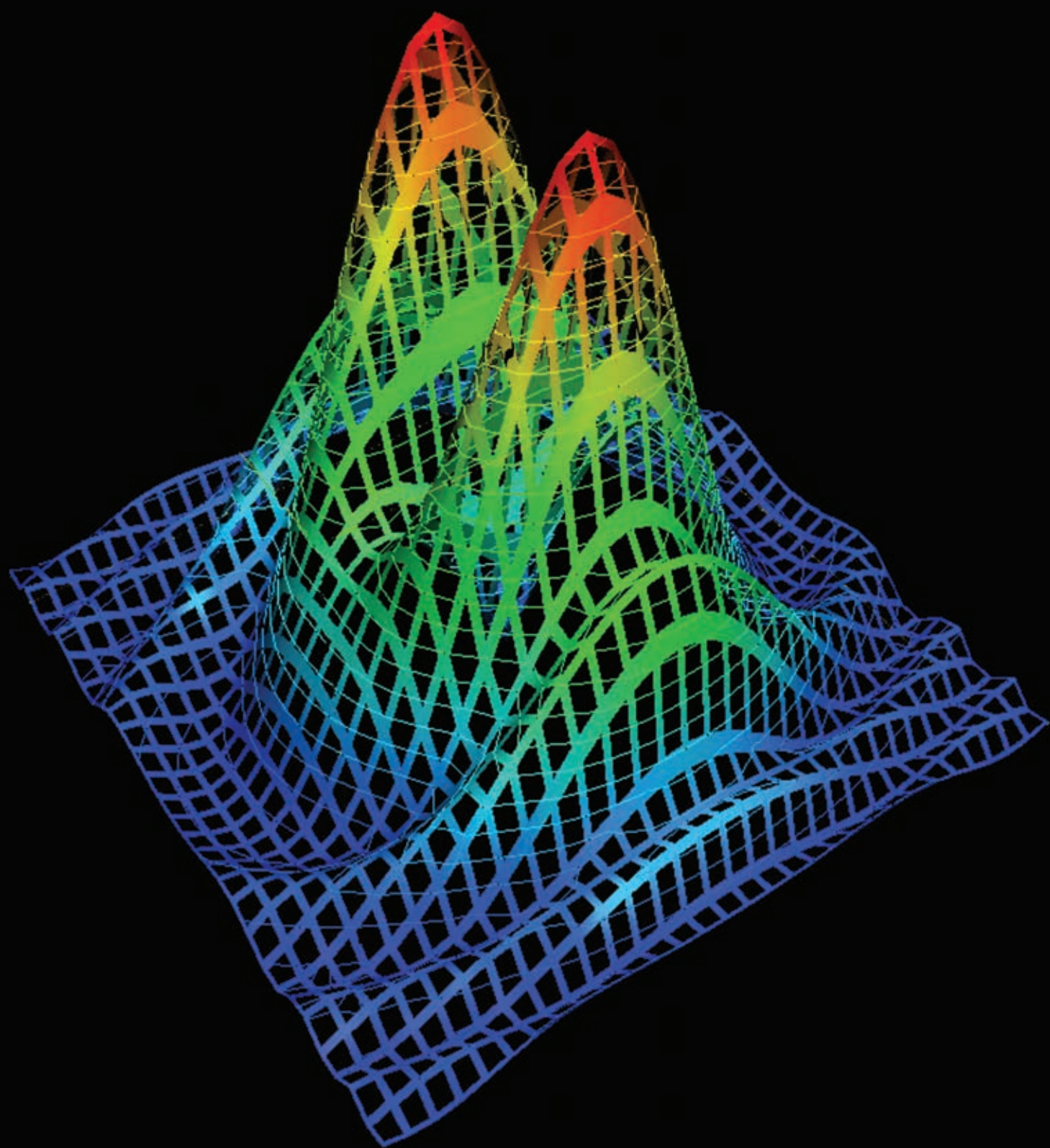


Figure 9.61: Reductions in embodied energy (data after Craig et al., 2009).

In addition, just one concrete mix has been investigated, and there clearly remains much work to do to investigate how changes in not only cement content, but also aggregate grading and size, influence the durability and surface properties of fabric cast concrete. Work is also required to extend the SEM and EDS analysis, considering multiple fabrics and the structure of the concrete during curing. Such a study would form part of broader research into the general behaviour of concrete during curing.

The limitations of the test results presented in this Chapter are found in the small scale of the test program undertaken, both in terms of specimen numbers and specimen size. It does not necessarily follow that the extremely advantageous durability results shown in this Chapter should be replicated in full size structural elements. Although durability testing is most often carried out on small samples (for ease of fabrication and testing) further work is required to affirm the results seen in this Chapter at full scale.

Chapter 9 has demonstrated that fabric cast concrete offers significant advantages for the durability of concrete structures. By providing a permeable mould, an advantageous release of water and air during curing results in a cement rich surface zone that provides improved resistance to chloride ingress and carbonation when compared to the same concrete cast into an impermeable mould. These results are supplemented by new investigations into the chemical and structural changes that occur within the surface zone of the concrete.



# Chapter 10 Analysis

## Fabric formed beams

### 10.1. Introduction

In Chapters 6, 7 and 8 a body of test data and analysis has been presented to meet the requirements of the test matrix first presented in §5.4 on page 122 to demonstrate how fabric formwork may facilitate a sustainable future in concrete construction. Additional and broader analysis is now presented in Chapter 10 to supplement this work and to consider:

1. Modelling techniques for fabric formed structures;
2. Prediction of the load deflection response of fabric formed beams;
3. Material use analysis including carbon data.

### 10.2. Load deflection predictions

#### 10.2.1. Introduction

A sectional analysis method to determine the full load deflection behaviour of variable section concrete beams is presented. The method is verified against test data for both ordinary Portland cement concrete beams (tested and analysed in detail in Chapter 6) and ultra-high performance fibre reinforced concrete beams (as described in §6.7 on page 206). It is shown that iterative routines can provide accurate predictions of the variable section beam's load deflection behaviour.

#### 10.2.2. Sectional analysis

Assuming that plane sections remain plane, reinforcement is perfectly bonded to its surrounding concrete, and that stress strain material models are known the following method has been used to predict the load deflection response of the variable section beams.



A strain profile is determined by the strain at the compression face and the depth of the neutral axis. Forces in both compression and tension are then determined based on the constitutive material models, and the correct neutral axis for a given value of strain at the compression face is determined by equilibrium. The moment capacity of this strain profile is then found by taking moments at any point on the section. Iterating this concept allows the full moment-curvature response to be developed for any cross section layout.

#### 10.2.2.1. Deflections

Given the assumption that plane sections remain plane, Eq. 10.1 and the definitions given in Eq. 10.2, the curvature at any point can be related to the strain at the compressive face and the depth of the neutral axis (Eq. 10.3).

$$\frac{M}{I} = \frac{\sigma}{y} = \frac{E}{R} \quad \text{Eq. 10.1}$$

$$E = \frac{\sigma}{\epsilon} \quad \kappa = \frac{1}{R} \quad \text{Eq. 10.2}$$

$$\kappa = \frac{\epsilon}{y} \quad \text{Eq. 10.3}$$

The deflection of an elastic beam subject to a vertical line load  $w$  may be described (Case *et al.*, 1983) by Eq. 10.4, after Bernoulli. The radius of curvature of the beam is related to its moment by Eq. 10.5 from which Eq. 10.6 is taken. Double integration of Eq. 10.6 yields the deflection, Eq. 10.7.

$$\frac{d^2}{dz^2} \left[ -EI \frac{d^2 v}{dz^2} \right] = \frac{dF}{dz} = -w \quad \text{Eq. 10.4}$$

Where  $z$  is the distance along the beam,  $v$  is the deflection,  $F$  is the shear force and  $w$  is a vertical line load.

$$\frac{1}{R} = \frac{M}{EI} \quad \text{Eq. 10.5}$$

$$\frac{d^2 v}{dz^2} = \kappa \quad \text{Eq. 10.6}$$

$$u = \iint \kappa dx \quad \text{Eq. 10.7}$$

Numerical integration is then applied to determine the deflection for a particular applied load. The required constants of integration are determined by the boundary conditions of the beam under consideration. Given that all beams tested in this thesis are simply supported, the vertical deflection at the supports is known to be zero.

#### 10.2.2.2. Automation

The process described above has been automated in a simple macro based program to predict the load deflection behaviour of various beams subject to uniform loading. In the following, each beam has been divided into a number of vertical sections, with the full moment-curvature behaviour of each section being determined as

shown in Figure 10.1. The full load-deflection behaviour is found as described in the flow chart given in Figure 10.2.

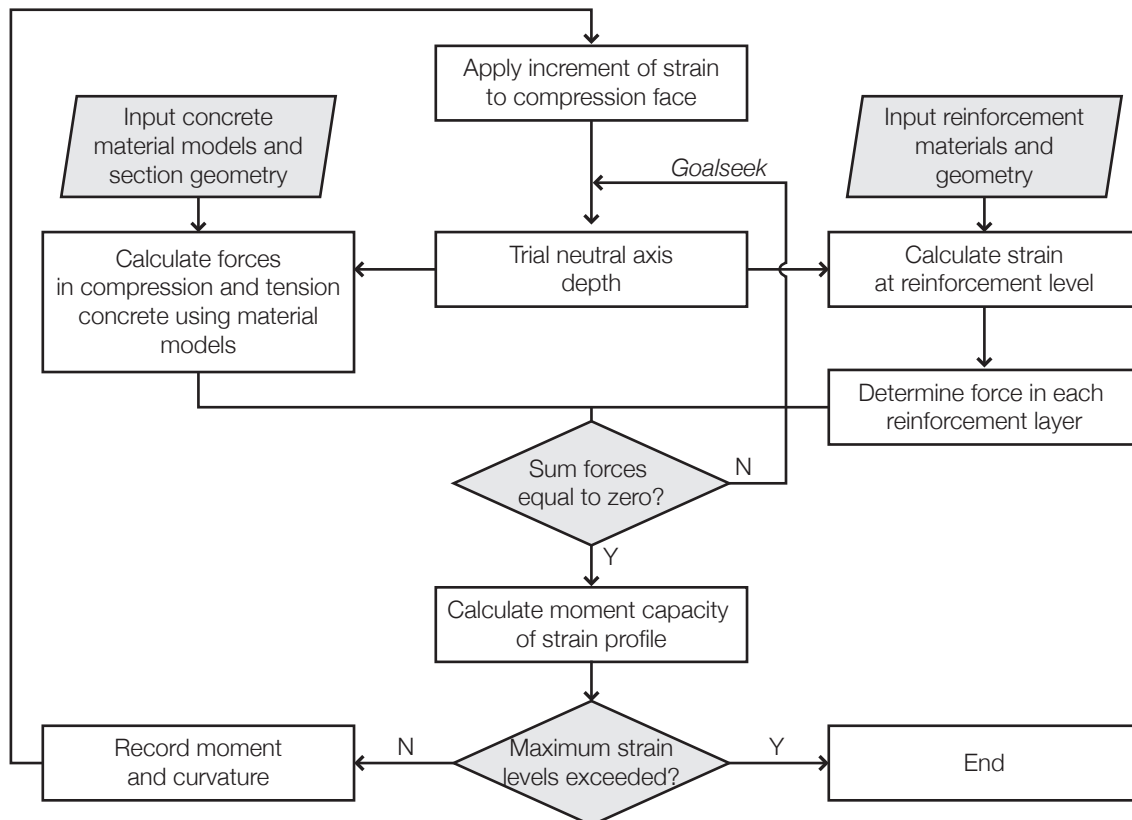


Figure 10.1: Moment-curvature relationship at a particular section.

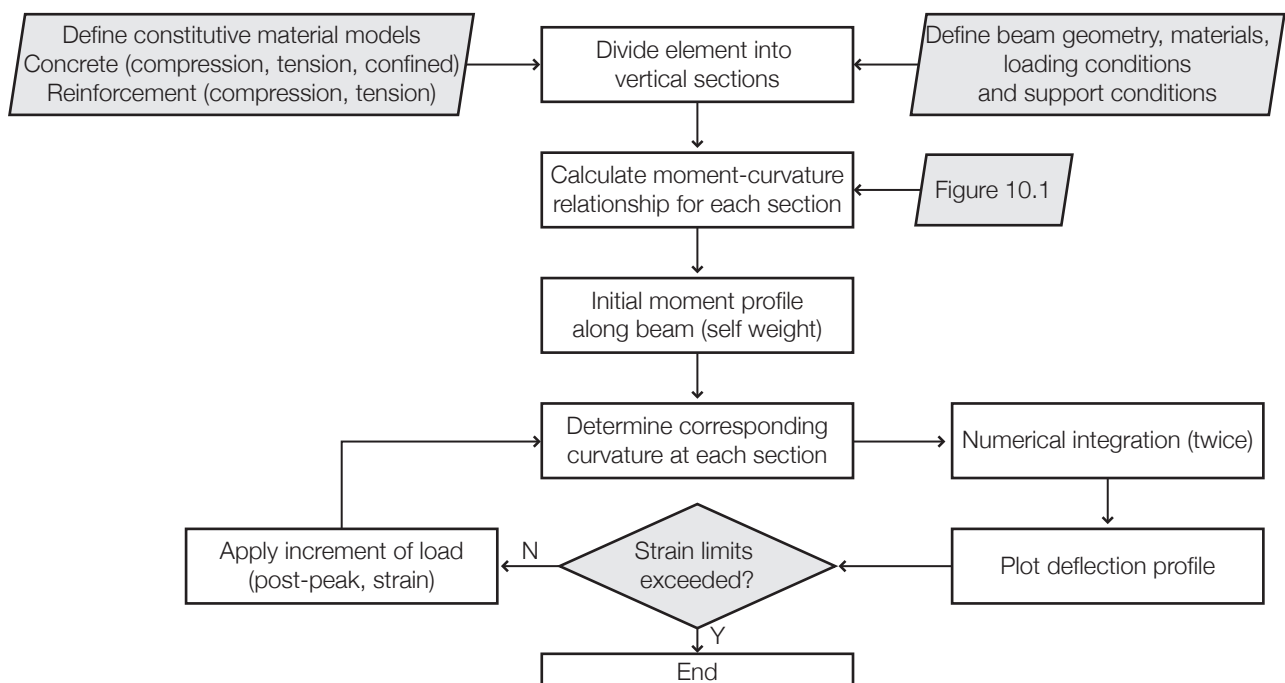


Figure 10.2: Load-deflection calculation for entire beam.

This process was implemented to predict the behaviour of the UHPFRC beams described in §6.7 on page 206. Material models and results are described below.

### 10.2.3. Verification - UHPFRC Beams

The 'Double T' Beam 7\_5 cast using UHPFRC was analysed using the procedure set out above. This element was chosen as it has an unusual concrete material model (as described below), compared to those elements analysed in subsequent sections which made use of ordinary Portland Cement Concretes. The design layout and test results of the Double T beam are described in full in §5.7.4 on page 150 and §6.7.4 on page 211 respectively.

#### 10.2.3.1. Material models

##### 10.2.3.1.1. Concrete

The Ductal® concrete material model is described in §3.2.2.1.2 on page 57 and summarised in Figure 10.3 below. The model has a linear compression relationship and rigid plastic (strain limited) tension behaviour.

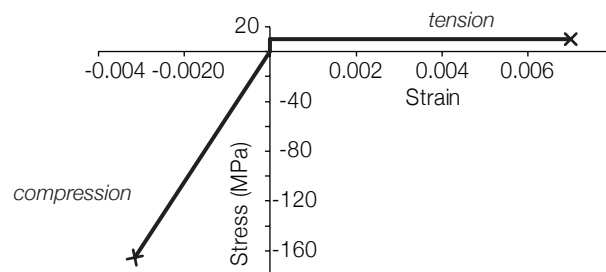


Figure 10.3: Uni-axial stress strain model for Ductal® (after Graybeal, 2006b).

##### 10.2.3.1.2. Steel

The material model for steel reinforcement was taken directly from BS EN 1992-1-1 (2004) and the relevant national annex and is summarised in Figure 10.4. The bilinear model has the same characteristic shape for both compression and tension.

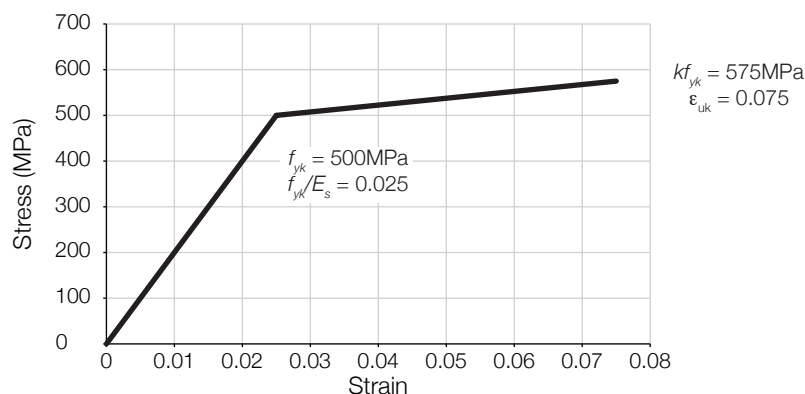


Figure 10.4: Material model for steel (after BS EN 1992-1-1 (2004)).

#### 10.2.3.2. Results

Implementing the method described above for the Ductal® cast double T beams resulted in the predictions of their load deflection behaviour shown in Figure 10.5. Whilst the behaviour of the section in the elastic and cracked ranges is well described, larger discrepancies occur in the post-peak range.

A second analysis was undertaken for the same beam geometry, but with all longitudinal reinforcement removed. The results of this are also shown in Figure 10.5, where it is apparent that the capacity of the unreinforced section is sufficient to carry approximately 47% of the load of the steel reinforced section. However, the unreinforced section would be expected to display significantly less deformation capacity.

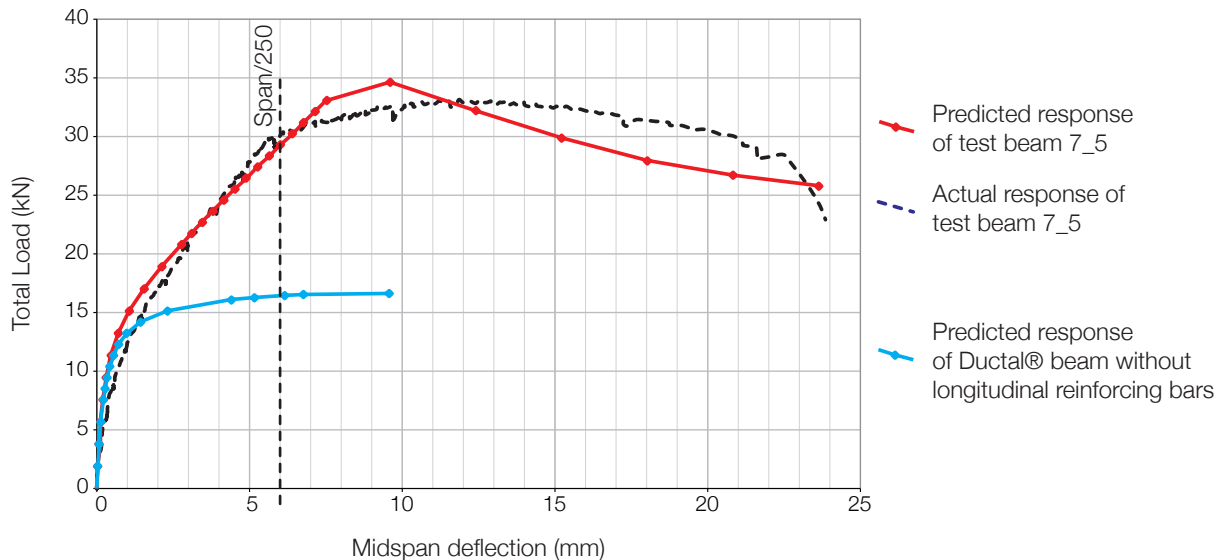


Figure 10.5: Results for Ductal® cast double T beam.

Shown alongside the load-deflection predictions for Beam 7\_4 in Figure 10.5 is a typical serviceability limit state deflection check for such elements (taken here as  $\text{span}/250$ ). The limit is found to be quite close to the maximum capacity of the section, and reflects the increased Young's Modulus of the UHPFRC used in this element when compared to an equivalent section cast using Ordinary Portland Cement Concrete (with a compressive strength of 160MPa, the UHPFRC is estimated (Eq. 3.4 on page 56) to have a Young's Modulus of 46GPa). This close matching of the ULS and SLS conditions requires that the optimisation process for such structures be considered carefully, and predictions such as those shown above should be included within the design process.

#### 10.2.4. Equivalent moment of inertia approach

In §10.2.3, the integration of curvatures along the length of variable depth concrete beams has been shown to provide accurate representations of their load-deflection behaviour. Such an approach can be time consuming and an alternative approach based on effective or equivalent moments of inertia is presented below before being verified against test results of both T and Double T beams presented in §6.5 on page 182 and §6.6 on page 195 of Chapter 6.

##### 10.2.4.1. Method outline

Calculation of beam deflections can be achieved using effective stiffness approaches, first proposed by Branson (1965) which provide a reduction in the element stiffness as it transitions from uncracked to a fully cracked state. The effective moment of inertia given by Branson (derived empirically from members tested in flexure) is given in Eq. 10.8.

$$I_e = \left( \frac{M_{cr}}{M_a} \right)^3 I_g + \left[ 1 - \left( \frac{M_{cr}}{M_a} \right)^3 \right] I_{cr} \leq I_g \quad \text{Eq. 10.8}$$

Where  $M_{cr}$  = cracking moment;  $M_a$  = moment at the critical section;  $I_g$  = gross moment of inertia;  $I_{cr}$  = cracked transformed moment of inertia.

Whilst this approach has been adopted by ACI 318 (2005) and in a modified form in ACI 440 (2006) design codes, an alternative method, proposed by Bischoff and Gross (2011) allows elements with variable stiffness along their length to be addressed in a similar manner by integrating effective stiffnesses along the length of the element. The advantage of this approach is that the entire load-deflection process can be determined in a single line of calculations, without requiring the complete moment-curvature relationships for each beam section to be determined, as is illustrated in the following.

Bischoff and Gross (2011) proposed calculating the effective moment of inertia at each section of a variable stiffness beam with the Eq. 10.9, whose factors are derived through virtual work considerations, as is described in detail by Bischoff and Gross (2011).

$$I_e = \frac{I_{cr}}{1 - \gamma \left( M_{cr} / M_a \right)^2} \leq I_g \quad \text{Eq. 10.9}$$

Where  $I'_e$  is the equivalent moment of inertia;  $M_{cr}$  is the cracking moment;  $M_a$  is the moment on the section,  $\gamma$  is a factor to account for integration (Eq. 10.10) and  $\eta$  is a factor to account for tension stiffening (see Bischoff and Gross, 2011), Eq. 10.12:

$$\gamma = \frac{1.6\xi^3 - 0.6\xi^4}{\left( M_{cr} / M_a \right)^2} + 2.4 \ln(2 - \xi) \quad \text{Eq. 10.10}$$

$$\xi = 1 - \sqrt{1 - M_{cr} / M_a} \quad \text{Eq. 10.11}$$

$$\eta = 1 - I_{cr} / I_g \quad \text{Eq. 10.12}$$

The analysis process is then undertaken as described in the flowchart shown in Figure 10.6. Results using this process were completed in one worksheet in Microsoft Excel. The method is undoubtedly quicker for simple beam calculations but the additional accuracy provided by the curvature method used previously may be better suited to a complete computational approach to be developed in future work.

The process is able to estimate the transition between the elastic, partially cracked and fully cracked conditions along the length of the beam under consideration. A further limit is placed on a steel reinforced section by the flexural capacity of the beam, which denotes the onset of yielding of the flexural reinforcement. This capacity may be calculated for each section, and once reached the beam load capacity is held essentially constant under an increasing deflection as the bars yield. The limit to this plastic behaviour may be found in one of three conditions,

which are considered in more detail in §10.3 on page 421: 1) fracture of the longitudinal bars; 2) debonding of the longitudinal bars and 3) crushing or sliding failure in the compression face of the concrete section.

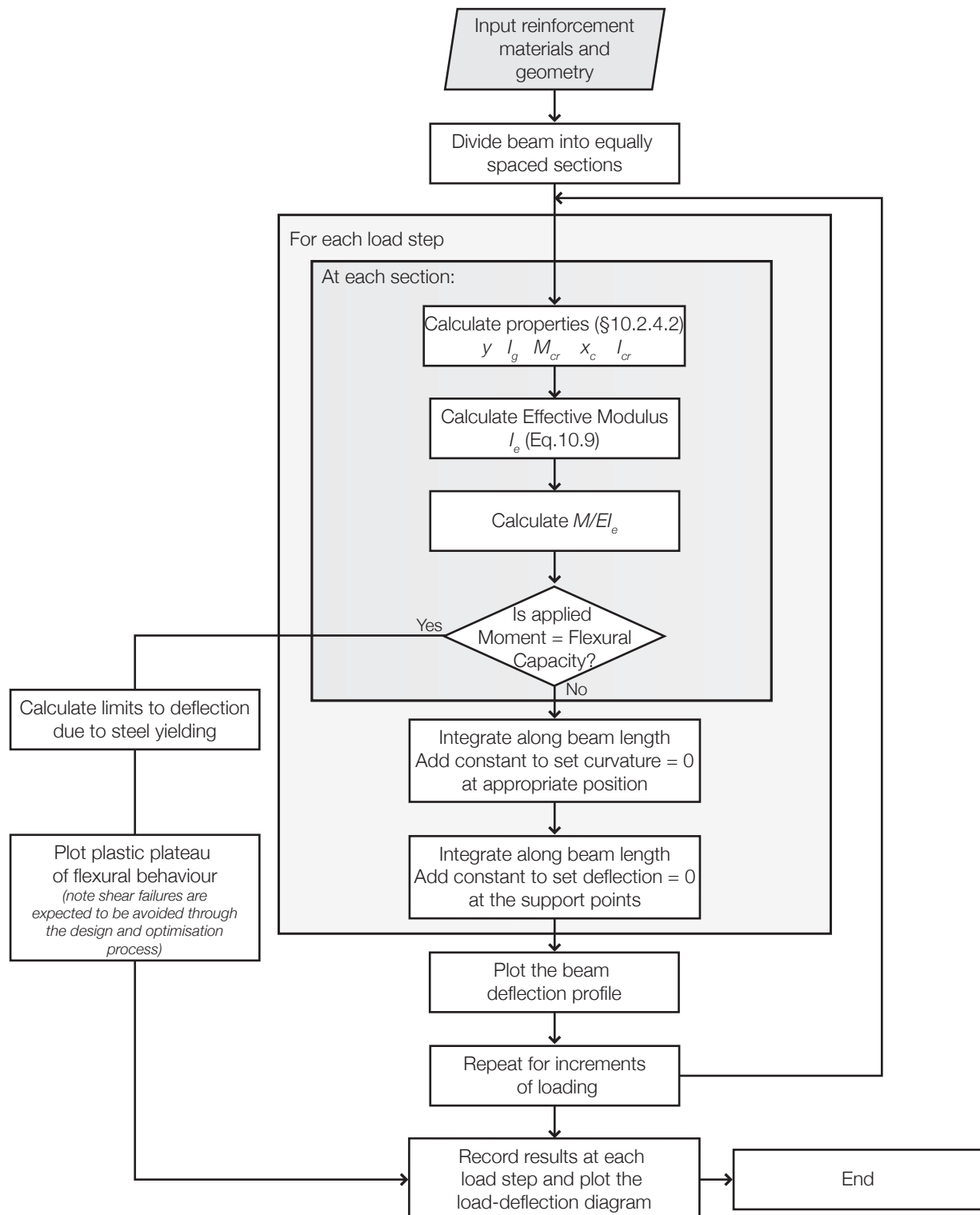


Figure 10.6: Flowchart showing deflection calculation process.



## 10.2.4.2. Verification

Two sets of beam data were chosen for analysis and verification using the proposed method. The beams are summarised in Figure 10.7 and Table 10.1. To calculate their respective section moduli, generic equations were derived for 'T' beams, with the Double T section being simplified into a 'T' for calculation simplicity, as provided in Table 10.2. Beam test data and photographs can be found in Chapter 6.

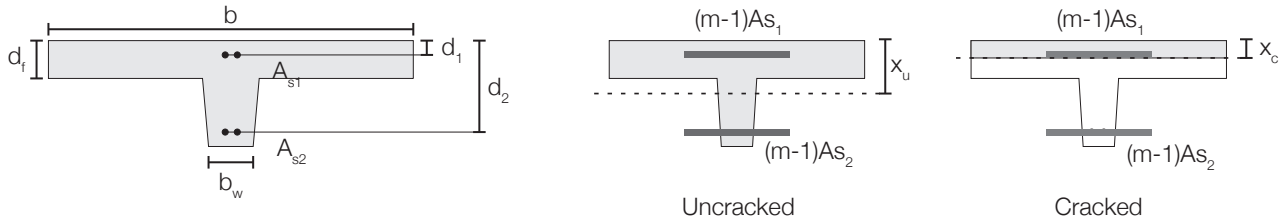


Figure 10.7: Summary of beam dimensions.

Table 10.1: Beams subject to the analysis method.

	b (mm)	d <sub>1</sub> (mm)	b <sub>w</sub> (mm)	d <sub>1</sub> (mm)	d <sub>2</sub> (mm)	A <sub>s1</sub> (mm <sup>2</sup> )	A <sub>s2</sub> (mm <sup>2</sup> )
Beam 6_4_1	975	50	120	22	Variable (§5.5)	201	201
Beams 5_1 and 5_2	975	100	125	28	Variable (§5.6)	157	226

Table 10.2: Equations for beam properties.

$x_u$	$x_u = \frac{b_1 \frac{d_f^2}{2} + b_w \left( \frac{D - d_f}{2} \right) + (m-1) A_{s1} d_1 + (m-1) A_{s2} d_2}{(m-1)(A_{s1}) + (m-1)(A_{s2}) + b_1 d_f + b_w (D - d_f)}$
$I_u$	$I_u = \frac{b_1 d_f^3}{12} + (b_1 d_f) \left( x_u - \frac{d_f}{2} \right)^2 + \frac{b_w (D - d_f)^3}{12} + b_w (D - d_f) \left( x_u - \left( \frac{D + d_f}{2} \right) \right)^2 + (m-1) A_{s1} (d_1 - x_u)^2 + (m-1) A_{s2} (d_2 - x_u)^2$
$x_c$	$x_c = \left( -((m-1) A_{s1} + m A_{s2}) + \sqrt{((m-1) A_{s1} + m A_{s2})^2 - 4(0.5b) \left( -(m-1) A_{s1} d_1 + m A_{s2} d_s \right)} \right) / b$
$I_c$	$I_c = \frac{b x_c^3}{3} + (m-1) A_{s1} (x_c - d_1)^2 + m A_{s2} (d_2 - x_c)^2$

The value for the modular ratio 'm' is given by Eq. 10.13. Values for the Young's modulus of concrete were estimated using Eq. 10.14, which is taken from BS EN 1992-1-1 (2004).

$$m = \frac{E_s}{E_c} \quad \text{Eq. 10.13}$$

Where  $E_s$  is the Young's Modulus of Steel and  $E_c$  is given by Eq. 10.14

$$E_{cm} = 22 \left[ f_{cm} / 10 \right]^{0.3} \quad \text{Eq. 10.14}$$

Where  $f_{cm} = f_{ck} + 8$  and  $f_{ck}$  is the characteristic concrete strength (MPa)

The deflection characteristics of a flexurally dominated section are heavily influenced by the point at which the longitudinal steel yields. This is calculated for each load step at each section by using Eq. 10.15, which is based on the sections drawn in Figure 10.7. It should be noted that the yield stress of steel used in construction in Europe has typical yield strengths of  $500\text{MPa} \leq \sigma_s \leq 650\text{MPa}$ . With Eq. 10.15 the maximum load capacity can be determined from the position at which the steel yields. In a simplified material model assuming no tension stiffening of the steel, this then provides a horizontal branch on the load-deflection plots, which is seen in the work presented in subsequent sections below.

$$\sigma_s = \frac{m M_x (d - x_c)}{I_e} \quad \text{Eq. 10.15}$$

Where  $\sigma_s$  is the stress in the steel;  $m$  is the modular ratio;  $M_x$  is the moment on the section under consideration;  $d$  is the effective depth;  $x$  is the neutral axis depth and  $I_e$  is the effective second moment of area.

#### 10.2.4.2.1. Beam 5\_1 and 5\_2

Beams 5\_1 and 5\_2 were tested in the early work of this thesis (§5.5 on page 124) and provided material savings of approximately 25%. Beams 5\_2 and 5\_1 have identical internal reinforcement layouts. Using the method shown above, the load-deflection response of the beams was determined for Load Case 2 (see §5.5.1 on page 124), which is the maximum sagging loading and final loading condition of the beams.

A concrete Young's Modulus for Beams 5\_2 and 5\_1 was determined from the specimen test data in Table 6.17 on page 183 (average compressive strength at 28 days of 39MPa).

For each loading step (taken in increments of 10% of the maximum beam capacity) the effective section moduli were calculated as described in Table 10.2. The value of  $M/E_e$  was then computed and integrated numerically to determine rotations along the beam. A constant of integration (determined by the boundary conditions shown in Figure 10.8 where the rotation at midspan is zero) was added, before a second integration was carried out to provide deflections, as described in previous sections. A constant of integration was then applied to these values to ensure that the vertical deflection at the support was equal to zero, as shown in Figure 10.8.

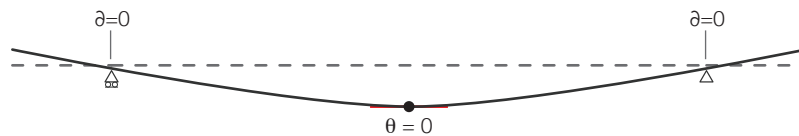


Figure 10.8: Beam 5\_1 and 5\_2 boundary conditions for integrations.

Following this process provides a quick method for determining the deflection along the beam for each load step, and the resulting load deflection plot is determined by repeating the process at each load step. The predicted response for Beam 5\_1 and 5\_2 is shown in Figure 10.9, where it is compared to the test results. The maximum flexural capacity is predicted at a value of 107kN (determined by considering the point at which the steel yields at the position of maximum moment, as described in §6.5.6 on page 192) and the beam response is seen to correlate well to this analysis.

Also shown in Figure 10.9 is a typical deflection limit for the serviceability limit state design of a concrete beam ( $\text{span}/250$ ). It is clear from this that this beam has sufficient stiffness for the serviceability condition to not be particularly onerous for the design process. This factor is a potential concern for variable stiffness elements, but the presence of a significant top slab has assisted Beams 5\_1 and 5\_2 in this respect.

In the load-deflection plot presented in Figure 10.9, a maximum deflection prediction is not estimated. The theoretical maximum deflection, given by the point at which the tension steel snaps, was included initially but results in extremely large deflection predictions at ultimate failure, as the steel material model provides strains to failure of greater than 7.5% (BS EN 1992-1-1 (2004)). Given that such a failure mode is not how the beams failed in testing, this maximum value was not included. Instead, the beams were seen to fail by crushing of the top slab concrete, with a wedge of concrete forming at the midspan. With the formation of this wedge, the beam redistributes stresses as the concrete crushes and thus the simplified analysis presented above is unable to calculate such effects. Additional work is shown in §10.3 to address this aspect of the failure process.

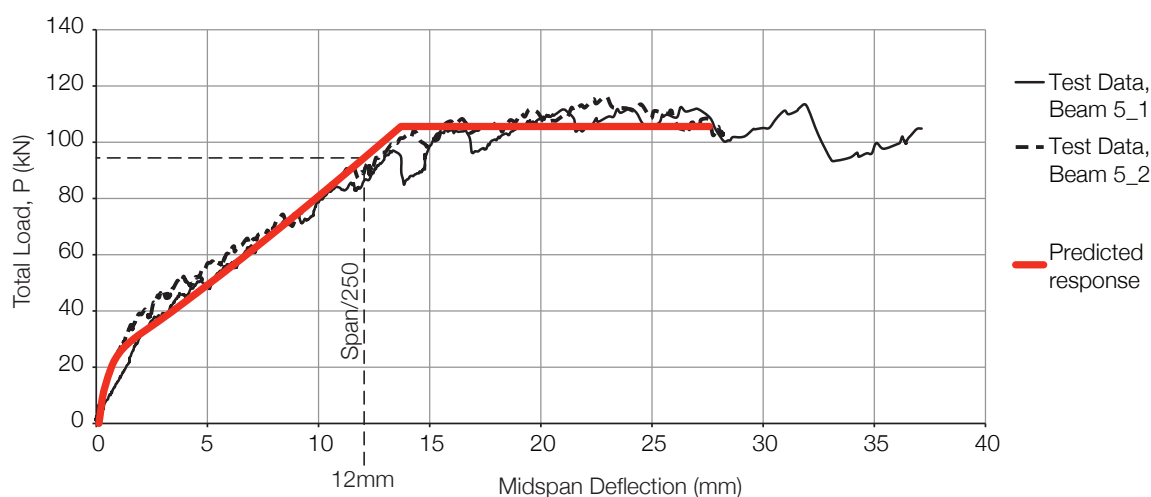


Figure 10.9: Predicted response of Beam 5\_1 and 5\_2, comparison with test data.

#### 10.2.4.2.2. Beams 5\_3 and 5\_4

Beams 5\_3 and 5\_4 had an identical design load envelope to Beams 5\_1 and 5\_2, but a different design process and internal steel layout. Following the same procedure as described above, predictions of the beams' load deflection responses were made. Full layouts of these elements can be seen in §5.5 on page 124, and their test results are shown in §6.5 on page 182. The average concrete strength of the two elements at the test date was

41MPa, and this value was thus used to calculate the concrete Young's modulus. The resulting beam deflection predictions are shown in Figure 10.10, where excellent agreement between the theoretical predicted deflections and those seen in the test procedure are again noted.

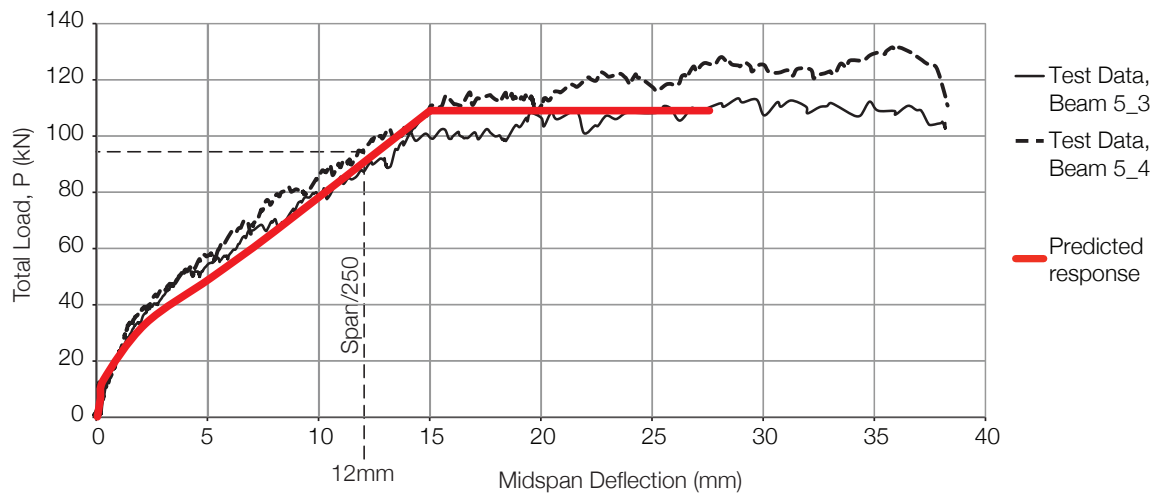


Figure 10.10: Predicted response of Beam 5\_3 and 5\_4, comparison with test data.

#### 10.2.4.2.3. Beam 6\_4\_1

The Double T Beam 6\_4\_1 was also subjected to the same load deflection analysis as Beams 5\_1 and 5\_2. The design of Beam 6\_4\_1 is presented in §5.6 on page 136 and its testing and results are shown in §6.6 on page 195. The same procedure of determining the load-deflection response was undertaken for Beam 6\_4\_1, and the results are shown in Figure 10.11. The tested concrete compressive strength of Beam 6\_4\_1 was 23MPa after 28 days, from which the concrete Young's Modulus was estimated as described previously.

The results of the load deflection analysis again show excellent agreement with the test data. The method is thus shown to be capable of providing quick predictions of the load-deflection behaviour of a concrete element with any cross sectional geometry, which is particularly important for fabric formed construction.

The maximum deflection prediction shown in Figure 10.11 is again estimated by considering the load at which the steel at midspan yields (as described for Beam 5\_1), and more accurate predictions of the post-peak behaviour are addressed in §10.3.

The analysis method described in Figure 10.6 on page 415 provides a load-deflection profile for the entire beam, and not just the midspan. This is shown for Beam 6\_4\_1 in Figure 10.12, where the load deflection profile at the peak load as measured during testing is compared to the predictions. It is again seen that the method provides excellent correlations with the test data at the test stages shown, and accurately addresses the cantilevering sections of this beam also.

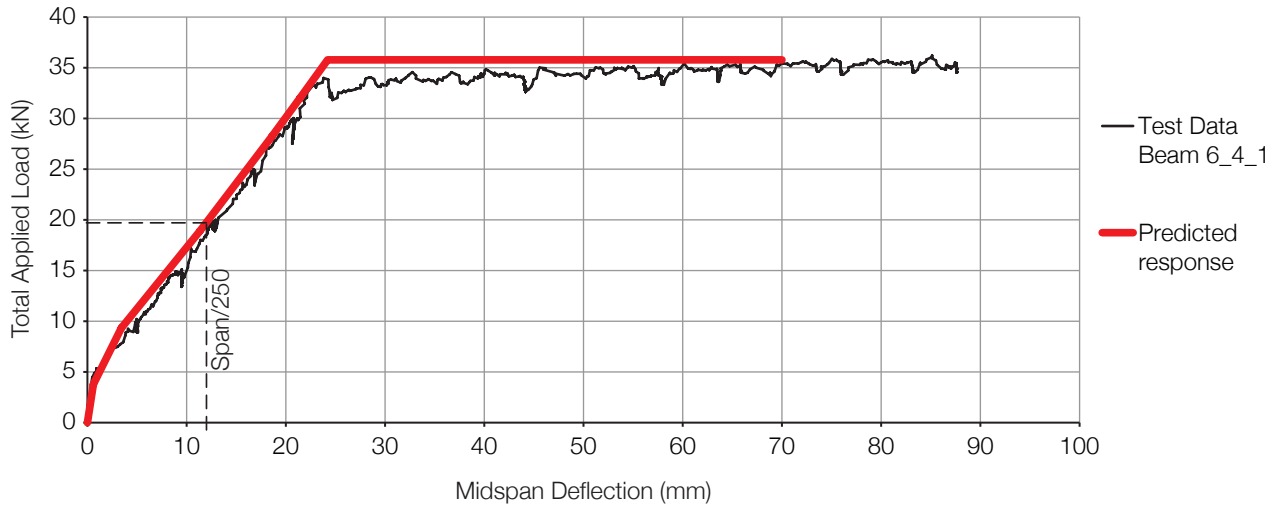


Figure 10.11: Predicted response (mid-span deflection versus total load) of Beam 6\_4\_1, comparison with test data.

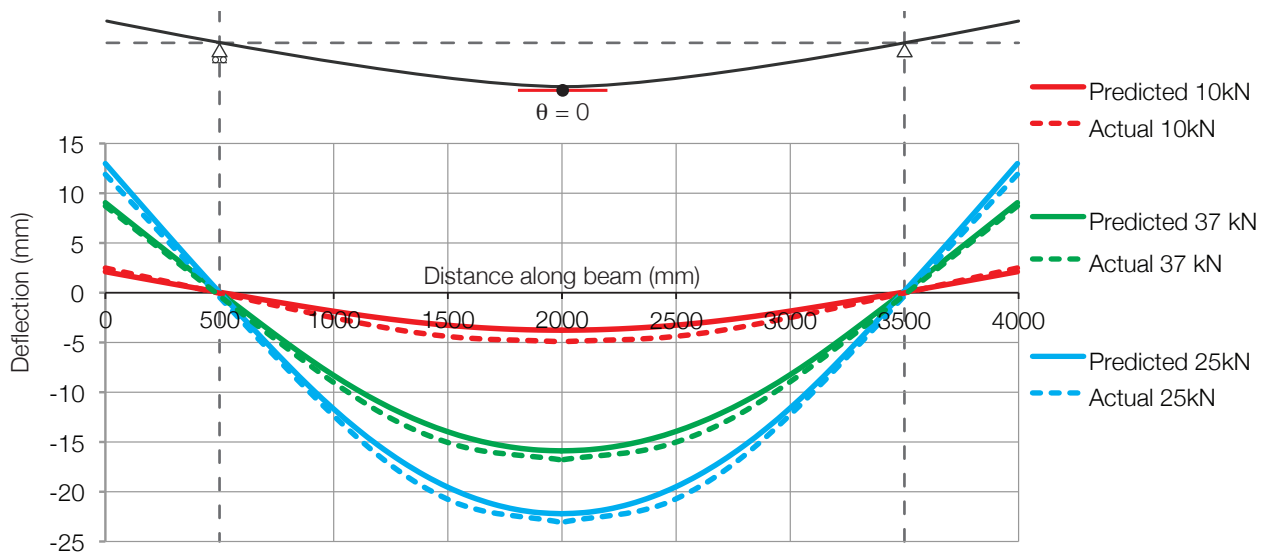


Figure 10.12: Deflection profile prediction for Beam 6\_4\_1, comparison with test data.

#### 10.2.4.2.4. Beam 8\_3i and 8\_3ii

A final verification of the load-deflection process was made on two non-prismatic beams which were not cast as 'T' or 'Double T' beams. The design and loading arrangements, and structural testing can be seen in §7.2 on page 218 and §8.2 on page 246 respectively.

The elements were assessed in the same manner as is described above. The average concrete strength at testing is recorded as 39.9 MPa, and this value was used to calculate the Concrete Young's Modulus and tensile strengths as described above. The equations presented for 'T' beams in Table 10.2 are easily modified for sections without top slabs.

The process was undertaken for the two beams, both of which were tested to failure, and the results are shown in Figure 10.13. Here, it is clear that the analysis procedure again provides an excellent prediction of the final beam load-deflection plots.

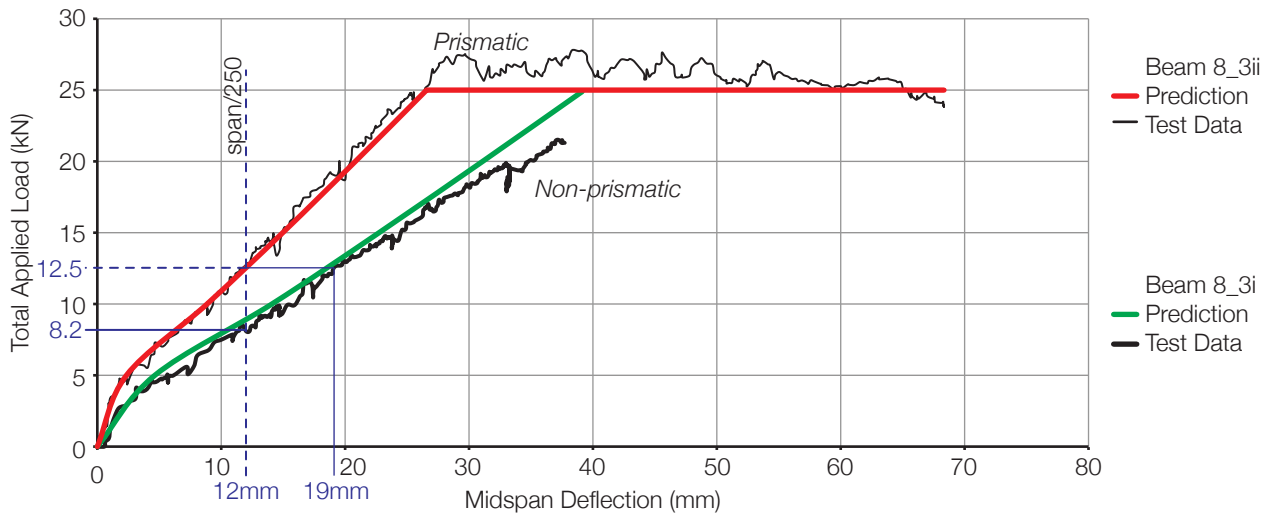


Figure 10.13: Predicted response (mid-span deflection versus total load) of Beams 8\_3i and 8\_3ii, compared to test data.

Whilst the method provides accurate descriptions of the beam load-deflection response it is, as described above, not able to completely model the final failure mode of the section, although the flexural capacity and plastic plateau can be modelled as before, since it is known that the steel at midspan will be yielding in this position. The failure mode of Beam 8\_3i (which was premature, and in shear) is particularly important as this is not able to be included in the prediction, and hence continues to the designed flexural capacity of 25kN. This area is considered further in §10.3 and in Chapter 12.

Shown also in Figure 10.13 is an illustration of how the serviceability limit state can become important in non-prismatic concrete beams. At the serviceability limit of  $\text{span}/250$ , the load capacity of the prismatic Beam 8\_3ii is 52% higher than that of the non-prismatic Beam 8\_3i (12.5kN versus 8.2kN, Figure 10.13). This suggests that in such a design, the capacity of the section will become severely limited by deflection considerations if the element stiffness is not carefully considered. This important concern is highlighted in the design guidance provided in Chapter 11.

### 10.3. Deflection limits

In the above it has been shown that the load-deflection of a non-prismatic concrete section using both UHPFRC and OPC designs can be predicted using the methods described, and that the behaviour of such elements can be accurately predicted in both serviceability and ultimate limit states. As the majority of the sections tested have displayed ductile responses to their applied loads, the maximum deflection of the elements should also be determined.

The 'T' and 'Double T' beams shown above have all been designed as under-reinforced sections, and hence their response is expected to allow the longitudinal steel to yield. There are three possibilities for the ultimate failure of the concrete section, as noted previously: 1) fracture of the longitudinal bars in tension; 2) debonding of the longitudinal reinforcement and 3) sliding failure in the concrete in compression. In the tests described above, the



limit at which the element was deemed to have failed was consistently recorded as a sliding/crushing failure in the top flange (no bar fractures or debonding were recorded).

During the testing regimes for the 'T' and 'Double T' beams cast in Ordinary Portland Cement Concrete (Beams 5\_1 - 5\_4 and Beam 6\_4\_1), failure was recorded at the onset of crushing in the top slab of the element. This form of failure occurs in the 'wedge' of concrete in compression.

For failure mode (1) above, a strain limit in the steel could be included in either model to highlight the position where the steel had fractured (such a limit would typically be  $\geq 7.5\%$  strain for 'Class C' steel, as detailed in BS EN 1992-1-1 (2004) Annex C). However, the inclusion of such a limit can result in large predicted deflections (in the plastic range) which were not seen in the testing regime. Mode (2) can also be included, provided a debonding model for the reinforcement is available. The third mode provides some additional challenges and is difficult to model using the method applied above.

An alternative approach, which may offer some solutions and can account for all three failure modes, is to consider a moment-rotation analysis of the section. Such a procedure is outlined in detail by Ohlers *et al* (2012) and Haskett (2010). The method is applied to a singly reinforced section as shown in Figure 10.14. For a given depth of the softening zone, forces in the concrete softening zone, the compression zone and the tension steel can be determined (as described by Haskett *et al.*, 2009 and Haskett, 2010).

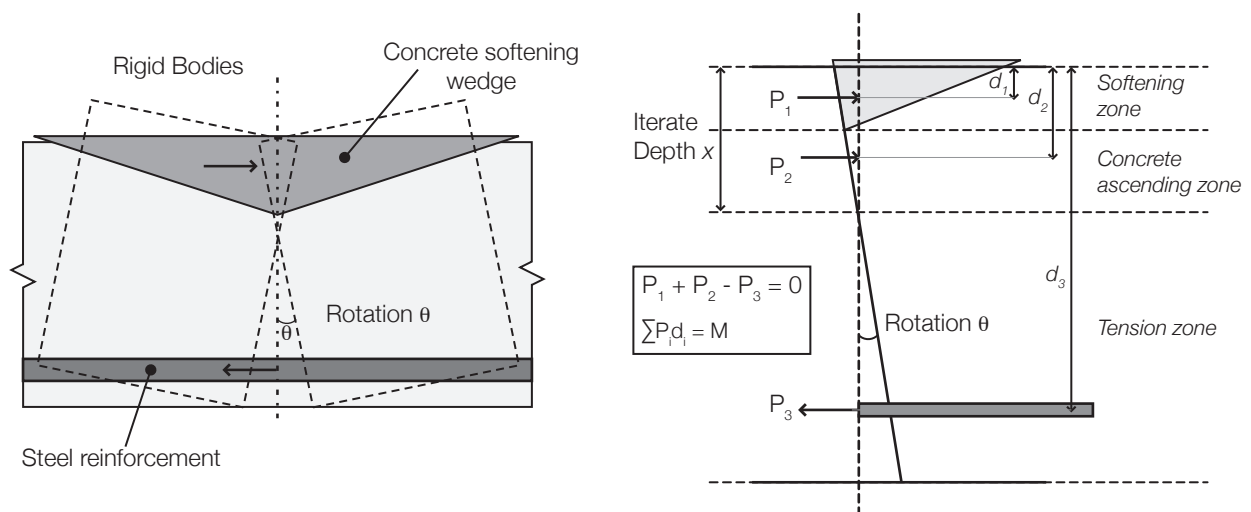


Figure 10.14: Principle of moment-rotation approach for a singly reinforced section (figure after Haskett *et al.*, 2008).

Haskett (2010) provides a detailed account of the complex approach that is required to determine the relevant equations for a singly reinforced concrete section, and demonstrates its efficacy against test data from Mattock (1964, cited by Haskett, 2010). However, the application of the model to doubly reinforced sections, and particularly sections with complex geometries, is not considered and requires further work to extend the model to such situations.

Within the model (and especially once the softening zone becomes dominant or where the tension steel is yielding and or debonding) a number of empirical relationships are required to determine material properties such as the Mohr-Coulomb friction angle for concrete; the bond-slip relationship of the steel; and most importantly the sliding of the concrete wedge. The method, which is demonstrated to be effective and has been used in many situations (including in work on FRP prestressed sections by Whitehead and Ibell (2005)), is therefore recommended for use in future work, where its applications could more effectively be explored. It is proposed that suitable tests be designed such that the three limits of failure can be tested completely, and that the element failure mode is considered in much more detail than was possible in this thesis, where the over riding concern was in the provision of a ductile failure mode. This aspect of future work is highlighted again in Chapter 12.

## 10.4. Modelling techniques

### 10.4.1. Introduction

The two dimensional modelling of fabric formed concrete structures using the principles of the elastica (§3.3.2 on page 61), as described by Foster (2010) has been used throughout this thesis. The principle of the method, and the extensions used in this work, are briefly described below to demonstrate how such a method can be integrated into the design process. Additional work is described in Chapter 12 to outline the potential modelling in three-dimensions of fabric cast structures, including within it the automated structural analysis of such elements.

### 10.4.2. Cross section modelling

The step-wise cross sectional modelling approach put forwards by Foster (2010) is summarised in Figure 10.15. This process uses an iterative Excel Macro to ‘walk-out’ from the deepest point on a section to plot the complete section profile from the relationship between depth and curvature (Foster, 2010). As is described in §3.3.2.2 on page 63, a relationship between the constant tension ( $T_0$ ) in the fabric, the variation in curvature ( $\kappa$ ) and the depth of the fluid ( $z$ ) is known (Eq. 10.16).

$$T_0 = \frac{\rho g z}{\kappa} \quad \text{Eq. 10.16}$$

By starting at the deepest point on a section, a perimeter is drawn based on this relationship between curvature and depth ( $z$ ). By controlling the relationship using a coefficient ( $k$ ), as described below, a range of curves for a given depth can be drawn (as shown by Foster, 2010). In the design process, the aim is to determine which curve will predict the cross section for a given depth and top opening width. It is therefore an iterative process to determine this curve, and this can be achieved using an excel goal-seeking routine.

Starting at the position (0,0), chosen to be at the deepest point on the centre line of the section, a constant increment length is chosen ( $\delta L$ ). The depth of the  $n^{\text{th}}$  increment is given by Eq. 10.17, and the angle between it and the previous increment by Eq. 10.18, as shown by Foster (2010). Since a constant increment length is taken, the coordinates at the end of the  $n^{\text{th}}$  increment are given by Eq. 10.19 on page 425. The iterative process shown in Figure 10.15 thus aims to set the value of the last coordinate point equal to the coordinates ( $0.5b$ ,  $d$ ). As the curve is symmetrical, this is simply mirrored to create the full cross section profile.

$$z_n = z - y_n \quad \text{Eq. 10.17}$$

Where  $z_n$  is the depth of the  $n^{\text{th}}$  step;  $z$  is the total hydraulic depth and  $y_n$  is the y coordinate of the  $n^{\text{th}}$  step.

$$\delta\theta_n = k z_n \quad \text{Eq. 10.18}$$

$\theta_n$  is the angle of the  $n^{\text{th}}$  increment,  $k$  is the coefficient and  $z_n$  is the depth of the  $n^{\text{th}}$  step

$$(x_n, y_n) = \left( \delta L \sum_{i=1}^n \cos \sum_{j=1}^{i-1} \delta \theta_j, \delta L \sum_{i=2}^n \sin \sum_{j=1}^{i-1} \delta \theta_j \right) \quad \text{Eq. 10.19}$$

This process can therefore determine the shape of the fluid filled fabric bag, and provides cross section predictions at discrete points along the length of an element. In this thesis, these sections were then joined together using CAD modelling software to create a prediction for the overall shape of a fabric cast beam for the purposes of structural analysis and three-dimensional image generation, as shown in Figure 10.16. Foster (2010) also shows how this process can be used in both partially full ( $z < d$ ) and over-full sections ( $z > d$ ), as shown in Figure 3.13 on page 65.

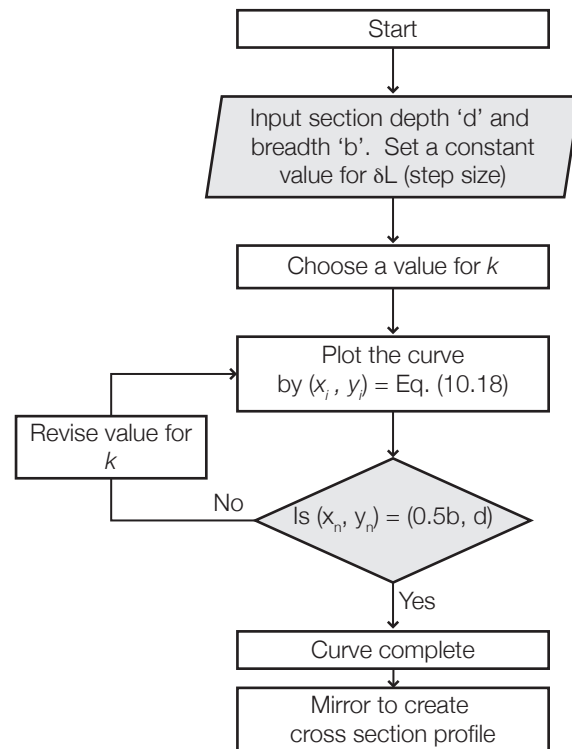
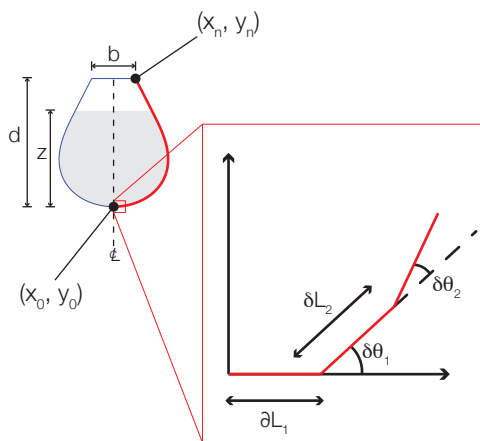


Figure 10.15: Method for cross sectional modelling.

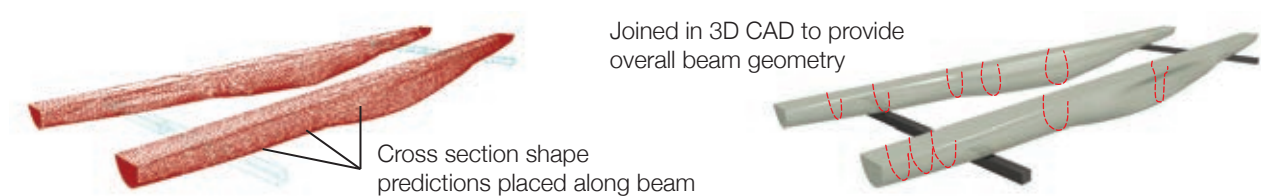


Figure 10.16: Generating three-dimensional images for beam design.

The use of a ‘cross-sectional’ approach, as shown in Figure 10.16, was considerably labour intensive and relied on additional macros to feed in the structural analysis data. Future work should aim to provide a single solution for modelling fabric formed structures in three-dimensions, and progress has been made in this area as seen in the work of Veenendaal *et al* (2010) and Bak (2012).

The modelling process of the fabric cast beams was not a focus of this thesis, and thus formed a periphery activity to the main structural testing that was undertaken and has been described in the preceding Chapters. Data was not collected to verify the cross-sectional geometry predictions made by the approach described above, although longitudinal profiles and steel layouts were checked to ensure the construction was correct.

Verification of the shape predictions is, however, provided by work carried out for the University of Manitoba. In the construction of a fabric-formed beam element, shape predictions were made using the method described above to facilitate the construction of both plaster models and full size elements. The comparison between shape predictions made using the iterative process described above and the plaster models are shown in Figure 10.17, where excellent agreements are seen. Additional work was undertaken by Veenendaal *et al* (2012), using a more sophisticated three-dimensional approach, that provided identical predictions and thus helps to verify the method.

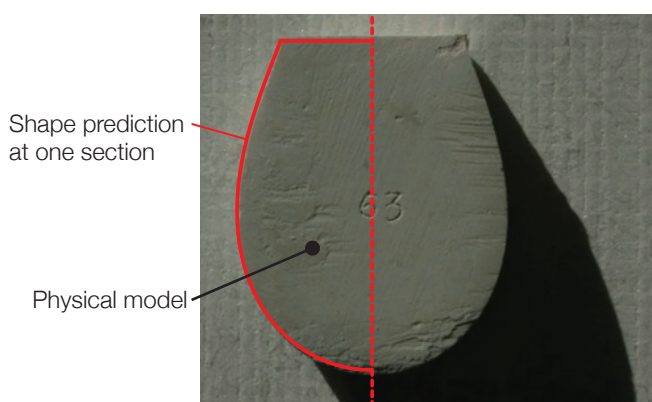


Figure 10.17: Comparison between plaster model and computer approach (model images courtesy Professor Mark West, University of Manitoba).

It is apparent from the above that further work is required to provide a more accessible solution to shape predictions and fabric modelling for architectural design and construction (Figure 10.18). Work in this area is underway, as is seen in publications by Bak (2012) and Veenendaal *et al* (2012), where the three-dimensional modelling of a draped or tensioned fabric cast concrete structure are shown. This area of work will be crucial to the future development of fabric formwork as a sustainable construction process for concrete structures.



Figure 10.18: Three-dimensional images generated from the cross sectional modelling approach (clockwise from top left: Double T Beams; Double cantilever beam; Ribbed slab on fabric cast beams; Continuous beam).

## 10.5. Parametric studies

### 10.5.1. Introduction

Two studies are introduced in the following section to highlight some of the design complexities of non-prismatic sections. First, the position of the inclined reinforcement is considered in terms of construction tolerances, and how these may affect the capacity of the section. Second, the calculation of forces in a truss model type approach is explained where it is also shown that in some situations conventional approaches for calculating the shear carried in the web of a tapered beam can be unconservative. This is an important consideration as the current guidance for BS EN 1992-1-1 (2004) does not specify a method for the calculation of this force, and the results of Chapter 8 have shown that such methods can provide unconservative designs.

### 10.5.2. Flexural design

The work presented in Chapter 5 and Chapter 6 has demonstrated the efficacy of the sectional analysis approach to flexural design for variable section beams. Whilst the design method for fabric cast beams in flexure has been verified, it is important to note that the construction process can result in misplaced reinforcement, which in a variable section member can make dramatic differences to the overall member capacity. A sensitivity analysis is undertaken to assess and analyse the likely results of misplaced reinforcement.

#### 10.5.2.1. Sensitivity analysis

Taking the reinforcement, geometrical layout and variables shown in Figure 10.19, a sensitivity analysis was undertaken. Assuming that the longitudinal reinforcement is fully anchored at the ends, and that at the ultimate limit state it yields, the neutral axis along the length of the beam was determined. The contribution of the inclined bar to the vertical force capacity was not included in this stage of analysis.

A 'design' value for  $\alpha$  of  $10^\circ$  was chosen. By varying the value of this angle within the small range of  $8^\circ$  -  $14^\circ$  (chosen such that the bar did not stray outside the dimensions of the designed beam), the change in moment capacity along the length of the tapered span could be determined. It was ensured that in all variations the strain in the reinforcement was sufficient to theoretically cause it to yield. These results are plotted in Figure 10.20.

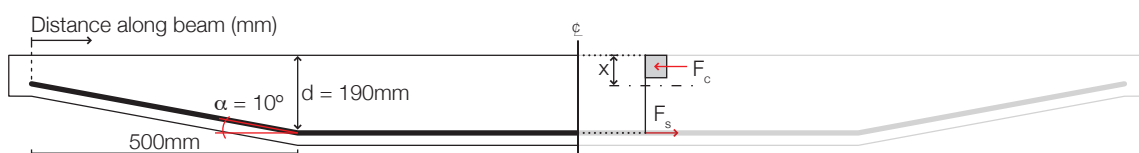


Figure 10.19: Beam layout for sensitivity analysis.



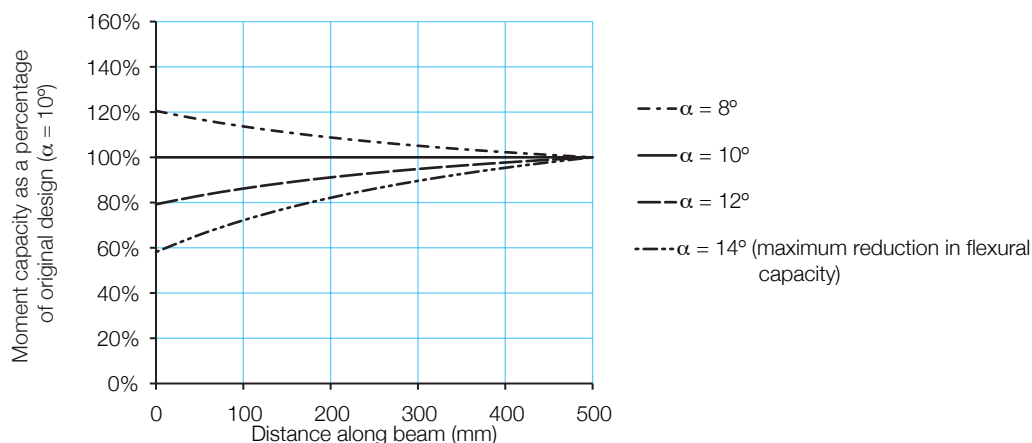


Figure 10.20: Sensitivity analysis results.



Figure 10.21: Bar position for different values of  $\alpha$ .

The results show that for a relatively small change in bar angle, there can be up to a 40% reduction in flexural capacity in the sections close to the end of the bar. The range of values for  $\alpha$  chosen in the above are illustrated in Figure 10.21, where it is apparent that in construction it would be fairly easy to achieve small variations in the bar position that would result in significant reductions in capacity.

It is therefore imperative that the fabric cast member have a robust construction method in which the position of the longitudinal reinforcement can be very accurately known. This has been achieved through the use of the keel mould (described in §2.3.1.2 on page 17) in work described in this thesis. In the provision of guidance for designers in Chapter 11 on page 443, the importance of construction tolerances is highlighted in order that the pitfalls described above can be avoided.

In the following section, the application of the 'Truss Model', as provided for shear design in BS EN 1992-1-1 (2004) is considered in its application to non-prismatic elements. A widely used design method is assessed, and shown to be inaccurate in some situations, with a solution based on equilibrium considerations provided.

### 10.5.3. Truss model applied to non-prismatic sections

The truss model, as used in BS EN 1992-1-1 (2004), for shear design is described for a prismatic section in §4.2.5.1 on page 88 and introduced for non-prismatic sections in §4.3.2.2 on page 96. An important part of this model is the ‘additional tension force’ which is generated as a result of the inclined compression struts in the web of the beam, and whose force is added to both compression and tension ‘chords’ of the model for equilibrium. Building on comments made in §4.3.2.2 on page 96, the following analysis is presented to show how existing approaches to calculating the shear carried in the web of a tapered beam can be unconservative in sections with an inclined compression chord and conservative in sections with an inclined tension chord, because this additional tension force is often excluded from the calculations.

#### 10.5.3.1. Sections with an inclined tension chord

For elements with an inclined tension chord, the truss model shown in Figure 10.22 may be applicable. The vertical component of force in the inclined tension chord provides a relieving effect to the magnitude of the shear force that must be carried in the web of the section. This force is normally calculated using Eq. 10.20. However, such an approach does not consider the additional tension force required for equilibrium of the truss model.

$$V_w = V - \frac{M}{z} \tan \beta \quad \text{Eq. 10.20}$$

Where  $V_w$  is the reduced shear force;  $M$  is the moment,  $z$  is the lever arm and  $\beta$  is the inclination.

A more detailed model is described below. The external forces are  $M$  and  $V$  are determined from analysis. The internal forces (denoted here with ‘ $N$ ’ as they are acting along the axis of the element under consideration) are the horizontal force in the top (compression) chord ‘ $N_1$ ’; the horizontal component of force in the inclined strut in the web ‘ $N_3$ ’ and the horizontal component of force in the inclined tension chord ‘ $N_2$ ’.

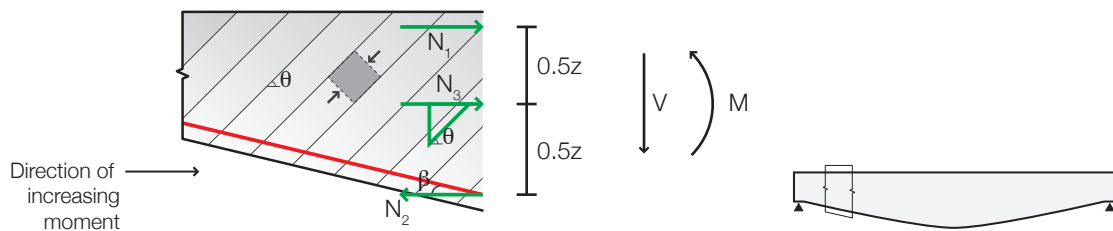


Figure 10.22: The variable angle truss model for a tapered beam with an inclined tension chord.

By equilibrium the following are obtained:

$$N_1 - N_2 + N_3 = 0 \quad \text{Eq. 10.21}$$

$$N_3 \tan \theta + N_2 \tan \beta - V = 0 \quad \text{Eq. 10.22}$$

$$N_3 \left( \frac{z}{2} \right) + M - N_2 z = 0 \quad \text{Eq. 10.23}$$

To obtain the force in the diagonal strut ( $N_3$ ) Eq. 10.22 and Eq. 10.23 are rearranged to give Eq. 10.24 and Eq. 10.25, which themselves are equated to provide the force  $N_3$ , Eq. 10.26. Note that when  $\beta = 0$ , Eq. 10.26 is simplified to Eq. 10.27 which is the conventional formula for prismatic sections.

$$N_2 = \frac{N_3}{2} + \frac{M}{z} \quad \text{Eq. 10.24}$$

$$N_2 = \frac{V}{\tan \beta} - \frac{N_3 \tan \theta}{\tan \beta} \quad \text{Eq. 10.25}$$

$$N_3 = \frac{V - (M \tan \beta) / z}{0.5 \tan \beta + \tan \theta} \quad \text{Eq. 10.26}$$

$$\text{when } \beta = 0, N_3 = \frac{V}{\tan \theta} \quad \text{Eq. 10.27}$$

The force in the inclined bottom chord ( $N_2$ ) may then be determined by substitution of Eq. 10.26 in Eq. 10.24, giving Eq. 10.28. Note again that for an element with parallel chords this equation reduces to that discussed in §4.3.2.2 on page 96 and given in BS EN 1992-1-1 (2004) including the additional tensile force. The first term in Eq. 10.28 is the additional tension force determined from the truss model.

$$N_2 = \frac{V - (M \tan \beta) / z}{\tan \beta + 2 \tan \theta} + \frac{M}{z} \quad \text{Eq. 10.28}$$

The force in the top chord is then given by substitution of Eq. 10.28 and Eq. 10.26 into Eq. 10.21 to give Eq. 10.29.

$$N_1 = \frac{M}{z} - \frac{V - (M \tan \beta) / z}{\tan \beta + 2 \tan \theta} \quad \text{Eq. 10.29}$$

Finally, the vertical component of the force  $N_3$  in the web that resists shear is given by Eq. 10.30 and Eq. 10.31. Note again that in the case of a prismatic section where all the shear is resisted by the web, Eq. 10.31 has the value of  $-V$ .

$$V_w = N_3 \tan \theta \quad \text{Eq. 10.30}$$

$$V_w = \frac{V - (M \tan \beta) / z}{(\tan \beta / 2 \tan \theta) + 1} \quad \text{Eq. 10.31}$$

Comparing Eq. 10.31 to the method given in much of the literature, where the force carried in the web is given by Eq. 10.32, the difference between them can be reduced to Eq. 10.33. By varying both  $\beta$  ( $0 < \beta \leq 30^\circ$ ) and  $\theta$  ( $22^\circ, 33.5^\circ$  and  $45^\circ$ ), it is seen that the conventional approach to calculating the shear force carried in the tapered section web is conservative by between 3% and 40%, as shown in Figure 10.23. Whilst this conservatism is entirely acceptable for design, it shows that a more detailed analysis can provide better calculations of the force in the web of the section.

$$V_w = V - \frac{M}{z} \tan \beta \quad \text{Eq. 10.32}$$

$$\Delta = \frac{1}{(\tan \beta / 2 \tan \theta) + 1} \quad \text{Eq. 10.33}$$

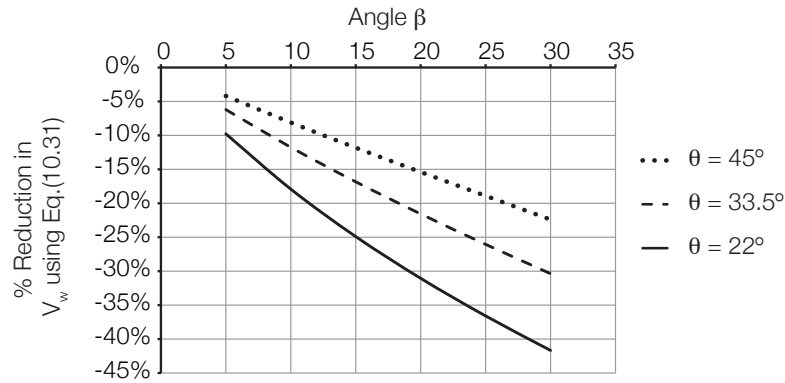


Figure 10.23: Reduction in shear carried by the web in beams with inclined tension chords.

#### 10.5.3.2. Section with inclined compression chord

In §10.5.3.1 it was shown that in a section with an inclined tension chord, the additional tensile force required for equilibrium increases the vertical component of force carried in the tension chord and thus can reduce the shear force carried in the web. In sections with inclined compression forces, the opposing argument is apparent. The inclined compression force is reduced by the additional tensile force, and thus the vertical force to be carried in the web is increased over that which would be calculated by Eq. 10.20. Following the same process as described above, but for the beam in hogging shown in Figure 10.24, the value for  $N_3$  can be found.

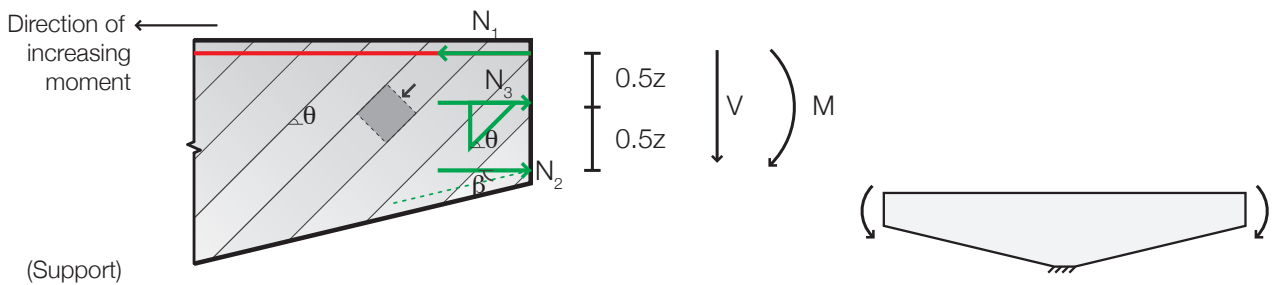


Figure 10.24: The variable angle truss model for a tapered beam with an inclined compression chord.

By equilibrium the values of  $N_1$ ,  $N_2$  and  $N_3$  are found as:

$$N_3 = \frac{V - M \tan \beta / z}{\tan \theta - 0.5 \tan \beta} \quad \text{Eq. 10.34}$$

$$N_2 = \frac{M}{z} - \frac{V - M \tan \beta / z}{2 \tan \theta - \tan \beta} \quad \text{Eq. 10.35}$$

$$N_1 = \frac{M}{z} + \frac{V - M \tan \beta / z}{2 \tan \theta - \tan \beta} \quad \text{Eq. 10.36}$$

The force carried in the web,  $N_3 \tan \theta$  is thus given by Eq. 10.37. This value is compared to that calculated by Eq. 10.20 in Figure 10.25. For the same range of  $\beta$  and  $\theta$  values as used previously, the method shows that the shear carried by the web in the beam with an inclined compression zone is increased significantly. It should be noted that the magnitude of the force calculated by Eq. 10.37 is still less than the total shear demand on the section (i.e. the inclined compression chord still provides some resistance to shear).

It would therefore be conservative to design sections with inclined webs to carry the entire shear force and to ignore the contributions from inclined areas. If these contributions are considered, then it is important that equilibrium is satisfied, for the reasons described above.

$$N_3 \tan \theta = \frac{V - M \tan \beta / z}{1 - (\tan \beta / 2 \tan \theta)} \quad \text{Eq. 10.37}$$

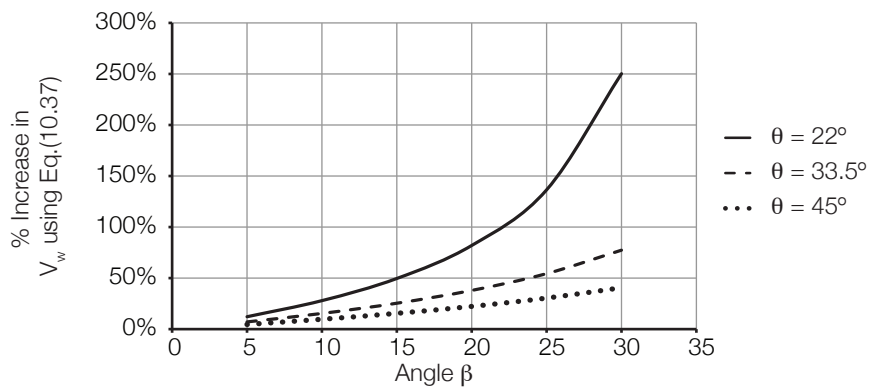


Figure 10.25: Change in shear carried by the web in beams with an inclined compression chord.

### 10.5.3.3. Analysis

From the analysis presented above it is clear that the conventional approach found in much of the literature for calculating the reduced shear force in beams with inclined chords can be unconservative in some situations. The magnitude of this unconservatism is potentially large for beams in hogging, although a design in which the entire shear force is carried by the web would always be conservative. The calculation of the relieving effect of the additional tensile force should always be included, as it is necessary for equilibrium.

Whilst this approach is useful for the calculation of forces to be carried in non-prismatic sections, its application to design must be used with caution, as the results presented in Chapter 8 demonstrate. In Chapter 8 it was shown that assumptions surrounding the yielding of both longitudinal and transverse steel can result in premature failures of the section. It is thus proposed that either the Compressive Force Path method, or a Strut and Tie model of the beam end zone should be adopted in the detailed design of transverse reinforcement for tapered beams. In this way, additional concerns in the end zones of steel capacity and yielding, anchorage and flexural failure capacity can also be addressed.

## 10.6. Material use

In this section the potential impact of fabric formwork on the construction industry is assessed in a broad sense. A summary of the material savings shown in this thesis is provided initially, taken from the wide range of tests that have been undertaken. Work is then presented that shows how these savings could be extended into concrete frame construction. This analysis further includes estimates of the embodied carbon of such structures, and demonstrates how low carbon approaches to concrete construction may be achieved using fabric formwork.

This thesis has demonstrated that fabric formed beam construction can provide concrete volume savings of, on average, 41% (Table 6.25 on page 215). In the following section, this analysis is extended to include formwork, fabric and construction processes to provide an estimate of the embodied energy of a fabric formed concrete beam.

### 10.6.1. Embodied energy analyses

In this section, the embodied energy of Beam 5\_1 ('T' Beam) and Beam 6\_4\_1 ('Double T' Beam) is calculated. It is shown that fabric formwork continues to provide significant advantages over conventional construction processes. The concrete used throughout this thesis has included fly ash or ground-granulated blast furnace slag replacements; here the embodied energy is calculated based on an RC25/30 concrete using 30% fly ash replacement (giving a 15% reduction in embodied energy when compared to a CEM I concrete mix with no cement replacements).

#### 10.6.1.1. Beam 5\_1

The design and construction of Beam 5\_1 is shown in §5.5 on page 124 and §6.5 on page 182. The materials used in each construction are illustrated in Figure 10.26, and summarised for Beam 5\_1 in Table 10.3 and for its equivalent strength prismatic section (denoted as Beam 5\_1\_P) in Table 10.4 on page 434, where the contribution of each material to the overall embodied energy is provided (all data taken from the inventory of carbon and energy (Hammond and Jones, 2011)). Comparisons between the two elements, and the overall embodied energy and embodied carbon savings achieved in Beam 5\_1 are given in Table 10.5 on page 434.

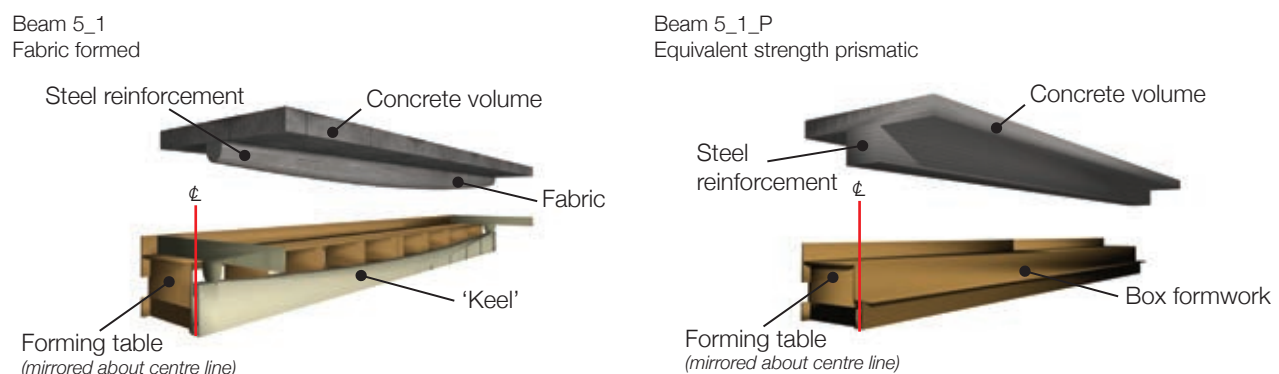


Figure 10.26: Materials used in the construction of Beam 5\_1 and an equivalent strength prismatic section (denoted Beam 5\_1\_P).



Table 10.3: Embodied energy of Beam 5\_1 (all values taken as 'Cradle to Gate' values where possible from Hammond and Jones, 2011).

Item	Description	m <sup>3</sup>	Density	kg	Embodied Energy	Embodied Carbon	Embodied Energy	Embodied Carbon
			kg/m <sup>3</sup>		MJ/kg	kgCO <sub>2</sub> e/kg	MJ	kg
Concrete <sup>1</sup>		0.065	2400	156.0	0.78	0.113	121.68	17.63
Steel	Longitudinal steel: 4H10 4m lengths; 2H12 4m length	2.15E-03	7850	16.9	17.40	1.40	294.03	23.66
	Links: ø3mm, 29m length	2.05E-04	7850	1.6	17.40	1.40	28.00	2.25
Plywood	Formwork, table tops and keel to secure fabric	0.1471	700	103.0	15.00	1.07	1544.55	110.18
Fabric <sup>2,3</sup>	Total area used to create beam mould	5.0m <sup>2</sup>	0.22kg/m <sup>2</sup>	1.1	90	3.40	99.00	3.74
<b>Total</b>							<b>2087.26</b>	<b>157.46</b>
Notes: <sup>1</sup> Concrete data RC25/30 with 30% Fly Ash replacement								
<sup>2</sup> A specific embodied energy and embodied carbon figure for the fabric used in this beam was not available, so figures of 90MJ/kg and 3.40kgCO <sub>2</sub> e/kg are taken from data given for Polypropylene in Hammond and Jones (2011). The fabric density is given by the supplier (Proserve, 2012).								
<sup>3</sup> The Embodied Carbon of the fabric material is an estimated based on the data available in Hammond and Jones (2011) and as such accounts for the difference in percentage savings shown in Table 10.5 when comparing embodied energy and embodied carbon (15.8% versus 18.6%).								

Table 10.4: Embodied energy of equivalent strength Beam 5\_1\_P (all values taken as 'Cradle to Gate' values where possible from Hammond and Jones, 2011).

Item	Description	m <sup>3</sup>	Density	kg	Embodied Energy	Embodied Carbon	Embodied Energy	Embodied Carbon
			kg/m <sup>3</sup>		MJ/kg	kgCO <sub>2</sub> e/kg	MJ	kg
Concrete		0.10	2400	240.0	0.78	0.113	187.20	27.12
Steel	Longitudinal steel: 4H10 4m lengths; 2H12 4m length	2.15E-03	7850	16.9	17.40	1.40	294.03	23.66
	Links: ø3mm, 29m length	2.33E-04	7850	1.8	17.40	1.40	31.86	2.56
Plywood	Formwork, table tops and prismatic box to make beam web	0.19	700	131.0	15.00	1.07	1964.80	140.16
<b>Total</b>							<b>2477.89</b>	<b>193.50</b>

Table 10.5: Savings in embodied energy for Beam 5\_1 when compared to Beam 5\_1\_P.

Item	Percentage saving in Embodied Energy for the fabric cast beam	Percentage Saving in Embodied Carbon for the fabric cast beam
Concrete	35.0%	35.0%
Steel - Longitudinal	0.0%	0.0%
Steel - Transverse	12.1%	12.1%
Plywood	21.4%	21.4%
Fabric	-	-
<b>Total saving</b>	<b>15.8%</b>	<b>18.6%</b>

It is seen in the analysis presented above that the fabric formed element provides significant reductions in the overall carbon and embodied energy of the 'T' beam under consideration. Whilst the savings presented in Table 6.25 on page 215, which consider only concrete material savings, are reduced it is important to note the significance in this analysis of the plywood used to support the fabric mould (and that acts as the complete formwork for the prismatic section). In the fabric cast beam, the plywood contributes 73% of the total embodied energy; in the prismatic section this figure is as high as 79%. The large contribution of the plywood highlights that additional challenges remain for fabric formwork to not only save large amounts of concrete, which has been achieved, but to provide a construction process that can do away with much more timber than is currently used.

It is further important that the use of a man-made fabric can have significant impacts on the overall embodied energy of the fabric cast construction. Whilst relatively little fabric is required to create Beam 5\_1, its estimated embodied energy of 90MJ/kg is by far the largest of all the materials used, and means that the fabric alone accounts for nearly as much embodied energy as the concrete for the beam. Whilst the fabric can be reused, it is also important that alternatives to synthetic fabrics are considered.

This aspect of optimisation of not just the structural element, but its construction process, will be considered in future work in this area. Alternatives to both plywood formwork and synthetic fabric should be sought.

#### 10.6.1.2. Beam 6\_4\_1

A similar analysis to that performed for Beam 5\_1 above is given below for Beam 6\_4\_1, described in full in §5.6 on page 136 and §6.6 on page 195. The materials used in the construction of this beam, and its equivalent strength prismatic section, are illustrated in full in Figure 10.27 and described in Table 10.6 for Beam 6\_4\_1 and Table 10.7 for Beam 6\_4\_1\_P.

The results are remarkably similar to those for Beam 5\_1 and 5\_1\_P, showing embodied carbon reductions of up to 18.1% for the fabric cast beam when compared to its equivalent strength prismatic section.

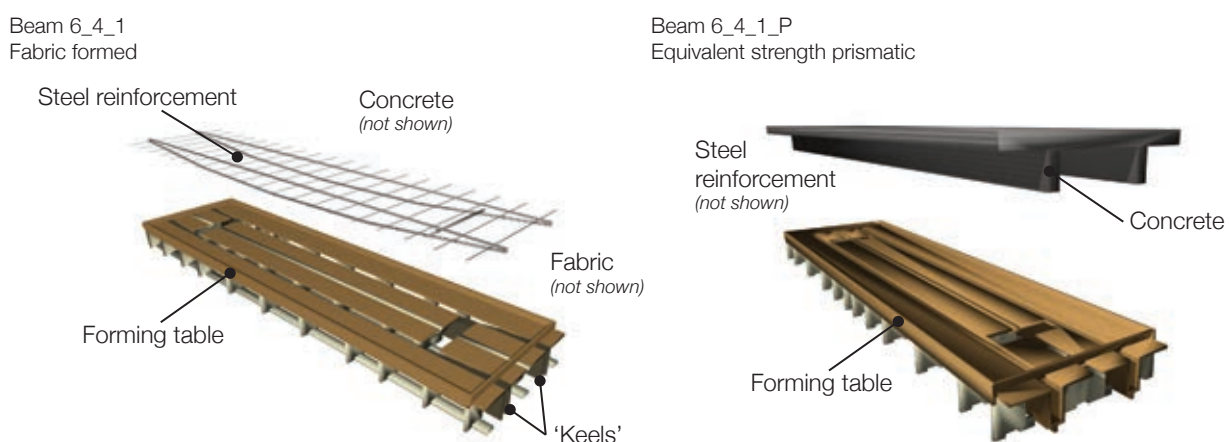


Figure 10.27: Materials used in the construction of Beam 6\_4\_1 and an equivalent strength prismatic section (denoted Beam 6\_4\_1\_P).

Table 10.6: Embodied energy of Beam 6\_4\_1 (all values taken as 'Cradle to Gate' values where possible from Hammond and Jones, 2011).

Item	Description	m <sup>3</sup>	Density	kg	Embodied Energy	Embodied Carbon	Embodied Energy	Embodied Carbon
			kg/m <sup>3</sup>		MJ/kg	kgCO <sub>2</sub> e/kg	MJ	kg
Concrete <sup>1</sup>		0.21	2400	499.20	0.78	0.11	389.38	56.41
Steel	Longitudinal steel: 8H8 4m lengths 20H8 0.95m lengths	2.58E-03	7.85E+03	20.28	17.40	1.40	352.90	28.39
	Links: ø3mm, 29.9m length	2.11E-04	7.85E+03	1.66	17.40	1.40	28.84	2.32
Plywood	Formwork, table tops and keel to secure fabric	0.14	700	99.88	15.00	1.07	1498.21	106.87
Fabric <sup>2,3</sup>	Total area used to create beam mould	5.50m <sup>2</sup>	0.22kg/m <sup>2</sup>	1.21	90.00	3.40	108.90	4.11
<b>Total</b>							<b>2378.23</b>	<b>198.11</b>
Notes: <sup>1</sup> Concrete data RC25/30 with 30% Fly Ash replacement								
<sup>2</sup> A specific embodied energy and embodied carbon figure for the fabric used in this beam was not available, so figures of 90MJ/kg and 3.40kgCO <sub>2</sub> e/kg are taken from data given for Polypropylene in Hammond and Jones (2011). The fabric density is given by the supplier (Proserve, 2012).								
<sup>3</sup> The Embodied Carbon of the fabric material is an estimated based on the data available in Hammond and Jones (2011) and as such accounts for the difference in percentage savings shown in Table 10.8 when comparing embodied energy and embodied carbon (15.0% versus 18.1%).								

Table 10.7: Embodied energy of equivalent strength Beam 6\_4\_1\_P (all values taken as 'Cradle to Gate' values where possible from Hammond and Jones, 2011).

Item	Description	m <sup>3</sup>	Density	kg	Embodied Energy	Embodied Carbon	Embodied Energy	Embodied Carbon
			kg/m <sup>3</sup>		MJ/kg	kgCO <sub>2</sub> e/kg	MJ	kg
Concrete		0.281	2400	674.40	0.78	0.11	526.03	76.21
Steel	Longitudinal steel: 4H10 4m lengths; 2H12 4m length	2.58E-03	7850	20.28	17.40	1.40	352.90	28.39
	Links: ø3mm, 29m length	2.99E-04	7850	2.35	17.40	1.40	40.81	3.28
Plywood	Formwork, table tops and prismatic box to make beam web	0.18		125.19	15.00	1.07	1877.83	133.95
<b>Total</b>							<b>2797.57</b>	<b>241.84</b>

Table 10.8: Savings in embodied energy for Beam 6\_4\_1 when compared to Beam 6\_4\_1\_P.

Item	Percentage saving in Embodied Energy for the fabric cast beam	Percentage Saving in Embodied Carbon for the fabric cast beam
Concrete	26.0%	26.0%
Steel - Longitudinal	0.0%	0.0%
Steel - Transverse	29.3%	29.3%
Plywood	20.2%	20.2%
Fabric	-	-
<b>Total saving</b>	<b>15.0%</b>	<b>18.1%</b>

In the above analysis it is again seen that although the fabric formed element saves considerable amounts of concrete material, the overall embodied energy is skewed by the use of a timber former to hold the fabric formwork. In Beam 6\_4\_1, the plywood used is estimated to account for 63% of the total embodied energy, and in Beam 6\_4\_1\_P for 67% of the total embodied energy. As noted above, this area should be considered in more detail in future work.

In the above comparison it is assumed that the plywood, fabric and other formwork materials are used only once and provide a full contribution to the embodied energy of the beams. This contribution therefore outweighs other embodied energy calculations. Further work is thus required to determine both the reusability of a fabric mould and a cradle-grave analysis of fabric formed construction. In such an analysis, the recyclability of the various formwork components would be included, and the ability to reuse the fabric formwork may lead to further reductions in total embodied energy.

The work presented in this section can be positively compared to a similar analysis undertaken by Lee (2010), where 27% savings in embodied energy were found in fabric cast 'T' beams (as described in §2.5.2 on page 31). However, these savings are based on only the concrete and steel contributions, and not that of the fabric and timber mould. Comparing the same parameters of concrete and steel use only for Beams 5\_1 and 6\_4\_1 with their prismatic counterparts, it is seen that they provide embodied energy savings of 14% and 16% respectively (Table 10.9). It is further noted by Lee (2010) that the necessarily simplistic calculations of embodied energy shown do not include site specific factors such as transport weights and distances, and worker behaviours (such as transport to site) that can impact the embodied energy. It should also be noted that in the fabric cast element, the use of an exposed finish can provide other benefits such as thermal mass and better day lighting (through tapered floor elements at windows) that can further reduce the in-service energy of the structure.

*Table 10.9: Material use comparison for Beams 5\_1 and 6\_4\_1 considering concrete and steel only.*

Embodied Energy	6_4_1	6_4_1_P	5_1	5_1_P
Concrete (MJ)	526.0	121.7	187.2	
Steel (MJ)	381.7	393.7	322.0	325.9
Total (MJ)	771.1	919.7	443.7	513.1
Reduction (%)	16%		14%	

In the above analysis, the embodied energy of the concrete has been taken with a 30% fly ash replacement value. This level of cement replacement is low, and further opportunities for embodied energy reductions exist in the use of low-carbon cements such as supersulfated cements (SSC), which can have up to 90% less embodied carbon than a conventional Portland cement concrete (Ioannou *et al.*, 2011). The disadvantage of such cements can be found in their increased susceptibility to carbonation (which in turn can lead to depassivation of internal steel reinforcement, and thus supports the case for using Fibre-reinforced polymer reinforcement in low-carbon concrete structures) and slow development of strength (which can reduce the speed at which a building is constructed and adds cost to the construction process).

### 10.6.2. Applications to building design

The analysis above has shown that the embodied energy of a concrete beam can be significantly reduced by the use of fabric formwork. Opportunities and challenges for further reductions in embodied energy have also been highlighted.

The potential for material and embodied energy savings throughout a concrete-framed building are now considered, taking the overall geometry shown in Figure 10.28. Sections showing the build up of the two construction processes being considered are shown in Figure 10.29. Material use analysis is undertaken and potentials for fabric formwork to influence the overall material use of concrete construction are shown in Table 10.10 and Table 10.11. Core walls are not included as they are assumed constant in both designs. Foundations are not included as they will vary depending on the site; however it should be recognised that where the structure has a lower self-weight, it may be possible to reduce the foundation size accordingly.

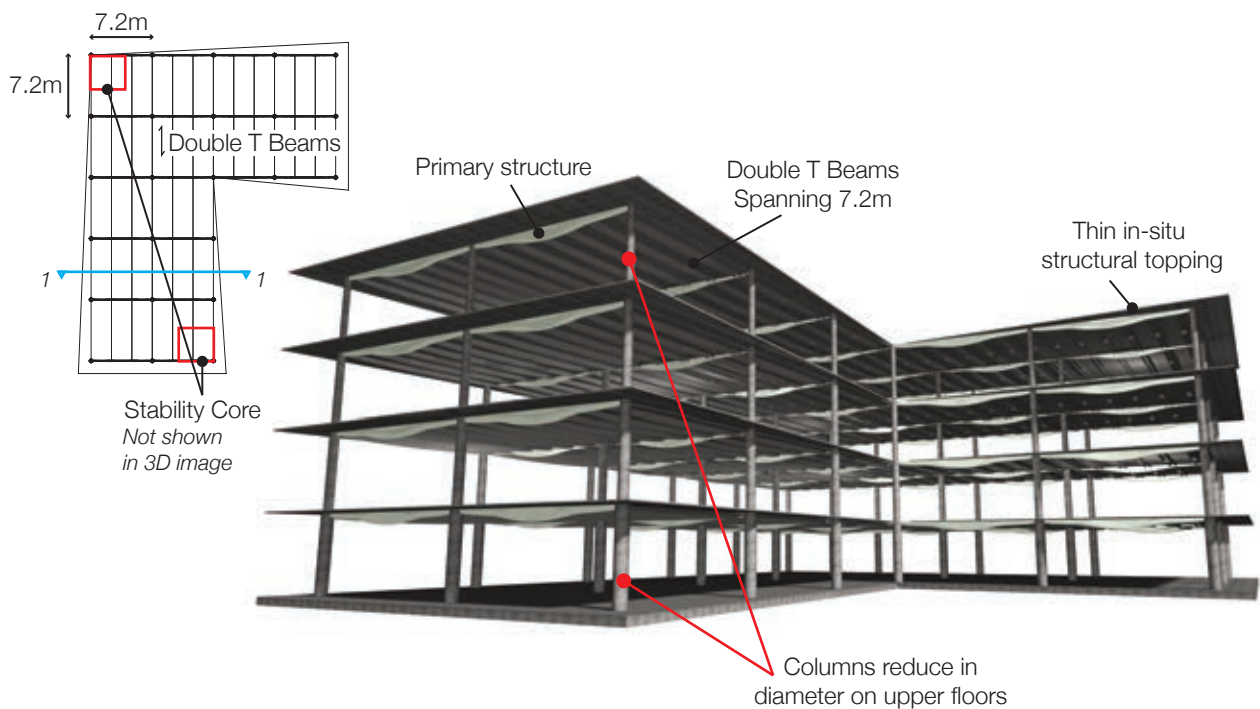
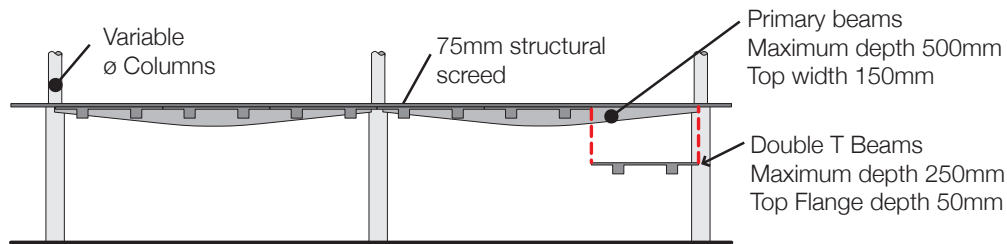
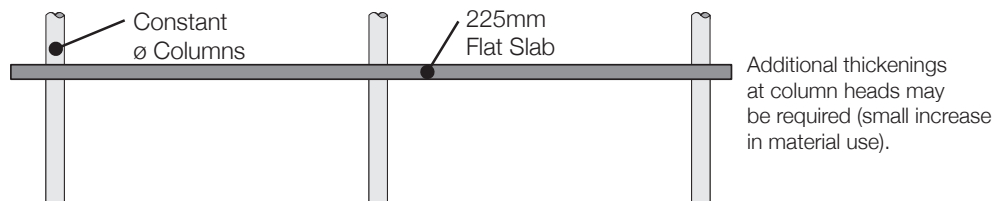


Figure 10.28: Layout of prototype building showing geometry and overall forms.



Section 1-1 (Figure 10.28) - Fabric formed construction



Section 1-1 (Figure 10.28) - Prismatic construction

Figure 10.29: Typical sections through the fabric formed and conventionally cast structure.

Table 10.10: Material use summary for the example fabric formed building shown in Figure 10.28 and Figure 10.29.

Floor		1	2	3	4	Total
Item						m <sup>3</sup>
Columns	24/floor	ø450mm, 3100mm long	ø350mm	ø300mm	ø250mm	27.90
Main Beams	18/floor	0.324m <sup>3</sup> /beam	0.324m <sup>3</sup> /beam	0.324m <sup>3</sup> /beam	0.324m <sup>3</sup> /beam	23.33
75mm Slab	850m <sup>2</sup> /floor	63.75m <sup>3</sup> /floor	63.75m <sup>3</sup> /floor	63.75m <sup>3</sup> /floor	63.75m <sup>3</sup> /floor	255.00
Double T Beams	42/floor	0.97m <sup>3</sup> /beam	0.97m <sup>3</sup> /beam	0.97m <sup>3</sup> /beam	0.97m <sup>3</sup> /beam	162.57
						<b>468.80</b>
Note: Core walls not included in the comparison as identical in both example buildings.						

Table 10.11: Material use summary for the example prismatic building shown in Figure 10.28 and Figure 10.29.

Floor		1-4	Total
Item			m <sup>3</sup>
Columns	24/floor	ø450mm, 3100mm long, 11.83m <sup>3</sup> /floor	47.33
225mm Slab	850m <sup>2</sup> /floor	191.25m <sup>3</sup> /floor	765.00
			<b>812.33</b>
Note: Core walls not included in the comparison as identical in both example buildings.			

A summary of the material use reductions provided in the above analysis is given in Table 10.12:

Table 10.12: Changes in material use, arranged by structural element (excluding core walls).

Item	% reduction when using fabric formed elements	Notes
Columns	41%	
Main Beams	-	Not used in prismatic form, increase in material use of 23m <sup>3</sup>
Concrete slab	67%	75mm structural screed compared to 225mm flat slab
Double T Beams	-	Not used in prismatic form, use a total of 163m <sup>3</sup> concrete
<b>Total</b>	<b>42%</b>	42% reduction correlates to 30-40% material savings achieved in structural test data presented in this thesis.



### 10.6.2.1. Material use: Columns

Thirion (2010) showed that the rate of work (peak actions divided by capacity) of columns in medium rise concrete framed buildings can be low. By simply varying the size and internal reinforcement of columns across the height of such a structure, material savings of as much as 60% were demonstrated. The work presented above suggests that similar material reduction are achievable (although it is noted that columns make up quite a small proportion of the total concrete in a structure, with the majority arising from the slab and beam construction).

### 10.6.2.2. Material use: Beams and Slabs

In this thesis it has consistently been shown that concrete material savings of up to 40% can be achieved through the optimisation of beam designs. In the comparison shown above, a fabric cast 'Double T' beam is compared to a 225mm flat slab (continuous, two way spanning). It is seen that the flat slab system, whilst easy to construct, uses significantly more material than the proposed 'Double T' system.

The comparison, which is a preliminary one that invites further work on this topic, demonstrates that the material use reductions seen throughout this thesis may also be achieved in complete building systems. Further work is required to determine additional savings in floor slab construction which may be possible - for example by using precast fabric formed shells to act as permanent participating formwork for an in-situ concrete slab, as shown in Figure 10.30. Steps towards achieving this in flat slab construction have been demonstrated in work by Bak *et al* (2012), as illustrated in §12.2.4 on page 467.

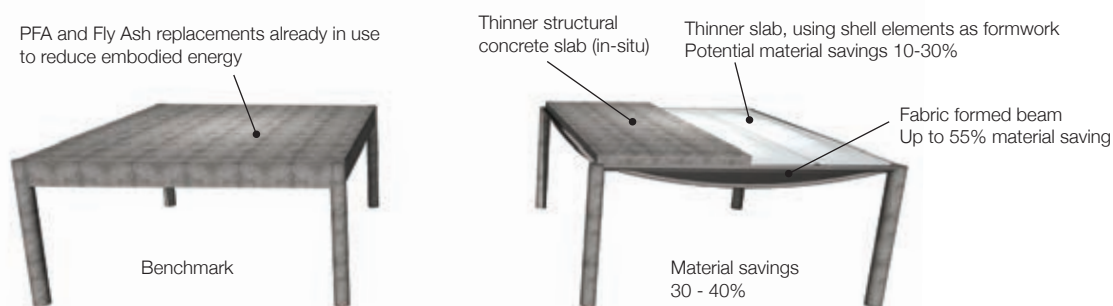


Figure 10.30: Future use of fabric cast shells as permanent formwork for in situ concrete construction.

### 10.6.2.3. Material use: Foundations and stability systems

In the above the foundations have not been included in the calculation of material use. However it is apparent that should it be possible to achieve an overall concrete volume saving of 40%, then the total vertical foundation load will be reduced proportionally. Depending on the ground conditions, this may allow significant reductions in the volume of concrete that is put into the ground.

Additionally, the core walls that form the stability system in this example are not included as both the prismatic and fabric formed buildings would be required to resist approximately the same horizontal (wind) loadings. Reductions may arise in the notional horizontal load requirements (as the building will have a lower mass, as mentioned

above), which could allow for further material savings, but these may be relatively small in comparison to the 40% savings available in the elements described above.

### 10.6.3. Summary

A summary of the material use savings shown above is provided in Table 10.12 on page 439, where concrete volumes only are calculated. Although significant potential for material use reductions are realised, it has been shown in §10.6.1 on page 433 that the embodied energy of the construction process must also be considered, and the application of this to a complete building structure is recommended as a topic of future consideration.

## 10.7. Conclusions

This Chapter has demonstrated that the load-deflection analysis of fabric cast beam sections can be undertaken using easily adapted and understood methods. A number of beams whose construction and testing has been the focus of this thesis have been used to verify these approaches. Opportunities for further work, including the application of the moment-rotation model, are highlighted. Such approaches will be key in allowing fabric cast elements to be designed with confidence in both their serviceability and ultimate limit state conditions.

The load-deflection prediction of fabric formed beams is equally as important as the prediction of the form of the fluid filled fabric bag, and this Chapter has demonstrated how this geometry can be modelled. Opportunities for extending the work into a more widely applicable approach are described.

Parametric studies were undertaken to show that construction tolerances in Fabric cast elements are hugely important, as small deviations in the location of a longitudinal bar can lead to large changes in element capacity. This work was then supplemented by an analysis the BS EN 1992-1-1 (2004), where it was shown that techniques for calculating the force in the truss elements can be unconservative if the additional tensile force is not properly accounted for and equilibrium satisfied.

Finally, this Chapter has shown that material savings in fabric cast construction have the potential to be highly significant - with embodied energy savings up to 15% and concrete material use savings of 40% highlighted. The potential for additional work in this area, considering not only the structural optimisation of the fabric formed beam but also the material use optimisation of the construction process, is highlighted.

In the following Chapter a design guide for fabric formed concrete beams is presented, including construction and detailing processes. Following this, Chapter 12 summarises the various areas of future work that this thesis has highlighted before final conclusions are drawn in Chapter 13.



# Chapter 11 Design guide

## Steel reinforced fabric formed beams

### 11.1. Introduction

The following Chapter sets out the design process for steel reinforced fabric formed concrete beams. An example beam design (single span element) is shown. Flexural and shear capacities are assessed using two methods described in this thesis before shape prediction techniques are demonstrated. A construction process and technique is provided based on the methods described in this thesis. The process of design is summarised in Figure 11.1 in §11.3 on page 445.

The design presented below is to intended to be undertaken with due consideration of the current relevant national standard. Design is undertaken using the partial factor method as described in BS EN 1990 (2005) cl.6. Symbols used in this Chapter are defined in §11.2.

### 11.2. Symbols

#### 11.2.1. Latin Upper Case

$A_b$	Area of longitudinal reinforcing bar ( $\text{mm}^2$ )
$a_{vx}$	The ratio ( $M_{ax}/V_{ax}$ ) (CFP)
CA	Centroidal Axis
CFP	Compressive Force Path Method
D	Section depth of fabric formed beam (external dimension, including cover) (mm)
EC2	Eurocode 2, BS EN 1992-1-1 (2004)
$E_d$	Design value of an action
$F_b$	Action - force in the longitudinal reinforcing bar (kN)
$F_{b,i}$	Action - horizontal component of force in the tensile longitudinal reinforcing bar, $i$ (kN)
$F_c$	Action - compressive force in the concrete (kN)
M	Moment (kNm)

$M_{ax}$	Bending moment at section 'x' (CFP) (kNm)
$M_{cx}$	The value of the moment corresponding to shear failure (CFP), Eq. 7.1 on page 215 (kNm)
$M_f$	Flexural capacity (CFP) (kNm)
NA	Neutral Axis
$R_d$	Design value of the member resistance
V	Shear Force (kN)
$V_{ax}$	Shear force at section 'x' (CFP) (kN)
$V_{cx}$	The value of the shear force corresponding to shear failure (CFP) (kN)
$V_f$	Shear corresponding to $M_f$ (CFP) (kN)

#### 11.2.2. Latin Lower Case

b	Top breadth of fabric formed beam
$b_1$	Web width (CFP)
d	Effective depth of a cross section
$f_{cd}$	Design strength of concrete, MPa
$f_{ck}$	Characteristic compressive cylinder strength of concrete, MPa
$f_{ck,c}$	Compressive strength of confined concrete, MPa
$f_{yk}$	Characteristic yield strength of steel reinforcement
k	Factor
s	Distance between successive vertical sections in design.
x	Neutral axis depth, Distance
y	Distance
z	Lever arm of internal forces

#### 11.2.3. Greek Lower Case

$\alpha$	Angle of inclination of the longitudinal reinforcement from the horizontal axis.
$\beta$	Angle
$\epsilon_b$	Strain in the longitudinal bar
$\epsilon_c$	Compressive strain in the concrete
$\epsilon_{c,1}$	Compressive strain in the concrete at peak stress ( $\epsilon_{c,1}$ for confined concrete)
$\epsilon_{cu}$	Ultimate compressive strain in the concrete ( $\epsilon_{cu,c}$ for confined concrete)
$\epsilon_{uk}$	Characteristic strain of reinforcement or prestressing steel at maximum load
$\gamma$	Partial factor (for permanent actions $\gamma_G$ and for variable actions, $\gamma_Q$ )
$\eta$	Effective strength factor
$\lambda$	Effective compression zone height factor
$\theta$	Angle of the compression strut
$\rho_w$	Ratio of tension steel to web concrete area
$\sigma_2$	Lateral confining pressure ( $= \sigma_3$ ) for concrete confined by spirals or closed links.

### 11.3. Process flow chart

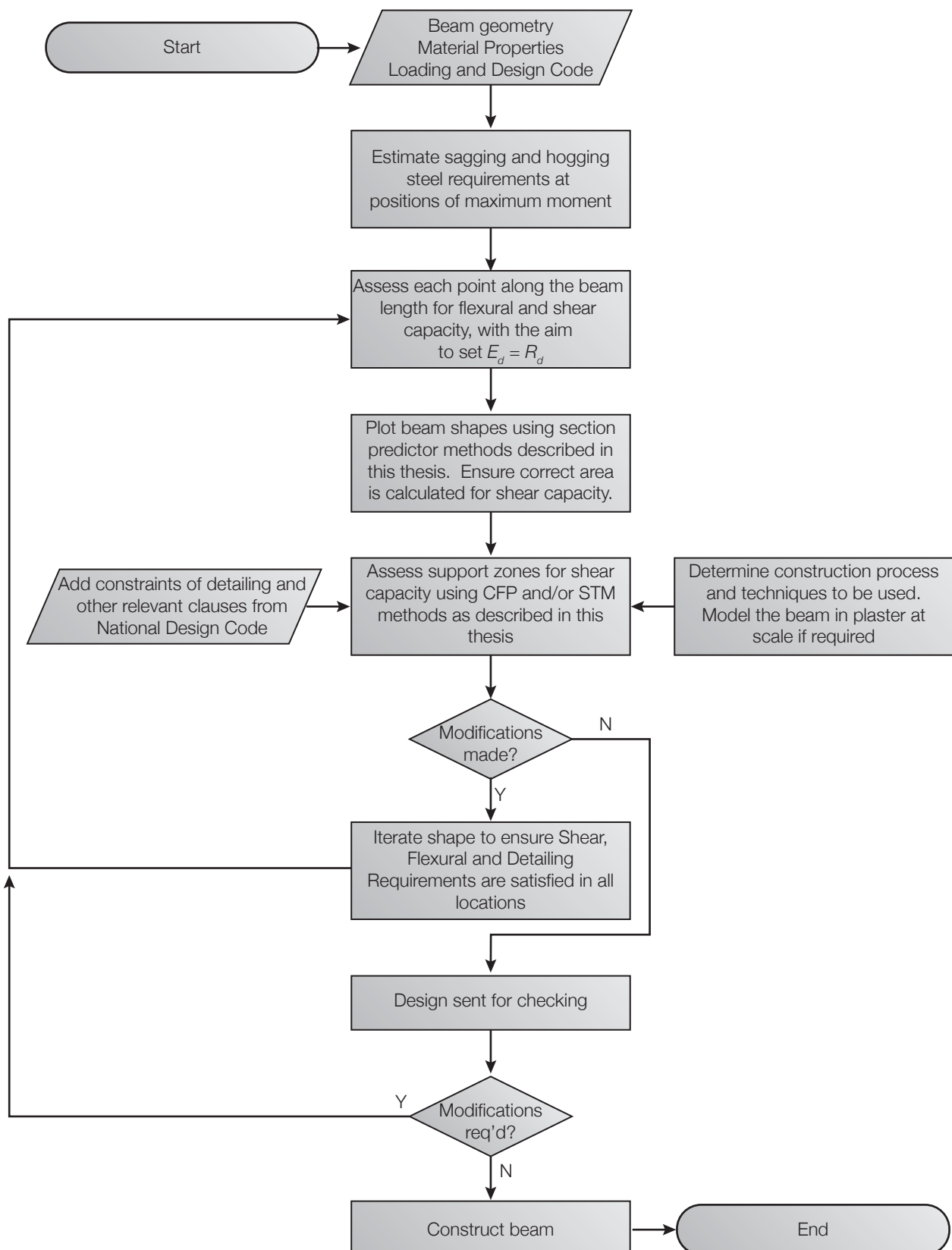


Figure 11.1: Design process flow chart summary.



### 11.3.1. Design considerations

In the design of a fabric formed beam there are a number of considerations that should be addressed throughout the design process, as listed and explained where necessary below:

#### 1. Material properties

- Fabric type, manufacturer and properties;
- Concrete type (Ordinary Portland Cement Concrete, Fibre reinforced, Ultra-high performance, low-carbon concrete) and concrete strength;
- Flexural and Transverse reinforcement type (FRP, Steel) and material properties.

#### 2. Dimensional requirements

- Beam span, support type and dimensions. Cover requirements (durability class required);

#### 3. Detailing

- Reinforcement detailing and conflicts with the fabric mould;
- Aesthetic considerations and architectural intent.

#### 4. Modelling

- Scale model using plaster and lightweight fabric; computational model of element geometry;

#### 5. Construction processes

- In-situ or precast construction;
- Quality of workmanship, and checking procedure to verify element geometry.

#### 6. Design

- Design code and appropriate standards to conform to;
- Checks on all actions acting on the element (bending, shear, torsion).

### 11.4. Sample beam design

The following section sets out the process of beam design that has been utilised throughout this thesis. It is applied to single span elements initially. Future work may consider continuous beams, which introduce new challenges including moment redistribution and areas of combined high shear and high moment at support zones.

#### 11.4.1. Span and loading envelope

The design process behind a 7m span simply supported beam is shown in the following section. A simplified loading envelope along with shear and bending moment diagrams are shown in Figure 11.2. Partial factors for the loads are taken as shown in this simple case in Table 11.1 (NA to BS EN 1990 (2002)). Plotting elastic bending moment diagrams assuming a constant value for  $EI$  is a simplification and in reality the fabric formed structure will not have a constant value of  $EI$ . The moment envelope could therefore be adjusted iteratively through the design process. The bending moment diagram must always be in equilibrium with the loads that the structure is to carry. The moment and shear envelopes for design are thus determined along the length of the beam by taking the maximum and minimum values of shear and moment at each point.

Table 11.1: Partial factors applied to loads (BS EN 1990 (2002)).

Factor	$\gamma_{G,j}$	$\gamma_{Q,1}$
Value	1.35	1.5

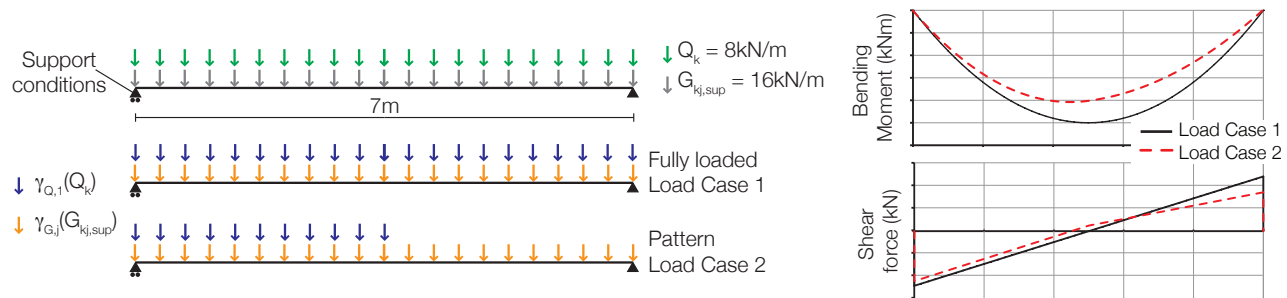


Figure 11.2: Beam layout and load envelope (l), with indicative bending and shear envelopes shown (r).

#### 11.4.2. Design to BS EN 1992-1-1 (2004)

The results of this thesis have shown that for elements loaded predominantly in shear the use of inclined tension reinforcement to provide both flexural and transverse capacity according to the provisions of BS EN 1992-1-1 (2004) can result in unconservative beam designs due to the manner in which yielding of the steel reinforcement is approached.

However, the BS EN 1992-1-1 (2004) shear design procedure for beams with transverse reinforcement that did not rely on the inclined tension reinforcement for transverse capacity was successfully applied to the design of 4m span 'T' and 'Double-T' beams under uniformly distributed loading. This method, which is part of the UK design code for concrete structures is used here in the design of an optimised fabric formed beam, before the results of the design are checked against those resulting from the use of the compressive force path method, which has

been shown in this thesis to be applicable and conservative for both uniformly distributed and point loaded beam elements. The design process using the compressive force path method is shown in §11.4.3 on page 453.

Following the general process described in Figure 11.1 the beam element may be designed in shear and flexure using BS EN 1992-1-1 (2004) in the following manner:

1. Divide the length of the beam into equally spaced strips (in this example they are 200mm apart);
2. At each location, determine from the loading envelope the maximum values of shear and bending that the section must resist;
3. Make a preliminary estimate of the longitudinal tension and compression steel requirements based on the peak moments determined from the loading envelope;
4. Using this preliminary steel layout, estimate the reinforcement lever arm based on the simplified stress block given in BS EN 1992-1-1 (2004) and reproduced in Figure 11.3 along the length of the beam for flexure only. Note that in positions of low moment very small effective depths may result, and these will be amended later in the design process;
5. Apply the shear design method given in BS EN 1992-1-1 (2004). The transverse steel spacing should not normally be less than the effective depth of the beam at that position. The value of  $\cot(\theta)$  given in BS EN 1992-1-1 (2004) may be taken provided crushing failures can be shown to be avoided. The vertical component of force in the longitudinal bars should not be used to resist shear (nor should bent up reinforcement be used) unless a full strut and tie model of the end zone of the beam, undertaken as described in Chapter 8 on page 245 of this thesis, is produced and verified;
6. The stress in the transverse steel should be considered in the support zone. Where the reinforcement is required to yield, it should be ensured that such a condition exists in the final section (as described below). A strut and tie model or design using the Compressive Force Path method may be produced to compare and verify the shear design;
7. Any transverse steel should be of sufficient length to be both fully anchored and to develop its full tensile strength, if this full tensile strength is to be relied upon for shear capacity. Minimum section depths, support widths, and detailing clauses from BS EN 1992-1-1 (2004) should be applied to the beam as necessary (Figure 11.4);
8. Anchorage and development of longitudinal flexural reinforcement should be verified such that the stress development required to satisfy the loading envelope can be achieved. Anchorage may be provided using conventional design methods, or innovative techniques such as splayed bars;

9. Based on the updated design incorporating considerations of shear forces, increased section depths are likely to be required in some positions (as noted previously). This data is then fed into the beam design for flexure. The beam capacity should then be checked along its length based on Steps 1-4 above.
10. Detailing of the beam for construction constraints (for example the inclusion of precasting joints or sockets, the use of end plates for lifting and/or support) should be included and checked for clashes with designed reinforcement (Figure 11.5 on page 450);
11. The final beam design (in elevation) is thus determined and may be plotted. Cover to the outer layer of reinforcement should be provided perpendicular to the line of the steel reinforcement (to ensure adequate cover distances) as required by BS EN 1992-1-1 (2004) and shown in Figure 11.6;
12. The beam shape in three dimensions may be plotted using the section prediction techniques described in Chapter 3 and Chapter 10 of this thesis, or by using other computational methods. A three-dimensional view of the beam should be created to ensure reinforcement clashes do not occur;
13. Visualisations of the beam using a plaster model at a suitable scale can be undertaken using a scaled fabric and timber mould to produce accurate representations of the beam geometry.

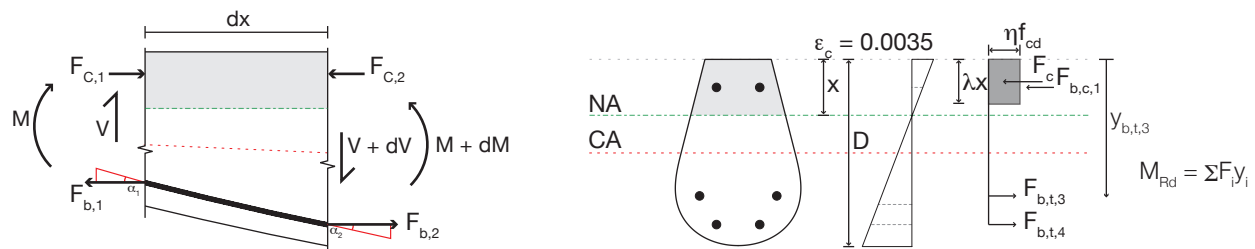


Figure 11.3: Stress strain profile for flexural capacity (note vertical component of bar is not included in shear force calculation for the BS EN 1992-1-1 method as per the recommendations found in Chapter 8 and the test results of this thesis).

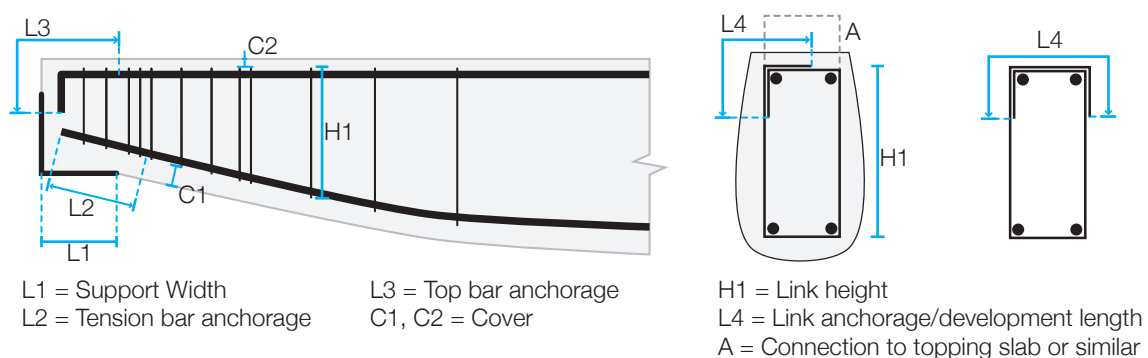


Figure 11.4: Anchorage and development lengths for flexural and transverse reinforcement.

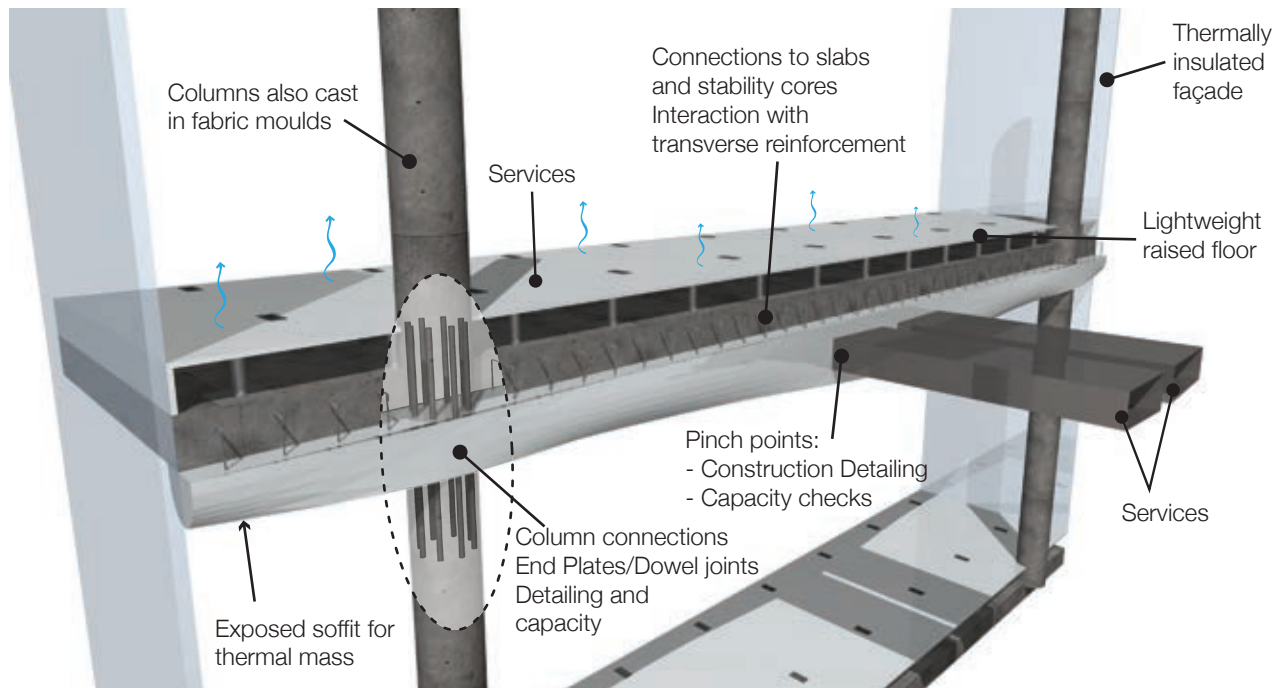


Figure 11.5: Construction joints, end zone detailing and other considerations.

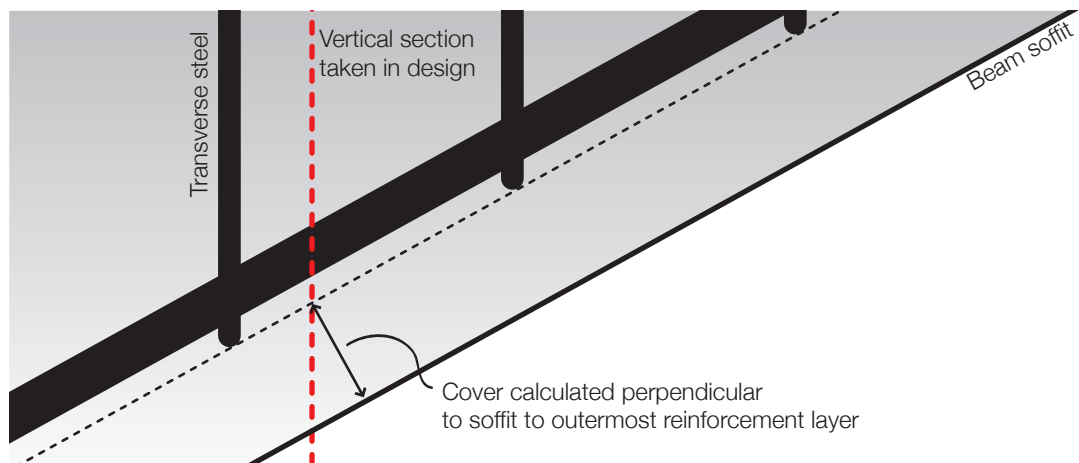


Figure 11.6: Cover requirements for longitudinal flexural reinforcement.

### 11.4.2.1. Design

Applying the requirements described above for design to BS EN 1992-1-1 (2004), a beam may be analysed and designed using a simple automated procedure in Microsoft Excel. Flexural design is undertaken by equilibrium considerations. Reinforcement layouts should be optimised for construction, which requires an iterative process to take into account the forces on the beam as it is designed.

The iterative design process will result in a changing beam profile, from one optimised only for flexure to one including full shear design and requirements of transverse and longitudinal reinforcement detailing. The reinforcement layout of the example beam was made constant throughout (as shown in Figure 11.7). The design process was then undertaken, as shown in Figure 11.8

Shown also in Figure 11.8 is a summary of the beam behaviour as realised in the design process, which illustrates how the cross-section variations react to the changing tension and compression paths along the length of the element. Such design is not only aesthetically pleasing, but illustrates the optimisation processes that have been undertaken. In the design process, assumptions of beam widths and depths must be made. Such considerations are closely linked with the construction process that is chosen for the element, as discussed in §11.7 on page 457.

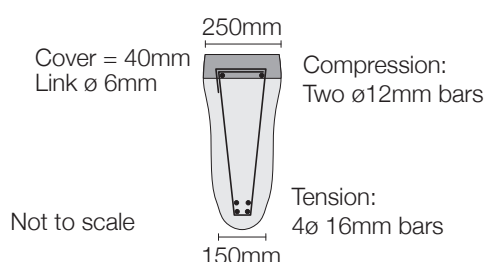


Figure 11.7: Cross section and reinforcement layouts assumed in design process.

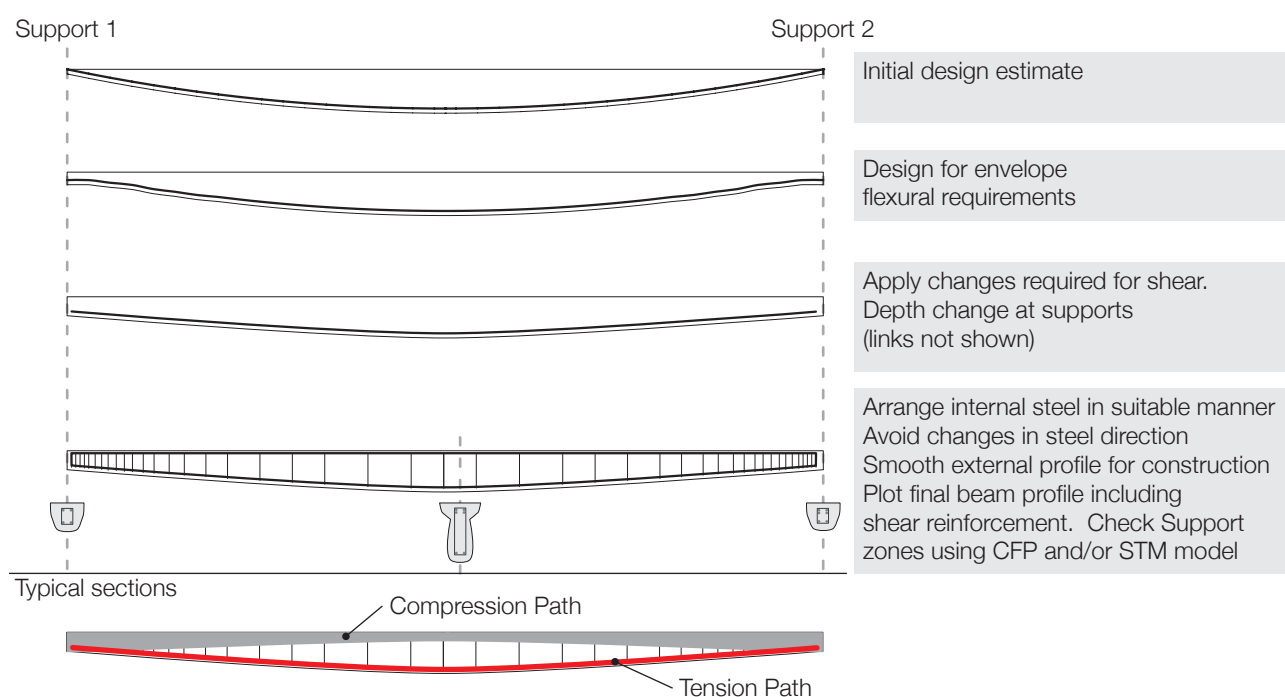


Figure 11.8: Progression of beam section design.



The process described above could be extended to a continuous beam as shown in Figure 11.9 (including hogging, sagging and support zones). Additional challenges of moment redistribution and support zone shear behaviour are highlighted previously as areas requiring further work.

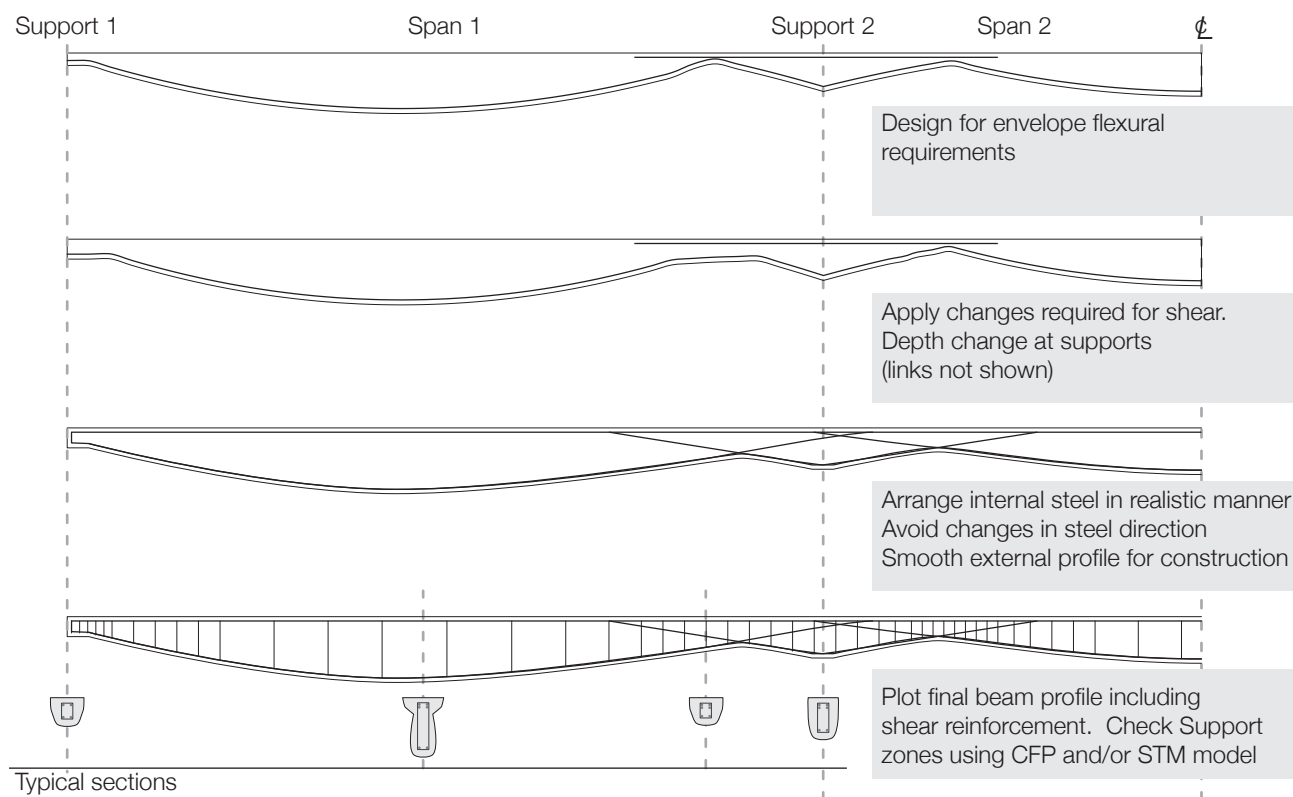


Figure 11.9: Indicative progression of beam section design for a continuous beam.

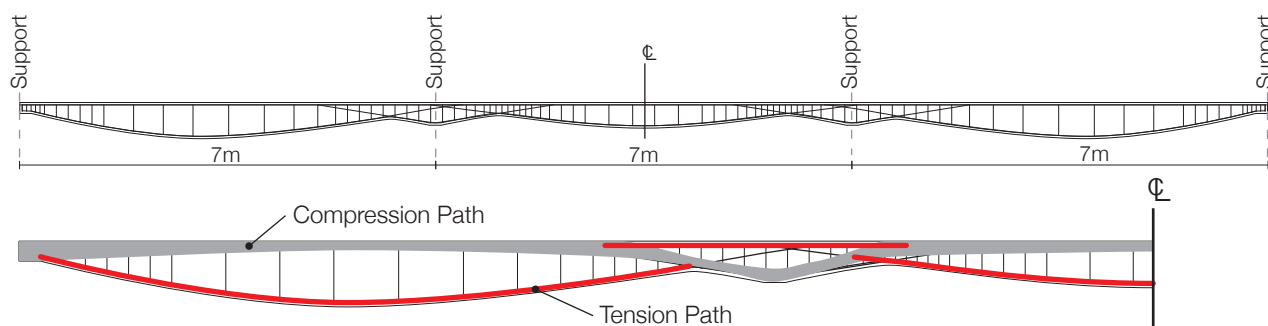


Figure 11.10: Example continuous beam design to BS EN 1992-1-1 (2004) including transverse reinforcement.

### 11.4.3. Design using the Compressive Force Path Method

It has been shown in this thesis that the compressive force path method can provide conservative designs that have a predictable failure mode. The process of design is undertaken as described below (also following the flow diagrams of Figure 11.1 and Figure 7.5 on page 222).

1. Divide the length of the beam into equally spaced strips;
2. At each location, determine from the loading envelope the maximum values of shear and bending that the section must resist;
3. Make a preliminary estimate of the longitudinal tension and compression steel requirements based on the peak moments determined from the loading envelope;
4. Using this preliminary steel layout, estimate the reinforcement lever arm based on the theory of plane sections (an initial estimation is used to guide the iterative design process and helps to avoid spurious results);
5. Calculate the value  $M_{cx}$  at each section (see §7.2.2 on page 219), from which  $V_{cx}$  is determined. If the value of  $V_{cx}$  is less than the shear force required to be carried by the load envelope, then the section depth should be amended;
6. Determine the failure mode. If the shear force corresponding to flexural failure ( $V_f$ ) is greater than the value of  $V_{cx}$  at a section then the section is denoted a 'shear failure area'. If the value of  $V_f$  is less than the value of  $V_{cx}$  then the section is denoted a 'flexural failure';
7. All areas denoted as shear failures can then be provided with transverse reinforcement such that the  $V_{cx}$  is made greater than  $V_f$ , as shown in Figure 7.5 on page 222;
8. Anchorage and development of longitudinal flexural reinforcement should be verified such that the stress development required to satisfy the loading envelope can be achieved. Anchorage may be provided using conventional design methods, or innovative techniques such as splayed bars (as described in §6.3 on page 172 of this thesis);
9. Based on the updated design incorporating considerations of  $V_{cx}$ , increased section depths are likely to be required in some positions;
10. Detailing of the beam for construction constraints (for example the inclusion of precasting joints or sockets, the use of end plates for lifting and/or support) should be included and checked for clashes with designed reinforcement (Figure 11.5);
11. The final beam design (in elevation) is thus determined and may be plotted. Cover to the outer layer of reinforcement should be provided perpendicular to the line of the steel reinforcement (to ensure adequate cover distances) as shown in Figure 11.6;

12. The beam shape in three dimensions may be plotted using the section prediction techniques described in Chapter 3 of this thesis, or by using other computational methods. A three-dimensional view of the beam should be created to ensure reinforcement clashes do not occur;
13. Visualisations of the beam using a plaster model at a suitable scale can be undertaken using a scaled fabric and timber mould to produce accurate representations of the beam geometry.

The method described above was then applied to the simply supported beam described in Figure 11.2 on page 447. An initial design (Figure 11.11(a)) shows the areas in which shear and flexural failures are predicted (note that the minimum section depth is greater than that seen in the initial design stages of BS EN 1992-1-1 (2004)). Transverse reinforcement is then added to this design such that the full flexural capacity can be attained at each section (Figure 11.11(b)), with these reinforcement layouts then being optimised for construction (Figure 11.11(c)).

Transverse reinforcement has been provided in this design only where the CFP method requires it for strength concerns, but it is recognised that in mid-span flexurally dominated areas additional links should be provided for robustness, to aid construction and to address potential surface cracking of the concrete. These additions are shown in Figure 11.11(d).

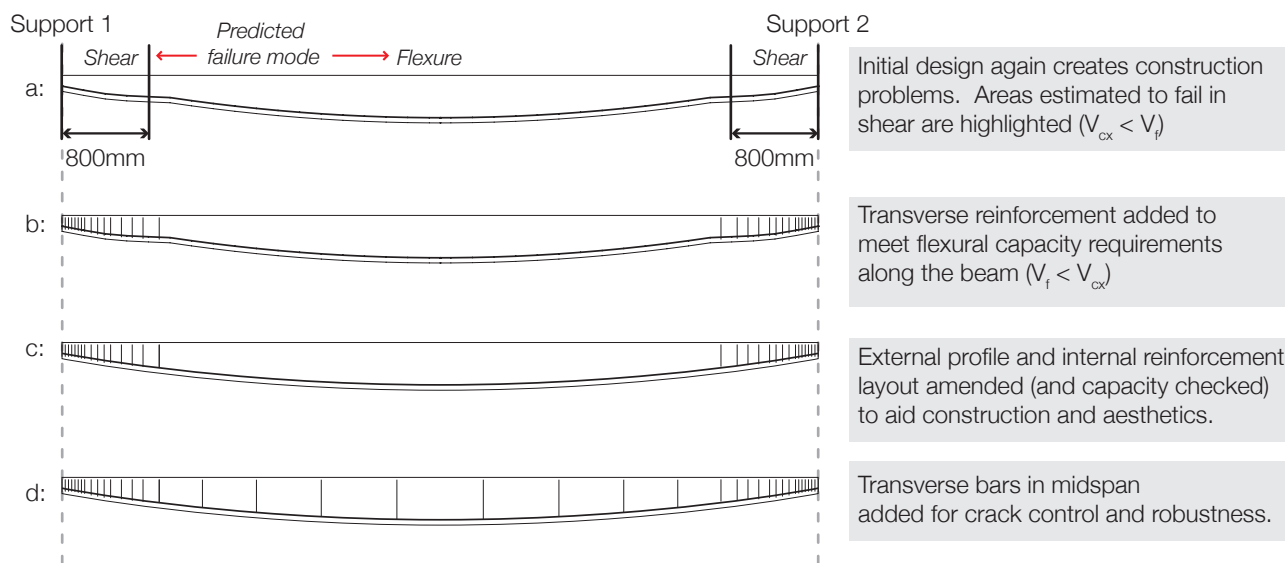


Figure 11.11: Beam designed according to the compressive force path method as described in this thesis.

#### 11.4.4. Design comparisons

The design of a simply supported beam has been provided above using both the Compressive Force Path method and the provisions of BS EN 1992-1-1 (2004). It is important in this situation to note the differences between the two method outputs, which are highlighted in Figure 11.12. From this, it is apparent that for the proposed beam design the two methods provide similar geometries but differ in their provision of transverse reinforcement. This difference is a key concern for areas of high shear forces and it is recommended that such 'disturbed' areas be the subject of further checks using strut and tie models (as described in full in §7.2.4 on page 236) to ensure that sufficient capacity is provided.

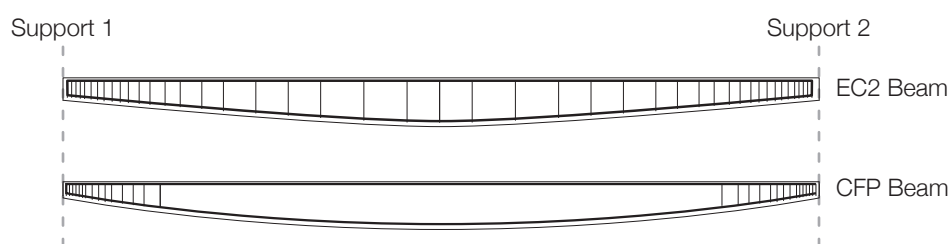


Figure 11.12: Comparison of BS EN 1992-1-1 (2004) and CFP method designs.

#### 11.4.5. Material savings

An indication of the material savings that can be achieved in the beam designed in the above sections are provided in Table 11.2. Comparing a prismatic concrete beam of the same maximum depth as the optimised section with a fabric cast beam with constant width demonstrates a material saving for the fabric cast beam of approximately 30%.

A second comparison is made between the prismatic beam and the fabric cast beam with additional 'pinch' points in the midspan to shape the cross section in areas of high moment and low shear. Such additional forming is simple, and could add 5-10% material savings for the beam as a whole.

Such results are verified by the structural testing and construction undertaken in this thesis, where average material savings of 41% were achieved (Table 6.25 on page 215).

Table 11.2: Material Savings achieved in example beam design.

Beam	Volume (m <sup>3</sup> )	Saving
Prismatic	0.477	-
Fabric formed, constant cross section	0.319	33%
Fabric formed, variable cross section	0.288	39%

### 11.5. Profile Predictions

Using the methods presented in Chapter 3, it is possible to estimate the shape of the concrete filled fabric formwork using an iterative Excel program. This was undertaken for a beam designed using the process described above as a continuous beam before the sections were then linked in a Rhino model to create the 3D image shown in Figure 11.13. Such a design is produced to be indicative of the final product, and there remains a body of work to do in completing the shape prediction software for commercial use.

Alternatively, plaster modelling at a suitable scale can provide accurate representations of the geometrical form that the full size element will have (provided the same construction process is used), and this technique has been successfully applied by researchers at the University of Manitoba on a number of occasions.



Figure 11.13: Example beam profile render in 3D.

### 11.6. Load Deflection Predictions

Methods for the prediction of a variable section concrete element's load-deflection behaviour are provided in full in Chapter 10 on page 409 and are verified against test data generated in this thesis. The prediction of concrete deflections for serviceability limit states using simple span/depth ratios should be carried out with caution for variable section elements, and simple checks using the procedures presented in Chapter 10 will help to provide accurate deflection checks.

The calculation of load-deflection behaviours in continuous beams adds a further dimension to the complexity of the analysis, and in this situation the methods given by Oehlers *et al* (2012), where the moment-rotation model is used, offer some advantages in terms of calculations.

## 11.7. Construction

The method of construction for the beam must be considered throughout the design process. In this thesis, the 'keel mould' has been used in the construction of optimised concrete beams as it provides good control over the final geometry and form. The method of construction is illustrated in §11.7.1 for completeness, before guidelines for the general design of formwork for fabric cast concrete beams are presented.

### 11.7.1. Keel Mould

The keel mould uses a piece of timber (or a metal spline) formed in the correct geometry to hold two sheets of fabric in position during casting. The mould allows the optimised geometry to be economically cast, with additional aesthetic and durability benefits being attained, as described in this thesis. In relation to the continuous beam described above, a formwork system such as that shown in Figure 11.14 may be employed, with construction proceeding as illustrated in Figure 11.15.

In this situation it is proposed to cast the element in one section close to its final construction position (i.e. casting at ground level but on the same site as the building) and lifting the entire beam over its supports. In such a way the fabric cast construction process could be used to create a fabrication facility for beams of any span and layout that are needed in a particular concrete framed building.

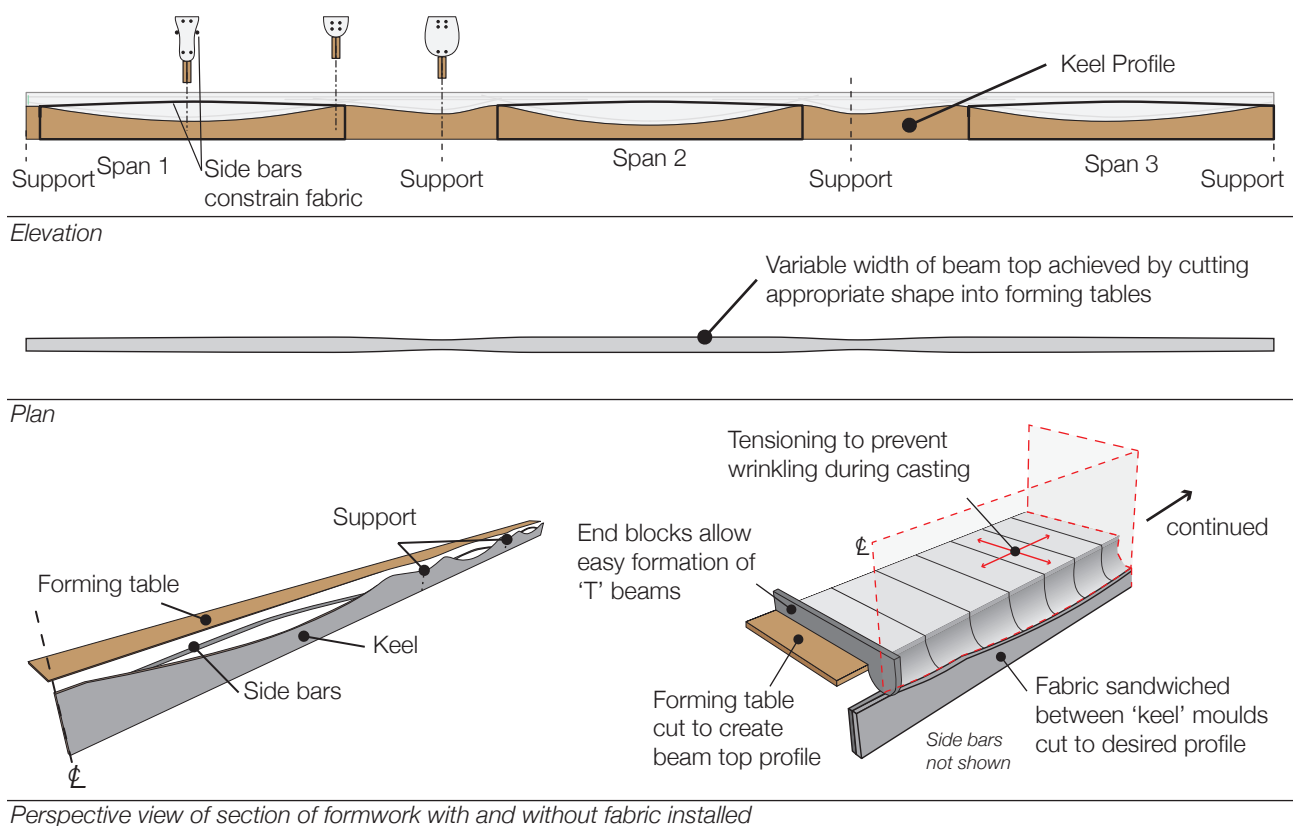


Figure 11.14: Example formwork system, shown for a continuous beam.



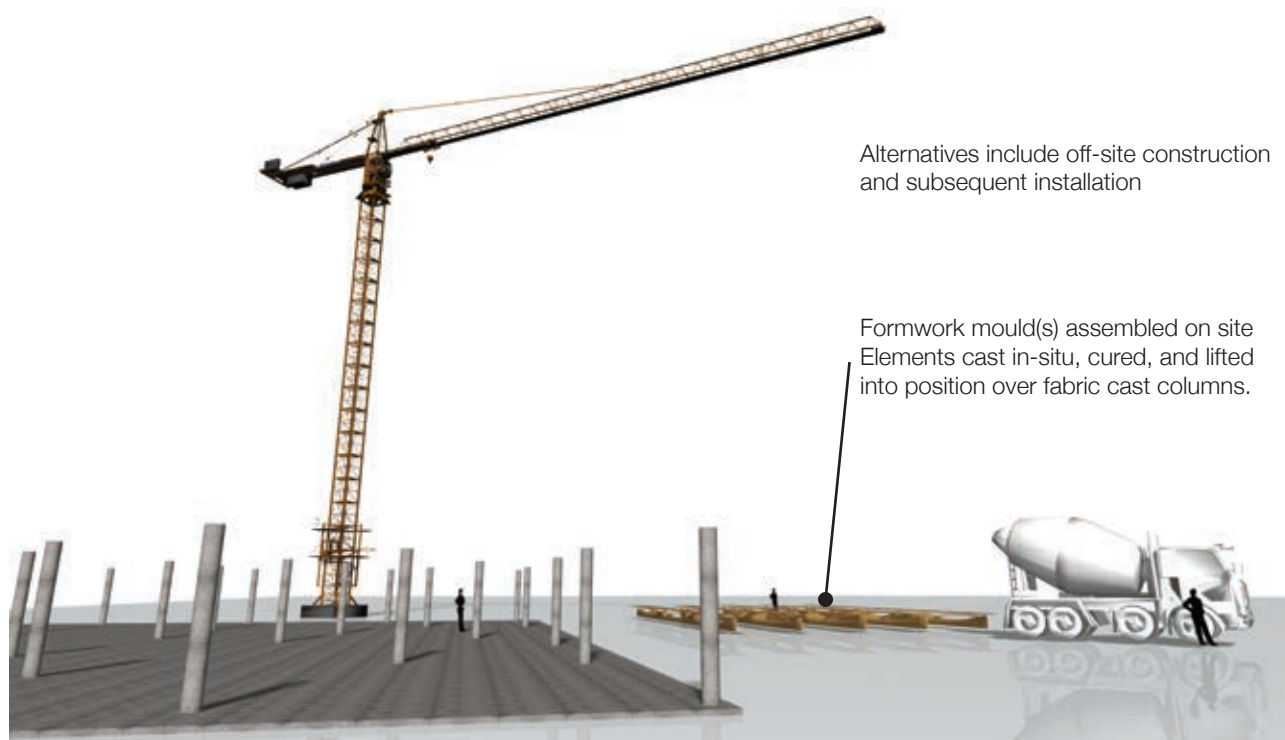


Figure 11.15: Construction process.

### 11.7.2. Formwork design

In common with the design of all formwork and falsework for concrete structures, the quality of the workmanship will greatly influence the resulting element. Skilled and experienced workers in this field are very much required. A number of areas of design must be considered for fabric cast construction, as outlined below:

#### 1. The fabric material properties

- The fabric chosen should be verified for use in concrete construction prior to first use (by casting sample elements or by reference to previous use of the fabric). This thesis has made extensive and successful use of a woven polyester fabric with the mechanical properties given in Table 9.3 on page 343.

#### 2. Fluid pressures

- Beams of modest spans, which tend to have relatively shallow depths, do not generally create very high fluid pressures in the formwork. However, where tall columns, or deep beams, or any element with a significant head of fluid concrete is to be cast, care should be taken to ensure that the fabric is able to resist the resulting fluid pressures.

#### 3. Timber falsework

- Shown in this thesis has been a system of using timber falsework to support sheets of fabric in which concrete is cast to create optimised structural elements. The timber (or steel) used to support the fabric should be verified to have sufficient capacity to not only support the weight

of wet concrete, but to not deform beyond the required tolerances for construction of the final element during the casting process. This should be checked prior to construction.

#### 4. Modelling and trial elements

- Construction of complex elements (trusses, continuous beams or non prismatic columns for example) can be aided by the construction of trial elements to verify the behaviour of both the fabric and the construction process. These may be undertaken on scale or full size prototypes.

Guidance on the design of concrete falsework and formwork does not currently include the use of fabric formwork, but documents including those by Grant and Pallet (2012) and BS 5975 (2011) set out many of the principles that must be considered for safe construction of fabric cast elements.

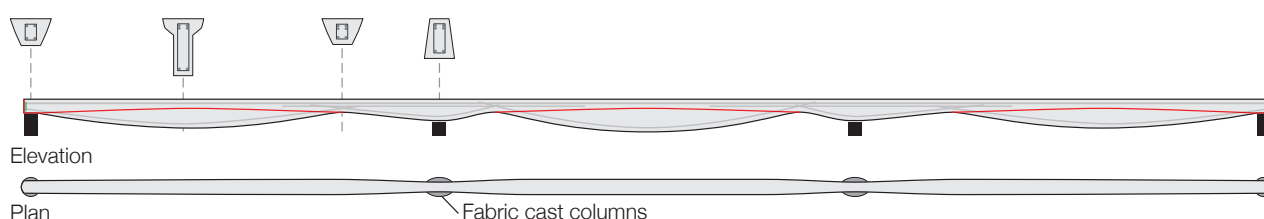


Figure 11.16: Continuous beam design and options for cross section variations.

## 11.8. Detailing considerations

### 11.8.1. Anchorage

One of the initial concerns with fabric formed elements had been the adequate anchorage of longitudinal reinforcement in sections with small end zones. Previous work had focused on using welded end plates (§2.5 on page 27) to provide anchorage. This thesis has demonstrated how looped or splayed bars may be used as an effective anchorage method. Some salient points for both methods are presented below.

#### 11.8.1.1. Loops

In the anchorage zone highlighted in Figure 11.17, the looped bar is used as described in detail in the test series presented in §8.3 on page 260. Simple design checks can be undertaken to both determine the force in a loop, and the required anchorage length of that loop to develop its capacity at the support point. An alternative method, using an 'L' bar is also possible (Figure 11.17(r)) provided there is sufficient end zone space for the anchorage.

It is recommended that a strut and tie model be used to estimate the forces in the bar. If the bar is yielding at the position from which anchorage is required, then the full capacity of the bar must be generated (calculations for this are described in BS EN 1992-1-1 (2004)). The stress  $\sigma_c$  (shown in Figure 11.17(c)) acts on the edge of the curved bar. Its action is to lead to splitting failure, which must be prevented in the concrete section (see Bruggeling and Huyghe (1991) for details).

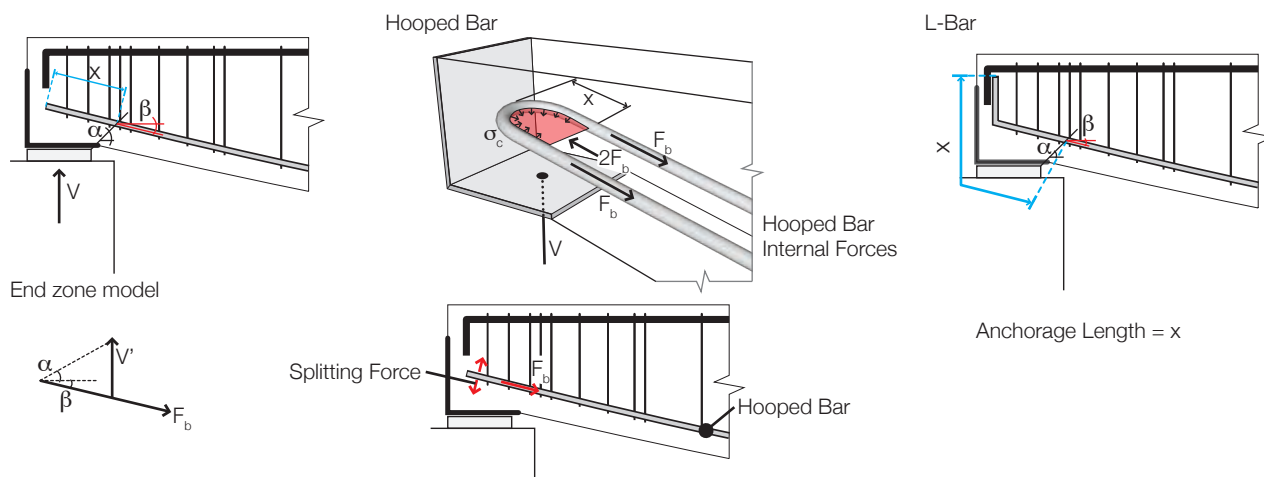


Figure 11.17: End zone of a tapered beam (l); Anchorage using a looped bar (c); Using an 'L' bar (r).

#### 11.8.1.2. Splayed bars

Through preliminary work on the use of splayed bars in concrete sections reinforced with both steel and FRP bars it was determined that the splayed bar (Figure 11.18) has the potential to provide full anchorage to longitudinal reinforcement. It is ideally used in fibre reinforced polymer bars, where local bends or welds are not a feasible construction method. The advantages and disadvantages of various anchorage methods are provided in Table 11.3.

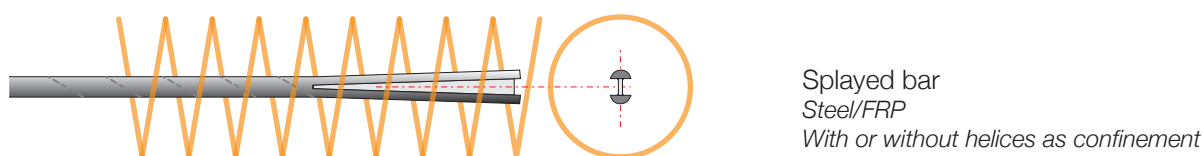


Figure 11.18: Splayed bar anchorage method for fabric formed beams.

Table 11.3: Summary of anchorage methods for fabric formed beam.

Method	Comments	Advantages	Disadvantages
Splayed bar	Use with both FRP and steel reinforcement, with or without confinement provided by steel or FRP helices.	Easy to build; Full anchorage achieved and shown to be effective in preliminary tests.	Limited test data.
Bent bars	Use with steel only.	Simple, well established design methods; Understood on site.	Requires deep end zone, may influence optimal design or be suited to larger span elements.
Welded end plates	Welded connection for steel bars only.	Easy to build; Simple, provides position for connection of elements in prefabricated construction	Requires very careful quality control to prevent brittle failure; Not suitable for site work.

### 11.8.2. Support zones

In this thesis beams with simple support conditions have been tested. Such conditions regularly occur in precast frame construction, where the elements may be supported in a number of ways. Two examples are shown in Figure 11.19.

Support zones may also be detailed as fixed connections, and here additional considerations should be made. Two examples of fixed connections, made between non-prismatic precast sections and columns are shown in Figure 11.20. Additional design guidance on such approaches is given in the literature (see for example Bruggeling and Huyghe, 1991, for many more approaches).

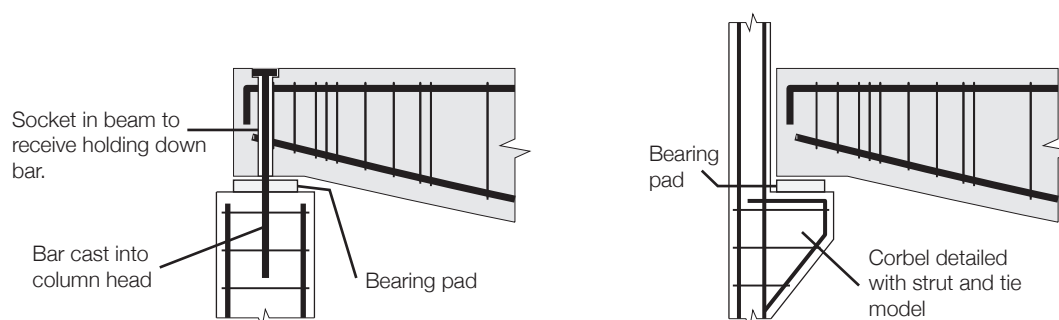


Figure 11.19: Detailing of simple supports. Column (l); Corbel (r).

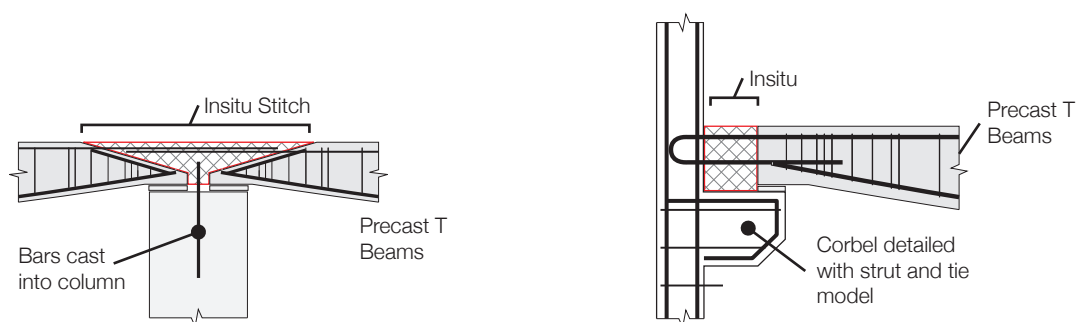


Figure 11.20: Detailing of fixed supports over a column (l); and at a corbel end (r).

### 11.8.3. Reinforcement

The positioning of longitudinal bars in a fabric formed beam is crucial to their behaviour in both flexure and shear, as was illustrated by the parametric studies presented in §10.5 on page 427. It is further important to ensure that any changes in direction of the tension reinforcement are properly considered in the design process.

This potential concern is illustrated in Figure 11.21(a), where a simply supported beam has been designed with longitudinal reinforcement whose contribution to the shear capacity of the section is disregarded. The 'ideal profile' for bending, which results in zero effective depth at the support zone, should not be used for the reasons explained in the shear behaviour analysis presented in Chapter 8, Figure 8.19 on page 256.

To ease construction, the bars may be placed along the bottom of the element, as shown in Figure 11.21(b). However, such an approach results in longitudinal reinforcement whose behaviour under loading can be to add a vertical force to the section at the end zone, as shown in Figure 11.21(c). This is clearly undesirable, and it is thus recommended that tension steel be given one curvature only, which should be such that it can only relieve the shear forces on the section if possible, as illustrated in the design example given above and in Figure 11.21(d).

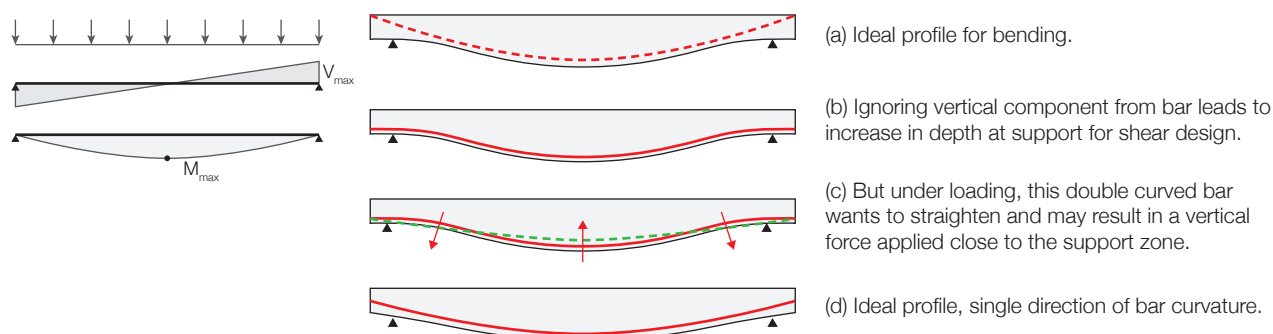


Figure 11.21: Theoretical profile of the beam (l); Additional depth at supports (c); Improved layout (r).

The practical provision of transverse reinforcement has been discussed throughout this thesis, with options including bent steel bars and fibre reinforced polymer reinforcement being explored. Detailing of the transverse reinforcement in a fabric formed structure is hugely important and sensible bar bending and arrangement schedules will be required. Although the transverse reinforcement sizes and shapes may be complicated, prefabricated reinforcement cages may provide a cost effective solution, the quality of which can be effectively monitored and assured.

## 11.9. Conclusions

Chapter 11 provides guidance for designers wishing to create efficient, fabric formed concrete beams. Within this Chapter, the knowledge developed during this thesis is summarised, with appropriate references made to relevant sections and Chapters when necessary.

The process of design has been highlighted for a simple beam, proceeding from the calculation of moment and shear envelopes, through the capacity predictions using two separate methods, to the design detailing of the steel reinforced concrete element. Consideration has been given to the load-deflection prediction of the structure, where the methods demonstrated in Chapter 10 may be applied. Construction processes that have been applied throughout this thesis are then summarised with potential site applications for fabric formwork shown. Finally, design and detailing considerations for general fabric formed construction are given.

In the following Chapter, areas of future work and investigation that have been highlighted throughout this thesis are presented in brief, before final conclusions are drawn in Chapter 13.







# Chapter 12 Future work

## Proposals

### 12.1. Introduction

This thesis has provided a significant body of practical and theoretical research in fabric formed concrete construction. Throughout the work, areas of potential future research have been highlighted, and these are now explored in the following sections before additional areas of interest for future research that have not been described previously in this thesis are described. The areas of future work are broadly split into:

1. Optimised construction;
2. Computational methods;
3. Shear behaviour;
4. Durability investigations; and
5. Extreme loading and Fire.

### 12.2. Optimised construction

#### 12.2.1. Serviceability limit states and loading conditions

The starting point for the design of a an optimised fabric formed beam is its loading condition, and these loads are generally taken from the relevant national standard. However, the early work of Mitchell and Woodgate (1970, 1971) has shown that office floor loadings often fall well below these values. These findings were reiterated in the work of Alexander (2002), who found opportunities for rationalisation of national loading standards to provide a more realistic design criteria. Note also that characteristic imposed loadings are multiplied in the load factor method to provide design loads, which are resisted by structures whose characteristic material properties

are reduced by further partial factors. A measure of the conservativeness of the initial loading condition is thus required to ensure that over design of concrete structures is avoided.

This aspect of loading is important for fabric formed structures that take their form from the loading envelope applied to them. In addition, the fabric formed element should be designed for serviceability under realistic conditions. Deflection limits should be chosen such they represent the requirements of the structure and do not impose undue stiffness requirements on the concrete elements. This area of imposed loading requirements and design conservativeness should be considered in future work.

### 12.2.2. Prestressed beams

As described throughout Chapter 6, a simple extension of the work presented in this thesis on passively reinforced beams is to consider actively reinforced beams. Prestressing and post-tensioning both offer new opportunities for material optimisation, and, importantly, can help reduce deflection to aid serviceability. Increased construction and design complexity, in addition to the uncertain use of fabric formwork in this situation, have meant that very few actively reinforced fabric cast elements have been created.

Therein lies a significant opportunity for the development of a design and construction method for uniform strength prestressed beams that save significant amounts of material, while potentially spanning greater distances than are possible with passive reinforcement.

### 12.2.3. Hollow structures

First illustrated in this thesis from the work of Miguel Fisac (Chapter 2), hollow structures provide a new means by which material can be placed only where it is required. Such structures could be both passively or actively reinforced, with forms as illustrated in principle in Figure 12.1. Future work should consider the feasibility of such elements, before the development of a design process. Hollow structures offer new methods for the routing of services and ventilation controls, and thus can utilise the full surface area of the exposed concrete.

A number of design options exist for prestressed fabric formed beams, as summarised in Figure 12.1 below. It is considered here that to fully realise the potential for UHPFRC to minimise material use, voided beams should be used if possible. The extraordinary compressive strength of Ductal® essentially means that it is irrelevant to the design process - massive prestress may potentially be applied to the section before 'compressive' failure might occur.

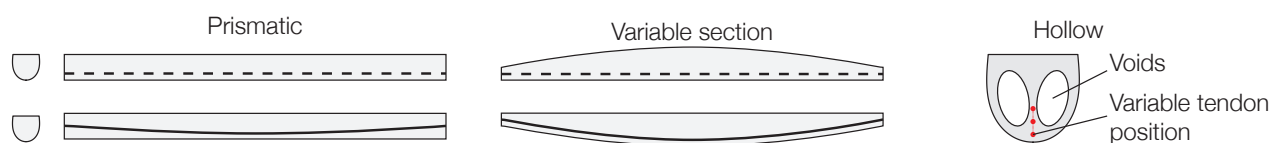


Figure 12.1: Design options for UHPFRC actively reinforced beams.

#### 12.2.4. Optimised flat slabs

This thesis has demonstrated that durable, optimised concrete beams can be designed and constructed using fabric formwork. Additional work is envisaged to continue this work in the area of floor slabs, plates and shells and might consider some of the work described and listed below.

Whilst steps have been made towards full computational approaches for beams in this thesis, there remains a great deal of work to be done in the optimisation and construction of flat slabs. Work undertaken by Bak (2012) demonstrates an excellent starting point for this work, which has subsequently been developed as a separate research topic. Taking the case of a square flat slab supported by a central column and carrying a uniformly distributed load, Bak (2012) developed a complex software package to optimise the three-dimensional structure based on strain energy limits. The optimised shape was then 'draped' with a fabric mesh, from which a cutting pattern can be created for the construction of optimised flat slabs. This work is illustrated in brief in Figure 12.2, where extracts from the computational work are shown.

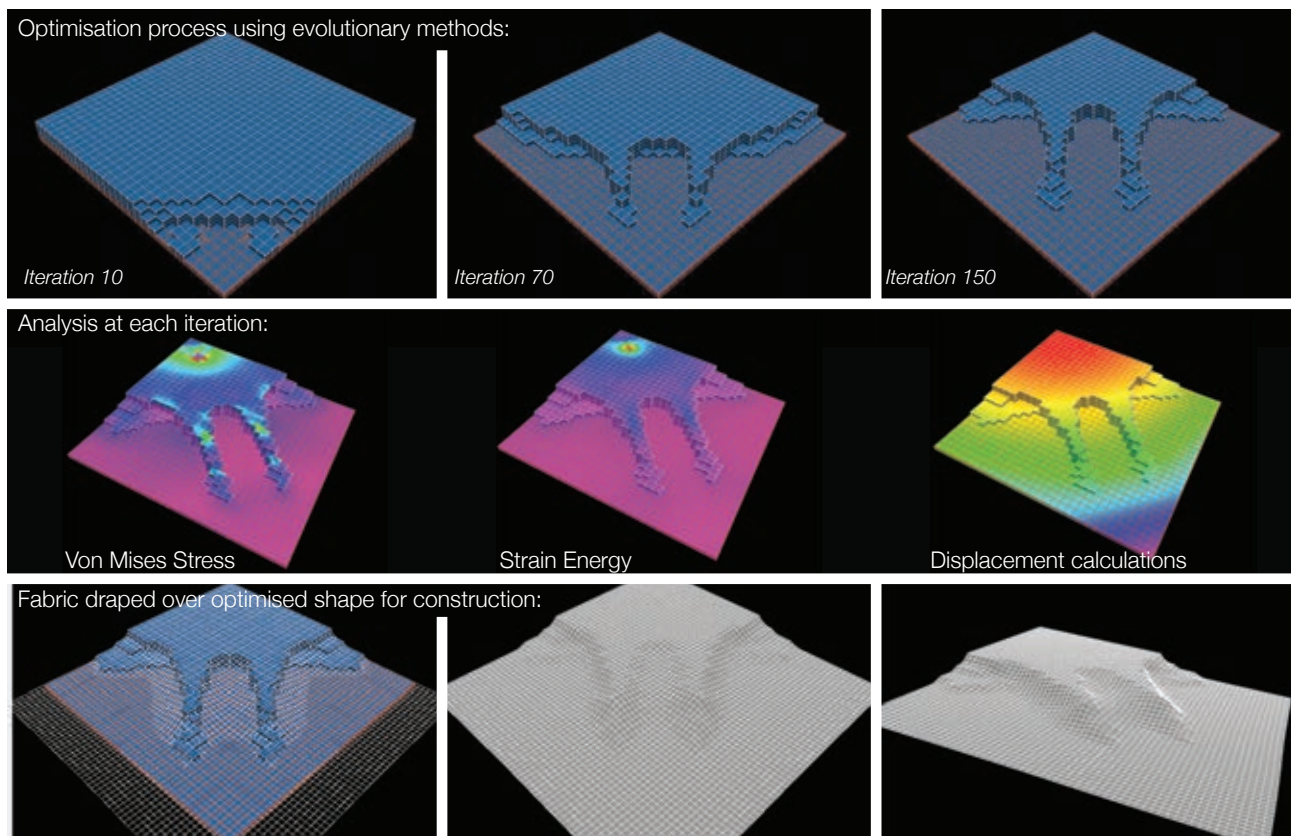


Figure 12.2: Computational optimisation of a flat slab (Bak, 2011).

### 12.2.4.1. Permanent (participating) slab formwork

Permanent, and possibly participating, formwork for flat slabs has previously been alluded to and is envisaged in use as prefabricated shell elements as formwork for a reinforced concrete slab. One of the many possible permutations of such elements is shown in Figure 12.3.

As imagined, the forms are very simple to construct - using a rectangular frame to hold a rectangular sheet of fabric at its edges. Concrete (steel fibre reinforced to carry tensile stresses during transport and limit cracking) is hand laid in a relatively thin layer over the fabric to create a hanging mould. This element may then be used directly, or can itself act as formwork for subsequent casts (to obtain multiple, identical copies of the element). The shell is then lifted into position between any form of support and reinforcement is placed in the correct positions before the concrete slab is poured. The shell is designed to carry only the concrete dead weight, and does not add reinforcement to the slab. The formwork shape may also be predicted using dynamic relaxation techniques, as shown in Figure 12.5.

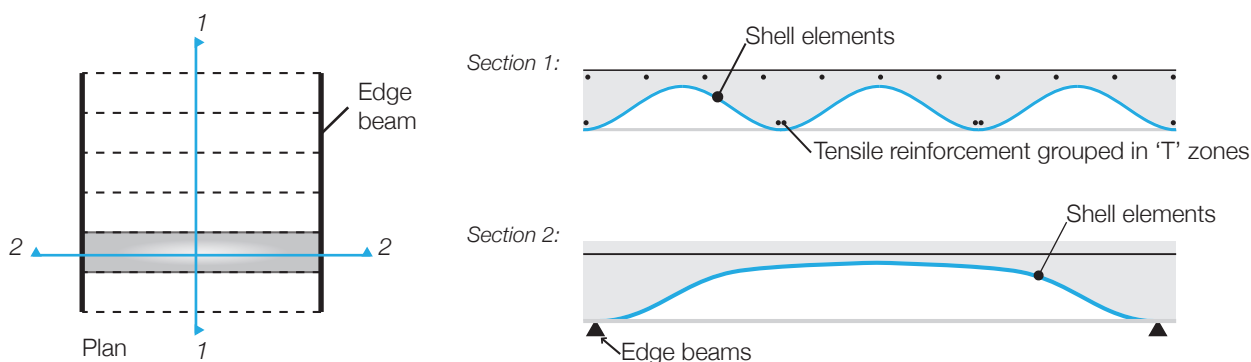


Figure 12.3: Shell formwork floor system.

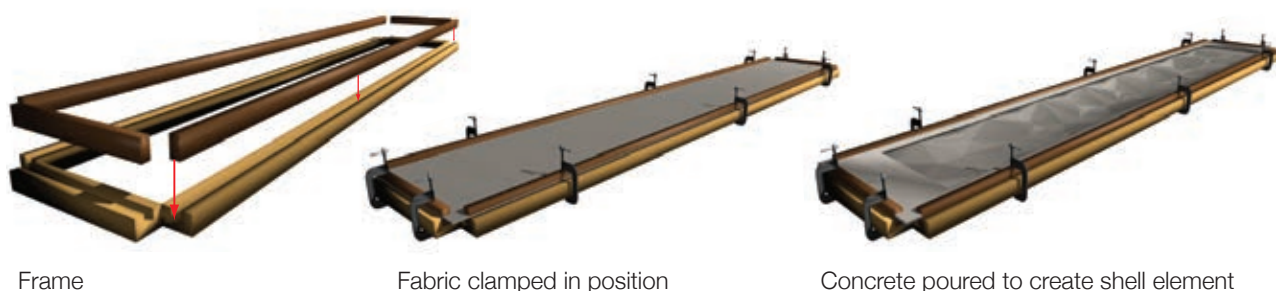


Figure 12.4: Shell formwork construction.

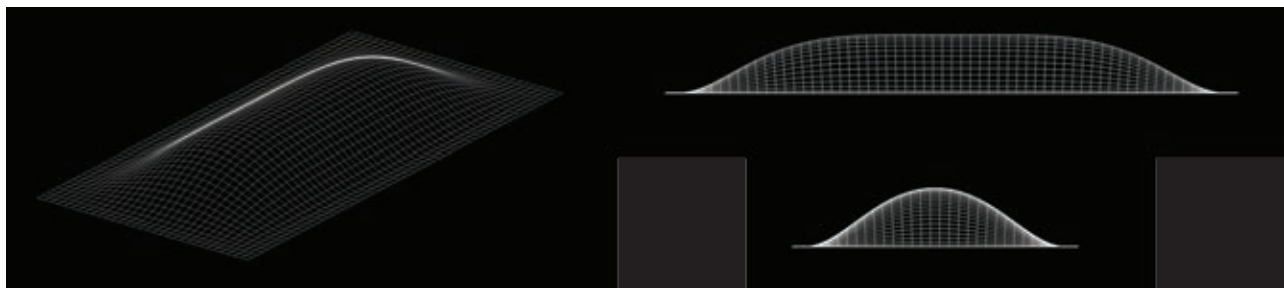


Figure 12.5: Form finding the shell using dynamic relaxation.

#### 12.2.4.2. Pole and fabric

The use of shell elements as formwork is simple and effective, although similar systems are already commercially available (Cobiax or Omnia systems, for example). An complete alternative is to use poles (shown here as standard scaffolding poles) to support a fabric sheet, into which concrete is poured to create a 'quilted' slab, as illustrated in Figure 12.6.

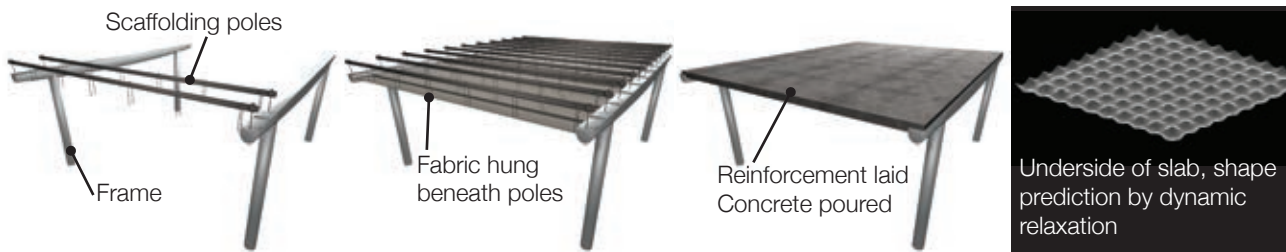


Figure 12.6: The fabric formed flat slab.

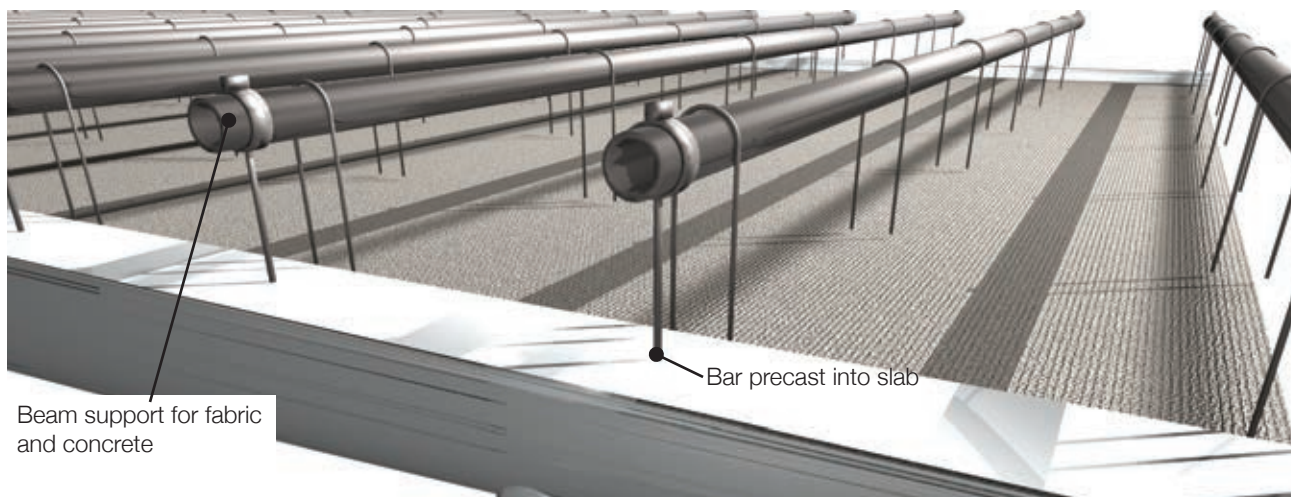


Figure 12.7: Support detail.

By supporting the poles on pre-cast bending moment shaped beams via a simple bar connection (Figure 12.7) the fabric can be supported at any point along the span, allowing for a multitude of designs. The slab has a 'quilted' underside, but crucially has a flat deck. The placement of reinforcement is more difficult, but should not be an insurmountable problem over short spans. The fabric ties could also be used to support the reinforcement, thereby ensuring its correct positioning.

The design of such a system will be guided by deflection criteria. Standard building tolerances limit slab flatness to within approximately  $\pm 5\text{mm}$ , and thus scaffolding poles ( $I_{xx} \approx 162,000\text{mm}^4$ ) would have to be closely spaced to carry the dead weight of the concrete, although any means may be used to span between supports. Dynamic relaxation may again be used to determine the shape of the hanging fabric (Figure 12.6), and the supports can be placed anywhere to create all sorts of interesting soffits.



## 12.2.5. Shell structures

The design and construction of shell structures using fabric formwork is an area that has been explored at the University of Edinburgh and the University of Manitoba, amongst others. The practical application of such techniques to the construction industry requires further work, specifically looking at how large scale optimised shell structures may be created (and not just designed) using fabric formwork. Work presented at the Second International Conference on Flexible Formwork (Orr *et al.* (Eds), 2012) has shown some interesting steps in this field.

The potential for shell and vault structures is illustrated in Figure 12.8, and work is currently being undertaken by the Author with Atkins to design a large scale shell structure in the Middle East ('Al-Akaria', Figure 12.8(r)) that may make use of fabric formwork. The use of fabric formwork on such a grand scale is a unique and exciting prospect. The design and construction of a shell could potentially make use of fabric formwork in an innovative way. One proposal is to use the fabric to create a 1:1 scale mould for the shell, over which concrete elements could be precast and then assembled on site. Already, work has been completed by the author to design shells using scale (1:300) models following techniques used by Heinz Isler, Figure 12.9. The fabric is pinned at predetermined locations to a wooden base before being coated in a light polyester resin and turned upside down. Similar methods are available using computational analysis, but the physical model is helpful in determining the desired architectural form.



Figure 12.8: Shell structures. CAST models (l) and 'Al-Akaria' shell design, courtesy Atkins UK (r).



Figure 12.9: Fabric scale model for the 'Akaria' shell.

### 12.2.6. Precast optimised frame structures

Reinforced concrete frame buildings make up a large proportion of the worldwide construction industry and the extension of fabric formed structures to this field is an exciting area of development. Figure 12.10 shows some potential designs, all of which are based on an extrapolation of the two-dimensional beam into a three-dimensional framing system.



Figure 12.10: Framing systems using fabric formwork.

The bending moment shaped beam offers an efficient method to provide a simply supported beam between column elements. This is, however, quite inflexible for design purposes and a more adaptable extended bending moment shaped beam is proposed. Here, two end cantilevers are provided to allow greater optimisation possibilities. The adjacent beams may be connected in shear, and both main and cantilever spans can be adjusted as desired. It would also be possible to divide the beam into three elements; a central span and two cantilevering pieces as shown in Figure 12.11. Using a drop in central span is sensible only on longer spans, and where the loading will be approximately constant throughout the life of the structure.



Figure 12.11: Drop in central span.



Figure 12.12: Application of double cantilevered beam to building frame.

Removing the drop in span of Figure 12.11 results in a cantilevering beam system, as shown in Figure 12.13. This method allows smaller beams to be constructed, and effectively collects bending and shear at the supports, where the deepest section is provided to resist them. The simple elevation of the beam is an advantage for construction, but equally the cantilevered nature of this design potentially requires the columns to take considerable bending during asymmetric loading on the floor above. Two designs are presented in Figure 12.13. The first is simpler to form, while the second provides a more accurate representation of the cantilevered beam's bending moment diagram. Similarly to previous designs, the use of precast shell elements is envisaged to act as permanent participating formwork for a concrete floor slab above. The cantilevered beam may also be extended to a prestressed system although there remains a potentially undesirable interaction between the beam and columns.

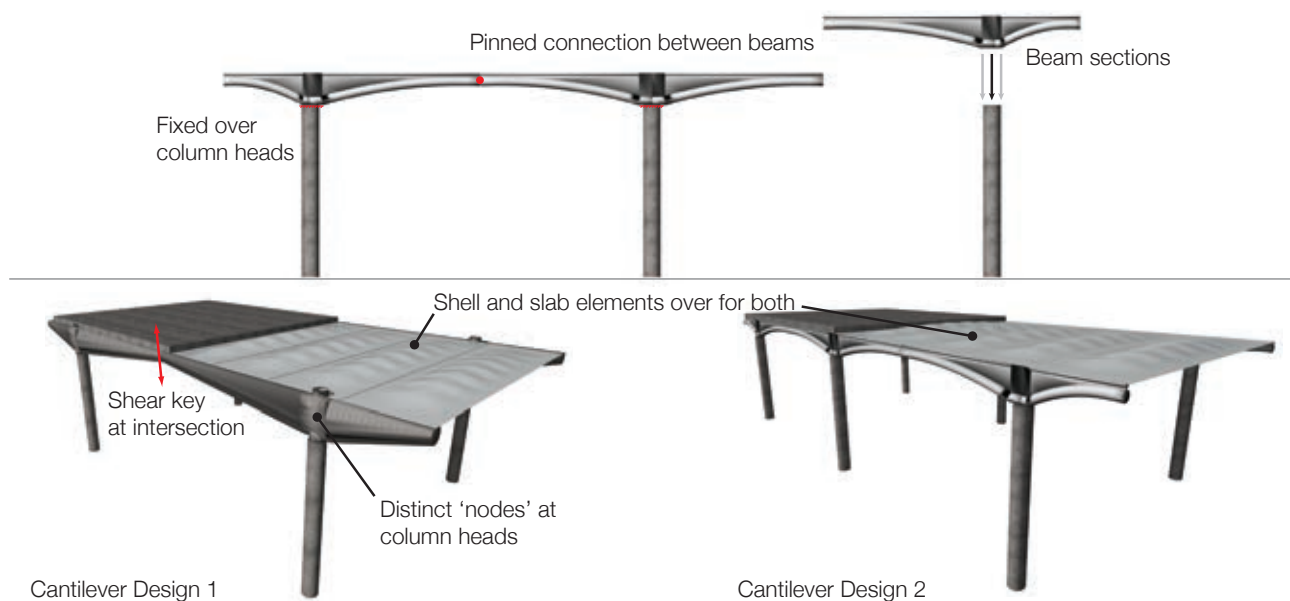


Figure 12.13: Cantilever Beam Designs.

The cantilever beam design lends itself well to use as a totally precast framing system, in which column, beam and slab (shell) elements could be assembled on site and stabilised by reinforced concrete cores, as illustrated in Figure 12.14. The downside to this design is a requirement for fixity at column locations.

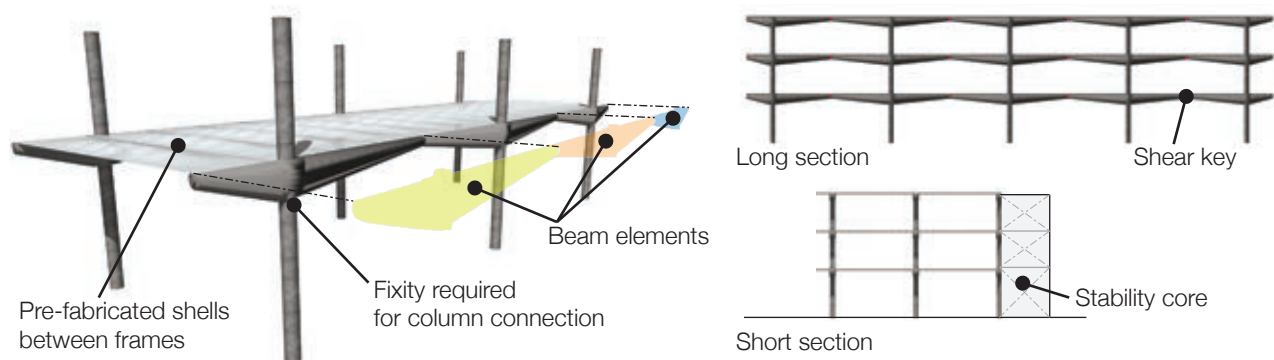


Figure 12.14: Prefabricated framing system.

### 12.2.6.1. Ultra-high performance concretes

The use of UHPFRC has been explored in this thesis in the design and construction of optimised 'T' beams. The elements offer an new opportunity to cast beams potentially without transverse reinforcement, in slender sections, offering quick production and easy pouring of complex shapes.

## 12.3. Construction processes

The construction processes presented in this thesis offer huge potential for further innovation. Future work could, for example, develop the cutting pattern and design tools required to create fabric 'socks' of the desired geometry, into which concrete is simply pumped. With the appropriate duct work, such a structure could be post-tensioned. Alternatively, new sewing techniques could be developed to allow the fabric bag to be pre-sewn with internal FRP reinforcement. In theory, such lightweight formwork could be fabricated anywhere and shipped around the world at very low cost.

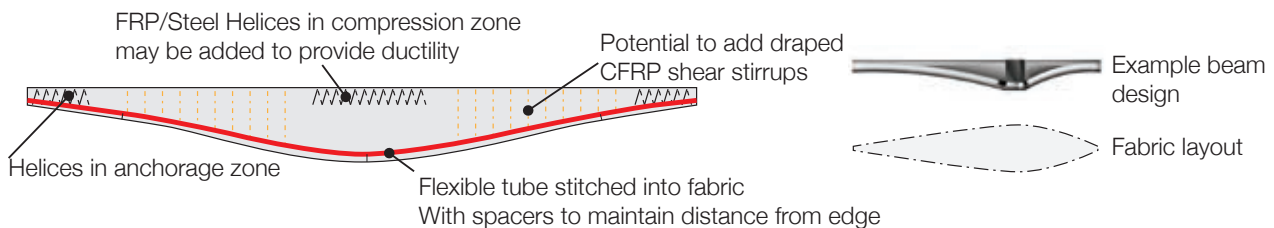


Figure 12.15: Fabric sock design principles.

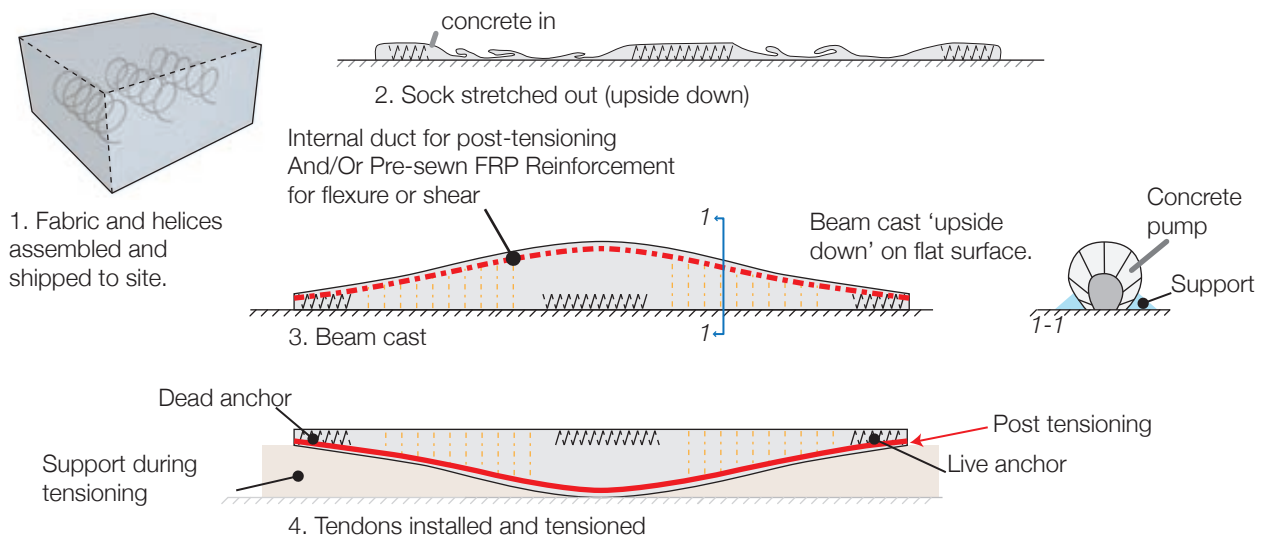


Figure 12.16: Pre-sewn fabric 'sock'.

## 12.4. Computational methods

Computational methods for fabric formed construction become increasingly important as architects and engineers begin to use the fabric formwork construction process. Although significant work has been completed in this field, encompassing shape prediction (Veenendaal (2008); Foster (2010)), design, and optimisation (Bak, 2012), future work must encompass the production of usable design tools for fabric formed construction.

Such tools should include:

1. Modelling of the fabric during casting to provide accurate construction templates for all types of concrete construction (beams, slabs and shells);
2. Modelling of the reinforced concrete section to automate the design and optimisation process;
3. Simple tools for CAD to generate fabric cast shapes as architectural models for initial scheming and design work.

In addition to the modelling of the fabric and concrete interaction, there is additional work that is required in the design and optimisation of the structure itself. In this thesis, optimisation has been undertaken using relatively simple Excel based approaches, which have provided robust, reliable and accurate results. However, such methods should now be incorporated into a widely available computer program.

In addition, the accurate modelling of the concrete itself is an area of huge potential. The work of Williams (2012) (Figure 12.17) has shown that concrete can be modelled as discrete particles using smoothed particle hydrodynamics, and this principle should be extended to include not just mass concrete elements but also steel and composite reinforced and prestressed building components. Combined with accurate modelling of the fabric behaviour, it may be possible to use the 'random fibres' to not only provide an accurate three-dimensional model of the fabric cast beam, but to also analyse its structural behaviour. Such an approach, with graphical output as shown below, would provide engineers with a simple tool to produce highly optimised and architecturally interesting concrete structures.

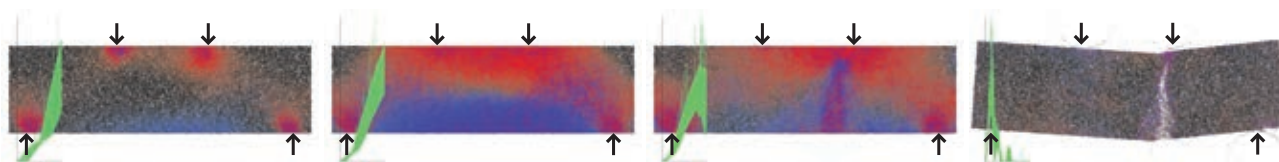


Figure 12.17: Modelling concrete using random fibres (increasing load left-right, blue showing tension, red compression) (after Williams, 2012).

## 12.5. Shear behaviour

The work presented in this thesis has shown that the shear behaviour of tapered non-prismatic steel reinforced concrete beams can be predicted with accuracy, provided a number of key considerations are taken into account. Future work should now look to address:

1. The behaviour of continuous and fixed-end beams, moving on from the assumption of simply supported end conditions of this thesis;
2. How sections with non-conventional reinforcement can be used to provide shear resistance (including the use of transverse FRP and steel- or plastic-fibre reinforced concretes);
3. Where the optimisation of flat slabs is undertaken, work is required to address how these structures behave in shear, especially around column heads;
4. A computational model (for example using random fibres as described in §12.4) of the shear behaviour of concrete in both prismatic and non-prismatic sections that is verified against test data.

## 12.6. Durability investigations

Chapter 9 on page 343 has shown that fabric cast concrete offers excellent opportunities for the creation of highly durable concrete structures. Throughout the Chapter, areas of required future work were highlighted, which are presented in brief below:

1. Work is required to accurately correlate accelerated carbonation test data to atmospheric conditions;
2. Chloride ingress testing on samples exposed to cyclically wet-dry conditions are required to verify the improvements in resistance to chloride ingress;
3. Simultaneous testing of samples exposed to chloride and carbonation to determine the combined effect of the two processes;
4. Surface hardness testing on large fabric cast panels or structural elements to address the current lack of testing on large specimens and to confirm the durability advantages seen in this thesis on small elements;
5. Determine to what extent shrinkage of the concrete is affected by the loss of water in the surface zone during the curing process when permeable moulds are used;
6. Determine the water/cement ratio in the surface zone of fabric cast concrete by direct measurement techniques;
7. Optimise the fabric weave and design to provide the best means of improving durability in fabric cast concrete, and quantify the optimum pore size for both woven and non-woven fabrics.



## 12.7. Fire

### 12.7.1. Introduction

Research has demonstrated that when exposed to fire, rapid changes in temperature in a concrete element can cause an increase in internal water pressure that can lead to spalling (Sullivan, 2001). Such spalling events can lead to considerable damage, such as that shown in Figure 12.18. It has been found that such effects are magnified in high performance concretes, which retain moisture inside the concrete due to their low permeability, combined with a dense cement paste that can restrict the movement of trapped water during heating, leading to high internal pressures and explosive spalling (Liu *et al.*, 2008).



Figure 12.18: Left: Spalling after the Channel Tunnel Fire, 1996 (Smith and Atkinson, 2010); Right: Fire damage during construction (Ingham, 2009).

### 12.7.2. Application to fabric formwork

It has been shown in Chapter 9 on page 343 that concrete cast into a fabric mould can have a reduced permeability when compared to ordinary Portland cement concretes. Whilst water is found to be removed from the surface of the fabric cast concrete, its reduced permeability may preclude the escape of water within the concrete element under fire conditions. It is therefore possible that the reduced permeability and other effects that provide fabric cast concrete with excellent durability characteristics may also make it susceptible to explosive spalling during fire, in a similar manner as is seen in High Performance Concrete (HPC).



Figure 12.19: Protecting concrete from explosive spalling using polypropylene microfibres (Shuttleworth, 2001, cited by Smith and Atkinson, 2010).

Solutions to explosive spalling in HPC have been demonstrated through the inclusion of polypropylene fibres within the concrete mix (Sullivan, 2001; Anderburg, 1997; Bentz, 2000a) (Figure 12.19). A common explanation is that the fibres are able to release the build up of steam pressure, but the mechanisms by which such fibres can prevent explosive spalling are still not fully understood and theories remain contentious (Heo *et al.*, 2012).

Given the potential for significant structural damage during fire events, it is proposed that further work should be undertaken to investigate the extent to which fabric cast concrete using ordinary Portland cements becomes susceptible to increased fire damage. The work should consider how the fabric used influences the concrete fire behaviour, and how the inclusion of synthetic fibres may be used to achieve resistance to such effects.

Fire design is often cited as a potential risk for fabric formed concrete structures. It is, however, simply a new load case for which the structure should be optimised, following the methods that have been presented in this thesis. Adding thermal stresses to the capacity requirements of a fabric formed beam could therefore quite easily be included in current design and optimisation processes. New challenges and research opportunities do arise, however, in the potential use of permanent participating fabric formwork systems.

## **12.8. Conclusions**

Chapter 12 has demonstrated that whilst this thesis has provided a significant body of test data, analysis and theoretical development, there remains a great deal of future work to be undertaken in this field to move fabric formwork into mainstream construction. The promulgation of such developments, especially those providing simple to use computational design tools, will be instrumental in the future success of this research area.



# Chapter 13 Conclusions

## Flexibly formed concrete structures

### **13.1. Introduction**

This work set out to progress our understanding in three aspects of fabric formed reinforced concrete beams - their structural behaviour, their long-term durability and the analytical methods required to design and subsequently build them. All three of these have been answered comprehensively in the course of this dissertation, which together supports the central thesis that fabric formwork can facilitate a sustainable future in concrete construction through the creation of optimised, durable, architecturally interesting concrete structures.

Fabric formwork is a growing field of research, design and construction, as shown in Chapter 2. Significant contributions to the field continue to be made, and huge scope for improvements in the way concrete is used as a structural material remain, both for architects and engineers. This dissertation has not set out to address every feasible aspect of flexible formwork for concrete structures, and acknowledges that there exist areas requiring further work, many of which are highlighted in Chapter 12.

In the following sections conclusions from the body of this dissertation are presented in brief, providing a summary of the detailed analysis and conclusions that have been drawn in each of the Chapters.

## 13.2. Structural behaviour

Design and optimisation processes presented in Chapter 5, Chapter 6, Chapter 7 and Chapter 8 have shown that optimised structures cast using fabric formwork can be readily achieved, with design and optimisation methods provided for both flexural and shear behaviour. A summary of the key conclusions made throughout each of these Chapters is given below.

1. Optimisation processes based on a sectional approach considering shear and flexural behaviour can provide a rapid means to design optimised concrete structures. The behaviour of the end zones must consider the combined effects of flexure and shear, and small variations in support depth can make the difference between shear and flexural failure modes (§8.2.5 on page 256);
2. Flexural design procedures in which plane sections remain plane appear to be valid in the range of 'T' and 'Double T' beam geometries tested within this dissertation. Accurate predictions of the flexural capacity of both 'T' and 'Double T' beams have been made using the procedures described in Chapter 10;
3. Through the design process described in Chapter 5, the flexural behaviour of optimised 'T' and 'Double T' beams cast in a fabric mould can be controlled such that ductility prior to failure is recorded, a crucial requirement;
4. The contribution of inclined steel acting primarily as flexural reinforcement in tension to the shear capacity of the optimised section should be limited (see §8.2 on page 246);
5. The shear behaviour of tapered sections, previously a topic of concern for designers, has been addressed for the case of non-prismatic fabric formed sections, and the use of either the compressive force path method or a modified strut and tie based approach have been shown to provide an appropriate and conservative design method for variable cross section steel reinforced concrete beams;
6. The behaviour of the compression path is crucially important when designing for shear behaviour. This is shown in the use of the compressive force path method for shear design;
7. During the design and optimisation process, flexure and shear forces acting on a section must be considered together, as the 'utilisation' (in shear and flexure) of each section may be high if an efficient design is to be realised. Methods to achieve this are described in Chapter 5 and Chapter 8. In addition, a distinction between areas of high shear and areas dominated by bending may be made to aid the design process, this distinction being analogous to the 'beam' and 'disturbed' regions of some existing design models;
8. The design of tapered beams using the provisions of BS EN 1992-1-1 (2004) is shown to be potentially unconservative in some situations. Close attention to the state of stress in the end zone of the beam must be paid to ensure that premature shear failures do not occur in the concrete section (as described

in §8.5.5 on page 319). The results of shear tests on tapered beams show that the EC2 model presented in Chapter 5 may be unable to model the behaviour of tapered beams. Whilst it is based on plastic theory, in which the steel is yielding to provide ductility, the actual behaviour of the beams in the end regions as recorded in the tests does not correlate to the predictions of the design model. The implications of this are explored in §8.5.6 on page 327;

9. In the design of optimised sections in shear, assumptions of plastic behaviour can lead to unconservative designs. Where the steel is assumed in the design process to be yielding, but is not able to in the built section, this can result in premature failures, as shown in §8.5 on page 301;
10. The compressive force path method has been demonstrated as an effective means by which the division between shear and flexural type failures can be determined, and its application to the range of tapering beam geometries tested in this dissertation has been demonstrated in Chapter 8;
11. Digital image correlation techniques have been used to demonstrate how the strain distribution in tapered sections is altered through the use of the various design methods. The avoidance of peak strains at the support zone is key to preventing brittle shear failures;
12. Draped reinforcement in the form of fibre reinforced polymer grids has been shown to be effective in providing shear capacity to the section (§8.6 on page 330);
13. Splayed bars acting as anchorage devices for both steel and fibre reinforced polymer reinforcement are effective in non-prismatic beam elements and may be used to provide an anchorage method in sections with shallow support zones;
14. The use of ultra-high performance fibre reinforced concrete (UHPFRC) as an alternative to ordinary Portland cement concretes has been shown to be effective. Fabric formwork provides a suitable means by which structures using ultra high performance concrete can be cast in slender and/or shallow sections to capitalise on the unique properties of such materials;
15. The prediction of the load capacity of UHPFRC fabric formed elements has been demonstrated in Chapter 10. Ultra-high performance fibre reinforced concrete can successfully be used in fabric formed elements, and its use should now be extended to panels, slabs and shells for full effect;
16. Construction tolerances are shown in Chapter 10 to be of crucial importance in the end zones, and construction processes and supervision should reflect this;
17. Overall material savings of between 30% and 40% could readily be achieved in concrete construction by undertaking simple optimisation processes and using fabric formwork as the construction method.



### 13.3. Durability

In light of the holistic approach to fabric formwork that has been taken throughout this dissertation, and to demonstrate that a sustainable future for concrete construction means not only reductions in material use at the point of design but also the provision of durable concrete structures that will remain serviceable throughout their design life, a considerable program of accelerated durability testing was undertaken in this dissertation. It has been demonstrated that significant improvements in the life-cycle durability of fabric cast concrete can be achieved, adding additional weight to the central thesis that fabric formwork can provide a sustainable future for concrete construction. The key conclusions are summarised below:

1. Fifty-percent reductions in carbonation depth over an accelerated testing period have been recorded;
2. Fifty-percent improvements in resistance to chloride ingress have been recorded;
3. Improvements in surface hardness of up to 13% were recorded;
4. The durability improvements demonstrated in Chapter 9 demonstrate that, in addition to Carbon savings achieved as a result of structural optimisation, casting concrete into fabric formwork can result in a more durable surface finish than an equivalent concrete cast into an impermeable mould. Such improvements in durability offer additional opportunities for reductions in embodied carbon;
5. Sorptivity test data suggests that whilst fabric cast concrete has fewer large pores and thus a lower initial absorption rate than concrete cast against an impermeable surface, the presence of smaller pores on the surface ensure water uptake remains an important process. This then suggests that there are proportionally more small pores in the fabric cast concrete as a ratio of large to small pores, and hence the long term sorptivity values were found to be similar in both concrete finishes;
6. Faced with environmental effects, fabric cast concrete shows a number of advantages. A harder finish is combined with a surface free from voids and blow holes to give a high quality visual finish. Significant improvements in resistance to both carbonation and chloride ingress further retard potential corrosion processes, and improve the durability of fabric cast concrete structures.

This web of durability advantages seen in fabric formed concrete are illustrated in full in Figure 9.60 on page 406.

### 13.4. Analysis

Chapter 10 provided a further body of work to support the use of fabric formed concrete construction. Methods for the prediction of both cross-sectional geometries and load-deflection behaviour of non-prismatic structures were presented. Material use analysis of the fabric formed elements presented in this dissertation are also shown, and new benefits in terms of material costs were found. In conclusion:

1. Techniques for the load-deflection prediction of non-prismatic elements are demonstrated, with iterative procedures used to calculate the behaviour of both ordinary Portland cement concrete and Ultra-High performance fibre reinforced concrete beams (Chapter 10);
2. Whilst fabric formed optimised elements can save significant volumes of concrete, it is important to consider also the embodied energy of the construction process that made the element. It is seen that the timber formwork used to hold the fabric may account for a significant proportion of the embodied energy of the construction process;
3. Theoretical investigations of this work as applied to complete building systems suggest large material savings, of a magnitude approximately equal to that shown in this dissertation for fabric formed beams (35-40%), may be possible. It is shown that flat slabs use a significant proportion of the concrete in a typical framed structure and these are therefore highlighted as areas that require significant future work and offer significant potential for reducing the embodied carbon of our new concrete structures;
4. Advantages in alternative analysis methods for the load-deflection and behaviour predictions of complex concrete structures (for example in the use of moment-rotation approaches) are shown, and the application of these to fabric formed concrete structures is highlighted;
5. Accurate load-deflection predictions were shown alongside generally good estimations of the final failure mode of the optimised concrete elements. Areas of future work required in this field were discussed in Chapter 12.

The work undertaken in this dissertation has shown that it is possible to accurately determine the structural behaviour and failure modes in both shear and flexure of highly optimised cross sections. This is a step forwards from previous work and provides the foundations for the creation of design guidelines for fabric cast members that are presented in Chapter 11.

### **13.5. Conclusion**

This Chapter has summarised the primary conclusions drawn throughout this dissertation and has shown again the advantages of flexible formwork as a construction process, design philosophy and architectural language.

In this dissertation it is shown that fabric formwork presents a viable alternative to conventional construction methods for reinforced concrete that can provide structurally optimised, architecturally interesting designs. The thesis that fabric formwork can facilitate a sustainable future in concrete construction has been advanced, challenged, and demonstrated in this dissertation through an extensive program of design, testing, and analysis.

[blank page]



# References

## A

- Abdelgader, H. S. and El-Baden, A. S. 2009. Compressive strength of concrete cast in fabric forms. *In: SBEIDCO - 1st International conference on sustainable built environment infrastructures in developing countries*, Oct.12-14 2009, Oran, Algeria.
- Abel, C., 2004. *Architecture, Technology and Progress*, London: Elsevier.
- Abramowitz, M. and Stegun, I. A., 2002. *Handbook of Mathematical Functions with Formulas, Graphs, and Mathematical Tables*.: U.S. Department of Commerce.
- Abrams, D. 1918. *Design of Concrete Mixtures. Bulletin 1*. Chicago: Structural Materials Research Laboratory, Lewis Institute.
- ACI 318: 1977, *Building Code Requirements for Structural Concrete and Commentary*. ACI.
- ACI 309: 1981, *Behaviour of fresh concrete during vibration*. ACI.
- ACI 318: 1989, *Building Code Requirements for Structural Concrete and Commentary*. ACI.
- ACI 318: 2005, *Building Code Requirements for Structural Concrete and Commentary*. ACI.
- ACI 440: 2006, *Fiber Reinforced Polymer Reinforcement: Guide for the Design and Construction of Structural Concrete Reinforced with FRP Bars*. ACI.
- Adrian, R. J., 1991. Particle imaging techniques for experimental fluid-mechanics. *Annual review of fluid mechanics*, 23, 261-304.
- AFGC, 2002. Bétons fibrés à ultra-hautes performances (Ultra High Performance Fibre-Reinforced Concretes): 2002, *Recommandations provisoires (Interim Recommendations)*. AFGC.
- Aldy, J. E., Orszag, P. R. and Stiglitz, J. E. 2001. Climate Change: An Agenda for Global Collective Action. *In: The Timing of Climate Change Policies*, 10-12 October 2001, Arlington, VA.
- Alexander, S. J., 2002. Imposed floor loading for offices: a re-appraisal. *The Structural Engineer*, 80.
- Allen, E., Zalewski, W. and Group, B. S., 2010. *Form and forces. Designing efficient, expressive structures*, Hoboken, NJ: John Wiley and Sons Inc.
- Anderberg, Y. 1997. Spalling Phenomena of HPC and OC. *In: NIST Workshop of Fire Performance of High Strength Concrete*, February 13-14, 1997, Gaithersburg. Gaithersburg: NIST.
- Ando, N., Matsukawa, H., Hattori, A. and Mashima, A. 1997. Experimental Studies on the Long-term Tensile properties of FRP Tendons. *In: Proceedings of the Third International Symposium on Non-Metallic (FRP) Reinforcement for Concrete Structures (FRPRCS-3)*, Sapporo, Japan. Tokyo: Japan Concrete Institute, 203-210.
- ASTM D123: 1994, *Standard Terminology Relating to Textiles*. ASTM: West Conshohocken, PA.



ASTM C1585: 2004, *Standard Test Method for Measurement of Rate of Absorption of Water by Hydraulic-Cement Concretes*. ASTM: West Conshohocken, PA.

## B

Bailiss, J., 2006. *Fabric-formed concrete beams: Design and analysis*. MEng Thesis, University of Bath.

Bak, A., Shepherd, P. and Richens, P. 2012. Intuitive interactive form finding of optimised fabric-cast concrete. In: Orr, J. J., et al., eds. *Second International Conference on Flexible Formwork*, 27-29 June 2012, University of Bath.

Balkaya, C., 2001. Behaviour and Modelling of non-prismatic members having T-Sections. *Journal of Structural Engineering*, 127, 940-946.

Bamforth, P. B. and Price, W. F. 1997. *An International Review of Chloride Ingress Into Structural Concrete*. Scotland: TRL.

Barnes, M., 1998. Form finding and analysis of prestressed nets and membrane. *Computers and Structures*, 30, 685-695.

Bazant, P. Z., 1993. Scaling laws in mechanics of failure. *Journal of Engineering Mechanics*, 119, 1828-1844.

Benmokrane, B., Tighiouart, B. and Chaallal, O., 1996. Bond strength and load distribution of composite GFRP reinforcing bars in concrete. *ACI Materials Journal*, 93, 246-253.

Bentz, D. P., 2000a. Fibers, Percolation, and Spalling of High-Performance Concrete. *ACI Materials Journal*, 97, 351-359.

Bentz, E. C., 2000b. *Sectional analysis of reinforced concrete members*. PhD, University of Toronto.

Bentz, E. C., Vecchio, F. J. and Collins, M. P., 2006. Simplified compression field theory for calculating shear strength of reinforced concrete elements. *ACI Structural Journal*, 103, 614-624.

Beukers, A. and van Hinte, E., 2005. *Lightness; the inevitable renaissance of minimum energy structures*. Rotterdam: 010 Publishers.

Billner, K. P. 1936. *Method of and apparatus for treating concrete*. United States of America, US Patent Number 2046867.

Bindhoff, E. W. and King, J. C., 1982. World's Largest Installation of Fabric-Formed Pile Jackets. *Civil Engineering*, March 1982, 68-70.

BIS 2010. *ESTIMATING THE AMOUNT OF CO2 EMISSIONS THAT THE CONSTRUCTION INDUSTRY CAN INFLUENCE: Supporting material for the Low Carbon Construction IGT Report*. London: BIS (Department for Business Innovation and Skills).

Bisby, L., Take, W. A. and Casparly, A. 2007. Quantifying strain variation in FRP confined concrete using digital image correlation: Proof of concept and initial results In: Smith, S. T., ed. *Asia Pacific Conference on FRP in Structures*, Hong Kong. Hong Kong: IIFC, 599-604.

Bischoff, P. H. and Gross, S. P., 2011. Equivalent moment of inertia based on integration of curvature. *Journal of Composites for Construction*, 15, 263-273.

Bobrowski, J. and Bardhan-Roy, B. K., 1969. A method of calculating the ultimate strength of reinforced and prestressed concrete beams in combined flexure and shear. *The Structural Engineer*, 5, 197-209.

Branson, D. E., 1965. *Instantaneous and time dependent deflections of simple and continuous reinforced concrete beams*, Montgomery, AL: Alabama Highway Department, Bureau of Public Roads.

- Bresler, B. and Pister, K., 1958. Strength of Concrete under Combined Stresses. *ACI Structural Journal*, 55, 321-345.
- Brown, M. D., Bayrak, O. and Jirsa, J. O., 2006. Design for Shear Based on Loading Conditions. *ACI Structural Journal*, 104, 541-550.
- Bruggeling, A. S. G. and Huyghe, G. F., 1991. *Prefabrication with concrete*, Rotterdam: Balkema.
- BS 1881-202: 1986, *Testing concrete — Part 202: Recommendations for surface hardness testing by rebound hammer*. BSI.
- BS 1881-124: 1988, *Testing concrete — Part 124: Methods for analysis of hardened concrete*. BSI.
- BS EN 1992-1-1: 1991a, *Eurocode 2: Design of concrete structures - Part 1-1: General rules and rules for buildings*. BSI.
- BS EN 1998-1: 1991b, *Eurocode 8: Design of structures for earthquake resistance — Part 1: General rules, seismic actions and rules for buildings*. BSI.
- BS 8110-1: 1997, *Structural use of concrete - Part 1: Code of practice for design and construction*. BSI.
- BS EN 206-1: 2000, *Concrete — Part 1: Specification, performance, production and conformity*. BSI.
- BS EN 12504-2: 2001, *Testing concrete in structures — Part 2: Non-destructive testing — Determination of rebound number*. BSI.
- NA to BS EN 1990: 2002, *UK National Annex for Eurocode 0 — Basis of structural design*. BSI.
- BS EN 1992-1-1: 2004a, *Eurocode 2: Design of concrete structures - Part 1-1: General rules and rules for buildings*. BSI.
- BS EN 13295: 2004b, *Products and systems for the protection and repair of concrete structures — Test methods — Determination of resistance to carbonation*. BSI.
- BS EN 1990:2002+A1: 2005, *Eurocode — Basis of structural design*. BSI.
- BS EN 14629: 2007, *Products and systems for the protection and repair of concrete structures — Test methods — Determination of chloride content in hardened concrete*. BSI.
- BS EN 12390-3: 2009a, *Testing hardened concrete. Part 3: Compressive strength of test specimens*. BSI.
- BS EN 12390-5: 2009b, *Testing hardened concrete. Part 5: Flexural strength of test specimens*. BSI.
- BS EN 12390-6: 2009c, *Testing hardened concrete. Part 6: Tensile splitting strength of test specimens*. BSI.
- DD CEN/TS 12390-11: 2010, *(Draft for Development) Products and systems for the protection and repair of concrete structures — Test methods — Determination of chloride content in hardened concrete* BSI.
- BS 5975:2008+A1: 2011, *Code of practice for temporary works procedures and the permissible stress design of falsework*. BSI.
- Budelman, H. and Rostasy, F. 1993. Creep Rupture Behaviour of FRP Elements for Prestressed Concrete. In: *International Symposium on FRP Reinforcement for Concrete Structures*. ACI.
- Burgoyne, C., 2001. Rational use of advanced composites in concrete. *Proceedings of the Institution of Civil Engineers: Structures and Buildings*, 146, 253-262.
- Buschow, K. H. J., Cahn, R. W., Flemings, M. C., Ilshner, B., Kramer, E. J. and Mahajan, S., 2001. *Encyclopedia of Materials - Science and Technology*, London: Elsevier.

- Buyle-Bodin, F. and Hadjieva-Zaharieva, R., 2002. Influence of industrially produced recycled aggregates on flow properties of concrete. *Materials and Structures*, 35, 504-509.
- Byatt, I., Castles, I., Goklany, I. M., Henderson, D., Lawson, N., McKittrick, R., Morris, J., Peacock, A., Robinson, C. and Skidelsky, R., 2006. The Stern Review: A Dual Critique. Part II: Economic Aspects. *World Economics*, 7, 199-232.

## C

- Cady, P. and Weyers, R., 1983. Chloride penetration and deterioration of concrete bridge decks. *Cement Concr Aggr*, 5, 81-87.
- Cairns, J., 1999. Enhancements in surface quality of concrete through the use of controlled permeability formwork liners. *Magazine of Concrete Research*, 51, 73-86.
- Callister, W. D., 2007. *Material science and engineering: an introduction*, USA: John Wiley and Sons.
- CARES 2004. *The CARES Guide to Reinforcing Steel - Part 3*. Sevenoaks: CARES.
- Carter, R. M., Freitas, C. R. d., Goklany, I. M., Holland, D. and Lindzen, R. S., 2006. The Stern Review: A Dual Critique. Part I: The Science. *World Economics*, 7, 165-198.
- CCAA 2009. *Cement Concrete and Aggregates Australia - Chloride Resistance of Concrete*. Sydney: CCAA.
- Concrete Centre, 2012. *Specifying Visual Concrete*. London: The Concrete Centre.
- Chandler, A. and Pedreschi, R., 2007. *Fabric Formwork*, London: RIBA.
- Chawla, A., 2010. *Fabric formed beams using splayed bars*. MEng Thesis, University of Bath.
- Chilton, J., 2000. *Heinz Isler (Engineer's Contribution to Architecture)*, London: Thomas Telford Ltd.
- Choi, M., 2002. *Primary anchorage zones for FRP-Prestressed concrete structures*. PhD, University of Bath.
- Choi, M. and Ibell, T. J., 2004. Behaviour of fiber-reinforced polymer-reinforced anchorage zones for post-tensioned concrete structures. *ACI Structural Journal*, 101, 625-632.
- Chomarat, ND. *Chomarat North America - C Grid* [Online]. Anderson, SC. Available: <http://tinyurl.com/384aw6w> [Accessed 04/01 2010].
- Christensen, R. M., 1979. *Mechanics of composite materials*, New York: Wiley Interscience.
- Chung, D. D. L., 1994. *Carbon Fiber Composites*, Newton, MA: Butterworth-Heinemann.
- Chung, S. F., 2000. *Friction development between FRP reinforcement and concrete*. BEng Thesis, University of Bath.
- Clarke, J. and Waldron, P., 1996. The reinforcement of concrete structures with advanced composites. *The Structural Engineer*, 74, 283-288.
- Clement, F. 2011. Fire protection in tunnels: Requirements, Solutions and Case histories. In: *IAT-AITES World Tunnel Congress*, May 21-26, Helsinki, Finland.
- Clift, R., Grace, J. R. and Weber, M. E., 1979. *Bubbles Drops and Particles*, New York: Academic Press.
- Collins, M. P., 1978. Towards a Rational Theory for RC Members in Shear. *Proceedings of ASCE*, 104, 649-666.

- Collins, M. P., Mitchell, D. and Bentz, E. C., 2008. Shear Design of Concrete Structures. *The Structural Engineer*, 86, 32-39.
- Conlon, C., 2011. *The Innovations and Influence of Irish Engineer James Hardress de Warrenne Waller*. MSc Thesis, University College Dublin.
- Conzett, J., Mostafavi, M. and Reichlin, B., 2006. *Structure as Space*, London: AA Publications.
- Cosenza, E., Manfredi, G. and Realfonzo, R., 1997. Behaviour and modelling of bond of FRP Rebars to Concrete. *Journal of Composites for Construction*, 1, 40-51.
- Costa, A., 2006. Permeability-porosity relationship: A reexamination of the Kozeny-Carman equation based on a fractal pore-space geometry assumption. *Geophysical Research Letters*, 33, 1-5.
- Craig, J. R., Vaughan, D. J. and Skinner, B. J., 1996. *Resources of the Earth: Origin, Use and Environmental Impact*, Upper Saddle River, NJ: Prentice Hall.
- CSA A23.3: 2004, *Design of concrete structures*. CSA.
- Cui, S.-Z. and Wang, S.-Y., 1999. Nonlinear creep characteristics of textile fabrics. *Textile Research Journal*, 69, 931-934.
- Culmann, K., 1865. *Die graphische Statik (Graphic Statics)*, Zurich: Verlag Von Meyer and Zeller.
- CurvedNFR. 2009. *Curved NFR* [Online]. Sleaford: Eurocrete Ltd. [Accessed 01/05 2011].

## D

- Dalziel, S. 2011. *Digiflow*. Cambridge: Department of Applied Mathematics and Theoretical Physics (DAMPT).
- Darby, A. D., Ibell, T.J., Tallis, S., and Winkle, C. 2007. End Anchorage for Internal FRP reinforcement. In: Triantafillou, T. C., ed. FRPRCS-8, July 16-18, University of Patras, Greece.
- Davies, G., Lamb, R. S. and Snell, C., 1973. Stress distribution in beams of varying depth. *The Structural Engineer*, 51, 421-434.
- Debaiky, S. Y. and Elneima, E. I., 1982. Behaviour and Strength of Reinforced Concrete Haunched Beams in Shear. *ACI Structural Journal*, 79, 184-194.
- Debruyne, D. and Lava, P. 2011. *Manual for MatchID 2D*. Ghent: Catholic University College Ghent.
- DECC. 2011. *Climate change statistics* [Online]. London: DECC. Available: [http://www.decc.gov.uk/en/content/cms/statistics/climate\\_stats/data/data.aspx](http://www.decc.gov.uk/en/content/cms/statistics/climate_stats/data/data.aspx) [Accessed 28/07 2011].
- Delijani, F., 2010. *The evaluation of changes in concrete properties due to fabric formwork*. MSc Thesis, The University of Manitoba.
- Dunster, A. M. 2000. *Accelerated carbonation testing*. London: BRE.
- DuPont 2007. *Zemdrain Classic Technical Properties* [online]. Available from [http://www2.dupont.com/Zemdrain/en\\_US/assets/downloads/datasheets/Propertiesclassic.pdf](http://www2.dupont.com/Zemdrain/en_US/assets/downloads/datasheets/Propertiesclassic.pdf) (Accessed June 2010).

## E

- EC 2010. *DIRECTIVE 2010/31/EU OF THE EUROPEAN PARLIAMENT AND OF THE COUNCIL of 19 May 2010 on the energy performance of buildings*. Brussels: European Union.

- EC 2011. *COMMUNICATION FROM THE COMMISSION TO THE EUROPEAN PARLIAMENT, THE COUNCIL, THE EUROPEAN ECONOMIC AND SOCIAL COMMITTEE AND THE COMMITTEE OF THE REGIONS: A Roadmap for moving to a competitive low carbon economy in 2050*. Brussels: European Commission.
- El-Mezaini, N., Balkaya, C. and Citipitioglu, E., 1991. Analysis of frames with nonprismatic members. *Journal of Structural Engineering*, 117, 1573-1592.
- El-Niema, E. I., 1988. Investigation of haunched concrete T-Beams under shear. *ASCE*, 114, 917-930.
- El-Turki, A., Ball, R., Carter, M A., Wilson, M A., Ince, C and Allen, G C., 2010. Effect of dewatering on the strength of lime and cement mortars. *Journal of the American Ceramic Society*, 93(7), 2074-2081
- Eligehausen, R., Popov, E. P. and Bertero, V. V. 1983. *Local bond stress-slip relationships of deformed bars under generalised excitations*. Berkeley, California: University of California.

## F

- Ferreira, T. and Rasband, W., 2011. *ImageJ User Guide*, Maryland: National Institutes of Health.
- FIB 2007. *FRP reinforcement in RC structures*. Lausanne: Federation Internationale du Beton.
- Focacci, F., Nanni, A. and Bakis, C. E., 2000. LOCAL BOND-SLIP RELATIONSHIP FOR FRP REINFORCEMENT IN CONCRETE. *Journal of Composites for Construction*, 4, 24-31.
- FortressStabilisation. 2009. *Concrete Mesh and Net for Commercial Applications* [Online]. Dexter, Michigan. Available: <http://www.fortressstabilization.com/> [Accessed 04/01 2010].
- Foster, R., 2010. *Form finding and analysis of fabric formed concrete beams*. MEng Thesis, University of Bath, Department of Architecture and Civil Engineering.
- Fritz, C., Naaman, A. E. and Reinhardt, D. H. W. 1992. Sifcon Matrix in RC Beams. In: Reinhardt, H. W. and Naaman, A. E., eds. *Proceedings of the RILEM-ACI International Workshop*, 23-26 June 1991, Mainz, Germany. EandFN Spon, 518-528.

## G

- Garbett, J., 2008. *Bone growth analogy for optimising flexibly formed concrete beams*. MEng Thesis, University of Bath, Department of Architecture and Civil Engineering.
- Garboczi, E. J., 1990. Permeability, Diffusivity and microstructural parameters: a critical review. *Cement and Concrete Research*, 20, 591-601.
- Ghaib, M. A. A. and Gorski, J., 2001. Mechanical properties of concrete cast in fabric formworks. *Cement and concrete research*, 31, 1459-1465.
- Glass, G. K. and Buenfeld, N. R. 1995. Chloride threshold levels for corrosion induced deterioration of steel in concrete. In: *Chloride penetration into concrete, Proceedings of the international RILEM Workshop*, Saint-Rémy-Les-Chevreuse, Bagneux, France. RILEM publications, 429-440.
- Glass, G. K. and Buenfeld, N. R., 2000. The influence of chloride binding on the chloride induced corrosion risk in reinforced concrete. *Corrosion Science*, 42, 329-344.
- Grant, M. and Pallet, P., 2012. *Temporary Works: Principles of Design and Construction*, London: ICE.
- Graybeal, B. A. 2006a. *Material Property Characterization of Ultra-High Performance Concrete*. McLean, VA: Federal Highway Administration.

- Graybeal, B. A. 2006b. *Structural Behaviour of Ultra-High Performance Concrete Prestressed I Girders*. McLean: Federal Highway Administration.
- Greenwood, M. 2001. Pultruded Composites Durability: A Key Value. In: *Proceedings of Composites 2001 CFA.*, Tampa, Florida.
- Guimares, G. B. and Burgoyne, C. J., 1992. Creep behaviour of a parallel-lay aramid rope. *Journal of Material Science*, 27, 2473-2489.
- Gummerson, R. J., Hoff, W. D., Hawkes, R., Holland, G. N. and Moore, W. S., 1979. Unsaturated water flow within porous materials observed by NMR Imaging. *Nature*, 281, 56-57.
- Guyon, Y., 1953. *Prestressed Concrete*, London: Contractors Record and Municipal Engineering.

## H

- Hall, C., 1989. Water sorptivity of mortars and concretes: A Review. *Magazine of Concrete Research*, 41, 51-61.
- Hall, C., 2007. Anomalous diffusion in unsaturated flow: Fact or Fiction? *Cement and Concrete Research*, 37, 378-385.
- Hall, C. and Hoff, W. D., 2002. *Water transport in brick, stone and concrete*, London: Spon Press.
- Hamill, J. and Knutzen, K., 2009. *Biomechanical basis of human movement*, Baltimore: Lippincott Williams and Wilkins.
- Hammond, G. P. and Jones, C. I., 2011. Embodied energy and carbon in construction materials. *Proceedings of the Institution of Civil Engineers: Energy*, In Press.
- Hansen, J. 2010. *Data.Giss: GISS Surface Temperature Analysis (GISTEMP)* [Online]. National Aeronautics and Space Administration, Goddard Institute for Space Studies. Available: <http://data.giss.nasa.gov/gistemp> [Accessed 11/07/10].
- Hansen, J., Sato, M., Ruedy, R., Lo, K., Lea, D. W. and Medina-Elizade, M., 2006. Global temperature change. *Proceedings of the National Academy of Sciences of the United States of America*, 103, 14288-14293.
- Hashemian, F, 2012. *Structural Behavior and Optimization of Moment-Shaped Reinforced Concrete Beams*. PhD thesis, University of Manitoba
- Haskett, M., 2010. *The discrete rigid body rotation of reinforced concrete beams using partial interaction and shear friction theory*. PhD, University of Adelaide.
- Haskett, M., Oehlers, D. J., Ali, M. S. and Wu, C., 2009. Rigid body moment rotation mechanism for reinforced concrete beam hinges. *Engineering Structures*, 31, 1032-1041.
- Hawkins, N. M., Kuchma, D. A., Mast, R. F., Marsh, M. L. and Reineck, K.-H. 2005. *Simplified Shear Design of Structural Concrete Members*. Washington DC: Transportation Research Board.
- Helm, D. R. and Hepburn, C., 2011. *The Economics and Politics of Climate Change*, London: OUP.
- Heo, Y.-S., Sanjayan, J. G., Han, C.-G. and Han, M.-C., 2012. Limited effect of diameter of fibres on spalling protection of concrete in fire. *Materials and Structures*, 45, 325-335.
- Hillen, H. F. J. 1969. *Form for constructing a slab for talus or bottom protection*. USA, US Patent Number 3425227.
- Hjelmstad, K. D., 2005. *Fundamentals of Structural Mechanics*, London: Springer.



- Holland, T. C., 2005. *Silica fume user's manual*. Silica Fume Association and the US Department of Transport Federal Highway Administration, National Technical Information Service: Springfield. Report No.FHWA-IF-05-016
- Hoult, N. A., Sherwood, E. G., Bentz, E. C. and Collins, M. P., 2008. Does the Use of FRP Reinforcement Change the One-Way Shear Behavior of Reinforced Concrete Slabs? *Journal of Composites for Construction*, 12, 125-133.
- Hull, D. and Clyne, T. W., 1996. *An introduction to composite materials*, Cambridge: Cambridge University Press.
- Hunkeler, F. 2005. Corrosion in reinforced concrete: processes and mechanisms. In: Hans, B. (ed.) *Corrosion in reinforced concrete structures*. Cambridge: Woodhead Publishing.

## I

- Ibell, T. J. and Burgoyne, C., 1999. Use of fibre reinforced plastics versus steel for shear reinforcement of concrete. *ACI Structural Journal*, 96, 997-1002.
- Ibell, T. J. and Darby, A. P. 2008. *Advanced Composites in Construction*. Bath: University of Bath.
- Ibell, T. J., Darby, A.P., Bailiss, J.A. 2007. Fabric formed concrete beams. In: Darby, A. P., ed. ACIC 2007, April 2-4, University of Bath, UK.
- Ingham, J., 2009. Forensic engineering of fire-damaged structures. *Proc. Instn Civil Engrs, Civil Engineering*, 162, 12-17.
- Ioannou, S., Paine, K. and Quillin, K. 2011. Resistance of Supersulfated Cement Concrete to Carbonation and Sulfate Attack. In: Papanikos, G. T., ed. *1st Annual International Conference on Construction*, 20-23 June 2011, Athens. Athens: ATINER.
- Iosilevskii, G., 2010. Shape of a soft container under hydrostatic load. *Journal of Applied Mechanics*, 77, 3.
- IStructE 1975. *Fire resistance of concrete structures: report of a Joint Committee*. London: IStructE.
- IStructE 2006. *Standard method of detailing structural concrete: a manual for best practice*. London: IStructE.

## J

- Jelic, I. 2002. *Behaviour of reinforced concrete beams: A comparison between the CFP method and current practice*. PhD, Imperial College London.

## K

- Kanakubo, K., Yonemaru, K., Fukuyama, H., Fujisawa, M. and Sonobe, Y. 1993. Bond performance of concrete members reinforced with FRP Bars. In: Nanni, A. and Dolan, C., eds. *Fiber reinforced plastic reinforcement for concrete structures - international symposium*. American Concrete Institute.
- Kani, G. N., 1967. How safe are our large reinforced concrete beams? *ACI Structural Journal*, 64, 128-141.
- Kasai, K., Nagano, M., Sato, K. and Suga, K., 1989. Study on the evaluation of concrete quality prepared with permeable forms and plywood forms. *Trans Japan Conc Inst*, 10, 59-66.
- Kaundinya, I. 1997. Protection of road tunnel linings in cases of fire. In: *European Conference of Transport Research Institutes Young Researchers Seminar 2007*, Brno. ECTRI.

- Klapatek, P., 2003. *Characterization of randomly rough surfaces in nanometric scale using methods of modern metrology*. PhD, MASARYK UNIVERSITY BRNO.
- Komi, P. V., 1986. Training of muscle strength and power: interaction of neuromotoric, hypertrophic, and mechanical factors. *International Journal of Sports Medicine*, 7, 10-15.
- Kostova, K., Ibell, T., Darby, A. P. and Evernden, M. 2012. Advanced composite reinforcement for fabric formed structural elements. In: Orr, J. J., et al., eds. *Second International Conference on Flexible Formwork*, 27-29 June 2012, University of Bath. University of Bath Press.
- Kotsovos, M. D., 1982. A fundamental explanation of the behaviour of reinforced concrete beams in flexure based on the properties of concrete under multiaxial stress. *Materials and Structures*, 15, 529-537.
- Kotsovos, M. D., 1988. Compressive Force Path Concept: Basis for Reinforced Concrete Ultimate Limit State Design. *ACI Structural Journal*, 85, 68-75.
- Kotsovos, M. D., 2007. Concepts Underlying Reinforced Concrete Design: Time for Reappraisal. *ACI Structural Journal*, 104, 675-684.
- Kotsovos, M. D., Bobrowski, J. and Eibl, J., 1987. Behaviour of reinforced concrete T-Beams in shear. *The Structural Engineer*, 65B, 1-10.
- Kotsovos, M. D. and Pavlovic, M. N., 1999. *Ultimate limit state design of concrete structures, a new approach.*, London: Thomas Telford.
- Kotsovos, M. D. and Pavlovic, M. N., 2006. Shortcomings of code methods for shear design of RC structures and the possible role of fibres. *The Structural Engineer*, 84, 44-49.
- Kropp, J. and Hilsdorf, H. K. 1995. *Performance Criteria for Concrete Durability - a State of the Art Report*. RILEM Technical Committee TC 116-PCD. London: EandFN Spon.
- Kudless, A. 2009. *P-Wall* [Online]. San Francisco: Museum of Modern Art. Available: [http://matsysdesign.com/category/projects/p\\_wall2009/](http://matsysdesign.com/category/projects/p_wall2009/) [Accessed 01/04 2011].
- Kupfer, H. B., Hilsdorf, H.K., Rusch, H., 1969. Behaviour of concrete under biaxial stress. *ACI Structural Journal*, 291-295.
- Kwan, A. K. H. and Mora, C. F., 2001. Effects of various shape parameters on packing of aggregate particles. *Magazine of Concrete Research*, 53, 91-100.

## L

- LABORSTA, 2010. *International Labour Organisation Online Database* [online]. ILO Department of Statistics. Available from: <http://laborsta.ilo.org/STP/guest> (Accessed: 07/13/10)
- Lafarge. 2009. *Ductal | Home* [Online]. Paris. Available: <http://www.ductal-lafarge.com> [Accessed 04/04 2009].
- Lake, L. W., 1989. *Enhanced Oil Recovery*, Englewood Cliffs, NJ: Prentice Hall Inc.
- Lamberton, B. A., 1989. Fabric forms for concrete. *Concrete international*, 58-67.
- Lamond, J. F., 2006. *Significance of Tests and Properties of Concrete and Concrete Making Materials*. ASTM International: West Conshohocken, PA.
- Lane, T. 2007. *Our dark materials* [Online]. London: Building. Available: <http://www.building.co.uk/comment/our-dark-materials/3099435.article> [Accessed 01/01 2011].

- Lava, P., Cooreman, S., Coppieters, S., Strycker, M. D. and Debruyne, D., 2009. Assessment of measuring errors in DIC using deformation fields generated by plastic FEA. *Optics and Lasers in Engineering*, 47, 747-753.
- Lava, P. and Debruyne, D. 2010. *MatchID*. Ghent, Belgium: Catholic University College Ghent.
- Lee, D. S. H., 2010. *Study of construction methodology and structural behaviour of fabric formed form-efficient reinforced concrete beam*. PhD, The University of Edinburgh.
- Lee, H. W., 2012. *Enhancement in Surface Quality of Concrete when Cast in Fabric*. MEng Thesis , University of Bath, Department of Architecture and Civil Engineering
- Lees, J. M. and Burgoyne, C. B., 1999a. Experimental Study of Influence of Bond on Flexural Behavior of Concrete Beams Pretensioned with Aramid Fiber Reinforced Plastics. *ACI Structural Journal*, 96, 377-386.
- Lees, J. M. and Burgoyne, C. J., 1999b. Transfer bond stresses generated between FRP tendons and concrete. *Magazine of Concrete Research*, 51, 229-239.
- Li, V. C. 1998. Engineered cementitious composites - tailored composites through micromechanical modelling. In: Banthia, N., ed. *Fibre Reinforced Concrete: Present and the Future*, Montreal, p67-97.
- Li, V. C., 2002. Large volume, high performance applications of fibres in civil engineering. *Journal of applied polymer sciences*, 83, 660-686.
- Liang, M. T., Qu, W. and C-H, L., 2002. Mathematical modelling and prediction of concrete carbonation and its applications. *Marine and Science Technology*, 10, 128-135.
- Lilienthal, L. W. G. 1899. *Fireproof Ceiling*. USA, United States Patent Office Number 619,769.
- Liu, X., Ye, G., Schutter, G. D., Yuan, Y. and Taerwe, L., 2008. On the mechanism of polypropylene fibres in preventing fire spalling in self-compacting and high performance cement paste. *Cement and Concrete Research*, 38, 487-499.
- Lockington, D. and Parlange, J. Y., 2003. Anomalous water absorption in porous materials. *Journal of Physics D: Applied Physics*, 36, 760-767.
- Loudon, N., Bell, B., Berry, B., Brown, P., Canning, L., Clarke, J., Darby, A., Denton, S., Drewett, J., Donnelly, E., Farmer, N., Hardie, A., Hughes, C., Ibell, T., Kaethner, S., Keble, J., Langdon, M., Luke, S., Mahon, M., Milligan, P., Moriarty, J., Richards, S., Richardson, M., Russell, P., Shave, J., Smith, I. and Walters, S. 2004. *Design guidance for strengthening concrete structures using fibre composite materials*. 2 ed. London: IStructE.

## M

- MacLeod, I. A. and Houmsi, A., 1994. Shear strength of haunched beams without shear reinforcement. *ACI Structural Journal*, 91, 79-89.
- Maki, A. C. and Kuenzi, E. W. 1965. *Deflection and stresses of tapered wood beams*. Madison, Wis: Forest Products Laboratory, Forest Service, US Department of Agriculture.
- Makitani, E., Irisawa, I. and Nishiura, N. 1993. Investigation of bond in concrete member with fiber reinforced plastic bars. In: Nanni, A. and Dolan, C., eds. *Fiber reinforced plastic reinforcement for concrete structures - International symposium*. American Concrete Institute.
- Malvar, L. J. 1994. *BOND STRESS-SLIP CHARACTERISTICS OF FRP REBARS*. Port Hueneme, CA: Naval Facilities Engineering Service Centre.

- Marchand, J. and Samson, E., 2009. Predicting the service-life of concrete structures – Limitations of simplified models. *Cement and concrete Composites*, 31, 515-521.
- Martin-Perez, B., Zibara, H., Hooton, R. D. and Thomas, M. D. A., 2000. A study of the effect of chloride binding on service life predictions. *Cement and Concrete Research*, 30, 1215-1223.
- Martin, H., Rauen, A. and Schiessl, P., 1975. Karbonatisierung von Beton aus verschiedenen Zementen (Carbonation of concrete from different cements). *Betonwerk + Fertigteil-Technik*, 12, 588-590.
- Martys, N. S., Toquato, S. and Bentz, D. P., 1994. Universal scaling of fluid permeability for sphere packings. *Physical Review E*, 50, 403-409.
- Matthews, T. J., Matthews, G. P. and Huggett, S., 1999. Estimating particle size distributions from a network model of porous media. *Powder Technology*, 104, 169-179.
- Maxwell, A. S., Broughton, W. R., Dean, G. and Sims, G. D. 2005. *Review of accelerated ageing methods and lifetime prediction techniques for polymeric materials*. National Physical Laboratory.
- Mayfield, B., 1990. THE QUANTITATIVE-EVALUATION OF THE WATER CEMENT RATIO USING FLUORESCENCE MICROSCOPY. *Magazine of Concrete Research*, 42, 45-49.
- Mehta, P. K. and Monteiro, P. J. M., 2006. *Concrete. Microstructure, Properties, and Materials*, London: McGraw-Hill.
- Metzler, R. and Klafter, J., 2000. The random walk's guide to anomalous diffusion: a fractional dynamics approach. *Physics Reports*, 2000, 1-77.
- Meyer, C. and Sheer, M. H., 2005. Do Concrete Shells Deserve Another Look? *Concrete International*, 27.
- Mitchell, D. and Collins, M. P., 1974. Diagonal Compression Field Theory - A Rational Model for Structural Concrete in Pure Torsion. *ACI Structural Journal*, 71, 396-508.
- Mitchell, G. R. and Woodgate, R. W. 1970. *A survey of floor loadings in office buildings*. London: CIRIA Report 25.
- Mitchell, G. R. and Woodgate, R. W. 1971. *Floor loadings in office buildings – the results of a survey*. London: BRE Current Paper 3/71.
- Moreno, M., Morris, W., Alvarez, M. G. and Duff, G. S., 2004. Corrosion of reinforcing steel in simulated concrete pore solutions Effect of carbonation and chloride content. *Corrosion Science*, 46, 2681-2699.
- Mörsch, E., 1908. *Der Eisenbeton, seine Theorie und Anwendung (Reinforced Concrete, theory and practical application)*. , Stuttgart: Wittwer.

## N

- Nagasaka, T., Fukuyama, H. and Tanigaki, M. 1993. Shear performance of concrete beams reinforced with FRP stirrups. In: Nanni, A., Dolan, C.W. (ed.) *Nonmetallic reinforcement and prestressing*, American Concrete Institute Special Publication 138.
- Nanni, A. 2001. Guide and Specifications for the Use of Composites in Concrete and Masonry Construction in North America. In: Reality, A., et al., eds. *Proceedings of the International Workshop Composites in Construction*, Reston. American Society of Civil Engineers.
- Nanni, A., Al-Zaharani, M. M., Al-Dulaijan, S. U., Bakis, C. E. and Boothby, T. E. 1995. Bond of FRP reinforcement to concrete - experimental results. In: Taerwe, L., ed. *2nd International RILEM Symposium (FRPRCS-2)*, 23-25 August 1995, Ghent.

- Narayanan, R. S., ed., 2002. *Manual for the design of concrete building structures to Eurocode 2*, London: IStructE.
- Nawy, E. G. and Neuwerth, G. E., 1971. Behaviour of fibre glass reinforced concrete beams. *Journal of the Structural Division, Proceedings of the American Society of Civil Engineering*, 97, 2203.
- Nervi, P. L., 1956. *Structures*: FW Dodge Corp.
- Nervi, P. L., 1963. *New Structures*, London: The Architectural Press.
- Nilsson, L. O., Sandberg, P. and Poulsen, E. 1994. *HETEK, A system for estimation of chloride ingress into concrete, theoretical background*,. Copenhagen: Road Directorate.
- Nordhaus, W. 2007. *The Stern Review on the Economics of Climate Change*. New Haven: Yale University.
- NT BUILD 357: 1989, *Concrete, repairing materials and protective coating: UDC carbonation resistance*. Nordtest.
- NT BUILD 443: 1995, *Concrete, hardened: Accelerated chloride penetration*. Nordtest.
- NT BUILD 208: 1996, *Concrete, hardened: Chloride content by volhard titration*. NordTest.
- NT BUILD 361: 1999, *Concrete, Hardened: Water-Cement Ratio*. NordTest.

## O

- Oehlers, D. J., Ali, M. S., Griffith, M. C., Haskett, M. and W, L., 2012. A generic unified reinforced concrete model. *Proceedings of the ICE - Structures and Buildings*, 165, 27-49.
- Orr, J. J., 2009. *Shear capacity of circular concrete sections*. MEng Thesis, University of Bath.
- Orr, J. J., Darby, A. P., Ibell, T. J., Evernden, M. C. and Otlet, M., 2011. Concrete structures using fabric formwork. *The Structural Engineer*, 89, 20-26.
- Orr, J. J., Evernden, M., Darby, A. P. and Ibell, T. J. 2012. Proceedings of the Second International Conference on Flexible Formwork (in press). In, 27th-29th June 2012, Bath, UK. University of Bath.

## P

- Pallet, P. 1994. *Introduction to the formworks scene*. Concrete Magazine, March/April.
- Pan, B., 2011. Recent Progress in Digital Image Correlation. *Experimental Mechanics*, 51, 1223-1235.
- Pan, B., Qian, K., Xie, H. and Asundi, A., 2009. Two-dimensional digital image correlation for in-plane displacement and strain measurement: a review. *Meas. Sci. Technol.*, 20, 17.
- Papadakis, V. G., Vayenas, C. G. and Fardis, M. N., 1991. Fundamental modelling and experimental investigation of concrete carbonation. *ACI Materials Journal*, 88, 363-373.
- Park, R. and Paulay, T., 1975. *Reinforced concrete structures*, USA: John Wiley and Sons.
- Perera, K., Ibell, T., Darby, A. and Denton, S. 2009. Bond mechanisms of various shapes of NSM CFRP bars. In: *Advanced Composites in Construction (ACIC 2009)*, 1-3 September 2009, Edinburgh.
- Price, W. F. 2000. *Controlled permeability formwork*. London: Construction Industry Research and Information Association.

Price, W. F. and Widdows, S. J., 1991. The effect of permeable formwork on the surface properties of concrete. *Magazine of Concrete Research*, 43, 93-104.

## Q

## R

Rankilor, P. R. 1994. *A technical manual for the design of UTF geosynthetics into civil and marine engineering projects*. NV: UCO Technical Fabrics.

Richard, P. and Cheyrezy, M., 1995. Composition of reactive powder concretes. *Cement and Concrete Research*, 25, 1501-1511.

Ritter, W., 1899. *Die bauweise hennebique (Construction techniques of Hennebique)*. Zurich: Schweizerische Bazeitung.

Rombach, G. and Nghiep, V. H., 2011. Versuche zue Querkrafttragfaeghigkeit von gevouteten Stahlbetonbalken ohne Querkraftbewehrung (Shear strength of Haunched Concrete Beams without Transverse Reinforcement). *Beton und Stahlbetonbau*, 106, 11-20.

Rossi, P., 2001. Ultra-high performance fibre reinforced concretes. *Concrete International*, 23, 46-52.

Rostasy, F. and Budelman, H., 1993. Principles of Design of FRP Tendons and Anchorages for Post-Tensioned Concrete. *ACI Struct J*, SP 138-38, 633-649.

Ruredil 2006. *Ruredil X Mesh Gold: Ultra high mechanical performance Polyparaphenylene benzobisoxazole (PBO) fibre mesh, with a stabilised inorganic matrix, for structural reinforcement of concrete*. Milan: Ruredil.

## S

Saettaa, A. V. and Vitaliani, R. V., 2004. Experimental investigation and numerical modelling of carbonation process in reinforced concrete structures. Part I: Theoretical formulation. *Cement and Concrete Research*, 34, 571-579.

Salek, M. S., Kotsovos, M. D. and Pavlovic, M., 1995. Application of the compressive-force path concept in the design of reinforced concrete indeterminate structures: A pilot study. *Structural Engineering and Mechanics*, 3, 475-495.

Schiessl, P. and Lay, S. 2005. Influence of concrete composition. In: Hans, B. (ed.) *Corrosion in Reinforced Concrete Structures*. Cambridge: Woodhead Publishing.

Schlaich, J., Schaefer, K. and Jennewein, M., 1987. Toward a consistent design of structural concrete. *PCI Journal*, May-June, 74-150.

Schlaich, J. and Schober, H., 1994. Steg uber die Autobahn bei Kirchheim/Teck (Bridge across the motorway near Kirchheim/Teck). *Beton und Stahlbetonbau*, 89, 40-44.

Schmitz, R. P. 2006. Fabric formed concrete. In: *17th Analysis and Computation speciality conference*, 2006 Structures Congress, May 18-20, St. Louis, MO.

Schneiders, J. 2003. CEPHEUS – measurement results from more than 100 dwelling units in passive houses. In: *ECEEE 2003 Summer Study – Time to turn down energy demand*. Panel 2, Passive House Institute: Darmstadt, p341-351.



- Seki, H., Sekijima, K. and Konno, T. 1997. Test Method on Creep of Continuous Fiber Reinforcing Materials. *In: Proceedings of the Third International Symposium on Non-Metallic (FRP) Reinforcement for Concrete Structures (FRPRCS-3)*, Saporro, Japan. Japan Concrete Institute, 195-202.
- Serafini, F. L. 1994. Corrosion protection of concrete using a controlled permeability formwork (CPF) system. *In: Corrosion and Corrosion Protection of Steel in Concrete*, 24-28 July 1994, Sheffield. 1114-1131.
- Shigekazu, H., Sadao, U. and Kozo, K. 1989. Improvement of concrete durability by permeable form. *In: 2nd East Asia Conference on Structural Engineering and Construction*, January 1989, Chiang Mai, Thailand. 112-118.
- Smith, K. and Atkinson, T. 2010. *PP fibres to resist fire-induced concrete spalling* [Online]. TunnelTalk. Available: <http://www.tunneltalk.com/Polypropylene-fibres-Nov10-Resistance-to-concrete-spalling-under-fire.php> [Accessed 26/03/2012].
- Spencer, R. W., 2008. *Climate confusion. How global warming hysteria leads to bad science, pandering politicians and misguided policies that hurt the poor.*, London: Encounter Books.
- Standring, S., 2008. *Gray's Anatomy: The Anatomical Basis of Clinical Practice, Expert Consult: The Anatomical Basis of Clinical Practice*, Philadelphia: Churchill Livingstone.
- Steffens, A., Dinkler, D. and Ahrens, H., 2002. Modelling carbonation for corrosion risk prediction of concrete structures. *Cement and Concrete Research*, 32, 935-941.
- Stern, N., 2007. *The Economics of Climate Change – The Stern Review*, Cambridge: Cambridge University Press.
- Stratford, T. 2008. *The shear of concrete with Elastic FRP reinforcement*. Bath: University of Bath.
- Stratford, T. and Burgoyne, C., 2003. Shear analysis of concrete with brittle reinforcement. *Journal of composites for construction*, 7, 323-330.
- Sturgis, S. and Roberts, G. 2010. *Redefining Zero: Carbon profiling as a solution to whole life carbon emission measurement in buildings*. London: RICS.
- Stuzman, P., 2000. Scanning electron microscopy in concrete petrography. *Materials Science of Concrete Special Volume: Calcium Hydroxide in Concrete (Workshop on the Role of Calcium Hydroxide in Concrete). Proceedings*. J. Skalny, J. Gebauer and I. Odler, eds., The American Ceramic Society. November 1-3, 2000, Anna Maria Island, Florida, 59-72 pp, 2001
- Stuzman, P., 2004. Scanning electron microscopy imaging of hydraulic cement microstructure. *Cement and Concrete Composites*, 26, 957-966.
- Sullivan, P. J. E. 2001. *Deterioration and spalling of high strength concrete under fire*. London: Health and Safety Executive.
- Suryavanashi, A. K. and Narayan Swamy, R., 1996. Stability of Friedel's salt in carbonated concrete structural elements. *Cement and concrete research*, 26, 729-741.
- Sutherland, R. J. M., Humm, D. and Chrimes, M., 2001. *Historic concrete: background to appraisal*, London: Thomas Telford.

## T

- Tallis, S., 2005. *Novel Anchorage of internal FRP reinforcement*. MEng Thesis, University of Bath, Department of Architecture and Civil Engineering.
- Tang, L. and Sorenson, H. E., 2001. Precision of the Nordic test methods for measuring the chloride diffusion/migration coefficients of concrete. *Materials and Structures*, 34, 479-485.

- Tans, P. 2010. *Trends in Carbon Dioxide* [Online]. US Department of Commerce National Oceanic and Atmospheric Administration, Earth System Research Laboratory. Available: <http://www.esrl.noaa.gov/gmd/ccgg/trends> [Accessed 11/07/10].
- Taylor, H. P. J. 1970. *Investigation of the forces carried across cracks in reinforced concrete beams in shear by interlock of aggregate*. London: Cement and Concrete Association.
- Taylor, S. C., Hoff, W. D. and Wilson, M. A. G., K M, 1999. Anomalous water transport properties of Portland and blended cement-based materials. *Journal of Material Science Letters*, 18, 1925-1927.
- TCG, 1991. *Code of practice for the design and construction of reinforced concrete structures* (In Greek), TCG.
- Tena-Colunga, A., 1996. Stiffness formulation for non prismatic beam elements. *Journal of Structural Engineering*, 122, 1484-1489.
- Tena-Colunga, A., Archundia-Aranda, H. I. and Gonzalez-Cuevas, O. M., 2008. Behaviour of reinforced concrete haunched beams subjected to static shear loading. *Engineering Structures*, 30, 478-492.
- Tepfers, R. and De Lorenzis, L., 2003. Bond of FRP Reinforcement in concrete - a challenge. *Mechanics of Composite Materials*, 39, 315-328.
- Teychenne, D. C., Franklin, R. E. and Erntroy, H. C. 1997. *Design of normal concrete mixes - second edition*. In: Establishment, B. R. (ed.). Watford: Building Research Establishment.
- Thirion, C., 2010. *Putting the material in the right place: the role of material-efficiency in reducing the environmental impact of building structures*. MRes, University College London.
- Thormark, C., 2001. Allow energy building in a life cycle—its embodied energy, energy need for operation and recycling potential. *Building and Environment*, 37, 429-435.
- Torrent, R. J. and Jornet, A. 1991. The quality of covercrete of low, medium and high strength concretes. In: *Proceedings Second CANMET/ACI International Conference Durability of Concrete*, 4-9 August 1991, Canada.
- Tumidajski, P. J., Schumacher, A. S., Perron, S., Gu, P. and Beaudoin, J. J., 1996. On the relationship between porosity and electrical resistivity in cementitious systems. *Cement and Concrete Research*, 26, 539-544..

## U

- USGS 2008. Cement statistics. In: KELLY, T. D., MATOS, G.R. (ed.) *Historical statistics for mineral and material commodities in the United States*. USGS.
- USGS. 2011. *Minerals Information* [Online]. US DoI, USGS. Available: <http://minerals.usgs.gov/minerals/> [Accessed 01/01 2011].

## V

- Vecchio, F. J. and Collins, M. P. 1986. The Modified Compression Field Theory for Reinforced Concrete Elements Subjected to Shear. *ACI Structural Journal*, 83, 219-231.
- Veenendaal, D. 2008. *Evolutionary optimisation of fabric formed structural elements*. Masters Thesis, University of Delft.

**W**

- Wagner, H., 1929. Ebene Blechwandtrager mit sehr dunnem Stegblech (Metal beams with very thin webs) *Zeitschrift für Flugtechnik und Motorluftschiffahrt*, 20.
- Waller, J. H. W. 1934. *Method of building with cementitious material applied to vegetable fabrics*. USA, US Patent Number 1,955,716.
- Walraven, J. C., 1981. Fundamental Analysis of Aggregate Interlock. *Journal of the Structural Division, Proceedings of the American Society of Civil Engineering*, 107, 2245-2269.
- West, M., 2007a. *C.A.S.T Construction*, Winnipeg: University of Manitoba.
- West, M., Abdelgader H.S., Gorski, J. 2007b. State-of-the-Art Report on Fabric Formwork. In: *Concrete: Construction's Sustainable Option*, 4-6 September, Dundee, UK.
- West, M., Araya, R. 2009. Fabric formwork for concrete structures and architecture. In: Kröplin, B. and Onate, E., eds. *International Conference on Textile Composites and Inflatable Structures*, 5-7 October, Barcelona, Spain. CIMNE.
- White, D. J., Take, W. A. and Bolton, M. D. 2001a. A deformation measuring system for geotechnical testing based on digital imaging, close-range photogrammetry, and PIV image analysis. In: *Proceedings of the 15th International Conference on Soil Mechanics and Geotechnical Engineering*, Istanbul, Turkey. Rotterdam: Balkema, 539-542.
- White, D. J., Take, W. A. and Bolton, M. D. 2001b. Measuring soil deformation in geotechnical models using digital images and PIV analysis. In: *Proceedings of the 10th International Conference on Computer Methods and Advances in Geomechanics*, 7-12 January 2001, Tucson, Arizona. Rotterdam: Balkema, 997-1002.
- Whitehead, P., 2002. *Fibre reinforced polymer reinforced beams*. PhD Thesis, University of Bath.
- Whitehead, P. and Ibell, T. J., 2005. Novel shear reinforcement for fibre reinforced polymer reinforced and prestressed concrete. *ACI Structural Journal*, 102, 286-294.
- Whitney, C. S., 1957. Ultimate shear strength of reinforced concrete flat slabs, footings, beams and frame members without shear reinforcement. *Journal of the American Concrete Institute*, 29, 265-298.
- Williams, C. J. K. W. 2012. Meshfree peridynamic computer modelling of concrete in three dimensions using randomly positioned particles. In: Orr, J. J., et al., eds. *Second International Conference on flexible Formwork*, 27-29 June 2012, University of Bath. University of Bath Press.
- Wise, C. 2010. *What if everything we did was wrong?* *Building Magazine* [online].
- WorldBank. 2009. *How we Classify Countries | Data* [Online]. Washington, DC: The World Bank. Available: <http://data.worldbank.org/about/country-classifications> [Accessed 05/05 2010].
- WorldBank. 2011. *GDP (Current US\$)* [Online]. Washington, DC: The World Bank. [Accessed 01/01 2011].
- WRI 2005. *Carbon Dioxide Emissions by Source 2005*. Earthtrends Data Tables: Climate and Atmosphere.

**X**

- Xi, Y. and Bazant, Z. P. 1999. Modelling chloride penetration in saturated concrete. *Journal of Materials in Civil Engineering*, 11, 58-65.

**Y**

Yamaguchi, T., Kato, Y., Nishimura, T. and Uomoto, I. 1997. Creep Rupture of FRP Rods Made of Aramid, Carbon and Glass Fibers. *In: Proceedings of the Third International Symposium on Non-Metallic (FRP) reinforcement for Concrete Structures (FRPRCS-3)*, Saporro, Japan. Japan Concrete Institute.

Yuan, Q., Shi, C., Schutter, G., Audenaert, K. and Deng, D., 2009. Chloride binding of cement-based materials subjected to external chloride environment - A review. *Construction and Building Materials*, 23, 1-13.

**Z**

Zia, P., Ahmad, S. and Leming, M. 1994. *High performance concretes. A state of the art report (1989-1994)*. U.S. Department of Transportation.

[blank page]